22nd International Conference on Cyclotrons and their Applications

science & technology

Department:
Science and Technology
REPUBLIC OF SOUTH AFRICA

NRF National Research Foundation

iThemba LABS
Laboratory for Accelerator Based Sciences

22 - 27 September 2019

Cape Town, South Africa

CYC2019

International Organising Committee

Sytze Brandenburg, KVI, Netherlands
Yuri Bylinski, TRIUMF, Canada
Lowry Conradie, iThemba LABS, South Africa (Chair)
Andrea Denker, HZB, Germany
Mitsuhiro Fukuda, RCNP, Japan
Ralf Gebel, FZJ, Germany
Boris Gikal, JINR, Russia
Pauli Heikkinen, JYFL, Finland
Yves Jongen, IBA, Belgium
Marc Loiselet, UCL, Belgium
Donald May, TAMU, United States
Yoshiharu Mori, RRI, Japan
Koji Noda, NIRS, Japan
Hiroki Okuno, RIKEN, Japan
Danilo Rifuggiato, INFN-LNS, Italy
Hermann Schweickert, ZAG, Germany
Mike Seidel, PSI, Switzerland
Vijay Shanker Pandit, VECC, India
Susan Smith, STFC, United Kingdom
Andreas Stolz, NSCL, United States
Damon Todd, LBNL, United States
Wenlong Zhan, IMP, China
Tianjue Zhang, CIAE, China
Hongwei Zhao, IMP, China

Themes

Cyclotron Technology
Theory, Models and Simulations
Operation and Upgrades
Cyclotron Applications
Cyclotron Concepts, FFA and new Projects
Session for young Scientists

Website: https://indico-jacow.cern.ch/event/14/


CYC 2019

12 November 2019

Foreword CYC2019

The 22nd International Conference on Cyclotrons and their Applications (CYC2019) took place from September 22 to 27 at the Westin Hotel in Cape Town, South Africa. The conference was proudly hosted by iThemba LABS (Laboratory for Accelerator Based Sciences) and coincided with the launch of the first phase of the much anticipated SAIF (South African Isotope Facility) project. iThemba LABS has a proud history of hosting the international cyclotron conference with the 14th edition of this conference also hosted in South Africa and opened by our former president, Nelson Mandela.

As has been the trend with previous cyclotron conferences, the focus and themes of the conference appear to be in a constant state of change. This movement reflects the vigorous research and development in the field, ultimately resulting in numerous practical benefits for the society as a whole. This is abundantly apparent from the number of new cyclotrons currently planned or being commissioned. Many of these cyclotrons are built for the medical fraternity with applications including proton therapy and the production of medical radioisotopes for early diagnosis of various conditions. The conference programme for CYC2019 sought to do justice to the energetic development in the field of cyclotrons. A remarkable number of high quality contributions were received from the various facilities operating cyclotrons around the world. These varied from contributions investigating complex interactions using numerical methods to reports discussing novel ideas to extend the current capabilities of ageing cyclotron facilities.

A particular focus of this conference was to foster good relations between the various cyclotron institutes around the world, with the ultimate goal of leading to constructive international collaborations. Another important goal of the conference was to encourage participation amongst the many young and talented cohort of students. In this regard funding was received from various institutes and these institutes are graciously acknowledged for their valuable contribution. The participation of students was however a concern compared to the student participation at the previous cyclotron conference hosted in Zürich, Switzerland. The host institution of CYC2022 is strongly encouraged to put systems in place to reverse this trend of declining student participation.

Finally, I would like to thank all the delegates for attending the conference. It is inconceivable that the conference could have been such a huge success was it not for the distinguished scientific contributions and participation of the esteemed delegates. A huge word of thanks also needs to be expressed to the various committees (IOC, SPC and LOC). It is largely due to their diligent contribution that the conference was such an astounding success.

Lowry Conradie

IOC and SPC Chair for CYC2019

ALL CYCLOTRON CONFERENCES

#	Conference and Location	Delegates	Host
1.	Cyclotrons’59, Sea Island, Georgia, 2-4 February 1959	(85)	ORNL
2.	Cyclotrons’62, UCLA, LA, California, USA, 1962	(139)	UCLA
3.	Cyclotrons’63, Geneva, Switzerland, 23-26 April 1963	(146)	CERN
4.	Cyclotrons’66, Gatlinburg, Tennessee, USA, May 1966	(224)	ORNL
5.	Cyclotrons’69, Oxford,17-20 September 1969	(202)	AERE Harwell
6.	Cyclotrons’72, Vancouver, Canada, 18-21 July 1972	(195)	UBC
7.	Cyclotrons’75, Zürich, Switzerland, 19-22 August 1975	(231)	SIN
8.	Cyclotrons’78, Bloomington, Indiana, USA, 18-21 September 1978	(205)	IUCF
9.	Cyclotrons’81, Caen, France, 7-10 September 1981	(225)	GANIL
10.	Cyclotrons’84, East Lansing, MI, USA, 30 April - 3 May 1984	(222)	MSU
11.	Cyclotrons’86, Tokyo, 13 - 17 October 1986	(206)	INS, RIKEN, RCNP
12.	Cyclotrons’89, Berlin, Germany, 8 - 12 May 1989	(213)	HMI
13.	Cyclotrons’92, Vancouver, BC, Canada 6-10 July 1992	(241)	TRIUMF
14.	Cyclotrons’95, Cape Town, South Africa, 8 - 13 October 1995	(204)	NAC
15.	Cyclotrons’98, Caen, France, 14-19 June 1998	(240)	GANIL
16.	Cyclotrons’01, East Lansing, MI, USA, 1-17 May 2001	(185)	MSU
17.	Cyclotrons’04, Tokyo, 18-22 October 2004	(210)	RIKEN
18.	Cyclotrons’07, Giardini Naxos, Catania, Italy, 1-5 October 2007	(241)	LNS
19.	Cyclotrons’10, Lanzhou, P.R. China, 6-10 September 2010	(194)	IMP
20.	Cyclotrons’13, Vancouver, Canada, 16-20 September 2013	(209)	TRIUMF
21.	Cyclotrons’16, Zürich, Switzerland, 11-16 September 2016	(205)	PSI
22.	Cyclotrons’19, Cape Town, South Africa, 23-27 September 2019	(194)	iThemba LABS

IOC			
Name	**Surname**	**Institute**	**Country**
Sytze	Brandenburg	KVI	Netherlands
Yuri	Bylinski	TRIUMF	Canada
Lowry	Conradie	iThemba LABS	South Africa
Andrea	Denker	HZB	Germany
Mitsuhiro	Fukuda	RCNP	Japan
Ralf	Gebel	FZJ-	Germany
Boris	Gikal	JINR	Russia
Pauli	Heikkinen	JYFL	Finland
Yves	Jongen	IBA	Belgium
Marc	Loiselet	UCL	Belgium
Donald	May	TAMU	USA
Yoshiharu	Mori	RRI	Japan
Koji	Noda	NIRS	Japan
Hiroki	Okuno	RIKEN	Japan
Danilo	Rifuggiato	INFN	Italy
Hermann	Schweickert	ZAG	Germany
Mike	Seidel	PSI	Switzerland
Vijay	Shanker Pandit	VECC	India
Susan	Smith	STFC	United Kingdom
Damon	Todd	LBNL	USA
Wenlong	Zhan	IMP	China
Tianjue	Zhang	CIAE	China
HongWei	Zhao	IMP	China
Stolz	Andreas	NSCL	USA

SPC			
Name	**Surname**	**Institute**	**Country**
Andreas	Adelmann	PSI	Switzerland
Rick	Baartman	TRIUMF	Canada
Sytze	Brandenburg	KVI-CART	Netherlands
Lowry	Conradie	iThemba LABS	South Africa
Andrea	Denker	Helmholtz Centre Berlin	Germany
Santo	Gammino	INFN-LNS	Italy
Wiel	Kleeven	IBA	Belgium
Yoshiharu	Mori	Kyoto University	Japan
Hiroki	Okuno	RIKEN	Japan
Marco	Schippers	PSI	Switzerland
Shizhong	An	CIAE	China
Daniel	Winklehner	MIT	USA

LOC		
Name	**Surname**	**Designation**
Lowry	Conradie	Manager
Fhumulani	Nemulodi	Poster Sessions JACoW
Naomi	Haasbroek	Conference Secretariat
Garrett	De Villiers	Proceedings JACoW
Joele	Mira	Proceedings JACoW
Melanie	Robertson	SPMS IT Support
Mike	Hogan	SPMS IT Support
Pieter	van Schalkwyk	Industrial Exhibition
Dirk	Fourie	Scientific Program
Rainer	Thomae	IThemba LABS tour coordinator
Michelle	Van Der Ventel-Bark	Website Design and Maintenance
Muneer	Sakildien	Chair / Student Support
Joshua	Lewis	AV Support, SPMS IT Support
Audrey	Sauls	Registration and Secretariat Assistant
William	Duckitt	Conference Sponsorship
Hugo	Barnard	Strategic Planning and Communications
Vanessa	De Jongh	Proceedings JACoW Secretary

JACoW Editorial Team			
Name	**Surname**	**Designation**	**Institute**
Jan	Chrin	Editor	PSI
Volker	Schaa	Editor	GSI
Garrett	De Villiers	Editor	iThemba LABS
Joele	Mira	Editor	iThemba LABS
Fhumulani	Nemulodi	Editor/Poster Police	iThemba LABS
Mike	Hogan	Speaker Preparation	iThemba LABS
Vanessa	De Jongh	Secretary	iThemba LABS

CONFERENCE SUMMARY

A. Denker
Helmholtz-Zentrum Berlin für Materialien und Energie, Berlin, Germany
also at Beuth University of Applied Sciences Berlin, Berlin, Germany

The 22nd International Conference on Cyclotrons and their Applications held in Cape Town, South Africa, attracted 194 delegates from 45 institutions located in 18 countries. Overall 119 contributions were presented, 52 oral presentations and 67 posters. For the latter, adequate time was allocated for presentation and discussion.

The addressed topics covered a very broad field. They ranged from concepts and new projects, theory and simulations, over cyclotron technology to operation and upgrades as well as applications. The different topics were very well balanced (Table 1).

Table 1: Share of the different presented topics.

Topic	Share
Cyclotron technology	32%
Operation and Upgrades	22%
Cyclotron Applications	19%
Theory, Models and Simulations	14%
Cyclotron and FFAG concepts	11%
Young Scientists	2%

A look at the various applications shows the extremely broad range of fields: accelerator driven systems (ADS), radioisotope production, particle therapy, radiation hardness testing, accelerator mass spectroscopy, and last, but not least – fundamental physics for a better understanding of the universe. All these various applications benefit from cyclotrons and a world without cyclotrons would be a poorer place. Just one example: It is important for our society to find a solution to the problem of long-lived radioisotopes from nuclear waste. The FFA accelerator complex in Kyoto accomplished the first experiments for transmutation of the minor actinides ^{237}Np and ^{241}Am.

Beside the charm and the beauty of cyclotron design in itself, these applications drive the development of the cyclotrons towards:

- Increased beam intensity, among others for ADS and radioisotope production.
- Precise beam delivery, e.g. for particle therapy.
- Increased efficiency: size, cost, energy consumption.
- Improved beam diagnosis and analysis.
- Driving the technical limits in terms of magnetic field, RF, and power.

The topic “Cyclotron technology” included magnets, injection and extraction, sources, and control systems. Mobile phones or tablets will be even more used in the future than today – so an interface to EPICS sounds fascinating.

Several sessions were dedicated to the topic “Operation and Upgrades”. Many “small” improvements resulted in higher intensities and better reliability. While GANIL and the IMP have long-term big upgrades based on a Linac, the upgrade plan for CIAE comprises a CW FFAG. Furthermore, complete refits of existing cyclotrons are underway.

The images of a Magnetic Resonance Imaging system (MRI) installed in a proton beam line showed little and predictable shifts due to the fringe field of the beam lines magnets. Furthermore, these are correctable. Improvements on the control of beam intensity for continuous line scanning were presented as well as transparent beam profilers based on secondary electron emission.

A new approach to design FFAs from their orbits was shown, however, most of the talks about simulations were dedicated to OPAL: Development and Surrogate models, a Multi-Objective Optimization which turned out to be good for a quick finding of reasonable solutions, and the inclusion of Monte Carlo methods for residual gas and dissociation by electromagnetic stripping.

There is a range of existing machines of various providers for radioisotope production, which has been extended in the 70 MeV energy range for protons. Furthermore, there are new installations to come in the future with energies up to 100 MeV. Within that topic there was an excellent presentation given by a young scientist about the design of a multi-purpose high-temperature superconducting skeleton cyclotron.

The presentations about accelerators for particle therapy included a proposal for a skeleton cyclotron as well, and a microtron-like design. Furthermore, several new projects for proton therapy sites in China were presented. A design for a 70 MeV/u for both $^{12}C^{6+}$ and H_2^+ is underway.

A very compact cyclotron for accelerator mass spectroscopy with an extraction radius of only 440 mm was presented for archaeometry.

For fundamental research both new designs as new machines were presented: e.g. a high power machine with permanent magnets for better transmission. The DC280 delivered first beam for super heavy elements in January 2019. For the ISIS upgrade a FFA option is considered.

This conference provided exciting and interesting contributions. The invited talks gave a very good overview of the addressed topics and were a perfect introduction into the corresponding sessions. New cyclotrons came into operation, are under construction and being designed. The status reports were honest and realistic, thus permitting a real experience exchange. There was time for intense discussions with colleagues, resulting in new ideas.

The author would like to thank the conference host, iThemba LABS, for running an extremely smooth conference, a very informative excursion to the iThemba LABS accelerators followed by a delicious braai, and giving us the chance to meet old friends and acquire new ones.

† email address denker@helmholtz-berlin.de

In memoriam: Jean-Pierre Blaser

by Werner Joho, Villigen, 22 September 2019

At the age of 96 J. P. Blaser, the former director of SIN, the Swiss Insitute of Nuclear Research, died in his home in Switzerland on the 29th of August 2019.

In 1948 J. P. Blaser finished his studies in physics at ETH Zurich, the Swiss Federal Institute of Technology. Afterwards he participated in the development of a cyclotron at ETH, built by professor Paul Scherrer during the second world war. In 1959 he was appointed as successor of Paul Scherrer, a popular lecturer at ETH, and inherited from him the planning group for a new cyclotron.

Originally Paul Scherrer wanted to copy the 88-inch cyclotron at Berkeley, California, and use it for research in nuclear physics. However J. P.Blaser wanted to realize a much more ambitious project. After getting advice from accelerator experts at CERN, among them Pierre Lapostolle, he proposed a 500 MeV cyclotron for the production of mesons. The key for such a meson factory was to extract the high intensity proton beam with very low losses. The competing projects for such a facility solved this problem with different approaches: At Los Alamos a Linear Accelerator was built, while the Canadian team TRIUMF in Vancouver planned to accelerate H- ions and extract them by stripping them to protons.

The leader of Blaser's cyclotron group was Hans Willax, who was previously delegated by Paul Scherrer to Berkeley for getting some expertise with cyclotrons. He realised, that a conventional cyclotron would have high losses at extraction. In 1962 he came up with the brilliant idea to break up the cyclotron magnets into separate sectors. This left space in between for high voltage cavities. This concept of a ring cyclotron ensured a large separation between the turns and thus very low losses on the extraction septum. J. P. Blaser immediately enthusiastically supported this new idea and pushed forward to get this expensive project approved by the Swiss government. Against all odds and against some strong opposition even from the physics community he finally succeded. In 1968 he founded the Swiss Institute for Nuclear Research (SIN) and was its director for the next 20 years.

Experiments at CERN showed, that the production of Pions would strongly increase with energy. In a last minute decision (supported by calculations from the author!) the energy of the cyclotron was increased from 500 MeV to 590 MeV. Even top accelerator specialists like the late Henry Blosser had doubts, that the SIN crew would reach the ambitious design goal of 100 μA, but Blaser and Willax were convinced, that the ring cyclotron had the potential for even higher intensities. They anticipated, that the original 72 MeV injector cyclotron, provided by the Philips company, would be the limiting factor and eventually would have to be replaced. Even before the construction of the ring cyclotron was completed the concept for a new Injector II was worked out. In the accelerator building a corresponding opening, which we called "the Philips provocation hole", was provided during construction.

In January 1974 the first protons were extracted from the ring, and at the end of 1976 the design current of 100 µA was reached. More highlights followed:

- 1985: First 72 MeV protons from the new Injector II.
- 1990: New high intensity targets for the production of mesons.
- 1995: With an upgraded RF-system 1.4 mA were achieved. With this current, the SIN cyclotron surpassed the Los Alamos Linac in beam power. This was a special pleasure for the cyclotron pioneer Henry Blosser, who as a true gentleman, admitted that he completly underestimated the potential of the Ring Cyclotron.
- 1996: Commissioning of the Neutron Spallation Source SINQ, replacing reactors as neutron sources
- 2006: Four new copper cavities with a voltage of 900 kV
- 2009: With 2.4 mA protons at 590 MeV, a new world record of 1.4 MW in beam power was achieved. This record still holds up to today.

These results gave J. P. Blaser a great satisfaction, even after his retirement in 1990. Before that date he initiated in 1988 the new "Paul Scherrer Institute, PSI", a combination of his own Institute SIN and the neighbouring reactor institute, EIR. For its first two years he acted as its director. All these achievments are summarized in a book by Andreas Pritzker: "History of the Swiss Institute for Nuclear Research".

From the beginning of the accelerator project J. P. Blaser saw the possibility to use particle beams for the irradiation of tumours. The first step was using pions for the treatment of deep seated tumours. A superconducting solenoid was constructed for this purpose and was in operation from 1982 to 1992. In 1984 the irradiation of eye tumours started, using the injector cyclotron. Up to today more than 7000 patients were treated this way. For deep seated tumours Eros Pedroni developed in 1996 the so called spot scanning technique. A small fraction of the 590 MeV beam was first degraded and then directed towards a rotating Gantry. Later a new superconducting cyclotron was acquired and two more Gantries are now in operation.

J. P. Blaser strongly supported all activities in medical application of cyclotrons. It was thus no surprise, that he was willing to give his advice to a corresponding new cyclotron project in South Africa. His help was strongly appreciated and in 1990 he was elected "Foreign Associate of the Royal Society of South Africa" for his efforts.

J. P. Blaser was blessed with great intuition, based on a thorough knowledge of the basic laws of physics. He was open to new and unconventional ideas. He fully supported young scientists and motivated them with his trust in their abilities. Team spirit was very high on his list of priorities. In his free time he enjoyed exploring the landscapes of Switzerland either by foot or as a pilot with an airplane. But the top priority was his familiy. He enjoyed enormously the company of his wife Frauke, their two daughters Claudine and Nicole and their four grandchildren. With Jean-Pierre his family and the accelerator community looses a great personality.

Andreas Adelmann delivered an obituary to the life of J. P. Blaser on
24 September at Cyclotrons'19, Cape Town, South Africa

Contents

Sunday 22 September 18:00-21:30 Registration and Welcome Reception (Venue: Two Oceans Aquarium)

Monday 23 September

Industrial Exhibition 08:30-18:00 in the Old Harbour Lobby

MOW	Conference Opening, Chair: Lowry Conradie
08:00	Registration
09:00	Welcome, Introduction
MOA	Facility Development and Upgrades, Chair: Yuri Bylinsky
09:30	MOA01: Yoshihiro Ishi - Recent Experimental Results of the Accelerator Drive System with a Sub-Critical Nuclear Reactor (ADS) Programme
10:00	MOA02: Weiqing Yang - Operating Status and Upgrading of Cyclotron in Lanzhou
10:20	MOA03: Omar Kamalou - Status Report on GANIL and Upgrade of SPIRAL1
10:40	Tea
MOB	Facility Development and Upgrades, Chair: Ralf Gebel
11:10	MOB01: Osamu Kamigaito - Recent Progress in RIKEN RI Beam Factory
11:40	MOB02: Jacobus Conradie - Progress With a New Radioisotope Production Facility and Construction of Radioactive Beam Facility at iThemba LABS
12:00	MOB03: William Beeckman - GFS-2 - The New Gas-filled Separator for Super-Heavy Elements in JINR. A Guided Walk through the Genesis of the Project from First Thoughts to Completion
12:20	Lunch
14:00	MOP POSTER SESSION
15:40	Tea
MOC	Cyclotron Technology: Ion Sources and Upgrades, Chair: Pauli Heikkinen
16:00	MOC01: Liangting Sun - Moving the Frontiers of the Production of Intense Beams of Highly Charged Ions With ECR Ion Sources
16:30	MOC02: Damon Todd - A Pathway to Accelerate Ion Beams up to 3 GeV with a K140 Cyclotron
16:50	MOC03: Markus Schneider - Upgrade of the PSI Injector 2 Cyclotron

Tuesday 24 September

Industrial Exhibition 08:30-18:00 in the Old Harbour Lobby

TUA	Cyclotron Applications: Isotopes, Chair: Hermann Schweikert
08:30	TUA01: Jean-Michel Geets - Radioisotopes production in accelerators and cyclotron use
09:00	TUA02: Saverio Braccini - Novel Irradiation Methods for Theranostic Radioisotope Production With Solid Targets at the Bern Medical Cyclotron
09:20	TUA03: Nicholas Philip van der Meulen - The Use of PSI's IP2 Beam Line Towards Exotic Radionuclide Development and its Application Towards Proof-Of-Principle Preclinical and Clinical Studies
09:40	TUA04: Martin Schulc - Characterization of Neutron Leakage Field Coming from 18O(p,n)18F Reaction in PET Production Cyclotron
10:00	TUA05: Mitra Ghergherehchi - Vanadium-48 Production Yield Investigation Using TiO2 Nan Powder Targets
10:20	Tea
TUB	Cyclotron Applications: Medical, Chair: Andrea Denker
10:50	TUB01: Daniel Winklehner - Status of the development of a fully iron-free cyclotron for proton beam radiotherapy treatment
11:10	TUB02: Oleg Karamyshev - SC230 Superconducting 230 MeV Proton Cyclotron for Therapy
11:30	TUB03: Erik Van Der Kraaij - MRI-Guided-PT: Integrating an MRI in a Proton Therapy System
11:50	TUB04: Serena Psoroulas - On-Line Dynamic Beam Intensity Control in a Proton Therapy Cyclotron
12:10	Lunch
13:50	TUP POSTER SESSION
15:30	Tea
TUC	Status Reports, Chair: Tianjue Zhang
15:50	TUC01: Mario Maggiore - Review and Current Status of the 70 MeV High Intensity Proton Cyclotron at Legnaro
16:20	TUC02: Andrea Denker - Status of the HZB Cyclotron
16:40	TUC03: Brian Jones - AGOR Status Report
17:00	TUC04: Hiroki Kanda - Status of the Cyclotron Facility at Research Centre for Nuclear Physics

Wednesday 25 September

Industrial Exhibition 08:30-14:00 in the Old Harbour Lobby

WEA	Magnet Design, RF and Upgrades, Chair: Yves Jongen
08:30	WEA01: GianLuca Sabbi - Future of High Field Superconducting Magnets
09:00	WEA02: Antonio Caruso - The Developments of the RF System Related to the K-800 Superconducting Cyclotron Upgrade
09:20	WEA03: Mitsuhiro Fukuda - Design for Upgrading the RCNP AVF Cyclotron
09:40	Tea
WEB	FFA Concepts, Beam Dynamics and Simulations, Chair: Yoshiharu Mori
10:10	WEB01: Jean-Baptiste Lagrange - Status of FFAs (Modelling and Existing/Planned Machines)
10:40	WEB02: Andreas Adelmann - Surrogate Models for Particle Accelerators
11:00	WEB03: Christiaan Baumgarten - Factors Influencing the Vortex Effect in High-Intensity Cyclotrons
11:20	WEB04: Hui Zhang - BDSIM Simulation for the Complete Radionuclide Production Beam Line on PSI Cyclotron Facility from Beam Splitter to Target Station
11:40	WEB05: Daniel Winklehner - Beam dynamics and preliminary design of the RFQ Direct Injection Project
12:00	Lunch
WEC	Young Scientists, Chair: Andreas Adelmann
13:15	WEC01: Hui Wen Koay - Conceptual Design of an Axial Injection System for High- Temperature Superconducting Skeleton Cyclotron (HTS-SC)
13:35	Introductory Talk and then Depart for Site Visit and Barbecue at iThemba LABS

Thursday 26 September

Industrial Exhibition 08:30-18:00 in the Old Harbour Lobby

THA	Beam Dynamics, Simulations and Control, Chair: Daniel Winklehner
09:00	THA01: Jochem Snuverink - Precise Modelling and Large Scale Multiobjective Optimization of Cyclotrons
09:30	THA02: Andreas Adelmann - Recent Developments of the Open Source Code OPAL
09:50	THA03: William Duckitt - Automation Studio: A New Face to Control Large Scientific Equipment
10:10	Tea
THB	High Power Cyclotrons and Diagnostics, Chair: Andreas Adelmann
10:40	THB01: Luciano Calabretta - Review of High Power Cyclotrons and Their Applications
11:10	THB02: Victor Smirnov - Production of 70-MeV Proton Beam in a Superconducting Cyclotron
11:30	THB03: Yu. Bylinskii - Conceptual Design of TR100+: An Innovative Superconducting Cyclotron for Commercial Isotopes Production
11:50	THB04: Christophe Thiebaux - Development of a Transparent Profiler Based on Secondary Electrons Emission for Charged Particle Beams
12:10	Lunch
THC	Radioactive Beams and New Concepts, Chair: Sytze Brandenburg
13:40	THC01: Igor Kalagin - Cyclotron Facility for Super Heavy Elements (SHE) Research
14:10	THC02: Donald Philip May - First Beams Produced by the Texas A&M University Radioactive-Beam Upgrade
14:30	THC03: Donghyup Ha - Design of Accelerator Mass Spectrometry Based on Cyclotron
14:50	THC04: Christian Rüdiger Wolf - 3D Printing for High Vacuum Applications
15:10	Tea
THD	Cyclotron Technology: Ion sources, Injection and Extraction, Chair: Danilo Rifuggiato
15:35	THD01: David Mascali - Physics and Technology of Compact Plasma Traps
16:05	THD02: Taneli Kalvas - Central Region Upgrade for the Jyväskylä K130 Cyclotron
16:25	THD03: Willem Kleeven - An Improved Concept for Self-Extraction Cyclotrons
17:35	Depart for Conference Dinner (Venue: The Bungalow)

Friday 27 September

Industrial Exhibition 08:30-10:00 in the Old Harbour Lobby

FRA	New Projects, Beam Dynamics, Simulations and Applications, Chair: Marco Schippers
08:30	FRA01: Tianjue Zhang - A New Solution for Cost Effective, High Average Power (2 GeV, 6 MW) Proton Accelerator and its R&D Activities
09:00	FRA02: Hiroshi Tsutsui - Status of Sumitomo's Cyclotron Development for Proton Therapy
09:20	FRA03: André Roth - Energy Reduction of Varian's ProBeam 250 MeV Cyclotron to 226 MeV
09:40	FRA04: Vasily Sergeevich Anashin - Cyclotrons Based Facilities for Single Event Effects Testing of Spacecraft Electronics
10:00	Tea
FRB	FFA Concepts and Upgrades, Chair: Andreas Stolz
10:30	FRB01: Thomas Planche - Designing Cyclotrons and FFAs From Their Orbits
11:00	FRB02: Semen Mitrofanov - FLNR JINR Accelerator Complex for Applied Physics Researches: State-of-Art and Future
	Conference Summary and Announcement of Host Institution for CYC2022, Chair: Lowry Conradie
11:20	Conference Summary presented by Andrea Denker
11:45	Announcement of the Host Institution for CYC2022
12:00	End of Conference

ISBN: 978-3-95450-205-9 doi:10.18429/JACoW-Cyclotrons2019-MOA01

RECENT EXPERIMENTAL RESULTS OF THE ACCELERATOR DRIVEN SYSTEM WITH A SUB-CRITICAL NUCLEAR REACTOR (ADS) PROGRAM

Y Ishi*, Y. Fuwa[1], Y. Kuriyama, H. Okita, H. Suga, T. Uesugi and Y. Mori
Institute for Integrated Radiation and Nuclear Science, Kyoto University, Osaka, Japan
[1]also at Japan Atomic Energy Agency, Ibaraki, Japan

Abstract

A series of studies on the accelerator driven system (ADS) has been carried out since 2009 at KURNS. In these studies, Kyoto University Critical Assembly (KUCA) has been used as sub-critical system connected with the proton beam line from FFAG accelerator facility (Fig. 1). A profile of accelerator facility and experimental results, including the first evidence of the transmutation of minor actinides at ADS, will be presented.

INTRODUCTION

Disposal of spent fuel generated after light water reactor (LWR) operation is an urgent worldwide issue that must be addressed. For instance in Japan, approximately 17,000 tons of spent fuel is stored as of April 2014. Twenty tons of spent fuel is generated with operation of a 1 GWe class LWR for one year. If we assume that 15% of electricity demand in Japan (forecast for 2030) is to be covered by nuclear power, 20 units of this class of LWRs (20 GWe) will be required, and 400 tons of spent fuel will be generated annually. One ton of spent fuel contains 1 kg of minor actinides (MAs). That is, if a group of LWRs generating the electric power of 20 GWe is operated for one year, 400 kg of MA will be generated.

Some MAs have an extremely long half-life. For instance, ^{237}Np has over 2 million years. It takes about 10,000 years to reduce the potential toxicity of ingestion of high-level radioactive waste from spent fuel containing MAs to the same extent as natural uranium. This fact makes it difficult to dispose high-level radioactive waste. With accelerator driven system (ADS) described in this report, long-lived MAs in spent fuel can be converted into stable or short-lived nuclei, and the potential toxicity decay time can be reduced from 10,000 years to a few hundred years. Therefore, ADS research and development, which greatly contributes to the disposal of spent fuel, is extremely significant from this social background.

ACCELERATOR DRIVEN SYSTEM

An accelerator driven system is composed of a nuclear reactor facility and an accelerator facility. It sustains a nuclear fission chain reaction induced by spallation neutrons obtained by irradiation of a heavy metal target using a high energy proton beam from the accelerator. The nuclear reactor plays a role of neutron booster which amplifies the neutron flux from the target.

* ishi@rri.kyoto-u.ac.jp

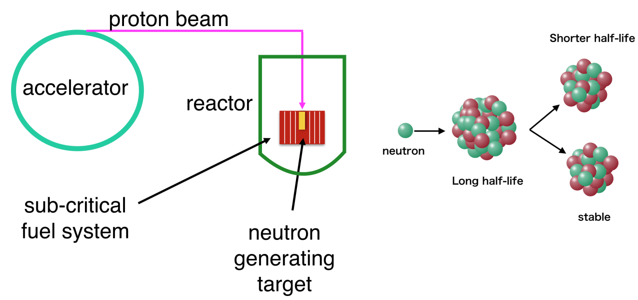

Figure 1: Concept of ADS.

In resent years,the ADS is paid attention not only as an energy production facility but as a device which transmutes long-lived radioactive materials such as the minor actinide (MA) to other materials whose lifetimes are much shorter than the original ones [1]. In the nuclear fuel cycle, MAs can be processed in a fast breeder. But in terms of the stability of the reactor operation in a critical state, the fraction of the MAs in the fuel system is limited as a few percent. On the other hand, in the ADS, MA can be loaded up to some 30 % because the fuel system is operated in a sub-critical state, in which more stable chain reaction can be obtained.

EXPERIMENTAL FACILITY FOR ADS STUDIES AT KURNS

At the Institute for Integrated Radiation and Nuclear Science, Kyoto University (KURNS), basic experimental studies on the ADS have been started since 2009 using a research reactor Kyoto University Critical Assembly (KUCA) [2]. A fixed field alternating gradient (FFAG) synchrotron has been constructed to deliver high energy proton beams to the KUCA. In these studies, the KUCA is used as a sub-critical reactor and the FFAG accelerator is used as a proton driver.

KUCA

The research reactor KUCA has been designed for precise study on reactor physics. It is a thermal reactor. Its typical output power is on the order of 10 W even in a critical state. It consists of 3 cores: A-Core, B-Core and C-Core. Polyethylene is used as moderators and reflectors of neutrons in A-Core and B-Core while H_2O is used in C-Core. For the ADS experiments, A-Core is used in a sub-critical state.

The A-Core accepts both 100-MeV proton beams from FFAG MAIN RING and 300-keV deuteron beams from a Cockcroft–Walton accelerator. The 100-MeV protons hitting heavy-metal targets such as W or Pb-Bi induce spallation neutrons, while the 300-keV deuterons hitting the Lithium

ISBN: 978-3-95450-205-9 doi:10.18429/JACoW-Cyclotrons2019-MOA01

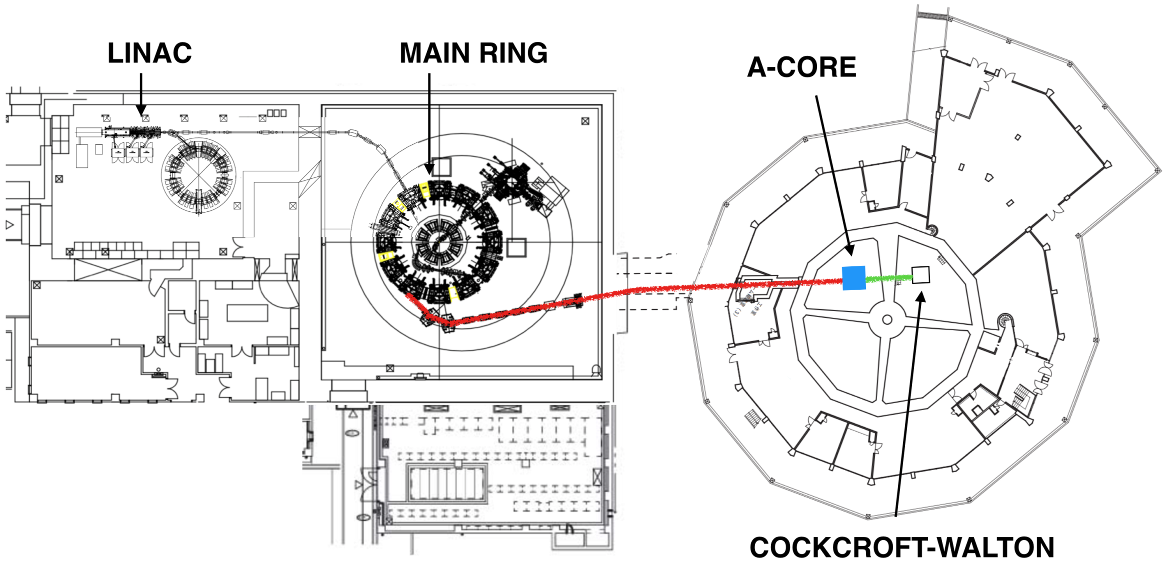

Figure 2: Layout of FFAG accelerator complex and KUCA.

target produce 14 MeV neutrons due to the D-T reaction. At the A-Core, two different types of accelerator driven neutron source can be used for the ADS study.

FFAG Accelerator Complex

The layout of the KURNS FFAG accelerator complex is shown in Figs. 2 and 3 [3]. The complex consists of an 11 MeV H^- injector LINAC, an 11-MeV H^- beam line, an FFAG synchrotron called MAIN RING and a 100-MeV proton beam line. Table 1 shows the basic parameters of the complex.

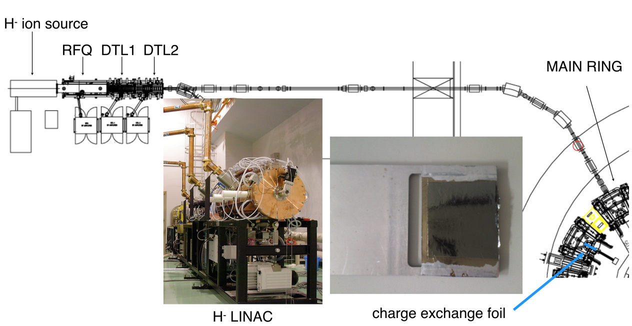

Figure 3: Detailed layout of FFAG accelerator complex.

The LINAC consists of RFQ, DTL1 and DTL2. H^- beams are injected into the MAIN RING through a charge stripping foil made of carbon, whose thickness is 20 μg/cm^2. In this injection scheme, no pulse device is used. Even orbit merging magnets are not necessary because the H^- beams are merged inside the main magnet of the MAIN RING. Proton beams from the MAIN RING is delivered as extremely short bunch such as 100 ns. The instantaneous beam power is a few ten kW. Therefore, dynamic characteristics of ADS can be investigated with these beams. The beam specification from the MAIN RING is summarized in Table 1.

Table 1: Basic Parameters of KURRI FFAG Accelerator Complex

LINAC	
Energy	11 MeV
Peak current	< 5 μA
Pulse length	< 100 μs (uniform)
Repetition rate	< 200 Hz
MAIN RING	
Energy	11 - 100 or 150 MeV
Field index k	7.5
Magnetic field	1.6 T (max.)
Revolution frequency	1.6 - 4.3 MHz
Rf voltage	4 kV
Repetition rate	< 30 Hz

Although the repetition rate of the LINAC is 200 Hz, that of the MAIN RING is limited up to 30 Hz because of a low accelerating speed. If the accelerating cavity voltage can be increased, high df/dt can be realized. Therefore, a higher repetition rate at the MAIN RING can be obtained.

FIRST MINOR ACTINIDE TRANSMUTATION BY ADS AT KURNS

The experimental studies at KURNS have been carried out since 2009. Numbers of results have been obtained. These can be seen in the articles [4–8]. On 14th and 15th February 2019, the first nuclear transmutation of minor actinides by the ADS was successfully demonstrated [9] in a sub-critical core at KUCA, detecting following reactions:

- fission reaction of ^{237}Np and ^{241}Am,
- capture reaction of ^{237}Np.

ISBN: 978-3-95450-205-9 doi:10.18429/JACoW-Cyclotrons2019-MOA01

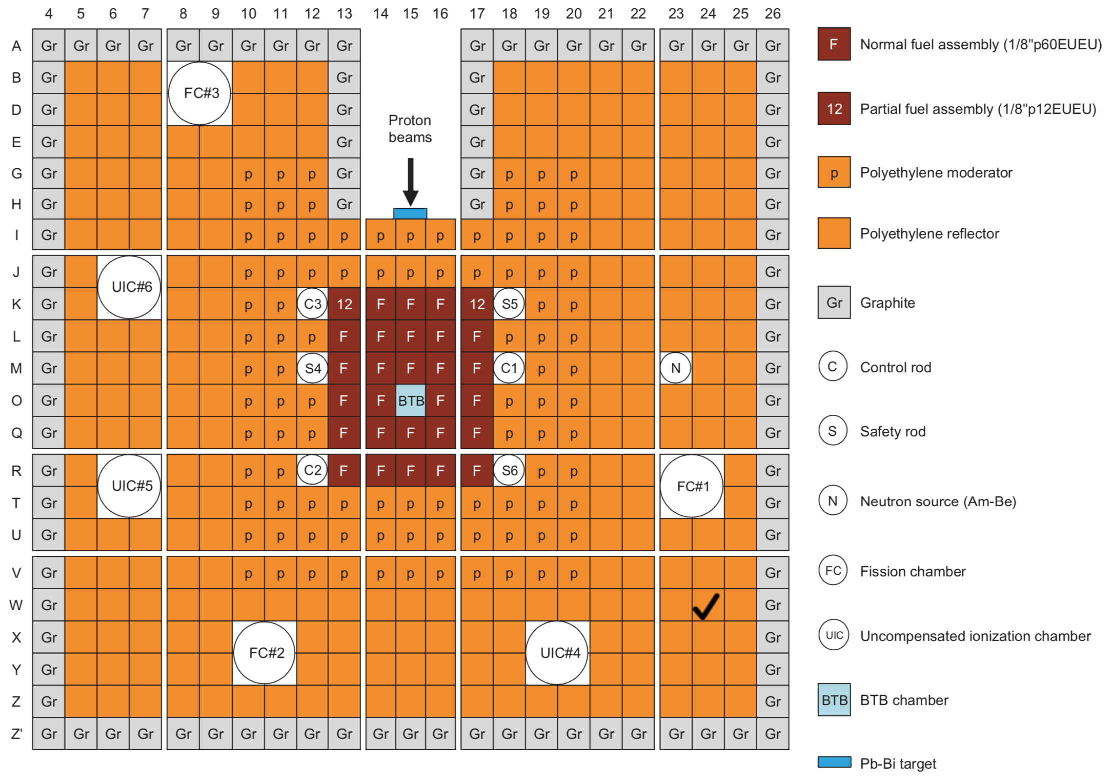

Figure 4: Configuration of sub-critical core (from the article [9]).

Core Configuration

A sub-critical core configuration for these experiments is shown in Fig. 4. The symbol “F” and “12” indicate the fuel assembly. The fuel used here was highly-enriched ^{235}U. A neutron production target made of solid state Pb-Bi was located at (15,H) on the core coordinate. The control and safety rods indicated by C1–C3 and S4–S6 were set in appropriate positions so that the sub-criticality was desired value.

The sample foils of ^{237}Np and ^{241}Am were installed in the special void element located at (15,O) with the reference ^{235}U foil and the back-to-back (BTB) fission chamber. The BTB chamber detects the signals of fission fragments due to the fission reaction in the sample foil and the reference one.

Proton Beams

A typical signal from the bunch monitor installed in the MAIN RING is shown in Fig. 5. The beam acceleration from 11 MeV to 100 MeV needs ~24.3 ms with the accelerating cavity voltage of 4 kV and synchronous phase of 30 deg. The repetition rate of the machine operation was 30 Hz. The characteristics of the proton beam for the experiments are summarized in Table 2.

There was a small amount of beam loss around 4 ms from the start of acceleration. It is attributed to the betatron resonance crossing. Except for this, no significant beam loss was observed after 4 ms from the start.

Table 2: Proton Beam Characteristics

Energy	100 MeV
Intensity	0.5 nA - 1 nA
Pulse width	100 ns
Repetition rate	30 Hz
Beam size at Pb-Bi target	40 mm in diameter

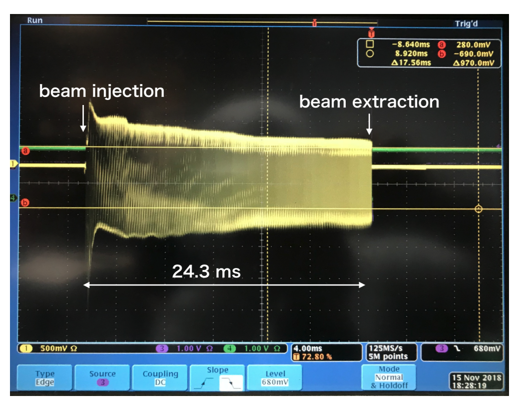

Figure 5: Typical signal from bunch monitor.

RESULTS

For the fission reaction, the pulse height distributions from BTB fission chamber for ^{237}Np and ^{241}Am were obtained as shown in Fig 6. The fission reactions in both the ^{237}Np and the ^{235}U foils were clearly observed over entire region of pulse height. For the case of ^{241}Am, signals lower than

ISBN: 978-3-95450-205-9 doi:10.18429/JACoW-Cyclotrons2019-MOA01

480 ch are attributed to α-ray induced by ^{241}Am. In the higher pulse height region, although the fraction is small, signals from fission reaction can be observed.

Also for the capture reaction, γ-ray emission was detected by germanium detector after the irradiation. Obtained γ-ray spectrum is shown in Fig. 7.

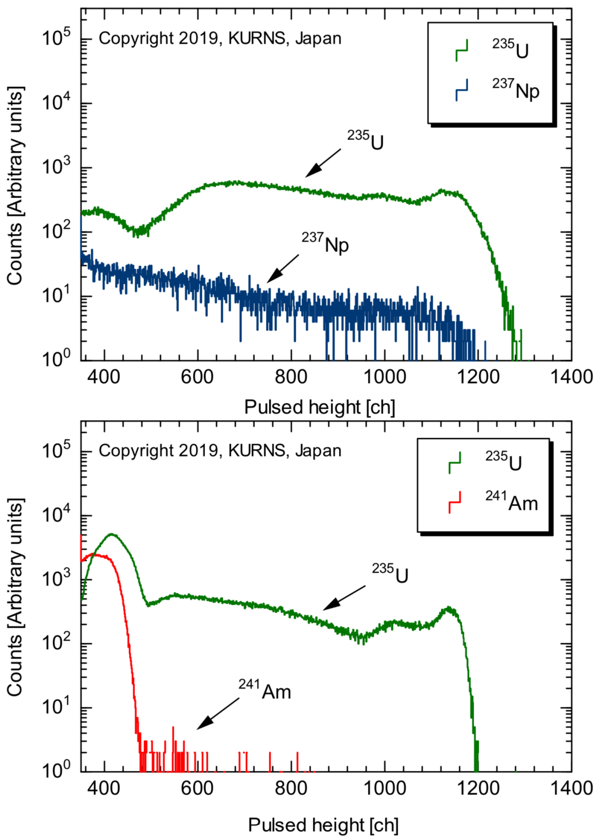

Figure 6: Pulse height distribution from BTB fission chamber for ^{237}Np and ^{241}Am.

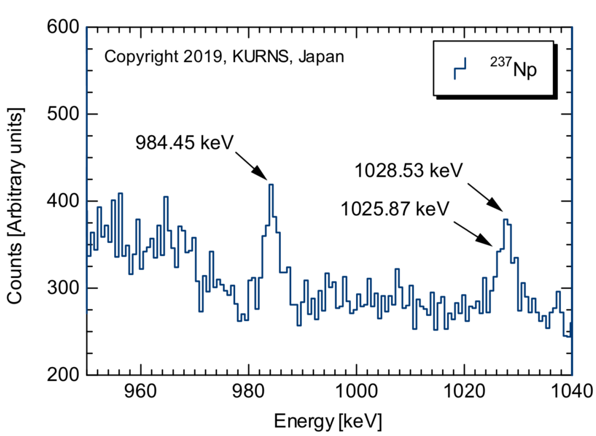

Figure 7: Measured γ-ray spectrum of capture reaction of ^{237}Np.

CONCLUSION

The world's first experiments for transmutation of minor actinide (^{237}Np and ^{241}Am) in accelerator driven system have been accomplished at the Institute for Integrated Radiation and Nuclear Science, Kyoto University.

ACKNOWLEDGMENTS

This work was supported by MEXT(the Ministry of Education, Culture, Sports, Science and Technology) of Japan in the framework of a task entitled "Research and Development for an Accelerator-Driven Sub-critical System Using an FFAG Accelerator".

REFERENCES

[1] K. Tsujimoto *et al.*, "Accelerator-Driven System for Transmutation of High-Level Waste" *Progress in Nuclear Energy*, vol. 37, pp. 339–344, Dec. 2000. doi:10.1016/S0149-1970(00)00068-8

[2] C. H. Pyeon *et al.*, "First Injection of Spallation Neutrons Generated by High-Energy Protons into the Kyoto University Critical Assembly" *J. Nucl. Sci. Technol.*, vol. 46, no. 12, pp. 1091-1093, Aug. 2009. doi:10.1080/18811248.2009.9711620

[3] Y. Ishi *et al.*, "Present Status and Future of FFAGs at KURRI and the First ADSR Experiment", in *Proc. IPAC'10*, Kyoto, Japan, May 2010, paper TUOCRA03, pp. 1327–1329.

[4] C. H. Pyeon *et al.*, "Preliminary study on the thorium-loaded accelerator-driven system with 100 MeV protons at the Kyoto University Critical Assembly", *Ann. Nucl. Energy*, vol. 38, pp. 2298-2302, Oct. 2011. doi:10.1016/j.anucene.2011.06.024

[5] C. H. Pyeon *et al.*, "Mockup Experiments on the Thorium-Loaded Accelerator-Driven System at the Kyoto University Critical Assembly", *Nucl. Sci. Eng.*, vol. 117, pp. 156-168, Jun. 2014. doi:10.13182/NSE13-21

[6] C. H. Pyeon *et al.*, "Experimental Analyses of Spallation Neutrons Generated by 100 MeV Protons at the Kyoto University Critical Assembly", *Nucl. Eng. Technol.*, vol. 45, pp. 81-88, Feb. 2013. doi:10.5516/NET.08.2012.003

[7] A. Sakon *et al.*, "Power spectral analysis for a thermal subcritical reactor system driven by a pulsed 14 MeV neutron source", *Nucl. Eng. Technol.*, vol. 50, pp. 481-492, Apr. 2013. doi:10.1080/00223131.2013.785268

[8] A. Sakon *et al.*, "Measurement of large negative reactivity of an accelerator-driven system in the Kyoto University Critical Assembly", *Nucl. Eng. Technol.*, vol. 51, pp. 116-126, Nov. 2014. doi:10.1080/00223131.2013.852488

[9] C. H. Pyeon *et al.*, "First nuclear transmutation of ^{237}Np and ^{241}Am by accelerator-driven system at Kyoto University Critical Assembly" *J. Nucl. Sci. Technol.*, vol. 56, no. 8, pp. 684-689, May 2019. doi:10.1080/00223131.2019.1618406

ISBN: 978-3-95450-205-9 doi:10.18429/JACoW-Cyclotrons2019-MOA02

OPERATION STATUS AND UPGRADING OF CYCLOTRON IN LANZHOU

W. Q. Yang†, L. T. Sun, J. C. Yang, L. J. Mao, J. W. Xia
Institute of Modern Physics, Chinese Academy of Sciences, 730000, Lanzhou, China

Abstract

IMP operates the Heavy Ion Research Facility in Lanzhou (HIRFL), which consists of the Sector Focusing Cyclotron, the Separated Sector Cyclotron, the Cooler Storage Ring, and a number of experimental terminals. The HIRFL is mainly used in fundamental research of nuclear physics, atomic physics, irradiation material and biology, and accelerator technology. This paper mainly introduces the operation status and upgrading of HIRFL. So far, HIRFL achieves all-ion acceleration from proton to uranium. In addition, in order to improve the efficiency of HIRFL, we will build two new Linac injectors for SSC and CSR, respectively.

INTRODUCTION

HIRFL (Heavy Ion Research Facility in Lanzhou) is the major facility of national laboratory of heavy ion accelerators. It is one of the national laboratories of China, which focused on nuclear physics, atomic physics and heavy ion related application and cross-disciplinary researches. As shown in Fig. 1. HIRFL consists of the ECR (Electron Cyclotron Resonance) ion sources, the Sector Focus Cyclotron (SFC), the Separated Sector Cyclotron (SSC) and the Cooler Storage Ring (CSR). SFC is a k = 69 and SSC is a k = 450. The CSR is a double cooler-storage-ring system consisting of a main ring (CSRm), an experimental ring (CSRe), and a radioactive beam line (RIBLL2). Presently, the heavy ion beams with an energy range of 1(U) – 10(C) MeV/u could be provided by the SFC and 10(U) – 100(C) MeV/u by the SFC + SSC.

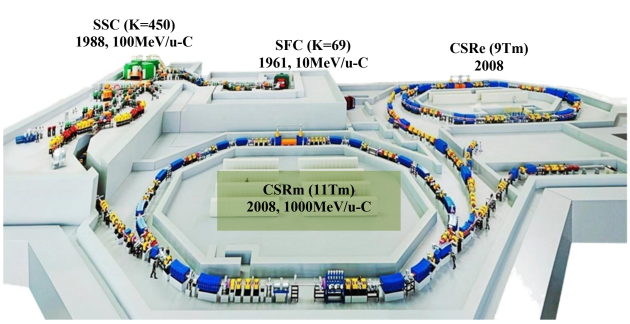

Figure 1: Present layout of the HIRFL.

OPERATION STATUS OF HIRFL

The machine combination operation modes of the HIRFL are SFC, SFC+SSC, SFC+CSRm and SFC+CSRm+CSRe. The time distribution of HIRFL operation consists preparation of machine, beam commissioning, the target beam and failure during the target beam. As shown in Fig. 2, HIRFL is operated about 7500 h during the last 5 years, the target beam time exceeds 70% of the total operating time. Average proportion of faults in each system during the five-year is shown in Fig. 3.

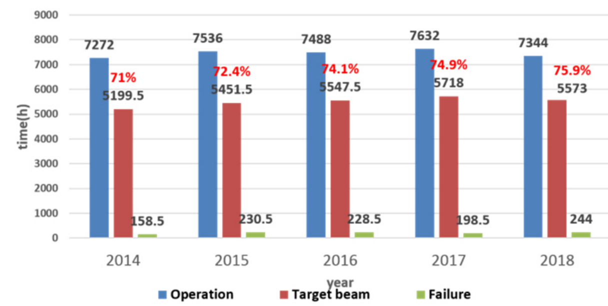

Figure 2: Operation time of the HIRFL.

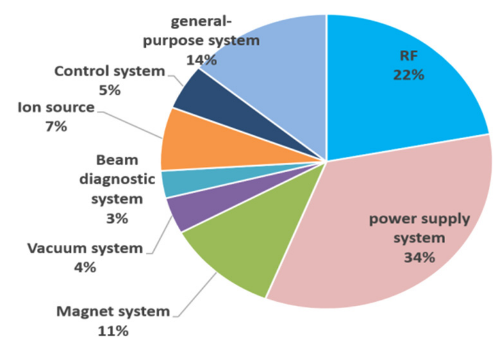

Figure 3: Average failure ratio of the accelerator subsystem during the recent five years.

The element types accelerated by HIRFL shown in Fig. 4, and 25 kinds of beams are provided annually. In the past five years, 61 kinds of new beams with different ions, different charge states and different energies have been produced. Typical ions accelerated by the HIRFL are listed in Table 1.

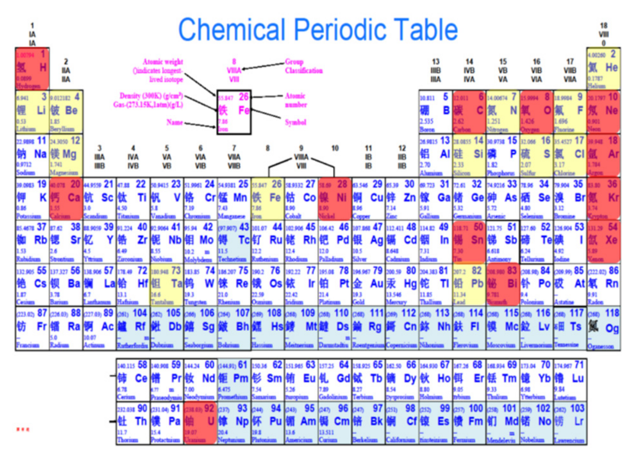

Figure 4: The element species provided by the HIRFL.

† ywq@impcas.ac.cn

ISBN: 978-3-95450-205-9 doi:10.18429/JACoW-Cyclotrons2019-MOA02

Table 1: Typical Ions Accelerated by the HIRFL

Ion beams	Energy (MeV/A) SFC	SSC	CSR	Intensity (eμA)
H_2^{1+}	10		400	30
$^{7}Li^{3+}$	9			2
$^{9}Be^{3+}$	6.89			0.55
$^{12}C^{5+/6+}$	8.47	100		0.4
$^{12}C^{4+}$	7		1000	3200
$^{26}Mg^{8+/12+}$	6.17	70		0.35
$^{36}Ar^{8+}$	2.07	22		3.3
$^{36}Ar^{8+}$	2.07	22	368	650
$^{22}Ne^{7+/10+}$	6.17		70	1700
$^{40}Ca^{12+}$	5.63			3.5
$^{56}Fe^{17+}$	6.3			1.5
$^{58}Ni^{19+}$	6.3		463.4	500
$^{78}Kr^{19+/28+}$	4		487	750
$^{112}Sn^{26+/35+}$	3.7		391	1000
$^{129}Xe^{27+}$	3		235	500
$^{129}Xe^{27+}$	1.84	19.5		0.4
$^{181}Ta^{31+}$	1.19	12.5		0.03
$^{208}Pb^{27+}$	1.1			1
$^{209}Bi^{31+}$	0.91	9.5		0.05
$^{209}Bi^{36+}$	2		170	60
$^{238}U^{26+}$	0.81			0.33
$^{238}U^{32+}$	1.22		100	160

In the past five years, more than 200 heavy ion experiments have been completed in the HIRFL. Users are from universities, enterprises and research institutes in China and abroad. The ratio of planned and implementation experiments are shown as Fig. 5.

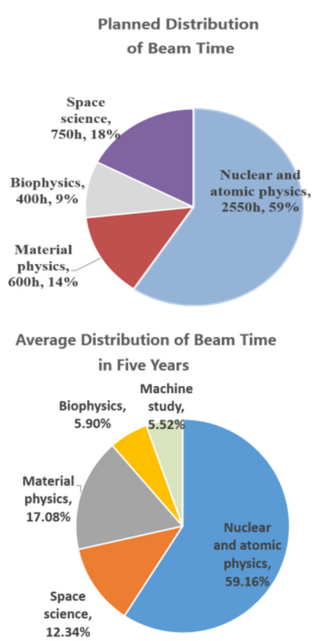

Figure 5: Planned and implementation time of experiments for the HIRFL.

SFC Operation Status

Presently, about 10 major terminals, which are TL1, TL2, RIBLL, CSR, nuclear pore membrane, Single Event Effects, New SEE, Super Heavy Elements and Micro-Beam, can be operated using the SFC. It provides users with about 15 kinds of beams and about 2000 hours of experimental time each year. As an injector of CSR, SFC provides matching beams to CSR according to experimental requirements. The operation time distribution of the SFC from 2014 to 2018 is shown in Fig. 6. SFC beam injection and extraction efficiency is shown in Fig. 7.

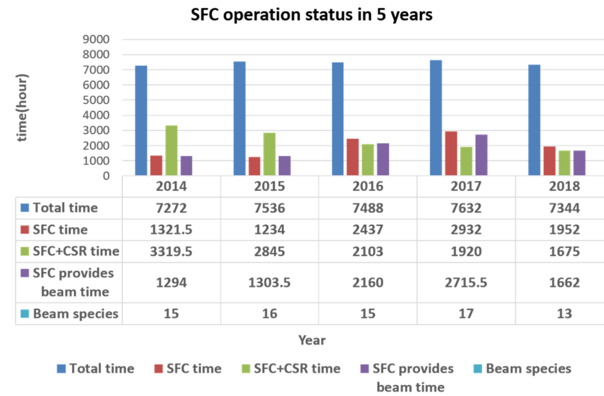

Figure 6: Operation time distribution of the SFC.

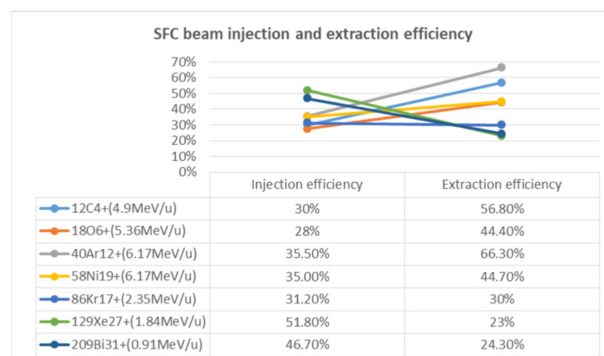

Figure 7: SFC beam injection and extraction efficiency.

SFC+SSC Operation Status

Currently, there are about 8 major terminals could be operated by using the SFC + SSC. The operation time distribution of the SFC + SSC is shown in Fig. 8. SSC beam injection and extraction efficiency is shown in Fig. 9. With the increasing demand for user experiments, the beam time of the experimental terminals around the SSC was still increased during the last 5 years.

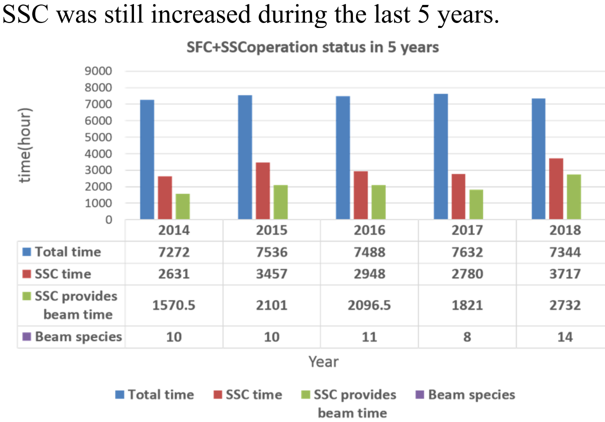

Figure 8: Operation time distribution of the SFC+SSC.

ISBN: 978-3-95450-205-9 doi:10.18429/JACoW-Cyclotrons2019-MOA02

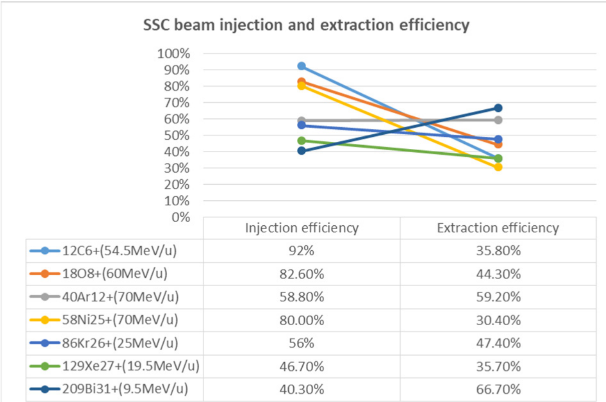

Figure 9: SSC beam injection and extraction efficiency.

Experiments and Studies

Experiments in the SFC and the SFC+SSC are focused on nuclear physics, atomic physics, biology, and ion irradiation physics. While satisfying the user's experimental needs, we should strengthen the study on the improvement and performance improvement of HIRFL. Examples of experiments and studies are:

- The SFC provides Ar, Ca, S, Mg, Ni and other beams for new nuclide synthesis experiments.
- The Sn^{35+} beam, provide by the SFC, is accumulated in CSRm with intensity of 1 emA, and accelerated to high energy of 401 MeV/u. Then, it is delivered to the CSRe to carry out nuclear mass measurement experiment.
- The SFC used as the injector to provide $^{12}C^{4+}$ - 10 eμA (7 MeV/u) beam for CSRm. Impulse electron beam cooling experiment is realized in the CSRm. The CSRe achieves stochastic cooling of beams.
- The SFC+SSC provides He, C, O, Ne, Si, S, Ar, Ni and other beams for RIBLL1. Many physical experiments have been completed in RIBLL1.
- The SFC+SSC used as injector to provide $^{36}Ar^{8+}$ 3.5 eμA (22 MeV/u) beam for CSRm. It accelerates to 368 MeV/u, beam intensity is 680 eμA.
- The SFC+SSC provides Kr, Bi, Ta, Xe and other beams for TR5 experiment terminal. The single event effect of many electronic components has been studied and tested.

HIRFL IMPROVEMENT AND UPGRADE

HIRFL was built-up in 3 periods, lasting about half century. We have made some equipment improvements and upgrade. Improvement of SFC vacuum chamber, vacuum pressure increased from 3×10^{-7} mbar to 5×10^{-8} mbar. The beam transmission line from SFC to SSC is equipped with a buncher to compress the longitudinal phase space of heavy ion beam, and the beam intensity of SSC is increased by two times. Replacement of SSC injection and extraction magnetic aging coils reduces the faults. The control system was changed to EPCIS. Power supply system gradually was changed to digital power supply. High frequency power source of SSC changed from Electron Tube Amplifier to Solid State Amplifier. The low-level system should be digitized, etc.

In the current accelerator, the SFC plays an important role in HIRFL operation. However, when the SFC provides ion beams to experiment terminals alone, the SSC and the CSR could not carry out other experiments. This cannot provide full-time operation for SSC and CSR simultaneously. Therefore, to enhance the performance of the HIRFL, two heavy-ion Linacs, called the SSC-LINAC and the CSR-LINAC, are proposed as a new injector of the SSC and the CSR, as shown in Fig. 10. Due to the limit of budget, SSC-Linac was built in first.

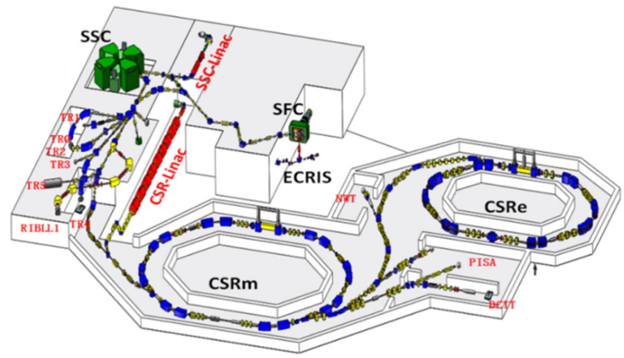

Figure 10: Layout of the new injector SSC-LINAC and CSR-LINAC.

Overview of SSC-LINAC

Focusing on the high intensity of heavy ion beam, the SSC-LINAC consists of a superconducting ECR ion source, LEBT, RFQ, MEBT, IH-DTL and HEBT, as shown in Fig. 11. The main parameters of the ECR ion source, RFQ and IH-DTL of the SSC-LINAC are listed in Table 2. As a high intensity heavy ion injector of the SSC, the SSC-LINAC could increase the beam intensity by 1 ~ 2 order.

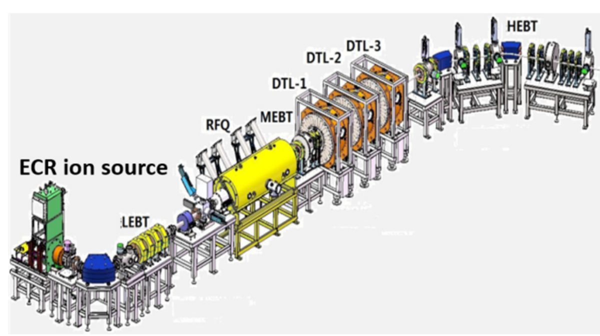

Figure 11: Layout of the SSC-LINAC.

ISBN: 978-3-95450-205-9 doi:10.18429/JACoW-Cyclotrons2019-MOA02

Table 2: The Main Parameters of the SSC-LINAC

Parameters	**Values**
Design ion	$^{238}U^{34+}$
ECR ion source	
Extraction voltage	25 kV
Max. axial injection field	2.3 T
Microwave frequency	18 GHz
4-rod RFQ	
Frequency	53.667 MHz
Input energy	3.728 keV/u
Output energy	143 keV/u
Inter-electrode voltage	70 kV
RF power	35 kW
Max. current	0.5 emA
IH-DTL	
Frequency	53.667 MHz
Input energy	0.143 MeV/u
Output energy	1.025 MeV/u

Overview of CSR-LINAC

The CSR-LINAC consists of a superconducting ECR ion source, a normal-conducting IH-RFQ, and six Interdigital H-type Drift Tube linac (IH-DTL) cavities. The main parameters of the CSR-Linac are listed in Table 3. Compared with the SSC, the CSR-LINAC could increase the beam intensity by 1 ~ 2 order, the beam current could be reached 1 ~ 10 pμA for various ions, and can accelerate all kinds of heavy ions to 7.272 MeV/u.

Table 3: The Main Parameters of the CSR-LINAC

Parameters	**Values**
Q/A	1/3-1/7
Frequency	108.48/216.96 MHz
Beam current	3 emA
Duration	3 ms
Repetition	10 Hz
RFQ input/out energy	4/300 keV/u
DTL input/out energy	0.3/7.272 keV/u
Transmission (design)	90%

CONCLUSION

The operation performance of the HIRFL has been improved significantly in the recent five years, and many important experiments are studied. To meet the requirement of nuclear physics, atomic physics and other related application, the two new injectors of the SSC-Linac and CSR-Linac will be built. The SSC-Linac is to commission in 2020 and the CSR-Linac is to be finished in the next few years. As a result, the whole performance of the HIRFL-CSR complex will be further enhanced.

ISBN: 978-3-95450-205-9 doi:10.18429/JACoW-Cyclotrons2019-MOA03

STATUS REPORT ON GANIL AND UPGRADE OF SPIRAL1

O. Kamalou, P. Delahaye, M. Dubois, A. Savalle, GANIL, CEA-DSM/CNRS-IN2P3, Caen, France

Abstract

The GANIL facility (Grand Accélérateur National d'Ions Lourds) at Caen is dedicated for acceleration of heavy ion beams for nuclear physics, atomic physics, and radiobiology and material irradiation. Nowadays, an intense exotic beam is produced by the Isotope Separation On-Line method at the SPIRAL1 facility since 2001. New demands from the physics community motivated the upgrade of this facility in order to extend the range of post-accelerated radioactive ions. A 2 MEuro project allowed the profound modification of the facility and the commissioning was achieved in 2017. The status of this facility and the last results will be presented. The review of the cyclotron operation from 2001 to 2019 will be presented as well.

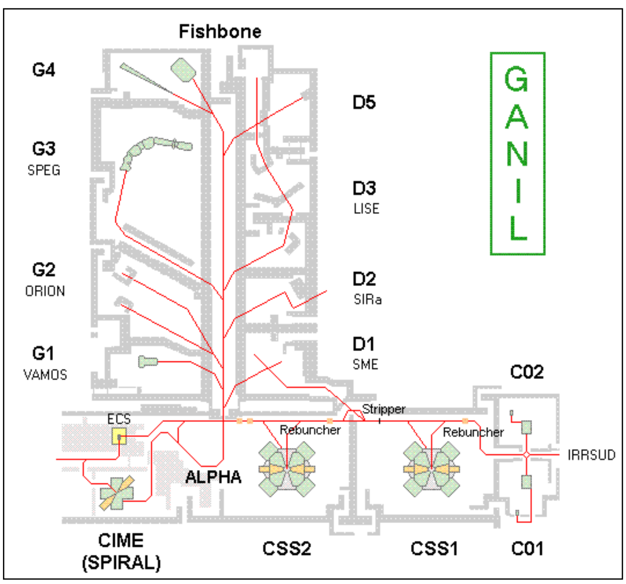

Figure 1: GANIL Layout.

OPERATION REVIEW

Multi-beam delivery is routinely done at GANIL using its 5 existing cyclotrons (Fig. 1):

1. Beams from C01 or C02 are sent to an irradiation beam line IRRSUD (<1 MeV/A)0.
2. A charge state among the ion distribution after the ion stripping foil downstream CSS1 is sent to atomic physics, biology and solid states physics line D1 (4 - 13 MeV/A).
3. A high-energy beam out of CSS2 is transported to experimental areas (< 95 MeV/A), for nuclear physics and previous applications.
4. Finally, stable beams from SPIRAL1 source can be sent to LIRAT (< 10 keV/q) or post-accelerated by CIME and used for testing detector for example.

During radioactive beam production with SPIRAL1, the two first cases are still possible, CSS2 beam is sent toward the SPIRAL1 target, and radioactive beam is sent to the experimental areas.

In addition, Ion sources are available in “hall D” building for atomic physics at very low energy.

2001-2019 GANIL OPERATION STATUS

Since 2001 (Fig. 2), more than 56000 hours of pilot beam time has been delivered by GANIL to physics, which correspond to 93% of scheduled experiments.

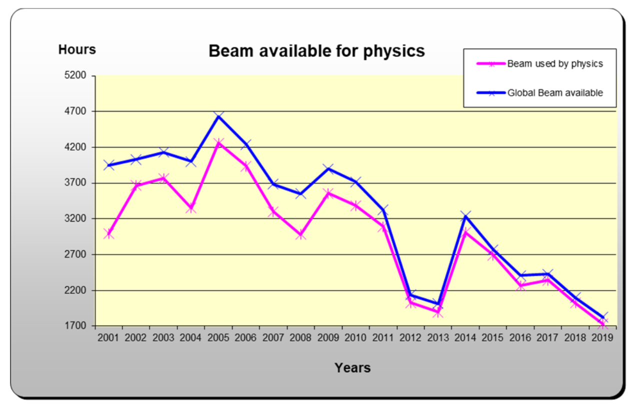

Figure 2: Beam time for physics.

In average, the number of beams delivered per year has increased until 2010. Owing to the construction and assembly of the new SPIRAL2 accelerator and upgrade of SPIRAL1, the running time has been shrinking to devote more human resources to the project SPIRAL2, in particular in 2012 and 2013 with only 2000 hours of experiments time (instead of 3500 hours per years).

Figure 3 shows the statistic running of the machine over 19 years. 67.8% of beam time is dedicated to Physics and 12.6% for machine tuning.

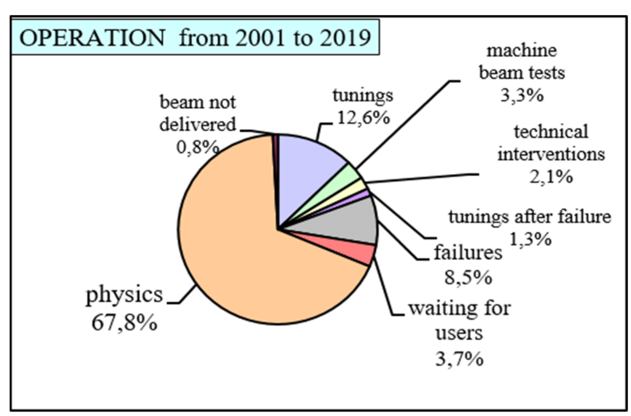

Figure 3: Statistic Running.

ISBN: 978-3-95450-205-9 doi:10.18429/JACoW-Cyclotrons2019-MOA03

In 2019 (April to July), the pilot beam time was 64%, the failure rate is 16% (highest value till 2013).

WATER LEAK NORTH RF CAVITY CSS1 AND BEAM TUNNING

In the past 2 years, the GANIL facility has encountered water leak problems mainly on the RF cooling circuits (an example given in Fig. 4 for CSS1 North cavity which is happening in 2018).

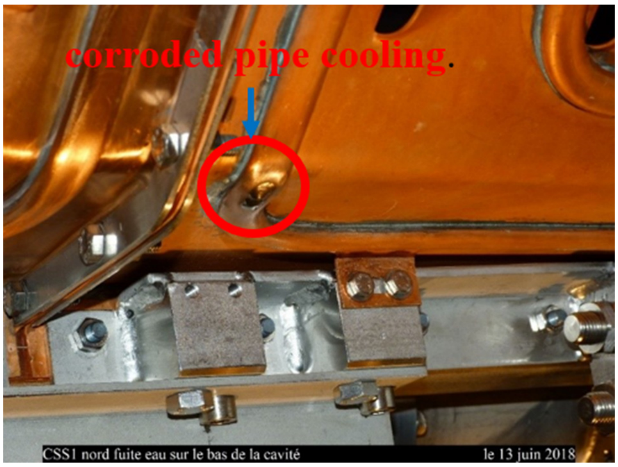

Figure 4: Corroded Pipe Cooling.

Instead of undertaking a water leak reparation, which would have caused a one-week time loss for experiment, the CSS1 cyclotron was tuned with one cavity as we can see in Fig. 5. Without North cavity, the magnetic fields should be decreased in the sectors D and A and increased in the sectors B and C. The optimized magnetic field for easy beam ejection could not be achieved in this degraded configuration. The beam time tuning was increased by a factor 3. Nevertheless, we managed to tune the CSS1 with only one cavity with 90% of efficiency for 16O at 95 MeV/A.

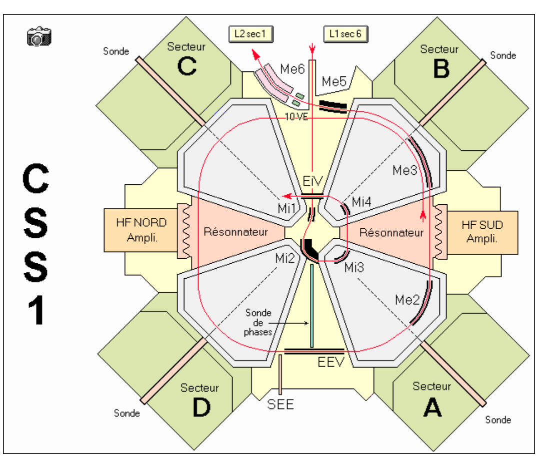

Figure 5: CSS1 Cyclotron.

SPIRAL1 UPGRADE

The first version of the Isotope Separator On Line System installed at GANIL, named SPIRAL1, has delivered radioactive ions for 13 years. Radioactive atoms produced by fragmentation of swift heavy ions on a carbon target are ionized in the Nanogan ECR multi-charged ion source before being post-accelerated in a cyclotron. The cyclotron energy is 1.2 to 25 MeV/A using harmonics 2 to 6. Several beams of gaseous elements (He, N, O, F, Ne, Ar, Kr) was produced for nuclear physics.

Due to the design of the Target Ion Source System (TISS), mainly gaseous ions were produced so far. To satisfy the request of physics community for extending the choice of ions to those made from condensable elements, with masses up to Xe, an upgrade of SPIRAL1 has been undertaken [1]. Beams and technical options considered during the prospective phase have been sorted out. A schematic of the ongoing upgrade is presented in Fig. 6.

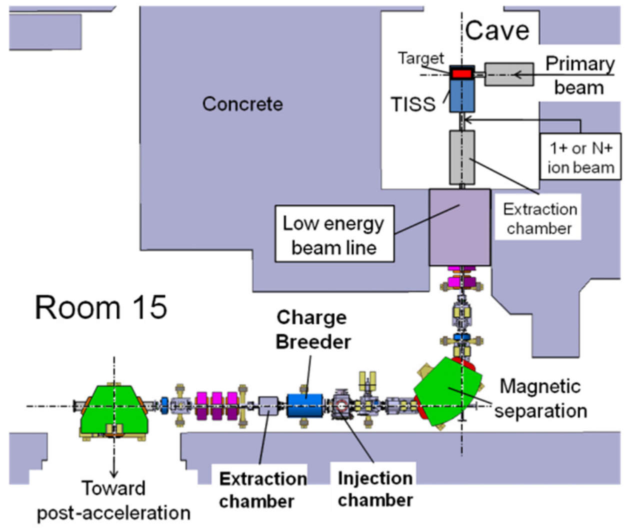

Figure 6: SPIRAL1 Upgrade Layout.

New targets (Nb, SiC,..) and new type of Surface ionization, FEBIAD (Forced Electron Beam Induced Arc Discharge) or ECR (Electron Cyclotron Resonance) ion sources [2, 3] can now be operated thanks to the modification of the production cave to provide 1+ beam of condensable elements. After mass separation the 1+ beam is injected into a Phoenix charge breeder, inserted in the low energy beam lines. The increase of charge state of the radioactive ions from 1+ to N+ for post-acceleration enables to access energy up to 25 MeV/A using the CIME accelerator.

The new TISS was tested at nominal power (1200W of 36Ar at 95 MeV/A) in the SPIRAL 1 beam lines in December 2013. The first scientific results obtained at SPIRAL 1 with a FEBIAD source was published [4, 5]. The integration of the charge breeder and the beam line modification were achieved between 2013 and 2016.

In 2017, the charge breeder and beam line off-line commissioning was started. The whole system was validated (performance, beam optics) by the end of 2017 [6].

In April and May 2018, the SPIRAL1 upgraded facility was ready for radioactive ion beam production. A beam of 95 MeV/A of 20Ne first impinged on the SPIRAL1 target

ISBN: 978-3-95450-205-9 doi:10.18429/JACoW-Cyclotrons2019-MOA03

for the production of a 17F beam at 10 MeV/A for the E750 experiment. The FEBIAD source failed after 6 hours of target irradiation. At that time, the failure was attributed to shortcut of the anode insulator [7], which was possibly caused by a deposition of direct C vapors generated by the primary beam impinging on the target. To fix this issue, a helical chicane was inserted in the transfer tube to stop the vapors from the irradiated target to the insulator (Fig. 7).

Figure 7: Helical Chicane Photo.

In 2019, the 40Ca, 95 MeV/A primary beam was sent to SPIRAL1 carbon target. An isomeric beam of 38 mK at 9 MeV/A was produced successfully and accelerated by the CIME cyclotron for E737 experiment. More than $5{\times}10^5$ pps of 38 K was sent to the experimental room for nuclear physics during two weeks. Following the experiment, a yield check showed degraded performances for the production of 33Cl, 23Mg and 25Na beams compared to 2013. We suspected the chicane to slow down significantly the release of these isotopes. The chicane was removed in an ultimate test with the FEBIAD TISS in 2019, with a primary beam of 36Ar at 95 MeV/A. For this last test, other tricks than the chicane were used to prevent deposition of C vapors on the insulators: a local screening of the insulators was improved, and Repieces, less conductive than the original Mo pieces, were used for the connection of the fragile insulators to the hot body of the anode. Once the chicane removed, we could measure as expected yields compatible with the measurements done in 2013.

The mass resolving of CIME cyclotron allow us to purify the beam in many cases for light element (A < 20). For heavier masses, and especially around 56Ni, which triggers a considerable scientific interest, a case by case study has to be done. In the coming years, the test of different stripping foils behind CIME to separate masses delivered from the FEBIAD TISS, and reaccelerated by CIME to energies of 10-12 MeV/A, will be investigated in details.

REFERENCES

[1] P. Jardin *et al.,* "Status of the SPIRAL I upgrade at GANIL", *Rev. Sci. Instrum.,* vol. 83, p. 02A911, Feb 2012. doi:10.1063.1.3672435

[2] S. Sundell *et al.,* "Ion source with combined cathode and transfer line heating", *Nucl. Instrum. Methods Phys. Res., Sect. B*, vol. 70, pp. 160-164, Aug. 1992. doi:10.1016/0168-583X(92)95926-I

[3] R. Vondrasek *et al.,* "Improved charge breeding efficiency of light ions with an electron cyclotron resonance ion source", *Rev. Sci. Instrum*., vol. 83, p. 113303, Nov. 2012. doi:10.1063.1.4768533

[4] J. Grinyer *et al., "*High-precision half-life measurements of the T=1/2 mirror beta decays 17F and 33Cl*", Phys. Rev. C,* vol. 92, p. 045503, Oct. 2015. doi:10.1103/PhysRevC.92.045503

[5] J. Grinyer *et al.,* "High-precision half-life measurement for the isospin T= ½ mirror β^+decay of ^{21}Na", *Phys. Rev. C*, vol. 91 p. 032501, Mar. 2015. doi:10.1103/PhysRevC.91.032501

[6] L. Maunoury *et al*., "SPIRAL1: A Versatile User Facility", in *Proc. 23th International Workshop on ECR Ion Sources (ECRIS'18)*, Catania, Italy, Sep. 2018, pp. 29-33. doi:10.18429/JACoW-ECRIS2018-MOC4

[7] P. Delahaye *et al.,* "New exotic beams from the SPIRAL1 upgrade"*, Nucl. Instrum. Methods Phys. Res., Sect. B,* to be published. doi:10.1016/j.nimb.2019.04.063

ISBN: 978-3-95450-205-9 doi:10.18429/JACoW-Cyclotrons2019-MOB01

RECENT PROGRESS IN RIKEN RI BEAM FACTORY

O. Kamigaito*, T. Dantsuka, M. Fujimaki, N. Fukunishi, H. Hasebe,
Y. Higurashi, E. Ikezawa, H. Imao, M. Kidera, M. Komiyama, K. Kumagai, T. Maie,
Y. Miyake, T. Nagatomo, T. Nakagawa, M. Nakamura, T. Nishi, J. Ohnishi, H. Okuno,
K. Ozeki, N. Sakamoto, K. Suda, A. Uchiyama, T. Watanabe, Y. Watanabe, K. Yamada
RIKEN, Nishina Center for Accelerator-Based Science, Wako-shi, Saitama, Japan

Abstract

Recent efforts at the RIKEN RI Beam Factory (RIBF) are aimed at increasing the beam intensity for very heavy ions such as xenon and uranium. This paper presents upgrade programs carried out over the past few years, including modifications of the RF cavities of the RIKEN Ring Cyclotron and improvements of the charge stripper. The current performance of the RIBF accelerators and future plans to further increase the beam intensity are also presented.

OVERVIEW OF RIBF

The Radioactive Isotope Beam Factory (RIBF) at RIKEN is a cyclotron-based accelerator facility that uses fragmentation or fission reactions of intense heavy-ion beams to produce intense RI beams over the whole atomic mass range [1, 2]. The RIBF started beam delivery in 2007, after the commissioning of the three ring cyclotrons, fRC, IRC, and SRC, that were constructed to boost the energies of the beams accelerated by the RIKEN Ring Cyclotron (RRC), shown in Fig. 1. The main specifications of the four ring cyclotrons are summarized in Table 1. There are currently three injectors, AVF, RILAC, and RILAC2, that provide a wide variety of heavy-ion beams, as described below.

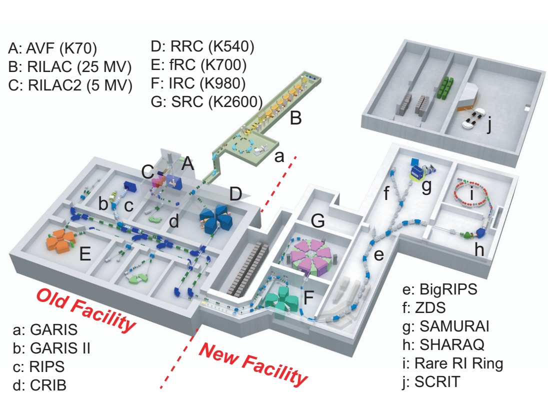

Figure 1: Schematic drawing of the RIKEN RI Beam Factory (RIBF). The accelerators (A–G) and experimental devices (a–j) are presented.

The scientific goals of the RIBF include establishing a new and comprehensive way of describing nuclei and improving the understanding of the synthesis of heavy elements in the universe. As shown in Fig. 1, distinctive experimental devices have been set up in the new facility, as well as in the old facility, which mainly uses the beams from the RRC.

We are also promoting applications of heavy-ion beams to various research fields, such as nuclear chemistry and biological science, using the heavy ion beams from RILAC, AVF, RRC, and IRC.

Table 1: Specifications of the RIBF Ring Cyclotrons

	RRC	fRC	IRC	SRC
Sectors	4	4	4	6
K [MeV]	540	700	980	2600
R_{inj} [cm]	89	156	278	356
R_{ext} [cm]	356	330	415	536
Weight [t]	2400	1300	2900	8300
Trim coils/ main coil	26	10	20	4 (SC) + 22 (NC)
RF system	2	2 + FT	2 + FT	4 + FT
Freq. [MHz]	18–38	54.75	18–38	18–38

One of the most important features of the RIBF accelerator system is the ability to accelerate all ions from hydrogen to uranium to 70% of the speed of light. To make this possible, three acceleration modes are used in the RIBF accelerators, as shown in Fig. 2.

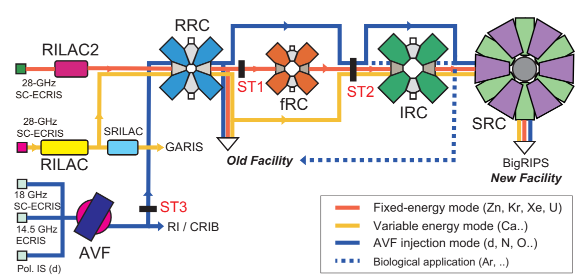

Figure 2: Accelerator chain of the RIBF. The three injectors, RILAC2, RILAC, and the AVF cyclotron, are followed by four booster cyclotrons, the RIKEN Ring Cyclotron (RRC), fixed-frequency Ring Cyclotron (fRC), Intermediate-stage Ring Cyclotron (IRC), and Superconducting Ring Cyclotron (SRC). The charge strippers are indicated by labels in red text (ST1–ST3). The superconducting linac booster, SRILAC, is under construction [3].

The first mode is a fixed-energy mode, originally intended for accelerating very heavy ions such as xenon and uranium. This mode uses the RILAC2 injector with a powerful 28-GHz superconducting ECR ion source, and boosts the beam energy up to 345 MeV/u with the four booster ring cyclotrons (RRC, fRC, IRC, SRC). Two charge strippers are used for the

* kamigait@riken.jp

ISBN: 978-3-95450-205-9 doi:10.18429/JACoW-Cyclotrons2019-MOB01

uranium beam. One is a helium gas stripper located at the exit of the RRC (E = 11 MeV/u), and the other is a rotating graphite-sheet stripper located between fRC and IRC (E = 50 MeV/u). Recently, the high performance of the ion source has made it possible to accelerate zinc and krypton beams in this mode using only the second charge stripper [4].

The second acceleration mode is a variable energy mode that uses the RILAC, RRC, IRC, and SRC to accelerate medium-mass ions such as calcium. The beam energy from the SRC can be changed over a wide range below 400 MeV/u by changing the RF frequency. The third mode uses the AVF cyclotron as an injector, with two boosters, the RRC and SRC. This mode is exclusively used for light ions such as deuterons, nitrogen, and oxygen. By changing the RF frequency, the beam energy from the SRC can also be changed in the range below 440 MeV/u.

RECENT RESEARCH & DEVELOPMENT

Among the heavy ion beams, the uranium beam is most effective because it can generate a medium-mass RI beam far from the stability line through fission reactions. Therefore, recent research and development efforts have concentrated on increasing the intensity of the uranium beam. This section gives some examples related to these efforts.

Ion Source [5]

Uranium ions are first generated in the 28-GHz superconducting ECR ion source (SC-ECRIS), and U^{35+} ions are accelerated by the RILAC2 and RRC. During the first few years after 2007, a sputtering method with a metallic uranium rod was used to generate uranium ions, and a U^{35+} beam of approximately 100 eμA could be extracted from the ion source during the beam time. However, the beam stability was not satisfactory. Therefore, in 2013, we started the development of a high-temperature oven (HTO) method. This method was expected to control the amount of vapor supplied to the ion source plasma.

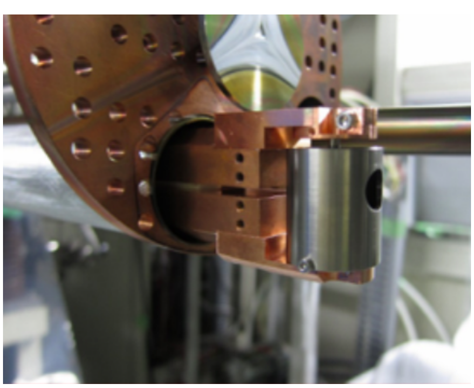

Figure 3: High-temperature oven (HTO) used in the 28-GHz superconducting ECR ion source (SC-ECRIS).

Figure 3 shows the HTO in the SC-ECRIS. The HTO is equipped with a pure tungsten crucible loaded with uranium oxide. The crucible is supported by a pair of copper rods that act as bus bars carrying DC current to heat the crucible directly. A temperature of 2000 °C is required for the crucible to bring the vapor pressure of uranium oxide to 0.1–1 Pa.

The HTO has been used in the uranium beam time since autumn 2016. In the first beam time, the U^{35+} beam was successfully supplied for 34 consecutive days with a current of 120 eμA or more. Although the vapor-ejection hole was blocked during the beam time in subsequent years, the beam intensity supplied to the RILAC2 injector was kept at 100–130 eμA at the ion source for more than one month.

Helium Gas Stripper [6]

The most important issue in the first few years of RIBF operation was the lack of a charge stripper for powerful uranium beams. In order to solve this problem, in 2012, we developed a window-less helium gas stripper based on a five-stage differential pumping system, as shown schematically in Fig. 4. The target cell of the stripper contains helium gas at approximately 7 kPa, while the gas leaked into the next stages is re-circulated to the target cell with the help of mechanical booster pumps. We found that the fraction of the charge state of 64+ is enhanced due to the atomic shell effect, and uranium ions with this charge state are accelerated by the next ring cyclotron, fRC. This system has played an essential role in increasing the uranium beam intensity. In fact, the present intensity of uranium beams injected into the stripper has reached 10^{13}/s.

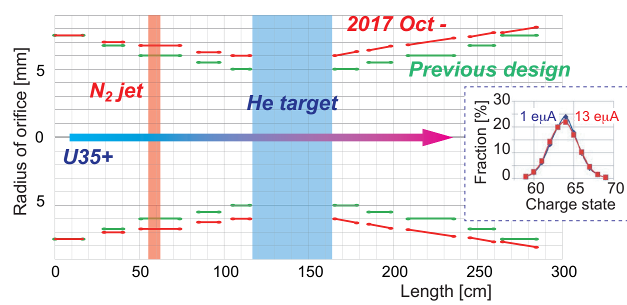

Figure 4: Orifice diameters in the helium gas stripper. The green lines represent the orifice diameters in the original structure. The N_2 gas-jet has expanded the orifice diameters to those represented by the red lines.

However, increasing the injected beam intensities has caused various difficulties in the operation of the helium gas stripper. The quality of beams injected into the stripper decreases during high-intensity operation due to space charge effects in the low energy section of the RILAC2. A small fraction of the beam loss in the stripper orifices can cause serious hardware failure or the generation of radioactivity. For efficient transmission of high intensity beams, the diameter of the orifices of the helium gas stripper had to be increased.

On the other hand, a slight leak of helium gas into the RRC located 7 m upstream of the stripper is a serious problem in high-intensity operation. Since the RRC has only cryogenic pumps, the leaked helium gas gradually accumulates in the RRC. Collisions between the uranium ions being accelerated

ISBN: 978-3-95450-205-9 doi:10.18429/JACoW-Cyclotrons2019-MOB01

and the helium atoms stored in the RRC can easily change the charge states and cause beam loss. Due to the acceleration of high-intensity uranium beams, such beam losses induce further losses because of local pressure increases due to gas desorption.

To overcome these difficulties, we developed a nitrogen gas-jet curtain method. By using a curtain-like nitrogen gas-jet separating the two chambers, the flow of helium to the low pressure side can be shut off, and the leaked gas is exchanged from He to N_2. Based on this, a N_2 gas-jet curtain was installed in the helium gas stripper and tested, as shown in Fig. 4. The sealing ability was found to be greatly improved. The gas leaked upstream in the beam line was successfully replaced with nitrogen, as desired. Also, we found that the N_2 gas-jet curtain works as a pre-stripper. Initial rapid stripping in the N_2 gas-jet curtain reduces the required pressure of helium gas by approximately 15%.

The improved system was used in the user beam time in 2017. The output intensity was increased by 25% due to improved transmission efficiency. No serious pressure rise in the RRC was observed. As shown below, the N_2 gas-jet curtain method contributed significantly to the new world record output intensity achieved in 2017 (71 pnA at 345 MeV/u).

RRC Cavity [7, 8]

The RIKEN Ring Cyclotron (RRC) has two acceleration cavities based on variable-frequency, half-wavelength resonator, constructed more than 30 years ago [9]. The resonant frequency of this cavity is varied by moving two boxes vertically, as shown in Fig. 5. The inner height of the cavities could be made as small as 2.1 m, while keeping a wide range of resonant frequency from 20 to 45 MHz. However, the frequency for uranium acceleration is 18.25 MHz, which is outside the designed range. The gap length between the dee electrode and the movable box had to be made as small as 20 mm, as shown in Fig. 5. During the acceleration of the uranium beam, the narrow gap between the dee electrode and the movable box caused a bottleneck problem limiting the cavity voltage to a maximum of 80 kV. In addition to frequent discharges during operation, this narrow gap increases the capacitance in the cavity, thus lowering the shunt impedance. Furthermore, due to the low acceleration voltage, the uranium beam current reached a space charge limit in the RRC [10].

Therefore, as shown in Fig. 5, the internal components of the cavity, the stems and the dee electrode, were replaced, leaving the external box and movable box of the cavity unchanged. The frequency range of the RRC cavity is shifted downward by the insertion of a notch into the stem, which was originally straight. Since the RRC cavities have not operated at frequencies above 39 MHz in recent years, the frequency range was set to 16–38 MHz after remodeling. The shunt impedance, voltage distribution, and frequency range were optimized by changing the notch size based on 3D electromagnetic calculations using the computer code Microwave Studio (MWS).

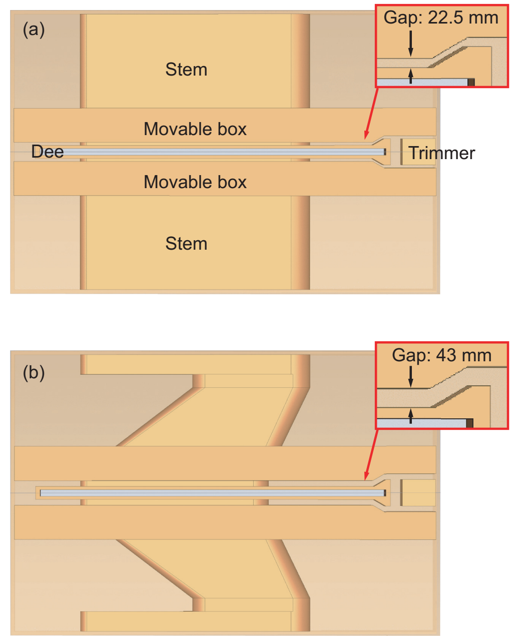

Figure 5: Calculation models for the original cavity (upper panel) and the modified cavity (lower panel). The gap length required for a resonant frequency of 18.25 MHz is shown in each panel.

The modification work was carried out from February to March 2018, and in April a low power RF test was performed with a network analyzer. Figure 6 shows a photo of the inside of the cavity after the modification. The test results showed that the frequency range covers the design range. In addition, as expected, the quality factor Q_0 almost doubled at 18.25 MHz. At the same time, the old degraded power supplies for the tetrode grids in the RF amplifiers were updated to improve the stability.

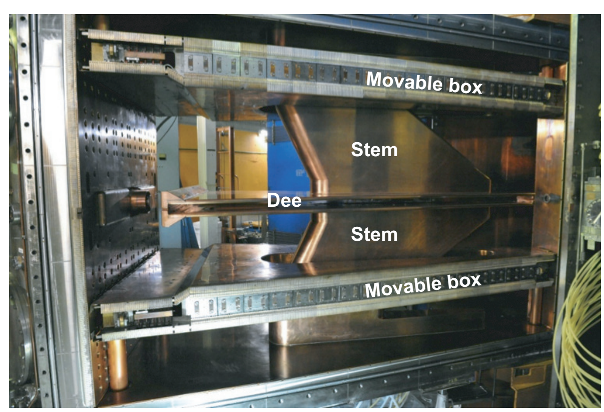

Figure 6: Internal view of the modified RRC cavity.

The new cavities have been used in beam time since May 2018 and show good operational performance from 18.25 to 32.6 MHz. In particular, stable operation was achieved at a voltage of 120 kV at 18.25 MHz. This is due to an improvement in shunt impedance and an increase in the gap length between the dee and the movable box. In fact, the

ISBN: 978-3-95450-205-9 doi:10.18429/JACoW-Cyclotrons2019-MOB01

frequency of voltage breakdown has decreased significantly, as shown in Fig. 7. The bottleneck problem during uranium acceleration was solved in this way. However, due to production problems, cooling water leaked into the vacuum several times, and we are currently considering countermeasures.

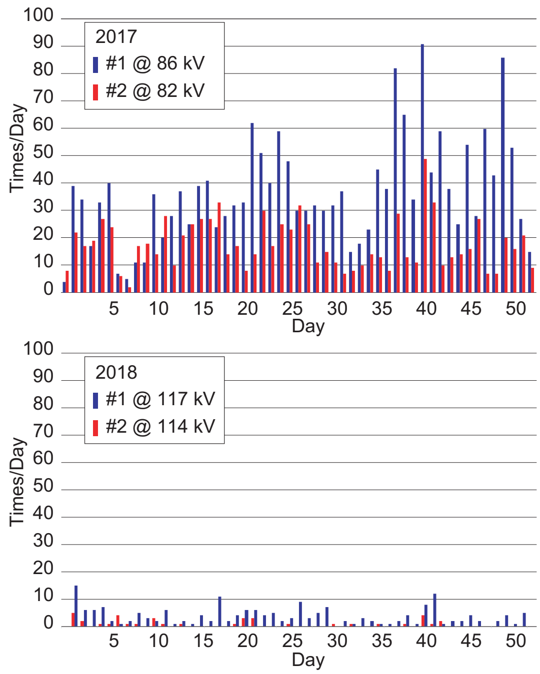

Figure 7: Comparison of frequency of voltage breakdown during the uranium beam time in 2017 (upper panel) and that in 2018 (lower panel). After the modification in 2018, the frequency of the breakdown decreased significantly despite the increased acceleration voltage.

PRESENT STATUS

The evolution of the maximum beam intensity for the ion beams accelerated at RIBF is shown in Fig. 8. Through continuous efforts including the research and development described above, the uranium intensity now exceeds 70 pnA and the beam power has reached 6 kW. The intensity of the xenon beam in 2019 is 70% higher than the previous value, mainly due to the RRC cavity modification. The beam power of medium-mass ions such as calcium and krypton already exceeds 10 kW, as shown in Fig. 8.

The transmission efficiency during uranium beam acceleration is also summarized in Fig. 9. It can be seen that the overall transmission efficiency has almost doubled over the past few years. The improvement in 2017 is due to a change in the beam tuning of the RRC with a reduced off-centering amplitude [11] in addition to the improvements in the helium gas stripper described above.

FUTURE PLANS

At present, the beam intensities extracted from the RIBF accelerator are the highest among rare isotope beam (RIB) facilities worldwide. However, a number of next-generation

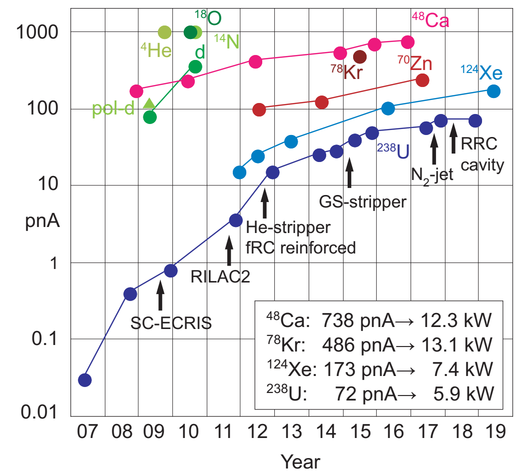

Figure 8: Evolution of the beam intensity at the exit of the SRC since the start of operation of RIBF in 2007. The maximum intensity achieved so far is presented for ^{48}Ca, ^{78}Kr, ^{124}Xe, and ^{238}U beams, along with the corresponding beam power. The main R&D items for increasing the uranium beam are also indicated.

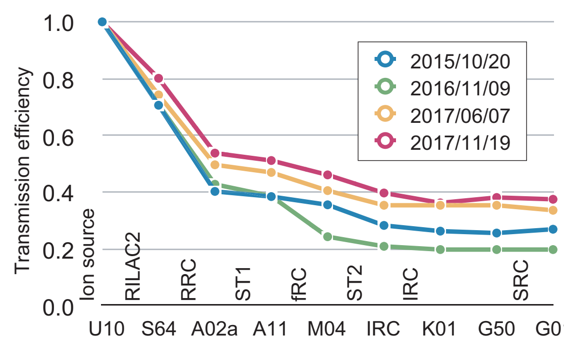

Figure 9: Transmission efficiency during uranium beam acceleration. The horizontal axis corresponds to the position of the Faraday cups in the accelerator chain. Note that the stripping efficiencies in the charger strippers are not included in the transmission efficiency.

RIB facilities are currently under construction in various parts of the world or are being planned. These include FRIB in the USA, FAIR in Germany, RAON in Korea, and HIAF in China. Some of them aim to achieve heavy ion beam acceleration at 400 kW by the early 2020s. Therefore, an upgrade plan is needed to maintain RIBF's future position as the world's leading facility in RIB science.

As mentioned above, two charge strippers are used during uranium acceleration at RIBF. In this acceleration scheme, the total stripping efficiency is 5% at most, as shown in Fig. 10. FRIB, on the other hand, will use a multi-charge acceleration method, where five charge states are accelerated simultaneously using the superconducting linac. The target effective efficiency of the stripper is approximately 85%. Unfortunately, this method is not applicable to acceleration schemes using cyclotrons.

ISBN: 978-3-95450-205-9 doi:10.18429/JACoW-Cyclotrons2019-MOB01

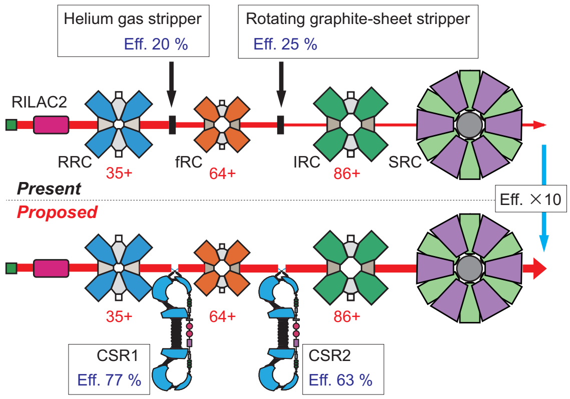

Figure 10: Present (upper panel) and proposed (lower panel) accelerator chains for the uranium beam at RIBF. The present stripping efficiency is 5%. Replacing the two charge strippers with charge stripper rings (CSR1 and CSR2) is expected to increase the total stripping efficiency to about 50%.

To reduce beam loss due to charge stripping at RIBF, a new charge stripping concept, the charge stripping ring (CSR), was proposed [6]. Figure 11 shows a schematic layout of the CSR optimized for the second stripper at 50 MeV/u. The U^{64+} beams are first injected into the ring with a charge exchange injection scheme. The energy losses in the stripper are recovered with the RF cavity following the stripper. The beams with U^{86+} are extracted using extractors based on static magnetic or electric fields. Ion beams other than those with the selected charge state (86+) circulate and reenter the stripper.

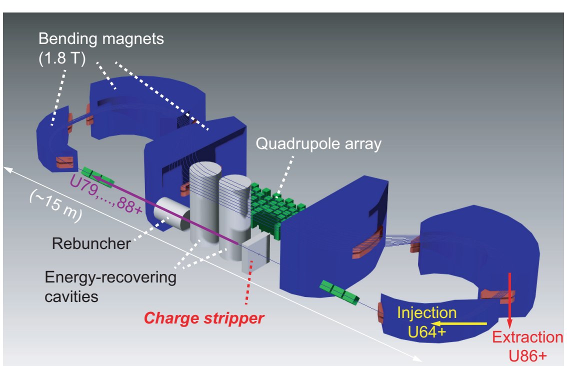

Figure 11: Schematic drawing of the charge stripper ring, optimized for the second stripping stage at the RIBF.

The key point of the CSR is that the ring is isometric for all the charge states and retains the bunch structure. In the present design, the magnetic field is 1.8 T and the size is about 15 m × 5 m. Specially designed quadrupole magnets are placed for orbits of all charge states independently at the dispersive region, where the orbit separation between two adjacent charge states is approximately 10 cm. The expected heat load on the stripper (3 mg/cm^2) is approximately 900 W. A rotating graphite-sheet stripper is a possible candidate.

According to the simulations, the effective stripping efficiency can be increased up to 77% and 63% for the first and second CSRs, respectively. Therefore, if we install the CSRs in place of the present charge strippers, the total efficiency of stripping during uranium acceleration will be 10 times the current value, as shown in Fig. 10.

ACKNOWLEDGMENTS

The authors would like to thank the SAS operators for making significant contributions to the RIBF accelerators.

REFERENCES

[1] Y. Yano, "The RIKEN RI Beam Factory Project: A status report", *Nucl. Instrum. Methods Phys. Rev., Sect. B*, vol. 261, pp. 1009–1013, 2007. doi:10.1016/j.nimb.2007.04.174

[2] H. Okuno, N. Fukunishi, and O. Kamigaito, "Progress of RIBF accelerators", *Prog. Theor. Exp. Phys.*, vol. 2012, pp. 03C002, 2012. doi:10.1093/ptep/pts046

[3] N. Sakamoto *et al.*, "Development of superconducting quarter-wave resonators and cryomodules for low-beta ion accelerators at RIKEN Radioactive Isotope Beam Factory", in *Proc. 19th Int. Conf. RF Superconductivity (SRF'19)*, Dresden, Germany, Jul. 2019. doi:10.18429/JACoW-SRF2019-WETEB1

[4] O. Kamigaito *et al.*, "Present status and future plan of RIKEN RI Beam Factory", in *Proc. 7th Int. Particle Accelerator Conf. (IPAC'16)*, Busan, Korea, May 2016, pp. 1281–1283. doi:10.18429/JACoW-IPAC2016-TUPMR022

[5] J. Ohnishi, Y. Higurashi, and T. Nakagawa, "Practical use of high-temperature oven for 28 GHz superconducting ECR ion source at RIKEN", in *Proc. 23th International Workshop on ECR Ion Sources (ECRIS'18)*, Catania, Italy, Sep. 2018, pp. 180–184. doi:10.18429/JACoW-ECRIS2018-WEB4

[6] H. Imao, "Development of gas stripper at RIBF", in *Proc. 9th Int. Particle Accelerator Conf. (IPAC'18)*, Vancouver, Canada, Apr.-May 2018, pp. 41–46. doi:10.18429/JACoW-IPAC2018-MOZGBE1

[7] K. Yamada, K. Suda, N. Sakamoto, and O. Kamigaito, "Remodeling of acceleration cavity resonators for RIKEN ring cyclotron", RIKEN Accelerator Progress Report, vol. 52, 2019, to be published.

[8] N. Tsukiori *et al.*, "Status report of the operation of RIBF ring cyclotrons", presented at the 16th Annual Meeting of Particle Accelerator Society of Japan, Kyoto, Japan, Jul. – Aug. 2019, paper FSPH002, in Japanese.

[9] T. Fujisawa *et al.*, "The Radiofrequency System of the RIKEN Ring Cyclotron", *Nucl. Instrum. Methods Phys. Res., Sect. A*, vol. 292, pp. 1–11, Jun. 1990. doi:10.1016/0168-9002(90)91728-T

[10] H. Okuno *et al.*, "Operational experience and upgrade plans of the RIBF accelerator complex", in *Proc. 21th Int. Conf. on Cyclotrons and their Applications (Cyclotrons'16)*, Zurich, Switzerland, Sep. 2016, pp. 1–6. doi:10.18429/JACoW-Cyclotrons2016-MOA01

[11] N. Fukunishi, "Overview of the RIBF Accelerators", presented at the 18th Nuclear Physics PAC Meeting for Nuclear-Physics Experiments at RI Beam Factory, Wako, Japan, Dec. 2017, unpublished.

ISBN: 978-3-95450-205-9 doi:10.18429/JACoW-Cyclotrons2019-MOB02

PROGRESS WITH A NEW RADIOISOTOPE PRODUCTION FACILITY AND CONSTRUCTION OF RADIOACTIVE BEAM FACILITY AT iTHEMBA LABS

J. L. Conradie, J. K. Abraham, H. Anderson, L. S. Anthony, F. Azaiez, S. Baard, R. A. Bark, A. H. Barnard, P. Beukes, J. I. Broodryk, B. Cornelius, J. C. Cornell, J. G. de Villiers, H. du Plessis, W. Duckitt, D. T. Fourie, M. E. Hogan, I. H. Kohler, C. Lussi, J. Mira, H. W. Mostert, C. Naidoo, F. Nemulodi, M. Sakildien, V. F. Spannenberg, G. F. Steyn, N. P. Stodart, I. L. Strydom, R. W. Thomae, M. J. van Niekerk, P. A. van Schalkwyk

iThemba LABS, National Research Foundation, P.O. Box 722, Somerset West 7129, South Africa

Abstract

With the termination of the neutron and proton therapy programs at iThemba LABS, the use of the Separated Sector Cyclotron (SSC) has now shifted to nuclear physics research with both stable and radioactive ion beams, as well as biomedical research. A dedicated isotope production facility with a commercial 70 MeV H-minus cyclotron has been approved and both the cyclotron and isotope production target stations will be housed in the vaults that were previously used for the therapy programs. The status of this new facility will be reported. In the future the SSC will mostly be used for nuclear physics research, as well as the production of isotopes that cannot be produced with the 70 MeV H-minus cyclotron. At present the production of the α-emitting radionuclide Astatine (^{211}At) with a 28 MeV alpha beam is being investigated. Progress with the construction of a facility for production of radioactive beams will be discussed. There will also be reports on development work on the ECR ion sources and progress with implementation of an EPICS control system.

DEDICATED 70 MeV CYCLOTRON FOR ISOTOPE PRODUCTION

The initial idea to simultaneously produce radioisotopes and radioactive ion beams with a dedicated 70 MeV H-minus cyclotron was discarded due to a number of reasons as explained in [1]. A feasibility study has shown that a very cost effective, dedicated isotope production facility can be constructed at iThemba LABS by making use of the existing infrastructure, which became available when iThemba LABS discontinued proton and neutron therapy. The layout of the proposed facility is shown in Fig. 1. There will be two isotope production vaults (Fig. 1, vaults A and B) with two bombardment stations in each. The 70 MeV H-minus cyclotron will be housed in a separate vault (Fig. 1, vault C) located between the two isotope production vaults. The irradiated targets will be transported via a rail transport system, through new labyrinths that will be connected to existing labyrinths, to the existing hot cells. Detailed FLUKA calculations have been done for the different vaults and labyrinths to ensure that all the radiation safety requirements will be met.

With a dedicated isotope production facility available, the bulk production of isotopes with the SSC will end. In future the SSC will then mainly be used for nuclear physics research and the development of new radioisotopes that cannot be produced with the dedicated isotope production facility, such as the alpha emitter ^{211}At.

Following approval of the project by the Board of the National Research Foundation, a contract for the manufacturing, delivery and installation of the 70 MeV cyclotron and associated beamlines has recently been signed after an open tender process. The 70 MeV H-minus cyclotron is capable of delivering two 375 μA beams simultaneously from two extraction ports placed 180 degrees apart. The consulting engineers for the design, development and construction of the required infrastructure have also been appointed. The infrastructure of the 70 MeV project will be completely separated from the infrastructure of the existing SSC facility to ensure that the new facility can operate independently from the SSC facility.

The time schedule for completion of this project is 3 years. The cyclotron and beamlines will be delivered within 2 years after contract signature. During this time, the infrastructure and the modifications to the 3 vaults will be completed and the 4 target stations will be designed, built and installed. Commissioning of the new equipment will take place during the third year.

ISOTOPE PRODUCTION TARGET STATIONS

The current plan is to build four new target stations that will receive beam from the 70 MeV cyclotron. They will be similar in design to the existing horizontal-beam target station (HBTS or Elephant) at iThemba LABS, but with thicker local radiation shields and several other smaller modifications and improvements. These target stations will be identical in all respects except for the aperture of the entrance collimator, which can have different sizes on different stations. During bombardment, a target will be completely surrounded by a composite radiation shield, consisting of an inner iron layer, a borated paraffin wax middle layer and a lead outer layer. This local shielding will reduce the neutron flux into the vault by about three orders of magnitude and reduce the thickness of the concrete shielding required for the vault significantly. More details on the station design can be found in [2]. Target transfer between a station and an electric rail transport system will be facilitated by a robot arm. All target handing, including the connection of cooling water, will be done by remote control.

ISBN: 978-3-95450-205-9 doi:10.18429/JACoW-Cyclotrons2019-MOB02

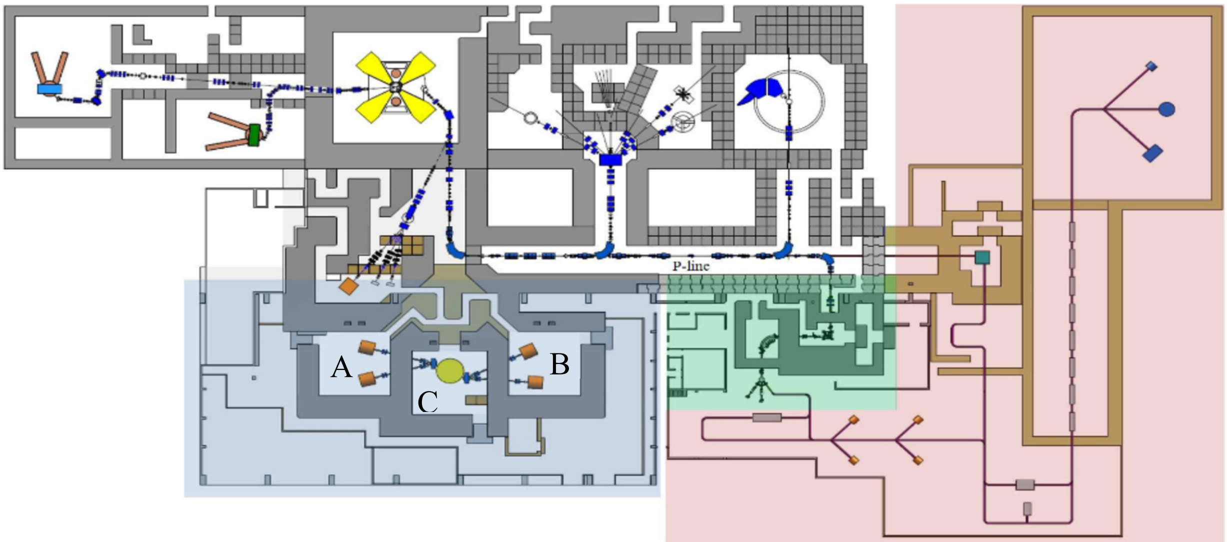

Figure 1: Layout of the main facility at iThemba LABS, with the new 70 MeV isotope production facility shaded in blue, the LERIB facility shaded in green and the second phase of the rare-isotope facility shaded in pink.

While target capsules with inner diameter sizes up to 52 mm have been foreseen for the future, it was not clear whether such large targets should be introduced from the outset. Currently, the largest target diameter of batch targets for radionuclide production in use by iThemba LABS is 40 mm, employing 66 MeV proton beams from the SSC with intensities up to 250 µA in the vertical-beam target station (VBTS). The decision was recently made to introduce the larger diameter of 52 mm from the outset with the new targetry for the long-lived radionuclides ^{22}Na, ^{68}Ge and ^{82}Sr on the 70 MeV cyclotron. This will increase the available target surface area in contact with cooling water, enabling an increase in beam intensity that a target can withstand. The thickness of individual cooling water layers will also be increased by 50% (from nominally 1 mm to 1.5 mm). This requires the volume flow rate of cooling water to be nearly double than currently being employed on the VBTS. Changes made to the cooling-water pusher arm and target holder will allow a flow rate of 250 l/min at a differential pressure of less than 10 bar. The new target holders will be very similar in design to the ones currently in use at iThemba LABS but upscaled to accommodate the bigger targets and increased flow rate.

PRODUCTION OF THE ALPHA EMITTER ASTATINE-211

The design of a dedicated target station for the production of the alpha emitter ^{211}At has recently been completed at iThemba LABS and construction is expected to start in due course. Targets consisting of a layer of Bi plated onto a water-cooled Al backing will be bombarded with a 28 MeV alpha-particle beam delivered by the SSC. A beam intensity up to 50 µA is anticipated. The targets will have a slant angle of 9° with respect to the beam axis to reduce the dissipated power density resulting from stopping the alpha particles within the Bi layer. The ^{209}Bi(α,2n)^{211}At reaction will be employed. The beam energy of 28 MeV is the maximum that can be employed as the ^{209}Bi(α,3n)^{210}At→^{210}Po reaction becomes significant above this energy. Since ^{210}Po is both long-lived and poisonous, its co-production has to be avoided. An agreement has recently been reached with the Department of Nuclear Medicine of the University of Pretoria, who will use the ^{211}At produced at iThemba LABS for targeted alpha-particle therapy (TAT).

RARE-ISOTOPES AT ITHEMBA LABS

Once the routine radionuclide production has been moved to the 70 MeV cyclotron, the SSC will be largely dedicated to research. To explore new frontiers in the field of nuclear physics, iThemba LABS has embarked on a project to establish a Low-Energy Rare-Isotope Beam (LERIB) facility, indicated in Fig. 1. The project will use the Isotope Separation On-Line (ISOL) method to produce radioactive isotopes of special interest in, for example, the study of neutron-rich nuclei involved in the r-process.

The project is proceeding in phases. Following a Memorandum of Agreement between the NRF and the Istituto Nazionale di Fisica Nucleare (INFN), a “front-end” Target/Ion Source (TIS) has been manufactured and delivered to iThemba LABS. It is being incorporated into an offline test facility as seen in Fig. 2. The TIS in the foreground, HV platform, extraction beamline complete with analysing magnet in the background is nearing completion and will be commissioned during the last quarter of 2019.

A complete EPICS-based control system is under development and will control all elements of the TIS, as well as the beamline components. With this test bench only stable beams will be produced by means of an oven technique and will be used to measure beam emittance from the TIS front end, ionisation yields of the surface ion source and efficiency of the extraction system. Provision is also made for experimenting with plasma and resonant laser ionisation techniques.

ISBN: 978-3-95450-205-9 doi:10.18429/JACoW-Cyclotrons2019-MOB02

Figure 2: The LERIB test-bench contains a target/ion source (foreground) on a high-voltage platform, and a beamline with an analysing magnet (background).

The next phase will see the construction of an on-line test facility, "LERIB Phase 0", over the next two to three years. RIBs will be produced through the bombardment of boron- and silicon carbide targets with a 1 μA, 66 MeV proton beam from the SSC. It will still be largely dedicated to the development of new RIB production techniques, such as the Versatile Arc Discharge Laser Ion Source (VADLIS) [3] and the use of carbonyl molecules to ionise refractory elements.

The construction of LERIB Phase 1 will follow, and will be capable of accommodating 66 MeV proton beams of up to 50 μA from the SSC. Uranium carbide targets will be fissioned in the TIS to produce neutron-rich ions of up to 60 keV energy. The facility will include a heavily shielded bombardment station, long term storage for spent targets, dedicated laboratories for target manufacture and later disposal, and an experimental hall.

The next step beyond LERIB, Phase 2 (see Fig. 1), will be to post-accelerate the low-energy RIBs to high-energies, sufficient to initiate nuclear reactions. Because LERIB will use the SSC as the driver accelerator, a new post-accelerator will be required. The requirement of high beam transport efficiency and beam purity leads to a system needing an RFQ beam cooler and high-resolution mass separator to refine the LERIB beams. Next, they will be charge bred for post-acceleration in one of two ion sources, i.e. an ECRIS or an EBIS. The post-accelerator is envisaged to be a LINAC in order to optimize transport efficiency. Post-accelerated energies will initially be approximately 5 MeV/A.

ECR ION SOURCE DEVELOPMENT

The two electron cyclotron resonance (ECR) ion sources at iThemba LABS can be operated simultaneously, i.e. the required beam for cyclotron acceleration is delivered from one source, while the second source can be used for beam development. ECRIS4, which was originally built by GANIL for the Helmholtz-Zentrum Berlin [4] delivers ion beams from gases and fluids. In addition, the source was equipped with an injection system for the so-called Metal Ions from Volatile Compound (MIVOC) method [5]. Due to the request for nuclear physics experiments with metallic ions of isotopes with low natural abundance, a program to produce metallocene from enriched elements was developed resulting in, for example, ion beam intensities of 30 eμA of $^{62}Ni^{8+}$ [6]. A second ECRIS (GTS2) that is based on the design of the Grenoble Test Source [7] is used to supply beams for nuclear physics experiments, which require elements like $^{1,2}H$, $^{3,4}He$, ^{12}C, ^{14}N, $^{16,18}O$, $^{20,22}Ne$, $^{36,40}Ar$, ^{86}Kr and $^{129,132,136}Xe$. In addition, under our collaboration with the ion source group of the Flerov Laboratory of Nuclear Reactions at the Joint Institute of Nuclear Research in Dubna, experiments for the production of intense metallic ion beams by oven technique were performed. With a modified micro oven [8] stable beams of Li, Mg, Ca and Bi with intensities of tens of μA were produced and are available for new fields of nuclear physics experiments at iThemba LABS [9].

NEW DIGITAL LOW-LEVEL RF CONTROL SYSTEM

iThemba LABS has successfully designed and implemented a new broadband digital low-level RF control system for cyclotrons that operates over a wide frequency range of 2-100 MHz and can achieve peak-peak amplitude and phase stabilities of 0.01% and 0.01°, respectively [10, 11, 12]. The systems have been successfully integrated at iThemba LABS into the K=8 and K=10 injector cyclotrons (SPC1 and SPC2), the K=200 separated sector cyclotron (SSC), the SSC flat-topping system, the pulse-selector system and three RF bunchers (AX, J and K-lines). In total there are 13 RF control systems now in full time operation since July 2017 [11, 12].

The systems have led to a substantial improvement in the beam quality of the SSC with a reduction in beam losses by more than 90% at high current intensities when 66 MeV proton beams are produced for isotope production [11]. The reduction in losses results in less activation of the extraction components.

Furthermore, the integration with EPICS and EtherCAT [12, 13] based actuator and motion control has resulted in a highly adaptable and easily implementable system at other facilities.

Not only have all the RF control systems at iThemba LABS been efficiently upgraded, but as a further indicator of the success of the system, ease of implementation and adaptability, the system was also installed and commissioned on the Helmholtz-Zentrum K=132 separated sector cyclotron in Berlin during April 2017 [14], contributing to the highly successful patient treatment program, as well as the execution of physics experiments.

EPICS AND ETHERCAT

iThemba LABS has made significant progress in migrating its distributed control system to EPICS [15, 16], a process made difficult by the need to support and upgrade 30-year-old legacy electronic systems. The adoption of EtherCAT [1, 10, 13] as the new industrial fieldbus has greatly simplified the migration process. The RF control systems upgrade project pioneered the way for the adoption of EtherCAT and EPICS templates that were created to implement several other projects such as the

ISBN: 978-3-95450-205-9 doi:10.18429/JACoW-Cyclotrons2019-MOB02

UPS monitoring system, water leak monitoring system, the Tandetron motion control, actuator and beamline control system, RF power amplifier automation, radiation protection and radiation monitoring systems.

The operator's displays used at iThemba LABS have evolved from MEDM [16] and QT displays to the industry standard in CSS. The need to keep up with modern trends in software prompted iThemba LABS to develop a modern React based progressive web app base front end [17]. This software, which is called React Automation Studio, is currently being used as a front end for the beam diagnostics system and the new LERIB Test Bench [13, 17]. We foresee many exciting times ahead with the React Automation Studio and will be open sourcing the framework for the greater EPICS community.

CONCLUSIONS

To stay relevant in an ever-evolving nuclear physics research environment, iThemba LABS reviewed its current capabilities and devised a number of new strategies to develop a long-range plan as a road map for moving into the future. The dedicated isotope production facility comprising a commercial 70 MeV H-minus cyclotron and beamlines to four target bombardment stations has been approved and will be implemented over the next 3 to 4 years. New targetry and bombardment stations are being developed to handle the higher intensity 70 MeV proton beams ranging up to 375 µA per target. Once radionuclide production has been moved to the 70 MeV cyclotron facility, the SSC will be largely dedicated to research. iThemba LABS has also embarked on a project to establish a Low-Energy Rare-Isotope Beam (LERIB) facility, of which an offline test facility is nearing completion. Later phases will establish a fully developed low-energy RIB facility including post acceleration. The design of a dedicated target station for the production of the alpha emitter ^{211}At has recently been completed and construction is expected to start soon. The introduction of 13 in-house developed variable frequency, low-level RF control systems has improved operational stability and reduced beam losses, and therefore extraction component activation, by more than 90%. iThemba LABS has made significant progress in migrating the distributed control system to the open source EPICS platform. The adoption of EtherCAT as the new industrial fieldbus has greatly simplified the migration process and opened more avenues for future control system developments.

REFERENCES

[1] J. L. Conradie *et al.*, "New developments at iThemba LABS", in *Proc. Cyclotrons'16*, Zurich, Switzerland, Sep. 2016, pp. 274-277. doi:10.18429/JACoW-Cyclotrons2016-THA02

[2] J. L. Conradie *et al.*, "The South African isotope facility", in *Proc. IPAC'18*, Vancouver, Canada, Apr.-May 2018, pp. 1240-1243. doi:10.18429/JACoW-IPAC2018-TUZGBF4

[3] Y. Martinez Palenzuela *et al.*, "Enhancing the extraction of laser-ionized beams from an arc discharge ion source volume", *Nucl. Instrum. Methods Phys. Res., Sect. B*, vol. B431, pp. 59-66, 2018. doi:10.1016/j.nimb.2018. 06.006

[4] P. Sortais, "Recent progress in making highly charged ion beams", *Nucl. Instrum. Methods Phys. Res. Sect. B,* vol. 98, pp. 508-516, 1995. doi:10.1016/0168-583X(95) 00177-8

[5] H. Koivisto, J. Arje, and M. Nurmia, "Metal ion beams from an ECR ion source using volatile compounds", *Nucl. Instrum. Methods Phys. Res., Sect. B,* vol. 94, pp. 291-296, 1994. doi:10.1016/0168-583X(94)95368-6

[6] N. Kheswa *et al.*, "Production of high intensity nickel-ion beams with high isotope purity with the metal ions from volatile compound (MIVOC) method", *AIP Conf. Proc.*, 2011, p. 040007, 2018. doi:10.1063/1.5053281

[7] D. Hitz, D. Cormier, and J.-M. Mathonnet, "A new room temperature ECR ion source for accelerator facilities", in *Proc. EPAC'02*, Paris, France, Jun. 2002, paper THPRI005, pp. 1718-1720.

[8] A. Efremov *et al.*, "Performance of the ion source DECRIS-14-2", *Rev. Sci. Instrum.,* vol. 69, no. 2, p. 662, 1998. doi:10.1063/1.1148567

[9] S. L. Bogomolov *et al.*, "Research on metallic ion beam production with electron cyclotron resonance ion sources", presented at Cyclotrons'19, Cape Town, South Africa, Sep. 2019, paper MOP017, this conference.

[10] W. Duckitt, J. Abraham, J. L. Conradie, M. J. van Niekerk, and T. R. Niesler, "A new digital low-level RF control system for cyclotrons", in *Proc. Cyclotrons'16*, Zurich, Switzerland, Sep. 2016, paper WEB01, pp. 258-262. doi:10.1016/j.nima.2018.03.064

[11] W. D. Duckitt *et al.*, "The design and implementation of a broadband digital low-level RF control system for the cyclotron accelerators at iThemba LABS", *Nucl. Instrum. Methods Phys. Res., Sect. A*, vol. 895, pp. 1-9, 2018. doi:10.1016/j.nima.2018.03.064

[12] W. D. Duckitt, "A digital low-level radio frequency control system for the particle accelerators at iThemba LABS", Ph.D. thesis, Eng. Dept., Stellenbosch University, Stellenbosch, South Africa, 2018.

[13] J. K. Abraham and W. Duckitt, "Integration of EtherCAT hardware into the EPICS based distributed control system at iThemba LABS", presented at Cyclotrons'19, Cape Town, South Africa, Sep. 2019, paper TUP004, this conference.

[14] T. Fanselow *et al.*, "Operational experience in the treatment of ocular melanomas with a new digital low-level RF control system", presented at Cyclotrons'19, Cape Town, South Africa, Sep. 2019, paper TUP007, this conference.

[15] J. L. Conradie *et al.*, "Current status of the cyclotron facilities and future projects at iThemba LABS", in *Proc. Cyclotrons'10*, Lanzhou, China, Sep. 2010, paper MOA2CCO02, pp. 42-44.

[16] I. H. Kohler *et al.*, "Progress in the conversion of the in-house developed control system to EPICS and related technologies at iThemba LABS", in *Proc. ICALEPCS'11*, Grenoble, France, Oct. 2011, paper MOPMS013, pp. 347-350.

[17] W. Duckitt and J. K. Abraham, "React automation studio: a new face to control large scientific equipment", presented at Cyclotrons'19, Cape Town, South Africa, Sep. 2019, paper THA03, this conference.

ISBN: 978-3-95450-205-9 doi:10.18429/JACoW-Cyclotrons2019-MOP001

DESIGN AND COMMISSIONING OF RF SYSTEM FOR SC200 CYCLOTRON

G. Chen†, G. Liu, Y. Zhao, Z. Peng, Y. Song, K. Ding, Y. Chen, ASIPP, Hefei, China
X. Zhang, C. Chao, X. Long, C. Yu, CIM, Hefei, China
O. Karamyshev, G. Karamysheva, G. Shirkov, JINR, Dubna, Russia
A. Caruso, L. Calabretta, LNS-INFN, Catania, Italy

Abstract

The SC200 proton therapy superconducting cyclotron is currently under construction by ASIPP (Hefei, China) and JINR (Dubna, Russia). The RF (Radio Frequency) system which provides an accelerating electric field for the particles, has been designed and tested in a high-power commissioning. The RF system consists of RF cavity, Low-level RF control system, RF source, transmission network and so on. The main performances of RF cavity meet design and use requirements in the cold test. The RF cavity achieved an unload Q factor of 5200 at the resonant frequency of 91.5 MHz, 65 kV (Center), ~115 kV (Extraction) accelerating voltage and coupling state of S11 < - 30 dB. The low-level RF (LLRF) system has been tested with an amplitude stability of < 0.2% and a phase stability of < 0.1 ºC in the high-power commissioning. What's more, the cavity has already operated in a ~50 kW continuous wave state after 4 weeks RF conditioning. Some risks have been exposed at higher power test, but related solutions and improvements have been developed. In future work, the target of RF system is effective operation under the overall assembly of cyclotron after further optimization and RF conditioning.

INTRODUCTION

The SC200 proton therapy superconducting cyclotron is currently under construction by ASIPP (Hefei, China) and JINR (Dubna, Russia). The RF system which provides an accelerating electric field for the particles, has been designed and tested in a high-power commissioning. The key components of RF system are Low-level RF control system, RF source, transmission network, which will be discussed in following paragraphs [1, 2]. The assembled RF system in commissioning stage is shown in Fig. 1.

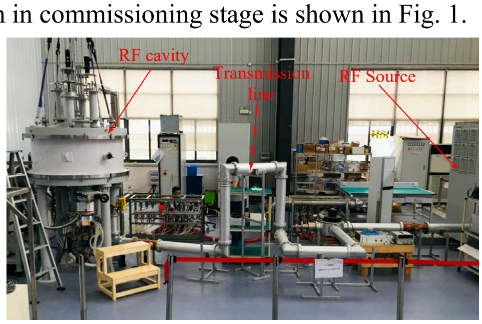

Figure 1: Assembled RF system in commissioning stage.

A high-power commissioning has been performed for the cavity. RF conditioning contributes to improve the performance RF cavity, so as to achieve high power feeding in cavity. Temperature record and X-ray calibration have also made for RF cavity to verify its performance. Moreover, some improvements have been done for cavity to solve related problems.

DESIGN OF RF SYSTEM

The RF system mainly consists of RF cavity, Low-level RF control system, RF source, transmission network. The RF source provides power to RF cavity through 6-inch coaxial transmission line under the control of Low-level RF control system. The RF cavity consists of Dee, Liner, Stems, Trimmers and coupling looping. The layout of RF cavity is shown in Fig. 2. Some optimizations have been made on the cavity based on the original physical model. Therefore, the Dee is optimized to a gradient shape with lighter weight. The inside of Dee has enough space for water cooling pipes. The design and manufacture of water - cooling paths on the rectangular Stem become easy. The new design also provides strong support for Dee to reduce the risk of deformation. The disc of trimmer and Dee form an equivalent capacitance, which is tuned by moving the trimmer up and down. In order to reduce the influence of high temperature under high power, water cooling pipes are also arranged on the outside of the cavity.

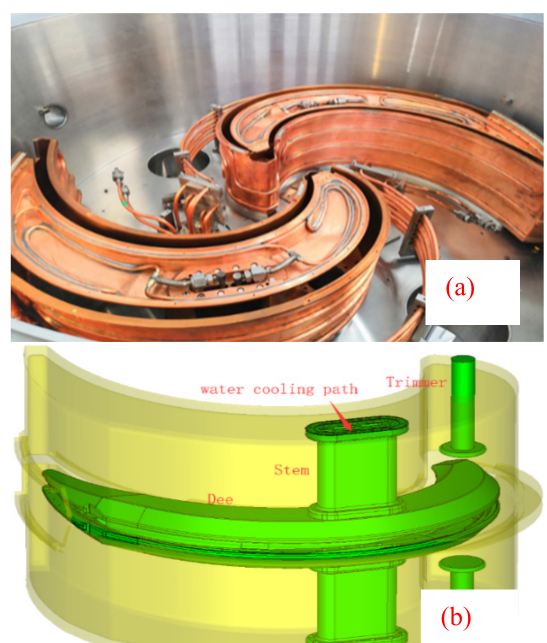

Figure 2: Layout of RF cavity. ((a) is half cavity with up and down symmetry, (b) is half cavity with left and right symmetry).

†chengen@ipp.ac.cn

ISBN: 978-3-95450-205-9 doi:10.18429/JACoW-Cyclotrons2019-MOP001

Moreover, a cold (no feeding power) test has been made on a mock-up cavity to verify its main parameters. The test results are shown in Table 1. The Resonant frequency is adjusted by 4 capacitance trimmers with moving distance of 100 mm. The tuning range in cold test is similar to the design. The Accelerating voltage is also the same. Due to a certain roughness on the mock-up cavity, the unload Q factor is lower than the design. But it also meets the requirements [3].

Table 1: Main Parameters of RF Cavity in Cold Test vs. Design

Parameter	Design	Cold Test
Frequency	91.5 MHz	91.5 MHz
Tuning range	±100 kHZ	91.4 MHz +180 kHz
Accelerating voltage	60 kV (Center) ~120 kV (Extraction)	65kV (Center) ~115 kV (Extraction)
Unload Q factor	5500	5200
Coupling state	$S_{11} < -30$ dB	$S_{11} < -30$ dB

The RF source is a Solid Amplifier with full power of 120 kW at frequency 91.5 ± 1 MHz. The Solid Amplifier signal flow is shown in Fig. 3. The Solid Amplifier consists of RF Gate, Driver module, Splitter, RF sub-Modules, Combiner and cooling auxiliary system. There are 48 RF sub-Modules and every Modules provides a redundant full power of 2.8 kW. The Low-level RF control system (LLRF) controls the Solid Amplifier to feed power to RF cavity. The composition chart of LLRF system is shown in Fig. 4. The adjustment process is implemented by three main loops. The amplitude loop compensates fast distortions for amplifier with a stability < 0.2%. The phase loop keeps the phase of cavity field to the desired value with a stability < 0.1°. The tuning loop contributes to automatic turning for cavity. The stabilities mentioned have been tested in the high-power commissioning.

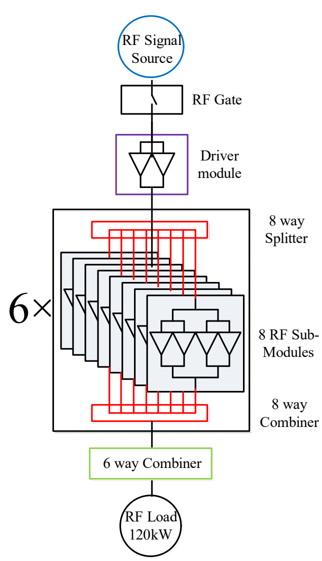

Figure 3: Amplifier signal flow.

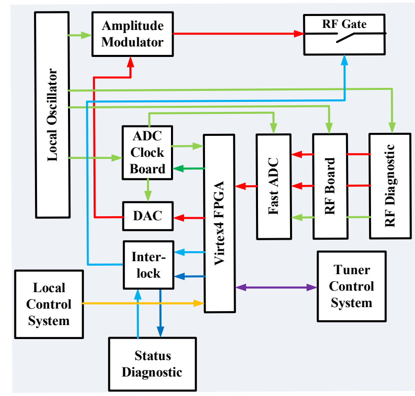

Figure 4: The composition chart of LLRF system.

THE COMMISSIONING OF HIGH-POWER TEST

We have made a high-power test for the prototype SC200 cyclotron under a suitable condition. The current of superconducting coil was 140 A with a magnetic field of ~3 T. The vacuum degree of cyclotron host is 1×10^{-4} Pa. The Pulse wave mode was used for RF conditioning under the control LLRF system [4]. The interface of LLRF system for RF conditioning is shown in Fig. 5. For RF conditioning, we increased the pulse wave power gradually under good coupling state. Amplitude in LLRF becomes stable gradually after a certain time. Pick-ups contributed to detect the multipactor in cavity in once RF conditioning [5]. Finally, the cavity could be fed ∼50 kW continuous wave power without reflection after 4 weeks of RF conditioning. In the whole RF conditioning process, we recorded the temperature of RF cavity. Thermal resistances detected three different points on the outside surface of RF cavity liner. The temperature rise of RF cavity is no more than 30 ℃ due to good cooling effect. The frequency deviation of cavity caused by temperature rise is estimated no more than -40 kHz based on previous multi-analysis [6].

Figure 5: The interface of LLRF system for RF conditioning.

Moreover, X-ray measurement has been made for cavity to the maximum accelerating voltage on Dee based on principle of bremsstrahlung. The detectors were suitable to collect the X-ray spectrum from Dee. The detectors were calibrated to acquire the relationship between energy and channel by Am241 source. The shunt impedance in test

ISBN: 978-3-95450-205-9 doi:10.18429/JACoW-Cyclotrons2019-MOP001

meets the design value 90 kΩ. The Dee voltage deviation between the two cavities is no more than 7 % [7].

IMPROVEMENTS FOR THE CAVITY

The high-power test stopped after running ~30 hours at ~50 kW continuous wave power due to the breakdown of RF window. We made some improvements for cavity to solve the problem. The structure of RF window was optimized to reduce the risk of multipactor. Venting holes (or gaps) were designed to increase gas circulation between RF window and the cavity to improve the vacuum degree. Cooling pipes were arranged on RF window and coupling to reduce thermal stress as shown in Fig. 6.

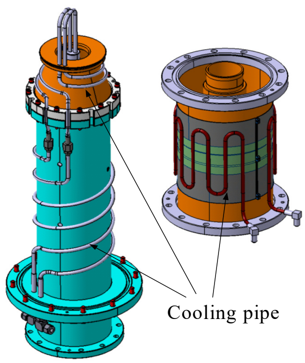

Figure 6: Cooling pipes on RF window and coupling.

We improved the electrical contact situation on Dee and Stem. The copper rings were used on Stem instead of the original copper braid. The “L” type RF contact fingers which have better condition within 2.5 mm are used between two Dees as shown in Fig. 7.

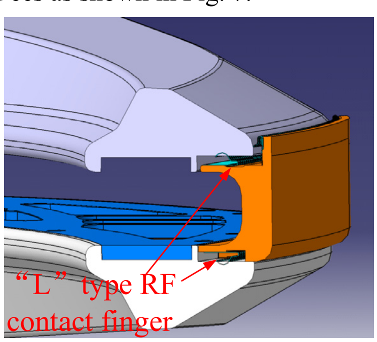

Figure 7: “L” type RF contact finger for Dee.

Last but not least, the water-cooling paths were modified on cavity. We designed semicircular groove for cooling pipes on Dee to increase heat dissipation area as shown in Fig. 8. A three-way connector was added to fix pipe on Dee.

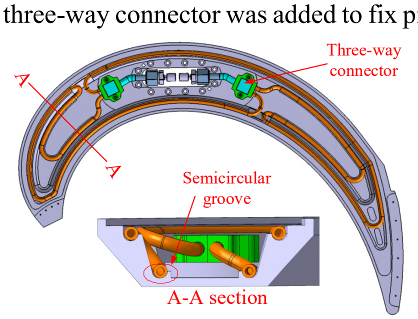

Figure 8: Water cooling optimization on Dee.

SUMMARY

The RF system of SC 200 mainly consists of RF cavity, Low-level RF control system, RF source and so on. The main parameters of RF cavity have been verified in a cold test. The RF cavity achieved an unload Q factor of 5200 at the resonant frequency of 91.5 MHz, 65 kV (Center) ~115 kV (Extraction) accelerating voltage and coupling state of S11 < -30 dB. The LLRF system has been tested with an amplitude stability of < 0.2% and a phase stability of < 0.1 degree. The cavity could be fed ~50 kW continuous wave power without reflection after 4 weeks of RF conditioning. Temperature record has contributed to thermal and frequency deviation analysis. The X-ray measurement has calibrated the maximum accelerating voltage on Dee. The improvements which are mainly about RF window, electrical contact and cooling system have been made to solve related problems. The future goal is to achieve 80 kW power smooth injection after the formal RF conditioning.

ACKNOWLEDGEMENTS

This work was supported by: (1) National Natural Science Foundation of China under grant No. 11775258, 11575237; (2) International Scientific and Technological Cooperation Project of Anhui (grant No. 1704e1002207). Authors very appreciate the support and assistance of Cryoelectra company; (3) China Fusion Engineering Experimental Reactor General Integration and Engineering Design (Grant No. 2017YFE0300503).

REFERENCES

[1] G. Chen *et al.*, “Preliminary design of RF system for SC200 superconducting cyclotron”, in *Proc. Cyclotrons'16*, Zurich, Switzerland, Sep. 2016, pp. 208-211. doi:10.18429/JACoW-Cyclotrons2016-TUP17

[2] G. A. Karamysheva *et al.*, “Compact superconducting cyclotron SC200 for proton therapy”, in *Proc. Cyclotrons'16*, Zurich, Switzerland, Sep. 2016, pp. 371-373. doi:10.18429/JACoW-Cyclotrons2016-THC03

[3] G. Chen *et al.*, “Research and development of RF system for SC200 cyclotron”, in *Proc. IPAC'18*, Vancouver, Canada, Apr.-May 2018, pp. 3616-3618. doi:10.18429/JACoW-IPAC2018-THPAL004

[4] G. Chen *et al.*, “Commissioning of RF system of the 200 MeV proton cyclotron”, in *Proc. IPAC’19*, Melbourne, Australia, May 2019, pp. 2877-2879. doi:10.18429/JACoW-IPAC2019-WEPRB030

[5] J. R. M. Vaughan, “Multipactor,” *IEEE Trans. Electron Devices*, vol. 35, no. 7, pp. 1172–1180, Jul. 1988. doi:10.1109/16.3387

[6] G. Liu, Y. Song, G. Chen *et al.*, “Thermal consideration and optimization for high-power operation of a cyclotron RF cavity”, *Nucl. Instrum. Methods Phys, Res., Sect. A*, vol 908, pp. 143-147, Nov. 2018. doi:10.1016/j.nima.2018.08.037

[7] G. Liu, Yuntao Song, Gen Chen *et al.*, “X-ray calibration of the Dee voltage of RF cavity based on a low-power test”, *Nucl. Tech. Rad. Prot.*, vol. XXXIV, Jan. 2019. doi:10.2298/NTRP190111023L

ISBN: 978-3-95450-205-9 doi:10.18429/JACoW-Cyclotrons2019-MOP002

RECENT PROGRESS ON ION SOURCE OF SC200 CYCLOTRON

Y. P. Zhao, Institute of Plasma Physics, Chinese Academy of Sciences, Hefei, China
S. W. Xu, University of Science and Technology of China, Hefei, China
G. Chen*, Institute of Plasma Physics, Chinese Academy of Sciences, Hefei, China
O. Karamyshev, G. Karamysheva, G. Shirkov, JINR, Dubna, Russia
L. Calabretta, LNS-INFN, Catania, Italy

Abstract

A 200 MeV compact superconducting cyclotron, named SC200, for proton therapy is under development by collaboration of ASIPP (Hefei, China) and JINR (Dubna, Russia). The ion source is a significant subsystem of the cyclotron. A hot cathode internal ion source has been designed and tested for SC200 cyclotron. The ion source has been successfully arc discharged on the test bench. The extracted beam current has been measured over 100 µA and filament lifetime of ion source exceeded 100 h, which indicated that the ion source meets the design requirements. The stability of the filament under strong magnetic field has also been tested and the differences between the two kinds of filament are compared.

INTRODUCTION

Per end of 2018 more than 220000 patients have been treated worldwide with Particle Therapy. About 190000 have been treated with protons, about 28000 with C-ions and about 3500 with He, pions and other ions. Proton therapy delivers radiation to tumor tissue in a much more confined way than conventional photon therapy thus allowing the radiation oncologist to use a greater dose while still minimizing side effects. Proton beam therapy uses special machines, a cyclotron and synchrotron being the most common, to generate and accelerate protons to speeds up to 60 percent the speed of light and energies of up to 250 million electron volts. These high-energy protons are steered by magnets toward the treatment room, and then to the specific part of the body being treated. In some older proton machines, additional pieces of equipment are needed to modify the range of the protons and the shape of the beam. Newer facilities make similar adjustments by fine tuning the energy of the beam and the magnetic fields which guide their path (“pencil beam scanning” or “scanning beam”). These modifications guide the proton beam to precise locations in the body where they deliver the energy needed to destroy tumor cells. The SC200 superconducting cyclotron for hadron therapy is under development by collaboration of ASIPP (Hefei, China) and JINR (Dubna, Russia) [1]. Superconducting cyclotron SC200 will provide acceleration of protons up to 200 MeV with maximum beam current of 400 nA in 2020. Internal ion source of PIG type will be used. The Penning ion source is perfectly suitable for the accelerator, as the structure of it is simple, compact, and discharging-efficient. The penning ion source produces plasma by heating cathode which will release thermoelectron. Under the effect of arc voltage electric field, the accelerated electron will collide hydrogen, then produces plasma. The proton of plasma will be extracted and then be accelerated to form proton beam [2].

* chengen@ipp.ac.cn

EXPERIMENTAL PROCEDURES

We established a test bed to carry out experiment so as to verify the proper functioning of ion source. The structure is shown as below Fig. 1. It includes six sections: magnet system, vacuum system, water cooling system, power system, data-collecting system and gas injection system. The magnet system consists of magnet power, coils and yoke. It can generate uniform magnet field with the maximum strength of 1 T around the arc chamber of ion source [3]. The beam extraction depends on the negative high voltage on the electrode. The beam extraction electrode was fixed outside the ion source by ceramic insulation, and the gap between the electrode and the ion source is kept at approximately 2 mm. The extraction electrode slit size is 4.3 mm × 1 mm with a 1 mm thickness. Because of space limitation, a bent copper block replaces the Faraday cup to collect the extracted ion beam. Such a system enables us to measure total amount of ion current extracted from the plasma chamber of the ion source. On this ion source test bench, a lot of ion source performance tests have been done, including the selection of ion source discharge parameters, the relationship between ion source discharge capacity and gas flow, arc voltage and other factors.

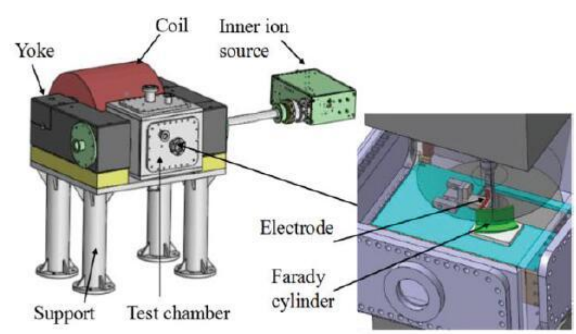

Figure 1: The components of the ion source test bench.

In order to verify that the filament can also maintain good performance in the central region of the SC200 cyclotron, we went to the high magnetic field laboratory of the Chinese Academy of Science and carried out repeated experiments under the 3T magnetic field generated by their equipment. The specific conditions of the device are shown in Fig. 2.

ISBN: 978-3-95450-205-9 doi:10.18429/JACoW-Cyclotrons2019-MOP002

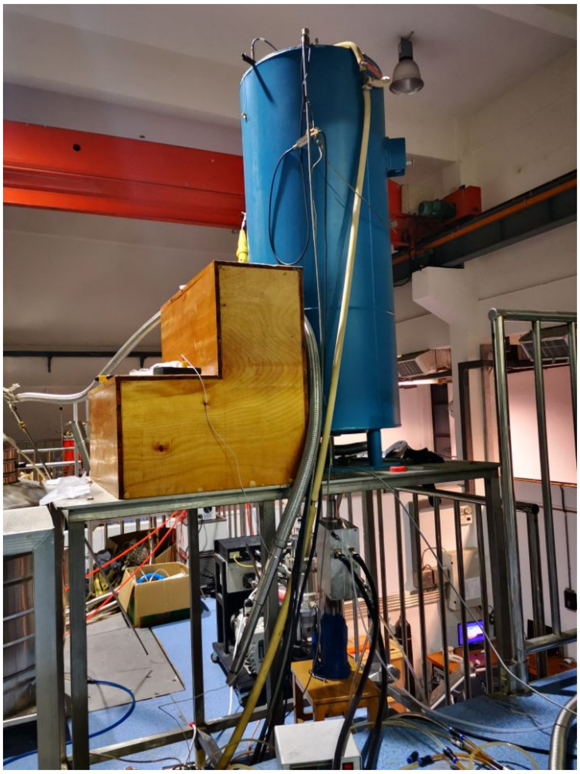

Figure 2: The test bench in the high magnetic field laboratory of the Chinese Academy of Science.

In addition, experiments have been carried out for filament with different materials and shapes. Figure 3 shows two different filaments, the difference being the thickness at the bottom which is to increase the mechanical properties of the filament. Experiments are also needed to verify the discharge capacity of the two types of filament.

Figure 3: Thin filament and thick filament.

RESULT AND DISCUSSION

Figure 4 shows the value and variation trend of the measured arc current under different filament current. The other general conditions were: gas flow 2 sccm, magnetic field 1 T and arc voltage 170 V. A thick filament requires a larger filament current to produce the same amount of arc current as a thin filament. With the increase of filament current, arc current rises rapidly in both thick filament and thin filament.

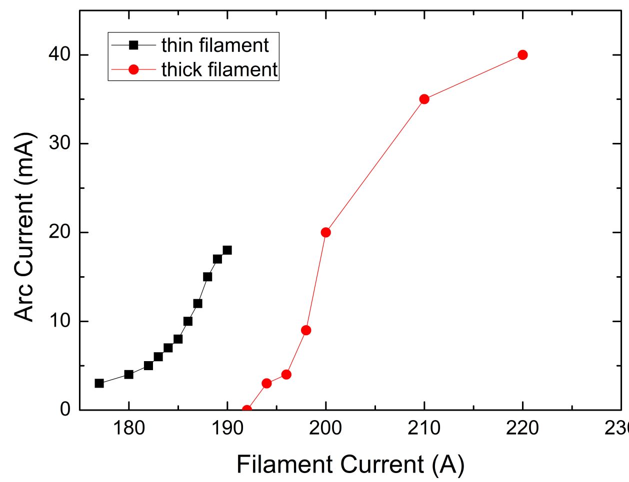

Figure 4: Arc current versus filament current.

The extracted beam intensity at various extraction voltage was measured under a magnetic field of 1 T, an arc voltage of 170 V and a gas flow of 2 sccm. The results are shown in Fig. 5. The thin filament current is set to 175 A, while the thick filament current is set to 215 A. With a current of more than 100 µA, we chose the thin filament as the final filament of our ion source, which will reduce the load on the filament power supply.In addition, high current will cause permanent damage to the filament and more easily cause the filament to break, as shown in Fig. 6.

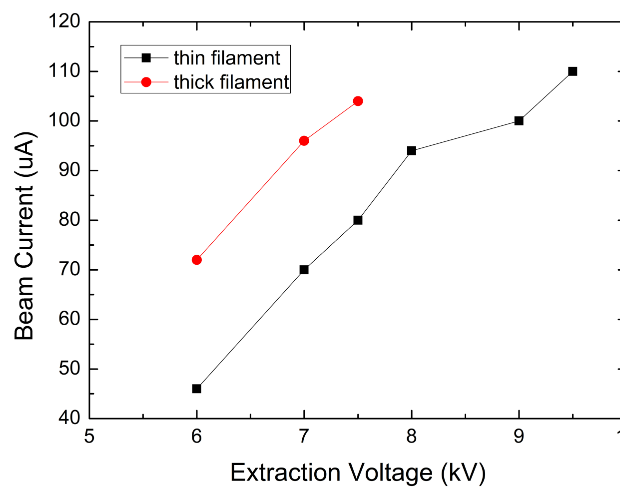

Figure 5: Results of beam extraction experiments of thin filament: beam current versus dc extraction voltage.

In addition, we did a long time stability test on the thin filament to verify whether it can meet the stable work in a treatment cycle. Figure 7 shows that the discharge is extremely stable for 1 h and the beam extraction for 0.5 h. The beam extraction strength exceeds the accelerator requirement of 100 µA.

ISBN: 978-3-95450-205-9 doi:10.18429/JACoW-Cyclotrons2019-MOP002

Figure 6: Fracture of thick filament at high current.

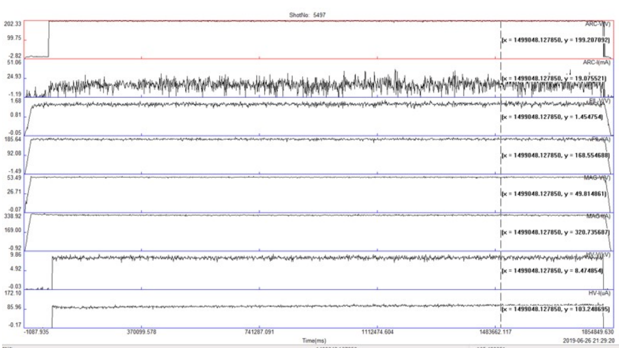

Figure 7: Waveform collected of the stable ion source discharge.

CONCLUSION

The hot cathode Penning inner ion source plays a very important role for the whole proton superconducting cyclotron system. The results obtained on our test bench confirm that the structure and operation state of the designed ion source is suitable for long pulses at high beam current. Thin filament can well meet the design requirements of the SC200 cyclotron. After extensive testing, the ion source is capable of generating beams of more than 100 µA and of stable operation for a long time. The integrated commissioning of the SC200 cyclotron will begin at the end of this year. The ion source will then be tested with other subsystems.

ACKNOWLEDGEMENTS

This work was supported by: (1) National Natural Science Foundation of China under grant No. 11775258, 11575237; (2) International Scientific and Technological Cooperation Project of Anhui (Grant No. 1704e1002207); (3) China Fusion Engineering Experimental Reactor General Integration and Engineering Design (Grant No. 2017YFE0300503).

REFERENCES

[1] G. A. Karamysheva *et al.*, "Compact superconducting cyclotron SC200 for proton therapy", in *Proc. 21th Int. Conf. on Cyclotrons and their Applications (Cyclotrons'16)*, Zurich, Switzerland, Sep. 2016, pp. 371–373. doi:10.18429/JACoW-Cyclotrons2016-THC03

[2] J. R. J. Bennett, "A review of PIG sources for multiply charged heavy ions", *IEEE Trans. Nucl. Sci*, vol. 19, pp. 48-68, Apr. 1972. doi:10.1109/TNS.1972.4326630

[3] Gen Chen *et al.*, "The construction of the inner ion source for SC200 compact superconducting cyclotron", *AIP Conference Proceedings*, vol. 2011, p. 090009, Sep. 2018. doi:10.1063/1.5053390

ISBN: 978-3-95450-205-9 doi:10.18429/JACoW-Cyclotrons2019-MOP003

OPTIMAL DESIGN AND FLUID-SOLID COUPLING THERMAL ANALYSIS OF SC200 SUPERCONDUCTING PROTON CYCLOTRON ELECTROSTATIC DEFLECTOR

Yue Xu[1], Kaizhong Ding[2,†], Xiongyi Huang[2], Kun Pei[2,3], Kangxin Gu[3], Junjun Li[2], Yuntao Song[2], Yonghua Chen[2,3]

[1]Anhui University, Hefei, Anhui, China

[2] Institute of Plasma Physics Chinese Academy of Science, China

[3] Hefei CAS Ion Medical and Technical Devices Co. Ltd., Hefei, China

Abstract

In recent years, the study of proton therapy equipment has received increasing attention in China. Hefei CAS Ion Medical and Technical Devices Co., Ltd. (HFCIM) is developing a proton medical device based on the superconducting proton cyclotron. The electrostatic deflector (ESD) is the key extraction component of the SC200 superconducting cyclotron, which uses a high-intensity electric field to bend the beam from the track. The fierce interaction between the proton beam and the deflector septum, causes a great loss of beam and unwanted excess heat accumulation and radiation. In order to minimize the risk of damage caused by the proton beam loss, the fluid solid-thermal coupling analysis of the deflector was performed by applying computational fluid dynamics (CFD) on ANSYS. The maximum temperatures of the septum in various cases of the cooling water speed, the septum thickness and material have been investigated respectively. The result based on analysis provide a valuable reference for the further optimization on the material selection and structural design for ESD.

INTRODUCTION

In modern society, the incidence of cancer has increased year by year. Proton therapy is becoming one of the main methods of cancer treatment because the proton beam provides superior dose distribution at several anatomical sites [1]. In recent years, proton therapy has received increasing attention in China and has made progress on a number of key technologies. Against this background, HFCIM is developing a proton medical device based on superconducting proton cyclotron (SC200). The extracted proton beam energy is designed to be 200 MeV and the beam current is higher than 400 nA. The proton beam extraction uses a precessional extraction method. The electrostatic deflector (ESD) is the first extraction element in the extraction system of the SC200 superconducting cyclotron, which uses a high-intensity electric field to strip the beam from the orbit.

Figure 1 shows the diagram of SC200 extraction system. In a cyclotron, the beam may be deposited at the extraction radius due to the extremely small turn separation. ESD cannot peel off the last turn without affecting the internal turns and the beam loss is much less, which is very difficult. Therefore, the thickness of the septum must be as thin as possible, and the specification range is 0.1 - 0.5 mm. The deposited beam energy is the most important risk of destroying ESD, and its performance directly affects the beam parameters. This paper mainly discusses the structural design and fluid-solid coupling thermal analysis of electrostatic deflector, and provides a valuable reference for further optimization.

† kzding@ipp.ac.cn

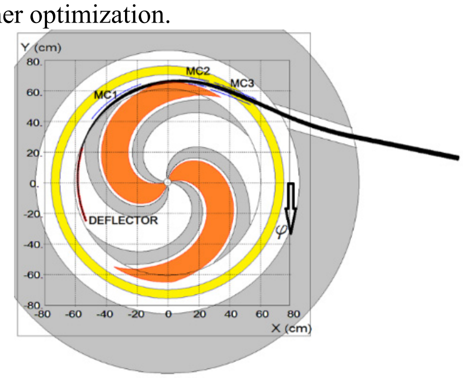

Figure 1: Schematic diagram of SC200 extraction system.

DESIGN AND SIMULATION

Simulation Model

The main structure of the electrostatic deflector is shown in Fig. 2. The septum is an integration design that is directly attached to the housing and has a thickness of only 0.1 mm. The outer surface of the septum is grooved, and the cooling water pipe is brazed in the groove to achieve the best cooling effect.

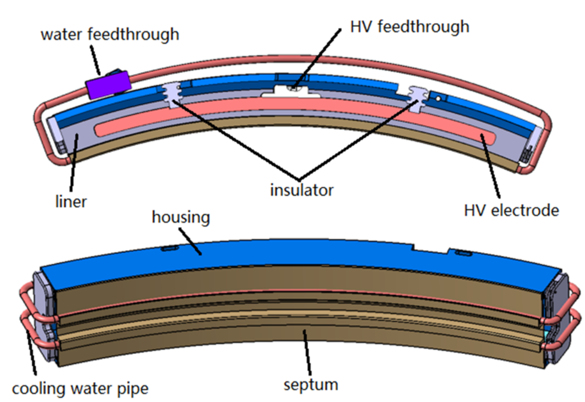

Figure 2: Main structure of ESD.

It is assumed that the beam loss rate at the entrance of the electrostatic deflector is 60%, which means that the

ISBN: 978-3-95450-205-9 doi:10.18429/JACoW-Cyclotrons2019-MOP003

deposition energy on the septum is 48 W. According to the Italian INFN research on the mechanism of breakdown, all materials of ESD have an effect on breakdown [2]. Because the high voltage electrode is loaded with a high voltage of -60 kV, we also care about the sparking phenomenon in the vacuum chamber. Therefore, in order to reduce the effects of thermal and sparking phenomena, we focus on structural optimization and material selection of electrostatic deflector. The main materials are listed in Table 1.

Table 1: Materials of Main Parts of ESD.

Part	Material
HV electrode	Titanium alloy
Septum	OFC
Liner	Stainless steel
Housing	Stainless steel
Insulator	Alumina ceramic

Simulation Calculation

The fluid-solid thermal coupling analysis of ESD is simulated by finite element analysis software ANSYS 17.2. It is known from previous experience that most of the beam loss is at the entrance of the septum [3]. And because the thermal conductivity of the septum is limited, heat will only accumulate near the entrance [4]. In order to simplify the calculation, the 1/4 length of the electrostatic deflector is used as a simulation model. The water cooling tube is brazed to the groove of the septum. The simulation model is shown in Fig. 3.

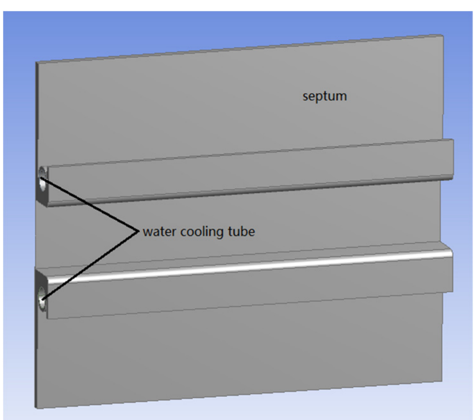

Figure 3: Simulation model in CFX.

It is approximated that the heat flux input Q at the entrance of the septum is Gaussian on the inlet surface. The Gaussian distribution equation is as follows:

$$Q = qe^{\frac{-x^2}{2\sigma^2}} \quad (1)$$

where q is a constant. The value of σ depends on the beam cross-section size, which is calculated by beam analysis to obtain σ = 3 mm. However, in actual operation, the relative position of the beam and the septum may change, and the area where the beam loss is also changed. In this limit condition, the load is all loaded on the surface of the 0.1 mm thick septum.

The total thermal power P is as follows:

$$P = \int Q\, sds = \sum_i^n Q(i)s(i) = \sum_i^n Q(i) * \Delta a(i) * b \quad (2)$$

where; i = 0, 1, ..., 9, Δa (i) = 0.25 mm, and b is the thickness of septum, b = 0.1 mm. P = 48 W for calculating the limit conditions.

The heat flux input of the Gaussian distribution as shown in Fig. 4 is distributed in the area shown in Fig. 5.

Both the septum and the water cooling tube are made of oxygen-free copper. Heat transfer is selected for each contact surface [5]. The boundary conditions at the inlet are set to a uniform temperature of 25 °C. The cooling water at 25 °C has a uniform water flow speed of 1 m/s. The outlet is set to 0Pa static pressure. The cooling water in the two water pipes flows to the same direction. The k-epsilon turbulence model is chosen for this analysis because it is suitable for most engineering conditions and provides better performance in terms of mathematical equations and precision. The solution strategy selects "Upwind", first-order discrete format. When the turbulent flow energy and heat transfer are less than 1×10^{-5}, the calculation is considered to be convergent.

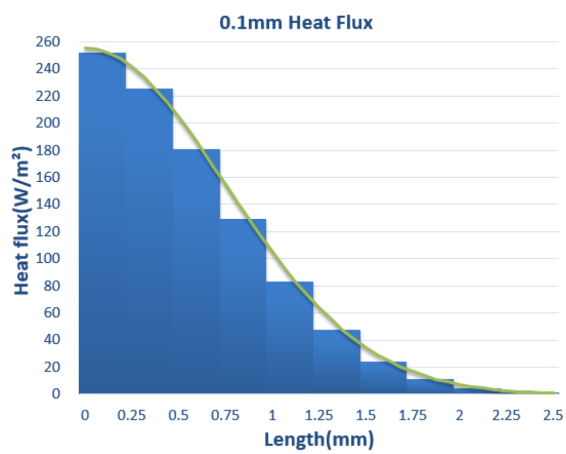

Figure 4: Input heat flux on surface of the septum.

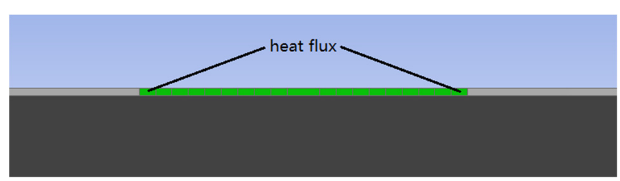

Figure 5: Input heat flux on surface of the septum.

SIMULATION RESULTS

Figure 6 shows the temperature distribution of the model under the conditions of an oxygen-free copper septum thickness of 0.1 mm, a cooling water flow speed of 1 m/s, and a beam loss power of 48 W. The results show that heat is mainly distributed around the heat source. The maximum temperature of 1027 °C appears at the center of the heat flux input, very close to the melting point of material. The septum is fixed to the housing, so the upper and lower ends are fixed. The septum is thermally deformed by being

ISBN: 978-3-95450-205-9 doi:10.18429/JACoW-Cyclotrons2019-MOP003

heated by the beam current to produce a protrusion of 0.11 mm, as shown in Fig. 7. This will cause more beam loss and heat accumulation, which worsens the problem. So the result is unacceptable.

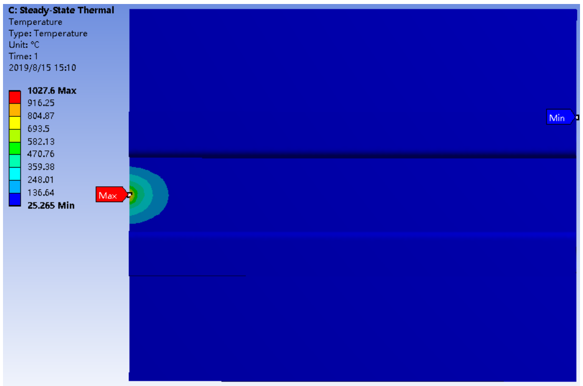

Figure 6: Temperature distribution of the model.

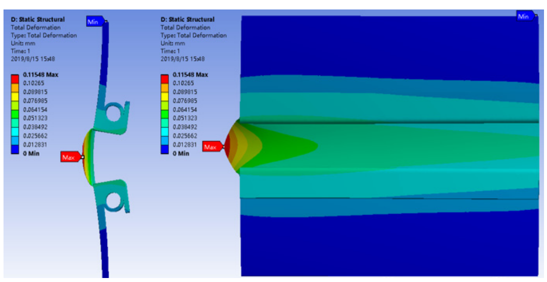

Figure 7: Structure deformation of the simulation model.

In order to reduce the thermal deformation, we consider the following points:

Material For the performance of the septum, perhaps a material with a higher melting point and heat transfer coefficient is more suitable. Table 2 lists the simulation results for several common dicing film materials. The thickness is 0.1 mm, the cooling water flow speed is 1 m/s, and the thermal power is 48 W.

Table 2: Simulation Results for Each Material

Material	Tmax (℃)	Δmax (mm)
OFC	1027.6	0.115
Mo	2764.3	0.082
Ta	6778.8	0.417
W	2184.6	0.058

From the point of view of temperature and deformation, tungsten is perhaps the best septum material.

Thickness The thinner the cut film thickness, the less the beam loss. However, the thickness also affects the heat transfer and de-formation of the septum. Under the conditions shown in Fig. 4, we believe that for every 0.1 mm increase in thick-ness, the beam will lose 10% more. The maximum temperature T and the maximum deformation ε of septa of different thicknesses were calculated. The results are shown in Fig. 8.

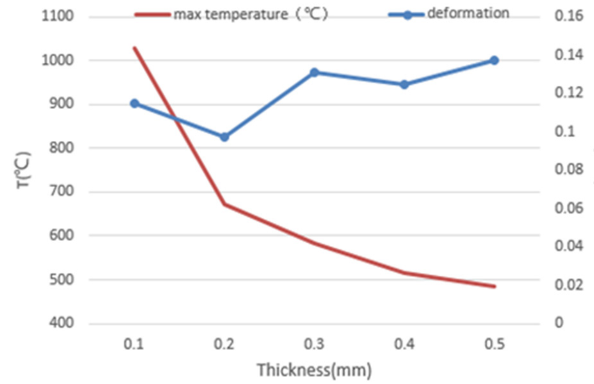

Figure 8: Maximum temperature and deformation of different thicknesses.

As the thickness increases, the maximum temperature decreases, but the deformation increases. Therefore, when we choose the thickness of the septum, we should also consider the structural properties and mechanical properties of the material.

Cooling Water Speed The rated pressure of the pump is 0.6 MPa, which can provides a cooling water speed of up to 1 m/s. Increasing the cooling water speed increases the heat exchange rate. According to the calculation equation of the pipeline resistance, the resistance of the cooling water is proportional to the square of the speed. As the resistance increases, the water cooling effect may change. We calculated the maximum temperature and deformation of the septum at different flow speeds and the results are shown in Fig. 9.

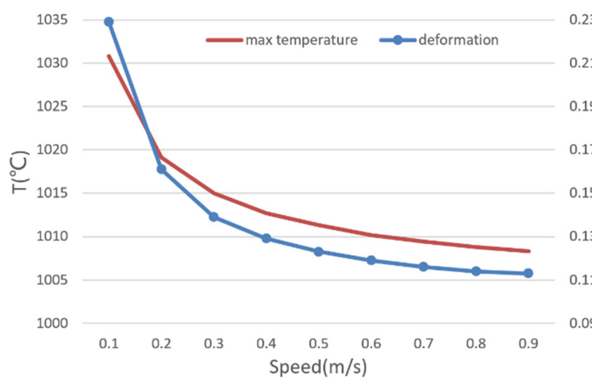

Figure 9: Maximum temperature and deformation of different water flow speeds.

CONCLUSION

This paper introduces the main structural design of the SC200 cyclotron electrostatic deflector and the fluid-solid coupling thermal analysis under extreme operating conditions. The actual work intensity will be lower than the simulation conditions. After analysis, a 0.1 mm thick tungsten septum may be a better choice. The simulation results will be compared to the experimental results at the end of this year.

ISBN: 978-3-95450-205-9 doi:10.18429/JACoW-Cyclotrons2019-MOP003

ACKNOWLEDGEMENT

Work supported by National Natural Science Foundation of China under grant No. 11775258 & 11575237, International Scientific and Technological Cooperation Project of Anhui grant No. 1704e1002207.

REFERENCES

[1] W. Wieszczycka and W. H. Scharf, "Proton radiotherapy accelerators", *World Scientific*, p. 344, August 2001. https://doi.org/10.1142/4617

[2] M. Re *et al.*, "Breakdown mechanisms in electrostatic deflector", in *Proc. 16th Int. Conf. on Cyclotrons and their Applications*, East Lansing, MI, USA, May 2001, p. 151.

[3] D. Poe *et al.*, "Status of electrostatic deflector at NSCL K1200 cyclotron", in *Proc. 15th Int. Conf. on Cyclotrons and their Applications*, Caen, France, Jun. 1998, pp. 229-231.

[4] J. DeKamp and F. Marti, "Thermo mechanical calculations of a cyclotron deflector", in *Proc. PAC'97*, Vancouver, Canada, May 1997, paper 8P022, p. 278.

[5] ANSYS, User's Guide Version 17.2, ANSYS Ltd., 2016.

ISBN: 978-3-95450-205-9 doi:10.18429/JACoW-Cyclotrons2019-MOP004

BEAM DYNAMICS SIMULATION OF THE EXTRACTION FOR A SUPERCONDUCTING CYCLOTRON SC240*

Z. Wu, University of Science and Technology of China, Hefei, China
K. Z. Ding†, J. J. Li, Y. T. Song
Institute of Plasma Physics, Chinese Academy of Sciences, Hefei, China
Z. Wang, Hefei CAS Ion Medical and Technical Devices Co. Ltd., Hefei, China

Abstract

In order to diversify the company's cyclotron, a design study has been carried out on a 240 MeV superconducting cyclotron SC240 for proton therapy, which is based on our experience in design of SC200. In order to increase turn separation and extraction efficiency, resonant precessional extraction method is employed in the extraction system. A first harmonic field consistent with the Gaussian distribution is added to introduce beam precessional motion. Its effects on phase space evolution and turn separation increase is studied by a high efficiency beam dynamics simulation code. According to the study, its amplitude and phase have been optimized to meet the requirements of extraction beam dynamics. Based on beam dynamics simulation, the parameters of extraction system elements (two electrostatic deflectors and six magnetic channels) are chosen. Besides, the effects of sectors spiral direction on beam extraction are studied. Extraction efficiencies and beam parameters have been calculated.

INTRODUCTION

In order to diversify the proton therapy cyclotron product series, ASIPP (Institute of Plasma Physics, Chinese Academy of Sciences) starts designing a superconducting cyclotron to extract 244 MeV, 500 nA proton beam [1]. The main parameters of SC240 cyclotron are listed in Table 1. In order to increase extraction efficiency and decrease the voltage of deflectors as much as possible, the proposed extraction method is resonance extraction [2].

BEAM PRECESSION DESIGN

Working Diagram

Figures 1 and 2 show that Qr drops quickly in extraction region. The beam will cross $Qr = 1$ resonance line when energy reaches 241 MeV. A first harmonic field bump will be added near $Qr = 1$ to increase coherent radial oscillation to generate big turn separation at entrance of first deflector.

Sector Spiral Direction

Before setting about designing the first harmonic field bump, we should choose an optimal sector spiral direction. As shown in Fig. 3, there are two different sector spiral direction: Case 1: beam moves in the direction of the sector spiral, and the position of entrance of first deflector is $\varphi = 44°$; Case2: beam moves against the direction of the sector spiral, and the position of entrance of first deflector is $\varphi = 91°$. We did beam precession simulation in extraction region under the 2 cases above with same amplitude of first harmonic field bump and optimal bump phase. The simulation conditions and results are shown in Fig. 4. The simulation shows that the extraction radius of case 1 is about 1.5 cm bigger than case 2.

Table 1: The Main Parameters of the Cyclotron SC240

Parameter	Value
Extracted beam energy	244 MeV
Extraction radius	80.88 cm
Extraction mechanism	Resonance crossing and precessional motion
Spiral angle (maximum)	71°
Pole radius	84 cm
Outer radius of yoke	160 cm
Hill/valley gap	5 cm/60 cm
Central field/Extraction field	2.39/3.01 T
Coil cross section	dx82×dy115 mm^2
Current density	62.56 A/mm^2
Number of cavity	4
RF frequency	72.79 MHz
Harmonic mode	2
Cavity voltage	~100 kV

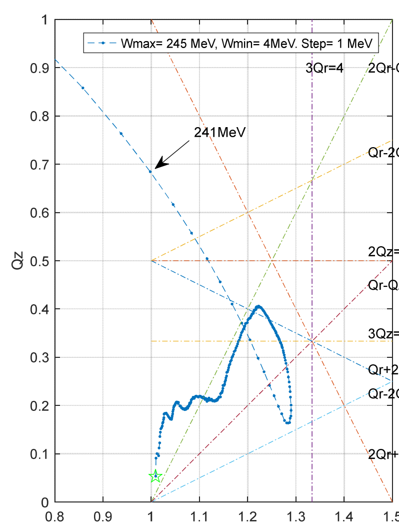

Figure 1: Working diagram of SC240 cyclotron.

* Work supported by National Natural Science Foundation of China under grant No. 11775258 & 11575237, International Scientific and Technological Cooperation Project of Anhui grant No. 1704e1002207.
† kzding@ipp.ac.cn

ISBN: 978-3-95450-205-9 doi:10.18429/JACoW-Cyclotrons2019-MOP004

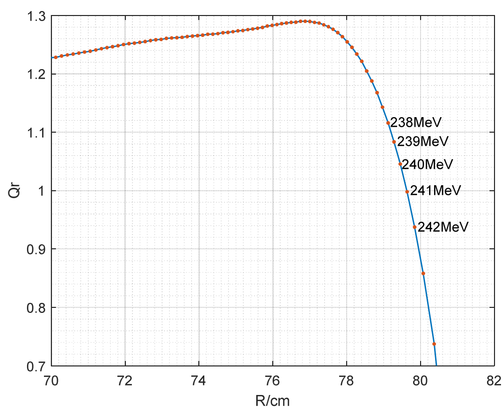

Figure 2: Qr vs. R at extraction region.

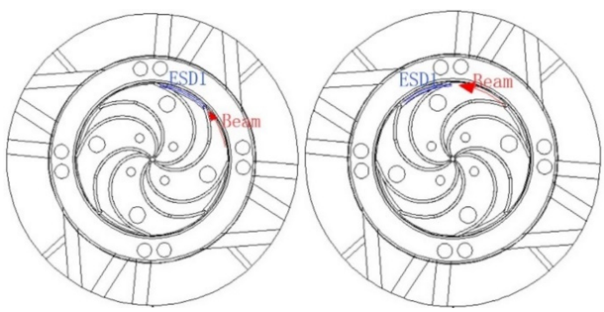

Figure 3: Two different spiral direction of sectors: left-Case1, right-Case2.

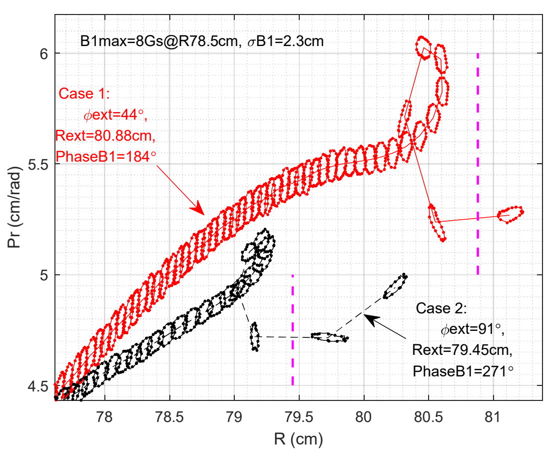

Figure 4: Different spiral direction make different extraction radius.

And the radial impulse at entrance of first deflector of case 1 is about 0.25 cm/rad bigger than case 2. Therefore, we can draw the conclusion that it's easier to deflect the beam in case 1 than in case 2. So we use the sectors whose spiral is in the same direction as the particle motion (case 1) to design beam extraction.

First Harmonic Field Bump

A suitable first harmonic field bump is designed to introduce desirable beam precession. The radial distribution of amplitude of first harmonic field is shown in Fig. 5. The radial distribution of the amplitude is consistent with the Gaussian distribution with a maximum amplitude equal to 8 Gs at center position $Rc = 78.5$ cm, and a width $\sigma = 2.3$ cm. After comparing the beam precession induced by first harmonic bumps with different phase, we found that the optimal phase of first harmonic is $\varphi = 184°$ when the entrance of first deflector is at $\varphi = 44°$.

With this first harmonic distribution shown in Fig. 5, we can observe the precession near extraction shown in Fig. 6. The simulation in Fig. 6 is done from 200 MeV, and the initial beam radial phase ellipse has emittance $\varepsilon_r \sim 0.3$ π·mm·mrad. Besides, the central proton is on AEO (accelerating equilibrium orbit). As shown in Figure 6, the turn separation increases about 5 mm due to the first harmonic bump.

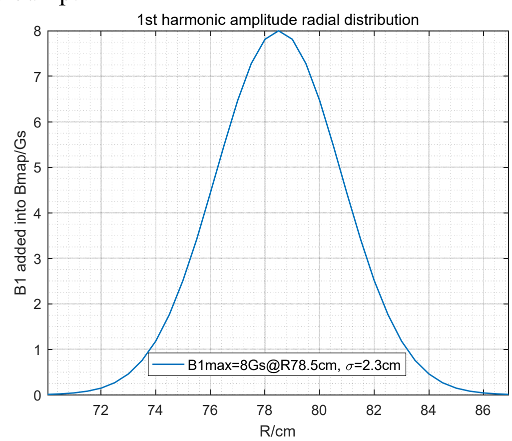

Figure 5: Radial distribution of amplitude of 1st harmonic field.

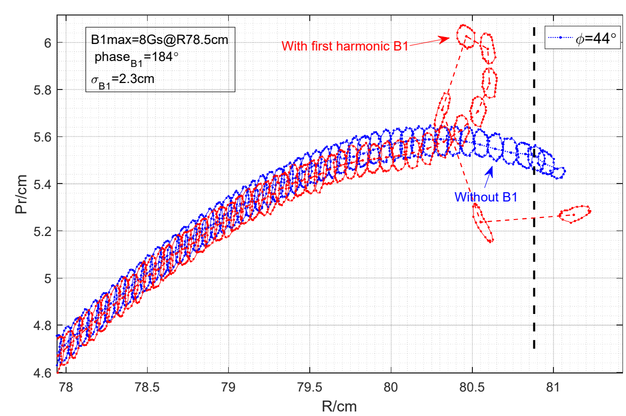

Figure 6: Radial phase space at extraction region.

Main Acceleration Region Simulation

The parameters of initial beam used for main acceleration region beam simulation is that: 1000 protons generated randomly in a phase ellipse around 200 MeV AEO with radial emittance, $\varepsilon_r \sim 0.3$ π·mm·mrad, and longitudinal emittance, $\varepsilon_z \sim 0.4$ π·mm·mrad, phase width = ±5° and energy spread = ±0.165%.

The axial profile of beam is shown in Fig. 7. From the radial phase space (Fig. 6) and the axial profile (Fig. 7), we can see that the optimal radial position of entrance of first deflector' septum is 80.88 cm. Then we can get the beam's parameters at the entrance of first deflector, which is shown in Figure 8. All of the 1000 protons at 200 MeV AEO are accelerated to the entrance of first deflector successfully.

ISBN: 978-3-95450-205-9 doi:10.18429/JACoW-Cyclotrons2019-MOP004

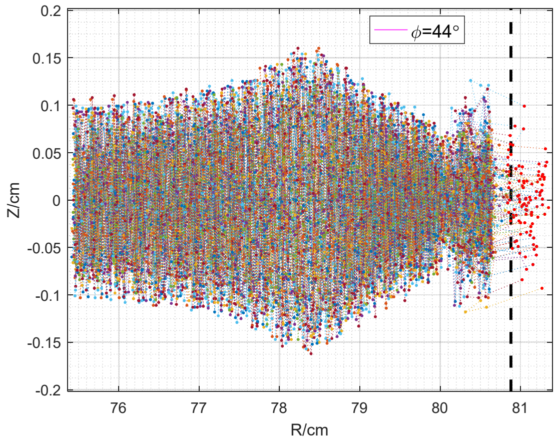

Figure 7: Axial profile of the beam.

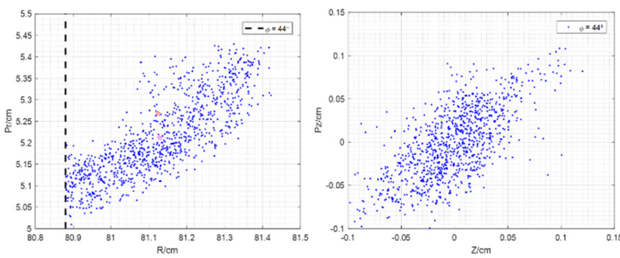

Figure 8: Position of protons on different planes at deflector entrance (Wave = 244 MeV).

EXTRACTION SYSTEM DESIGN

Extraction Trajectory and Envelop

There are two steps to design the extraction system. Firstly, based on the central proton at the entrance of first deflector, we design the radial component of electric field *Er* in deflectors and magnetic field response ΔB in channels to get a suitable central extraction trajectory. Secondly, we design suitable magnetic field gradient based on multi-particle beam simulation with all of the protons at the entrance of first deflector to make beam envelope as small as possible.

The plan view of central extraction trajectory and extraction elements are shown in Figure 9. The geometry and field parameters of all elements are shown in Table 2 and Table 3. There are 2 deflectors placed at the adjacent hills and 6 passive magnetic channels in the extraction system. Electric field strength in deflectors does not exceed 110 kV/cm, gradients of magnetic field in channels are in a range of 2–3 kGs/cm. Five channels focus the beam in horizontal direction. MC4 and edge magnetic field focus the beam in vertical direction. As shown in Fig. 10, the beam envelop at exit of cyclotron (R = 160 cm) does not exceed 5 mm in both horizontal and vertical direction. Figure 11 shows the parameters of extracted beam at the external radius of yoke (R = 160 cm) when the initial beam at 200 MeV AEO has emittance $\varepsilon_r \sim 0.3\ \pi\cdot$mm$\cdot$mrad and $\varepsilon_z \sim 0.4\ \pi\cdot$mm$\cdot$mrad. The output beam at R = 160 cm has emittance $\varepsilon_x = 7.81\ \pi\cdot$mm$\cdot$mrad, $\varepsilon_z = 1.01\ \pi\cdot$mm$\cdot$mrad, average energy = 244 MeV and energy spread = ±0.25%.

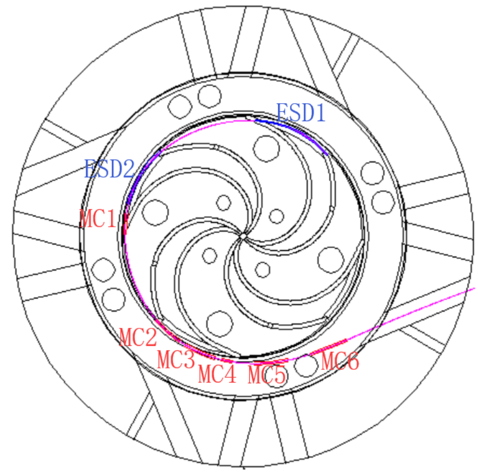

Figure 9: Plan view of extraction system and central extraction trajectory.

Table 2: Geometry Parameters of MCs and ESDs

Element	φ1 (°)	φ2 (°)	Xc (cm)	Yc (cm)	Rc (cm)
MC1	169	179	-3.181	3.568	78.935
MC2	224	239	-0.384	-8.181	77.974
MC3	242	257	4.734	-0.471	87.261
MC4	260	265	7.134	7.258	95.376
MC5	275	290	8.194	25.809	114.012
MC6	300	315	-41.92	181.892	278.180
ESD1	44	84	6.103	12.092	68.479
ESD2	134	164	-11.26	4.209	71.000

Table 3: Field Parameters of MCs and ESDs

Element	ΔB (kGs)	dB/dx (kGs/cm)
MC1	-0.5	2.5
MC2	-0.2	2.5
MC3	-0.2	2.5
MC4	-0.2	-2.0
MC5	-0.2	3.2
MC6	-0.2	3.2
ESD1		Er = 110 kV/cm
ESD2		Er = 100 kV/cm

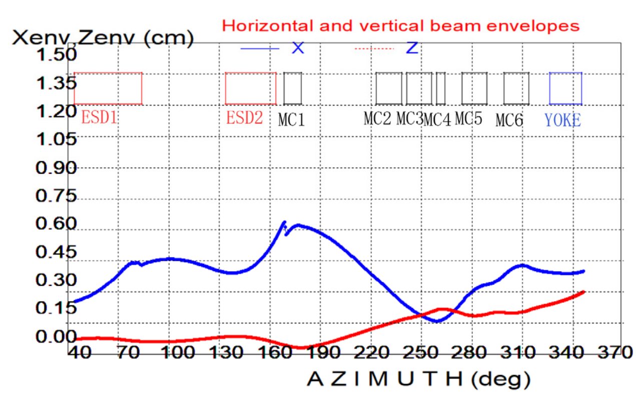

Figure 10: Beam envelop in extraction system.

ISBN: 978-3-95450-205-9 doi:10.18429/JACoW-Cyclotrons2019-MOP004

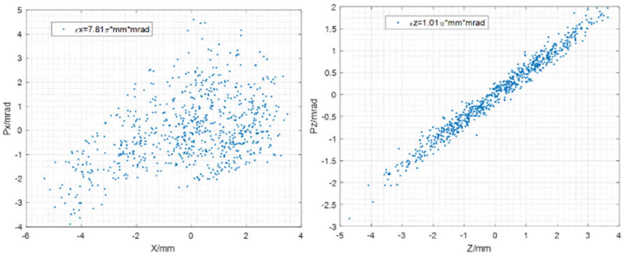

Figure 11: Beam parameters at the exit of cyclotron (R=160 cm).

Beam Loss and Efficiency

The distribution of beam loss is given in Table 4. The protons are mainly lost on ESD1 and MC1 in horizontal direction. The extraction efficiency achieves 76.4%.

Table 4: Beam Loss Distribution in Extraction System

Lost on ESD1	Lost on MC1	Extracted
11.7%	11.9%	76.4%

CONCLUSION

It is easier to deflect beam in a resonance extraction system when the sector's spiral is in the same direction as the particle motion. We have generated a 5 mm turn separation by adding an 8 Gs 1st harmonic bump near $Qr = 1$. In addition to 2 electrostatic deflectors, the proposed extraction system contains 6 sets of passive magnetic channels. The extracted beam envelop is less than 5 mm and extraction efficiency is about 76.4%.

REFERENCES

[1] F. Jiang *et al.*, "Design study of a compact superconducting cyclotron SC240 for proton therapy", in *Proc. IPAC'19*, Melbourne, Australia, May 2019, pp. 3506-3509. doi:10.18429/JACoW-IPAC2019-THPMP029

[2] T. I. Arnette, H. G. Blosser, M. M. Gordon, and D. A. Johnson, "Cyclotron programs for a small computer", *Nucl. Instrum. Methods*, vol. 18-19, pp. 343-345, 1962. doi:10.1016/S0029-554X(62)80044-5

ISBN: 978-3-95450-205-9 doi:10.18429/JACoW-Cyclotrons2019-MOP006

THE DESIGN AND SIMULATION ON THE EXTRACTION SYSTEM FOR CYCIAE-50

Shizhong An†, Yinlong Lv, Huidong Xie, Luyu Ji, Sumin Wei, Ming Li, Lipeng Wen,
Xia Zheng, Jiansheng Xing, Fengping Guan, Peng Huang, Tianjue Zhang
China Institute of Atomic Energy, Beijing 102413, P. R. China

Abstract

A 50 MeV H^- compact cyclotron as a proton irradiation facility is under construction at China Institute of Atomic Energy (CYCIAE-50). The proton beam with the energy of 30 MeV to 50 MeV and the current of 10 μA will be extracted by a single stripping extraction system. In order to reduce the beam loss, the combination magnet is fixed inside the magnetism yoke. The positions of stripping points for the different extraction energy are calculated and the extracted beam trajectories after stripping foil are simulated in detail in this paper. The extracted beam distribution after stripping foil and the extracted beam characters will be studied in this paper. The beam parameters after extraction will be given by the extracting orbit simulation. The design on the whole stripping extraction system has been finished and will be presented in this paper.

INTRODUCTION

China Institute of Atomic Energy (CIAE) has been devoted to the development of the technologies on proton cyclotrons with high intensity and medium & high energy superconductive proton cyclotrons since 1958, when the first cyclotron had been built at CIAE [1]. CIAE has successively built a series of high intensity beam proton cyclotron with different energy ranges of 10 - 100 MeV [2-5]. For 100 MeV H^- cyclotron at CIAE (CYCIAE-100), more than 1 mA beam has been used on the internal target and maximum proton beam current of 520 μA was used on the power target last year [6, 7]. In order to study the radiation damage to spacecraft materials and devices induced single-particle effects in the space radiation environment, a 50 MeV H^- compact cyclotron as a proton irradiation facility is under construction at CIAE (CYCIAE-50).

CYCIAE-50 consists of a 50 MeV proton cyclotron, two beam lines and two radiation effect simulation experimental target station. The 50 MeV proton cyclotron is a compact cyclotron with the proton beam energy from 30 - 50 MeV, and the beam intensity is from 10 nA to 10 μA. The cyclotron is about 3.2 m in diameter, 3.5 m in total height and 80 t in total weight. The proton beam will be extracted by a single movable stripping extraction system. In order to reduce the beam loss, the combination magnet is fixed inside the magnetism yoke. The extracted proton energy can be extracted continuously by changing the stripping position in the radial direction under the fixed magnetic field and RF frequency. A single stripping probe with a piece of carbon foil will be inserted radially from the main magnet pole. The proton beams with the energy range of 30 - 50 MeV will be extracted by charge exchange with stripping foil and then be transported into the crossing point in a combination magnet center separately under the fixed main magnetic field. The combination magnet is fixed between the adjacent yokes of main magnet in the direction of valley region. The difference of stripping extraction system between CYCIAE-50 and CYCIAE-100 is only single stripping probe is chosen and no foil changing system is used for CYCIAE-50 due to the much lower extracted beam current of 10 μA.

The extracted beam optic trajectories are studied in detail in this paper. To keep all the proton beams with various energies transported through the same crossing point in the combination magnet, the stripping probe can be moved in the radial direction and rotated in the angular direction. The positions of stripping points for the different extraction energy are calculated. The extracted beam trajectories after stripping foil and the extracted beam distribution on the stripping foil are simulated in detail in this paper. The design on the combination magnet will be given in this paper too.

THE POSITIONS OF COMBINATION MAGNET AND STRIPPING FOIL

The positions of the stripping points and the combination magnet are chosen by calculating the extraction trajectories of extracted proton beams after stripping foil for different energy with the code CYCTR, which is developed by CIAE [8]. The main magnetic field used to calculate the extraction trajectories is assumed to have mid-plane symmetry. The extracted beam energy is chosen by the corresponding static equilibrium orbit, which is calculated with the code CYClOP [9].

For CYCIAE-50, the radius of magnet pole is 1.0 m and the combination magnet will be set at the position of ($R = 1.75$ m, $\theta = 100°$). Figure 1 shows the position of combination magnet and the extracted beam trajectories from the stripping foil to the combination magnet center for different energies. The red lines are the equilibrium orbits. Table 1 shows the positions of stripping foil with the extraction energy between 20 MeV and 50 MeV. The stripping probe is inserted in the radial direction from the main magnet pole and proton beam will be extracted from the direction of valley. The stripping foil is at ($R = 0.9374$ m, $\theta = 58°$) for 50 MeV and ($R = 0.7399$ m, $\theta = 56°$) for 30 MeV. So, the stripping probe needs to be

† szan@ciae.ac.cn

ISBN: 978-3-95450-205-9 doi:10.18429/JACoW-Cyclotrons2019-MOP006

inserted radially from the magnetism pole and the minimal radius of inserting the foil is 0.6 m.

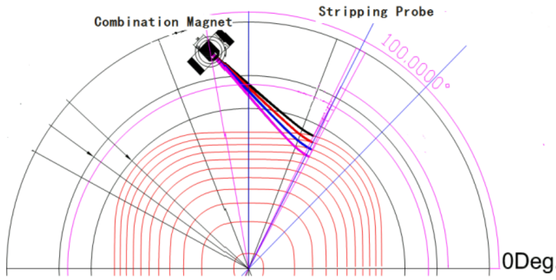

Figure 1: Stripping probe and position of combination magnet. (The red lines are equilibrium orbits).

Table 1: Position of Stripping Foil with Different Extraction Energy, Combination Magnet is Located Closed to the Magnet Yoke with (1.75 m, 100°)

E (MeV)	**R** (M)	**θ** (Degree)
50	0.9374	57.99
40	0.8464	56.97
30	0.7399	56.05
20	0.6092	55.28

THE EXTRACTING TRAJECTORIES WITH COMBINATION MAGNET

Figure 2 shows the extraction trajectory including the fields of combination magnet for the extracted energy of 30 - 50 MeV. The field of combination magnet is different for different extracted energy and the bending angle is ±5°. The field is zero for the extracted energy of 40 MeV. With the different fields, the extracted proton beam with different energy after stripping foil will go through the crossing point of the combination magnet center which is located at the position of (1.75 m, 100°) and will be extracted along the same direction afterwards. The extracted proton beam trajectories for the energy of 30 MeV to 50 MeV can be calculated with the code of CYCTR.

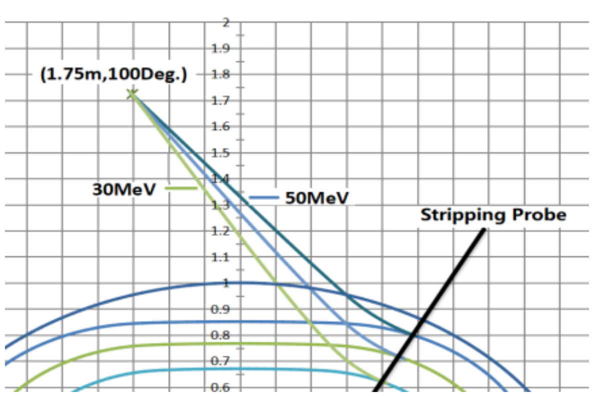

Figure 2: The extracted trajectories with the combination magnet fields for different energies.

THE EXTRACTED BEAM DISTRIBUTION ON THE STRIPPING FOIL

The extracted beam distribution on the stripping foil can be got from the multi-particle tracking code COMA [10]. The H^- beam is injected from the symmetry center of valley with azimuth $\theta = 0°$, and the beam will be tracked along the inserting direction of stripping probe. The initial beam energy is 1.85 MeV at the radius of R = 17.4 cm. The choice of the initial normalized emittance of 0.01 cm^2 or $\varepsilon_x = \varepsilon_z = 4\,\pi$·mm·mrad for CYCIAE-50, which is the same as the case of CYCIAE-100 used in the COMA. The input phase space distributions are uniform in transverse direction and Gaussian in longitudinal direction with the phase extension of $\Delta\phi = \pm 20°$, 20000 macro particles are used in the simulation. Figure 3 shows the input initial phase space distribution and Fig. 4 shows the extracted beam phase space distributions on the stripping foil with the energy of 50 MeV.

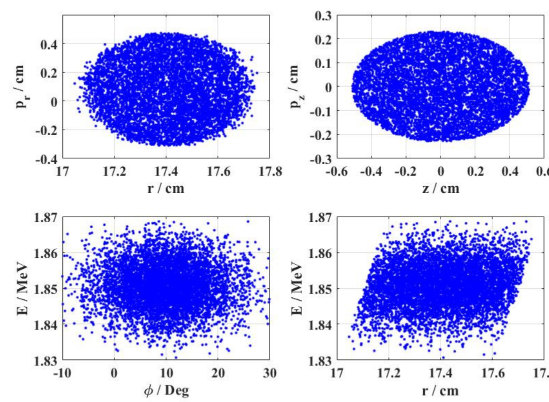

Figure 3: Initial phase space distribution with the normalized emittance of 4.0 π·mm·mrad and phase width of ±20°.

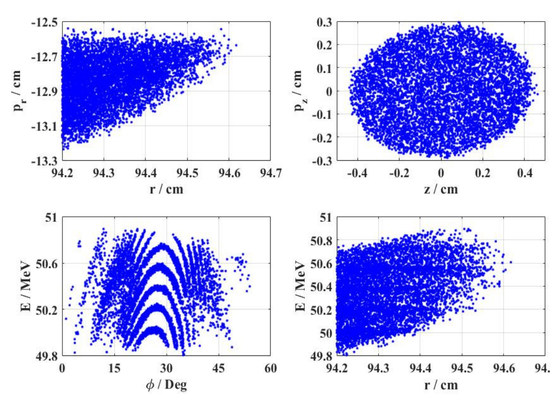

Figure 4: The extracted beam phase space distribution for 50 MeV on the stripping foil.

The extracted beam phase space distribution for 30 MeV on the stripping foil is similar as the case of 50 MeV. From the simulation, the normalized emittance for the extracted proton beam on the foil is almost the same as the initial case. The beam profile on the foil is

ISBN: 978-3-95450-205-9 doi:10.18429/JACoW-Cyclotrons2019-MOP006

about 5mm×9mm and the energy spread is about ±1.0% for 50 MeV.

THE DESIGNS OF THE EXTRACTED SYSTEM

The designs for stripping extracted system of CYCIAE-50 have been finished. A single movable stripping probe with a piece of carbon foil can move from 30 MeV to 50 MeV. Figure 5 shows the structure of the movable stripping probe. The stripping probe can be moved along the radial direction and rotated along the angle direction. The precision of radial movement is limited about 0.01 cm. The minimum radius which the stripping probe can be inserted is 0.7 m and the rotation range of the probe is ±3°. Only one piece of carbon foil is used for the system and the foil thickness of 120 - 150 μg/cm^2 is enough for CYCIAE-50. The stripping efficiency is about 99.99%.

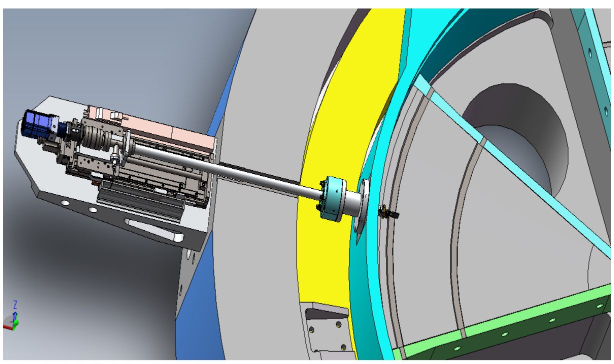

Figure 5: The structure of the movable stripping probe.

The combination magnet in the 50 MeV stripping exchange extraction system is placed at the position of R= 1.75 m, θ =100°. The combination magnet design is very similar as the case of CYCIAE-100 [11]. The structure of the combination magnet is shown in Fig. 6. The maximum of the field is 0.35T. The maximum bending angle of beam is 5°. The field is -1.5 kG for 30 MeV and 3.5 kG for 50 MeV. The Bending radius is 2968 mm and the gap is 82 mm.

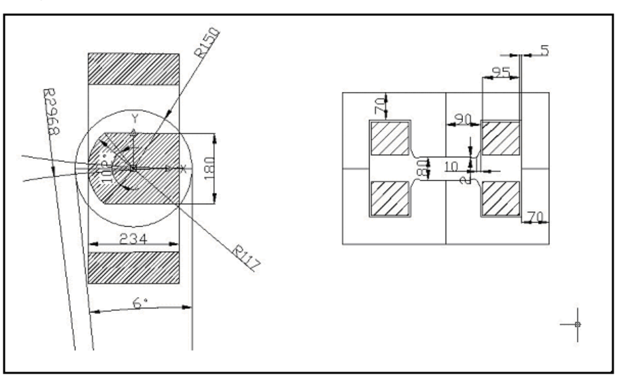

Figure 6: The structure of the combination magnet.

CONCLUSION

All the calculation and simulation on the stripping extraction system has been finished for CYCIAE-50. It is very similar as the case of CYCIAE-100. A single movable stripping probe is adopted in the extraction system. Because the extracted proton beam current is limited less than 10 μA, only a piece of carbon foil will be used to extract the proton beam from 30 - 50 MeV and no foil changing system is used in this machine. All the detail design of the stripping extraction system for CYCIAE-50 has been finished and is being manufactured now. Beam commissioning is expected to be done at the end of the next year.

ACKNOWLEDGEMENTS

The authors are very much grateful to Dr. Yi-Nong Rao from TRIUMF, who give us considerable help and providing materials concerning the cyclotron and the use of the code COMA and CYCLOP. Also the authors would like to give the grateful acknowledge to Dr. Gerardo Dutto, George Mackenzie, R. Baartman from TRIUMF, Dr. Werner Joho from PSI, Jingyu Tang from IHEP-Beijing, for the extraction discussion and lots of useful suggestions.

REFERENCES

[1] Fan Mingwu, Zhang Xingzhi, Li Zhenguo *et al.*, “Construction of high current proton cyclotron CYCIAE-30”, Chinese Science Bulletin, 1995， CN 11-1784/N, vol. 40, no. 1, p. 825.

[2] T. J. Zhang, L. I. Zhenguo, A. N. Shizhong *et al.*, “The cyclotron development activities at CIAE”, *Nucl. Instrum. Methods Phys. Res., Sect. B*, vol. 269, no. 24, pp. 2863-2870, Dec. 2011. doi:10.1016/j.nimb.2011.04.047

[3] T. J. Zhang, Li Zhen-Guo, Chu Cheng-Jieo, *et al.*, “Test stand design and construction for high intensity, cyclotron development”, *Chinese Physics C*, vol. 32, no. S1, p. 237, 2008.

[4] T. J. Zhang, Lu Yinlong, Yin Zhiguo, *et al.*, “Overall design of CYCIAE-14, a 14 MeV PET cyclotron”, *Nucl. Instrum. Methods Phys. Res., Sect. B*, vol. 269, no. 24, pp. 2950-2954, Dec. 2011. doi:10.1016/j.nimb.2011.04.049

[5] T. J. Zhang, J. Yang, “The beam commissioning of BRIF and future cyclotron development at CIAE”, *Nucl. Instrum. Methods Phys. Res., Sect. B*, vol. 376, pp. 434-439, 2016. doi:10.1016/j.nimb.2016.01.022

[6] T. Zhang, S. An, Y. Lv, *et al.*, “mA beam acceleration efforts on 100 MeV H$^-$ cyclotron at CIAE”, *Nucl. Instrum. Methods Phys. Res., Sect. B*, vol. 406A. A, pp. 250-255, Sept. 2017. doi:10.1016/j.nimb.2016.11.024

[7] Sumin Wei, Tianjue Zhang, Feng Wang, Shizhong An *et al.*, “Study and construction of a 100 MeV high power proton beam line”, Atomic Energy Science and Technology, ISSN 1000-6931, CN 11-2044/TL, 2019.

[8] An Shizhong, Guan Fengping, Xie Huaidong *et al.*, “Stripping extraction calculation and simulation for CYCIAE-100”, *Chinese Physics C*, vol. 33, no. S2, pp. 42-47, Jun. 2009. doi:10.1088/1674-1137/33/S2/011

[9] M. M. Gordon, “Computation of closed orbits and basic focusing properties for sector-focused cyclotrons and the design of cyclops”, *Part. Accel*, vol. 16, pp. 39-62, 1984.

ISBN: 978-3-95450-205-9 doi:10.18429/JACoW-Cyclotrons2019-MOP006

[10] C. J. Kost, G. H. Mackezie, "COMA – A linear motion code for cyclotron", *IEEE Transact. Nucl. Sci.*, vol. 22, no. 3, Jun. 1975. doi:10.1109/TNS.1975.4328029

[11] S. M. Wei, M. Li, C. Wang, M. Yin, T. J. Zhang, and X. Zheng, "Design and construction of combination magnet for CYCIAE-100", in *Proc. Cyclotrons'13*, Vancouver, Canada, Sep. 2013, paper TUPSH002, pp. 221-223.

ISBN: 978-3-95450-205-9 doi:10.18429/JACoW-Cyclotrons2019-MOP007

THE DESIGN AND CALCULATION ON THE INJECTION AND CENTRAL REGION FOR CYCIAE-50

Luyu Ji†, Xianlu Jia, Shizhong An, Yinlong Lv, Xia Zheng, Fengping Guan, Tianjue Zhang, Shenglong Wang, Chuan Wang
China Institute of Atomic Energy, Beijing 102413, P. R. China

Abstract

A 50 MeV cyclotron is being built at China Institute of Atomic Energy (CYCIAE-50). CYCIAE-50 is a compact H^- cyclotron with the proton beam energy of 30 MeV to 50 MeV and the beam current of 10 μA. A multi-cusp H^- ion source with the beam current of 5 mA will be used for this machine. The design on the injection and central region of CYAIAE-50 has been finished. The way of matching the beam from ion source to central region and the design of central region will be present in this paper. In addition, some significant problems in central region will be discussed, including radial alignment, axial focusing, longitudinal focusing, etc.

INTRODUCTION

A compact H^- cyclotron, CYCIAE-50, is being constructed for Space Science and Applied Research (CSSAR). H^- beams are injected through a spiral deflector with the energy of 30 keV, and extracted by a stripping foil in the range 30 - 50 MeV with the current of 10 μA. There are four straight pole sectors in CYCIAE-50 and the magnetic field in central region is 0.9 T. Forth harmonic acceleration is adopted with two 50 kV, 65.5 MHz cavities in the valleys.

A 30 keV, 5 mA external H^- multi-cusp ion source is adopted, which is the same as the case of CYCIAE-100 [1]. The injection system is very simple design. The H^- beam from the ion source enters the spiral inflector in the center region only through a solenoid. The ion source and the injection beamline are being manufactured. The design procedure and results of central region, spiral inflector and injection line are displayed in this paper.

CENTRAL REGION DESIGN

The following problems should be concerned for the central region designs:

- Central region must fit the structures of RF cavities and shimming bars.
- Beams should pass through electrodes from their center line.
- Good axial focussing and radial centering.

CYCLONE is a particle tracking code especially fitting the calculation in central region. The magnet field is got from finite element method program [2] and the 3D electric potential map can be obtained from code of RELAX3D [3]. When we design central region, we usually adjust electrode structure and sometimes shimming bars if necessary.

The process of central region design is shown as follows:

- According to the magnetic field, RF cavities, shimming bars and injection energy, the central region will be designed, partly referring to the design of cyclotrons at CIAE [4-8].
- Finding the reference particle in accelerating region by orbit tracking, who needs the least turn to be accelerated to 50 MeV and has the least amplitude of radial oscillation.
- Tracking reference particle backwards to injection point, by which optimizing electrode structure.
- Tracking multiparticle from injection to extraction and optimizing electrode structure until getting a good beam dynamical result.

The Electrode structure, electric field distribution and particles' trajectory in central region are shown in Fig. 1. Central rays within ±20° phase width is tracked, whose phase history is shown in Fig. 2 and radial misalignment is shown in Fig. 3. It needs 272 turns for the reference particle from 30 keV to 50 MeV and less than 279 turns for particles within ±20° phase width. As shown in Fig. 2, the 40° phase width is compressed to 25° in central region. The amplitudes of radial oscillation around static equilibrium orbit (SEO) are less than 1.5 mm.

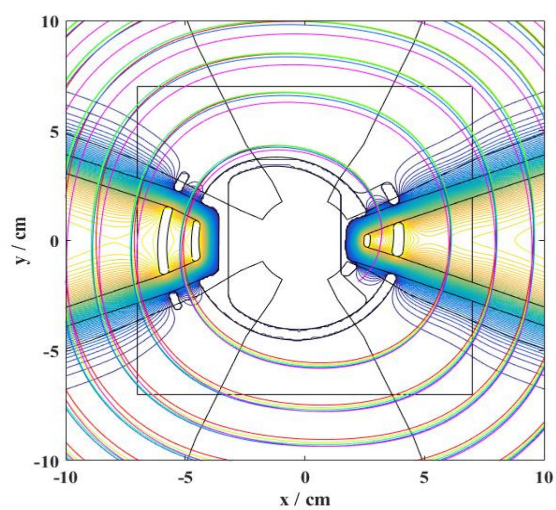

Figure 1: Electrode structure, electric field and particles' trajectory in central region.

The vertical focussing includes magnetic focussing and electric focussing. Vertical electric focussing plays an important role at low energy, which depends on electrode structure and the phase of particles [9].

†luyu_ji@163.com

ISBN: 978-3-95450-205-9 doi:10.18429/JACoW-Cyclotrons2019-MOP007

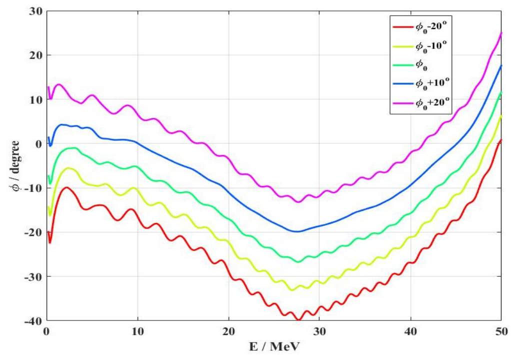

Figure 2: Phase history of central rays within ±20° phase width.

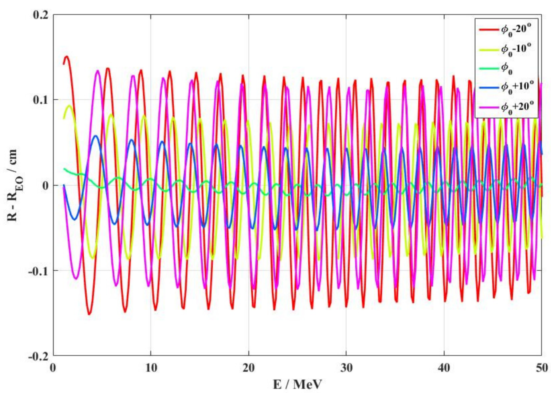

Figure 3: Radial misalignment of central rays within ±20° phase width.

Figure 4 gives the results of tracking particles with different phase and axial coordinates. The top one is particles start at $z = 1$ mm and the bottom one is particles start at $p_z = 1$ mm. We can see that positive phases leads a bigger v_z in central region.

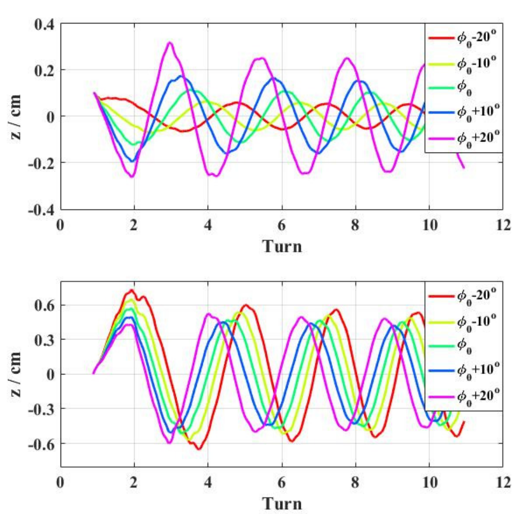

Figure 4: Axial motion of particles with different starting RF phase. (The top one for the starting particles at $z = 1$ mm and the bottom one for the starting particles at $p_z = 1$ mm).

INFLECTOR DESIGN

After finishing central region design, the orbit of reference particle is obtained. Inflector design needs the coordinates of inflector's central particle closely to the reference particle at the exit of spiral inflector. The simulation was done by program CASINO [10] and INFLECTOR [11]. Table 1 shows some main parameters of inflector. Figure 5 shows the surface of inflector electrodes and the trajectory of central particle.

Table 1: Main Parameters of Inflector

Parameter(unit)	Value	Unit
Injection energy	30	keV
Electric bend radius	32	mm
Tilt parameter	-0.75	
Electrode spacing	8	mm
Electrode width	16	mm
Voltage	12.60	kV
Matching point θ	313.23	°
Matching point R	2.81	cm
Matching point P_R	0.61	cm

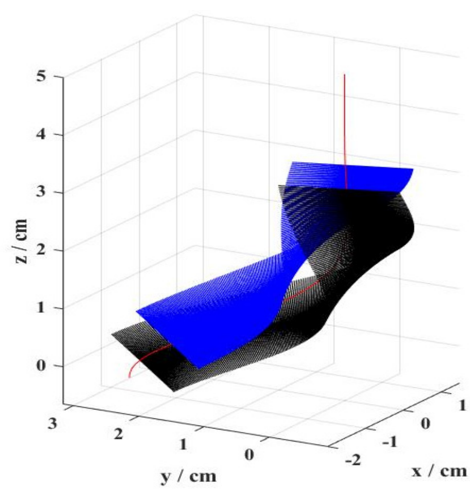

Figure 5: The surface of inflector electrodes and the trajectory of central particle.

INJECTION LINE DESIGN

As shown in Fig. 6, the injection line is about 1.4 m, which consists of ion source, vacuum chamber, x-y steering, solenoid and spiral inflector. The DC beam is injected from the ion source which is upper the magnet of the cyclotron. The solenoid has a effective length of 35 cm with a field of 1.9 kG. The transfer matrix of spiral inflector is calculated by orbit tracking. The ion source provides a 5 mA beam, whose normalized emittance is 0.4 π·mm·mrad [12]. A more than 10^{-4} Pa vacuum makes the 95% neutralization achieved [13]. The parameters of the ion source and injection beamline are shown in Table 2 and the beam size (FWHM) is shown in Table 3.

ISBN: 978-3-95450-205-9 doi:10.18429/JACoW-Cyclotrons2019-MOP007

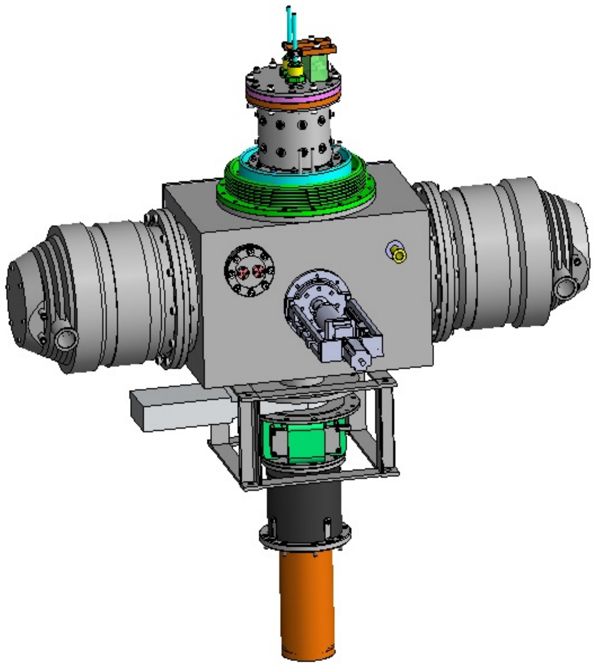

Figure 6: Injection line of CYCIAE-50.

Table 2: The Parameters of the Ion Source and Injection Beamline

Parameter	Value	Unit
Beam energy	30	keV
Normalized emittance	0.4	π·mm·mrad
Beam current	5	mA
Inflector voltage	±10	kV
Injection beamline	~1.4	m
Inflector gap	8	mm

Table 3: Beam Parameters in the CYCIAE-50 Beam Line

Position	*x* [mm]	*x'* [mrad]	*y* [mm]	*y'* [mrad]
Exit of ion source	4.0	22.0	4.0	22.0
Entrance of inflector	1.0	50.9	1.0	50.9
Exit of inflector	2.4	55.7	1.2	41.6

CONCLUSION

All the calculation and simulation on the injection system has been finished for CYCIAE-50. The central region design results are described in detail in this paper. From the calculation, the beam is well centered and more than 40° RF phase width can be accepted. Spiral inflector is designed to match the injection point and reference particle in central region. The beam line from ion source to central region is matched with a 5 mA, 0.4 π·mm·mrad H^- beam. The main parts of the cyclotron such as the main magnet are being manufactured now. The final structure of the central region will be fixed after finishing the magnet filed measurement and shimming. Beam commissioning is expected to be done at the end of the next year.

REFERENCES

[1] H. J. Yao *et al.*, "Matching from H− multicusp source to central region of a 100 MeV compact cyclotron for high current injection", *Rev. Sci. Instrum.*, vol. 79, no. 2, p. 02C708, 2008. doi:10.1063/1.2801646

[2] S. L. Wang *et al.*, "Study on the main magnet design of 50 MeV H^- Cyclotron", Atomic Energy Science and Technology, Aug. 2019. www.aest.org.cn/CN/10.7538/yzk.2019.youxian.0130

[3] C. J. Kost and F. W. Jones, "RELAX3D User's Guide and reference Manual", Triumf, Vancouver, BC, Canada, Rep. TRI-CD-88-01, 1988.

[4] T. J. Zhang *et al.*, "Overall design of CYCIAE-14, a 14 MeV PET cyclotron", *Nucl. Instrum. Methods Phys. Res., Sect. B*, vol. 269, no. 24, pp. 2950-2954, Dec. 2011. doi:10.1016/j.nimb.2011.04.049

[5] T. J. Zhang *et al.*, "Spiral inflector and central region study for three cyclotrons at CIAE", *Nucl. Instrum. Methods Phys. Res., Sect. B,* vol. 261, no. 1-2, pp. 60-64, Aug. 2007. doi:10.1016/j.nimb.2007.04.230

[6] J. J. Yang *et al.*, "The injection line and central region design of CYCIAE-70", in *Proc Cyclotrons'10*, Lanzhou, China, 2010, paper MOPCP030, pp. 111-113.

[7] T. J. Zhang *et al.*, "The study and design of spiral inflector and central region for CYCIAE-100 cyclotron", in *Proc. Cyclotrons'07*, Giardini Naxos, Italy, Oct. 2007, pp. 57-59.

[8] D. S. Zhang *et al.*, "Some initial results of central region orbit tracking for superconducting cyclotron CYCIAE-230", in *Proc. SAP'17*, Jishou, China, Aug. 2017, paper MOPH04, pp. 34-36. doi:10.18429/JACoW-SAP2017-MOPH04

[9] H. J. Yao *et al.*, "Vertical focusing study in the central region of the CYCIAE-100 cyclotron", *Chin. Phys. C*, vol. 33, no. S2, p. 39, Jun. 2009. doi:10.1088/1674-1137/33/S2/010

[10] B. F. Milton *et al.*, "CASINO User Guide and Reference Manual", Triumf, Vancouver, BC, Canada, Rep. TRI-DN-89-19, 1989.

[11] L. Milinkovic, "RELAX3D Spiral Inflectors", Triumf, Vancouver, BC, Canada, Rep. TRI-DN-89-21, Sep. 1992.

[12] T. J. Zhang *et al.*, "Experimental study for 15–20 mA dc H^- multicusp source", *Rev. Sci. Instrum.*, vol. 81, p. 02A705, Oct. 2010. doi:10.1063/1.3266148

[13] R. Baartman, "Injection line optics", Triumf, Vancouver, BC, Canada, Rep. TR30-DN-25, 1989.

ISBN: 978-3-95450-205-9 doi:10.18429/JACoW-Cyclotrons2019-MOP008

MECHANICAL DESIGN OF BEAM LINES FOR 230 MeV SC CYCLOTRON AT CIAE

Meng Yin*, Tianjue Zhang, Sumin Wei, Shizhong An, YunlongLv, Fengping Guan, Feng Wang, Lipeng Wen, Fei Wang, Gaofeng Pan, Xiaofeng Zhu
China Institute of Atomic Energy, P.O. Box 275(3), Beijing 102413

Abstract

A 230MeV SC cyclotron (CYCIAE-230) is under construction at CIAE, which can extract 230MeV proton beam for proton therapy. To develop the proton beam transfer system which used in the field of proton therapy, the mechanical design of proton beam lines based on the CYCIAE-230 has been finished at CIAE. The proton beam transfer system includes the beam lines, beam dump, gantry, nozzle, couch, image guidance system, etc. Two beam lines are designed at CIAE this moment. One is for the nozzle system, the other is for the beam dump. The beam lines include four systems: the energy selection system (ESS), the beam transportation systems (BTS), gantry system, and beam dump. The beam lines are very compact in order to match the beam optics and the space limitation. The gantry can be rotated ±180°. The collimation of beam lines is very important to get the better beam quality for the proton therapy. There are several key components in beam lines, such as magnets, energy degrader, beam diagnostics components, vacuum components, etc. The designed mechanical tolerance of the magnets is limited less than 0.1 mm. There are at least four targets on each magnet for collimation and all the components can be adjusted in three dimensions. The magnets are being manufactured now. The mechanical design of proton beam lines based on the CYCIAE-230 will be presented in this paper.

INTRODUCTION

To build a healthy China, improving cancer 5-year survival rate is one of the most important actions. In China, the deaths caused by cancer are 2.5 million, and the new cancer cases are 3.5 million each year [1]. Proton therapy is an effective way for the cancer treatment. More than 4 million cancer patients in China will be beneficial from proton therapy each year.

To meet urgent needs for proton therapy, one of the technology innovation plan in "Dragon 2020 — major medical equipment - medical cyclotron key technology and engineering research" had launched by China National Nuclear Corporation (CNNC) [2]. In this project, a 230 MeV compact superconducting cyclotron is developing at China Institute of Atomic Energy (CIAE) to extract 230 MeV proton beam [3]. Beam lines for the 230 MeV SC cyclotron to transport the beam to the nozzle system and to the beam dump are under construction at the same time.

*mythtom@gmail.com
+This work was supported in part by the National Natural Science Foundation of China under Grant 11475269 and 11375274.

The whole project consists of a 230 MeV SC cyclotron (CYCIAE-230), the energy selection system (ESS), the beam transportation systems (BTS), a gantry and a beam dump, as shown in the Fig. 1 [4].

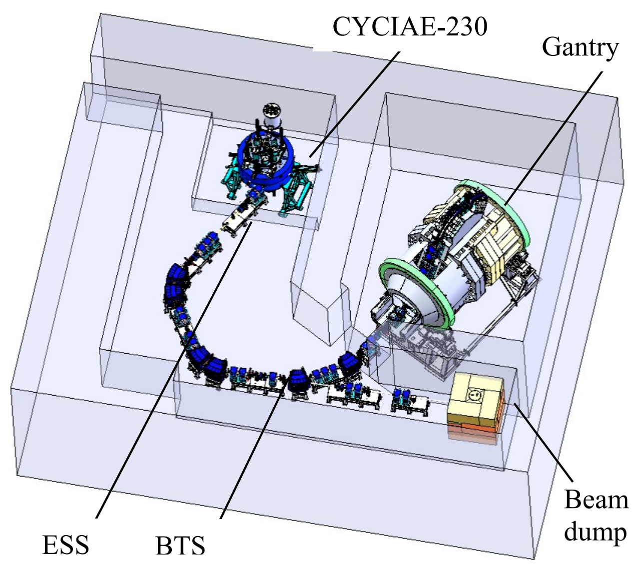

Figure 1: Layout of CYCIAE-230 and beam lines.

The beam line is about 47 m long. The ESS is 5.2 m long. The BTS is 19.8 m long, which is the longest system in beam lines. The beam line on gantry is 13.5 m long and the beam line to beam dump is 8.5 m long.

BEAM LINES ON GROUND

The beam lines on ground divided into three parts, include ESS, BTS and the beam line to beam dump. The height of the beam on ground is 1.25 m, all of the components in beam lines on ground are designed to meet this requirement.

There are trenches at both sides of the beam lines on ground. Along the beam direction, cables are put into the left trench and water pipes are put into the right trench. All of the components are designed to meet this layout. The mechanical specifications of the components in beam lines on ground are listed in Table 1.

There are many components in ESS, one of the most important component is the energy degrader. The energy degrader is used to adjust the proton energy, which can fit to the depth of the tumor [5]. To test the performance of the degrader, two types of degrader had been made. The shape of the two degraders are wedge and circle, as shown in the Fig. 2. The energy distribution of the circular degrader is

ISBN: 978-3-95450-205-9 doi:10.18429/JACoW-Cyclotrons2019-MOP008

discrete and the energy distribution of the wedge degrader is continuous.

Tabel.1: Mechanical Specifications of Components on Ground

Code	Components	Dimensions [mm]	Weight [kg]	System
ED	Energy Degrader	691× φ 640	570	Degrader
Q	Quadrupole	385×700 ×708	700	magnet
SXY	Steering Magnet	187×339 ×364	260	
B30	30° Dipole	(R1007-R2005)× 30° ×978	5800	
BPM	Beam Position Monitor	170×240 ×563	17	Beam diagnostics
FC	Faraday Cup	230×260 ×755	30	
RC	Round Hole Collimator	100× φ 145	22	
C	Four Collimator	220×836 ×836	26	
T	Turbo Pump	430× φ 230	27	Vacuum
RV	Release Valve	200× φ 92	2	
G	Gauge	80× φ 15.5	0.5	
V	Valve	60×166× 506	18	

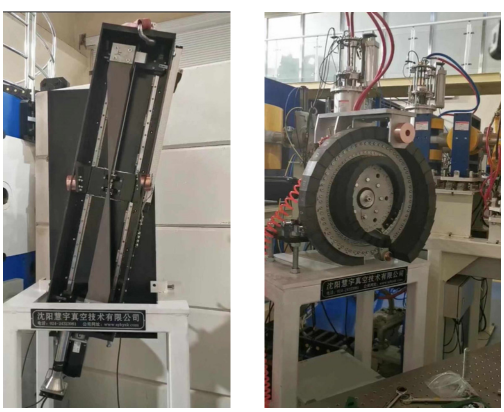

Figure 2: Photos of two types of energy degrader (left: wedge right: circle).

A spiral rotating disk, which is driving by motor, is fixed on the cylinder. There are twenty blocks with different thickness on the disk, which can adjust the energy step by step. The material of blocks is graphite. Two collimators are fixed at beam entrance and exit of the energy degrader to guarantee the quality of the beam [6].

The magnets are another important component on the beam line. They are all water-cooled conventional ac electromagnets. The changes of magnetic field should be 300 Gauss/20 ms to meet the requirement of pencil beam scanning.

There are three kinds magnets in BTS, among them, the 30°-dipoles are used to deflect the beam. Neutrons are produced when the beam through the energy degrader. To protect the patients from irradiation by neutrons, the protons are deflected to the treatment room and the neutrons are shield by thick cement walls.

The 30°-dipoles have a large leakage magnetic field, which can influence the performance of the components nearby. So two magnetic shielding plates are added at each ends of the magnets [7], as shown in Fig. 3. There are at four targets on each 30° dipoles for collimation. There are beam entering and beam extracting vacuum pipes welding on the vacuum chambers of 30°-dipoles, and a third vacuum pipe welding right to beam entering pipe at opposite direction for collimation at installation stage and installing fluorescent target at beam debugging stage. There are two bellows before and after the 30°-dipoles vacuum pipes for easy installation. There is an adjustable support under 30° dipoles. The designed mechanical tolerance of the 30° dipoles is limited less than 0.1 mm.

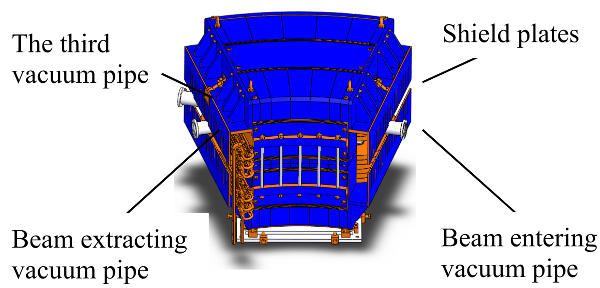

Figure 3: Model diagram of 30°-dipoles.

BEAM LINE ON GANTRY

The beam energy is continuously adjustable from 70 MeV to 230 MeV in the beam line on gantry [8]. At the exit of the gantry, the beam enters the nozzle and transmit to the isocenter where the tumor is located. The beam line is composed of a 60°-dipole, three double quadrupoles, a pair of 75°-dipoles with thin-thick-thin triple quadrupoles between them, the diagnostic components and vacuum components, as shown in Fig. 4 [9]. All the magnets on gantry are room temperature to get rapid change. The two 75° dipoles are arranged symmetrically with the thin-thick-thin triple quadrupoles between them which can eliminate the dispersion on the beam line [10]. The pair of XY fast scanning magnets are installed in the nozzle just after the second 75°-dipole for the fast pencil beam scanning.

One 60°-dipole and two 75°-dipoles fixed on gantry to bend the beam from level to vertical. These dipoles are rotate on gantry ±180°. At both sides of each dipole, there is an adjustable support to fix the dipole on gantry and to adjust the X and Y position, the Z position can be adjusted by add gasket into the gap between the dipole and the support, as shown in Fig. 5. The connectors of electricity and water are integrated in a box on the top of the dipole.

ISBN: 978-3-95450-205-9 doi:10.18429/JACoW-Cyclotrons2019-MOP008

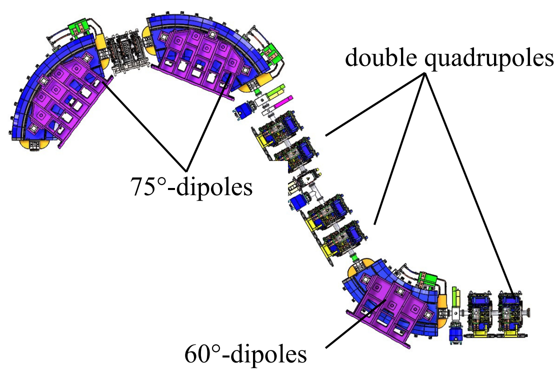

Figure 4: Layout of beam line on gantry.

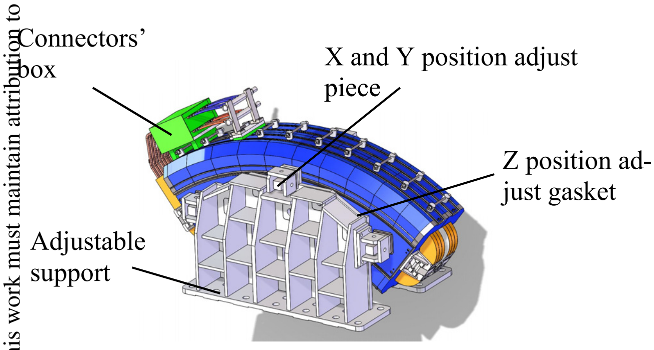

Figure 5: Model diagram of 75°-dipoles.

There are three kinds of quadrupoles in beam lines. All of the quadrupoles have iron outside with water-cooled copper coils inside. The coils are wound into individual "saddle" coils. Each coils are fixed surround the poles of the quadrupoles. The diameters of the bore are large enough to fit the diameter of the beam tubes. Different numbers of quadrupoles form different combinations to meet the requirement of beam optics. There are four kinds of combinations, including single quadrupole, double quadrupoles, triple quadrupoles and thin-thick-thin triple quadrupoles. There is an adjustable support under each combination to adjust the quadrupoles together, as shown in the Fig. 6.

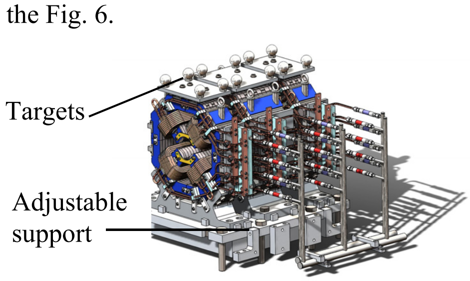

Figure 6: Model diagram of thin-thick-thin triple quadrupoles.

The designed mechanical tolerance of the quadrupole is limited less than 0.1 mm. There are four targets on each quadrupole for collimation.

CONCLUSIONS

Based on the beam optical design and considering the space limitation, the design of the beam lines layout had been finished, including ESS, BTS, the beam line on gantry and the beam line to beam dump. According to the layout of the beam lines, the mechanical design of beam lines and the main components on beam lines had been finished. In the design process of the magnets, many technical details had been considered, such as magnetic shielding plates, a third vacuum pipes in 30°-dipoles and position adjust gaskets in 60°- and 75°-dipoles on gantry. The designed mechanical tolerance of the magnets is limited less than 0.1 mm.

The beam lines are under construction now. The assembly of the beam lines will finish in 2019, and the beam debugging of the beam lines will start in 2020.

REFERENCES

[1] W. Chen, R. Zheng, P. Baade *et al.*, "Cancer statistics in China", 2015 [J]. *CA Cancer journal for Clinicians*, vol. 66, pp 115-132, Mar. 2016. doi:10.3322/caac.21338

[2] T. Zhang, C. Wang, M. Li *et al.*, "Developments for 230 MeV superconducting cyclotrons for proton therapy and proton irradiation", *Nucl. Instrum. Methods Phys. Res., Sect. B*, vol. 406, pp. 244-249, Sept. 2017. doi:10.1016/j.nimb.2016.11.010

[3] T. Zhang, C. Wang, T. Cui, *et al.*, "Design and Construction of the main magnet for a 230 MeV superconducting cyclotron", *IEEE Trans. Appl. Supercond.*, vol. 28, no. 3, pp. 1-5, April 2018, doi:10.1109/TASC.2017.2777469

[4] S. Wei, F. Guan, and T. Zhang, "Cyclotron-based proton therapy system", China, 201610616075.1. doi:patents.google.com/patent/CN106139420A/en.

[5] F. Guan, S. Wei, and F. Wang, "Double disc rotary compact energy degrader and using method", China, 201610614151.5. doi:patents.google.com/patent/CN106267584B/en

[6] F. Guan, S. Wei, and F. Wang, "Device and method for effectively controlling proton beam emittance after energy degrader", China, 201610616069.6. doi:patents.google.com/patent/CN106211535B/en

[7] Y. Chen and W. Kang, "Design of current septum magnet for injection system of China spallation neutron source", *High Power Laser and Particle Beams*, vol. 24, no. 2, Feb. 2012. doi:10.3788/HPLPB20122402.0453

[8] W. Chen *et al.*, "Design of prototype magnets for HUST proton therapy beamline", *IEEE Trans. Appl. Supercond.*, vol. 28, no. 3, pp. 99, Nov. 2017. doi:10.1109/TASC.2017.2772868

[9] S. Wei, F. Guan, F. Wang *et al.*, "Gantry for treating tumors", China, 201610616041.2. doi:patents.google.com/patent/CN106139419A/en

[10] A. C. Paul *et al.*, "The beamline for the second axis of the dual axis radiographic hydrodynamic test facility", in *Proc. 18th Particle Accelerator Conf. (PAC'99)*, New York, NY, USA, Mar. 1999, paper THP126, pp. 3254-3256.

ISBN: 978-3-95450-205-9 doi:10.18429/JACoW-Cyclotrons2019-MOP010

A 50 MeV PROTON BEAM LINE DESIGN

S. M. Wei†, S. Z. An, L. Y. Lv, L. L. Guan
China Institute of Atomic Energy, Beijing, 102413, China

Abstract

The cyclotron center at the China Institute of Atomic Energ (CIAE) is now developing a medium-energy proton irradiation device that provides a proton beam with an energy range of 30 MeV to 50 MeV to simulate a space proton radiation environment, which has a significant impact on spacecraft. A beam transport line is designed for irradiation effect study based on this 50 MeV compact cyclotron, which requires continuous adjustment of the beam energy and the beam spot on the target requires high uniformity. The proton beam extracted from the cyclotron is adjusted to the energy required by using the degrader and the energy selected system, then the proton beam will be transported to the target. In order to obtain uniform large-diameter beam spot on the target, a wobbling magnet is installed on the beam line to uniformly sweep the proton beam on the target and finally obtain the proton beam with energy of 10 MeV-50 MeV, current of 10 μA and beam spot of 20 cm*20 cm on the target.

INTRODUCTION

Protons are the main components of the space radiation environment, causing radiation damage to spacecraft materials and devices, as well as induced single-particle effects, which seriously threaten satellite safety, especially the scientific satellite payload is more sensitive to damage caused by space protons. The Research Center of Cyclotron in China Institute of Atomic Energy (CIAE) has designed a medium-energy proton irradiation device, which is mainly composed of a 50 MeV proton cyclotron, a beam transport line and an experimental terminal. The center has already developed several compact cyclotrons and proton beam lines [1-4].

The 50 MeV cyclotron is designed as a compact structure that extracts protons from 30 MeV to 50 MeV, with a lower energy range, a degrader is provided on the beam line to reduce beam energy to 10 MeV. For irradiation effect study in this case, the energy dispersion required is small so the energy selected system is necessary.

A wobbling magnet is installed a few meters in front of the target to provide a magnetic field with periodic rotation changes, which make the beam spot uniformly sweep on the target.

The layout of the beam line and element design is shown in this paper.

LAYOUT OF THE 50 MeV PROTON BEAM TRANSFER SYSTEM

The layout of the 50 MeV irradiation dedicated proton beam transport system is shown in Fig. 1. Since the proton energy extracted by the cyclotron is adjustable in the range of 30 MeV~50 MeV, a combination magnet is placed inside the yoke which will combine proton beams with different energies to one beam line. The diagnostic box is including faraday cup (FC), fluorescent target (SS) and the beam profile monitor (BPM), which are used to measure the beam intensity and the beam profile; D1 is the degrader, which can reduce the beam energy extracted from the cyclotron to a lowest energy 10 MeV by using different thicknesses of graphite; C is a collimator; B1 and B2 are two 45° bending magnets that deflect the proton beam by 90°, and these two bending magnet and the collimators can select proton energy to reduce energy dispersion; Q is a quadrupoles for proton beam focusing; SXY is steering magnet for correcting the particle center; T is the vacuum pump for obtaining the vacuum of the pipe; W is the wobbling magnet that provide a magnetic field with periodic rotation changes. This magnetic field causes the beam on the target to periodically rotate and scan to improve the uniformity and the size of the beam spot on the target [5].

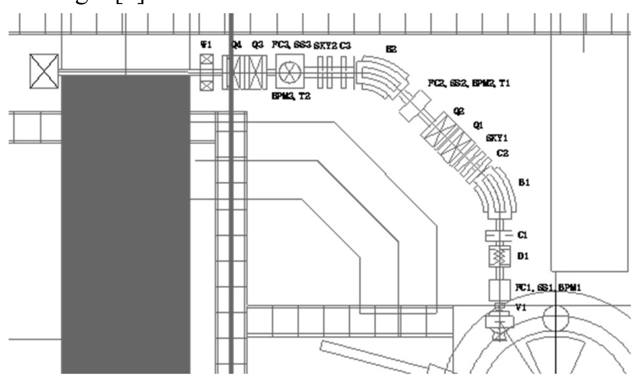

Figure 1: The layout of the 50 MeV beam transfer system.

The total length of the beam line is about 12 m, the inner diameter of the beam pipe is Φ78 mm, and the material is aluminium. The optics and the magnets design will be given in detail.

OPTICS RESULTS

The 50 MeV compact proton cyclotron uses a stripping method to extract the proton beam with the energy range 30 MeV~50 MeV, the maximum beam intensity is 10 μA, and the minimum intensity is 10 nA. The beam with different energy after the stripping foil is transported through the combination magnet into the same beam pipe. The initial input parameters for the optical matching are the σ matrix of the beam on the stripping film provided by the extraction system (calculated by using the COMA program) and the beam transfer matrix of the stripping foil to the exit of the combination magnet (by using GOBLIN and STRAPUBC). The optical matching of the beam line

† 3517267@qq.com

ISBN: 978-3-95450-205-9 doi:10.18429/JACoW-Cyclotrons2019-MOP010

is using TRACE 3-D, which uses matrix multiplication to obtain beam characteristics for any section of the beam line [6].

The layout of the beam line, as shown in Fig. 1, has two bending magnets and four quadrupoles to assist with the optics matching.

In the matching, the proton beam of 10 MeV-50 MeV and 10 μA was simulated respectively, and the parameters of each quadrupole were adjusted in the matching to get the size of the beam spot on the target is Φ20 mm.

Figure 2 shows the optics matching results for 30 MeV and 50 MeV. The protons in this energy range can be directly extracted from the cyclotron without the degrader. The matching starts from the exit of the cyclotron. Figure 2 also shows the envelope in both horizontal and vertical directions, the upper one is the optics result of 50 MeV beam and the nether on is 30 MeV. The magnetic field gradient of each quadrupole is shown in Table 1. The beam spot on the target for both 50 MeV and 30 MeV is Φ20 mm.

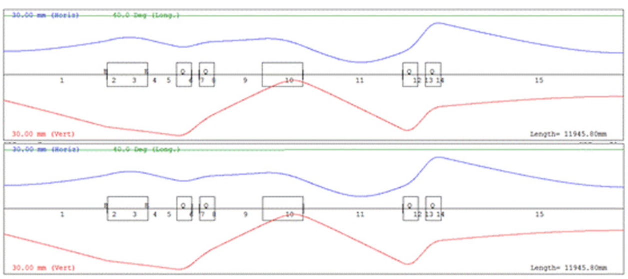

Figure 2: The optics results of 50 MeV (upper) and 30 MeV (lower).

Since the minimum energy extracted from the cyclotron is 30 MeV, the lower energy beam requires by using a degrader, the parameters of the proton beam after the degrader are determined by the collimators. In the matching, after the degrader, the beam parameter is chosen as x=y=8 mm, and x'=y'=3 mrad. The matching is starting at the outlet of the degrader. The optical matching results of the 20 MeV and 10 MeV proton beam are shown in Fig. 3, the upper one is the optics result of 20 MeV beam and the nether on is 10 MeV, the magnetic field gradient of each quadrupole is also shown in Table 1.

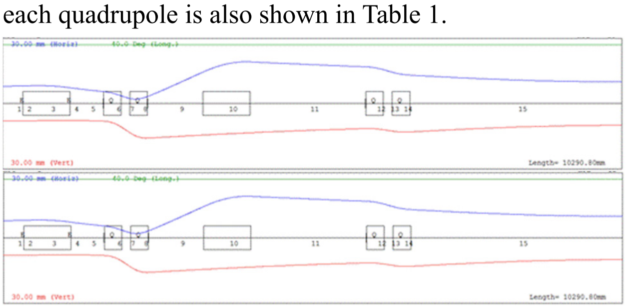

Figure 3: The optics results of 20 MeV (upper) and 10 MeV (lower).

In summary, we can adjust the parameters of each collimators and magnets to obtain the beam energy, beam spot size, envelope size and other parameters that meet the design requirements.

Table 1: Field Gradient of the Quadrupoles for Different Beam Energies

Field / Energy	Q1 T/m	Q2 T/m	Q3 T/m	Q4 T/m
50 MeV	-2.91	1.36	-5.48	5.40
30 MeV	-2.25	1.05	-4.22	4.15
20 MeV	4.18	-2.88	0.91	-1.00
10 MeV	2.95	-2.03	0.64	-0.71

MAGNET DESIGN

Bending Magnet Design

There are two 45° bending magnets on the beam line, which deflects the 10 MeV~50 MeV proton beam to the terminal station and selected the beam energy. The magnetic rigidity of the 50 MeV proton is 1.034 Tm, and the bending radius of the magnet is 1 m, so the maximum magnetic field of the magnet is 1.034 T. The magnet is designed to take a maximum magnetic field of 1.1 T. According to the envelope size of the proton beam in the magnet, the field of the magnet is required to be ±25 mm, and the uniformity of the magnetic field is better than 5×10^{-4}.

The cross section of the magnet is shown in Fig. 4. This figure is a 1/4 model of the magnet cross section. To improve the uniformity of the magnetic field, the padding is added on both sides of the magnetic pole surface. Figure 4 is also shows the distribution of the magnetic field in the magnet. The magnetic field distribution in the magnet is calculated, as shown in Fig. 5. It is calculated that within ±25 mm of the good field, the calculated uniformity of the magnetic field is 1.28×10^{-4}, which satisfies the design requirements.

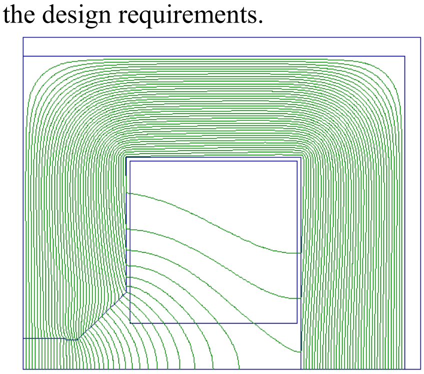

Figure 4: Cross section of the bending magnet.

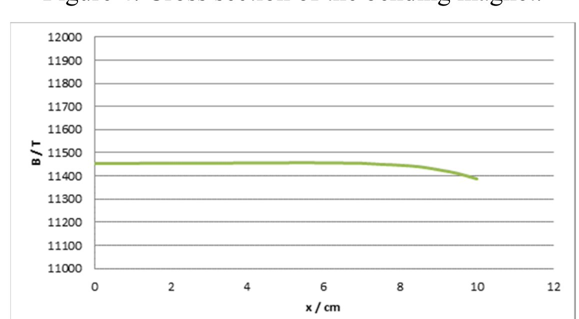

Figure 5: Field distribution along the radial center.

ISBN: 978-3-95450-205-9 doi:10.18429/JACoW-Cyclotrons2019-MOP010

Quadrupole Design

With the field gradient, the effective length, and the inner bore of the quadrupole, we can determine the pole face width and pole face shape of the magnet and the yoke thickness. Based on these basic parameters, we designed a quadrupole magnet using the two-dimensional computational magnetic field calculation program POISSON.

Based on accurate numerical analysis of magnetic fields and the past experience, here we choose a quadrupole structure with a polygonal tip section as a fold line instead of the theoretical hyperbolic structure. Such a structure has the advantages of simple processing, easy installation and positioning, etc. The difficult is to accurately designing the shape of the magnetic pole through accurate numerical analysis of the magnetic field.

Since the quadrupole magnet is an axisymmetric component, in the design we chose one-eighth model to calculate the field. The specific structure is shown in Fig. 6. The figure also shows the magnetic field of one-eighth of the magnet. distributed.

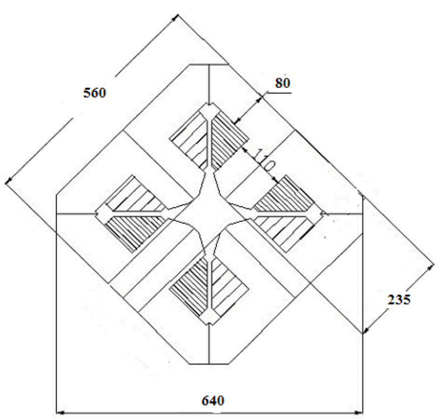

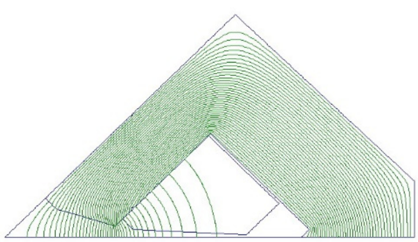

Figure 6: Cross section of the quadrupole.

Wobbling Magnet Design

The wobbling magnet produces a periodic magnetic field perpendicular to the direction of particle motion, which produces a periodically varying force on the particle that causes the particle to scan over the target, as shown in Fig 7.

The voltage applied to the wobbling magnet changes periodically, so that the magnetic field generated by the magnet also changes periodically. The force applied to the particles changes periodically, too. The radius of the particles scanned on the target periodically changes and then get a large uniform beam spot.

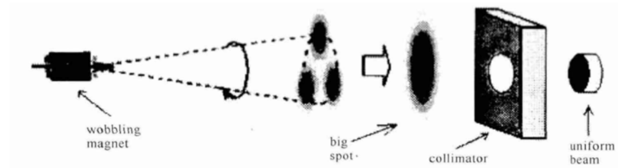

Figure 7: Working principle of the wobbling magnet.

CONCLUSION

Based on the development of a 50 MeV compact cyclotron in the cyclotron center of CIAE, a radiation-specific proton beam line is designed to get the proton beam of 10 MeV-50 MeV, 10 nA-10 μA.

At present, the layout design and optical matching of the beam line have been completed, and various elements such as magnets and diagnostic systems are in the process of mechanical design and processing. It is expected that the installation and beam commission will be completed in 2020.

REFERENCES

[1] T. Zhang *et al.*, "The cyclotron development activities at CIAE", *Nucl. Instr. Methods Phys. Res., Sect. A*, vol. 269, no. 24, pp. 2863-2870, Dec. 2011. doi.org/10.1016/j.nimb.2011.04.047

[2] T. Zhang and J. Yang, "The beam commissioning of BRIF and future cyclotron development at CIAE", *Nucl. Instr. Methods Phys. Res., Sect. B*, vol. 376, pp. 434-439, Jun. 2016. doi.org/10.1016/j.nimb.2016.01.022

[3] S. Wei *et al.*, "Beam line design for a 100 MeV high intensity proton cyclotron at CIAE", *Nucl. Instr. Methods Phys. Res., Sect. B*, vol. 261, no. 1-2, pp. 65-69, Aug. 2007. doi.org/10.1016/j.nimb.2007.04.232

[4] S. Wei *et al.*, "Transfer beamline design after stripping", *Nucl. Instr. Methods Phys. Res., Sect. B*, vol. 266, no. 19-20, pp. 4697-4701, Oct. 2008. doi:10.1016/j.nimb.2008.05.119

[5] Xianlu Jia *et al.*, "Wobbling magnet design on the beam line for a 30 MeV medical cyclotron", High Energy Physics and Nuclear Physics, no. 3, pp. 292-295, 2007.

[6] K. R. Crandall and D. P. Rusthoi, *TRACE 3-D Documentation*, Third Edition, May 1997, Los Alamos National Laboratory.

ISBN: 978-3-95450-205-9 doi:10.18429/JACoW-Cyclotrons2019-MOP011

MAGNETIC FIELD MEASUREMENT AND SHIMMING FOR A MEDICAL COMPACT CYCLOTRON

Leilei Guan†, Ming Li, Tianjue Zhang, Tao Cui, Peng Huang, Fei Wang, XianLu Jia, ShiZhong An
China Institute of Atomic Energy, Beijing 102400, China

Abstract

A compact cyclotron is developed by Cyclotron Research and Design Center at China Institute of Atomic Energy (CIAE) to extract 14 MeV proton beam for medical radioisotopes production, so as to meet the market demands of early diagnosis of malignant tumors, cardiovascular and cerebrovascular diseases. Owing to the small size and limited space of small medical cyclotrons, critical requirements are imposed on magnetic field measurement. For this reason, a magnetic field measurement system, with high-precision and high-stability, suitable for small cyclotrons is adopted and then an efficient magnetic field shimming method is used, which greatly reduces the construction period. It provides a strong guarantee for the stable operation of medical small cyclotrons.

INTRODUCTION

The Cyclotron Research and Design Center at China Institute of Atomic Energy developed a 14 MeV medical cyclotron for boron neutron capture therapy (BNCT). The main magnet of the cyclotron adopts a compact size, and the diameter is 1 m. Four straight sectors are adopted and the harmonic number is 4 in the cyclotron. The gap between the magnetic poles is between 23 mm and 26 mm, and the beam current is 1 mA. For the above characteristics of the BNCT cyclotron, a fully automated magnetic field measurement system for the magnetic field mapping and shimming is adopted.

DESIGN OF THE MAGNETIC FIELD MAPPING INSTRUMENT

Principally it should be ensured that the components of the field mapping system placed inside the accelerator are non-magnetic and the eddy current is not obvious during the movement of the system. Hall probe is used for measuring the magnetic field ranging from 400 G to 20 kG with the calibrated precision of 10^{-4} which means the field measurement errors is less than 2 G. The measuring arm can rotate freely clockwise and counterclockwise around the central axis of the accelerator with the angular positioning precision of 20 s. The Hall probe on the measuring arm can move in the radial direction with the range from -2 cm to 50 cm based on the center of the cyclotron and the radial positioning precision reaches 0.1 mm. The period of the magnetic field measuring is less than 8 hrs for one mapping in which the radial interval is 1 cm and the angular interval is 1° [1]. The random error and system error are shown in Table 1.

Table 1: Parameters of Measuring Precision

Random Error	Value
Magnetic field measuring error/Gs	2
Radial measuring error/mm	0.1
Radial positioning error/mm	0.1
Angle measuring error/s	12
Angle positioning error/s	20
System Error	**Value**
Measuring arm horizontal error/mm	0.1
Measuring arm axial error/mm	0.2
Center shaft tilt error/deg	0.2

MECHANICAL STRUCTURE

The main mechanical structure is mainly composed of the support rail, the measuring arm, the Hall probe base, the angular rotating component, the radial driving component, and the center shaft component [2]. The support rail adopts aluminum alloy material, which is the support of the measuring arm with two rounds of balls supporting between to reduce the resistance during the movement. The angular rotating component built-in circular grating drives the arm rotation via the central shaft. Both ends of the Hall probe base are connected to the transmission rope, and the radial movement is driven by the radial drive component, and the radial position is indirectly determined according to the rotation angle of the rope wheel. The mechanical structure is shown in Fig. 1.

CONTROL MODULE

The radial motion controller sends the analog signal to the servo motor driver to drive the motor according to the position reference and feedback. In the angular direction, the controller drives the stepping motor by calculating the output count pulse to realize open loop control. Indirect closed-loop control is implemented by a software algorithm according to the position signal fed back by the

† guanll_1988@126.com

ISBN: 978-3-95450-205-9 doi:10.18429/JACoW-Cyclotrons2019-MOP011

angle encoder. The control flow is shown in Fig. 2.

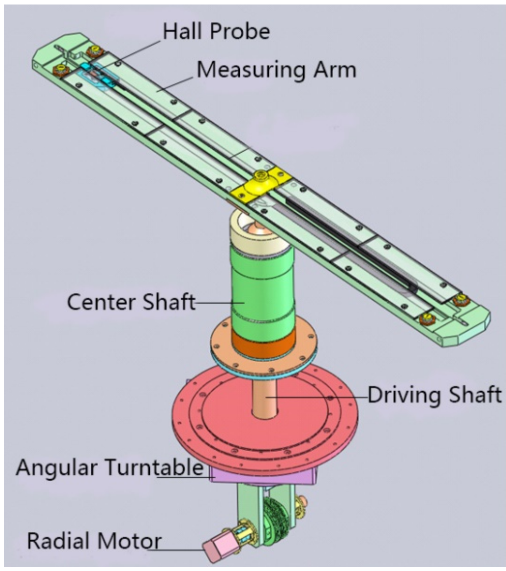

Figure 1: Mechanical structure of the measuring instrument.

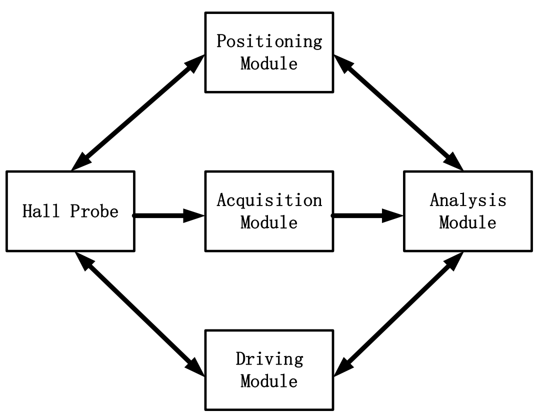

Figure 2: Control flow chart.

The issuance of the control commands of the control system and the data recording are implemented by the industrial computer. In the automatic mode, the magnetic field value of each point is measured in turn, and finally the measurement result file is formed, and the magnetic field measurement task is automatically completed. The manual mode is set as a motion mode for debugging and moving to a certain position to set working origin, positive and negative soft limit.

SHIMMING METHOD

The center plane magnetic field is shimmed by adjusting the width of the strips on both sides of the magnetic poles of the main magnet by the strip shimming method. For the purpose of improving the convergence speed of the magnetic field shimming process and reducing the period of shimming, the strips are divided into odd and even triangles in the radial direction, as shown in Fig. 3.

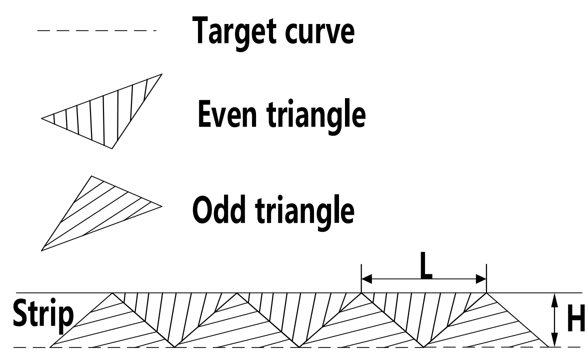

Figure 3: Even and odd triangle on the strip.

The effect on the average magnetic field, by cutting the triangular areas of length L and height H on the region near one point on the strip in the radial direction, is calculated by finite element method. To calculate the average field variation caused by the odd-even triangle, the same split mesh is used in the finite element simulation to reduce the magnetic field deviation. The shimming results are shown in Fig. 4.

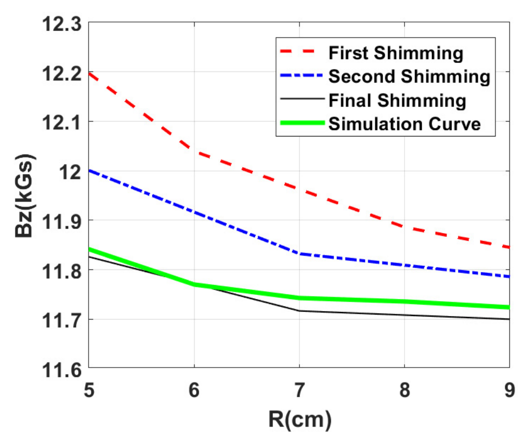

Figure 4: Average magnetic field of shimming results in the BNCT cyclotron.

RESULTS

The BNCT 14 MeV cyclotron has completed the final task after five times of magnetic field mapping and three times of shimming under the condition of ensuring the measurement accuracy and repeatability, which has experienced a total of 6 weeks. Through the final measurement results, the average field can meet the physical design requirements of the isochronism of the magnetic field.

The first harmonic is controlled at a lower level. The amplitude of the first harmonic in the small radius is less than 10 G, and the amplitude of the first harmonic in the large radius is less than 5 G, which is crucial for the 1 mA beam of the cyclotron, as shown in Fig. 5. Figure 6 shows that integral phase slip can be kept within ±15°.

ISBN: 978-3-95450-205-9 doi:10.18429/JACoW-Cyclotrons2019-MOP011

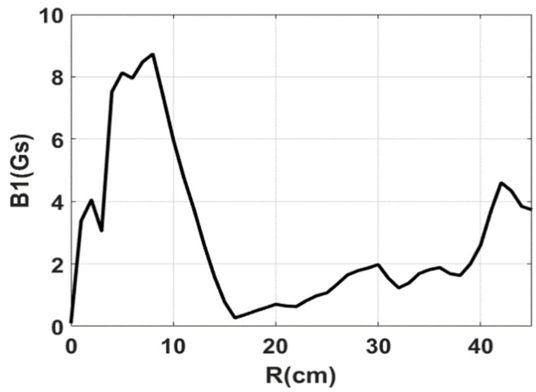

Figure 5: Amplitude of first harmonic.

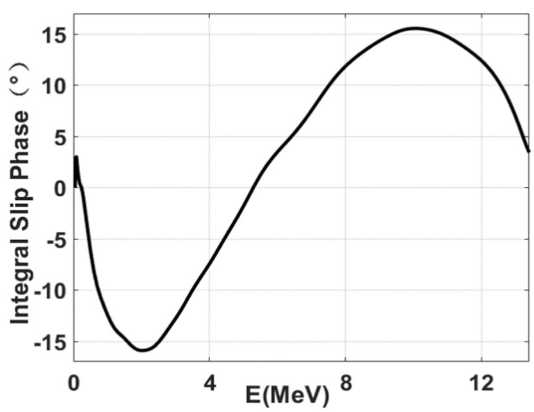

Figure 6: Integral phase slip of the final shimming.

CONCLUSION

There are still many aspects to be considered in the work of magnetic field measurement, such as magnetic performance test of main magnet, main magnet power supply stability test, cyclotron temperature monitoring, environmental humidity monitoring, and so on, which are also important factors affecting the magnetic field distribution. During the measurement process, the measuring system has been further improved and completed, which laid a solid foundation for the subsequent industrialization of medical compact cyclotron.

REFERENCES

[1] W. Beeckman *et al.*, “The C235 IBA-SHI protontherapy cyclotron for the NPTC project: Magnetic system design and construction”, in *Proc. 14th Int. Cyclotron Conf. and Their Applications (Cyclotrons'95)*, Cape Town, South Africa, Oct. 1995, paper E-13, pp. 218-221.

[2] A. Roy *et al.*, “Median plane magnetic field mapping for superconducting cyclotron (SCC) in VECC”, in *Proc. 4th Asian Particle Accelerator Conf. (APAC'07)*, Indore, India, Jan.-Feb. 2007, paper THPMA016, pp. 652-654.

22nd Int. Conf. on Cyclotrons and their Applications Cyclotrons2019, Cape Town, South Africa JACoW Publishing
ISBN: 978-3-95450-205-9 doi:10.18429/JACoW-Cyclotrons2019-MOP013

MECHANICAL MODIFICATIONS OF THE MEDIAN PLANE FOR THE SUPERCONDUCTING CYCLOTRON UPGRADE

G. Gallo, G. Costa, L. Allegra, L. Calabretta, A. Caruso,
G. Messina, M. Musumeci, D. Rifuggiato, E. Zappalà
INFN - Laboratori Nazionali del Sud, Via S. Sofia 62, 95125 Catania, Italy

Abstract

The Superconducting Cyclotron (CS) is a three sectors, compact accelerator with a wide operating diagram, capable of accelerating heavy ions with q/A from 0.1 to 0.5 up to energies from 2 to 100 MeV/u. Recently a significant upgrade has been proposed to increase the light ion beam intensity by means of extraction by stripping. For the implementation of the new extraction mode, many relevant modifications are needed in the median plane. The biggest upgrade action is the replacement of the present superconducting magnet with a new one, compatible with the beam trajectory and envelope in the extraction by stripping. The extraction by stripping mode implies the installation of two stripper systems, one in a hill and the other in a valley, that allow to extract all the ions requested by the users. Finally, since the present electrostatic extraction mode will be maintained, several relevant mechanical issues have to be faced when switching from one extraction mode to the other one, the location of one electrostatic deflector being the same as the stripper system. The focus of this paper will be the presentation of the different mechanical features involved in the upgrade.

INTRODUCTION

The Superconducting Cyclotron (CS) is an accelerator which was designed for low intensity beams, whose main limitations to extract high beam power are the two electrostatic deflectors. The goal of the upgrade is to make extraction by stripping possible, interchanging the stripper with one of the two electrostatic deflectors, to achieve high power beams for the set of beams of interest and, at the same time, to maintain the versatility of the CS [1]. To reach our aim, it is necessary to design a stripper device, to be implemented when the Electrostatic deflector is not used and removed. To achieve fast extraction trajectories when we use the extraction by stripping, compatible with simulation studies, it is necessary to design a new extraction channel that overlaps geometrically with the tubes of the electrostatic deflectors movements, increasing the complications of the two setup functioning. These features cause the definition of a new median plane and the redesign of some components of the CS.

MEDIAN PLANE REDEFINITION

To satisfy all the extraction by stripping equipment, the median plane of the CS will be modified (Fig. 1).

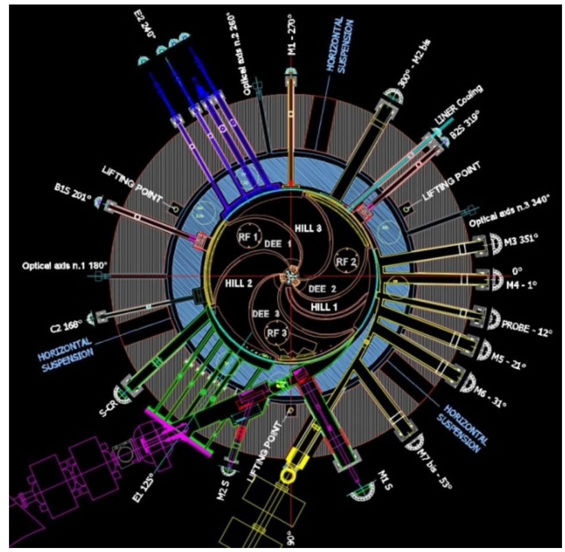

Figure 1: The new median plane.

Due to the new extraction channel, it has been necessary to optimise the position of the three lifting points and of the three horizontal suspensions of the vacuum chamber [2]. The design of the new extraction channel must allow the arrangement of two new magnetic channels, M1S and M2S, in addition to those already existing in the cyclotron, to locally reduce the magnetic field and focus the beam in the radial direction. These new magnetic channels have interferences with the electrostatic extraction mode. The M1S shaft collides with the actual extraction channel and so to solve that, the shaft has a suitable gap to permit the beam trajectory of the electrostatic extraction mode. The M2S channel has an interference with one of the electrostatic deflector handlings; therefore, we designed the new extraction channel to make the M2S channel and the electrostatic deflector setting compatible. The M1S and M2S are made of three iron bars, that need of a housing to contain them and a shaft, connected with the housing, that allows to modulate their position, for our selected ions. For the two magnetic channels, the geometrical dimensions and the resultant forces of the iron bars are different.

For both magnetic channels, the resultant forces are tilted in relation to the penetrations axis, we implemented mechanical simulations by means of Comsol Multiphysics, a FEM (Finite Element Method) software. To obtain acceptable stress and strain values for the two housings and shafts, we optimized the mechanical design and the choice of the materials. Moreover, for the extraction by stripping, two identical compensation bars, B1S and B2S

ISBN: 978-3-95450-205-9 doi:10.18429/JACoW-Cyclotrons2019-MOP013

are necessary, in order to compensate the imperfections of the new magnetic field. B1S and B2S are made up of one iron bar, contained in a housing, and a shaft, connected with the housing, allowing to adjust the position. Unlike the magnetic channels M1S and M2S, the bars resultant forces are radial, along the penetration axis.

CONSEQUENCES OF THE NEW SUPERCONDUCTING MAGNET

For the CS upgrade with the extraction by stripping, the focus was the design of a new superconducting magnet. A preliminary study, relating to the dynamics of the beam along the stripping trajectories and the following magnetic, structural, thermal analysis, including the consumption of helium and liquid nitrogen, confirm the feasibility of the new superconducting magnet. The whole replacement of the Cryostat, that will contain all the tubes, the actual ones and the new ones, causes the geometrical modification of the six iron sectors of the yoke. The changes with respect to the CS present configuration, turned to be so significant that the central ring of the yoke will be completely replaced.

LINERS

Due to the dimensions of the beam spot, it is mandatory to increase the vertical gap of the acceleration chamber, from the present 24 mm to 30 mm. This will cause the whole replacement of the lower Liner and upper Liner, because it is impossible to keep the present ones. The two liners were redesigned, simplifying them appropriately and considering the possibility of using more modern construction techniques.

STRIPPER DEVICES

To realise the extraction by stripping mode, the design of two stripper devices is necessary. The two stripper devices have to permit the extraction of all ions requested by the users. Some extraction points are located in one valley, others in one hill. The valley stripper device is made up of an automatic and sequential structure, that holds a revolving carousel (Fig. 2).

The carousel has to move sequentially, around a vertical axis A1, five stripper foils, that have to be hit by the ion beams.

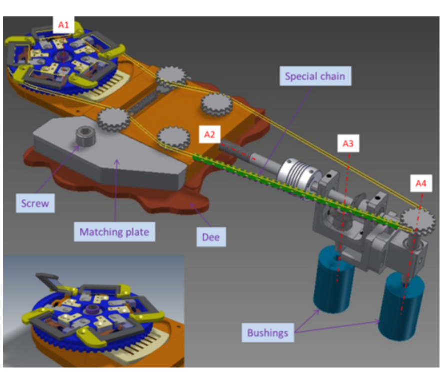

Figure 2: The valley stripper device.

The foils rotation is allowed by a special chain that transfers a shaft rotation (A4) to a gear, integral with the carousel. In the rest condition, all frames are lowered and one frame at a time, can be raised and lowered through a cam profile. The carousel can translate along an axis (A2), perpendicular to the axis A1. This translation movement is assured through two conical gear wheel, that transfer a shaft rotation (A3), to a screw integral with the carousel [3]. The device is arranged from the top to one of the three positions, in the DEE number three (Fig. 3).

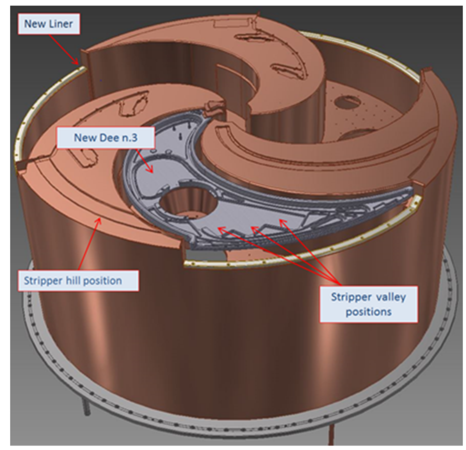

Figure 3: The stripper devices positions.

To allow the placement of the valley stripper device, it is necessary the redesign of several RF components [4, 5].

The two shafts, A3 and A4, are linked, by two bushings, to two shafts inside the RF cavity and there is a lateral matching plate that traps and leads the system. The device is disassembled through a little rotation of a screw and the matching plate is removed. This process allows a fast and safe disassembly in a radioactive zone and gives us the possibility of assembly a new device, outside the machine. If the magnetic simulations will allow to extract all the ions with the hill extraction, this device will not be necessary. Instead the hill stripper device is definitely mandatory. This device is made up of an arm hinged in a fixed point; the arm must rotate around this point, of a 4 degree.

A crank, that transforms a linear movement in a rotating one, converts the translational movement of a shaft, in the arm rotation. In the arm, there is a track with a chain, that moves some housings for the stripper foils, in a carousel system. A kinematic chain (gears, bearings and pulleys), transfers a rotation shaft to the chain [3]. Every housing is equipped with four foils and for every ion, only one foil will be hit (Fig. 4). The hill stripper device is arranged from the top to the liner surface, in the same area of the electrostatic deflector E1 (Fig. 3), because we must have all at the ground potential. The device is disassembled by disconnecting the rotation shaft, through the bushing and the translation shaft, through the screw, inside the lever. Then, it's possible to release definitively the arm, unscrewing the special screw, to

ISBN: 978-3-95450-205-9 doi:10.18429/JACoW-Cyclotrons2019-MOP013

achieve the assembly of a new device, outside the machine. The two shafts are moved from outside of the Cyclotron and their combined control, allows to reach all the hill extraction points for the ion beams of our interest.

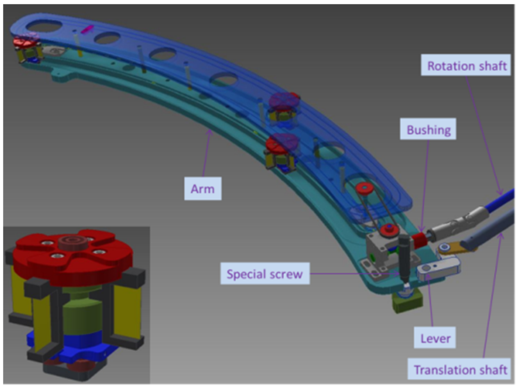

Figure 4: The hill stripper device.

MECHANICAL COMPATIBILITY OF THE TWO EXTRACTION MODES

In addition to the explained modifications inside the CS, the extraction by stripping requires a design of mechanical parts located outside, to make compatible the new extraction mode with the present electrostatic extraction mode (Fig. 5).

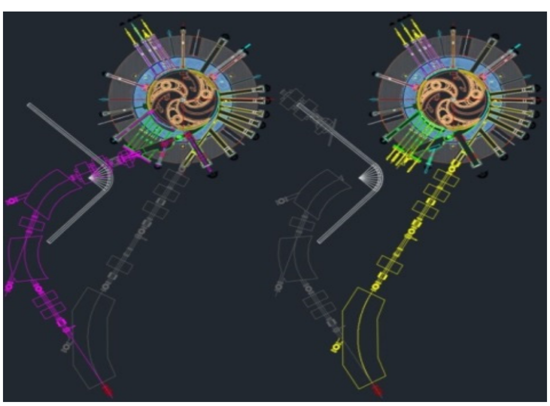

Figure 5: The two extraction settings.

When we work with the stripping setting (magenta in Fig. 5), the electrostatic deflector E1 assembly must be disassembled and removed. When we work with the deflector setting (yellow in Fig. 5), a whole section of beam line must be disassembled and translated (to as semble the electrostatic deflector E1 handlings), using a carriage over a track, that allows its translation movement.

So we have the possibility of move one of the two settings out of the operation area, while the other one is working. Anyway all choices regarding other devices (vacuum, cabling, control, etc.) will be subjected to a future revaluation.

CONCLUSION

To realise the CS upgrade, the extraction by stripping mode will be implemented. To satisfy the physical and mechanical requirements, we redesigned the median plane and we investigated on the feasibility of the new superconducting magnet construction. We designed two stripper devices to reach all extraction points for the ion beams of interest. Moreover, to make the two extraction modes compatible, a study was necessary to define the possible movements of the two settings and to obtain their simultaneous presence and alternative operation.

REFERENCES

[1] L Calabretta, A. Calanna, G. Cuttone, G. D'Agostino, D. Rifuggiato, and A. D. Russo, “Upgrade of the LNS superconducting cyclotron for beam power higher than 2-5 kW”, in *Proc. 21th Int. Conf. on Cyclotrons and their Applications (Cyclotrons'16)*, Zurich, Switzerland, Sep. 2016, pp. 7-10. doi:10.18429/JACoW-Cyclotrons2016-MOA02

[2] G. Gallo, L. Allegra, G. Costa, E. Messina, and E. ZappalÃ, “Mechanical aspects of the LNS superconducting cyclotron upgrade”, in *Proc. 21th Int. Conf. on Cyclotrons and their Applications (Cyclotrons'16)*, Zurich, Switzerland, Sep. 2016, pp. 322-324. doi:10.18429/JACoW-Cyclotrons2016-THP09

[3] G. Gallo *et al.*, “Mechanical aspects of the LNS superconducting cyclotron upgrade”, INFN-LNS, Catania, Italy, internal report.

[4] G. Torrisi *et al.*, “3D radio frequency simulation of the INFN-LNS superconducting cyclotron”, presented at the 22nd Int. Conf. on Cyclotrons and their Applications (Cyclotrons'19), Cape Town, South Africa, Sep. 2019, paper FRB03, this conference.

[5] A. C. Caruso *et al.*, “The developments of the RF system related to the K-800 superconducting cyclotron upgrade”, presented at the 22nd Int. Conf. on Cyclotrons and their Applications (Cyclotrons'19), Cape Town, South Africa, Sep. 2019, paper WEA02, this conference.

ISBN: 978-3-95450-205-9 doi:10.18429/JACoW-Cyclotrons2019-MOP014

3D MAGNETIC OPTIMIZATION OF THE NEW EXTRACTION CHANNEL FOR THE LNS SUPERCONDUCTING CYCLOTRON

L. Neri†, L. Calabretta, D. Rifuggiato, G. D'Agostino, A. D. Russo, G. Gallo, L. Allegra, G. Costa, G. Torrisi, Istituto Nazionale di Fisica Nucleare Laboratori Nazionali del Sud, Catania, Italy

Abstract

The upgrade of the Superconducting Cyclotron operating at INFN-LNS is the main objective of the general upgrade of the LNS facility, consisting in the enhancement of light-medium ion beam intensity. To overcome the present maximum power of 100 W of the beam extracted by electrostatic deflector and achieve a beam power as high as 10 kW, the implementation of the extraction by stripping method has been proposed. Intense ion beams with mass in the range 10 to 40 amu (^{12}C, ^{18}O, ^{20}Ne, ^{40}Ar) in the energy range of interest (15-70 MeV/u) will be delivered to the NUMEN experiment, as well as used for production of in-flight radioactive beams. The present work consists in the optimization of the magnetic channels needed to limit the radial and axial beam envelopes. The design of the magnetic channels has been accomplished by fully three-dimensional magneto-static simulations using Comsol Multiphysics and a custom transport code developed in Matlab along the last year at INFN-LNS. The effect of a magnetic shielding structure in the extraction channel is presented, together with the possibility of producing a magnetic gradient from an asymmetric coil.

INTRODUCTION

A custom transport code was developed at INFN-LNS to support the design of different parts of the extraction by stripping system. In particular stripping foil area, extraction channel geometry and magnetic channels. The tool is fully three dimensional and starting from the measured middle-plane magnetic field map deduce the three-dimensional magnetic field map in the acceleration region of the cyclotron. The stationary beam envelope in the radial and vertical phase-space diagrams are found for all the beams of interest. An example of what called auto-ellipses is shown in Fig. 1 in the case of $^{18}O^{6+}$ at 45.6 AMeV, nominal beam condition considered in all this paper for comparison reason.

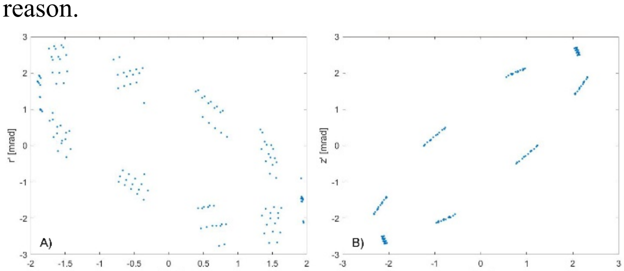

Figure 1: Auto-ellipse beam particle distributions of $^{18}O^{6+}$ at 45.6 AMeV, A) radial phase-space diagram, B) vertical phase-space diagram.

The size of the beam envelope was chosen to be close to the normalized beam emittance of 1π·mm·mrad for 99% of the beam envelope, value estimated for our accelerated beam. The stationary beam envelope along a full turn was also calculated, and the intersection with the stripping foil region (shown in red in Fig. 2) were saved every approximately 0.03 degree. The showed magnetic field map is a merge between measured map in the acceleration region, and the remaining part coming from a fully 3D magnetic model of the entire cyclotron joke and superconductive coils. Acceleration region was not extracted from the 3D simulation because of missing trimmer coil in the simulation model. The black contour of Fig. 2 marks the walls of the vacuum chamber. If the beam trajectory crosses this black contour the code mark the particle as lost. In the centre of the cyclotron a black circle represents a beam forbidden area in correspondence of the central region.

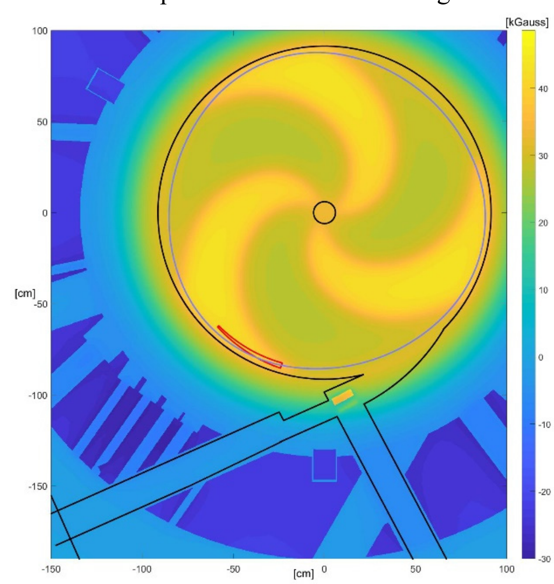

Figure 2: Magnetic field map of the cyclotron with vacuum region delimited by black line, foil region in red and stationary trajectory in blue.

After, the beam is fully stripped by the stripping foil the trajectory changes drastically. By selecting carefully, the stripping foil location it is possible to drive the deflected beam through the new extraction channel. Figure 3 shows the fully stripped trajectory in blue. Immediately after the cyclotron joke there are red dots representing hit of lost particles. Figure 4 shows the behaviour of the stripped beam by showing in light blue the magnetic field along the central particle trajectory. In black the number of remaining particles divided by two (for graphical reason). Then the beam envelope is represented showing the maximum distance between the central particle and the farther beam

† neri@lns.infn.it

ISBN: 978-3-95450-205-9 doi:10.18429/JACoW-Cyclotrons2019-MOP014

particle in the middle plane (in red) and in the vertical coordinate (in blue). The abscissa is in arbitrary time unit. The beam envelope suffers of strong variation in correspondence of the magnetic field drop when the beam exit from the acceleration region. This is due to the magnetic field gradient.

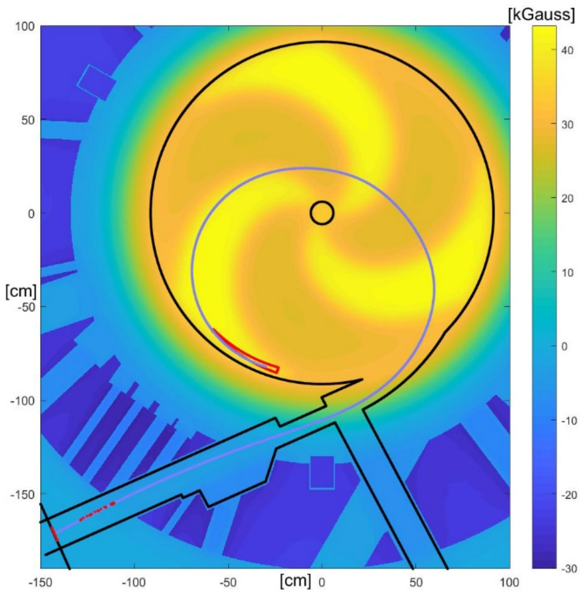

Figure 3: Fully stripped beam trajectory (light blue line) superimposed in magnetic field map (colour map), vacuum chamber (black line), stripping area (red line) and beam losing point (red dots). (mettere line nere e line rosse, togliere titolo, mm negli assi)

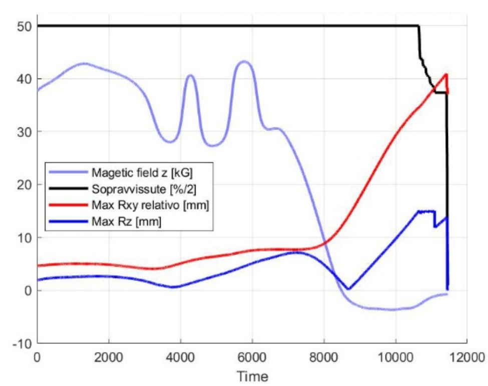

Figure 4: Beam behaviour along the fully stripped trajectory.

Strong defocusing is observed for the envelope in the middle plane, while strong focusing occur in the vertical direction. The result is that after the cyclotron the envelopes of the beam are bigger than the acceptance of next set of quadrupoles for both directions. Further disagreement with respect next acceptance is that the transverse and the vertical envelope of the beam need to be one convergent and the other divergent, doesn't matter the order. Figure 4 shows a focusing point of the vertical envelope and consequently a divergent beam, both vertically and horizontally.

MAGNETIC OPTIMIZATION

Scope of the magnetic optimization is to counteract the magnetic field drop effect trying to move the focusing point as far as possible, keep vertical envelope convergent and reduce the divergency of horizontal envelope. The magnetic element typically used in this scenario is a magnetic channel composed by three ferromagnetic bars shaped to obtain a magnetic gradient. Two different magnetic channels were planned for our cyclotron named respectively MC1s and MC2s. Different steps were done during different years of the design upgrade of our cyclotron summarized in the following paragraph for MC1s. The main parameter that identify the strength with which the magnetic channel act on the beam is the magnetic field gradient orthogonal to beam trajectory.

Current Sheet Approximation

First magnetic optimization step [1] was done by using Opera and the current sheet approximation. This computational method is fast but suffer of precision when considering that the magnetic channel extends up to 30 mm out of the middle plane and the magnetic field is not uniform as in the present case. The preliminary achievement was to define a preliminary geometry able to perform a gradient up to 180 mT/cm. With beam particle transport code, we have seen that this gradient amount is not enough. Stronger gradient is needed and higher accuracy in the magnetic simulation is needed to obtain a more homogeneous magnetic field gradient with respect to what obtained with this method.

FEM and Genetic Algorithm Approach

For a more accurate simulation we moved to a FEM description of the problem using Comsol Multiphysics as solver and developing environment. To increase the magnetic field gradient, we investigate the use of permendur vanadium, while to perform a more efficient geometry optimization we used a genetic algorithm approach implemented with a custom Matlab code. Genetic algorithm approach implies several thousand of tries, consequently the test of the geometry needs to be as fast as possible. This was done by using a 2D description of the problem. The design was done in case of the magnetic channel inserted in a uniform magnetic field. More details can be found in [2]. Magnetic channel performances were improved in amplitude, from 180 to 250 mT/cm and in uniformity. But when we used this result in the 3D model of the entire cyclotron, we found that the assumption of uniform magnetic field was a poor estimation. Figure 5 shows the magnetic field over a slice perpendicular to the magnetic channel, and centred with respect it, in the case of 3D simulation.

ISBN: 978-3-95450-205-9 doi:10.18429/JACoW-Cyclotrons2019-MOP014

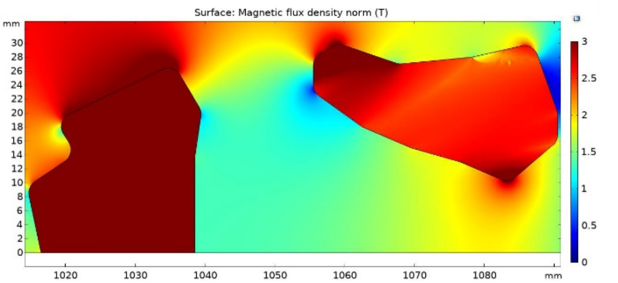

Figure 5: Slice of 3D magnetic field in correspondence of the MC1s centre.

Symmetry with respect middle plane was used and so only half of the magnetic channel is shown. It is evident that there is a magnetic field gradient from left to right in the central region, but with a more detailed analysis, Fig. 6, it is clear that the uniformity is poor. Figure 6 shown the magnetic field gradient in the region where the beam crosses the magnetic channel. We considered not only the gradient produced in correspondence of the middle plane, blue line, but also 5 mm (green line), 10 mm (red line) and 15 mm (light blue line) far from middle plane. The length of the four lines is equivalent to the expected beam size outside of the middle plane.

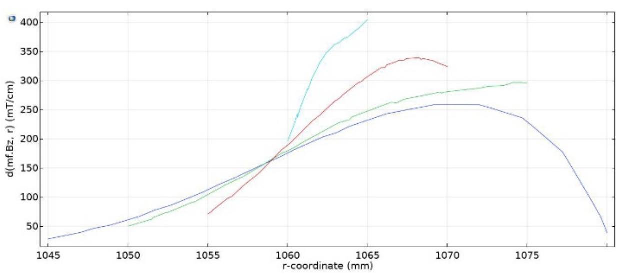

Figure 6: 3D magnetic field gradient at the centre of MC1s, see the text for the meanings of the lines.

3D-Equivalent Optimization

3D magnetic simulation of cyclotron and magnetic channel is more realistic with respect 2D simulation but can't be used with a genetic algorithm approach because of the huge amount of time needed for each simulation (20 hours) and the huge amount of try needed for the optimization algorithm (≈ 1000). However, we found how to improve the reliability of 2D simulation and made a 3D-equivalent simulation. Figure 7 shows the 3D model with a blue line centred with respect MC1s. From a 3D magnetic simulation without MC1s we extracted the magnetic field profile along this line. Then a genetic algorithm approach was used to generate a 2D cyclotron-like geometry, showed in Fig. 8, that generate 3D-like magnetic field profile. Finally, we used this environment to perform a 2D geometrical optimization using the genetic algorithm approach. The result (Fig. 9) was excellent with an extreme agreement between 2D and 3D simulation, see Fig. 10.

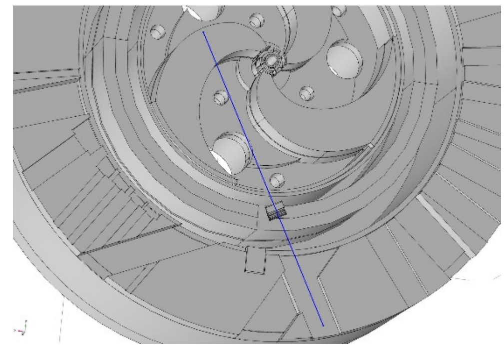

Figure 7: 3D magnetic simulation drawing of half of cyclotron joke, superconductive coil and MC1s, blue line is the reference for the magnetic field profile with which MC1s need to be optimized.

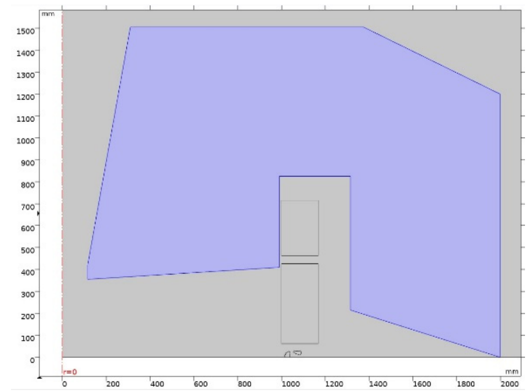

Figure 8: 2D geometry able to provide same magnetic field profile of 3D simulation, low carbon steel 1010 in light blue, the two rectangular superconductive coils, and close to the middle plane at coordinate r = 0 and y = 1000 the drawing of the magnetic channel.

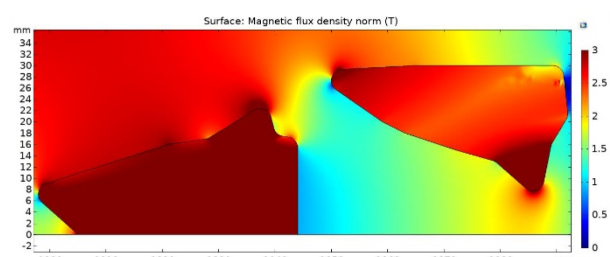

Figure 9: Slice of 3D magnetic field in correspondence of the MC1s optimized with 3D-equivalent method.

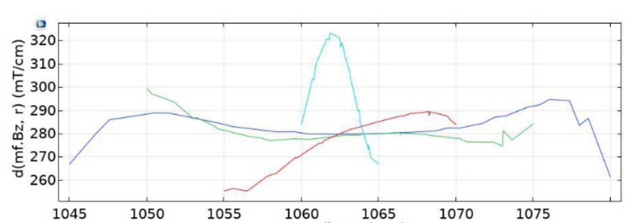

Figure 10: 3D magnetic field gradient at the centre of new MC1s.

ISBN: 978-3-95450-205-9 doi:10.18429/JACoW-Cyclotrons2019-MOP014

RESULT

The evolution in magnetic optimization ended with best result achievable with state-of-the-art software and algorithm. The optimum magnetic gradient and uniformity achieved were tested with our beam transport code. Figure 11 shown the beam envelope for the new MC1s that is almost inside the acceptance of next quadrupoles elements. The strong magnetic field gradient of MC1s was able to move the focusing point of vertical envelope from 8800 to 10800 time unit (corresponding to a position quite near to exit of the yoke), no particle were lost, and the horizontal size of the beam was reduced from 40 to 20 mm radius. Figure 12 shown the extracted beam envelope in the two-phase space planes, ellipse-like shape and consequently emittance was preserved due to the optimum homogeneity of the magnetic field gradient of the new MC1s.

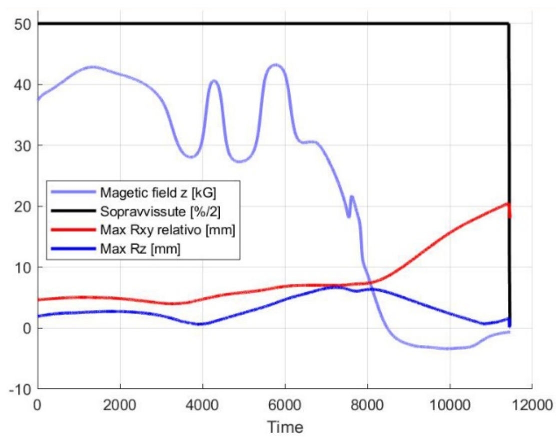

Figure 11: Beam behaviour along the fully stripped trajectory in the case of new MC1s.

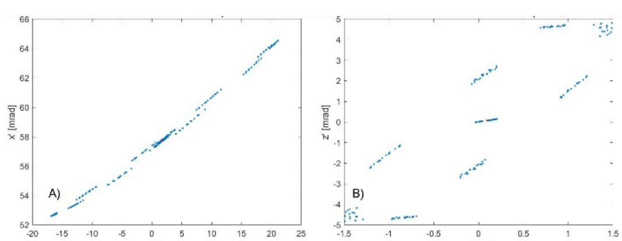

Figure 12: Beam particle distributions of extracted O_{18}^{6+} at 45.6 AMeV, A) radial phase-space diagram, B) vertical phase-space diagram.

CONCLUSION

The optimization of MC1s reached satisfactory result and no more steps are needed for it design. An additional magnetic channel is required to achieve a better match between beam envelope and acceptance of the first set of quadruplets after the cyclotron. For this second element instead to modify the existing magnetic field to obtain a magnetic field gradient, it was chosen a different magnetic approach. The magnetic field coming from the joke was shielded as much as possible and the magnetic field gradient was generated by an asymmetric coil. Coil current of asymmetric coil and obtained magnetic field gradient intensity introduce a new tuning parameter that will make easier the matching of the different beams of interest with the transport line. The design of this active channel is in progress.

REFERENCES

[1] L. Calabretta *et al.*, "Overview of the future upgrade of the INFN-LNS superconductive cyclotron", *Mod. Phys. Lett. A*, vol. 32, no. 17, 2017. doi:10.1142/S0217732317400090

[2] L. Calabretta, O. Karamyshev, L. Neri, and D. Rifuggiato, "New method to design magnetic channels with 2D optimization tools and using Permendur Vanadium", presented at the 14th Int. Conf. on Heavy Ion Accelerator Technology (HIAT'18), Lanzhou, China, Oct. 2018, paper TUOZA01.

ISBN: 978-3-95450-205-9 doi:10.18429/JACoW-Cyclotrons2019-MOP016

VERTICAL FOCUSSING WITH A FIELD GRADIENT SPIRAL INFLECTOR

A. H. Barnard†, J. I. Broodryk, J. L. Conradie, J. G. de Villiers, J. Mira, F. Nemulodi, R. W. Thomae, iThemba Laboratory for Accelerator Based Science, Cape Town, South Africa

Abstract

Traditional spiral inflectors suffer from vertical defocussing, leading to beam loss. In this study the electrode shape of an inflector is modified to intentionally produce transverse electric field gradients along the beam path, which have a significant influence on the optics. This is done by placing the traditionally parallel electrodes at an angle relative to each other in the transverse plane, creating a quadrupole field on the central path. Varying the electrode angle along the path length creates an alternating-gradient effect. The electrode entrance and exit faces are also shaped to create quadrupoles inside the fringe field. By numerical optimisation a design with good vertical focussing is obtained. Experiments show a roughly 100% improvement in transmission in cases where the buncher is turned off. However, high losses at extraction are observed with the buncher turned on, due to RF-phase spread introduced by longitudinal defocussing in the inflector. This results in an improvement of only 20% during normal cyclotron operation, and shows that an inflector should ideally focus vertically and longitudinally at the same time. Ongoing work to achieve such combined focussing is briefly described.

INTRODUCTION

Spiral inflectors based on the Belmont-Pabot [1] design are known to have very good transmission, but suffer from vertical defocussing, which can lead to beam loss in the inner region of the cyclotron [2]. This undesired vertical behaviour is illustrated in Fig. 1, where the beam passing through the C-inflector of the Solid-Pole-Cyclotron 2 (SPC2) [3] at iThemba LABS is modelled in TOSCA [4]. A substantial portion of the beam strikes the vertical slits downstream from the inflector, or is lost vertically on the puller electrode.

Solutions to the vertical defocussing problem implemented in the past include the addition of an electrostatic or magnetic quadrupole behind the inflector, but this requires additional space in the cramped inner region [5], and does not prevent emittance blow-up in the inflector itself. Another solution proposed at Dubna, is to give the electrodes a V-shape to create focussing electric fields, similar to the vertical direction of a spherical electrostatic bend [2]. In this article a design is introduced that involves shaping the inflector electrodes to create quadrupole electric fields in the transverse plane, and varying their strengths along the path length, to create an effect similar to strong focussing.

† hbarnard@tlabs.ac.za

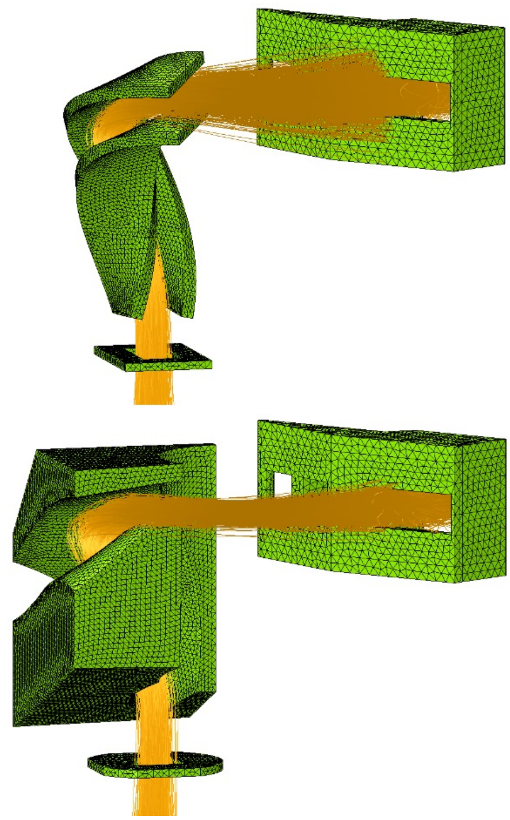

Figure 1: Beam passing through the inflector and striking the vertical slit in an ordinary spiral inflector (top), and in a field gradient inflector with vertical focussing (bottom).

ELECTRIC FIELD GRADIENTS

The traditional spiral inflector design by Belmont and Pabot specifies the electric field on the central trajectory, but places no constraints on the field gradients. Since the first order optics of the device depends on these gradients, it might be possible to control the focussing of an inflector by selecting appropriate electric field gradients.

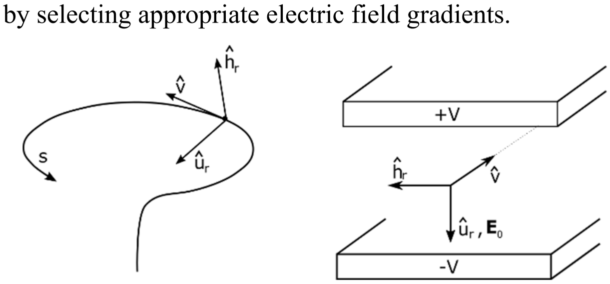

Figure 2: Standard inflector coordinate system (left) and the positioning of the electrodes to create the central field $\boldsymbol{E_0}$ (right).

ISBN: 978-3-95450-205-9 doi:10.18429/JACoW-Cyclotrons2019-MOP016

Standard inflector coordinates are used here, as illustrated in Fig. 2: The coordinates (u_r, h_r, s) form a right handed system, where s is the path length and the transverse (u_r, h_r) plane is Cartesian so that $\hat{u}_r$ points in the direction of the central electric field $\boldsymbol{E_0}$.

First order electric field gradients on the central path can intentionally be created by tilting the electrodes relative to one another, as shown in Fig 3.

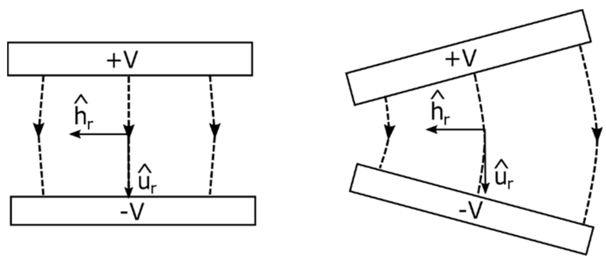

Figure 3: Electrode cross sections in the transverse plane. Traditional parallel electrodes (left) keep the electric field as uniform as possible, while tilting the electrodes (right) intentionally creates electric field gradients.

For simplicity, when ignoring the 3D bending and rotation of the central path, the electric field can be approximated by a 2D field in the (u_r, h_r) transverse plane. The tilting of the electrode surface then produces a quadrupole field:

$$\frac{\partial E_{h_r}}{\partial u_r} = \frac{\partial E_{u_r}}{\partial h_r} = -QE_0$$

Where the titling parameter Q is given by the relative slope of the internal electrode surface in the (u_r, h_r) plane:

$$Q = \frac{1}{u_r}\frac{\partial u_r}{\partial h_r}$$

The strength of the tilting, expressed by $Q(s)$, can be varied along the path length, to create a strong focussing effect similar to a doublet or triplet lens. Additionally, the entrance and exit faces of the electrodes can be cut at an angle in the (h_r, v) plane, as shown in Fig. 4, producing electric field gradients in the fringe field region.

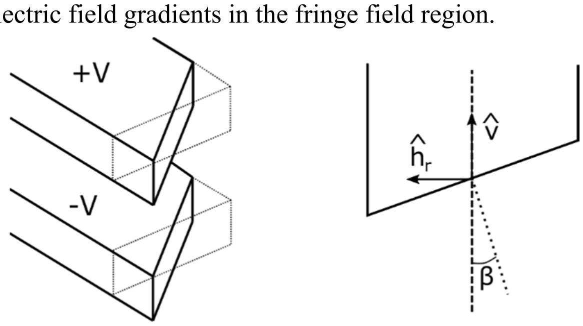

Figure 4: Modifying the electrode entrance and exit angles to produce field gradients in the fringe field region. The main field changes in strength along h_r, producing a quadrupole with $\frac{\partial E_{h_r}}{\partial u_r} = \frac{\partial E_{u_r}}{\partial h_r}$.

The entrance and exit edge angles β_1, β_2 can then be selected to enhance the gradients produced by $Q(s)$, in the internal part of the inflector.

EFFECTIVENESS OF THIS METHOD

To see how effective these gradients can be, consider a simplified situation where the inflector has been "straightened out" so that its central trajectory is a straight line. If the first half of the inflector is then given a positive Q, and the second half a negative Q, a doublet lens is formed, as shown in Fig. 5. Note that the maximum electrode gradient that can easily be obtained in an inflector is around Q ≈ 60 m^{-1}. For a typical inflector with a path length of 10 cm, electric bending radius 6 cm and electrode tilt Q = ±60 m^{-1}, the point-to-point focussing distance obtained by such a doublet is 17 cm. This is very similar to the distance between the collimator in front of the inflector and the slit behind the inflector, so clearly the field gradients can have a substantial effect on the optics.

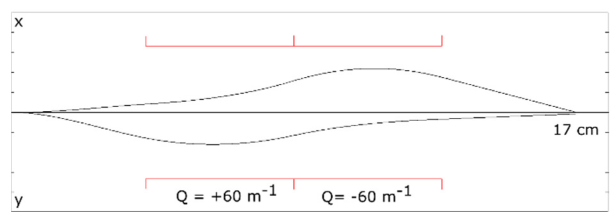

Figure 5: TRANSPORT calculation of a doublet equivalent to a "straightened out" inflector with alternating electric field gradients.

DESIGN PROCEDURE

The design of a field gradient spiral inflector consists of specifying a Belmont-Pabot type central path, the electrode gradient $Q(s)$ along the length of the path, as well as the entrance and exit angles β_1, β_2. The transfer matrix for the inflector, written as $R(Q, \beta_1, \beta_2)$, is very complicated and must be obtained numerically. A Matlab program was created to quickly compute the transfer matrix:

$$R = TransferMatrixProgram(Q, \beta_1, \beta_2)$$

To do this the function $Q(s)$ was discretized and represented by in a piecewise linear fashion. The discretization only consisted of 3 points along the path length (inflector entrance, middle and exit), which is the minimum needed to represent a triplet-like shape, and these values are indicated by (Q_1, Q_2, Q_3). The *TransferMatrixProgram* had to be able to compute R within a few seconds. This was done by ray-tracing through the electric and magnetic fields. The same magnetic field was always used, and obtained from a TOSCA-based numerical model of the SPC2 cyclotron [6]. Using an accurate magnetic field is important due to the strong solenoid focussing and rotation occurring as the beam enters the main magnetic field through the axial entrance hole in the magnet yoke.

ISBN: 978-3-95450-205-9 doi:10.18429/JACoW-Cyclotrons2019-MOP016

When performing ray tracing, the electric field has to be constantly adapted, depending on the gradient parameters Q_1, Q_2 ... etc. Since a full TOSCA simulation of the electric field is too time consuming, a simplified method was used. This method only requires performing a small number of TOSCA simulations, and then using their pre-calculated results to estimate the electric field during run time. To do this, it was assumed that the electric field can, in all of space, be approximated by the first derivatives of the field with respect to the electrode parameters:

$$\boldsymbol{E}(Q_1, Q_2, \dots) = \boldsymbol{E}|_0 + \frac{\partial \boldsymbol{E}}{\partial Q_1} Q_1 + \frac{\partial \boldsymbol{E}}{\partial Q_2} Q_2 + \cdots$$

Where $\boldsymbol{E}|_0$ refers to the 3D TOSCA electric field when all the parameters are zero, while the derivatives with respect to the gradient parameters were estimated by:

$$\frac{\partial \boldsymbol{E}}{\partial Q_1} \approx \frac{1}{\Delta Q}\left(\boldsymbol{E}|_{Q_1=\Delta Q} - \boldsymbol{E}|_0\right)$$

Where $\boldsymbol{E}|_{Q_1=\Delta Q}$ refers to the 3D TOSCA field calculated when $Q_1 = \Delta Q$ and all the other parameters zero. The value of $\Delta Q = 20$ was chosen since it lies roughly in the middle of the range of obtainable gradients. In this way, only 6 pre-calculated TOSCA models were required. The complete *TransferMatrixProgram* was validated by comparing it to the full TOSCA simulation in a number of cases.

The transfer matrix $R(Q_1, Q_2, Q_3, \beta_1, \beta_2)$ was numerically optimised so that the resulting beam height and vertical divergence at the first acceleration gap were kept to a minimum. This optimisation was performed using a combined method of random sampling, to obtain promising starting positions, followed by steepest descent, to reach the optimal values.

DESIGN OF A NEW INFLECTOR FOR SPC2

The SPC2 injector cyclotron at iThemba LABS uses a spiral inflector, called inflector C1, to accelerate heavy ions. Inflector C1 is equivalent to a standard spiral inflector with properties shown in Table 1. A new vertically focussing inflector, called C2, was designed to replace C1.

Table 1: Specifications of Inflector C

Description	Parameter	Value
Magnetic bending radius	R_m	4.9 cm
Electric bending radius	A	6.0 cm
Tilt parameter	k'	0.38

In the design of the C2 inflector, a beam with a 3 mm x 30 mrad elliptical transverse profile and a 0.5% momentum spread was used as the input, and the beam profile at the first acceleration gap was optimised. The final design is shown in Fig. 6. It was found that a doublet-type design, where Q goes from negative to positive along the path length, worked well. The entrance and exit angles β_1, β_2 were set at 20° and oriented to enhance the gradients produced by Q.

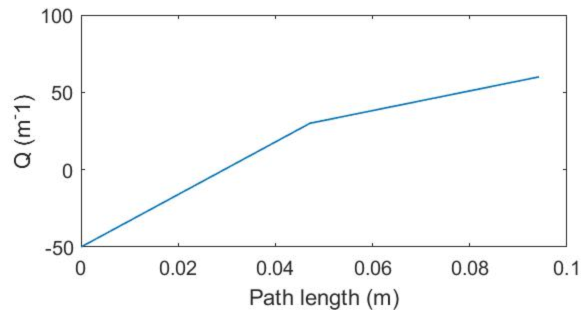

Figure 6: Design of the C2 inflector, showing how the tilting parameter Q changes along the path length.

The simulated vertical performance of C2, shown in Table 2, is very good. In particular, there was a 65% decrease in the beam spot size compared to C1. The horizontal behaviour did not change much. The longitudinal spread introduced by C2 is however substantially more than C1, by a factor of around 2. The phase space plots of the final beam, as determined by ray tracing in the full 3D inflector model in TOSCA, are shown in Fig. 7.

Table 2: Comparison of the C1 and C2 Beam Parameters at the First Acceleration Gap

Parameter	C1	C2
Vertical emittance growth (%)	+45	+5
Vertical half-width (mm)	8.9	2.9
Horizontal emittance growth (%)	+45	+30
Horizontal half-width (mm)	3.0	1.5
Longitudinal half-width (mm)	5.5	12.9
RF phase spread (degrees)	±39	±90

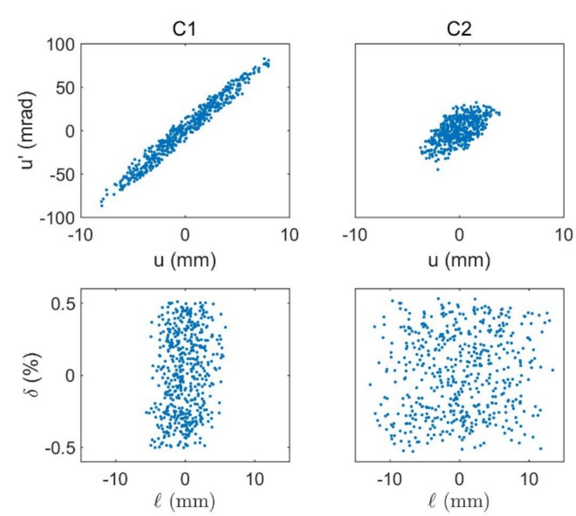

Figure 7: Vertical (top) and longitudinal (bottom) emittance plots at the first acceleration gap.

ISBN: 978-3-95450-205-9 doi:10.18429/JACoW-Cyclotrons2019-MOP016

EXPERIMENTAL TESTING

Inflectors C1 and C2 were experimentally tested by measuring their transmission throughout SPC2. The transmission was defined as the beam current measured at a certain point divided by the beam current on the last Faraday cup before the inflector. The results of all four experiments performed so far are shown in Fig. 8. It should be noted that performing experiments with SPC2 is difficult since it displays large differences in performance (at least 20%) between consecutive runs, so it is important to look at the trends in the data rather than the individual values.

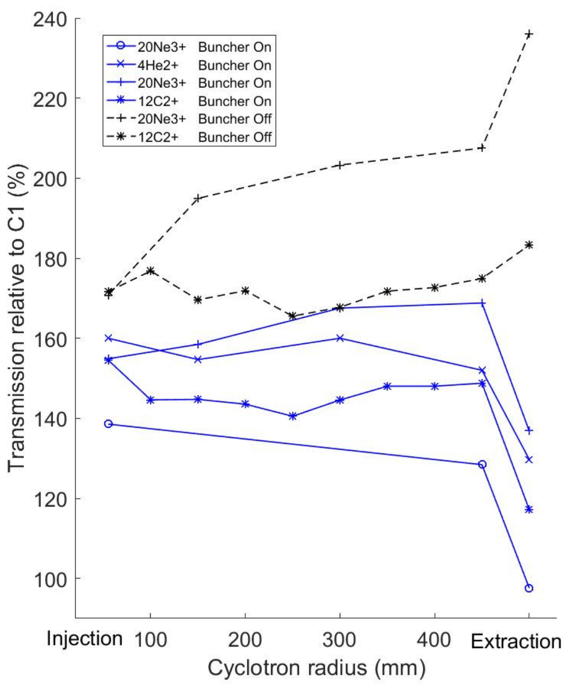

Figure 8: Experimental transmission through SPC2 when using the field gradient inflector C2, compared to the transmission with the ordinary spiral inflector C1.

When the buncher is turned off, so that the longitudinal behaviour of the inflector plays no role, the C2 inflector improved transmission by between 80% - 120%. With the buncher activated, C2 improves the injection efficiency by about 50% and it then maintains this improvement throughout the cyclotron, but suffers from bad extraction. This meant that the average total improvement in transmission was only about 20%.

IMPORTANCE OF LONGITUDINAL BEHAVIOUR

The experimental results can be explained as follows: C2 has very good vertical focussing and loses relatively few particles on the puller slits, resulting in the good performance when the buncher is turned off. But C2 also has a large longitudinal spread (see Table 2 and Fig. 7), resulting in a large RF phase spread when the buncher is turned on. The inflector is in effect de-bunching the beam. This leads to decreased performance, with a larger energy spread probably resulting in a wider beam with poor extraction.

It was attempted to improve the longitudinal behaviour of C2, while still maintaining its vertical focussing, using the electrical gradient method described in this article. Unfortunately, this was unsuccessful. Instead, a new more general method for the control of all possible electric gradients has been developed, resulting in quadratic electrode profiles in the transverse plane. This doubles the degrees of freedom available to control the first order electric field gradients. The development of a new inflector, C3, capable of controlling both the vertical and longitudinal focussing is ongoing.

CONCLUSION

By tilting the electrode surfaces of a spiral inflector it is possible to create electric field gradients along the central path that greatly influence the optics. Selecting an appropriate tilting profile Q(s) results in good vertical focussing and much improved transmission through the cyclotron. However, an increase in longitudinal spread reduces the effectiveness of this method, and a possible solution is being investigated.

REFERENCES

[1] J. L. Belmont and J. L. Pabot. “Study of axial injection for the Grenoble cyclotron”, *IEEE Trans. Nucl. Sci.*, vol. 13, no. 4, pp. 191-193, 1966. doi:10.1109/TNS.1966.4324204

[2] B. N. Gikal, G. G. Gulbekian, and I. A. Ivanenko, “Compensation of the beam vertical defocusing at the exit of U400 cyclotron spiral inflector”, in *Proc. 21st Russian Particle Accelerator Conf. (RuPAC'08)*, Zvenigorod, Russia, Sep.-Oct. 2008, paper TUAPH12

[3] Z. B. Du Toit *et al.*, “Commissioning of the injector cyclotron for polarised and heavy ions at NAC”, in *Proc. 14th Int. Cyclotron Conf. and their Applications (Cyclotrons'95)*, Cape Town, South Africa, Oct. 1995, paper A-04, pp. 28-31.

[4] TOSCA, http://operafea.com

[5] I. A. Ivanenko, “The methods of compensation of the beam vertical divergence at the exit of spiral inflector in cyclotrons”, in *Proc. 21st Int. Conf. on Cyclotrons and their Applications (Cyclotrons'16)*, Zurich, Switzerland, Sep. 2016, pp. 221-223. doi:10.18429/JACoW-Cyclotrons2016-TUP25

[6] J. G. de Villiers *et al.*, “Numerical Orbit Tracking in 3D Through the Injector Cyclotron for Heavy Ions at iThemba LABS”, in *Proc. 21th Int. Conf. on Cyclotrons and their Applications (Cyclotrons'16)*, Zurich, Switzerland, Sep. 2016, pp. 71-74. doi:10.18429/JACoW-Cyclotrons2016-MOP10

ISBN: 978-3-95450-205-9 doi:10.18429/JACoW-Cyclotrons2019-MOP017

RESEARCH ON METALLIC ION BEAM PRODUCTION WITH ELECTRON CYCLOTRON RESONANCE ION SOURCES

S. Bogomolov†, A. Efremov, D. Pugachev, K. Kuzmenkov, N. Yazvitskiy
Joint Institute for Nuclear Research (JINR), Dubna, Russia
R. Thomae, J. Mira, F. Nemulodi, N. Kheswa, L. Conradie, D. Fourie
iThemba LABS, Faure, South Africa

Abstract

Many experiments in nuclear physics request the production of metallic ion beams. All elements from Lithium up to Uranium are of interest and most of them are required as a specific isotope which demands commonly enriched materials. Depending on the material properties, beams of rare isotopes can be produced from solid materials or solid compounds. In this report the results of experiments carried out under a collaboration of JINR and iThemba LABS on the production of metallic ions from Electron Cyclotron Resonance (ECR) Ion Sources using resistive oven evaporation, Metal Ions from VOlatile Compounds (MIVOC) method and sputtering technique will be presented.

INTRODUCTION

Several methods for the production of ions from solid materials have been developed. Solid materials can be evaporated from a resistor or inductive oven inserted into a source chamber [1, 2]. Refractory metals can be sputtered by plasma ions [3] or inserted into plasma with subsequent heating by energetic plasma electrons ("insertion technique") [4, 5]. Another way of producing ions of solids is to feed plasma of an organometallic compound using the MIVOC method [6]. The selection of the best method to feed solids into ECR ion sources strongly depends on specific properties of materials.

OVEN EXPERIMENTS

Development of the oven evaporation method for production of ions of solids for FLNR JINR ECR ion sources was stimulated by the requirements of production of intense ^{48}Ca beam, which is the key ingredient in the experiments on synthesizing of new heavy nuclei.

To solve this problem, a new method for the solid material feed into the ECR source was developed. The combination of a micro oven with a hot tantalum liner inside the discharge chamber allowed the production of intense beams of ions of metals with relatively low evaporation temperature (Li, Mg, Ca, Bi) [7]. This development allowed long-term experiments on synthesis of super heavy elements during last 20 years and led to discovery of new super heavy elements with Z = 113–118 [8].

The experience of FLNR ECR ion source group was successfully applied in a collaboration of JINR and iThemba LABS on the production of metallic ions from ECR ion sources at iThemba LABS.

The experiments on production of ions of solids by oven evaporation method were performed with the GTS2 ECR ion source [9]. The layout of the beam line used for the experiments is shown in Fig. 1. In all experiments the source was operated with 14 GHz frequency.

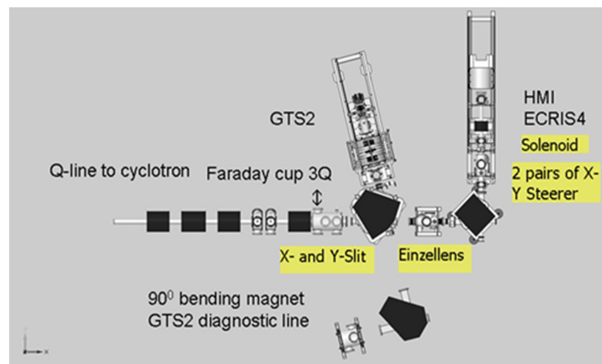

Figure 1: Experimental layout for the oven and MIVOC experiments.

The GTS2 ECR ion source is equipped with two ports through which electrically heated ovens can be introduced into the plasma chamber. The oven used for the measurements was designed and manufactured by the ion source group at FLNR. The design is based on the micro oven [10], which has been successfully used for several years for the production of ^{48}Ca and Li ion beams. The present design of the oven allows using a crucible with an inner volume of 480 mm^3, which is about 6 times more than that of the original design. The calibration for the oven inner temperature as a function of the oven electrical heating power is shown in Fig. 2. The oven was mechanically and electrically connected to the oven support of the GTS2. The oven is positioned inside the plasma chamber in a way that the tip of the oven has a distance of 30 mm to the bias disc. In addition, a liner made from 0.1 mm stainless steel sheet was installed inside the plasma chamber. The liner has folds on both ends to keep it in 1 mm distance to the plasma chamber wall to reduce the thermal contact. This results in a higher temperature of the liner by means of microwave and plasma heating thereby preventing the condensation of the oven material.

The beam extracted from GTS2 was either analysed with Faraday cup 3Q behind the 104°-bending magnet in the Q-line or with Faraday cup Q2 in the diagnostic beam line behind the 90°-bending magnet (see Fig. 1).

† sbogomolov@jinr.ru

ISBN: 978-3-95450-205-9 doi:10.18429/JACoW-Cyclotrons2019-MOP017

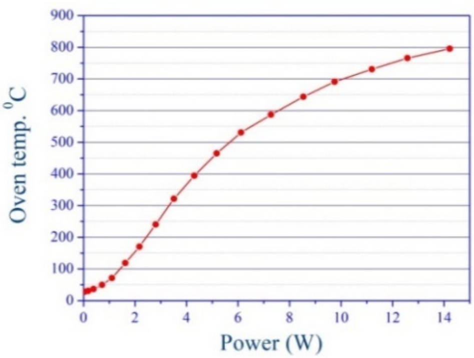

Figure 2: Oven inner temperature vs electrical heating power.

Calcium Experiments

The stainless steel crucible was loaded with approximately 500 mg of natural Ca granulate (97% ^{40}Ca). The granulate surface was prepared with a smooth file. The oven and the liner were conditioned for 15 hrs with 100 W of RF power with He support gas and oven heating power of 1.1 W (~100 °C).

The source was optimized for the extraction of $^{40}Ca^{9+}$ ions. Fig. 3 shows the spectrum of extracted Ca ions at extraction voltage of 10 kV, RF power P_{rf} = 250 W, horizontal slit width SLX = 20 mm, vertical slit width SLY = 30 mm, oven heating power P_o=5.6 W. For this experiment He gas was used as a supporting gas. A $^{40}Ca^{9+}$ ion current of 100 eμA was measured in Faraday cup 3Q.

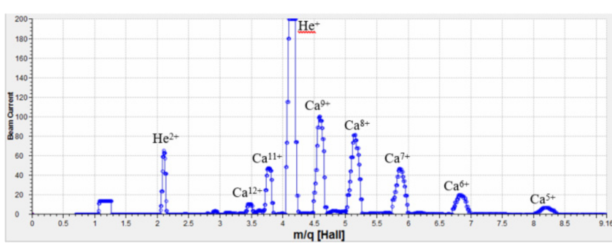

Figure 3: Spectrum of the extracted Ca ion beam.

The Faraday cup current for $^{40}Ca^{9+}$ ions was monitored for constant source settings over 12 hours in which the current dropped by 20%.

Lithium Experiments

After experiments with Ca the crucible was loaded with approximately 200 mg of Li. For Li operation it is essential that the oven opening is closed with a small ball twirled of 0.2 mm Ta wire because the material's melting point is below its operation temperature. The oven was then moved into the source at the same position as described before. The oven was conditioned by gradually increasing the oven temperature to 100 °C. The source was then started up, optimized for Li^{2+} and after one hour of operation the spectrum shown in Fig. 4 was measured in Faraday cup 3Q at extraction voltage U_{ex} = 10 kV, RF power P_{rf} = 200 W, horizontal slit width SLX = 20 mm, vertical slit width SLY = 30 mm, oven heating power P_o=3.8 W (~350 °C). The source is also operated with He supporting gas.

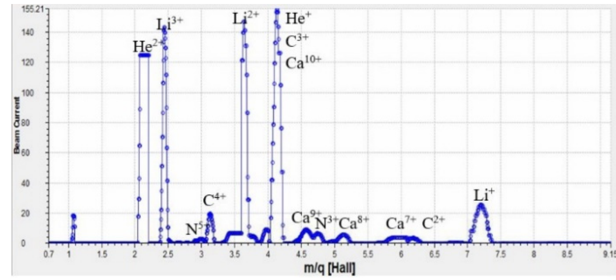

Figure 4: Spectrum of the extracted Li ion beam.

Three observations from the spectrum are evident: firstly, there is still some Ca left in the source from the previous experiment (appears as Ca^{7-10+} peaks). Secondly, C ions are detected which were not measured in the Ca experiment (see Fig. 4). This contamination can be explained by the fact that the Li material was stored in oil. Thirdly, the source is very well conditioned which is obvious from the low intensities of the N^{3+} and N^{5+} peaks. This is important for the determination of the Li beam intensity because all charge states of Li ions are interfered by Nitrogen ions with corresponding double charge states.

Intensities measured for Li ions with charge state 2+ and 3+ were more than 100 eμA. Next the beam extracted from the source was directed into the diagnostic beam line for long-term experiments. The transmission through this beam line is roughly half of that of the Q-line. The 90°-bending magnet was adjusted for Li^{2+}.

The source was operated with Li beam for a total period of 6 days. During this period of time the Li^{2+} beam current dropped from 55 to 40 eμA. The short term stability was better than +/-5 %. Only once the gas flow of the supporting gas was slightly adjusted to improve the source stability.

The source was then tuned for Li^{3+} production and the beam was transported through Q-line to the entrance of the Solid Pole Cyclotron (SPC2). For cyclotron injection the slits in the Q-line were closed to 10 mm (horizontal) and 20 mm (vertical) resulting in a beam current of 17 eμA measured in Faraday cup in front of SPC2. This beam was then injected into SPC2 and accelerated to 10 MeV. The Li^{3+} current extracted from SPC2 was 2.3 eμA.

Magnesium Experiments

The stainless steel crucible was loaded with approximately 350 mg of natural Mg (79 % ^{24}Mg, 10 % ^{25}Mg, 11 % ^{26}Mg). The material was chipped with a knife from a solid disc. The chips were compressed inside the crucible. The oven was conditioned with 1.1 W (~160 °C) of oven heating power for 12 h. In addition, the source was operated with 60 W of RF power with He as support gas. The source was then optimized for the extraction of $^{24}Mg^{7+}$ ions. The spectrum shown in Fig. 5 was obtained at following source settings: extraction voltage U_{ex} = 10 kV, RF power P_{rf} = 430 W, oven heating power P_o = 3.8 W (the oven temperature is approximately 390 °C), horizontal slit width SLX = 5 mm, vertical slit width SLY = 15 mm. Furthermore, beside the main peaks

ISBN: 978-3-95450-205-9 doi:10.18429/JACoW-Cyclotrons2019-MOP017

for the ^{24}Mg peaks for the isotopes 25 and 26 can be identified.

A maximum $^{24}Mg^{7+}$ ion current of 40 eμA was measured in Faraday cup 3Q. When the extraction voltage was increased to 15 kV, the $^{24}Mg^{7+}$ current amounted to 90 eμA. This can be either due to extraction conditions (Child-Langmuir) and/or due to a higher transmission through the bending magnet into the Q-line. The Faraday cup current for $^{24}Mg^{7+}$ ions was monitored for constant source settings over 12 hours in which the intensity varied by less than 5%.

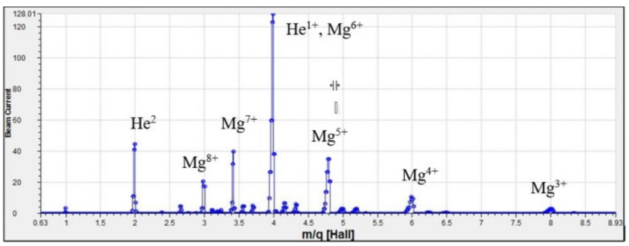

Figure 5: Spectrum of the extracted Mg ion beam.

Bismuth Experiments

The crucible was loaded with approximately 2 g of Bi. For Bi operation it is essential that the oven opening is closed with a small ball twirled of 0.2 mm Ta wire because the material's melting point (270 °C) is below its operation temperature (630 °C). The oven was then moved into the source at the same position as described before. The oven was conditioned at a temperature of 200 °C for 12 hrs.

The source was optimized for Bi^{27+}. The spectrum, shown in Fig. 6 shows the intensities of 23 and 16 eμA for Bi^{27+} and Bi^{30+}, respectively. The source parameters are: extraction voltage $U_{ex} = 15$ kV, RF power $P_{rf} = 460$ W, horizontal slit width SLX = 15 mm, vertical slit width SLY = 35 mm, oven heating power $P_o = 5.7$ W (510 °C).

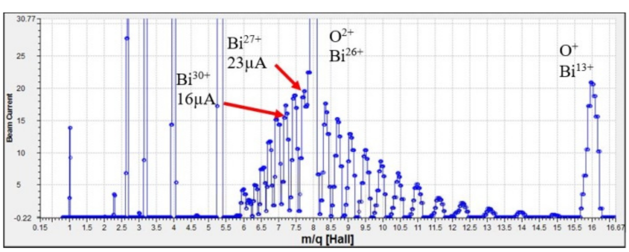

Figure 6: Spectrum of the extracted Bi ion beam.

The results so far suggest that the oven position might be too close to the plasma for Bi operation. This is because maximum beam intensities were obtained at lower oven heating powers than expected. Experiments at FLNR gave best Bi operation at oven temperature of 630 °C corresponding to oven heating powers of 8.4 W. The heating power of 5.7 W used in our experiments corresponds to only 510 °C, the additional oven heating could be from plasma heating. Further experiments in which the oven position will be varied need to be carried out.

MIVOC EXPERIMENTS

The MIVOC technique was first developed in Finland in 1994 [6]. In the MIVOC technique, solid state volatile metallic compounds can produce vapor gas having metallic atoms even at room temperature. Compounds are placed in a separate vacuum chamber connected to the plasma stage of the ECR ion source.

In FLNR the investigations on MIVOC method were motivated by the demand on production of intense ^{50}Ti ion beam for further progress in synthesis of super heavy elements. The series of experiments with natural and enriched compounds of Ti $(CH_3)_5C_5Ti(CH_3)_3$ were performed at the ECR test bench leading to production of intense beams of Ti ions (80 µA $^{48}Ti^{5+}$ and 70 µA $^{48}Ti^{11+}$) [11]. Experiments on the production of Co, Cr, Ni, V, Ge and Hf ion beams were also performed at the test bench of ECR ion sources.

This development allowed long-term experiments with accelerated ^{50}Ti and ^{54}Cr ion beams at the U-400 cyclotron.

The experience obtained during MIVOC method development in FLNR was applied in a collaboration of JINR and iThemba LABS for production of Ni ion beam from isotopes with low natural abundance. The experiments were performed with ECR4 [12] ion source in experimental layout shown in Fig. 1.

The experiments were performed with commercial Nickelocene $(Ni(C_5H_5)_2)$ with natural abundance, in-house produced 99 % enriched 60-Nickelocene and in-house produced 98 % enriched 62-Nickelocene. The procedure of Nickelocene synthesis and details of the experiments are described in [13]. Currents of 30 µA for charge state 8+ were obtained.

From the performed experiments we can conclude, that the drift length of the Nickelocene molecules into the plasma chamber should be reduced by excluding the insulator of the injection system, and the injection system should be kept on source potential to prevent possible gas discharges which might interact with the Nickelocene flow. The other possible way to increase the conductivity of the injection system and thus increase the beam current is the modification of the ECR4 ion source like similar CAPRICE-type ECR source mVINIS [14].

SPUTTERING EXPERIMENTS

The experiments on production of ions of solids by sputtering method were performed using the DECRIS-SC ion source [15] at the CI-100 cyclotron [16].

The CI-100 cyclotron is mainly tuned for acceleration of ions with A/Z ratio close to 5 ($^{132}Xe^{26+}$, $^{86}Kr^{17+}$ and $^{40}Ar^{8+}$) for the energy of about 1.2 MeV/n. To avoid the changing of RF system tuning $^{51}V^{10+}$ ion was chosen for the first experiments. The DECRIS-SC is equipped with two ports, one of these ports can be used for insertion of oven or sputtering sample. The experimental equipment includes a negatively biased metal sample positioned close to the ECR plasma. The metal sample of V was supported by water cooled

ISBN: 978-3-95450-205-9 doi:10.18429/JACoW-Cyclotrons2019-MOP017

supporting rod. The position of rod was remotely controlled. The rod position and high voltage for sputtering were optimized for maximizing the beam intensity of V^{10+} ions. Ar gas was used as a sputtering gas. One of the spectrum is shown in Fig. 7, where the position of V^{6+}, V^{7+}, V^{8+} and V^{10+} peaks are indicated.

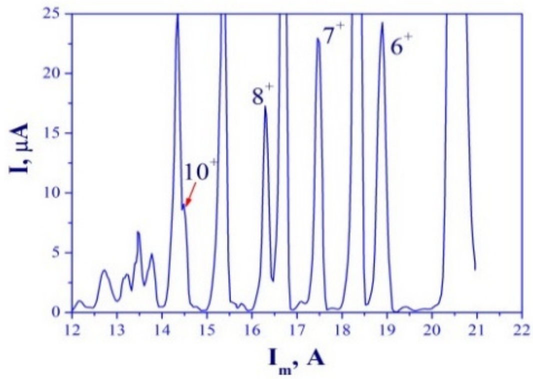

Figure 7: Spectrum of the extracted V ion beam. Positions of V^{6+}, V^{7+}, V^{8+} and V^{10+} peaks are indicated.

Due to the pure resolution of the injection system the tuning of the source was performed with accelerated beam at the final radius of cyclotron. The intensity of accelerated beam was 50 – 60 nA at the final orbit. The beam was produced at an extraction voltage of 14.65 kV, 250 W of RF power. The sputtering voltage and current amounted to 5 kV and 8 mA, respectively.

The accelerated beam was used for irradiation of ceramics samples during 125 h. The energy of accelerated beam was measured and constitutes of 62.4 MeV. The material consumption was measured as 1.32 mg/h.

In future experiments we plan to produce $^{181}Ta^{35+}$ (A/Z = 5.17) and study the effect of argon and oxygen as sputtering/mixing gases. Also, similar system can be applied at the GTS2 source.

CONCLUSION

Over the past few years, notable results and significant progress have been achieved by FLNR JINR and iThemba LABS collaboration in the production of intense multiply charged metal ion beams in ECR ion sources. Stable beams of Li, Mg, Ca and Bi were produced with a resistive oven from the GTS2 ion source. The Li^{3+} ion beam was accelerated to 10 MeV with SPC2; the extracted current was 2.3 eµA. Further optimisation of this method is required from the point of view of oven position and preventing oven overheating by plasma. The MIVOC method allows the production of intense ion beams with long-term stability. The further increase in beam intensity can be achieved by optimization of the injection line and remote tuning of compound flow.

The first experiments with sputtering technique were performed at FLNR JINR, and the accelerated beam of V^{10+} was produced at CI-100 cyclotron. This method can be also applied at the GTS2 source.

REFERENCES

[1] D. J. Clark and C. M. Lyneis, "The production of beams from solid materials at the LBL ECR source", *J. Phys. Colloq.* vol. 50, pp. 759-766, 1989.

[2] R. Harkewicz, "Efficient production of a ^{48}Ca beam from oxide material in an electron cyclotron resonance ion source using a low power miniature oven", *Rev. Sci. Instrum.*, vol. 67, pp. 2176–2178, 1996.

[3] R. Harkewicz *et al.*, "Ion plasma sputtering as a method of introducing solid material into an electron cyclotron resonance ion source", *Rev. Sci. Instrum.*, vol. 66, pp. 2883–2887, 1995.

[4] R. Geller, P. Ludwig, and G. Melin, "Metal ion production in ECRIS", *Rev. Sci. Instr.*, vol. 63, pp. 2795–2800, 1992.

[5] T. Nakagawa *et al.*, "Recent developments of RIKEN ECR ion sources", in *Proc. 10th Int. Workshop on ECR Ion Sources*, ORNL, Oak Ridge, USA, 1990, pp. 163-172.

[6] H. Koivisto, J. Arje, and M. Nurmia, "Metal ions from the volatile compounds method for the production of metal ion beams", *Rev. Sci. Instrum.*, vol. 69, no. 2, pp. 785–787, 1998. doi:10.1063/1.1148539

[7] V. B. Kutner, S. L. Bogomolov, A. A. Efremov *et al.*, *Rev. Sci. Instrum.*, vol. 71, no. 2, pp. 860-862, 2000. doi:10.1063/1.1150290

[8] Yu. Ts. Oganessian, A. Sobiczewski, and G. M. Ter-Akopian, "Superheavy nuclei: from predictions to discovery", *Phys. Scr.*, vol. 92, p. 023003, 2017. doi:10.1088/14024896/aa53c1

[9] R. Thomae *et al.,* "First commissioning results with the Grenoble test electron cyclotron resonance ion source at iThemba LABS", *Rev. Sci. Instrum.*, vol. 83, p. 02A323, 2012. doi:10.1063/1.3669790

[10] A. Efremov *et al.*, "Performance of the ion source DECRIS-14-2", *Rev. Sci. Instrum*, vol. 69, no. 2, pp. 662 – 664, 1998. doi:10.1063/1.1148567

[11] S. L. Bogomolov, A. E. Bondarchenko, A. A. Efremov *et al.*, "Production of intense metal ion beams from ECR ion sources using the MIVOC method", *Phys. Part. Nucl. Lett.*, vol. 12, no. 7, pp. 824–830, Dec. 2015. doi:10.1134/S1547477115070043

[12] P. Sortais *et al.*, "ECRIS development at GANIL", *Rev. Sci. Instrum.*, vol. 61, p. 288, 1990. doi:10.1063/1.1141324

[13] N. Kheswa, R. Thomae, F. Nemulodi *et al.*, "Production of high intensity nickel-ion beams with high isotope purity with the metal ions from volatile compound (MIVOC) method", *AIP Conf. Proc.*, vol. 2011, p. 040007, 2018. doi:10.1063/1.5053281

[14] A. Efremov *et al.*, "Upgrading of the CAPRICE type ECR ion source", *AIP Conf. Proc.*, vol. 2011, p. 040017, 2018. doi:10.1063/1.5053291

[15] A. Efremov *et al.*, "Status of the ion source DECRIS-SC", *Rev. Sci. Instrum.*, vol. 77, p. 03A320, 2006. doi:10.1063/1.2165268

[16] B. Gikal, S. Dmitriev, G. Gulbekian *et al.*, "Cyclotron based complex IC-100 for scientific and applied research", in *Proc. 18th Int. Conf. on Cyclotrons and their Applications (Cyclotrons'07)*, Giardini Naxos, Italy, Oct. 2007, pp. 27–32.

ISBN: 978-3-95450-205-9 doi:10.18429/JACoW-Cyclotrons2019-MOP018

SIMULATION OF THE AXIAL INJECTION BEAM LINE OF DC140 CYCLOTRON OF FLNR JINR

N. Yu. Kazarinov†, G. G. Gulbekyan, I. A. Ivanenko, I. V. Kalagin, J. Franko
Joint Institute for Nuclear Research, 141980, Dubna, Russia

Abstract

Flerov Laboratory of Nuclear Reaction of Joint Institute for Nuclear Research carries out the works under creating of FLNR JINR Irradiation Facility based on the cyclotron DC140. The facility is intended for SEE testing of microchip, for production of track membranes and for solving of applied physics problems. The main systems of DC140 are based on the DC72 cyclotron ones that now are under reconstruction. The DC140 cyclotron is intended for acceleration of heavy ions with mass-to-charge ratio A/Z within interval from 5 to 5.5 up to two fixed energies 2.124 and 4.8 MeV per unit mass. The intensity of the accelerated ions will be about 1 pμA for light ions (A<86) and about 0.1 pμA for heavier ions (A>132). The injection into cyclotron will be realized from the external room temperature 18 GHz ECR ion source. The simulation of the axial injection system of the cyclotron is presented in this report.

INTRODUCTION

Flerov Laboratory of Nuclear Reaction of Joint Institute for Nuclear Research carries out the works under the creating of Irradiation Facility based on the DC140 cyclotron. The DC140 will be a reconstruction of the DC72 cyclotron [1, 2]. Table 1 presents the main parameters of DC140 cyclotron

Table 1: DC140 Cyclotron Main Parameters

Pole (Extraction) Radius, m	**1.3 (1.18)**	
Magnetic field, T	1.415 to 1.546	
Number of sectors	4	
RF frequency, MHz	8.632	
Harmonic number	2	3
Energy, MeV/u	4.8	2.124
A/*Z* range	5.0 to 5.5	7.577 to 8.25
RF voltage, kV	60	
Number of Dees	2	
Ion extraction method	electrostatic deflector	
Deflector voltage, kV	70	

The irradiation facility will be used for Single Event Effect (SEE) testing of microchips by means of ion beams (^{16}O, ^{20}Ne, ^{40}Ar, ^{56}Fe, $^{84,86}Kr$, ^{132}Xe, ^{197}Au and ^{209}Bi) with energy of 4.8 MeV per unit mass and having mass-to-charge ratio *A*/*Z* in the range from 5.0 to 5.5.

Besides the research works on radiation physics, radiation resistance of materials and the production of track membranes will be carrying out by using the ion beams with energy of about 2.124 MeV per unit mass and A/Z ratio in the range from 7.577 to 8.25.

The working diagram of DC140 cyclotron is shown in Fig. 1. The acceleration of ion beam in the cyclotron will be performed at constant frequency f = 8.632 MHz of the RF-accelerating system for two different harmonic numbers h. The harmonic number $h = 2$ corresponds to the ion beam energy $W = 4.8$ MeV/u and value $h = 3$ corresponds to $W = 2.124$ MeV/u. The intensity of the accelerated ions will be about 1 pμA for light ions ($A \le 86$) and about 0.1 pμA for heavier ions ($A \ge 132$).

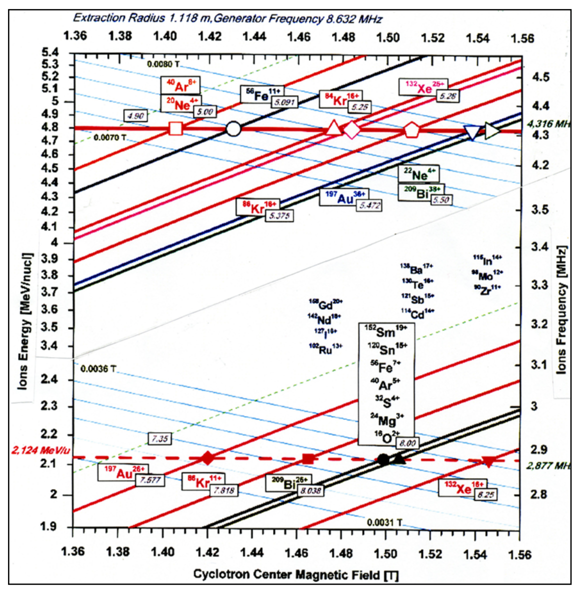

Figure 1: Working diagram of DC140 cyclotron.

The axial injection system of DC140 cyclotron will be adapted from the existing DC72 cyclotron one [3].

This report presents the simulation of the beam dynamic in the axial injection beam line of DC140 cyclotron. The simulation was carried out by means of MCIB04 program code [4].

ECR ION SOURCE

The ion beams are produced in superconducting ECR ion source DECRIS-SC designed in Flerov Lab of JINR [5]. The working frequency DECRIS-SC is equal to 18 GHz. It is able to produce the beams of ion from ^{22}Ne to ^{209}Bi. The ion beam currents at the source exit sufficient for the facility operation are contained in Table 2.

† nyk@jinr.ru

ISBN: 978-3-95450-205-9 doi:10.18429/JACoW-Cyclotrons2019-MOP018

Table 2: Ion Beam Current Extracted from DECRIS-SC

Ion	Current, pmcA	Ion	Current, pmcA
$^{22}Ne^{4+}$	~ 50	$^{132}Xe^{23+}$	~ 4
$^{40}Ar^{7+}$	~ 30	$^{132}Xe^{24+}$	~ 4
$^{56}Fe^{10+}$	~ 4	$^{197}Au^{34+}$	~ 0.3
$^{84}Kr^{15+}$	~ 8	$^{209}Bi^{37+}$	~ 0.2

The charge state distribution of argon beam current used in simulation is shown in Fig. 2.

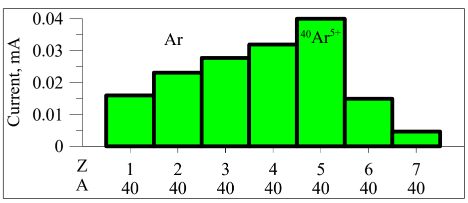

Figure 2: Ar beam current distribution.

The parameters of the ion beams at the extraction hole of ECR ion source are contained in Table 3.

Table 3: Parameters of Ion Beam Used in Simulation

Injected ions	$^{209}Bi^{38+}$	$^{132}Xe^{16+}$
A/Z	5.5	8.25
Extraction voltage U_{inj}, kV	17.26	14.31
Beam current [μA]	10	10
Beam diameter, [mm]	8	8
Emittance, π·mm·mrad	225	200

BEAM LINE SCHEME

The scheme of the beam line is shown in Fig. 3.

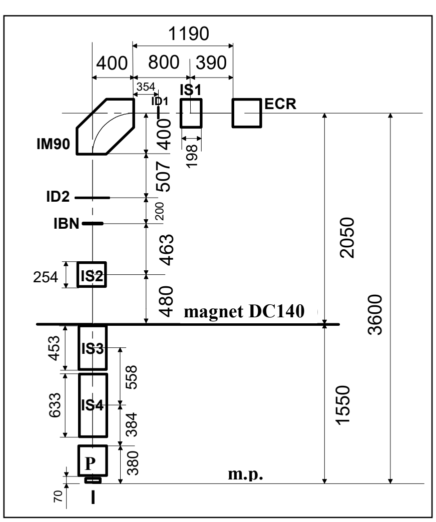

Figure 3: Scheme of the axial injection beam line.

The length of the beam line is equal to 5.018 m. The 90-degree analysing magnet IM90 separates the injected beam. The solenoidal lenses IS1-4 focus and match beam with the acceptance of the spiral inflector I for all level of the cyclotron magnetic field. The sinusoidal buncher IBN increases the beam capture into acceleration. Two movable diaphragms ID1,2 are used for analysis of the beams spectra.

ANALYZING MAGNET IM90

The analysing magnet IM90 has a bending radius R_M equal to 0.4 m, gap 80 mm and maximum magnetic field 0.2 T. This magnet was used in U400M cyclotron axial injection beam line before it upgrading.

SOLENOIDS IS1-IS4

The solenoids IS1-IS4 are the part of existing DC72 cyclotron axial injection beam line [3]. Its on-axis magnetic fields are shown in Fig. 4.

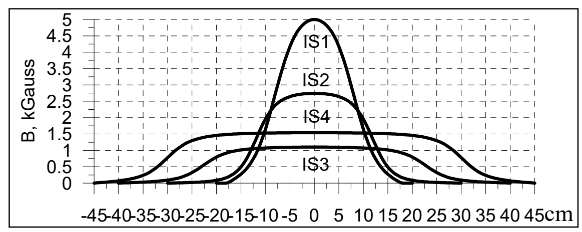

Figure 4: On-axis magnetic field of solenoids.

MAGNETIC PLUG

The parameters of the magnetic plug (P in Fig. 3) of the DC72 cyclotron were used in the calculation. The channel aperture in plug is shown in Fig. 5.

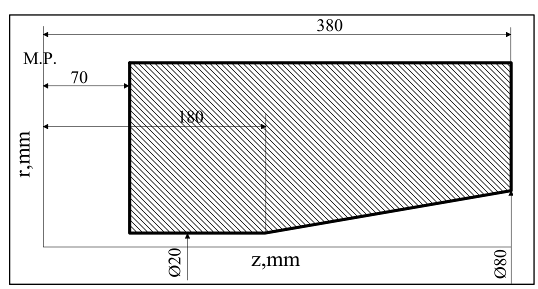

Figure 5: Magnetic plug scheme.

SINUSOIDAL BUNCHER IBN

To improve the efficiency of beam capture into the acceleration a sinusoidal (one harmonic) buncher IBN, located outside the yoke of the magnet at a distance of 2.493 m from the median plane of the cyclotron, is used. The maximum applied voltage at the grids of buncher is 423.4 V for the injecting ions having A/Z = 5.5($^{209}Bi^{38+}$). The efficiency of bunching is approximately equal to 2 (see Fig. 6).

ISBN: 978-3-95450-205-9 doi:10.18429/JACoW-Cyclotrons2019-MOP018

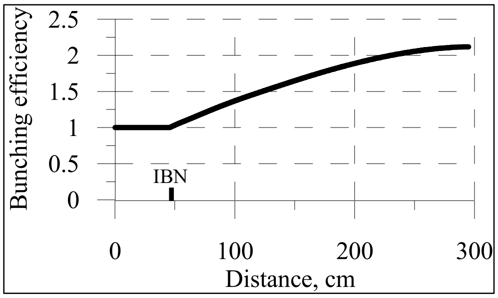

Figure 6: Bunching efficiency.

SPIRAL INFLECTOR I

The spiral inflector I rotates the beam onto the median plane of the cyclotron. In the case of harmonic number h = 2, the inflector of DC72 cyclotron with magnetic radius ρ_M of 28.7 mm is used. The ECR extraction voltage U_{inj} varies from 15.69 kV to 17.27 kV for ions having A/Z in the range 5.0 ($^{40}Ar^{8+}$) to 5.5 ($^{209}Bi^{38+}$).

In the case h = 3 the new inflector with magnetic radius ρ_M = 32.0 mm is used. Then the voltage U_{inj} varies from 13.14 kV to 14.31 kV in the case of injection of ions having A/Z in the range from 7.577 ($^{197}Au^{26+}$) to 8.25 ($^{132}Xe^{16+}$).

SIMULATION RESULTS

The calculations of ion injection with the parameters specified in Table 3 were carried out. In all cases, the transfer efficiency is equal to 100%.

A/Z=5.5, B0=1.546 T, ρ_M=28.7 mm, h=2

Transport of $^{209}Bi^{38+}$ ion beam was considered. In this case the magnetic field at the center of the cyclotron B_0 = 1.546 T is maximal. The horizontal (H) and vertical (V) envelopes of $^{209}Bi^{38+}$ ions in the beam line is shown in Fig. 7.

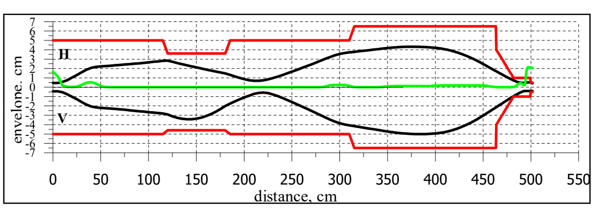

Figure 7: Horizontal (H) and vertical (V) $^{209}Bi^{38+}$ beam envelopes, aperture (red line) and longitudinal magnetic field (green line).

A/Z=8.25, B0=1.546 T, ρ_M =32.0 mm, h=3

Transport of $^{132}Xe^{16+}$ ion beam was considered. In this case the magnetic field at the center of the cyclotron B_0 = 1.546 T. The horizontal (H) and vertical (V) envelopes of $^{132}Xe^{16+}$ ions in the beam line is shown in Fig. 8.

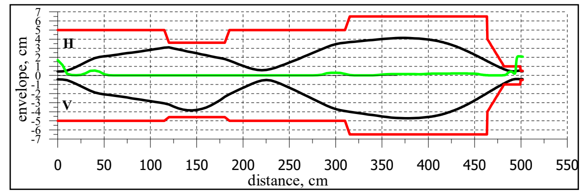

Figure 8: Horizontal (H) and vertical (V) $^{132}Xe^{16+}$ beam envelopes, aperture (red line) and longitudinal magnetic field (green line).

Beam Spectrum Analysis

Two movable diaphragms ID1,2 are used in the beam spectrum analysis. The first diaphragm ID1, has the form of a square with a side of 10 mm and shown in Fig. 9, is located at a distance of 354 mm in front of the IM90 magnet.

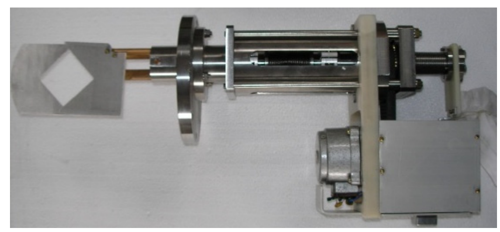

Figure 9: Diaphragm ID1.

The second one ID2 is a slit with a width of 5 mm < d < 10 mm, located at distance of 507 mm after IM90 magnet. The distance between diaphragm ID2 and Faraday cap is equal to 100 mm.

The beam emittance is decreased at diaphragm ID1 in 16 times that give opportunity to separate two neighbour charges in the beam spectrum by means of diaphragm ID2.

The distribution of ions $^{209}Bi^{37+,38+,39+}$ in front of the diaphragm ID2 is shown in Fig. 10.

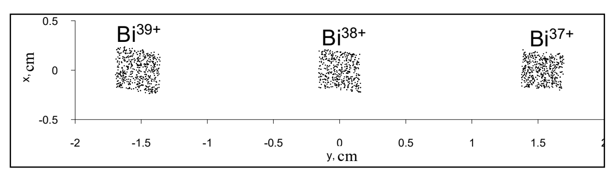

Figure 10: Bi ions distribution.

SUMMARY

The axial injection system of DC140 cyclotron allows transporting with of 100% efficiency all ion beams declared in the working diagram of FLNR JINR Irradiation Facility (Fig. 1).

The proposed system of beam spectrum analysis allows to separate ion charge up to value Z=38.

In the calculation the parameters of the existing solenoids IS1-4 of the axial injection channel of the DC-72 cyclotron have been used. The magnitudes of their magnetic fields are in the design range.

ISBN: 978-3-95450-205-9 doi:10.18429/JACoW-Cyclotrons2019-MOP018

REFERENCES

[1] B. N. Gikal, "Dubna cyclotrons – status and plans", in *Proc. 17th Int. Conf. on Cyclotrons and Their Applications (Cyclotrons'04)*, Tokyo, Japan, Oct. 2004, paper 20A1, pp. 100-104.

[2] G. Gulbekian, I. Ivanenko, J. Franko, and J. Keniz, "DC-72 cyclotron magnetic field formation", in *Proc. 19th Russian Particle Accelerator Conf. (RuPAC'04),* Dubna, Russia, Oct. 2004, paper WENO12, pp. 147-149.

[3] G. G. Gulbekyan, S. L. Bogomolov, V. V. Bekhterev, I. V. Kalagin, N. Yu. Kazarinov, and M. V. Khabarov, "Axial injection channel of the DC-72 cyclotron", in *Proc. 19th Russian Particle Accelerator Conf. (RuPAC'04),* Dubna, Russia, Oct. 2004, paper WENO11, pp. 144-146.

[4] V. Aleksandrov, N. Kazarinov, and V. Shevtsov, "Multi component ion beam code-MCIB04", in *Proc. 19th Russian Particle Accelerator Conf. (RuPAC'04),* Dubna, Russia, Oct. 2004, paper THBP09, pp. 201-203.

[5] A. A. Efremov *et al.*, "Status of the ion source DECRIS-SC", *Review of Scientific Instruments*, vol. 77, pp. 235-239, p. 03A320, 2006. doi:10.1063/1.2165268

ISBN: 978-3-95450-205-9 doi:10.18429/JACoW-Cyclotrons2019-MOP019

THE RESULTS OF MAGNETIC FIELD FORMATION AND COMMISSIONING OF HEAVY-ION ISOCHRONOUS CYCLOTRON DC280

G. Gulbekian, V. Semin, I. Ivanenko[#], I. Kalagin, G. Ivanov, FLNR, JINR, Dubna 141980, Russia

Abstract

The DC280 cyclotron is the new accelerator of FLNR Super Heavy Elements Factory. It was commissioned in the beginner of 2019. DC280 is intended for production of high intensity, up to 10 pmkA, beams of heavy ions with mass to charge ratio A/Z = 4 - 7. The wide range of accelerated ions from Helium to Uranium and smooth variation of extracted beam energy in the range W = 4 to 8 MeV/nucl. are provided by varying of the level of main magnetic field from 0.64 T to 1.32 T. The DC280 magnetic field was formed in a good conformity with results of computer modelling. In spite of the commissioning of cyclotron still is in progress, the first experiments gave the intensity 1.35 pmkA of $84Kr^{14+}$ and 10 pmkA of $12C^{2+}$. At the present work the results of calculations, magnetic field measurements and first experiments are presented.

INTRODUCTION

The main feature of new DC280 cyclotron is a wide range of operational modes and a high intensity of accelerated beams [1].

The cyclotron can accelerate heavy ions from Helium to Uranium with mass to charge ratio of A/Z = 4 – 7. The extracted energy of the beams can be smoothly varied in the range of W = 4 – 8 MeV/nucl. by changing of main magnetic field level and shape. The main challenge of DC280 magnetic system formation is covering all possible operational modes with minimal power consumption. According to the working diagram, Fig. 1, the magnetic field level should be varied in the wide range from 0.64 T to 1.32 T. In parallel, the isochronous radial growth of average magnetic field should be varied from 30 Gs to 100 Gs. For that, the 11 radial and 4 pairs of harmonic correcting coils are utilized and provide the needed operational correction.

DC280 is a compact type cyclotron. It has H-shape main magnet with 4-meter pole diameter, Table 1. Four pairs of straight, 45-degrees sectors form the variation of magnetic field, that keeps betatron frequencies in the ranges $1.005 < Qr < 1.02$ and $0.2 < Qz < 0.3$. The isochronous magnetic field is formed by variation of sectors height from the pole side. The sectors surfaces from median plane side stay flat. It decreases the sensitivity of replay function and, as a result, decreases the requirement to accuracy of sector shaping. DC280 magnet was manufactured and assembled with designed accuracy. Table 1 presents some important parameters with accuracies that were measured after assembling.

For DC280 magnetic field formation the original magnetometer was created. As a result of mapping and final formation, the magnetic field was formed in a good agreement with results of computer modelling. The first harmonic amplitude was decreased to about 1 Gs.

The first experiments have shown the efficiency of beam transmission from the inner radiuses until deflector has reached up to 90%.

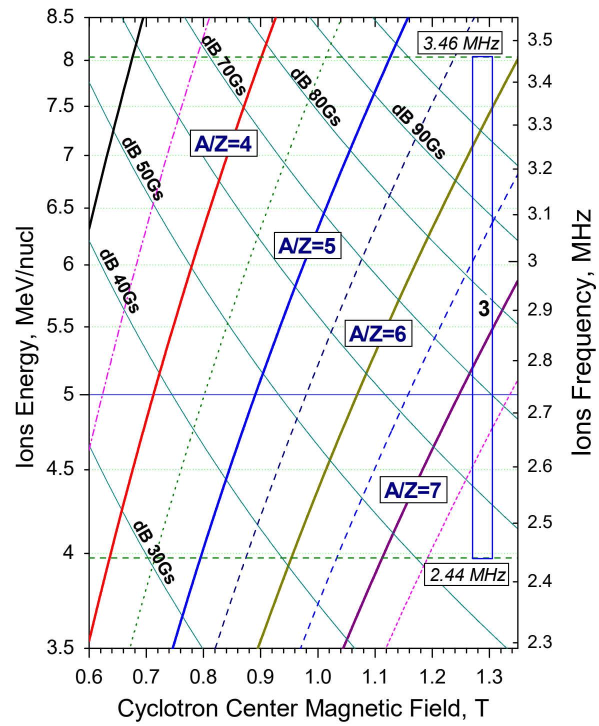

Figure 1: DC-280 Working diagram.

Table 1: Main Parameters of DC-280 Cyclotron Magnet

Parameter	Value
Main magnet size, mm	8760x4080x4840
Pole, mm	4000
Pole to pole gap, mm	500, accuracy ±0.2
Sector to sector gap, mm	208, accuracy ±0.17
Poles axis centering, mm	accuracy 0.53
Sector angular extent (spirality)	45° (0°)
Main magnet power, kWt	280
Correcting coils power, kWt	18

MAPPING SYSTEM

For final magnetic field formation, the DC280 mapping system was created [2]. The mapping system is based on 14 Hall probes and measures the magnetic field in a polar coordinate system with accuracy 10^{-4}. The Hall probes are placed on the plank with radial distance of 160 mm one to another. The plank is moved radially with a step of 10 mm

[#]ivav@jinr.ru

ISBN: 978-3-95450-205-9 doi:10.18429/JACoW-Cyclotrons2019-MOP019

or 20 mm in a range of 160 mm. The maximal radius of mapping is 160 mm x 14 = 2240 mm. All Hall probes were calibrated at the special test magnet in the range of 0.1 T – 2.9 T with NMR magnetometer. The possible errors between calibration functions of the neighbour probes are controlled by extra radial step of the plank, when previous probe is placed on the start position of the next probe. The usage of 14 probes decreases a time of mapping: the mapping of full, 360° azimuth range with 1° azimuthal and 10 mm radial steps takes about 7 hours. The 90° range mapping with 2° and 20 mm steps takes about 1 hour. The mechanisms of radial and azimuthal motions are equipped with pneumatic engines, Fig. 2. The standard poly-urethane toothed belt is placed around bottom pole and provides discreet azimuthal steps with a high accuracy.

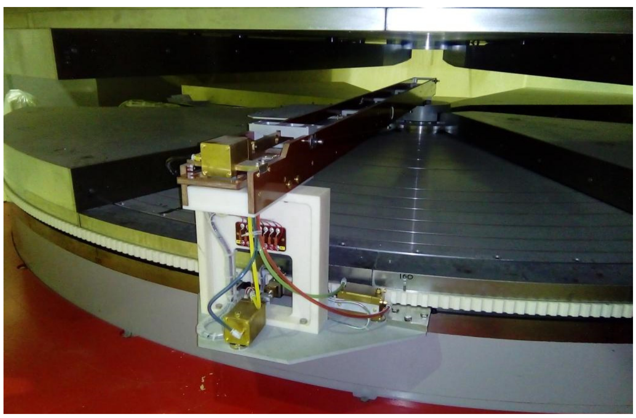

Figure 2: DC280 magnetometer with toothed belt.

RESULTS OF MAPPING

DC280 magnetic field measurements took about 3 months. During the mapping the database of main magnetic fields and additional fields of correcting coils was collected at different levels in the range 0.6 T to 1.32 T.

The time, required for magnetic field stabilization at a first turning on was measured. It takes about 40 minutes to reach the magnetic field stability of 10^{-4}, Fig. 3. The changing of the magnetic field level between different operational modes, including turning on of the correcting coils, are progressed faster and takes less than 10 minutes.

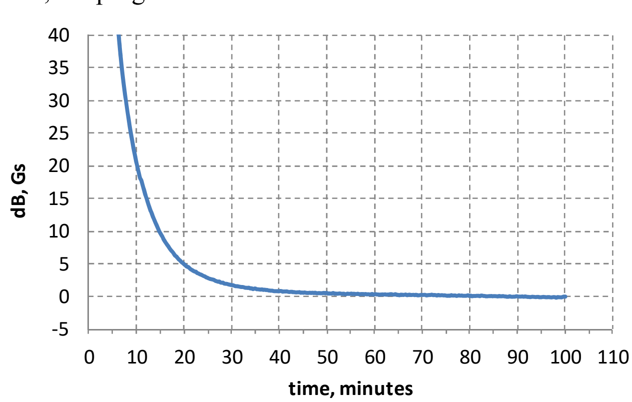

Figure 3: The time of magnetic field stabilization.

Figure 4 presents the signal from Hall probe, positioned at the cyclotron centre during the azimuthal motion of the magnetometer plank. It demonstrates good centring of the magnetometer and the low level of probe noises, not more than $2x10^{-5}$.

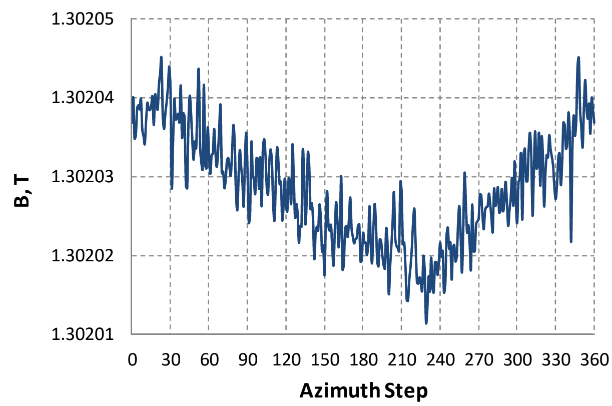

Figure 4: Signal from Hall probe at cyclotron centre.

To correct magnetic field, the sectors are equipped with removable shims. The shims have the shape of 10 mm width plates and are placed at edges of sectors. The shims could be easily removed and machined.

The results of the magnetic field measurements have shown a good coincidence with results of the numerical simulations, Fig. 5. At this case, correction of the average magnetic field by means of shaping of the sector shims was not required.

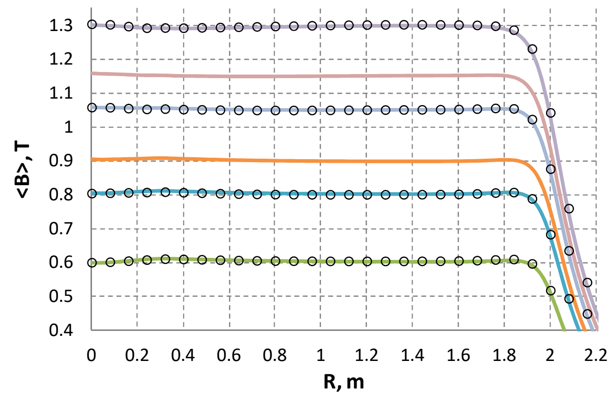

Figure 5: The calculation of the average magnetic field (circles) and the results of the measurements (line).

During DC280 magnetic field measurements, decreasing of pole to pole gap under magnetic field forces was investigated. For the magnetic field of 1 T the poles converging was not uniform azimuthally and varied from 0 to 0.2 mm.

The not uniform converging of the poles as well as finite accuracy of the manufacturing and assemblage leads to asymmetry of cyclotron magnetic system and cause the first harmonic of the magnetic field. The results of magnetic field measurements have shown the presence of the first harmonic with amplitude up to 10 Gs, Fig. 6.

ISBN: 978-3-95450-205-9 doi:10.18429/JACoW-Cyclotrons2019-MOP019

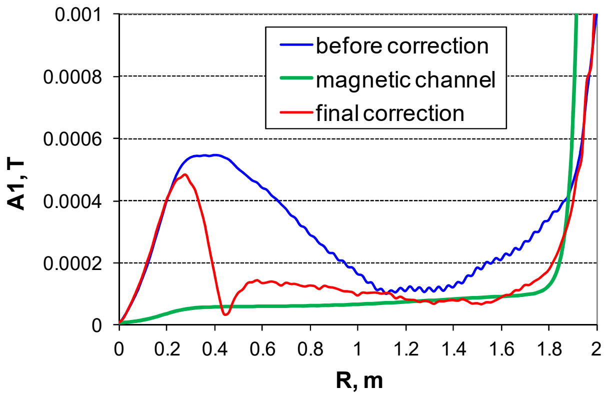

Figure 6: The amplitudes of first harmonic before and after correction and caused by magnetic channel installation.

DC280 magnet is equipped with focusing magnetic channel as a part of cyclotron extraction system. The channel is placed after electrostatic deflector at the radiuses 1900 mm – 2100 mm. Magnetic channel restricted the magnetometer motion. For field correction, the calculation results of the channel contribution to the first harmonic were used. Because a high distance between DC280 sectors is 208 mm and between the poles is 500 mm, the magnetic channel produces first harmonic with amplitude about 1 Gs up to extraction radius, Fig 6. Analysis of combination of measured first harmonic without magnetic channel and calculated first harmonic, produced by magnetic channel, gave the final shapes of sectors shims to compensate the total first harmonic. The final measurements shown that first harmonic was decreased to 1 – 2 Gs. Because sector shims have a technological restriction, the first harmonic could not be corrected on inner radiuses 0 – 400 mm and stays with permissible amplitude about 5 Gs at the centre.

RESULTS OF COMMISSIONING

In the first half-part of 2019 the beams of $84Kr^{14+}$, $12C^{2+}$ and $40Ar^{7+}$ were accelerated to energy 5.9 MeV/nucl. The intensities of extracted beams from cyclotron were 1.35, 6 and 10 pmkA respectively.

For $84Kr^{14+}$ beam the efficiency of injection into cyclotron was 14% without buncher, and 62% with buncher. Efficiency of acceleration inside cyclotron, with losses on residual gases as 10%, was 85%. Efficiency of beam extraction to the ion transport channel was 89%. The total efficiency from injection line to transport channel was about 42%.

For $12C^{2+}$ beam the efficiency of injection into cyclotron was 11.5% without buncher, and 54% with buncher. Efficiency of acceleration to the extraction radius was 83% and efficiency of extraction was 64%.

Figure 7 displays the experimental dependence of relative current of $84Kr^{14+}$ beam on magnetic field level for different radiuses of acceleration. The figure demonstrates that DC280 magnetic system forms the operational magnetic field in a good coincidence to isochronous. It is confirmed by a good transmission factor of acceleration. Because the presented results were received at the first experiments during cyclotron commissioning, the increasing of beam transmission factor at following experiments is expected.

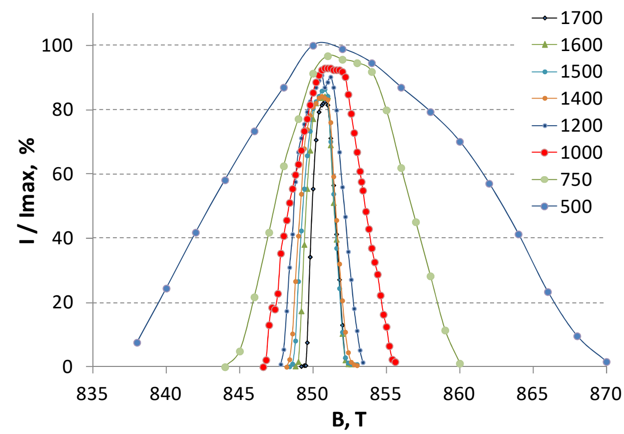

Figure 7: The dependence of relative current of $84Kr^{14+}$ beam on magnetic field level at different radiuses.

CONCLUSION

DC280 cyclotron was commissioned in the beginning of 2019. Despite the cyclotron is still in the progress of adjusting, the first experiments have shown a good efficiency of beam acceleration. In particular, it demonstrates that cyclotron magnetic system forms the operational magnetic field in a good coincidence to isochronous. To reach planned intensities of ion beams with middle atomic masses (A~50) up to 10 pmkA, the more operational time, improvement of vacuum conditions in the cyclotron chamber, adjustment of flat-top and usage of magnetic field database for programmer optimization of the operational modes parameters are needed.

REFERENCES

[1] I. V. Kalagin *et al.*, “Status of the DC-280 cyclotron project”, in *Proc. 21th Int. Conf. on Cyclotrons and their Applications (Cyclotrons'16)*, Zurich, Switzerland, Sep. 2016, pp. 363-365. doi:10.18429/JACoW-Cyclotrons2016-THP25

[2] I. A. Ivanenko, V. V. Aleinikov, G. N. Ivanov, and V. V. Konstantinov, “Measuring system for FLNR cyclotrons magnetic field formation”, in *Proc. 25th Russian Particle Accelerator Conf. (RuPAC'16)*, Saint Petersburg, Russia, Nov. 2016, pp. 544-546. doi:10.18429/JACoW-RUPAC2016-THPSC004

[3] I. A. Ivanenko, B. Gikal, G. G. Gulbekyan, V. P. Kukhtin, E. A. Lamzin, and S. E. Sytchevsky, “The feature of magnetic field formation of multi-purpose isochronous cyclotron DC280”, in *Proc. 8th Int. Particle Accelerator Conf. (IPAC'17)*, Copenhagen, Denmark, May 2017, pp. 2352-2354. doi:10.18429/JACoW-IPAC2017-TUPVA113

ISBN: 978-3-95450-205-9 doi:10.18429/JACoW-Cyclotrons2019-MOP020

SIMULATION OF THE BEAM EXTRACTION SYSTEM OF DC140 CYCLOTRON OF FLNR JINR

N. Yu. Kazarinov†, G. G. Gulbekyan, I. A. Ivanenko
Joint Institute for Nuclear Research, 141980, Dubna, Russia

Abstract

Flerov Laboratory of Nuclear Reaction of Joint Institute for Nuclear Research carries out the works under creating FLNR JINR Irradiation Facility based on the cyclotron DC140. The facility is intended for SEE testing of microchip, for production of track membranes and for solving of applied physics problems. The main systems of DC140 are based on the DC72 cyclotron ones that now are under reconstruction. The DC140 cyclotron is intended for acceleration of heavy ions with mass-to-charge ratio *A/Z* within interval from 5 to 5.5 up to two fixed energies 2.136 and 4.8 MeV per unit mass. The intensity of the accelerated ions will be about 1 pμA for light ions (*A*<86) and about 0.1 pμA for heavier ions (*A*>132). The beam extraction system consists of electrostatic deflector and two magnetic channels. The simulation of the extraction system of the cyclotron is presented in this report. The extracted beams characteristics outside the cyclotron, that will serve as initial conditions for the design of experimental beam lines of FLNR JINR IF are determined.

INTRODUCTION

Flerov Laboratory of Nuclear Reaction of Joint Institute for Nuclear Research carries out the works under the creating of Irradiation Facility based on the DC140 cyclotron. The DC140 will be a reconstruction of the DC72 cyclotron [1, 2]. Table 1 presents the main parameters of DC140 cyclotron.

Table 1: DC140 Cyclotron Main Parameters

Parameter	Value	
Pole (extraction) radius, m	1.3 (1.18)	
Magnetic field, T	1.415 - 1.546	
Number of sectors	4	
RF frequency, MHz	8.632	
Harmonic number	2	3
Energy, MeV/u	4.8	2.124
A/*Z* range	5.0 - 5.5	7.577 - 8.25
RF voltage, kV	60	
Number of Dees	2	
Ion extraction method	electrostatic deflector	
Deflector voltage, kV	70	

The irradiation facility will be used for Single Event Effect (SEE) testing of microchips by means of ion beams (^{16}O, ^{20}Ne, ^{40}Ar, ^{56}Fe, ^{84,86}Kr, ^{132}Xe, ^{197}Au and ^{209}Bi) with energy of 4.8 MeV per unit mass and having mass-to-charge ratio *A*/*Z* in the range from 5.0 to 5.5.

Besides the research works on radiation physics, radiation resistance of materials and the production of track membranes will be carrying out by using the ion beams with energy of about 2.124 MeV per unit mass and *A/Z* ratio in the range from 7.577 to 8.25.

The working diagram of DC140 cyclotron is presented in report MOP019 at this conference [3]. The acceleration of ion beam in the cyclotron will be performed at constant frequency f = 8.632 MHz of the RF-accelerating system for two different harmonic numbers h. The harmonic number h = 2 corresponds to the ion beam energy W = 4.8 MeV/u and value h = 3 corresponds to W = 2.124 MeV/u. The intensity of the accelerated ions will be about 1 pμA for light ions (A ≤ 86) and about 0.1 pμA for heavier ions (*A* ≥ 132).

The extraction system of DC140 cyclotron differs from DC72 cyclotron one, based on extraction by stripping foil [4], and consists of electrostatic deflector and two magnetic channels. The first is the passive channel placed in the region of strong magnetic field of the cyclotron. The second is permanent magnet channel placed in the region of low level magnetic field.

This report presents the simulation of the ^{209}Bi^{38+} ion beam dynamic in the extraction beam line of DC140 cyclotron.

CYCLOTRON MAGNETIC FIELD

The magnetic field of DC140 cyclotron within the project range is formed by variation of the currents in the main and in ten correcting coils. Radial distribution of the magnetic fields for acceleration of ^{209}Bi^{38+} ions up to energy W = 4.8 MeV/u is shown in Fig. 1 [5].

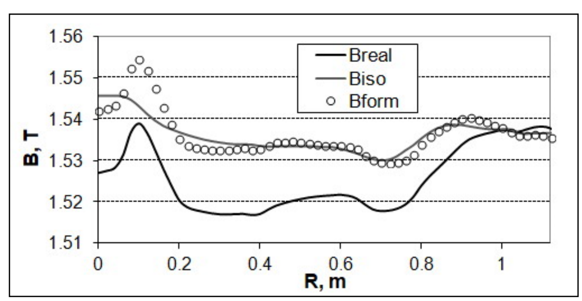

Figure 1: Magnetic fields for acceleration of ^{209}Bi^{38+} ions. Breal – magnetic field formed by main coils ; Biso – isocronous magnetic field ; Bform – magnetic field formed by main and correcting coils.

For the other kind of ions, the form of magnetic field is similar to the considering case.

† nyk@jinr.ru

ISBN: 978-3-95450-205-9 doi:10.18429/JACoW-Cyclotrons2019-MOP020

EXTRACTION BEAM LINE SCHEME

The scheme of the working region of DC140 cyclotron is shown in Fig. 2. The ion motion is considered in the polar coordinates system (R,Φ) having origin coincided with cyclotron center. The line $\Phi = 0$ (see Fig. 2) is the valley middle line. Ions move counterclockwise.

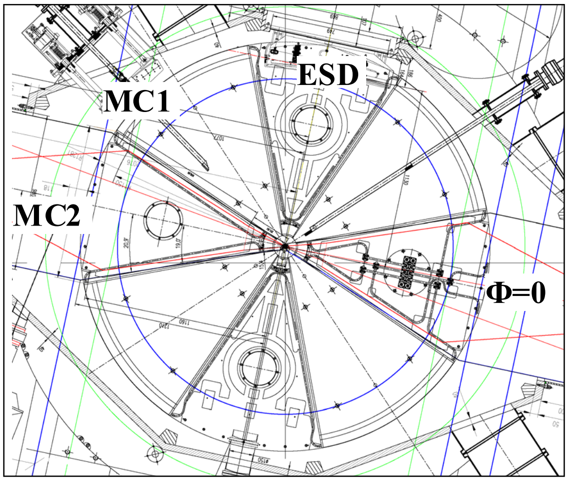

Figure 2: DC140 cyclotron working region. ESD – electrostatic deflector; MC1 – passive magnetic channel; MC2 – permanent magnet channel.

The closed orbit of the cyclotron corresponded to ion energy of 4.8 MeV/u and extraction orbit with final point at middle of special window in the wall of vacuum chamber (R = 197.1 mm, Φ = 194.60) are shown in Fig. 3. The length of extraction orbit is equal to 306.4 cm.

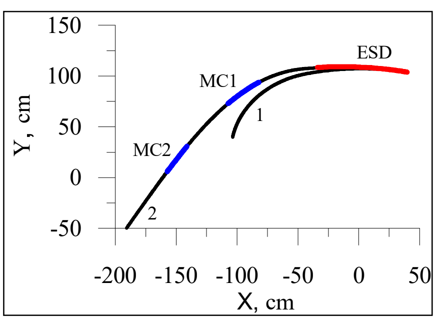

Figure 3: Closed (curve 1) and extraction (curve 2) orbits of DC140 cyclotron.

The cyclotron magnetic field B_z and its gradient along the direction of normal vector to the extraction orbit $\partial Bz/\partial x$ are shown in Fig. 4.

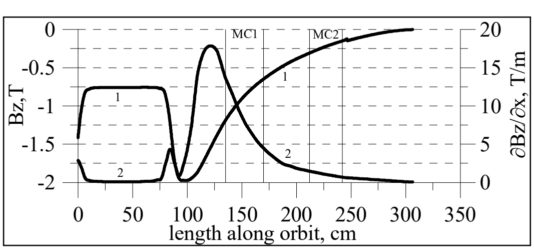

Figure 4: Cyclotron magnetic field B_z (curve 1) and its gradient (curve 2) distributions along the extraction orbit.

The entrance of electrostatic deflector ESD is placed at the common point of closed and extraction orbits having coordinates (R_{ex} = 111.20 cm, Φ_{ex} = 69.0°). The angular length of the deflector is equal to 42^0. The length along the extraction orbit equals 81.6 cm. The deflector gap is 0.9 cm. The deflector voltage U_{ESD} is equal to 70 kV (maximum) in the case of $^{209}Bi^{38+}$ ions extraction.

The passive magnetic channel MC1 is placed in the region of strong magnetic field B_z and its gradient (see Fig.4). The entrance of MC1 has coordinates (R = 126.16 cm, Φ = 135.64°). It length along the extraction orbit equals to 35.0 cm.

The permanent magnet channel MC2 is placed in the region of low level magnetic field B_z and its gradient (see Fig.4). The entrance of MC1 has coordinates (R = 144.61 cm, Φ = 167.65°). Its length along the extraction orbit is equal to 30.0 cm.

CLOSED ORBIT PARAMETRS

The betatron functions $\beta_{H,V}$ and horizontal dispersion function D_H for the closed orbit corresponding to beam energy W = 4.8 MeV/u are shown in Fig. 5.

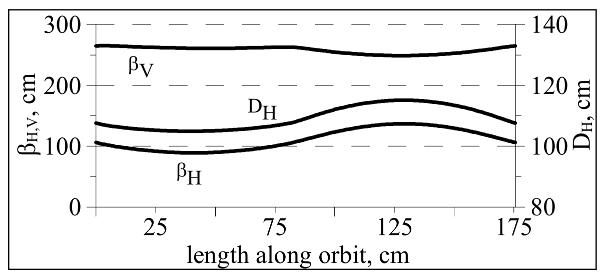

Figure 5: Horizontal β_H, vertical β_V betatron functions and horizontal dispersion function D_H. W = 4.8 MeV/u.

The frequencies of betatron oscillation at this orbit are equal to Q_H = 1.031, Q_V = 0.433.

These quantities give opportunity to evaluate one turn transfer matrix to compute of the extracted beam parameters.

ION DISTRIBUTION AT ESD ENTRANCE

The method of computation of ion distribution at electrostatic deflector ESD entrance is the same as being used in [6]. The radial shift ΔR of the orbit due to energy gain per turn ΔW = 0.031 MeV/u is evaluated as ΔR = 3.7 mm. The septum of the deflector is placed at radius $R_s = R_{ex} - \Delta R/2$. The radial (horizontal) beam size is evaluated as a_H = 8.6 mm and number of turns N_t needed for 100% beam extraction, is equal to 3.

The distribution of the ions at entrance of ESD was found by macro particle simulation. The coordinates of particle in five-dimensional phase was transformed by means of one turn transfer matrix for each N_t extracted turns. The particle having radius greater than R_s was accumulated and did not consider in the calculations of the next turns. The distributions of the ion $^{209}Bi^{38+}$ in the various phase space planes are shown in Figs. 6 and 7.

ISBN: 978-3-95450-205-9 doi:10.18429/JACoW-Cyclotrons2019-MOP020

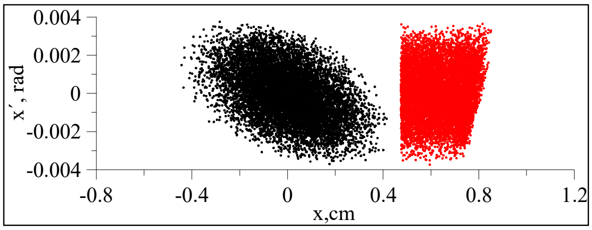

Figure 6: Horizontal plane (x,x′). Accelerated beam – left, beam at ESD entrance – right.

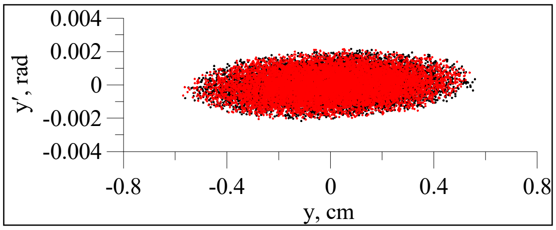

Figure 7: Vertical plane (y,y′). Accelerated beam – black dots, beam at ESD entrance – red dots.

The beam distribution in vertical plane (y,y′) (see Fig. 7) does not differ significantly from accelerated one.

ION DISTRIBUTION AT FINAL POINT

The fitting of magnetic field gradients in magnetic channels MC1, 2 gives the optimum values G_{MC1} = -12 T/m and G_{MC1} = -9 T/m.

The betatron functions $\beta_{H,V}$ and dispersion function D_H along the extraction orbit from are shown in Fig. 8.

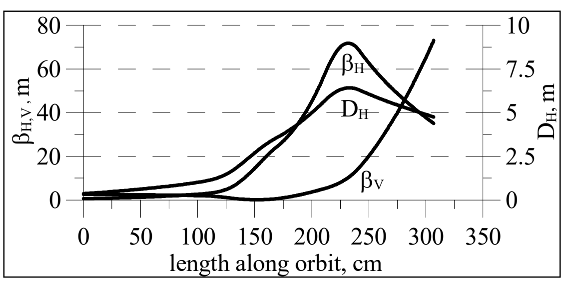

Figure 8: The betatron $\beta_{H,V}$ and dispersion D_H functions along the extraction orbit.

The changing of the beam envelopes (2σ) along the extraction orbit are given in Fig. 9.

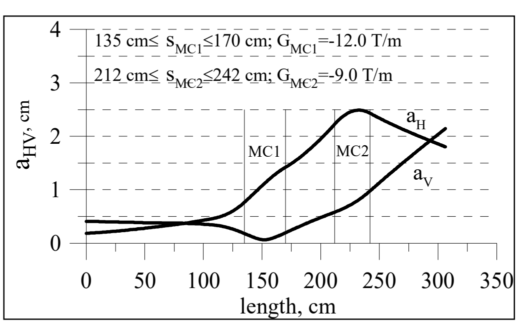

Figure 9: Horizontal (a_H) and vertical (a_V) $^{209}Bi^{38+}$ beam envelopes along the extraction orbit.

The ion distribution in the plane (x,y) at the final point of the extraction beam line is shown in Fig. 10.

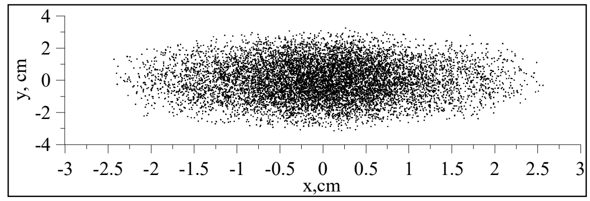

Figure 10: $^{209}Bi^{38+}$ ion distribution in plane (x,y) at final point of extraction beam line.

The ion distributions in horizontal (x,x′) and vertical (y,y′) planes at the final point of the extraction beam line are shown in Figs. 11 and 12.

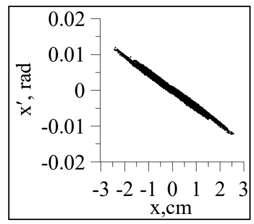

Figure 11: Plane (x,x′).

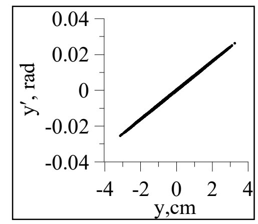

Figure 12: Plane (y,y′).

SUMMARY

The extraction system of DC140 cyclotron allows to extract all ion beams declared in the working diagram of FLNR JINR Irradiation Facility [3].

The parameters of the extraction system such as U_{ESD} and $G_{MC1,\,2}$ have reasonable values.

REFERENCES

[1] B. N. Gikal *et al.*, “Dubna cyclotrons – status and plans”, in *Proc. 17th Conf. on Cyclotrons and their Applications (Cyclotrons'04)*, Tokyo, Japan, Oct. 2004, pp.100-104.

[2] G. Gulbekyan, I. Ivanenko, J. Franko, and J. Keniz, “DC-72 Cyclotron magnetic field formation”, in *Proc. 19th Russian Part. Acc. Conf. (RuPAC'04)*, Dubna, Russia, Oct. 2004, pp. 147-149.

[3] N. Kazarinov *et al.*, “Simulation of the axial injection beam line of DC140 Cyclotron of FLNR JINR”, presented at Cyclotrons’19, Cape Town, South Africa, Sep. 2019, paper MOP019, this conference.

[4] O. N. Borisov, G. G. Gulbekyan, and D. Solivajs, “Numerical simulation of beam extraction from DC-72 AND U-400R Cyclotron by Stripping”, in *Proc. 19th Russian Part. Acc. Conf. (RuPAC'04)*, Dubna, Russia, Oct. 2004, pp. 180-182.

[5] G. G. Gulbekyan, I. A. Ivanenko, I. V. Kalagin, N. Yu. Kazarinov, and J. Franko, “Creation of the magnetic system of the new isochronous cyclotron DC140 based on the electromagnet of DC72 cyclotron”, *PEPAN Lett.*, to be published.

[6] N. Kazarinov *et al.*, “Simulation of beam extraction from TR24 cyclotron at IPHC”, presented at Cyclotrons’19, Cape Town, South Africa, Sept. 2019, paper MOP021, this conference.

ISBN: 978-3-95450-205-9 doi:10.18429/JACoW-Cyclotrons2019-MOP021

SIMULATION OF BEAM EXTRACTION FROM TR24 CYCLOTRON AT IPHC

N. Kazarinov#, I. Ivanenko, JINR, Dubna, Russia
F.Osswald, T. Adam, E. Traykov, IPHC/IN2P3/CNRS, Unistra, 67037 Strasbourg, France

Abstract

The CYRCé (CYclotron pour la ReCherche et l'Enseignement) TR24 cyclotron is used at IPHC (Institut Pluridisciplinaire Hubert Curien) for the production of radio-isotopes for diagnostics, medical treatments and fundamental research in radiobiology. The TR24 cyclotron produced and commercialized by ACSI delivers a 16-25 MeV proton beam with intensity from few nA up to 500 µA. The TR24 is a compact isochronous cyclotron with normal-conducting magnet and stripper foil for the beam extraction. The calculation model for OPERA 3D program code is described. The magnetic field map in the working region of the cyclotron is generated. The beam characteristics outside the cyclotron, that will serve as initial conditions for the design of future beam lines are determined.

INTRODUCTION

The study of beam extraction from TR24 [1] cyclotron is mandatory for the design of the future beam lines and the specification of the performances in regard of the different applications. The simulation of the ion trajectories for different azimuthal positions of the stripper, the influence of energy dispersion taking into account the 3D cyclotron fringe field and field of the combo magnet will help us to define the reference orbit, the best beam extraction and the optimal settings of the optical elements.

MAIN PARAMETERS OF PROBLEM

H^- ion beam is produced in the CUSP ion source [2] with kinetic energy of 30 keV The beam emittance is strongly dependent on beam current.

For H^- ion beam currents equal to 5 mA the initial beam emittance is equal to 50 π·mm·mrad. The main parameters of the TR24 cyclotron and H- ion beam are indicated in Table 1.

CYCLOTRON MAGNETIC FIELD

The main magnet of TR24 compact cyclotron is intended to produce the isochronous magnetic field with the level of 1.36 T at the cyclotron centre. Magnet has 170 x 170 x 110 cm closed yoke with pole diameter of 120 cm. Four azimuthally-profiled sectors provide the isochronous acceleration and focusing of the H^- beam up to the extraction radius of about 51 cm.

For analysis of the extraction efficiency and beam characteristics along the extraction trajectory a 3D computer model of the cyclotron magnet was created. Magnetic field calculations were performed with TOSCA OPERA 3D. The calculated average magnetic field and flutter distributions along cyclotron radius are presented in Fig. 1.

Table 1: Cyclotron and H^- Beam Parameters

Parameter	Value
Center magnetic field, T	1.36
RF frequency, MHz	85.085
Harmonic number	4
Dee voltage, kV	50
Number of dee	2
Maximum extraction radius, cm	51
Charge	-1
Mass number	1
Maximum current, mA	5
Injection energy, keV	30
Extraction energy, MeV	18-24
Injected Beam emittance, π·mm·mrad	50

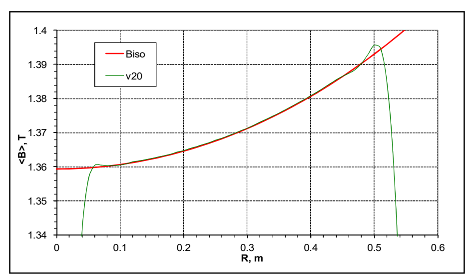

Figure 1: Isochronous (red line) and simulated (green line) average magnetic field.

The results of calculations are used for trajectory analysis of the extracted beam from the last orbits to the object point in the beam transporting line placed beyond the cyclotron at the entrance of the combo magnet at radius of 132 cm. The median plane distribution of the inner magnetic field, the field in the yoke and the field outside magnet up to 150 cm from cyclotron center is shown in Fig. 2.

CLOSED AND EXTRACTION ORBITS

In contrast to [3], closed orbits exist for the entire range of output energies without any correction of the average magnetic field.

The closed and extraction orbits for extraction energy W_{ex} range (Table 1) are shown in Fig. 3.

The main parameters of the closed orbits for various values of the extraction energy W_{ex} at extraction point are shown in Figs. 4-5.

#nyk@jinr.ru

ISBN: 978-3-95450-205-9 doi:10.18429/JACoW-Cyclotrons2019-MOP021

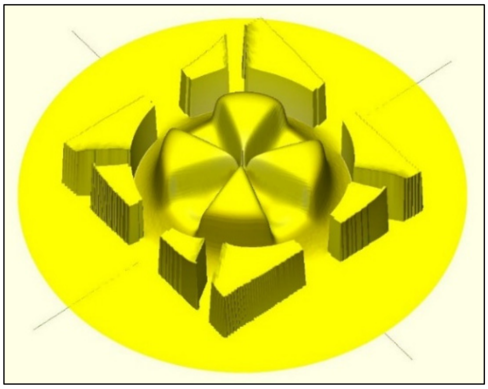

Figure 2: The distribution of the inner and outer magnetic field in median plane of the cyclotron.

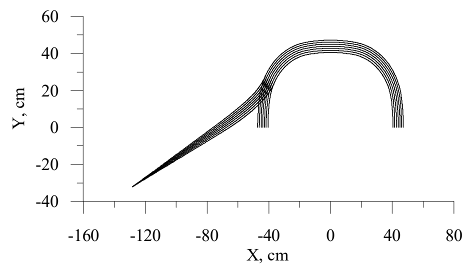

Figure 3: Closed and extraction orbits for extraction energy range 18 MeV ≤ W_{ex} ≤ 24 MeV.

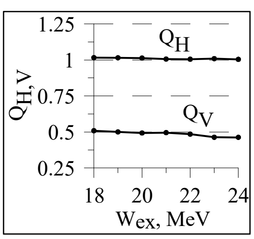

Figure 4: Frequencies $Q_{H,V}$.

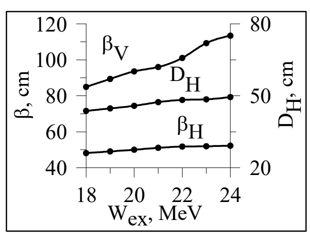

Figure 5: Horizontal (H) and vertical (V) β-functions. Dispersion function D_H.

Periodic solutions for betatron functions $\beta_{H,V}$, and dispersion function D_H can be obtained by using the calculated values and its derivative with respect to length along the orbit as initial conditions. These solutions for the closed orbit corresponding to the extraction energy W_{ex} = 24 MeV are shown in Fig. 6.

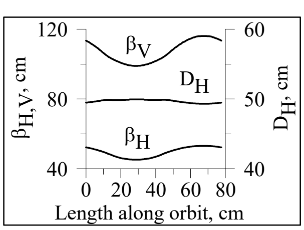

Figure 6: Periodic solutions for $\beta_{H,V}$ and D_H, W_{ex}=24 MeV.

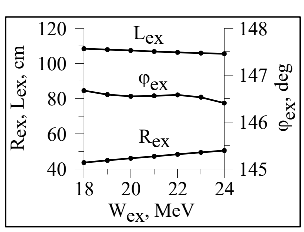

Figure 7: Extraction radius R_{ex}, angle φ_{ex} and orbit length L_{ex}.

The extraction orbit begins at the point with the coordinates (R_{ex}, φ_{ex}) of the closed orbit corresponding to extraction energy W_{ex}. The angle φ_{ex} and the length of the extraction orbit L_{ex} have to be fitted to provide the coincidence of the radial and angular position of the final point in focusing plane with the position of the object point of the beam line. The dependencies of extraction radius R_{ex}, angle φ_{ex} and orbit length L_{ex} on energy W_{ex} are shown in Fig. 7.

STRIPPING FOIL POSITIONING

The angular position of the stripping foil coincides with extraction angle φ_{ex}. Its radial position depends on extraction energy W_{ex}, extraction radius R_{ex} and the energy gain per turn ΔW. For TR24 cyclotron the value ΔW is equal to 0.2 MeV. The energy gain ΔW leads to the increasing of the extraction radius by amount $\Delta R = 2$ mm. With this definitions the inner bound of the stripping foil is defined as $R_f = R_{ex} - \Delta R/2$.

ION DISTRIBUTION AT STRIPPING FOIL

The ion distribution at the stripping foil is dependent on the horizontal dimension a_H of the beam. The value of the horizontal dimension a_H is approximately constant in the extraction energy range and may be evaluated as $a_H = 5$ mm. The ratio $a_H/\Delta R$ define the number of turn N_t that is needed for 100% beam extraction:

$$N_t = \lceil a_H/\Delta R \rceil = 3 \;;\; N_{sh} = N_t - 1 = 2 \qquad (2)$$

The number Nsh defines the value of the shift from initial radius R_i and energy W_i of the beam to the extraction ones R_{ex} and W_{ex}:

$$R_{ex} = R_i + N_{sh}\Delta R \;;\; W_{ex} = W_i + N_{sh}\Delta W \qquad (3)$$

The distribution of the ions accumulated at stripping foil was found by macro particle simulation. The coordinates of each particle in five-dimensional phase space was transformed by means of one turn transfer matrix for each N_t extracted turns. The particle that had radius greater than R_f was accumulated and do not consider in the calculations of the next turns. The distributions of the ion with extraction energy of 24 MeV in the various phase space planes are shown in (Figs. 8, 9).

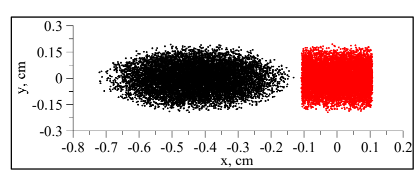

Figure 8: Plane (x,y). Accelerated beam – left, beam at stripping foil – right.

ISBN: 978-3-95450-205-9 doi:10.18429/JACoW-Cyclotrons2019-MOP021

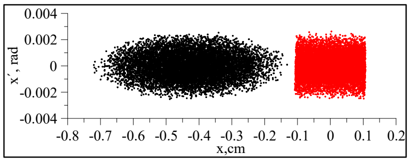

Figure 9: Horizontal plane (x, x′). Accelerated beam - left, beam at stripping foil – right.

The beam distribution in vertical plane (y, y′) (see Fig. 10) does not differ significantly from accelerated one.

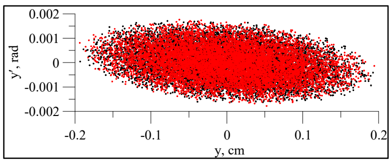

Figure 10: Plane (y, y′). Accelerated beam – black dots, beam at stripping foil – red dots.

ION DISTRIBUTION AT OBJECT POINT

The betatron functions $\beta_{H,V}$ and dispersion function D_H along the extraction orbit from the stripping foil to object point of the beamline are shown in Fig. 11.

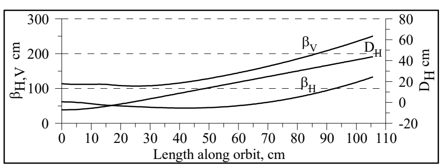

Figure 11: The betatron $\beta_{H,V}$ and dispersion D_H functions along the extraction orbit at 24 MeV.

The changing of the rms beam emittance along the extraction orbit is shown in Fig. 12. Due to the influence of the momentum spread, the horizontal rms emittance changes in the presence of a non-zero bending magnetic field of the cyclotron.

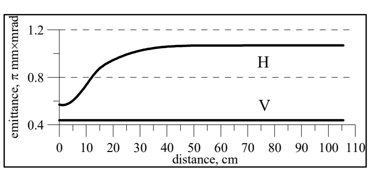

Figure 12: The horizontal (H) and vertical (V) rms beam emittance along the extraction orbit at 24 MeV.

The ion distributions in horizontal (x, x′) and vertical (y, y′) planes at the object point of the beamline are shown in (Figs. 13, 14).

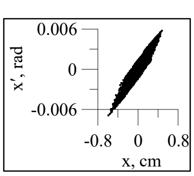

Figure 13: Plane (x,x′).

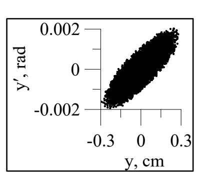

Figure 14: Plane (y,y′).

TRANSPORT IN BEAMLINE

The initial part of experimental beam-line [4] is shown in Fig. 15. The betatron functions $\beta_{H,V}$ and dispersion function D_H along the beamline from the object point to DIAG2 are shown in Fig. 16 (quads are switched off).

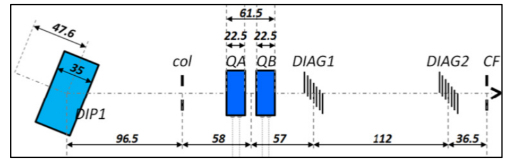

Figure 15: Experimental beam line [4]. *DIP1* – combo magnet; *QA*, *QB* – quadrupole lenses; *DIAG1,2* – diaphragms, *CF* – Faraday's cap.

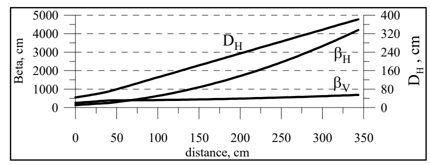

Figure 16: The betatron $\beta_{H,V}$ and dispersion D_H functions along the experimental beamline at 24 MeV.

The changing of the rms beam emittance along the experimental beamline is shown in Fig. 17. The horizontal rms emittance changes in the presence of a non-zero bending magnetic field of the combo magnet.

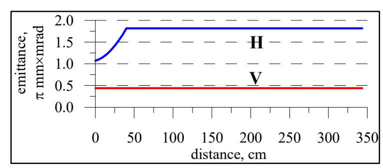

Figure 17: The horizontal (H) and vertical (V) rms beam emittance along the experimental beamline.

The ion distribution in the plane (x, y) at the DIAG2 is presented in Fig. 18. The horizontal ion density at the same point is given in Fig. 19.

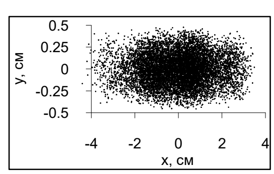

Figure 18: The ion distribution at DIAG2.

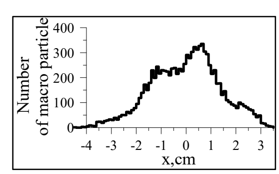

Figure 19: The horizontal ion density at DIAG2.

The horizontal ion density has a multi-peak form as it was observed in [4]. This is explained by presence in the extracted beam of three groups of the ions with energies of $W_{ex} - \Delta W$, W_{ex} and $W_{ex} + \Delta W$.

ISBN: 978-3-95450-205-9 doi:10.18429/JACoW-Cyclotrons2019-MOP021

REFERENCES

[1] Advanced Cyclotron Systems Inc., http://www.advancedcyclotron.com/cyclotron-solutions/tr24/

[2] K. Jayamanna, M. McDonald, P. W. Schmor, and D. H. Yuan, "The TRIUMF Compact DC H-/D- ion source", in *Proc. EPAC'90*, Nice, France, 12-16 June 1990, pp. 647-649.

[3] N. Yu. Kazarinov, I. A. Ivanenko, and F. R. Osswald, "Beam extraction from TR24 cyclotron at IPHC", in *Proc. 9th Int. Particle Accelerator Conf. (IPAC'18)*, Vancouver, BC Canada, Apr.-May 2018, pp. 3218-3220. doi:10.18429/JACoW-IPAC2018-THPAK007

[4] E. Bouquerel *et al.*, "Design of a beamline from a TR24 cyclotron for biological tissues irradiation", in *Proc. 8th Int. Particle Accelerator Conf. (IPAC'17)*, Copenhagen, Denmark, May 2017, pp. 564-566. doi:10.18429/JACoW-IPAC2017-MOPIK030

ISBN: 978-3-95450-205-9 doi:10.18429/JACoW-Cyclotrons2019-MOP022

PROJECT OF A NOVEL MULTI-ORBITAL BEAM BUNCHING AND EXTRACTION FROM THE U-120M CYCLOTRON

M. Čihák[†], J. Štursa, P. Krist, R. Běhal, T. Matlocha, V. Zach, Nuclear Physics Institute of the Czech Academy of Sciences, p.r.i., Husinec-Řež 130, CZ 250 68, Czech Republic

Abstract

We introduce the bunching system for a time structure control of the U-120M cyclotron beam. The system is based on a unique pulsed vertical deflection of the selected final orbits of the internal accelerated beam of the H^- ions to an extractor-stripper (a thin carbon foil positioned below the cyclotron median plane). A set of home-made programs have been developed for simulations and parameters determination of the system. Results of some simulations (i.e. dimensions of the deflection system, parameters of the pulsed high voltage power supply, position of the stripper, beam trajectories, beam parameters, beam losses, Be target position etc.) are presented. The system will be used for fast neutron generation and consequently for spectrometric measurement of neutron energy by the time of flight (TOF) method. The system will provide beam bunch interval up to 2000 ns range of a defined beam time structure (up to beam bunch period to beam bunch width ratio min 100).

INTRODUCTION

Motivation

For wide range of applications and advanced technological systems (i.e. nuclear power reactors, accelerator driven systems (ADS), fusion technology) neutron induced reactions play irreplaceable role. The data for neutronic calculations is based on transport codes with evaluated data libraries, supported by measurements and experimental tests of reaction models. Proposed chopping system supplies pulsed proton beam of the cyclotron U-120M which in connection with the Be target provide necessary tool for precise measurement of angle/energy-dependent cross-sections by neutron TOF method. Planned facility will be complementary with the parameters of the European TOF facilities (nTOF CERN, GELINA Geel, NFS Ganil [1]). The NPI has a long-term experience with the design, manufacture and operation of targets for production of fast neutrons and their use in various projects and experiments [2]. Study and project of the TOF system [3] on the new cyclotron TR-24 (repetition frequency 85 MHz/pulse width 2.3 ns) which was based on the double deflection (sinusoidal and pulsed) was not implemented also due to very strict requirements for the parameters of deflection voltage. For that reason, we focused on the design and implementation of the TOF system on the cyclotron U-120M (26 MHz/5 ns).

Beam Pulse Parameters

For the fast neutron generation, the maximum H^-/proton beam energy (i.e. 36 MeV) of the cyclotron U-120M was chosen. In this case the width of the beam pulse should be approx. 5 ns (FVHM) and period of approx. 40 ns. The required beam pulse width to beam pulse period should be approx. 1/100. The proportion of unwanted or parasitic pulses extracted between working pulses should not exceed 1 %.

PROPOSED SOLUTION AND DESIGN

We were inspired by the system implemented in 60 s on the cyclotron in Karlsruhe [4]. Internal vertical H^- beam deflection we combined with the stripping extraction method. The beam of accelerated, H^- ions is directed after vertical deflection to the stripping foil and extracted to an external Be target located outside the acceleration chamber. In order to solve this task, the program of simulation of acceleration and extraction of beams on the cyclotron U- 120M – Durycnm18 [5] was extended by additional modules. Due to the narrow aperture (20 mm) inside the 180° Dee the accelerated beam is shifted above the regular median plane using the built-in correction coil of the cyclotron.

This vertical beam shift provides more space for vertical deflection of the beam in working pulses. The beam accumulated between the working pulses in the range of radii 47–50 cm is vertically deflected by the two-section deflector to the stripping foil and extracted to the short beam line with Be target at the end. Bunching system layout is demonstrated in the Fig. 1.

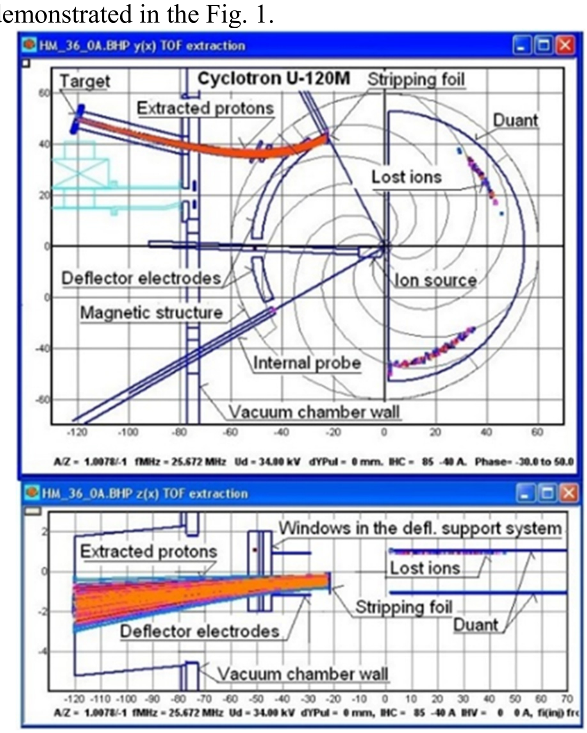

Figure 1: TOF extraction system arrangement.

† cihak@ujf.cas.cz

ISBN: 978-3-95450-205-9 doi:10.18429/JACoW-Cyclotrons2019-MOP022

BUNCHING SYSTEM

Description, Parameters

The deflection system consists of two parts. The gap in between the electrodes is 20 mm. According to the detailed simulations optimal amplitude of pulsed high voltage energized simultaneously each electrode should be min. + 4.5 kV and − 4.5 kV, respectively. The photo of the manufactured deflection system is in the Fig. 2.

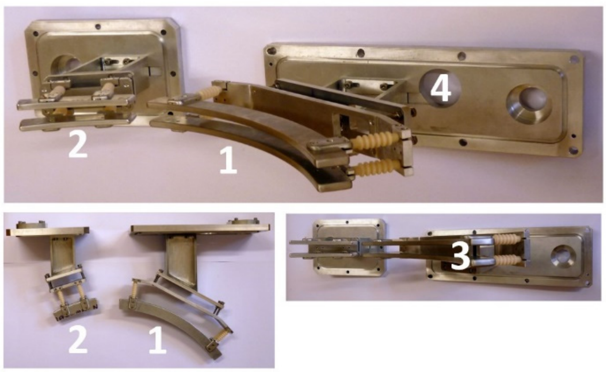

Figure 2: Two section of the deflection bunching system. 1) 1st deflector section, 2) 2nd deflector section, 3) beam entry, 4) beam exit window.

Time Structure

The time structure of the beam and HV pulses with respect to the Dee voltage is shown in the Fig. 3. The widths tn and td are maximum values which prevent from extraction of unwanted ions outside the working periods.

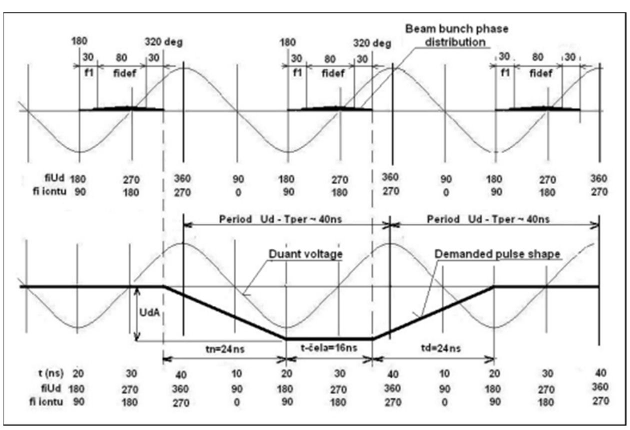

Figure 3: Time structure of the HV pulses.

RESULTS OF COMPUTER SIMULATIONS

Deflection During Acceleration

Vertical motion of the deflected ion during first period after HV pulse is show in the Fig. 4.

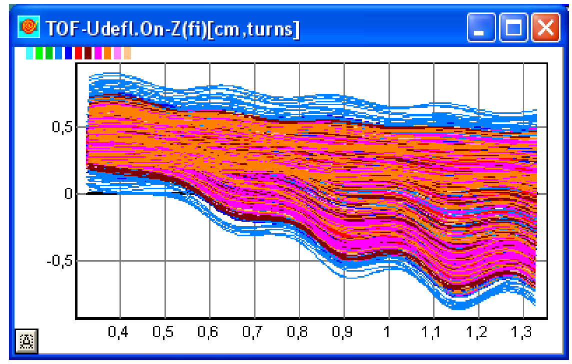

Figure 4: Vertical motion of the deflected ion during first period after HV pulse.

Characteristics of Extracted Beam

The beam cross-section and the extracted beam densities distribution are shown in the Fig. 5. By suitable choice of the position of the stripping foil it was achieved that the extracted beam covers the target area well.

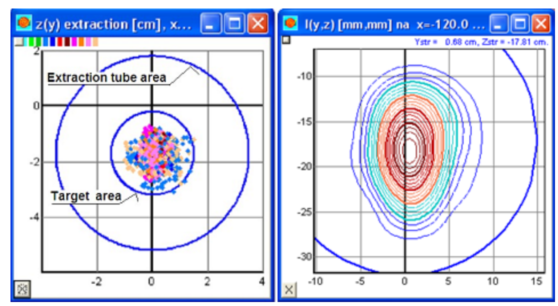

Figure 5: Extracted beam cross-section at the Be target.

The average energy of the extracted beam is 34 MeV with SQR dispersion about 0.9 MeV (see the Fig. 6).

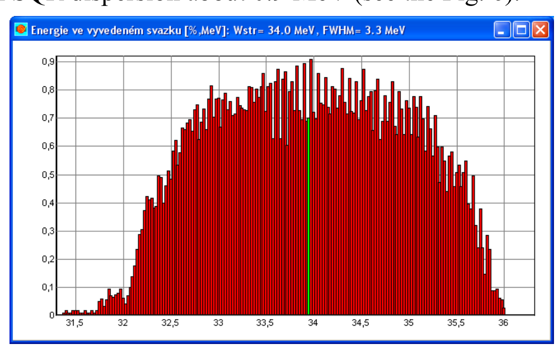

Figure 6: Extracted beam energy dispersion.

The calculated horizontal RMS emittance is 740 π·mm·mrad, vertical 59 π·mm·mrad. The extraction efficiency depends on the number of the beam turns between working pulses. At a low number, the space above the foil is not fully filled, at a high one the ions continue in acceleration to the target placed on the inner probe at higher radius. Maximum efficiency is achieved when ions accelerated between working pulses just fulfil the space above the foil. Suppression of unwanted ions extracted between the working pulses is achieved by correctly adjusting the vertical deflection of the magnetic median plane, the vertical position of the upper edge of the foil, and the

ISBN: 978-3-95450-205-9 doi:10.18429/JACoW-Cyclotrons2019-MOP022

amplitude of the HV pulses delivered to the deflectors. Unfortunately, the stray electric field of the deflectors on the inner radii in the periods following the HV pulse causes vertical oscillations of non-extracted ions in front of the foil. These ions can hit the upper side of the Dee or the foil with the subsequent extraction between the working pulses. This undesirable effect can be minimized by appropriately selected the radial position of the foil relative to the adjusted magnetic medial plane distortion. However, these effects may be negligible on cyclotrons with greater aperture of the accelerator system elements.

The stripping foil was positioned so that ions on radii 47 and 50 cm were directed to a target centre in the distance of approximately 40 cm from the wall of the acceleration chamber. At the beam rotation period of 40 ns, the HV pulse repetition interval of 2 µs was selected, corresponding to 50 periods during which the radius area above the foil is filled by accelerated ions. The FWHM time of the extracted beam bunch is approximately 5 ns. From the 90 accelerated ions, 2118 ions entered the extraction process. From these ions, 1712 (80.8 %) good ions were extracted at the time of the first pulse period, 395 (18.7 %) were lost on the duant, 9 (0.4 %) were stopped on the foil frame, and 2 (0.1 %) undesired ions were extracted outside working period. Ions distribution is demonstrated in the Fig. 7. If the repetition interval is longer, the extraction efficiency and the power lost on the duant will be reduced. At shorter intervals, efficiency decreases because accelerated ions do not completely fill the space above the foil.

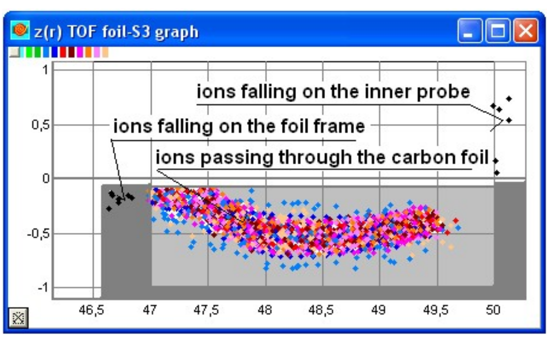

Figure 7: Ion beam distribution in the stripping foil area.

PULSED POWER SUPPLY

Design and development of the pulsed power supply based on the SiC MOSFET transistors (amplitude up to + 6 kV resp. − 6 kV, HV voltage pulse front edge 24 ns/amplitude 16 ns/back edge 24 ns, repetition frequency up to 1 MHz) as well as the pulse synchronization with the cyclotron RF are described on an individual poster of the conference [6].

CONCLUSION

The article briefly introduces unique "deflection-bunching" TOF system which is based on the vertical deflection of the internal negative H^- beam deflected with the two-section deflector to the striper and converted into the proton beam by means of the stripping method. Compared to the standard selection of working bunches for TOF measurement on an extracted cyclotron beam, the described system has a number of advantages. In the working pulse, it emits about 20 times more ions at an incomparably lower level of residual radioactivity caused by collimator slits activation with the ion beam deflected between working pulses. Positioning of the Be target outside the acceleration chamber allows greater flexibility in spatial arrangement and easier manipulation of the target without risk of vacuum chamber contamination. On the other hand, the disadvantage is the much wider energy spectrum and greater horizontal emittance extracted proton beam. However, for the purpose of TOF measurements, deterioration of these properties does not matter. In accordance with the results of the performed simulations, a system of electrostatic deflectors with an external beam line system and a pulsed HV power supply have been manufactured. Extraction of the beam into the beam line was tested on the U-120M cyclotron in the static mode. Testing of the complete system on the cyclotron is under preparation. We expect the 34 MeV proton beam pulse of width of approx. 5 ns (FWHM) and period up to 2 µs directed to the external Be target. The pulse width to the period ratio should be up to 1:400 which meets well the required parameters. After implementation the system should provide white spectrum of neutrons up to 34 MeV, TOF neutron flux $7\cdot10^6$ n/s/cm^2 at 3 m distance and energy resolution ≤ 4 % FWHM at 15 m distance.

ACKNOWLEDGEMENT

This work was supported by OP RDE, MEYS, Czech Republic under the project reg. No. CZ.02.1.01/0.0/0.0/16_003/0001812.

REFERENCES

[1] X. Ledoux *et al.*, "The neutron for science facility at SPIRAL-2", *EPJ Web of Conferences*, vol. 146, p. 03003, 2017. doi:10.1051/epjconf/201714603003

[2] M. Stefanik *et al.*, "Neutron field measurement of p(35)+Be source using multi-foil activation method", *Radiat. Prot. Dosim.*, vol. 180, no. 1-4, Aug. 2018, pp. 377-381. doi:10.1093/rpd/ncx249

[3] J. Stursa, M. Cihak, M. Gotz, and V. Zach, "Physical design of external two-stage beam chopping system on the TR 24-Cyclotron", in *Proc. Cyclotrons'16*, Zurich, Switzerland, Sep. 2016, pp. 45-48. doi:10.18429/JACoW-Cyclotrons2016-MOP02

[4] S. Cierjacks *et al.*, "A novel deflection-bunching system at the Karlsruhe Isochronous Cyclotron", in *Proc. Cyclotrons'66*, Gatlinburg, Tennessee, USA, 1966, pp. 355-359.

[5] M. Cihak *et al.*, "Beam dynamic simulation in the isochronous cyclotron U-120M", in *Proc. Cyclotrons'07*, Giardini-Naxos, Italy, 2007, pp. 385-387.

[6] P. Krist, D. Poklop, J. Stursa, V. Cervenka, and J. Vozáb, "Synchronization and high-speed high voltage switcher for pulse bunching system of the cyclotron U-120M", presented at the 22nd Int. Conf. on Cyclotrons and their Applications (Cyclotrons'19), Cape Town, South Africa, Sep. 2019, paper MOP023, this conference.

ISBN: 978-3-95450-205-9 doi:10.18429/JACoW-Cyclotrons2019-MOP023

SYNCHRONIZATION AND HIGH SPEED HIGH VOLTAGE SWITCHER FOR PULSE BUNCHING SYSTEM OF THE CYCLOTRON U–120M

P. Krist†, D. Poklop, J. Štursa, Nuclear Physics Institute, Řež, Czech Republic
V. Červenka, HiLASE Centre, Dolní Břežany, Czech Republic
J. Vozáb, Radan s.r.o., Barchov, Czech Republic

Abstract

Pulse bunching system for neutron time of flight (TOF) measurements on the cyclotron U-120M exploits a unique pulsed vertical deflection of the selected final orbits of the internal accelerated beam of the H^- ions to an extractor-stripper. This system is described in details on an individual poster of this conference. A key device is the pulse high voltage (HV) power supply (HV switcher) which is supplying the deflector and elevates H^- ions in defined time structure to an extractor-stripper. The developed HV switcher is based on the SiC MOSFET transistors. It can provide HV pulses with the following pulse parameters: amplitude up to 13 kV, front edge less than 20 ns, flat top 20 ns, back edge less than 20 ns and repetition frequency up to several hundred of kHz. We have also developed the pulse synchronization with the cyclotron RF (25 MHz), which enables to set up front edge of bunching pulses within 2π with accuracy 80 ps. Human-machine interface is based on SCADA software Reliance and PLC Tecomat Foxtrot.

INTRODUCTION

U-120M Cyclotron

The U-120M cyclotron was originally designed as an accelerator of light positive ions (A/Z = 1–2.8) with the maximum energy up to tens of MeV. Since the early 1990s, the cyclotron has undergone major upgrade in terms of acceleration of negative ions H^-, D^- in order to increase external beam intensities [1].

The cyclotron is equipped with a beam line system for the transport of the accelerated and extracted ions to the experimental and target facilities. This system includes also a short beam line for the transport of ions extracted from negative regimes [2].

Protons can by used for neutron production (deuterons and ^{3}He particles were tested as well) for ToF, and are extracted from the beam using the stripping foil. The proton beam is directed to the target installed at the end of the beam pipe. In the negative ion mode of acceleration, the protons resp. deuterons with energies of 6–36 MeV resp. 10–20 MeV with good beam current stability are obtained and used for neutron production at the suitable targets. An average beam current for neutron production is usually 10–15 μA [2].

† krist@ujf.cas.cz

Time Structure of the Cyclotron Beam

The cyclotron radiofrequency (RF) system is not operated at the continuous wave regime. In order to protect the RF accelerating system against discharges and to control the beam current, the RF frequency is modulated by a dedicated 150 Hz macropulsed signal. A duty cycle of the corresponding 6.67 ms signal period is adjustable and determines a time interval in-between the macropulses filled with proton bunches. For the lowest RF (≈10 MHz), the duty cycle can reach rather high values of about 65 %. On the other hand, for the highest RF (≈25 MHz) the maximum duty cycle is limited to 25 %. The cyclotron radiofrequency depends on required output beam energy [3].

Time Structure of the Buncher

For measured of neutron energy by the TOF method the required beam pulse width to beam pulse period should by lower than 1/400. The proportion of unwanted or parasitic pulses extracted between working pulses should not exceed 1 %.

We assume to use 25 MHz cyclotron RF. The period of the bunches is therefore t_{acc} = 39 ns and bunch duration is approximately t_b = 6.5 ns. Principle of the proposed bunching system of the cyclotron U-120M is shown in the Fig. 1. The deflection system consist of two parts with total length of 742 mm. The time of flight of the 36 MeV proton bunch through deflection system is t_{flight} = 11.1 ns.

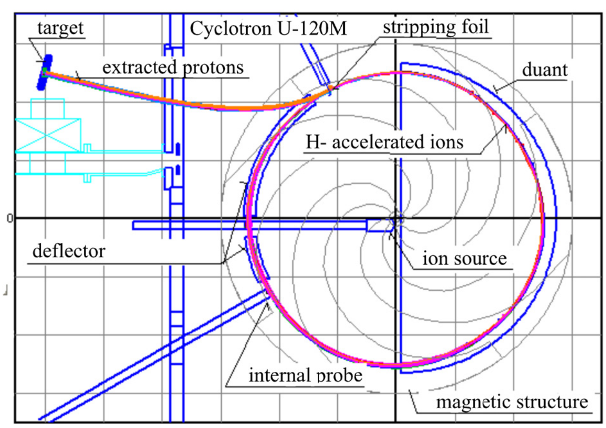

Figure 1: Schematic diagram of U-120M cyclotron with deflection and extraction system.

In the Fig. 2. is shown necessary time structure of pulsed deflection voltage U_{def} for trouble-free beam deflection. Amplitude of the voltage is 10 kV.

Flat top of deflection pulse have to be minimally $t_{ft} = t_b + t_{flight}$. So, t_{ft} = 17.6 ns. The time for switch on or switch off is $t_{switch} = t_{acc} - t_{ft}$. Thus, maximum possible time

ISBN: 978-3-95450-205-9 doi:10.18429/JACoW-Cyclotrons2019-MOP023

for deflection voltage change is 21.4 ns. We expect the commonly usable repetition rate of extracted bunches to be about 260 kHz, so $t_{rep} \approx 3.8$ µs.

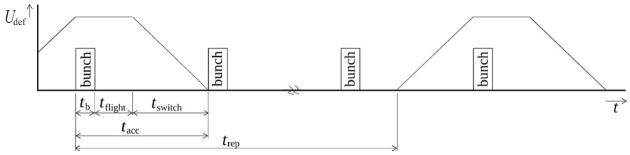

Figure 2: Deflection voltage timing. t_b – bunch duration, t_{flight} – ion time of flight through deflectors, t_{switch} –maximum possible time of switch on or switch off deflection voltage, t_{acc} – repetition time of bunches in accelerator, t_{rep} – repetition time of extracted bunches, U_{def} – deflection voltage.

HV SWITCHER

As described in the previos section, HV switcher should generate pulses supplying the deflector with flat top duration approximately 20 ns, rising and falling edge of pulses shorter then 20 ns and voltage amplitude about 10–12 kV. For this reason, a Silicon Carbide (SiC) power MOSFET transistor was selected as the switching element. Deflector capacitance was estimated to be 40 pF. The current flowing through the switch to the deflector was estimated by simulation to by up to tens of amps. A transistor meeting these conditions is manufactured by CREE with the type designation C3M0065090J [4].

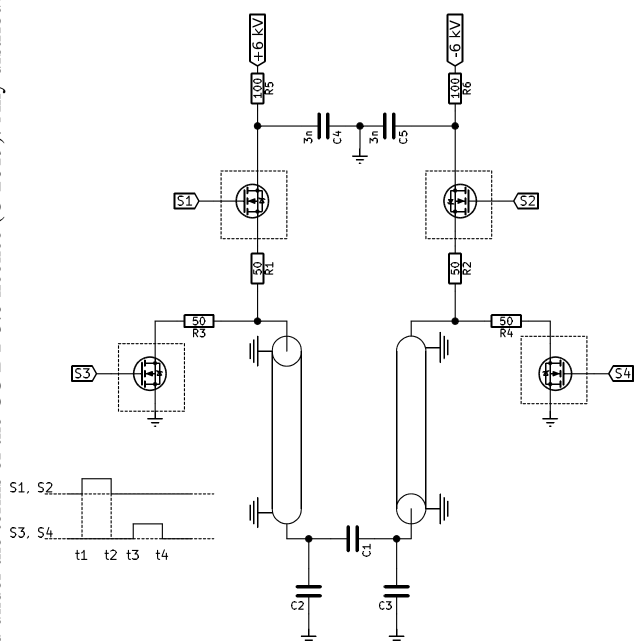

Figure 3: Wiring diagram of HV switcher with deflector. C1 – deflector capacitance, C2 and C3 – parasitic capacitance, S1–S4 – control pulses for SiC MOSFET switch, HV pulse is in time interval (t1; t3).

We can generate HV pulses with electrical circuit as shown in the Fig. 3. At the time t_1 the switch S1 and S2 turn on and deflector is charged to 12 kV. At the time t_2 the switch S1 and S2 turn off and the deflector remains charged. At the time t3 switch S3 and S4 turn on and deflector is discharged.

Each switch S1–S4 must be designed for min. 6 kV. We connected 8 transistors in series. Each transistor has separate driving of its gate with galvanically isolated coupling. The coupling is realized by transformer with one thread on the primary and one thread on the secondary side. Separate driving allows accurate timing of each transistor (block delay in the Fig. 4). We reached time mismatch between transistors better than 1 ns. Wiring diagram of one switch channel (one driver and one transistor) is shown in the Fig. 4.

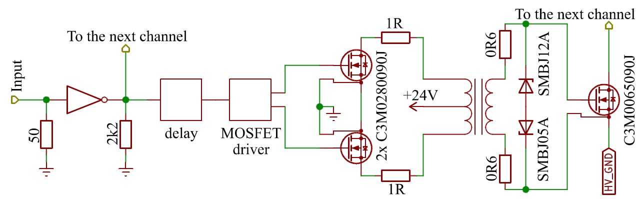

Figure 4: Wiring diagram of one channel of SiC MOSFET switch.

Control pulses at gates of C3M0280090J transistors [5] are shown in the Fig. 5. It is possible to set-up rising edge and also puls duration at gate of C3M0065090J by overlapping pulses.

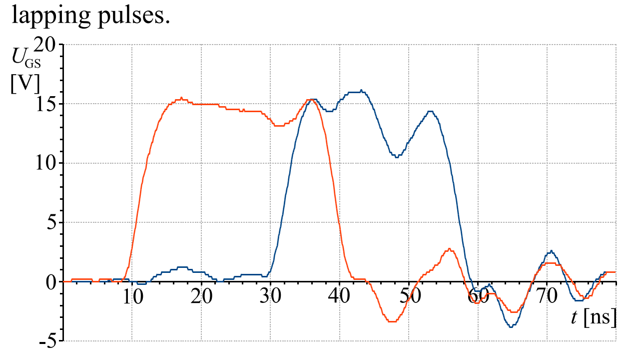

Figure 5: Gate-source voltage at C3M0280090J SiC MOSFET transistors.

The Fig. 6 shows voltage between gate and source (U_{GS}) each HV SiC transistor. Thanks to bipolar driving, the transistor reaches a very fast rising edge. Gate voltage limitation is provided by a pair of transils in anti-series connection.

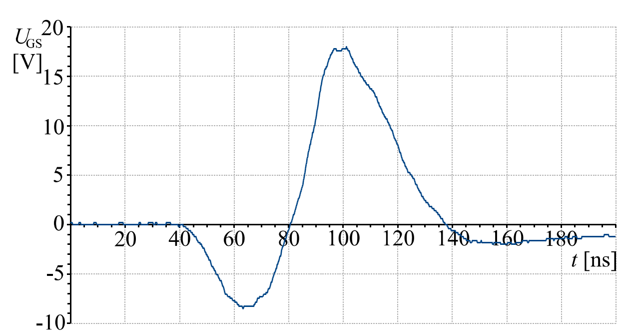

Figure 6: Gate-source voltage at C3M0065090J HV SiC MOSFET transistors.

We can see the rising edge of the HV switch in the Fig. 7. The measurement was provided with 2 m long

ISBN: 978-3-95450-205-9 doi:10.18429/JACoW-Cyclotrons2019-MOP023

coaxial cable between switch and load (deflector) and with 40 Ω serial resistor. The switch was turned off at the time value 67 ns and after this time the deflector is charged through high impedance resistor.

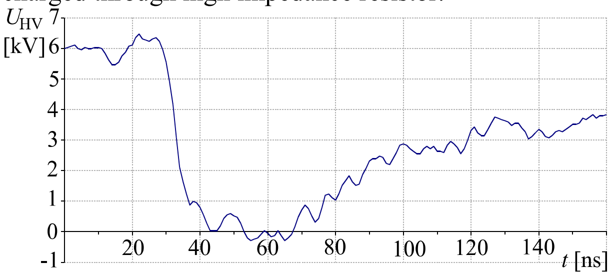

Figure 7: Rising edge of the HV switch.

SYNCHRONISATION SYSTEM

The synchronisation system for accurate timing of HV switcher at the optimal phase of accelerating RF is developed as a standalone device. The system enable turn on HV switcher in any phase within 2π of accelerating RF. The system generate all signals for each switch. Block diagram of the synchronisation system is shown in the Fig. 8.

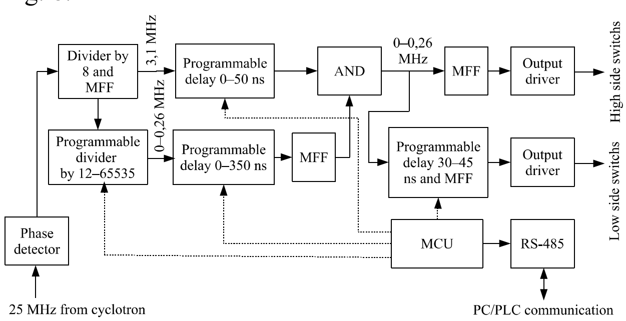

Figure 8: Synchronization system with phase tuning in 2π of accelerating RF. MFF – monostable flip-flop, MCU – microprocessor ATmega328, RS-485 – communication serial line.

The programmable delay 0–50 ns enable scanning accelerating voltage within 2π of RF with 80 ps steps. It enable setting up the turn on the HV switcher in any phase of the accelerating voltage. Programmable divider allows to set repetition rate of extracted bunches. With programmable delay 30–45 ns we can tune HV pulses duration. MCU ATmega328 [6] ensure communication with superior system eg. PLC or PC.

HUMAN–MACHINE INTERFACE

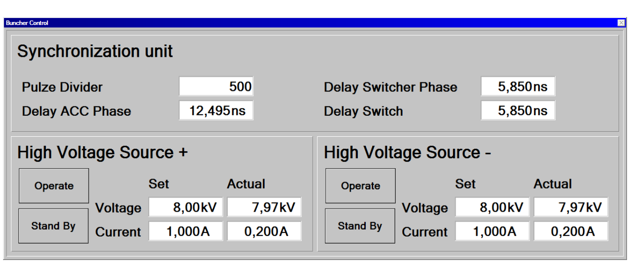

Figure 9: Human-machine interface for HV switcher.

For control the described HV switcher by the operator, a PLC with SCADA/HMI system is commonly used at our laboratory. The PLC was supplied by Teco company. The type designation is Tecomat Foxtrot with central unit CP-1003 [7]. The SCADA software is called Reliance [8]. In the software we prepare basic window for human–machine interface, which allow to control also the HV power supplies feeding the HV switcher (Fig. 9).

CONCLUSION

The HV switch allow the high voltage to be switched in very short time with very short pulse duration. The switch was tested with satisfactory result. We reached rising edge of the HV pulse to be shorter then 20 ns. Flat top duration of the pulse is adjustable and we achieve the value less than 20 ns. These results allow us to start working on assembling of the system as it is shown in the Fig. 3.

After realization of the whole bunching system we are expecting the width of 34 MeV proton beam bunch of approx. 5 ns (FWHM) and period up to 2 µs. The pulse width to the period ratio should be up to 1:400 which meets well the required parameters. After implementation the system should provide white spectrum of neutrons up to 34 MeV, TOF neutron flux $7{\cdot}10^6$ n/s/cm^2 at 3 m distance and energy resolution ≤ 4 % FWHM at 15 m distance [9].

ACKNOWLEDGEMENTS

This work was supported by OP RDE, MEYS, Czech Republic under the project reg. No. CZ.02.1.01/0.0/0.0/16_003/0001812.

REFERENCES

[1] Department of accelerators, Nuclear Physics Institute CAS, http://www.ujf.cas.cz/en/departments/department-of-accelerators/.

[2] M. Majerle *et al.*, "Laboratory of fast neutron generators of the NPI", in *Proc. 25th Int. Conf. Nuclear Energy for New Europe (NENE2016)*, Portorož, Slovenia, Sep. 2016, pp. 203.1–203.12.

[3] F. Křížek *et al.*, "Irradiation setup at the U-120M cyclotron facility", *Nucl. Instr. Meth.*, vol. 894, pp. 87–95, 2018. doi:10.1016/j.nima.2018.03.066

[4] C3M0065090J 900V 65 mOhm 35A SiC MOSFET, https://www.wolfspeed.com/c3m0065090j

[5] C3M0280090J 900V 280 mOhm 11.5A SiC MOSFET, https://www.wolfspeed.com/c3m0280090j

[6] ATmega328 – 8-bit AVR Microcontrollers, https://www.microchip.com/wwwproducts/en/ATmega328

[7] CP-1003 basic modules – PLC Tecomat Foxtrot, https://www.tecomat.com/Products/cz/plc-tecomat-foxtrot/zakladni-moduly/125-cp-1003/.

[8] Reliance industrial SCADA/HMI system https://www.reliance-scada.com/en/main

[9] M. Čihák *et al.*, "Project of a novel multi-orbital beam bunching and extraction from the U-120M cyclotron", presented at the Int. Conf. on Cyclotrons and their Applications (Cyclotrons'19), Cape Town, South Africa, Sep. 2019, paper MOP022, this conference.

ISBN: 978-3-95450-205-9 doi:10.18429/JACoW-Cyclotrons2019-MOP024

DEVELOPMENT OF A REPLACEMENT FOR THE LONG RADIAL PROBE IN THE RING CYCLOTRON

R. Dölling†, M. Rohrer, G. Gamma, R. Senn, P. Rüttimann, V. Ovinnikov
Paul Scherrer Institut, 5232 Villigen PSI, Switzerland

Abstract

The long radial probe in PSI's Ring cyclotron delivers a radial pattern of all but the first few turns. In recent years, the measurement has been plagued by artefacts and mechanical problems. We report here on the development of a replacement, which should also provide a more flexible basis for extended measurement capabilities.

INTRODUCTION

In 1993 the actual long radial probe RRL1 was installed in the ring cyclotron [1]. It replaced a multi-finger probe operated since 1974 [2], which covered the turns from 110 MeV to 590 MeV at low beam currents.

The almost 3 m long probe is parked in a separately supported chamber connected to an 'intermediate sector' between two of the eight sector magnets. When moved by a wire rope into the cyclotron (Fig. 1), the forks upper and lower trolleys have to transfer from outer to inner rails over a gap of ~5 cm required by the vacuum valve. By using a 33 um vertical carbon fibre, the radial profile of all but ~6 innermost turns can be measured at full beam current up to 2.4 mA. The probe wire is biased to +60 V in order to suppress thermionic electrons at lower beam energies [3] and to decrease artefacts. From 2002 - 2009, upper and lower fingers from 100 µm SiC, extending vertically until 1 mm from the midplane, were installed to get vertical information at beam currents up to 500 µA.

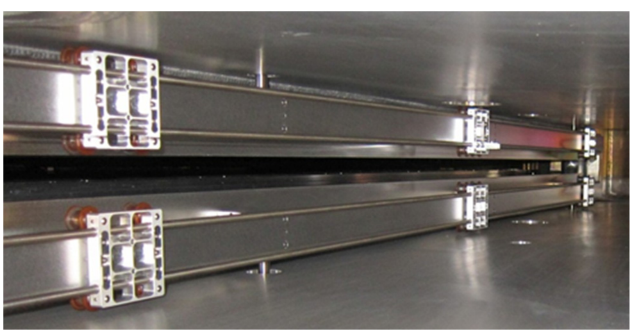

Figure 1: Actual probe fully inserted. The last trolley to the left (not shown) which combines upper and lower arm of the fork stays in the outer chamber. Some of the seven fixtures of the rails are visible.

The probe has delivered nice results. However, two problems are impeding the probe signal. Since the installation of the more powerful RF cavities until 2008, artefacts attributed to plasma clouds [4] occur frequently and are often dominant (Fig. 2). A repetition of a probe measurement often leads to a gradual decrease of the disturbance. Possibly charging of surfaces at the probe and its surroundings plays also a role here.

Since 2014, we observe a severe noise, occurring only with beam and outside a certain machine radius, with this radius being smaller for the foregoing inward than for the outward movement and changing over time. The reason is not identified, plasma may again be a candidate. In addition, there is a problem affecting the probe movement. At venting and pumping of the cyclotron, the overdetermined mounting of each rail at several points at the vacuum chamber results in relative movements between these rails and also with respect to the rails in the external chamber. To prevent the probe to be stuck, the rails must be positioned accordingly, which requires a tedious adjustment, for which a reproducible procedure has not been found. This has to be repeated every time the intermediate sector has moved, which happens, e.g., at a change of the Indium or double O-ring sealed adapter flange towards the downstream magnet chamber.

We also learned that the internal low-noise signal cables, which are useful to minimize microphonic noise at cable bending during probe movement, are badly outgassing softeners. Hence, a replacement of the ageing internal probe cables may improve the noise problem, but in exchange may contribute to the plasma-related problems, for which the exact mechanisms are not known.

Two years ago we started the development of a replacement for RRL1. Besides solving the actual problems, it should also provide a more flexible platform for extended measurement capabilities as a phase probe or diagonal wires [1] to get information on the vertical beam profile.

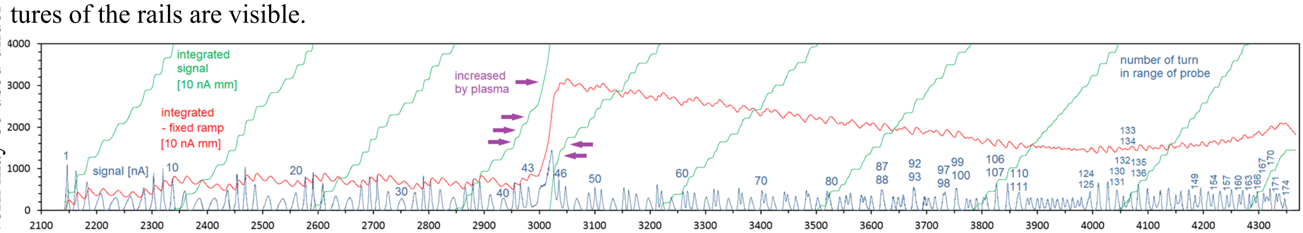

Figure 2: A nicer example of a measurement taken at a beam current of 2200 µA. It is affected by plasma only in a narrow range. A day later, the maximum disturbance was 30 times larger and affected many more turns. With the beam switched off but RF still on, the artefact from the plasma cloud decays within seconds.

† rudolf.doelling@psi.ch

ISBN: 978-3-95450-205-9 doi:10.18429/JACoW-Cyclotrons2019-MOP024

BASIC MECHANICAL SETUP

The foreseen probe arrangement is depicted in Fig. 3. A 3.1 m long carrier made of aluminium is rolled from the service chamber into the intermediate sector chamber by a gear operated manually from outside. It will be retracted only for service or repair. The lower and the upper traverse of the carrier are connected at both ends, with the aperture including all turns (Fig. 4). The C-clamp is shaped to fit in the narrow space besides the inflector septum EIC [5]. Suspension by the wheels at both ends of the carrier provides a decoupling of the carrier position from the 'breathing' of the vacuum chamber.

On both sides of each traverse, a trolley guided by rails can be moved by a motor via a perforated metal belt driven by toothed pulleys (Fig. 5) [6]. At one side, upper and lower trolley are moved synchronously by a single motor which drives the pulleys via gear wheels. This allows, e.g., the radial movement of vertical and diagonal carbon fibres in the midplane. Drag chains support the cabling from service chamber to carrier and from traverse to trolley (Fig. 6).

Although located relatively far away from the acceleration cavities, RF stray fields may have an impact to carrier and probe. 40 contact springs provide the grounding of the carrier at several points at ceiling and bottom of the intermediate sector chamber. Carrier temperature will be measured by thermocouples.

Carrier mechanics can be accessed by removing the large flanges. It can be also removed from the vault together with the service chamber by using the vault internal crane.

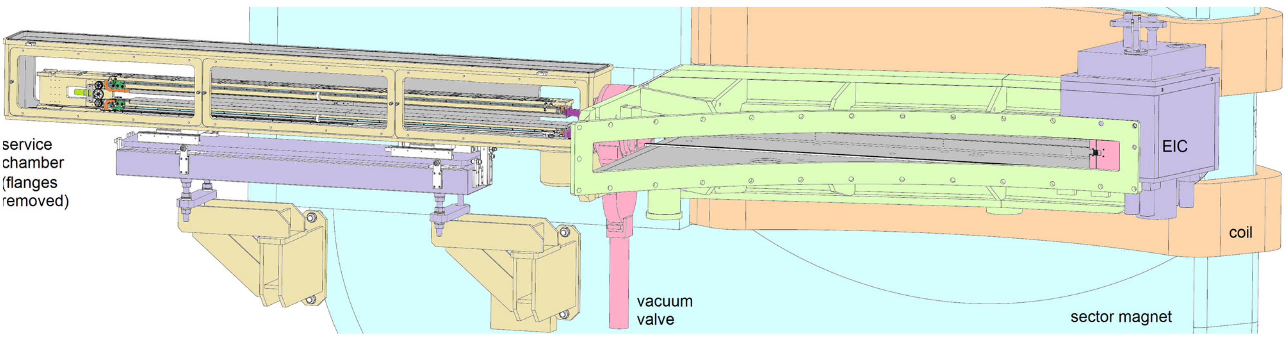

Figure 3: Foreseen arrangement at intermediate sector vacuum chamber. Carrier retracted to service chamber.

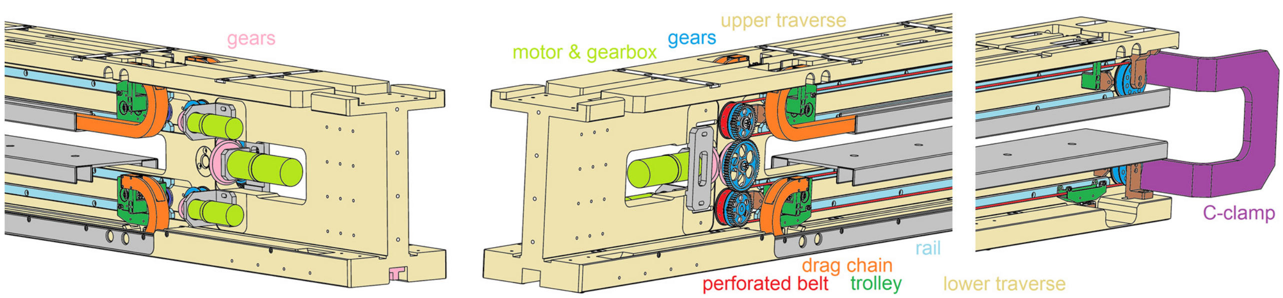

Figure 4: Carrier with drive mechanics. The trolleys carry probe wires, fingers or other sensor.

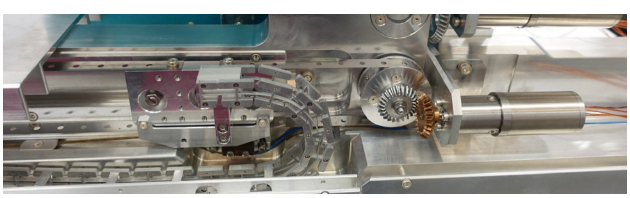

Figure 5: Test setup with motor, drive belt and an earlier version of drag chain installed.

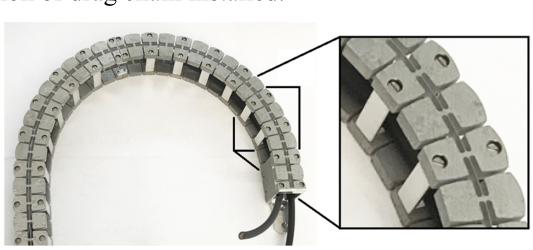

Figure 6: Vacuum compatible aluminium drag chain. Flexor hinges are cut by water jet. The thin fillet is only 0.25 mm wide. Mean radius in operation 34 mm.

COMPONENT TESTS

Shielded Kapton or PEEK insulated cables [7, 8] are well suited for vacuum environments and probably sufficiently radiation hard for the given location, although in the foreseen configuration, the cables stay permanently inside the cyclotron. However, the internal cables must also be well shielded, microphonic noise from the cable movement must be low and cables must survive repeated bending.

Currently we are evaluating these aspects for several cables in the lab. This includes a low-noise coax cable similar to the actually installed ones, coax cables designed for vacuum, as well as individual unshielded Kapton insulated wires combined in a braid with no outer jacket.

Microphonics were roughly tested by placing the cable into the 1.4 m long drag chain to a trolley and moving the trolley with 20 mm/s along 2.5 m forth and back, while injecting 920 pA DC current close to the LogIV [9] logarithmic amplifier module, which was coupled to the fixed

ISBN: 978-3-95450-205-9 doi:10.18429/JACoW-Cyclotrons2019-MOP024

cable end to detect the signal current. An effect of electromagnetic interference from the motor cable was excluded by repeating the same with the tested cable laid closely besides the drag chain. With the low-noise cable, no effect of movement was detected, while for the dedicated vacuum cables the noise level increased quite differently (Table 1). We have to keep in mind that the performance may be different in the real environment or after extensive use or with a bias voltage applied to the wire.

The quality of the cable shield will be tested by placing the cable in a metal tube to which a ±10 V 1 kHz rectangular signal will be applied by a voltage generator. Tests of the mechanical life time of the cable in the drag chain are also pending.

Table 1: Microphonic Noise in Moving Drag Chain

* equals electronics noise level ** already too stiff for actual drag chain	type	diam. [mm]	noise [pA_{rms}] at 20 ms/sample integration time
Huber & Suhner G_01130_HT-03	low noise	3.2	~1.4*
VACOM KAP-LCOAX50-AWG26	coax (vacuum)	2.3	~21
VACOM KAP-LCOAX50-AWG30		1.7	~33
Allectra 311-KAP50-RAD		2.3	~76
Allectra 311-KAPM-060-COAX		1.4	~2.8
Allectra 310-PEEK50-TRIAX (shields combined)**		2.7	~2.4
3x Kapton AWG26 (within Allectra 316-BRAID3)	shielded multi-wire (vacuum)	2.6	~8
4x Kapton AWG26 (within Allectra 316-BRAID4)		2.8	~6
4x Kapton AWG30 (within Allectra 316-BRAID4)		2.6	~8

Outgassing rates for ~3 m long cable samples were determined, with a connector attached. Differences of about a factor of 10 were observed (Fig. 7). With the dedicated vacuum cables, mainly desorption of water and air was observed. With the low-noise cables the amount of hydrocarbons of 40 to 100 atomic mass units, probably softeners, was larger by a factor of ~40.

Synthetics drag chains were also strongly outgassing. In this aspect, the in-house developed all-metal drag chain is a clear improvement. An endurance tests was performed with a shorter piece of chain at the design radius of 34 mm, using a pressured air actuator. After 2000 cycles no apparent damage was observed. This has to be repeated with the full length and cables inside.

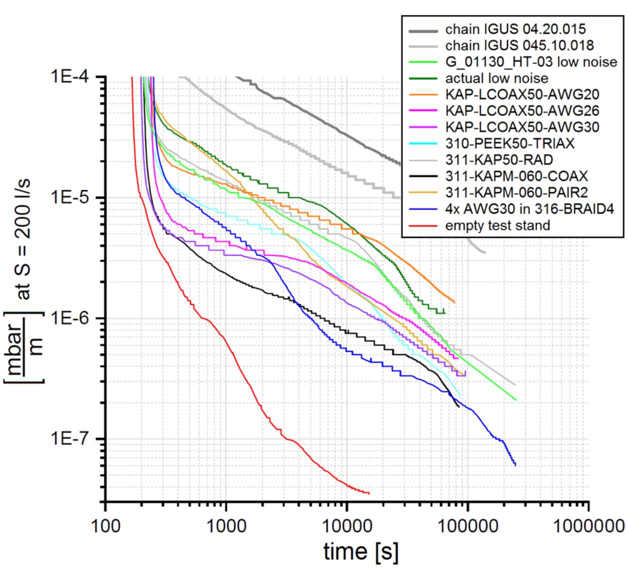

Figure 7: Outgassing rates of cables and drag chains.

While the solutions for the drag chain as well as the non-magnetic and radiation hard materials seem satisfactory, we are still looking for improvements with the cables.

OPTIONAL EXTENDED CAPABILITIES

A 2D-scan of the beam halo could be provided by small ionization chambers at the probe head, moved vertically towards the beam core until a certain signal level is reached (Fig. 8). Beam fractions of the order of 0.1 nA to 1000 nA, limited by background radiation respectively saturation and heating, should be detectable. In the beam lines, a comparable dynamic range could also be delivered by halo monitors, and is already available, however only with little spatial resolution, from beam loss monitors.

Mutual collision by beam protons do not lead to a significant loss of information on the 6-dimensional beam distribution, since the relaxation time of the 'non-neutral plasma' exceeds the duration of the transport through the facility. Also, collisions with the residual gas are not significant in this respect. With this, it seems unlikely that the observation of the beam halo down to fractions of 10^{-7} of the full beam current, over some 170 turns, would not reveal information on the beam distribution, which could be used to better understand beam losses. To a degree, this may allow to design countermeasures, which help to lower activation of machine components. Combination with detailed beam dynamics simulations [10-12, and Refs. in 11, 13] may even allow a prediction of beam losses. However, it is discussed controversially, if this will be ever possible at the limited precision of the available field maps of the magnetic elements and RF cavities which determine the beam transport.

Whether this or other optional probe equipment is to be realized will depend on the future strategy for accelerator development, directed at reducing beam losses, and in general. This applies also to dedicated beam dynamics studies, developments to OPAL [14, 15] as a tool for detailed beam dynamic simulations, as well as to other beam diagnostics systems that deliver the corresponding detailed information, as, e.g., 4-dimensional emittance measurement [13] or bunch-shape monitors [3].

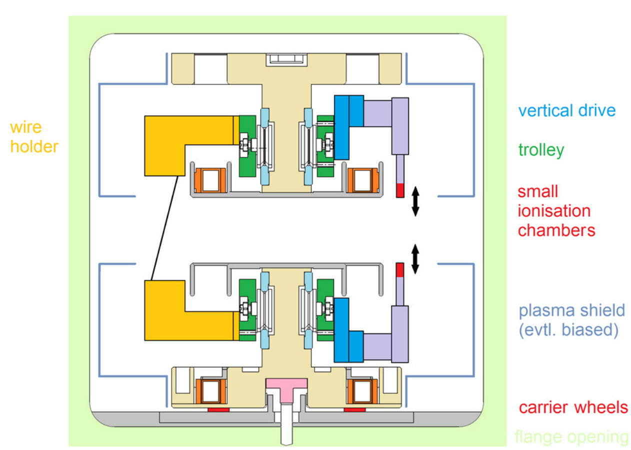

Figure 8: A possible extended configuration of probe heads (schematic, beam from left to right).

ISBN: 978-3-95450-205-9 doi:10.18429/JACoW-Cyclotrons2019-MOP024

OUTLOOK

Delivery of the service chamber is projected for spring 2020, followed by completion of the setup and in-vacuum lab testing of the mechanics. We intend to install in the cyclotron first a basic probe configuration with three carbon wires. Later, shielding electrodes may be added (Fig. 8), which could be biased to ±100 V and, hopefully, prevent disturbances by plasma clouds.

AUTHOR CONTRIBUTIONS

RD specified the physics layout, guided the development and wrote the paper. MR developed the mechanics concept and detailed layout and oversaw fabrication. RD and RS contributed to the design. RS mounted the mechanical setup and run the cable tests together with GG, who also provided testing software and connector solutions. PR contributed the outgassing tests and its interpretation. VO and GG provided hardware and software for motor tests.

REFERENCES

[1] L. Rezzonico *et al.*, "Diagnostics for high intensity beams", in *Proc. BIW'94,* Vancouver, BC, Canada, Oct. 1994, *AIP Conf. Proc.,* vol. 333, pp. 398-494, 1995.

[2] M. Olivo, "Beam diagnostic equipment for cyclotrons", in *Proc. Cyclotrons'75*, Zurich, Switzerland, Aug. 1975, paper E-01, pp. 331-340.

[3] R. Dölling, "Bunch-shape measurements at PSI's high-power cyclotrons and proton beam lines", in *Proc. Cyclotrons'13*, Vancouver, BC, Canada, Sep. 2013, paper TU3PB01, pp. 257-261.

[4] D. Goetz *et al.*, "Disturbance effects caused by RF power leaking out from cavities in the PSI ring cyclotron", in *Proc. Cyclotrons'10*, Lanzhou, China, Sep. 2010, paper WEM2CCO03, pp. 341-343.

[5] R. Dölling and J. Brutscher, "Fast recharging of electrostatic injection or extraction septa", presented at the Cyclotrons'19, Cape Town, South Africa, Sep. 2019, paper MOP025, this conference.

[6] Belt Technologies, Inc., www.belttechnologies.com

[7] allectra, www.allectra.com

[8] VACOM, www.vacom.de

[9] P. A. Duperrex *et al.*, "Latest diagnostic electronics development for the Proscan proton accelerator", in *Proc. BIW'04*, Knoxville, TN, USA, May 2004, *AIP Conf. Proc.*, vol. 732, pp. 268-275, 2004.

[10] A. Adelmann *et al.*, "Precise simulations of high-intensity cyclotrons", Paul Scherrer Institute, Villigen, Switzerland, Scientific Report 2010, pp. 54-55.

[11] M. Frey *et al.*, "Matching of turn pattern measurements for cyclotrons using multiobjective optimization", *Phys. Rev. Accel. Beams*, vol. 22, p. 064602, Jun. 2019. doi:10.1103/PhysRevAccelBeams.22.064602

[12] Y. J. Bi *et al.*, "Towards quantitative simulations of high power proton cyclotrons", *Phys. Rev. ST Accel. Beams*, vol. 14, p. 054402, May 2011, doi:10.1103/PhysRevSTAB.14.054402

[13] R. Dölling and M. Rohrer, "A 4D emittance measurement device for the 870 keV HIPA injection line", in *Proc. HB'18*, Daejeon, Korea, Jun. 2018, pp. 329-333. doi:10.18429/JACoW-HB2018-WEP2PO030

[14] https://amas.web.psi.ch/

[15] A. Adelmann *et al.*, "OPAL a versatile tool for charged particle accelerator simulations", May 2019. arXiv:1905.06654

ISBN: 978-3-95450-205-9 doi:10.18429/JACoW-Cyclotrons2019-MOP025

FAST RECHARGING OF ELECTROSTATIC INJECTION AND EXTRACTION SEPTA AFTER BREAKDOWN

R. Dölling†, Paul Scherrer Institut, 5232 Villigen PSI, Switzerland
J. Brutscher, 01324 Dresden, Germany

Abstract

We propose to recharge an electrostatic injection or extraction septum in a high-power cyclotron fast enough to omit the need for switching off the beam at a high voltage breakdown.

INTRODUCTION

In the Ring cyclotron, a proton beam of up to 2.4 mA is injected and extracted with the help of electrostatic septa [1]. Depending on tuning status, conditioning, actual problems and actual beam current, 5 to 300 short beam trips occur per day, from which ~1/10 include high voltage (HV) breakdowns in these septa. However, we do not know whether the breakdown is the reason or a consequence of beam switch off and related interlocks of loss monitors indicating errant beam. Anyhow, then the beam is switched off and ramped up again in about half a minute. This already amounts to a large fraction of the unscheduled downtime of the accelerator [2]. Some 5% of the experiments at the subsequent spallation source SINQ, as 2D or 3D imaging of processes, suffer from information loss due to these interruptions [3]. Also, the frequent beam switch-off and corresponding thermal cycling may accelerate the ageing of the SINQ target [4]. As a remedy for that fraction of beam trips, which are caused by a septum, we propose a recharging of the septum within 1 ms, which would allow to keep the beam running, being lost only for this short time. The amount of uncontrolled beam loss and the needed reaction times for surveillance is comparable to the switching of the full beam between beam lines routinely performed for the operation of the ultra-cold neutron source UCN [5]. Furthermore, for interlocks caused by other transients, detected, e.g., by loss monitors, a fast recharge of the septa may also allow to keep the beam running, if the causes decay correspondingly fast. The required fast surveillance will be eased by the new generation of loss monitor read-out electronic under preparation [6].

ACTUAL SETUP

The electrical (Fig. 1) and mechanical (Fig. 2) setup is discussed in the context of the injection septum EIC. The HV supply located outside the vault is connected to the septum via a long HV cable, a CERN type [7] external isolation resistor, a vacuum feedthrough, an in-vacuum damping resistor and a flexible connection to the cathode, which allows the mechanical adjustment of the septum during operation. A breakdown nearly fully discharges septum and short cable to isolation resistor, but not the long cable, since the discharge cannot be maintained with a low current. The exchange of charge already stored in the long cable and the power supply takes ~8 ms and recharges the cathode already to ~93% of the nominal 134 kV. Then the power supply delivers a charging current, typically limited to 100 µA, for ~0.6 s. With most breakdowns, a standard load curve is precisely reproduced (Fig. 3). During loading, the beam is already switched off due to beam losses or the low-voltage indication of the HV supply. Occasionally, multiple breakdowns occur (Fig. 4), or deeper breakdowns, which are also likely to be “assembled” by consecutive, but not resolved sparks. We also see switch off due to low-voltage indication resulting from overly increased dark current induced by operation of the nearby radial probe RRL [8].

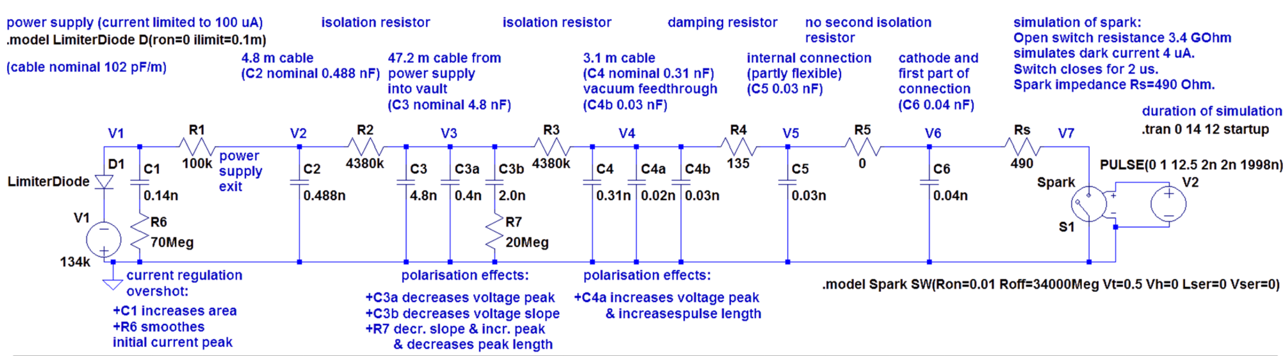

HV supply cur limit	R3	R4	R5	Rs		V2max	V3max	V4max	I1max	I2max	I3max	I4max	I5max	Ismax	V6 deficit after 1 ms	V6 deficit <1 kV after	HV supply in cur limit for
100 uA	4.38 MΩ	135 Ω	0 Ω	490 Ω	actual operation	-126.2 kV	-125.2 kV	~0 kV	168 uA	937 uA	31 mA	178 A	-	266 A	82 kV	511 ms	559 ms
500 uA	4.38 MΩ	135 Ω	0 Ω	490 Ω	increased current limit	-128.3 kV	-125.5 kV	~0 kV	553 uA	1.16 mA	31 mA	173 A	-	266 A	82 kV	107 ms	79 ms
500 uA	350 kΩ	135 Ω	0 Ω	490 Ω	lower Risol	-127.9 kV	-124.0 kV	~0 kV	561 uA	2.0 mA	382 mA	173 A	-	266 A	10.2 kV	105 ms	80 ms
500 uA	350 kΩ	1 MΩ	0 Ω	1200 Ω	plus 2nd Risol (instead Rdamp)	-134.0 kV	-132.3 kV	-122.3 kV	370 uA	370 uA	32 mA	134mA	-	111 A	1.8 kV	13 ms	-
500 uA	350 kΩ	135 Ω	1 MΩ	1600 Ω	plus 2nd Risol (new)	-134.0 kV	-133.0 kV	-125.8 kV	217 uA	217 uA	23 mA	123 mA	134 mA	83 A	1.05 kV	1.1 ms	-
100 uA	350 kΩ	135 Ω	1 MΩ	1600 Ω	plus 2nd Risol (new)	-133.6 kV	-133.0 kV	-125.8 kV	109 uA	201 uA	23 mA	123 mA	134 mA	83 A	1.05 kV	1.1 ms	29 ms

Figure 1: Present electrical circuit. Rs chosen to approximate calculated curves in Fig. 5 by V6. Its value corresponds to arc resistance at passing 75 kV. C4b, C5, C6 estimated from geometry. Simulation results are given for variants as well.

† rudolf.doelling@psi.ch

ISBN: 978-3-95450-205-9 doi:10.18429/JACoW-Cyclotrons2019-MOP025

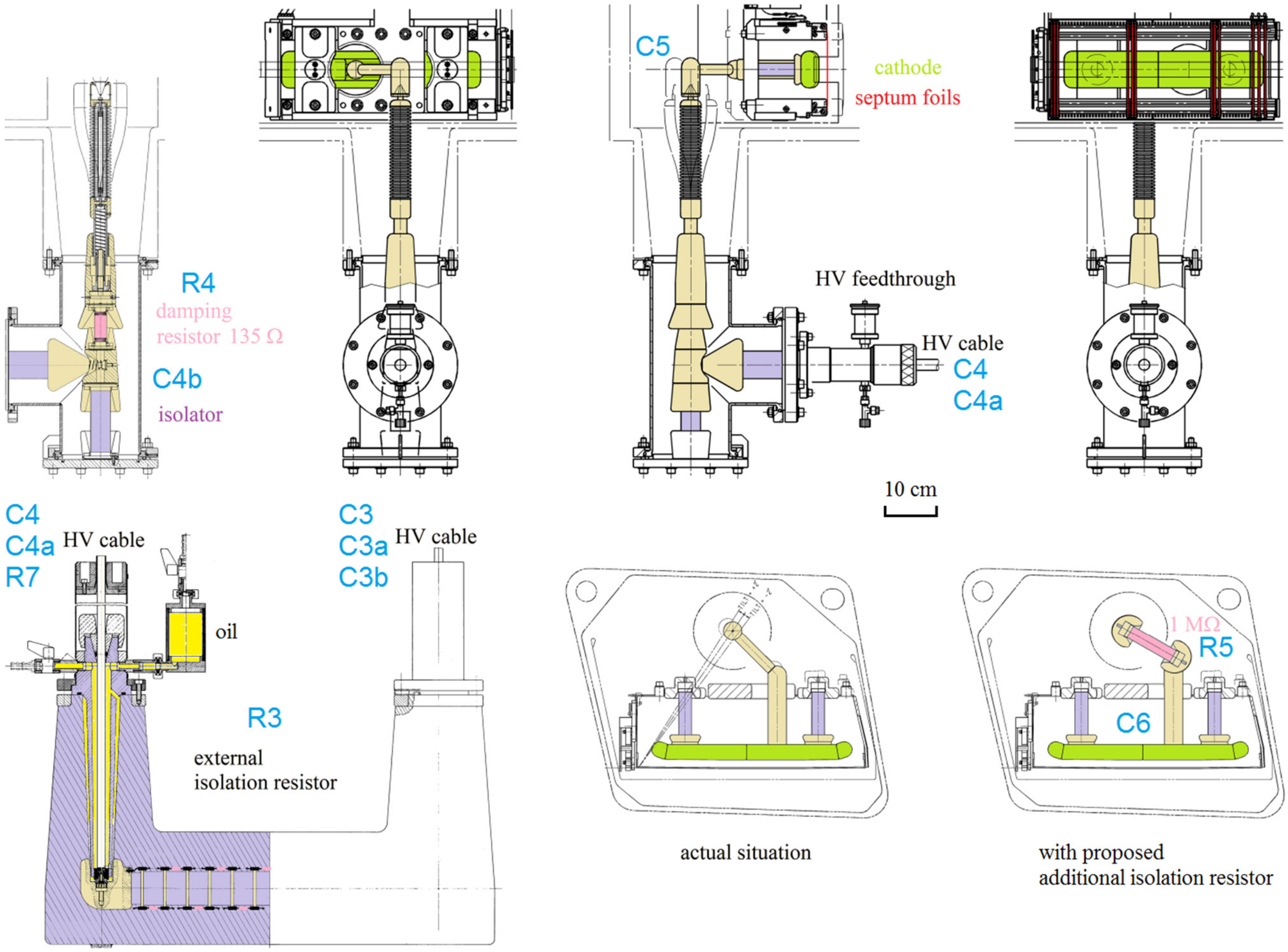

Figure 2: Mechanical setup of injection septum EIC of the Ring cyclotron. Shielded HV cables of type 2134 [9].

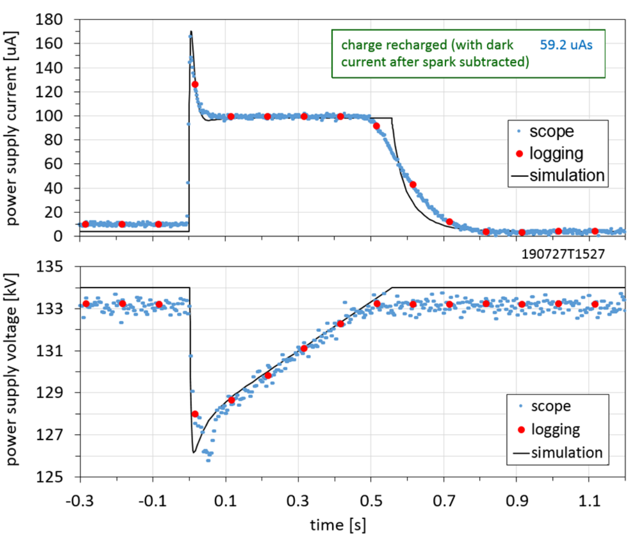

Figure 3: HV supply load curves for a “standard” spark. Current and voltage readings from HV supply analogue outputs at a scope. In addition, the data logged by the control system and the results from the LTspice simulation from Fig. 1 are depicted.

The initial current peak is probably caused by a non-ideal current regulation. In the LTspice simulation [10], this is roughly reproduced by adding C1, R6. The initial voltage peak, as well as the final slow current drop, result from polarisation currents in the dielectrics of the isolators. This is represented in the simulation by C3a, C3b, R7, C4a. However, the final current drop could not be reproduced exactly. Also, the result is still reasonable with R7 much lower, even 0 Ohm. In any case, cable capacitance is significantly increased above the specified value.

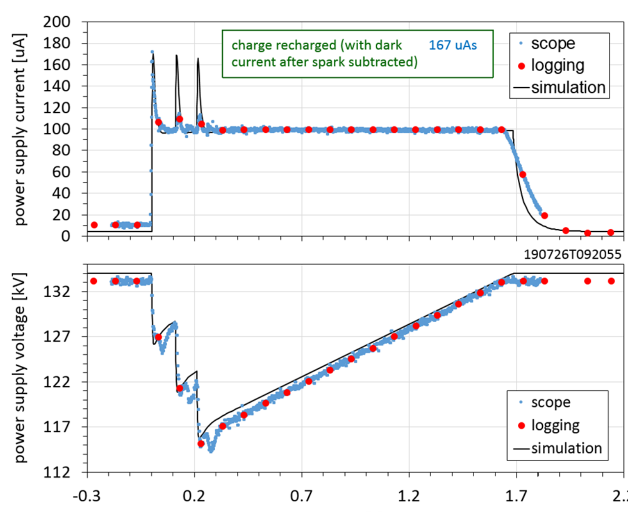

Figure 4: Triple breakdown.

ISBN: 978-3-95450-205-9 doi:10.18429/JACoW-Cyclotrons2019-MOP025

For the long cable, this, e.g., corresponds to an increase of the diameter of the inner conductor from 5.6 mm (4.8 nF) to 8.5 mm (7.2 nF), thereby decreasing the isolation distance from 6.9 mm to 5.4 mm. Possibly, this is an indication of degradation of the cable isolator. It will be interesting to see if this could help to identify critically aged cables.

PROPOSED SETUP

In an improved setup, the external isolation resistor close to the vacuum chamber would be smaller, e.g., 350 kΩ, as used for the CERN PSR septa [11], leading to a much faster initial redistribution of charge. 124 kV would be reached after the critical loss duration of 1 ms. Tests with deactivated beam centring demonstrated, that a static beam of 1730 µA or less is transported within a window of cathode voltage of ~120 kV to 140 kV. With a delayed switch-off, the shortly interrupted beam should be transported as well.

However, at higher beam currents, the voltage window will decrease. (Actually, for other reasons, operation is limited to about 1900 µA.) Here, in addition, a 1 MΩ isolation resistor can be placed much closer to the septum in vacuum (Fig. 1 R5, Fig. 2 bottom right), thereby reducing the charge consumed by the breakdown. With this, the cathode voltage deficit after 1 ms would decrease to 1 kV. We assume that in vacuum a resistor of 100 mm length will hold the full voltage which is applied for ~40 µs, although commercially available items are specified for much lower voltages for long-term operation in air. However, this has to be proven experimentally. If needed, the resistor may be prolonged to 180 mm.

In 2001, a similar proposal intended to speed up the charge exchange from the long cable by a lower-ohm external isolation resistor, eventually augmented by switching an additional charge from a dedicated storage capacitor [12]. With doubts that the isolation resistor would be able to prevent the charge from the long cable to be consumed in the breakdown, coupled with small value attached to the envisaged benefit, it was not pursued.

BREAKDOWN MECHANISM

A common approach to describe a sparkover in vacuum is that it starts with a point on the cathode, where plasma is generated, and the plasma is expanding towards the anode with a velocity of about 20 km/s (see, e.g., [13, 14]). In [15] a formula is derived to describe the time dependent voltage at a spark gap, which discharges a capacitance parallel to it. The ratio of voltage U to start voltage U_0 is described as $u = U/U_0 = [1 + Bz/2]^{-2}$ with time dependence

$$z = \frac{\tau^2}{2} + 0.244\left\{\frac{(1-\tau)^2}{2} - 1.5 + 3\tau + 3\ln(1-\tau) + \frac{1}{1-\tau}\right\}$$

and $\tau = vt/d$ the time relative to the time the plasma needs to cross the gap width d at a plasma velocity v, $B = \frac{A\sqrt{U_0}d}{vC}$ with constant $A = 3\cdot10^{-5}\,\mathrm{A/V^{1.5}}$, and C the capacitance to be discharged. The formula is valid for times $\tau < 1$, i.e. until the plasma has bridged the gap, and not too large capacitances, so that $B > 1$. Despite the complexity of the analytical formula, the results must be considered as a crude estimate. De facto, the plasma has heavy fluctuations and limited reproducibility.

In case the plasma has bridged the gap, the current is limited only by external components (e.g., cable inductance), and the gap voltage is given by the vacuum arc burning voltage of around 50 V. For continuous plasma generation, a current flow of a few Amperes is needed, otherwise the plasma would dissipate to the walls, and after a few µs the gap would be isolating again [16]. Hence, with an isolation resistor of 350 kΩ, a feeding of the discharge by the charge from the long cable is not likely, even in the case of reflections at not well-terminated ends of the transmission lines formed by the setup.

We evaluate the formula for 410 pF, 70 pF and 40 pF, which are assumed as discharged capacitances behind the isolation resistor in the variants of the LTspice simulation listed in Fig. 1, using $v = 20$ km/s as the plasma velocity, $d = 17$ mm as the gap distance and a starting voltage of $U_0 = 134$ kV. The time until the plasma has crossed the gap ($\tau = 1$) is, in our case, $t = d/v = 17\ \mathrm{mm}/20\ \mathrm{mm/\mu s} = 850$ ns. Using $B = \frac{3\cdot10^{-5}\,\mathrm{A/V^{1.5}}\ \sqrt{134000\mathrm{V}}\ 0.017\mathrm{m}}{20000\mathrm{m/s}\ C}$, we find that for $C = 410$ pF, $B = 22.8$, for $C = 70$ pF, $B = 133$, and for $C = 40$ pF, $B = 233$.

The corresponding voltage decay curves are depicted in Fig. 5, together with the current $I = C\cdot dU/dt$. In all cases the capacitance is discharged before the spark plasma bridges the gap. However, whereas for the 410 pF capacitance the decay to 10% of original voltage takes nearly 500 ns, it needs only 220 ns with 70 pF and only 160 ns with 40 pF. Currents are decayed to a few Amperes a little later, and hence we expect that the cathode is close to fully discharged when the gap gets isolated again. This corresponds well with the observed occurrence of a standard load curve.

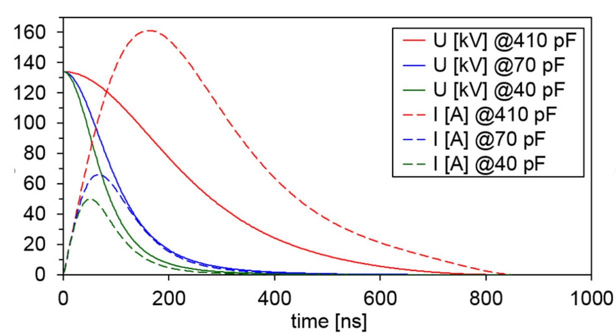

Figure 5: Voltage and current during sparkover.

OTHER ASPECTS

At the larger extraction septum EEC, capacitance and actual and improved recharge time are nearly doubled. However, the effect on damage caused by the beam will be counteracted by the initially lower stopping power and scattering of the lost higher energy protons. Also, for EEC, the total width of the usable septum voltage window already shrinks from 26 kV to 11 kV when the beam current is increased from 1330 µA to 1730 µA. This can be studied in detail, when the higher beam current is available again.

ISBN: 978-3-95450-205-9 doi:10.18429/JACoW-Cyclotrons2019-MOP025

At a breakdown, the beam interlocks triggered by loss-monitors and low-voltage indication must be suppressed for about a ms. But in case of a repeated breakdown, the beam should be switched off to prevent damage.

In case of a breakdown, the feedback control of the amplifiers of the acceleration cavities could cope with the sudden drop of beam current. However, the regulation of the actual flat-top cavity amplifier, which is already at its limits, would not [17]. An upgrade of the cavity, which is under discussion for other reasons, would be required.

CONCLUSION

Based on the developed understanding, we assume that the proposed changes would allow keeping the beam running over individual discharges of the injection and extraction septa of the Ring cyclotron.

AUTHOR CONTRIBUTIONS

RD initiated this work, performed the measurements and LTspice simulations and wrote the manuscript. JB contributed the breakdown theory and suggested the in-vacuum isolation resistor. Both discussed the whole topic and verified the paper.

ACKNOWLEDGEMENTS

We like to thank Martin Baumgartner, Dietmar Götz and Thomas Rauber for providing information on the built-in septa, cables, resistors and power supplies. We thank Dr. Bräunlich from FKH for useful comments and literature. Thanks to Steffen Schnabel for help with LTspice and to Oliver Dölling for cleaning the underlying drawings for Fig. 2.

REFERENCES

[1] M. Olivo, "The electrostatic extractor channel for the SIN 590-MeV ring cyclotron", in *Proc. Cyclotrons'75*, Zurich, Switzerland, Aug. 1975, paper D-18, pp. 292-296.

[2] M. Seidel, J. Grillenberger, and A. C. Mezger, "High intensity operation and control of beam losses in a cyclotron based accelerator", in *Proc. HB'12*, Beijing, China, Sep. 2012, paper THO1C01, pp. 555-559.

[3] S. Janssen, Paul Scherrer Institute, private communication, June 2019.

[4] B. Blau *et al.*, "Investigations on the premature failure of SINQ target #11 and its countermeasures", to be presented at ICANS XXIII, Chattanooga, USA, Oct. 2019, to be published.

[5] D. Reggiani, "Extraction, transport and collimation of the PSI 1.3 MW proton beam", in *Proc. HB'12*, Beijing, China, Sep. 2012, paper WEO3A03, pp. 373-377.

[6] R. Dölling, E. Johansen, M. Roggli, W. Koprek, and D. Llorente Sancho, "Development of new loss monitor electronics for the HIPA facility", presented at the IBIC'19, Malmö, Sweden, Sep. 2019, paper MOPP024.

[7] D. Götz, PSI, private communication, May 2019.

[8] R. Dölling *et al.*, "Development of a replacement for the long radial probe in the ring cyclotron", presented at Cyclotrons'19, Cape Town, South Africa, Sep. 2019, paper MOP024, this conference.

[9] `http://dielectricsciences.thomasnet.com/Asset/2134.pdf`

[10] `https://www.analog.com/en/design-center/design-tools-and-calculators/ltspice-simulator.html`

[11] J. Borburgh, CERN, private communication, May 2019.

[12] R. Dölling, "Möglichkeit einer schnellen Regeneration der Spannung elektrostatischer Elemente nach Durchschlägen", Paul Scherrer Institute,, Villigen, Switzerland, Internal Rep. HIPA-ELSTAT-DR84-003.00-100801, Aug. 2001.

[13] B. Jüttner, "Vacuum breakdown", *Nucl. Instrum. Methods Phys. Res., Sect. A*, vol. 268, pp. 390-396, 1988.

[14] G. A. Mesyats and D. I. Proskurovski, "Pulsed electrical discharge in vacuum", Springer Verlag, 1989.

[15] Jörg Brutscher, "Experimentelle und theoretische Untersuchungen zum Hochvakuumdurchschlag", Ph.D. thesis, Frankfurt 1992.

[16] H. J. Lippmann, "Schalten im Vakuum", VDE Verlag 2003.

[17] M. Schneider, Paul Scherrer Institute, private communication, July 2019.

ISBN: 978-3-95450-205-9 doi:10.18429/JACoW-Cyclotrons2019-MOP028

DESIGN OF 5.8 MHz RF ELECTRODE FOR AMS CYCLOTRON

D.-H. Ha[1], M. Ghergherehchi[1], H. Kim[2], J. Lee[2], H. Namgoong[1], K. M. M. Gad[2], J.-S. Chai[1†]
Sungkyunkwan Universtity, 2066 Seobu-ro, Jangan-gu, Suwon, Gyeonggi-do, Korea
[1]Dept. Electrical and Computer Engineering
[2]Dept. Energy Science

Abstract

Accelerator Mass Spectrometry (AMS) is a powerful method for separating isotopes, and electrostatic tandem accelerators are widely used for AMS. Sungkyunkwan University is developing AMS that can be used in a smaller space based on cyclotron. Unlike conventional cyclotrons used in PET or proton therapy, cyclotron-based AMS provides high turn number and high resolution. In this study, we proposed a cavity with a frequency of 5.8 MHz and an accelerating voltage of 300 V to accelerate the particles in the cyclotron. The proposed cavity was designed as an electrode and verified by CST Microwave studio.

INTRODUCTION

AMS has been developing rapidly since the 1980s. As a new application of accelerators, AMS has been widely applied in archeology, earth and planetary science, materials and environmental sciences. Especially AMS has a bright future in biomedical applications.

In general, the accelerator used in the AMS system is an electrostatic accelerator Tandem. This is because tandem accelerators are electrostatically accelerated and can be applied to a wide variety of particles, regardless of their weight.

Cyclotrons can be used to separate particles on their own. so cyclotron is suitable for use in AMS systems. This can benefit greatly from the size and cost of AMS systems compared to tandem accelerators. However, cyclotrons can only be used for specifically targeted particles and have a major weakness in resolution and sample acquisition which are key variables in AMS systems.

Sungkyunkwan University has developed a cyclotron-based AMS system targeting carbon which is the most widely used particle in AMS systems. The cyclotrons were developed with a focus on particle classification which is a key variable of AMS rather than acceleration efficiency which is an important variable of the accelerator. In order to improve the resolution, a design with a high turn number and a high Harmonic number was carried out and artificial intelligence was applied to have high accuracy at a low sample acquisition number. The final specifications are as follows.

In this study, we describe a cavity in the cyclotron's components that accelerates particles. The cavity is designed and impedance matched through the RF circuit, verified by CST MICROWAVE STUDIO.

† jschai@skku.edu

DESIGN FEATURE

The resolution of cyclotron is as follows:

$$\text{Resolution} = \pi h n$$

Where h is the harmonic number and n is the number of turns. According to the equation, the higher the harmonic number and the number of turns the greater the resolution. Cyclotrons induce the movement of particles through the magnetic field of the electromagnet and accelerate the particles through the electric field of the cavity. Because it affects each other, the electromagnet and the cavity are designed to have one side design first, and the other side design according to the design side first.

In this study, the design of the electromagnet was carried out and the cavity was designed according to the design of the electromagnet. The requirements are shown in Table 1.

Table 1: Specification of AMS Cyclotron

Specification	Value	Unit
E	200	keV
R_{in} / R_{ext}	138 / 453.6	mm
Mass Resolution	5000	
Turn number	159	
Dee voltage	300	V
Frequency	5.8	MHz
E_{in}	25	keV
Dee angle	20	°
Number of Dees	2	

By default, the size of the cavity is proportional to the wavelength of the frequency. The larger the band of frequencies used, the shorter the wavelength of the frequency. So the size of the cavity is usually smaller. At 5.8 MHz, the wavelength is approximately 51724 mm. The types of cavities commonly used in cyclotrons are λ/4 and λ/2 resonators. In this case, 12931 mm for the λ/4 type and 25862 mm for the λ/2 type are required. The acceleration section of the particle required in Table 1 is very different from 138 mm to 453.6 mm.

ISBN: 978-3-95450-205-9 doi:10.18429/JACoW-Cyclotrons2019-MOP028

The frequency follows the formula:

$$f = \frac{1}{2\pi\sqrt{LC}}$$

L means inductance component and C means capacitance component. According to the equation, the frequency can be adjusted by adding an inductance component and a capacitance component to the cavity.

In general cyclotron, high power is used to increase acceleration efficiency. In this case, power cannot be tolerated at the device level of inductance or capacitance. Create L and C structurally to adjust the frequency.

In this study, AMS cyclotron is focusing on high-resolution rather than acceleration efficiency. So, Acceleration voltage is very low as 300 V. In addition to the cavity, the RF circuit box is designed for impedance matching and frequency tuning such as shown in Fig. 1.

By using CST, the field data in Fig. 2 can be obtained.

Computer simulation results show that the acceleration voltage 145840 V is generated when the power of 6656 W is consumed. Power consumption and generated voltage are generated in proportion to the square. Using this, it can be seen that the power required to generate 300 V requires about 0.03 W. Because of the very small power dissipation, you can see that impedance matching and frequency matching are possible at the device level.

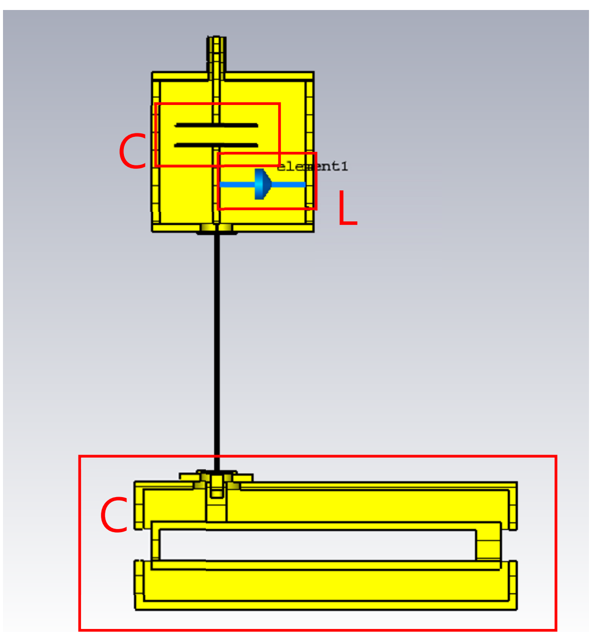

Figure 1: RF cavity.

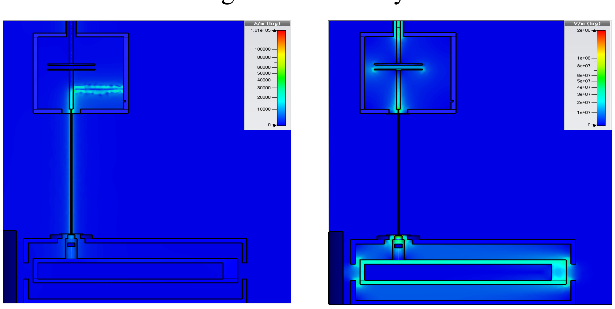

Figure 2: H-field and E-field created in the cavity.

Impedance matching and frequency matching were performed by adjusting L and C of the external RF circuit box, and the results are shown in Figs. 3 and 4.

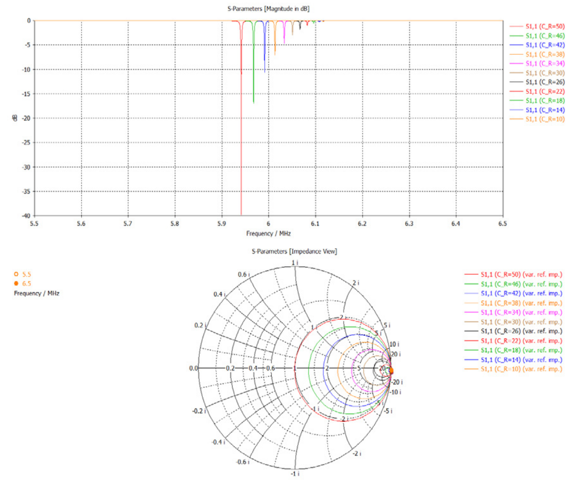

Figure 3: matching with variable capacitance.

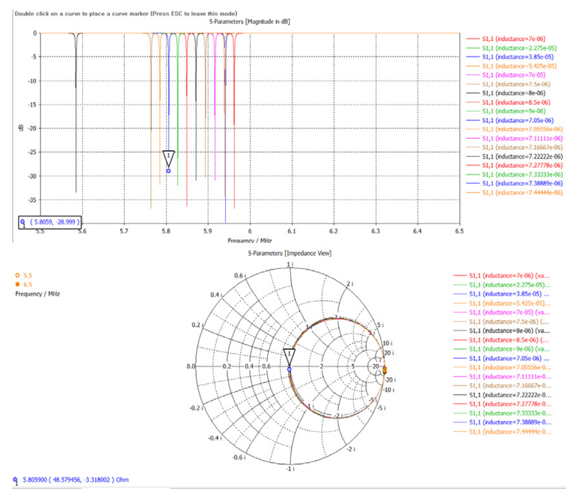

Figure 4: Matching with variable inductance.

Figure 3 shows the change in frequency and impedance with capacitance. Impedance matching changes significantly compared to the change in frequency as shown in Fig. 3. However, there is almost no change in impedance matching compared to the frequency change in Fig. 4, which shows the change in frequency and impedance with inductance. Therefore, the design was carried out by adjusting the inductance to adjust the frequency near 5.8 MHz and then adjusting the capacitance to match the impedance and frequency. Finally, an RF cavity with impedance 50 Ω and frequency 5.8 MHz was designed.

DISCUSSION

In the currently designed RF cavity, Dee is in the air with only a physical design in progress. Engineering design, such as fixing between liner and Dee with dielectric material, is necessary and additional changes should be considered.

ISBN: 978-3-95450-205-9 doi:10.18429/JACoW-Cyclotrons2019-MOP028

ACKNOWLEDGEMENTS

This work was supported by the Radiation Technology R&D program through the National Research Foundation of Korea funded by the Ministry of Science, ICT and Future Planning (Grant No. 2017M2A2A4A02020347).

ISBN: 978-3-95450-205-9 doi:10.18429/JACoW-Cyclotrons2019-MOP029

DESIGN AND MANUFACTURE OF 10 kW, 83.2 MHz 4-WAY POWER COMBINER FOR SOLID STATE AMPLIFIER

D.-H. Ha[1], M. Ghergherehchi[1], H. Kim[2], J. Lee[2], H. Namgoong[1], K. M. M. Gad[2], J.-S. Chai[1†]
Sungkyunkwan Universtity, 2066 Seobu-ro, Jangan-gu, Suwon, Gyeonggi-do, Korea
[1]Dept. Electrical and Computer Engineering
[2]Dept. Energy Science

Abstract

The purpose of this study is to improve the insertion loss of a 20 kW solid-state RF power amplifier and the power coupling efficiency by reducing reflected power. For this purpose, a power combiner, which is a core component of a solid-state RF power amplifier, was designed and fabricated. The 4-way power combiner employs the Wilkinson type, which has excellent power coupling efficiency and isolation, and operates at 83.2 MHz. This paper covers the design and cold test results.

INTRODUCTION

RF amplifiers for particle accelerators require high frequency, power and phase stability. Depending on the type of particle accelerator, the power requirement is 10 kW to 2 MW or more for continuous sources and a maximum of 150 MW for pulse sources.

These high frequency, power and phase safety requirements have led to the use of tube amplifiers as the source of particle accelerators. Tube amplifiers include Tetrode amplifiers, Inductive output tubes, Klystrons, Magnetrons and Gyrotrons. Tube amplifiers have been used as a power source for particle accelerators because they can supply frequencies up to 10 GHz and power up to 100 MW. Recently, however, limitations of tube amplifiers have begun to emerge. All tube amplifiers have the same problem, and typical problems include heat loss, voltage breakdown, output window failure, and multipactor discharge. Semiconductor amplifiers have emerged to solve impedance problems during beam loading and reflection problems during multipacing.

In the case of a semiconductor amplifier, the output power of a single amplifier is lower than that of a tube amplifier, but when sufficient power cannot be obtained, the output of several amplifiers can be combined to achieve a target output. In addition, semiconductor amplifiers have low voltage requirements and low maintenance costs. The cost of amplifiers (including replacement preamplifiers) in the total operating cost of a particle accelerator system is quite high. Therefore, the maintenance cost of a semiconductor amplifier with low voltage requirements is much lower than that of a tube amplifier because the power efficiency of an RF amplifier determines the power consumption and the power consumption soon determines the operating cost. In addition, the semiconductor amplifier is modularized, so that the failure of a single amplifier unit does not affect the whole system, and it is easy to find the fault part, so that maintenance is easy and cost is low. In the future, as the efficiency of MOSFETs, a key component of semiconductor amplifiers, increases, the amount of power available for output is expected to increase.

However, semiconductor amplifiers still have a lower maximum output power than tube amplifiers and have some disadvantages. Semiconductor amplifiers require a compact system that has high RF power per unit volume due to low acceleration efficiency per unit volume. In addition, the LDMOS device, a key component of the semiconductor amplifier, is sensitive to increased junction temperature, requiring a heat sink design with good thermal management efficiency.

There is also a problem of lowering power coupling efficiency due to unbalance of amplitude and phase. The semiconductor amplifier combines the power of single amplifier units to achieve the target power. When single amplifier units have different powers and phases and ignore them and combine them, there is a risk of damage to the equipment due to the reflected power generated by the phase and power difference. To solve this problem, amplitude and phase trimmers have been developed and individual PA phase adjustments have been used to compensate for phase imbalance, but no perfect solution has yet emerged. In this paper, we designed a power combiner that increases the power coupling efficiency and minimizes the reflection power to solve the problem of power coupling efficiency degradation due to the amplitude and phase imbalance of semiconductor amplifiers.

DESIGN FEATURE

The most suitable type for power combiners that must combine large powers of 10 kW is Gysel power combiners. Gysel power combiners are superior to Wilkinson power combiners in terms of thermal endurance and power handling, making them suitable for high power applications.

However, the proposed 4-way power combiner has the goal of improving insertion loss and reflected power. The advantages of Gysel power combiners, thermal endurance and power handling, have no direct impact on insertion loss and improved return power. Therefore, Wilkinson power combiner, which has low loss type, is more suitable for the target than Gysel power combiner. In addition, the

† j.schai@skku.edu.

ISBN: 978-3-95450-205-9 doi:10.18429/JACoW-Cyclotrons2019-MOP029

matching frequency is distorted due to the slight characteristic change due to heat generated during power coupling. In order to minimize the loss caused by this phenomenon, a wide bandwidth Wilkinson power combiner is adopted.

Since it was difficult to ignore the heat generation problem of the resistive component, which is the disadvantage of Wilkinson's power coupler, the isolation resistor was directly coupled to the heat sink and a cooling fan was installed to improve thermal durability. Based on these considerations, the 4-way power combiner proposed in this paper is designed by adopting Wilkinson type.

Before designing a 4-way power combiner, a conceptual 4-way Wilkinson combiner was designed to verify the shape, impedance, and matching of circuit components and patterns. The Term was placed at 50 ohms for both input and output ports, with 100 ohms between the input ports for isolation, according to Wilkinson divider theory. The transmission line is set to 1/4 wavelength and the impedance is designed to 70.7 ohms. As a result, the 4-way power combiner was completed by combining three 3-way power combiners as shown in Fig. 1.

The S-parameter simulation results show that S (2,2) is about –100 dB at 83.2 MHz and S (1,2) is about –6 dB as shown in Fig. 2.

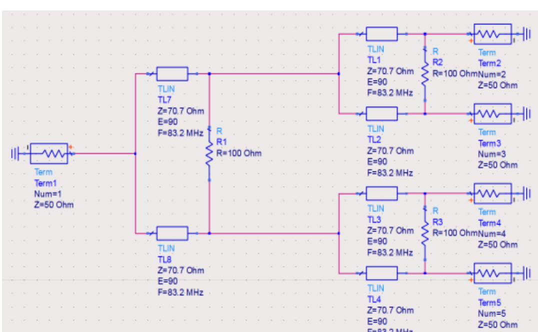

Figure 1: Ideal 4-way wilkinson power combiner matched at 83.2 MHz.

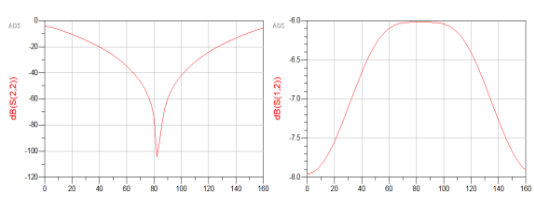

Figure 2: S-parameter simulation result S (2,2), S (1,2).

Considerations for circuit design include pattern width and pattern length, thickness of PCB board, thickness of gold foil, conductivity of gold foil, dielectric constant of Teflon and PCB dissipation factor. PCB board is adopted for accurate circuit design (Table 1).

Table1: Characteristics of Teflon Base PCB Board

Parameter	Value
Base Material	Teflon
Board Thickness	2.6 mm
Copper Thickness	2 OZ (0.07 mm)
Dielectric Constant	2.1
Dissipation Factor tan	0.0004
Conductivity	5.8E+7

After layout and simulation of the completed circuit diagram, it is possible to manufacture after checking the matching and S-parameter. After that, if you go into production without patterning, a pcb board about 1.2 m long is completed.

The already developed semiconductor amplifier of Sungkyunkwan University does not have enough space to mount a board about 1.2 m long. In addition, if the distance between the input port and the output port is 1.2 m away, the power coupling efficiency is expected to decrease due to the phase change depending on the position of the connector and the length of the transmission line. In order to prevent such reduction in power coupling efficiency, a patterning process is required.

Figure 3 shows the proposed 4-way power combiner circuit. Table 2 shows the main difference between the circuit design and the pattern design S-parameters.

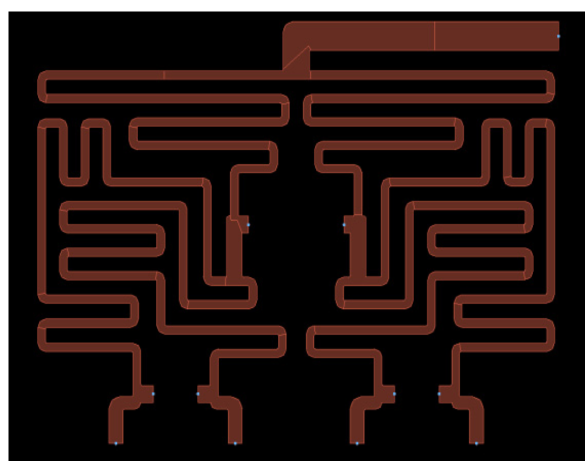

Figure 3: Pattern of the proposed 4-way power combiner circuit.

ISBN: 978-3-95450-205-9 doi:10.18429/JACoW-Cyclotrons2019-MOP029

Table 2: Difference between Circuit Design and Pattern Design S-parameter

S-Parameter	Circuit Design	Pattern Design
Insertion Loss	6.162 dB	6.241 dB
Input Return Loss	29.874 dB	25.144 dB
Output Return Loss	19.467 dB	13.319 dB
Near Isolation	25.241 dB	16.587 dB
Far Isolation	42.353 dB	38.646 dB

The measurement was performed in the 70 ~ 100 MHz section and the measurement equipment was used as a network analyzer (NA). Table 3 lists the S-parameters measured in the cold test in the order of Insertion Loss, Input Return Loss, Output Return Loss, Near Isolation, and Far Isolation. Figures 4 and 5 show the insertion loss and input return loss measured at ports 2 and 5, respectively. In the cold test of the fabricated power combiner, the characteristics of the S-parameter were many different from those of the designed value.

Table 3: Cold Test S-parameter versus Simulation S-Parameter

S-Parameter	Cold Test	Pattern Design
Insertion Loss	-6.17 dB	-6.241 dB
Input Return Loss	-25.738 dB	-25.144 dB
Output Return Loss	-13.659 dB	-13.319 dB
Near Isolation	-16.148 dB	-16.587 dB
Far Isolation	-35.245 dB	-38.646 dB

In the existing design, the frequency was precisely matched to the target frequency of 83.2 MHz, and the flat power did not differ by more than 5 dB even if the target frequency differed by up to 40 MHz. However, the actual measurements showed that the matching frequency was formed at about 87 MHz and the reflection power was as good as -30 dB when matched. At 83.2 MHz, the reflection power was about –25.6 dB, which is better than the simulation value. It is expected that the end part designed by wider line width has less influence than the simulation to protect the damage caused by current, so that the flat power is reduced and the reflection power which is reduced by widen the line width is expected to be higher than the design value.

In case of insertion loss, there was also a slight difference between the simulation value and the measured value. The simulation result was –6.241 dB and the insertion loss measured during cold test was –6.17 dB. It is expected that the characteristics of the actual measurement are better because the dielectric constant of the gold foil is higher than the value set in the simulation.

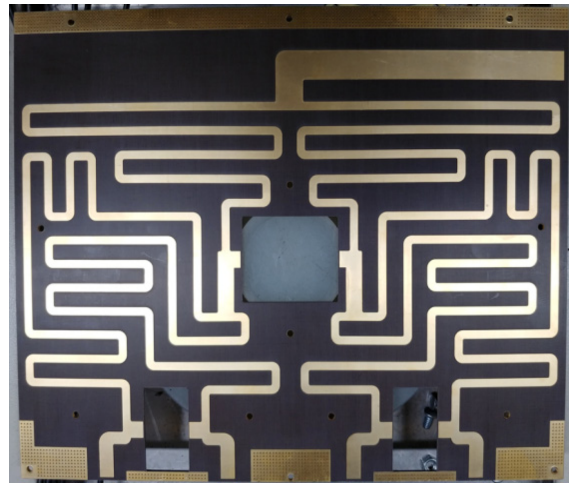

Figure 4: 4-way combiner.

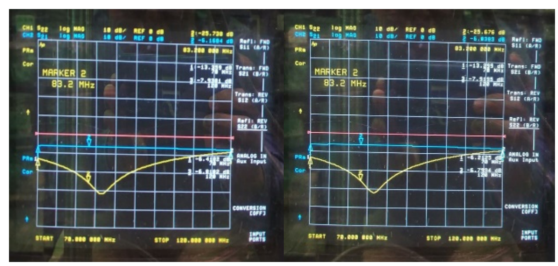

Figure 5: Cold test.

CONCLUSION

Cold test results showed similar trends with simulation values. In particular, the insertion loss and the Input Return Loss values were better than the simulation results. This is expected to be due to the lower conductivity of the gold foil, resulting in better actual conductivity and less impact on the end of the wider pattern width for overcurrent protection. As a result of the cold test, the values of Insertion Loss, Input Return Loss, Output Return Loss, Near Isolation, and Far Isolation respectively were -6.17, -25.144, -13.319, -16.587 and -38.646 dB.

These results confirm that the 4-way power combiner is designed in a way that meets the purpose. It is considered that the results of the study on the high power pcb combiner for semiconductor amplifiers are extremely rare.

ACKNOWLEDGEMENT

This work was supported by the Radiation Technology R&D program through the National Research Foundation of Korea funded by the Ministry of Science, ICT and Future Planning (Grant No. 2017M2A2A4A02020347)

ISBN: 978-3-95450-205-9 doi:10.18429/JACoW-Cyclotrons2019-MOP030

RF MEASUREMENT OF SKKUCY-10 RF CAVITY FOR IMPEDANCE MATCHING

J. Lee[1], M. Ghergherehchi[2], H. Kim[1], D.-H Ha[2], H. Namgoong[2], K. M. M. Gad[1], J.-S. Chai[2,†]
Sungkyunkwan Universtity, 2066 Seobu-ro, Jangan-gu, Suwon, Gyeonggi-do, Korea
[1]Dept. of Energy Science
[2]College of Information and Communication Engineering

Abstract

The 10 MeV cyclotron was designed for next version in Sungkyunkwan University, after the SKKUCY-9 had developed for medical application for PET. The RF cavity, which generates the electric field in cyclotron, was designed based on a half-wavelength resonator and optimized to improve the unloaded quality factor (Q_0). The design specifications of RF cavity were resonance frequency 83.2 MHz, Q_0 5830 and Dee voltage 40 kV with geometrical values resonator length 560 mm, Dee angle 35° and Stem radius 16 mm. The RF cavity of the SKKUCY-10 was fabricated and installed inside the electromagnet, and RF characteristics were measured with a network analyzer. The RF coupling coefficient and characteristic impedance for desired condition were selected at 1.08 and 52 Ω, respectively. The RF coupling coefficient and characteristic impedance were measured 0.8-1.2, 52-49 Ω according to temperature as 15-21°C. The power coupler was checked for optimization of RF coupling coefficient and characteristic impedance, and the results show good agreement with simulated and measured data.

INTRODUCTION

RF cavity generates electric field with resonant frequency in cyclotron and is developed based on coaxial resonator to improve RF power efficiency according to electric field [1]. Cyclotrons aimed at producing radio tracers have been developed as isochronous magnets with azimuthally varying magnetic fields, and fix frequency RF cavities with constant dee voltages [2].

An isochronous cyclotron using fixed frequency has developed to optimize the magnetic field to satisfy the synchronous phase of charged particles by equilibrium-orbit. However, due to the thermal and beam loading effect at cyclotron operation, the RF coupling state and the dee voltage variation can occur inside the RF cavity. To overcome this, the capacitive type fine tuner, the amplitude of the RF amplifier, and the phase control are applied to keep the stable condition of the RF cavity, which are regulation of dee voltage, resonant frequency and RF critical coupling state [3].

The medical AVF cyclotron (named SKKUCY-10) is developing for 10 MeV proton at Sungkyunkwan university, and the RF system based on half-wavelength coaxial resonator was designed to have 83.2 MHz resonant frequency and 50 Ω characteristic impedance [4].

In this paper, the RF coupling state and characteristic impedance was analyzed with considerations of thermal and beam loading effect. The initial conditions of temperature and beam power were assumed based on the specification of SKKUCY-10, and the RF coupling coefficient and characteristic impedance were calculated by simulation code. In addition, the RF coupling coefficient and characteristic impedance were measured according to environment temperature in RF system, and compared with simulation results.

METHODS AND MATERIALS

The RF cavity, capacitive power coupler and fine tuner structure of the 10 MeV cyclotron are shown in Fig. 1. The power coupler is designed as a 50 Ω, 3.125 inch standard coaxial rigid line, and the inner conductor of the rigid line is coupled by capacitance adjacent to the side of the dee. The fine tuner consists of an electrically grounded plate and movement motor. The plate is coupled by capacitance adjacent to the side of the dee, and the plate diameter was designed to be 50 mm to compensate for wide variations in the RF cavity.

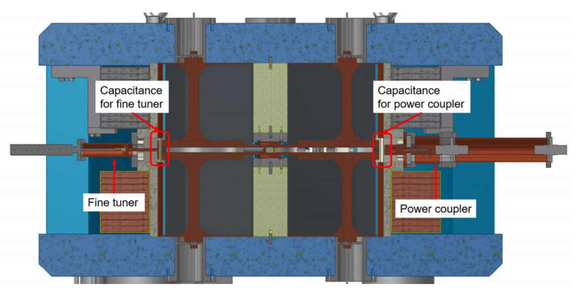

Figure 1: Power coupler and fine tuner for SKKUCY-10.

In the RF system of SKKUCY-10, the power coupler was considered with impedance matching as 50 Ω to satisfy critical coupling state, and the RF specification is shown in Table 1. The fine tuner was designed to have a tuning range of ±0.5 MHz with 83.2 MHz, and the RF coupling coefficient was optimized to 1.03 when the coupler gap distance is 18.7 mm.

†jschai@skku.edu

ISBN: 978-3-95450-205-9 doi:10.18429/JACoW-Cyclotrons2019-MOP030

Table 1: RF Specifications

Parameter	Value
Resonance frequency [MHz]	83.2
Coupling coefficient	1.03
Tuning range [MHz]	±0.5
Coupler gap distance [mm]	18.7
Tuner gap distance [mm]	5

In order to understand the thermal effect of the RF cavity, the resistivity of the copper property was changed by temperature in Eq. (1), where T is temperature, β_T is temperature coefficient as $1/(233.54 + \mathrm{T})$, $\rho_{T1,2}$ is the specific resistivity at temperature from T_1 to T_2 [5]. The conductivity of the RF cavity, is expressed as the inverse of resistivity, and the change of unloaded quality factor caused by the conductivity can break the matching of β and Z_0.

$$\rho_{T2} = \rho_{T1}(1 + \beta_T(T_2 - T_1)) \qquad (1)$$

The β with beam loading effect is expressed by equation (2) in the RF cavity, where i is the beam current and r_s is the shunt impedance, p_c is the cavity dissipation power [6].

$$\beta = [\frac{i}{2} \cdot \sqrt{\frac{r_s}{p_c}} + \sqrt{1 + \frac{i^2 r_s}{4p_c}}]^2 \qquad (2)$$

The β, and Z_0 of the RF cavity due to thermal effects were simulated by using the Microwave Studio in Computer Simulation Technology [7]. The structure of power coupler for critical coupling state was calculated by changing the gap distance between dee and coupler as shown in Fig. 2.

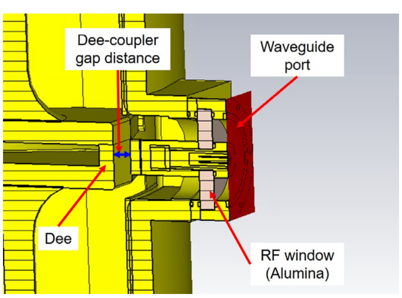

Figure 2: Scheme of power coupler.

RESULTS AND DISCUSSION

The calculation result of RF coupling coefficient (β) caused by beam loading effect is shown in Fig. 3. The β was increased, when the beam current was increased based on equation (2). Our desired beam current 100 μA with β = 1, so β should be optimized to 1.08 for beam loading effect.

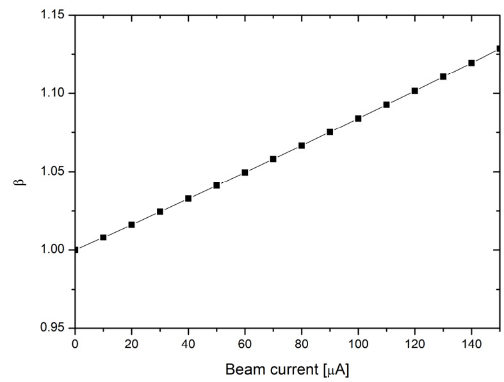

Figure 3: Calculation result of RF coupling coefficient according to beam current.

The results of β and characteristics impedance (Z_0) of RF cavity are shown in Fig. 4, and compared with measured value. For the measurement of β the network analyser was used and scattering parameter was investigated, and Z_0 was measured in smith chart. As the conductivity of copper was decreased with increasing of temperature, the β was decreased based on reduction of unloaded quality factor (Q_0). The Z_0 was decreased, and the coupling state was slightly under-coupled.

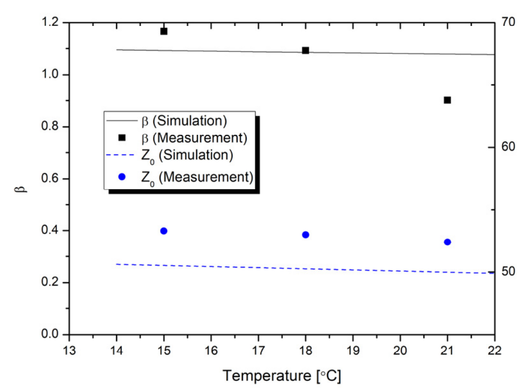

Figure 4: Results of RF coupling coefficient and characteristics impedance according to temperature.

In our RF system, the β was simulated 1.08 ±0.01 for operating condition of 100 μA beam current and ±5 °C. The power coupler and RF cavity was simulated by optimizing the β, and compared with measured value. The gap distance between dee and power coupler was changed for measurement as shown in Fig. 5.

The results of β and Z_0 are shown in Fig. 6, and the simulation results were compared with measurement data. The resonant frequency was kept as constant value 83.2 MHz by moving the tuner plate position at all gap distance of power coupler. When the gap distance between dee and power coupler was increased, the β was decreased and Z_0 was increased.

ISBN: 978-3-95450-205-9 doi:10.18429/JACoW-Cyclotrons2019-MOP030

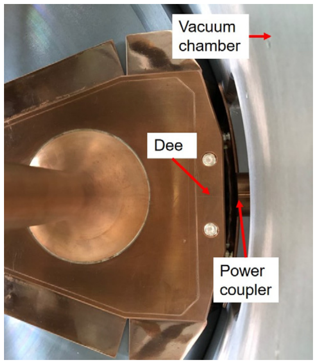

Figure 5: Dee and power coupler in SKKUCY-10 RF cavity.

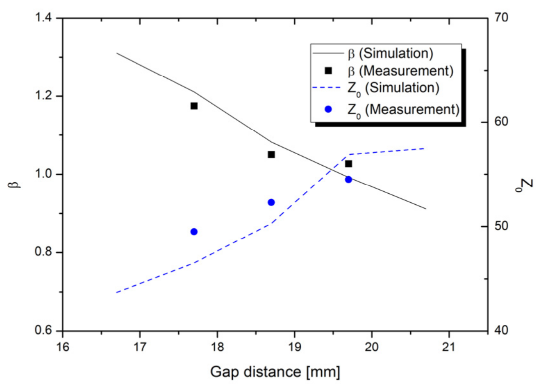

Figure 6: Results of RF coupling coefficient and characteristics impedance by power coupler.

CONCLUSION

The RF coupling coefficient and characteristic impedance were simulated and measured with consideration s of thermal and beam loading effect. The RF system of 10 MeV cyclotron (SKKUCY-10) was analysed with specifications, resonant frequency 83.2 MHz, Q_0 5830 and Dee voltage 40 kV with geometrical values resonator length 560 mm, Dee angle 35° and Stem radius 16 mm. The RF cavity of the SKKUCY-10 was fabricated and installed in side the electromagnet, and RF characteristics were measured with a network analyzer. The RF coupling coefficient and characteristic impedance for desired condition were selected at 1.08 and 52 Ω, respectively. The RF coupling coefficient and characteristic impedance were measured 0.8-1.2, 52-49 Ω according to temperature as 15-21°C. The power coupler was checked for optimization of RF coupling coefficient and characteristic impedance, and the results show good agreement with simulated and measured data.

ACKNOWLEDGEMENTS

This work was supported by the Radiation Technology R&D program through the National Research Foundation of Korea (NRF) funded by the Ministry of Science and ICT (2017M2A2A4A02020347).

REFERENCES

[1] J. J. Livingood, *Principles of Cyclic Particle Accelerators*: Van Nostrand, 1961.

[2] A. I. Papash and Y. G. Alenitsky, "Commercial cyclotrons. Part I: Commercial cyclotrons in the energy range 10–30 MeV for isotope production", *Physics of Particles and Nuclei,* vol. 39, no. 4, pp. 597-631, 2008. doi:10.1134/S1063779608040060

[3] P. K. Sigg, "RF for cyclotrons", *CAS-CERN Accelerator School: Specialized Course on Small Accelerators*, May-Jun. 2005, Zeegse, The Netherlands, pp. 231-251. doi:10.5170/CERN-2006-012.231

[4] J. Lee *et al.*, "Design of 83.2 MHz RF cavity for SKKUCY-10 cyclotron", *Nucl. Instr. Methods Phys. Res., Sect. A,* vol. 939, pp. 66-73, 2019. doi:10.1016/j.nima.2019.05.072

[5] C. D. Association, *High Conductivity Coppers*: CDA Publication, 1998.

[6] B.-N. Lee *et al.*, "Design study of an S-band RF cavity of a dual-energy electron LINAC for the CIS", *J. Korean Phys. Soc.,* vol. 64, no. 2, pp. 205-211, 2014. doi:10.3938/jkps.64.205

[7] CST Microwave Studio, https://www.cst.com

ISBN: 978-3-95450-205-9 doi:10.18429/JACoW-Cyclotrons2019-MOP031

DESIGN OF HIGH SENSITIVE MAGNET AND BEAM DYNAMICS FOR AMS CYCLOTRON

H. Namgoong[1], H. S. Kim[2], J. C. Lee[2], D.-H. Ha[1], M. Ghergherehchi[1] J.-S. Chai[1†]
Sungkyunkwan University, 2066 Seobu-ro, Jangan-gu, Suwon, Gyeonggi-do, Korea
[1]Dept of Electrical and Computer Engineering
[2]College of Information & Communication Engineering

Abstract

To produce a Carbon 14 for Accelerator Mass Spectrometry (AMS), AMS Cyclotron magnet was designed. For AMS system, Cyclotron magnet has been required high mass resolution. In order to realize high mass resolution, the phase error is designed within ±10 and the mass resolution was 5000. Cyclotron electromagnet was designed with a mass resolution of 5000, a harmonic number of 10, a center magnetic field of 0.5332 T, a maximum energy of 200 keV, a minimum turn separation of 1.2 mm. and a size of 1580 mm × 800 mm. We used CST particle studio and Cyclone for beam dynamics simulation of this cyclotron magnet. This paper describes AMS cyclotron magnet and beam dynamics design.

INTRODUCTION

Design of high sensitive magnet and beam dynamics study of AMS Cyclotron magnet was started in 2017 May at Sungkyunkwan University. The main purpose of AMS Cyclotron is accelerator mass spectrometry for medical purpose. Accelerated Carbon-14 beam can be used for mass spectrometry [1, 2].

This paper presents a design of high sensitive magnet and beam dynamics for AMS cyclotron. A magnet of AMS cyclotron is made of DT-4 steel with 10th harmonics. The main parameters of magnet are decided by 200 keV Carbon-14 beam. These main parameters are relation with size of magnet, power consumption, beam parameters. The accelerators for AMS system require high mass resolution.

DESIGN AND SYSTEM DESCRIPTION

The design process of cyclotron magnet is shown in Fig. 1. The main design parameter is decided at initial calculation. The maximum beam energy, dimension of cyclotron magnet size is the part of main design parameters. From the initial calculation, maximum energy of Carbon-14 beam is decided from the magnetic rigidity. The extraction radius set as 453.6 mm and central magnetic field is set to 0.5332 T so RF frequency is 5.8 MHz when the 10th harmonic is used. The approximate 3D modelling of the electromagnet was performed based on calculated main design parameters. The magnetic field of the 3D model of the electromagnet is analysed using TOSCA. After that, the phase error is calculated using the CYCLONE code and the reference field is designed using the phase error

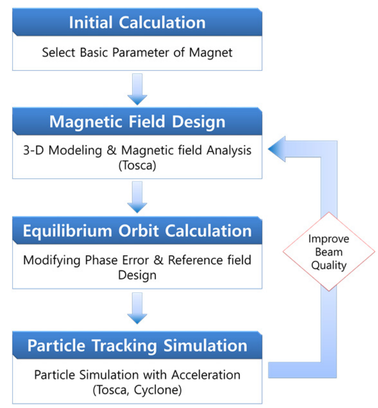

Figure 1: Cyclotron design process.

The designed magnetic field result from TOSCA were imported into CYCLONE. CYCLONE code calculates equilibrium orbit, phase error, single particle trajectory, tunes of designed magnetic field. The magnetic field error between reference field and designed field has calculated by using

$$\frac{\Delta B(r)}{B(r)} = \gamma^2(r)\frac{\Delta f_p(r)}{f_p(r)}. \quad (1)$$

The magnetic field was modified by magnetic field error from Eq. (1) [3]. The magnetic field error between reference field and designed field should be less than 10 Gauss for get high quality of Carbon-14 beam (Fig. 2).

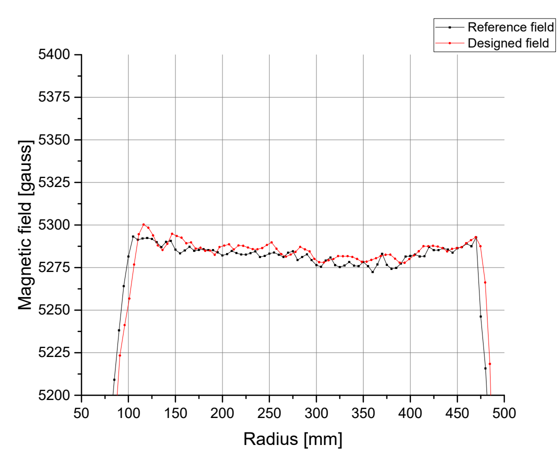

Figure 2: Magnetic field design.

† jschai@skku.edu

ISBN: 978-3-95450-205-9 doi:10.18429/JACoW-Cyclotrons2019-MOP031

The 3D drawing of AMS cyclotron magnet is shown as Fig. 3. This magnet has been adopted to design of low valley which can reduce the power consumption of magnet. The cyclotron ion source is injected vertically and a small hole in the center of the cyclotron was made for this purpose. A hole for the vacuum pump was also made in the center of the valley. The magnetic field design is based on basic design parameter and calculated by Opera 3D (TOSCA) [4]. The coil of AMS cyclotron specification is shown as Table 1 and the magnet specification is shown in Table 2. The power consumption of magnet coil was set as 2.75 kW. The power consumption has been modified by coil design.

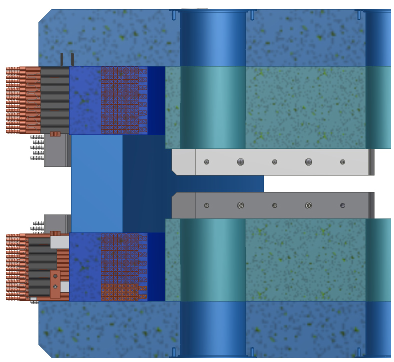

Figure 3: AMS magnet side view.

Table 1: AMS Cyclotron Coil Specification

Parameter	Value
Square	9 mm
Hole	4.5 Phi
Coil Turn	160
A-T	13700
Current	85 A
Voltage	32 V
Power	2.75 kW

RESULTS AND DISCUSSIONS

Figure 4 shows designed magnetic field and reference field. vertical tune is around 0.4, radial tune is around 1.01. Estimated RF Dee voltage is 300 V.

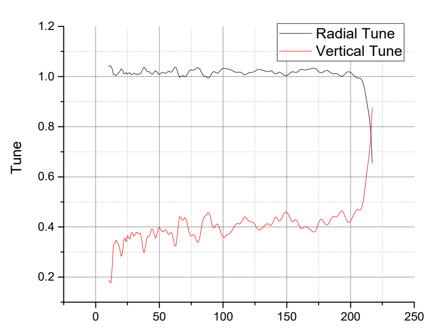

Figure 4: Tunes of magnetic field.

The reference particle is start with 20 keV and accelerated up to 200 keV. The location of RF cavity was set as the valley. Accelerating voltage was 5.8 MHz with the 10th harmonics. The beam trajectory is shown in Fig. 5.

Table 2: AMS Cyclotron Magnet Specification

Parameter	Value
Maximum energy	200 keV
Beam species	Carbon-14 negative
Ion source	Cs sputtering
Number of sectors	4
Hill angle	60°
Valley angle	40°
Pole radius	0.510 m
Extraction radius	0.453 m
Hill / Valley gap	0.25
Harmonic number	10
Radio frequency	5.8 MHz
Radial tune	~ 1.01
Vertical tune	0.4
B-field (min., max.)	0.137, 0.687 T

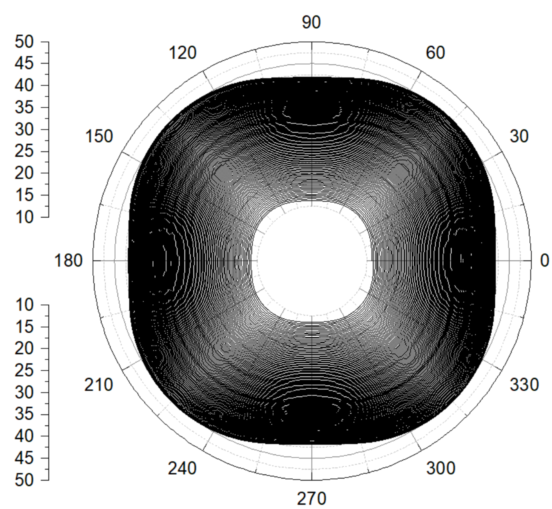

Figure 5: Single particle trajectory of Carbon-14.

The distribution of magnetic field on the z = 0 plane of the magnet is form 0.137 T to 0.687 T. A Carbon-14 beam is produced for an ion source and is injected on the cyclotron in the vertical direction. It is bent 90º through the inflector and starts acceleration at a radius of 138 mm. The Carbon-14 beam is accelerated to a Dee voltage of 300 V and rotates a total of 160 turns to 200 keV. Cyclotron for AMS require high mass resolution, which is calculated as

$$\frac{M}{\Delta M} = \frac{f}{\Delta f} \approx \pi h N. \qquad (2)$$

This cyclotron has 10th harmonics and 160 turns, the mass resolution is about 5000 according to Eq. (2) [5].

ISBN: 978-3-95450-205-9 doi:10.18429/JACoW-Cyclotrons2019-MOP031

The space where the Carbon-14 beam is accelerated is 315 mm (138 mm to 453 mm). The Carbon-14 beam rotates 160 turns in a space of 315 mm, the turn separation is optimized and the turn separation is shown in Fig. 6. Through magnetic field optimization, the minimum turn separation was optimized to 1.2 mm.

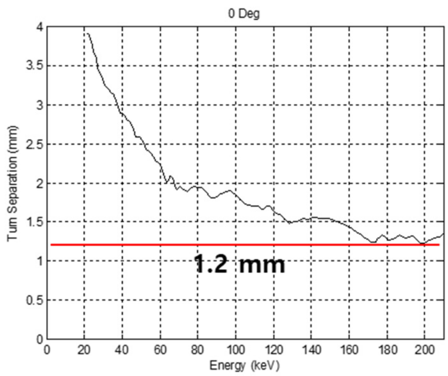

Figure 6: Turn separation of Carbon-14 beam.

CONCLUSION

In this study, Design of High Sensitive Magnet and Beam Dynamics for AMS cyclotron was done. The cyclotron for AMS with 200 keV Carbon-14 beam was designed and its mass resolution was 5000. To develop cyclotron for AMS system, magnetic field design for 200 keV Carbon-14 beam was performed and magnetic field optimization was performed within 10 Gauss. The optimized magnetic field was analysed using cyclone code. This cyclotron was manufactured by Korean company. The AMS cyclotron is being shimming with the goal of starting in 2020.

ACKNOWLEDGMENT

This work was supported by Radiation Technology R&D program through the National Research Foundation of Korea funded by the Ministry of Science, ICT & Future Planning. [2017M2A2A4A02020347, Development of an Accelerator Mass Spectrometer based on Artificial Intelligence].

REFERENCE

[1] J-W. Kim *et al.*, "Design study of a compact cyclotron for accelerator mass spectrometry." *J. Kor. Phys. Soc.*, vol. 54, no. 2, pp. 580-585, Feb. 2009.

[2] M. Chen *et al.*, "A New Type of Mini Cyclotron as Accelerator Mass Spectrometer", in *Proc. 14th Int. Cyclotron Conf. and Their Applications (Cyclotrons'95)*, Cape Town, South Africa, Oct. 1995, paper C-02, pp. 107-110.

[3] P. L. Rossiter, *The electrical resistivity of metals and alloys*, Cambridge University Press, 1987.

[4] operafea, http://operafea.com/

[5] D. J. Clark, "Cyclotrons as mass spectrometers", in *Proc. 10th Int. Cyclotron Conf. and their Applications (Cyclotrons'84)*, East Lansing, MI, USA, Apr.-May 1984, paper L03, pp. 534-539.

ISBN: 978-3-95450-205-9 doi:10.18429/JACoW-Cyclotrons2019-MOP032

CONTROL SYSTEM IN 10 MeV CYCLOTRON BASED ON IoT

M. Mohamadian†, H. Pashaei, N. Salmani, S. Babaee, M. Ghergherehchi[1], H. Afarideh,
Amirkabir University of Technology, Tehran, Iran
[1]also at Sungkyunkwan University, Suwon, South Korea

Abstract

Many The Internet of Things is one of the new most advanced technologies in the world. One of the applications of this technology is using it in places where remote control is preferred or it needs to control various processes at different times throughout the day. The cyclotron accelerator is one such system in which the start-up process until radio medicine production requires continuous monitoring and inspection. In this research, we have tried to use the internet of things technology in the process of cyclotron control system specially in fine tuning section.

INTRODUCTION

Every process needs control and monitoring to properly execute and monitor performance. The purpose of the cyclotron accelerator control system is to do the same. System control will also prevent possible damage and facilitate troubleshooting.

In the past, the cyclotron control system was fully hardware designed by relays and then wired. The major drawback of this method was that, if there was a change in the control system, the hardware and wiring of the relays would also have to be changed. This increased the cost and time. Relay systems also had a slower operating speed and were much more difficult to troubleshoot due to wired communication.

With the advent of intelligent control devices and the use of a series of programmable tools and software that operate intelligently, the above issues have been resolved, as well as with the benefits of smaller system dimensions and the possibility to exchange information with other systems, causes that using the Internet of Things for ease of communication.

Our 10 MV cyclotron is comprised of several components including: magnet, RF system, vacuum system, cooling section and ion source. Each of these parts contains components that must be carefully monitored by accurate sensors during the process, and if necessary, automatically assigned the commands to these parts. As a result, it is better to have all of its subsystems intelligently controlled and monitor in order to sustain the cyclotron accelerator performance. All of these subsystems are controlled by programable components and have a communication through the IoT protocols. In this research, we have tried to use the internet of things technology in the process of cyclotron control system specially in fine tuning section.

CYCLOTRONS

As mentioned, the cyclotron accelerator is composed of various components, including ion sources, magnets, cavities, and the vacuum system. When the charged particles leave the ion source, they travel through the space between the poles and accelerate as they pass through the cavity. What drives the charged particles in this device is a variable electric field generated by the cavity. And what holds the particles in a circular path is the force of the magnetic field. Thus, the particle is accelerated through the electric field and driven by the magnetic field, both focal and in a circular path, after being injected into the middle plane and positioned in the appropriate rotation plane. Finally, the particle is extracted by a stripper in a radius of proper energy [1].

Accelerators are used in the medical field to produce diagnostic radio-medicine, radiotherapy, and rapid neutron production for the treatment of cancers. The 10 MeV cyclotron was designed to produce FDG radio-medicine for PET spectroscopy.

INTERNET OF THINGS (IoT)

IoT technology is the creation of a global network of uniquely addressable objects based on a standard communication protocol. Active involvement of "objects" in commerce, information gathering and processing processes while being able to interact with each other and with the environment, with the ability to transmit information and to respond automatically to natural or physical events by performing a process or without direct human intervention in many industries can be helpful.

Not long after the idea of the IoT was developed by Kevin Ashton, who pointed to factors such as increasing data volume in the world, the importance of controlling objects, human limitations, time, speed and accuracy. But in various industries and everyday life is expanding rapidly.

In the IoT structure, the human structural system is inspired by the way that equipment and sensors play the same role as the human five senses and wireless cellular networks, local area networks, data storage and processing security, and transactional and analytical systems, replaces the brain. As a result, the system consists of three main parts: sensors, communications and protocols, and data processing.

In each application, the sensors are characterized by what is appropriate for that control system. In the selection of sensors, the type of sensor and the its accuracy should be specified and taken into account.

For the cyclotron, these sensors include pick up probes for feedback from the RF field inside the cavity, directional coupler outputs to investigate the rate of return wave at the beginning of the tuning system, tuner capacitor location, phase and frequency of the RF signal from the LLRF section, temperature and Pressure sensors, output beam flow, etc. [2].

† m.mohamadian@gmail.com

ISBN: 978-3-95450-205-9 doi:10.18429/JACoW-Cyclotrons2019-MOP032

In order to achieve the goals of IoT and what it is intended for, smart devices must be able to seamlessly exchange information. The collected information should then be sent to the server through the infrastructure, then the data analysed and the commands sent to the devices, applications, or individuals, as shown in Fig. 1. In cyclotron control system, these communications are considered in two ways: Wi-Fi and cable communications. Also, data processing in the central operating system and data transfer is done through PLC and Raspberry Pi interacting with each other according to expected performance.

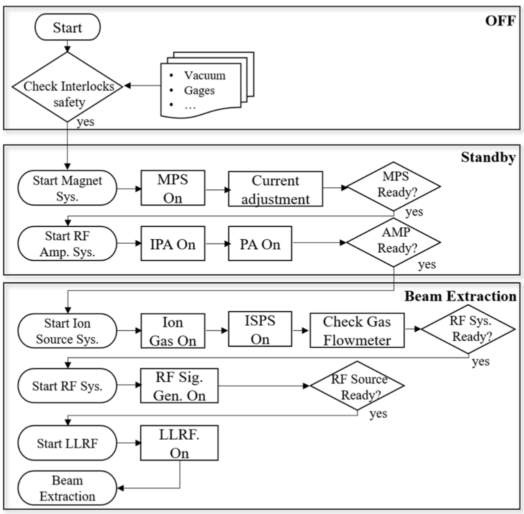

Figure 1: The different parts relation to each other and the algorithm used in programming.

CYCLOTRON CONTROL SYSTEM

As mentioned, cyclotron controlled subsystems include: cooling system control, cyclotron vacuum control, magnet system control, RF system control, etc., as shown in Fig. 2.

In order to launch the cyclotron correctly, all of these sections will start in order of priority, at specified intervals and after checking all the necessary conditions at each step. The below flowchart shows the sequence of these steps [3].

One of the major obstacles to the development of IoT equipment is the sometimes costly expense of producing it. But due to tools such as Raspberry Pi and the ever expanding ecosystem development, IoT projects should not be expensive. There are four models of the Pi Machine: Model A, Model B, Compute and Zero. In this system uses a 32-bit Raspberry Pi 3 B with 1 GHz processor and 512 MB of RAM, which is shared with the GPU. An array of general-purpose input/output (GPIO) pins are provided at Raspberry Pi. For example, the PWM module in the GPIO of Raspberry is used to control the tuner servo motor. These pins can be used for various control tasks. Python programming is also used for its programming.

In this research, we sought to streamline and smarting the cyclotron control process and to enable remote control and monitoring by IoT devices. Therefore, all control processes previously controlled through the LLRF and PLC sections were seamlessly designed in a new context as remote controls.

CONCLUSION

IoT can be used in various industries to increase efficiency, reduce costs, as well as control the system, making it easier to prevent potential damage and troubleshooting systems. In the design of the desired 10 MVA cyclotron, all control systems, in an integrated context, allow remote control and monitoring using IoT protocols. All processes are remotely done at the start of the system and all control signals are evaluated side by side. And during operating the system, the need to be near the device should be eliminated. This improves the safety of users and also controls the performance of the device more precisely.

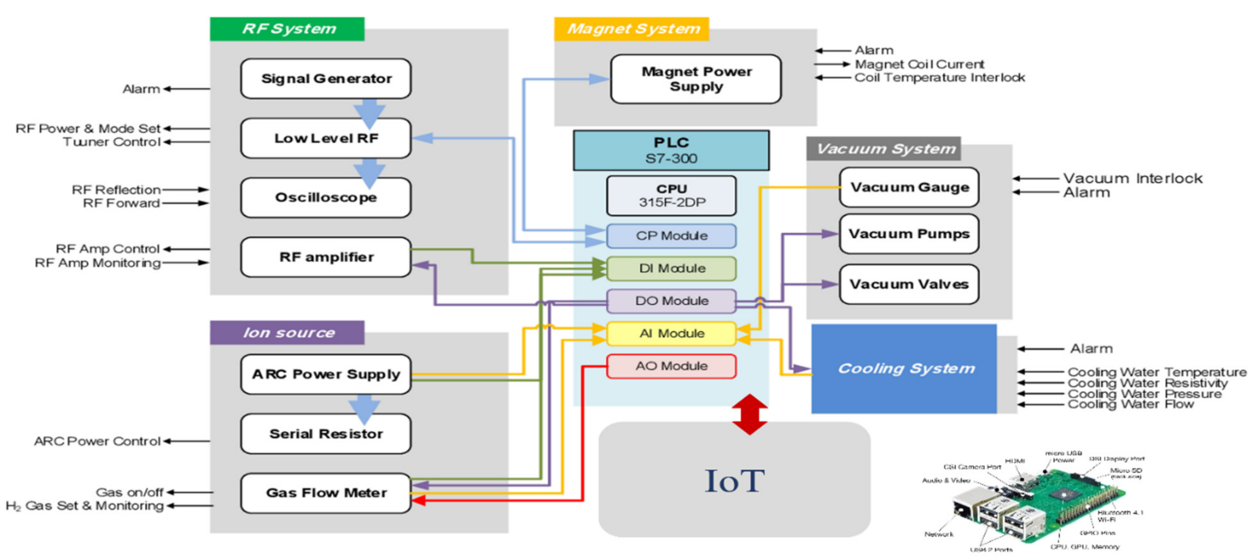

Figure 2: The 10 MeV cyclotron control system.

ISBN: 978-3-95450-205-9 doi:10.18429/JACoW-Cyclotrons2019-MOP032

REFERENCES

[1] M. Mohamadian, H. Afarideh, and M. Ghergherehchi, "Accurate Electromagnetic Simulation and design of cyclotron cavity", *IEEE Trans. Nucl. Sci.*, vol. 64, no. 2, pp. 809-815, Feb. 2017. doi:10.1109/TNS.2016.2646841

[2] M. Hassani, H. Afarideh, and Y. Ghorashinejad, "Development of control system for 10 MeV cyclotron", in *Proc. 21st Int. Conf. on Cyclotrons and their Applications (Cyclotrons'16)*, Zurich, Switzerland, Sep. 2016. doi:10.18429/JACoW-Cyclotrons2016-THP07

[3] A. Abdorrahman, S. Malakzade, H. Afarideh, G. Aslani, A. Afshar, M. Ghergherehchi, and J. Chai, "Control system of 10 MeV Baby Cyclotron", in *Proc. 20th Int. Conf. on Cyclotrons and their Applications (Cyclotrons'13)*, Vancouver, BC, Canada, Sep. 2013, paper TUPPT001, pp. 156-158.

ISBN: 978-3-95450-205-9 doi:10.18429/JACoW-Cyclotrons2019-MOP034

BEAM STRIPPING INTERACTIONS IMPLEMENTED IN CYCLOTRONS WITH OPAL SIMULATION CODE

P. Calvo*, C. Oliver, CIEMAT, Madrid, Spain
A. Adelmann, M. Frey, A. Gsell, J. Snuverink, Paul Scherrer Institut, 5232 Villigen PSI, Switzerland

Abstract

Beam transmission optimization and losses characterization, where beam stripping interactions are a key issue, play an important role in the design and operation of compact cyclotrons. A beam stripping model has been implemented in the three-dimensional object-oriented parallel code OPAL-CYCL, a flavor of the OPAL framework. The model includes Monte Carlo methods for interaction with residual gas and dissociation by electromagnetic stripping. The model has been verified with theoretical models and it has been applied to the AMIT cyclotron according to design conditions.

INTRODUCTION

Compact cyclotrons are one of the most versatile accelerators involved in radioisotope production employed in PET scans as diagnostic tools in hospitals. Due to short lifetimes of some radioisotopes, it is recommended that the accelerator facility is located inside the hospital, thus the compactness is a relevant factor. Hence, superconducting magnets can be used to increase the magnetic field, minimizing the acceleration region and consequently reducing the overall cyclotron size. An internal ion source must be considered as well. However, technical complications arise in the design and manufacturing processes. Given the worsening of the vacuum due to the internal source, combined with the limited space of acceleration region and the amount of components in the accelerator, the vacuum conditions could be a considerable source of losses, even more in the case of H$^-$ beams. As a consequence, beam current will be reduced, as well as the efficiency and radioisotope production. Additionally it could increase the activation of the machine. Thus, optimization of beam transmission as well as minimization of activation associated with lost particles, is of great importance in compact cyclotrons. Specifically, it is essential to study the effect of some residual physics phenomena, as the interaction of the beam with residual gas and electromagnetic stripping. In this paper a general beam stripping model is presented being integrated into the particle accelerator framework OPAL [1]. It allows a more realistic description of the beam dynamics and a characterization of the losses.

AMIT CYCLOTRON

A compact cyclotron is being developed as part of the AMIT project, aimed at the production of single doses of ^{18}F and ^{11}C radioisotopes. The AMIT cyclotron has been designed to improve the size and cost efficiency limitations through a careful study of the electromagnetic design [2] and the beam dynamics [3]. The machine aims to produce a 10 μA beam of 8.5 MeV protons. It is a Lawrence type cyclotron with weak focusing. It employs two superconducting coils in a Helmholtz arrangement and magnetic iron yoke to provide the 4 T magnetic field and a 180° Dee attached to the RF cavity, with a 60 kV accelerating peak voltage imposed by the non RF-particle isochronism, to accelerate H$^-$ ions produced by a cold cathode Penning Ion Source, and with stripping mechanism for beam extraction. The superconducting magnet [4] of NbTi has a warm iron configuration, where only the coils are kept cold inside a common cryostat. It is cooled down with two-phase helium, circulating in a closed circuit and recondensed externally.

Figure 1: General arrangement of the AMIT cyclotron.

BEAM STRIPPING

H$^-$ ions have become increasingly popular in cyclotrons due to high efficiency extraction process. However, the second electron of this type of hydrogen has a low bounding energy (0.75419 (2) eV [5]). Therefore, the electron has a high probability of being stripped by interaction with residual gas or with electromagnetic field, increasing beam losses. Other types of ions, or even neutral particles, are also affected, although with less probability. The processes are classified according to the charge state of the particle, $\sigma_{qq'}$, where q represents the charge state before and q' after the process. The processes to be considered in case of H$^-$ are single- or double-electron-detachment (σ_{-10} or σ_{-11}). Regarding protons, the process available is electron capture.

Assuming that particles are normally incident on a homogeneous medium and that they are subjected to a process with a mean free path λ between interactions, the probability density function for the interaction of a particle after travelling a distance x is [6]:

$$F(x) = \frac{1}{\lambda} \cdot e^{-x/\lambda} \qquad (1)$$

where $F(x)dx$ is the probability of having an interaction between x and x+dx. Hence, the probability of an interaction

* pedro.calvo@ciemat.es

ISBN: 978-3-95450-205-9 doi:10.18429/JACoW-Cyclotrons2019-MOP034

before reaching a path length x can be deduced:

$$P(x) = \int_0^x F(x)dx = 1 - e^{-x/\lambda} \tag{2}$$

where $P(x)$ is the statistic cumulative probability of the interaction process. In case of interaction between a beam with particles of a material, the process is generally described under some considerations in terms of the cross section, σ, and the number of interaction particles per unit volume, N: $\lambda = 1/N\sigma$.

Residual Gas Interaction

The fraction loss of the beam travelling a unit length is, according to Eq. (2):

$$f_g = 1 - e^{-x/\lambda_{total}} \tag{3}$$

where λ_{total} is the summation over all gas components and over all physical processes for each component, supposing a beam flux incident in an ideal gas.

The cross section data have been measured experimentally for the most important gases [7–11]. However, analytic expressions fitted to cross section data have been semiempirically developed for collisions of hydrogen atoms and ions with some gaseous atoms and molecules [12]:

$$\sigma_{qq'} = \sigma_0 \left[f(E_1) + a_7 \cdot f(E_1/a_8) \right] \tag{4}$$

where σ_0 is a convenient cross section unit ($\sigma_0 = 1 \cdot 10^{-16}$ cm^2); and $f(E)$ and E_1 are given by:

$$f(E) = \frac{a_1 \cdot \left(\frac{E}{E_R}\right)^{a_2}}{1 + \left(\frac{E}{a_3}\right)^{a_2+a_4} + \left(\frac{E}{a_5}\right)^{a_2+a_6}} \tag{5}$$

$$E_R = hcR_\infty \cdot \frac{m_H}{m_e} = \frac{m_H e^4}{8\varepsilon_0^2 h^2} \tag{6}$$

$$E_1 = E_0 - E_{th} \tag{7}$$

where E_0 is the incident projectile energy in keV, E_{th} is the threshold energy of reaction in keV, and a_i $(i = 1, \ldots, 8)$ denote adjustable parameters. Experimental data and analytical function results for σ_{-10} on H_2 are shown in Fig. 2.

Electromagnetic Stripping

When a particle is in a magnetic field, electrons and nucleus are bent in opposite directions according to their electric charge. If magnetic field is strong enough, the slightly bounded electron can be stripped. Electromagnetic stripping for ions in an accelerator are able to be analysed as the decay of an atomic system in a weak and static electric field, as the magnetic field produces an electric field according to Lorentz transformation, $E = \gamma\beta cB$.

The fraction of particles dissociated by electromagnetic fields after a travelled distance x during a time t is a function of energy and magnetic field B, according to Eq. (2):

$$f_{em} = 1 - e^{-x/\beta c\gamma\tau} = 1 - e^{-t/\gamma\tau} \tag{8}$$

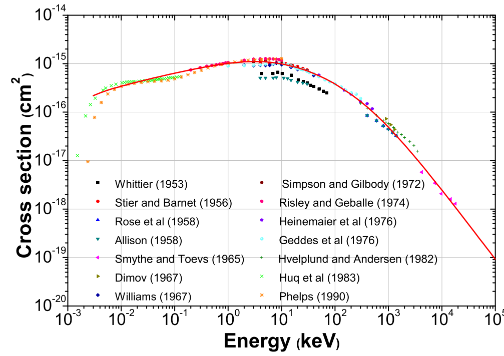

Figure 2: Single electron detachment cross sections experimental data for H^- on H_2 with analytic fit.

where τ is the particle lifetime in the rest frame.

Theoretic studies [13] have determined the lifetime τ of an H^- ion in an electric field E. Nevertheless, it is more common to parametrize the decay time taking into account approximations according to experimental approach [14]:

$$\tau = \frac{A_1}{E} \cdot \exp\left(\frac{A_2}{E}\right) \tag{9}$$

where A_1 and A_2 are functions of binding energy experimentally determined [15]: $A_1 = 3.073\,(10) \cdot 10^{-6}$ s V/m and $A_2 = 4.414\,(10) \cdot 10^9$ V/m.

RESULTS AND DISCUSSION

One of the unique features of OPAL is to perform not only the particle tracking through an accelerator or beam line, but also a Monte Carlo simulation of the beam interaction with matter. Hence, beam stripping has recently been incorporated in OPAL-CYCL to improve physical interaction models. The variables that determine vacuum conditions have been included through assignment of pressure and temperature, considered constant in the first approximation. The magnetic field map, already incorporate in OPAL-CYCL, is taken into account. Thus, beam fraction lost is evaluated individually for each particle in each step of the tracking through a Monte Carlo method according to the description presented in previous section. The implementation for beam stripping is focused on atomic hydrogen ion interaction although the model can be easily extended to other ions as H_2^+. The cross section values are derived from Eq. (4) and evaluated as function of particle energy. Furthermore the code development for beam stripping allows to trace optionally secondary particles produced during the interaction.

The implementation of the residual gas interaction has been validated evaluating beam losses in simulations of H^- particles in air at different energies in a drift space at $P = 1.0 \cdot 10^{-6}$ mbar, compared in Fig. 3 with theoretical fraction lost. In a similar way, the electromagnetic stripping has also been tested for a beam at 100 MeV in a 2.3 T magnetic field, getting a fraction lost of 0.570 (10) m^{-1}, which is in a good agreement with the theoretical results (0.571 m^{-1}).

ISBN: 978-3-95450-205-9 doi:10.18429/JACoW-Cyclotrons2019-MOP034

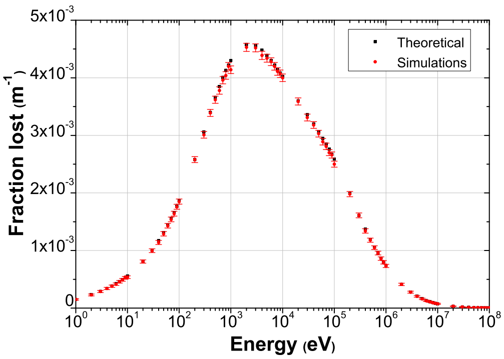

Figure 3: Fraction lost by residual gas interaction of a H^- beam as function of energy.

Once the code validation was achieved, simulations applied to the AMIT cyclotron have been carried out to evaluate losses due to beam stripping. The vacuum conditions are of special relevance, since being a compact cyclotron, ultra high vacuum cannot be achieved. An internal study concludes that a vacuum level between 10^{-5} and 10^{-4} mbar could be achieved. However, the level depends on the nominal flow in the ion source. Thus, firstly, some characterization measurements of the AMIT internal ion source have been performed in a versatile test bench designed for the optimization of ion sources [16]. The flow rate has been optimized considering the discharge characteristics of the source and reached beam current. Beam stripping analysis allows us to obtain the relationship between vacuum level and beam losses (Fig. 4), as well as characterize the energy profile of the losses (Fig. 5), which would increase the activation of the facility, and could cause hot spots in some components.

CONCLUSION

A new feature of physics interaction model in the beam dynamics code OPAL for beam stripping reactions was presented. The model uses analytic expressions to evaluate individually the cross section of different reactions as function of energy of the particles and theoretical studies about

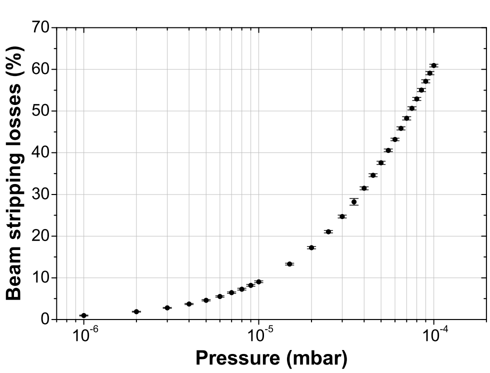

Figure 4: Beam stripping losses as a function pressure for optimum AMIT operational conditions.

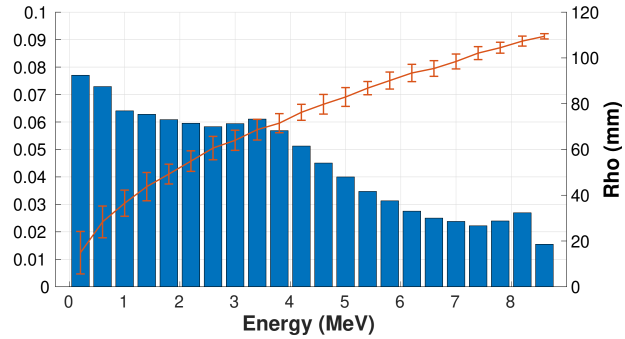

Figure 5: Beam stripping losses characterization at $P = 1.0 \cdot 10^{-5}$ mbar. Energy distribution normalised (left side) and confidence interval of radial position (right side) of corresponding particles to each bar of the histogram.

lifetime of hydrogen ions in electromagnetic fields. The model implementation shows excellent agreement with the analytical model. Moreover, this new implementation is an essential tool that allows us to optimize the design of the AMIT cyclotron to characterize beam transmission and minimize losses.

ACKNOWLEDGEMENTS

The main author thanks the Laboratory for Scientific Computing and Modelling at Paul Scherrer Institute (LSM-PSI) and the OPAL developers core for the opportunity to perform this research. This work was partially supported by the computing facilities of Extremadura Research Centre for Advanced Technologies (CETA-CIEMAT), funded by the European Regional Development Fund (ERDF). CETA-CIEMAT belongs to CIEMAT and the Government of Spain.

REFERENCES

[1] A. Adelmann *et al.*, "OPAL a versatile tool for charged particle accelerator simulations", May 2019. arXiv:1905.06654

[2] D. Gavela *et al.*, "Calculation and design of a RF cavity for a novel compact superconducting cyclotron for radioisotope production (AMIT)", in *Proc. IPAC'15*, Richmond, VA, USA, May 2015, pp. 3055–3057. doi:10.18429/JACoW-IPAC2015-WEPMN057

[3] C. Oliver *et al.*, "Optimizing the radioisotope production with a weak focusing compact cyclotron", in *Proc. Cyclotrons'13*, Vancouver, BC, Canada, Sep. 2013, paper WE4PB03, pp. 429-431.

[4] L. García-Tabarés *et al.*, "Development of a superconducting magnet for a compact cyclotron for radioisotope production", *IEEE Trans. Appl. Supercond.*, vol. 26, no. 4, art. seq. no. 4402004, pp. 1–4, 2016. doi:10.1109/TASC.2016.2548429

[5] K. R. Lykke, K. K. Murray, and W. C. Lineberger. "Threshold photodetachment of H^-", *Phys. Rev. A*, vol. 43, no. 11, p. 6104, 1991. doi:10.1103/PhysRevA.43.6104

ISBN: 978-3-95450-205-9 doi:10.18429/JACoW-Cyclotrons2019-MOP034

[6] W. R. Leo, *Techniques for Nuclear and Particle Physics Experiments*. Berlin, Heidelberg: Springer-Verlag, second edition, 1994. doi:10.1007/978-3-642-57920-2

[7] P. Hvelplund and A. Andersen, "Electron loss by fast He^+, He, H^- and He^- projectiles in collisions with atomic and molecular hydrogen", *Phys. Scr.*, vol. 26, no. 5, p. 370, 1982. doi:10.1088/0031-8949/26/5/004

[8] Y. Nakai, A. Kikuchi, T. Shirai, and M. Sataka, "Data on collisions of hydrogen atoms and ions with atoms and molecules (i)", JAERI, Tokai, Japan, Rep. JAERI-M 83-013, Feb. 1983.

[9] M. S. Huq, L. D. Doverspike, and R. L. Champion, "Electron detachment for collisions of H^- and D^- with hydrogen molecules", *Phys. Rev. A*, vol. 27, no. 6, p. 2831, 1983. doi:10.1103/PhysRevA.27.2831

[10] Y. Nakai, A. Kikuchi, T. Shirai, and M. Sataka, "Data on collisions of hydrogen atoms and ions with atoms and molecules (ii)", JAERI, Tokai, Japan, Rep. JAERI-M 83-143, Sep. 1983.

[11] A. V. Phelps, "Cross sections and swarm coefficients for H^+, H_2^+, H_3^+, H, H_2 and H^- in H_2 for energies from 0.1 eV to 10 KeV", *J. Phys. Chem. Ref. Data*, vol. 19, p. 653, 1990. doi:10.1063/1.555858

[12] Y. Nakai, T. Shirai, T. Tabata, and R. Ito, "Cross sections for charge transfer of hydrogen atoms and ions colliding with gaseous atoms and molecules", *At. Dat. Nucl. Dat. Tables*, vol. 37, no. 1, p. 69, 1987. doi:10.1016/0092-640X(87)90005-2

[13] L. R. Scherk, "An improved value for the electron affinity of the negative hydrogen ion", *Can. J. Phys.*, vol. 57, no. 4, pp. 558–563, 1979. doi:10.1139/p79-077

[14] G. M. Stinson, W. C. Olsen, W. J. McDonald, P. Ford, D. Axen, and E. W. Blakmore, "Electric dissociation of H-ions by magnetic fields", *Nucl. Instrum. Meth.*, vol. 74, p. 333, 1969. doi:10.1016/0029-554X(69)90359-0

[15] P. B. Keating, "Electric-field-induced electron detachment of 800-MeV H^- ions", *Phys. Rev. A*, vol. 52, no. 6, p. 4547, 1995. doi:10.1103/physreva.52.4547

[16] D. Obradors-Campos *et al.*, "Characterization of the AMIT internal ion source with a devoted DC extraction test bench", in *Proc. IPAC'17*, Copenhagen, Denmark, May 2017, pp. 1740–1742. doi:10.18429/JACoW-IPAC2017-TUPIK030

ISBN: 978-3-95450-205-9 doi:10.18429/JACoW-Cyclotrons2019-MOP035

EXTRACTION BEAM ORBIT OF A 250 MeV SUPERCONDUCTING CYCLOTRON*

H. J. Zhang, K. J. Fan†, Y. Yan
State Key Laboratory of Advanced Electromagnetic Engineering and Technology,
L. G. Zhang, Huazhong University of Science and Tech., Hubei, China, HUST, Wuhan, China
Y. N. Rao, TRIUMF, Vancouver, BC Canada

Abstract

A superconducting cyclotron based on proton therapy facility is being developed at Huazhong university of science and technology (HUST). Due to the compact size of the main magnet, the beam orbits at the extraction region are distributed densely, which creates difficulties for beam extraction leading to severe beam loss. In order to deal with these challenges, the orbit precession method has been employed in the extraction system design. In this paper, we introduce a method of employing a first harmonic field near the $\nu_r = 1$ resonance where the beam energy is about 248 MeV to adjust the amplitude of beam orbit oscillation. The optimum amplitude and phase of the first harmonic field are designed to obtain a large turn separation in the extraction region. Three different ways of generating the first harmonic field are compared for optimization.

INTRODUCTION

As a kind of radiotherapy, proton therapy is becoming increasingly more accepted, which is preferred for most tumors due to minimal damage to healthy tissues and precise local dose control. Proton therapy is considered to be the most effective radiotherapy for cancer, with a cure rate of 80% [1].

The superconducting cyclotron HUST-SCC250 based on proton therapy facility has excellent advantages of economy and compactness, but it also complicates the electromagnetic structure. The orbit separation at the extraction region is usually smaller than the beam size, which makes the extraction efficiency very low. Resonant extraction denotes the focusing oscillation is coherently excited, thus enhancing the distance between successive turns and facilitating extraction of the beam.

In this paper, particle tracking code CYCLOPS is used to analyze the magnetic field and find the location of $\nu_r = 1$ resonance, where the first harmonic covering a radial range of 2 cm is introduced to increase the turn separation [2]. In order to find the appropriate phase of the first harmonic field, the particles are tracked by CYCLONE code so that the amplitude of the field is determined to be 12 Gs, and the phase is 20°~45°. Finally, there are three ways to create the first harmonic field.

* The work is supported by the National Nature Science Foundation of China (11775087).
† kjfan@hust.edu.cn

STATIC ORBIT PROPERTIES ANALYSIS

The static equilibrium orbit (SEO) characteristics of the given magnetic field maps plays an important role in the study of cyclotron extraction orbit. The level of isochronism of the field is represented by the difference of the nominal rf angular frequency ω_0 and the revolution angular frequency of particle along the SEO ω, which is given as $(\omega_0/\omega - 1)$. Figure 1 shows the evolution of the isochronism from low energy of 5 MeV to the extracted beam energy of 252.6 MeV, which is calculated with an energy step of 0.4 MeV.

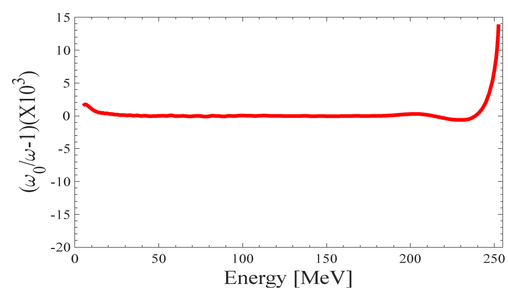

Figure 1: The isochronism parameter $(\omega_0/\omega - 1)$ vs. energy.

The isochronism of the given magnetic, which varies around zero over the energy range, provides essential information for calculating the phase shift by the well-known phase-energy equation:

$$\Delta(\sin\phi) = \sin\phi_f - \sin\phi_i = \frac{2\pi h}{\Delta E}\int_{E_i}^{E_f}\left(\frac{\omega_0}{\omega} - 1\right)dE \qquad (1)$$

where h is the rf harmonic number, ΔE is the energy gain per turn. Figure 2 shows the results calculated with h = 2 and ΔE = 0.4 MeV/Turn.

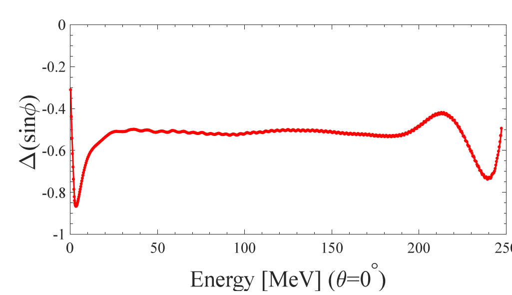

Figure 2: The phase shift $\Delta(\sin\phi)$ vs. energy.

The initial phase $\phi_i = 32.8°$ is chosen such that the integral of $\sin\phi$ over the whole energy range equals to zero, so

ISBN: 978-3-95450-205-9 doi:10.18429/JACoW-Cyclotrons2019-MOP035

as to minimize the energy spread of beam at the extraction region.

DESIGN OF EXTRACTION ORBITS

The precession extraction basically is achieved by a perturbation of the first harmonic which provides a driving force in resonance, namely:

$$b(r,\theta) = b_1(r)\cos(\theta-\theta_0) \tag{2}$$

where $b_1(r)$ is more nearly Gaussian distributed. Applying the WKB approximation (neglecting non-linear effects) to analyze the resonance, the oscillation amplitude after the effective duration n_{eff} is as follows:

$$A=\pi R n_{eff}\frac{b_1}{B_0} \tag{3}$$

where

$$(n_{eff})^{-2}=\left|\frac{d\nu_r}{dn}\right| \tag{4}$$

ν_r is the radial oscillation frequency, R is the orbit radius at ν_r=1, and the average field B_0 is calculated at R. The radial position of particles near the extraction can be expressed as:

$$r = r_0 + A\cos\varphi \tag{5}$$

where r_0 is the radial position without harmonic field, φ is the phase of the radial oscillation caused by the harmonic field. The turn separation at the extraction region is:

$$\begin{aligned}\Delta r &= \Delta r_0 + A\cos[\varphi+2\pi(\nu_r-1)] - A\cos\varphi \\ &= \Delta r_0 + A\sin[2\pi(\nu_r-1)]\end{aligned} \tag{6}$$

Choosing the appropriate initial phase and effective duration to make $\varphi \approx \pi/2$ at the extraction region, the first harmonic covers the range of the radial oscillation frequency ν_r from 1.2 to 0.8, to obtain the required turn separation [3]. Using a field bump with amplitude of 12 Gs, the enough turn separation Δr=5 mm can be obtained. Figure 3 shows the resulting turn ν_r vs. energy.

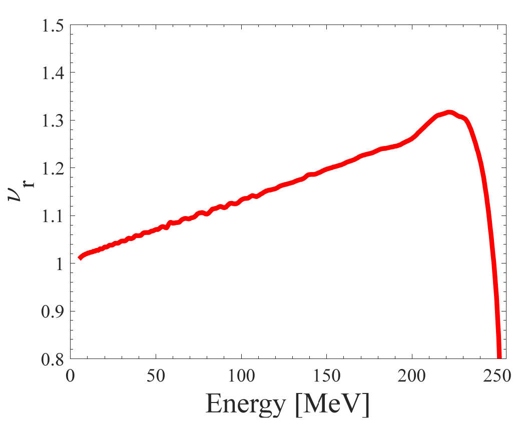

Figure 3: The ν_r vs. energy.

Figure 3 implies that the ν_r=1 resonance occurs at E=247.8 MeV so that the first harmonic field should distribute between E=240 MeV and 251 MeV. Assuming the phase search range of the first harmonic is 0~2π, Fig. 4 shows the evolution of the radial phase space from E=240 MeV to 251 MeV with harmonic field phase of 0°, 90°, 180° and 270° when the amplitude of the field is 12 Gs.

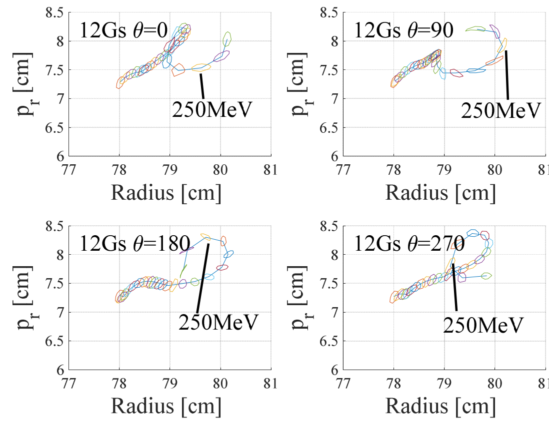

Figure 4: The phase diagrams (12 Gs $\theta_0=0^\circ\sim270^\circ$). Phase space motion with precession near the extraction region.

For the harmonic magnetic field with phase of 90°~270° the orbit is staggered and compressed near the extraction, which cannot satisfy the purpose of increasing the turn separation at the extraction region. A set of phase diagrams of beam radial motion was calculated with field phase of 20°, 45° and 70°, as shown in Fig 5.

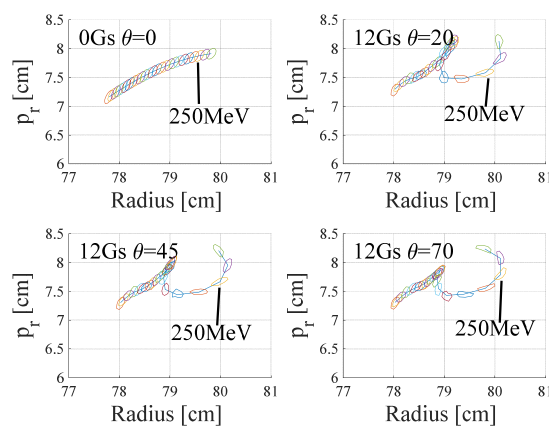

Figure 5: The phase diagrams of the extracted beam under different phase. The turn separation of more than 4.7 mm can be obtained in the phase range between 20°~45°.

As the beam accelerates through ν_r=1 resonance, there is a slowly growth in orbit displacement up to 4.7mm for the first harmonic field with phase of 20°~45°, which is beneficial to beam extraction. With appropriate harmonic field phase of θ_0 the precession extraction will yield a large space between orbits at the entrance angular position of the electrostatic deflector (ESD) θ=182°. For the harmonic field with amplitude of 12 Gs and with phase of 45°, the single particle acceleration orbit is obtained as shown in the right portion of Fig. 6. Compared with the

ISBN: 978-3-95450-205-9 doi:10.18429/JACoW-Cyclotrons2019-MOP035

orbit without harmonic field in the left portion of Fig. 6, the turn separation increases obviously.

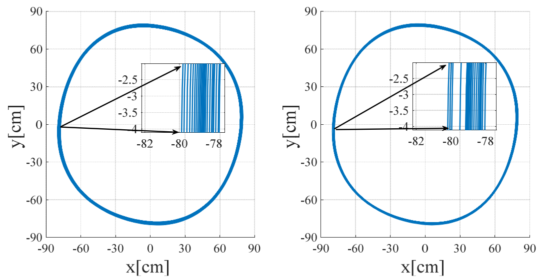

Figure 6: Left: the acceleration orbit without harmonic field. Right: the acceleration orbit When the amplitude of the harmonic field is 12 Gs and the phase is 45°. The turn separation increases obviously.

THE WAY OF INTRODUCING FIRST HARMONIC

The generation of the first harmonic can generally be achieved by two methods: (1) In active method, the magnetic field is introduced by trim coils. (2) In passive method, the trim-rods or magnet shimming is employed to generate a disturbance field by changing the structure of the magnet at the extraction region.

Trim Coil

Trim coils distributed on the hills of the main magnet are employed at the extraction region to create the desirable field. By independently controlling the current of the four coils, the continuous and adjustable amplitude and phase of the first harmonic field can be obtained. The ampere turn of coils should be calculated by 150 to ensure that the amplitude of the field reaches 12 Gs [2].

Trim-rod

Compared with the trim coil, the magnetic field generated by the trim-rods which are located on the central line of the magnetic pole is more predictable and stable. In order to adjust the amplitude of the first harmonic field from 0 to 10 Gs, the depth of trim-rod should exceed 15 cm [4]. Due to the wider radial distribution of the magnetic field generated by the trim-rod, its side effect on the isochronal field is inevitable. Therefore, it is necessary to re-shimming the magnet after determining the position of the rest positions of trim-rods.

Magnet Shimming

Trim coil and trim-rod are always avoided in superconducting cyclotron accelerating single particle species. The beam extraction of this kind of cyclotron is mainly achieved by radial and axial pole shaping.

The magnet shimming is an iterative process, which consists of two steps: (1) Determining the field error (2) Predicting the modification of the magnet pole shape according to the field error in step (1) [5].

For the second step, the modification of the pole shape can be achieved by three methods: (1) The methods based on analysis or experience; (2) Linear transformation of magnetic field errors using hard-edge approximation; (3) Matrix method including non-linear edge field effect. The hard-edge approximation can be used to transform field errors into shape changes, thus a series of studies discussed the magnet model and the effect of edge cutting on the local magnetic field. A. Papash et al. proposed a shimming algorithm based on a set of analytic formulas [6]. W. Kleeven et al. introduced a more sophisticated solution to relate pole shaping with a large computational matrix containing the effect of isochronous field errors and harmonic field effects [7].

CONCLUSION

This paper introduces the design of beam orbit on the extraction of 250 MeV superconducting cyclotron. Utilizing several codes, such as MATLAB, CYCLOPS and CYCLONE, to track the orbit, an optimized first harmonic with the phase of 20°~45° is selected, which contributes a turn separation of 4.7 mm. Three ways of generating the first harmonic are introduced, which are trim coil, trim-rod, magnet shimming, respectively.

REFERENCES

[1] C. Baumgarten, A. Geisler, U. Klein *et al.*, "Isochronism of the ACCEL 250 MeV medical proton cyclotron", *Nucl. Instrum Methods Phys., Sect. A*, vol. 570, no. 1, pp. 10-14, Jan. 2007. doi:10.1016/j.nima.2006.09.112

[2] L. G. Zhang, K. J. Fan, S. W. Hu *et al.*, "Extraction channel design based on an equivalent lumped parameter method for a SCC-250 MeV superconducting cyclotron", *Nucl. Instrum. Methods, Sect. A,* vol. 897, pp. 66-71, Jul. 2018. doi:10.1016/j.nima.2018.04.049

[3] E. Fabrici and F. G. J. N. I. Resmini, "A survey of beam dynamics prior to extraction in the K-500 cyclotron at M.S.U.", *Nucl. Instrum. Methods,* vol. 180, no. 1-2, pp. 319-333, Jun. 1981. doi:10.1016/0029-554X(81)90073-2

[4] D. S. Zhang, M. Li, C. Wang, J. J. Yang, and T. J. Zhang, "Physical design of the extraction trim-rods in a 230 MeV superconducting cyclotron", in *Proc. 21th Int. Conf. on Cyclotrons and their Applications (Cyclotrons'16)*, Zurich, Switzerland, Sep. 2016, pp. 61-63. doi:10.18429/JACoW-Cyclotrons2016-MOP06

[5] B. Qin, D. Z. Chen, L. C. Zhao *et al.*, "An improved matrix method for magnet shimming in compact cyclotrons", *Nucl. Instrum. Methods Phys., Sect. A*, vol. 620, no. 2, pp. 121-127, 2010. doi:10.1016/j.nima.2010.03.135

[6] A. Papash, "Field shimming of commercial cyclotrons", in *Proc. 17th Int. Conf. on Cyclotrons and their Applications (Cyclotrons'04)*, Tokyo, Japan, Oct. 2004, paper 20P03.

[7] W. Kleeven, W. Beeckman, S. Lucas, S. Zaremba, D. Vandeplassche, and Y. Jongen, "Magnetic field calculation and shimming of the self-extracting cyclotron", in *Proc. 16th Int. Conf. on Cyclotrons and their Applications (Cyclotrons'01)*, East Lansing, MI, USA, May 2001, paper P3-27, pp. 348-350.

ISBN: 978-3-95450-205-9 doi:10.18429/JACoW-Cyclotrons2019-MOP036

THE MAGNETIC FIELD DESIGN OF CYCLOTRON AT IMP

Q. G. Yao#, B. M. Wu, L. Yang, W. Wu, B. Wang
Institute of Modern Physics, Chinese Academy of Sciences, 730000, Lanzhou, China

Abstract

A cyclotron magnet is studied at Institute of Modern Physics, Chinese Academy of Sciences (IMP, CAS), and the whole system include one main magnet and other magnetic gradient correctors, which is used to accelerate the Kr^{26+} beam. The structure of superconducting coils and room-temperature iron core are adopted for the main magnet. This paper describes the magnetic field design of the cyclotron, and several shimming methods are used to meet the isochronous magnetic field of Kr^{26+} beam, including pole face shimming method and side shimming method. The final optimization results show that the error between simulation and theory value is small. In addition, the magnet structure is also described.

INTRODUCTION

At present, the activities on the development of isochronous cyclotron are carried out at IMPCAS (Fig. 1). This project includes cyclotron and several beam lines, which intended for obtaining the Kr^{26+} beam to produce nuclear track membrane. The cyclotron magnet has the pole diameter size of 1.64 m and provides the maximum magnetic fields 2.8 T between sectors. Its main parameter is shown in Table 1.

Table1: Main Parameters of the Cyclotron

Parameter	Value
Maximum energy [MeV]	10
Beam species	$^{86}Kr^{26+}$
Number of sectors	4
Ion source	outer
Hill angle [°]	56
Valley angle [°]	34
Max. average Mag. field [T]	2
Harmonic number	4
Magnet aperture [mm]	50-80

The main magnet has a round yoke, four pairs of straight-line sectors. In this paper, we introduce the main magnet with particular emphasis on the isochronous mangetic field design. In addition, we would ensure the cyclotron magnet structure of accordance with the magnetic field calculation.

MAGNETIC FIELD DESIGN AND OPTIMIZATION

The shape of the magnet yoke is optimized by OPERA- 3D magnetic field calculation [1], The OPERA-3D program was used to calculate the three-dimensional field. In the Modeller, the 1/16 model is created according to the symmetry of the magnetic field. Figure 1 shows the geometry of the cyclotron model by the OPERA. Consider with the vacuum and RF systems, there are four holes at the valley centre was designed. Figure 2 shows the radial magnetic field along the "hill" median line at the centre plane. We have been able to obtain a reasonable isochronous magnetic field by some optimization methods.

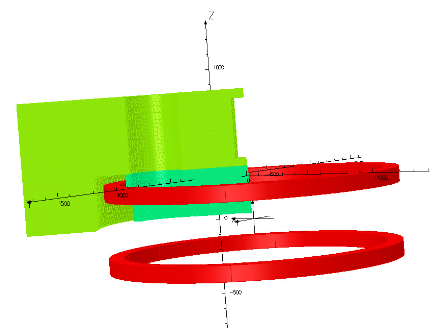

Figure 1: OPERA 3D model.

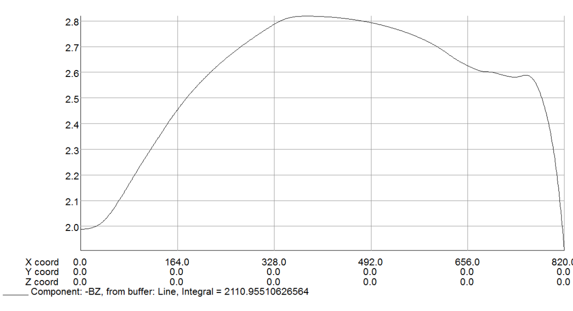

Figure 2: Radial magnetic field distribution.

By successive approximation, cylinder side is optimized as the final shape. In addition, to avoid the rapidly decreasing field in the center region and at the final radius, two special shimming shapes are adopted in these two areas. The optimization structure of sector is shown in Fig. 3. The comparison between the calculation and theory is shown in the Fig. 4, the result shows the deviation does not exceed 10 Gauss over a large area.

In addition, horizontal and vertical focusing frequencies are also obtained from the equilibrium orbit calculation. Generally, we hope the focusing frequency away from the resonances, especially the vertical focusing frequency. Figure 5 shows the two focusing frequencies, the vertical focusing frequency is below 0.5 except some points in final radius [2].

yaoqinggao@impcas.ac.cn

ISBN: 978-3-95450-205-9 doi:10.18429/JACoW-Cyclotrons2019-MOP036

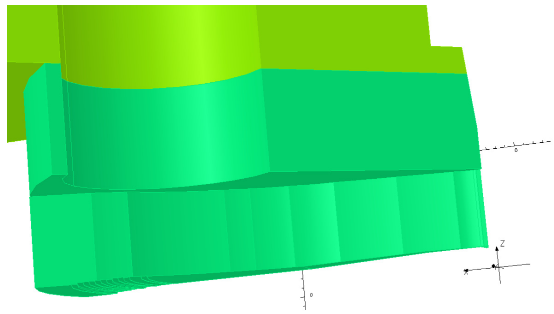

Figure 3: The optimized shape of pole.

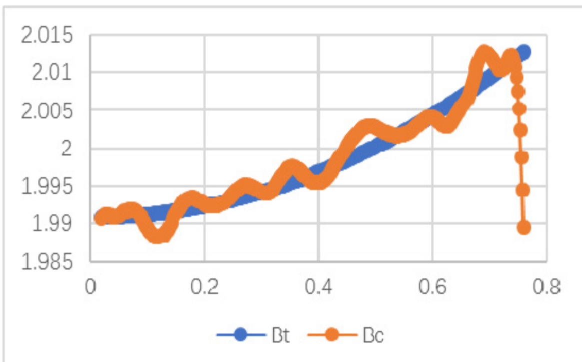

Figure 4: Comparison between calculation and theory values.

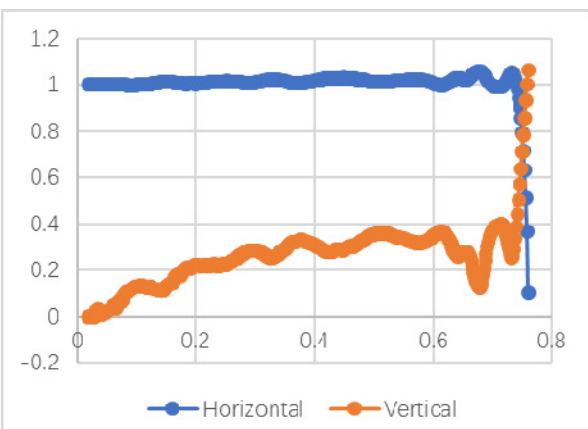

Figure 5: Focusing frequency.

When the optimization of isochronous magnetic field has been finished, the extraction elements need to be designed. Extraction elements such as electrical septum and gradient correctors would be used to extract the Kr beams.

MAGNET STRUCTURE

For the main magnet system, we adopt the structure of superconducting coils and room-temperature iron core. Figure 6 gives the sectional dimension of cyclotron. The outer diameter of cyclotron is 2.98 m, the height is 1.72 m.

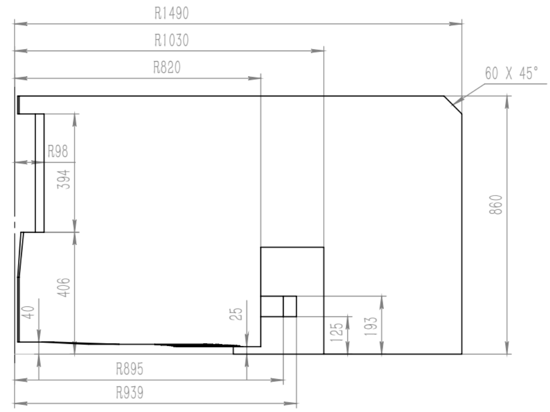

Figure 6: Sectional dimension.

Low carbon steel, electrical pure iron DT4 for the pole and No. 10 Steel for the yoke is the main material of the magnet. The weight of iron core is about 72 t. DT4 is annealed and forged, to improve the material magnetic properties. In the shimming optimization process, the real B-H curves of the magnet material must be taken into account, because different materials, especially the sector material, influence the isochronous field.

Accordance with the basic magnetic field calculation, the total current is 306000 A. The size of coil conductor wires is 1.565×1.040 mm, the critical current@4.2 K is 1200 A (2 T), the ratio of Cu/non-Cu is 5. RRR (273 K/10 K) is 100. Table 2 shows the main parameters of coil system. The superconducting coil is about 0.3 t and the cryogenic system is about 4.7 t.

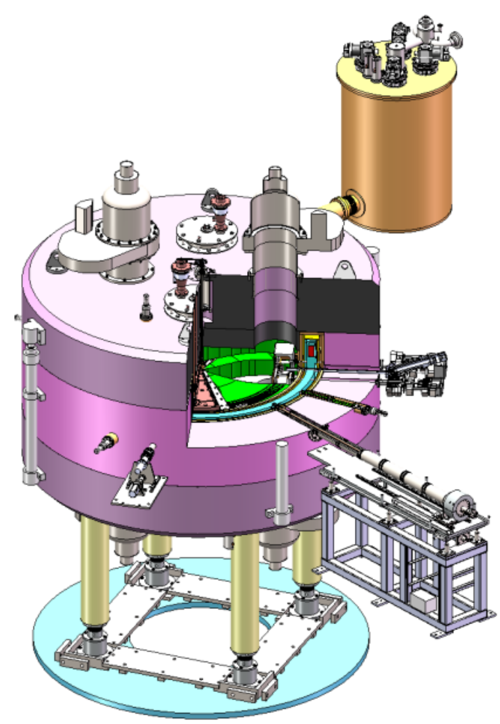

Figure 7: The preliminary structure of cyclotron.

ISBN: 978-3-95450-205-9 doi:10.18429/JACoW-Cyclotrons2019-MOP036

Table 2: Main Parameters of the Coil System

Item	Value
Number of coils	2
Inner radius of coils	895 mm
Outer radius of coils	939 mm
Height of coils	68 mm
Distance between two coils	250 mm
Design current	243 A
Number of turns	1258
Number of layers	34
Number of per layer	37
Load line	32%

The cryogenic system of superconducting cyclotron consists of two coil windings, two coil cases, thermal shield, outer vacuum vessel, valve box, four two-stage GM cryocoolers which are installed for re-condensing the evaporated helium gas, two single-stage GM cryocoolers which are used for thermal shield cooling, a pair of high temperature superconducting (HTS) current leads, and other auxiliary devices (see Fig. 7). The cryostat for the two sets of superconducting coil windings are separated into upper and lower parts. The circulation of helium between the re-condensing vessel and each coil case is performed by the natural convection.

CONCLUSION

Magnetic field calculation of main magnet for a 10 MeV Kr^{26+} cyclotron have been finished. The purpose of the work is to obtain the resonable isocoronous magnetic field, an effective method has been carried out. By complicated chamfering, the isocoronous magnetic field could satisfy the design requirements. The next step is the optimization of extraction system and cryogenic system.

REFERENCES

[1] Cobham Technical Services, www.cobham.com/technicalservices

[2] Q. G. Yao, L. Z. Ma, H. F. Hao, X. Y. Zhang, S. F. Han, B. Wang, and P. Yuan, "The magnetic field design of HITFiL cyclotron", *IEEE Trans. Appl. Supercond.*, vol. 22, no. 3, Jun. 2012, art. seq. no. 4401004. doi:10.1109/TASC.2011.2175190

ISBN: 978-3-95450-205-9 doi:10.18429/JACoW-Cyclotrons2019-MOC02

A PATHWAY TO ACCELERATE ION BEAMS TO 3 GeV WITH A K140 CYCLOTRON*

D. Z. Xie†, L. Phair, D. S. Todd
Nuclear Science Division, Lawrence Berkeley National Laboratory, Berkeley, CA 94720, USA

Abstract

The capabilities of the K140, 88-Inch Cyclotron at Lawrence Berkeley National Laboratory (LBNL) have been significantly enhanced through the addition of three successive generations of electron cyclotron resonance ion sources (ECRISs). These ion sources have helped the 88-Inch Cyclotron to evolve from a light-ion accelerator to one that has accelerated over half of the naturally-occurring elements in the periodic table, and in particular has accelerated ultra-high charge state heavy ions, such as xenon and uranium. Recently, with $^{124}Xe^{49+}$ ions injected from the superconducting ECRIS VENUS, the 88-Inch Cyclotron reached a new peak extracted kinetic energy of ~2.6 GeV. This is approximately a fifteen-fold energy increase over what this K140 cyclotron could achieve when it started operation almost six decades ago. A next-generation ECRIS, MARS-D, is under development and will further raise the extracted beam energy from the cyclotron. It is anticipated that the higher charge state ions produced by MARS-D will result in the 88-Inch Cyclotron accelerating ions in excess of 3 GeV for use by the radiation effects testing community. This paper will present and discuss the development of the MARS-D ECRIS and the 88-Inch Cyclotron's recent and possible future achievements.

INTRODUCTION

The K140, 88-Inch Cyclotron at Lawrence Berkeley National Laboratory (LBNL) has, in its nearly six decades of service, evolved from a light ion accelerator to one that has successfully accelerated ions ranging in mass from protons to the heaviest naturally-occurring element, uranium [1, 2]. The enhancement of this cyclotron's capabilities has continued through the addition of three successive generations of Electron Cyclotron Resonance Ion Sources (ECRISs). To date the 88-Inch Cyclotron has accelerated the 49 elements indicated in Fig. 1, which represents more than half of the naturally occurring elements including quite a number of their isotopes.

The wide range of ions capable of being accelerated by the 88-Inch Cyclotron has led to its use for a diverse range of applications, such as nuclear chemistry, syntheses of super heavy isotopes, nuclear structure, neutron beams for isotope breeding, space effects testing, etc. The very first single event effects (SEE) tests in the world were conducted using beams from LBNL's 88-Inch Cyclotron by the Aerospace Corporation in 1979 [3]. The combined versatility of the ECRIS, coupled with flexibilities in both the 88-Inch Cyclotron's magnetic field and accelerating frequency, allowed for the development of a number of "cocktail beams" in the mid-1980s where a collection of ions with very similar mass-to-charge ratios are injected into the cyclotron simultaneously and by employing small accelerating frequency changes, single ion species are fully accelerated and extracted [1, 4]. This capability led to the establishment of the Berkeley Accelerator Space Effects (BASE) Facility operating in conjunction with the 88-Inch Cyclotron to provide beams of heavy ions, protons, and neutrons for radiation effects testing. The continued advancement of different generations of ECRIS has led to great enhancement of both ion energy and variety enabling the BASE Facility continue to be at the forefront of radiation effects testing.

Though older, 88-Inch Cyclotron has not yet reached its full potential and the proposed ion source discussed below could push this accelerator to new heights. A brief introduction to ECRISs is given, followed by a description of how advancements in ECR technology at LBNL have enhanced the capabilities of the 88-Inch Cyclotron. Finally, a case is made the novel design of a next-generation ECRIS at LBNL may present the easiest path to the 88-Inch Cyclotron producing 3 GeV ion beams.

ECR ION SOURCE BASICS

The production of multiply-charged ions via ECR ion source was first reported by Geller at GANIL in 1972. This ion source uses a superposition of axial solenoids and a radial multipole (typically a sextupole) to confine a plasma in a magnetic field where that increases in all directions from the source center, i.e., a minimum-B field. Microwaves are injected into the source chamber at frequencies that allow for resonant electron heating on closed shells of constant magnetic field. These energetic electrons ionize neutrals and ions in a step-wise fashion.

The ionizing electrons are more energetic and are more likely to ionize if their source lifetime is long, therefore better plasma confinement leads to both higher currents and higher charge states. Geller developed semi-empirical scaling laws [5] predicting that extracted ion currents will increase as the square of both the injected microwave frequency and the confining magnetic field ($I_q \propto f^2 \propto B^2$). These scaling laws have continued to hold for three generations of ECRIS development, and it is expected that source performance will continue to improve with increased confining magnetic field.

ECRIS development since its invention has shown that

* Work was supported in part by the U.S. DOE, Office of Science, Office of Nuclear Physics under contract number DE-AC02-05CH11231.
†zqxie@lbl.gov

ISBN: 978-3-95450-205-9 doi:10.18429/JACoW-Cyclotrons2019-MOC02

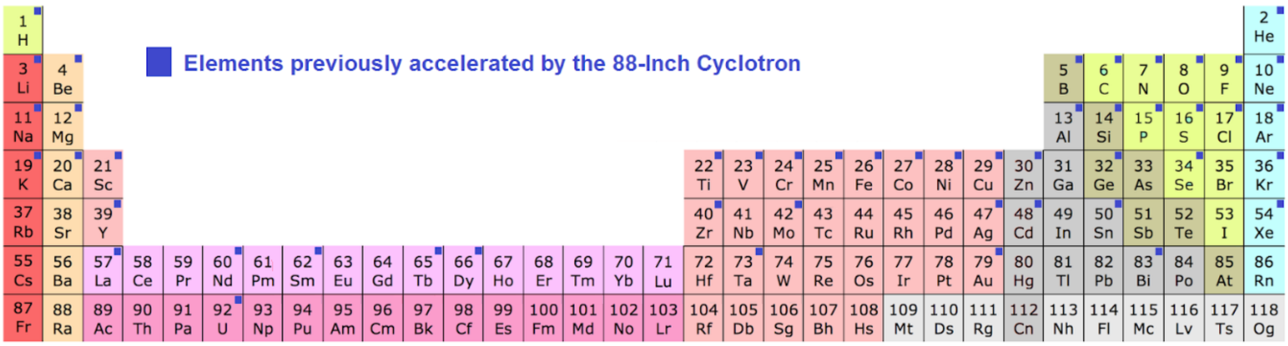

Figure 1: Since its commencement in 1962, so far the 88-Inch Cyclotron at Lawrence Berkeley National Laboratory has accelerated 49 elements (indicated with blue color squares), which is more than one half of the natural elements, and a great number of isotopes.

the source plasma is insensitive to the specific magnetic geometry of the source and all that is required is a high-strength minimum-B field [6]. Further, recent studies at LBNL have demonstrated that a cylindrical plasma chamber is not necessary for a high charge state ECRIS as the centimeter-or-smaller microwave wavelengths can easily travel into and resonate in a large complex-shaped plasma chamber [7]. This insensitivity to both magnet geometry and chamber geometry allows considerable flexibility when designing a high charge state ECRIS.

ECR ION SOURCES AT LBNL

Motivated by Geller's new ion sources, a 1st generation ECRIS named the LBL ECR replaced the 88-Inch Cyclotron's PIG sources in 1984 [1]. The increased versatility this ion source provided the cyclotron led to the construction and implementation of a 2nd and a 3rd generation ECR ion sources, AECR-U and VENUS, that were installed in 1996 and 2002, respectively [2, 8]. Each successive generation of added ion source had higher confining magnetic field and microwave frequencies, culminating with VENUS, the first 3rd generation ECR ion source built with a superconducting magnet. VENUS is capable of producing maximum axial and radial fields at the plasma chamber walls of 4 and 2.2 T, respectively and utilizing 18 and 28 GHz microwave heating.

Figure 2 clearly shows the greatly enhanced capability of the 88-Inch Cyclotron with each successive generation of ECR ion source. With the introduction of each new ECRIS, the 88-Inch Cyclotron's ability to accelerate heavier ions at higher currents followed. As can be seen in Fig. 2, before the introduction of AECR-U (the 2nd generation ECRIS) only ions with mass numbers up to 40 could be accelerated by the cyclotron to energies that reach the coulomb barrier for nuclear reactions (~5 MeV/nucleon). The AECR-U increased the mass of ion species reaching this energy threshold up to uranium, while the addition of the 3rd generation source VENUS increased beam intensities, as indicated in Fig. 2 by "Present with AECR-U" and "Present with VENUS," respectively. In particular, going from a 2nd to a 3rd generation ECRIS increased the intensity of cyclotron-extracted uranium from 10s of epA to 1 enA.

Listed in Table 1 are a few of the ultra-high charge state ion beams that have been accelerated through the cyclotron in recent years with maximum total energies in the 2.4-2.7 GeV range. This represents an energy increase of about fifteen-fold over what the 88-Inch Cyclotron could achieve almost six decades ago, and has been greeted enthusiastically by BASE Facility users desiring higher energy beams. Two of these high-energy beams, Xe^{49+} and Au^{63+}, are believed to represent the highest charge states of these species that the cyclotron can accelerate using VENUS as an injector source. Any further energy advancement will require the development of a more advanced ion source operating at higher confining fields and microwave frequencies in order to produce higher charge state ions with higher currents. Drawing on over 35 years of ECR ion source development at LBNL, we believe the development of a 4th generation ECRIS is the best path forward for this facility to acceleration ions in excess of 3 GeV in the near future.

Table 1: Ultra-High Charge State Ions Produced with VENUS and Accelerated by the 88-Inch Cyclotron

Ion	Ip# (keV)	E (MeV/n)	E_{total} (GeV)	$I_{ex}{}^{\alpha}$ (epA)
$^{124}Xe^{47+}$	7.76	19.2	2.38	62
$^{124}Xe^{48+}$	8.02	20.0	2.48	10.5
$^{124}Xe^{49+}$	8.62	20.8	2.58	2.1
$^{179}Au^{63+}$	6.64	13.5	2.66	~1

#: Ip the ionization potential.
α: I_{ex} the current extracted from the 88-Inch Cyclotron.

CHALLENGES OF DEVELOPING A 4TH GENERATION ECRIS

All existing 3rd generation ECRISs, including LBNL's VENUS, have been built using NbTi superconducting coils. These advanced sources have two different, successful magnet geometries to produce the source magnetic fields: the radially-confining racetrack sextupole coils are either inside or outside of the axially-confining solenoids. For either coil configuration, however, existing 3rd generation sources are operating very near the NbTi conductor limits for safe operation in their high field environments. A

ISBN: 978-3-95450-205-9 doi:10.18429/JACoW-Cyclotrons2019-MOC02

4th generation ECR ion source using one of these geometries would therefore need to employ a superconducting material capable of safe operation at even higher magnetic fields. The present leading candidate for a higher field material is Nb_3Sn. However, this material has never been successfully used in the construction of the very complex ECRIS magnet. To use Nb_3Sn many issues and challenges need to be addressed and overcome, such as conductor brittleness, increased coil fabrication complexity due to the heat-and-react processes, substantially poorer Nb_3Sn quench propagation requiring very demanding quench protection, etc.

Although there has been conceptual exploration into the design of a Nb_3Sn magnet for a future ECRIS [9], the ion source group at the Institute of Modern Physics in Lanzhou, China, is the only group currently working on the fabrication of an ECRIS utilizing Nb_3Sn coils (attempting sextupole-inside-solenoids geometry. This Nb_3Sn magnet is being designed to generate magnetic fields on axis and radially at the chamber walls of 6.5 and 3.3 tesla, respectively, which will allow for operation at 45 GHz [10]. Unfortunately, the progress of the magnet fabrication has been exceedingly slow as they attempt to address the expected challenges and complexities.

The difficulties faced in utilizing a new superconducting material to increase ECRIS magnetic fields motivates one to ask whether source geometry changes could be used to reach these higher fields while still employing NbTi coils. Reaching these higher fields using a coil material with nearly two decades of successful ECR ion source application could offer an easier route to a 4th generation, 45 GHz ECRIS.

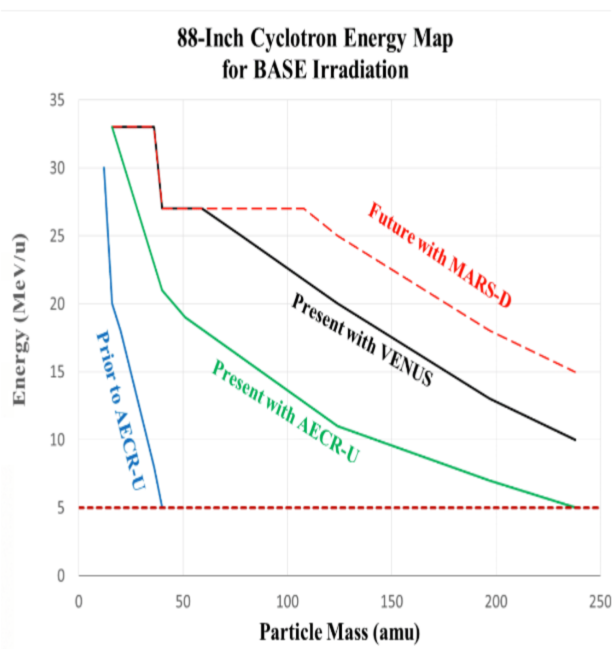

Figure 2: This plot shows the energy-mass curves achieved by the 88-Inch Cyclotron with the existing ECRISs and extrapolation with a future ECRIS for the BASE Facility.

MARS-D: A 4TH GENERATION ECRIS

A 4th generation ECRIS, MARS-D, capable of operation at 45 GHz is under continuing development at LBNL. This advanced source is expected to serve many roles, but it will be a key element in the quest for using the 88-Inch Cyclotron to accelerate ions in excess of 3 GeV total energy.

MARS-D employs a new magnet geometry: a Mixed Axial and Radial field System (MARS), that will allow NbTi-magnet-based ECR ion sources to achieve higher confining fields [11]. The critical component of MARS is a closed-loop-coil with a hexagonally-shaped cross section, as shown schematically in Fig. 3 (a). The major difference between the MARS geometry and a conventional racetrack design comes in the connections between the long sextupole sections. The closed-loop-coil is one continuous winding, and as a result the currents in the ends of the sextupole structure all rotate in the same sense about the long axis of the sextupole. This is not true for the six racetrack coils that make up a more typical electromagnetic sextupole, where neighboring racetrack coils have end currents with opposite rotations about the long axis. This difference presents two major advantages for the closed-loop-coil over a set of racetrack coils: there is a net solenoidal field at each end of the closed-loop-coil so that this structure alone generates a minimum-B structure, and the forces on each end of the structure are always in the same direction (outward) which makes for much easier coil clamping. By generating its own axial magnetic field, smaller additional solenoid coils can be used, which keeps the internal coil fields for the superposed structure further from critical operation points. A design using relatively small solenoids combined with a closed-loop-coil to construct a NbTi magnet for MARS-D is shown in Fig. 3 (b). Generally, ECRIS design requires that the maximum axial fields within the source, B_{inj} and B_{ext} (injection and extraction), along with the radial field at the chamber wall, B_{rad}, be related to the magnetic field for ECR heating via injected microwave, B_{ECR} in the following manner: $B_{inj} \sim 3.5 - 4\ B_{ECR}$ and $B_{ext} \approx B_{rad} \geq 2\ B_{ECR}$. Based on these requirements, MARS-D has been designed to produce maximum fields of 5.7 T on axis and 3.2 T radially at the plasma chamber walls: sufficient for supporting operations at 45 GHz.

The two main advantages of the MARS magnet come at the cost of a more complex winding for the closed-loop-coil. Specific tooling and a new winding technique have allowed for the successful construction of a closed-loop-coil using copper wires. Field mapping of this coil agrees very well with the computations demonstrating the feasibility of fabricating a NbTi closed-loop-coil [12]. The MARS-D plasma chamber and the warm bore of the cryostat are to have a hexagonal cross-section to match the shape of the closed-loop-coil and more efficiently use its confining radial field.

Full construction of MARS-D is anticipated to begin soon with scheduled completion in approximately four to five years. Initial commissioning is planned by using multiple-frequency heating, such as a combination of commercially available microwave generators of 22, 28, 35 and

ISBN: 978-3-95450-205-9 doi:10.18429/JACoW-Cyclotrons2019-MOC02

45 GHz with a total power of ~4-5 kW. This power level is estimated to be sufficient for the production of ultra-high charge state ion beams for use by the BASE facility. A full power solution for MARS-D would be 15-20 kW and that will be treated as a power upgrade for the production of intense highly-charge ion beams for other applications.

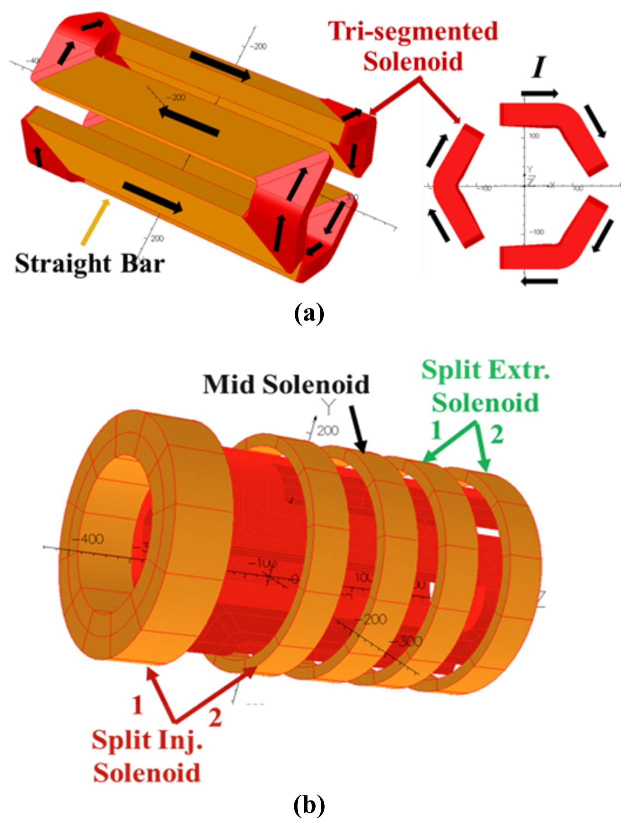

Figure 3: (a). Schematic layout of a closed-loop-coil, the MARS critical component. It combines six rectangular straight bars (yellow color) and two three-segmented solenoids (red color) into a closed-loop-coil. (b). The solenoids superimposed magnet system for producing the minimum-B field with high mirror ratios for MARS-D ECRIS.

Table 2: Possible Ultra-High Charge State Ions Produced with MARS-D and Accelerated by the 88-Inch Cyclotron

Ion	Ip# (keV)	E (MeV/n)	E_{total} (GeV)
$^{124}Xe^{52+}$	9.57	23.4	2.90
$^{124}Xe^{54+}$	40.3	25.2	3.12
$^{179}Au^{69+}$	8.26	16.2	3.19
$^{179}Au^{70+}$	17.1	16.6	3.27
$^{179}Au^{73+}$	18.3	18.0	3.55

#: Ip the ionization potential.

With a higher density of hotter electrons and a longer plasma confinement time compared to VENUS, MARS-D is anticipated to enhance the production of higher charge states heavy ions, such as xenon, gold, and uranium. Listed in Table 2 are a few ultra-high charge state ion beams with ionization potentials in the 10-40 keV range that are anticipated to be produced with MARS-D. The 88-Inch Cyclotron should be capable of accelerating these ions to a total energy in excess of 3 GeV, thus furthering the achievements of this nearly 60-year-old machine and benefitting the radiation testing community.

REFERENCES

[1] C. M. Lyneis, "Invited paper: Operational performance of the LBL 88-Inch cyclotron with an ECR source", in *Proc. 11th Int. Cyclotron Conf. and Their Applications (Cyclotrons'86)*, Tokyo, Japan, Oct. 1986, paper M-02, pp. 707-712.

[2] Z. Q. Xie, D. J. Clark, A. Guy, S. A. Lundgren, and C. M. Lyneis, "Vacuum Improvements for Ultra High Charge Ion Acceleration", in *Proc. 15th Int. Cyclotron Conf. and Their Applications (Cyclotrons'98)*, Caen, France, Jun. 1998, paper B-07, pp. 179-182.

[3] E. L. Petersen, R. Koga, M. A. Shoga, J. C. Pickel, and W. E. Price, "The single event revolution", *IEEE Trans. Nucl. Science*, vol. 60, no. 3, pp. 1824-1834, Jun. 2013. doi:10.1109/TNS.2013.2248065

[4] M. A. McMahan *et el.*, "Using a cyclotron plus ECR source for detector evaluation and calibration", *Nucl. Instrum. Methods Phys. Res., Sect. A*, vol. 253, pp. 1-9, Nov. 1986. doi:10.1016/0168-9002(86)91118-6

[5] R. Geller, "Electron cyclotron resonance ion source and ECR plasmas", *Institute Phys. Publishing*, vol. 28, p. 395, 1996.

[6] D. Z. Xie, "A new structure of superconducting magnetic system for 50 GHz operations", *Rev. Sci. Instrum.*, vol. 83, p. 02A302, Feb. 2012. doi: 10.1063/1.3655530

[7] D. Z. Xie, W. Lu, J. Y. Benitez, and M. J. Regis, "Recent production of ultra-high charge state ion beams with VENUS," presented at the 23rd Int. Workshop on ECR Ion Sources, Catania, Italy, Sep. 2018, unpublished.

[8] D. Leitner *et al.*, "Next generation ECR ion sources: First results of the superconducting 28 GHz ECRIS – VENUS", *Nucl. Instrum. Methods Phys. Res., Sect. B*, vol. 235, pp. 486-493, July 2005. doi:10.1016/j.nimb.2005.03.230

[9] C. M. Lyneis *et al.*, "Fourth generation electron cyclotron resonance ion sources", *Rev. Sci. Instrum.*, vol. 79, p. 02A321, 2008. doi:10.1063/1.2816793

[10] H. W. Zhao and L. T. Sun, "FECRAL - a 45 GHz fourth generation ECR ion source and its technical challenge", presented at the 22nd Int. Workshop on ECR Ion Sources, Busan, Korea, Aug. 2016, paper MOBO01, unpublished.

[11] D. Z. Xie *et al.*, "Development status of a next generation ECRIS: MARS-D at LBNL", *Rev. Sci. Instrum.*, vol 87, p. 02A702, Sep. 2016. doi:10.1063/1.4931713

[12] D. Z. Xie, W. Lu1, G. Sabbi, and D. S. Todd, "Possible optimizations of existing magnet structures for the next generation of ECRIS", presented at the 22nd Int. Workshop on ECR Ion Sources, Busan, Korea, Aug. 2016, paper MOBO02, unpublished.

ISBN: 978-3-95450-205-9 doi:10.18429/JACoW-Cyclotrons2019-MOC03

UPGRADE OF THE PSI INJECTOR 2 CYCLOTRON

M. Schneider†, J.Grillenberger, Paul Scherrer Institut, 5232 Villigen PSI, Switzerland

Abstract

The high intensity proton accelerator facility at Paul Scherrer Institute (PSI) is capable of providing beam currents of up to 2.4 mA at a kinetic energy of 590 MeV. PSI is following an upgrade plan to further increase the beam power and to further minimize proton losses. Up to now, this has mainly been achieved by the installation of high gradient copper resonators in the Ring cyclotron and the installation of more powerful RF-amplifiers. Currently, PSI follows a similar approach for the Injector 2 cyclotron providing 72 MeV protons for the injection into the 590 MeV Ring cyclotron. In order to increase the turn separation in the injector cyclotron which results in lower relative beam losses, the two 150 MHz resonators operated in accelerating mode are replaced with two 50 MHz Aluminum resonators providing higher acceleration voltage. This paper describes the status of the upgrade, i.e., the replacement of the first resonator and related hardware.

INTRODUCTION

The Injector 2 cyclotron was commissioned in the 1984. The rf system consists of the Resonators 1 & 3, which are 50 MHz double cap cavities for the main acceleration. In addition, the injector is equipped with two flat top Resonators 2 & 4 operated at a frequency of 150 MHz, initially to provide a broad phase acceptance. However, it was later discovered that space charge forces lead to a Vortex motion of the particles and thus a self-focusing of the bunches [1]. It turned out that changing the phase of the Resonators 2 & 4 by 180 degrees and thus providing additional energy gain per turn leads to even lower proton losses in the cyclotron. In this configuration during several shifts of 8 hours the operation of the Injector 2 cyclotron at 2.4 mA was demonstrated.

To further increase the beam current to 3 mA and consolidate the rf system, an upgrade program of the Injector 2 rf system was started [2, 3]. This upgrade is as well essential for the amplifier chains because some of the tetrodes used in the amplifiers up to 10 kW are not anymore available on the market.

THE NEW RF SYSTEM

In the new rf system the Resonators 2 & 4 will be replaced by 50 MHz single gap cavities with a higher voltage and a field distribution with the peak shifted toward the outer radius of the Injector 2. This will lead to an even higher energy gain per turn and a better turn separation at the extraction. The gap voltage of the old and new cavities is compared in Fig. 1. Because of the change in the frequency from 150 MHz to 50 MHz, the old analog LLRF system and the amplifiers need to be replaced.

In a second phase the 50 MHz LLRF system and the amplifiers for the Resonators 1 & 3 will be as well renewed.

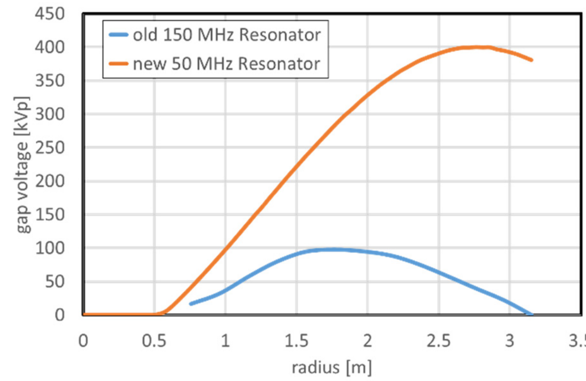

Figure 1: Gap voltage of Resonators 2 & 4.

The New 50 MHz Resonator

The rf volume of the new Resonator has an 8 shape in the cross section. On both sides there are two wings which serve as vacuum chamber towards the sector magnets (see Fig. 2). Within this space diagnostic elements and in the Resonator 4 the extraction magnets AXA/AXB are installed.

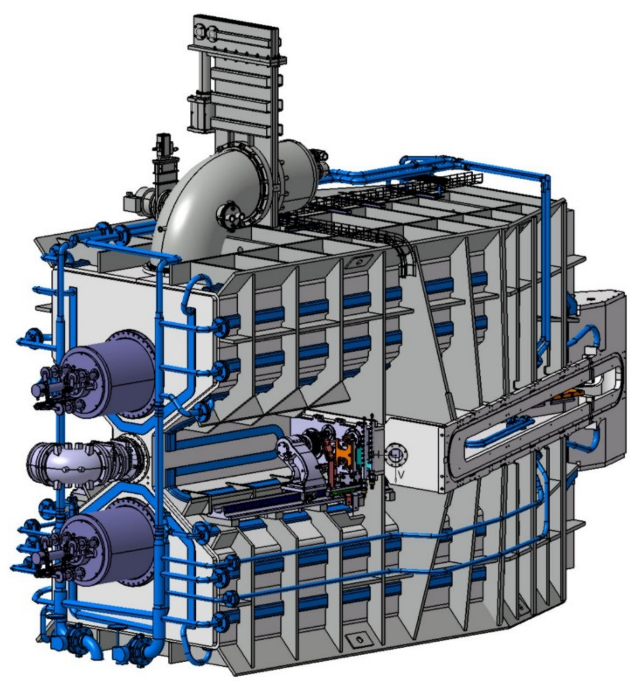

Figure 2: Isometric view of Resonator 4 with tuner, coupling loop in the front and vacuum pump on the top.

The new Resonators were made of Aluminum allowing using the existing cooling infrastructure of the Resonators 1 & 3. Both resonators were designed at Paul Scherrer Institute (PSI) and manufactured in France by the company SDMS. Some key parameters are listed in Table 1.

† markus.schneider@psi.ch

ISBN: 978-3-95450-205-9 doi:10.18429/JACoW-Cyclotrons2019-MOC03

Table 1: Parameters of the New 50 MHz Resonator

Parameter	Value
Resonance Frequency	50.6328 MHz
Q_0	24'500
Peak gap Voltage	400 kVp
Dissipated Power	50 kW
Tuning Range	200 kHz
Material Cavity RF-wall	EN AW 1050
Material Structure	EN AW 5083
Cooling Water Flow	15 m3/h
Dimension	5.6 x 3.3 x 3 m
Weight	7000 kg

Test of the new Resonator 2 The new Resonator 2 was successfully tested in our rf test stand in 2017. The cavity was first conditioned within a day to a power level of 100 kW. During a 24 hours long term run the distribution of the thermal losses in resonator was tested by measuring the temperatures with thermocouples at about 50 different locations.

For the beam entrance and exit the rf volume the resonators have a slit of 40 mm in height and 2.4 m in length on both sides. To quantify the rf leaking into the cyclotron's vacuum chamber, the leaking power into the wings was measured with a capacitive probe. First the voltage distribution along the slit was measured with the network analyzer. Afterwards the leaking power was measured at different power levels. By shifting the electrodes of the cavity, the asymmetric leaking power on one side could be reduced significantly as shown in Table 2. The measured leaking power is in the range of 20 µW.

Table 2: Measurement of Leaking RF Power

Position of Pickup in Wing	Resonator Wall Losses	Pickup signal before shifting	Pickup signal after shifting
Beam exit	50 kW	233.5 mV	22.2 mV
Beam exit	70 kW	271.8 mV	25.1 mV
Beam entrance	50 kW	41.7 mV	25.0 mV
Beam entrance	70 kW	33.3 mV	30.4 mV

Finally, the accelerating voltage of the resonator was determined by measuring the Bremsstrahlung. Therefore, a CZT-detector (SPEAR™-detector of Kromek) was installed in a lead housing with a 1.5 mm aperture pointing towards the area with the highest electrical field of the resonator. The resonator was operated on different power levels for 8 hours and from the measured Bremsstrahlung spectrum the highest energy at the zero crossing was determined. The measurements of Resonator 2 are listed in Table 3. To be able to determine the gap voltage during regular operation of the cavity, the voltage on a reference pickup was measured. The measured wall losses of 50.3 kW for 400 keV kinetic energy is comparable to the simulations of 50 kW wall losses for a gap voltage of 400 kVp.

Table 3: Results from the Bremsstrahlung Spectrum Measurements of the New Resonator 2

RF Power	Voltage on Reference Pickup	Zero Crossing in Bremsstrahlung Spectrum
35 kW	2.936 V	323 keV
46 kW	3.402 V	382 keV
56 kW	3.714 V	422 keV
66 kW	4.040 V	467 keV
75 kW	4.280 V	483 keV
85 kW	4.560 V	500 keV

Installation of the new Resonator 2 During the shutdown 2018 the old 150 MHz Resonator 2 was removed from the Injector 2 and replaced by the new 50 MHz Resonator (see Fig. 3). This requires the decommissioning of the old 150 MHz rf system (amplifiers and LLRF) and setting up the new 50 MHz system during beam operation. The resonator was installed without coupling loop and without tuners and is therefore used as vacuum chamber only. Since only 3 resonators are available, the Injector 2 is currently operated at a reduced beam current of 2 mA. Nevertheless, the new resonator was already equipped with all necessary parts for beam control and diagnostic and the beam operation with 3 resonators could successfully be started after the shutdown in 2018. The Injector 2 is presently operating in this regime.

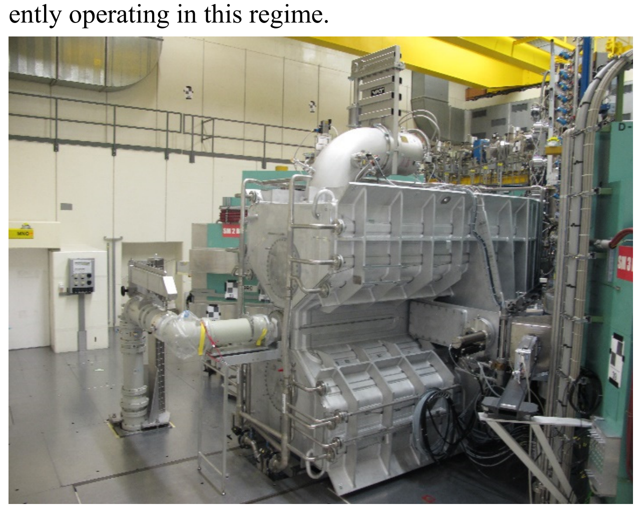

Figure 3: The new 50 MHz Resonator 2 installed in the Injector 2 Cyclotron.

Test of the new Resonator 4 The Resonator 4 was manufactured first and previously tested in 2016/ 2017 at full power without any problems. The Resonator 4 was then stored in a separated building, because the test stand was used for the tests of Resonator 2, which was intended to be installed in the cyclotron first. At the end of 2018, the Resonator 4 was moved back to the test stand and the test program was restarted. During a long term run at 60 kW

ISBN: 978-3-95450-205-9 doi:10.18429/JACoW-Cyclotrons2019-MOC03

we observed a 27 °C higher temperature on the bottom than on the top side of the cavity. This problem is still under investigation. We observed a change of the input impedance at about 3 kW incident power, which indicates the ignition of a discharge in the cavity which persist up to higher power levels. Obviously, a suitable treatment of the wall surface of the bottom has to be performed to avoid this effect. This could be cleaning or painting with Aquadag® to change the secondary emission coefficient of electrons.

Tuning system For tuning the cavity two plungers of about 500 mm diameter are installed. The plungers can be shifted by a hydraulic system by 200 mm, which results in a frequency shift of 200 kHz. Figure 4 illustrates the tuner.

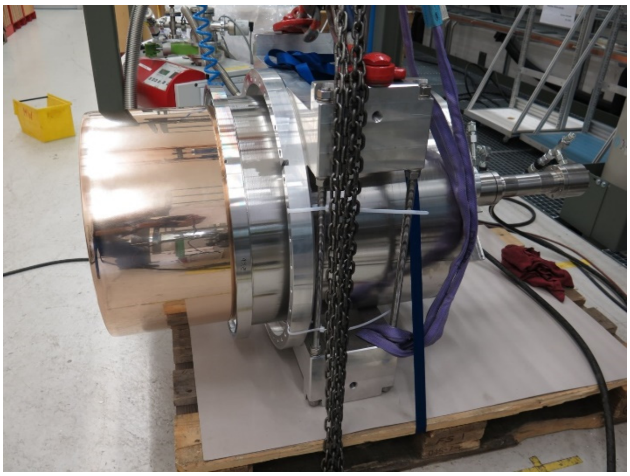

Figure 4: The tuner for the new 50 MHz resonator.

The plungers are made out of copper and are water cooled. The plungers are hard gold coated on the outside and there are finger contacts of silver graphite for the rf current flow to the cavity wall. During the tests the finger contacts showed some weakness requiring a consolidation before going into operation. After 1 month of tests abrasion of the silver graphite contact material was observed which leads to dust in the cavity and scratches in the gold plated copper. This is not acceptable for an operation in the cyclotron and caused a delay of the project. Until now different materials and contact types were tested, but no satisfactory results have been found. At the moment a version of the tuner without finger contacts is under test.

Coupling loop To couple the power into the resonator an inductive coupling loop is used. During the power runs in the test stand the input impedance of the resonator was matched to 50 Ohm. For the operation in the Injector 2 the impedance will be adapted to 81 Ohm, which results in a loop length of 84 mm. Due to the beam loading a perfect matching to 50 Ohm will be reached at a beam current of 2.0 mA.

Transmission Line

The transmission lines between the resonators and the final stage of the amplifiers are purchased from the German company Spinner. The standard RL 100-230 is used at the connection of the amplifier and on the resonator side: In between, the line is reduced to EIA 6 1/8”. The length of the transmission line between the amplifier and the cavity is matched by high power phase shifters to a multiple length of lambda half to avoid having impedance transformation along the transmission line.

Amplifiers

The power requirements of the amplifiers for the different resonators are listed in Table 4. These levels include some margin for the LLRF system, load mismatches, higher beam currents and an operation with only 3 resonators.

Table 4: Amplifier Power Requirements

RF System	Driver	IPA	PA
Resonator 1	2 kW	35 kW	360 kW
Resonator 2		10 kW	180 kW
Resonator 3	2 kW	35 kW	360 kW
Resonator 4		10 kW	180 kW

Power Amplifiers (PA) The final stage is a tetrode (RS2074HF) based amplifier, running in grounded grid configuration. This amplifier was designed at PSI for the Ring cyclotron where it is running at a power level of 650 kW. For the Injector 2 upgrade project the same rf design is used with an adapted working point on lower power level. As the rf circuits are installed in a trolley, the amplifier can be used either for the Injector 2 or for the Ring cyclotron. This facilitates stock-keeping of spare parts and allows for the flexibility to switch between the accelerators. Five new amplifiers were produced for the Injector 2 upgrade project (see Fig. 5). In case of a failure, the amplifier can be replaced within 3 hours.

Figure 5: Amplifier hall with 5 power amplifiers.

The plate voltage power supply is capable to deliver up to 15 kV and 40 A. It is a Pulsed Step Modulator, where the output Voltage can be adjusted. The advantage of this technology is to have less stored energy and no crowbar system is needed. The prototype was tested by the manufacturer on a load. All 4 power supplies were delivered to PSI and currently the installation is ongoing. The grid and screen power supplies are commercial power supplies from the industry. PSI is now performing the system integration and building up the amplifier control system for the final stage.

ISBN: 978-3-95450-205-9 doi:10.18429/JACoW-Cyclotrons2019-MOC03

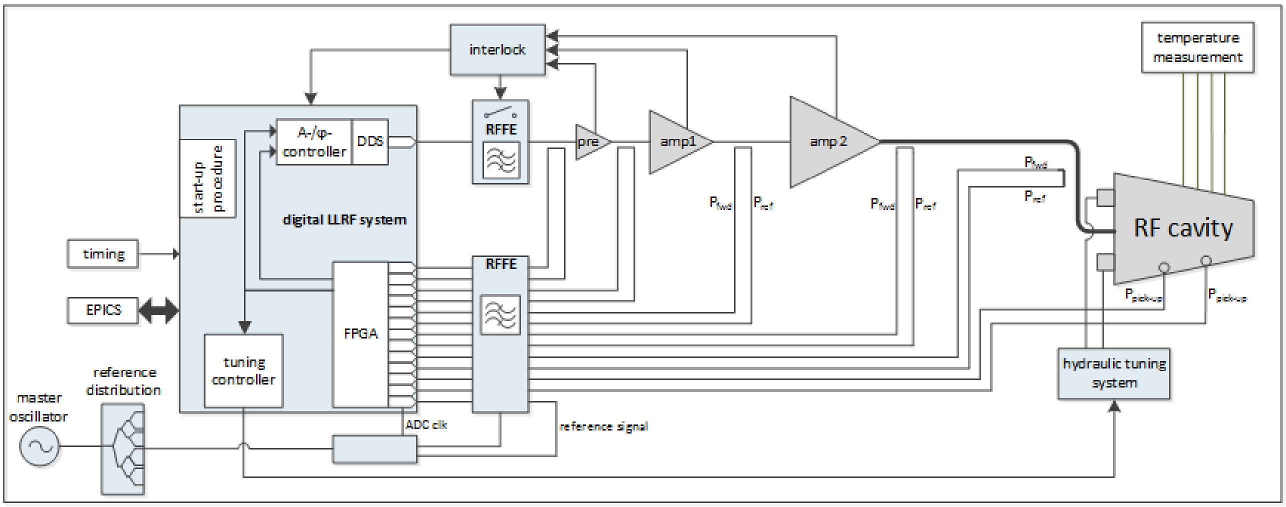

Figure 6: Overview layout of an rf station with digital LLRF system, amplifiers and cavity.

Intermediate Power Amplifier (IPA) In the rf stations for Resonator 2 & 4 a 10 kW solid state amplifier (SSA) is used as driver. Two BBL200A10000 were bought from the company Rhode & Schwarz. Both amplifiers have been delivered to PSI in 2019 and were successfully tested on a load.

For resonator 1 & 3, we consider a tetrode based IPA with a 2 kW SSA or alternatively a 35 kW SSA.

The first amplifier chain will be tested in 2020 on an rf load.

Digital LLRF System

A new digital system is intended to replace the existing analog LLRF System and will improve maintainability due to better diagnostics capabilities and integration into the control system (EPICS). The concept foresees a new LLRF system that is based on PSI's standard processing board, FMC mezzanine cards and a specific rf front-end to condition the rf signal for direct sampling. The demodulated signals are used for amplitude and phase feedback, for monitoring and calculation of the drive signal for the mechanical cavity tuners. In Fig. 6 an overview of an rf station is given.

The tuning system is realized as a master/slave system. The slave tuner follows the positon of the master tuner. The master can either be in position control, where the plunger moves to a given position or in the phase control mode, where the resonator is kept on resonance by comparing the phase of the incident power of a directional coupler with the phase of a cavity pickup.

The main objective of the LLRF system is to keep the amplitude and phase of the cavity in the required stability by setting the rf signal feed to the amplifier chain. To start up the system a startup sequence is implemented to bring the cavity quickly through the multipactoring levels by pulsing the rf [4].

The LLRF system includes an interlock system that supervises the whole rf station and can switch it of in case of any failure. The rf is inhibited in case of a subsystem, a bad vacuum, if the cooling water for the cavity, tuner or plunger is missing, and in case of a temperature of the cavity is too high.

CONCLUSION

The new Resonator 2 was successfully tested and characterized under full power. Different redesign options to solve the issues with the finger contacts on the tuners are under investigation. The installation of the amplifier chain and new digital LLRF system should be finish until summer 2020 for the commissioning of the new system in the second half of 2020 and to demonstrate the operation of Resonator 2 with beam. This will allow to operate the Injector 2 at a beam current of 2.4 mA beam currents and to complete the upgrade with the implementation of Resonator 4.

ACKNOWLEDGEMENTS

There a many different groups at PSI involved in this upgrade and without their effort for the project we wouldn't have reached the current state. Many thanks to all the people involved.

A special thanks goes to Hansruedi Fitze, Sebastian Jetzer and Erich Wüthrich of the rf group, who performed many measurements and tests on the new resonators.

REFERENCES

[1] S. Adam, "Calculation of Space Charge Effects in Isochronous Cyclotrons", in *Proc. 11th Particle Accelerator Conf. (PAC'85)*, Vancouver, Canada, May 1985, pp. 2507-2510.

[2] L. Stingelin, M. Bopp, and H. Fitze, "Development of the new 50 MHz resonators for the PSI Injector II Cyclotron", in *Proc. 18th Int. Conf. on Cyclotrons and their Applications (Cyclotrons'07)*, Giardini-Naxos, Italy, Oct. 2007, pp. 467-469.

[3] L. Stingelin *et al.*, "High power RF systems and resonators for sector cyclotrons", in *Proc. 19th Int. Conf. on Cyclotrons and their Applications (Cyclotrons'10)*, Lanzhou, China, Sep. 2010, paper WEM2CIO01, pp. 332-337.

[4] J. Cherix and P. Sigg, "Pulsed-RF to start the cyclotron cavities in a short time", in PSI - Scientific and Technical Report 2004 / Volume VI, Paul Scherrer Institute, Villigen PSI, Switzerland, 2004, pp. 16-17.

ISBN: 978-3-95450-205-9 doi:10.18429/JACoW-Cyclotrons2019-TUA02

NOVEL IRRADIATION METHODS FOR THERANOSTIC RADIOISOTOPE PRODUCTION WITH SOLID TARGETS AT THE BERN MEDICAL CYCLOTRON*

S. Braccini[1,†], C. Belver Aguilar[1], T. S. Carzaniga[1], G. Dellepiane[1], P. D. Häffner[1], P. Scampoli[1,2]
[1] Albert Einstein Center for Fundamental Physics (AEC), Laboratory for High Energy Physics (LHEP), University of Bern, Sidlerstrasse 5, 3012 Bern, Switzerland
[2] Department of Physics "Ettore Pancini", University of Napoli Federico II, Complesso Universitario di Monte S. Angelo, 80126 Napoli, Italy

Abstract

The production of medical radioisotopes for theranostics is essential for the development of personalized nuclear medicine. Among them, radiometals can be used to label proteins and peptides and their supply in quantity and quality for clinical applications represents a challenge. A research program is ongoing at the Bern medical cyclotron, where a solid target station with a pneumatic delivery system is in operation. To bombard isotope-enriched materials in form of compressed powders, a specific target coin was realized. To assess the activity at EoB, a system based on a CZT detector was developed. For an optimized production yield with the required radio nuclide purity, precise knowledge of the cross-sections and of the beam energy is crucial. Specific methods were developed to assess these quantities. To further enhance the capabilities of solid target stations at medical cyclotrons, a novel irradiation system based on an ultra-compact ~50 cm long beam line and a two-dimensional beam monitoring detector is under development to bombard targets down to few mg and few mm diameter. The first results on the production of ^{68}Ga, ^{64}Cu, ^{43}Sc, ^{44}Sc and ^{47}Sc are presented.

INTRODUCTION

The availability of novel medical radioisotopes is a key issue for advances in nuclear medicine. Of particular interest are the so-called theranostic pairs, which consist of one radionuclide used for diagnostics (β^+ or γ emitter for PET or SPECT) and one for therapy (β^-, Auger or α emitter for radio-immunotherapy). The two radionuclides must have very similar or identical chemical properties, as in the case of isotopes of the same element. They can be used to label the same biomolecules that, once injected into the patient's body, undergo the same metabolic processes. In this way, they allow treating the disease and, at the same time, assessing their uptake and following the evolution of the therapy by means of medical imaging. Along this line, radiometals can be bound to proteins and peptides and a few of their isotopes form the most promising pairs , such as ^{43,44}Sc/^{47}Sc and ^{61,64}Cu/^{67}Cu.

The availability of these radionuclides represents the bottle-neck for the development of theranostics in nuclear medicine. To solve this problem, the large number (> 1000 worldwide) of compact medical cyclotrons [1] could be exploited to produce the diagnostic partner of the pair and, in some cases, also the therapeutic one. Being designed to produce ^{18}F, which is presently the main PET radioisotope, medical cyclotrons provide proton beams of low energy (about 20 MeV) and relatively high intensity (>100 µA). For the production of radiometals, very rare and expensive isotope enriched materials have to be bombarded. They are often available in form of powder and, to obtain high yields, the use of a solid target station represents the best solution. Solid target stations for compact medical cyclotrons are rare. They are designed to irradiate target coins on which the enriched material is electroplated, a methodology that is not suitable for the production of several radiometals. For the bombardment of compressed materials in form of powder and to irradiate solid targets of small dimensions (about 6 mm diameter or less) novel irradiation instruments and methods have to be conceived and developed.

We report here about some of the developments and results obtained in the framework of the research programs ongoing at the cyclotron laboratory in operation at the Bern University Hospital [2, 3]. This facility is based on an IBA Cyclone 18/18 medical cyclotron (18 MeV proton beams, max. 150 µA extracted current, 8 out ports), which is used for routine production of ^{18}F during the night and for multidisciplinary research activities during the day. For the last purpose, it is equipped with a 6 m long Beam Transport Line (BTL) bringing the proton beam to a second bunker with independent access. Although uncommon for a hospital-based facility, this solution was fundamental to obtain the results reported in this paper.

SOLID TARGET DEVELOPMENTS AND FIRST RESULTS

To pursue our research program on novel medical radioisotopes, an IBA Nirta Solid target station was installed in one of the out ports of the cyclotron together with a pneumatic solid target transfer system (STTS) by TEMA Sinergie. The STTS was customised in such a way that the shuttle containing the irradiated target can be sent either to one hot cell in the nearby GMP radio-pharmacy or to a receiving

* Work partially supported by the Swiss National Science Foundation (SNSF). Grants: 200021_175749, CRSII5_180352, CR23I2_156852
† saverio.braccini@lhep.unibe.ch

ISBN: 978-3-95450-205-9 doi:10.18429/JACoW-Cyclotrons2019-TUA02

station located in the BTL bunker. The latter option is used for all non GMP activities and when the irradiated target is transported to external research laboratories for separation and labelling.

The solid target station was designed to bombard a disk (24 mm diameter, 2 mm thick) on which the target material is electroplated, as in the case of ^{64}Cu production via the reaction ^{64}Ni(p,n)^{64}Cu. This method is not suitable to produce scandium isotopes that can be obtained by irradiating powders compressed in pellets made of $CaCO_3$ or CaO. For this purpose, a specific magnetic "coin" target disk was conceived and constructed. As shown in Fig. 1, the coin has the same external dimensions as an ordinary disk but is composed of two halves kept together by small permanent magnets. The choice of its components and its manufacturing

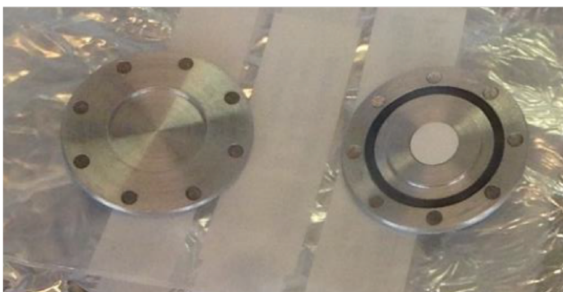

Figure 1: The two halves of the "coin" target. The front part (on the left) is used to degrade the beam to the desired energy. The rear half (on the right) contains the 6 mm diameter pellet and hosts an o-ring to assure gas tightness.

is challenging. In particular, the magnets should not loose their properties due to the high temperatures (>200 °C) that are reached during irradiation, although the disk is cooled by water on the back and by helium on the front side. The coin is constructed using an aluminum alloy (EN AW-6082) while other materials characterised by high melting point and low residual activation (such as niobium) are considered. The front window of the coin is used to adjust the energy of the protons reaching the target material. Due to the high cost of enriched materials, 30 mg of CaO were used for the case of ^{44}Sc, giving a 6 mm diameter and 500 µm thick pellet. It is important to remark that a very good thermal contact between the two halves of the magnetic coin and the target material is mandatory to assure good cooling, thus avoiding target and coin melting.

Being the beam extracted from the cyclotron ~12 mm FWHM at the solid target station in standard irradiation conditions, only about 25% of the extracted protons are effectively used to produce the desired isotope if a 6 mm pellet is used. This fact produces unwanted residual activity in the coin with consequent radiation protection and transport limitations. Furthermore, overheat is produced during the irradiation with limitations on the total beam current. To improve this issue, a novel irradiation system described later in this paper is under development. It has to be remarked that some powder materials are available in form of oxide and the reaction ^{16}O(p,α)^{13}N produces a relevant amount of activity in gas form provoking radiation protection issues. For this reason, an o-ring was embedded in the coin to contain the radioactive gas (Fig. 1). For the case of scandium, this is particularly critical if $CaCO_3$ is used due the increase of pressure caused by the production of CO_2 by dissociation. For this reason, a method for the production of CaO targets was developed [4].

The produced activity and the radionuclidic purity can be optimised on the basis of an accurate knowledge of the reaction cross-sections by choosing the appropriate thicknesses of the cyclotron exit window, of the front part of the coin and of the pellet. Several versions of the magnetic coin target were therefore realised for each specific radionuclide to be produced. In particular, a coin was made to irradiate thin foils at the maximum possible beam energy featuring a front part made of a ring without any absorber in front of the target material. On the basis of the cross sections and by measuring the current on target during irradiation, the produced activity can be estimated. To experimentally assess the produced activity after EoB and the delivery of the shuttle, a CZT detector system was designed and installed about 1 m away from the receiving station. Based on a ~1 cm^3 CdZnTe crystal (GBS Elektronik), this detector allows recoding the energy spectra of the gamma rays emitted by the target (coin and pellet). The low detection efficiency due to the distance and the small volume of the crystal is well suited for the high produced activities. Once calibrated by means of an HPGe detector, the signal of the CZT allows measuring the produced activity with an accuracy of a few per cent [5].

Thanks to these developments, several radionuclides have been produced during the first two years of operation of the solid target station, as reported in Table 1. In particular, the production of about 15 GBq of ^{44}Sc represents a promising

Table 1: Main Achievements in Non-Standard Radioisotope Production Obtained During the First Two Years of Operation of the Solid Target Station at the Bern Cyclotron. The Beam Current Corresponds to the Protons Hitting the Target Material.

Isotope	Reaction	Target Material	Beam Current [µA]	Irradiation Time [h]	A_{EOB} [GBq]
^{44}Sc	(p,n)	Enriched CaO pellet	5	5	~15
^{64}Cu	(p,n)	Enriched Ni deposition	15	10	~20
^{68}Ga	(p,n)	Enriched Zn pellet	5	0.5	~15
^{48}V	(p,n)	Ti metal foils	10	1	~0.15
^{65}Er	(p,n)	Ho metal disk	10	10	~1.5

ISBN: 978-3-95450-205-9 doi:10.18429/JACoW-Cyclotrons2019-TUA02

result in view of theranostic clinical applications. Production tests of ^{43}Sc and of the therapeutic partner ^{47}Sc are foreseen in the near future using the same methodology. In particular, we expect to obtain about 10 GBq of ^{47}Sc, an adequate quantity for clinical trials. The results we obtained on the production of ^{68}Ga [5] are at the basis of on-going developments aimed at improving the scarce supply of this radionuclide by Ge/Ga generators. Developments in fundamental physics were also pursued. $^{143-147}$Pm radioisotopes from a Nd oxide target were produced in enough quantities to be studied by high-precision laser spectroscopy. The production of very thin ^{48}V positron sources may open new avenues to obtain positron beams for fundamental and applied research using a table-top apparatus [6].

BEAM CHARACTERIZATION

To enhance the production capabilities of compact medical cyclotrons in the production of unconventional radioisotopes, an accurate knowledge of the beam characteristics is mandatory in order to be able to effectively bombard small targets (6 mm diameter or less) and to reduce to a minimum the irradiation of other materials.

Beam Monitoring Detectors

Beam monitoring detectors are essential in accelerator facilities and our group is engaged in developing specific devices to complement the standard equipment (destructive beam viewers) provided by the manufacturer of the cyclotron and the BTL.

A high sensitivity Faraday cup was developed [7] to measure beam currents down to the pA range.

The UniBEaM detector [8] is an optical wire scanner that consists of a 200 µm diameter 10 cm long doped silica fibre passed through the beam. The collected light allows measuring the beam profile in an almost non-destructive way with a precision of about 0.1 mm. This instrument can detect beams in a wide range of intensities (from 1 pA to about 10 µA) and, being linear up to about 1 µA, can be used to assess the total beam current by integrating the beam profile. This device is commercialised by the Canadian company D-Pace [9] and can provide profiles in two orthogonal axes by using two fibres moved in orthogonal directions.

The π^2 detector is based on the collection by a CCD camera of the light produced by the beam on a few µm thick P47 phosphor screen deposited on a 1 µm aluminum foil (Fig. 2). The foil can be removed from the beam path via a pneumatic mechanism. This device allows measuring a two-dimensional beam profile in an almost non destructive way.

Transverse Beam Emittance

The transverse beam emittance was first assessed using the BTL by means of the standard and time consuming quadrupole variation method. Based on four UniBEaM detectors located at a distance of about 50 cm one another along the beam path, a novel system (dubbed ^{4}PrOBεaM)

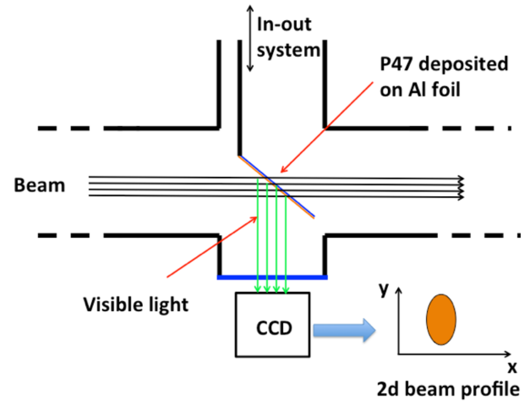

Figure 2: Scheme of the π^2 beam-monitoring detector. The intensity of the light emitted by the P47 coating is proportional to the intensity of the beam and is recorded by a CCD camera.

capable of measuring the transverse beam emittance quasi on-line was realised [10]. Based on the acquisition of four consecutive beam profiles, the transverse beam emittance can be measured in less than one minute. This system allowed to study the transverse beam emittance as a function of several parameters such as the current in the main coil of the cyclotron or the radio-frequency peak voltage.

Beam Energy

The beam energy of the pristine proton beam is an essential parameter for an optimised radioisotope production with solid targets. We measured the beam energy with different methods based on the assessment of the beam current after passive absorbers of different thickness [10], on a multi-leaf Faraday cup [11] and on Rutherford Back Scattering (RBS) [12]. A further apparatus based on the deflection of the beam by a dipole electromagnet and on the measurement of the beam position by a UniBEaM detector was conceived and realised to assess the beam energy as a function of cyclotron operational parameters as the current in the main coil. The beam energy extracted on the BTL was measured to be (18.3 ± 0.3) MeV in resonance conditions, a slightly higher value with respect to the nominal value of 18 MeV due to the modified position of the stripper foil [3].

CROSS SECTION MEASUREMENTS

A novel method to measure cross-sections with a medical cyclotron was developed [13]. It relies on the irradiation of a known mass with a flat beam current surface density instead of the usual method based on the irradiation of a homogeneously thick target. The beam is flattened by means of the optical elements of the BTL and monitored on-line by means of the UniBEaM and the π^2 detectors. Before hitting the target, protons cross thin aluminum discs used to degrade their energy that was calculated on the basis of our measurement of the pristine beam energy and by Monte Carlo simulations (SRIM). The integrated charge due to the protons passing through the collimator is recorded and the

ISBN: 978-3-95450-205-9 doi:10.18429/JACoW-Cyclotrons2019-TUA02

obtained activity measured by HPGe gamma spectroscopy. With this method, the production cross section of several radioisotopes (^{43}Sc, ^{44}Sc [13, 14], ^{48}V [13], ^{68}Ga [5] and ^{44m}Sc, ^{47}Sc, ^{48}Sc, ^{47}Ca [15]) was measured.

FUTURE DEVELOPMENTS

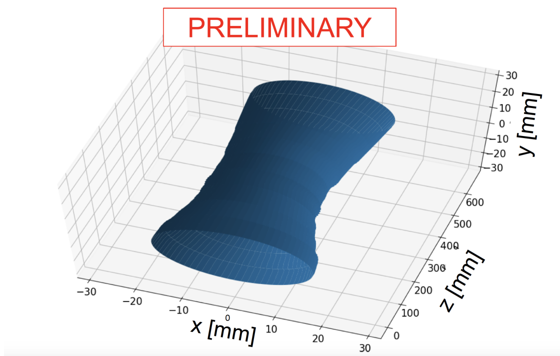

Figure 3: Three dimensional reconstruction of the beam envelope based on the measurements by the π^3 detector.

To enhance and optimise the production capabilities of solid target stations at compact medical cyclotrons, a novel irradiation system able to focus the beam down to the diameter of the pellet (~6 mm or less) and to keep it always on target is under development. With this system, we expect to enhance the production activity at EoB of a factor five for the same extracted current of 20 µA for the case of ^{44}Sc. Since basically all the hospital-based cyclotron facilities do not dispose of a long beam line, this apparatus must be very compact (about 1 m long) to be installed in the same bunker as the accelerator. This apparatus is composed of a compact 50 cm long Mini-Beam-Line (MBL) and a two-dimensional beam monitoring detector (dual axis UniBEaM or π^2) located just in front of the solid target station. The MBL is produced by the company D-Pace [16] and consists of a quadrupole doublet with embedded two (one vertical and one horizonal) steering dipoles. A software feedback system collects and analyses the data from the detector and, if necessary, acts on the power supplies of the MBL to correct the beam position and shape. For this purpose, an accurate characterisation of the MBL is necessary and beam tests are on-going by means of the BTL. Simulations of the beam optics with the MAD-X software are performed. Due to the compactness of the optical elements of the MBL, beam optics has to be studied carefully. For this purpose an innovative three dimensional beam monitoring detector has been conceived and built, dubbed π^3. This detector consist of a small foil like the π^2 and a small camera connected to it that operates under vacuum. The screen and the camera are moved inside the beam pipe and images of the beam are acquired at distances of 1 mm inside the magnetic elements of the MBL. Focusing, defocusing and steering effects can be directly measured and a full three-dimensional reconstruction of the beam obtained [17]. A first preliminary reconstruction of the beam envelope is shown in Fig. 3.

CONCLUSIONS AND OUTLOOK

A research program aimed at the production of non-conventional radioisotopes is on-going at the Bern cyclotron laboratory. Novel irradiation instruments and methods were conceived, realized and tested based on accelerator and detector physics developments. The promising results obtained represent a valuable step towards the establishment of efficient and reliable radioisotope supply using compact medical cyclotrons in view of theranostic applications in nuclear medicine.

ACKNOWLEDGEMENTS

We acknowledge contributions from LHEP engineering and technical staff. We are thankful to Gianni Molinari (TERA Foundation and CERN) for contributions to the first prototype of the π^2 detector and to Riccardo Bosi and the SWAN Isotopen AG maintenance team for the collaboration in the set-up and operation of the solid target system.

REFERENCES

[1] S. Braccini, “Compact medical cyclotrons and their use for radioisotope production and multi-disciplinary research”, in *Proc. Cyclotrons’16*, Zurich, Switzerland, Sep. 2016, pp. 229–234. doi:10.18429/JACoW-Cyclotrons2016-TUD01

[2] S. Braccini, A. Ereditato, P. Scampoli, and K. von Bremen, “The new Bern cyclotron laboratory for radioisotope production and research”, in *Proc. IPAC’11*, San Sebastian, Spain, Sep. 2011, paper THPS080, pp. 3618–3620.

[3] S. Braccini, “The new Bern PET cyclotron, its research beam line, and the development of an innovative beam monitor detector”, *AIP Conf. Proc.*, vol. 1525, p. 144-150, Apr. 2013. doi:10.1063/1.4802308

[4] N. van der Meulen *et al.*, “Targetry developments for 44Sc production using enriched CaO”, in *Proc. of the 17th WTTC workshop*, Coimbra, Portugal, Aug. 2018, paper OP24, to be published.

[5] D. Wüthrich, Master thesis, University of Bern, 2018.

[6] L. Gerchow *et al.*, “High efficiency cyclotron trap assisted positron moderator”, *Instruments* 2018, vol. 2(3), art. no. 10, Jun. 2018. doi:10.3390/instruments2030010

[7] M. Auger *et al.*, ‘Low current performance of the Bern medical cyclotron down to the pA range”, *Meas. Si. Technol.*, vol. 26, p. 094006, Jul. 2015. doi:10.1088/0957-0233/26/9/094006

[8] M. Auger *et al.*, “A detector based on silica fibers for ion beam monitoring in a wide current range”, *J. Instrum.*, vol. 11, p. P03027, Mar. 2016. doi:10.1088/1748-0221/11/03/P03027

[9] D. E. Potkins *et al.*, “A low-cost beam profiler based on Cerium-doped silica fibers”, *Physics Procedia*, vol. 90, pp. 215-222, Oct. 2017. doi:10.1016/j.phpro.2017.09.061

[10] K. P. Nesteruk *et al.*, “A system for online beam emittance measurements and proton beam characterization”, *J. Instrum.*, vol. 13, pp. P01011, Jan. 2018. doi:10.1088/1748-0221/13/01/P01011

ISBN: 978-3-95450-205-9 doi:10.18429/JACoW-Cyclotrons2019-TUA02

[11] K. P. Nesteruk *et al.*, "Measurement of the beam energy distribution of a medical cyclotron with a multi-leaf faraday cup", *Instruments*, vol. 3(1), art. no. 4, Jan. 2019. doi:10.3390/instruments3010004

[12] L. Campajola *et al.*, "Measurement of the proton beam energy of a medical cyclotron based on Rutherford Back-scattering Analysis", *Nucl. Instrum. Methods Phys. Res.* B, vol. 440, pp. 114-117, Feb. 2019. doi:10.1016/j.nimb.2018.12.017

[13] T. S. Carzaniga *et al.*, "Measurement of ^{43}Sc and ^{44}Sc production cross-section with an 18 MeV medical PET cyclotron", *Appl. Radiat. Isot.*, vol. 129, pp. 96-102, Nov. 2017. doi:10.1016/j.apradiso.2017.08.013

[14] T. S. Carzaniga *et al.*, "Measurement of the ^{43}Sc production cross-section with a deuteron beam", *Appl. Radiat. Isot.*, vol. 145, pp. 205-208, Mar. 2019. doi:10.1016/j.apradiso.2018.12.031

[15] T. S. Carzaniga and S. Braccini, "Cross-section measurement of ^{44m}Sc, ^{47}Sc, ^{48}Sc and ^{47}Ca for an optimized ^{47}Sc production with an 18 MeV medical PET cyclotron", *Appl. Radiat. Isot.*, vol. 143, pp. 18-23, Jan. 2019.

[16] M. P. Dehnel, D. E. Potkins, and T. M. Stewart, "An integrated self-supporting mini-beamline for PET cyclotrons", in *Proc. Cyclotrons'13*, Vancouver, Canada, Sep. 2013, paper TUPSH014, pp. 251–253.

[17] A. Gsponer, Bachelor thesis, University of Bern, 2019.

ISBN: 978-3-95450-205-9 doi:10.18429/JACoW-Cyclotrons2019-TUA03

THE USE OF PSI's IP2 BEAM LINE TOWARDS EXOTIC RADIONUCLIDE DEVELOPMENT AND ITS APPLICATION TOWARDS PROOF-OF-PRINCIPLE PRECLINICAL AND CLINICAL STUDIES

N. P. van der Meulen†, R. Eichler, P. V. Grundler, R. Hasler, W. Hirzel, S. Joray, D. C. Kiselev, R. Sobbia, A. Sommerhalder, Z. Talip, H. Zhang
Paul Scherrer Institut, 5232 Villigen PSI, Switzerland
S. Braccini, Laboratory of High Energy Physics, University of Bern, Bern, Switzerland

Abstract

Paul Scherrer Institute (PSI) runs a High Intensity Proton Accelerator (HIPA) facility, where a maximum of 100 µA protons is gleaned from high intensity 72 MeV protons from Injector 2, a separated sector cyclotron, into the IP2 target station. These protons irradiate various targets towards the production of exotic radionuclides intended for medical purposes.

Many radiometals in use today are for the diagnosis of disease, with the most popular means of detection being Positron Emission Tomography. These positron emitters are easily produced at low proton energies using medical cyclotrons, however, developments at these facilities are lacking. The fixed 72 MeV proton beam is degraded at IP2 using niobium to provide the desired energy to irradiate targets to produce the likes of ^{44}Sc, ^{43}Sc, ^{64}Cu and ^{165}Er. Once developed, these proofs-of-principle are then put into practice at partner facilities.

Target holders and degraders require development to optimize irradiation conditions and target cooling. Various options are explored, with pros and cons taken into consideration based on calculations and simulations.

INTRODUCTION

Paul Scherrer Institute (PSI), Switzerland's premier research facility, runs a High Intensity Proton Accelerator (HIPA) amenity as part of its Large Facilities, where three accelerators are connected in series to increase proton beam energy. A Cockroft-Walton accelerator accelerates protons at 870 keV to the Injector II separated sector cyclotron, where the protons are accelerated to 72 MeV at an intensity of ~2.5 mA to the Ring cyclotron. The Ring cyclotron accelerates the protons further to 590 MeV, which is then sent down the beam line to various experimental vaults, before the remainder of the beam is collected in a Pb beam dump, which serves as a neutron spallation source for the Swiss Neutron Source (SINQ) [1].

Along the beam line between Injector II and the Ring cyclotron, the Radionuclide Development/production irradiation station (known as IP2) currently gleans ~50 µA protons from Injector 2, by means of a beam splitter, into the IP2 target station (Fig.1). These protons irradiate various targets towards the production of exotic radionuclides intended for medical purposes.

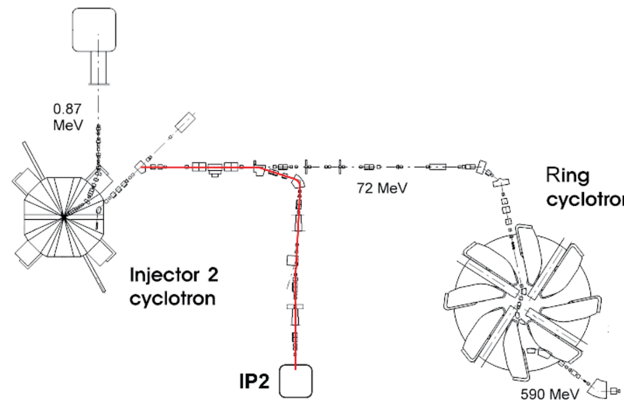

Figure 1: The beam transfer from the Cockroft Walton accelerator via the Injector II cyclotron to the Ring cyclotron. The red line indicates the 72 MeV beam gleaned from Injector II to IP2. Figure adapted from [2].

Many radiometals currently used in nuclear medicine are for the diagnosis of disease, with the most popular means of detection being Positron Emission Tomography (PET). These positron emitters are easily produced at low proton energies using medical cyclotrons, however, development using such facilities are rare.

The irradiation station at IP2 is used for ~9 months of the year and, as a result, cannot be considered for use in any commercial setting. The system is still put to good use, however, towards the development of novel, non-standard radiometals. The station was used to produce the likes of ^{18}F [3] and ^{124}I [4] in a novel way by utilizing its higher beam energy, as well as ^{67}Cu [5], ^{82}Sr and ^{68}Ge, but these activities were halted over a decade ago. As the use of PET increased in popularity for the diagnosis of cancer, the strategy of the station's use was adjusted to meet the growing demand for positron-emitting radionuclides.

Positron-emitting radionuclides are popular, too, because they can easily be produced at medical cyclotrons (with an installed solid target station) utilizing the (p,n) nuclear reaction in the vicinity of 13 MeV protons. To apply this to the revised strategy of IP2's use, it was necessary to degrade from 72 MeV to the desired energy of the radiometal to be produced. Once developed, these proofs-of-principle can then be put into practice at partner facilities.

† nick.vandermeulen@psi.ch

ISBN: 978-3-95450-205-9 doi:10.18429/JACoW-Cyclotrons2019-TUA03

BEAM DEGRADATION

The 72 MeV proton beam is degraded at IP2 using niobium (Nb) at various thicknesses to provide the desired energy to irradiate the target in question. The size of degraders range from 1.0 to 3.5 mm and the degradation of the beam (Fig. 2), calculated using SRIM-2013, is listed in Table 1. The values stated are more of an approximation, as this does not take the beam spread, as a result of the degradation of the proton beam, into consideration. Radionuclides developed and produced using this concept include ^{44}Sc [6], ^{43}Sc [7], ^{64}Cu [8] and ^{165}Er [9, 10].

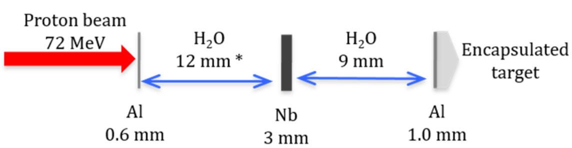

Figure 2: Degrading of the 72 MeV proton beam at the IP2 target station at PSI. The water jacket between the encapsulated target and the degrader remains constant.

Table 1: Nb Degraders used in the 72 MeV Proton Beam at IP2 Irradiation Station at PSI and their Degrading Effect

Nb Degrader Thickness (mm)	Proton Beam Energy on Target (MeV)
1.0	34.1
1.8	28.1
2.0	26.4
2.2	24.7
2.4	22.8
2.8	18.6
3.0	16.2
3.1	14.9
3.2	13.4
3.3	11.8
3.4	10.3
3.5	8.6

The target holders used for the irradiation of targets have not changed much over the years, however, there is place for the fitting of the degrader (Fig. 3). There have been concerns raised with regard to the cooling of the target and initial simulations indicate that there are areas where the water cooling of the target may be optimized (Fig. 4).

Currently, an updated system is being designed such that multiple degraders (maximum of 1 mm thick) are used for the same effect, so that the flow of water through the holder is increased, thereby, improving the cooling of the target. Initial simulations have been performed and, based on the result, a prototype created using a 3D printer (Fig. 5). The prototype was tested in a hot cell, using manipulators, to determine the practicality of installation and removal of the target capsule and degrader stack, respectively.

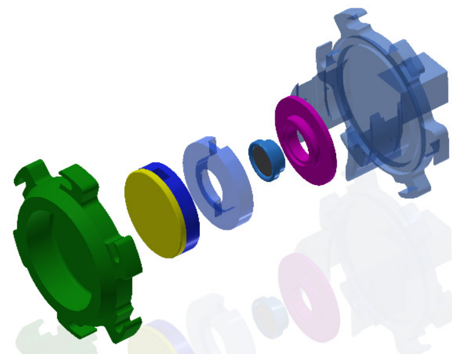

Figure 3: Blown-up layout of target holder containing the target capsule and degrader (blue and yellow).

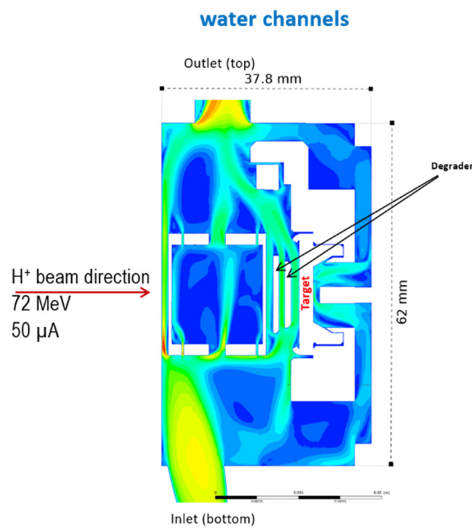

Figure 4: Contour plot of the velocity profile from fluid dynamics simulations through the target holder and degrader in an earlier prototype. Blue indicates a slow velocity (1x10^{-3} m.s^{-1}), green ~1 m.s^{-1}, yellow ~1.5 m.s^{-1} and red the highest velocity at ~ 2 m.s^{-1}.

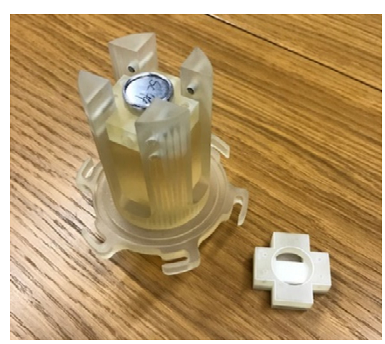

Figure 5: Prototype of target holder, containing a ^{44}Sc target capsule, with a stacked degrader lying next to it.

TARGET PREPARATION

As the (p,n) nuclear reaction is often utilized for irradiation purposes and radionuclidic purity of products for nuclear medicine purposes is vital, one has to turn to the use of enriched target material to obtain the desired nuclear reaction and product. These materials are generally expensive and one has to be able to optimize the targets such that

ISBN: 978-3-95450-205-9 doi:10.18429/JACoW-Cyclotrons2019-TUA03

enough activity is produced from as little material as possible. Sometimes, the target material cost is such that one has to devise a means of recycling the target material post production.

Enriched oxide targets have been designed to be 6 mm in diameter and 0.5 mm thick (Fig. 6), while the target for ^{64}Cu production consists of an enriched Ni-plated Au foil, 10 mm in diameter [8]. This concept has been slightly adapted for use at the cyclotron facility at the University of Bern, however, the capsule and target design has been used directly towards the design of the solid target station (with an IBA Cyclone 18/9) recently built at ETH Zurich.

Figure 6: Pressed salt target, 6 mm in diameter, nestled in the indentation of an Al (99.5 % pure) capsule.

RADIONUCLIDE DEVELOPMENT AT IP2

^{44}Sc

^{44}Sc is seen as a potentially ideal radiometal for PET, as its half-life ($T_{1/2}$ = 3.97 h) is longer than ^{68}Ga (currently the most popular radiometal in use for PET; $T_{1/2}$ = 68 min) and has better resolution than its Ga counterpart. ^{44}Sc was initially obtained from a ^{44}Ti/^{44}Sc generator, where the parent (^{44}Ti) radionuclide would decay into the daughter (^{44}Sc) and the daughter would be eluted (or “milked”) from the generator. The disadvantage of such a system is two-fold: the production rate for producing ^{44}Ti (from Sc) is extremely low, thereby, only producing low-activity generators from which ^{44}Sc can be obtained. Secondly, the half-life of the parent ($T_{1/2}$ = 60 a) is such that breakthrough from the generator could have disastrous consequences in a clinical setting [6].

^{44}Sc can also be produced at a cyclotron via the ^{44}Ca(p,n)^{44}Sc nuclear reaction. Initially, enriched $CaCO_3$ targets were pressed onto graphite and irradiated at ~11 MeV protons at 50 µA beam intensity (currently using a 3.4 mm degrader – Table 1), however, the targets were not homogeneous and 6 mm pressed pure carbonate targets were developed to replace them. It was subsequently discovered that the carbonate targets would easily dissociate in the beam, with the release of radioactive oxygen, and it was decided to further develop the target material. Enriched carbonate targets were converted to oxide targets, which were found to be far more robust under irradiation conditions [11].

Irradiated targets were dissolved in nitric acid and loaded onto a column containing DGA extraction resin, where the ^{44}Sc was retained and the Ca target material passed through the system. This was collected separately and subsequently recycled to make new targets. The desired ^{44}Sc was eluted with dilute hydrochloric acid and concentrated onto a second, smaller, resin column. The final product was eluted in a small volume such that it could be used effectively for preclinical [12] and clinical studies [13].

The system was converted and implemented at the medical cyclotron facility at the University of Bern, which houses an IBA Cyclone 18/18 with a solid target station. The enriched CaO pellet was the same, however, the encapsulation design was customized to fit into the target station [11].

^{43}Sc

While ^{44}Sc is an attractive PET radionuclide, it has the disadvantage of the emission of a γ-ray at 1157 keV, with almost 100 % intensity, having implications on radiation protection and image quality. A suggested alternative is ^{43}Sc, with a similar half-life ($T_{1/2}$ = 3.89 h), but its γ-emission at 373 keV is at 22.5 % intensity, thereby, decreasing dose to the clinical operator and patient and slightly improving image resolution.

^{43}Sc is more difficult to produce than its ^{44}Sc counterpart: production cross sections using the two most popular production routes is lower than for ^{44}Sc [7] and the means to produce it is more expensive, thereby, making it less attractive to introduce into the clinic. It is produced at IP2 via the ^{46}Ti(p,α)^{43}Sc nuclear reaction (using a 3.2 mm Nb degrader – Table 1) or via the ^{43}Ca(p,n)^{43}Sc nuclear reaction using similar irradiation conditions to that of ^{44}Sc production.

The $^{46}Ti_2O_3$ was initially reduced to Ti powder and then pressed into a graphite pellet for irradiation. The beam intensity was reduced to 20 µA for optimum irradiation and target dissolution conditions. The Ti target was dissolved in concentrated hydrochloric acid, diluted slightly and passed through a DGA extraction resin column, where the Sc was retained and the Ti collected for recycling. The Sc was eluted in dilute hydrochloric acid and concentrated on a small SCX cation exchange column. The product was eluted in a small volume of hydrochloric acid/sodium chloride solution. While radionuclidic purity was high (>98 %), the separation was time-consuming and the yields relatively poor [7].

^{43}Sc production and separation from enriched Ca was performed as for ^{44}Sc. Enrichment of ^{43}Ca determines radionuclidic purity of the product, in this case, 57 % enriched ^{43}Ca produced 66.6 % ^{43}Sc and 33.3 % ^{44}Sc. The chemical separation, in comparison to the Ti route, was simple and fast and the yield considerably higher, however the target material is prohibitively expensive.

A more recent approach was taken to make this radionuclide, namely, via the ^{44}Ca(p,2n)^{43}Sc production route [14].

Enriched ^{44}CaO pellets were encapsulated and irradiated as for ^{44}Sc, instead, the Nb degrader used was 2.0 mm thick – coinciding with ~26.4 MeV protons. High yields were

ISBN: 978-3-95450-205-9 doi:10.18429/JACoW-Cyclotrons2019-TUA03

obtained, with >70 % ^{43}Sc obtained along with co-produced ^{44}Sc. The product was of high chemical purity, confirmed by the ability to use it for high-specific radiolabelling of biomolecules.

^{64}Cu

^{64}Cu is a medically-interesting PET radionuclide with a longer half-life than many of its radiometal counterparts used for similar purposes ($T_{1/2}$ = 12.7 h). It is known to produce images of high resolution. The means of producing it is via the $^{64}Ni(p,n)^{64}Cu$ nuclear reaction and the target material required to produce this radionuclide is expensive. A thin layer of enriched Ni is electroplated onto 0.5 mm thick gold foils as preparation of targets for irradiation.

The irradiated ^{64}Ni (irradiated with a proton beam degraded with 3.4 mm Nb at 50 µA beam intensity) was dissolved from the gold foil in hydrochloric acid and subsequently diluted to obtain a concentration of 0.1 M hydrochloric acid and 60 % acetone mixture. This resultant solution was passed through a macroporous cation exchange resin column (AG MP-50), where both Cu and Ni were retained. The concentration of acetone was adjusted to elute the ^{64}Cu final product first, while the Ni is finally eluted in hydrochloric acid and collected for recycling purposes [8]. The radionuclide has been used extensively for preclinical studies.

^{165}Er

^{165}Er is a pure Auger-emitting radiolanthanide and is regarded as an interesting option towards targeted radionuclide therapy. It emits no γ-rays and can be detected with its low energy X-rays. It can be produced by means of low-energy protons via the $^{nat}Ho(p,n)^{165}Er$ nuclear reaction (referred to as the "direct" route) or at higher proton energies via the $^{166}Er(p,2n)^{165}Tm \rightarrow ^{165}Er$ nuclear reaction (referred to as the "indirect" production route).

The direct route utilized pressed Ho_2O_3 targets 13 mm in diameter, as the 6 mm diameter target produced relatively low activities of product. The beam settings had to be adjusted accordingly, however, the beam intensity had to be reduced to 20 µA, as any higher intensity had a negative impact on the production yield. The same irradiation parameters were applied to the indirect production route, however, a 6 mm target was prepared for the irradiation of enriched target material (Fig. 6) [9, 10].

An adapted chemical separation method, based on that determined for ^{161}Tb production at PSI [15] was adopted.

CONCLUSIONS AND OUTLOOK

The IP2 target station at PSI has proven to be an effective tool towards proof-of-principle development of exotic radionuclides in Switzerland. Its effectiveness has resulted in small, long overdue upgrades planned to improve irradiation conditions. A new target holder has been designed and is under construction, with initial tests planned within the next year. Other upgrades, such as beam position diagnostics, are envisaged in the near future.

REFERENCES

[1] M. Seidel *et al.,* "Production of a 1.3 MW proton beam at PSI", in *Proc. 1st Int. Particle Accelerator Conf. (IPAC'10)*, Kyoto, Japan, May 2010, pp. 1309-1313.

[2] Y. J. Bi *et al.,* "Towards quantitative simulations of high power proton cyclotrons", *Physical Review Special Topics - Accelerators and Beams*, vol. 14, p. 054402, May 2011. doi:10.1103/PhysRevSTAB.14.054402

[3] R. Schwarzbach *et al.,* "Production of ^{18}F from sodium-metal-target", in *Proc. 5th International Workshop on Targetry and Target Chemistry*, Upton, NY, USA, Sep. 1993, pp. 77-81.

[4] R. Weinreich and E. J. Knust. "Quality control of ^{124}I", in *Proc. 6th International Workshop on Targetry and Target Chemistry*, Vancouver, BC, Canada, Aug. 1995, pp. 84-86.

[5] R. Schwarzbach, K. Zimmernann, I. Novak-Hofer, and P. A. Schubiger, "A comparison of ^{67}Cu production by proton (67 to 12 MeV) induced reactions on ^{nat}Zn and on enriched $^{68}Zn/^{70}Zn$", *Supplement: J. Labelled Compd. Radiopharm*, vol. 44, no. S1, pp. S809-811, May 2001. doi:10.1002/jlcr.25804401284

[6] N. P. van der Meulen *et al.*, "Cyclotron production of ^{44}Sc: from bench to bedside", *Nucl. Med. Biol.*, vol. 42, pp. 745-751, 2015. doi:10.1016/j.nucmedbio.2015.05.005

[7] K. A. Domnanich *et al.*, "Production and separation of ^{43}Sc for radiopharmaceutical purposes", *EJNMMI Radiopharmacy and Chemistry,* vol. 2, p. 14, 2017.

[8] N. P. van der Meulen *et al.,* "Implementation of a new separation method to produce qualitatively improved ^{64}Cu", *J. Labelled Compd. Radiopharm.,* vol. 62, pp. 460–470, 2019. doi:10.1002/jlcr.3730

[9] N. Gracheva *et al.,* "Production and separation of ^{165}Er – a medically interesting Auger emitter", Villigen-PSI, Switzerland, Laboratory of Radiochemistry Annual Report 2017-57, Apr. 2018.

[10] N. Gracheva, R. Schibli, and N. P. van der Meulen. "Production and purification of the pure Auger electon emitter Erbium-165", Villigen-PSI, Switzerland, Laboratory of Radiochemistry Annual Report 2018-58, Apr. 2019.

[11] N. P. van der Meulen *et al.,* "Targetry for ^{44}Sc production using enriched CaO", submitted to Proc. 17th International Workshop on Targetry and Target Chemistry, Coimbra, Portugal, Aug. 2018, OP24.

[12] C. Müller, K. A. Domnanich, C. A. Umbricht, and N. P. van der Meulen, "Scandium and terbium radionuclides for radiotheranostics: Current state of development towards clinical application", *Br. J. Radiol.,* vol. 91, p. 20180074, 2018. doi:10.1259/bjr.20180074

[13] A. Singh *et al.,* "First-in-human PET/CT imaging of metastatic neuroendocrine neoplasms with cyclotron-produced ^{44}Sc-DOTATOC: A proof-of-concept study", *Cancer Biotherapy and Radiopharmaceuticals*, vol. 32, May 2017. doi:10.1089/cbr.2016.2173.

[14] N. van der Meulen and R. Hasler. "The possibility of producing ^{43}Sc from ^{44}Ca via the (p,2n) nuclear reaction", *Nucl. Med. Biol.,* vol. 72-73, Supplement 1, p. S9, July 2019. doi:10.1016/S0969-8051(19)30215-X

[15] N. Gracheva *et al.,* "Production and characterization of no-carrier-added ^{161}Tb as an alternative to the clinically-applied ^{177}Lu for radionuclide therapy", *EJNMMI Radiopharmacy and Chemistry,* vol. 4, p. 12, Jun. 2019. doi:10.1186/s41181-019-0063-6

ISBN: 978-3-95450-205-9 doi:10.18429/JACoW-Cyclotrons2019-TUA04

CHARACTERIZATION OF NEUTRON LEAKAGE FIELD COMING FROM ^{18}O(p,n)^{18}F REACTION IN PET PRODUCTION CYCLOTRON

M. Schulc*, M. Kostal, E. Losa, J. Simon, F. Brijar, T. Czakoj, V. Rypar
Research Centre Rez, Husinec-Rez, Czechia
Z. Matej, F. Mravec[1], Masaryk University, Brno, Czechia
M. Antos, S. Vadjak, M. Cuhra[2], UJV Rez, Husinec-Rez, Czechia
F. Cvachovec[3], University of Defence, Brno, Czechia

Abstract

The paper shows a new method for characterization of the secondary neutron field quantities, specifically a neutron spectrum leaking from ^{18}O enriched H_2O XL cylindrical target in IBA Cyclone 18/9 in the energy range of 1–15 MeV. This leakage spectrum is measured by stilbene scintillation detector in different places. The neutron spectra are evaluated from the measured proton recoil spectra using deconvolution through maximum likelihood estimation. A leakage neutron field is not only an interesting option for irradiation experiments due to a quite high flux, but also for a validation of high energy threshold reactions due to a relatively high average energy. The measured neutron spectra were compared with calculations in MCNP6 model by using TENDL-2017, FENDL-3, and default MCNP6 model calculations. TENDL-2017 and FENDL-3 libraries results differ significantly in the shape of the neutron spectrum for energies above 10 MeV while MCNP6 gives incorrect angular distributions. Activation measurements of the different neutron induced reactions support the characterization. The ^{18}F production yield is in a good agreement with TENDL-2017 proton library calculation within a respective uncertainties. The shape of the measured spectrum is also compared with the calculations with TALYS-1.9 using the different models.

INTRODUCTION

All experiments were performed using IBA Cyclone 18/9 accelerator (18 MeV for H$^-$, 9 MeV for D$^-$ particle) which is located in UJV cyclotron laboratory. The most common radioisotope product of the facility is 2-fluoro-2-deoxy-D-glucose (FDG) labeled by ^{18}F which origins from ^{18}O(p,n)^{18}F reaction. Furthermore, it has the capacity to produce the other positron-emitting medical isotopes such as ^{11}C, ^{13}N, ^{15}O. The cyclotron is surrounded by a 4 m wide and 5.75 m long ferroconcrete shielding bunker as a biological shielding. The accelerator has 2 m in diameter and is centered to the shorter side and the same distance from the side wall.

Measurements were performed during irradiation (by 18 MeV protons) of 2.7 ml ^{18}O enriched water (minimal content of 98%). The water is placed in a niobium pin which is sealed by a Havar foil. Accelerator window is covered by a Ti foil. The current, generated by the proton beam on the target, was approximately 75 µA in case of the activation experiments, while it was 0.92 µA in the case of neutron spectra measurements near target. The current was approximately 80 µA in the case of neutron and gamma spectra measured further from the target.

EXPERIMENTAL AND CALCULATION METHODS

The 10×10 mm stilbene scintillation detector was used for measuring neutron leakage spectra in the range of 1.0–14 MeV in the steps of 100 keV. Energy calibration was tested at LVR-15 reactor in Research centre Rez by means of a silicon filtered beam [1]. The efficiency calibration employs a measurement using a pure ^{252}Cf neutron source. This upgraded two-parameter spectrometric system NGA-01 [2, 3] is fully digitized and is now able to process up to 500 000 impulse responses per second. Pulse shape discrimination unit is used to distinguish the type of the detected particle by analyzing the pulse shape, while particle energy is evaluated from the integral of the whole response (energy integral). The pulse shape discrimination value is computed by the field-programmable gate array using an integration method which uses the comparison of the area delimited by part of a trailing edge of the measured response with the area delimited by the whole response. Then the neutron spectra are evaluated from the acquired recoiled proton spectra by means of deconvolution using Maximum Likelihood Estimation [4]. The substantial sources of uncertainty in the measurement were: an energy calibration uncertainty of 3–5%, an uncertainty in the efficiency crystal calibration factor 2.1%, and an uncertainty in the total emission of the neutron ^{252}Cf source 1.3%. Total measurement uncertainty, including statistical uncertainty and dispersion between measurements, is between approximately 2.4%–15% in the measured region.

In the case of activation experiments, the experimental reaction rates were derived from the gamma activities of irradiated samples. Irradiated samples were measured by means of a well-defined HPGe detector with verified geometry and efficiency calibration, for more details see [5]. The reaction rates were derived using the following formula:

$$q = C(T_m)\frac{\lambda \times k}{\epsilon \eta N}\frac{1}{1-e^{-\lambda T_m}}\frac{1}{e^{\lambda \Delta T}}\frac{1}{1-e^{\lambda T_{ir}}}, \qquad (1)$$

where: q is the experimental reaction rate per atom per second, N is the number of target isotope nuclei, η is the detector efficiency, ϵ is gamma branching ratio, λ is the decay constant, ΔT is the time between the end of irradiation

* martin.schulc@cvrez.cz

ISBN: 978-3-95450-205-9 doi:10.18429/JACoW-Cyclotrons2019-TUA04

and start of HPGe measurement, $C(T_m)$ is the measured number of counts, T_m is the time of measurement by HPGe, k is coincidence summing correction factor and T_{ir} is the time of irradiation.

Various types of samples were used, pure natural Ni, Fe and Al. The evaluated monitoring reactions were: ^{58}Ni(n,p)^{58}Co, ^{60}Ni(n,p)^{60}Co, ^{58}Ni(n,X)^{57}Co, ^{54}Fe(n,p)^{54}Mn, ^{54}Fe(n,α)^{51}Cr and ^{27}Al(n,α)^{24}Na. The samples were placed and measured on the end cap of the HPGe detector. Very important is fact that the reaction ^{18}O(p,n)^{18}F produces gammas with very high energy up to 18 MeV. Those gammas can induce for instance (γ, n) reactions which have the same product as (n,2n) reactions. Hence, the monitor reactions should be selected very carefully or contribution of parasitic reactions should be evaluated.

All calculations were performed using the MCNP6 Monte Carlo code [6] in coupled proton neutron transport mode. Default settings containing the Cascade-Exciton Model (CEM) is used for accelerated protons in the MCNP6 simulations. The CEM model, originally proposed in Dubna, incorporates all three stages of nuclear reactions: intranuclear cascade, pre-equilibrium, and equilibrium (or compound nucleus) [7] and [8]. In our case, mostly pre-equilibrium and equilibrium stages are applicable to our problem. The proton transport nuclear data libraries from TENDL-2017 [9] and FENDL-3 [10] proton transport libraries were also tested for mutual intercomparison. ENDF/B-VII.1 nuclear data library [11] was used for simulation of neutron interactions in structural materials and for ^{58}Ni(n,x)^{57}Co reaction. All other tested cross sections were calculated using dosimetric IRDFF-1.05 library [12]. It is worth noting that the structural components have special importance in the formation of the secondary neutron field. The lower part of the neutron spectrum arises from the backscattered neutrons from walls and structural components. The uncertainties in the calculated reaction rates were below 2 %. The calculation uncertainties in the neutron fluence rate were about 2 % in lower regions and 5-9 % in upper regions.

Spectrum of outgoing neutrons from ^{18}O(p,n)^{18}F reaction was also calculated using TALYS-1.9 code [9] with different models. TALYS-1.9 is a system for the analysis and simulation of nuclear reactions. It can simulate nuclear reactions that involve neutrons, photons, protons, deuterons, tritons, ^{3}He$^-$ and alpha particles, in the 1 keV–200 MeV energy range and for target nuclides of mass 12 and heavier.

RESULTS

Differential Neutron Spectra in Different Positions

As a first test, the reaction rate of production of ^{18}F isotope was investigated by measuring of its activity in a certified geometry, within 5% uncertainty. The TENDL-2017 cross section of ^{18}O(p,n)^{18}F reaction was used for comparison. The production rate of ^{18}F agrees well within uncertainties including uncertainty in enrichment and uncertainty in loses of enriched water in piping preceding activity measurement.

The neutron spectra were measured in different places of the cyclotron room using the stilbene detector. For real geometry, see Fig. 1. The places were following: position in the labyrinth (Labyrinth), position 1 (Position 1) and position 1 with Bi (Position 1 Bi filter). In the case of Position 1, the detector was surrounded by 30 cm of lead except top of the detector. In the case of position 1 with Bi, the additional 12 cm of Bi was placed in front of the top of the detector. The detector was always placed one meter above the ground. In these cases the proton current was approximately 80 µA. Results are shown in Fig. 2. The shape of spectra is very similar for energies higher than 3 MeV.

The neutron spectrum measured in position 80 cm from ^{18}O enriched H_2O target was compared with calculations using various incident proton nuclear data libraries, MCNP6 default calculations, FENDL-3 and TENDL-2017 libraries. The comparison is presented in Fig. 3. All calculations are comparable and reasonable up to 9 MeV. As can be seen, the calculations with TENDL-2017 differ significantly for energies higher than 9 MeV, the same can be stated for FENDL-3 calculations, however the discrepancy is smaller. The most reasonable agreement with experiment is in the case of MCNP6 calculation. The C/E-1 comparison is presented in Fig. 4. It is clear that the discrepancy in the 2–6 MeV interval is 2–3 times higher than the related uncertainty and in for energies higher than 10 MeV, the difference can be up to five times higher the respective uncertainty. More details can be found in [13].

The gamma spectrum was measured by stilbene detector in the labyrinth, see Fig. 5. The gamma spectrum is very hard, thus one have to be aware of gamma induced reactions in the case of evaluation of some monitor reactions.

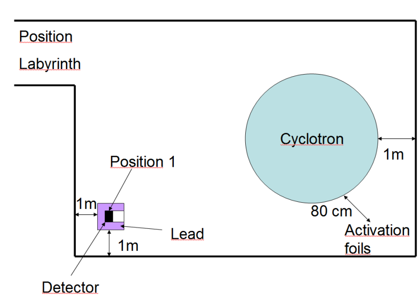

Figure 1: Geometry of the measurements.

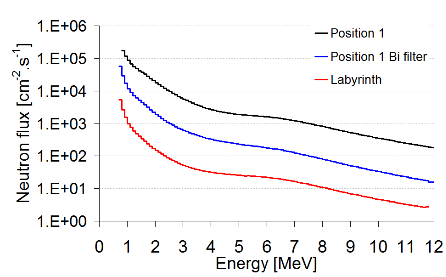

Figure 2: Measured neutron spectra in different places.

ISBN: 978-3-95450-205-9 doi:10.18429/JACoW-Cyclotrons2019-TUA04

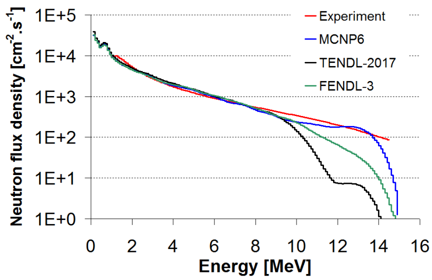

Figure 3: Comparison of measured and calculated neutron spectrum 80 cm from cyclotron end.

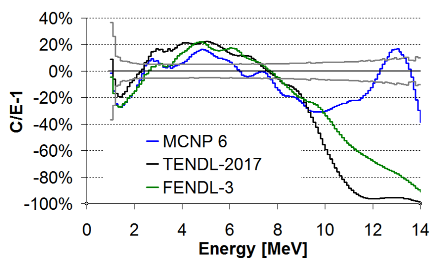

Figure 4: C/E-1 comparison of calculated and measured neutron spectrum 80 cm from cyclotron end.

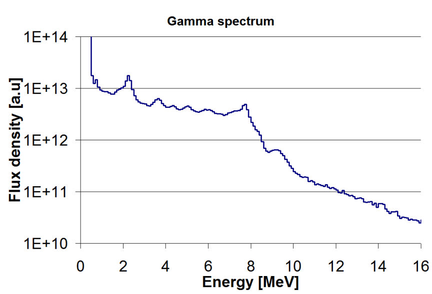

Figure 5: Measured gamma spectrum in the labyrinth.

Reaction Rates Measurement

Table 1 shows comparison of measured and calculated reaction rates by means of Calculation(C) to Experiment(E) ratios. The samples for irradiation were placed in distance of 80 cm in cyclotron vertical axis from the target, i.e. in the same place as neutron spectra were measured. The cross sections for reactions under study except ^{58}Ni(n,X)^{57}Co were taken from IRDFF-1.05 library because these reactions are dosimetric and are validated in different neutron spectra. In the case of FENDL-3 calculations, the results are not satisfactory for all reactions.

TENDL-2017 performs better with very good agreement for ^{58}Ni(n,p)^{58}Co and ^{54}Fe(n,p)^{54}Mn reactions. All other reaction rates are reproduced very poorly. Concerning default MCNP6 model results, the agreement is satisfactory and overall best from these three calculations with maximum discrepancy almost 20%.

Table 1: C/E-1 of the Measured Reaction Rates 80 cm from the Cyclotron End

Reaction	MCNP6	FENDL-3	TENDL-2017
^{58}Ni(n,p)^{58}Co	13.4%	23.1%	-2.8%
^{54}Fe(n,p)^{54}Mn	19.8%	29.4%	1.4%
^{54}Fe(n,α)^{51}Cr	-5.0%	-20.6%	-49.3%
^{60}Ni(n,p)^{60}Co	-7.3%	-18.9%	-47.0%
^{27}Al(n,α)^{24}Na	-13.2%	-34.1%	-62.2%
^{58}Ni(n,X)^{57}Co	-2.5%	-73.2%	-96.3%

Comparison with TALYS-1.9

Figure 6 shows comparison of shapes of measured and TALYS-1.9 calculated neutron spectra. Generally, the agreement is satisfactory for neutron energies higher than 2 MeV. The lower energies are influenced by the scattered neutrons by walls and structural components in the case of experiment. In the case of simulation with no compound nucleus, the agreement is the worst. The reasonable agreement is also achieved with disabled the pre-equilibrium reaction mechanism. The best agreement is achieved with default calculation using widthmode 0, it corresponds to the case where no width fluctuation corrections in compound nucleus are implemented, i.e. calculations use pure Hauser-Feshbach model.

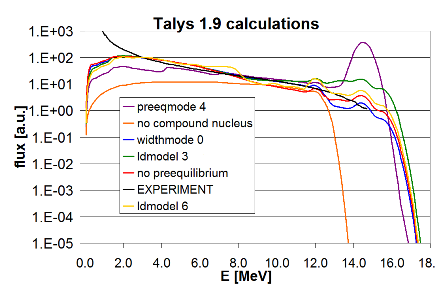

Figure 6: Comparison of measured spectrum with ones calculated using TALYS-1.9.

CONCLUSION

The leakage neutron field of the ^{18}F production reaction was measured at IBA Cyclone 18/9 cyclotron with XL cylindrical target for the first time. This technique can be used in principle in any cyclotron for measuring neutron evaporation spectra up to 15 MeV. The employed proton libraries show significant discrepancies, thus they are not suitable for a precise description of the secondary neutron field to be used as a scientific instrument. The TENDL-2017 and FENDL-3 libraries differ significantly in the shape of the spectrum in the high-energy tail, whereas MCNP6 default model is incorrect in the angular distribution. However, the calculations of the ^{18}F production yields, the TENDL-2017 cross section gives a very good results with discrepancy about 3 % which is comparable with the respective uncertainties. Either neutron and photon spectrum can be effectively characterized

ISBN: 978-3-95450-205-9 doi:10.18429/JACoW-Cyclotrons2019-TUA04

using a stilbene scintillation detector and the flux with neutron activation analysis performed with suitable samples. However, the reactions to be under study must be carefully selected due to the influence of the parasitic photonuclear reactions. Concerning TALYS-1.9 calculations, the shape of the spectrum is reproduced very well. The best agreement is achieved with the calculations using pure Hauser-Feshbach model.

ACKNOWLEDGEMENTS

Presented results were obtained with the use of the infrastructure Reactors LVR-15 and LR-0, which is financially supported by the Ministry of Education, Youth and Sports Czech Republic – project LM2015074 and – project LQ1603 Research for SUSEN. This work has been realized within the SUSEN Project (established in the framework of the European Regional Development Fund (ERDF) in project CZ.1.05/2.1.00/03.0108 and of the European Structural Fundsand Investment Funds (ESIF), Czech Republic in the project CZ.02.1.01/0.0/0.0/15_008/0000293), which is financially supported by the Ministry of Education, Youth and Sports, Czech Republic – project LM2015093 Infrastructure SUSEN.

REFERENCES

[1] M. Kostal, J. Soltes, L. Viererbl, *et al.*, "Measurement of neutron spectra in a silicon filtered neutron beam using stilbene detectors at the LVR-15 research reactor", *Appl. Rad. and Isot.*, vol. 128, pp. 41–48, Oct. 2017. doi:10.1016/j.apradiso.2017.06.026

[2] M. Veskrna, Z. Matej, F. Mravec, V. Prenosil, F. Cvachovec, and M. Kostal, "Digitalized two parametric system for gamma/neutron spectrometry", in *Proc. 18th Topical Meeting of the Radiation Protection and Shielding Division of ANS*, Knoxville, TN USA, Sep. 2014. https://pdfs.semanticscholar.org/f6dc/a5a72824d730d0a54a145097fd2cdace6acc.pdf

[3] Z. Matej, *Digitalization of spectrometric system for mixed field of radiation*, Saarbrücken, Germany: LAP LAMBERT Academic Publishing, Sep. 2014. ISBN 978-3-659-59970-5.

[4] J. Cvachovec and F. Cvachovec, "Maximum likelihood estimation of a neutron spectrum and associated uncertainties", *Advances in Military Technology*, vol. 3, no. 2, Dec. 2008. https://www.researchgate.net/publication/267992287_Maximum_Likelihood_Estimation_of_a_Neutron_Spectrum_and_Associated_Uncertainties

[5] M. Kostal, M. Schulc, V. Rypar, *et al.*, "Validation of zirconium isotopes (n,g) and (n,2n) cross sections in a comprehensive LR-0 reactor operative parameters", *Appl. Rad. and Isot.*, vol. 128, pp. 92—100, Oct. 2017. doi:10.1016/j.apradiso.2017.06.023

[6] T. Goorley *et al.*, "Initial MCNP6 release overview", *Nucl. Technol.*, vol. 180, pp. 298–315, Aug. 2012. doi:10.13182/NT11-135

[7] K. K. Gudima, S. G. Mashnik, and V. D.Toneev, "Cascade-exciton model of nuclear reactions", *Nucl. Phys. A*, vol. 401(2), pp. 401-329, Jun. 1983. doi:10.1016/0375-9474(83)90532-8

[8] A. C. Kraan, "Range verification methods in particle therapy underlying physics and Monte Carlo modeling", *Front. Oncol.*, vol. 5, 2015. doi:10.3389/fonc.2015.00150

[9] A. J. Koning and D. Rochman, "Modern nuclear data evaluation with the TALYS code system", *Nucl. Data Sheets*, vol. 113, pp. 2841–2934, Dec. 2012. doi:10.1016/j.nds.2012.11.002

[10] R. A. Forrest *et al.*, "FENDL-3 library summary documentation", Report INDC(NDS)-628, 2013. https://40.68.46.107/publications/indc/indc-nds-0628.pdf

[11] M. B. Chadwick, M. Herman, P. Oblozinsky, *et al.*, "ENDF/B-VII.1: Nuclear data for science and technology: Cross sections, covariances, fission product yields and decay data", *Nucl. Data Sheets*, vol. 112, pp. 2887—2996, Dec. 2011. doi:10.1016/j.nds.2011.11.002

[12] R. Capote, K. I. Zolotarev, V. G. Pronyaev, and A. Trkov, "Updating and extending the IRDF-2002 dosimetry library", *J. ASTM Int.* (JAI)- 9, Issue 4, pp. 1-9, Apr. 2012. doi:10.1520/JAI104119

[13] M. Kostal *et al.*, "The methodology of characterization of neutron leakage field from PET production cyclotron for experimental purposes", *Nucl. Instrum. Methods Phys. Res., Sect. A*, vol. 942, art. no. 162374, 2019. doi:10.1016/j.nima.2019.162374

ISBN: 978-3-95450-205-9 doi:10.18429/JACoW-Cyclotrons2019-TUB02

JINR PROJECTS OF CYCLOTRON FOR PROTON THERAPY

O. Karamyshev†, K. Bunyatov, S. Gurskiy, G. Karamysheva, V. Malinin, D. Popov, G. Shirkov, S. Shirkov, V. Smirnov, S. Vorozhtsov, JINR, Dubna, Russia

Abstract

The physical design of the compact superconducting cyclotron SC230 (91.5 MHz) has been performed. The cyclotron can deliver up to 230 MeV beam for proton therapy and medical and biological research. As the cyclotron will have a relatively small magnet field, it is possible to use both superconducting and resistive coil. Besides a superconducting cyclotron we simulate design of the cyclotron with a conventional copper water-cooled coil.

INTRODUCTION

Since 2016 the project of SC200 superconducting cyclotron for hadron therapy has been jointly developed by JINR and ASIPP (Hefei, China) [1]. The production of the cyclotron faced a lot of engineering challenges which are mainly aroused due to high magnetic field of the accelerator.

Recent developments of superconducting cyclotrons for proton therapy, such as SC200, Pronova [2], Sumitomo 230 MeV [3] share similar parameters that define the structure of the cyclotron. All projects are four-sector cyclotrons with ~3 T central field. Such parameters were chosen in pursuit of compact dimensions. None of those cyclotrons are yet in operation. It was, therefore, decided to rethink some design decisions after careful analysis of SC200, other projects and operating cyclotrons for proton therapy.

There are two most successful accelerators in the proton therapy: Varian Proscan [4], design proposal by H. Blosser et al. in 1993, and C235 (IBA Belgian) [5]. Both cyclotrons have much smaller central field, 2.4 and 1.7 T. First of all, we increased the pole of the cyclotron in order to decrease mean magnetic field to about 1.5 T in the center. Corresponding RF frequency for this value of the magnetic field is about 90 MHz at 4th harmonics operation mode. As the cyclotron will have a relatively small magnet field, it is possible to use both superconducting and resistive coil. Both solutions have their pros and cons. Earlier [6] we reported design of the SC230 cyclotron with superconducting coil. Its parameters are recapitulated in Table 1.

SC-230 CYCLOTRON

Computer Simulations of the Magnet

Simulations were performed in CST studio [7] in the parametrized model of the magnet (see Fig. 1) created in Autodesk Fusion 360. The dimensions of the yoke (see Fig. 2) were chosen to restrict the magnetic stray field in the range of 200 - 300 G just outside accelerator, providing full saturation of the iron poles and yoke. Average magnetic field and flutter from CST simulation are presented in Fig. 3.

Betatron tunes calculated with CYCLOPS-like code are presented in Fig. 4.

† olegka@jinr.ru

Table 1: Parameters of the Cyclotron SC230

Parameter	Value
Magnet type	Compact, SC coil, warm yoke
Ion source	PIG
Final energy, MeV	230
Pole radius, mm	1350
Mean mag. field (center), T	1.5
Dimensions (height×diameter), m	1.7 × 4
Weight, tonnes	130
Hill/Valley gap, mm	50/700
A·Turn number	170 000
RF frequency, MHz	91.5
Harmonic number	4
Number of RF cavities	4
Voltage, center/extraction kV	35/90
RF power, kW	40
Number of turns	600
Beam intensity, μA	1.0
Extraction type	ESD

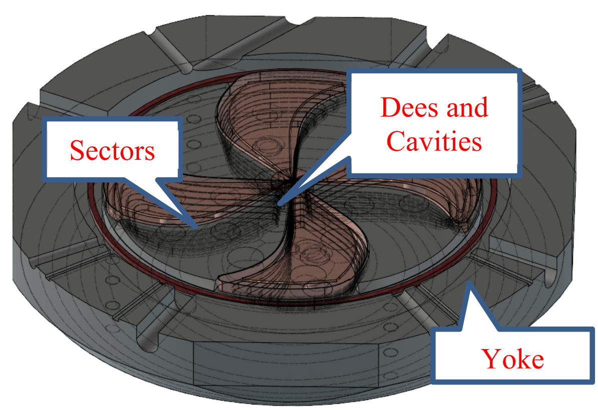

Figure 1: Layout of the cyclotron's 3D computer model (magnet and accelerating system).

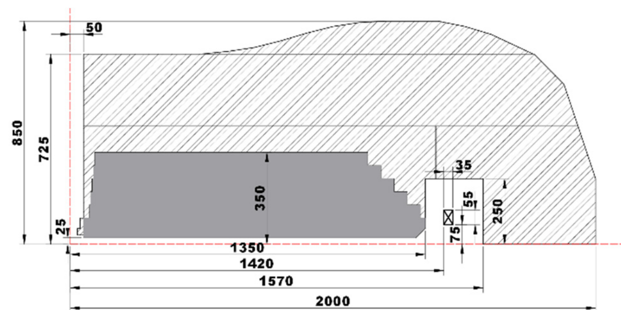

Figure 2: SC230 magnet yoke and SC coil general dimensions.

ISBN: 978-3-95450-205-9 doi:10.18429/JACoW-Cyclotrons2019-TUB02

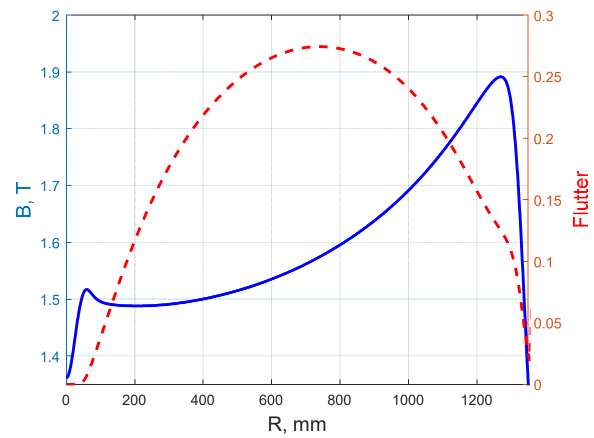

Figure 3: Average magnetic field and flutter along the radius.

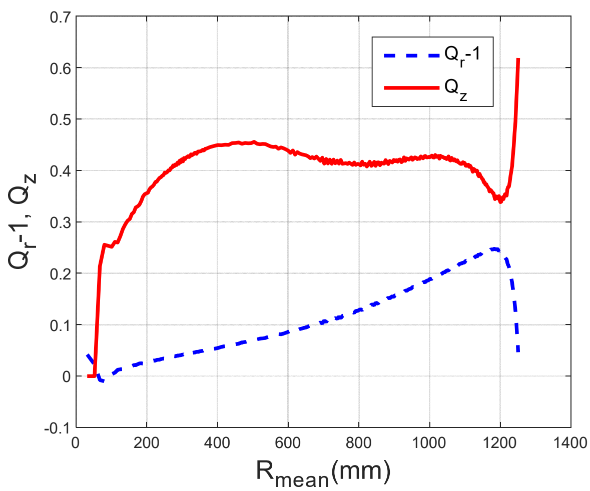

Figure 4: Vertical and radial betatron tunes in SC230.

ACCELERATING SYSTEM DESIGN

RF cavities are located at the valleys of the magnet, the geometry of the RF cavity is restricted by the size of spiral sectors. For proton acceleration, we are planning to use 4 accelerating RF cavities, operating on the 4th harmonic mode. All four RF cavities will be connected in the center and will be working on approximately 91.5 MHz frequency. Cavities can be equipped with an inductive coupling loop and will be adjusted by capacitance trimmers like in SC200 [8].

Computer Model

The characteristic parameters of the half-wavelength coaxial resonant cavity with two stems have been obtained from simulation. The RF cavity resonator solution for the SC230 cyclotron can be seen in Fig. 5.

Azimuthal extension of the cavity (between middles of accelerating gaps) is about 40 degrees. As the beam will be accelerated in the fourth harmonic mode we believe that the RF magnetic field will not have noticeable effect on the beam. Suitable accelerating frequency and voltage along radius were achieved.

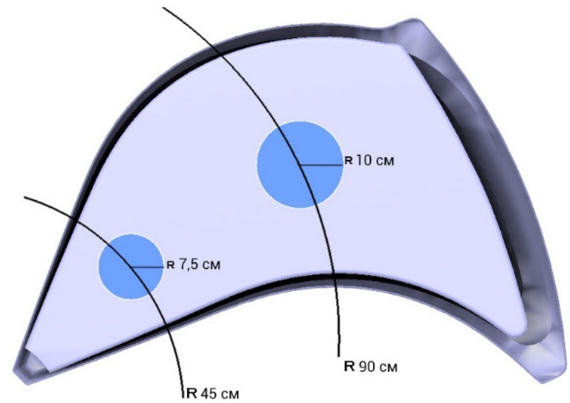

Figure 5: View of the model of the cavity.

Power Losses

Power dissipation in the model was calculated assuming the wall material is copper with a conductivity $\sigma = 5.8\mathrm{x}10^{7}$ $(\Omega\mathrm{m})^{-1}$. The quality factor was about 13800 and power losses of all cavities were: for storage energy 1 joule voltage in the center/extraction 35 - 95 kV, thermal losses are 43 kW.

Overall power and cooling requirements of the RF system are rather small.

Extraction from this cyclotron will be performed by electrostatic deflector. The height of the deflector is 50 mm, which makes it possible to place it in an axial gap between the sectors. The ESD voltage, required for extraction is just 100 kV/cm.

A CYCLOTRON FOR PROTON THERAPY RC240.

Magnet System

We simulate a cyclotron similar to the SC230 cyclotron, but with some changes optimizing the accelerator design with resistive coils (RC).

Relying on modern computing capabilities it is possible to design a cyclotron with resistive coils with sizes smaller than the leader of the proton therapy market C235 (IBA).

To have more compact design of the cyclotron with resistive coil the vertical gap between sectors needs to be as small as possible. In the proposed design the gap between the sectors is 15 mm, which resulted in a low current value in the coil, and the weight of the magnet was about 140 tonnes. It is important that the gap between sectors is constant, compared to IBA C235 design with elliptic gap, that decreases towards the extraction down to 9 mm. It is much easier and cheaper to manufacture and easier to control during installation. The diameter of RC240 is below 4 m, in order to simplify the logistics of the magnet. It is important for the cyclotron that needs to be delivered to the hospitals in different location to be fairly simple for the transportation. Therefore, each element of yoke is below 30 tonnes.

Table 2 displays the main RC240 parameters. Figure 6 shows the magnetic flux through the median plane.

ISBN: 978-3-95450-205-9 doi:10.18429/JACoW-Cyclotrons2019-TUB02

Table 2: Parameters of the Cyclotron RC240

Parameter	**Value**
Magnet type	resistive
Ion source	PIG
Final energy, MeV	240
Pole radius, mm	1350
Mean magnetic field (center), T	1.45
Dimensions (height×diameter), m	1.62 × 3.95
Weight, tonnes	140
Hill/Valley field, T	1.8/0.4
Hill/Valley gap, mm	15/700
A·Turn number	120 000
Magnet power consumption, kW	140
RF frequency, MHz	89
Harmonic number	4
Number of RF cavities	2
Voltage center/extraction, kV	50-110
RF power, kW	50
Turn number	800
Beam intensity, μA	1.0
Extraction type	ESD

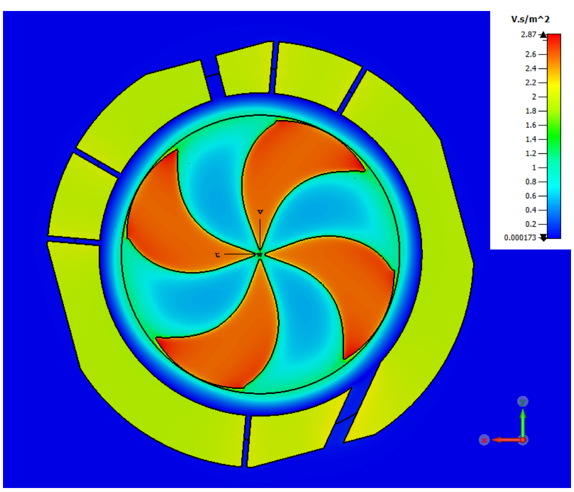

Figure 6: Magnet flux through median plane.

The number of A·Turn is 120000 and therefore it's power consumption is rather small 140 kW.

The average magnetic field and flutter from CST simulation is presented in Fig. 7.

The RC240 needs 2 times less A-turns in the coils compared to IBA C235, so we are able to use a much smaller coil cross-section. The RC240 coil is only 272x170 mm^2, and IBA C235 coil is about 600 x 500 mm^2. So even having much smaller field and bigger sectors radius, thanks to much smaller coil the overall size and weight of the RC240 is much smaller and it consumes less power.

Results of simulations of the magnetic field were exported to Matlab to be analysed with CYCLOPS-like code. Orbital frequency shows rather good isochronism of the field (see Fig. 8).

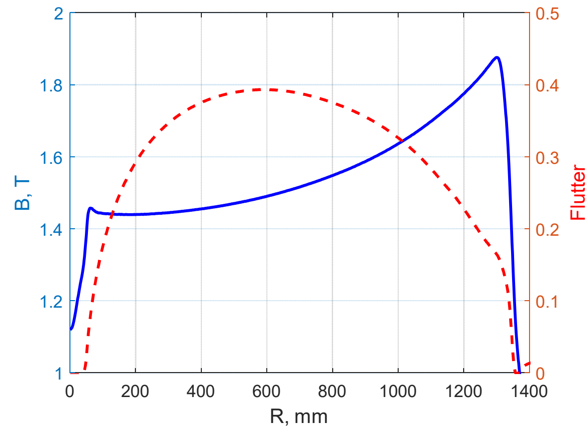

Figure 7: Average magnetic field and flutter along the radius.

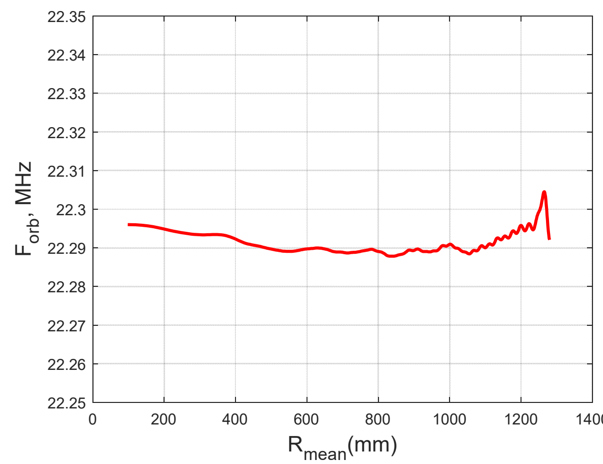

Figure 8: Orbital frequency.

The RC240 needs 2 times less A-turns in the coils compared to IBA C235, so we are able to use a much smaller coil cross-section. The RC240 coil is only 272x170 mm^2, and IBA C235 coil is about 600 x 500 mm^2. So even having much smaller field and bigger sectors radius, thanks to much smaller coil the overall size and weight of the RC240 is much smaller and it consumes less power.

Results of simulations of the magnetic field were exported to Matlab to be analysed with CYCLOPS-like code.

Figure 9 shows that working point does not cross dangerous resonances. This cyclotron has different path of the working point. In both IBA C235 and Varian as well as in projects with 3 T magnetic field (SC200, Sumitomo and Pronova) Q_z (vertical tune) stays below 0.5. In case of the RC240 the flutter is too high, so we immediately "jump" over Qz = 0.5 and stay over the Qr = 2Qz resonance. Particle tracking in realistic 3D electric and magnetic fields have been performed in order to prove that such unconventional path is indeed ok.

ISBN: 978-3-95450-205-9 doi:10.18429/JACoW-Cyclotrons2019-TUB02

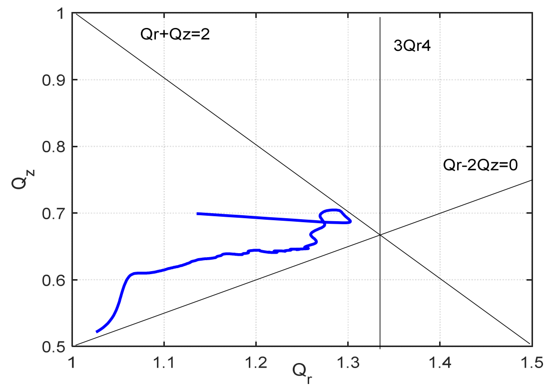

Figure 9: Working diagram.

Accelerating System

Two RF cavities are located at the opposite valleys of the magnet. Accelerating RF cavities will operate at 89 MHz (acceleration on the 4th harmonic mode). Space in the valley is enough to place cavities with azimuth extension about 40 degrees.

The characteristic parameters of the half-wavelength coaxial resonant cavity with two stems have been obtained from simulation in CST studio. Quality factor of the cavity is about 14000.

RF cavities will be connected in the center, can be equipped with an inductive coupling loop and will be adjusted by capacitance trimmers.

Extraction from this cyclotron will be performed by ESD placed in empty valley. The ESD voltage, required for extraction is about 100 kV/cm.

As a result, we have a design of both options of cyclotron with:

- Low power consumption.
- High quality of the beam.
- Minimum engineering efforts and challenges.
- Reasonable size and weight.

CONCLUSION

We chose a low level of the magnetic field in the cyclotron and found out that dimensions of the cyclotron can be reasonable. Low magnetic field will provide efficient extraction with electrostatic deflector. The superconducting option is lighter, consumes less power, has bigger gap between poles, however superconducting coil is more expensive to build and to run. Both options are great candidates for JINR to be used for medical research program.

REFERENCES

[1] G. A. Karamysheva *et al.*, "Present status of the SC202 superconducting cyclotron project", in *Proc. 8th Int. Particle Accelerator Conf. (IPAC'17)*, Copenhagen, Denmark, May 2017, pp. 4730-4732. doi:10.18429/JACoW-IPAC2017-THPVA120

[2] V. Smirnov, S. Vorozhtsov, Z. Neville, G. Blosser, X. Wu, and J. Vincent, "The R&D of a K230 superconducting cyclotron for proton therapy", presented at the 41st European Cyclotron Progress Meeting (ECPM'18), Sep. 2018, Dubna, Russia.

[3] H. Tsutsui *et al.*, "Status of SUMITOMO's superconducting isochronous cyclotron development for proton therapy", in *Proc. 13th Int. Topical Meeting on Nuclear Applications of Accelerators (AccApp'17)*, Quebec City, Canada, Jul.-Aug. 2017, pp. 412-419.

[4] J. M. Schippers *et al.*, "The SC cyclotron and beam lines of PSI's new proton therapy facility PROSCAN", *Nucl. Instrum. Methods Phys. Res., Sect B*, vol. 261, pp.773-776, 2007. doi.org/10.1016/j.nimb.2007.04.052

[5] D. Vandeplasche, W. Beeckman, S. Zaremba, Y. Jongen, and T. Tachikawa, "Extracted beams from IBA's C235", in *Proc. 1997 Particle Accelerator Conf. (PAC'97)*, paper 7W022, p. 1045 (3 pages).

[6] O. Karamyshev *et al.*, "Conceptual design of the SC230 superconducting cyclotron for proton therapy", in *Proc. 9th Int. Particle Accelerator Conf. (IPAC'19)*, Melbourne, Australia, May 2019, pp. 2058-2060. doi:10.18429/JACoW-IPAC2019-TUPTS059

[7] CST Studio Suite, https://www.cst.com

[8] G. Chen *et al.*, "Research and development of RF system for SC200 cyclotron", in *Proc. 9th Int. Particle Accelerator Conf. (IPAC'18)*, Vancouver, Canada, Apr.-May 2018, pp. 3616-3618. doi:10.18429/JACoW-IPAC2018-THPAL004

ISBN: 978-3-95450-205-9 doi:10.18429/JACoW-Cyclotrons2019-TUB03

MRI-GUIDED-PT: INTEGRATING AN MRI IN A PROTON THERAPY SYSTEM

E. van der Kraaij†, J. Smeets, Ion Beam Applications S.A., 1348 Louvain-la-Neuve, Belgium
L. Bertora, A. Carrozzi, A. Serra, ASG Superconductors S.p.A., 16152 Genova, Italy
B. Oborn, Centre for Medical Radiation Physics (CMRP),
University of Wollongong, Wollongong, NSW 2500, Australia
S. Gantz, A. Hoffmann, L. Karsch, A. Lühr, J. Pawelke, S. Schellhammer
OncoRay – National Center for Radiation Research in Oncology, Faculty of Medicine and
University Hospital Carl Gustav Carus, Technische Universität Dresden,
Helmholtz-Zentrum Dresden – Rossendorf, Dresden 01307, Germany

Abstract

Integration of magnetic resonance imaging (MRI) in proton therapy (PT) has the potential to improve tumor-targeting precision. However, it is technically challenging to integrate an MRI scanner at the beam isocenter of a PT system due to space constraints and electromagnetic interactions between the two systems. We present a concept for the mechanical integration of a 0.5 T MRI scanner (MR-Open, ASG Superconductors) into a PT gantry (ProteusONE, IBA). Finite element modelling (FEM) simulations are used to assess the perturbation of several of the gantry's elements on the homogeneity of the scanner's static magnetic field. Results show that only the perturbations by the bending magnet are significant and to be taken into account during treatment planning and dose delivery.

INTRODUCTION

Image guidance in conventional PT systems is provided by X-ray or (cone-beam) CT systems. Better image guidance and adaptive therapies for several tumor sites can be achieved by changing to MRI guidance. The first benefit of MRI is the absence of ionizing radiation dose: an advantage in for example paediatric cases and an enabler for continuous imaging. Daily adaptations of the treatment plan and organ motion visualization in for example the abdomen or the thorax become feasible. Secondly, MRI provides unparalleled soft-tissue contrast, enabling margin reduction in the treatment planning and potentially hypo-fractionation. For more information and an overview of the subject the reader is referred to [1].

Challenges

Before an MRI-guided-PT system can be designed there are several technical challenges to overcome. We mention the four most pressing issues. Firstly, there is the problem how to mechanically integrate the two large complex devices. Secondly, there is the mutual magnetic interference to be taken into account: the perturbation of the image quality by the PT system and the perturbation of the beam quality by the MRI's magnetic fields. Thirdly, there is the integration of a Faraday cage to shield the MRI from surrounding RF sources and it needs to be confirmed that the MRI receiver coils function correctly in or near the beam path, without altering the beam properties. Finally, methods for dosimetry in the presence of a magnetic field need to be established. All of this, and more, requires adjustment of the treatment workflow for a synchronized operation of both the imaging and the treatment equipment.

Scope of Proceedings

In these proceedings we discuss the mechanical integration of an MRI scanner on a PT gantry and an FEM study to assess the perturbation of the gantry's elements on the homogeneity of the MRI scanner's magnetic field.

A PT gantry comprises strong magnets mounted on heavy, ferromagnetic, iron support structures. These can be detrimental to the B-field homogeneity of an MRI scanner. Two possible sources of perturbation are studied. Firstly, the gantry rotation: Moving ferromagnetic objects can cause a change in the B-field. Secondly, the magnetic fringe field of the 60° bending magnet on the gantry: This last magnet on the gantry is closest to the MRI scanner and has a field that varies with beam energy.

Further Research

To test the technical feasibility, a first experimental setup was realized at the PT center in Dresden, combining a 0.22 T open MRI scanner with a static proton beam line. For more information, the reader is referred to [2].

MECHANICAL INTEGRATION

A 0.5 T open MRI scanner is the preferred choice for the integration with an IBA ProteusONE system [3]. The scanner's design would be based on that of the MR-Open manufactured by ASG Superconductors [4], see Fig. 1.

The low field strength scanner is foreseen to provide a good contrast-to-noise ratio and adequate image resolution [5]. At the same time, the liquid helium free scanner is based on a dry-cooled, superconducting magnet and has a large opening for patients between the magnet coils.

By modifying the C-shaped yoke of the MR-Open to a closed yoke, the integration of the MR on the PT system is foreseen as shown in Fig. 2. The beam exiting from the gantry to the isocenter is parallel to the B-field of the MRI

† erik.vanderkraaij@iba-group.com

ISBN: 978-3-95450-205-9 doi:10.18429/JACoW-Cyclotrons2019-TUB03

scanner at isocenter (B_0), assuring the least possible deflection of the proton beam. The beam passes through a hole in the yoke, visible in the blue yoke of Fig. 1 (right).

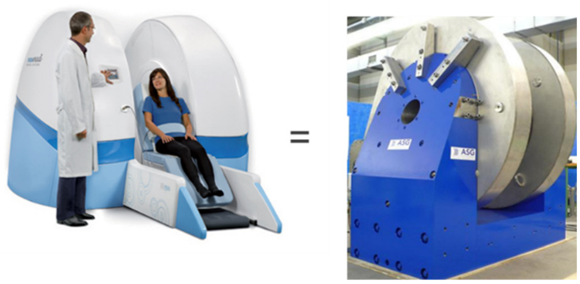

Figure 1: Left is shown a clinical version of the MR-Open scanner. Right is the MRI yoke with the coil structures.

The structure in Fig. 2 has several benefits: the MRI scanner is coupled to the gantry for simultaneous rotation. The rotating structures can be decoupled for maintenance purpose. The patient opening is large, reducing as much as possible claustrophobic anxieties and giving easy access for QA.

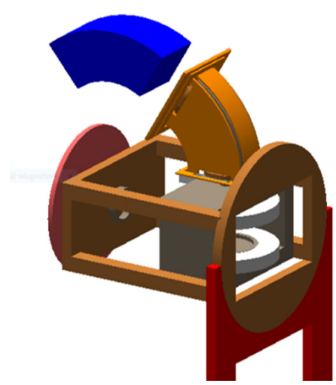

Figure 2: Conceptual drawing of an open MRI scanner mounted at the PT gantry's isocenter. Shown are the gantry's last two bending magnets, the MRI yoke, the MRI coils and support structures.

FINITE ELEMENT ANALYSIS

For the FEM simulations, Opera3D v.18R2x64 was used with its Magnetostatic solver [6]. To ensure mesh independence of the analysis, one large model was created, as depicted in Fig. 3. It contains a slightly simplified model of the gantry, including its counterweight and its last 60° bending magnet, two support structures (the gantry's "chair") and the MRI scanner. Table 1 lists several dimensions of the MRI scanner and gantry. In real life, more ferromagnetic material will surround the system. The gantry's chair is however by far the largest element rotating around the scanner and was thus for now taken as the only rotating perturbation source.

Model Setup

The model has been recreated nine times, with the gantry rotated by -30°, 0°…, 210° relative to the chair[1]. For each angle model, after the meshing, the solver was run with the chair set to either air or iron and the current in the bending magnet was set to 0% or 100% of its maximum value. The MRI coils always had the same current setting.

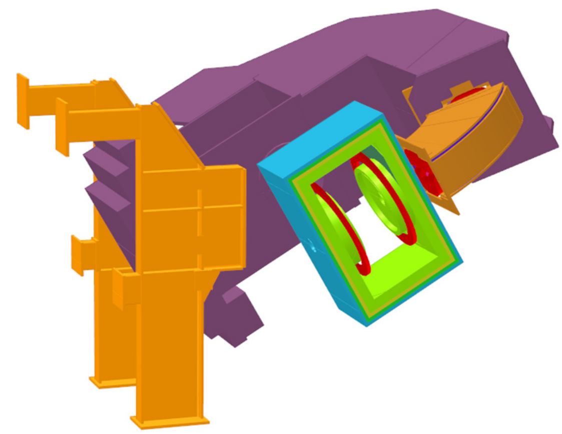

Figure 3: Opera3D model of the gantry (purple), the gantry's chair (orange), the MRI scanner and the 60° bending magnet at isocenter. This model has the gantry and scanner rotated relative to the vertical position by +60°. The scanner model can be seen to consist of several layers, to study different yoke thicknesses.

Table 1: Model Properties as Simulated

Parameter	Value
MRI:	
Pole gap	600 mm
Pole diameter (=depth)	1166 mm
Inner width	2000 mm
Yoke thickness (min - max)	150 - 300 mm
Yoke height (max)	1730 mm
B at isocenter (B_0)	0.53 T
Iron mass (min - max)	13 – 24 ton
PT system:	
Gantry iron mass, incl. 60°-bend	82 ton
Gantry chair iron mass	10 ton
Bending magnet B-field (max)	1.5 T

To study the perturbations on the B-field homogeneity as a function of the MRI scanner's yoke thickness, the inner part of the yoke was always simulated as iron. Three extra layers of 50 mm each were present in all models and the solver was run with these layers set to either air or iron. Thus, the MRI was simulated with different yoke thicknesses of 150, 200, 250 and 300 mm.

Solver Settings

As the calculations are at the ppm level of the magnetic field, the TOSCA 'Nonlinear iteration convergence tolerance' was set to 10^{-6}. A lower setting did not result in better performance.

The integration method for calculations in Opera3D could not be used. In a recent upgrade a stochastic element has been added to this calculation method [7],

[1] The ProteusONE can rotate from 0° up to 220°.

ISBN: 978-3-95450-205-9 doi:10.18429/JACoW-Cyclotrons2019-TUB03

speeding up the calculation, but also introducing a fluctuation. The Field Calculation Method was therefore set to Nodal Interpolation mode.

Legendre Polynomial Fitting

The field homogeneity at isocenter in the MRI scanner was analyzed by fitting for each solved model the Legendre polynomial

$$\frac{(B_z - B_0)}{B_0} \cdot 10^6 =$$

$$\sum_{n=0}^{N} \sum_{m=0}^{n} P_{nm}(\cos(\theta))[\alpha_{nm}\cos(m\varphi) + \beta_{nm}\sin(m\varphi)]$$

up to N=15, at a radius of 200 mm. Spherical coordinates (r, θ, φ) are used, with z parallel to the beam direction and x along the gantry rotation axis. B_z is the magnetic field in vertical direction. B_0 is defined as B_z at isocenter, for the model at 0° rotation angle, with the yoke fully made of iron and all other elements set to air.

To assure mesh independence, only relative measurements were analyzed: the results with the chair set to iron were subtracted by the results of the chair set to air, and the results with the bend current at 100% were subtracted by those at 0%. In other words, the perturbations were obtained by subtracting coefficient by coefficient:

$$\alpha_{nm}^{\text{pert rot}} = \alpha_{nm}^{\text{chair set to iron}} - \alpha_{nm}^{\text{chair set to air}}$$

and

$$\alpha_{nm}^{\text{pert bend}} = \alpha_{nm}^{\text{bend current 100\%}} - \alpha_{nm}^{\text{bend current 0\%}}.$$

RESULTS

Due to symmetry reasons, almost all β-coefficients are zero. The discussion of the results is therefore mostly on the α-coefficients.

Unfortunately, the angle model of 210° did not converge for all its different settings. The set of 210° is thus not included in the final analysis.

Perturbation by Gantry Rotation

For this perturbation study the current in the gantry's bending magnet was always at 0%.

In Fig. 4 the results are shown for $\alpha_{00}^{\text{pert rot}}$ at different rotation angles. This value is the perturbation effect of the chair on the average of the magnetic field in the MRI scanner as it rotates around the gantry axis. This figure shows the results with the gantry set to air.

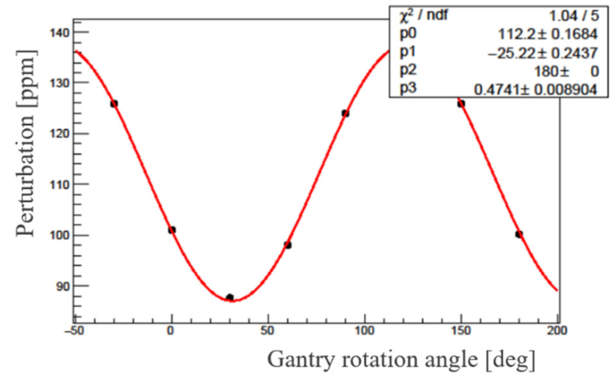

Figure 4: $\alpha_{00}^{\text{pert rot}}$ versus gantry rotation angle.

In the figure, the value at rotation angle 0° is non-zero, as B_0 is defined for the model with the chair and gantry set to air. The average of the figure has thus no significant meaning. It requires only passive compensation and can be compensated by magnet shimming at installation.

The amplitude of the fluctuation of the perturbation in the figure is fitted with a sinusoidal function to 25 ppm. This perturbation amplitude means that over a full rotation around the gantry axis, a maximum shift of ±25 ppm of the average B_z in a sphere of 400 mm diameter at isocenter can be expected.

Repeating the above sinusoidal fit on the set of results with the gantry set to iron and with different MRI yoke thicknesses, the perturbation amplitudes in Fig. 5 were obtained.

Perturbations due to rotation during system operation require active compensation. For $\alpha_{00}^{\text{pert rot}}$, the MRI receiver coil frequency can be adjusted and the maximum of ~45 ppm is easy to adapt to. The $\alpha_{n=1,m}^{\text{pert rot}}$ reflect linear perturbations on the field homogeneity and can be compensated for by the MRI gradient coils. Note that $\alpha_{10}^{\text{pert rot}}$ is along the z-axis and $\alpha_{11}^{\text{pert rot}}$ is along the rotation axis. $\beta_{11}^{\text{pert rot}}$ is perpendicular to both.

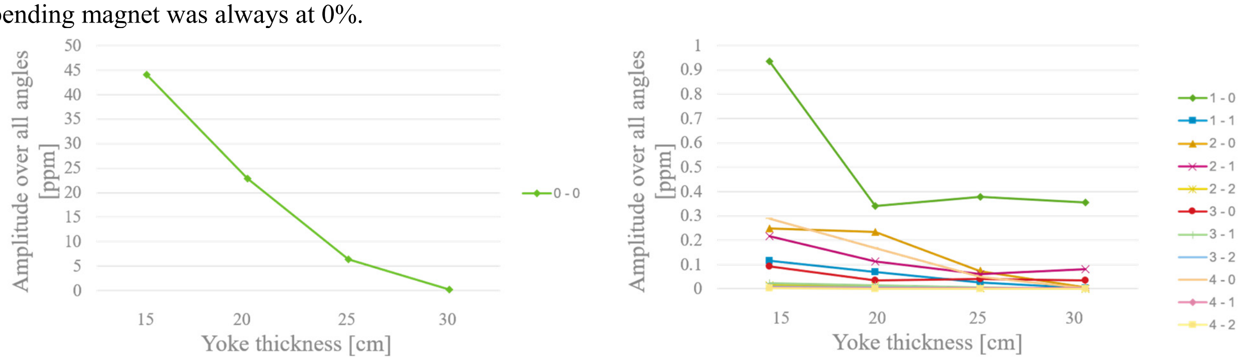

Figure 5: Fitted perturbation amplitudes versus yoke thickness for $\alpha_{00}^{\text{pert rot}}$ (left) and for higher orders with $n \geq 1$ (right). The legends list the $n - m$ parameters.

ISBN: 978-3-95450-205-9 doi:10.18429/JACoW-Cyclotrons2019-TUB03

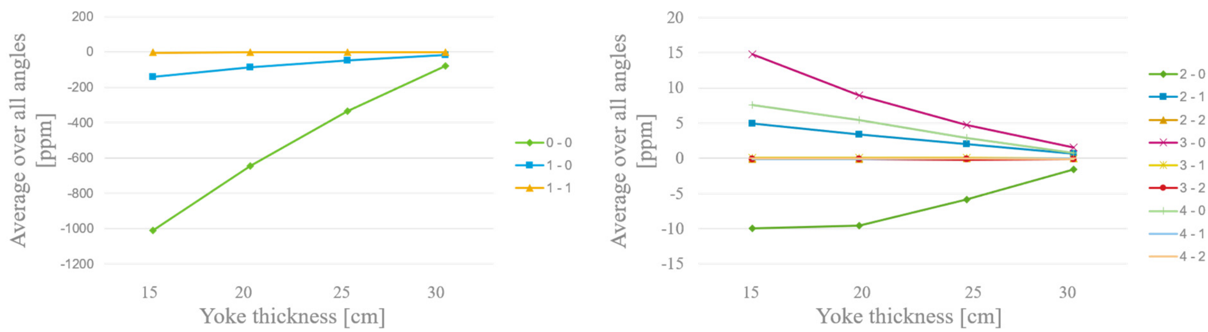

Figure 6: Fitted perturbation averages versus yoke thickness for the first orders of $\alpha_{nm}^{\text{pert bend}}$ (left) and for higher orders with $n \geq 2$ (right). The legends list the $n - m$ parameters.

For the MR-Open, linear adjustments by the gradient coils can be taken care of up to 100 ppm. The higher order perturbations (n ≥ 2) can be seen in Fig. 5 to be below the ppm level and need no compensation.

Perturbation by 60° Bending Magnet

For this perturbation study the gantry and the gantry's chair were all included as iron.

The results for $\alpha_{nm}^{\text{pert bend}}$ versus gantry rotation angle show no significant fluctuation as function of the angle. The average of the perturbations over the angles is therefore studied.

In Fig. 6 the fitted perturbation averages are given for $\alpha_{nm}^{\text{pert bend}}$, with $(n, m) \leq (4,2)$. Higher order perturbations are negligible, i.e. < 1 ppm. In Fig. 7 the fitted perturbation averages are given for the β coefficients.

The lowest order coefficients $(n, m) \leq (1,1)$ are within reach for active compensation with the default MR-Open, even with yoke thicknesses down to 20 cm. The perturbations by the bending magnet on the higher order coefficients $\alpha_{20}, \alpha_{21}, \alpha_{30}, \alpha_{40}, \beta_{21}$ are in the 1-10 ppm range for a yoke thickness of 30 cm. Active compensation coils can be designed and added to the system to cancel these levels of perturbations.

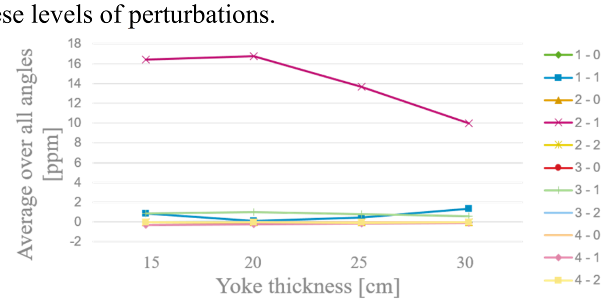

Figure 7: $\beta_{nm}^{\text{pert bend}}$ versus yoke thickness. The legend lists the $n - m$ parameters.

CONCLUSION

An option for the integration of a liquid helium free 0.5 T open MRI scanner based on the ASG MR-Open into an IBA ProteusONE PT gantry has been presented. An FEM analysis has been performed to assess the magnetic field perturbations by rotating ferromagnetic elements around the MRI, and by the fringe field of the 60° bending magnet mounted on the gantry.

The analysis shows that the rotations cause perturbations below the 50-ppm level, which can be actively compensated for with the default MR-Open system.

The bending magnet's fringe field causes perturbations, which cannot all be compensated for with the default MR-Open: With the maximum yoke thickness of 30 cm, non-linear perturbations remain up to the 10-ppm level.

Consequently, in the synchronization of the operation of the MRI and the PT system, an image can be acquired simultaneously with the changing of the magnet's field only if active compensation coil sets are added to the system. Without these coils, image acquisition and changing magnet setpoints should be done successively. The two scenarios correspond to different trade-offs between treatment delivery speed and commissioning efforts.

REFERENCES

[1] B. Oborn *et al.*, "Future of medical physics: real-time MRI-guided proton therapy", *Med. Phys.*, vol. 44, no. 8, pp. e77-e90, Aug. 2017. doi:10.1002/mp.12371

[2] S. Schellhammer *et al.*, "Integrating a low-field open MR scanner with a static proton research beam line: proof of concept.", *Phys. Med. Bio.*, vol. 63, no. 23, p. 23LT01, Nov. 2018. doi:10.1088/1361-6560/aaece8

[3] E. Pearson *et al.*, "Magnet developments and commissioning for the IBA compact gantry", *IEEE Trans. App. Supercond.*, vol. 24, no. 3, p. 4401004, Jun. 2014. doi:10.1109/ TASC.2013.2284719

[4] ASG Superconductors – Paramed MRI Unit, https://www.paramedmedicalsystems.com/

[5] J. Marques *et al.*, "Low-field MRI: An MR physics perspective", *J. Magn. Reson. Imaging*, vol. 49, no. 6, p. 1528, Jun. 2019. doi:10.1002/jmri.26637

[6] Vector Fields Software, "OPERA Simulation Software", http://operafea.com

[7] Vector Fields Software Support, Klaus Hoffner, private communications, Dec. 2016.

ISBN: 978-3-95450-205-9 doi:10.18429/JACoW-Cyclotrons2019-TUB04

ON-LINE DYNAMIC BEAM INTENSITY CONTROL IN A PROTON THERAPY CYCLOTRON*

Serena Psoroulas, Pablo Fernandez Carmona, David Meer, Damien Charles Weber[1]
Paul Scherrer Institut, 5232 Villigen PSI, Switzerland
[1]also at University of Zurich, Zurich, Switzerland, and University of Bern, Bern, Switzerland

Abstract

Modern proton therapy facilities use the pencil beam scanning (PBS) technique for the treatment of tumours: the beam is scanned through the tumour volume sequentially, i.e. stopping the beam at each position in the tumour for the amount of time necessary to deliver the prescribed dose for that position, and then moving to the next position (dose-driven delivery). This technique guarantees robustness against fluctuations in the beam current. Modern cyclotrons however offer very stable beam currents, and allow regulating the beam intensity online to match the requested intensity vs. time profile of the beam ('time-driven' delivery). To realise time-driven delivery at the COMET cyclotron at the Paul Scherrer Institute (PSI), we have designed a beam intensity controller which is able to partially compensate for the non-linearity and the delay introduced by the physical limitations of the beam line elements and its drivers; this is particularly important when trying to achieve a very fast modulation of the beam, as required by clinical plans. Experimental results have shown good performance for most current clinical scenarios, and we are investigating more advanced solutions for higher dose rates scenarios.

INTRODUCTION

Proton therapy (PT) is a radiation therapy technique which established itself recently as treatment of choice of many tumours, particularly paediatrics [1]. Modern PT facilities use the pencil beam scanning technique (PBS) for the treatment of deep-seated tumours, because it provides better tissue sparing and less neutron contamination than other delivery techniques, such as passive scattering. In PBS, the beam is moved sequentially through the target volume, and stopped at each point through the volume for the amount of time needed to deliver the amount of protons defined by the treatment plan (therefore is also called 'discrete scanning'). About 75% of all PT facilities feature a cyclotron [2], as this technology offers high intensities and a very reliable beam current output, which are both advantageous to keep treatment times within predefined limits (about 2 Gy/minute needed to irradiate a 1-liter volume). Despite this excellent timing performance, PBS is currently mostly used to treat static tumours (for example, brain tumours) and in some cases used to treat tumours with limited periodical motion due to respiration, such as lung or liver, with or without motion mitigation strategies. This is due to the fact that the reciprocal/independent motion of the beam and the target cause an interference pattern in the resulting dose distribution, that worsens the delivered dose distribution (the so-called the interplay effect) and makes in the end the treatment ineffective. PBS can be used to treat such tumours only in combination with motion mitigation techniques [3], to ensure the dose degradation remains within acceptable limits.

At PSI, in the clinical treatment unit Gantry 2, we are investigating a new delivery technique, continuous line scanning (CLS), which offers substantially lower treatment times and better dose conformity of moving targets treatments, particularly when combined with motion mitigation. In recent papers [4, 5] we compared it with the two main discrete scanning techniques used for PBS, the so-called spot scanning [6] and raster scanning [7], showing that CLS brings clear advantage over the other techniques for liver tumours treated with motion mitigation.

One of the keys of CLS performance is its high flexibility and speed in the dose modulation, which is achieved by both quickly adapting the beam transverse scanning speed as well as beam intensity to what is specified for the treatment. This however requires fast intensity changes to be performed already at the cyclotron. Though the PSI COMET cyclotron is designed to match such a requirement, achieving a reliable intensity control that also meets the stringent safety requirements for patient routine treatments represent a challenge not fully considered at the time of design. We have preliminarily reported [8] a first attempt at designing a beam intensity controller for this application, and the challenges of the final design and implementation [9]. After summarising the main challenges and the characteristics of our design, we will report in this paper the experimental validation of the implemented solution.

BEAM INTENSITY CONTROL AT THE PSI PROTON THERAPY CYCLOTRON

The COMET Cyclotron at PSI and its Intensity Regulation

The COMET cyclotron (ACCEL/Varian) [10] provides a beam of 250 MeV to the treatment rooms at PSI. The beam energy is then lowered to what needed for the treatments in a degrader and energy selection section placed downstream. The beam intensity is defined at the cyclotron and gets considerably lowered when passing through the energy selection system. For keeping the beam delivery efficiency high, stable beam currents and a high cyclotron output are of utmost importance.

Inside the cyclotron, the beam is extracted from a cold-cathod-type proton source by a puller, and then accelerated

ISBN: 978-3-95450-205-9 doi:10.18429/JACoW-Cyclotrons2019-TUB04

passing through four dees. The source output is tuned once a day and kept stable during operation [11], while the regulation of the beam current is done in the next turn, by passing the beam through a vertical electrostatic deflector (VD) followed by collimators [12]. When the VD is charged, it deflects the beam off the central plane. This will cause a part of the beam to be collimated in the collimators placed in the following dee. The larger the VD electric field, the more protons will be stopped. With such a system, we can achieve intensity variations from 0 to maximum current within 50 µs.

Beam Intensity Regulation Challenges

VD voltage versus current relationship The beam current is constant at the treatment room. However, because of the losses caused by the energy selection, which are higher for lower energies, the beam output requested at the cyclotron depends strongly on the energy to be delivered at the patient. This means that we need a large range of VD voltages during treatments, with the highest values required for higher energy treatments, and values close to 0 required for low-energy treatments.

As shown in Fig. 1, to achieve a current of 1e6 protons/ms at the patient, we may require about 0.4 kV at 150 MeV, but only 0.05kV at 70 MeV. Additionally, because of fluctuations in the current extraction efficiency, ion source operation etc., the relationship between VD voltage and current at the patient can strongly vary between different days and even within the same day [8]. To better correct for such fluctuations, we perform measurements of this relationship regularly through the day, and use this information to make a first estimate of the VD voltage operating point requested by each line before delivery.

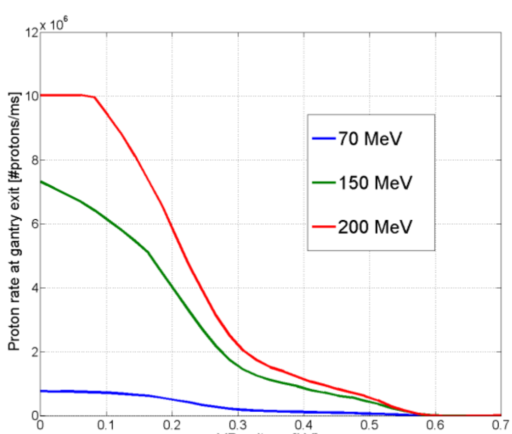

Figure 1: Vertical deflector (VD) voltage vs beam intensity at patient relationship for three energies [3].

Reaction time of the monitoring system The beam current delivered at the patient, inside the treatment room, defines the reference current for the regulation. This however introduces a systematic delay, caused respectively by the time needed for the communication between our treatment control system and the VD power supply, the time needed for the beam acceleration inside the cyclotron and the transport to the treatment room, and finally the time needed for the measurement of the beam intensity in the Gantry 2 monitoring system (which uses ionisation chambers with a collection time of about 90 µs). In total, the latency caused by the delays amounts to about 200 µs. In clinical practice, the smallest lines we want to deliver are about 300 µs long. This makes the regulation of the beam current for such lines particularly challenging.

Power supply hardware constraints Due to the harsh radiation environment in the cyclotron bunker, the power supply has been installed outside. The long cable thus required causes adds a capacitance of approximately 5 nF to the load of the system; in comparison, the capacitance due to the copper plates of the VD is only of the order of 100 pF. Together with the producer of the power supplies [13], we have optimised the impedance matching between the power supply and the load to avoid problems as much as possible. However, such a high capacitance presents a limitation to the highest speed of intensity change reachable by the power supply. Furthermore, the power supply is internally built using switched stages of 90 V, which makes the internal regulation faster but causes unpredictable overshoots to appear whenever the power supply switches stages [9].

Intensity Controller Design

We considered the different challenges identified in the previous section in the design of the intensity controller [9]. From data collected over a year of operation we realised that the large variability of the system as well as the presence of large overshoots (particularly for low voltage variations) required different parameters for the controller, depending on the expected range of possible overshoots. Therefore, our implementation foresees the presence of three different controllers, with different degrees of reaction time and robustness (the slower the controller to reach the set point, the more robust and less prone to oscillations). Each controller is better suited for different levels of overshoot and voltage variations. All three controllers have the same structure, only different parameters. During beam irradiation, the Gantry 2 control system selects the desired controller parameters based on the intensity variation (the 'gain' caused by the voltage variation) requested. Furthermore, a Smith predictor has been integrated in the controller design to cope with the 200 µs latency. We refer the reader to another paper [9] for a detailed report of the design and implementation of the intensity controller in our beam delivery FPGA.

ISBN: 978-3-95450-205-9 doi:10.18429/JACoW-Cyclotrons2019-TUB04

RESULTS

Figure 2 shows the comparison between the old version of the controller (whose behavior was explained in a previous report [8]) and the new version. It also highlights the difference between a controller without Smith predictor and a controller with Smith predictor. The latency compensation introduced by the predictor reduces the settling time, without causing instabilities in the system. Based on these results, we concluded that the delay compensation brings substantial improvements and therefore is a fundamental part of our design, despite adding complexity to the system. However, the predictor is only as good as the quality of the model of the plant. For this reason, we will commission the controller over a long period, as we have particularly observed seasonal variations in the behaviour of the facility.

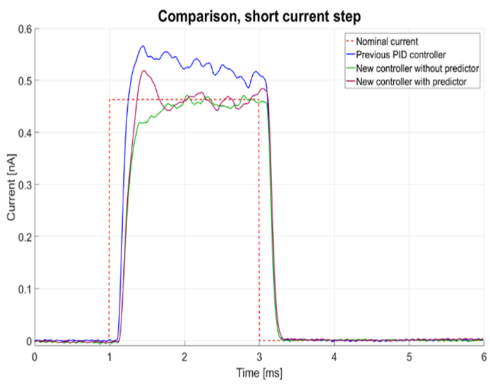

Figure 2: Comparison between controller with and without Smith predictor [8].

Concerning robustness, we tested two different scenarios: in the first case, we derived controller parameters which allowed a faster reaction time (but were less robust with respect to instabilities), while in the second scenario we derived controller parameters achieving a slower but more robust operation. We indeed could observe the faster controller become unstable after a few hours of operation, particularly when variations on the current output of the cyclotron (such as extracted beam current and transmission to the gantry room) occurred. An example of such behavior is shown in Fig. 3. From our clinical experience, we know such variations can occur almost unexpectedly during clinical operation (depending on ion source performance worsening, beam centering in the central region of the cyclotron, and other effects currently under investigation). At PSI, we are looking into possible ways to automatically tune the accelerator settings to stabilize these variations. However, since we are currently running without an automatic correction of such effects, for the time being we need to rely on a more robust controller, and therefore need to accept some compromises on the maximum settling time for the beam current in line scanning plans. Another possibility being investigated is adapting the controller parameters to the beam conditions; this solution though is not currently preferred, since it adds complexity to the Gantry 2 operation.

We could also observe the effect of the 90 V stage switching on the stability of the delivery; an example is reported in Fig. 4, where several small beam current overshoots/undershoots can be seen. In this example, one such overshoot is high enough to go beyond our safety tolerance at the beginning of the delivery, where it would have caused a beam intensity interlock. To solve this problem, we are considering the option of a linear regulation of the power supply (without discrete steps) for a future upgrade of the facility.

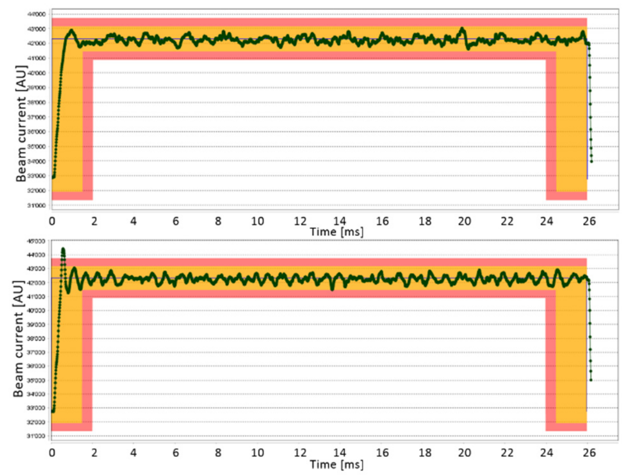

Figure 3: Beam current plots; the target current (horizontal blue line) is overlaid to the measurements (markers). The red bands represent the warning level, exceeding such bands would trigger an interlock when operating the system in clinical mode. In the example, we show the same patient file, delivered once and after one hour, with the same controller parameters; in the second irradiation, instabilities in the beam delivery arise, due to variations in the current output of the cyclotron.

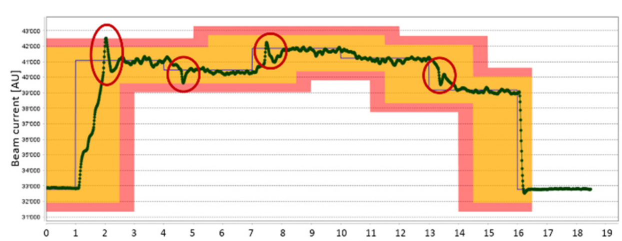

Figure 4: Effect of the 90 V stage switching: small overshoots appear during the delivery of the line.

Despite the compromises mentioned above, we could verify that the precision of the delivery meets the requirements of line scanning experiments. One example of a dose distribution delivered with the current controller is shown in Fig. 5. In this example considered, the beam current is quickly lowered to 0 and then again to maximum towards the middle of the line. The good agreement of the delivered dose distribution and the expected dose distribution is an indirect confirmation that the fast beam current modulation at the vertical deflector is working as expected. However, further testing (particularly regarding

ISBN: 978-3-95450-205-9 doi:10.18429/JACoW-Cyclotrons2019-TUB04

robustness and reliability) are necessary before the technology will be fully integrated in clinical practice.

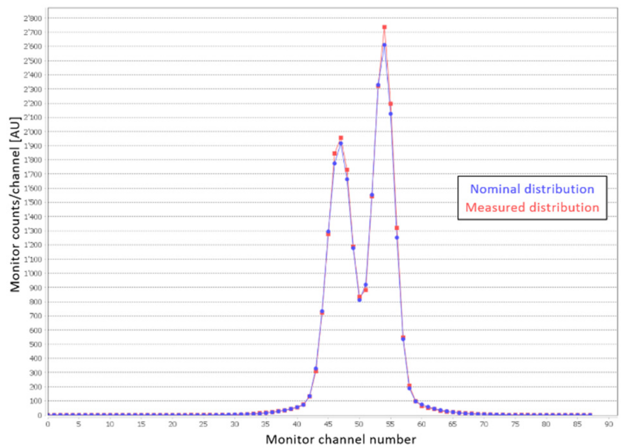

Figure 5: Dose distribution for a single line: comparison between expected ('nominal') and measured dose distributions, measured in the nozzle monitor strip chamber.

CONCLUSIONS

We reported the results of the implementation of an on-line dynamic beam intensity controller for CLS at a proton therapy cyclotron. Our design features a gain-scheduled controller, which, depending on the intensity variation required for the treatment, selects the controller parameters according to three possibilities: from slowest but more robust, to fastest but less robust to fluctuations, depending on the expected range of possible overshoots. Furthermore, to compensate for the large latency in our system, it features a Smith predictor. We have shown that the presence of the predictor substantially increases the speed of the controller. However, the large variability of the accelerator output as well as some features of the VD power supply design pose still substantial challenges to the reaction times of the system, and therefore for a first implementation we chose a more robust, though slower, version of the controller. In this implementation, currently available for experiments, most of the patient plans from our center can be delivered with a precision of few percent; however, due to the speed of the controller chosen, the settling time of the beam current might still come short of the requirements for patient cases we would like to investigate in the future. For this reason, we are planning a further upgrade of the hardware (including new power supply specifications).

ACKNOWLEDGEMENTS

We are grateful to the dedication of all members of the line scanning team. We would like to acknowledge V. Minnig's work and the collaboration with A. Karimi from EPFL on the beam intensity controller. Special thanks to our colleagues from PSI, M. Eichin, C. Bula and U. Rechsteiner's, for their involvements on the control system developments at Gantry 2. The patient plans tested in this work were prepared using the line scanning planning tools developed by G. Klimpki and A. Mayor at PSI. Lastly, we would like to acknowledge the support of our PSI colleagues M. Schippers, M. Kostezer, P. Frey and A. Muelhaupt on the accelerator challenges.

REFERENCES

[1] R. L. Foote *et al.*, "The clinical case for proton beam therapy", *Radiation Oncology*, vol. 7, no. 1, p. 174, 2012. doi:10.1186/1748-717X-7-174

[2] PTCOG statistics webpage, https://ptcog.ch/index.php/facilities-in-operation

[3] J. Y. Chang *et al.*, "Consensus guidelines for implementing pencil-beam scanning proton therapy for thoracic malignancies on behalf of the PTCOG thoracic and lymphomasSubcommittee", *Int. J. Radiat. Oncol. Biol. Phys.*, vol. 99, no. 1, pp. 41–50. doi:10.1016/ J.IJROBP.2017.05.014

[4] G. Klimpki *et al.*, "A beam monitoring and validation system for continuous line scanning in proton therapy", *Phys. Med. Biol.* vol. 62, no. 15, p. 6126, 2017. doi:10.1088/1361-6560/aa772e

[5] G. Klimpki *et al.*, "The impact of pencil beam scanning techniques on the effectiveness and efficiency of rescanning moving targets", *Phys. Med. Biol.*, vol. 63, no. 14, p. 145006, 2018. doi:10.1088/1361-6560/aacd27

[6] E. Pedroni *et al.*, "The 200 MeV proton therapy project at the Paul Scherrer Institute: conceptual design and practical realization", *Med. Phys.*, vol. 22, pp. 37–53, 1995. doi:10.1118/1.597522

[7] T. Haberer *et al.*, "Magnetic scanning system for heavy ion therapy", *Nucl. Instrum. Methods Phys. Res., Sect. A*, vol. 330, pp. 296–305, 1993. doi:10.1016/0168-9002(93) 91335-K

[8] S. Psoroulas *et al.*, "Challenges in fast beam current control inside the cyclotron for fast beam delivery in proton therapy", in *Proc. Cyclotrons'16*, Zurich, Switzerland, Sep. 2016, pp. 126-129. doi:10.18429/ JACoW-Cyclotrons2016-TUA02

[9] P. Fernandez Carmona *et al.*, "Continuous beam scanning intensity control of a medical proton accelerator using a simulink generated FPGA gain scheduled controller", *Proc. PCaPAC'18*, Hsinchu City, Taiwan, Oct. 2018, pp. 242-247. doi:10.18429/JACoW-PCaPAC2018-FRCC2

[10] H.-U. Klein *et al.*, "New superconducting cyclotron driven scanning proton therapy systems," *Nucl. Instrum. Methods Phys. Res., Sect B*, vol. 241, no. 1–4, pp. 721–726, Oct. 2005. doi:10.1016/j.nimb.2005.07.123

[11] M. Schippers *et al.*, "Beam intensity stability of a 250 MeV SC cyclotron equipped with an internal cold-cathode ion source", in *Proc. Cyclotrons'07*, Giardini Naxos, Italy, Oct. 2007, pp. 300–302.

[12] M. Schippers *et al.*, "Fast scanning techniques for cancer therapy with hadrons – a domain of cyclotrons", in *Proc. Cyclotrons'10*, Lanzhou, P. R. China, Sep. 2010, paper FRM1CIO04, pp. 410–415.

[13] SIGMAPHI Electronics, Haguenau, France.

ISBN: 978-3-95450-205-9 doi:10.18429/JACoW-Cyclotrons2019-TUP004

INTEGRATION OF EtherCAT HARDWARE INTO THE EPICS BASED DISTRIBUTED CONTROL SYSTEM AT iThemba LABS

J. K. Abraham, W. D. Duckitt, iThemba LABS, Somerset West, South Africa

Abstract

iThemba Laboratory for Accelerator Based Sciences (iThemba LABS) has, over the past 30 years, carried out several upgrades to its control electronics and software. This culminated in the adoption of EPICS as the de-facto distributed control system at the lab. In order to meet the changing technology and user requirements, iThemba LABS adopted EtherCAT as its new industrial communication standard. Building on an open EtherCAT master implementation and prior community development, iThemba LABS has successfully integrated a variety of EtherCAT hardware into its EPICS control system (Fig. 1). This paper presents the open source software toolchain that has been developed and is used at iThemba LABS and showcases several hardware installations at the facility and abroad. Community involvement and future plans for this initiative are also presented.

Figure 1: 19-inch rack mountable EtherCAT enclosures designed at iThemba LABS.

INTRODUCTION

iThemba Laboratory for Accelerator Based Sciences (iThemba LABS) is a multidisciplinary facility conducting research in subatomic physics, material research, radiobiology, and the research and development of unique radioisotopes for nuclear medicine and industrial applications. The facility operates and maintains a number of accelerators, the largest of these a K=200 separated sector cyclotron can accelerate protons to energies of 200 MeV. The control systems of these machines have been continually upgraded over the last 30 years in order to keep equipment failure to a minimum and to enhance technical capabilities.

Evolution of the iThemba LABS Control Architecture

The original control system was developed in the late 1970s around a few mini-computers with the control electronics and instrumentation interfaced via CAMAC. This system was then upgraded in the early 1990s to a distributed PC-based system running OS/2 and communication over Ethernet LAN. An in-house “simple” interface (SABUS) was also developed to supersede the ageing CAMAC bus and an assortment of I/O cards were developed to gradually replace the existing CAMAC modules.

With the OS/2 operating system no longer being supported by IBM, the decision was made in the late 2000s to migrate the control system onto the EPICS platform. The SABUS hardware interface was retained on account of robustness, noise-immunity and the large amount of re-cabling that would have to be done if this was changed. The various EPICS client user interfaces were developed in MEDM and Qt. By the mid-2010s about 60% of the control hardware was under EPICS control using SABUS cards to control power supplies, stepper motors, pneumatic actuators, all aspects of the vacuum, slits and scanner systems [1–3].

Migration to EtherCAT

The long design cycles involved in developing custom in-house SABUS cards resulted in a number of legacy OS/2 CAMAC systems still remaining. CAMAC hardware was becoming increasingly difficult to find and the rapid rate of obsolescence of modern electronic components meant that the in-house SABUS cards had to be periodically redesigned. In light of these challenges, and after an investigation of various industrial bus technologies, iThemba LABS adopted EtherCAT as its new industrial communication bus in 2015 due to its high-speed performance, existing integration with EPICS and wide selection of commercial off-the-shelf hardware.

SOFTWARE STACK

EtherCAT is an open real-time Ethernet fieldbus developed by Beckhoff (Verl, Germany) and maintained by the EtherCAT Technology Group (ETG) [4]. The EtherCAT topology employs a master/slave principle, where the master node (typically the control system) sends Ethernet frames to the slave nodes, the slave nodes then extract data from and insert data into these frames with a few nanoseconds delay. Each EtherCAT slave includes a controller with a Fieldbus Memory Management Unit (FMMU). The FMMU allows the mapping of logical addresses in the Ethernet frame to physical ones within the slave modules. The registers in each slave that can be mapped by the FMMUs are known as either Process Data Objects (PDOs) or Service Data Objects (SDOs).

ISBN: 978-3-95450-205-9 doi:10.18429/JACoW-Cyclotrons2019-TUP004

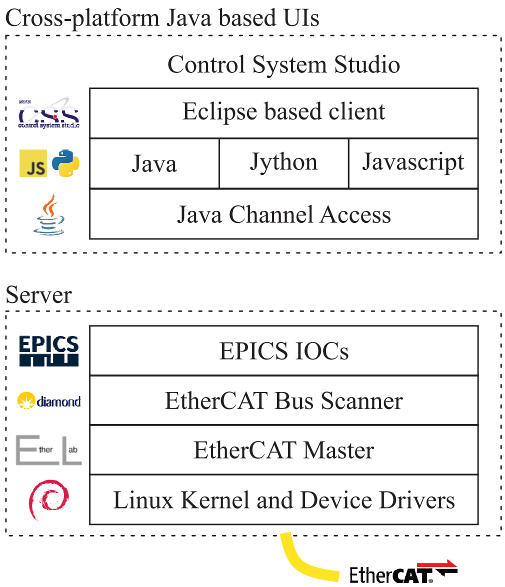

Figure 2: EtherCAT master/slave software stack used at iThemba LABS.

Figure 2 shows the server/client open-source software stack developed and used at iThemba LABS. The server, which implements the EtherCAT master, runs on a "headless" Debian Linux machine patched with a real-time kernel patch. The real-time kernel patch ensures the deterministic performance of EtherCAT can be achieved. The client user interfaces are based on Control System Studio (CS-Studio) and can be deployed on regular Windows/Linux machines as they are cross-platform.

The server stack is built on an open-source EtherCAT master from EtherLab.org and a bus scanner and Asyn drivers developed by Diamond Light Source UK (Diamond) [5, 6].

EtherLab EtherCAT Master

The EtherLab kernel module implements an EtherCAT master conforming to IEC/PAS 62407. The master provides, amongst others: the finite state machine that reads the slave states cyclically, dynamic slave configuration (including PDOs and SDOs), Userspace API via a C-library and a command-line tool 'ethercat' for diagnosis and maintenance of the bus.

Diamond Bus Scanner and Asyn Drivers

The Diamond bus scanner generates the cyclical EtherCAT packets. On start-up it reads an XML configuration file, configures the FMMUs, and puts the slaves into operational (OP) mode. A Python script is used to generate the XML configuration file from the EtherCAT Slave Information (ESI) files and the active bus topology.

Finally, Asyn drivers deliver the slave I/O data and configuration information on each bus cycle to the EPICS application layer through asynInt32 parameters. Sample EPICS hardware templates are generated from the ESI file for each slave device using the Python libxml2 library.

EPICS IOCs

The majority of the development undertaken at iThemba LABS has been on the application layer using EPICS (low level hardware control) and a combination of State Notation Language (sequencing and state machine) and Java/Python (high level scripting). Using these tools, real-time control of various field sensors and actuators have been developed, including: pneumatic control of Faraday cups, harps etc.; movement of slits, trolleys, tape stations and various RF elements using motors; water flow, temperature monitoring and heat exchangers systems; interfacing with in-house and commercial meters such as radiation sensors and vacuum gauges; serial communications with third party devices and power supplies; and vault clearance and safety interlocking systems [3, 7–10].

Closed loop PID motion control algorithms have also been developed for various servo, DC and stepper motors. Positioning of these systems are done using potentiometers, encoders or using the drive's internal counters[1]. Motion systems have also been developed that use multiple feedback sensors simultaneously to ensure failsafe operation should a particular sensor fail mid-movement.

Large Scale Software Architecture A range of hardware expertise and software applications were developed through the upgrade of the RF motion control elements of the iThemba LABS cyclotrons. With the procurement of a 3 MV Tandetron from High Voltage Engineering Europa B.V. (HVE) in 2016, these tools were used to develop the complete beamline control, man-machine, safety, vault clearance and interlocking systems for the Tandetron. It is also envisioned that future projects such as the Low Energy Radioactive Ion Beam facility (LERIB) and the South African Isotope Facility (SAIF) will utilise these tools.

User Interfaces

All present user interfaces for new installations are being developed in CS-Studio. CS-Studio is a product of the collaboration between different laboratories and universities and provides a collection of tools to monitor and operate large scale control systems [11].

Concurrently, iThemba LABS is also developing a browser based user interface development framework called React Automation Studio [12]. This framework implements a modern tool chain with a React [13] front-end and a PyEpics [14] back-end as a progressive web application. This enables efficient and responsive cross platform and cross device operation. We hope to release it to the community soon.

HARDWARE INTEGRATION

Once EtherCAT was adopted as the new industrial communication bus, a selection of vendor hardware was tested with the open source master stack. The Beckhoff range of modular EtherCAT terminals was chosen as the preferred

[1] Internal counters only applicable for stepper motor drives.

ISBN: 978-3-95450-205-9 doi:10.18429/JACoW-Cyclotrons2019-TUP004

Figure 3: Unistrut EtherCAT cabinets designed at iThemba LABS.

hardware vendor for three reasons: (1) 25 years hardware support on all modules; (2) wide selection of I/O modules catering for most of our process control requirements; and (3) ease of integration and stability with the open master software stack.

A variety of EtherCAT slave I/O have been successfully interfaced into EPICS using customised hardware templates at iThemba LABS, these include:

- **Analogue inputs/outputs -** ±10 V and 0 to 20 mA; 12 to 24-bit
- **Digital inputs/outputs -** 5 to 24 V, potential free contacts and negative switching I/O
- **Temperature -** thermocouples and resistance thermometer devices (RTD)
- **Communication -** RS232, RS485 and RS422
- **Motion -** Servo, DC and Stepper motors
- **Position measurement -** potentiometers, absolute mechanical encoders and incremental optical encoders

SYSTEM INSTALLATIONS

iThemba LABS utilises the 19-inch racking standard for mounting most of its electronic enclosures and equipment. The EtherCAT terminals attach to commercially available 35 mm mounting rails (DIN rails according to EN 60715). Several form factor electronic enclosures, with DIN rail mounted slaves, have been developed at iThemba LABS, both to fit within the 19-inch rack standard and for alternate applications. Figures 1, 3 and 4 show some of the electronic enclosures installed at iThemba LABS.

International Collaborations

iThemba LABS has also, through collaborations, deployed a dual DC motor motion control system at Helmholtz-Zentrum Berlin (HZB) Germany and is jointly developing the control system for the SPES tape station at Laboratori Nazionali di Legnaro (LNL) Italy using EtherCAT hardware and the above mentioned software tools [8, 9].

Figure 4: Custom 19-inch rack mountable EtherCAT cabinets designed at iThemba LABS.

CONCLUSIONS AND FUTURE DEVELOPMENT

Building on the work done by EtherLab and Diamond, a stable and mature EtherCAT software stack has been developed at iThemba LABS. A variety of hardware I/O modules have been successfully integrated and deployed with this software architecture. The move to industrial off-the-shelf hardware has mitigated our obsolescence risk, shortened product development time and increased product life cycles. This process has also expedited the migration of our control system onto the EPICS platform.

Further investigations are needed into integrating I/O cards from other vendors and integrating the new ELM series of modules from Beckhoff (built for laboratory and testing technology environments) with the EtherCAT software stack. iThemba LABS will also be working to prepare a release candidate of its React Automation Studio front end software framework. The framework is cross device and cross platform. The operational readiness and stability of this software has been demonstrated and we encourage the EPICS community to test, evaluate and contribute to React Automation Studio.

REFERENCES

[1] J. L. Conradie *et al.*, "Current status of the cyclotron facilities and future projects at iThemba Labs", in *Proc. 19th Int. Conf. on Cyclotrons and their Applications (Cyclotrons'10)*, Lanzhou, China, Sep. 2010, paper MOA2CCO02, pp. 42–44.

ISBN: 978-3-95450-205-9 doi:10.18429/JACoW-Cyclotrons2019-TUP004

[2] I. H. Kohler *et al.*, “Progress in the conversion of the in-house developed control system to EPICS and related technologies at iThemba LABS”, in *Proc. 13th Int. Conf. on Accelerator and Large Experimental Control Systems (ICALEPCS’11)*, Grenoble, France, Oct. 2011, paper MOPMS013, pp. 347–350.

[3] J. L. Conradie *et al.*, “New developments at iThemba LABS”, in *Proc. 21th Int. Conf. on Cyclotrons and their Applications (Cyclotrons’16)*, Zurich, Switzerland, Sep. 2016, pp. 274–277. doi:10.18429/JACoW-Cyclotrons2016-THA02

[4] Dirk Jansen and Holger Buttner, “Real-time ethernet: the ethercat solution”, *Computing and Control Engineering*, vol. 15(1), pp. 16–21, 2004. doi:10.1049/cce:20040104

[5] EtherLab, http://etherlab.org

[6] R. Mercado, I. J. Gillingham, J. Rowland, and K. G. Wilkinson, “Integrating EtherCAT based IO into EPICS at Diamond”, in *Proc. 13th Int. Conf. on Accelerator and Large Experimental Control Systems (ICALEPCS’11)*, Grenoble, France, Oct. 2011, paper WEMAU004, pp. 662–665.

[7] J. L. Conradie *et al.*, “Progress with a new radioisotope production facility and construction of radioactive beam facility at iThemba LABS”, presented at the 22nd Int. Conf. on Cyclotrons and their Applications (Cyclotrons’19), Cape Town, South Africa, Sep. 2019, paper MOB02.

[8] M. Montis *et al.*, “EPICS based control system for SPES tape station for beam characterization: Motion system and controls”, presented at the 17th Int. Conf. on Accelerator and Large Experimental Control Systems (ICALEPCS’19), New York, NY, USA, Oct. 2019, paper MOPHA097.

[9] T. Fanselow *et al.*, “Operational experience in the treatment of ocular melanomas with a new digital low-level RF control system”, presented at the 22nd Int. Conf. on Cyclotrons and their Applications (Cyclotrons’19), Cape Town, South Africa, Sep. 2019, paper TUP008.

[10] William Duckitt, “A digital low-level radio frequency control system for the particle accelerators at iThemba LABS”, PhD thesis, Stellenbosch: Stellenbosch University, 2018.

[11] Control System Studio, http://controlsystemstudio.org/

[12] W. Duckitt and J. K. Abraham, “React Automation Studio: A new face to control large scientific equipment”, presented at the 22nd Int. Conf. on Cyclotrons and their Applications (Cyclotrons’19), Cape Town, South Africa, Sep. 2019, paper THA04.

[13] React, https://reactjs.org/

[14] PyEpics, https://cars9.uchicago.edu/software/python/pyepics3/

ISBN: 978-3-95450-205-9 doi:10.18429/JACoW-Cyclotrons2019-TUP005

THREE YEARS OPERATION OF CYCIAE-100

Tao Ge#, Yinlong Lyu, Tianjue Zhang, Yaoqian Li, Shiqiang Li, Zhenwei Liu, Lei Wang, Lei Cao, Zhenhui Fu, Hao Jiang, Lipeng Wen, Bin Ji, Zhiguo Yin, Shigang Hou, Gaofeng Pan
China Institute of Atomic Energy, Beijing, PR China

Abstract

The 100 MeV high intensity proton cyclotron (hereinafter referred to as CYCIAE-100) developed by China Institute of Atomic Energy is a multi-purpose variable energy AVF cyclotron for nuclear fundamental research and nuclear technology application. Its design specifications are: energy from 75 to 100 MeV continuously adjustable, beam intensity 200 μA, beam current can be extracted in both directions. The first physics experiment was carried out in November 2016 right after the national acceptance. By June 2019, we completed the construction of multiple experimental terminals for CYCIAE-100, such as single-event effect experimental terminal, ISOL experimental terminal, and white-light neutron experimental terminal. Several typical physics experiments of CYCIAE-100 have been carried out. Such as: The physics experiment of CYCIA-100 driving ISOL device to generate radioactive nuclear beam, white light neutron experiment, SiC and SRAM proton irradiation experiments, calibration experiment of high-energy proton electron total dose detector probe, and proton irradiation damage effect experiment of photoelectric devices. At present, the beam time for beam development of CYCIAE-100 is about 5000 hours, providing effective beam time for more than 3000 hours for many users at home and abroad, and the other beam time for beam development. This paper introduces the operation of CYCIAE-100 in the past three years, as well as the construction of experimental beam lines and terminals and typical experiments carried out.

CONSTRUCTION OF BEAMLINES AND EXPERIMENTAL TERMINALS

At the beginning of the design, the CYCIAE-100 had multiple beam lines and experimental terminals. Further, due to lack of funds and other factors, construction of some beam lines and experimental terminals were not completed when the accelerator was first beamed out in 2014. Then, as the accelerator gradually putting into the operation and while carrying out physical experiments, the construction of some beam lines and experimental terminals were also gradually carried out [1]. By July 2019, we completed the construction of multiple experimental terminals for CYCIAE-100, such as single-event effect experimental terminal, ISOL experimental terminal, and white-light neutron experimental terminal.

Single-event Effect Beam Line and Experimental Terminal

The single-event effect beam line and experimental terminal are located on the east side of the physical experiment hall. They are mainly used to carry out experiments on single-event effect and anti-radiation reinforcement of aerospace devices. Figure 1 shows the single-event effect beam line and the experimental terminal. The proton beams are transmitted along the south to the common beam line, after they are extracted from CYCIAE-100. Then, after the proton beams are deflected by the southward switching magnet, they enter the single-event effect beam line. At present, a large number of experiments about single-particle effects and radiation-resistant reinforcement have been carried out at the experimental terminal.

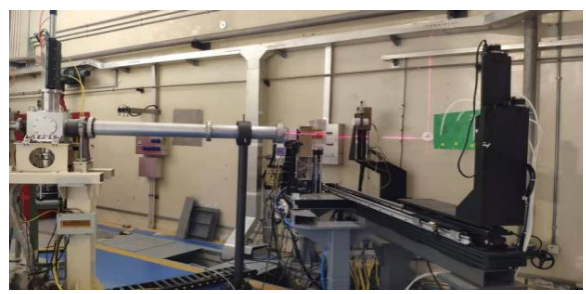

Figure 1: Beam line and experimental terminal of single-event effect.

Construction of ISOL Beam Line and Experimental Terminal

The ISOL beam line and experimental terminal are one of the important components in the HI-13 Tandem Accelerator Upgrade Project. The ISOL experimental terminal uses the proton beams generated by CYCIAE-100 to bombard the target material to produce medium- and short-lived radionuclides. Subsequently, the neutral radionuclide atoms generated in the target are converted into charged particles, and the required radioactive nuclear beams are sorted by a magnetic analyzer and accelerated up to 300 keV. A new set of superconducting post-accelerators and existing HI-13 tandem accelerators can further accelerate ions. The proton beams generated by CYCIAE-100 are transmitted through the north common beam line, pass through the northward switching magnet, enter the ISOL beam line, and are transmitted to the ISOL target chamber. The proton beams interact with the selected target material to generate the desired radioactive nucleus. The radionuclide atoms diffuse out from the target and enter the ion source ionization chamber to be ionized.

18610094847@163.com

22nd Int. Conf. on Cyclotrons and their Applications Cyclotrons2019, Cape Town, South Africa JACoW Publishing
ISBN: 978-3-95450-205-9 doi:10.18429/JACoW-Cyclotrons2019-TUP005

The ISOL experimental terminal is shown in Fig. 2. At present, the ISOL beam line and experimental terminal have been completed, and we have carried out the radioactive nuclides experiments such as ^{38}K and ^{20}Na.

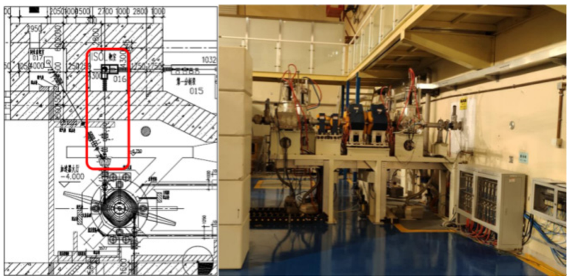

Figure 2: ISOL Beam line and experimental terminal.

Construction of Quasi-Single Neutron Beam line and Experimental Terminal

The study of neutron reference radiation field and calibration method in the energy region above 20 MeV is the hotspot of neutron metrology international research. The operation of CYCIAE-100 has laid a research foundation for the study of high-energy neutron reference radiation field in China. After the construction of the quasi-single-neutron beam line and the experimental terminal are completed, we will carry out research on high-energy neutron reference radiation field and calibration technology.

The quasi-single-energy neutron beam line and experimental terminal are located on the west side of the physical experiment hall. The proton beams generated by CYCIAE-100 pass through the south common beam line and are deflected by the south switching magnet to inject the quasi-single-energy neutron beam line. Figure 3 shows the quasi-single-energy neutron beam line and experimental terminal. At present, the beam line and experimental terminal have been completed, and relevant experimental work will be carried out soon.

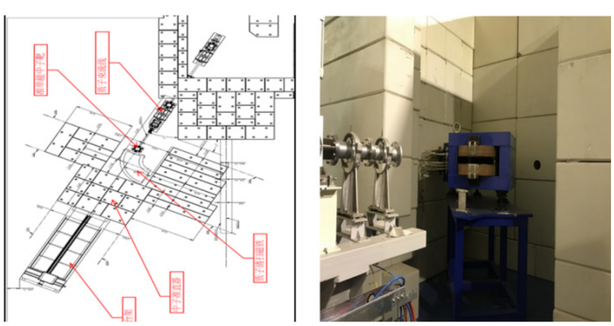

Figure 3: Quasi-single-energy neutron beam line and experimental terminal.

Construction of White Neutron Beam Line and Experimental Terminal

The operation of CYCIAE-100 laid the foundation for the research of white neutrons in China. After the construction of the white neutron beam line and the experimental terminal are completed, we will obtain the best pulse beams in China (pulse width/2.6 ns, 1 MeV-20 MeV neutron energy resolution is better than 1%). White light fast neutrons have a relatively broad energy spectrum, relatively high pulse frequency (1M/500 kHz), and the white light fast neutron yield and irradiation fluence rate are the highest in China. The best time-resolved white light neutron source in China is suitable for time-of-flight measurement methods.

The white neutron beam line and the experimental terminal are located in the middle of the physical experiment hall and are divided into two beam lines of 0° and 15°. The proton beams generated by CYCIAE-100 passes through the south common beam line and the south switching magnet. Then, they enter the white-light neutron beam stream, and finally hit the white-light neutron target. At present, the beam line and the experimental terminal have been constructed. Upon completion, the first test was carried out and a white neutron beam was obtained. Figure 4 shows the installed white light neutron target and pipe.

Figure 4: White light neutron target and beamline.

TYPICAL EXPERIMENT

Since the CYCIAE-100 was put into operation, dozens of users at home and abroad have used the accelerator to carry out various types of experiments. For example, the CYCIAE-100 design index debugging experiment was carried out, and the maximum extracted beam on the target reached 520 μA with a power of 52 kW. Achieve a supply beam range from 1 pA to 520 μA, and the beam intensity stability is 1%/8 hours. An experimental study on the sub-second half-life (445 ms) $^{20}Na^{+}$ radioactive nuclear beam, several β–γ–α singular decay sequences of ^{20}Na discovered for the first time in the world [2].

Proton irradiance effect test for single-event effect of large-capacity SRAM memory and DSP, etc. Total dose effect and displacement damage effect based on 100 MeV energy region wide beam intensity range proton beam were first carried out in China.

For the first time in China, the single crystal diamond wafer proton irradiation experiment for LHC/ATLAS applications was carried out. Table 1 shows some typical experiments.

Index Debugging Experiment of CYCIAE-100

The CYCIAE-100 has two radial insertion stripping targets, each with twelve carbon films, which can be replaced online. By adjusting the radial insertion position of

ISBN: 978-3-95450-205-9 doi:10.18429/JACoW-Cyclotrons2019-TUP005

the stripping target, the stripping extraction of H-ion in the energy range from 75 MeV to 100 MeV can be realized. After the H-ion is accelerated to a certain energy, it passes through the stripped membrane, loses two electrons and becomes a proton. By fine-tuning the angle of the stripped membrane, it changes the direction of motion under the effect of magnetic field, and is drawn out of the main vacuum and injected into the corresponding beam line.

Table 1: Some Typical Experiments

No	Experiment name	User Name	Beam Intensity	Experimental Time
1	^{20}Na decay study	CIAE	5 µA	150 h
2	Proton irradiation experiment of Single Crystal Diamond Module	Nanjing University	300 nA	50 h
3	Reinforcement test from check main nucleus in 28nm SOC asymmetric mode	Xi'an Jiaotong University	2 nA	3 h
4	The relationship between luminescence efficiency of scintillating fiber and proton irradiation dose was studied	Tsinghua University	2.5 nA	2.5 h
5	High-energy proton electron and total dose detector probe calibration experiment	Aerospace Fifth Research	1.6 pA	4 h

The accelerator debuted its first beam extraction in 2014 and first physics experiment in 2016. On this basis, 2018 has carried on the accelerator design index debugging experiment. By means of further increasing the main vacuum of the accelerator (the highest vacuum is 4.8×10^{-8} mbar), improving the stability of the high-frequency system under high power conditions, and improving the efficiency of the buncher, etc. The maximum stripping beam intensity of 520 µA was obtained on Beamdump target. Figure 5 shows the beam measurement curve for the Beamdump target.

Proton Irradiation Test of Single Crystal Diamond Module

The next-generation upgrade plan for the Large Hadron Collider (LHC) is to increase the transient brightness by a factor of ten. When the upgrade is complete, the original material will not be able to withstand such high colliding brightness. So they hope to place a diamond mini-FCal module in front of ATLAS's Liquid-Argon front-end energy meter, using the diamond module as a buffer to resist such high-brightness particle beams. Therefore, the high-energy Proton beam produced by the CYCIAE-100 was used to study whether the single crystal diamond module can maintain more than 5% signal output after being exposed to a beam dose equivalent to that of the LHC for 10 years. Single crystal diamond chips are widely used, not only as energy meter modules, but also as dose detection windows, track detectors, Pixel detectors, etc. Therefore, this experiment has important reference significance for the development of detector modules in large-scale Collider such as CEPC.

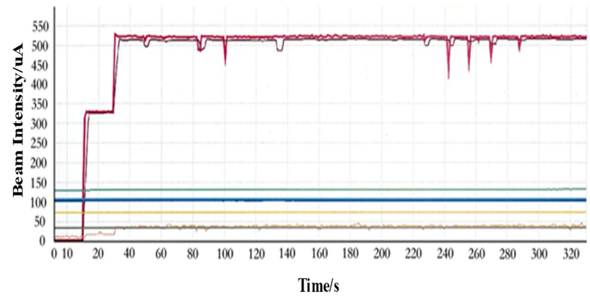

Figure 5: The beam curve of the beamdump target.

The data of one of the two samples in the experiment were processed. The sample was exposed to about 1.5×10^{17} p/cm^2 of Proton radiation, and the final output signal was about 5.6% of the initial signal. Figure 6 shows a photo of the experiment.

Figure 6: Proton irradiation experiment of single crystal diamond.

CONCLUSION

The steady operation of the CYCIAE-100 for nearly three years and a large number of experiments show that the design of the accelerator is reasonable and the index is advanced. The results demonstrate the China Institute of Atomic Energy's extensive experience in building and debugging cyclotron. The China Institute of Atomic Energy has the ability to develop high energy, high power, high current proton cyclotron.

REFERENCES

[1] T. J. Zhang *et al.*, "Research progress on several aspects of advanced high intensity accelerator technology at CIAE", *Atomic Energy. Sci. Techno.*, vol. z1, pp. 129-146, 2009.

[2] Y. Wang *et al.*, "Study of the exotic decay mode of 20Na with an intense ISOL beam", *Nucl. Phys. Rev.*, vol. 35, no. 4, Sep. 2018. doi:10.11804/NuclPhysRev.35.04.445

THE INJECTION AND CHOPPER-BASED SYSTEM AT ARRONAX C70XP CYCLOTRON

F. Poirier[†,1], F. Bulteau-harel, T. Durand, X. Goiziou, C. Koumeir, H. Trichet, A. Sengar
ARRONAX, Saint-Herblain, France
G. Blain, M. Fattahi, F. Haddad, J. Vandenborre, IN2P3/SUBATECH, Nantes, France
S. Chiavassa, G. Delpon, ICO, Saint-Herblain, France
[1] also at CNRS - DR17, Rennes, France

Abstract

The multi-particle cyclotron of the Arronax Public Interest Group (GIP) is used to perform irradiation up to hundreds of µA on various experiments and targets. To support low and high average intensity usage and adapt the beam time structure required for high peak intensity operation and experiments such as pulsed experiments studies, it has been devised a pulsing system in the injection of the cyclotron. This system combines the use of a chopper, low frequency switch, and a control system based on the new extended EPICS network. This paper details the pulsing system adopted at Arronax, updates and results for various intensity experimental studies performed with alpha and proton beams. Updated work on the simulation of the injection is also shown, specifically towards high intensity future irradiation.

INTRODUCTION

The Arronax cyclotron has been performing irradiation for 9 years delivering beams with intensities ranging over several orders of magnitudes. Typically for experimental studies, the average intensity is below one µA, while highest intensity irradiation for radio-isotope production can be at least up to 350 µA for proton and 20 µA for alpha in a single beamline. The cyclotron provides bunches interspaced by 32.84 ns (RF frequency = 30.45 MHz) translating into 7.8×10^7 particles per bunch for protons. To conform to the needs of the users for the range of beam intensities, several techniques are being employed based on the tuning of the source and the various magnet elements throughout the accelerator and specifically in the injection.

Additionally, a new chopper-based system located in the injection has been added and its characteristics and impact on the beam are being investigated in order to extend its use for high intensity operations.

CONCEPT AND LAYOUT

The pulsing chopper based system is designed to provide a variable number of trains of bunches to users from an initial continuous bunch structure, typical of cyclotrons. The present prototype design and functioning system allows thus to modify train duration and repetition. It is detailed in [1] as well as the first results at low intensity and the monitoring system that is being used.

The chopper system allows to bend away bunches at low energy (~40 keV for protons and 20 keV for other particles) in the injection. Its main components are:

- Two parallel copper plates within the beampipe
- A High Voltage (HV) switch (Behlke type) located outside the beampipe and closed (<30 cm) to the plates.
- Control electronics and a Raspberry Pi3 server within an EPICS network environment.
- A Control System Studio-based (CSS) interface with a simple visualisation terminal.

At the present time, the CSS interface gives operators the possibilities to manually modify the duration, repetition and number of trains that the experimenters require.

The control electronics located outside the cyclotron vault serves as a counting board for the number of RF buckets, a trigger for the desired state (closed/open) of the switch and a mirror trigger for experimental use.

When the HV switch is closed, 3.3 kV is applied to the plates, ejecting bunches to the injection beampipe wall.

EXPECTED CAPACITIES

At low intensity, the resulting trains have been checked using a light detector and have indicated rise and fall times of the order of a few microseconds [1]. An extended scan over the repetition frequency and train duration has been performed and has shown the potential usage from 10 Hz to 50 kHz with trains from 164 ns up to the continuous case.

A relatively good linearity has been obtained for duration above a few hundreds of ns and with repetition below 10 kHz. With this configuration at Arronax, Fig. 1 illustrates the average intensity <I> required for protons to reach, in a single train, dosimetry level of 33 Gy/s at the plateau before the Bragg peak as a function of the train duration. The figure indicates that a 6.4 ms train at <I> = 500 nA can reach the considered dosimetry level, and 320 µs at <I> = 10 µA.

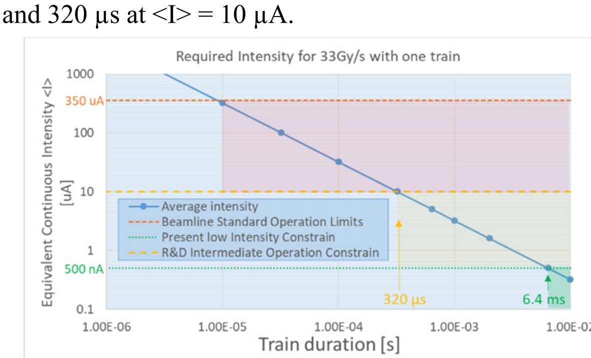

Figure 1: Avg. intensity as a function of the train duration to reach a dosimetry of 33 Gy/s at the Bragg peak plateau.

† poirier@arronax-nantes.fr

ISBN: 978-3-95450-205-9 doi:10.18429/JACoW-Cyclotrons2019-TUP006

INTENSITY STUDIES

A study of the use of the chopper is performed in comparison to the standard usage.

Low Intensity Tune

For low intensity, the arc source is minimised such that the beam remains stable, e.g. not too low. To reach very low and ultra-low intensity of the order of a few pA, solenoids in the injection are detuned. Three solenoids, of glaser-type, i.e. with a bell-shaped z-axial field distribution, are used: The source solenoid (SG) located downstream the source; the injection glaser (IG); and upstream the central region of the cyclotron, the cyclotron solenoid (CG). Figure 2 shows the impact of the intensity of the detuning of each solenoid. SG has the most drastic effect and is thus primarily used to decrease intensity to very low levels. Using this intensity degradation, the method has also shown that particles were lost mainly prior to acceleration below 1 MeV. It benefits operation ease, as only one knob is used.

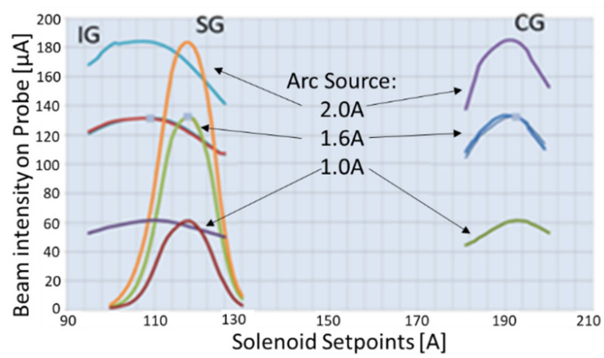

Figure 2: Intensity on the probe at 150 mm inside the cyclotron according to the settings of the three solenoids at various arc source.

High Intensity Tune

Traditionally for operations at high intensity the arc source is tuned to increase the beam intensity. All magnet elements are modified in accordance to allow maximum transmission from the injection faraday cup down to the irradiation station or experiment area.

The chopper-based system has been used to check its compatibility with high intensity runs (~50 µA on target). For the tests, the system was fixed at a 100 Hz repetition (or 10 ms time length) and a train duration from 0.5 ms up to 9.995 ms. Results are presented below: Figure 3 shows the linearity of the intensity on target using only this system and Fig. 4 depicts the beam geometry as given by a 4-independent fingers collimator. The difference of the right and left fingers electrical deposit (R-L) is here given, and represents in the case of a symmetric beam, the position of the transverse beam. Both techniques to lower down the average intensity, with the chopper or the source only, are used, to check the beam position. Without further retuning of any magnets, the chopper-based technique points to a better global stable beam when intensity modification occurs. This is also the case when the intensity is dropped by unwanted events such as breakdowns.

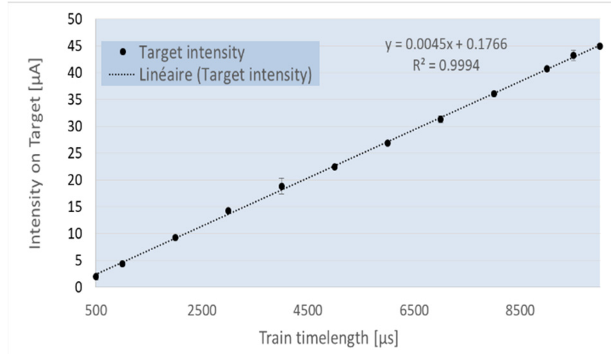

Figure 3: Target intensity up to 45 µA as a function of the train duration as driven by the injection chopper system.

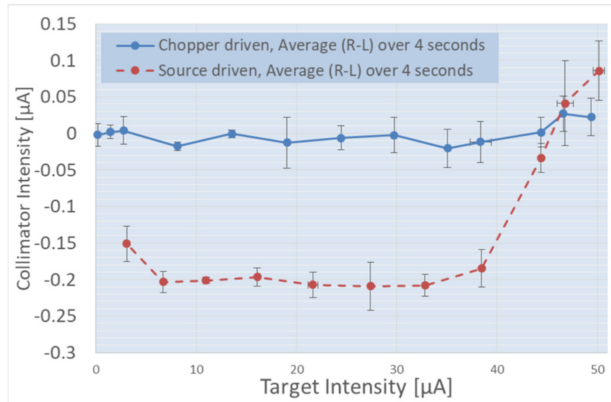

Figure 4: Average horizontal beam position at collimator for both techniques, i.e. source and pulsed-chopper driven, vs the intensity on target. 3×Standard Deviation are used for vertical error bars.

Discussion

First, the techniques based on the chopper has shown that it can be used with any particles and is applicable to any of the 8 beamlines of Arronax.

Second, the chopper can be used at high intensity, and suggest a certain reliability for short runs within the Arronax environment. For present test-runs, the integrated dose, measured with a Landauer neutron dosimeter on the switch, reached more than 110 mSv.

Taking into account the rise time of chopper in terms of the measured end-of-line intensity (<3 µs), the system shows it could potentially be integrated in the machine protection scheme. The results point that use of the switch to lower down the intensity when a breakdown occurs could provide a faster and more stable beam. This has to be reviewed in light of the difficulty to apply the right algorithm to lower down the beam intensity and then increase it again after breakdowns occurred downstream the chopper.

INJECTION STUDIES AND SIMULATION

Previous experimental studies have revealed that particles can still be accelerated depending on the settings of SG, mostly when defocalisation occurs with the solenoid being at low settings. This has asked to check the intensity

ISBN: 978-3-95450-205-9   doi:10.18429/JACoW-Cyclotrons2019-TUP006

prior to fix the settings of the solenoid when the chopper is used.

To verify various operational scenarios and study several potential optimisations, simulations of the injection are on-going.

Injection Simulation

G4Beamline, a particle tracking simulation program based on Geant4, is used at Arronax to perform detailed simulation that requires field and particle matter interaction impact for the various accelerator parts [2, 3].

A simplified model of the injection has been gathered and includes the field from all main magnetic elements and also the plates of the chopper-based system.

Magnet Field Construction

The models of the magnetic fields are based at the present time on approximated calculation and, when available, on the measurements performed by the magnets provider, SigmaPhi. Simulated field maps are constructed by applying a simple differential minimisation algorithm with the experimental measurements for the quadrupoles, solenoids and dipoles. This helped to perform integration to a more global model of the injection. Figure 5 shows the entire injection modelled in G4Beamline.

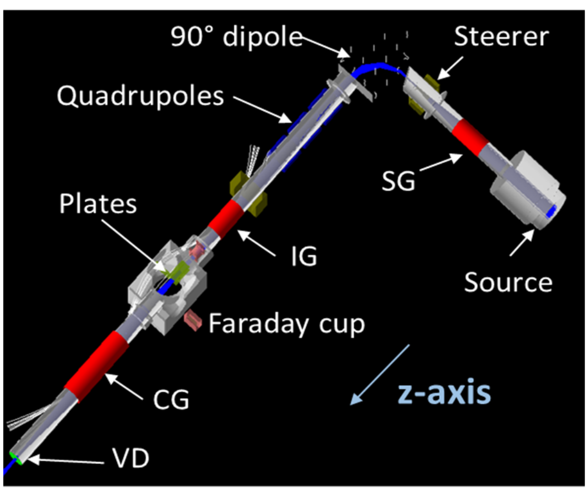

Figure 5: The overall G4Beamline model of the injection.

Simulation Input and Tune

From the experimental resulting field, fringe factors (= 0.3) as defined in G4beamline have been applied. Several emittances with a round beam at the exit of the source have been studied. For the present studies a beam of transverse dimension $\sigma_{x,y}$ = 9.9 mm, $\sigma_{x',y'}$ = 0.0018 (Here $\delta_{x,y}/\delta_z$ slope) has been used.

Simulation Results

The scenario with a beam approximately centered along the vertical z-axis has been chosen. This needed to kick the beam upstream the 90°-dipole with the steerer. With this scenario, the core of the beam is going between the chopper plates. Virtual Detectors (VD) located along the z-axis serves as ideal beam monitors. The results are depicted in Fig. 6 concerning the two extreme operation modes of the chopper: Stop mode, the chopper is kept at 3.3 kV, and continuous mode, the chopper is at 0 kV.

Similar to the experiments reported in [1], it can be observed that in the stop mode of this scenario and without any collimators, several particles can pass through. A collimator, upstream the chopper plates, helps to lower down the quantity of particles in the stop mode.

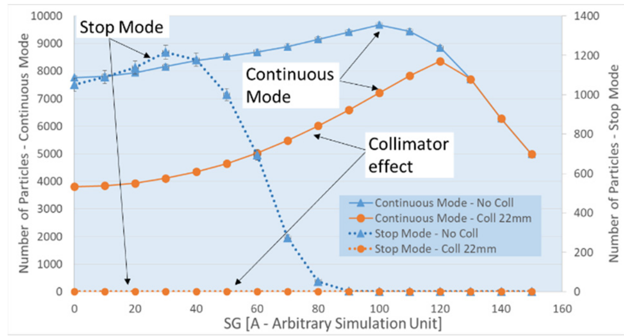

Figure 6: Number of particles on VD vs the solenoid setpoints for both extreme modes and impact of a 22 mm aperture collimator.

Experimental tests with a collimator are foreseen though still several simulation scenarios have to tackle various hypothesis on the beam.

CONCLUSION

Within the Arronax injection section, a chopper-based pulsed system has been added and is fully functional for low and high intensity beam. It helps to provide a temporally defined train of bunches, and if chosen to drive the average intensity, can contribute to further stabilise the beam. Though, optimisation for potential high intensity standard irradiation is needed.

A first model of the injection has also been built and already helps to explore various scenarios in view of the decision making towards optimisation. Further realistic field models have to be implemented.

ACKNOWLEDGEMENTS

This work has been, in part, supported by grants from the Région Pays de la Loire and the French National Agency for Research called "Investissements d'Avenir", Arronax-Plus n°ANR-11-EQPX-0004, IRON n°ANR-11-LABX-18-01 and Next n°ANR-16-IDEX-0007 and by Institut de Cancérologie de l'Ouest (internal call Emergence 2018).

REFERENCES

[1] F. Poirier *et al.*, "The pulsing chopper-based system of the Arronax C70XP cyclotron", in *Proc. IPAC'19,* Melbourne, Australia, June 2019. doi:10.18429/JACoW-IPAC2019-TUPTS008

[2] F. Poirier *et al.,* "The C70 ARRONAX and beam lines status", in *Proc. IPAC'11,* San Sebastian, Spain, Sep. 2011, paper WEPS069, pp. 2661-2663.

[3] A. Sengar *et al.*, "Development of a beam loss monitor and transverse beam dynamics studies at ARRONAX C70XP cyclotron", in *Proc. IPAC'19*, Melbourne, Australia, June 2019. doi:10.18429/JACoW-IPAC2019-WEPGW006

ISBN: 978-3-95450-205-9 doi:10.18429/JACoW-Cyclotrons2019-TUP007

OPERATIONAL EXPERIENCE IN THE TREATMENT OF OCULAR MELANOMAS WITH A NEW DIGITAL LOW-LEVEL RF CONTROL SYSTEM

T. Fanselow†, J. Bundesmann, A. Denker[1], U. Hiller
Helmholtz-Zentrum Berlin für Materialien und Energie (HZB), Berlin, Germany
J. K. Abraham, J. L. Conradie, W. Duckitt, iThemba LABS, Somerset West, South Africa
[1]also at University of Applied Sciences, Beuth Hochschule für Technik Berlin, Berlin, Germany

Abstract

Ocular melanomas have been treated for the last 20 years at the Helmholtz-Zentrum Berlin in collaboration with the Charité – Universitätsmedizin Berlin. However, parts of the initial control system electronics date back to the 1970s, when the machine was installed. Facing a critical shortage of legacy and obsolete components and with the down-time due to failures in the electronics on the increase, a decision was made to install the digital low-level RF control system, developed by iThemba LABS, on our k=132 cyclotron. A short description of the installation and commissioning process, which occurred in April 2017, and the experiences of the first two years of operation with the new digital low-level RF control system is presented.

INTRODUCTION

The HZB cyclotron with its two 30 kW RF amplifiers was built 45 years ago [1]. Over time some components of the whole cyclotron have been renewed, rebuilt or optimized. Especially in the high frequency systems, the 1 kW tube driver amplifiers were replaced by 2 kW semiconductor amplifiers, the system frequency generator was replaced by a network compatible device and various analogue displays were replaced by digital displays.

However, many components in both the low level and high level system of the RF are still from the early days. The two RF amplifiers in the high level system are still in their original condition, with the exception of minor optimizations, and are very robust. Spare parts for the amplifiers are available or can be made by ourselves. Some main components like e.g. the 100 kW amplifier tubes are still manufactured. Failures in the high level systems occur mainly due to leaks and defects in the water cooling system, and can be fixed by replacing or repairing the unit. The electronic modules in the low level systems were constructed using the wire wrap technology common at the time (Fig. 1), which is relatively compact despite the large number of components, but makes repair and maintenance more difficult. With the increasing age of the electronic modules, contact problems and wire breaks on the wire wrap cards occurred in addition to defective components.

Since various built-in special high frequency components and high-level logic ICs are no longer available, repairs were made even more difficult by increasingly scarce spare parts. Due to these problems and the desire for a better overview and diagnosis of the RF parameters, it was decided to replace the complete low level control of the two RF systems. An in-house development was rejected due to lack of personnel and time, and adaptable ready-made solutions were sought.

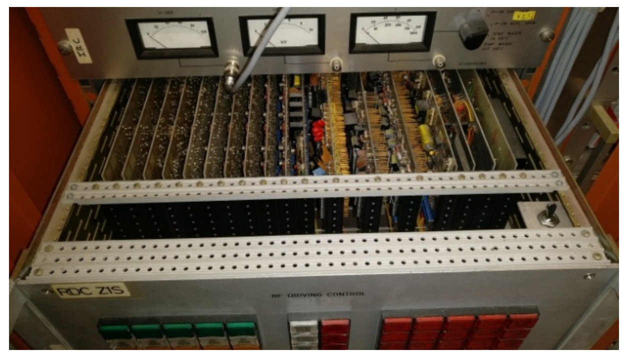

Figure 1: Old low level RF control system.

The digital low level RF (LLRF) control system newly developed and built by W. Duckitt at iThemba LABS [2] in Cape Town South Africa seemed to be suitable to replace the low level electronics of the RF systems at the HZB cyclotron. At this time in 2015, the digital LLRF control system was already successfully used with both injector cyclotrons SPC1 and SPC2 at iThemba LABS and the installation at the main cyclotron SSC and various buncher systems were planned. In October 2015, after clarification of the adaptability of the system and the technical implementation at the HZB cyclotron, it was decided to use the LLRF control system from iThemba LABS on both our RF systems.

PREPARATIONS AND INSTALLATION

From the beginning of 2016 to May 2017, all preparations, conversions and necessary measurements and tests were carried out in addition to normal accelerator operation during the maintenance periods. iThemba LABS built five LLRF control system modules for the HZB cyclotron and delivered them in March 2017. Two of the modules are planned for the north and south system at the cyclotron, one module serves as reference oscillator and two modules are intended as reserve or in the future for the buncher at the accelerator. For a synchronized operation of the modules, a distribution of the reference frequency and a 10 MHz clock signal had to be prepared using existing RF splitters. Since the installation of the LLRF control system had to take place without disturbing the accel-

†timo.fanselow@helmholtz-berlin.de

ISBN: 978-3-95450-205-9 doi:10.18429/JACoW-Cyclotrons2019-TUP007

erator operation, no modules of the old RF control system could be removed to create space for the new system. In order to allow the installation of the new modules, some of the old RF control modules were moved or rebuilt. The three LLRF control system modules with 6 rack units each were installed and connected to the reference and clock signal distribution. For the hardware connection of all actuators, read-outs, interlocks, analogue and digital signals of the RF systems to the control software, four 4-rack large modules units were built. In these modules, the signals are read or output via Beckhoff EtherCAT terminals and made available to the control software as parameters. For this purpose, two modules for motion control and one module each for the analogue and digital signals were set up (Fig. 2).

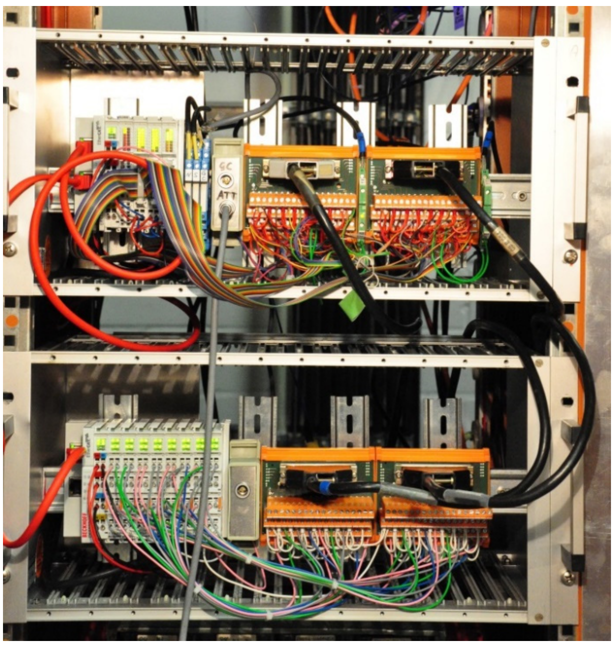

Figure 2: Modules with Beckhoff EtherCAT terminals for analogue and digital signals.

In addition, two server PCs with Linux operating systems were set up and installed, which represent the central interface between the LLRF, the Beckhoff EtherCAT terminals and the client PCs in the control and electronics room. The two Motion Control modules were then tested in interaction with all motors and position read-outs in the resonance tuning and control of the RF systems, and the respective limit parameters were determined. In order to ensure a fast connection of the analogue, RF, control and interlock signals of the new RF system and a fast change between the old and the new RF control, all signals of both RF systems were connected on patch panels (Fig. 3).

Subsequently, all analogue and RF signals were measured at the patch panels under different operating conditions of the cyclotron RF.

Amplifiers and attenuators were prepared to adjust the level differences between the measured and the required signal levels of the LLRF. The necessary software adaptation of the LLRF to the resonance control system at the HZB cyclotron, which differs from the iThemba LABS cyclotrons, was performed by iThemba LABS.

Figure 3: Patch panel for RF signals.

COMMISSIONING

The commissioning of the LLRF at the HZB cyclotron took place at the beginning of May 2017 [3], for which W. Duckitt and J. Abraham from iThemba LABS were on site. Since small changes and adaptations to both the software and the hardware are still necessary during the piecewise commissioning of the LLRF, two weeks were planned for the entire process.

Changes in the software mainly included adjustments of the gain and attenuation factors as well as phase and delay values in the resonance control. In addition, the limit values of all motion control actuators in the software were adjusted. On the hardware side, additionally required floating contacts were created and some interlocks were linked, and level adjustments were made with the prepared amplifiers and attenuators. In the first step, the EPICS based user interface was set up on the client PCs and the two server PCs were configured. The RF systems were tuned with the old RF control to the standard therapy frequency of 19.3187 MHz to obtain a starting value of the resonance tuning for the LLRF. Then the RF was switched off again and all signals at the patch panels were plugged into the new LLRF modules. In the next step, the north RF system was first started with the LLRF and, after optimizing the amplitude, phase and resonance control, stable operation under therapy conditions with 115 kV amplitude was achieved.

Subsequently, the same procedure was successfully performed for the south RF system, and both RF systems could be operated with the new LLRF after only two days (Fig. 4).

In the next step, resonance tuning to standard operating frequencies in the range of 10-20 MHz and further optimizations in the control loops in the LLRF were performed for both systems.

Finally, the interlock to block the operator interface, which is important for therapy when treating patients, was integrated.

In total, only one week was needed for commissioning instead of the planned two weeks. After commissioning, stability tests and several changes between the old and the new RF control were carried out in the second week. Comparative measurements of the therapy beam with the

ISBN: 978-3-95450-205-9 doi:10.18429/JACoW-Cyclotrons2019-TUP007

new and old RF control showed identical results at the target site.

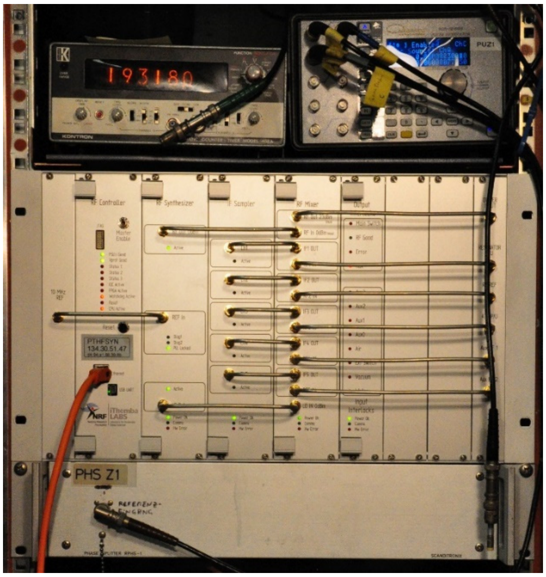

Figure 4: One of the LLRF modules installed at HZB.

TWO YEARS OF OPERATION

The therapy block in May 2017 was still carried out with the old RF control, as some adjustments still had to be made in the CAMAC control system for the new LLRF. The first therapy performed with the new LLRF followed in June 2017. Already during the adjustment of the accelerator the starting of the RF systems by the automatic resonance search of the LLRF was easier and faster than the manual resonance search of the old system.

Thus, the cold start of the RF systems after the maintenance period can be carried out by all operators themselves without any problems and without the help of the RF group. A further simplification for the operators is the visualization of the status as well as the short- and long-term display of the amplitudes and phases of both RF systems on the operator interface in the control room (Fig. 5).

This allows a better assessment of the status of the RF systems during the beam time. Both systems now run more stable, with phase stability improving from 0.1° to 0.02° and amplitude stability from 0.5% to 0.7%. The three bunchers and the pulse suppressor used only for experiment operation were synchronized with the new LLRF via the reference frequency. Thus the bunchers and pulse suppressor could be used identically to the old RF control for beam optimization at the cyclotron. Test measurements with bunched and pulsed 68 MeV proton beams with multi turn and single turn extraction showed a stable interaction of the RF systems.

The failures of the RF systems have been significantly reduced since operation with the new LLRF and are now mainly limited to problems with cooling water lines and power supply defects in the anode and grid voltage.

In the last two years only one problem has occurred: In October 2017, after a change of cyclotron frequency, the LLRF of the south system's phase modulator became sporadically unstable.

Figure 5: Operator interface for the north and south RF.

After consultation with W. Duckitt of iThemba LABS, the problem was identified as a suboptimal tuning of the RF power amplifiers output stage, resulting in the loop instability.

To solve the problem, the integral coefficient of the phase modulator's PID controller was first lowered. This allowed the power amplifier to be optimised at rated power. Thereafter the integral coefficient was returned to its nominal value and normal operation continued.

Downtime for magnet power supplies of the cyclotron, water leaks or RF are all counted in one number. Thus the trend of reduced downtime thanks to the LLRF is not immediately visible in Fig. 6, however, half of the downtime in 2017 was due to problems with water leaks and a power supply of a trim coil magnet.

Since June 2017 both the proton therapy and the experiment operation have been carried out successfully exclusively with the new LLRF.

Besides the standard 68 MeV proton beam (f_{RF} = 19.3187 MHz) a 90 MeV ^{4}He beam (f_{RF} = 17.2576 MHz) has been delivered successfully for experiments.

OUTLOOK

The next step is the conversion of the buncher systems to the LLRF, as problems with the procurement of spare parts are increasingly occurring here as well. This would also provide a better overview of the condition of the buncher and an easier optimization of the phase relationships of the RF systems.

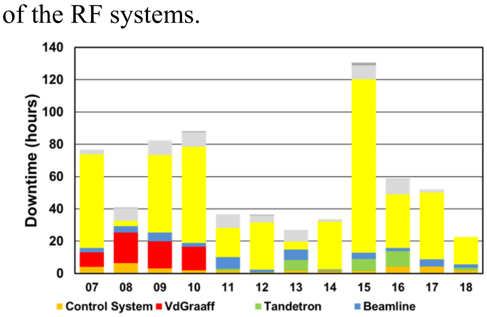

Figure 6: Downtime of the accelerator over the years. Since the installation of the new LLRF the downtime due to the cyclotron has been reduced. In 2017, only half of the cyclotron downtime was due to problems with the RF.

ISBN: 978-3-95450-205-9 doi:10.18429/JACoW-Cyclotrons2019-TUP007

CONCLUSION

The preparations and installation went without any major problems and could be carried out during the maintenance periods or parallel to operation. Commissioning was faster than planned, with the installed patch panels and previous testing of the motion control modules proving essential. The RF systems are now more stable and provide a better overview of their condition. Support from iThemba LABS for LLRF replacement modules as well as for problems or changes to the EPICS software is essential. More than 400 patients have been treated since the commissioning with the new LLRF.

REFERENCES

[1] K. H. Maier, "Status of the VICKSI project", in *Proc. Cyclotrons'75*, Zurich, Switzerland, Aug. 1975, paper A-08, pp. 68-75.

[2] W. Duckitt, J. Abraham, J. L. Conradie, M. J. Van Niekerk, and T. R. Niesler, "A new digital low-level RF control system for cyclotrons", in *Proc. Cyclotrons'16*, Zurich, Switzerland, Sep. 2016, pp. 258-262. doi:10.18429/JACoW-Cyclotrons2016-WEB01

[3] W. Duckitt, "A digital low-level radio frequency control system for the particle accelerators at iThemba LABS", Ph.D. thesis, Stellenbosch University, Stellenbosch, South Africa, 2018.

ISBN: 978-3-95450-205-9 doi:10.18429/JACoW-Cyclotrons2019-TUP008

THE CYCLOTRON TR-FLEX AT THE CENTER FOR RADIOPHARMACEUTICAL CANCER RESEARCH AT HELMHOLTZ-ZENTRUM DRESDEN-ROSSENDORF

M. Kreller*, T. Knieß, Helmholtz-Zentrum Dresden-Rossendorf e.V. ,
Institute of Radiopharmaceutical Cancer Research, Bautzner Landstraße 400, Dresden, Germany
S. Preusche, Helmholtz-Zentrum Dresden-Rossendorf e.V. ,
Central Technical Services Department, Bautzner Landstraße 400, Dresden, Germany

Abstract

The new Center for Radiopharmaceutical Cancer Research was established at Helmholtz-Zentrum Dresden-Rossendorf e.V. to centralize the main units: a high current proton cyclotron, a radiopharmaceutical production – GMP unit including quality control, laboratories for PET-radiochemistry, chemical laboratories, laboratories for biochemical investigation, laboratories for small animal imaging and an animal keeping facility.

The cyclotron TR-Flex was put into operation in 2017 and it is equipped with two extraction ports. Both are movable to adjust the energy of the extracted proton beam in the range from 15 MeV up to 30 MeV. One extraction port is coupled with a combination magnet and two beam lines. A [^{123}I]-iodine gas target station is installed at the first beam line and a four-port target selector is installed at the end of beamline two. The second extraction port has no beamlines but is equipped with a four-port target selector. Two [^{18}F]- water targets, one [^{18}F]F_2 gas target, one [^{11}C]CH_4 gas target, one [^{11}C]CO_2 gas target, one 30° and one 90° solid state target are mounted on two target selectors.

In our contribution we report our experience of the new cyclotron TR-Flex during the first two operation years. Typical beam parameters, saturation yields and the reliability of the TR-Flex are presented. Furthermore we describe the new home-built Radionuclide Distribution System.

INTRODUCTION

Radiopharmaceutical research and the production of radiopharmaceuticals have a long history at the Research Center in Rossendorf. The production of radiopharmaceuticals started in 1958. The basis were a nuclear research reactor (10 MW) and the Cyclotron U-120 (Leningrad). A broad scale of radiolabeled products based on ^{14}C, ^{131}I, ^{123}I, ^{32}P, ^{75}Se, ^{67}Ga, ^{85}Sr, ^{111}In, ^{211}At and fission radionuclides such as ^{90}Sr/ ^{90}Y, ^{99}Mo were provided. Furthermore, the Research Center was the second producer of fission ^{99}Mo/ ^{99m}Tc-generators with an amount of 20 TBq ^{99}Mo per week. A wide-spread research to ^{99m}Tc coordination chemistry and radiopharmacology and ^{99m}Tc-kits was established including a wide range of labelled compounds for human use.

The Cyclotron U-120, Leningrad (1958 - 1999) was used for routine production of ^{67}Ga, ^{85}Sr, ^{111}In, ^{123}I, ^{211}At and the corresponding labelled compounds for human use. The start for research for PET was in 1982. The first [^{18}F]FDG (electrophil) production was in 1983.

1997 marked the official opening of Rossendorf PET-Center for research and application including the manufacturing authorization for PET drugs. The marketing authorization includes [^{18}F]FDG (GlucoRos), [^{18}F]Fluoride (NaFRos) and [^{18}F]FDOPA (DOPARos). Furthermore, there are 15 different radiopharmaceuticals available on demand.

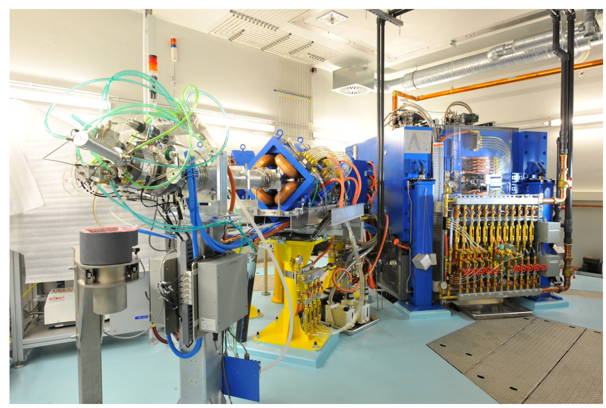

Figure 1: The TR-Flex cyclotron at the HZDR. The beamline 1B with a 4-port target selector is shown in the foreground. The second 4-port target selector is at the opposite side of the Cyclotron. Picture: HZDR/Frank Bierstedt

The former cyclotron of the HZDR, an IBA Cyclone 18/9, was put in operation in autumn 1996. After 18 years of routine operation comprehensive upgrades would have to be necessary to fulfill the new demands in the second decade of the 21th century. On the other hand HZDR could not forego the RN production with the Cyclone 18/9 during the ZRT building phase. Thus, HZDR decided to install a new cyclotron with higher ion energy and higher ion bean current.

THE TR-FLEX CYCLOTRON

The TR-Flex cyclotron, shown in Fig. 1, from Advanced Cyclotron Systems Inc. (ACSI, Canada) [1] was put into operation in 2017. The cyclotron is equipped with two extraction ports. Both extraction foils are radially movable to adjust the energy of the extracted proton beam in the range of 15 MeV up to 30 MeV. Two beamlines are connected behind a combo magnet on the extraction port 1. Two 4 port

* m.kreller@hzdr.de

ISBN: 978-3-95450-205-9 doi:10.18429/JACoW-Cyclotrons2019-TUP008

target selectors are installed at one beamline and the second extraction port. The following targets are installed:

- two [^{18}F]F^{-} water targets and one [^{18}F]F_2 gas target
- one [^{11}C]CH_4 gas target and one [^{11}C]CO_2 gas target
- one 30° and one 90° solid state target
- one [^{123}I]I^{-} gas target

ION ENERGY

The cyclotron is designed to extract ions in the range of 18 MeV up to 30 MeV. But it is of real interest to extract ions at lower ion energies. The reaction cross section for a lot of radionuclides are higher and the impurities are lower for lower ion energies. Hence, experiments were done to determine the lowest possible ion extraction energy. Autoradiography measurements at ion beam energies of 14 MeV and 30 MeV were executed to determine the profile of the proton beam hitting the solid target installed at the beamline target selector. The Autoradiographic measurement of a 30 µA beam current with an energy of 30 MeV is shown in Fig. 2.

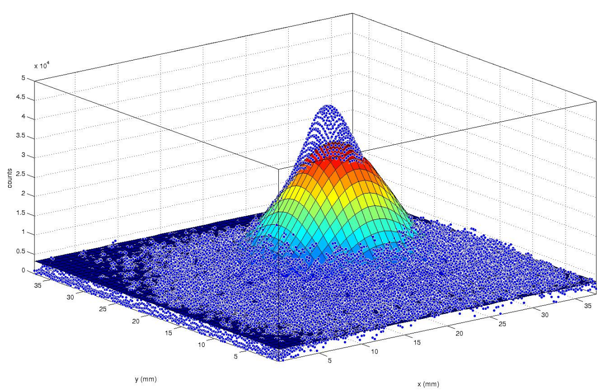

Figure 2: Autoradiographic measurement of an irradiated gold disk at the 90°-solid state target, beam energy 30 MeV. (blue dots: measured values, colored surface: fitted curve)

A two dimensional Gaussian function was fitted to the measured profile to determine the beam size in x- and y-direction.

$$I(x,y) = I_0 \cdot e^{-\left(\frac{(x-\mu_x)^2}{2\cdot\sigma_x^2}+\frac{(y-\mu_y)^2}{2\cdot\sigma_y^2}\right)} \quad (1)$$

We measured a pretty well shaped beam profile for lower and higher energies at the target selector at the end of the beamline. The FWHM value in x- and y-direction was for low and high energies in the range of 13(1) mm. We extract the beam at an energy above 15 MeV because of a higher beam loss in the beamline for lower energies.

ENERGY DEGRADER

A 700 µm thick Al-disk was installed at the 90° solid state target instead of the vacuum foil to reduce the energy below 15 MeV. SRIM-calculations shows an energy loss within the Al-disk in in the range of 3.0 MeV to 4.5 MeV depending on the initial beam energy.

The Al-disk is manufactured produced from one piece and a water cooling is installed. A schematic view of the energy degrader is shown in Fig. 3. It is an Al-flange with a diameter of 40 mm and a beam window with a diameter of 16 mm with a thickness of 700 µm. The flange is directly water cooled. FEM simulations show an maximum temperature of 500 °C in the center of the beam window at an ion current of 80 µA.

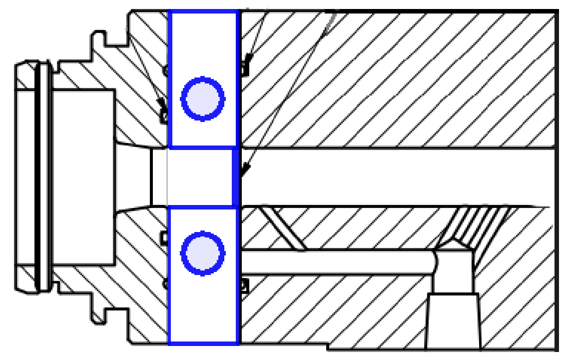

Figure 3: The energy degrader (blue part) is installed instead of the vacuum foil in front of the solid target system.

The energy degrader was tested for the ^{64}Cu production using 13 MeV protons for the ^{64}Ni(p,n)^{64}Cu reaction [2, 3] were carried out and evaluated. Typical irradiation parameters for the copper production are an ion current of 70 µA and an irradiation time of 90 min. The molar activity of the ^{64}Cu is about 1 TBq µmol^{-1}. We achieved an activity of 18 GBq that is corresponding to a saturation yield of 4.0 GBq µA^{-1} strongly depending on the ^{64}Ni mass on the gold disk.

PRODUCED RADIONUCLIDES

The following radionuclides are produced reliably with the TR-Flex since the beginning of 2018. Typical production parameters of the new TR-Flex and the achieved activities are presented in Table 1.

Table 1: Typical Production Parameters of the TR-Flex

Isotope	Chem. Form	Typ. Current	Irr. Time	Actitvity
^{18}F	F^-	80 µA	20 min	95 GBq
^{18}F	F_-	105 µA	70 min	355 GBq
^{18}F	F_2	30 µA	60 min	20 GBq
^{11}C	CO_2	40 µA	35 min	155 GBq
^{11}C	CH_4	30 µA	40 min	55 GBq
^{64}Cu	Cu	70 µA	90 min	16 GBq
^{123}I	I^-	150 µA	360 min	350 GBq

ISBN: 978-3-95450-205-9 doi:10.18429/JACoW-Cyclotrons2019-TUP008

THE RADIONUCLIDE DISTRIBUTION SYSTEM

A new Radionuclide Distribution System was developed and installed by the Department of Research Technology at HZDR. The liquid and gas targets are unloaded through capillaries to a central hot cell. Henceforward the radionuclides can be distributed automatically to the 25 hot cells in the whole Center for Radiopharmaceutical Cancer Research.

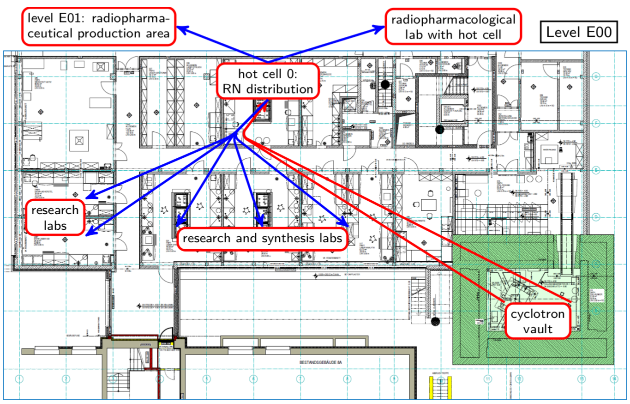

Figure 4: Schematic view of the radionuclide distribution in the building. red lines: unload the targets to the hot cell “0”, blue lines: radionuclide distribution within the ZRT building.

The system controls the target unload and the transport to the hot cells within the whole building. The gas is transported by stainless steel capillaries with an inner diameter of 1.4 mm and the liquid is transported by PTFE capillaries with an inner diameter of 0.8 mm. The transport distances can reach up to 100 m. The supervision of the relevant parameters and interlock system for the radiation protection (shielding of the hot cells, correct transportation path, correct ventilation system) and generation of the target unload clearance signal sent to the cyclotron is done automatically by the Radionuclide Distribution System.

Normally this is an automatic transport but also an manual operation and a so-called emergency mode, that allows to abrogate the interlock system, is possible. A schematic view of the distribution is shown in Fig. 4. Solid targets are unloaded to a transport container on a hand cart. An unload clearance signal is generated when the hand cart is docked at the solid target system and the cooling water blow out as well as the unload process is done by the control system of the cyclotron. Also the iodine target is unloaded into a transport container. The container is docked the a hot cell and the target is washed out through PTFE capillaries into the container.

CONCLUSIONS

In our contribution we introduced the new cyclotron TR-Flex including first results of the radionuclide production and beam characterization measurements. We presented the energy degrader to reduce the energy of the solid targt system. The Al-flange was dismounted and checked after more than 40 production runs with a total amount of about 3800 µA h deposited charge. A very slight plastic deformation was seen. The integration of the Al-flange was successful. The production of further radionuclides will be started in the future step by step.

REFERENCES

[1] R. Watt, W. Gyles, and A. Zyuzin, “Building on TR-24 success: Advanced cyclotron systems Inc. launches a new cyclotron model”, *J. Radioanal. Nucl. Chem*, vol. 305, pp. 93–98, Jul. 2015. doi:10.1007/s10967-015-4048-y

[2] D. W. McCarthy, R. E. Shefer, R. E. Klinkowstein, L. A. Bass, W. H. Margeneau, C. S. Cutler, C .J. Anderson, and M. J. Welch, “Efficient production of high specific activity ^{64}Cu using a biomedical cyclotron”, *Nucl. Med. Biol.*, vol. 24, pp. 35–43, Jan. 1997. doi:10.1016/S0969-8051(96)00157-6

[3] S. Thieme, M. Walther, H.-J. Pietzsch, J. Henniger, S. Preusche, P. Maeding, and J. Steinbach, “Module-assisted preparation of ^{64}Cu with high specific activity”, *Applied Radiation and Isotopes*, vol. 70, pp. 602–608, Apr. 2012. doi:10.1016/j.apradiso.2012.01.019

ISBN: 978-3-95450-205-9 doi:10.18429/JACoW-Cyclotrons2019-TUP009

CYCLOTRON CAVITY POLLUTION RECOVERY

J. Dabin§, P. Cailliau, E. Forton, Ion Beam Applications, B-1348 Louvain-la-Neuve, Belgium
B. Adant, K. Ellis, J. Mandrillon, P. Verbruggen, T. Ponter
Ion Beam Applications, B-1348 Louvain-la-Neuve, Belgium

Abstract

In a cyclotron, RF cavities are usually among the most reliable subsystems, provided minimal care and maintenance. Nevertheless, several parameters may affect cavity performance after several years of operation. To name a few typical causes of degradation: decreasing vacuum quality, various gas loads or gas qualities triggering adverse effects, deposition of highly emissive material on the cavity due to overheating of components like pass-through connectors, accidental use of chemicals or not-suited greases. The cavity status can be monitored but, in the worst cases, the RF tuning may become difficult and it is important to apply methods in order to recover a better cavity Q-factor. In this paper, cases of cavity pollution will be shown, their potential root causes discussed and some recovery methods described.

INTRODUCTION

RF Cavities, Equivalent Circuit and Power Characterization

RF cavities are a key subsystem of cyclotrons. They create the necessary electric field required to accelerate charged particles. The RF system of a cyclotron can be seen as a RLC circuit that resonates at the pulsation $\omega_{res} = \frac{1}{\sqrt{LC}}$.

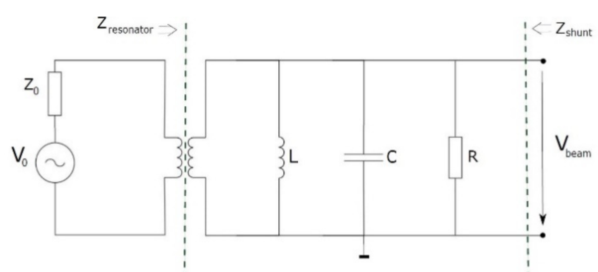

Figure 1: RLC equivalent circuit of a RF system. Adapted from F. Caspers [1].

The inductor and capacitor represent a lossless resonator, while the resistor characterizes the losses of the circuit. Equation (1) gives the impedance seen by the beam, called the shunt impedance, and at resonance it is equal to the ohmic resistor.

$$Z(\omega) = \frac{1}{\frac{1}{R}+j\omega C+\frac{1}{j\omega L}} \text{ and } Z(\omega_{res}) = R \quad . \tag{1}$$

The average dissipated power is defined as the power emitted by Joule losses. Therefore, for a constant accelerating voltage, the higher the shunt impedance, the lower the dissipated power.

$$P = \frac{V_{max}^2}{2R} \quad . \tag{2}$$

The challenge faced by cyclotron users is therefore the following: tune the system to work at resonance and limit the power dissipated by the cavities by maximizing the shunt impedance. In order to understand the parameters involved in this challenge, we need to introduce the cavity scaling laws given by Eqs. (3) and (4) and the skin depth depicting the surface thickness where most of the RF current flows (8):

$$\frac{R}{Q} = const \quad , \tag{3}$$

$$Q * \frac{\delta}{\lambda} = const \quad , \tag{4}$$

$$\delta = \sqrt{\frac{2}{\omega\sigma\mu}} \quad , \tag{5}$$

where Q is the quality factor of the RF system, $\frac{R}{Q}$ is called the characteristic or geometric impedance, δ is the skin depth, σ is the electric conductivity and μ is the magnetic permeability.

From these relationships, we can conclude that if the skin depth of the cavity increases (by decreasing the conductivity at the same resonance frequency) the Q factor must decrease, and so does the shunt impedance. The power dissipated rises, for a set voltage.

This phenomenon can be also understood by introducing the surface resistance of the RF cavity:

$$R_{surf} = \frac{1}{\sigma\delta} = \sqrt{\frac{\omega\mu}{2\sigma}} \quad . \tag{6}$$

And the power dissipated in the cavity walls due to ohmic heating is given by [2]:

$$P = \frac{1}{2} R_{surf} \int |H|^2 dS \quad , \tag{7}$$

where H is the magnetic field [A/m] induced by the RF electric field.

Increasing the skin depth (by decreasing the conductivity at the same resonance frequency) increases the surface resistance seen by the current and therefore also increases the power dissipated. The shunt impedance and the surface resistance behave thus inversely.

In the equivalent RLC model described in Fig. 1, R is the resistor across which the voltage driving the beam is generated. It represents the losses of the resonator for that given voltage. The surface resistance describes the losses due to the ohmic heating as well, but from an electric and magnetic field point of view. The oscillating electric field creates in turn an oscillating magnetic field, inducing cur-

§ john.dabin@iba-group.com

ISBN: 978-3-95450-205-9 doi:10.18429/JACoW-Cyclotrons2019-TUP009

rent that shapes the total current to flow mainly on the surface of the cavity (skin effect). For a given magnetic field, the higher the surface resistance, the higher the ohmic losses.

Multipactor and Secondary Electron Emission

Multipactor refers to RF discharges occurring inside particle accelerators. Secondary electron emission resulting from electronic bombardment of an emissive surface, coupled to a RF field, leads to a sinusoidal electron avalanche phenomenon. When that happens, the RF load to achieve beam performances becomes so high that running the RF can become impossible.

It was shown by Yves Jongen [3] that the essential conditions for multipactor to happen can be met in the C230 cyclotron (gap between dee and valley, voltage, frequency, electrons starting phase).

Another primordial parameter for multipactor is the secondary emission yield (SEY) of a surface, which represents the number of secondary electrons emitted per incident primary electron. For multipactor to happen, the SEY needs to be equal or superior to one.

$$SEY = \frac{I_s}{I_p} \quad . \tag{8}$$

POISONING OF RF CAVITIES

A recurring problem observed over time on multiple IBA sites consists in a sudden and increasing change in the forward power fed to the RF cavities, becoming more and more problematic to handle over time, to the point where the RF drops and extracting beam must pause until RF is resumed. The power dissipation seems not to be localized, but rather spread over the 4 dees and cavities. While a typical power lies around 50 kW, when this issue arises the power can increase by 20 or 30 kW. Observations have revealed typical and recurring traces on all cavities suffering that kind of issue.

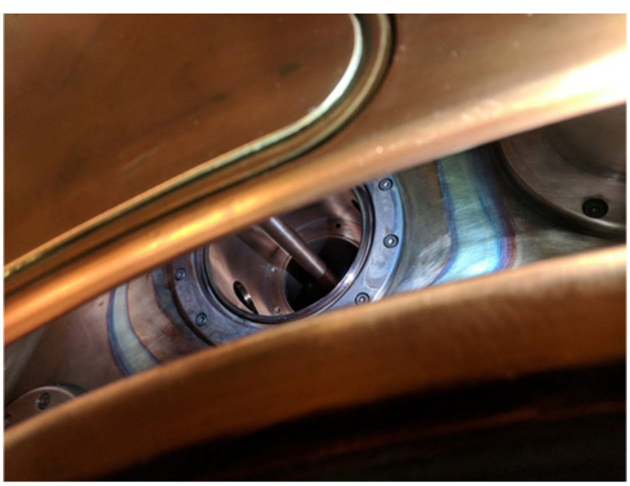

Figure 2: Typical poisoning traces inside RF cavities.

A common symptom can be observed through measuring the shunt impedance of the cavities: the shunt impedance drops and no longer stays constant with the applied cavity RF voltage (the observed change further increasing over time). The drop is easily understandable as the shunt impedance is inversely proportional to the power. The variability may lead one to believe that a multipactor phenomenon is occurring with a different intensity in function of the amplitude of the RF voltage, meaning that the power is not evolving as the square root of the dee voltage anymore because the intensity of the multipactor leads to dissipating more or less heat.

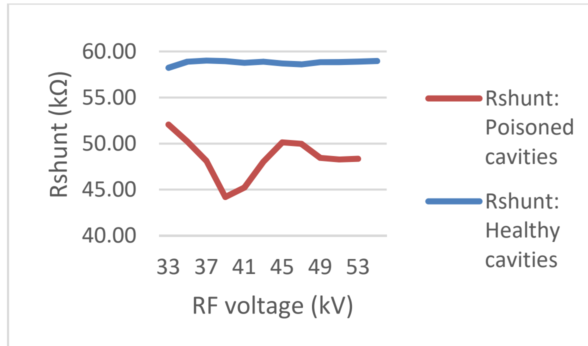

Figure 3: Rshunt of a healthy RF system vs Rshunt of a poisoned RF system.

ANALYSIS & HYPOTHESIS

The problem was qualified as “poisoning”, or sometimes “pollution” of the cavities because in every case, an external contaminant was found in the RF system. Most of the time, a strong correlation between the oxygen partial pressure and the increase in forward power was found. In some other cases, water, cadmium or silicon oxide was found on the cavities.

Oxygen Poisoning

Oxygen inside a cyclotron can originate from different sources: a leak with the atmosphere, a water leak or from the oxygen sprayed on the extraction electrostatic deflector.

When oxygen poisoning occurs, traces of copper oxide are most often found on the RF cavities. It is therefore believed that an oxygen plasma is created because of the RF multipactor: the electrons oscillating between the dees and the valleys hit and ionize oxygen molecules, and the free radicals recombine with the ionized surface of the copper.

It was shown that copper oxide exhibits a higher SEY than pure copper. While the SEY of copper lies around 1.3, the secondary emission yield of copper oxide can exceed 2 [4]. This increase in SEY leads to a more intense multipactor phenomenon, and therefore more power is dissipated inside the RF cavities. Furthermore, this phenomenon is self-maintaining / self-enhancing as the increase in multipactor will induce more oxygen ionization, and therefore a larger production of copper oxide. The cycle continues and the situation further degrades.

ISBN: 978-3-95450-205-9 doi:10.18429/JACoW-Cyclotrons2019-TUP009

Silicon Oxide Poisoning

Silicon-based greases are to be prohibited inside cyclotrons. Indeed, silicon oxide also exhibits a high SEY, leading once again to enhanced multipactor. Instead, if lubrication can't be avoided, it is encouraged to use ODP oil, as it can have a beneficial effect on the secondary emission yield of the cavities as explained in the next section.

Water Poisoning

It was shown by Baglin et al. [4] that deposition/adsorption of water on a copper surface also increases the SEY. This can happen when the cooling lines of the dees and cavities suffer from a leak. It can be easily diagnosed by observing the vacuum level: a water leak most often describes successive vacuum peaks, as the water freezes under vacuum, sealing the leak source, until it vaporizes with sufficient heating.

Cadmium Poisoning

The brazing of a few components of IBA RF cavities is partially composed of cadmium. This is for instance the case for the capacitive cavity tuner flaps, connecting the capacitor to the RF cavity, which are constantly solicitated in order to adapt the resonance frequency of the system. As the flaps move, defects in the brazing sometimes occur. This leads to an increase of temperature due to the induced RF currents in that area, leading in turn and in some extremely rare cases to outgassing of the brazing and deposition of cadmium inside the RF cavities.

It was shown by Walker et al. [5] that the cadmium secondary emission yield is lower than copper (maximum SEY around 1.1). This means that the increase in RF power is not due to a multipactor increase. Moreover, most of the traces of cadmium were found on the top of the dees and side of the cavities, where the multipactor is less likely to occur. Therefore, another phenomenon must be responsible for the power dissipation increase.

Figure 4: Cadmium deposition on RF system after outgassing of the mobile capacitor brazing.

Because cadmium has a lower conductivity than copper (around 5 times smaller), it can be shown that the skin depth at 106 MHz will double its thickness (from 6.3 µm for copper, to 13.2 µm for cadmium). As this depth is within the probable thickness of the cadmium layers deposited on the cavity surface, we can assume that all the current will flow into this layer. The surface resistance of a cadmium layer with this skin depth is therefore twice the one of copper, at the same frequency. As shown by Eq. (7), the local power dissipation could double if all the cavity surface was plated or recovered with cadmium.

This hypothesis is valid only for materials with electric conductivity and magnetic permeability in the range of e.g. copper and cadmium. Indeed, as long as the skin depth is in the range of the layer deposited on the surface, we can consider that the surface resistance will be solely influenced by the poisoning material. For copper oxide, the behaviour is different: the physical properties of the cavity surface are modified as its structure gets oxidized. A. Ogwu et al. [6] have shown that for CuO and Cu_2O formed with RF power, the resistivity lies around 25 Ohm.cm, which translates to a conductivity in the range of 10^{-4} S/m, while it is in the range of 10^{+7} S/m for copper and cadmium. The resulting theoretical skin depth is extremely large (5 meters), showing that the copper oxide behaves as an insulator. Therefore, the current will mainly flow in the copper bulk and not the oxidized surface. As a result, the power dissipation is not impacted by the surface resistance, but rather by the previously discussed increase of SEY.

PREVENTIVE ACTIONS & RECOVERY METHODS

Preventive Actions

Decreasing the O_2 Load Any cyclotron operator should minimize the O_2 load of the accelerator by reducing the partial pressure of O_2 willingly injected in the cyclotron to avoid some poisoning factors.

Leak Checking & Fixing Even minor vacuum leaks that have little impact on the cyclotron base vacuum are potential pollution factors. A good practice is therefore to make sure that sensitive locations are regularly checked. Cooling pipes, for instance, are first-hand potential culprits and should be checked, i.e. by injecting pressurized air and monitoring the vacuum level. In case of pollution, the very first measure to be taken is to diagnose, localize and repair potential leaks.

Recovery Methods

Once vacuum has been validated, it is necessary to evacuate the contaminants from the system. In order to do so, different recovery methods exist, with or without opening the cyclotron. Recovering with a closed cyclotron takes time, usually a few weeks to a month, and hence require patience combined with rigor. Other methods require to open the cyclotron; they have a higher impact on system uptime but are sometimes much more effective and/or simply mandatory.

High Vacuum and ODP Oil Effect In order to flush the system from its contaminants, it is necessary to allow time for the system to be under high vacuum: the hydrogen

ISBN: 978-3-95450-205-9 doi:10.18429/JACoW-Cyclotrons2019-TUP009

and oxygen load should be stopped for at least two to four hours each night in order to let the vacuum system pump to its maximum abilities. If the contaminant has been adsorbed by the surface, it can be useful to heat the system in order to help its desorption.

The secondary emission yield will slowly drop, and it is believed that this can be helped and enhanced with the natural deposition of ODP oil in the RF system. When pumping with oil diffusion pumps, the vaporized hydrocarbon oil often finds its way out of the pump, and deposits itself on the dees and in the valleys, lowering the SEY.

H_2 Bake If copper oxide has developed in the RF system, high vacuum is not sufficient to get rid of it. So called "H_2 bakes" are performed by flooding the cyclotron with hydrogen (up to a global pressure approaching the 10^{-4} mbar) and running high power RF (60 to 70 kW) in order to induce heating, catalysing the reduction reaction. The reducing power of the hydrogen helps to unravel the copper oxide molecules, reducing them to solid metallic copper and water vapor, which is then pumped out of the machine. It was shown by Kim et al. [7] that temperature and time are intricated for the reduction process of the two types of copper oxides: the higher the temperature, the faster the reduction (CuO reduces to metallic Cu slightly quicker than Cu_2O).

$$CuO(solid) + H_2(gas) \rightarrow Cu(solid) + H_2O(gas) \quad (9)$$

$$Cu_2O(solid) + H_2(gas) \rightarrow 2Cu(solid) + H_2O(gas) \quad (10)$$

For temperatures below 300°C, one can observe an induction period before the start of the reduction process (during this induction period, the reduction takes place at a much slower pace than afterwards). This induction period gets larger with the decrease of temperature (around 60 min for a temperature of 230 °C, around 100 min at 200 °C). Therefore, the recovery process for RF systems takes time and patience; when performing H_2 bakes a few hours per night, sites usually see lasting effects after several weeks.

Pulse Conditioning During "pulse conditioning", RF is pulsed inside the cavities, leading to a behaviour resembling to the charge and the discharge of a capacitor. This induces outgassing of the surface of the cavities, purging it from its contaminants. This can also be coupled with a high H_2 load in order to induce the reduction of the copper oxide (the O_2 gas load being once again totally shut off during the conditioning).

Simultaneously, it is possible to sweep the current of the main coil, modifying the magnetic field seen by the RF plasma induced, and modifying the trajectories of its particles. It is believed that this method allows a real sweep of the cavities surfaces by this plasma, however no simulation or systematic studies of the results have yet been done, nor any systematic comparison to a simple H_2 bake (without RF pulsing and magnetic sweeping).

Performing this method should be avoided if the presence of any leak of O_2 is still suspected. Indeed, the plasma induced with oxygen would have an adverse effect, as described in the section about oxygen poisoning.

Mechanical Cleaning In some cases, the poisoning is too intense for any conditioning methods described hereabove to be efficient. In some other cases, the situation is not viable for the cyclotron users as the symptoms are too painful to pursue the activity (i.e. patient treatment) and opening the cyclotron and cleaning the RF cavities becomes necessary. In order to remove the contaminants of the surface, the dees must be dismantled from the cavities. In some extreme case, the cavities should be removed if the back is poisoned as well. One needs to use abrasive hand pads to remove the contaminated layers over the copper. To ensure the rest of the machine is not polluted with the dust, the cyclotron subsystems such as deflectors, poles, central region etc are protected with protective rugs or removed. The dust is then vacuumed out of the cyclotron, and all the cavities and dees surfaces are cleaned with isopropyl alcohol.

Chemical Cleaning IBA recently experimented chemical cleaning on a site facing cadmium poisoning. The purpose was to avoid etching the surface with any abrasive pads, but rather by using a mild hydrochloric acid solution (mass diluted to 15%) that would remove the cadmium from the copper surfaces, and then rinsing the surfaces with bi-carbonated water in order to neutralize the acid action and protect the copper. The effectiveness of the method has been observed through a significant drop in RF forward power; initially at 60 kW for 50 kV of dee voltage, it dropped to 38 kW for the same dee voltage after the chemical cleaning. It has also been observed that the cavity copper turned slightly pink, with no impact on RF system operation.

REFERENCES

[1] F. Caspers and M. Wendt, "JUAS 2018 RF Engineering", Joint Universities Accelerator School, 2018.

[2] M. Sosa Guitron, "RF Cavities I", Mexican Particle Accelerator School, 2015.

[3] Y. Jongen, "Some reflections on multipactor", IBA internal document, 2008, unpublished.

[4] V. Baglin *et al.*, "The secondary electron yield of technical materials and its variation with surface treatments", in *Proc. 7th European Particle Accelerator Conf. (EPAC'00)*, Vienna, Austria, Jun. 2000, paper THXF102.

[5] C. G. H. Walker *et al.*, "The secondary electron emission yield for 24 solid elements excited by primary electrons in the range 250-5000 eV: A theory/experiment comparison", *The J. of Scanning Microscopies*, vol. 30, no. 5, pp. 365-380, 2008. doi:10.1002/sca.20124

[6] A. A. Ogwu *et al.*, "Electrical resistivity of copper oxide thin films prepared by reactive magnetron sputtering", *J. Achiev. in Mater. & Manuf. Eng.*, vol. 24, no. 1, pp. 172-177, 2007.

[7] J. Y. Kim *et al.*, "The reduction of CuO and Cu_2O with H_2: H embedding and kinetic effects in the formation of suboxides", *J. Am. Chem. Soc.*, vol. 125, no. pp. 10684-10692, 2003. doi:10.1021/ja0301673

ISBN: 978-3-95450-205-9 doi:10.18429/JACoW-Cyclotrons2019-TUP010

BUNCHER FOR THE OPTIMIZATION OF THE INJECTION OF A 70 MeV CYCLOTRON

P. Antonini*, A. Lombardi, M. Maggiore, L. Pranovi INFN/LNL, Legnaro, Italy
L. Buriola, Univ. degli Studi di Padova, Padova, Italy

Abstract

The design of an injection buncher for the 70 MeV cyclotron in use at Laboratori Nazionali di Legnaro (LNL) labs of INFN is under way. This buncher is to be installed between the ion source and the injection, to match the injected beam to the acceptance angle of the cyclotron's injection.

The planned design is a 3/2 beta-lambda double-gap driven with one or two harmonics of the 56 MHz cyclotron's frequency.

Remotely-driven variable capacitors will be used for easy tuning of the matching box from the control system.

The mechanical layout and simulations will be presented.

DESIGN OF THE BUNCHER

The injection buncher for the 70 MeV cyclotron at Laboratori Nazionali di Legnaro (LNL) of INFN is on design stage since a while, due to the commitment of the cyclotron's team to other activities. Nevertheless, slowly but constantly the design is being carried out by the team.

Relatively to older presentations [1, 2], the mechanical design is reconsidered and implemented in stability and accuracy. Beam dynamics simulations have been started, and the results are shown here. A chopper is also being considered.

GENERAL LAYOUT

The buncher will be installed along the injection line, between the multi-casp H^- ion source and the central region, in a dedicated vacuum box, placed between two focusing solenoids. The vacuum box can be isolated from the ion source and the cyclotron closing two gate valves, placed before and after the position of the buncher. The ion source provides up to 10 mA of DC current at 40 keV. The frequency of the buncher will of course be the same as the radiofrequency (RF) of the cyclotron, e.g. 56 MHz. The length of the buncher is calculated upon the $\frac{3}{2}\beta\lambda$, that is 73.995 mm, where $\beta\lambda$ is the distance covered by the ions accelerated by the source during one RF cycle.

Mechanical Layout

To improve the beam dynamics, the ground electrodes should be not too short. Two different configurations have been studied: a $\frac{3}{2}\beta\lambda$ buncher that has a longer drift tube, and a $\frac{1}{2}\beta\lambda$, that allows longer ground electrodes.

It is not possible to have long ground electrodes and long drift tube at the same time, due to the limited longitudinal dimensions: the two gate valves are placed at short distances before and after the position of the buncher.

The $\frac{3}{2}\beta\lambda$ and the $\frac{1}{2}\beta\lambda$ configurations have both been calculated and compared.

The $\frac{3}{2}\beta\lambda$ buncher This configuration allows the use of two separate electrodes for the injection of two different harmonics of the radiofrequency power.

Using the $\frac{3}{2}\beta\lambda$ configuration, and 5 mm between the RF electrode (the drift tube) and the ground (GND) electrodes, the length of the drift tube will be of 69 mm, and the total length of the whole buncher is 119 mm, with 20 mm of GND electrode's length.

To determine the inner diameter of the buncher we remind that it must be as small as possible, with respect to the diameter of the beam, to increase the transit time factor [3,4].

The dimensions of the $\frac{3}{2}\beta\lambda$ configuration are specified in Table 1.

Table 1: Dimensions of the $\frac{3}{2}\beta\lambda$ Buncher: Drift Tube and Ground (GND) Electrodes

Element	Length (mm)	Diameter (int/ext)
GND1	20	40/50
Gap1	5	-/-
Drift tube	69	40/50
Gap2	5	-/-
GND2	20	40/50

The rendering of the new design of the $\frac{3}{2}\beta\lambda$ can be seen in the following Fig. 1.

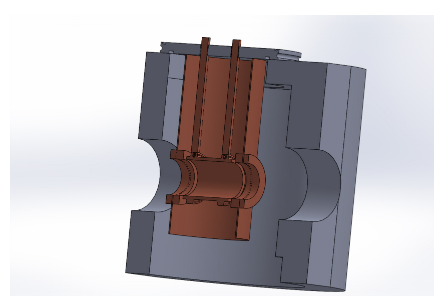

Figure 1: Rendering of the section of the buncher. The ground electrodes will be screwed with the external screen. Two electrodes are foreseen to feed the RF power to the buncher, at one ore two harmonics.

The Fig. 2 shows the calculation of the electric potential in the plane cutting the buncher along ts axis, where the Fig. 3 shows the detail of the potential along the axis of the drift tube.

* antonini@lnl.infn.it

ISBN: 978-3-95450-205-9 doi:10.18429/JACoW-Cyclotrons2019-TUP010

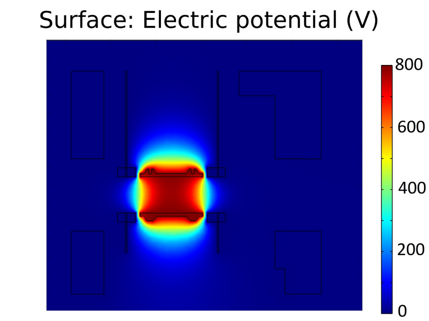

Figure 2: Simulation of the electric field for the $\frac{3}{2}\beta\lambda$ buncher. The beam travels horizontally.

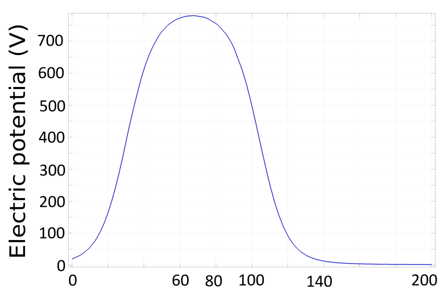

Figure 3: Simulation of the electric field along the axis for the $\frac{3}{2}\beta\lambda$ buncher.

With this configuration, the phase/energy plot can be seen in Fig. 4.

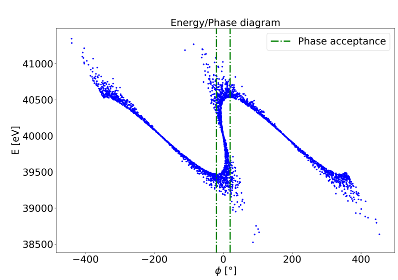

Figure 4: Phase/energy diagram for the $\frac{3}{2}\beta\lambda$ buncher.

The distribution of the particles inside the buncher is as in Fig. 5.

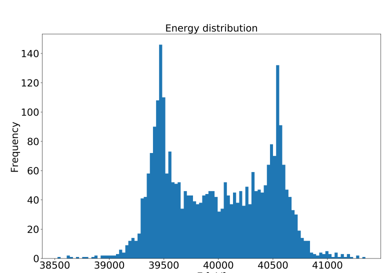

Figure 5: Distribution of the particles inside the bunches, for the $\frac{3}{2}\beta\lambda$ buncher.

The vertical (y) emittance was also calculated,and it is shown in Fig. 6.

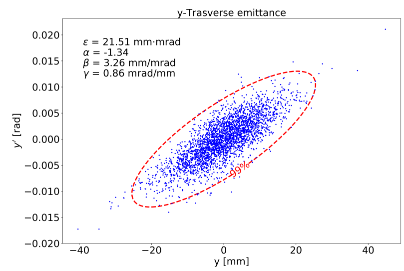

Figure 6: Vertical (y) emittance calculations the $\frac{3}{2}\beta\lambda$ buncher.

The horizontal (x) emittance was also calculated,and it is shown in Fig. 7.

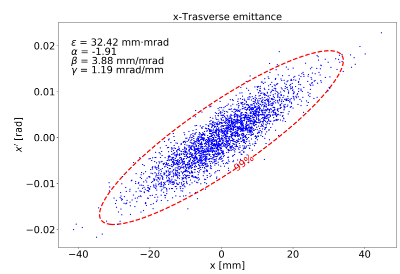

Figure 7: Horizontal (x) emittance calculations the $\frac{3}{2}\beta\lambda$ buncher.

The $\frac{1}{2}\beta\lambda$ buncher The rendering of the design of the $\frac{1}{2}\beta\lambda$ can be seen in the following Fig. 8.

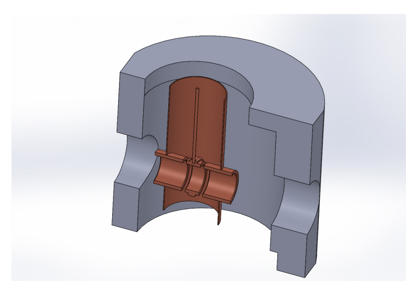

Figure 8: Rendering of the $\frac{1}{2}\beta\lambda$ buncher. The ground electrodes will be screwed with the external screen.

This second configuration has some advantages. The first one is that the ground electrodes can be longer, this improves the emittance of the injected beam. The second advantage is that the ground screen is at larger distance from the drift tube electrode: this decreases the capacitance of the buncher, allowing for a better matching impedance circuit between the RF amplifier and the buncher. Nevertheless, as can be seen in the electric potential simulations of Figs. 9 and 10, in the axis of the buncher the electric voltage is lower than in the border, paving the way for a worsening of the Transit Time Factor.

ISBN: 978-3-95450-205-9 doi:10.18429/JACoW-Cyclotrons2019-TUP010

The dimensions of the $\frac{1}{2}\beta\lambda$ configuration are specified in Table 2.

Table 2: Dimensions of the $\frac{1}{2}\beta\lambda$ Buncher: Drift Tube and Ground (GND) Electrodes

Element	Length (mm)	Diameter (int/ext)
GND1	40	40/50
Gap1	5	-/-
Drift tube	20	40/50
Gap2	5	-/-
GND2	40	40/50

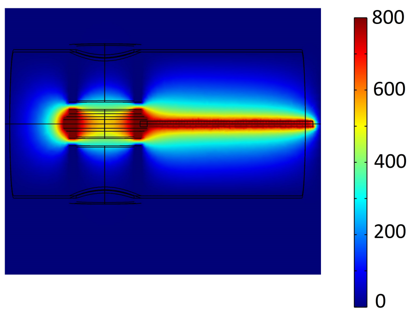

Figure 9: Simulation of the electric field for the $\frac{1}{2}\beta\lambda$ buncher. The beam travels vertically.

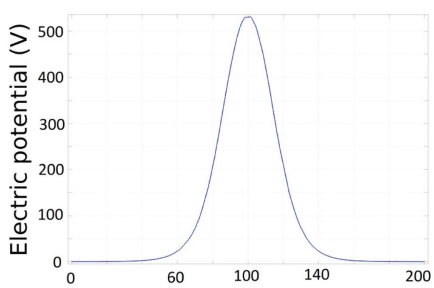

Figure 10: Simulation of the electric field on axis for the $\frac{1}{2}\beta\lambda$ buncher.

With this configuration, the phase/energy plot can be seen in Fig. 11.

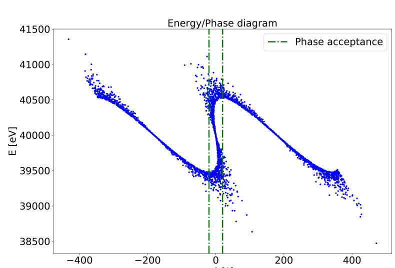

Figure 11: Phase/energy diagram for the $\frac{1}{2}\beta\lambda$ buncher.

The distribution of the particles inside the buncher is as in Fig. 12.

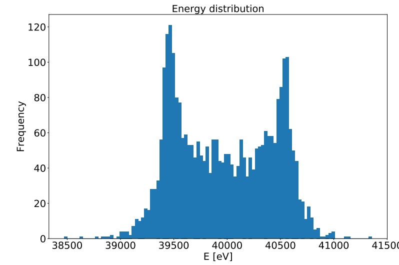

Figure 12: Distribution of the particles inside the bunches, for the $\frac{1}{2}\beta\lambda$ buncher.

The vertical (y) emittance was also calculated,and it is shown in Fig. 13.

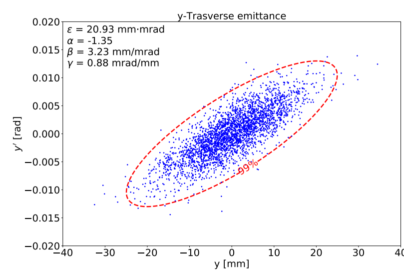

Figure 13: Vertical (y) emittance calculations the $\frac{1}{2}\beta\lambda$ buncher.

The horizontal (x) emittance was also calculated,and it is shown in Fig. 14.

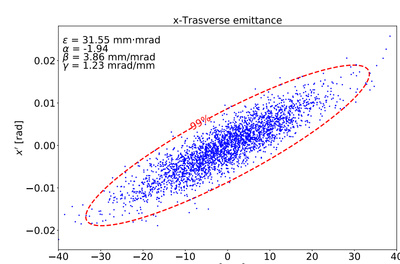

Figure 14: Horizontal (x) emittance calculations the $\frac{1}{2}\beta\lambda$ buncher.

COMPARISON OF THE TWO CONFIGURATIONS

The emittances of the two configurations are shown in the next Table 3. It can be seen that the two different drift tube lengths do not change much the emittance. For this reason the choice between the two configurations will be made based on mechanical stability or electronic circuitry.

ISBN: 978-3-95450-205-9 doi:10.18429/JACoW-Cyclotrons2019-TUP010

Table 3: Vertical (y) and Horizontal (x) Emittances (in mm·mrad) for the Two Different Configurations. It can be seen that there is no large difference.

Emittance	$\frac{3}{2}\beta\lambda$	$\frac{1}{2}\beta\lambda$
ϵ_y	21.5	20.9
ϵ_x	32.4	31.5

REFERENCES

[1] P. Antonini *et al.*, "Design of an injection buncher for the 70 MeV cyclotron", *European Cyclotron Progress Meeting (ECPM) 2017*, Legnaro, Italy.

[2] P. Antonini *et al.*, "Design of an injection buncher for the SPES cyclotron", *INFN-LNL Annual Report (2017)*, pp. 3-4.

[3] W. J. G. M. Kleeven, "Injection and extraction for cyclotrons", *CAS - CERN Accelerator School and KVI: Specialised CAS course on small accelerators*, 2005, pp. 271-296. doi:10.5170/CERN-2006-012.271

[4] W. J. G. M. Kleeven, W. Gelbart, and J. Sura, "Optical properties of a two-gap buncher", *Nucl. Instr. Methods Phys. Res., Sect. B*, vol. 64, pp. 367-370, Feb. 1992. doi:10.1016/0168-583X(92)95496-E

ISBN: 978-3-95450-205-9 doi:10.18429/JACoW-Cyclotrons2019-TUP011

UPGRADE OF THE CENTRAL REGION OF THE SUPERCONDUCTING CYCLOTRON AT INFN-LNS

G. D'Agostino*, L. Calabretta, D. Rifuggiato, INFN-LNS, 95123 Catania, Italy
W. Kleeven, IBA, B-1348 Louvain-la-Neuve, Belgium

Abstract

The Superconducting Cyclotron (CS) at INFN-LNS is regularly operated with beam power up to 100 W. The present efforts in upgrading the cyclotron are directed towards an increase of beam power up to 10 kW for ions with mass number A≤40 and energies between 15 and 70 AMeV by means of increase of beam intensity. Moreover, a beam energy resolution of 0.1% is requested by the NUMEN project at INFN-LNS. We plan to achieve high beam power by increasing the efficiency of the injection and extraction processes. The current extraction efficiency is lower than 60%. We expect to increase it to a value close to 100% by extracting the specific ion beams by stripping and no longer by electrostatic deflectors. A spiral inflector is used to inject onto the median plane the ion beams produced by the two ECR ion sources. Including the effect of a drift buncher placed in the axial injection line, the current injection efficiency is about 15%. The study of an upgraded CS central region is ongoing at INFN-LNS. First results of simulation study aimed to increase the injection efficiency are presented.

INTRODUCTION

The Superconducting Cyclotron at INFN-LNS in Catania, known as CS, has about 25 years track-record of accelerating ion beams to support the nuclear physics community of the laboratory. Furthermore, it is also used for the treatment of ocular melanoma by proton beam.

It is a multi-particle variable energy cyclotron with a wide operating diagram. The CS accelerates ions with charge-to-mass ratio Q/A in the interval 0.1 - 0.5. For any Q/A, the maximum energy per nucleon is determined by either the bending limit $E/A = 800 \cdot (Q/A)^2$ or the vertical focusing limit $E/A = 200 \cdot Q/A$.

The CS is very compact with a pole radius of 90 cm. The isochronous magnetic field in the range 2.2 – 4.8 T is produced by two superconducting main coils, three fully-saturated iron pole sectors and twenty trim coils wound around each hill [1]. Three RF-cavities provide the accelerating voltage for the beams and operate in the frequency range 15 - 48 MHz in harmonic mode 2. Ion beams, generated by two ECR ion sources, are axially injected.

The extraction system consists of two electrostatic deflectors placed on consecutive hills and eigth passive magnetic focusing channels [2]. The extraction by electrostatic deflectors limits the maximum beam intensity because of losses and induced heat-load on the septum of the first device. The current extraction efficiency is lower than 60% and the maximum beam power that the CS can deliver is about 100 W [3]. The constraint on the maximum beam intensity prevents to inject in the cyclotron high current, although the ion sources are able of high performance.

The cyclotron will be under an upgrade process in the near future to increase the beam intensity. High beam intensity is required by the NUMEN project at INFN-LNS [4]. It aims at accessing experimental-driven information on nuclear matrix elements involved in the half-life of neutrinoless double beta decay, by high-accuracy measurements of cross section of heavy ion induced double charge exchange reactions. The project requires mainly beams of carbon, oxygen and neon with intensity up to $10^{13} - 10^{14}$ pps. The required energies for these beams are in the range 15 - 70 AMeV, which corresponds to a beam power in the range 1 - 10 kW. Furthermore, a good beam energy resolution (~1/1000) is required.

In order to deliver high beam intensity, it is planned to increase the overall efficiency, including beam injection, acceleration and extraction processes.

The extraction by stripping for ions with $A \leq 40$ has been proposed. It will allow to inject into the cyclotron, accelerate and to extract beam current higher than the actual one. According to data in Ref. [5], for the ion beams and energies required by NUMEN, the percentage of fully-stripped ions after the stripping process is higher than 99%. Consequently, an extraction efficiency close to 100% is expected. The implementation of the stripping extraction is not trivial because it requires substantial changes in the cyclotron [6].

The improvement of the injection efficiency is another important aspect of the CS upgrade project to achieve the desired high beam intensity. The overall efficiency is strongly constrained by the NUMEN requirement on the energy spread. Therefore, the evaluation of the energy spread of the extracted beam is essential.

THE EXISTING CS CENTRAL REGION

During the first four years of operation, the CS worked as a booster of the 15 MV Tandem at INFN-LNS [7]. Since the year 2000, the machine works in stand-alone mode.

A spiral inflector is used for 90° bending of ion beams from the vertical direction into the cyclotron median plane. It has a bending radius A of 27 mm and the so-called tilt-parameter k' is zero. The electrode distance d is 6 mm and the aspect-ratio s/d is 2. The inflector is surrounded by a copper housing to isolate the device from the RF-fields driving the CS. A copper collimator with a circular aperture of 6 mm diameter is placed before the device entrance to protect the inflector electrodes from the ion hits.

The CS central region is composed of a set of electrodes attached to the dees and dummy-dees. Pillars crossing the

* dagostino@lns.infn.it

ISBN: 978-3-95450-205-9 doi:10.18429/JACoW-Cyclotrons2019-TUP011

median plane are placed on each electrode. The vertical gap between the accelerating electrodes in the CS centre is 19 mm. The CS central region operates in the so-called constant orbit mode [8] in order to be valid for the acceleration of all the ions within the operating diagram of the cyclotron [9]. This imposes the existence of a scaling rule for the voltage of the ion source, spiral inflector and dees, as compared to a reference case:

$$\frac{V}{\omega_0 \cdot B_0} = constant \qquad (1)$$

where V is the peak voltage of the dees, ω_0 the ion orbital frequency and B_0 the magnetic field in the cyclotron centre.

Figure 1 shows the Opera-3d [10] model of the existing spiral inflector and central region of the CS.

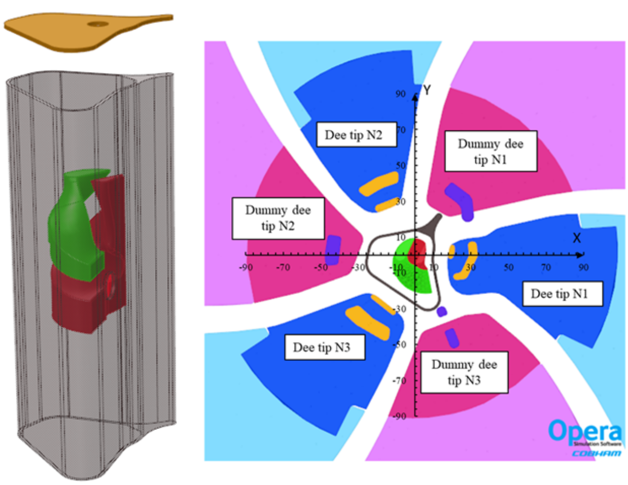

Figure 1: Opera-3d model of the existing spiral inflector (on the left) and central region (on the right) of the CS.

IMPROVEMENT OF THE TRANSMISSION IN THE CENTRAL REGION

The approach used can be divided in the following steps:

1) Choice of the reference ion. According to the scaling law given by Eq. (1), an ion that requires the highest dee and injection voltage has been selected within the operating diagram of the CS. Our choice is the ion $^{16}O^{8+}$ accelerated at the maximum energy of 100 AMeV.
2) Creation of an Opera-3d model of the cyclotron magnet and use it to create the isochronous field map for the chosen reference ion and a detailed 3D field map in and around the inflector volume as needed by the tracking code AOC.
3) Creation of an Opera-3d model of the cyclotron central region and use it to create a 3D potential map around the median plane and the inflector volume as needed by the tracking code AOC.
4) Study of the beam optics through the axial bore of the CS to find the best match with the optical properties of the CS axial bore. The transverse normalized beam emittance at the entrance of the cyclotron axial bore was defined equal to 1 π mm-mrad.
5) Evaluation of the RF phase acceptance for different angular positions of the whole inflector assembly with respect to the vertical direction to estimate the optimum orientation of the device with respect to the central region electrodes.
6) Evaluation of the present injection efficiency by beam tracking from the axial bore entrance, through the spiral inflector up to the central region exit of the CS.
7) Optimization of the position of the pillars to increase the clearance reserved to the ions for their escape from the central region.
8) Increase of the dee voltage to reduce the radial hits of the ions with the electrodes intersecting the median plane.

The injection efficiency is determined by the losses on the whole inflector assembly and on the central region electrodes. It has been evaluated considering three different models of the CS central region, that we named model I, II and III respectively [11]. The first model is the existing design and the other ones have been obtained from the existing design changing slightly the position of the pillars of 1-2 mm.

Figure 2 shows the differences between the models. Only the pillars, that have been moved, are shown. On the left, the differences between model I and II are shown and on the right the ones between model II and III.

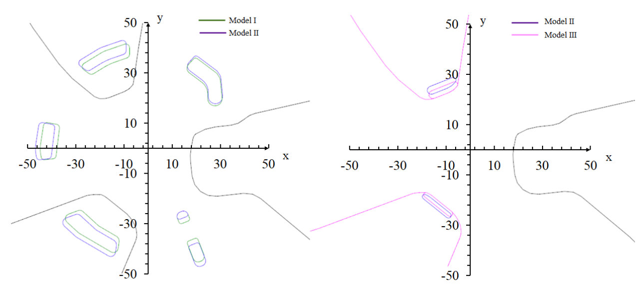

Figure 2: On the left differences between the models I and II and on the right the ones relative to the model II and III of the CS central region.

For each of the models of the CS central region, the injection efficiency has been evaluated for four values of the dee voltage: 86 kV (the nominal value for acceleration of the chosen reference ion), 90 kV, 95 kV and 100 kV.

Table 1 reports the values of the injection efficiency in percentage for the above-mentioned cases. It supposes particle RF-phases on a interval of 30° at the starting tracking position corresponding to the axial bore entrance.

Simulations show that, when the nominal dee voltage is applied to the existing electrodes of the central region, the ion losses are especially radial and concentrated on the pillars. The use of dee voltages higher than the nominal one has the effect to help a high number of ions to move away from the pillars reducing the hits, as shown in Fig. 3. When the model III and 100 kV dee voltage are considered, the increase of injection efficiency is really relevant and it is

ISBN: 978-3-95450-205-9 doi:10.18429/JACoW-Cyclotrons2019-TUP011

Table 1: Injection Efficiency in Percentage as Function of the Different Models of the CS Central Region and the Dee Voltage

	Dee voltage			
	86 kV	90 kV	95 kV	100 kV
Model I	29.7 %	39.2 %	43.5 %	41.1 %
Model II	25.0 %	38.1 %	47.3 %	52.5 %
Model III	35.6 %	43.2 %	50.5 %	53.0 %

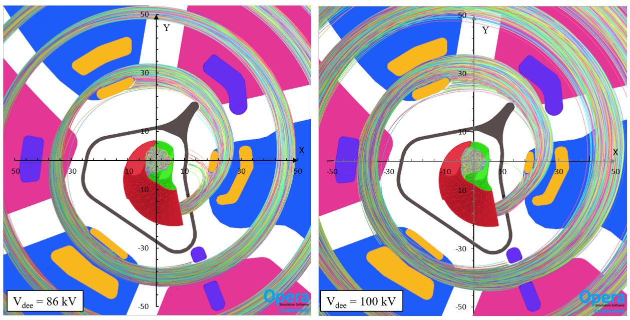

Figure 3: Beam particles in the existing CS central region, when the voltage applied to the dees is equal to 86 kV (on the left) and 100 kV (on the right).

almost 78% with respect to the present situation. Supposing to inject a DC beam into the CS and considering a buncher able to guarantee a buncher efficiency of 50% within 30° RF-phase width, the injection efficiency becomes close to 25% and therefore increases of a factor 1.7 with respect to the actual one of 15%.

The current maximum voltage applicable to the dees is about 82 kV. Although the simulations on the injection efficiency have been carried out for dee voltages higher than this value, the obtained results are valid for all the ion species accelerated at low and medium energies because they require a dee voltage less than or equal to this value, according to Eq. (1).

CONSIDERATIONS ON THE TOTAL EFFICIENCY AND BEAM ENERGY SPREAD AT THE EXTRACTION

The expected beam energy resolution at the extraction for all the ion beams to be extracted by stripping is about 0.3 - 0.4%, according to the analytical formula in Ref. [12]. Simulations have confirmed this value, that is higher than the NUMEN requirement of about a factor 4 [11].

Simulations of beam tracking starting at 120 mm from the CS centre up to the extraction system have been carried out for the evaluation of the beam energy spread at the extraction. Figure 4 shows the energy distribution at the extraction of a beam of 5000 particles with 10° RF phase width at the starting position. In order to reduce the energy spread of the extracted beams, an energy selection process is foreseen outside the CS. FRAISE, the new FRAgment In-flight SEparator at INFN-LNS, will be also used as a

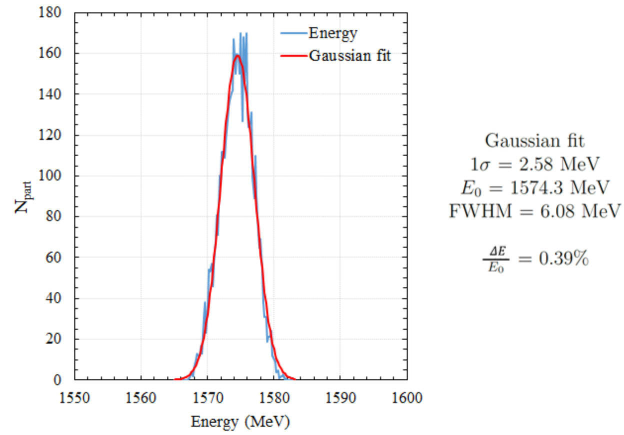

Figure 4: Beam energy distribution at the extraction of a sample of 5000 particles accelerated from 120 mm from the CS centre up to the extraction system.

beam energy selector [13]. This implies that only a portion of the accelerated beams could be transported to the NUMEN experimental hall. It is clear that the improvement of the injection efficiency, described in the previous section, can be a solution to avoid a relevant reduction of the total efficiency due to the beam energy selection process after the beam extraction.

Alternative solutions to the improvement of the beam energy resolution are under investigation at INFN-LNS. A solution could be the use of a wedged degrader, placed in the FRAISE beam line. It would allow to reduce the beam energy spread without significant loss of beam intensity. Other possible solutions could be the use of phase-slits installed within the CS, just outside the central region, for reducing the RF-phase width of the beam and the use of the existing harmonic coils installed at outer radii in the cyclotron to produce a first harmonic precession able to increase the separation between last turns at the stripper foil position. However, simulations have demonstrated that the energy gain per turn contributes only partially to the energy spread at the extraction and the main contribution to it is the large emittance injected in the central region of the LNS cyclotron. Also a good quality of the accelerated beam is necessary because an initial beam offset in the central region implies a further increase of the beam energy spread at the extraction. More details about all these aspects can be found in Ref. [11].

CONCLUSION

The project of the CS and the INFN-LNS facility upgrade (POTLNS PON Ricerca e innovazione 2014-2020) is funded by MIUR (Italian Ministry of Instruction, University and Research). The present study has allowed to establish a roadmap to be followed for the improvement of the CS performance.

ISBN: 978-3-95450-205-9 doi:10.18429/JACoW-Cyclotrons2019-TUP011

REFERENCES

[1] G. Bellomo and L. Serafini, "Design of the magnetic field for the Milan superconducting cyclotron", *INFN report*, INFN/TC-84/5, 1984.

[2] E. Fabrici and A. Salomone, "The extraction system for the Milan superconducting cyclotron", *INFN report*, INFN/TC-87/4, 1987.

[3] D. Rifuggiato *et al.*, "Variety of beam production at the INFN LNS superconducting cyclotron", in *Proc. 20th Int. Conf. on Cyclotrons and their Applications (Cyclotrons'13)*, Vancouver, Canada, Sep. 2013, paper MOPPT011, pp. 52–54.

[4] F. Cappuzzello *et al.*, "The NUMEN project: NUclear Matrix Elements for Neutrinoless double beta decay", *Eur. Phys. J. A*, vol. 54:72, May 2018. doi:10.1140/epja/i2018-12509-3

[5] K. Shima *et al.*, "Equilibrium charge fractions of ions of Z = 4 – 92 emerging from a carbon foil", *At. Data Nucl. Data Tables*, vol. 51, no. 2, pp. 173-241, 1992. doi:10.1016/0092-640X(92)90001-X

[6] L. Calabretta, A. Calanna, G. Cuttone, G. D'Agostino, D. Rifuggiato, and A. D. Russo, "Overview of the future upgrade of the INFN-LNS superconducting cyclotron", *Mod. Phys. Lett. A*, vol. 32, no. 17, p. 1740009, Apr. 2017. doi:10.1142/S0217732317400090

[7] D. Rifuggiato *et al.,* "First years of operation of the LNS superconducting cyclotron", in *Proc. 15th Int. Cyclotron Conf. and their Applications (Cyclotrons'98)*, Caen, France, Jun. 1998, paper I–03, pp. 599–602.

[8] G. Bellomo, "The central region for compact cyclotrons", in *Proc. Cyclotrons'89*, Berlin, Germany, 1989, paper F6–01, pp. 325–334.

[9] D. Rifuggiato and L. Calabretta, "Axial injection in the superconducting cyclotron", Internal Report INFN, Frascati, Italy, INFN/TC–00/01, 2000.

[10] http://operafea.com

[11] G. D'Agostino, "Orbit dynamics studies of injection, acceleration and extraction of high-intensity beams for the upgrade of the INFN-LNS Superconducting Cyclotron", Ph.D. dissertation, Phys. Dept., University of Catania, Catania, Italy, 2019.

[12] S. S. Tomic and E. V. Samsonov, "Analytical description of stripping foil extraction from isochronous cyclotrons", *Phys. Rev. E*, vol. 65, p. 036504, Feb. 2002. doi:10.1103/PhysRevE.65.036504

[13] A. D. Russo, L. Calabretta, G. Cardella, and P. Russotto, "Preliminary design of the new FRAgment In-flight SEparator (FRAISE)", *Nucl. Instrum. Methods Phys. Res., Sect. B*, Apr. 2019, in press. doi:10.1016/j.nimb.2019.04.037

ISBN: 978-3-95450-205-9 doi:10.18429/JACoW-Cyclotrons2019-TUP012

UPGRADE OF THE FAST NEUTRON BEAM VAULT AT iTHEMBA LABS TO A METROLOGY FACILITY

N. B. Ndlovu*, P. P. Maleka, F. D. Smit
Department of Subatomic Physics, iThemba LABS, Cape Town, South Africa
V. Lacoste, Institut de Radioprotection et de Sûreté Nucléaire, Saint-Paul lez-Durance, France
A. Boso, National Physical Laboratory, Teddington, United Kingdom
A. Buffler, D. Geduld, T. Hutton, T. Leadbeater
Department of Physics, University of Cape Town, Cape Town, South Africa

Abstract

Quasi-monoenergetic neutron beams are typically produced at the iThemba LABS fast neutron beam facility by the ^{7}Li(p,xn) or ^{9}Be(p,xn) reactions. With the proton beams available from the separated sector cyclotron, the neutron energy range from about 30 MeV to 200 MeV can be covered almost continuously. The facility first became operational in the late 1980s. The fast neutron beam facility at iThemba LABS has been designated by the National Metrology Institute of South Africa (NMISA) as an entity responsible for providing traceability for the medium and high-energy neutron measurements in South Africa. As a result, the facility is undergoing a major upgrade and development in order for it to meet the requirements for a medium and high-energy neutron metrology facility. As part of the ongoing upgrade, Monte Carlo (MC) simulations aimed at benchmarking the experimental data are ongoing.

INTRODUCTION

iThemba LABS (Laboratory for Accelerator-Based Sciences) is one of the few facilities in the world that can provide quasi-monoenergetic neutron beams in the energy range of up to 200 MeV [1]. Quasi-monoenergetic neutron beams that range from about 30 MeV to 200 MeV are produced in the D-line experimental vault (Fig. 1) via the ^{7}Li(p,xn) or ^{10}Be(p,xn) reactions [2] for varying thicknesses of Li and Be targets, using proton beams available from the separated sector cyclotron (SSC). The iThemba LABS neutron beam facility has been designated by the National Metrology Institute of South Africa (NMISA) as an entity responsible for providing traceability for the medium and high-energy neutron measurements in South Africa. Thus, the facility is intended to be recognised and supported by the international neutron physics and metrology communities for calibrations of neutron detectors and radiation protection dosemeters; including those with a strong sensitivity to epithermal and thermal neutrons such as survey meters. Moreover, cross-section measurements of neutron-induced reactions in the medium and high-energy region (with as low uncertainties as possible) will be performed. In this regard, the neutron beam facility at iThemba LABS is undergoing a major upgrade and development in order for it to meet the requirements for a medium and high-energy neutron metrology facility.

* nbndlovu@tlabs.ac.za

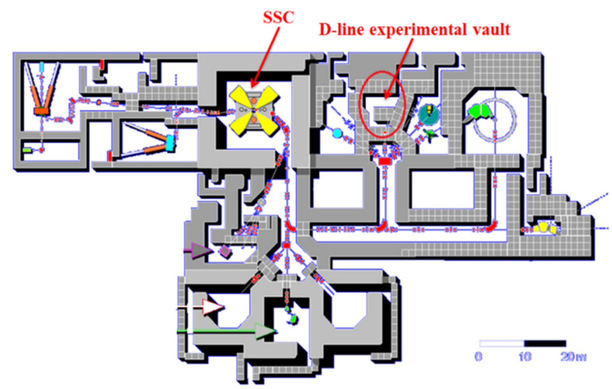

Figure 1: Layout of the iThemba LABS facility showing the location of SSC and the D-line experimental vault.

An ISO-accreditation of the facility will provide it the ability to participate in international key-comparison studies in the area of neutron metrology for medium to high-energy neutrons.

iTHEMBA LABS NEUTRON BEAM FACILITY

At the iThemba LABS neutron beam facility, neutron production targets (Li or Be) are mounted on a target ladder (Fig. 2, label 1) that has four positions, with one permanently occupied by a quartz viewer. At beam currents of a few nanoAmpere (nA), the position of the beam spot can be monitored using the quartz viewer. Out of the three other positions, one is left empty for background target runs while the remaining two are dedicated for neutron production targets. The target ladder is operated remotely. The proton beam is deflected into the beam dump after passing the target. At this point, the Faraday cup that is positioned in the proton beam dump is used to measure the beam charge. The neutron production area of the neutron beam facility at iThemba LABS is separated from the experimental area by an iron shielding wall with collimators at 0°, 4°, 8°, 12° and 16° neutron emission angles (Fig. 2). The collimator channels have rectangular cross sections of about (5 × 5) cm^2. Optimized neutron beam collimator inserts with conical shapes are required in order to improve the uniformity of the beam profile throughout the irradiated target.

ISBN: 978-3-95450-205-9 doi:10.18429/JACoW-Cyclotrons2019-TUP012

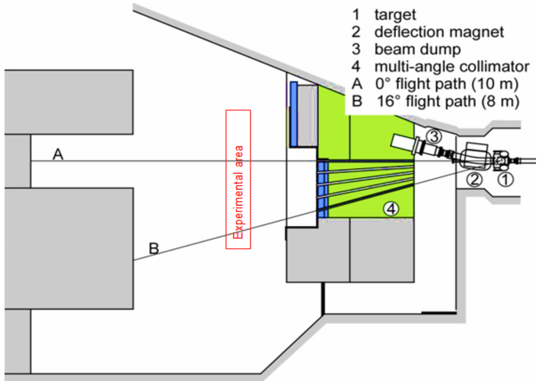

Figure 2: Layout of the fast neutron beam facility at iThemba LABS.

The lateral spatial distribution of the neutron beam depends on the positioning of the ion beam on the Li target and on the collimator shape. The collimator exits are located at a distance of 4 m from the neutron production point. Possible neutron flight paths in the D-line extend from about 4 m to about 10 m. At 0° neutron emission angle, the maximum distance from the target is about 10 m. The beam size at this position is about (13 × 13) cm^2. At 16°, the maximum distance has only been about 8 m, with a correspondingly smaller beam size. For the ongoing refurbishment plans, this 16° flight path has been extended to more than 10 m.

In order to simulate a quasi-mono-energetic neutron energy distribution via ^{7}Li(p,xn), the energy spectra of neutron beams generated by the Li + p reaction at neutron emission angles of 0° and 16° are simultaneously measured. The neutron energy distributions from these emission angles feature a prominent peak and a continuum (Fig. 3).

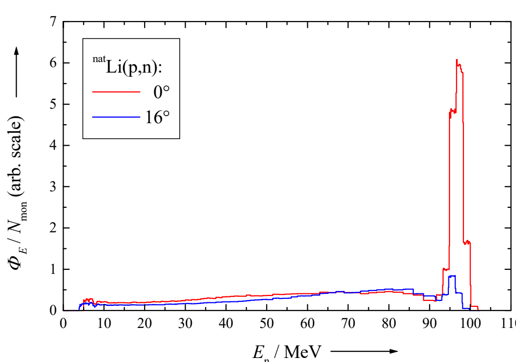

Figure 3: Neutron spectra (measured by time-of-flight) from 100 MeV protons on a 6 mm ^{nat}Li target.

The prominent peak is associated with direct reaction transitions mainly to the ground state and to the unresolved first excited state of ^{7}Be. The continuum at lower energies is associated primarily with the three-body break up process; ^{7}Li(p,n^{3}He)^{4}He. The intensity of the prominent peak in the 0° spectrum is high and rapidly decreases with increasing neutron emission angle. For the low energy continuum, the intensity is almost independent of the neutron emission angle for angles up to 16°. The yield produced by irradiation with the neutron beam in the 0° emission angle includes components due to reactions initiated by both the high-energy peak neutrons (prominent peak) and the continuum. On the other hand, the yield resulting from irradiation with the neutron beam in the 16° emission angle is dominated by reactions initiated by the low-energy continuum alone. Therefore, a yield determined for the quasi-monoenergetic neutron energy is obtained through a “difference spectrum”, by subtracting the yield produced in the 16° beam from that simultaneously produced in the 0° (Fig. 4) [3-7]. Before obtaining the “difference spectrum”, the two spectra are normalized to equalize the total number of counts in the continuum region.

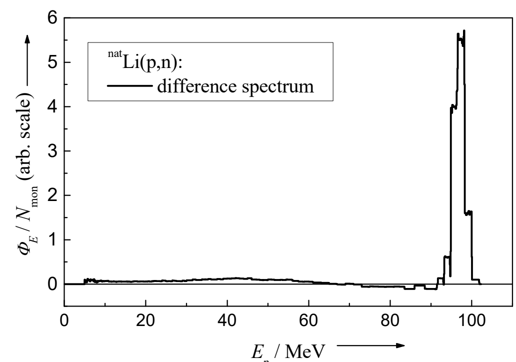

Figure 4: Difference spectrum obtained by subtracting the 16° spectrum from the 0° spectrum.

Neutron beams at iThemba LABS have been well characterized over the years [4, 7, 8]. In Fig. 5, some of the normalised neutron spectra produced at iThemba LABS are shown [9]. The intrinsic widths indicated by the red horizontal bars in Fig. 4 refer to the spread in neutron energy associated with the Li target thickness.

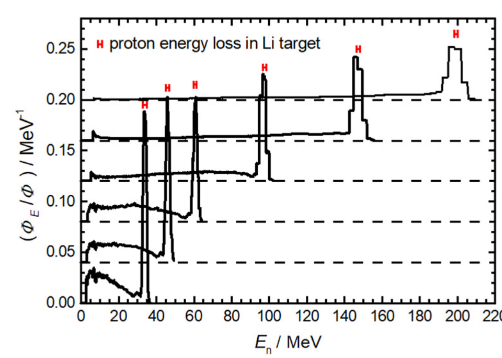

Figure 5: Normalised neutron spectra from Li targets at various energies produced at iThemba LABS [9].

The iThemba LABS neutron beam facility first became operational in the late 1980s [2, 10]. Some of the major challenges of the current set-up were identified based on the results from a measurement campaign performed in the facility by [8]. These challenges include the epithermal neutron background due to leakage from the target

ISBN: 978-3-95450-205-9 doi:10.18429/JACoW-Cyclotrons2019-TUP012

area to the experimental area (Fig. 6), instability of the spatial neutron beam profile due to movement of the proton beam spot on the neutron production target and unstable neutron energy distributions caused by protons hitting the target holder (both due to the insufficient control of the proton beam). This is unacceptable for the intended use since some of the dosemeters which will have to be calibrated in the facility tend to be highly sensitivity to epithermal and thermal neutrons.

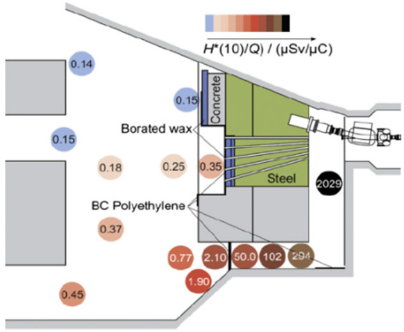

Figure 6: Ambient dose equivalent, *H*(10),* at various locations within the fast neutron beam vault at iThemba LABS measured for a 200 MeV proton beam on a 6 mm Li target [8].

FACILITY UPGRADE

As part of the ongoing upgrade, considering the findings by [8] and the advice from [10], a new design for the D-line vault is proposed as presented in Fig. 7.

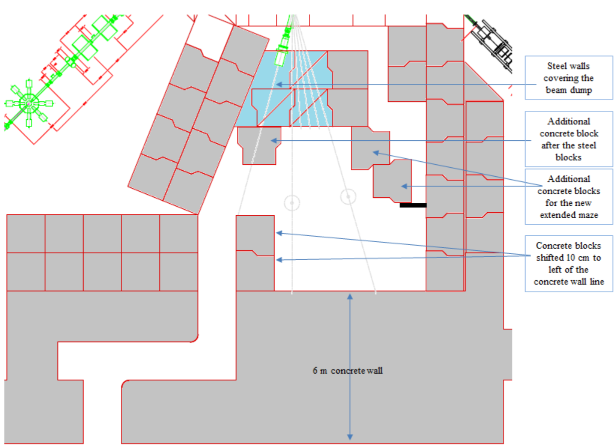

Figure 7: The proposed new configuration of the iThemba LABS neutron beam vault.

In order to reduce the effect on epithermal background, an improved shielding on neutrons from the target area was produced based on a qualitative analysis of data from the previous investigations of the neutron background using the Institut de Radioprotection et de Sûreté Nucléaire (IRSN) Bonner sphere spectrometer HERMEIS. Emphatically in this design, the leakage of epithermal neutrons from the target area through the door is reduced by additional concrete blocks. Moreover, the area between the 0°and 16° has been opened up, providing an extended 16° flight path and providing more space for the experiments. An additional concrete block (~1.5 m thick) has also been added in the vault behind the beam dump after the original steel blocks (~ 2 m thick). The layout as shown in Fig. 7 does not include an additional neutron beam dump to be installed at the end of each flight path. The neutron beam dump is meant to reduce the effect of neutrons striking the concrete wall and scattering back. This will improve shielding of background neutrons in the experimental area. The two concrete blocks along the passage have been moved 10 cm to the left (towards the passageway), in order to increase the space around the 0° measuring axis. Also, this shift has improved the direct line of sight from the beam dump towards the passageway way, which has been travelling straight to the corner of the concrete block. A test experiment aimed at validating the improved shielding in the D-line is anticipated for the beginning of 2020.

Also critical for the success of the measurements is a proper adjustment of the proton beam transport. In order to avoid parasitic sources of neutrons, the beam should have no halo and should not hit any structural material on the target chamber. Thus, the beam should be centred in such a way that only the target material is hit by the beam. At low beam currents, monitoring of the beam is accomplished by using a quartz viewer with a central hole, which takes the central part of the proton beam and makes only the outer parts of the beam to be visible on the TV screen. At higher intensities, the existing quartz viewer cannot be used since it cannot withstand higher beam currents. To enable regular on-line monitoring of the proton beam position and spot size on the neutron production target by the cyclotron operators, a radiation-hard monitor must also be installed close to the target. The expected new beam position monitoring system should be able to withstand the intended current range of ≤ 10 μA. Plans are underway to install proton beam position monitors along the beamline, which will provide continuous information about the proton beam spot during experiments. For scanning procedures, new designs for collimator insert which will provide steeper beam profiles are required and planned. Moreover, a new water-cooled target ladder, which should be able to withstand higher beam currents, will be incorporated into the system. Radiation dose levels of the facility will be investigated to test the limits on maximum beam current allowed on targets. Monte Carlo (MC) simulations aimed at benchmarking the experimental data from the D-line are ongoing. Numerous MC simulation codes are available for radiation transport using random sampling methods. For benchmarking purposes, the experiments and simulations have to be consistent in the description of the physical system for the comparison to work [11]. For the system at iThemba LABS, the standard MCNPX ver. 2.7 with tabulated values of cross-section ENDF/B-VII.0 and ENDF70prot (3007.70 h and 13027.70 h) [12] is used. As part of preparations for an ISO[1]-accreditation as a fast neutron beam reference facility, new instrumentation will be procured, characterized and tested in the D-line. In this regard, a

[1] International Organization for Standardization.

ISBN: 978-3-95450-205-9 doi:10.18429/JACoW-Cyclotrons2019-TUP012

new proton recoil telescope for 30 MeV - 200 MeV energies will be designed for fluence measurements, in addition to a modified and characterised version of the existing ^{238}U fission chamber. Moreover, a new digital data acquisition system will be procured for acquiring data during measurements. Once all the structural modifications of the vault have been done and the instrumentation optimized, the upgraded facility will be tested for metrology capabilities.

CONCLUSION

The fast neutron beam facility at iThemba LABS is undergoing a major upgrade and development in order for it to meet the requirements for a medium and high-energy neutron metrology facility. More experimental tests are planned and simulations are ongoing to benchmark the experimental data. Once the fast neutron beam facility at iThemba LABS obtains the ISO-accreditation as a fast neutron facility in the energy range from 30 MeV to 200 MeV, it will be recognised and supported by the international neutron physics and metrology communities. The facility will then be more suitable for cross-section measurements of neutron-induced reactions and for calibration of neutron detectors and radiation protection dosemeters (including those with strong sensitivity to epithermal and thermal neutrons such as survey meters). Traceability of measurements carried out using fast neutron beam facility at iThemba LABS will be ensured by setting up a primary standard for neutron measurements in the energy range from 30 MeV to 200 MeV. Furthermore, as an ISO-accredited facility, the fast neutron facility at iThemba LABS will be able to participate in international key-comparison studies in the area of neutron metrology for medium to high-energy neutrons. The key-comparison studies in the area of neutron metrology are organized by the Consultative Committee for Ionizing Radiation (CCRI) of the International Committee for Weights and Measures (CIPM).

ACKNOWLEDGEMENTS

This work is based on a research project supported by the National Research Foundation of South Africa, NMISA (South Africa), UCT[2] (South Africa), PTB[3] (Germany), IRSN (France), and the NPL[4] (United Kingdom). The authors would like to acknowledge NMISA for designating the neutron beam facility at iThemba LABS as a neutron metrology for quasi-monoenergetic neutrons in the 'medium to high energy region' in South Africa. The consortium for fast neutron metrology facility at iThemba LABS is thankful to thank Dirk Fourie, Lowry Conradie and the rest of the iThemba LABS accelerator department team for assisting them with the layout drawings and information regard the iThemba LABS neutron beam facility. Ralf Nolte from PTB is also acknowledged for his critical input and review of this paper.

[2] University of Cape Town
[3] Physikalisch-Technische Bundesanstalt
[4] National Physical Laboratory

REFERENCES

[1] S. Pomp *et al.*, "High-energy quasi-monoenergetic neutron fields: existing facilities and future needs", EURADOS, Braunschweig, Germany, EURADOS Rep. 2013-02, May 2013. https://uu.diva-portal.org/smash/get/diva2:621911/FULLTEXT01.pdf

[2] W. R. McMurray *et al.*, "The Faure cyclotron neutron source and a particle spectrometer for neutron induced emission of charged particles at energies between 60 and 200 MeV", *Nucl. Instrum. Methods Phys. Res., Sect. A*, vol. 329, pp. 217-222, 1993. doi:10.1016/0168-9002(93)90939-F

[3] N. Nakao, *et al.*, "Development of a quasi-monoenergetic neutron field using ^{7}Li(p,n)^{7}Be reaction in the 70-210 MeV energy range at RIKEN", *Nucl. Instrum. Methods Phys. Res., Sect. A,* vol. 420, pp. 218-231, 1999. doi:10.1016/S0168-9002(98)01146-2

[4] R. Nolte *et al.*, "High-Energy neutron reference fields for the calibration of detectors used in neutron spectrometry", *Nucl. Instrum. Methods Phys. Res., Sect. A,* vol. 476, pp. 369-373, 2002. doi:10.1016/S0168-9002(01)01472-3

[5] Y. Iwamoto *et al.*, "Characterization of quasi-monoenergetic neutron source using 137, 200, 246 and 389 MeV ^{7}Li(p,n) reactions", *Prog. Nuclear Science Tech.*, vol. 4, pp. 657-660, 2014. doi:10.15669/pnst.4.657

[6] Y. Iwamoto *et al.*, "Characterization of high-energy quasi-monoenergetic neutron energy spectra and ambient dose equivalents of 80–389 MeV ^{7}Li(p,n) reactions using a time-of-flight method", *Nucl. Instrum. Methods Phys. Res., Sect. A*, vol. 804, pp. 50-58, 2015. doi:10.1016/j.nima.2015.09.045

[7] J. M. Sisterson *et al.*, "Cross-section measurements for neutron-induced reactions in copper at neutron energies of 70.7 and 110.8 MeV", *Nucl. Instrum. Methods Phys. Res., Sect. B,* vol. 240, pp. 617-624, 2005. doi:10.1016/j.nimb.2005.06.005

[8] M. Mosconi *et al.*, "Characterisation of the high-energy neutron beam at iThemba LABS", *Rad. Meas.*, vol 45, pp. 1342-1345, 2010. doi:10.1016/j.radmeas.2010.06.044

[9] R. Nolte *et al.*, "Cross sections for neutron-induced fission of ^{235}U, ^{238}U, ^{209}Bi, and ^{nat}Pb in the energy range from 33 to 200 MeV measured relative to n-p scattering", *Nucl. Sci. Eng.*, vol. 156, pp. 197-210, 2007. doi:10.13182/NSE06-14

[10] J. C. Cornell, D. T. Fourie, and G. C. W. Lloyd, "A neutron beam facility at NAC", in *Proc. 12th Int. Cyclotron Conf. and Their Applications (Cyclotrons'89)*, Berlin, Germany, May 1989, paper J-08, pp. 594-597.

[11] S. G. Mashnik and J. S. Bull, "MCNP6 simulation of quasi-monoenergetic ^{7}Li(p,n) neutron sources below 150 MeV", *Nucl. Data Sheets*, vol. 118, pp. 323-325, 2014. doi:10.1016/j.nds.2014.04.070

[12] D. B. Pelowitz (ed), *MCNPX^{TM} User's Manual, version 2.6.0*, LA-CP-07-1473, Los Alamos National Laboratory, U.S., Apr. 2008. https://www.mcnp.ir/admin/imgs/1354176297.2.6.0_UsersManual.pdf

ISBN: 978-3-95450-205-9 doi:10.18429/JACoW-Cyclotrons2019-TUP014

DEFLECTING SYSTEM UPGRADE INITIAL SIMULATIONS FOR 37 MeV CYCLOTRON AT NPI REZ

T. Matlocha*,[1], Nuclear Physics Institute of the CAS, Rez, Czech Republic
[1]also at Czech Technical University in Prague, FNSPE, Prague, Czech Republic

Abstract

NPI Rez U-120M multi-particle variable energy cyclotron system for positive ions extraction consists of three electrostatic deflectors, one active magnetic channel and an electromagnetic bump exciter. The deflectors transmission ratio for deuterons, alpha particles and Helium 3 ions is rather low, usually about 10 %, for protons it is far below 5 %. Based on an experience from other cyclotron laboratories, the general concept of the extraction system has been modified and the last two electrostatic deflectors were replaced with two magnetic channels. In the early stage of the upgrade, simulations were performed for protons at 28 MeV and Helium 3 ions at 44 MeV with and without the magnetic bump exciter. The extraction efficiency and beam losses along the extraction path are evaluated. The presented modified extraction system simulations suggest promising results. The total transmission ratio of the deflecting system has increased significantly, allowing work to continue and expect a positive final result.

ACTUAL SITUATION OVERVIEW

The isochronous cyclotron U-120M is a four sector machine with a pole diameter 120 cm, 18 trim coils. It is in operation from 1977. Initially it was built in JINR as a positive ions accelerator, an option for negative ions was enabled circa 15 years later. Complete list of accelerated ions with their maximal energies is specified in Table 1. For both ion polarities an internal cold cathode Penning type ion source is used. The negative ions are extracted using a stripping foil with efficiency close to 100 %.

The extraction of positive ions is rather problematic and requires a significant improvement. There are two main issues related to the low extraction ratio. Firstly, it is the low extracted beam current, but usually this can be compensated by a prolonged irradiation time. Secondly, it is very high activation of the cyclotron equipment, especially the extraction elements, which prevents an efficient maintenace.

Table 1: Possible positive ions with their energy ranges and maximal internal currents at the U-120M cyclotron.

Particle	Energy range	Maximal current int.
protons	6 – 37 MeV	200 µA
deuterons	7 – 20 MeV	80 µA
α	12 – 40 MeV	40 µA
$^3He^{2+}$	17 – 54 MeV	20 µA

* matlocha@ujf.cas.cz

Extraction System Concept

The original concept of the extraction system described in [1] is shown in Fig. 1. The system had consisted of an electrostatic first harmonic exciter (EE) and an electrostatic compensator (EC), three electrostatic deflectors (ESD) and one magnetic channel after ESD III (not in figure). Extraction efficiency of this configuration was close to 40 %. After the compensator part failed, the electrostatic exciter was replaced by a magnetic bump coil. This change was made in about 1980 and the extraction efficiency had dropped significantly.

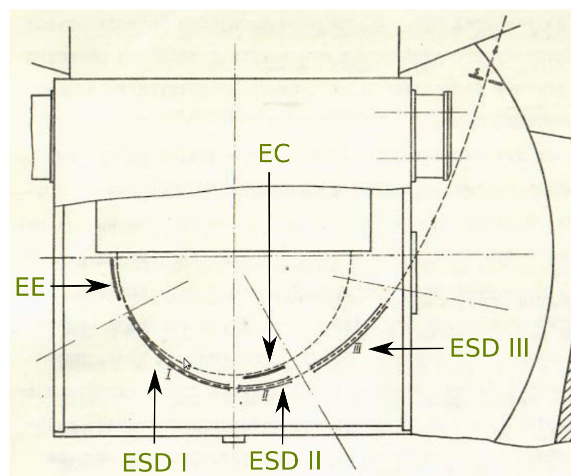

Figure 1: The original concept of the extraction system [1].

Electrostatic Deflectors

The system consists of three ESD's located at azimuths 120°, 182° and 215°. Septum of the first electrostatic deflector is placed near extraction radius 510 mm where ν_r is still ~1.03.

The original intention was that the electrostatic deflectors would also have vertical beam focusing properties. This resulted in their rather complicated shape (see Fig. 2). Moreover the first ESD is divided into a part for the beam deflection and a part for the beam deflection and vertical focusing. The nontrivial shape of the septums and electrodes are responsible for a part of the high extraction losses. Second part is due high radial beam dispersion, as the beam passes all three deflectors without any kind of radial focusing.

Magnetic Field Bumper

The beam is extracted by a Brute force method as the $\nu_r = 1$ region is crossed very fast [2]. The magnetic bump coil is a dipole magnet with the center at azimuth 98°, 12°

ISBN: 978-3-95450-205-9 doi:10.18429/JACoW-Cyclotrons2019-TUP014

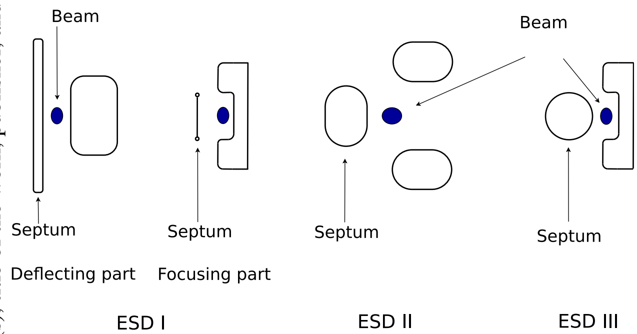

Figure 2: Eletrostatic deflectors profiles. Not labeled profiles belongs to high voltages electrodes.

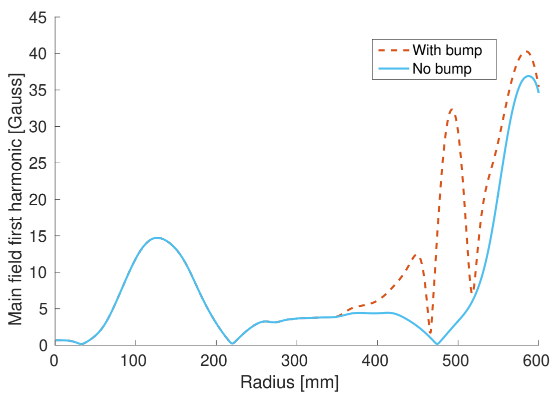

Figure 3: First harmonic introduced by the magnetic field bumper at proton regime for 28 MeV.

width and with a variable radial position 460 mm–500 mm. The introduced magnetic field perturbation is not compensated resulting in a slight phase shift of the accelerated beam. The influence of the bump magnet to the first harmonic component of the main magnetic field is shown in Fig. 3.

Harmonic Coils

The U-120M cyclotron has two sets of harmonic coils. Internal coils are placed at radius 140 mm and are used for the beam centering. Outer harmonic coils are placed at radius 420 mm, too far from the extraction radius 510 mm. They were originally not intended as extraction coils and currently they are not in operation.

SIMULATIONS

Beam dynamic simulations were performed in an "in house" Durycnm18 code [3] and in the SNOP – free to use beam analysis code for compact cyclotrons [4]. Durycnm18 was used for proper beam centering and the magnetic bump amplitude and radial position tuning. The SNOP code was used for phase slits influence evaluation, deflector septum and magnetic channels optimization and a beam loss analysis.

Two regimes were used for the transmission ratio calculations, protons at 28 MeV and $^3He^{2+}$ at 44 MeV as they are about 80 % of the maximal energy. Based on other laboratories experience, the general concept of the extraction system has been modified. The ESD II and ESD III were replaced by analytically introduced magnetic channels MC, which provide radial beam focusing. With this configuration, three basic modifications of the extraction system were evaluated:

- Bump coil was turned off. Beam extracted without additional separation.
- Bump coil was replaced by a short ESD 0. Outer harmonic coils used for a turn separation. Phase slits introduced to the cyclotron central region.
- Bump coil used for the turn separation and phase slits introduced to the central region.

Beam Centering

Good beam centering can be obtained for the central particle by fine tuning of the inner harmonic coils. Surrounded RF phases are well centered for about ± 15°, depending on the accelerated ion type and its final energy. With proper centering, the beam radial size is about 2.5 mm at the ESD enter. Beam center coordinates for the three above mentioned modifications are show in Fig. 4.

It seems that there is a natural first harmonic at azimuth 270° in the magnetic field. As the deflector is located at

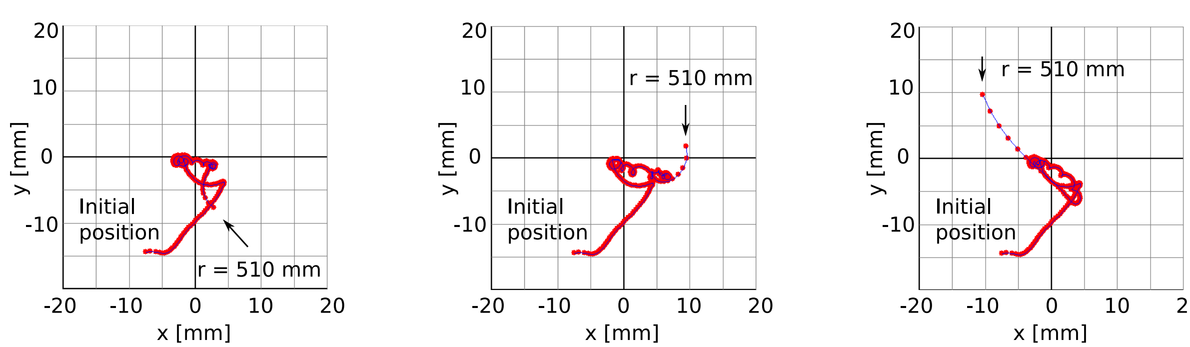

(a) Centered beam. Intrinsic first harmonic at azimuth ~270°.

(b) Centered beam with outer harmonic coils. Center shifts to azimuth ~70°.

(c) Centered beam with the field bump at azimuth 98°.

Figure 4: Beam center coordinates for the central RF phase and different harmonic coil settings. Septum of the first deflector located at azimuth 113.5°.

ISBN: 978-3-95450-205-9 doi:10.18429/JACoW-Cyclotrons2019-TUP014

113.5°, this intrinsic field perturbation push the beam just the opposite direction. The intrinsic first harmonic can be observed in Fig. 3 where it starts at radius 480 mm and also in Fig. 4a as a tail of the beam center path.

Phase Slits

Phase slits introduced into the central region need to respect the actual geometry and space restrictions in the area. In past years there was an attempt to introduce the phase slit as one piece slit placed in the central region. Resulting beam properties were not satisfactory and the phase slit idea was abandoned. By a detailed analysis of the central region, we observed a better solution. It is beneficial to split the phase slit into two separate parts, placed at different positions in the central region. Respecting the necessity of remote position controlling, there are only two possible locations. First is in the region of the ion source head, at the first orbit, where the slit limits lower RF phases. Here the phase slit position control can be done by a piston-rod hidden in the ion source support. Second position is inside the puller at the second beam orbit, where the upper RF phases are restricted. By a proper phase slits setting it is possible precisely tune the beam RF phase range leaving the central region. Figure 5 shows comparison of the initial and accelerated beam RF phase distribution for the phase slits setting ±15° around the central RF phase −7°.

We afraid that the second phase slit position control could be a difficult mechanical and engineering task, as it is placed inside the puller. Nevertheless its use is highly appreciated. We consider a hydraulic driving of the second phase slit.

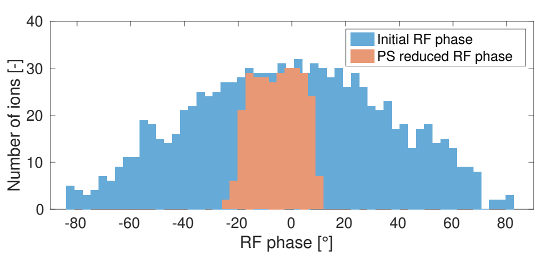

Figure 5: RF Phase distributions for initial and for the accelerated beam.

Turn Separation

Without using the field bump or the outer harmonic coils, the beam is not separated at the extraction radius 510 mm and aziuth 114° at all. Experimentally, we switched on the external harmonic coils and evaluated their benefit to the extraction process. The beam center at the extraction radius is shifted towards aziuth ~70° as can be seen in Fig. 4b. Results were promising for part of the acceleration regimes, but not for all.

Better results are achieved using the bump magnet, for which the degree of the turn separation is similar to the effect ot the outer harmonic coils, but the azimuth is more appropriate. Plot of orbits from radius 470 mm with the turns separated by the bump coil is in Fig. 6. Corresponding beam centering is plotted in Fig. 4c.

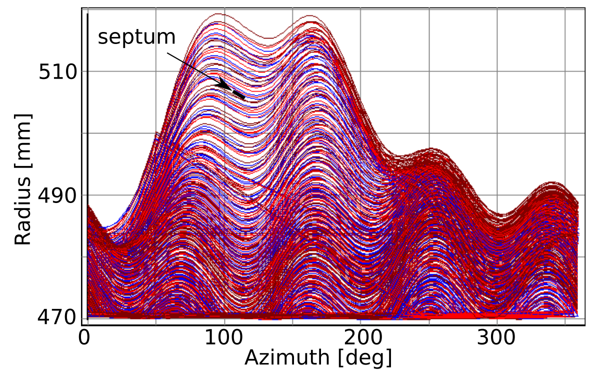

Figure 6: Orbit separation at azimuth 110° by a magnetic field bump and ESD septum position.

Extraction Elements

At this early stage of the U-120M extraction system upgrade, the extraction elements are simulated using analytical electromagnetic fields inserted into the acceleration region. In the future, when CAD models of the deflector and magnetic channels will be created and simulated, their real fields will replace the analytical fields.

The deflector septum shape is derived from the central particle path and its CAD model is inserted to the SNOP code for particle losses evaluation.

SIMULATION RESULTS

For the case without an additional turn separation, i.e. when the bump coil was turned off, we were not able to reach extraction ratio better than 40%. This is partly caused by not using the phase slits to reduce the RF width of the beam. After we introduced the phase slits and improved the turn separation by using the outer harmonic coils, we also tried to introduce short electrostatic deflector ESD 0 before ESD I, instead of the bump coil. Transmission ratio improves dramatically, but at some regimes the effect was not beneficial.

Best results were achieved by using the phase slits in the central region and the bump coil together. In this case we prolonged the first electrostatic deflector by 6° moving its beginning to azimuth 113.5°. One optimized septum shape was used for both evaluated regimes, just with different positions and angles. Results of this third modification are presented in the Table 2, where initial vs. accelerated beam stands for the beam leaving the ion source vs. the beam after the phase slits. Emittances are calculated for two standard deviations of the mean. The transmission ratio was evaluated at the cyclotron output to a beam transmission line located at radius ~1050 mm. No losses are considered in the magnetic channels. The magnetic channels settings were optimized for a proper beam focusing.

ISBN: 978-3-95450-205-9 doi:10.18429/JACoW-Cyclotrons2019-TUP014

Table 2: Simulation Results

		p 28.0 MeV	**$^3He^{2+}$ 44.0 MeV**
RF phase beam width		30°	55°
Central RF phase		−7°	−2°
Extracted beam radial emittance		7.8 π mm mrad	13 π mm mrad
Extracted beam vertical emittance		0.9 π mm mrad	1.1 π mm mrad
Losses on septum	From initial beam :	3.5 %	3.6 %
	From accelerated beam:	11.8 %	7.1 %
ESD transmission ratio	From initial beam:	25.8 %	47.9 %
	From accelerated beam:	88.2 %	2.9 %

Losses Distribution

Figure 7 shows comparison of the septum losses distribution for the two compared regimes. The proton 28 MeV regime has the major part of beam loss located at the beginning of the septum and the rest on the first few centimeters (see Fig. 7a). On the other end for the $^3He^{2+}$ at 44 MeV regime, the septum touches the beam also with its end, as can be seen in Fig. 7b. This can be further optimized by a small change of the septum shape or by further decrease of the RF phase beam width.

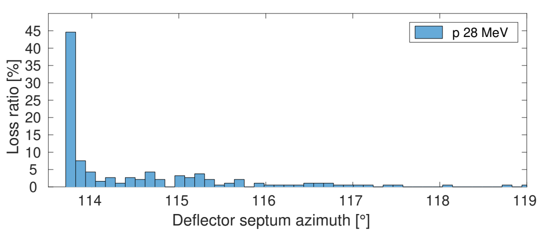

(a) Regime for p 28 MeV. Detail of the septum beginning.

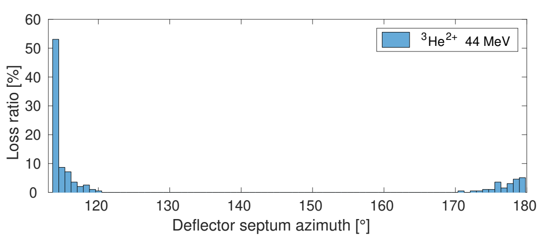

(b) Regime for 3He^{2+} 44 MeV. Full septum length.

Figure 7: Losses distribution along the electrostatic deflector septums for two evaluated regimes.

CONCLUSION

For the intended positive particles extraction system upgrade at the U-120M cyclotron, three basic modifications of the current configuration were simulated. Mode without an additional turn separation by the bump coil, a mode using the outer harmonic coils for the turn separation with a short electrostatic deflector ESD 0 instead of the bump coil and a mode using the bump coil for the turn separation and slightly prolonged the first electrostatic deflector ESD I were compared. Surprisingly the best results were obtained for the configuration with the bump coil. We originally thought the bump coil is not suitable for the extraction, but with a proper beam RF phase reduction, its use is justified. It now seems necessary to install the phase slits in the cyclotron central region. The simulated first electrostatic deflector transmission ratio increased significantly, for both regimes close to one order.

By replacing the second and the third electrostatic deflector by magnetic channels for an additional radial focusing, also a considerable increase in the total extracted beam can be expected.

In the next step we will concentrate on a design of suitable magnetic channels as they will be an indispensable part of the final extraction system.

ACKNOWLEDGEMENTS

This work was supported by Ministry of Education, Youth and Sports under the project CANAM - LM2015056.

REFERENCES

[1] V. P. Dmitrievskii, V. V. Kolga, N. L. Polumordvinova, and Z. Treibal, "Calculation of the electrostatic system for beam extraction of cyclotron", *in 3rd Symposium on the isochronous cyclotron U-120M and its uses for studies on nuclear science*, Ceske Budejovice, Czechoslovoakia, May 1973, Joint Inst. for Nucl. Res., Dubna, USSR, Rep. JINR-R9-7339, pp. 102-105, pp. 102-105 (in Russian).

[2] P. Heikkinen, "Injection and extraction for cyclotrons", *CAS - CERN Accelerator School : 5th General Accelerator Physics Course*, Jyväskylä, Finland, Sep. 1992, CERN, Geneva, Switzerland, Rep. CAS CERN 94/01, pp. 819-839, 1994, http://cds.cern.ch/record/398439/files/p819.pdf

[3] M. Cihak, J. Stursa, and O. Lebeda, "Beam dynamic simulation in the isochronous cyclotron U-120M", *in Proc. 18th Int. Conf. on Cyclotrons and their Applications (Cyclotrons'07)*, Giardini-Naxos, Sicily, Italy, Oct. 2007, pp. 285-387. http://accelconf.web.cern.ch/AccelConf/c07/PAPERS/385.pdf

[4] V. Smirnov and S. Vorozhtsov, "SNOP – Beam dynamics analysis code for compact cyclotrons", *in Proc. 23rd Russian Particle Accelerator Conf. (RuPAC'12)*, Saint Petersburg, Russia, Sep. 2012, paper TUPPB008, pp. 325–327. doi:10.13140/2.1.2035.9684

ISBN: 978-3-95450-205-9 doi:10.18429/JACoW-Cyclotrons2019-TUP016

NEW CENTRING BEAM MONITOR FOR HIGH POWER PROTON BEAM ROTATING TARGET

P.-A. Duperrex†, P. Baumann, S. Joray, D. Kiselev, D. Laube, D. Reggiani
Paul Scherrer Institut, 5232 Villigen PSI, Switzerland

Abstract

The high intensity proton accelerator (HIPA) at the Paul Scherrer Institute (PSI) delivers 590 MeV c.w. proton beam with currents of up to 2.4 mA, i.e., 1.4 MW beam power. For experiments of nuclear and material research the beam is directed to the 4 or 6 cm graphite 1 Hz rotating target (Target E). Centring the beam on the target is an important task for the operation and has safety issues in case of beam misalignment. Transmission monitoring has been the standard method to optimize the beam position on the target, though not very sensitive. A new method is currently being tested that provides a more sensitive off-axis detection. It is based on the detection of beam intensity modulation from the milled grooves at the target edge. This paper presents the concept and preliminary experimental results that can be obtained with this method.

INTRODUCTION

At the 1.4 MW high intensity proton accelerator facilities (HIPA) at Paul Scherrer Institute (PSI), the proton beam is accelerated from a Cockcroft-Walton source followed by two cyclotrons: the so-called Injector 2 cyclotron accelerating the beam from 870 keV to 72 MeV and the so-called Ring cyclotron accelerating it to 590 MeV. The beam is then directed through 2 meson graphite targets (Target M and E) to the spallation neutron source SINQ [1]. The energy deposit on Target E is 20 kW mA^{-1} with a beam 2-sigma width of 1.5 mm in the horizontal direction and 1.7 mm in the vertical direction.

The correct centring of the beam on the Target E is important since the rim of the wheel is only 6 mm wide. Missing partly the target would not only reduce the meson production rate but also leads to a pencil beam hitting the SINQ target window, which could not withstand such power densities.

Transmission minimization has been the standard method to center the beam position on the Target. The transmission is the ratio of the beam current measured after and before the target. For this method, a beam position scan is performed to identify the range and the optimum position corresponding to the minimum transmission. This is however an indirect measurement and is not very sensitive.

The new method currently being tested allows a more sensitive detection of off-axis beam conditions. The method is based on the detection of beam current modulations induced by grooves milled at the target rim. Evidence of these modulations is indicative of off-axis beam conditions, the modulation amplitude giving some information about how far off-axis the beam is located.

† pierre-andre.duperrex@psi.ch

EXPERIMENTAL SETUP

The Grooved Target

The Target-E for this experiment is shown in Fig. 1. The tests took place in the summer 2019 during 2 months, the target then had to be replaced due to bearing problems.

Figure 1: The Target-E used for the experiment.

The 60 mm wide rim of the target is divided into 12 segments. Between the segments a 1 mm wide gap allows for thermal expansions as well as dimensional changes due to irradiation.

The grooves on each segments are easily visible in Fig. 2. The spaces between each groove have been calculated so that, for a target rotating at 1 Hz, a beam current modulation at either 114 Hz (left off-axis) or 138 Hz (right off-axis) will be measured. These two frequencies have been chosen so that they are located exactly between two harmonics of the 12 Hz signal generated from the target blades.

Four groove milling depths were tested on this target: 0.3, 0.5, 0.7 and 0.9 mm on groups of 3 elements distributed equally to investigate the sensitivity of the detection and the possible physical defects. One groove on each side was milled deeper (1 mm) to act as an absolute marker (see Fig. 2).

ISBN: 978-3-95450-205-9 doi:10.18429/JACoW-Cyclotrons2019-TUP016

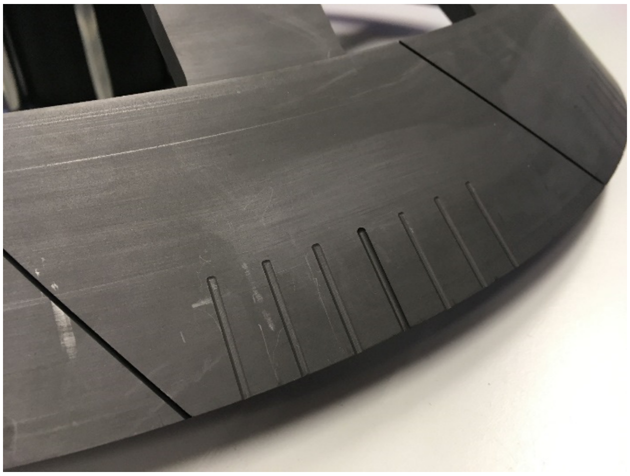

Figure 2: Detail of a segment showing the grooves. On that particular segment the middle groove is milled 1 mm deep (the other grooves of this segment are 0.3 mm deep). This groove acts as absolute marker.

Control of the Beam Position

The relative position of the beam on the target is controlled by a set of steering magnets. They have been used for this experiment to change the beam position on the target from -1.3 mm to 1.3 mm.

Beam Current Monitors

Two beam current monitors have been used for this study. They are resonators tuned at the 2nd harmonic of the RF (101.26 MHz). The first monitor, called MHC4, is located before the target and the 2nd one (MHC5) after it.

Measurement Chain

The beam current signals have been recorded using a 16-bit data logger at a 10 kHz sampling frequency. LabVIEW was used to remotely control the data logger, perform the modulation detection and to configure an EPICS server for easy access to the results.

Signal Processing

To detect the groove modulation on the MHC5 signal, it was necessary to filter the broadband noise already present on the signal. The MHC4 signal was used for that purpose. By subtracting the correctly weighted MHC4 signal from the MHC5 one, most of the noise contributions prior to the target E can be removed. An example of such filtering is shown in Fig. 3. The 12 Hz modulation from the blades are easily visible as well as a 1 Hz rotation wobbling.

The FFT of the filtered MHC5 is then performed to detect the possible presence of the 114 Hz or 138 Hz spectral lines, as well as their corresponding harmonics.

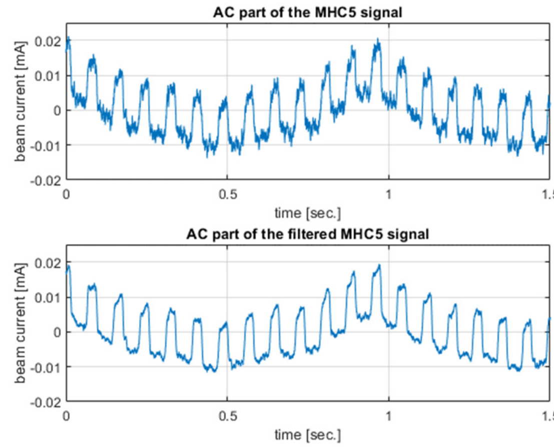

Figure 3: Raw and filtered MHC5 signals.

EXPERIMENTAL RESULTS

Figure 4 shows an example of the data for +1.3 mm beam off-set at beam intensity of 0.388 mA.

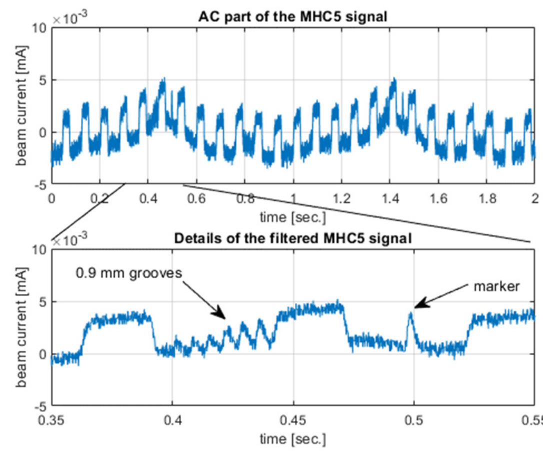

Figure 4: Example of modulations for off-axis position.

The beam intensity modulation due to the absolute marker on the first segment is clearly visible as well as the 138 Hz 0.9 mm groove effects.

The groove modulation level dependency on the off-axis beam position has been analysed for 1.6 mA beam intensity conditions. For this study, the beam position on the target has been changed from -1.3 to +1.3 mm with 0.1 mm increment. The 114 Hz and 138 Hz spectral line amplitudes have been measured for each position using the FFT routine and the results are shown in Fig. 5.

ISBN: 978-3-95450-205-9 doi:10.18429/JACoW-Cyclotrons2019-TUP016

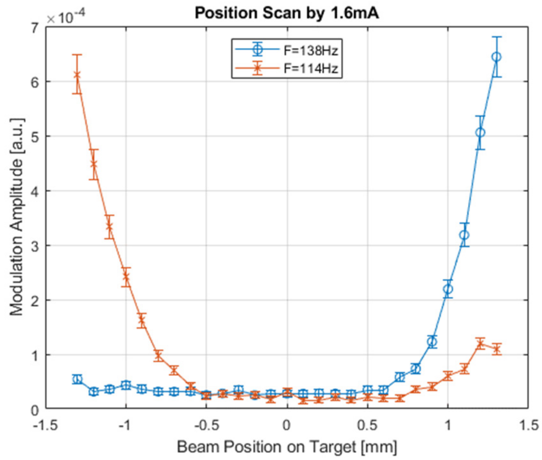

Figure 5: 114 Hz and 138 Hz spectral lines as function of the beam position on the target.

For centred beam conditions, no spectral lines at 114 Hz and 138 Hz are detected the noise level. For off-axis distance larger than 0.7 mm the spectral lines have been clearly detected. The non-linear dependency stems from the shape and profile of the beam.

To compare the performance of the new method with the transmission measurements, the transmission level as function of the beam position is shown in Fig. 6. The transmission is clearly much less sensitive compared to the groove modulation detection.

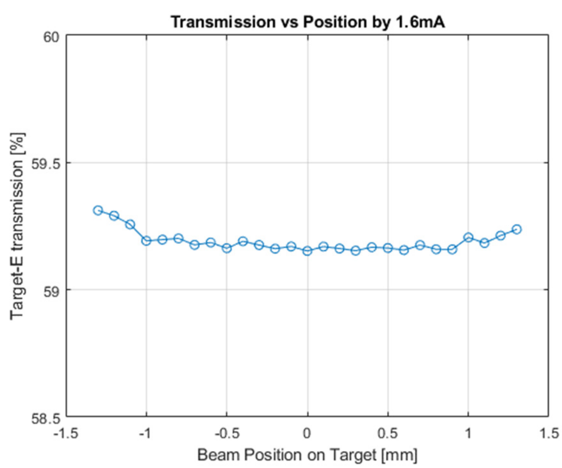

Figure 6: Transmission as function of the beam position.

DISCUSSION

The preliminary results show that the groove modulation method can detect an off-axis position of 0.7 mm or more in the present configuration. Using simple considerations, modulations are expected to appear for an off-axis position larger than 0.6 mm. Indeed, with a 6 mm target width, 2 sigma beam width of 1.5 mm and 0.9 mm deep grooves, one gets: 3 -1.5 - 0.9 mm = 0.6 mm.

Inspection of the target after 2 months of operation show no particular sign of damage like deformations or cracks even for the 0.9 mm grooves. It was a major concern that the milling of the grooves on both sides of the target rim would weaken the stability of the graphite.

This method may potentially lead to beam size estimate though more detailed analysis and simulation are needed. Indeed, measuring the exact modulation amplitude during a position scan should give an estimate of the beam width: a wider beam would generate a groove modulation for a smaller off-axis position, but the relative increase for larger off-axis position would not be as steep as for narrower beams.

This new method also overcomes some short-comings of the transmission measurements. It is more sensitive and it doesn't suffer from calibration issues faced by the MHC5 [2]. Indeed, the MHC5 resonator is exposed to the particles scattered from the Target-E. The resulting deposited power can heat up the resonator up to typically 130 °C. This has some direct impact on the stability of its calibration factor.

CONCLUSION

A method for measuring the beam position on the meson target Target-E has been tested during 2 months of beam operation in the summer 2019. It is based on the detection of beam intensity modulation from the milled grooves at the target rim. The results show that this method is sensitive enough to measure 0.7 mm off-axis conditions. These results motivate further development and optimisation to provide in the future a fully operational system.

REFERENCES

[1] D. Kiselev, P. Baumann, B. Blau, K. Geissmann, D. Laube, T. Reiss, R. Sobbia, A. Strinning, V. Talanov, and M. Wohlmuther, "The Meson target stations and the high power spallation neutron source SINQ at PSI", *in Proc. 27. Int. Conf. of the Nuclear Target Development Society (INTDS'14)*, Tokyo, Japan, Aug.-Sep. 2014, *J. Radioanal. Nucl. Chem.*, vol. 305, no. 3, pp. 769-775. 2015. doi:10.1007/s10967-015-3999-3

[2] J. Sun, P. A. Duperrex, and G. Kotrle, "Design of a new beam current monitor under heavy heat load", in *Proc. 54th ICFA Advanced Beam Dynamics Workshop on High-Intensity and High-Brightness Hadron Beams (HB'14)*, East Lansing, MI, USA, Nov. 2014, paper MOPAB48, pp. 154-156.

ISBN: 978-3-95450-205-9 doi:10.18429/JACoW-Cyclotrons2019-TUP017

MANUFACTURING AND COMMISSIONING OF CYCLOTRONS IN A SERIES PRODUCTION AT VARIAN

O. Boldt, M. Eichel, S. Lucht, L. Netterdon, A. Roth, M. Seher, T. Stephani, M. Wiesner
Varian Medical Systems GmbH, Troisdorf, Germany

Abstract

On 16th of March 2019 Varian celebrated the 10th anniversary of first patient treatment in the Munich Proton Center.

Since the first cyclotron installation, 22 cyclotrons have successfully been manufactured, commissioned, and tested in Troisdorf production.

A better understanding of the cyclotron mechanisms and physics allowed for significant faster commissioning lead times without changing the hardware setup substantially.

Essential improvements in area of qualification of magnetic field configuration, RF conditioning, and beam commissioning are presented.

KEY PERFORMANCE INDICATORS

Varian's superconducting AC250 cyclotron delivers proton beams with a fixed energy of 250 MeV with beam currents of up to 800 nA. This compact cyclotron is a four-sector cyclotron operating at an RF frequency of approx. 72 MHz, which is the second harmonic of the orbital frequency, see [1] and [2] for more key parameters of the cyclotron.

During the last years, several improvements were introduced in the phase of production and factory commissioning of the cyclotron. This allowed an increased number of fully commissioned cyclotrons, which were tested and optimized to the medical specifications needed for clinical operation, especially with respect to extraction efficiency as well as beam shape and stability.

After the superconducting coil is cooled down to liquid helium temperature of 4.2 K the magnetic is excited for the first time followed by the field mapping process. By using a pre-shimmed cyclotron, i.e. omitting several shimming / field mapping iterations, the number of field maps could be reduced significantly. During the commissioning of the first cyclotrons, several iterations were performed, i.e. the magnetic field configuration was optimized incrementally by adjustments of the shimming pattern. Afterwards the magnetic field was mapped. Starting with cyclotron #7 (C7), the number of shimming iterations and corresponding field maps was gradually decreased towards a pre-shimming first time used with cyclotron #15, see Fig. 1. This means, that a default shimming pattern is used for each cyclotron and the magnetic field configuration is only verified via field mapping.

Although test criteria (e.g. extraction efficiency, max. beam intensity, and beam position stability) have simultaneously become more elaborate and strict over the past years, improvements of the test processes as well as hardware changes result in a significant reduction of needed working hours for RF and beam commissioning as well, see Fig. 2. Details of the improvements will be described in the following section.

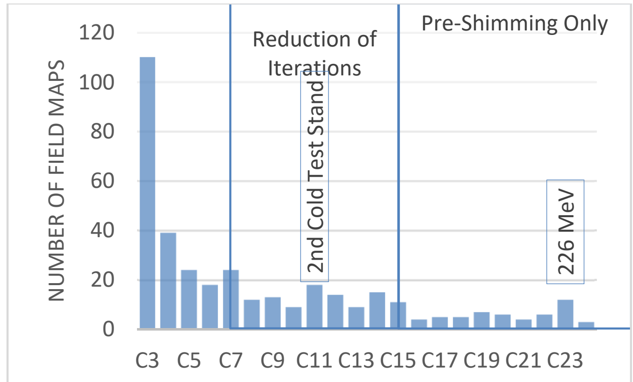

Figure 1: Number of collected field maps for different projects (indicated by C followed by integer).

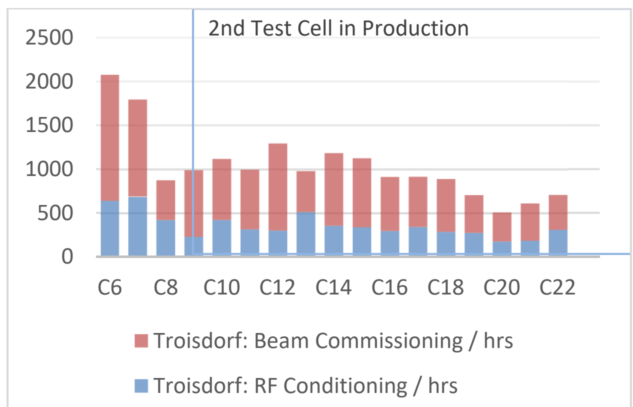

Figure 2: Used working hours for RF and beam commissioning in the Troisdorf cyclotron test cells.

IMPROVEMENTS

Several hardware changes were introduced with the goal to make commissioning processes faster, more reliable, and reproducible. During beam commissioning, a so-called foil irradiation is performed several times. After each beam characterization and optimization iteration, beam width and position are checked via the irradiation of radiation sensitive foils. These foils are attached to the entrance and exit of the extraction deflectors and focusing bars. Figure 3 shows a schematic overview of the cyclotron and the position of the different extraction elements.

Instead of pasting the foil pieces directly to the respective component, foil frames and holders were designed for easier and more reliable installation of the foils.

ISBN: 978-3-95450-205-9 doi:10.18429/JACoW-Cyclotrons2019-TUP017

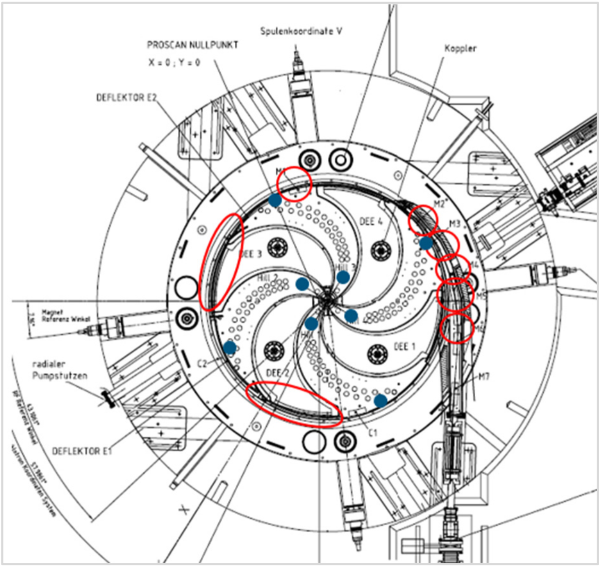

Figure 3: Sketch of cyclotron layout. The red circles depict the extraction element positions (see Fig. 5).

In addition, the design of the Dee Rims, which connect the RF cavity structure of both pole caps, has been changed. At the early stage of RF commissioning, the electrical field inside the cavity might not be well balanced yet. This may result in strong current flows at the four Dee Rims, causing their contact fingers to burn. After changing the design at this point, burned Dee Rim contact fingers only rarely occur. Figure 4 shows both Dee Rim designs, where the top one shows partly burned contact fingers. The bottom picture shows a new-designed Dee Rim which was in operation throughout RF and beam commissioning.

Besides hardware changes, processes throughout all phases of cyclotron commissioning have been reorganized to enhance effectivity and robustness of test procedures and results. This was possible especially by gathering data and experience from former cyclotron commissioning procedures. The first example is in the field of the field mapping and shimming process, see above. Regarding RF commissioning, a self-developed automatization tool is in operation. This tool was designed to support the cyclotron operator during RF and beam commissioning and is an extension to the current cyclotron control system. Together with the existing control system functions this tool is able to continue RF operation after an RF trip without any action needed from the operator. This in tool in principle allows a completely automatic RF commissioning in the sense of slowly ramping up RF power and self-adjusting the power level towards stable conditions. It has proven to significantly speed up the conditioning process, as it is now possible to run 24 hours a day, even when no cyclotron operator is present.

[1]The beam distribution and position is processed via Python by analysing a video with respect to a distribution of bright pixels.

Figure 4: Top: Dee Rim with old design of contact fingers. Starting from the edge of the Dee Rim, the contact fingers are melted due to high currents caused by disbalanced EM fields. Bottom: Dee Rim with new-designed contact fingers. No sign of deterioration is noticeable. Note, that this Dee Rim was installed during RF and beam commissioning.

Moreover, meanwhile the superconducting coil is prealigned before the cyclotron enters the test cell. The coil was previously aligned using foil irradiations in order to avoid a tilted coil and, thus, vertical oscillations of the proton beam while being extracted, see [3] for details. Nowadays, the forces of the coil support links are balanced in a way that the torsional moment is minimized as far as possible. This results in much less foil irradiations and, thus, faster beam commissioning. Figure 5 shows examples of irradiated foils before and after the coil was tilted. By optimizing the coil position beforehand, the first foil irradiations can be omitted.

On the other hand, the vertical position of the coil still needs to be optimized using a proton beam. For this purpose, so-called viewer probe is used. This basically consists of a CCD camera at the top of a lance, which can be moved radially inside the cyclotron to visualize vertical position and shape of the proton beam. By tracking the vertical position from the inner region up to the extraction channel, the vertical coil alignment can be evaluated. Data acquisition and evaluation of this process has recently been fully automatized using a self-developed blob[1] detection algorithm, see Fig. 6.

Beside imaging the beam, another important part of the cyclotron beam commissioning is the so-called characterization for different settings. For this purpose, various parameters (e.g. main coil current, electro-static beam steerers, or variable collimators) are scan whilst recording beam position, shape, and intensity.

ISBN: 978-3-95450-205-9 doi:10.18429/JACoW-Cyclotrons2019-TUP017

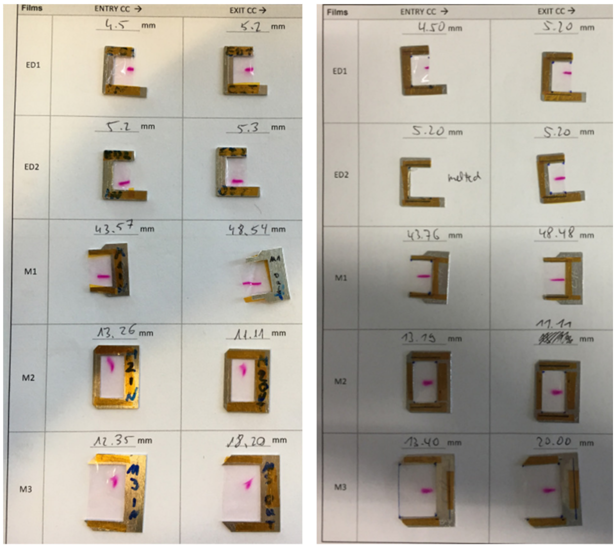

Figure 5: Examples of foil irradiations performed during beam commissioning. Left: vertical beam oscillations are visible along the beam path due to misaligned (tilted) coil. Right: coil pre-alignment eliminates oscillation and allow an straight beam path through the extraction.

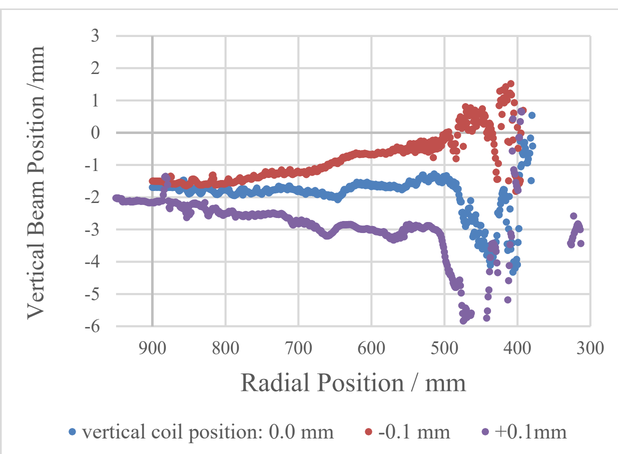

Figure 6: Vertical beam oscillation along cyclotron radius for 3 different vertical coil positions (please note: radial position axis is inverted, 360 mm corresponds to outermost radius/ extraction).

For this procedure, automatic routines were adapted to test cell commissioning, which are already used during clinical cyclotron operation on-site. This allows an improved data collection and comparability at different stages of beam commissioning as well as between different cyclotrons in the test cells.

CONCLUSION AND OUTLOOK

Several improvements of the cyclotron factory tests and commissioning process have been presented. This comprises hardware changes as well as an improvement of test processes to make the commissioning process faster, more reliable, and enhance the robustness of test results. For the future, further improvements are currently being planned. Among others, one very promising approach is to perform beam commissioning and optimization using pulsed RF instead of continuous wave operation. By doing so, beam commissioning would become independent of stable RF conditions at higher powers, where the actual RF conditioning is done automatically overnight. First test runs have successfully been carried out and show comparable results of measured beam properties.

REFERENCES

[1] A. Geisler, “Status report of the ACCEL 250 MeV medical cyclotron”, in *Proc. 17th Int. Conf. on Cyclotrons and their Applications (Cyclotrons'04)*, Tokyo, Japan, Oct. 2004, paper 18A3.

[2] H. U. Klein *et al.*, “New superconducting cyclotron driven scanning proton therapy systems”, *Nucl. Instrum. Methods Phys. Res., Sect. B*, vol. 241, no. 1–4, pp. 721-726, Dec. 2005. doi:10.1016/j.nimb.2005.07.123

[3] J. W. Kim, “Effects of vertical misalignment of superconducting coils in cyclotrons”, *AIP Conf. Proceedings*, vol. 600, no. 1, pp. 405-407, 2001. doi:10.1063/1.1435289

ISBN: 978-3-95450-205-9 doi:10.18429/JACoW-Cyclotrons2019-TUP019

RECENT EXTENSIONS OF JULIC FOR HBS INVESTIGATIONS

O. Felden, N. Demary, N.-O. Fröhlich, R. Gebel, M. Rimmler, Y. Valdau
Forschungszentrum Jülich, IKP-4, Germany

Abstract

At the Forschungszentrum Jülich (FZJ) the energy variable cyclotron JULIC is used as injector of the Cooler Synchrotron (COSY) and for low to medium current irradiations of different types. Recently a new target station was set up and is mainly used for tests of new target materials, neutron target development and neutron yield investigations with high power proton or deuteron beam in perspective of a high brilliance accelerator based neutron source (HBS) with the Jülich Centre for Neutron Science (JCNS). Beside this, ToF-experiments are performed to investigate and optimize the pulsing structure for HBS. The target station is installed inside an Experimental area close to the cyclotron bunker, offering space for complex detector and component setups for nuclear and neutron related experiments. It is used for other purposes like electronic or detector tests and irradiation as well. This report briefly summarizes the history of JULIC and the activities for its future perspectives.

INTRODUCTION

The Institute for Nuclear Physics (IKP) [1] is focusing on the tasks given by the Helmholtz Association (HGF). This comprises the design and preparations for the High Energy Storage Ring (HESR) of FAIR [2] with the PANDA experiment. The hadron physics program at the Cooler Synchrotron COSY exploits the internal experimental setups PAX, KOALA and the PANDA Cluster-Jet Target Development. The Jülich Electric Dipole Moment Investigation project (JEDI) [3] profits from the availability of polarized beams from the injector cyclotron and the unique capabilities and experiences at the COSY facility. The extracted beam is used for the PANDA experiment, detector tests and for high-energy irradiation in the area of the finished TOF experiment. The JESSICA and Big Karl-Experiment areas are also used with extracted beam for other FAIR related detector tests and developments like CBM, e.g., Fig. 1 presents the layout of the COSY facility with the JULIC cyclotron and the experimental areas.

The COSY accelerator facility [4], operated by the Institute for Nuclear Physics at the Forschungszentrum Jülich, consists of the injector cyclotron JULIC and the Cooler Synchrotron COSY. Both accelerators are originally dedicated to fundamental research in the field of hadron, particle, and nuclear physics, to study the properties and behaviour of hadrons in an energy range that resides between the nuclear and the high energy regime. Operation of the cyclotron JULIC started 1968 and it provides mainly 45 MeV H^- respectively 76 MeV D^- with beam currents up to ~10 μA.

Within the framework of the High Brilliance neutron Source project [5], Jülich is developing a scalable pulsed accelerator-based neutron source capable to support the large scale facilities and provide an efficient network of small and medium neutron sources throughout Europa.

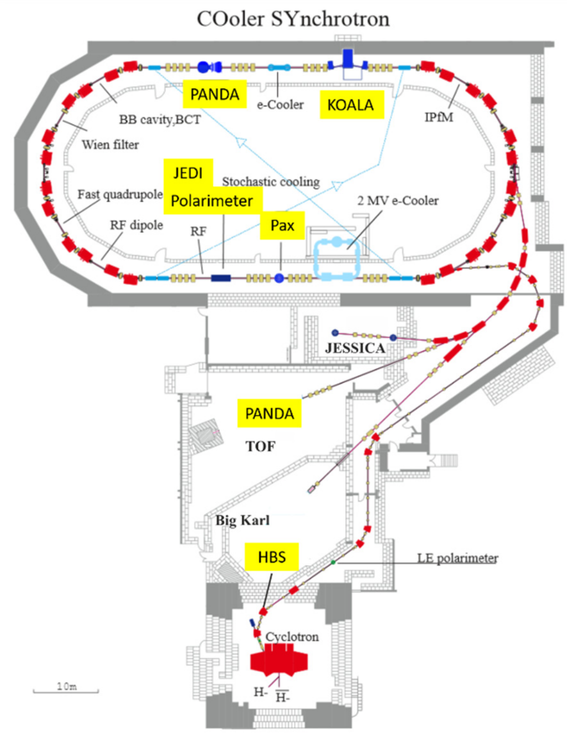

Figure 1: Layout of the COSY facility with the new beamline from the cyclotron into the Big Karl Experiment area

The HBS JULIC Neutron Platform is going to be installed at the Big Karl experimental area aside the JULIC cyclotron providing experimental space for the development, testing and operation of components of pulsed accelerator based neutron sources within the HBS project together with the Jülich Centre for Neutron Science. Figure 2 shows the planned experimental setup in Big Karl-area.

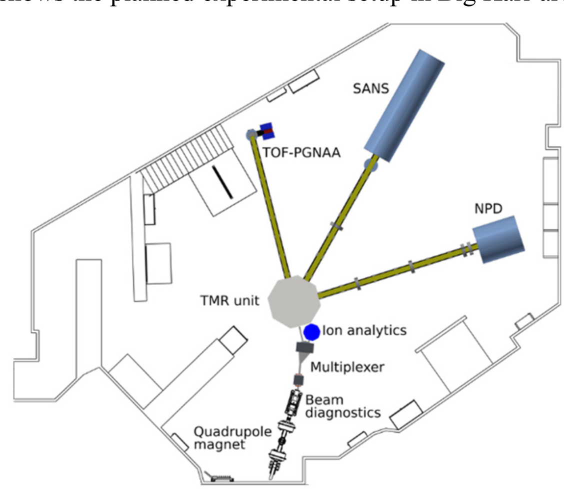

Figure 2: Planned experimental setup in Big Karl area.

ISBN: 978-3-95450-205-9 doi:10.18429/JACoW-Cyclotrons2019-TUP019

It further allows the design, construction and operation of basic scientific neutron scattering and neutron analytic instruments for development, training, education and research in collaboration with university groups and industry.

CURRENT STATUS OF HBS ACTIVITIES

For experiments related to the HBS project, a dedicated beam line at the JULIC cyclotron at the COSY facility has been finalized (Fig. 3).and is shown later in the text. It is in use since beginning of 2019 in the Big Karl area.

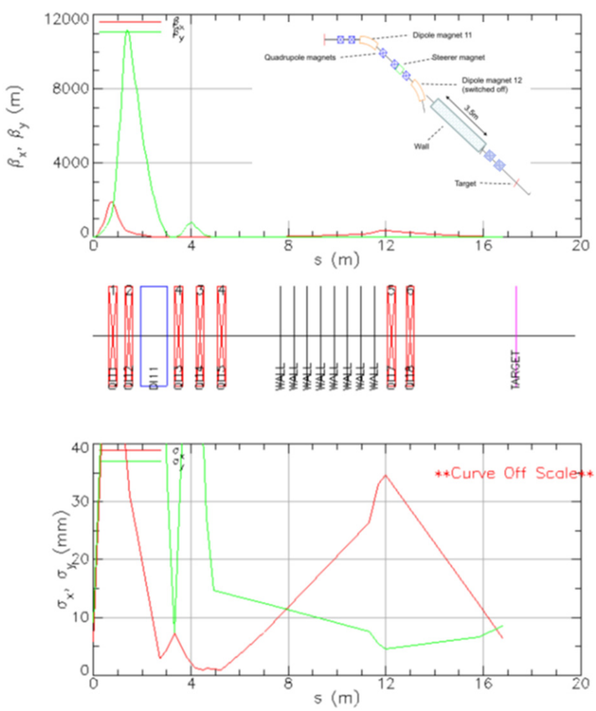

Figure 3: Beamline to Big Karl area. The figure shows the simulation results of transport calculations starting at the cyclotron, passing the shielding wall as well as the quadrupole setup.

At this beamline, experimental validations of cross section measurements and component tests for the HBS target development are being performed and will be used further for such experiments.

The needed proton and deuteron energies are obtained by use of an energy degrader providing fixed energies of 10, 20, 30 and 40 MeV for both species (Fig. 4) and enabling fast switching between these energies instead of changing the working point of JULIC. The frameless energy degrader is made from graphite giving maximum beam spots of 15 mm reducing halo particles. The necessary material thicknesses to obtain the different energy degradations have been calculated with SRIM [6] and checked with Bragg Peak-measurements of the protons respectively deuterons penetrating into PMMA using GAFchromic® films (Fig. 5).

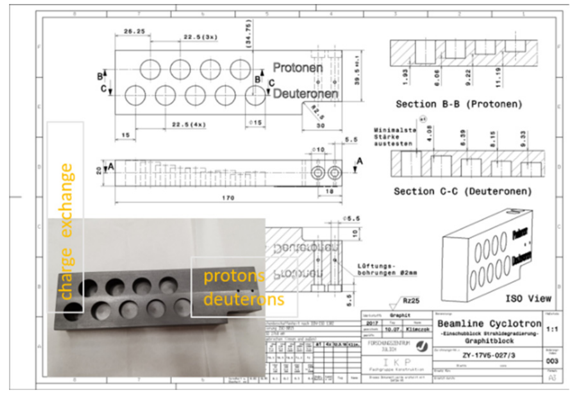

Figure 4: Frameless energy degrader made from graphite.

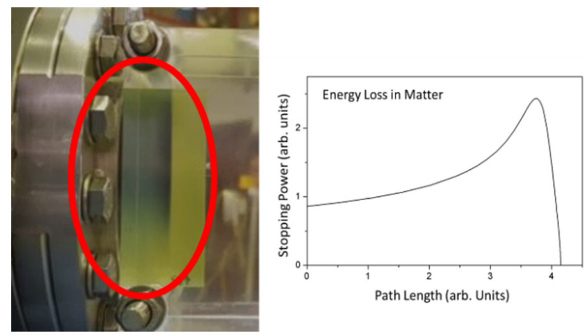

Figure 5: Determination of the proton energy by measurement of penetrating depth into PMMA using GAFchromic® films and comparison with SRIM-calculation.

To reduce the neutron background at the detector setup in the Big Karl-area the degrader is installed inside the Cyclotron bunker right behind the cyclotron exit. The protons and deuterons are deflected by ~30° with a dipole magnet into the Big Karl Experiment area while the neutrons, produced inside the graphite are going straight and will be stopped in the bunker shielding walls (Fig. 6).

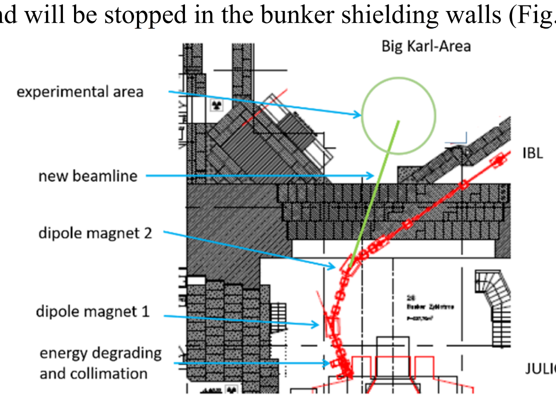

Figure 6: Beamline into Big Karl area with energy degrader and dipole magnets inside the cyclotron bunker.

For safety reasons two beam stops are installed inside the bunker, which can be used as faraday cups for beam current measurement as well. Inside the Big Karl-area beam current is measured with a Bergoz Fast Current Transformer (FCT) [7, 8] and on the target directly.

ISBN: 978-3-95450-205-9 doi:10.18429/JACoW-Cyclotrons2019-TUP019

Beam profile measurements (see Fig. 7) with a Multi Wire Proportional Chamber (MWPC) is used for optimizing the beam spot on target regarding to the experimental needs.

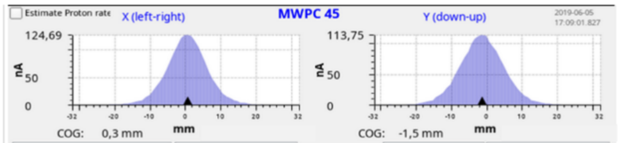

Figure 7: Beam profile at Big Karl target station. The beam size shown is ~15 mm FHWM.

Beam position is measured in both X and Y planes with a capacitive Beam Position Monitor System (BPM) [9, 10] (Fig. 8) utilizing four electrically isolated electrodes. Signal processing is done with preamplifiers FEMTO DHPVA-201 and lock-in-amplifiers Stanford Research SR844 [11] and data recorded via EPICS IOCs [12]. Newly developed graphical user interfaces based on Control System Studio (CSS) [13] allow for display of measured beam orbit and currents.

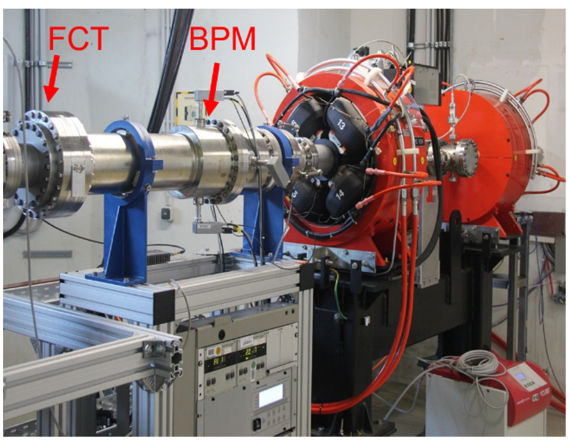

Figure 8: Beamline inside Big Karl area with Beam Position Monitor System (BPM) and Fast Current Transformer (FCT).

The current permission for the radiation controlled area limits the operation to beam intensities of up to 10 nA. The area is going to be upgraded to the capabilities of the cyclotron.

Based on the routine parameters of the proton and deuteron beams offered by the JULIC the cyclotron can be used efficiently as part of a pulsed neutron source as in the concept for the NOVA ERA [14] or as existing accelerator based neutron facilities in Japan [15].

The pulsing scheme for proton beam of duration between 10 to 50 µsec has been realized

FUTURE ACTIVITIES

Based on the existing experimental station of the HBS project at the Big Karl area a prototype of the HBS target-moderator-reflector (TMR) assembly is intended. This assembly will allow to develop further the compact neutron source concept with regards to targetry, neutron provision, moderator development and optimization of the TMR unit. Tests and developments of target handling, target cooling systems, biological shielding and any other development to improve neutron provision will be made possible. In addition, proton beam transport devices, beam control and dynamics, beam multiplexing or beam dump systems will be installed and tested at the platform. The multiplexer system, consisting of a fast kicker (see Fig. 9), deflects the beam up to 40° into a dedicated septa magnet, guiding the beam to three target stations is actually under construction at IKP and will be mounted in 2020.

The new platform allows designing, constructing and operating versatile neutron instruments for neutron scattering purposes as well as neutron analytics with competitive neutron flux. Shielding and Radiation protection calculations to run with 10 µA into the Big Karl-Area and per-mission process are in preparation.

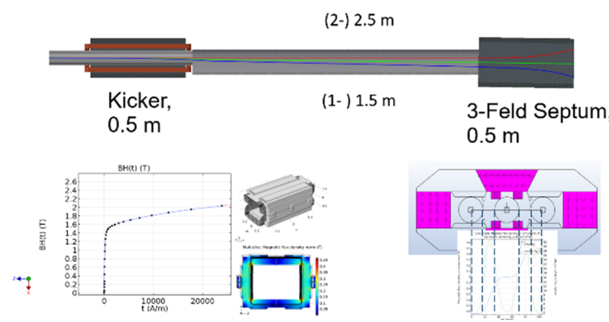

Figure 9: Multiplexer configuration with a fast kicker and a septa-magnet.

Taking into account possible upgrades of the beam current of the JULIC cyclotron up to 10 µA beam power up to 30 W are achievable, as listed in Table 1. This upgrade would promote the JULIC Neutron Platform in beam power and neutron flux an order of magnitude above current operated compact accelerator based neutron (CANS) facilities. It will allow for a full test of individual HBS structures including proof-of-principle experiments of components and performance tests of potential neutron scattering and analytic instruments an extension of the current installed experimental possibilities for HBS at the Big Karl area is in-tended. This extension will lead to a versatile platform for the operation and development of compact accelerator based neutron sources with dedicated neutron instrumentation used also by universities and industry for training, development and scientific service.

Table 1: Parameters of the JULIC Neutron Platform

Description	**Proton**	**Deuteron**
Energy [MeV]	45	76
Current [µA]	10	10
Duty cycle [%]	4	4
Peak power [W]	450	760
Average power [W]	18	30

CONCLUSION

Using the JULIC cyclotron, it is possible to demonstrate a small accelerator-based neutron source with protons or deuterons in the energy range from 10 MeV to 45 MeV

ISBN: 978-3-95450-205-9 doi:10.18429/JACoW-Cyclotrons2019-TUP019

(76 MeV for deuterons) at COSY. This allows testing and developing critical components for the HBS project. In addition, it can provide access to neutron beam time for research and industry and with the expected performance of the neutron source at JULIC it is a unique option to strengthen the research with neutrons at the Forschungszentrum Jülich with the local universities, research institutions and industry.

REFERENCES

[1] Institute for Nuclear Physics, Forschungszentrum, Jülich, http://www.fz-juelich.de/ikp/en

[2] FAIR, GSI, http://www.gsi.de/fair

[3] http://www.collaborations.fz-juelich.de/ikp/Jedi

[4] R. Maier, "Cooler synchrotron COSY – performance and perspectives", *Nucl. Instr. Methods Phys. Res., Sect. A*, vol. 390, pp. 1-8, May 1997. doi.org/10.1016/S0168-9002(97)00324-0

[5] U. Rücker *et al.*, "The Jülich high-brilliance neutron source project", *Eur. Phys. J.*, vol. 131, Jan. 2016. doi.org/10.1140/epjp/i2016-16019-5

[6] SRIM - The stopping and range of ions in matter, http://www.srim.org/index.htm

[7] Y. Valdau *et al.*, "Development of high resolution beam current measurement system for COSY-Jülich", in *Proc. IBIC'16*, Barcelona, Spain. doi:10.18429/JACoW-IBIC2016-TUPG41

[8] *Bergoz Instrumentation, Fast Current Transformer, User's Manual, Rev. 3.1*, 2015. devices 3272 and 3273 FCTCF10"-147.6-40-UHV-5.0-CAW. https://www.bergoz.com

[9] J. Biri *et al.*, "Beam position monitor electronics at the cooler synchrotron COSY Jülich", *IEEE Trans. Nucl. Sci.*, vol. 41, no. 1, pp. 221-224, Feb. 1994. doi:10.1109/23.281493

[10] R. Maier *et al.*, "Non-beam disturbing diagnostics at COSY Jülich", *EPAC'90*, Nice, France, June 1990, pp. 800-802.

[11] *Stanford Research Systems, User manual*, "Model SR844 RF Lock-In Amplifier", rev. 2.9, USA, 2016. https://www.thinksrs.com/downloads/pdfs/manuals/SR844m.pdf

[12] Experimental Physics and Industrial Control System (EPICS), http://www.aps.anl.gov/epics

[13] Control System Studio Webpage, http://controlsystemstudio.org

[14] Eric Mauerhofer *et al.*, "Conceptual design report - NOVA ERA (Neutrons Obtained Via Accelerator for Education and Research Activities) - A Jülich high brilliance neutron source project", volume 7 of Schriften des Forschungszentrums Jülich Reihe Allgemeines / General. Forschungszentrum Jülich GmbH Zentralbibliothek, Verlag, Jülich, 2017.

[15] Y. Kiyanagi, "Jcans network of compact neutron facilities in Japan", *Eur. Phys. J.*, May 2016. doi:10.1140/epjp/i2016-16132-5

ISBN: 978-3-95450-205-9 doi:10.18429/JACoW-Cyclotrons2019-TUP020

BEAM PROPERTIES AT THE EXPERIMENTAL TARGET STATION OF THE PROTON THERAPY IN BERLIN

J. Bundesmann†, A. Denker[1], J. Holz auf der Heide
Helmholtz-Zentrum Berlin für Materialien und Energie, Berlin, Germany
[1]also atBeuth University of Applied Sciences Berlin, Berlin, Germany

Abstract

Beside the therapy station for ocular tumours, we have an experimental area for irradiations with protons and other ions either in air or in vacuum. The beam spot can be focused to a diameter of 1 mm in air. For larger homogeneous irradiated areas, we can use beam scanning with up to10 nA spot current. If scanning is not possible due to experimental needs, scattering foils are used.

For protons, the energy can be set to a mono-energetic beam of 68 MeV or to spread-out Bragg peaks with a mechanical range shifter. Very quick energy changes are achieved by absorber plates to reduce the energy.

THE EXPERIMENTAL AREA

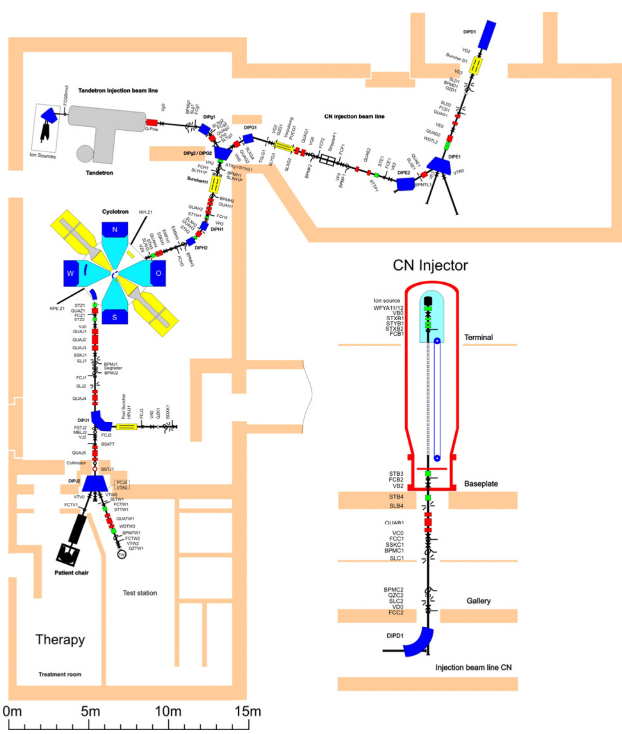

Figure 1: Layout of the accelerators and target stations.

The experimental area is located just beside the installation for the treatment of ocular tumours (Fig. 1). Thus, the beam as used for therapy can be brought to the target station in short time by switching the last dipole magnet in the beamline. The standard therapy beam is a quasi-DC 68 MeV proton beam with a beam size of 40 mm in diameter and a very homogenous beam profile (see Fig. 5). The beamline in the experimental area also permits to focus the beam down to a diameter of 1 mm.

†bundesmann@helmholtz-berlin.de

As from beam time to beam time slight changes in the settings of the beam line were needed to obtain the same beam position on target, the beam line settings were recalculated: Instead of a focal point between two quadrupole triplets the beam is now kept parallel at this position. With this setting, only tiny adjustments are needed on the last elements in the beamline to compensate slight differences when extracting the beam from the cyclotron.

Different settings for experiments are possible: The beam can be extracted in air via a thin Kapton foil and the samples to be irradiated are mounted on a xy table with a stroke of 50 cm and a positioning precision of 0.1 mm. The maximum weight for the samples is 50 kg. Large and sensitive objects can be irradiated: The largest sample was a painting with a size of 1 m × 1.4 m. Behind the xy table is a 2 m long optical bench. This is used mainly for irradiations in vacuum in order to avoid scattering of the beam in air.

The samples are aligned on the beam line axis with the help of an adjusted Laser system. The proton intensity is measured on-line using an ionisation chamber of PTW Freiburg. Radiation safety limits the quasi-DC proton beam intensity to about 10 nA in the experimental area. For most experiments this is largely sufficient.

BEAM SIZE ADAPTATION

The two-dimensional distribution of the beam is measured using a CCD camera with an x-ray converter foil (Sensicam QE from PCOAG). The resolution of the camera is 50 µm per pixel. For a quick determination of the beam spot, films are used.

Widening of the Beam Using a Scanning System

For higher proton intensities and passive irradiations a scanning system may be used. The scanning system consists of two scanners: a 21 cm long y-scanner, 5 cm distance, and a 21 cm long x-scanner. Settings of the power supplies for the scanning system is done with a LabView code.

This code also corrects for influences of the scanning frequency on the current of the power supplies and for the geometric differences due to the fact that the scanners are in different positions on the beam axis. To define the irradiation field, the user can choose between various functions, repetition rates, and distances of the scan lines. The user also has to define the shape of the beam spot, which was determined using a quartz, a film or the CCD camera. The dose distribution for the chosen parameters is then simulated and visualised. Figure 2 shows in the top row two different shapes of a focused beam. Identical settings

ISBN: 978-3-95450-205-9 doi:10.18429/JACoW-Cyclotrons2019-TUP020

of the scanners would lead to different homogeneities of the simulated dose distribution.

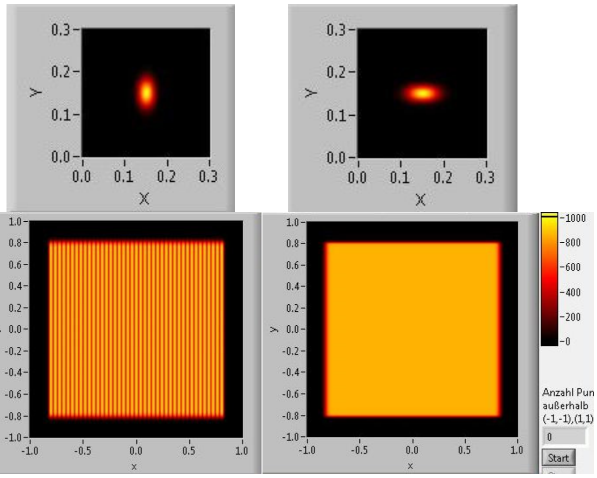

Figure 2: The top row shows two different beam spots used for scanning. The simulated dose distribution for identical settings of the scanner is shown in the lower row.

Using the scanning system together with an aperture, homogenous dose distributions with sharp lateral fall-offs can be produced. In the example shown in Fig. 3 the dose varies less than 5% over the 20 mm of the aperture width.

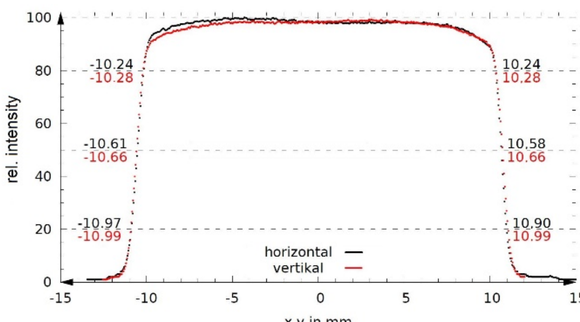

Figure 3: Line scan in x and y of a scanned irradiation field with a quadratic aperture having 20 mm edge length [1].

Besides rectangular or quadratic irradiation fields, irregular fields can be created (Fig. 4). The field size is about 30 mm x 30 mm at the position of the xy table. The maximum size depends on the position of the sample with respect to the scanning system.

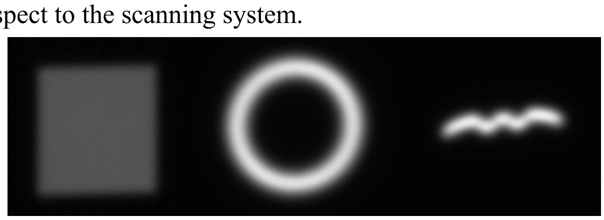

Figure 4: CCD images of the proton beam using the scanning system. Rectangular, circular or irregular shapes are feasible.

However, for devices which are actively tested, the beam size has to be adapted in a different way to avoid interplay effects when the proton beam scans over the internal structures of the devices.

Widening of the Beam by Scattering Foils

For the therapy of ocular melanomas the beam is widened by a 50 µm thick Ta-foil about 8 m upstream of the isocentre. About 90% of the extracted proton beam is thus lost, but the result is a very homogenous distribution (see Fig. 5).

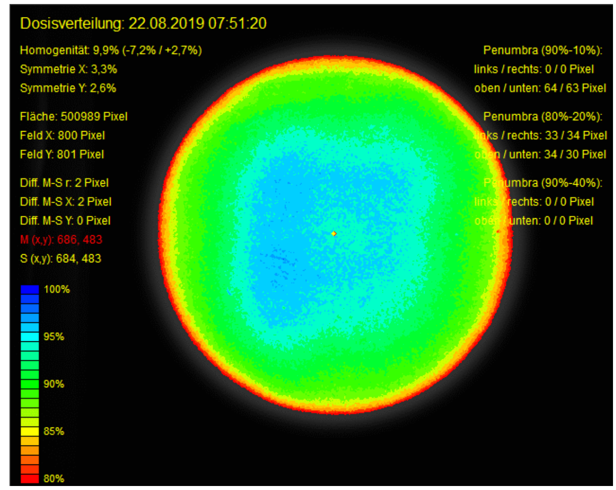

Figure 5: CCD image in false colours of the proton beam using the scattering foil upstream, showing a very homogenous dose distribution.

The same foil can be used for the experimental target area, providing a beam diameter of 50 mm. The irradiation area is set using a pair of slits in x and y for rectangular samples or adequate apertures are used for round samples. This reduces activation of the samples. However, for small devices needing high proton intensities the beam losses and activation of slits or apertures are not negligible. In addition, for radiation hardness tests variations of the beam homogeneity of 10% are acceptable.

For this reason, a second scattering system (Fig. 6) was installed in the beamline 1 m upstream of the target position. Using SRIM [2], the required foil thickness for various beam diameters have been estimated, making simplifications on the start parameters of the beam on the foil. The foils were mounted on a moving mechanism. A quartz on the moving mechanism allows to check the size and position of the proton beam.

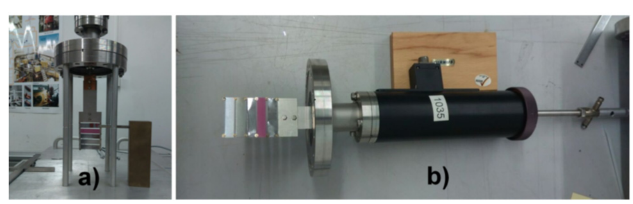

Figure 6: Adjustment unit for positioning of the foils on the beam line axis (a), moving mechanism with three different foils and a ruby quartz.

The beam size for the different scattering foils was measured using the CCD camera (see Fig. 7). Using the software Image – ProPlus an intensity profile from the grey values of the images was calculated and compared to the estimations by SRIM (Table 1).

ISBN: 978-3-95450-205-9 doi:10.18429/JACoW-Cyclotrons2019-TUP020

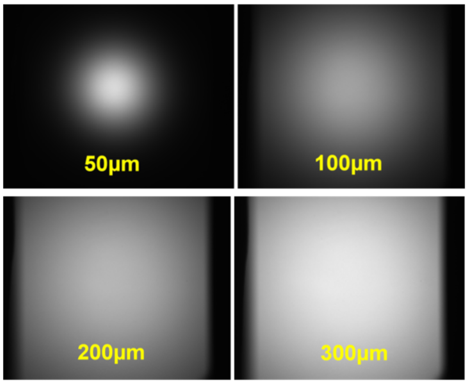

Figure 7: CCD images of the full beam spot using different scattering foils. For 200 µm and 300 µm thickness, the overall beam spot is larger than the entrance aperture of the CCD camera.

Typical dimensions of solar cell samples or electronic components are less than 20 mm in one direction. Thus, the 100 µm foil together with a corresponding aperture is used to confine the irradiation field to 20 mm in diameter. The transmission using an aperture was measured and is 35%. For this beam size the gain in intensity is about a factor 20 compared to the scattering system 8 m upstream.

Table 1: Comparison of the Beam Diameter with Intensity Variations of 80% to 100%. The Error for the Diameter is Estimated to be About ±1 mm

Foil Thickness	Diameter (SRIM)	Diameter (measured)
50 µm	9 mm	10 mm
100 µm	14 mm	20 mm
200 µm	22 mm	31 mm
300 µm	28 mm	40 mm

ENERGY VARIATION

Our standard beam is the 68 MeV proton beam used for therapy. A change of the setting of the accelerators in order to achieve a different energy takes at least 4 hours, mainly due to the ramping time of the main magnets of the cyclotron. In most cases, especially for radiation hardness tests, a mono-energetic beam is not necessary. Thus, for quick changes in energy, aluminium plates of different thicknesses are introduced in the beam path. The final energy is determined with a special Multi-Leaf Faraday cup [3].

EXAMPLES

Radiation Hardness Tests

The experimental area is used mainly for dosimetry and radiation hardness tests. Besides experiments for the German Space Agency DLR, solar cells [4, 5] for space applications are irradiated. These require comparable high proton doses of 10^{11}-10^{13} protons/cm², while the irradiation time should not exceed an hour. Depending on the experimental needs, JV-curves are acquisitioned or the proton induced currents is measured in-situ.

PIXE and PIGE

Small beam spot sizes and intensities are needed for material analysis with Proton Induced X-ray Emission (PIXE) and Proton Induced γ-ray Emission (PIGE) [6]. Especially for light elements in a heavy matrix, PIXE provides information of the material composition close to the surface, while PIGE yields information from larger depths. For a good lateral resolution, the beam diameter is focused to 1 mm. The proton beam intensities are below 0.1 pA. Silver coins from the Münzkabinett (museum for coins and medals) in Berlin have been investigated [7].

CONCLUSION

The experimental area is a flexible, versatile room which permits the irradiation of sensitive and large objects. The beam intensity is varied between 10^3 protons/sec up to 10^{10} protons/sec. The time structure of the beam ranges from a quasi-DC beam, where the cyclotron frequency defines the repetition rate, over pulse trains to single pulses. The possible beam size ranges from 1 mm up to 50 mm in diameter. Very homogenous dose distributions can be provided employing either the scanning system or the scattering foil used for therapy. Using the second scattering system, 10^{13} protons/cm² can be applied within less than one hour with acceptable losses in homogeneity.

REFERENCES

[1] N. Bernt, "Erzeugung und Messung von komplexen zweidimensionalen Protonenfeldern", Bachelor thesis, TU Berlin, p. 30, 2015.

[2] SRIM, `https://www.srim.org`

[3] S. Seidel, J. Bundesmann, T. Damerow, A. Denker, C. S. G. Kunert, and A. Weber, "A multi-leaf faraday cup especially for proton therapy of ocular tumors", in *Proc. 21th Int. Conf. on Cyclotrons and their Applications (Cyclotrons'16)*, Zurich, Switzerland, Sep. 2016, pp. 118-120. doi:10.18429/JACoW-Cyclotrons2016-MOE02

[4] F. Lang *et al.*, "Radiation hardness and self-healing of Perovskite solar cells", *Adv. Materials*, vol 28, pp. 8726–8731, Aug. 2016. doi:10.1002/adma.201603326

[5] F. Lang *et al.*, "Efficient minority carrier detrapping mediating the radiation hardness of triple-cation perovskite solar cells under proton irradiation", *Ene. Env. Science*, vol. 12, pp. 1634-1647, 2019. doi:10.1039/c9ee00077a

[6] A. Denker, *et al.*, "Non-destructive analysis of coins using high-energy PIXE", *Nucl. Instrum. Methods Phys. Res., Sect. B.*, vol. 226, pp. 163-171, Nov. 2004. doi:10.1016/j.nimb.2004.03.015

[7] S. Röhrs *et al.*, "A study of medieval polish denars of the piast dynastry – alloy composition and determination of surface deposits by a multi-analytical methodology", Jahrestagung der Archäometrie und Denkmalpflege, Wien Austria, Sep. 2019.

ISBN: 978-3-95450-205-9 doi:10.18429/JACoW-Cyclotrons2019-TUP021

TOWARDS FLASH PROTON IRRADIATION AT HZB

G. Kourkafas*, J. Bundesmann, A. Denker, T. Fanselow, J. Roehrich
Helmholtz-Zentrum Berlin für Materialien und Energie (HZB), Berlin, Germany
V. H. Ehrhardt, J. Gollrad, J. Heufelder, A. Weber, Charité – Universitätsmedizin Berlin, Germany

Abstract

The HZB cyclotron has been providing protons for eye-tumor treatment for more than 20 years. While it has been very successful using conventional dose rates (15-20 Gy/min), recent studies indicate that rapid irradiation with very high dose rates (FLASH) might be equally efficient against tumors but less harmful to healthy tissues. The flexible operation schemes of the HZB cyclotron can provide beams with variable intensities and time structures, covering a wide unexplored regime within the FLASH requirements (>40 Gy/s in <500 ms). This paper presents the results of the first FLASH beam production at HZB towards the establishment of an in-vivo clinical irradiation in the future.

INTRODUCTION

The cyclotron of Helmholtz-Zentrum Berlin (HZB) in Germany has been providing protons for the treatment of ocular tumors to more than 3600 patients since 1998, with a local tumor control of 96% five years after the treatment [1]. However, according to recent studies, side effects to healthy nearby tissues may be significantly reduced by using high dose-rate FLASH irradiation [2].

In short, the FLASH scheme utilizes much higher dose rates in much shorter irradiation times compared to conventional radiotherapy — regardless of the type of radiation being used. With its exact specifications not yet universally acknowledged, most studies categorize an irradiation of more than 40 Gy/s within 500 ms or less into the FLASH regime. Under these conditions, the normal cells appear to experience an equivalent dose of ~70% with respect to the dose received by the tumorous cells (1.4 dose-modifying factor), sparing thus selectively healthy tissues from radiation damage and enabling higher dose delivery to the tumor [3]. The underlying biological mechanism as well as the optimal irradiation parameters are still under investigation.

Different institutes worldwide are currently trying to test this new radiotherapy concept and prove its potential benefits. The first application to a human was recently conducted on a skin tumor using a 5.6 MV electron linac, which generated 15 Gy in 90 ms, delivered in 10 pulses of 1 µs each with a 100 Hz repetition rate [4]. Experiments with protons are also under preparation to be applied to small animals using a clinical system [5].

The HZB cyclotron, originally designed for ion experiments requiring various intensities and time structures, is nowadays an ideal machine for testing a broad unexplored regime of the FLASH radiotherapy — even in-vivo. Towards this direction, this paper demonstrates the first FLASH proton-beam production at HZB, the currently feasible parameters and finally the short- and mid-term plans of applying ocular proton irradiation on mice using the FLASH scheme for the first time.

* georgios.kourkafas@helmholtz-berlin.de

MACHINE AND EXPERIMENTAL SETUP

The HZB cyclotron can be operated with two different types of injectors:

- A Tandetron (tandem accelerator), abbreviated as *TT*, which is routinely used for the medical operation due to its increased stability,
- a Van-de-Graaff accelerator, abbreviated as *CN*, which provides bunched beams of higher intensity and is equipped with a fast kicker (pulser) to selectively guide bunches within a specified time window into the cyclotron.

For the standard machine settings, the proton beam extracted from the cyclotron has a kinetic energy of 68 MeV, a repetition rate of 20 MHz and a bunch duration in the order of 5 ns when using the TT injector, or down to 1 ns when using the CN injector. These timescales are negligibly short for radiotherapy — even that of FLASH — meaning that the delivered beam is considered as approximately continuous (quasi-DC). Nevertheless, a pulsing scheme with a time window of at least 50 ns and a repetition rate of up to 2 MHz can be applied when using the CN injector. Regarding the average beam current at the end of the beamline, around 40 nA can be reached with the TT and 10 times more with the CN.

Considering the future plan of irradiating eyes of mice, whose tumors are typically located in a depth of 5 mm from the eye's front surface, a reduced proton energy will be needed at the irradiation target. Therefore, a 16 mm-thick aluminum plate was used as a range shifter between the exit port of the accelerator beamline and the target. In order to block the scattered protons downstream and irradiate only the desired area of the target (a circular field of ~9 mm diameter for mouse eyes), a holder for interchangeable round collimators of different diameter was placed in between. An Advanced Markus® ionization chamber [6], which is indicated for measuring high dose rates, was installed at the target position. A photo of this experimental setup can be seen in Fig. 1. Before and after measuring the dose rate, the dose monitor was replaced by a 12-bit CCD camera to capture the transverse profile of the beam with a resolution of 1280 × 1024 pixels and a scaling of 48 ± 2 µm/pixel.

The above setup was used to measure the delivered dose rate, range (Bragg-peak) and transverse distribution of the quasi-DC proton beam at the target for each injector.

ISBN: 978-3-95450-205-9 doi:10.18429/JACoW-Cyclotrons2019-TUP021

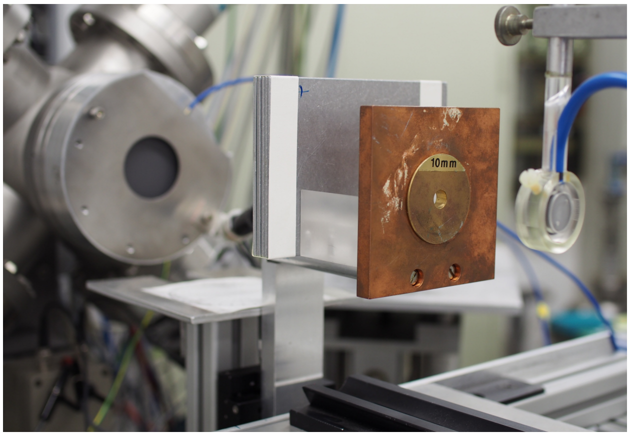

Figure 1: Photo of the experimental setup. The protons travel from left (vacuum beamline exit port) to right (dose monitor with blue cable) in air, while passing through an aluminum plate and a round bronze collimator.

MEASUREMENT RESULTS AND SIMULATION VALIDATION

After setting up the machine to the nominal operation parameters, the beam was centered with steerers and focused with quadrupoles at the target to a round transverse RMS width of ~1 mm, in the absence of the aluminum range shifter/scatterer. After inserting the aluminum plate, the dose rate at the target was recorded, while varying the average beam current with the accelerator's low-energy collimating slits and measuring it with a Faraday cup at the end of the vacuum beamline. The results from both injectors are plotted in Fig. 2. In these first measurements no statistical errors were recorded, but they were observed to be small due to the stability of the accelerator and the dose monitor.

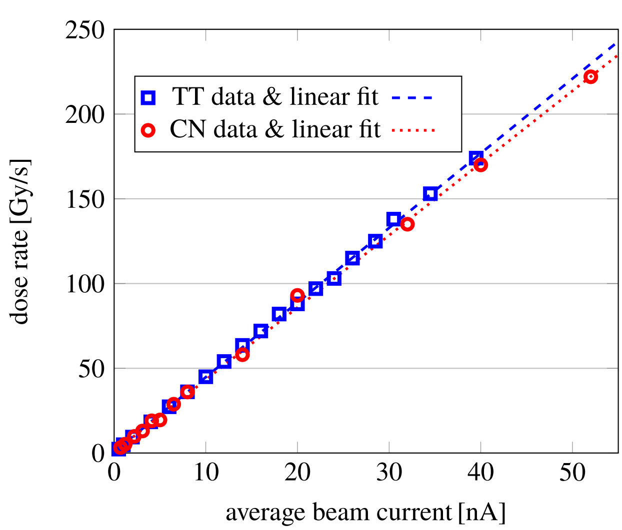

Figure 2: Measured dose rate at the target from each injector.

The measured dose rates indicate that the FLASH requirements can be covered to a wide extent by both injectors. The data show a good linearity with respect to the average beam current and a good accordance between the two injectors. As expected, higher intensities are available with the CN, which provided dose rates even higher that the plotted values (exceeding 1 kGy/s) not shown here due to very short measurement times as a precaution against damaging the involved components and triggering radiation-safety interlocks. Potential saturation and recombination effects of the dose monitor were not taken into consideration, which might imply that the presented data could be underestimated [7].

The measured values were already predicted by calculations and simulations using the LOOKUP code [8]. With the measured beam energy and transverse dimensions at the vacuum port as initial parameters, our experimental setup was simulated to deliver 22.84 MeV protons with an uncollimated transverse RMS width σ = 9.1 mm at the target. At this energy the protons have a mass stopping power S/ρ = 23.4 MeV·cm^2/g and a 5.4 mm penetration depth in water [9]. The dose rate $\dot{D}$ is given by:

$$\dot{D} = \frac{i_p}{A}\frac{S}{\rho}, \tag{1}$$

where i_p is the proton current at the detector's sensitive area A, which corresponds to a 2.5 mm radius in our case and collects only 3.7% of the total beam current for the expected σ, fairly uniformly. As a result, an i_p = 335 pA or a total average beam current of 9.1 nA is required for $\dot{D}$ = 40 Gy/s, in accordance with the measurements. In addition, σ was measured by the CCD camera to be 8.8 ± 0.4 mm.

As a further validation step, the dose monitor was put inside a water phantom and shifted in the direction of the beam in order to measure the Bragg peak. The resulting curve in Fig. 3 shows a good agreement with the simulation, measuring the distal 90% and 80% points at 5.4 mm and 5.6 mm respectively and a 1 mm sharp fall-off between 90% and 10% of the delivered dose.

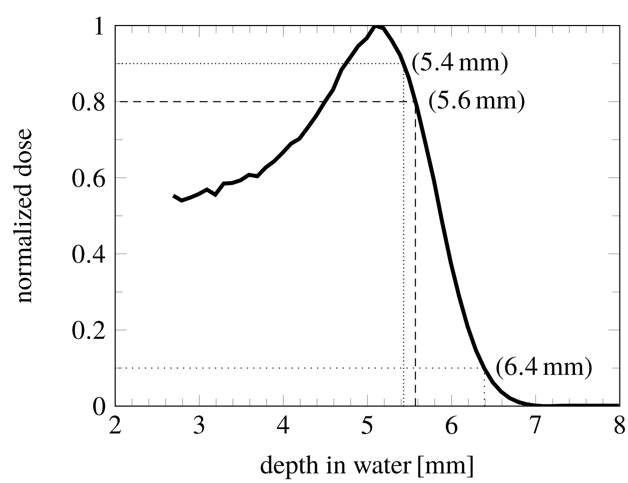

Figure 3: Measured Bragg peak with corresponding distal points in a water phantom for mouse irradiation.

At last, the transverse profile of the beam was captured at the target position after collimation through different apertures. It appeared that a 5 mm diameter aperture yielded a

ISBN: 978-3-95450-205-9 doi:10.18429/JACoW-Cyclotrons2019-TUP021

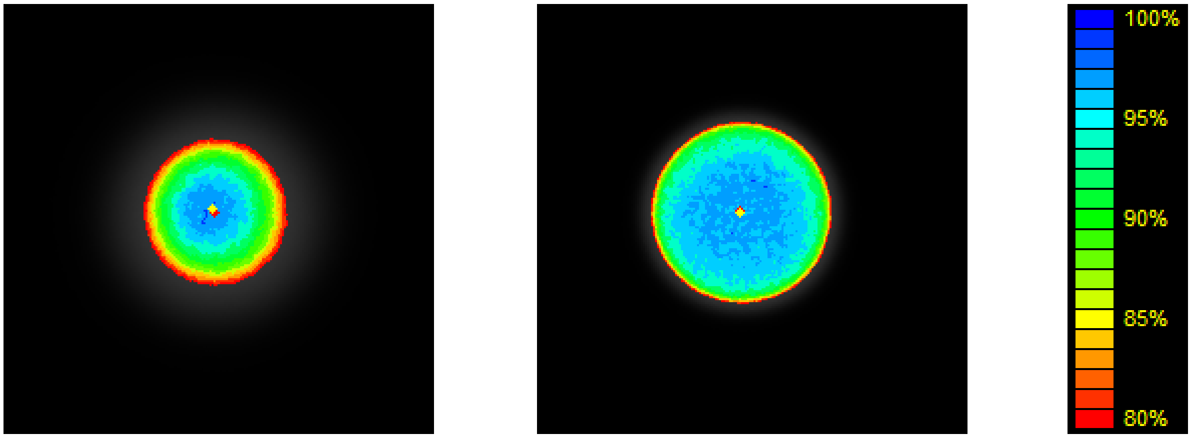

(a) Original setup with 5 mm aperture. (b) Modified setup with 7.6 mm aperture.

Figure 4: Measured normalized intensity of the transverse beam profiles at the target in grayscale, color-contoured between 80%–100%.

circular field of 9.2 mm as desired, but with a lateral width uniformity of 27% (Fig. 4a), which might not meet clinical standards. A much better uniformity of 6% was achieved for a similar field of 9.4 mm by moving the aluminum plate 19 cm upstream and using a 7.6 mm aperture (Fig. 4b). However this position shift reduced the proton intensity within the area of the dose detector by 82% with respect to the original setup using the same aperture, corresponding to an equal dose-rate reduction according to Equation (1). Even in this (far from optimized) case, a clinically acceptable FLASH beam can already be delivered to mice when reviewing Fig. 2.

OUTLOOK

The next steps towards clinical application include optimizing the setup for maximimum dose-rate delivery and lateral width uniformity, while applying an effective modulation scheme for a spread-out Bragg peak. For this purpose a number of components such as a fast transverse beam scanner, double or contoured scatterers and ridge filters are planned to be simulated and tested. From the machine side, a fast beam shutter that allows a precise dose delivery has to be developed and the efficiency of the existing beam diagnostics has to be verified for such short time scales. Moreover, the dosimetry of such intense beams has to be checked for limitations and potential correction models have to be applied. The forthcoming milestone is the first FLASH ocular irradiation of mice in collaboration with the Charité – Universitätsmedizin Berlin.

CONCLUSION

The HZB cyclotron is currently able to deliver FLASH proton irradiation with dose rates of more than 200 Gy/s and flexible pulsing schemes, qualifying as a powerful machine for the investigation of wide unexplored regimes of this promising radiotherapy technique. This first attempt already delivered a clinically usable beam for ocular irradiation of mice, which is under preparation together with Charité in Berlin. After an upcoming optimization of the involved components, further improvements of the reported performance and the first clinical results are expected to be published.

REFERENCES

[1] A. Denker *et al.*, "Status of the HZB Cyclotron", presented at the 22nd Int. Conf. on Cyclotrons and their Applications (Cyclotrons'19), Cape Town, South Africa, September 2019, paper TUC02, this conference.

[2] M.-C. Vozenin, J. H. Hendry, and C. L. Limoli, "Biological benefits of ultra-high dose rate FLASH radiotherapy: Sleeping beauty awoken", *Clinical Oncology*, vol. 31, no. 7, pp. 407-15, 2019. doi:10.1016/j.clon.2019.04.001

[3] J. Bourhis *et al.*, "Clinical translation of FLASH radiotherapy: Why and how?", *Radiotherapy and Oncology*. doi:10.1016/j.radonc.2019.04.008

[4] J. Bourhis *et al.*, "Treatment of a first patient with FLASH-radiotherapy", *Radiotherapy and Oncology*. doi:10.1016/j.radonc.2019.06.019

[5] A. Patriarca *et al.*,"Experimental set-up for FLASH proton irradiation of small animals using a clinical system", *Int. J. Radiat. Oncol. Biol. Phys.*, vol. 102, no. 3, pp. 619–626, 2018. doi:10.1016/j.ijrobp.2018.06.403

[6] PTW-Freiburg, *Ionizing Radiation Detectors*, 2019, p. 17; https://www.ptwdosimetry.com/fileadmin/user_upload/DETECTORS_Cat_en_16522900_12/blaetterkatalog/index.html#page_16

[7] K. Petersson *et al.*, "High dose-per-pulse electron beam dosimetry — A model to correct for the ion recombination in the Advanced Markus ionization chamber", *Med. Phys.*, vol. 44, no. 3, pp. 1157–1167, 2018. doi:10.1002/mp.12111

[8] B. Gottschalk's talks and software archive, https://github.com/maggiemcfee/gottschalk

[9] NIST Standard Reference Database, https://physics.nist.gov/PhysRefData/Star/Text/PSTAR.html

ISBN: 978-3-95450-205-9 doi:10.18429/JACoW-Cyclotrons2019-TUP022

STATUS OF A 70 MeV CYCLOTRON SYSTEM FOR ISOL DRIVER OF RARE ISOTOPE SCIENCE PROJECT IN KOREA*

J.-W. Kim#, J. S. Kang, J. H. Kim, T.S. Shin
Rare Isotope Science Project, Institute of Basic Science, Daejeon, Korea

Abstract

A 70 MeV H^- cyclotron commercially available for medical isotope production will be used as an ISOL driver for rare isotope science project in Korea. The cyclotron is scheduled to be installed in 2021 for beam commissioning in the following year. In fact the building to house the cyclotron is currently almost complete so that the cyclotron system newly contracted needs to fit into the existing building, which brings some challenges in equipment installation and adaptation to utilities. Two beam lines to transport high-current proton beams into ISOL targets have been designed and are described along with other issues associated with the interface of the ISOL system.

INTRODUCTION

A 70 MeV cyclotron system was contracted with a company in May 2017 to be used as the driver of the ISOL system for rare isotope science project (RISP) in Korea [1, 2] and a building to house the system has been constructed since 2017. However, the contract was broken in early 2019 while the building is near completion. A new contract was made with IBA in July 2019 after reviewing the building interface and the design of ISOL beam lines. It was then mutually confirmed no major modification of the present building is needed to accommodate the cyclotron system of IBA [3].

The major parameters of cyclotron are listed in Table 1. The cyclotron size is slightly smaller than the previous one so that minor modifications are sufficient for installation. The primary use of cyclotron will be to provide ISOL target with proton beams in a diameter of 2-5 cm. with a beam power up to 10 kW for RISP. A wobbler magnet will be installed in the cyclotron vault and then the drift length to the target is over 8 m, which may cause some instability of the beam spot at the target.

Table 1: Main Cyclotron Parameters

Item	Value
Beam energy range	30 – 70 MeV
Max. beam current	0.75 mA
Extraction port number	2
Weight	140 tons
Beam size at ISOL target	20-50 mm

*Work supported by Rare Isotope Science Program (RISP) through the National Research Foundation of Korea (NRF) funded by Ministry of Science, ICT and Future Planning (MSIP) (NRF-2013M7A1A1075764)
#jwkim@ibs.re.kr

BUILDING INTERFACE

Construction of the cyclotron building is nearly completed in 2019 with its design fit for the cyclotron of BEST Cyclotron Systems, Inc. [4, 5]. Hence, the building design was checked before the new contract was made whether any major modification of the current building is needed such as new penetration holes on the walls designed for radiation shielding, but no significant work was found.

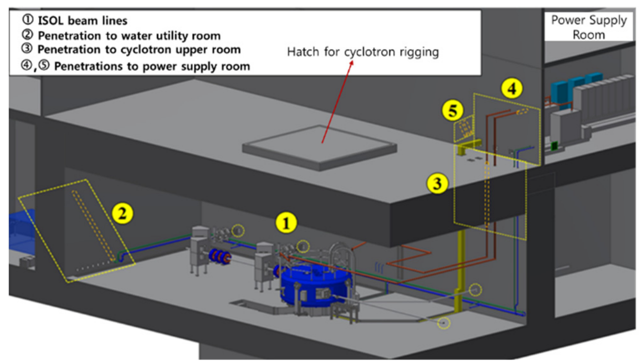

Figure 1: Penetration holes and a hatch in the cyclotron vault and in the upper room. The vault is located in B1. In ④ there are holes for rf transmission line of the final amplifier located in the power supply room, which is not needed for the IBA cyclotron.

The cyclotron will be rigged and installed through the hatch shown in Fig. 1 with one or two cranes anchored outside of the building. Also shown in Fig. 1 are utility connections through the shielding walls, which are grouped into four depending on their usage as denoted. A major difference in cyclotron component is that the final RF amplifier is directly attached to the cyclotron dee rather than placed in the power supply room. Hence, two high-power transmission lines of over 10 m long and their penetration holes are saved.

In the current building, there is no crane inside the vault so that it is expected to have some difficulty during installation and maintenance later. To relieve this issue we plan to install a simple jib crane near the cyclotron, which can also cover some beam line components.

The cyclotron pit was constructed to accommodate the ion source and injection beam line located under the cyclotron, but the IBA system has them on the top of the cyclotron. The lower space will be utilized to house some components such as for vacuum, so it is actually thought to be useful.

The beam loss inside the cyclotron and along the beam line is expected to be less than the loss used for the design of shielding walls. At the maximum current of 750 μA,

ISBN: 978-3-95450-205-9 doi:10.18429/JACoW-Cyclotrons2019-TUP022

the beam delivered to the target vault will be around 700 μA if the loss by the beam collimator is not included. The loss inside the cyclotron by magnetic and gas stripping during acceleration is calculated to be less than 3%.

TWO ISOL BEAM LINES

Two target bunkers are prepared for the ISOL system as shown in Fig. 2 but only one beam line to cave 1 will be extended up to the target during RISP. For high-power beam test the beam will be delivered to cave 2 bombarding a beam dump cooled by flowing water to carry away up to 50 kW at 70 MeV.

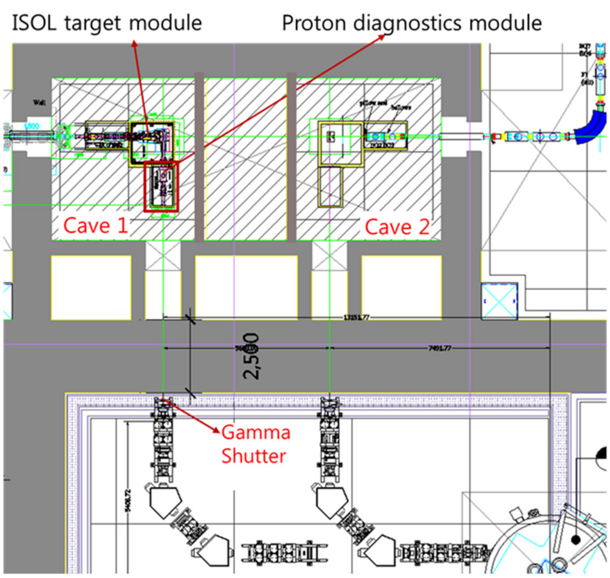

Figure 2: Two caves for the ISOL target. Two modules called as ISOL target and proton diagnostics will be installed with remote handling capability.

A concern in the target room design is the distance between a multi-slice ISOL target and wobbler magnet is over 8 m due to a long tunnel in between. An AC beam formed by the wobbler should travel the distance without any active beam steering component due to high radiation inside the cave, which requires sophisticate remote handling capability for maintenance. As indicated in Fig. 2 only two modules adapted to remote handling will be installed in the cave. Each module has gate valves and pillow seals, which are connected to the upper plate of the module for detachable connections. As a result any jittering of the wobbler can induce significant shift of the beam.

A gamma shutter will be used to enter the cyclotron vault when ISOL target being irradiated stays in the target cave. The ideal location of the shutter is near the wall inside the cave, but then its maintenance is not easy without resorting to complicate remote handling. Therefore the proper location considered is to be close to the wall inside the cyclotron vault as indicated in Fig. 2. A movable thick steel plate in vacuum will be used to shield gamma radiation

Figure 3 shows the layout of three beam components in the diagnostics module. The Faraday cup is retractable while the wire scanner needs to be further evaluated for the maximum beam power density sustainable without direct cooling. The 4-jaw collimator physically shapes the beam with a maximum cooling capacity of 15 kW. In addition, a beam position detector will be needed to monitor the beam shift non-destructively, which is not shown in Fig. 3.

As site acceptance, the beam line in cave 1 will be tested using the components of the diagnostics module and also with radio-chromic film at the target location for beam wobbling with two diameters of 2 cm and 5 cm. The beam jitter, which is worsened by the long drift distance, will be measured. A current plan is to install a collimator in front of target with a maximum power handling of 1 kW to remove stray beam.

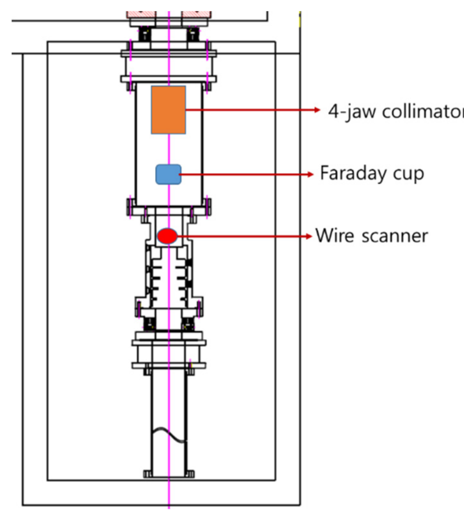

Figure 3: Layout of the proton diagnostics module including three beam components.

ISOLATION OF ISOL TARGET VACUUM

The beam energy of 70 MeV is rather too low to install a beam window to isolate the ISOL target vacuum from the beam line and cyclotron. We plan to use a fast protection valve which can react within tens of ms in case of vacuum failure. However, there is concern of continuous molecular flow during irradiation, which will contaminate the entire system.

A couple of options have been thought to reduce the flow as follows [6]: 1) cold trap using liquid nitrogen, 2) a thin rotating target with vacuum pumping system. Other possibility may be to apply plasma window with a high-voltage system to isolate the vacuum almost non-interactively. Difficulty is a small aperture of a few mm while we need an aperture of over 10 mm. Further consideration including the possibility of plasma window will be made.

ISBN: 978-3-95450-205-9 doi:10.18429/JACoW-Cyclotrons2019-TUP022

CONCLUSIONS

A 70 MeV H^- cyclotron is recently contracted with a new vendor IBA to be used as the ISOL driver. The design of existing building and its interface were reviewed, which are fit with the previously contracted cyclotron system. Especially, utilities, wall penetrations and control system have been checked and no major modification required was found.

The initial design of two beam lines for ISOL targets has been performed also identifying the beam diagnostic components to be located inside the target cave. A long distance between the wobbler and the target may cause some difficulty in the stability of high-power beam. A non-destructive beam position monitor will be used close to the target to compensate for beam jitter, which may cause severe thermal stress problem. A beam collimator will be added in front of the target with a maximum power handling capacity of 1 kW.

The cyclotron system will be delivered to the RISP site in 2021 for installation and beam commissioning will follow.

REFERENCES

[1] J.-W. Kim, Y. Choi, S. Hong, and J. H. Kim, "Plan of a 70 MeV H- Cyclotron System for the ISOL Driver in the Rare Isotope Science Project", in *Proc. Cyclotrons'13*, Vancouver, Canada, Sep. 2013, paper MOPPT015, pp. 64-66.

[2] J. Kang, H. M. Jang, B. Kang, J.-W. Kim, and J. H. Lee, "Status of the ISOL cyclotron system in RISP", in *Proc. Cyclotrons'16*, Zurich, Switzerland, Sep. 2016, pp. 356-358. doi:10.18429/JACoW-Cyclotrons2016-THP22

[3] B. Nactergal *et al.*, "Installation and commissioning of the first Cyclone®70p", in *Proc. Cyclotrons'16*, Zurich, Switzerland, Sep. 2016, pp. 173-174. doi:10.18429/JACoW-Cyclotrons2016-TUP05

[4] V. Sabaiduc *et al.*, "New high intensity compact negative hydrogen ion cyclotrons", in *Proc. Cyclotrons'10*, Lanzhou, China, Sep. 2010, paper MOPCP017, pp. 81-83.

[5] V. Sabaiduc *et al.*, "BEST 70P cyclotron commissioning at INFN LN Legnaro", in *Proc. Cyclotrons'16*, Zurich, Switzerland, Sep. 2016, pp. 241-243. doi:10.18429/JACoW-Cyclotrons2016-TUD04

[6] Private communication with Dr. L. Calabretta of INFN.

ISBN: 978-3-95450-205-9 doi:10.18429/JACoW-Cyclotrons2019-TUP024

MUON CYCLOTRON FOR TRANSMISSION MUON MICROSCOPE

T. Yamazaki*, T. Adachi, Y. Nagatani, Y. Miyake
High Energy Accelerator Research Organization(KEK), 1-1 Oho, Tsukuba, Ibaraki, Japan
J. Ohnishi, A. Goto, RIKEN Nishina Center, 2-1 Hirosawa, Wako, Saitama, Japan
Y. Kumata, S. Kusuoka, T. Onda, H. Tsutsui
Sumitomo Heavy Industries, Ltd., ThinkPark Tower, 1-1 Osaki 2-chome, Shinagawa, Tokyo, Japan

Abstract

A transmission muon microscope is an unprecedented tool which enables its users to reconstruct 3D image of samples such as a living cell. Muons can gain penetrative power as their energy increase, though electrons above 1 MeV start to trigger electromagnetic showers and protons above 1 GeV cause nuclear reactions. Muons accelerated up to about 5 MeV are able to penetrate a living cell (~10 µm), which is impossible with ultra-high voltage (1 MeV) electron microscopes. In order to accelerate muons, efficient acceleration is necessary because the lifetime of muons is only 2.2 µm.

In addition, it is important to accelerate muons without increasing their energy dispersion. Cyclotron with a flat-top acceleration system is the best suited for the transmission muon microscope and is being developed at the J-PARC muon facility (MUSE). In this paper, the transmission muon microscope project and the development of the muon cyclotron will be presented.

INTRODUCTION

Muons at muon beam facilities are generated from pion decays, and these pions are produced via nuclear reactions of a proton beam in a muon production target. The conventional muon beams have been utilized for varieties of sciences such as magnetism study using the µSR (muon spin rotation) technique, non-destructive element analysis from muonic x-ray using a negative muon beam, and so on. However, the beam size of a conventional muon beam is relatively wide ($O(10)$ mm). Development of a high-intensity muon microbeam will open a unprecedented research area using muon microscope (a transmission muon microscope and scanning muon microscope), therefore it is a very important milestone in muon science and materials research.

A high intensity muon beam, so-called "surface muon" beam (4 MeV), is obtained from positive pion decays near the surface of a muon production target, but its energy spread is large (~10 %), which is determined by a momentum bite of bending magnets in the muon beamline. The large energy spread makes it impossible to obtain a muon microbeam due to chromatic aberration. Therefore, we re-accelerate ultra-slow muons to produce a high-intensity muon microbeam. At the J-PARC muon facility (MUSE) [1], ultra-slow muons are generated by laser ionization of a muonium (Mu, a bound state of μ^+ and e^-) [2]. Since muoniums are emitted from a hot tungsten target (2000 K), the initial energy of ultra-slow muons is cooled down to 0.2 eV. We plan to re-accelerate ultra-slow muons up to 5 MeV while keeping its energy spread less than 500 eV ($\Delta E/E = O(10^{-5})$), and then the beam is focused to a muon microbeam using a superconducting lens. The novel positive muon microbeam can be used for a transmission muon microscope. The penetrative power of muons enables us to obtain image of thick sample, such as a living cell (~10 µm).

An AVF cyclotron with a flat-top RF system is adopted to re-accelerate muons. Cyclotron's efficient acceleration is inevitable because the lifetime of a muon is only 2.2 µs. A flat-top RF system is also necessary not to increase energy spread. Ultra-slow muons are first accelerated electrostatically up to 30 keV and then injected into the muon cyclotron and accelerated up to 5 MeV. The muon intensity is about 10^4 /pulse with a repetition rate of 25 Hz. The beam parameters are summarized in Table 1.

Table 1: Beam Parameters

Particle	Positive muon μ^+
Mass	m_μ = 105.6 MeV/c^2
Lifetime	τ_μ = 2.2 µs
Injection	
Number of particles	10^4 /pulse
Repetition rate	25 Hz
Kinetic energy	30 keV
Pulse width	200 ps
Emittance (1σ)	1 π mm mrad
Extraction	
Kinetic energy	5 MeV
Energy width ($\Delta E/E$)	$O(10^{-5})$
Emittance (1σ)	0.1 π mm mrad

BASIC DESIGN OF MUON CYCLOTRON

Toward the installation of the muon cyclotron in FY2020, detailed design of the muon cyclotron has been almost finished and its fabrication is on-going simultaneously. Figure 1 is a schematic of our muon cyclotron. The external structure of the cyclotron is inherited from the HM-10 cyclotron of the Sumitomo Heavy Industries, Ltd., but the internal design is quite different. Major changes are as follows:

- Built-in ion source → external injection,
- installation of a flat-top RF cavity,
- increase of gaps between poles to extract the muon beam.

* takayuki@post.kek.jp

ISBN: 978-3-95450-205-9 doi:10.18429/JACoW-Cyclotrons2019-TUP024

Two acceleration cavities are used and one flat-top RF cavity to supply the 3rd harmonic wave is separately installed in the valley gaps. The remaining valley gap will be used for a muon beam probe. A 5 MeV muon beam is extracted obliquely upward and then bent to a downward direction where a superconducting objective lens, a sample to image, and a camera (muon detector) are placed.

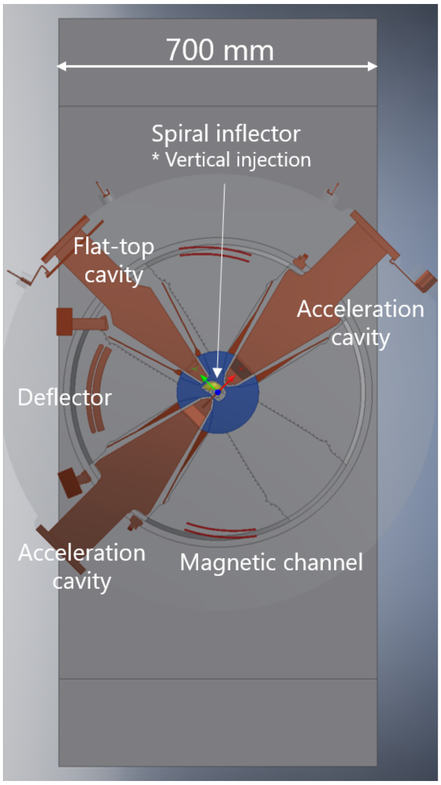

Figure 1: Muon cyclotron.

Parameters of the muon cyclotron are summarized in Table 2. Hill gaps are increased from the HM-10 cyclotron in order to install an electrostatic deflector and a passive-type magnetic channel to extract the muon beam. The RF frequency of the acceleration cavities is 108 MHz. In order to inject a 30 keV muon beam into the cyclotron, a spiral inflector is used.

MAGNET DESIGN

Isochronous condition is severe to suppress energy spread of the muon beam. The phase acceptance of a flat-top RF acceleration using the 3rd harmonic wave is 8.23° to achieve $\Delta E/E = 10^{-5}$. We designed the shape of the magnet using Opera-3D [3]. The 1/4 model implemented in the simulation is shown in Fig. 2. A passive-type magnetic channel is also implemented in the simulation to be used in the calculation of beam extraction.

Figure 3 shows deviation from the isochronous magnetic field and acceleration phase as a function of the radius of a beam orbit. The fluctuation of the acceleration phase is less than 5 % even without passive shimming of the magnet. For fine tuning of the isochronous condition, the magnet

Table 2: Cyclotron Parameters

Magnet	
Average field	0.4 T
Number of magnet sectors	4
Hill gap	54 mm
Valley gap	200 mm
Extraction radius	262 mm
Trim coils	None
RF	
Number of dees	2(main) / 1(flat-top)
Harmonic mode	2
RF frequency	108 MHz
Dee voltage	50 kV
Flat-top RF frequency	324 MHz
Flat-top dee voltage	10 kV
Injection	
Spiral inflector	±4.5 kV
Extraction	
Deflector	±7.5 kV/mm
Magnetic channel	Passive

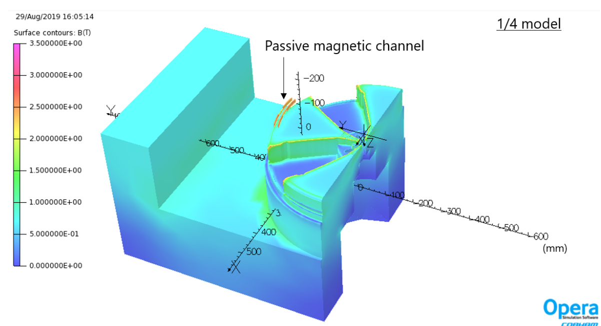

Figure 2: Opera 3D model of the magnet and the magnetic channel.

has shimming plates in the $R > 90$ mm region with a step of $\Delta R = 10$ mm. The thickness of shimming plates can be changed by ±3 mm with a precision of 0.1 mm.

DESIGN OF RF CAVITIES

RF cavities are designed using CST Microwave Studio [4]. The main acceleration cavities are 1/4-wave resonators and connected via a copper bar. Its resonant frequency is 108 MHz and the Q-value is 5400. The dee voltage with 12 kW RF power is shown in Fig. 4. Beam couplers (feeder and pickup) are also designed, and the reflection of the RF power is enough small as shown in Fig. 5.

The flat-top RF cavity to provide the 3rd harmonic wave is a 1/2 wave resonator (Fig. 6) based on an open patent [5]. The Q-value is 5700 and the radial distribution of its voltage is shown in Fig. 4.

ISBN: 978-3-95450-205-9 doi:10.18429/JACoW-Cyclotrons2019-TUP024

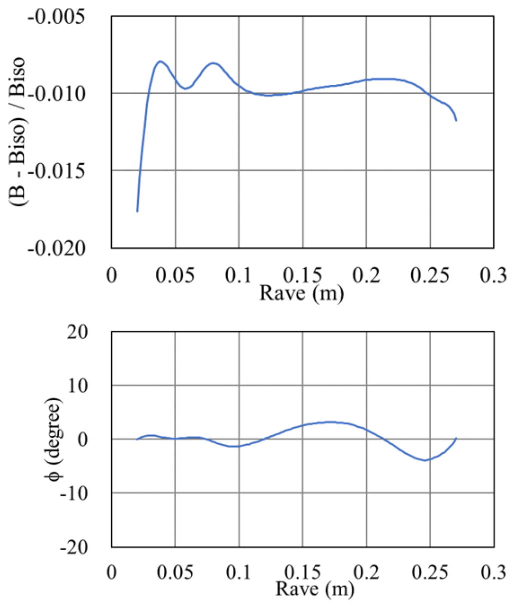

Figure 3: (Top) Deviation from the isochronous magnetic field and (bottom) acceleration phase (bottom) as a function of the radius of a beam orbit.

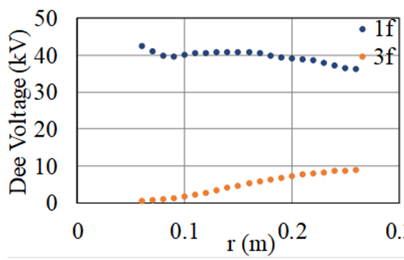

Figure 4: Acceleration voltages of the main (1f) and the flat-top RF (3f) cavities.

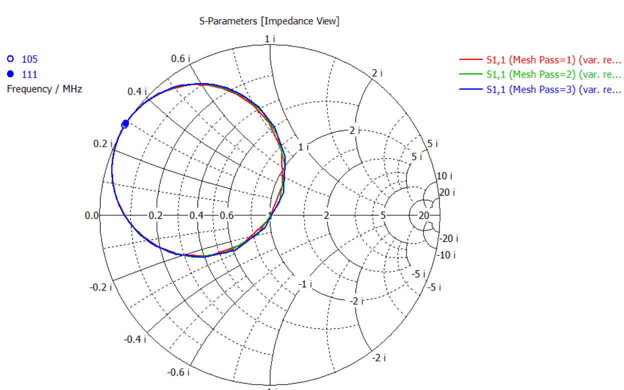

Figure 5: S-parameter (S11) of the feeder of the main acceleration cavity.

SPIRAL INFLECTOR

A spiral inflector is used to inject 30 keV muons vertically into the muon cyclotron. The electric radius of the inflector is 40 mm, and the tilt parameter (k') is -0.42. The magnetic field in the injection region is not constant is the muon cyclotron, therefore the inflector is designed considering the change of the magnetic radius. The gap of the electrodes is 6 mm and voltages of about ±4.5 kV are supplied. The electric field distribution is calculated using Opera-3D (Fig. 7).

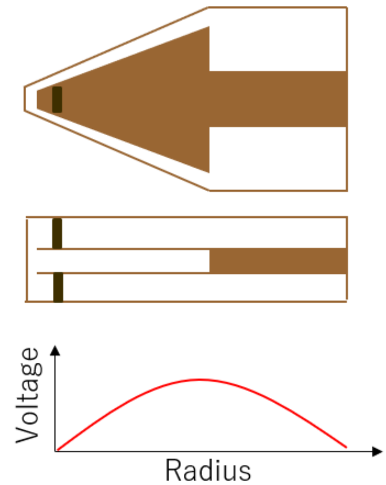

Figure 6: Schematic design of a flat-top RF cavity.

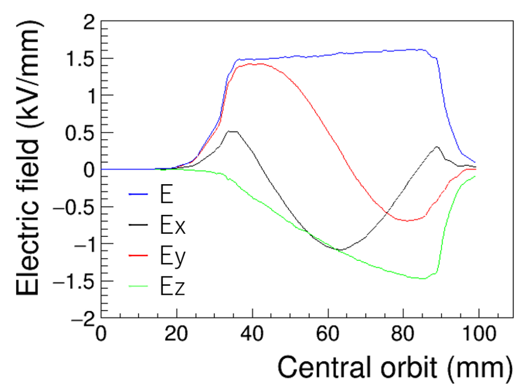

Figure 7: Electric field distribution in the spiral inflector.

BEAM ORBIT CALCULATION

Beam dynamics of muons is calculated using electromagnetic fields obtained by 1.1 μs, half of the lifetime of muons), therefore 60 % of injected muons can survive the acceleration period. Multiparticle tracking is performed assuming Gaussian distributions of 1 π.mm.mrad (1σ). Figure 8 shows the beam orbit inside the cyclotron, and the extraction loss in the deflector is only 2 %, which is negligible compared to the loss due to the muon's short lifetime. The rms emittances of R- and z-direction of the extracted muon beam are about 0.3 π.mm.mrad.

Figure 9 shows the energy spread as a function of the turn number. The energy spread of the extracted muon beam is less than 1 keV ($\Delta E/E < 2 \times 10^{-4}$). The current values of the emittance and the energy spread is quite small, but we are now trying to improve more by re-designing the central region of the cyclotron.

ISBN: 978-3-95450-205-9 doi:10.18429/JACoW-Cyclotrons2019-TUP024

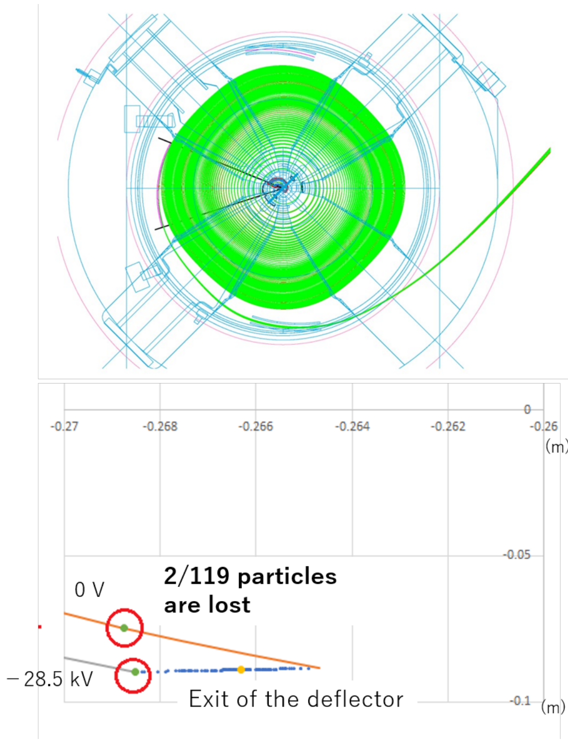

Figure 8: Beam orbit in the muon cyclotron. When 119 muons are injected, only 2 muons are lost near the exit of the electrostatic deflector.

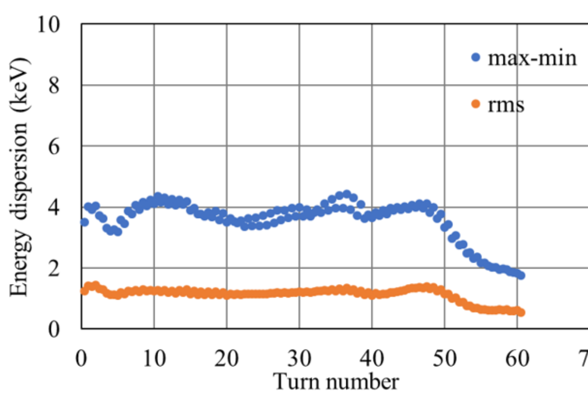

Figure 9: Change of the energy dispersion as a function of the turn number.

ACKNOWLEDGEMENT

The authors would like to thank Dr. S. Kurashima of QST for helpful discussions. This work was supported by JSPS KAKENHI Grant Numbers JP17H06126 and JP19H05194.

CONCLUSION

We are developing the muon cyclotron for the transmission muon microscope, which will be installed in the J-PARC muon facility (MUSE) in FY2020. An AVF cyclotron with a flat-top RF system is adopted to re-accelerate ultra slow muons without increasing energy spread. The detailed design is performed using 3D electromagnetic field simulations and multiparticle beam orbit calculation. Energy spread less than 2×10^{-4} has been achieved already, but we are trying to reduce it down to $O(10^{-5})$ by tuning the design of the central region of the cyclotron.

REFERENCES

[1] W. Higemoto *et al.*, "Materials and life science experimental facility at the Japan proton accelerator research complex IV: The muon facility", *Quantum Beam Sci.*, vol. 1, p. 11, Jun. 2017. doi:10.3390/qubs1010011

[2] Y. Miyake *et al.*, "Ultra slow muon project at J-PARC MUSE", *JPS Conf. Proc.*, vol. 2, p. 010101, 2014. doi:10.7566/JPSCP.2.010101

[3] Opera Simulation Software, https://operafea.com

[4] CST Studio Suite®, https://www.3ds.com

[5] Y. Kumata, Japan patent JP2002-043097

ISBN: 978-3-95450-205-9 doi:10.18429/JACoW-Cyclotrons2019-TUP025

FEASIBILITY STUDY FOR CONVERTING THE CS-30 INTO A VARIABLE ENERGY CYCLOTRON FOR ISOTOPE PRODUCTION USING THE INTERNAL TARGET SYSTEM*

H. A. Kassim, King Saud University, Riyadh, Saudi Arabia
F. M. Alrumayan†, A. M. Hendy
King Faisal Specialist Hospital & Research Center, Riyadh, Saudi Arabia
F. Akhdar, Imam University, Riyadh, Saudi Arabia

Abstract

This paper reports a method to reduce the beam energy of the CS-30 cyclotron from 26.5 down to 10 MeV using the internal target system in CS-30 cyclotrons for isotopes production. Irradiations of solid targets, in this type of cyclotrons, take place when the target is positioned horizontally inside the cyclotron tank. In its final position, the target plate interrupts the beam from completing its orbit and nuclear reactions take place. Calculations are made to determine the beam energy as a function of radius. Verification of the new method was achieved by producing pure Ga-68 at an energy level of 11.5 MeV.

INTRODUCTION

Production of radioisotopes by CS-30 cyclotron at KFSHRC started in 1982 with seven targets, each positioned at the end of a beamline. In addition to these seven beamlines, it is also possible in this type of cyclotron to irradiate a solid target internally. A special ISO-RABBIT mechanical system connects the cyclotron with one of the hot cells to receive the target before irradiation and deliver it after irradiation. The internal target is located inside the cyclotron tank at the edge of the pole where the proton has gained full energy of 26.5 MeV [1]. Table 1 illustrates the specification of the CS-30 cyclotron [2].

Cyclotrons have an extraction system, comprising the equipment that extracts the beam from the accelerated region to the main beamline of the cyclotron. In negative ion cyclotrons (whose accelerated particles are negative ions), this is done by stripping electrons from the negative ions using carbon foils. In positive ion machines, the mechanism is more complicated, consisting of an electrostatic deflector (which has two parts: a septum. Septum made of tungsten, held at zero potential, and a high voltage electrode) and a magnetic channel to eliminate the magnetic field effect of the extracted beam. On the last rotation, particles experience a strong electric field capable of modifying slightly the trajectory of their orbit [3-6].

Figure 1 illustrates the internal target mechanism of a CS-30 cyclotron, which holds the target plate (to be irradiated) in final position at the edge of the pole where the proton energy is 26.5 MeV.

Table 1: Main Specification of CS30

Parameter	Value
Proton Energy	26.5 MeV
Deuteron Energy	15.0 MeV
He-3 Energy	38.0 MeV
He-4 Energy	30.0 MeV
External Beam Power	2000 W
Pole Diameter	38 inch
Weight	22 t
Number of Dees	2
Acceleration mode	fundamental
Voltage Gain Per Turn	100 kV

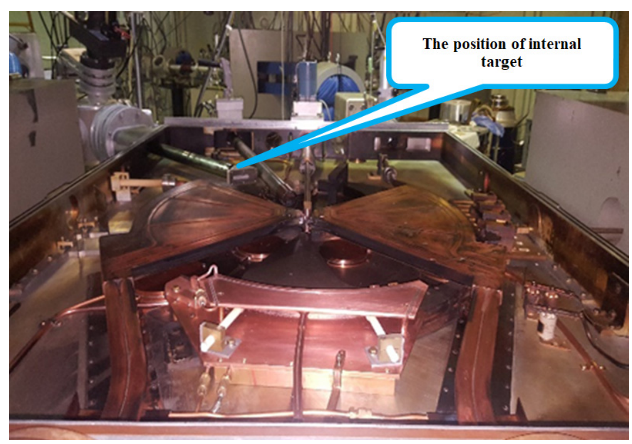

Figure 1: The normal position of the internal target during irradiation at 26.5 MeV.

This paper reports the possibility of reducing the cyclotron energy from 26.5 down to 10 MeV by moving the internal target mechanical system toward the central region of the cyclotron. The low energy beam, then, can be used to produce low energy-produced isotopes such as Ga-68 (produced at 11.5 MeV).

*Work supported by NSTIP strategic technologies program in the kingdom. Award No. (14-MAT-1233-20).
†rumayan@kfshrc.edu.sa

ISBN: 978-3-95450-205-9 doi:10.18429/JACoW-Cyclotrons2019-TUP025

CALCULATIONS OF BEAM ENERGY AND TARGET MODIFICATIONS

Calibration Curve of the CS30 Cyclotron

In order to, precisely, specify the energy level as a function of radius, the calibration curve was calculated as following [3]:

Consider the isochronous field of a cyclotron, i.e.:

$$\langle B \rangle = \gamma B_0 \,, \tag{1}$$

where B_0 is the cyclotron average magnetic field and γ equals to:

$$\gamma = \frac{1}{\sqrt{\left(1-\frac{r^2}{\alpha^2}\right)}} , \tag{2}$$

where;

$$\alpha = \frac{E_0}{ecB_0} \,, \tag{3}$$

$$E_0 = m_0c^2 = 938.2 \; MeV \,, \tag{4}$$

$$T = (\gamma - 1)E_0 \,, \tag{5}$$

where T is the energy level at different radii. Figure 2 shows the calibration curve of the CS30 Cyclotron.

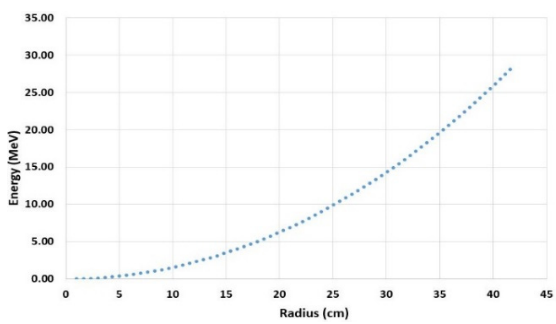

Figure 2: Energy-radius relationship of the CS30.

Beam Position at 11.5 MeV

In order to produce Ga-68 at 11.5 MeV [7], the internal target system was moved inward into a distance of 27 cm from the central region. This value is with respect to an energy level of 11.5 MeV. Beam position on target was examined in two energy levels: at 26.5 MeV Fig. 3 (A) and at 11.5 MeV Fig. 3 (B). At 11.5 MeV, the beam is off-centre and hit the top part of the target plate. Therefore, it is clearly indicated that the radius of curvature is not aligned with the new position of the target as it is in the outer radius case at 26.5 MeV. Therefore, target holder needs to be modified.

Modification of Target Geometry

The target mechanical shaft is off-centre, as shown in Fig. 4. The perpendicular distance between the canter and the shaft centreline d is 10.67 cm. The target surface should be tangential to the beam orbit. From geometry, the angle of the target to be tangential will be:

$$\theta = sin^{-1}\frac{d}{r} , \tag{6}$$

where d = 10.67 cm is the distance between canter and shaft centreline, and r is the orbit radius.

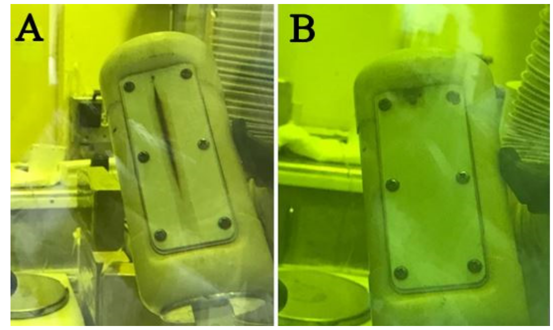

Figure 3: The beam position on the ISO-RABBIT target at (A) 26.5 and (B) 11.5 MeV.

For beam energy of 26.5 MeV, r is 41 cm and θ is 15.04° and for beam energy of 11.5 MeV, r is 27.6 cm, and θ is 22.74°. Target holder should be modified to fit the target carrier. From this perspective, the new dimensions of the target for an energy level of 11.5 MeV (as shown on upper right of Fig. 4) are: a = 7.1 cm, b = 3.6 cm, c = 8.0 cm and d = 0.5 cm.

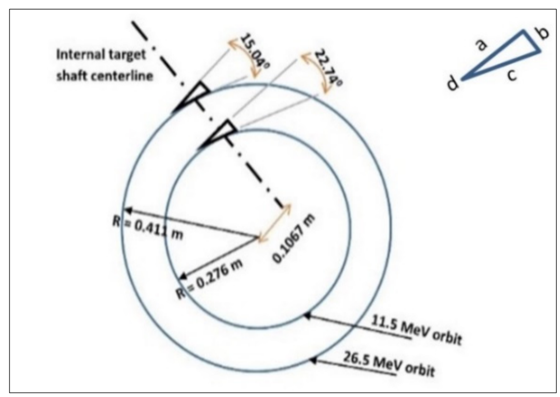

Figure 4: The target surface should be tangential to the beam orbit.

It should be noted that the production of Ga-68 was produced before modifying the target geometry, in order to verify the energy of the cyclotron with respect to the radius.

Ga-68 Production

The enriched Zn-68 was electrodeposited onto a copper disc as target support using a solution comprised of $^{68}ZnCl_2$ and 0.05 N HCl (concentration of Zn-68: 25–30 mg/mL) and a current density of 350 mA (43.75 mA/cm^2). The electroplating process was performed for 20 minutes. The weight of deposited Zn-68 on the copper disc was around 166.0 milligrams. The target was then transferred and mounted in the cyclotron. Figure 5 illustrates the shape of the target before and after being coated with the Zn-68.

Target Irradiation

Ga-68 can be produced by the cyclotron via the ^{68}Zn(p,n)^{68}Ga reaction in a solid target. The copper disc target was transferred into the internal target holder via an automated target transfer system. After that, the target was irradiated by proton-beam energy of 11.5 MeV with beam currents of 40–50 µA for 120 minutes. After irradiation, the

ISBN: 978-3-95450-205-9 doi:10.18429/JACoW-Cyclotrons2019-TUP025

target was transported from the target holder in the cyclotron vault to the processing hot cell within the radiochemistry laboratory. In the hot cell, the solid target was dissolved. The chemical separation of Ga-68 was per-formed.

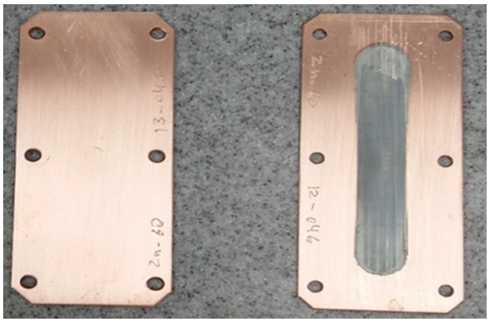

Figure 5: The copper target before and after being coated with the Zn-68.

RESULTS AND DISCUSSION

The radionuclide purity was assessed using gamma-ray spectroscopy equipped with a high purity germanium detector (CANBERRA, model: GC1518) and GENEI 2000 software was utilized. Figure 6 shows the main gamma lines of the Ga-68. To assess the presence of radio isotopic contaminants such as Ga-66 or Ga-67. Such Ga-67 impurities cannot be chemically separated, and the labelled compounds will have the same bio-distribution and kinetics as Ga-68. Measurements of Ga-67 and Ga-66 were made after 12 hours' decay of Ga-68. The Sample was counted for 5 minutes immediately after the end of separation.

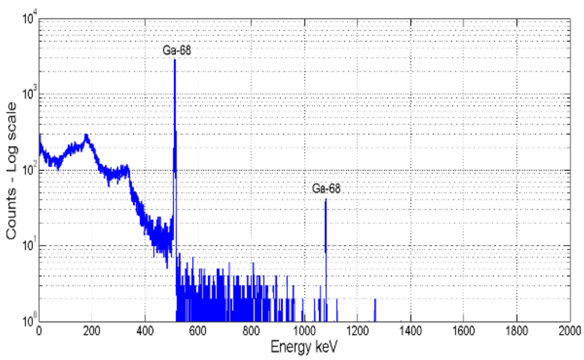

Figure 6: Characterization of Ga-68 by high purity germanium detector after production.

CONCLUSION

The possibility for reducing the cyclotron energy from 26.5 to 10 MeV was achieved in the CS30 cyclotron at KFSHRC. Calculations are made to determine the beam energy as a function of radius. Verification of the new method was achieved by producing pure Ga-68 at an energy level of 11.5 MeV.

ACKNOWLEDGMENTS

We would like to thank Mr. Ahmed Alghaith (Cyclotron engineer), Mr. Hussain Aldossery and Abdulrahman Alomar (Radiochemists) for excellent technical support. This project was supported by the NSTIP strategic technologies program in the kingdom. Award No. (14-MAT-1233-20).

REFERENCES

[1] F. M. Alrumayan, M. S. Shawoo, and M. Vora, "Status report of the cyclotrons C-30, CS-30 and RDS-111 at KFSHRC, Saudi Arabia", in *Proc. Cyclotrons'13*, Vancouver, Canada, Sep. 2013, paper MOPPT001, pp. 28-30.

[2] F. M. Alrumayan *et al.*, "Magnetic field measurement system of CS-30 cyclotron", in *Proc. Cyclotrons'16*, Zurich, Switzerland, Sep. 2016, pp. 196-198. doi:10.18429/JACoW-Cyclotrons2016-TUP13

[3] J. Livingood, "*Principles of Cyclic Particle Accelerators*", D. Van Nostrand Company Inc., 1962.

[4] H. L. Hagedoorn and P. Kramer, "Extraction studies in an AVF cyclotron", *IEEE Trans. Nucl. Sci*. vol. 13, no. 4, p. 64, Aug. 1966. doi:10.1109/TNS.1966.4324177

[5] W. Joho, "Extraction from medium and high energy cyclotrons", in *Proc. Cyclotrons'69*, Oxford, UK, Sep. 1969, paper CYC69C01, pp. 159-179.

[6] W. Kleeven *et al.*, "The IBA self-extracting cyclotron project", in Proc. *XXXIII European Cyclotron Progress Meeting*, Nukleonika 48 supplement 2, pp. 59-67, 2003.

[7] M. Pandey *et al.*, "Cyclotron production of ^{68}Ga via the ^{68}Zn(p, n)^{68}Ga reaction in aqueous solution", *American J Nucl. Med. Mol. Imaging,* vol. 4, pp. 303-310, June 2014.

ISBN: 978-3-95450-205-9 doi:10.18429/JACoW-Cyclotrons2019-TUP026

EMBEDDED LOCAL CONTROLLER FOR THE CS-30 CYCLOTRON*

A. M. Hendy†, F. M. Alrumayan,
King Faisal Specialist Hospital & Research Center, Riyadh, Saudi Arabia
H. A. Kassim, King Saud University, Riyadh, Saudi Arabia

Abstract

The Embedded Local Controller is used for upgrading the old CS-30 cyclotron control system at King Faisal Specialist Hospital and Research Centre. It is installed inside the cyclotron vault and connected to the control room using CAN serial bus. This is to avoid adding more wires from cyclotron vault to the outside, because there is no room for extra wires in the feed through conduits. The system is carefully designed to be fault tolerant so that it can run in a radiation environment without failure. Details of the design and field test results are presented.

INTRODUCTION

Production of radioisotopes by CS-30 cyclotron at KFSHRC started in 1982 with seven targets, each positioned at the end of a beamline. In addition to these seven beamlines, it is also possible in this type of cyclotron to irradiate a solid target internally. A special ISO-RABBIT mechanical system connects the cyclotron with one of the hot cells to receive the target before irradiation and deliver it after irradiation. The internal target is located inside the cyclotron tank at the edge of the pole where the proton has gained full energy of 26.5 MeV [1, 2]. Table 1 illustrates the specification of the CS30 cyclotron

In our attempts to upgrade the control system of our old CS-30 cyclotron, we always face the wiring problem. The wiring channels are full of heavy gauge wires and there is no room to add more wires for our upgrade. This raised the need to add a part of this upgrade locally inside the cyclotron vault, and motivated us to design our robust embedded controller to use inside cyclotron vault. Cyclotron local controller is placed inside cyclotron vault to overcome the wiring problem, therefore, it is subjected to a high ionizing and non-ionizing radiation, and must be carefully designed to guarantee reliable operation for a long time [3].

A prototype of the system was produced and as a first try, it is used as a cyclotron vacuum system controller. It has been placed under actual field-testing for more than a year without any failure.

SYSTEM OVERVIEW

The control system consists of backplane, controller board, optional signal conditioning board, and power supply, all placed inside a 19”, 3U sub-rack (see Fig. 1). Figure 2 shows that system is placed inside the cyclotron vault and connected to the remote user interface computer though CAN serial bus.

*Work supported by NSTIP strategic technologies program in the kingdom. Award No. (14-MAT-1233-20).
†ahendy@kfshrc.edu.sa

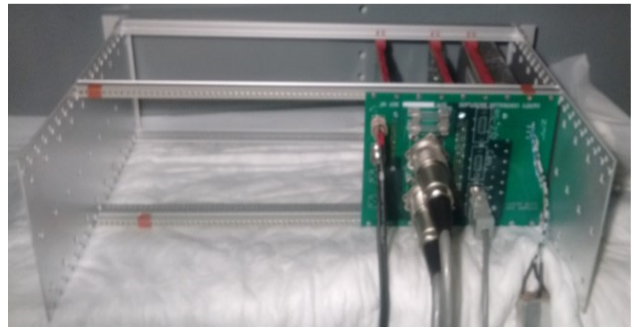

Figure 1: Embedded local controller system.

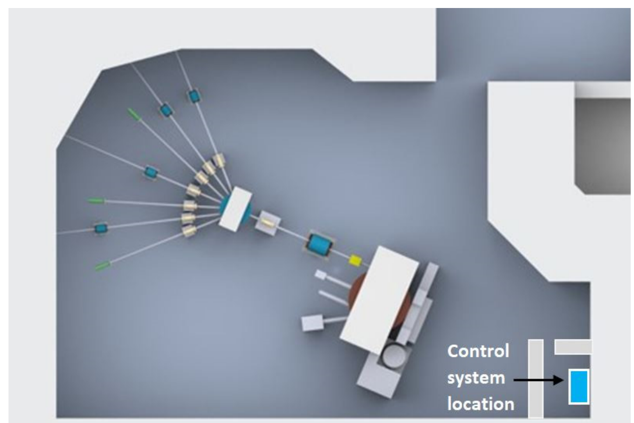

Figure 2: Control system location inside cyclotron vault.

CONTROLLER BOARD DESCRIPTION

Figure 3 shows the PCB of the controller and block diagram of this board is shown in Fig. 4. This board has all sub-circuits that allow it to be high reliability standalone controller. At the top is TMS570LS0432 safety microcontroller (Texas Instruments) that has many features, which make it very robust in the radiation environment [4]. There is a digital I/O sub-circuit, with 16 lines output (24 V, 0.5 A), 24 lines input (24 V), and four high-speed inputs (24 V) that can be used as quadrature encoder input. Additionally, there is an analogy I/O sub-circuit, with 8 analogy inputs (programmable range) and 8 analogy outputs (programmable rage). In addition, there are two CAN ports, one isolated and the other non-isolated, and one isolated RS-232 port. All sub-circuits power supplies are protected and can be on/off controlled, and can be monitored through the microcontroller, this feature is crucial to monitor current variation due to the effect of radiation.

ISBN: 978-3-95450-205-9 doi:10.18429/JACoW-Cyclotrons2019-TUP026

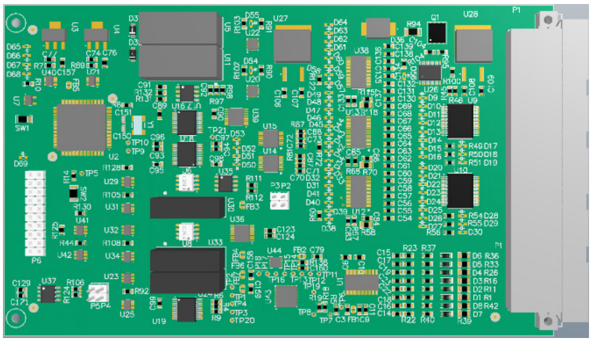

Figure 3: Controller PCB.

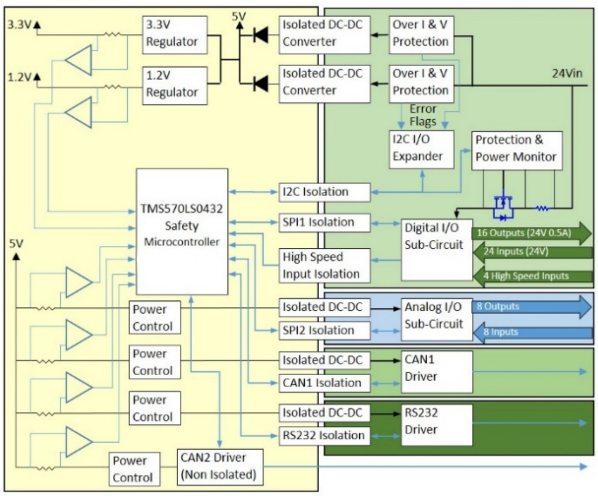

Figure 4: Controller block diagram.

Microcontroller Sub-circuit

Power supply of this sub-circuit utilizes two parallel connected DC-DC converters with two protection circuits. This ensures the operation of the circuit even with one DC-DC converter failure, thus increasing system reliability. The protection circuit provide flags to the microcontroller indicating over current or voltage.

LDO voltage regulators are used to generate 3.3 V and 1.2 V for microcontroller supply.

Current consumption of 3.3 V and 1.2 V supplies can be monitored by the microcontroller such that detect any abnormalities due to ionizing radiation.

Microcontroller used is Texas Instruments TMS570LS0432 safety microcontroller. It is a high-performance automotive-grade microcontroller for safety systems. The safety architecture includes dual CPUs in lockstep, CPU and Memory BIST (Built-In Self-Test) logic, ECC (Error Correcting Code) on both the flash and the data SRAM, parity on peripheral memories, and loop-back capability on peripheral I/Os. All these feature make it ideal for high reliability, fault tolerant system.

Digital I/O Sub-circuit

Figure 5 shows the block diagram of the digital I/O sub-circuit, which comprises digital output, digital input, and high-speed digital input. Digital output is implemented using two VNI8200XP (ST Microelectronics) high side driver which capable of driving up to 0.7 A, 32 VDC. It converts serial data at the SPI port into the parallel high current output.

Digital input is implemented using three SCLT3-8BT (ST Microelectronics) protected digital input with serializer. It accepts up to 35 VDC parallel input and convert into serial data that can be read by microcontroller SPI port.

Finally, the high speed input comprises two PCLT-2A (ST Microelectronics) that convert the high voltage signal to a low voltage logic signal that can be fed to the microcontroller. The high speed digital inputs can be used for quadrature encoder interface. This encoder interface can be used for motor speed measurement, flow sensor, or any other quadrature signal interface.

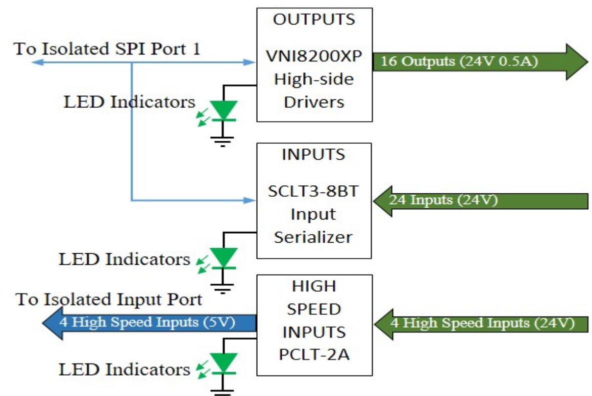

Figure 5: Digital I/O sub-circuit.

The power supply of digital I/O sub-circuit is controlled and monitored using TPS2483PW (Texas Instruments) by which we can turn the power on or off and can measure the voltage and current drawn by this sub-circuit. This can help in discovering the circuit abnormalities before complete failure.

Analog I/O Sub-circuit

The analog I/O sub-circuit (see Fig. 6) comprises ADS8688A 8 channels, 16 bits ADC (Texas Instruments) for analog input, and LTC2668 16 channels 16 bits DAC (Linear Tech) for the analog output.

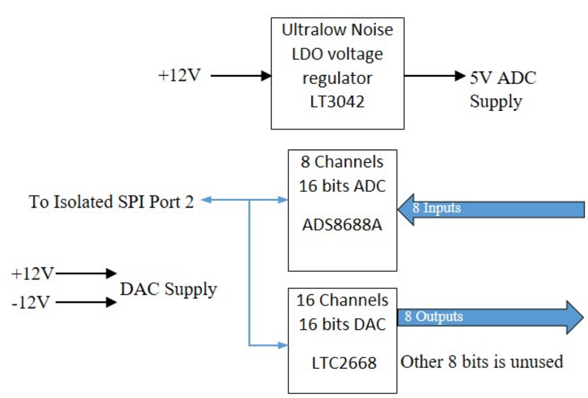

Figure 6: Analog I/O sub-circuit.

ISBN: 978-3-95450-205-9 doi:10.18429/JACoW-Cyclotrons2019-TUP026

Also, LT3042 Ultralow Noise LDO voltage regulator (Linear Tech) is used to generate the supply of the ADC. The power supply current of this sub-circuit is monitored by the microcontroller for any abnormalities to give early warning before complete failure.

Serial Communication

There are one isolated CAN port, one non-isolated CAN port, and one isolated RS-232 port. The supply of these ports can be on/off controller, and measured by the microcontroller to monitor the effects of radiation on the IC's. The isolated CAN port (CAN1) is used for communication with host computer at the control room. Non-isolated CAN port (CAN2) can be used for communication between modules on the same backplane, allowing the use of more than one controller board to increase the number of I/O, or to make a redundancy to improve the reliability of the system. The isolated RS-232 port can be used to interface with other external equipment that equipped with that port.

Software

The host PC at the control room is connected to the controller through CAN bus using Remote Procedure Call RPC [5]. It is a simple way to transfer control and data across a communication network (CAN bus). Figure 7 shows the components of the RPC system.

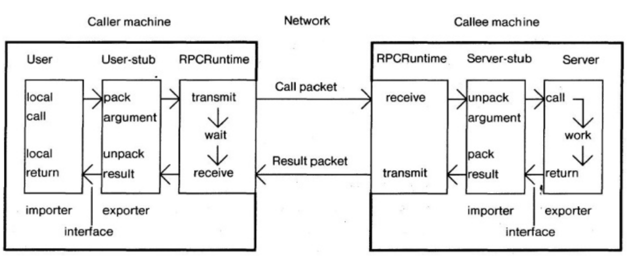

Figure 7: Components of RPC system and their interactions.

In this preliminary version of the software, we have the minimal number of RPCs that can work the system, and it can be extended to get more functionality. Table 1 lists the currently implemented RPCs.

BACKPLANE DESCRIPTION

The backplane is customized according to the requirements (see Fig. 8). At least, it contains connectors for the one power supply, and one Controller board. It may contain a connector for signal conditioning board that is used to interface with different sensors in the system (e.g. Vacuum sensor). Also, it contains the cable connectors that interface with different actuators and sensors of the system. The following figure shows the backplane used to control the cyclotron vacuum system.

Table 1: RPCs

Proc. ID	Procedure
0	void SetOutputBit(uint8_t OutputNumber, uint8_t Out-putState);
1	void SetOutputValue(uint32_t OutputValue);
2	uint32_t GetOutputValue(void);
3	uint32_t GetOutputInterlockValue(void);
4	uint8_t GetInputValue (uint32_t* InputData);
5	uint16_t GetAnalogValue (uint8_t ChannelNumber);
6	uint32_t GetFlowRate(void);
7	uint32_t GetErrorFlags(void);
8	uint32_t GetFirwareVe (void);
9	void SetAlarmHi(uint8_t Channel Number, uint16_t AlarmHiValue);
10	void SetAlarm Lo(uint8_t Channel-Number, uint16_t AlarmLoValue);
11	Errors Get UcErrors (void);
12	void InjectError (uint8_t Index, uint8_t DualBit);

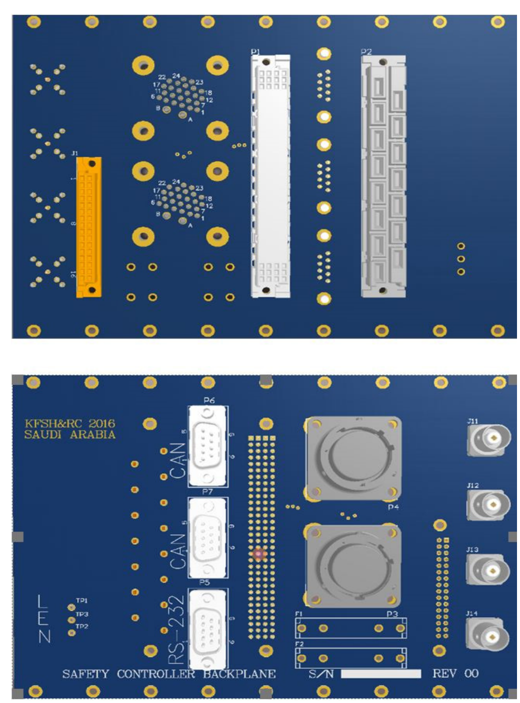

Figure 8: Backplane front (up) and back (down).

ISBN: 978-3-95450-205-9 doi:10.18429/JACoW-Cyclotrons2019-TUP026

FIELD TEST

The system was installed inside the cyclotron vault and was under full operation for more than one year. Table 2 lists the run history during this duration.

Table 2: Cyclotron Production Run

Isotope	Target	Run Time	Average Current (μA)	Number of Runs
^{123}I	Internal	3 Hr	18	39
^{81m}Kr	Line 5	1 Hr	13	34
^{13}N	Line 7	5 Min	10	34
^{67}Ga	Internal	7.5 Hr	45	6
^{201}Tl	Internal	5 Hr	80	5

During this duration, the microcontroller detected only one correctable error.

CONCLUSION

Embedded Local Controller is a way to place the control system inside the cyclotron vault. This has a great advantage to reduce the wiring complexity and cost. It also allows easy extend and modify the functionality. This raises the issue of semiconductor operation in the radiation environment. By carefully designing the system and using a powerful microcontroller with redundancy, we can achieve the required working time using COTS components.

ACKNOWLEDGEMENTS

This project was supported by the NSTIP strategic technologies program in the kingdom. Award No. (14-MAT-1233-20).

REFERENCES

[1] F. Alrumayan, M. Shawoo, and M. Vora, "Status report of the cyclotrons C-30, CS-30, and RDS-111 at KFSHRC, Saudi Arabia", in *Proc. Cyclotrons'13*, Vancouver, BC, Canada, paper MOPPT001, pp. 28-30.

[2] G. O. Hendry, "Compact cyclotron engineering for application", in *Proc. Cyclotrons'81*, Caen, France, 1981, *AIP Conf. Proc.*, vol. 9, p. 616, 1972. doi.org/10.1063/1.2946412

[3] B. Hallgren, H. Boterenbrood, H. J. Burckhart, and H. Kvedalen, "The Embedded Local Monitor Board (ELMB) in the LHC front-end I/O control system", in *7th Worshop on Electronics for LHC Experiments*", Stockholm, Sweden, Sep. 2001, pp. 325-330 (CERN-2001-005). doi:10.5170/CERN-2001-005.325

[4] K. Greb and D. Pradhan, Hercules™ microcontrollers: Real-time MCUs for safety-critical products, http://www.ti.com/lit/wp/spry178/spry178.pdf

[5] A. D. Birrell and B. J. Nelson, "Implementing remote procedure calls", *ACM Trans. Comput. Syst.*, vol. 2, no. 1, Feb. 1984. doi:10.1145/2080.357392

ISBN: 978-3-95450-205-9 doi:10.18429/JACoW-Cyclotrons2019-TUP028

BREMSSTRAHLUNG PHOTONS EMISSION IN 28-GHz ELECTRON CYCLOTRON RESONANCE PLASMA

M. J. Kumwenda*, University of Dar es Salaam, Dar es Salaam, Tanzania
J. K. Ahn and J.W. Lee, Korea University, Seoul, Republic of Korea
I. J. Lugendo, University of Dar es Salaam, Dar es Salaam, Tanzania
S. J. Kim, J.Y. Park and M. S. Won, Busan Center, KBSI, Busan, Republic of Korea

Abstract

Radial measurements of bremsstrahlung photons show high-energy intensity beyond a critical energy from electron cyclotron resonance (ECR) heating and its nature is not well understood so far. For the first time we have measured the bremsstrahlung photons energy intensity from 28-GHz ECR ion source at Busan Center of KBSI. Three round type NaI(Tl) detectors were used to measure the bremsstrahlung photons emitted at the center of the ECRIS at the same time. Another NaI(Tl) detector was placed downstream from the ECR ion source for monitoring photon intensity. The ECR ion source was operated at Radiofrequency (RF) power of 1 kW to extract ^{16}O beam with a dominant fraction of O^{3+}. Bremsstrahlung photons energy spectra were measured at the center of the ECR ion source. We studied possible systematic uncertainties from different characteristics among the three NaI(Tl) detectors by repeating measurements alternatively. Geant4 simulation was performed to take the geometrical acceptance and energy-dependent detection efficiency into account due to large non-uniformity in the material budget. We extracted true bremsstrahlung energy spectra from the 28-GHz ECR ion source using the inverse-matrix unfolding method. The unfolding method was based on a full geometry Geant4 model of the ECR ion source. The high energy intensities of the bremsstrahlung photons at the center of the ECRIS were explained by the internal structure and shape of ECR plasma.

INTRODUCTION

An electron cyclotron resonance ion source (ECRIS) is one of the most used ion source types for high charge state heavy ion production [1]. Most electron cyclotron resonance (ECR) ion source including Korea Basic Science Institute (KBSI), rely on the superposition of solenoid and hexapole magnetic fields for plasma confinement [2]. The ECR plasma state depends on various operation conditions such as radiofrequency (RF) power, the pressure of the injected gas and the solenoid coil current. Also, ECR on sources are usually built for a specific maximum resonance frequency, e.g 28 GHz [3]. The ECR plasma used in this study is 28 GHz was developed as injector equipment for the heavy ion linear accelerator at the KBSI.

In ECR radio frequency microwaves heat plasma electrons in order to provide ionization of neutral gases. As a result of ECR heating very high electron energies are produced which can generates a large amount of bremsstrahlung photons [1,4]. Two process in the ECR plasma lead to the emission of bremsstrahlung radiations in the form of x-rays. First bremsstrahlung is created by electron-ion collisions within the plasma volume. The second process is when electrons are lost from the plasma, collide with the plasma chamber wall and radiate bremsstrahlung due to their sudden deceleration [1,5].

The produced bremsstrahlung photons deposits energy in the structure of ion sources and turns out to be substantial heat load to the cryostat in the case of superconducting ECR ion sources [4,6]. The cryogenic system can remove only a limited amount of the heat from the cryostat. If more heat is added to the system than can be removed, the temperature of the liquid helium rises and can cause the superconducting coils to quench [2].

Bremsstrahlung photons produced in ECR ion source have been made since late 1960s [7]. Nevertheless, many of these experiments used to measure the bremsstrahlung photons in only one direction, axially using one or two detectors but under different conditions. However, since the bremsstrahlung photons emitted from the ECR is expected to be anisotropic due to various effects [5]. This paper presents the first measurements results of the bremsstrahlung photons energy intensity at the center of the ECR ion source at three azimuthal angles.

EXPERIMENTAL SETUP

The data that is presented in this paper was carried out to measure bremsstrahlung photons energy intensity from 28 GHz superconducting ECR ion source of the compact linear accelerator facility at Korea Basic Science Institute (KBSI), cyclotron research centre.

ECR ion source developed at KBSI is composed of a six racetrack hexapole coils and three mirror solenoid magnets [8]. The axial magnetic field is about 3.6 T at the beam injection area and 2.2 T at the extraction region, respectively. A radial magnetic field of 2.1 T can also be achieved on the plasma chamber wall. A higher current density NbTi wire was selected for winding of sextupole magnet. The inner face of the 5 cm thick solenoid coil is placed at a distance of 44 cm from the beam axis. The 10 cm thick iron shielding structure is 120 cm wide, 122 cm high and 170 cm long [9].

The experiment setup to measure bremsstrahlung photons spectra in this study is totally different from previous experiment conducted by other researchers. Photon energy spectra were measured using three round type NaI(TI) detectors as shown in Fig. 1 facing the edge of ECRIS at the center of the ECR ion source.

* kmwingereza@yahoo.com

22nd Int. Conf. on Cyclotrons and their Applications Cyclotrons2019, Cape Town, South Africa JACoW Publishing
ISBN: 978-3-95450-205-9 doi:10.18429/JACoW-Cyclotrons2019-TUP028

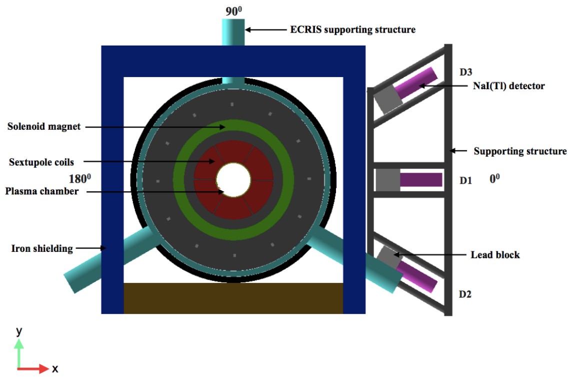

Figure 1: The three NaI(Tl) scintillation detectors at the center of the ECR ion source.

For easy reference, all detectors are labeled with letters D1, D2, D3 and D4, which were operated at +1300 V. The three detectors (D1, D2 and D3) were mounted on the support structure for measurements at azimuthal angles, as shown in Fig. 1, while the D4 detector was mounted at the view port for monitoring the intensity of ECR plasma (Fig. 2).

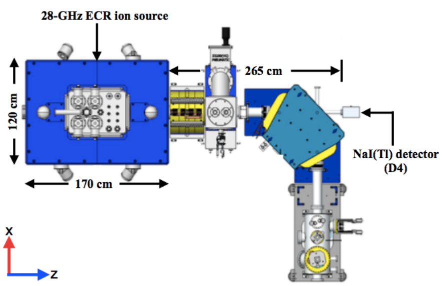

Figure 2: Detector D4 at the view port. The D4 detector was used to monitor a possible variation in ECR plasma intensities throughout the measurements.

The photon energy intensity was measured at 3 angles in a 30° interval at the ECR ion source. The three detectors were attached at a single support structure, and changed the positions, in order to cover the angular region. For a systematic study among the three detectors, the three detectors were replaced at the same angular position.

Each NaI(Tl) detector was placed in a lead (Pb) collimator of a 0.5 cm hole. The Pb collimator covered a full dimension of the NaI(Tl) crystal. The 500 MHz FADC system was used for data acquisition as illustrated in Fig. 3.

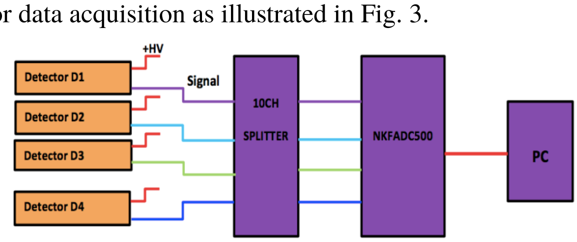

Figure 3: Schematic of an electronic illustration showing the signal from each detector was fed to the splitting module and then to other electronic devices.

The detector signal was fed to splitting module and then to a (500 MHz flash ADC) NKFADC and recorded in a coincidence with a reference signal from the detector D4 placed at the view port. The 4-channel flash ADC module (Notice Co.) recorded full pulse information from four NaI(Tl) detectors in every 1000 ns. The ring-buffer data were then fed to a PC. Due to a huge data size the measurement was performed in every 3 minutes. Trigger logic OR provide event triggering condition. The data recorded by using the NKFADC500 flash ADC were in raw binary form. The raw binary data were decoded to get ROOT format data for analysis [10].

DATA ANALYSIS

Energy and Efficiency Calibrations

Throughout the measurement the energy calibration of the spectrum was taken using standard radioactive gamma rays' sources namely, ^{60}Co source with gamma-ray energies of 1173 keV and 1332 keV and ^{137}Cs source gamma-ray energy of 662 keV [11]. Then, the three calibrated data points were fitted using a least-squared chi-square linear fit to convert channel number to its corresponding energy value. The background photon energy spectrum was measured for 10 hours and was normalized with the data taking time and subtracted from the raw spectra for bremsstrahlung photon measurement.

In order to take the geometric acceptance and also the energy-dependent detection efficiency into account a Monte Carlo simulation based on Geant4 package was performed. To perform a Monte Carlo simulation based on Geant4 package a fully Geant4 model based on the KBSI ECR ion source design was considered during the simulation. Monte Carlo simulation was performed due to complicated structure of the ECR ion source, the material budget differs largely depending on the azimuthal angles.

In the first step Geant4 simulation was performed with gamma ray spectra ranging from 0.1 to 2 MeV with an interval of 0.1 MeV. Then each peak was fitted to the Gaussian functions and the peak region were calculated by taking 1.96σ value which makes 95 % confidence level for the peak region. The peak regions boundary was established as $(\mu - 1.96\sigma, \mu + 1.96\sigma)$ and counts under this region were recorded for each peak and angle.

Unfolding Procedures

The measured spectrum in physical experiment are usually distorted and transformed by different detector effects, such as finite resolution, perturbations produced by the electronic device, etc. In order to reproduce true photon spectrum from the measured distributions it is necessary to take into accounts these effects by means of response function [12–15]. Normally the response functions are obtained by response matrix. From the basic mathematical relationship, the measured spectrum M(E) can be given as follows:

$$M(E) = R(E, E_0)T(E_0)\,, \tag{1}$$

where T(E_0) is the original or true energy distribution of gamma rays emitted by the source and R(E,E_0) is the response function or sensitive matrix of the detector.

ISBN: 978-3-95450-205-9   doi:10.18429/JACoW-Cyclotrons2019-TUP028

The task is to obtain the true gamma ray spectrum given the measured energy spectrum. Thus, the desired photon spectrum $T(E_0)$ is calculated from the matrix equation as follows:

$$T(E_0) = R^{-1}(E, E_0)M(E)\,, \tag{2}$$

R^{-1} is the inverse of the response matrix.

The procedure for obtaining $T(E_0)$ from M(E) is known as the unfolding (Deconvolution) of the measured spectrum. The matrix multiplication of M(E) and $R^{-1}(E, E_0)$ matrices gives another row matrix, which is true gamma ray spectrum of the detector. The pulse height distributions from various mono-energetic gamma ray spectra were obtained from Monte Carlo simulation based on Geant4 package using NaI(Tl) scintillation detector.

RESULTS AND DISCUSSIONS

Deconvolution of Mono-energetic Measured Spectrum

We have checked the correctness of the response matrix by multiplying R and R^{-1} and we have found that all elements along the diagonal are unity while in the inverse matrix all elements above the diagonal are negative numbers. These are physically justifiable. When measured spectrum (column vector M) is multiplied by the inverted matrix R^{-1} due to photons of a given energy the number of photons fall entirely in the channel corresponding to the given energy in the true spectrum (column vector T). Since the diagonal elements are positive the above statement can be true only if all elements above the diagonal are negative [16].

In order to check the practicality of the inverted matrix in the analysis of the continuous gamma ray spectrum we have first used it for the inversion of the spectrum from standard mono-energetic gamma ray source. The use of inverse matrix approach which shifts low pulse height counts into their photo-peak energy region by unscrambling the energy distribution recorded by NaI(Tl) scintillation detector. The typical measured and deconvolute gamma ray spectra are overlaid in Fig. 4. By means of the direct matrix inversion unfolding method, the backscattered peak and Compton continuum are significantly eliminated from the measured spectra into the corresponding photo-peak. In order to quantify the efficiency of the deconvolution technique the peak-to-total ratio (P/T) after applying direct matrix inversion unfolding method was calculated and was increased to 0.93 from 0.50 (0.43 increment) for ^{137}Cs radioactive source. Therefore, the number of counts in the photo-peak region increased approximately by factor of 0.43 after deconvolution.

Unfolding of Energy Spectrum of Bremsstrahlung Photons

This subsection is describing the bremsstrahlung photons energy spectra at the center position of the ECR ion source as represented in Fig. 5. All the measured spectra in azimuthal angles were normalized to the number of events taken in the same time interval by the detector D4. It is observed that

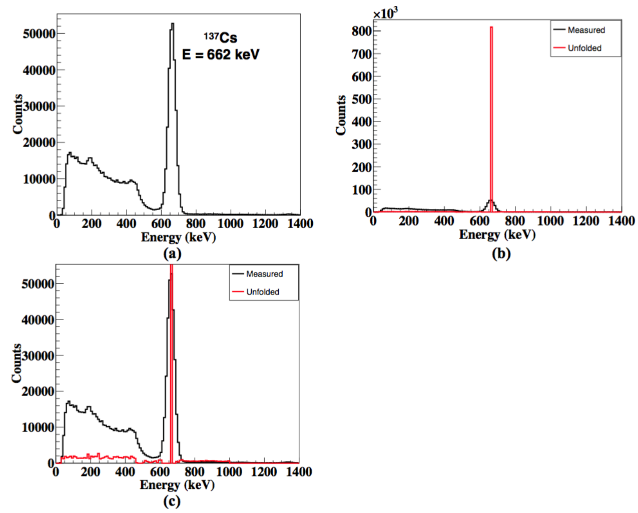

Figure 4: (a) The measured energy spectrum of ^{137}Cs (overlaid as black histogram) (b) The deconvoluted spectrum (overlaid as red histogram) using matrix inversion method.

both spectra at angles 30° and 330° shows the bump around 0.25 MeV for all three configurations.

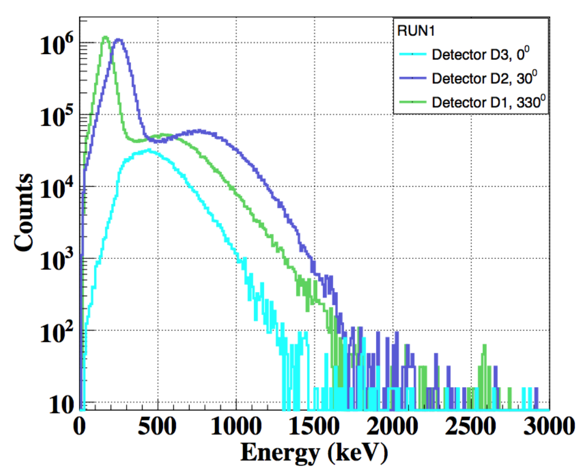

Figure 5: Bremsstrahlung photons energy intensity measured in three angles for detectors D1, D2 and D3.

The comparisons of unscrambled spectra after the application of inverted response matrix to the experimental measured bremsstrahlung photons for the detectors D1, D2 and D3 at the center position of the ECR ion source to all three azimuthal angles are well described by Fig. 6 for RUN1, the other two configurations namely RUN2 and RUN3 shows similar behavior. By the application of inverse matrix deconvolution method to the continuous spectrum, the results show a more precise identification of the bremsstrahlung photons end-point energy intensity in the spectrum. The end-point energies in a radial direction at angle 0° reaches 1.450 MeV while 30° and 330° reaches 1.710 MeV and 1.690 MeV respectively, which is beyond predicted maximum energy of 1.330 MeV. The maximum energy (T_{max}) that an electron can attain from ECR heating at cyclotron frequency ω can be given as follows:

$$T_{\max} = E_{\max} - m_e\,, \tag{3}$$

ISBN: 978-3-95450-205-9 doi:10.18429/JACoW-Cyclotrons2019-TUP028

where m_e is the mass of an electron and E_{max} is the total energy of an electron.

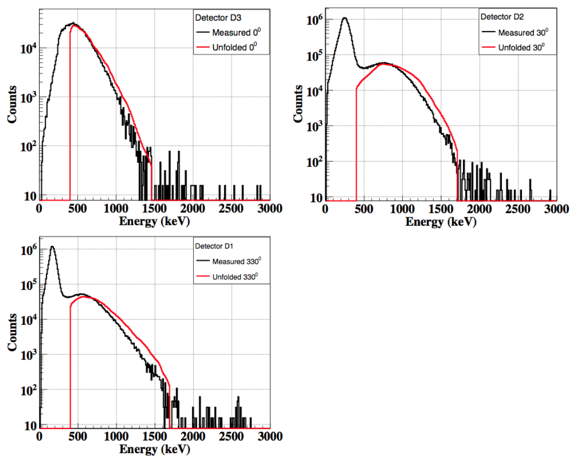

Figure 6: Deconvoluted energy spectra at angles 0° (D3), 30° (D2) and 330° (D1) respectively obtained after unfolding.

CONCLUSIONS

For the first time we measured bremsstrahlung photons energy intensity from the 28-GHz ECR ion source at Busan Center of KBSI at the center position. The detection system consists of three NaI(Tl) scintillation detectors placed 620 mm radially from the beam axis and one NaI(Tl) scintillation detector framed 3500 mm away at the extraction port for monitoring the photon intensity along the beam axis. At the center position, the ECR plasma is formed in the shape basically the same with the six-arm star (hexagon) [17, 18], due to the hexapole magnetic fields. The six corners of the plasma shape correspond to the angles of 30°, 90°, 150°, 210°, 270° and 330°, that means after every 60° there should be maximum angle. During the data measurement, we managed to measure three angles 0°, 30° and 330° other angles were not accessible due to the ECR supporting structure. Electrons at two angles namely 30° and 330° of the hexagon shapes at the center position of the ECR ion source can collide easily with the chamber wall and produce the bremsstrahlung photons. Hence, the high photon intensities at angles 30° and 330° can be explained by the shape of the ECR plasma. The gaps between the adjacent hexapole coils could account for high photon intensity and end-point energy observed at angles of 0°.

ACKNOWLEDGEMENTS

The authors would like to gratefully acknowledge support by National Research Foundation of Korea, Korea University, KBSI and University of Dar es Salaam.

REFERENCES

[1] T. Ropponen *et al.*, “The effect of magnetic field strength on the time evolution of high energy bremsstrahlung radiation created by an electron cyclotron resonance ion source”, *Nucl. Instrum. Methods Phys. Res., Sect. A*, vol. 600, pp. 525-533, 2009. doi:10.1016/j.nima.2008.12.065

[2] J. Y. Benitez *et al.*, “Current developments of the VENUS ion source in research and operations”, in *Proc. ECRIS’12*, Sydney, Australia, Sep. 2012, paper THXO02, pp. 153–158.

[3] B.S. Lee *et al.*, “Manufacturing of a superconducting magnet system for 28 GHz electron cyclotron resonance ion source at KBSI”, *Rev. Sci. Instrum.*, vol. 83, p. 02A347, 2012. doi:10.1063/1.3680266

[4] D. Leitner *et al.*, “Status report of the 28 GHz superconducting electron cyclotron resonance ion source VENUS”, *Rev. Sci. Instrum.*, vol. 77, p. 03A302, 2006. doi:10.1063/1.2149298

[5] J. Noland *et al.*, “Measurement of radial and axial high energy x-ray spectra in electron cyclotron resonance ion source plasmas”, *Rev Sci. Instrum.*, vol. 81, art. no. 02A308, 2010. doi:10.1063/1.3258614

[6] H. Zhao *et al.*, “Measurements of Bremsstrahlung radiation and X-ray heat load to cryostat on SECRAL”, in *Proc. ECRIS’10*, Grenoble, France, Aug. 2010, paper TUPOT009, pp. 134–136.

[7] J. Noland, PhD Theses, 2011.

[8] J. Y. Park *et al.*, “Superconducting magnet performance for 28 GHz electron cyclotron resonance ion source developed at the Korea Basic Science Institute”, *Rev Sci. Instrum.*, vol. 85, art. no. 02A928, 2014. doi:10.1063/1.4832136

[9] J. Y. Park, “Development of a superconducting magnet system for the 28-GHz ECR ion source at KBSI”, PhD Thesis, Pusan National University, 2014.

[10] M. J. Kumwenda, “Measurements of Bremsstrahlung photons in 28-GHz electron cyclotron resonance plasma”, PhD Thesis, Korea University, 2018, unpublished.

[11] G. F. Knoll, *Radiation Detection and Measurement*, Third Edition, New York, NY, USA: John Wiley & Sons, Inc., 1999.

[12] K. Tackmann and A. Hoecker, “SVD-based unfolding: implementation and experience”. arXiv:1112.2226

[13] S. Gallardo *et al.*, “Application of unfolding techniques to obtain the X-ray spectrum”. https://pdfs.semanticscholar.org/4c89/844643e9e04f63ad0b571296ba5b08e304ef.pdf

[14] J. Kluson, “Environmental monitoring and in situ gamma spectrometry”, *Radiat. Phys. Chem.*, vol. 61, pp. 209-216, 2001. doi:10.1016/S0969-806X(01)00242-0

[15] G. H. Golub and C. F. Van Loan, *Matrix Computations*, 3rd edition, Johns Hopkins University Press Baltimore, MD, USA, 1996.

[16] P. Subrahmanyam and P. Ammiraju, “An analytical method of analysing gamma-ray pulse height spectra”, *Nucl. Instrum. Methods*, vol. 33, pp. 87-92, 1965. doi:10.1016/0029-554X(65)90220-X

[17] J. Benitez *et al.*, “High energy component of X-ray spectra in ECR ion sources”, in *Proc. ECRIS’08*, Chicago, IL, USA, Sep. 2008, paper MOPO–08, pp. 77–84.

[18] V. Mironov *et al.*, “Numerical model of electron cyclotron resonance ion source”, *Phys. Rev. ST Accel. Beams*, vol. 18, p. 123401, Dec. 2015. doi:10.1103/PhysRevSTAB.18.123401

ISBN: 978-3-95450-205-9 doi:10.18429/JACoW-Cyclotrons2019-TUP029

A 15-20 MeV/NUCLEON ISO-CYCLOTRON FOR SECURITY AND RADIOISOTOPE PRODUCTION*

C. Johnstone†, R. Agustsson, S. Boucher, S. Kutsaev, A. Y. Smirnov
Radiabeam, Santa Monica, CA, USA
R. C. Lanza, Massachusetts Inst. of Technology, Cambridge, MA, USA

Abstract

Cargo inspection systems exploit the broad bremsstrahlung spectrum from a 6 - 10 MeV, low-duty cycle electron accelerator which in the presence of significant backgrounds presents challenges in image and material identification. An alternative approach is to use ions which can excite nuclear states either directly, or through generation of secondary high-energy signature gammas which are produced from nuclear interactions in a target. RadiaBeam is designing a compact sector isocyclotron ~1.2 - 1.5 m extraction radius, with high-gradient cavities to accelerate multi-ion species up to 15 - 20 MeV/u, respectively, with large turn-to turn, centimeter-level separation for low-loss extraction without lossy foil stripping. A strong-focusing radial field profile will be optimized in a separated-sector format for control over machine tune simultaneous with isochronous orbit requirements for high-current (~0.5 mA) operation. Innovation in injection will be introduced to replace the high-loss central region. Non-security applications of the cyclotron include medical isotope production, ion radiobiology, as well as material science research and ion instrumentation development.

INTRODUCTION

In cargo scanning for Special nuclear material (SNM), detection can be performed by either passive or active interrogation. The approach proposed here is an active, accelerator-based interrogation systems based on an ion accelerator capable of 15 - 20 MeV/nucleon.

Commercially-available accelerator-based security inspection systems generally exploit the broad bremsstrahlung spectrum generated using a 6 - 10 MeV, pulsed, low-duty cycle electron accelerator (i.e. linac or betatron) which in the presence of significant backgrounds presents difficulties in image and material identification which can make precise analysis challenging [1, 2]. An alternative approach is to use low energy (10 - 20 MeV/u) ions, which can excite nuclear states either directly, or through generation of secondary high-energy signature gammas produced from nuclear interactions in a target [3]. In the presence of nuclear materials, a beam of ions or secondary gammas will excite characteristic nuclear states which can be selectively identified by an appropriate detector array via spectral absorption or emissions eliminating the broad bremsstrahlung photon background that can avalanche a detector. The multiple monoenergetic gammas can be used in transmission to differentiate materials based on density and Z. Further, the Continuous Wave (CW) beam proposed here is well matched to detector systems in both collection and response times, facilitating low-dose scans and/or a much higher gamma ray energy spectrum for signature nuclear state excitation and applying established gamma-ray spectroscopy techniques. The idea is to use low energy nuclear reactions to produce mononenergetic gammas to improve the measurement of average density and Z; improving identification of lead and uranium, for example.

Designing for a charge to mass of ½ as proposed in Table 1 would allow either protons in the form of H_2+ or deuteron beams to be accelerated, for example, and delivered using the same system with deuterons adding neutron scanning capability. Another active detection approach which uses a CW accelerator for interrogation relies on measurement of delayed radiation [4] from induced photofission uniquely identifying SNM. What is unique to beam in a CW accelerator is that it can be triggered/inhibited on an RF timescale (~25 to 50 ns) through RF control systems, optimally tailoring to detection and maximizing signal to noise ratio by controlling both the strength and duration of the delayed radiation.

Table 1: Preliminary Accelerator Parameters for Q/A = ½

Parameter	Value
Accelerated Ions	H_2^+ (p), deuterons, He, B, Li, C, O, Ne, Si
Sectors	4
Extraction Energy	15-20 MeV/u
Injection Energy	0.5-1 MeV/u
Peak Current (avg)	0.5-1 mA (CW)
Inject/Extract Radius	0.1 / 1.3-1.5m
Field @ extraction	1.3T
Acceleration	400 kV/turn (2 cavities)
RF frequency	~40 MHz (8^{th} harmonic)

The high-current machine under design (Table 1) is also ideal for producing radioisotopes with many applications in medicine, biology, physics, chemistry, agriculture, national security and environmental and materials science. The most direct benefits are realized in medical diagnosis and therapy – expanding the availability of key or currently rare isotopes domestically is considered a high, even critical priority. One medical application is Radioimmunotherapy (RIT), a promising, new modality that selectively delivers radionuclides that emit α-particles, β-particles, or Auger electrons to tumours. The isotope group of the Nuclear Science Advisory Committee (NSAC), recognizing the gap between production and demand of α-particle-

* Work supported by U.S. Department of Energy, Office of Defense Nuclear Nonproliferation under SBIR grant DE-SC0020009
†johnstone29w@gmail.com

ISBN: 978-3-95450-205-9 doi:10.18429/JACoW-Cyclotrons2019-TUP029

emitters, advises in their long-range plan that the United States should "invest in new production approaches of ^{211}At emitters with high priority for ^{211}At and ^{225}Ac"; the latter, Actinium 225 is produced using a proton beam and Astatine 211 with an alpha beam both of which can be produced with the machine proposed here. Other isotopes in high demand in the U.S. in medical research, clinical nuclear medicine, science, oil exploration, construction, homeland security, national security, and defense include: Americium-241 Californium-252 Molybdenum-99 Uranium-232 Gadolinium-153 Promethium-147 Copper-67 Zirconium-89 Tin 117m.

In response, RadiaBeam is developing a novel compact sector iso-cyclotron, with dual, high-gradient, 0.2 MV cavities to accelerate ion species with charge to mass of ½ up to 20 MeV/u with large turn-to turn, centimeter-level separation for low-loss extraction removing the need for foil charge-changing extraction. The design will be optimized for radioisotope production and nuclear security applications – with a size and weight that allows transport between inspection sites on a truck. The higher extraction energy of 20 MeV/u and high currents are preferred for radioisotope production. The use of separated sectors allows extraction or insertion of targets at optimal energies for isotope production. With multi-ion capability (H_2^+ and He^{2+}) both ^{211}At and ^{225}Ac can be mass produced. Additionally, an intense neutron beam can be generated using a high current of protons on a Be target for production of Moly-99. This reaction requires less energy per secondary neutron than a current approach which uses a DT source – the Be target can be located inside the sub-critical assembly generating more neutrons and increasing the effective shielding.

TECHNICAL APPROACH

Two established approaches are available for ion acceleration: a linear or a recirculating machine. Ion linear accelerators (or linacs) have limited transportability and represent the highest cost due to the size of the accelerator and number of independent components and power sources needed to accelerate a hadron beam to the energies required for cargo inspection. For neutrons this is 14 MeV, or 14 MeV/u when applied to ions [5].

At these energies, AVF cyclotrons are a proven commercial and cost-effective technology for high current and compact proton applications. In this low-energy, non-relativistic regime (unlike electrons), cyclotrons can be designed with isochronous orbits and therefore can deliver a continuous beam in bunches spaced at the RF cavity frequency; a distinct advantage over low duty cycle pulsed systems and they have lower power requirements than a CW linac. AVF cyclotrons, however, have unavoidable high losses – 80% at injection during beam capture from the source in the central region and up to 60 - 80% at extraction due to closely-spaced proximate, turn-to-turn orbits; an artifact of low-gradient acceleration attributed to Dee cavities (which must fit in the gap between the poles, usually in the valley region [6]). Due to the closely spaced orbits, H^- is nominally accelerated in compact AVF machines instead of protons because foil stripping of electrons is required to charge change in order to extract. For ions, charge-changing extraction is not a practical option due to the already decreased charge to mass available for acceleration – for compact acceleration ions must be in their highest charge state. For light ions, a charge to mass of ½ is the highest charge state and allows a range of ions, H_2^+; or protons, through potentially to Ca^{20+}, to be accelerated in the same high-gradient accelerator.

Superconducting cyclotrons are similarly compact and much lighter than conventional AVF cyclotrons, but the associated cryogenics systems are not mobile nor insignificant [7, 8]. The iron-free cyclotron [9] must be superconducting as air-core normal conducting coils cannot generate strong magnetic fields without iron to reach MeV energies. As in the AVF cyclotron, only low-gradient cavities can be integrated into the accelerator, but H^- stripping extraction is unlikely to be an option at high currents to avoid potentially quenching the coils. Further, the degree of isochronism required for acceleration, and coil/machine tolerances depend directly on the accelerating voltage and therefore the type of cavity deployed.

For preferred CW operation, only separated-sector cyclotrons support high-gradient accelerating cavities (inserted in the gaps between sector magnets), high beam intensities with acceptable losses, and can accelerate multi-species of ions with the same charge to mass ratio without operational or configurational changes. The sector cyclotron was therefore chosen to allow insertion of high-gradient cavities, achieve the orbit separation required to support low-loss injection and extraction channels, and reduce costly precision machine-manufacturing tolerances.

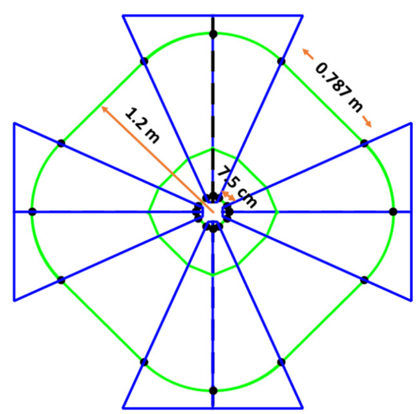

Figure 1: Schematic of the proposed cyclotron with injection drift (7.5 cm), extraction drift (0.8 m) at the extraction radius of 1.2 m

General Concept

RadiaBeam is developing a compact sector iso-cyclotron, 1.25 – 1.5 meters at the extraction radius as shown in Figure 1, with dual, high-gradient, 0.2 MV cavities to accelerate multi-ion species up to 15 - 20 MeV/u with large turn-to turn, centimeter-level separation for low-loss extraction eliminating the need for problematic ion charge changing via foil stripping. The focusing and compact foot-

ISBN: 978-3-95450-205-9 doi:10.18429/JACoW-Cyclotrons2019-TUP029

print of the AVF cyclotron will be reproduced by optimizing a radial field gradient in a sector, linear-edge magnet format with harmonic coils. Conventional shimming will attain the required isochronism for high-current (~0.5 mA) operation.

The injection energy to the cyclotron will be around 1 MeV at a radius of 12 cm, past the high-beam-loss central region plug of compact AVF and conventional cyclotrons. An innovative solid-state tandem system or RFQ with an ECR source is proposed to replace the high-loss central region – a critical design upgrade required to support high-current ion beams. Injection will occur in one of the unoccupied straight sections between sector magnets and use an inflector-type injector. The large acceleration gradient supports single-turn CW injection as the next energy orbit does not overlap the injector. A 2 mm extraction septum has been selected, given the large, meter spacing between sector magnets at extraction. A high-current, cost-effective and compact ion cyclotron based on high-gradient acceleration and low loss injection has not been built to date and the anticipated beam intensity could potentially achieve an order of magnitude higher intensity than existing ion cyclotrons.

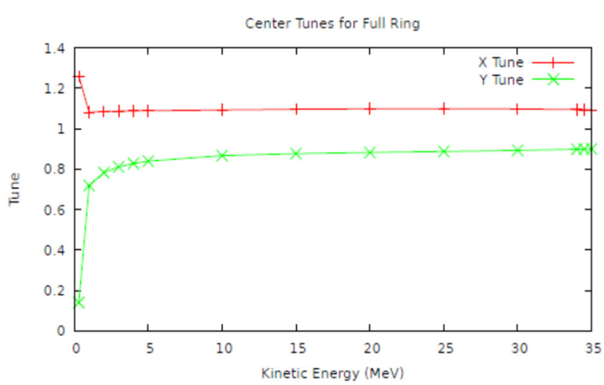

Figure 2: Design lattice machine tunes for charge to mass of ½ up to ~18 MeV/u.

Cyclotron Design

A 4-sector radial-gradient design lattice is being developed with a linear edge profile using an Enge-function end-field expansion to an isochronous specification of 10^{-5} to 10^{-4} in the Time-of-Flight (ToF) as a function of energy. Even-fold periodicity is important for the transverse dynamics and optimal when RF cavities are placed in opposing straight sections between sector magnets. The isochronous field profile will be designed for ions with a charge to mass of ½ which allows for acceleration over a wide range of light ions from protons in the form of H^{2+}, deuterons, and alphas up to Si as listed in Table 1. With strong acceleration gradients (400 keV/turn, 200 keV/cavity) and the specified field ToF field tolerance, ions with charge to mass of ½ can be accelerated in this machine without re-shimming, strong trim coils, or hardware reconfiguration of the accelerator and with fixed-frequency RF (fixed frequency RF can be retuned at the 1% level if needed). The rapid acceleration compensates for the very small changes in nuclear mass due to the nuclear binding energy. Radial field profile will not only support the ToF tolerance, linear edge-angle design and body field will be adapted to support strong, constant machine tunes in both the horizontal and vertical. The gradient radial field profile will perform the tune function of the spiral AVF pole design, serving to increase the flutter, or vertical tune (which typically decreases with radial compactness). Projected machine tunes for a preliminary concept are given in Fig. 2 for ions with a charge to mass of ½ up to ~18 MeV/u. Orbit separation at extraction for this acceleration gradient is currently estimated to be ~0.7 cm, center-to-center; sufficient for a 2 mm extraction septum. Additional extraction techniques can be applied such as inducing a betatron oscillation, as is done at PSI or a field fall-off near the extraction radius to increase the orbit to orbit separation if needed.

RF Concept

The electromagnetic design of the accelerating cavities will be driven by the cyclotron beam dynamics and magnet design. We estimate that the cavities should provide acceleration of at least 200 keV/u for the particles with charge-to-mass ratio of ½. The optimal frequency is ~40 MHz; a trade-off between acceleration gradient, stable longitudinal emittance and physical cavity size.

There are several types of RF cavities with large apertures for separate sector cyclotrons. They can be divided into two groups: double-gap (λ/4 or λ/2 transmission line type) resonators, also called 'coaxial' resonators and single-gap, waveguide-type resonators [10]. Coaxial resonators in particular can be made wide at outer radii (piece-of-pie shape, see Fig. 3, left). Double-gap coaxial type resonators can be made compact since they operate in TEM mode. However, the energy gain can vary along the aperture due to the phase difference between two gaps (transit-time factor) [11] (see Fig. 3, right).

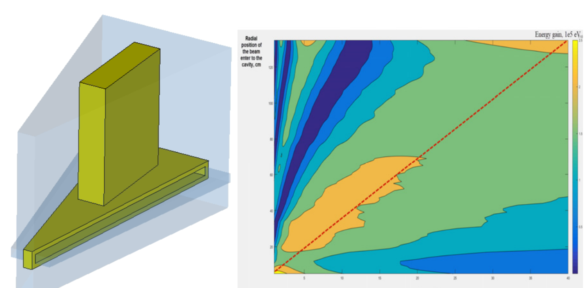

Figure 3: Quarter-wave double-gap (left) sector RF cavity, and the energy gain of the particle depending on the aperture position in a quarter-wave resonator (right), calculated in CST Particle Studio. Red line corresponds to the expected positions of the beam for the designed energy gain.

CONCLUSION

Ion accelerators have lagged technically behind advances in compact, high intensity proton accelerators. The light ion accelerator proposed here represents an innovative advance in accelerator technology for nuclear security applications including material interrogation and special

ISBN: 978-3-95450-205-9 doi:10.18429/JACoW-Cyclotrons2019-TUP029

nuclear maetrials non-proliferation which require a compact transportable and cost-efficient CW accelerator capable of producing high current ion beams with energies of 10 - 20 MeV/u and the intensities up to ~mA. This accelerator will further be an enabling technology for the commercial production of critical and currently rare radioisotopes such as At-211 and Ac-225 and also Moly-99. The most common method for producing At-211 is the bombardment of natural bismuth with α-particles. Since the threshold for the reaction is approximately 20 MeV and then peaks near 31 MeV (or 15.5 MeV/u [12]), this production channel can be accessed with the proposed cyclotron. The proposed accelerator can also be used as the injector for an ion therapy machine.

REFERENCES

[1] S. Ogorodnikov and V. Petrunin, "Processing of interlaced images in 4 - 10 MeV dual energy customs system for material recognition", *Phys. Rev. Spec. Top. Accel. Beams*, vol. 5, p. 104701, Oct. 2002.

[2] F. D. McDaniel *et al*., "Understanding X-ray cargo imaging", *Nucl. Instrum. Methods Phys. Res., Sect. B*, vol. 241, no. 1, pp. 810-815, 2005.

[3] E. S. Marshall, "New considerations for compact cyclotrons", Master Thesis, Massachusetts Institute of Technology, Massachusetts, USA, 2012.

[4] G. R. Keepin, T. F. Wimmett, and R. K. Zeigler, "Delayed neutrons from fissionable isotopes of Uranium, Plutonium, and Thorium", *Phys. Rev.*, vol. 107, p. 1044, Aug. 1957.

[5] V. Valkovic, *14 MeV Neutrons: Physics and Applications*, Boca Raton, FL, USA, CRC Press, 2015.

[6] J. H. Oh, J.-S. Chai, H. W. Kim, and B. N. Lee, "Design of RF system for compact AVF cyclotron", in *Proc. 19th Int. Conf. on Cyclotrons and their Applications (Cyclotrons'10)*, Lanzhou, China, Sep. 2010, paper MOPCP024, pp. 99-101.

[7] M. M. Maggiore, L. Bromberg, C. E. Miller, J. V. Minervini, and A. Radovinsky, "Study of a superconducting compact cyclotron for delivering 20 MeV high current proton beam", in *Proc. 20th Int. Conf. on Cyclotrons and their Applications (Cyclotrons'13)*, Vancouver, Canada, Sep. 2013, paper MOPPT020, pp. 76-78.

[8] L. García-Tabarés, "Superconducting compact cyclotrons for isotope production", presented at Academia industry matching event on superconductivity CEIMAT, May 27-28, 2013.

[9] A. L. Radovinsky *et al.,* "Variable energy acceleration in a single iron-free synchrocyclotron", MIT, Cambridge, MA, USA, Rep. PSFC/RR-13-9, Sep. 2013.

[10] P. K. Sigg, "RF for cyclotrons", *CAS - CERN Accelerator School and KVI: Specialised CAS Course on Small Accelerators*, May-Jun. 2005, Zeegse, The Netherlands, pp. 231-251. doi:10.5170/CERN-2006-012.231

[11] T. Wangler, *Principles of RF Linear Accelerators*, Wiley, New York, USA, May 1998.

[12] M. R. Zalutsky and M. Pruszynski, "Astatine-211: Production and Availability", *Current Radiopharmaceuticals*, vol. 4, no. 3, pp. 177-185, 2011. doi:10.2174/1874471011104030177

ISBN: 978-3-95450-205-9 doi:10.18429/JACoW-Cyclotrons2019-TUP030

REINFORCEMENT LEARNING BASED RF CONTROL SYSTEM FOR ACCELERATOR MASS SPECTROMETRY

H. Kim[1], M. Ghergherehchi[2], J. Lee[1], D.-H. Ha[2], H. Namgoong[2], K. M. M. Gad[1], J.-S.Chai[2,†]
Sungkyunkwan Universtity, 2066, Seobu-ro, Jangan-gu, Suwon, Gyeonggi-do, Korea
[1]Dept. Energy Science
[2]Dept. Electrical and Computer Engineering

Abstract

Accelerator Mass Spectrometry (AMS) is a powerful method for separating rare isotopes and electrostatic type tandem accelerators have been widely used. At SungKyunKwan University, we are developing AMS that can be used in a small space with higher resolution based on cyclotron. In contrast to the cyclotron used in conventional PET or proton therapy, the cyclotron-based AMS is characterized by high turn number and low dee voltage for high resolution. It is designed to accelerate not only ^{14}C but also ^{13}C or ^{12}C. The AMS cyclotron RF control model has nonlinear characteristics due to the variable beam loading effect of the acceleration of various particles and injected sample amounts. In this work, we proposed an AMS RF control system based on reinforcement learning. The proposed reinforcement learning finds the target control value in response to the environment through the learning process. We have designed a reinforcement learning based controller with RF system as an environment and verified the reinforcement learning based controller designed through the modelled cavity.

INTRODUCTION

Accelerator mass spectrometry is an instrument for analysing the mass of radioactive isotopes. It accelerates various ions such as ^{10}Be, ^{14}C, ^{28}Al, ^{38}Cl, ^{41}Ca, and ^{129}I and it is used in clinical experiments. AMS has higher resolution than conventional Mass Spectrometry. For general mass spectrometry, it has 10 - 12 parts per trillion (ppt) level sensitivity, but for accelerator mass spectrometer it has a high sensitivity of 10 - 15 ppt and tandem accelerators type AMS has been widely developed. However, cyclotron-based AMS is still under study because of its potential for miniaturization and efficiency compared to existing tandem accelerators [1, 2].

Unlike conventional cyclotron used for PET or proton therapy, AMS cyclotron has relatively low voltage and high rotation number for resolution. There is also the feature of accelerating various kinds of particles. This feature leads to non-linearity in control and interferes with performing precise beam and RF control. The external environment of the accelerator is continuously changed according to the type of particles and the quantity of the incident sample. In order to solve such a problem, it is inappropriate as a control system based on the existing linear section.

Reinforcement learning is one of the methods of machine learning such as Supervised Learning and unsupervised learning. It is a way to improve the behaviour through reward based on mutual relation of environment. Reinforcement learning does not require prior knowledge of the environment and is used for robots and games because it guarantees learning and adaptability [3].

In this work, reinforcement learning based RF control system was developed. From the viewpoint of reinforcement learning structure, we can redefine the controller as an agent and the cyclotron control variable as environment and to interconnect environment between agent, state, action and reward should be defined as shown in Fig. 1.

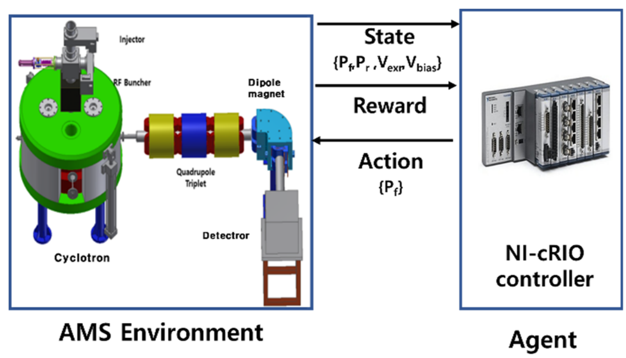

Figure 1: Reinforcement Learning based AMS control block diagram.

SYSTEM DESIGN

In AMS RF cavity, the electric field from rf source can be calculated by following formula.

$$E_{PK} = \kappa_e \sqrt{P_t} \ ,$$

where κ_e is coefficient which is determined using computer code and P_t is transmitted power. P_t is changed by cavity coupling coefficient and resonant-frequency mismatch and is related to beam loading effect and reflected power. Those parameters are used to describe state as follows:

$$\{P_f, P_r, V_{exr}, V_{bias}\} \quad ,$$

where P_f is forward power from rf source, P_r is reflected power and V_{exr}, V_{bias} is extraction and biases voltage, which effect injection beam quality from ion source, respectively.

To measure forward and reflected power, ZFBDC20-61HP+ bi directional coupler was installed between cavity and RF amp and NI-cRio was communicated with ion source process controller station. The action space for the RF controller can be expressed by:

$$A = \{a| -\Delta f, 0, \Delta f\} \ ,$$

†jschai@skku.edu

ISBN: 978-3-95450-205-9 doi:10.18429/JACoW-Cyclotrons2019-TUP030

where Δf is the Increment of RF input frequency. Since we use a relatively low frequency, we choose an AFG 3021 function generator as an RF input and ACTION is implemented by remote control. Agent's actions are evaluated by the reward:

$$\text{Reward} = \{+1, \text{ if } P_{r\,t+1} > P_{r\,t} \text{ and } -1, \text{ if } P_{r\,t+1} \leq P_{r\,t}\},$$

where $P_{r\,t+1}$, $P_{r\,t}$ are reflected power at two successive time steps. Agent will get positive reward when reflected power decrease. In other cases, it gets a negative reward.

SOFTWARE DEVELOPMENT

AMS controller was implemented by NI CompactRIO systems. By using the Scan Engine, we programmed Actor-critic structure and data communication with other AMS devices for data acquisition and monitoring. CompactRIO consist of CPU module, input output module and communication module. The devices such as signal generator and ion source were connected through RS 232,485 serial communications.

In AMS controller, we programmed Actor-critic method [4]. Actor-Critic is type of reinforcement learning and also time difference method that can be used directly without an environment model, and has the advantage of doing the learning directly with raw experience.

In Actor-Critic structure, Both Actor and Critic are parameterized with neural networks and those function determines whether to pass through or update the neural network through Boolean input.

In the former case, the input data passes through each layer of the neural network. At this time, the weight and bias values remain at their stored values.

In the update process, the neural network calculates the gradient of the weight and bias according to the input through backpropagation, as shown in Fig. 2.

The calculated gradient is used as input to the ADAM optimizer [5] and updates the weights and biases. The weights and biases of neural networks that make up actors and critics are initialized before training. We performed the initialization using a He uniform variance scaling initializer. This is accomplished using a uniform white noise function with a square root of 6 / (number of layer inputs), as shown Fig. 3.

Actor and Critic perform optimization work by using ADAM Optimizer to reduce loss function through training. The ADAM optimizer is a kind of Stochastic Gradient Descent that allows you to quickly find the optimal value using only a few data when training. Figure 4 shows the loss function reduction during training of actors and critics.

Verification of the A2C-based resonant controller was carried out through the forward and reflected power. A2C controller was simulated when the resonance point did not change at 5.8 MHz to verify whether the A2C model can track the resonance point and confirmed that it converged to the 5.8 MHz band after the initial search, as shown Fig. 5.

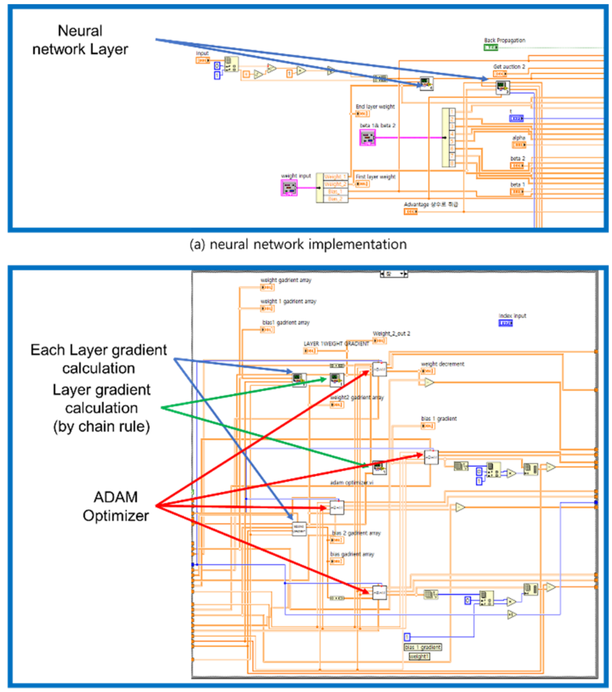

(a) neural network implementation

(b) neural network weight and biases update process

Figure 2: Neural network block diagram.

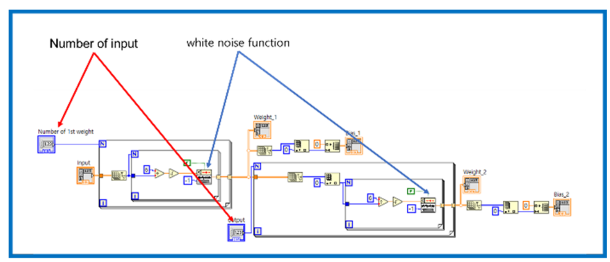

Figure 3: He uniform variance scaling initializer.

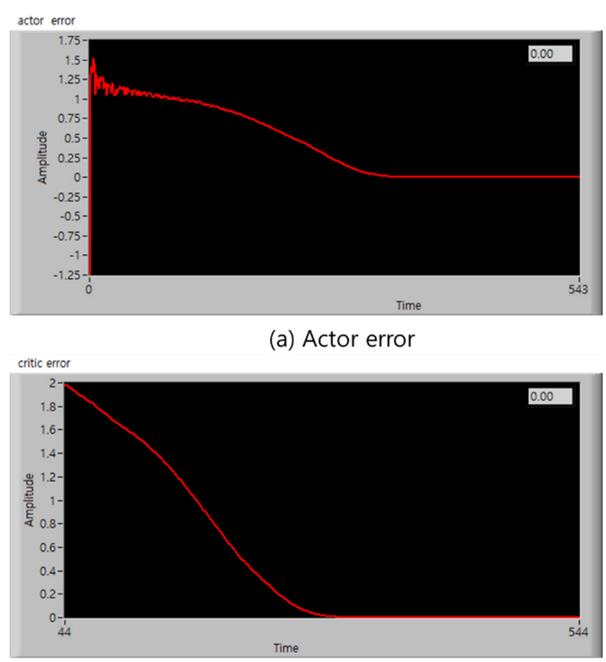

(a) Actor error

(b) Critic error

Figure 4: Actor and critic loss function test in training.

ISBN: 978-3-95450-205-9 doi:10.18429/JACoW-Cyclotrons2019-TUP030

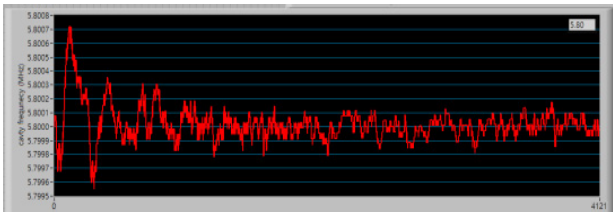

Figure 5: A2C Resonance controller learning process at 5.8 MHz constant resonance point.

The resonance point variation model was also trained by adding a sinusoidal function with an amplitude of 1.5 kHz to the resonance point, as shown Fig. 6.

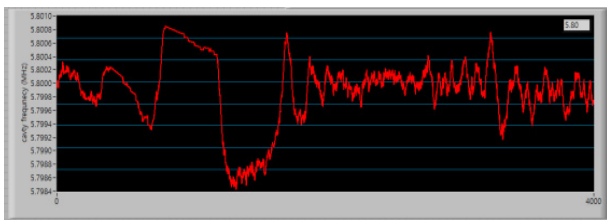

Figure 6: A2C Resonance controller learning process in resonance point shift model.

DISCUSSION

A2C based AMS control system design and simulation was performed in this paper. This method is currently being tested with the ion source controller hardware information.

ACKNOWLEDGEMENTS

This work was supported by the Radiation Technology R&D program through the National Research Foundation of Korea funded by the Ministry of Science, ICT and Future Planning (Grant No. 2017M2A2A4A02020347).

REFERENCE

[1] J.-W. Kim *et al.,* “Design study of a compact cyclotron for accelerator mass spectrometry”, *J. Korean Phys. Soc.*, vol. 54, no. 2, pp. 580-585, Feb. 2009.

[2] W. Kutschera, “Progress in isotope analysis at ultra-trace level by AMS”, *Int. J. Mass Spectrom.,* vol. 242, no. 2-3, pp. 145-160, Apr. 2005. doi.org/10.1016/j.ijms.2004.10.029

[3] R. S. Sutton and A. G. Barto, *“Reinforcement learning: An introduction”*, Cambridge, MA, USA and London, England: MIT press, 2014, 2015.

[4] I. Grondman *et al.*, “A survey of actor-critic reinforcement learning: Standard and natural policy gradients”, *IEEE Trans. Syst. Man and Cybern. Part C Appl. Rev.,* vol. 42, no. 6, pp. 1291-1307, 2012. doi:10.1109/TSMCC.2012.2218595

[5] D. P. Kingma and J. Ba, “Adam: A method for stochastic optimization”, 2014. arXiv:1412.6980

ISBN: 978-3-95450-205-9 doi:10.18429/JACoW-Cyclotrons2019-TUP031

DESIGN AND CONSTRUCTION PROGRESS OF CYCLOTRON BASED PROTON IRRADIATION FACILITY FOR SPACE SCIENCE

Yinlong Luy†, Shizhong An, Bin Ji, Xianlu Jia, Shenglong Wang, Tao Cui, Tao Ge, Tianjue-Zhang
China Institute of Atomic Energy, Beijing, China

Abstract

The proton irradiation facility for space science research and application consists of a 50 MeV proton cyclotron, two beam lines and two radiation effect simulation experimental target stations. And the shielding plant facilities is constructed at the same time. The equipment provided by CIAE mainly includes a 50 MeV proton cyclotron, beam transport lines and experimental terminals, as well as dose monitoring and installation equipment. The 50 MeV proton cyclotron CYCIAE-50 is a compact, negative hydrogen ion cyclotron with the proton beam energy from 30 - 50 MeV, and the beam intensity is from 10 nA to 10 uA. The CYCIAE-50 is about 3.2 m in diameter, 3.5 m in total height and 80 t in total weight. The magnet of the cyclotron is a compact AVF structure electromagnet at room temperature with 30 kW exciting power. The diameter of the pole is 2 m, the outer diameter of the yoke is 3.2 m, and the height of magnet is 1.5 m. The cyclotron uses an external multi-cusp H^- ion source. The H^- beam from the ion source is injected into the center region through the axial injection beamline. Then the H^- beam is injected into the accelerating orbit by the spiral inflector. The cyclotron frequency is about 16 MHz. The RF system of the cyclotron is a pair of $\lambda/2$ cavities driven by a 23 kW transmitter. The fourth harmonic accelerating frequency is about 65 MHz. The proton beam is extracted by a single movable stripping carbon foil and the stripping extraction efficiency is more than 99%. The CYCIAE-50 has now been designed in detail, and its main components, such as the main magnets and RF cavities, are being manufactured in the factories in China.

This paper introduces the design and construction progress of the proton irradiation facility based on a 50 MeV cyclotron. The proton irradiation facility for space science is oriented to space proton radiation environment simulation. The proton radiation has an important influence on the spacecraft, and the energy of more than half of the protons in the space is no more than 50 MeV. The Proton Irradiation Facility could provide proton beam with energy range of 30-50 MeV, and beam density in the range of $5 \times 10^5 \sim 5 \times 10^9$ $p \cdot cm^{-2} \cdot s^{-1}$. It is suitable for the ground simulation test of displacement damage of optoelectronic devices, as well as the proton single particle effect ground simulation test of deep submicron devices and nanodevices. It provides technical support for the development of scientific satellite load and optoelectronic devices. Compared with the large accelerator facility, the proton irradiation facility based on the compact cyclotron is a type of space proton radiation environment simulation device with high performance and lower price. The layout diagram of the proton irradiation facility for space science is shown in Fig. 1. The proton beam from the cyclotron passes through two 45˚ deflection magnets and the energy selection system. At the experimental hall, there are two experimental beam lines for different proton radiation effects.

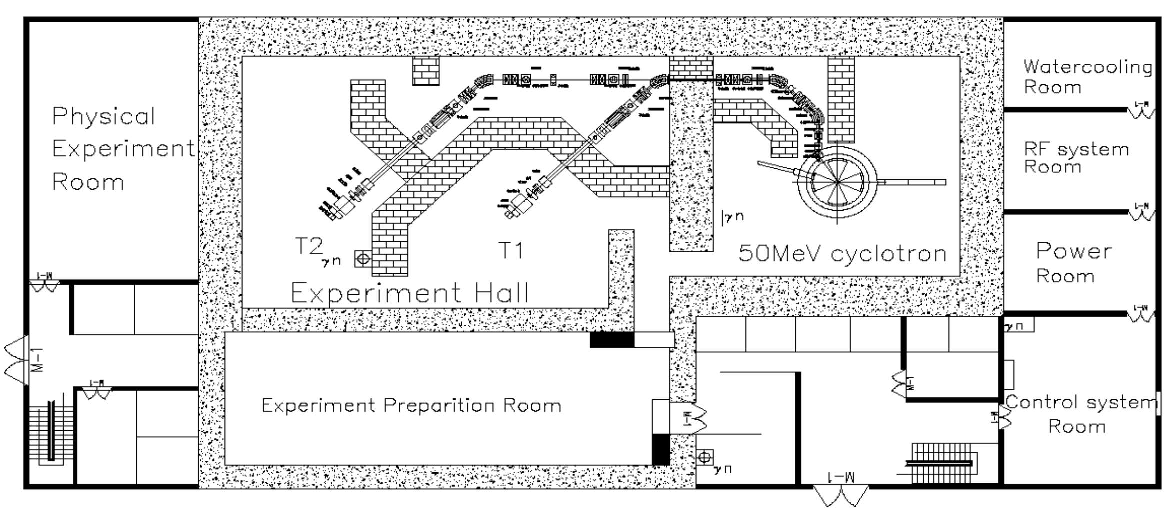

Figure 1: Layout of the proton irradiation facility based on 50 MeV cyclotron.

† yllv401@126.com

ISBN: 978-3-95450-205-9 doi:10.18429/JACoW-Cyclotrons2019-TUP031

The Progress of the 50 MeV Cyclotron

The 50 MeV proton cyclotron for the Proton Irradiation Facility for Space Science is a compact, negative hydrogen ion cyclotron. Thanks to the movable stripping extraction carbon foil, the proton beam energy is from 30 to 50 MeV. The beam intensity is from 10 nA to 10 μA. The CYCIAE-50 cyclotron is about 3.2 m in diameter, 3.5 m in total height and 80 t in total weight. The cyclotron uses an external multi-cusp H^- ion source is installed above the main magnet. The H^- beam from the ion source is injected into the center region through the axial injection beamline. Then the H- beam is injected into the accelerating orbit by the spiral inflector. The cyclotron frequency is about 16 MHz. The RF system of the cyclotron is a pair of 1/2 RF cavities driven by a 23 kW transmitter. The fourth harmonic accelerating frequency is about 65 MHz. The proton beam is extracted by a single movable stripping carbon foil that's stripping extraction efficiency is more than 99%. Design of main vacuum is 5×10E-7 mbar for the cyclotron. The main vacuum chamber is cylinder sealed by rubber O-rings. The Two GM cryogenic vacuum pumps are fixed on the top of the main magnet, and two turbine molecular pumps are fixed under the main magnet. The total power of the cyclotron is about 200 kW. Table 1 shows the main parameters of the 50 MeV cyclotron.

Table 1: The Parameters of the 50 MeV Proton Cyclotron

Parameter	Value
Beam Energy	30-50 MeV
Beam intensity	1 nA - 10 μA
Accelerated Particle	H-
Ion Source	H-Multi-Cusp
Magnetic field	1-1.6 T
Particle rotation frequency	16 MHz
Cyclotron Size	Φ3.5 m×2.5 m
Weight	~ 80 t
Vacuum Degree	5×10^{-7} mbar
Beam stability	1/2 hr
Total Power	~ 200 kW
standby power	~ 50 kW

The Main Magnet of CYCIAE-50

The main magnet of the cyclotron is a compact AVF structure electromagnet at room temperature. The diameter of the poles is 2 m, the outer diameter of the yokes is 3.2 m, and the height of magnet is 1.5 m. The main magnet is one of the most important components of the cyclotron, which forms an isochronous magnetic field that restricts particles to rotate along the designed orbit. The system includes magnet, excitation coils, synchronous hydraulic lifting device, high precision magnetic field measuring device, on-line temperature monitoring device, on-line magnetic field monitors, high precision and high stability power supply, etc. The main magnet adopts straight sectors and deep valleys structure without adjusting coils. Figure 2 shows the structure of the main magnet. The magnetic poles are 4 pairs of 50° sector poles, the air gap is from 40 mm to 32 mm. The average field is 1.0-1.6 T. The shimming bars used to adjust the isochronous magnetic field are embedded at the edges of the magnetic poles. The magnet material is pure iron with carbon content less than 0.025%. The manufacturing accuracy of the main parts of the magnet is better than 0.05 mm. The coils are fixed between the magnetic poles and the yokes. The excitation coils are wound by the copper hollow tubes with internal cooling water. The total exciting power of the coils is about 30 kW, and the total weight is about 5 t.

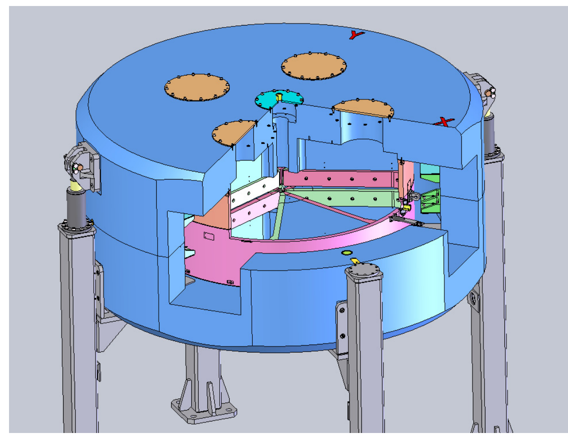

Figure 2: The main magnet of CYCIAE-50.

The main magnet structure is poles and yokes integral blank structure. That is, the poles and yokes and so on are machined from one pure iron disc blank. The magnet blank parts are vacuum smelting and vacuum casting ingots, and then forged by a free forging machine of 18500 t to create round cake-like blank parts. The magnet parts are currently being processed on a milling machine and are expected to be finished in October. Figure 3 shows that the magnet blank parts are being forged, and Fig. 4 shows that the magnet parts are being machined on a milling machine.

The RF System of CYCIAE-50

The RF system of the 50 MeV proton cyclotron consists of a RF power source with rated output power of 23 kW, a 3 in transmission line system, a low level control system and two high frequency cavities. The 23 kW RF power source is designed with easy maintenance and antireflection. The two cavities of the 50 MeV cyclotron are connected by a high frequency bridge at the central position. RF power feeds into the cavities by a coupling capacitor. The low level control system includes amplitude stable loop and frequency tuning loop. The two loops are used to stabilize the acceleration voltage of the RF cavities and control the fine tuning capacitance to compensate the deformation caused by heating. The RF power source, RF cavities, and low level control system have been designed and are being manufactured. The parameters of the RF system are detailed in Table 2.

ISBN: 978-3-95450-205-9 doi:10.18429/JACoW-Cyclotrons2019-TUP031

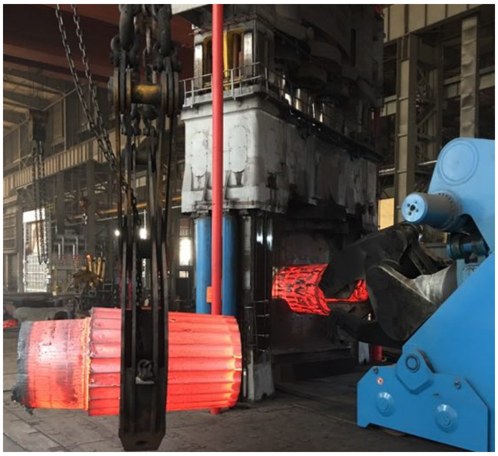

Figure 3: The magnet blank parts are being forged.

Figure 4: The magnet parts are being machined on a milling machine.

Table 2: The Parameters of the RF System

Parameter	**Value**
RF frequency	~ 65.4 MHz
Voltage stability	1/1000
Cavity number	2
Work model	4th harmonic acceleration
Cavity form	λ/2
Acceleration voltage	~ 50 kV
Coupling capacitor number	1
Frequency tuning	1

Other System of the 50 MeV Cyclotron

There is a permanent magnet multi-cusp H- ion source on the top of the cyclotron main magnet. The maximum H- beam intensity from the source is 5 mA, and the beam energy is 30 keV. The injection system is very simple design. The H- beam from the ion source enters the spiral inflector in the center region only through a solenoid. The ion source and the injection beamline are being manufactured. Table 3 is the main parameters of ion source and injection beamline.

Table 2: The Parameters of the Ion Source and Injection Beamline

Parameter	**Value**
Ion source	Multi-cusp H- source
Beam energy	30 keV
Beam intensity	5 mA
Inflector voltage	±10 kV
Injection beamline	~1 m
Inflector gap	8 mm

The 50 MeV cyclotron has a single movable stripping carbon foil that can move from 30 - 50 MeV. Ordinary the stripping extraction efficiency is more than 99%, and the beam loss is no more than 100 μA. Figure 5 shows the structure of the movable stripping target.

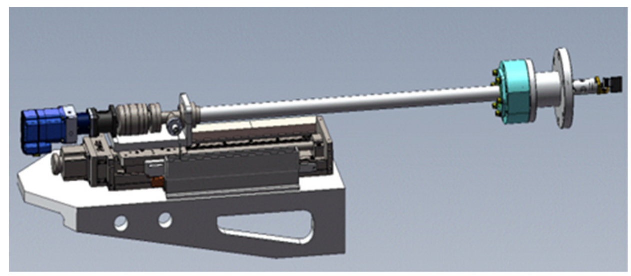

Figure 5: The structure of the movable stripping target.

CONCLUSION

The proton irradiation facility based on the 50 MeV proton cyclotron is a compact and lower price space proton radiation environment simulation facility with high performance. Now all the detail design of the 50 MeV cyclotron has been finished at CIAE. The main parts of the cyclotron such as the main magnet are being manufactured now. Beam commissioning is expected to be done at the end of the next year.

REFERENCES

[1] T. J. Zhang, Z. G. Li, and Y. L. Lyu, "Progress on construction of CYCIAE-100", in *Proc. 19th Int. Conf. on Cyclotrons and their Applications (Cyclotrons'10)*, Lanzhou, China, Sep. 2010, paper TUA2CIO01, pp. 308-313.

[2] W. Kleeven, M, Abs, J. L. Delvaux, *et al.*, "Recent development and progress of IBA cyclotrons", *Nucl Instrum. Methods Phys. Res., Sect. B*, vol. 269, no. 24, pp. 2857-2862, Dec. 2011. doi:10.1016/j.nimb.2011.04.031

[3] T. Zhang, Y. Lyu, J. Zhong, *et al.*, "Design, construction, installation, mapping, and shimming for a 416-ton compact cyclotron magnet", *IEEE Trans. Appl. Supercond.*, vol. 26, no. 4, pp. 1-5, Jun. 2016. doi:10.1109/TASC.2016.2524535

ISBN: 978-3-95450-205-9 doi:10.18429/JACoW-Cyclotrons2019-TUP033

CONCEPT OF 15 MeV CYCLOTRON FOR MEDICAL ISOTOPES PRODUCTION

O. Karamyshev†, JINR, Dubna, Russia

Abstract

The purpose of this article is to show the prospects of cyclotrons with resistive coils and prove that even in such a well-established field there is still room for innovation. The concept of a 15 MeV cyclotron accelerating H^- ions with a current of up to 1 mA is presented. The design features significantly lower weight and power consumption compared to the majority of existing cyclotrons of the same energy.

INTRODUCTION

Cyclotrons are widely used, delivering 10 - 70 MeV proton (mostly) beams for medical isotopes production such as PET, SPECT isotopes and 200 - 250MeV proton beams for hadron therapy. The modern trend is to apply superconducting coils to increase magnetic field strength of the cyclotron in order to make the accelerator more compact, and thus reduce the overall cost of the cyclotron setup. Nowadays superconducting cyclotrons and synchrocyclotrons are successfully operating not just for proton therapy (Varian Proscan [1], S2C2 (IBA) [2], Mevion [3]) but also for isotope production (Ionetix [4]). Some of them appeared quite recently, and some work for years and have proved their effectiveness.

However, the author believes that at least at the low-energy area there is still room for improvements of the resistive-coil machines.

To summarize, here are the reasons why the author believes that cyclotrons with resistive coils are still a good choice for medical applications:

- There are opportunities for optimization, examples are presented further in the paper.
- Compared to superconducting cyclotrons, power consumption and dimensions are not necessarily higher, but in some cases could be lower, as cryocoolers consume power, and also occupy space around the magnet.
- Low magnet field is easier to shim, the isochronizing requirements are lower.

A NEW 15 MeV CYCLOTRON RC3/6

Usually, cyclotrons dedicated for isotope production accelerate H^- ions to get use from extraction by stripping on the foil. Extraction by stripping has about 100% efficiency, low energy H^- ions has only one disadvantage, high vacuum is required.

Concept RC3/6

The cyclotron needs to be compact, cheap, reliable and to have a low power consumption. Concept RC3/6 lead us to more efficient design of the cyclotron than typical four-sector accelerator. What is the essence and specific feature of the concept 3/6? The three-sector cyclotron operating at the 6 harmonic mode of acceleration allows to have an effective magnetic system due to wide sectors providing higher mean field and narrow valleys sufficient for placing resonators corresponding to 6th harmonic of acceleration (see Figure 1). The sectors of the magnet are 90° azimuthal width, and valleys are about 30 degrees. In such case the 6th harmonic mode is optimal for acceleration and the resonance frequency must be 128 MHz for magnetic field equal to 1.4 T.

Such configuration is beneficial for both magnet and RF design, as the magnet, while having necessary average magnet field is being very efficient (has small number of A·turns), high frequency RF system is very compact and power-efficient.

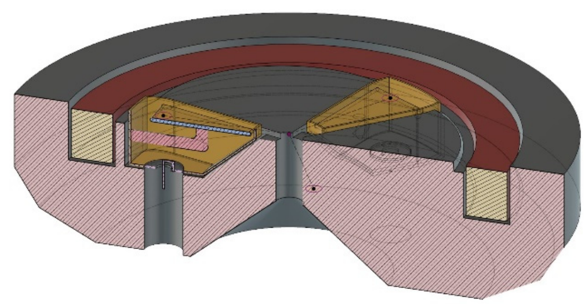

Figure 1: Layout of the 3D computer model of the cyclotron.

Table 1. Parameters of the Cyclotron

Magnet Type	Resistive
Ion source	external
Final energy [MeV]	15
Final radius [mm]	370
Mean Magn. field [T]	1.4
Dimensions (height×diameter) [mm^2]	720 × 1420
Weight [kg]	6500
Hill/Valley field [T]	1.8/0.4
Hill/Valley gap [mm]	25/300
A*Turn number	17 000
Magnet power consumption [kW]	1.5
RF frequency [MHz]	128
Harmonic number	6
Voltage [kV]	20
RF power [kW]	4
Turn number	120
Beam intensity [μA]	Up to 1000
Extraction type	stripping foil

† olegka@jinr.ru

ISBN: 978-3-95450-205-9 doi:10.18429/JACoW-Cyclotrons2019-TUP033

Resistive coils and rather big pole diameter reduce the effort and cost of producing this machine.

The main specific feature of this cyclotron is very low coil current 17000 A·turns. Coil cross-section is 120x100 mm^2, therefore the current density is 17000/120/100 = 1.41 A/mm^2. It is possible to keep this coil even air-cooled. Magnet power consumption is just about 1.5 kW.

If it would be more feasible to use water cooling coil, it is optimal to keep the current density at about 3 A/mm^2 and make the yoke more compact. This would save some money on copper and steel, however increase power consumption.

What makes the magnet of this cyclotron so efficient is low A·turns number in the coil. Such a low value is possible because the magnetic flux inside the magnet remains below the saturation of the Steel 1010 (which is commonly used for cyclotron magnets), so almost all the energy of magnetic field is concentrated between the poles, and the steel is in the mode of an efficient magnet conductor.

Magnetic Field Analysis and Preliminary Beam Dynamics Estimations

As the concept is rather unusual, particle tracking has been carried out to confirm the principle.

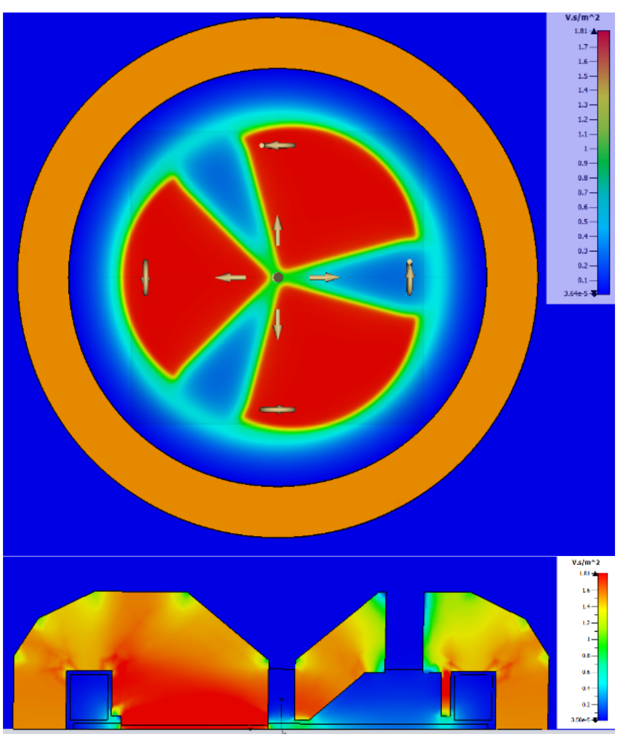

Figure 2: Magnet flux distribution through median plane (up), inside the yoke of the magnet (down).

Average magnetic field and flutter from CST simulation (Figure 2) are presented in Figure 3.

It can be seen from Figure 4 that the three wide sector structure of the cyclotron has high 6th and 9th Fourier harmonics in the structure of the magnetic field, which together with the third harmonic lead to a sufficiently large value of the flutter (Figure 3).

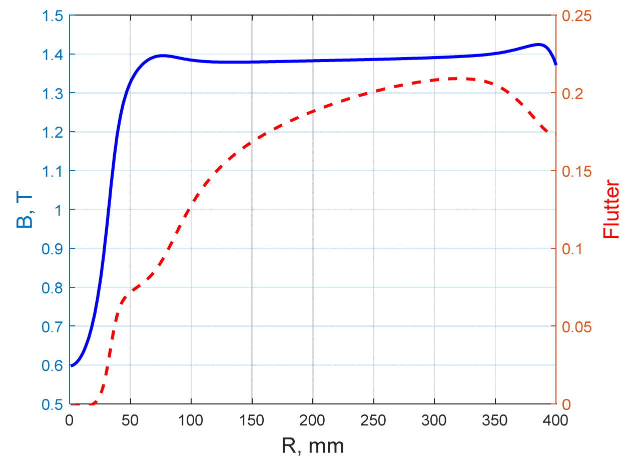

Figure 3: Average magnetic field and flutter along the radius.

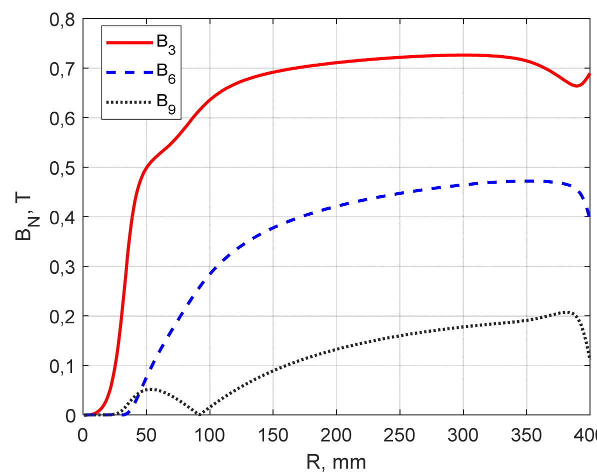

Figure 4: Fourier harmonics of the cyclotron magnetic field.

It can be seen from Figure 4 that the three wide sector structure of the cyclotron has high 6th and 9th Fourier harmonics in the structure of the magnetic field, which together with the third harmonic lead to a sufficiently large value of the flutter (Figure 3).

Orbital frequency and betatron tunes calculated in equilibrium orbits by CYCLOPS-like code are presented in Figure 5 and Figure 6 correspondently.

Isochronism of the model is good enough for beam dynamics simulation. The beam has been accelerated in the 3D magnetic and 3D RF electric field maps with initial amplitudes of betatron oscillations up to 5 mm (see Figure 7). Total number of turns with 20 kV accelerating voltage was equal 120. There were no losses of particles in any radius.

The beam is injected from the external CUSP ion source, using usual electrostatic spiral inflector or magnetostatic inflector. Accurate 3D model of the inflector and the central region is not finished yet but it is clear that center region should not cause any troubles.

ISBN: 978-3-95450-205-9 doi:10.18429/JACoW-Cyclotrons2019-TUP033

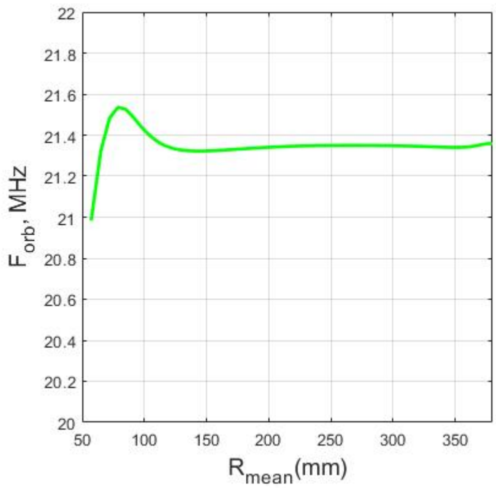

Figure 5: Orbital frequency.

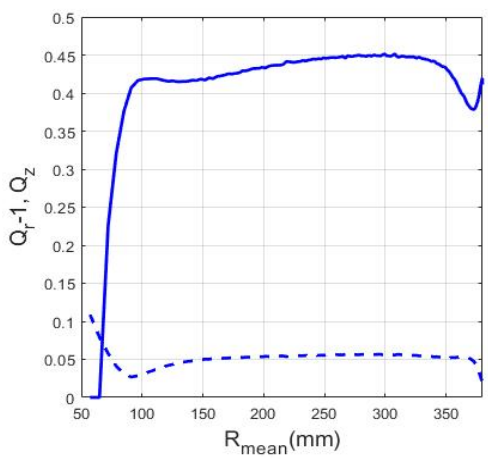

Figure 6: Betatron frequencies.

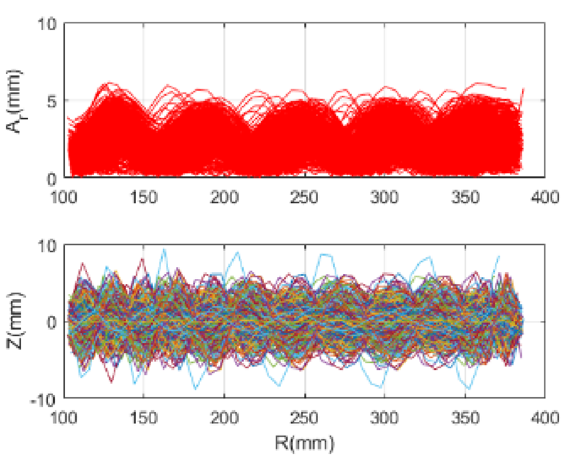

Figure 7: Amplitudes of radial oscillations and vertical motion of the beam during acceleration.

Accelerating System

Geometric model of the double gap delta cavity housed inside the valley of the magnetic system of the cyclotron RC3/6 simulated in the CST STUDIO SUITE is presented in Figure 8. Suitable accelerating frequency and voltage along radius were achieved. All 3 cavities will be powered independently with a coupling loop. It is not possible to have galvanic connection in the center region, because of a spiral inflector. All coupling loops can be connected to the coaxial power line, going in 100 mm hole through the yoke from the top of the cyclotron. All cavities operated in the same phase. Top/bottom Dees should be connected via contact fingers at the extraction end.

The active tuning system must be designed to bring the cavities on the frequency initially to compensate detuning for temperature variations due to RF heating and can be realized by capacitance tuner from radial direction. Simulations show that the frequency is about 128 MHz.

Power dissipation in the model was calculated assuming the wall material is copper with a conductivity $\sigma = 5.8\text{x}10^7$ 1/(Ωm). The quality factor was about 5500 and power losses of the model were:

For accelerating voltage 20 kV, calculated losses in one cavity are about 1.3 kW.

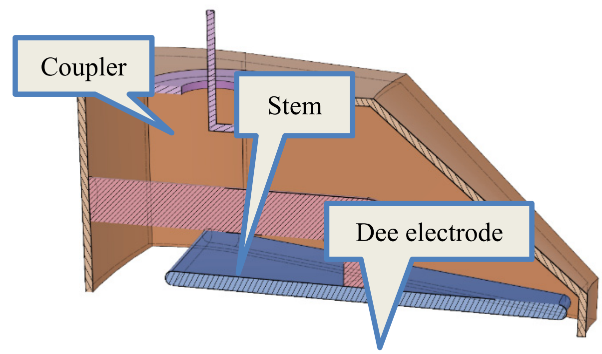

Figure 8: RF cavity overview (one fourth).

Vacuum

Vacuum chamber wall 30 mm width between the end of the sectors and coil. The rest of the vacuum chamber is the magnet itself. Vacuum seals in the RF/vacuum pump holes. Three holes from the bottom will be used for vacuum pumping.

Expected pressure in the cyclotron is 2 to 5 x10^{-7} Torr, by using three turbo-molecular pumps, pumping through 100 mm holes placed at the distance 0.5 m away from median plane.

The limitation for H^- acceleration is the energy of about 70 MeV, as further acceleration would result in magnetic dissipation of H^- ions, and require reduction of magnetic field, making the cyclotron big, and therefore expensive. The 15 MeV cyclotron RC3/6 is just an example, the concept RC3/6 can work at least up to 70 MeV.

CONCLUSION

The optimization possibilities of the design of cyclotrons with resistive coils are not exhausted.

The design of the RC3/6 is quite unusual. The main advantage of the RC3/6 cyclotron is its low power consumption and small size. Dimensions are even smaller than those of the superconducting ION-12SC cyclotron [4].

The concept RC3/6 of a three-sector cyclotron operating in 6th harmonic mode will be an effective solution for accelerating to higher energies. The author will continue to

ISBN: 978-3-95450-205-9 doi:10.18429/JACoW-Cyclotrons2019-TUP033

develop this concept and design different cyclotrons for the alpha-emitting isotopes production, such as ^{211}At and up to the 70 MeV H$^-$ cyclotron.

Also, similar approach is possible for proton cyclotrons of a higher energies, such as 230 MeV for proton therapy.

REFERENCES

[1] J. Schippers, R. Dölling, J. Duppich *et al.*, "The SC cyclotron and beam lines of PSI's new proton therapy facility PROSCAN", *Nucl. Instrum. Methods Phys. Res., Sect. B*, vol. 261, no. 1, pp. 773-776, 2007. doi: 10.1016/j.nimb.2007.04.052

[2] J. G. M. Kleeven *et al.*, "The IBA Ssperconducting synchrocyclotron project S2C2", in *Proc. 20th Int. Conf. on Cyclotrons and their Applications (Cyclotrons'13)*, Vancouver, Canada, Sep. 2013, paper MO4PB02, pp. 115-119.

[3] http://www.mevion.com/products/mevion-s250-proton-therapy-system

[4] X. Wu *et al.*, "Recent Progress in R&D for Ionetix Ion-12SC superconducting cyclotron for production of medical isotopes", in *Proc. 10th Int. Particle Accelerator Conf. (IPAC'19)*, Melbourne, Australia, May 2019, pp. 3568-3570. doi:10.18429/JACoW-IPAC2019-THPMP052

ISBN: 978-3-95450-205-9 doi:10.18429/JACoW-Cyclotrons2019-TUP034

STUDY OF MERIT RING FOR INTENSE SECONDARY PARTICLE PRODUCTION

H. Okita*[1], Y. Kuriyama[2], T. Uesugi[2], Y. Ishi[2], Y. Mori[2]
[1] Graduate School of Engineering and Faculty of Engineering, Kyoto University, Kyoto, Japan
[2] Institute for Integrated Radiation and Nuclear Science, Kyoto University, Osaka, Japan

Abstract

An intense negative muon source MERIT (Multiplex Energy Recovery Internal Target) for the nuclear transformation to mitigate the long-lived fission products from nuclear plants have been proposed. For the purpose of proof-of-principle of MERIT scheme, a FFA (Fixed Field Alternating focusing) ring has been developed. In this paper, the results of study for proof-of-principle experiment on MERIT scheme will be reported.

INTRODUCTION

Recently, nuclear transmutation with negative muons has been conceived as one of the ways to mitigate the radioactive nuclear wastes such as long lived fission products (LLFPs) [1]. In muonic atom, which is formed by trapping negative muon, the atomic nucleus absorbs a negative muon with large probability (95%) [2], if the atomic number Z is more than 30 and then, it transforms to stable nucleus by beta decay and the emission of several neutrons. For example, long lived cesium isotope ^{135}Cs ($\tau_{1/2}$=2.3 million years) which is produced from the nuclear power plant in burning out one ton of enriched the nuclear fuel including 3% of ^{235}U can be transformed to non-radioactive Xe isotopes within about five years, if the yield of negative muon is $10^{16}\mu^-$/s.

Negative muons decayed from negative pions are efficiently produced by the nucleon-nucleon interactions with high energy hadron beam using the target nucleus containing neutrons. In order to generate negative muons effectively, MERIT (Multiplex Energy Recovery Internal Target) scheme has been proposed. The principle of the MERIT scheme is shown in Fig. 1. Contrary to the original ERIT scheme [3,4], the transverse emittance growth caused by multiple scattering is rather modest since a primary hadron beam energy is relatively high. On the other hand, the longitudinal emittance growth rate becomes large. The wedge-shaped target placed at the dispersive orbit could reduce this effect and also the injection beam energy becomes lower, which could cure the load of the injector.

The characteristics of the MERIT scheme are shown as follows.

- Energy recovery and ionization cooling;
- CW operation with fixed RF frequency beam acceleration and storage;
- Negative pion production using internal thin target;

There are a couple of difficulties in negative pion production. One is the energy loss of the projectile proton by ionization of target. The efficiency of negative pion production drops until the particle energy reaches the threshold energy of pion production at about 250 MeV/u. Another problem is the absorption of negative pions in the solid target. The absorption cross section of negative pions with the target nucleus is so large that a thinner target must be used. Thus, a high beam current and a thin target are both essential to improve the efficiency in negative muon production.

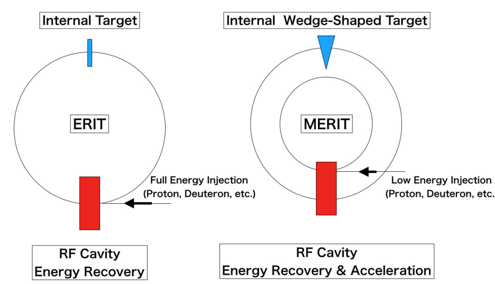

Figure 1: Schematic diagram of ERIT and MERIT scheme.

In MERIT scheme, the fixed RF frequency acceleration makes a cw beam operation with low energy beam injection. Negative pion production using a thin target has advantages for reducing the negative pion loss in the target and keeping high reaction rate with energy recovering and cooling by RF re-acceleration.

To prove a principle of MERIT scheme, in particular, on the fixed RF frequency beam acceleration and storage with a wedge type of thin internal target, a scaling type of FFA ring, the name is MERIT-PoP (Proof-of-Principle) ring has been developed with remodeling the FFA-ERIT ring [3,4], which was built at the Institute for Integrated Radiation and Nuclear Science in Kyoto University (KURNS). As preparation for the experimental study on MERIT scheme, beam study on the closed orbit distortion (COD) correction and measurement of betatron tune of the MERIT-PoP ring was carried out [5]. In this paper, study for the PoP experiment on MERIT scheme using the MERIT-PoP ring is reported.

MERIT-POP RING

The MERIT-PoP ring has been developed with several modifications of existing the FFA-ERIT proton ring. A semi-isochronous acceleration in the scaling FFA is useful for the fixed RF frequency acceleration [6], where it is essential to keep a slippage factor(η) close to zero. In case of the scaling FFA, η depends only on the field index k and Lorentz factor

* okita.hidefumi.43x@st.kyoto-u.ac.jp

ISBN: 978-3-95450-205-9 doi:10.18429/JACoW-Cyclotrons2019-TUP034

γ as shown in Eq. (1).

$$\eta = \frac{1}{k+1} - \frac{1}{\gamma^2} \tag{1}$$

The injection beam energy of the MERIT-PoP ring is about 10.0 MeV. Thus, the field index k was changed from the original value of 1.92 to about 0.07 by changing the magnetic pole shape as shown in Fig. 2, which led the slippage factor of −0.044. With this modification, the energy range of

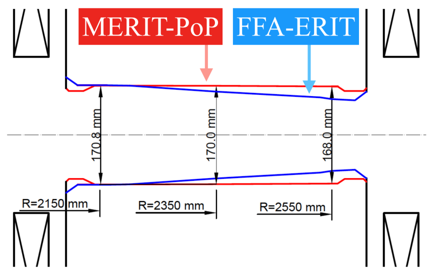

Figure 2: Schematic view on modification of magnetic pole shape. This figure shows the pole shape of focusing magnet of the FFA-ERIT ring and the MERIT-PoP ring, respectively.

the MERIT-PoP ring was extended to accelerate the proton beam from approximately 9.5 to 12.0 MeV. All parameters are shown in Table 1.

Table 1: Parameters of MERIT-PoP Ring

Ring Paramters		
Particle		Proton
Number of Cells		8
Lattice		FDF-triplet
Field Index	k	0.07
Energy Range	[MeV]	9.5 – 12.0
Orbit Radius	[mm]	2250 – 2500
Slippage Factor	η	-0.044
Betatron Tune	H/V	1.03 / 1.25
Magnetic Field F/D	[T]	0.59 / 0.14
Opening Angle of F/D magnet	[deg.]	6.4 / 5.1
Minimum Half Gap of F/D magnet	[mm]	84.0 / 85.2
RF Voltage	[kV]	75–225
Harmonic Number		6
RF Frequency	[MHz]	18.12

In the scaling FFA, the horizontal tune can be obtained approximately from Eq. (2). The horizontal tune of MERIT-PoP ring becomes $\nu_H \sim 1.03$. In Fig. 3, the betatron tune of the MERIT-PoP ring plotted in the tune diagram is shown.

$$\nu_H \sim \sqrt{k+1} \tag{2}$$

INTERNAL TARGET

In order to show the beam acceleration and storage in MERIT scheme experimentally, a semi-wedge type of internal target was designed and made. The design of the internal

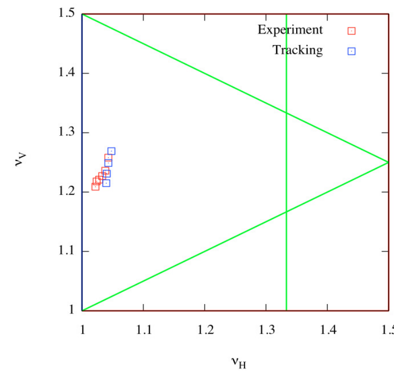

Figure 3: Betatron tune of the MERIT-PoP ring. Red and blue plots show the results of measurement and tracking simulation, respectively. Betatron tunes were measured and calculated by changing the focusing and defocusing magnetic field strength.

target is shown in the Fig. 4. The target material is carbon, which is composed of two stages in thickness. The thickness of the inner stage is 720 µg/cm^2 and the outer stage is 980 µg/cm^2, respectively. The width and height of the target are 140 and 115 mm, which corresponds to approximately 40% and 80% of the region of the vacuum chamber in horizontal and vertical direction, respectively. The energy loss at each stage for 11 MeV proton beam is about 27 and 37 keV, respectively. Also, the scattering at each stage for 11 MeV proton beam is about 1.9 and 2.2 mrad, respectively.

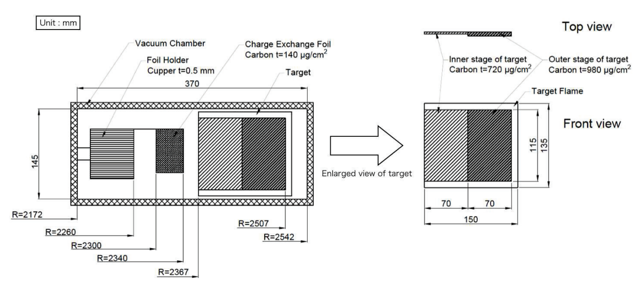

Figure 4: Design of the internal target.

TRACKING SIMULATION WITH G4beamline

In order to evaluate the particle motions in detail, the particle tracking simulation code, G4beamline (G4BL), was used. The G4BL code is basically a single particle tracking and simulation code based on the Geant4 toolkit, which enable to estimate the particle interactions and tracking in collision with the materials [7]. The three dimensional field distribution of the ring magnet, which is required for the beam tracking, were calculated with the OPERA3D/TOSCA code [8].

The result of G4BL beam tracking in longitudinal direction for two different cases are shown in Fig. 5. Figure 5 shows the results when RF voltage is 75 kV. Upper and lower graph in Fig. 5 show the result in case without and with the internal target, respectively. As can be seen from Fig. 5, the

ISBN: 978-3-95450-205-9 doi:10.18429/JACoW-Cyclotrons2019-TUP034

beam is lost until about 50 turn in case without the internal target because the beam hit the radial outside of physical aperture located around the 12.0 MeV. In contrast, in case with the internal target, the beam starts to hit the internal target after about 20 turns, and reaches maximum energy of 11.5 MeV after 40 turns. After that, beam circulates more than 100 turns with acceleration and storage although the beam intensity decreases gradually because of the emittance growth.

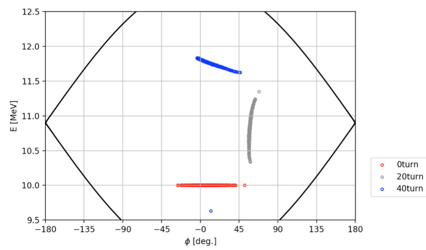

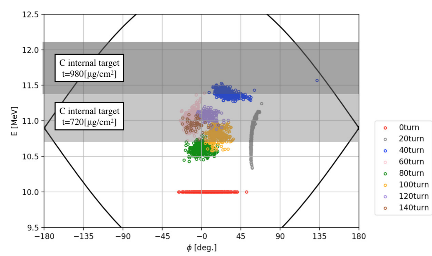

Figure 5: Results of G4BL tracking in longitudinal direction for all 20 turns for MERIT-PoP ring for two different cases; upper and lower graph show the result without and with the internal target, respectively. The two grey regions in the lower graph indicate the position of each stage of the internal target.

SUMMARY

This paper presents study for the PoP experiment on MERIT scheme, which has been proposed as an intense negative muon source. The MERIT-PoP ring was formulated by remodelling the existing ring for neutron source with energy recovering internal target with ionization cooling [3, 4]. To evaluate the particle motion for the PoP experiment on MERIT scheme using the MERIT-PoP ring in detail, tracking simulation using the G4BL was performed. The results showed beam circulation more than 100 turns with acceleration and storage with the internal target.

ACKNOWLEDGEMENTS

This work is partially supported by the ImPACT Program of Council for Science, Technology and Innovation (Cabinet Office, Government of Japan).

REFERENCES

[1] Y. Mori *et al.*, “Intense negative muon facility with MERIT ring for nuclear transmutation”, *JPS Conf. Proc.*, vol. 21, p. 011063, Hokkaido, Japan, Jun. 2017. doi:10.7566/JPSCP.21.011063

[2] S. Devons and I. T. Duerdoth, “Muonic Atoms”, in *Advances in nuclear physics*, M. Baranger, E. Vogt (eds.), New York, NY, USA: Springer, 1969, vol. 21, pp. 295–423. doi:10.1007/978-1-4684-8343-7_5

[3] Y. Mori, “Development of FFAG accelerators and their applications for intense secondary particle production”, *Nucl. Instrum. Methods Phys. Res., Sect. A*, vol. 562, pp. 591–595, 2006. doi:10.1016/j.nima.2006.02.044

[4] Y. Mori *et al.*, “Neutron source with emittance recovery internal target”, in *Proc. PAC’09*, Vancouver, BC, Canada, May 2009, paper TH4GAC04, pp.3145–3147.

[5] H. Okita *et al.*, “Beam optics study on FFA-MERIT ring”, in *Proc. IPAC’19*, Melbourne, Australia, May 2019, pp. 613–615. doi:10.18429/JACoW-IPAC2019-MOPRB019

[6] E. Yamakawa *et al.*, “Serpentine acceleration in zero-chromatic FFAG accelerators”, *Nucl. Instrum. Methods Phys. Res., Sect. A*, vol. 716, pp. 46–53, 2013. doi:10.1016/j.nima.2013.03.061

[7] T. Roberts, *G4beamline User’s Guide*, Muons, Inc., http://g4beamline.muonsinc.com

[8] *Opera-3d User Guide*, Vector Fields Limited, Oxford, England.

ISBN: 978-3-95450-205-9 doi:10.18429/JACoW-Cyclotrons2019-TUP035

DEVELOPMENT OF A CENTER REGION FOR NEW SUMITOMO CYCLOTRON

N. Kamiguchi, H. Oda, J. Kanakura, Y. Kumata, M. Hirabayashi, Y. Mikami, H. Murata, T. Tachikawa, N. Takahashi, T. Tsurudome, H. Tsutsui, J. Yoshida
Sumitomo Heavy Industries, Ltd. Tokyo, Japan

Abstract

We Sumitomo Heavy Industries, Ltd. have been newly developing an AVF cyclotron which employs the superconducting magnet. This cyclotron purposes medical use, especially proton therapy fields and is most compact and high intensity among AVF cyclotrons which can accelerate to the energy for proton therapy. In this paper we report and focus on its center region. The center region consists of an ion source, a beam shaper, RF electrodes and two functional pair of centering coils that use Bz 1st harmonic (C-H coils). These components were finished manufacturing and await the component test after the assembly.

INTRODUCTION

This cyclotron is a compact cyclotron which has a 2.8 m diameter and 1.7 m height yoke, thus also that center region becomes compact and is equipped into a tiny space of it within about 0.2 m diameter [1]. Figure 1 shows external view of a whole center region. There are many small components in the center region and these components will be introduced in the following sections.

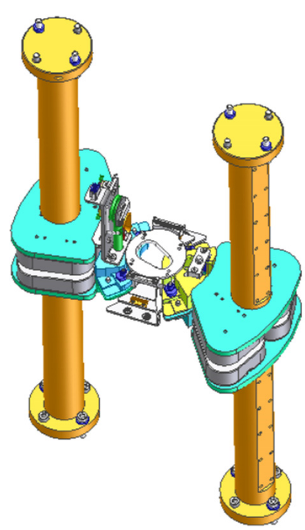

Figure 1: 3D schema of a whole center region.

COMPONENTS OF CENTER REGION

Ion Source

The PIG ion source with hot cathode is applied and located at the center of the cyclotron as an internal ion source. The structure of the ion source is classic and simple PIG ion source because of tiny space of the center region. An anti-cathode which is set against the filament and floating on the ground reflects thermal electron. As this cyclotron has 3.0 T magnetic field, the filament heated by current receives the Lorentz force strongly. It may be a problem that this force deforms the filament. To avoid the deformation, AC current heating is newly introduced into this ion source. This method made application of hot cathode PIG ion source under high magnetic field possible.

The performance of this ion source have been confirmed on our test bench (Fig. 2). The performance test was conducted under the condition that 3.2 T magnet field and static extraction. The H^+ beam current was measured about 300 μA at most (Fig. 3) [2].

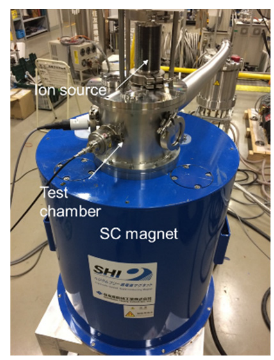

Figure 2: Test bench of ion source.

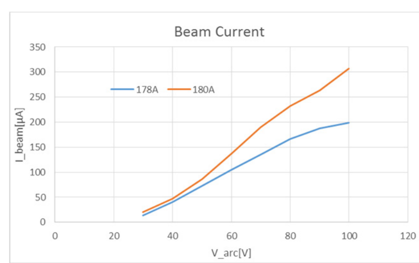

Figure 3: Extracted beam current on the test bench. This shows arc voltage vs extracted beam current in case of two type of filament current.

In case of hot cathode type PIG ion sources, filaments are supplies and must be exchanged periodically. As the mechanical driving system which evacuate the ion source from the cyclotron without broking vacuum is equipped under the cyclotron, a maintenance of ion source is possible to be performed easily and rapidly.

Dee and Counter Dee Electrode

The extraction of the proton beam from the ion source is conducted with RF electric field made by the dee electrode. The voltage of 50 kV is loaded between the puller and the ion source and the beam is extracted to accelerated orbits. Extracted beams turn around 15 mm radius and RF field

ISBN: 978-3-95450-205-9 doi:10.18429/JACoW-Cyclotrons2019-TUP035

accelerates beam gradually. Figure 4 shows actual Dee and C-Dee electrodes.

On one counter dee electrode, beam chopper (electrostatic vertical deflector) is equipped and on the other counter dee electrode, phase slits, a pair of vertical beam dumpers and a beam measurement prove are equipped.

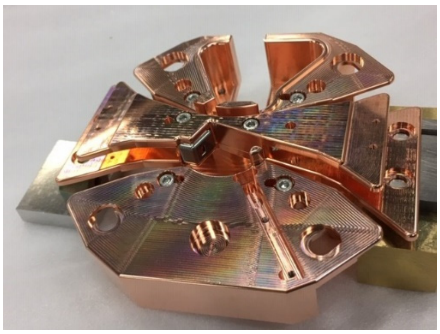

Figure 4: Pre-assembled electrode. This can be included within 100 mm diameter.

To control the beam current from the cyclotron, static electric beam chopper deflects the beam direction vertically. The beam is kicked out from 1st turn and is dumped within 4 turns before accelerated to 1 MeV (Fig. 5 and Fig. 6). Thus, there is no matter of the activation.

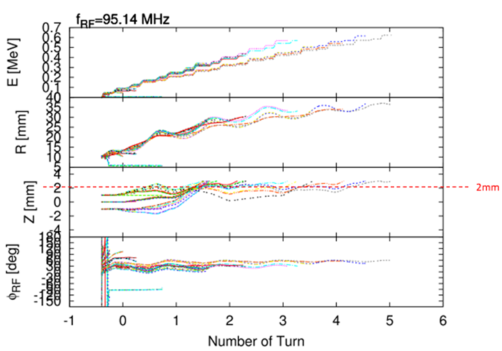

Figure 5: Parameters of deflected beam orbit till the beam dumps.

The phase slit limits the phase acceptance of extracted beam and vertical beam dumpers cut off unnecessary beam to improve the extraction efficiency of the cyclotron.

The beam measurement probe is located at 42 mm radius and can measures the beam current at the center region to perform the Smith – Garren measurement and to confirm the status of the ion source.

Central Harmonic Coil: C-H Coil

C-H coils are put on outside of the center region in the valley. Because of limited vacant space, all pairs of C-H coils are put into a pair of the valley though they are ordinarily put on each sectors in case of other cyclotrons. Though C-H coils do not form the 90° symmetric alignment but 180° symmetric one in this composition, Bz output is possible to be gained enough by organizing the output of magneto motive force (Fig. 7).

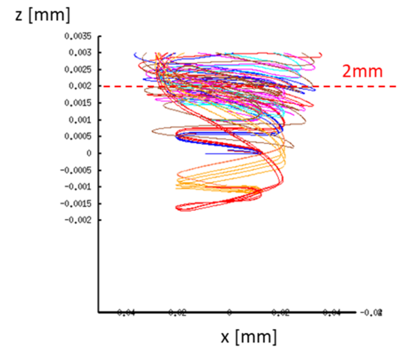

Figure 6: Schema of chopping beam.

C-H coils have been already winded around their bobbins as shown in Fig. 8 and unit test has been completed.

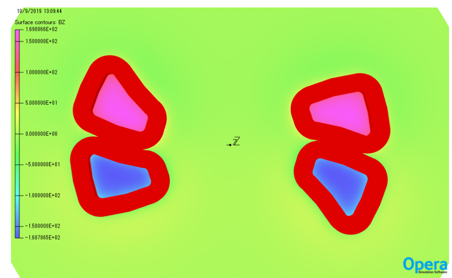

Figure 7: Bz 1st harmonic element calculation with 3D calculator. This case shows 1st harmonic condition for y-axis direction.

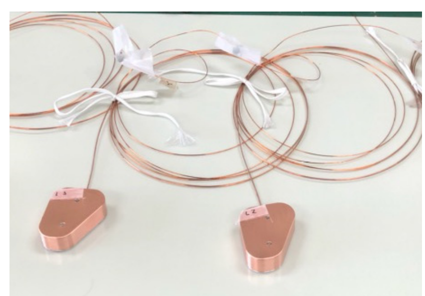

Figure 8: Processed C-H coil.

CONCLUSION

The design of the components of the center region for new Sumitomo Super-conducting cyclotron have been completed and manufacturing them have already been finished.

The component tests are going to be planed and these components will be installed into the inside of cyclotron after passing the tests and the assembly in Ehime works of ours.

REFERENCES

[1] H. Tsutsui *et al.*, “Current status of Sumitomo's superconducting cyclotron development for proton therapy”, presented at the 22nd Int. Conf. on Cyclotrons and their Applications (Cyclotrons'19), Cape Town, South Africa, Sep. 2019, paper FRA02, this conference.

[2] N. Kamiguchi *et al.*, presented at the 17th Int. Conf. on Ion Sources, Geneva, Switzerland, Oct. 2015, unpublished.

ISBN: 978-3-95450-205-9 doi:10.18429/JACoW-Cyclotrons2019-TUP036

OPTICAL DESIGN OF AVF WEAK-FOCUSING ACCELERATOR

C. Hori*, T. Aoki, T. Hae, T. Seki, K. Hiramoto, Hitachi, Ltd., Hitachi, Japan

Abstract

A trend in proton beam therapy systems is downsizing their footprints. A larger main magnetic field for the downsizing, however, requires a septum magnet to generate a larger magnetic field for beam extraction. In order to relax the specification of the septum magnet, we consider an azimuthally varying field (AVF) weak-focusing accelerator. The magnetic fields of its hills and valleys can be designed while maintaining the average magnetic fields over the design orbits. Thus, by locating the septum magnet near one of the valleys, the specification is relaxed while keeping the footprint of the accelerator. In this study, we show an optical design of an AVF weak-focusing accelerator with cotangential orbits. The magnetic field in the valleys is smaller than the average magnetic field over the maximum energy orbit by 0.2 T. We evaluate gradient magnetic fields required for beam extraction and find the possibility of variable energy extraction by the static gradient fields.

INTRODUCTION

A trend in proton beam therapy (PBT) systems is downsizing their footprints. We have proposed a compact accelerator for PBT with cotangential orbits [1, 2]. Figure 1 shows a schematic of the accelerator. Its concept is to achieve both compactness and variable energy extraction. For compactness, a superconducting magnet which generates a weak-focusing magnetic field of approximately 4-5 T and an RF cavity which can modulate its frequency are applied. For variable energy extraction, the orbits are not concentric but cotangential like the classical microtron, and an RF kicker and gradient fields (generated by a peeler and a regenerator) are combined. Due to the characteristic orbit configuration, there is small turn separation region on one side, where the RF kicker is installed. Each orbit between 70 MeV and 235 MeV passes through the RF kicker. By turning on the RF kicker, the beam trajectory is moved toward the outside of the circulating region. The beam moved by the RF kicker is eventually affected by the gradient magnetic fields generated by the peeler and the regenerator. The gradient magnetic fields bring about 2/2 resonance, and the beam arrives at the entrance of the extraction channel. Along the extraction channel, septum magnetic fields are applied to extract the beam from the accelerator.

A larger main magnetic field requires septum magnets to generate larger magnetic fields for extraction. Since the proposed accelerator is designed to extract low energy (approximately of 70 MeV) beams, it requires the septum magnets to generate even larger magnetic fields compared with cyclotrons and synchrocyclotrons. Among the septum magnets, the first septum magnet, which is located at the entrance of the extraction channel, is under the severest conditions. Hence, we considered a new idea to relax the specification of the first septum magnet.

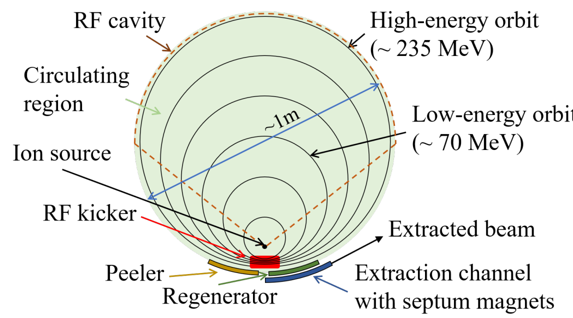

Figure 1: Schematic of compact accelerator.

AVF WEAK-FOCUSING ACCELERATOR

We denote the fringe magnetic field at the entrance of the extraction channel by B_f, and the first septum magnetic field by $-\delta B$. Then the curvature radius of the beam at the entrance is given by

$$\rho(K) = \frac{\sqrt{K(K+2E_0)}}{cq\left(B_f - \delta B\right)}, \tag{1}$$

where c denotes the speed of light, and q, E_0, and K denote charge, rest energy, and kinetic energy of the beam, respectively. We denote the maximum kinetic energy and the average main magnetic field over the maximum kinetic energy orbit by K_M and B_M, respectively. In order to extract the beam with its energy of K, $\rho(K)$ has to be larger than ρ_M, where ρ_M is given by

$$\rho_M = \frac{\sqrt{K_M(K_M+2E_0)}}{cqB_M}. \tag{2}$$

If B_f is reduced, δB is also reduced while $\rho(K)$ maintained. The easiest approach to reduce B_f is to reduce B_M. However, if B_M is reduced, not only B_f is reduced, but also ρ_M is increased, indicating a larger footprint of the accelerator and larger $\rho(K)$ for extraction. Hence for relaxing the specification of the first septum magnet, B_f should be reduced without reducing B_M. To satisfy this condition, we consider an azimuthally varying field (AVF) weak-focusing accelerator. By locating the extraction channel near one of the valleys, B_f at the extraction channel is reduced while B_M maintained.

The AVF field is normally applied to cyclotrons to satisfy both isochronism and stable betatron motion. Since isochronism requires a magnetic field to increase with radius, the average magnetic fields of usual AVF cyclotrons increase

* chishin.hori.cj@hitachi.com

ISBN: 978-3-95450-205-9 doi:10.18429/JACoW-Cyclotrons2019-TUP036

with radius. In contrast to the usual AVF cyclotrons, the proposed accelerator does not require isochronism, since the frequency of the RF cavity is modulated. The average magnetic field should decrease with radius in accordance with the weak-focusing principle.

OPTICAL DESIGN

Method

A special tool is required to design the optics of the AVF weak-focusing accelerator with cotangential orbits. We developed a design tool based on the transfer matrix method for an isochronous accelerator with cotangential orbits [3]. We have applied this tool to design the optics of the AVF weak-focusing accelerator. Since it does not require isochronism, we give the average magnetic field $\bar{B}$ as the function of the beam velocity β by

$$\bar{B}(\beta) = \begin{cases} -b_1 \left(\dfrac{\beta}{\beta_M}\right)^{p_1} + B_{\max} & 0 \le \beta \le \beta_m \\ b_2 \left[1 - \left(\dfrac{\beta}{\beta_M}\right)^{p_2}\right] + B_{\min} & \beta_m \le \beta \le \beta_M \end{cases}, \quad (3)$$

where p_1, p_2, $B_{\max}$, $B_{\min}$, and β_m are adjustable parameters, and β_M is determined by K_M. The other parameters b_1 and b_2 are determined by the condition that $\bar{B}$ and its first derivative with respect to β are continuous at $\beta = \beta_m$. We note that $B_{\max}$ and $B_{\min}$ are maximum and minimum of $\bar{B}$, respectively. Hence the magnetic field at the hills is larger than $B_{\max}$, and the magnetic field at the valleys is smaller than $B_{\min}$.

Design Orbits and Tunes

In the following, we show an example of the optical design, where K_M and B_M are fixed at 235 MeV and 4.5 T, respectively.

Figure 2 shows the design orbits and the magnetic fields. The magnetic field at the hills is 5.04 T, while the magnetic field at the valleys is 4.28 T, which is smaller than B_M by approximately 0.2 T. This difference is expected to contribute to reducing the first septum magnet field.

Figure 3 shows the horizontal and the vertical tunes, which are denoted by ν_h and ν_v, respectively. The solid curves indicate design tunes by the tool, while the plotted symbols are obtained by the beam tracking simulation code GPT [4]. The design tunes and the tracking simulation results agree within the accuracy of 10%. Since the tool models the magnetic fields by the hard edge model, it is not applicable to the low energy region. Hence the tunes are evaluated above the energy of 10 MeV. In order to utilize 2/2 resonance by the peeler and regenerator for extraction, the horizontal tunes are designed to be more than 0.95 in all energy regions. The vertical tunes are designed to avoid the second resonance line $\nu_v = 0.5$.

Figure 4 shows the tune diagram, where the resonance lines up to the fourth order are drawn. The Walkinshaw resonance ($\nu_h = 2\nu_v$) is avoided.

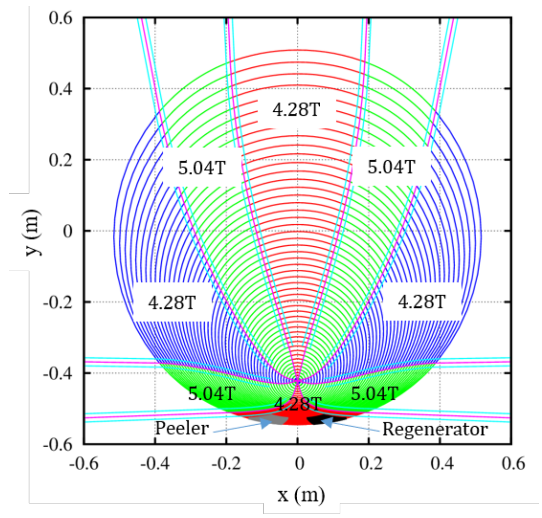

Figure 2: Design orbits and magnetic fields.

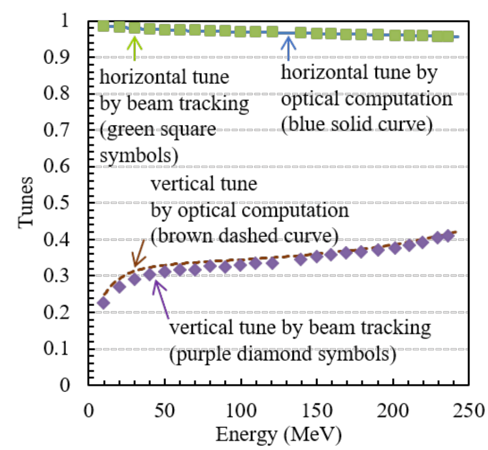

Figure 3: Betatron frequencies (tunes).

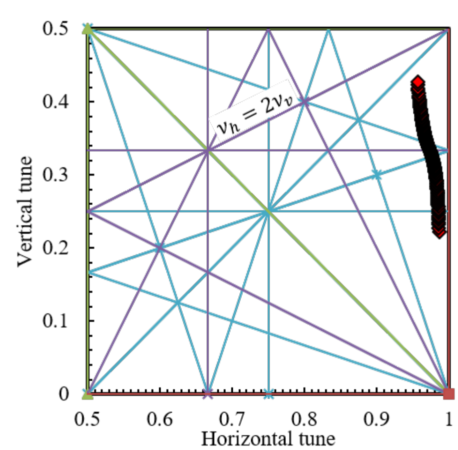

Figure 4: Tune diagram.

Gradient Magnetic Fields for Extraction

As is shown in Fig. 1, the peeler and the regenerator are located outside the circulating region. In order to estimate required strengths of those fields, however, the peeler and the

ISBN: 978-3-95450-205-9 doi:10.18429/JACoW-Cyclotrons2019-TUP036

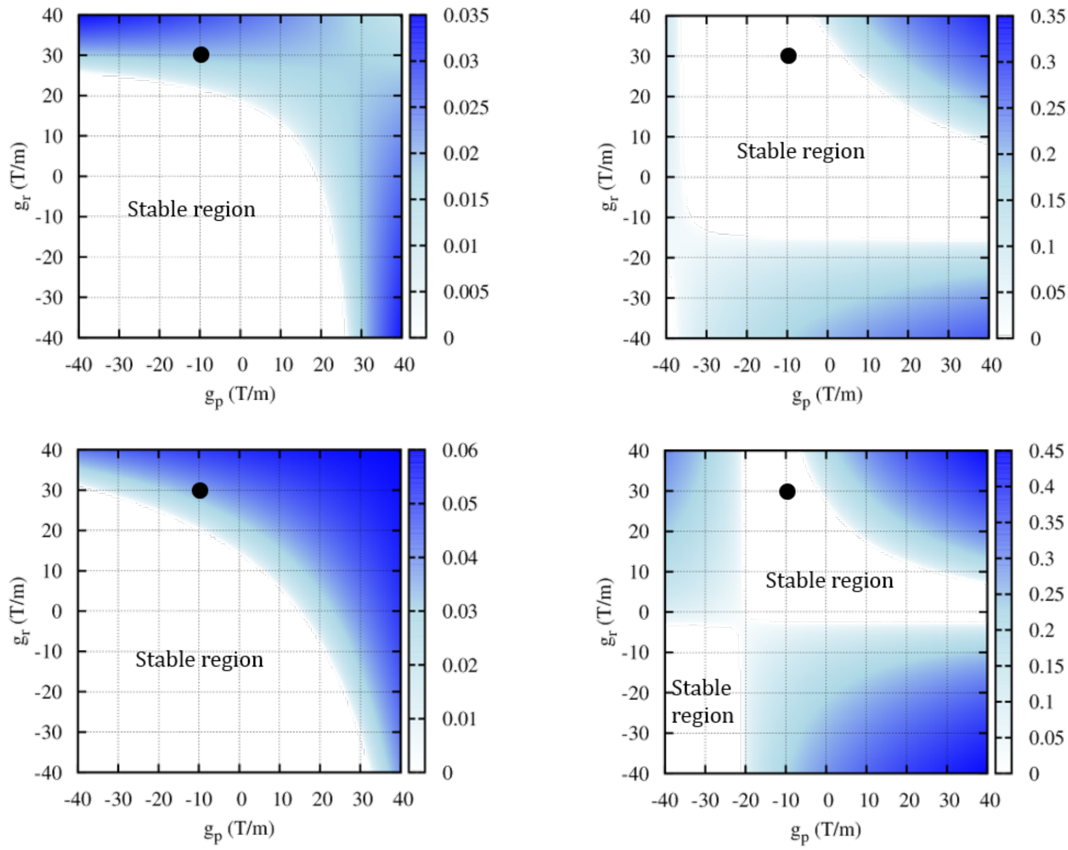

Figure 5: Imaginary parts of tunes. Upper left and upper right are horizontal and vertical tunes at 67.8 MeV, respectively. Lower left and lower right are horizontal and vertical tunes at 236.3 MeV, respectively.

regenerator are assumed to be in the valley shown in Fig. 2 for simplicity, and the imaginary parts of the tunes are evaluated by the transfer matrix method. Figure 5 shows color maps of the imaginary parts, where g_p and g_r denote the strengths of the peeler and the regenerator, respectively. The betatron motion becomes unstable when the corresponding tune has a nonzero imaginary part. For extraction, $\mathrm{Im}\,(\nu_h)$ has to be larger than zero, while $\mathrm{Im}\,(\nu_v)$ has to remain zero. For example, the point of $(g_p, g_r) = (-10, 30)$, which is indicated by the black circle symbol in Fig. 5, satisfies that condition for both 67.8 MeV and 236.3 MeV. This result indicates the possibility of static gradient magnetic fields for variable energy extraction.

CONCLUSION

We considered the AVF weak-focusing accelerator with cotangential orbits for proton beam therapy to achieve both compactness and variable energy extraction. By locating the first septum magnet outside the valley, its specification was relaxed. The possibility of variable energy extraction by the static gradient magnetic fields was indicated. We noted that the idea of the AVF weak-focusing accelerator would be applicable to axisymmetric synchrocyclotrons.

REFERENCES

[1] T. Aoki, T. Hae, C. Hori, T. Seki, Y. Nakashima, and F. Ebina, "Concept of frequency modulated variable-energy accelerator", in *Proc. 14th Annual Meeting of Particle Accelerator Society of Japan (PASJ'17)*, Sapporo, Japan, Aug. 1-3, 2017, paper THOL02, pp. 150-154.

[2] T. Hae *et al.*, "Compact cotangential orbits accelerator for proton therapy", in *Proc. 22nd Int. Conf. Cyclotrons and their Applications (CYC'19)*, Cape Town, South Africa, Sep. 22-27, 2019, paper TUP037, this conference.

[3] C. Hori, T. Aoki, and T. Seki, "Variable-energy isochronous accelerator with cotangential orbits for proton beam therapy", *Nucl. Instrum. Methods Phys. Res., Sect. A*, vol. 922, pp. 352-356, Apr. 2019. doi:10.1016/j.nima.2019.01.005

[4] GPT, http://www.pulsar.nl/gpt/index.html

ISBN: 978-3-95450-205-9 doi:10.18429/JACoW-Cyclotrons2019-TUP037

COMPACT COTANGENTIAL ORBIT ACCELERATOR FOR PROTON THERAPY

T. Hae, T. Aoki, C. Hori, H. Nakashima, F. Noda, T. Seki, K. Hiramoto
Hitachi Ltd., Hitachi city, Japan

Abstract

A new type accelerator is being developed for the next generation particle therapy system. This accelerator utilizes a weak focusing DC magnetic field and a frequency modulated RF acceleration. Since a superconducting magnet is applicable to the main magnet, the accelerator can be compact. The accelerator characteristically has cotangential orbits to form an orbit-concentrated region. A beam is extracted from the region by using a new extraction method with the transverse RF kicker, peeler and regenerator magnetic fields. In this method an extracted beam energy can be controlled by applied time of the acceleration RF voltage without using an energy selection system (ESS). Intensity and pulse width of the extracted beam can be controlled by a voltage and/or a frequency pattern of the RF kicker.

INTRODUCTION

Currently, a cyclotron type accelerator (AVF cyclotron, synchrocyclotron) and a synchrotron are provided to practical use of particle therapy.

Since a superconducting magnet is applicable to a cyclotron type accelerator with a DC main magnetic field, it is a merit to be able to downsize the accelerator. However, it is necessary to install an ESS outside the accelerator in order to obtain various desired beam energy levels for treatments. A degrader in an ESS generates unnecessary radiation and reduces beam utilization efficiency. There is also a problem of fragmentation that makes it difficult to apply the cyclotron type accelerator to uses other than proton therapy.

On the other hand, a synchrotron has a merit to extract a variable energy beam without the ESS. In addition, transverse RF-driven slow extraction technology [1] has made it possible to control both the position and the intensity of the extracted beam with high accuracy. Thus, a synchrotron is advantageous for scanning irradiation. However, since the synchrotron requires an AC main magnetic field, it is difficult to adopt the superconducting magnet as a means to achieve a smaller body.

The cotangential orbit accelerator that combines the merits of both a cyclotron type accelerator and a synchrotron has been proposed as a next-generation accelerator for particle beam therapy [2]. This new accelerator uses the DC main magnetic field and the frequency-modulated RF acceleration. The accelerator body can also be downsized by applying the superconducting magnet. It is more nortable that a variable energy beam can be extracted without the ESS by the new method. The accelerator can be applied to both proton and heavy ion beam therapies. In particular, the result of the conceptual design study on the accelerator for proton therapy is described in this paper. The main specifications of the accelerator are listed in Table 1.

Table 1: Margin Specifications

Parameter	Value
Diameter of yoke	2.7 m
Total weight	60 t
Magnetic field	4.0 T at injection point, 3.94 T at max. energy orbit
Main coil	NbTi cable, conductive cooling
Magnetomotive force of main coil	1.8 MA
Harmonic number	1
RF frequency	61.0 ~ 48.5 MHz
RF voltage, required power	10 kV, 30 kW
Extracted beam energy	70 MeV to 225 MeV without degrader
Extraction method	Slow extraction, RF kicker + peeler regenerator
Pulse repetition rate	< 500 Hz

DISTRIBUTION OF ORBITS

The orbits are decentered as shown in Fig. 1 (a) to create the orbit-concentrated region with the radial width of about 10 mm. This region is located at orbits from 70 MeV to 225 MeV, and that corresponds to the extraction energy range needed for treatment. There are two reasons for forming the orbit-concentrated region.

- Extracting the beam from the orbit-concentrated region allows for reduction of the required radial displacement from the equilibrium orbit for each beam within the extraction energy range.
- Installing the RF kicker on the orbit-concentrated region makes it easier to apply the transverse RF electric field to each beam within the extraction energy range.

These two points are essential to realize the new extraction method. Figure 1 (b) shows the ideal main magnetic field distribution on the midplane that realizes such an orbital arrangement. The tune diagram is shown in Fig. 2. It has been confirmed that there is sufficient horizontal and vertical acceptance based on results of a tracking analysis with the ideal main magnetic field distribution [3].

ISBN: 978-3-95450-205-9 doi:10.18429/JACoW-Cyclotrons2019-TUP037

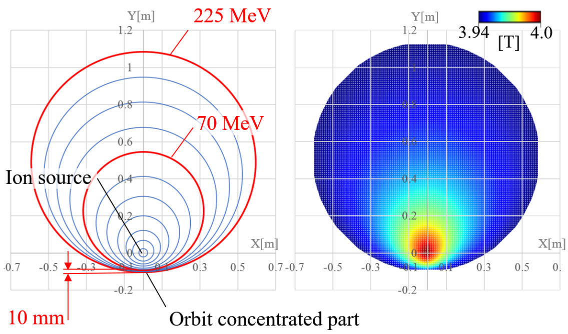

(a) Orbit distribution (b) Main magnetic field

Figure 1: Orbits and main magnetic field.

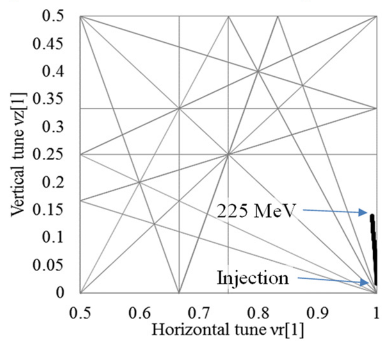

Figure 2: Tune diagram.

ACCELERATOR CONFIGURATION

Figure 3 shows schematic drawings of the accelerator. The main components of the accelerator include the main magnet, the ion source, the RF accelerating system and the extraction system.

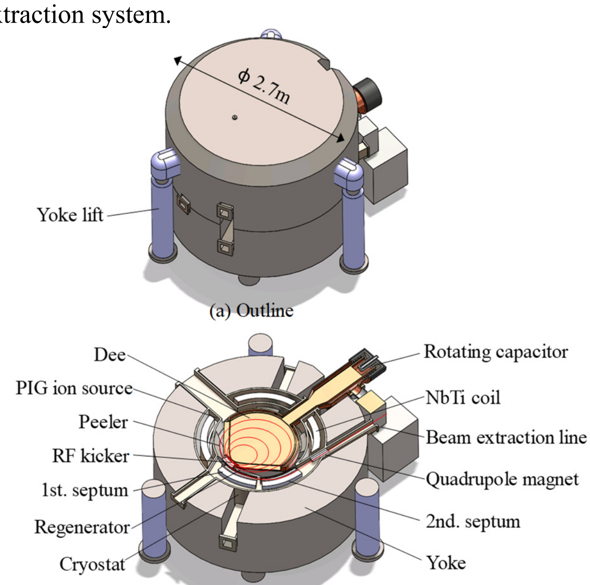

(a) Outline

(b) Cross-sectional view on mid plane

Figure 3: Schematic drawings of the accelerator.

Main Magnet

A conduction-cooled superconducting magnet is applied to forms the ideal magnetic field by weak focusing. The shape of the magnetic pole has been obtained by singular decomposition calculation. NbTi wire is selected for the coil winding, based on its relatively low cost and satisfactory mechanical strength.

Ion Source

A compact PIG ion source is applied. Hydrogen gas is introduced into the chimney between the upper and lower cold cathodes. A plasma is generated by applying a DC high voltage and discharging the gas. An RF acceleration electric field formed by an accelerating cavity is used to extract the beam from the plasma.

RF Accelerating System

An accelerating cavity with λ/2 resonant mode is applied to the system. The resonant frequency of the cavity must be modulated because of the non-isochronous magnetic field. Hence either the inductance or the capacitance of the cavity must be varied in time. Thus, the resonant frequency is modulated at the cycle of 2 ms with a rotating capacitor that is attached at the open end of the accelerating cavity opposite the accelerating gap. The shunt impedance of the accelerating cavity was calculated by 3D electromagnetic field analysis, and as a result, the required RF power is about 30 kW. A solid-state amplifier is used for the RF power supply.

Extraction System

The new extraction method utilizes the system consisting of the RF kicker, the peeler and regenerator fields and septum magnets.

Figure 4 shows a schematic diagram explaining the extraction method. The RF kicker is the electrode pair having holes that the circulating beam passes through. Beam orbits of any energy within the extraction energy range are included between the electrode pairs. After the beam is accelerated to reach the extraction energy, the RF accelerating voltage is turned off, and then the RF kicker begins to apply a transverse RF electric field to the circulating beam so as to excite horizontal betatron oscillation. The frequency band of the transverse RF electric field is set to include $f_{rev} \cdot (1-\nu_r)$, where f_{rev} is the circulating beam frequency and ν_r is the horizontal tune of the beam. While the transverse RF electric field is turned on, the circulating beam eventually reaches the peeler and regenerator fields on the outer peripheral side of the equilibrium orbit of 225 MeV. As a result, half-integer resonance ($2\nu_r = 2$) is driven by the peeler and regenerator fields, and a large turn separation can be obtained that cannot be realized by the RF kicker only. The peeler and regenerator fields have been designed by trajectory analysis to obtain sufficient turn separation at the entrance of the septum magnet while keeping the vertical betatron oscillation stable for the beam of any energy within the extraction energy range. The extraction system utilizes several septum magnets whose excitation currents are changed according to the extraction energy.

An example of the timing chart regarding the beam extraction is shown in Fig. 5. The pulse width of the extracted beam is controlled by the application time of the RF kicker

ISBN: 978-3-95450-205-9 doi:10.18429/JACoW-Cyclotrons2019-TUP037

in order to match the requirement of spot scanning irradiation. The beam current is controlled by the amplitude and/or the frequency of the transverse RF electric field. The RF captured and accelerated beam can be effectively utilized by this slow extraction, which can contribute to a higher dose rate for proton therapy.

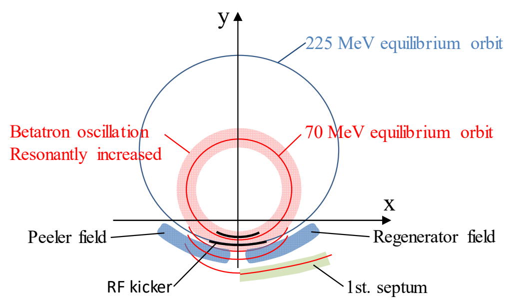

Figure 4: Schematic drawing explaining the extraction method.

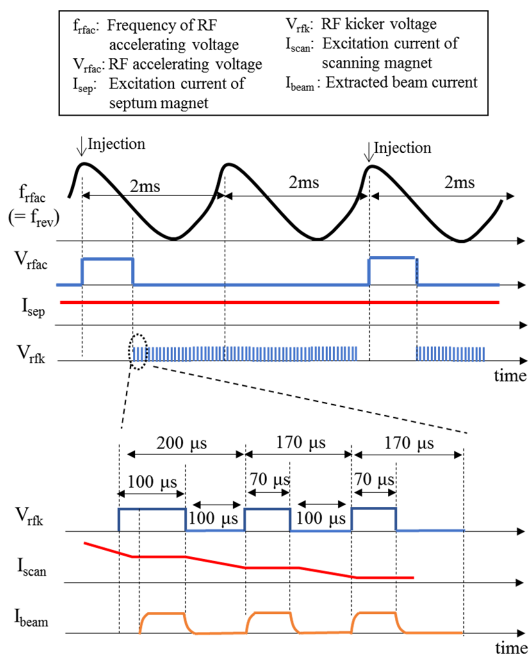

Figure 5: Timing chart of beam extraction.

BEAM EXTRACTION SIMULATION

Figure 6 shows the simulation results of single particle tracking by using the analysis code GPT [4]. In these results, only the RF kicker voltage V_{rfk} = 2 kV is applied without the RF acceleration. And the trajectory is calculated from each initial position to the septum entrance. The initial position is set to the place displaced +1 mm horizontally from each equilibrium orbit. In these conditions, for the lowest extraction energy of 70 MeV, the minimum turn separation of 11 mm can be obtained and it exceeds the septum conductor thickness of 7.5 mm. The turn separation becomes larger as extracted beam energy increases. Because the higher energy beam is more affected by the peeler and regenerator fields in this extraction method. For the highest extraction energy of 225 MeV, the turn separation reaches 53 mm, and the beam utilization efficiency is maximized.

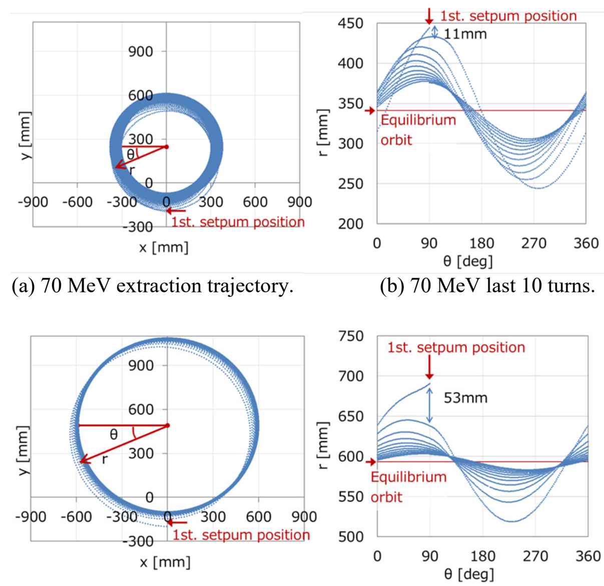

(a) 70 MeV extraction trajectory. (b) 70 MeV last 10 turns.

(c) 225 MeV extraction trajectory. (d) 225 MeV last 10 turns.

Figure 6: Tracking simulation result of beam extraction.

CONCLUSION

The conceptual design has been done for the cotangential orbit accelerator using the DC main magnetic field and the frequency modulated acceleration. And the new extraction method utilizing combination of cotangential orbits, RF kicker, and peeler and regenerator magnetic fields has been proposed. The tracking simulation indicated the possibility to extract proton beam of the energy range of 70 to 225 MeV without an ESS. The new extraction method enables slow beam extraction, therefore both a high beam utilization efficiency and high-accuracy dose control suitable for a scanning irradiation can be realize.

ACKNOWLEDGEMENTS

The authors are grateful to Dr. Masahito Tomizawa and Dr. Ryotaro Muto of KEK for providing very useful advice when designing septum magnets.

REFERENCES

[1] K. Hiramoto, J. Hirota, M. Nishi, and M. Tadokoro, “Resonant beam extraction with constant separatrix”, in *Proc. 15th Particle Accelerator Conf. (PAC'93)*, Washington D.C., USA, Mar. 1993, pp. 309-312.

[2] T. Aoki *et al.*, “Concept of frequency modulated variable energy accelerator”, *in Proc. of the 14th Annual Meeting of Particle Accelerator Society of Japan*, Sapporo, Japan, Aug. 2017, pp. 150-154.

[3] T. Aoki *et al.*, "Study of transverse motion in cotangential trajectory accelerator", *in Proc. 15th Annual Meeting of Particle Accelerator Society of Japan*, Nagaoka, Japan, Aug. 2018.

[4] `http://www.pulsar.nl/gpt/index.html`

ISBN: 978-3-95450-205-9 doi:10.18429/JACoW-Cyclotrons2019-TUC01

REVIEW AND CURRENT STATUS OF THE 70 MeV HIGH INTESITY PROTON CYCLOTRON AT LNL

M. Maggiore, P. Antonini, A. Lombardi, L. Pranovi
Laboratori Nazionali di Legnaro, INFN, Legnaro, Italy
Z. Filipovsky, Institute for Positron Emission Tomography, Skopje, Rep. of Macedonia

Abstract

In 2017 the new cyclotron has been successfully commissioned and started the operation at Laboratori Nazionali di Legnaro (LNL) of INFN. The cyclotron is the proton driver foreseen for the Selective Production of Exotic Species (SPES) project, providing the high power beam for radioactive ion beams (RIBs) production by the ISOL technique. The SPES facility is today under construction and first low energy RIBs are expected to be available in 2021. The facility has been designed in order to exploit the versatility of the cyclotron in terms of wide range of energy and beam current extracted: 35 - 70 MeV energy and 20 nA - 500 µA of average current. Moreover, the possibility to extract at the same time two proton beams allows to share these both for experimental physics session and applications. In particular, at LNL a collaboration between private company and public institution will lead to a profitable synergy in R&D of new radioisotopes and the related production. In the session the results of the commissioning and the operation of cyclotron will be presented as well as the description of the SPES facility together with its potentiality in nuclear physics research and applications.

SPES PROJECT STATUS

The SPES project [1] is developing in the international framework of the new facilities producing radioactive ion beams for experiments exploring the frontiers of nuclear physics. It will mostly provide neutron-rich exotic beams, through the production of fission fragments by the interaction of high power proton beam (8 kW) with UCx targets. The neutron rich exotic ions produced by the above direct reaction, will be selected in mass with a very high resolution on the order of 1/20000 and then, once the charge breeding process increases the charge to mass ratio, the ions are accelerated with ALPI linac booster up the energy of 10 MeV/amu (A~130).

SPES project is developing in several branches spreading from fundamental research to applications and interdisciplinary physics. The complexity of the project has required to separate it in four phases with the aim to provide a multipurpose facility:

- α-phase: construction of main building and installation and commissioning of the high intensity accelerator delivering the high power proton beams.
- β-phase: installation and commissioning of Radioactive Ion Beams (RIB) facility. It consists on ISOL targets, low energy beam transport lines, beam cooling device and High Resolution Mass Separator (HRMS), charge breeding system, new RFQ injector and re-acceleration.
- γ-phase: installation and commissioning of equipment and laboratories for production and R&D of radioisotopes for medical applications.
- δ-phase: realization of experimental hall for the production of neutrons beam by interaction of high intensity protons with heavy and light targets.

The SPES project entered in the construction phase in 2010 with the assignment of the tender for the cyclotron supply to Best Cyclotron System Inc. (BCSI) Canadian company.

The α-phase has been accomplished out at the end of 2017: the main building has been constructed and principal plants, services and auxiliary systems were supplied in order to allow the first operation of the accelerator. The cyclotron has been installed in 2015 and finally commissioned in 2017. From mid-2018, in the SPES building several activities have started in order to complete the services (electrics, hydraulics, thermo-mechanics) and the infrastructures (laboratories, finishing of irradiation rooms, additional shielding) necessary to carry out the β-γ-δ phases.

Certainly the β-phase is the most complex and articulated of the project. It includes not only the realization of the items described above but also additional works to provide a significant upgrade of the actual ALPI superconducting linac (cryogenics system, controls, etc..) in order to improve both the performance and reliability. The works related this phase are still ongoing: the ISOL target station is ready to be installed in the dedicated bunker and the low energy beam transport line components are under construction. The beam cooler device is being realized in collaboration with LPC of CNRS at Caen (France). The HRMS design has been completed and the tender for the construction will be launched in few months. The charge breeder has been installed and ready for the commissioning with stable beams. The resistive RFQ to be used as new injector for ALPI booster is under construction. The main schedule foresees the commissioning at low energy of the first beam extracted from ISOL target in 2021. The completion of the SPES commissioning with RIBs at fully energy is expected in 2023.

The γ and δ phases are related to the applications of high intensity proton beam extracted from the cyclotron.

The γ-phase foresees the setting-up of 3 bunkers dedicated to the production of innovative radioisotopes for diagnostics and therapy in medical environment. One low intensity irradiation area is being prepared for nuclear cross-section measurements. Moreover, the laboratories for chemical treatment of the produced radionuclides and for special targets preparation will be equipped. The project funded for this purpose is LARAMED [2].

ISBN: 978-3-95450-205-9 doi:10.18429/JACoW-Cyclotrons2019-TUC01

Finally, the δ-phase concerns the neutron sources. The final goal is to set-up an experimental hall allocating two dedicated beamlines: one for the production of quasi-mono energetic neutron flux by the interaction of few micro-ampere proton beam with thin target made of composite of Beryllium and Lithium and the second for the production of a neutron beam with continuous energy spectrum (in the range of a few keV to 70 MeV) to emulate the atmospheric neutron flux [3].

While the γ-phase progresses in an advanced construction stage and his partial completion (1 irradiation station at high power (35 kW) and 1 irradiation station at low power (35 W)) is scheduled for the end of 2022, the δ-phase is still in the design step.

HIGH INTENSITY FACILITY STATUS

The SPES project involves all the infrastructures of the LNL and the new building above discussed is the main area where the high power proton beam is accelerated, transported and delivered to the targets. This facility [4] was designed in order to exploit the possibility to extract simultaneously two proton beams from the cyclotron and deliver them to the maximum number of irradiation target stations. In such a way to realize a multipurpose facility for providing research and applications in parallel sessions.

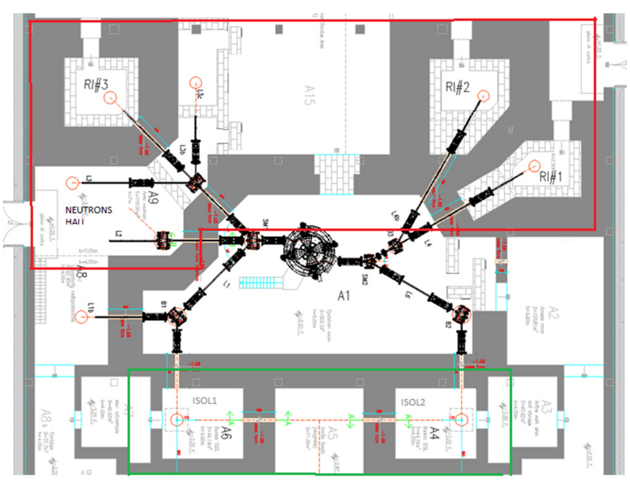

Figure 1: Main layout of high intensity facility at SPES building. The areas dedicated to the applications and R&D on radioisotopes are red underlined. The two bunker for RIBs production by ISOL target are highlighted in green.

General Layout

Mainly the facility is divided into two macro-regions: the EAST area (shown in red in Fig. 1) is dedicated to the applications as radioisotopes production and neutron sources and the WEST (shown in green in Fig. 1) area where the two bunkers for the ISOL target stations have been placed (ISOL1 and ISOL2 shown in Fig. 1).

The core of the facility is the area A1, just in the center of building, which accommodates the cyclotron. Two main beamlines come in opposite direction from the accelerator to the distribution magnets SM1 and SM2. From these, different beamlines guide the beam up to 9 irradiation points.

Three bunkers RI1, RI2, RI3 will be equipped with high power target stations for production and research of radioisotopes for medical use. The pneumatic transport system is expected to deliver the irradiated targets up to hot cells in the radio-chemical laboratories placed on second floor.

Cyclotron C70

The SPES Cyclotron is a four sectors compact cyclotron capable to accelerate H^- ions up to the maximum energy of 70 MeV. The protons are extracted by the stripping of the H- ions passing thru a thin graphite foil where the two electrons were stopped.

The proton beams are available in the energy range within 30-70 MeV and with an average current varying from few tens of nA up to the nominal value of 750 µA.

In the following Table 1 are summarized the performances.

Table 1: Cyclotron Parameters

Parameter	Value/Description
Cyclotron type	Compact, resistive magnet
Sectors number	4 straight sectors
Accelerated particle	H^- (protons extracted)
Beam energy range	35÷70 MeV
Beam current range	50 nA÷750 µA
Magnetic field at centre	1 Tesla
Peak magnetic field	1,6 Tesla
Pole radius	135 cm
Weight	~200 ton
RF system	2 delta-type cavities λ/2
RF frequency	56 MHz, harmonic=4
Extraction system	Stripping process
Injection system	Axial from external IS
Ion Source (IS)	Volumetric multi-cusp
Nominal intensity IS	6÷10 mA
Voltage IS	40 KV

The vacuum system is equipped with four cryogenic pumps CTI-10 of Brooks Company installed into the two valleys, providing a vacuum level of 3×10^{-6} Pa. A scroll pump allows to get the primary vacuum level of 1.5 Pa. The system is able to achieve high vacuum (5.5×10^{-6} Pa) level, even with only two cryopumps operational, giving very good margins for beam operations.

The RF system consists of 2 delta-type cavities (half-wave) placed in the valleys, providing up to 70 kV of accelerating voltage. The devices operate in 4th harmonic mode at the frequency of 56 MHz. In order to optimize the performance of the whole system, the cavities are fed by two separated amplifiers (dual stage, tetrode based) able to provide up to 55 kW RF power each.

The injection of the beam is axial and a multicusp H^- ion source (IS) is placed underneath the cyclotron in the pit.

ISBN: 978-3-95450-205-9 doi:10.18429/JACoW-Cyclotrons2019-TUC01

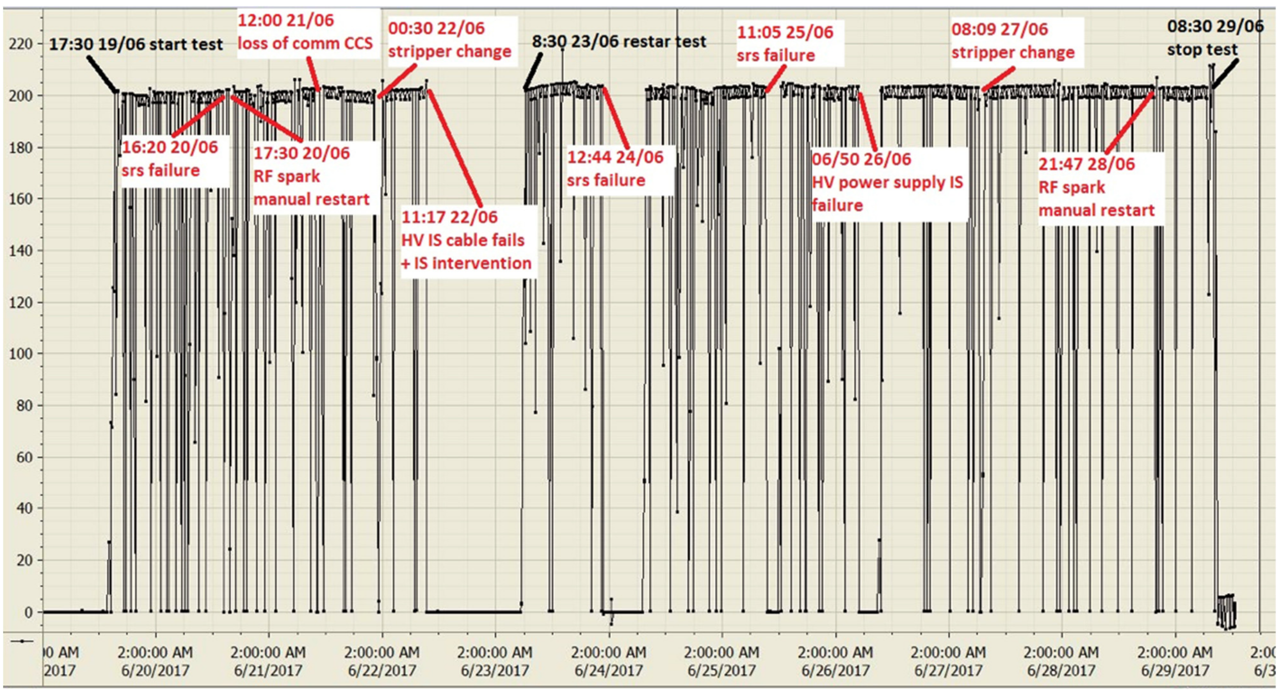

Figure 2: The plot shows the average current trend of beam on target during the endurance test of the cyclotron. In red the most significant events (system failure, stripper changes) were also reported.

A beam stop is placed downstream the IS for current measurement. The injection line is composed by two magnetic solenoids for focusing the beam in series with a couple of quadrupoles needed for beam matching with the inflector entrance. The central region has been designed in order to maximize the phase acceptance up to the value of 50 RF deg. It allows to have margin for optimizing the injected current. A beam stop is placed into the cyclotron intercepting the accelerated particles once they have made few turns (1 MeV energy). It permits to setup the best conditions of the injected beam before the full acceleration and extraction.

The extraction mechanism allows changing the stripper foil without breaking the vacuum in the main chamber. The device has been designed in order to hold up to 20 stripper foils quickly movables and easy to re-charge entirely.

Beamlines and Related Components

Two main extraction lines come from the Cyclotron. Each line ends with a switching magnet (10 tons) bending the beam along three potential lines to be used exclusively.

Each beamline is equipped with a cryogenic pump CTI-8 type and with the necessary beam diagnostics device. A fast gate valve is installed along each beamline line arm, in order to prevent any damage coming from potential vacuum breaks at the target stations.

The four jaw collimators (Aluminium made) placed along the beamlines allows to detect the halo of the beam in order to know the relative alignment. Vertical and horizontal steerers will provide the needed correction to minimize the beam losses. A the end of each beamline, a current monitor (DCCT transformer type) measures the average current of the beam which can be compared to the value measured with a similar device placed just downstream the cyclotron extraction ports. This comparison is used to calculate the transport efficiency of each beamline.

The commissioning of the cyclotron was carried on along the beamline L1 which connect the accelerator to the ISOL1 bunker. Actually this beamline is the only in operation. Two additional beamlines are currently being installed: the beamline L2 which allows to deliver the beam to ISOL2 bunker and the beamline that connect the cyclotron to the bunker RI3 for LARAMED project. The completion of this work is expected by mid of 2020.

BEAM COMMISSIONING AND OPERATION

BCSI team accomplished out the commissioning of the Cyclotron supply in September 2017. After doing a dedicated training session for LNL operators, the supply was definitively delivered to INFN. The Cyclotron group of LNL has then carried on the beam operation until March 2018, when temporary authorization for beam commissioning expired.

Commissioning Results

The commissioning phases have concerned each system of the accelerator complex installed by BCSI including all the ancillary equipment needed for beam operation.

One of the most important test regarded the long-term run in order to verify the performance in term of beam current stability, reliability and control system efficiency. The test consisted to run the beam on target for 5 days 24 h with a limited number of operator interventions allowed.

The beam specs were chosen to reproduce the operation condition expected for RIBs production: 200 µA of average

ISBN: 978-3-95450-205-9 doi:10.18429/JACoW-Cyclotrons2019-TUC01

current and 40 MeV energy. The beam was then transported along the BL1 and stopped into the beam dump provided by INFN.

The above test has failed two times because of technical failures of the HV insulator transformer providing voltage for ion source platform, whose replacement has required 5 months of machine stop. Once the device was replaced with one more robust then previous, the above test was successfully passed. During the endurance test, a limited number of beam-trips occurred due to the spark of RF system, extraction electrode of ion source and inflector. The frequency of these trips decreases better is the main conditioning of the machine. The plot in Fig. 2 summarize the events which have characterized the above test.

Beam Operations

The beam operations have been carried by out by the personnel of cyclotron team in order to complete the training and to establish the operational limits of the machine as well as its performance in terms of reliability.

Concerning the maximum beam power, the team has achieved the power of 35 kW by delivering 70 MeV protons at 500 µA. Such a value has been reached different times in several days and kept for tens of minutes without particular problems. Due to a vacuum leakage problem occurred in the Beam Dump device, the endurance test at the nominal maximum power (50 kW) has not been accomplished out. Figure 3 shows the ramp-up current session of the accelerating beam at 70 MeV to get the value of 500 µA. The procedure takes several tens of minutes in order to stabilize the operation parameters and minimize the beam losses along the transport beamline

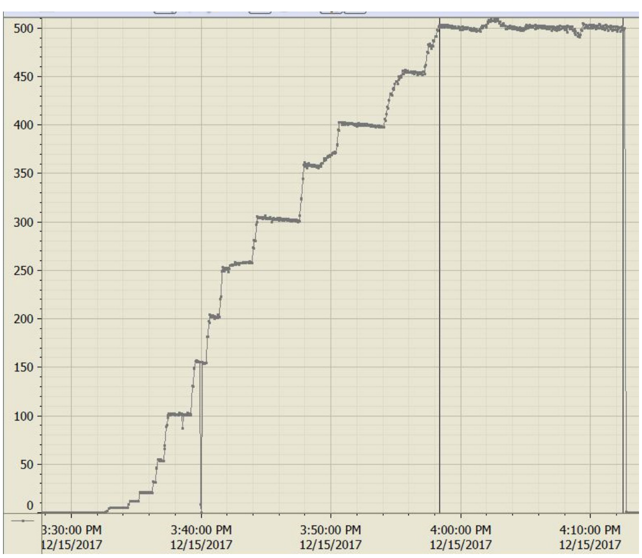

Figure 3: The graph shows the average current (in µA) of proton beam delivered to the beam dump at 70 MeV versus time.

The optical properties of the beam along the transport line BL1 have been verified and a good matching with the simulations has been observed. The transversal size of the delivered beam was measured in different points along the beamline by using the three wire scanners (see Fig. 4). It has permitted to check the behavior of beam envelop by modifying the operational parameters of the magnet devices (dipoles and quadrupoles) as well as the extraction conditions from the cyclotron.

The beam operations stopped in March 2018 to allow the preventive maintenance of cyclotron systems and to provide the needed installations expected for SPES project.

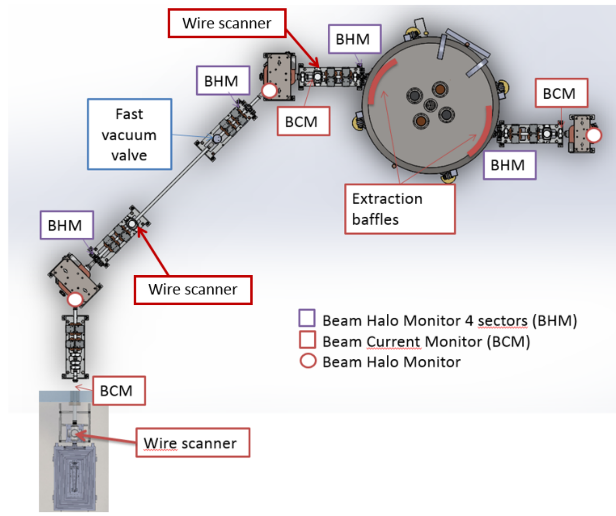

Figure 4: The picture shows the layout of actual installation of the Cyclotron and beamlines in SPES building. The positions of wire scanners used as active beam diagnostic are shown.

Cyclotron Systems Upgrade

As mentioned above, the Cyclotron facility is being expanded with the installation of 3 beamlines by the 2020: two lines will be dedicated to radioisotopes research within the LARAMED project environment. A third beamline is foreseen as complementary ISOL target in the bunker ISOL2.

Actually the cyclotron systems are under preventive maintenance: the hydraulic system was purged and the oil re-filled, the vacuum system and cryogenics equipment were refurbished and the RF power amplifiers were retuned.

As future upgrades expected to improve the cyclotron performance, two main devices are under study and design: a collimator system to be installed along the injection line in order to varying the average current of extracted beams avoiding to do it by modifying the voltage of the RF cavities; an axial buncher allowing to optimize the ion source performance and the related injected current to improve the reliability and to get more flexibility [5].

As suitable upgrade of the Cyclotron facility, a new beam dump dedicated for high power beam test has been proposed. The main purpose is to realize a dedicated beamline for Cyclotron testing which is equipped with a beam dump able to sustain 50 kW beam power.

ISBN: 978-3-95450-205-9 doi:10.18429/JACoW-Cyclotrons2019-TUC01

The high power test beamline will be derived from the second switching magnet placed along the ISOL1 beamline. The high power beam dump will be placed into the wall separating the A1 and A8 room (see Fig. 1). It will allow to have the concrete shield for neutron and gamma radiations generated during the irradiation.

A preliminary study of the new beam dump was accomplished out from the Cyclotron team in order to set the technical parameters of the device: a graphite made structure embedded in an aluminium holder has been studied and the related cooling water circuit has been preliminarily dimensioned (see Fig. 5).

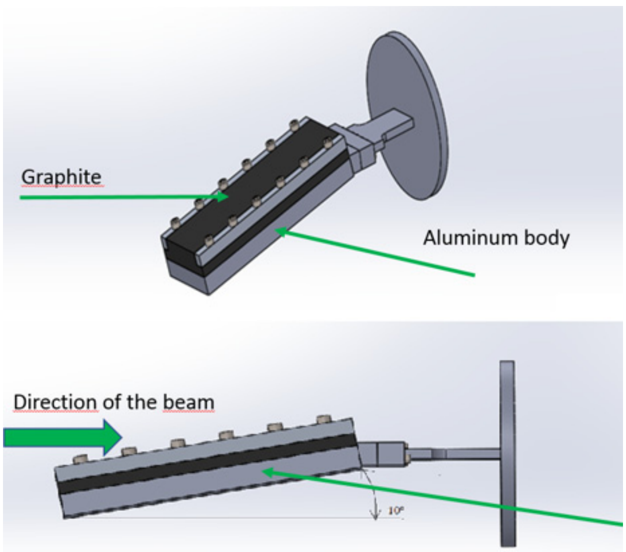

Figure 5: The plots show the preliminary model of the beam dump graphite made to be placed at the end of beamline foreseen for high power beam test.

CONCLUSION

The high power Cyclotron has been delivered at LNL and first beam operations were carried on in 2018. The accelerator has achieved the requested performance and it has demonstrated a satisfactory reliability (even if additional tests will be necessary) and, generally, a very good manufacturing. The LNL cyclotron group is involved in the operation and an intensive program of upgrades is being carried on. In parallel, the high intensity facility is expanding in order to make operational the beamlines and make available the first beams for nuclear research and medical applications. In fact, at LNL the SPES project is entered in the installation phase and most of main components (ISOL targets, low energy beamlines) will be available to work in the next three years.

REFERENCES

[1] F. Gramegna *et al.*, "The SPES exotic beam ISOL facility", *Il Nuovo Cimento C*, vol. 41, no. 5, art. 195, 2018. doi:10.1393/ncc/i2018-18195-3

[2] J. Esposito *et al.*, "LARAMED: A laboratory for radioisotopes of medical interest", *Molecules*, vol. 24, no.1, art. 20 (14 pages), 2019. doi:10.3390/molecules24010020

[3] D. Bisello *et al.*, "LINUS: the integrated LNL neutron source facility", in *Proc. 22nd meeting of the International Collaboration on Advanced Neutron Sources (ICANS XXII)*, 27–31 Mar. 2017, Oxford, UK, *J. Phys. Conf. Ser.*, vol. 1021, p. 012010, 2018. doi:10.1088/1742-6596/1021/1/012010

[4] M. Maggiore *et al.*, "SPES: a new cyclotron-based facility for research and applications with high-intensity beams", *Mod. Phys. Lett. A*, vol. 32, no. 17, 2017. doi.org/10.1142/S0217732317400107

[5] P. G. Antonini *et al.*, "Buncher for the optimization of injection of 70 MeV cyclotron", presented at the 22nd Int. Conference on Cyclotrons (Cyclotrons'19), Cape Town, South Africa, Sept 2019, paper TUP010, this conference.

ISBN: 978-3-95450-205-9 doi:10.18429/JACoW-Cyclotrons2019-TUC02

STATUS OF THE HZB CYCLOTRON

A. Denker[†,1], J. Bundesmann, T. Damerow, T. Fanselow, D. Hildebrand, U. Hiller, I. Kailouh, G. Kourkafas, S. Ozierenski, S. Seidel, C. Rethfeldt, J. Röhrich, C. Zimmer
Helmholtz-Zentrum Berlin für Materialien und Energie, Berlin, Germany
D. Cordini, J. Heufelder, R. Stark, A. Weber, Charité – Universitätsmedizin Berlin, Berlin, Germany
[1]also at Beuth University of Applied Sciences Berlin, Berlin, Germany

Abstract

For more than 20 years eye tumours are treated in collaboration with the Charité – Universitätsmedizin Berlin. The close co-operation between Charité and HZB permits joint interdisciplinary research. Irradiations with either a sharp, well focused or a broad beam, either in vacuum or in air are possible. In addition, a ^{60}Co-source for γ-irradiations is available. Experiments now comprise dosimetry, detector comparisons, and ambulant mouse irradiations. Furthermore, radiation hardness tests on detectors, CCD-cameras and other electronics are performed.

In order to improve the beam diagnosis between the 2 MV injector Tandetron and the cyclotron a harp has been installed, leading to new beam line calculations for the injection line.

ACCELERATORS AND OPERATION

The k=130 cyclotron of HZB is served by two injectors: a 6 MV Van-de-Graaf and a 2 MV Tandetron (see Fig. 1 in [1]). The Tandetron is our usual injector for therapy, delivering an extremely stable beam. The Van-de-Graff injector is used as backup, for rare gas beams, and if a beam with a different time structure is required.

The standard beam is a 68 MeV quasi-DC broad proton beam. For experiments, time structures vary from quasi-DC to single pulses with a pulse width of less than 1 ns. The beam spot may be 50 mm in diameter with a homogenous distribution or may be focused to less than 1 mm.

Operation of the accelerator complex went smoothly. As the scheduled beam time is only little more than one week in two shift mode per month, major break-downs have an enormous effect on the relative down time, e.g. the high downtime in 2015 was due to faulty operation during run-up of the cyclotron. With exception of 2015, the relative down-time of the accelerator was below 5%. Furthermore, as can be seen in Fig. 1, most of the downtime occurs during the start-up phase of the accelerator complex. Since 2011 the Tandetron is our usual injector for therapy, improving the downtime. The main cause for down-time is the cyclotron. Here, the installation of the new low-level RF control [2] reduced the RF faults. 10% of the down-time is due to cuts in the electricity supply.

BEAM UTILIZATION

By far most of the beam time (85%) is delivered for therapy. The experimental use of the beam time is: accelerator development 8%, medical physics and dosimetry 5%, and radiation hardness tests about 2%.

† denker@helmholtz-berlin.de

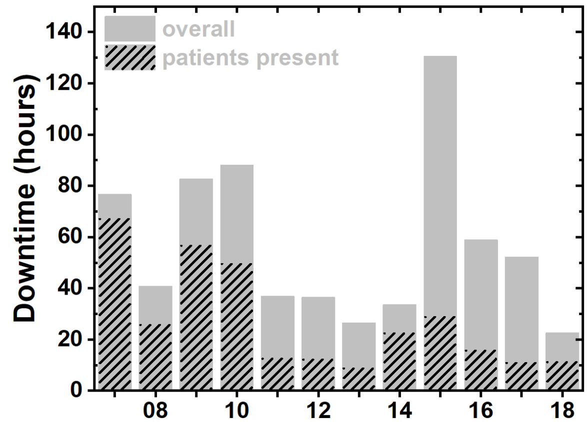

Figure 1: Downtime in hours for the past years. With exception of 2015, the relative downtime was below 5%.

Therapy of Ocular Melanomas

We now look back to more than 20 years of accelerator operation for proton therapy. Overall, more than 3500 patients have been treated. For the past ten years, nearly 220 patients have been irradiated each year in a routine workflow. Special cases were children, pregnant and breast-feeding patients.

In Tables 1 and 2 the clinical results of different radiation types used for the treatment of ocular melanomas of different centres as well as of Charité are shown. Compared to other radiation techniques, protons provide an excellent tumour control of 96% after 5 years as well as a very good eye retention rate.

Table 1: Tumour Control after 5 Years

Radiation	Others	Charité
^{106}Ru [3,4]	91%	ca. 92%
^{125}I [3]	91%	
Protons[3,5,6]	96%	ca. 96%
LINAC (SRT) [3,7]	94%	
Cyberknife (SRS) [8,9]	73%	

Table 2: Eye Retention Rate after 5 Years

Radiation	Others	Charité
^{106}Ru [10,4]	91%	ca. 92%
^{125}I [11]	91%	
Protons[5,12,6]	96%	ca. 96%
LINAC (SRT) [7]	94%	
Cyberknife (SRS) [8,9]	73%	

ISBN: 978-3-95450-205-9 doi:10.18429/JACoW-Cyclotrons2019-TUC02

Medical Physics

An observed side effect of radiation therapy is the radiation induced retinopathy one to two years after treatment. For a better understanding of the causes, ophthalmologists want to irradiate single mice eyes to observe the chemical and biological changes in eye tissue. The challenge lies in the small size of a mouse eye compared to the human eye. Thus, a very small irradiation field with sharp dose fall-offs to the sides as well as in depth is required. A Spread Out Bragg Peak with a maximum range of 7 mm and full modulation length is provided (Fig. 2). A second absorber of 2 mm thickness reduces the maximum proton range further down to 5 mm. Thus, the second eye is non-irradiated due to the sharp distal fall-off of less than 1 mm and can be used as a control. The irradiation is an ambulant procedure: The mice are transported from the animal husbandry of the Charité to HZB, have time for acclimatization, and are anesthetised. The mouse is positioned in front of the beam line with one eye placed at the isocenter. The position of the mouse during irradiation is monitored using the same camera as for clinical treatment. After irradiation the mice are transported back to the Charité. Up to now, about 60 mice have been irradiated with doses from 0 Cobalt Gray Equivalent (CGE) to 15 CGE.

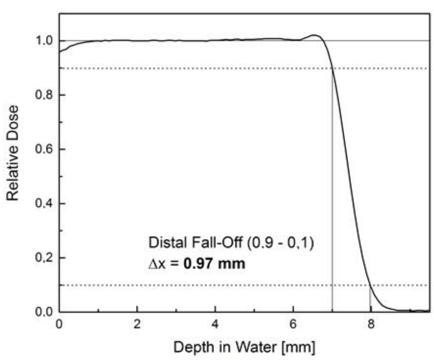

Figure 2: Spread Out Bragg Peak used for irradiations of mice eyes. The distal fall-off from 90% to 10% of the dose is less than 1 mm.

Dosimetry

Experiments on dosimetry comprised, among others:

- Determination of the radiation exposure to the foetus of a pregnant patient during eye tumour treatment with protons [13].
- Characterization of thin-film TLD, type LiF:Mg, Cu, P for the dosimetry with 68 MeV protons [14].

Radiation Hardness Tests

Radiation hardness tests can be performed using either γ-rays from a ^{60}Co source or protons from the cyclotron. At the ^{60}Co source, total ionising dose (TID) tests are performed using dose rate between 1 Gy/h to 100 Gy/h. The TID tests and proton irradiations can be performed on one site with short distances between the two irradiation rooms.

The proton beam size is adjusted to the size of the devices using different scattering systems or a wobbling system. The proton intensity varies between 10^4 p/cm² to 10^{13} p/cm². When irradiation times of more than 15 min are requested, the low proton intensities are challenging for precise measurements.

Radiation hardness tests are performed for industry, the German Aerospace Center (DLR), and research. Examples are e.g. commercial of the shelf electronics for space missions [15, 16] or solar cells [17].

Accelerator Development

For the installation of the 2 MV Tandetron, which replaces our RFQ, we had to accept constraints for the position of the Tandetron in beam direction: It had to fit to the existing beamline, and access to the cyclotron and emergency exits had to be maintained. Figure 3 shows the Ootran [18] calculations performed for the RFQ prior to its installation. The position of the Tandetron is marked with the yellow line. The beam profile monitor (BPM), a rotating wire scanner, had to be moved closer to the cyclotron. Thus, the BPM is not on a focal point, and tuning of the beam is ambiguous. Furthermore, the Tandetron is equipped at the end of the acceleration tube with an electrostatic quadrupole. This quadrupole is a triplet with only three power supplies and thus, asymmetric properties. Normal beam line calculation programmes cannot handle it.

A harp has been installed in the beamline to quantify the beam size. It consists of 25 wires in x and y, mounted on a standard movement unit [19]. The connection of the wires is done with flat cables and a printed circuit board (PCB). For the vacuum feed-through we used a second PCB board and epoxy (see Fig. 4). The leak rate of this connection is $1{\cdot}10^{-9}$ mbar/(l·s). Tests on a mass spectrometer revealed no out-gassing material which might be dangerous for the electrostatic quadrupole nearby. The read-out is done with the harp electronics from iThemba labs.

The beam profile measured with the usual BPM (Fig. 5, left) had shown two peaks in y. This was in the beginning explained as a slight misalignment of the beam. However, the measurements with the harp also revealed two peaks (Fig. 5, right). Further investigations showed that we have two beams: a proton beam and a beam of neutral hydrogen particles which is due to incomplete stripping in the Tandetron.

These measurements together with finite element calculations of the electrostatic quadrupole using SIMION [20] permitted to estimate the beam properties at the exit of the quadrupole. Thus, the beam line settings between the Tandetron and the cyclotron can be now be calculated.

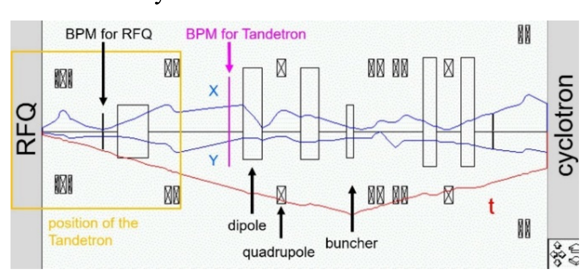

Figure 3: Ootran calculations for the beam line between RFQ and cyclotron.

ISBN: 978-3-95450-205-9 doi:10.18429/JACoW-Cyclotrons2019-TUC02

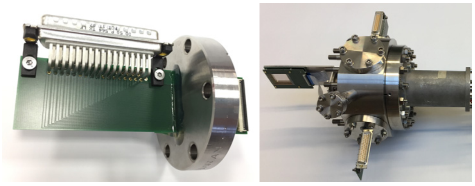

Figure 4: Vacuum feed through of the harp (left) and the connection to a standard movement unit with flat cables (right).

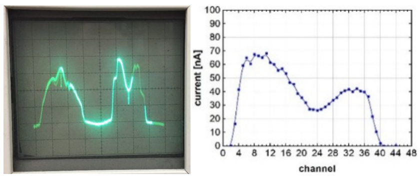

Figure 5: Beam profile after the Tandetron. Left: as measured with a BPM, showing the profile in x and y. Right: y profile measured with the harp.

CONCLUSION

Accelerator operation was reliable. With one exception, the relative down-time in the past years was less than 5%. Most of the down-time occurs during start-up of the accelerator. We will continue with our on-going improvements and developments in order to keep the down-time low.

In 2018, we celebrated the 20th anniversary of eye tumour therapy in Berlin, the only facility for proton therapy for ocular melanomas in Germany. End of June 2019, more than 3500 patients had been treated with protons in Berlin. The clinical data for protons show excellent tumour control and eye retention rate.

Experiments comprise accelerator research and development, radiation hardness testing for space applications, dosimetry, as well as radiobiological experiments.

The authors are indebted to iThemba labs for providing the electronic for the harp.

REFERENCES

[1] J. Bundesmann *et al.,* "Beam properties at the experimental target station of the proton therapy in Berlin", presented at the 22nd Int. Conf. on Cyclotrons and their Applications (Cyclotrons'19), Cape Town, South Africa, Sep 2019, paper TUP020, this conference.

[2] T. Fanselow *et al.*, "Operational experience in the treatment of ocular melanomas with a new digital low-level RF control system", presented at the 22nd Int. Conf. on Cyclotrons and their Applications (Cyclotrons'19), Cape Town, South Africa, Sep 2019, paper TUP007, this conference.

[3] M. Y. Chang *et al.*, "Local treatment failure after globe-conserving therapy for choroidal melanoma", *Br. J. Ophthalmol.,* vol. 97, no. 7, pp. 804-811, Jul. 2013.

[4] N. Krause *et al.*, "Langzeitergebnisse bei Aderhautmelanom nach 106Ruthenium-Brachytherapie", Dissertation, FU Berlin, Germany, 2015.

[5] E. Egger *et al.*, "Maximizing local tumor control and survival after proton beam radiotherapy of uveal melanoma", *Int. J. Radiat. Oncol. Biol. Phys.*, vol. 51, no. 1, pp. 138-147, Sep. 2001.

[6] I. Seibel *et al.*, "Local recurrence after primary proton beam therapy in uveal melanoma: Risk factors, retreatment approaches, and outcome", *Am. J. Ophthalmol.,* vol. 160, no. 4, pp. 628-636.

[7] R. Dunavoelgyi *et al.*, "Local tumor control, visual acuity, and survival after hypofractionated stereotactic photon radiotherapy of choroidal melanoma in 212 patients treated between 1997 and 2007". *Int. J. Radiat. Oncol. Biol. Phys.,* vol. 81, no. 1, pp. 199-205, Sep. 2011.

[8] K. Eibl-Lindner *et al.,* "Robotic radiosurgery for the treatment of medium and large uveal melanoma", *Melanoma Res.*, vol. 26, no. 1, pp. 51-57, Feb. 2016.

[9] G. Yazici *et al.*, "Stereotactic radiosurgery and gractionated stereotactic radiation therapy for the treatment of uveal melanoma", *Int. J. Radiat. Oncol. Biol. Phys.,* vol. 98, no. 1, pp. 152-158, May 2017.

[10] K. M. S Verschueren *et al.*, "Long-term outcomes of eye-conserving treatment with Ruthenium(106) brachytherapy for choroidal melanoma", *Radiother. Oncol.,* vol. 95, no. 3, pp. 332-338, Jun. 2010.

[11] D. T. Vonk *et al.*, "Prescribing to tumor apex in episcleral plaque iodine-125 brachytherapy for medium-sized choroidal melanoma: A single-institutional retrospective review", *Brachytherapy*, vol. 14, no. 5, pp. 726-33, Sep.-Oct. 2015.

[12] K. K. Mishra: "Proton therapy for the management of uveal melanoma and other ocular tumors", *Chin. Clin. Oncol.* vol. 5, no. 4, p. 50, Aug. 2016.

[13] A. Mirus, "Ermittlung der Strahlenbelastung während einer Augentumortherapie mit Protonen im Fetus einer schwangeren Patientin", master thesis, Beuth University for applied sciences, Berlin, Germany, 2017.

[14] S. Pensold, "Charakterisierung von Dünnfilm-TLD des Typs LiF:Mg, Cu, P für die Dosimetrie am 68 MeV Protonenstrahl in der Augentumortherapie", Diploma thesis, Martin-Luther-Universität, Halle, Germany, 2013.

[15] H. J. Sedlmayr *et al.*, "COTS for (deep) space missions", *Radiation Effects on Integrated Circuits and Systems for Space Applications,* München, Germany, Oct. 2017, pp. 381-401.

[16] H. J. Sedlmayr *et al.*, "Radiation test of a BLDC motor driver component", *IEEE Nuclear and Plasma Sciences Society*, NSREC2018, Jul. 2018, Kona, USA, pp. 109-115. doi:10.1109/NSREC.2018.8584281

[17] H.-C. Neitzert *et al.*, "Electroluminescence efficiency degradation of crystalline silicon solar cells after irradiation with protons in the energy range between 0.8 MeV and 65 MeV", *Phys. Stat. Sol. (b),* vol. 245, no. 9, pp. 1877–1883, 2008. doi:10.1002/pssb.200879543

[18] A. Ninane, *et al.*, "An object-orient program for charged-particle beam transport design". *Nucl. Instrum. Methods Phys. Res., Sect. A* , vol. 293, pp. 468 – 474, 1990.

[19] M. Burmeister, "Aufbau und Entwicklung einer zweidimensionalen Strahlprofilanalyse für die Protonentherapie am Helmholtz Zentrum Berlin", Master thesis Beuth University for applied sciences, Berlin, Germany, 2016.

[20] SIMION, https://simion.com/

ISBN: 978-3-95450-205-9 doi:10.18429/JACoW-Cyclotrons2019-TUC03

AGOR STATUS REPORT

B. N. Jones, S. Brandenburg, M.-J. van Goethem, KVI-Center for Advanced Radiation Technology, University of Groningen, 9747AA Groningen, The Netherlands

Abstract

The operations of the superconducting cyclotron AGOR over the past years will be reviewed. Reliability issues encountered after nearly 25 years of operation and mitigation measures to warrant reliable operation for the coming decade will be discussed.

The research performed with AGOR has significantly shifted from fundamental physics to radiation biology and medical radiation physics, both in collaboration with the Groningen Proton Therapy Center, and radiation hardness studies. The radiation biology research will be substantially expanded in the coming years with a new beam line for image guided preclinical research. For this research new dose delivery modalities including scanning, spatial fractionation and very high dose rates are developed. In addition, a new program has been started on the production of exotic nuclei, for which a new superconducting solenoid fragment separator will be developed.

For the radiation hardness testing a cocktail beam at 30 MeV/amu with several ion species up to Xe has been developed and is now routinely delivered for experiments. A cocktail at 15 MeV/amu up to Bi is under development.

INTRODUCTION

The superconducting AGOR cyclotron, built by a French-Dutch collaboration in the period 1987 – 1994, has, after being transferred from Orsay (France), been operational in Groningen since the beginning of 1996. It can deliver beams of all elements, as is illustrated in the operating diagram in Fig. 1. The upper limit on the beam energy is determined by K_{bend} = 600 MeV and K_{foc} = 200 MeV; the lower limit by the lowest RF-frequency of 24 MHz and the location of the $\nu_r + 2\nu_z = 3$ resonance. The dots in the figure indicate the beams delivered for experiments over the years.

In the period 1996 – 2013 the beams delivered have mainly been used for research in nuclear physics (light ions) and on fundamental symmetries (heavy ions). Since 2014 the emphasis has shifted towards biomedical research, detector development and radiation hardness testing.

OPERATION

The cyclotron is operated 120 hours per week for about 26 weeks per year, which still meets current demand. From a technical perspective it is feasible to operate the cyclotron about 40 weeks per year; this would require additional operating staff to be recruited and trained.

With the shift from fundamental physics to radiation biology and physics and technology of particle therapy the number of individual experiments has significantly increased while their duration has strongly decreased from several days to typically 16 hours. It regularly happens that the cyclotron has to deliver a different beam every day of the week.

Over the past few years proton beams have been provided for over 80 % of the beam time, accelerated either as protons ($E_p \geq 120$ MeV) or as molecular hydrogen ($40 \leq E_p \leq 90$ MeV). The remainder of the beam time helium, carbon and oxygen beams with energies in the range 30 – 90 MeV/amu have been provided.

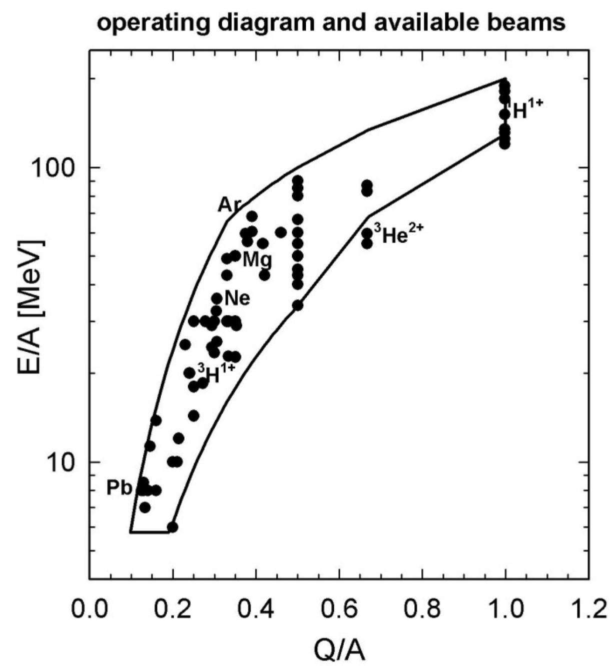

Figure 1: Operating diagram of the AGOR cyclotron.

RELIABILITY ISSUES

After nearly 25 years of operation reliability issues start to appear on certain sub-systems of the accelerator. These are to a large extent related to availability of spare parts and components and, for the control system, incompatibility with current hardware and standards for communication. In addition, wear and tear necessitates replacement of certain components.

Control System

The central control system of the AGOR accelerator facility is based on the commercial Vsystem software package [2]. We have recently ported the system from the 32-bit to the 64-bit version in order to maintain compatibility with modern hardware. Depending on the specific requirements local control is performed by PLC's (vacuum, cryogenics, cooling) and locally developed microprocessor-based systems communicating over BITBUS (power supplies, beam diagnostics). Both suffer from obsoles-

ISBN: 978-3-95450-205-9 doi:10.18429/JACoW-Cyclotrons2019-TUC03

cence. We have therefore started a program stretching over several years to gradually replace all PLC's and to phase out BITBUS. Upgrade of the PLC-based systems to the latest version is nearly complete. BITBUS-based systems are replaced by PLC's where possible, thus creating a stock of spare parts. Options for replacement of the remaining BITBUS-based systems, in particular in the RF-system are being evaluated.

Radiofrequency System

The RF-system of the AGOR cyclotron operates rather reliably. The tetrodes of the 55 kW RF amplifiers, which for all beams operate below 22 kW, all have well in excess of 100,000 running hours and we observe no degradation of the cathode emission. Breakdown of power transistors in the dual 1 kW solid state preamplifiers of each amplifier is the main source of malfunctioning and we are considering replacement. The low-level electronics (amplitude, phase and tuning regulation) and the position control of the RF-cavities require, although reliable, overhaul because of obsolescence of key components.

Extraction Channels

The extraction system of the AGOR cyclotron consists of an electrostatic deflector (ESD), a room temperature electromagnetic channel (EMC1) and two superconducting electromagnetic channels (EMC2 and QPOLE). EMC1 and EMC2 consist of the dipole, gradient and compensation winding; QPOLE consists of a quadrupole doublet with horizontal and vertical steering.

The ESD operates at moderate voltage ($V \leq 50$ kV) and field strength ($E \leq 10$ MV/m), resulting in very reliable operation. Occasionally reconditioning by means of flowing oxygen gas in the gap is required.

The EMC1 operates at high current densities (up to 140 A/mm^2) and small winding dimensions (3 x 4 mm^2 with 2 mm $\varnothing$ cooling channel). The total power dissipation in the channel is up to 80 kW in less than 2 kg of Cu. Adequate cooling necessitates high flow velocities, resulting in erosion in the sharp bends of the windings at the entrance and exit of the channel. Both the original EMC1 and a copy put into operation ten years ago increasingly suffer from water leaks in bends. The repair of these leaks is a major source of downtime, which can only be mitigated by building another EMC1. In order to avoid the sharp bends, the channel has been completely redesigned exploiting an in-house developed bending technique. An additional benefit of the new design is a reduction of the number of brazings by a factor four from over 200 to 52. The new EMC1 is currently under construction in our workshop and will be commissioned in 2020.

The superconducting channels operate very reliably. Malfunctioning of the redundant quench detection caused a rupture of the superconducting wire of the QPOLE. While the repair itself was straightforward, getting access was complicated due to the need to cut the cryostat wall and weld it again after the repair.

Cryogenic System

The main coils and the two superconducting extraction channels are cooled by a Linde TCF-50 cryoplant operating in mixed mode: for the main coils it acts as a refrigerator (gas return at 4.5 K) while for the extraction channels it supplies liquid helium (gas return at 300 K). Overall, this system has proved to be very reliable over the years. However, for the past year we experienced a transient instability during filling of any of the three cryostats precluding operation for a period of several days up to two weeks. No signs of excessive heat loss in either transfer lines or cryostats were observed and also detailed analysis of the extensive diagnostics information did not provide an insight in the cause of this problem. After the last standard maintenance cycle, during which essentially all transfer lines are warmed up and evacuated the problem now seems to have disappeared.

At the end of 2018, we installed a new Kaeser helium compressor and upgraded the cryogenic control system. The motivation for this project were energy savings and spare parts running out at the manufacturer. The new compressor operates at variable frequency, which has resulted in an energy savings of 15% for the accelerator facility as a whole. The payback time for this investment is six to seven years. The new compressor has been equipped with a heat recovery system that provides about 75 % of the heat needed for heating the building.

PLANS FOR THE FUTURE

In 2018 funding has been obtained for further expansion of the biomedical research at the AGOR cyclotron and for a research programme on the properties of neutron-rich heavy nuclei. For both programmes new experimental platforms will be installed at existing beam lines. Consequently, the BBS magnetic spectrometer [3] used for nuclear structure research and the TRIμP fragment separator [4] are being decommissioned. In Fig. 2 the new lay-out of the experimental hall is displayed.

Biomedical Research

The University of Groningen (UG) and the University Medical Center Groningen (UMCG) have recently established a clinical proton therapy center, which started treating patients at the beginning of 2018, at the UMCG-campus. In conjunction with this center an extensive R&D programme encompassing radiation biology, physics and technology as well as clinical studies has been established. The AGOR accelerator facility is the key infrastructure for in particular the radiation biology and physics and technology R&D in this programme.

For the radiation biology research a new beam line with 3D X-ray and bioluminescence imaging at the irradiation position, thus providing the capability to perform individually optimized small animal irradiations, will be built in the coming years. At the new irradiation platform several new dose delivery modalities will be available, including pencil beam scanning, spatial fractionation and very high

ISBN: 978-3-95450-205-9 doi:10.18429/JACoW-Cyclotrons2019-TUC03

dose rates (> 1000 Gy/s). The platform will be operated as an open access facility.

Plans for a further additional beam line for particle therapy physics and technology R&D are currently being developed.

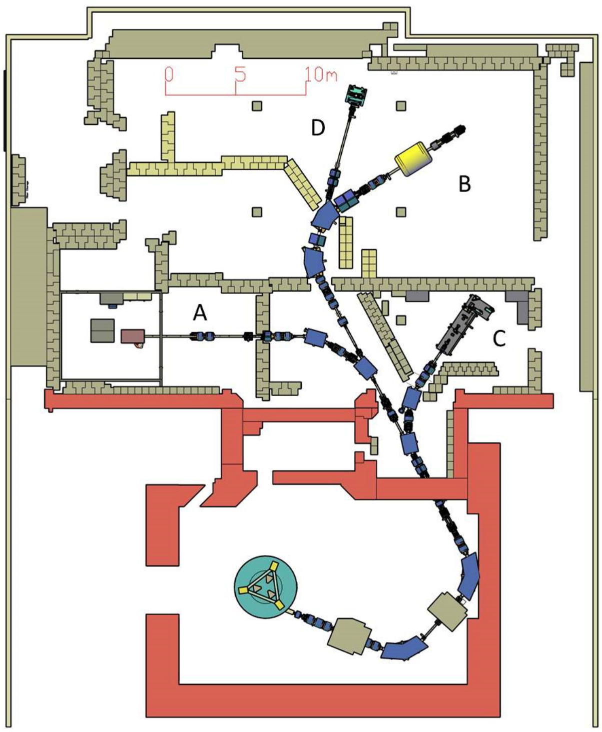

Figure 2: New floorplan of the AGOR facility.
A: image guided radiation biology.
B: superconducting solenoid separator
C: in-air irradiation
D: in-vacuum irradiation

Heavy Element Research

A new experimental research program on the production of neutron-rich heavy nuclei using multi-nucleon transfer in reactions between heavy nuclei (e.g. 136Xe on 208Pb) [5] has recently been started at the University of Groningen. The AGOR cyclotron will provide the heavy ion beams in the mass range A = 140 – 160 with energies around 10 MeV/A for the experiments, requiring substantial development work to produce rare earth elements beams. A new experimental station consisting of a 3 T superconducting solenoid fragment separator followed an MR-ToF mass spectrometer will be installed at one of the existing beam lines (see Fig. 2).

Radiation Hardness Testing

The radiation hardness testing at our facility is expanding. In addition to the proton beams we now also provide heavy ion beams for this. We have commissioned a cocktail of various ions up to 129Xe with an energy of 30 MeV/amu for in air testing. Using a thin Au scatter foil ions fluxes $\geq 10^6$ ions/(cm^2s) in a field of 30 × 30 mm are available for all ions. The homogeneity of the field is better than 10 %. foil. Higher fluxes and larger fields can be achieved with the scanning system that has been installed at both the in-air and in –vacuum irradiation stations. Beam purity is warranted by producing the various ions in the cocktail in two different ECR-sources. Switching between sources requires changing the setting of one switching magnet only. First experiments by external users will be performed in the autumn of 2019.

A cocktail with ions up to 209Bi at 15 MeV/amu, to be delivered to the vacuum irradiation facility, is under development.

ACKNOWLEDGEMENTS

The operation of the AGOR facility is supported by the European Union Horizon 2020 programme (contract nr. 654002 and 730983) and the CORA IBER program of the European Space Agency.

The new platform for image-guided radiation biology research is funded by the Dutch Cancer Foundation KWF (projects 11766 and 12092).

The operation of the AGOR accelerator would not be possible without the strong support of the KVI-CART technical staff.

REFERENCES

[1] S. Galès for the AGOR project group, "AGOR: A superconducting cyclotron for light and heavy ions", in *Proc. ICCA'11,* Tokyo, Japan, Oct. 1989, paper f01, pp. 184–190.

[2] Vista Control Systems, Inc., https://www.vista-control.com/

[3] A. M. van den Berg, "The big bit Spectrometer for AGOR", *Nucl. Instr. Methods Phys. Res., Sect. B*, vol. 99, pp. 637–640, 1995. doi:10.1016/0168-583X(95)00309-6

[4] G. P. A. Berg *et al.*, "TRIμP – a radioactive isotope trapping facility under construction at KVI", *Nucl. Instr. Methods Phys. Res., Sect. B*, vol. 204, pp. 532–535. doi:10.1016/S0168-583X(02)02127-4

[5] J. V. Kratz, W. D. Loveland, and K. J. Moody, "Syntheses of transuranium isotopes with atomic number Z ≤ 103 in multi-nucleon transfer reactions", *Nucl. Phys. A*, vol. 944, pp. 117-157, 2015. doi:10.1016/j.nuclphysa.2015.06.004

ISBN: 978-3-95450-205-9 doi:10.18429/JACoW-Cyclotrons2019-TUC04

STATUS OF THE CYCLOTRON FACILITY AT RESEARCH CENTER FOR NUCLEAR PHYSICS

H. Kanda†, M. Fukuda, S. Hara, T. Hara, K. Hatanaka, K. Kamakura, H. W. Koay, S. Morinobu, Y. Morita, M. Nakao, K. Omoto, T. Saito, K. Takeda, H. Tamura, Y. Yasuda, T. Yorita
Research Center for Nuclear Physics, Osaka University, Ibaraki, Japan

Abstract

Research Center for Nuclear Physics (RCNP), Osaka University operates a K140 AVF cyclotron and a K400 ring cyclotron. We promote the nuclear physics, accelerator physics and related scientific fields using its unique beams. From 2018, the RCNP started the Research Center of Subatomic Sciences as the International Joint Usage/Research Center in Japan. It enables more efficient support for the researches using the resources of the RCNP facility. We have carried out the stable operation until Feb. 2019 when the 2 years of shutdown period starts for the upgrade works. We have been carrying out a program of the upgrade of the K140 AVF cyclotron. We aim at 10 times higher intensity for the proton beam than before and further stability of the operation. We also carried out the upgrade of the cyclotron building and related facilities to handle beams with higher intensity. The upgrade works are planned to be completed in the beginning of 2021. These upgrades are the most important programs to reinforce the function of the newly established center.

INTRODUCTION

Research Center for Nuclear Physics (RCNP), Osaka University operates a K140 AVF cyclotron which was completed in 1973 and a K400 ring cyclotron which was completed in 1992 and promotes the nuclear physics, accelerator physics, and related scientific fields since its foundation in 1971. Several kinds of the electron cyclotron resonance ion sources and a low energy beam transport system provide various ion beams including polarized proton and deuteron beams for injection to the K140 AVF cyclotron. The K140 AVF cyclotron have been used for providing medium energy beams to the experimental station and for injecting the beams to the K400 ring cyclotron. The K400 ring cyclotron accelerates protons up to 420 MeV at the maximum and other ions with their charge number Q and mass number A up to $400(Q/A)^2$ MeV. Precision of the beam energy is uniquely high ($\Delta E/E \sim 10^{-4}$) and it is taken advantage of in the precise measurement of the nuclear energy structures combined with the distortion matched beamline [1] and the world's most precise spectrometer Grand Raiden [2]. The proton beams with energy of 396 MeV is used for the production of secondary beams of muons as described in the later section and neutrons. The neutron beam with a broad energy spectrum is called as the white neutron beam which approximates the energy spectrum of cosmic ray neutrons on the ground level [3]. It is used for the test of the radiation-induced soft errors of semiconductor integrated circuits mainly by the industrial researchers. The middle energy beams are mainly used for the production of radioactive isotopes (RIs). We allied with 5 accelerator facilities in Japan and have provided short-lived RIs which are difficult to be commercially purchased. The accelerator building and the structure inside with the cyclotrons, spectrometers and the beam lines are shown in Fig. 1.

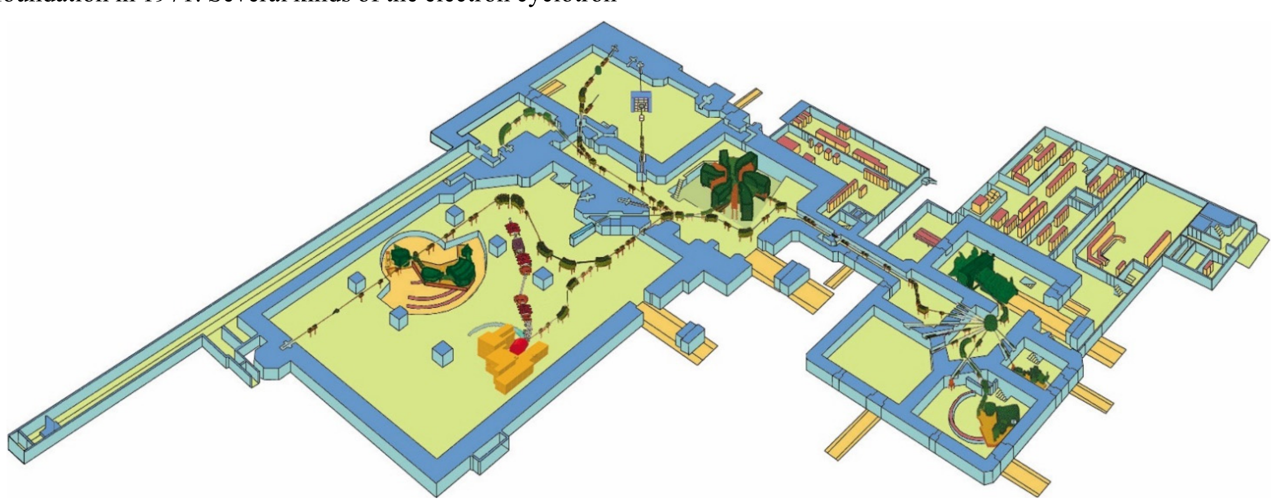

Figure 1: A birds-eye view of the RCNP cyclotron facility.

† kandah@rcnp.osaka-u.ac.jp.

ISBN: 978-3-95450-205-9 doi:10.18429/JACoW-Cyclotrons2019-TUC04

OPERATION STATUS

The operation status is summarized in Fig. 2. The operation time of the cyclotron system was 5784 hours in year 2018. Main use of the beam is the experiments in the nuclear physics. Proton, deuteron and helium beams were used in physics experiment mainly at the WS beam course in combination with the Grand Raiden spectrometer. Polarized proton beam was used at the ENN beam course for the investigation of the three body nuclear force. Light to heavy ion beams were used at the EN course for the production of exotic nuclei to study their structures. The next frequent use was the RI production. Alpha beam was mainly used for the production of ^{211}At which is one of the nuclides attracting interest in Japan as one of the alpha emitter to be used in the targeted alpha therapy of the cancers. The unscheduled shutdown was 111 hours. The usual causes of the troubles were water leaks from the plastic tubes used for the electric insulation and faults of electric power lines. Times needed for the recovery from these troubles were a few hours per trouble at the longest but we have to try to reduce the frequency of their occurrence. The troubles with the power lines may be resolved by the renovation of the power systems in the upgrade works of the cyclotron facilities. The troubles with the water leakage from the plastic tubes should be investigated and we have to make some countermeasures against them. We finished the machine operation on 11 Feb. 2019 for the upgrade works. The machine operation is scheduled to start from the beginning of 2021 after the completion of the upgrade of the K140 AVF cyclotron.

MUON BEAMLINE

We constructed a new continuous (DC) muon beamlines, MuSIC (MUon Science Innovative Channel) which consists of a superconducting solenoid systems for the pion capture and the muon transport [4, 5]. A 396 MeV proton beam with an intensity of 1.1 μA is impinging on a graphite target at the frequency of 16.8 MHz. Produced charged pions are captured by the pion capture magnet with B = 3.5 T and the muons emitted from the decay of the pions are transported to the beam line. The intensity of the negative muon is ~ 10^5 counts per second and that of the positive muon is ~ 10^6 counts per second. Its construction and commissioning were finished in 2017 and it have been used for nuclear physics experiments to investigate the three body nuclear force and muonic nuclear transmutaion, material analysis with specific muonic X-rays, and the estimation of the soft error rates of the integrated circuits induced by muons. The number of users have been constantly increased and many important results have been reported from the experiments.

UPGRADE OF THE RCNP FACILITIES

The upgrade program of the K140 AVF cyclotron and the RCNP facility was planned for the reinforcement of the function of the RCNP as the center to support the communities of researchers. Increasing the primary beam intensity

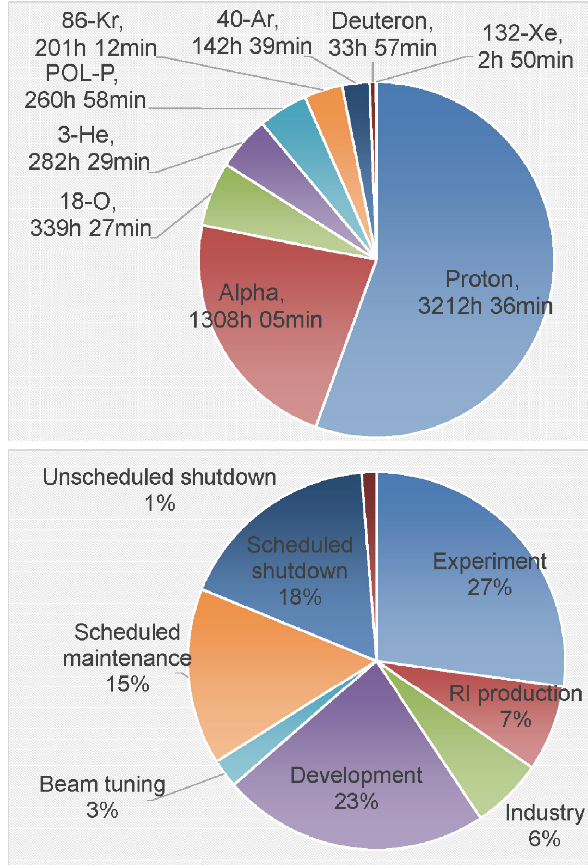

Figure 2: Summary of the beam time with respect to ion species (upper panel), with respect to uses (lower panel).

will increase the amount of produced RIs, the intensities of the secondary beams and the beam quality needed for the precise measurement. In this upgrade, we estimate that at least 10 times higher beam intensity will be achieved.

The RCNP started the Research Center of Subatomic Sciences as the International Joint Usage/Research Center in Japan in 2018 financially supported by Japanese Ministry of Education, Culture, Sports, Science and Technology because of the high reputation to the efforts which the RCNP has been spent to support the researches and the communities of the researchers. In order to promote the activity of the center, the upgrade of the facility is important. The upgrade consists of three elements and they are described in the following of this section.

Ion Sources and the Low Energy Beam Transport

In order to increase the intensity of the accelerated beams, increasing the brightness of the ion sources is inevitable. We are developing a high intensity ECR ion source for proton and light ions referring to the IFMIF type ion source [6, 7]. We also prepared a duoplasmatron ion source which enables substantially low emittance and high intensity. We plan to increase the extraction voltage of all the ion sources from 10 – 15 kV to at least 50 kV and design a low energy beam transport to treat the higher energy ion beams. Reducing the emittance to match the acceptance of

ISBN: 978-3-95450-205-9 doi:10.18429/JACoW-Cyclotrons2019-TUC04

the K140 AVF cyclotron will increase the beam amount injected into the cyclotron.

Upgrade of the K140 AVF Cyclotron

The beam with higher intensity may more strongly affected by the space charge effect. It is better to finish acceleration in shorter time before the beam spreads by the repulsive force. We plan to replace the current single Dee electrodes of the K140 AVF cyclotron to double Dee electrodes covering ~ 90 degrees. With harmonic = 2 acceleration, a beam bunch can be accelerated 4 times in one turn and thus the number of turns needed to reach the maximum energy. The RF system consisting resonators, couplers, amplifiers are newly designed to match this replace of Dee electrodes. Deflectors and gradient correctors are also designed to deal with the change of beam trajectory. Inflector electrodes and phase slits have to be newly designed for accepting 50 kV accelerated ions. All the probes are newly designed to handle the higher power dissipated by the more intense beams. The old trim coils and valley coils are replaced to new ones. The vacuum chamber and pumping system are also renewed. Thus the K140 AVF cyclotron is almost completely renewed. Only the main coils, yokes, and poles are to be reused.

Readers are referred to the reference [8] for the detail of the upgrade of the K140 AVF Cyclotron.

Upgrade of the Cyclotron Buildings and Facilities

In order to handle more intense beam, the apparatuses are also renewed:

1. Thicker shielding wall, especially surrounding the beam line from the AVF cyclotron to the ring cyclotron.
2. The cooling towers for higher cooling capacity.
3. The RI drainage system to handle larger radioactivity.

Adding to them, old apparatuses, floors, roofs are also renovated. The construction work started from the April 2019 and planned to be completed in March 2020.

We also plan to renovate the white neutron beam line. The radiation shielding on the ceiling is added to handle the higher radiation. The diameter of the hole for the neutron beam duct is enlarged to enable the neutron beam with larger diameter so that larger area of the printed board is irradiated at one time. This renovation will serve for more efficient use of the beam time.

SUMMARY

The RCNP operates AVF cyclotrons that are more than 40 years old and ring cyclotrons that are more than 20 years old with unchanged stability in operation. We constructed the new beam line for DC muons and made steady progress in nuclear physics, nuclear chemistry, nuclear medicine and information science. From this year, the upgrade works of the K140 AVF cyclotron has been started. And the renovation of the buildings and the apparatuses has started for handling of beams with increased intensity and for repairing or replacing the aged apparatuses which are nearly out of order. Through these upgrade and renovation, we aim at improving the functions of research center in related fields and further development.

REFERENCES

[1] T. Wakasa *et al.*, "High resolution WS beam line at RCNP", in *Proc. 16th Int. Conf. on Cyclotrons and their Applications (Cyclotrons'01)*, *AIP Conf. Proc.* vol. 600, no. 1, p. 458, 2001.

[2] M. Fujiwara *et al.*, "Magnetic spectrometer Grand Raide", *Nucl. Instrum. Methods in Phys. Res., Sect. A*, vol. 422, pp. 484–488, 1999.

[3] Y. Iwamoto *et al.*, "Evaluation of the white neutron beam spectrum for single-event effects testing at the RCNP cyclotron facility", *Nucl. Tech.*, vol. 173, no. 2, pp. 210–217, 2011. doi:10.13182/NT11-A11550

[4] D. Tomono *et al.*, "Muon Beamline Commissioning and Feasibility Study for μSR at a New DC Muon Beamline, MuSIC-RCNP, Osaka University" in *Proc. 14th Int. Conf. on Muon Spin Rotation, Relaxation and Resonance (μSR2017)*, *JPS Conf. Proc.* vol. 21, p. 011057, Mar. 2018. doi:10.7566/JPSCP.21.011057

[5] S. Cook *et al.*, "Delivering the world's most intense muon beam", *Phys. Rev. Accel. Beams,* vol. 20, no. 3, p. 030101, 2017. doi:10.1103/PhysRevAccelBeams.20.030101

[6] R. Gobin *et al.*, "High intensity ECR ion source (H+, D+, H−) developments at CEA/Saclay", *Rev. Sci. Instrum.* vol. 73, no. 2, pp. 922–924, 2002. doi:0.1063/1.1428783

[7] R. Gobin *et al.*, "A 140 mA cw deuteron electron cyclotron resonance source for the IFMIF-EVEDA project", *Rev. Sci. Instrum.* vol. 79, p. 02B303, 2008. doi:10.1063/1.2801976

[8] M. Fukuda *et al.*, "Design for upgrading the RCNP AVF cyclotron", presented at the 22nd Int. Conf. on Cyclotrons and their applications (Cyclotrons'19), Cape Town, South Africa, Sep. 2019, paper WEA03, this conference.

ISBN: 978-3-95450-205-9 doi:10.18429/JACoW-Cyclotrons2019-WEA02

THE DEVELOPMENTS OF THE RF SYSTEM RELATED TO THE K-800 SUPERCONDUCTING CYCLOTRON UPGRADE*

A. Caruso†, L. Calabretta, G. Gallo, G. Costa, A. Longhitano, D. Rifuggiato, A. Spartà, G. Torrisi, E. Zappalà, Istituto Nazionale di Fisica Nucleare –Laboratori Nazionali del Sud, Catania, Italy

Abstract

The K-800 superconducting cyclotron has been in operation at Laboratori Nazionali del Sud for almost 25 years. It has been subjected to continuous upgrades and modifications since 1994: the RF couplers have been redesigned, the new dees have been changed from aluminium to copper, as has the new central region from radial to axial injection of the beam, the hybrid configuration solid state - tube of the power amplifiers, the digital LLRF, etc. The next scheduled important upgrade of the Cyclotron mainly consists in a new extraction beam line able to support the increase of the beam current intensity. The accelerated beam will be extracted in two ways: by stripper and by electrostatic deflector and, consequently, one of the most important features of the new upgrade is the new cryostat. Further upgrades and refurbishments of the other main parts of the cyclotron, such as a new liner, the modification of the RF cavities and dees, the refurbishment of HLRF-LLRF, the insertion of the stripper extraction system, to name but a few, are in progress, too. This work focuses on the RF system upgrade.

INTRODUCTION

The LNS Superconducting cyclotron has been operating at LNS since 1995. The original design was thought up to produce beams for nuclear physic experiments in the range of a few dozen watts. In the initial configuration, the cyclotron was a booster of the 16 MV Tandem. The injection was radial and the Tandem and Cyclotron operated together as a coupled accelerator system. The introduction of the axial injection and the redesign of the central region means the cyclotron has been a stand-alone accelerator since 2000. The two accelerators, Tandem and Cyclotron, have been operating independently for the last 19 years. In the meanwhile, the cyclotron's good results with the axial injection were a sort of flywheel to develop, through the EXCYT project, the production of radioactive ion beams on a thick target with the ISOL technique [1]. However, the limitation, in terms of maximum output power (<150 Watts) of our extraction system due to some intrinsic constraints and efficiency around 50 - 60% of the electrostatic deflector (ED), became quite clear. Yet the strong interest, in terms of demand, for high intensive beams is still valid. A new important project, in fact, has requested this kind of beam. The project, called NUMEN (NUclear Matrix Elements for Neutrinoless double beta decay), proposes an innovative technique to measure the nuclear matrix that is of relevant interest for the double β decay without neutrino emission. This ambitious technique needs beams of $^{12}C^{4+}$ $^{18}O^{6+}$ $^{20}Ne^{4+}$ mainly, with a maximum beam current intensity of 10^{14} pps, which means a cyclotron beam power between 1 and 10 kW. This is more or less 10 - 100 times the present maximum beam power of 100 W. In any case, some preliminary experimental results, obtained at the INFN-LNS with the present version of the superconducting cyclotron, have provided an encouraging indication of the capability of the proposed technique to access relevant quantitative information for NUMEN [2]. Another facility, strongly interested in high intensive beams, using the inflight technique to produce RIBs is FRIBs@LNS (in Flight Radioactive Ion BeamS at LNS), already installed at LNS, allows one to carry out nuclear physics experiments investigating the properties of short-lived nuclear species. The maximum power delivered with the upgraded Superconducting Cyclotron, suggests a specific study to design, a proper beam line with a new fragment separator, named FRAISE (FRAgment Inflight SEparator) too [3].

MAIN MODIFICATIONS

The main difference between the present configuration of the cyclotron and the future upgraded one, is the introduction of a second extraction technique by stripping. In this way the extraction efficiency is enough to achieve the high intensity requests. The new median plane of the cyclotron with both extraction channels, by stripper and through electrostatic deflector (E.D.), is shown in Fig. 1.

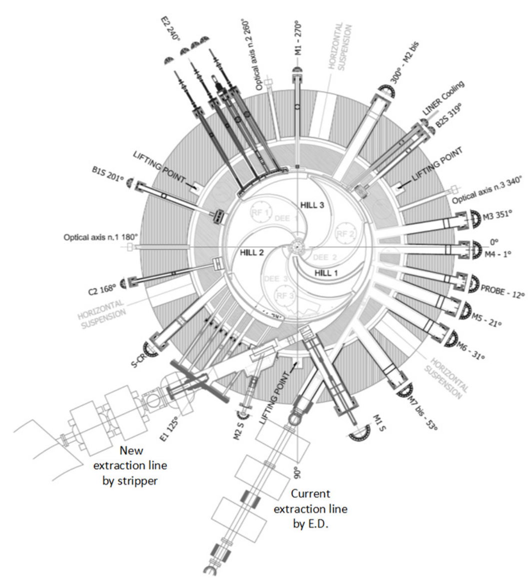

Figure 1: Median plane of the upgraded cyclotron.

* INFN-LNS
† caruso@lns.infn.it

ISBN: 978-3-95450-205-9 doi:10.18429/JACoW-Cyclotrons2019-WEA02

The extraction by stripper requires many parts of the cyclotron to be redesigned. A new hole/penetration along the median plane is necessary to introduce this new extraction channel. This means redesigning the magnet, cryostat and making some other modifications including the RF system. A detailed beam dynamic study has optimized the extraction trajectory of the stripped beams with the extraction trajectory by E.D. This perfect overlap trajectory allows for the interchanging of the two systems in the present ED position [4]. To reduce the interchanging phases, two sessions have been scheduled during the year: one for high intensive beams and the other for the beam extracted by E.D. [5].

RF SYSTEM UPGRADE

The upgrade of the cyclotron involves the RF system too. The most important reasons for changing something in the RF field are mostly related to the power and size of the stripped beam during the acceleration phase, inside the median plane and subsequently in the extraction channel. Two fronts are opened in the RF system to match the next stripper configuration goal of the cyclotron: one related to the new geometry of the median plane, the other related to the final dissipated power. These two reasons can also be seen as two opportunities to improve and refurbish the RF system in terms of mechanics, vacuum quality improvement, with new liner design and high/low level electronic.

Mechanic modifications

The present vertical distance between the upper and lower dees and inside the liner is 24 mm, not enough for all the future beams extracted with the stripper technique. An extra space of ± 3 mm in the vertical gap should be enough to allow for the acceleration of the high intensive beams and to also minimize the beam loss inside the acceleration chamber. To increase the distance between the acceleration electrodes, from 24 to 30 mm, a reduction of the upper and lower conical connection length between the dees and the inner coaxial of ±3 mm has to be made.

In Fig. 2 (ABC), a sequence shows how to increase the vertical gap through decreasing the conical connection length. The red arrows show the present conical length and vertical gap, in green the future (ones) length and gap. Particular attention, in terms of voltage and power dissipation, has to be paid to the main ceramic insulator area. A reduction in length between the connection of dee and stem increases the high voltage around the ceramic of the coaxial cavity. The high voltage ceramic insulator allows for the separation between air and vacuum inside the RF cavity. The position of the ceramic inside the magnet at 62 cm from the median plane of the cyclotron is enough for the sliding short to tune the cavity up to 50 MHz. The shape and the dimension of the ceramic are strongly influenced by this high frequency parameter and consequently the design was particularly critical. The ceramic inside the cavity is shown in Fig. 2D during a maintenance phase, the lower Dee was removed and the white ceramic between the inner and outer coaxial is visible. A detailed vertical cross section of the upper side cavity ceramic insulator is shown too, together with the copper conical Dee-Stem connection.

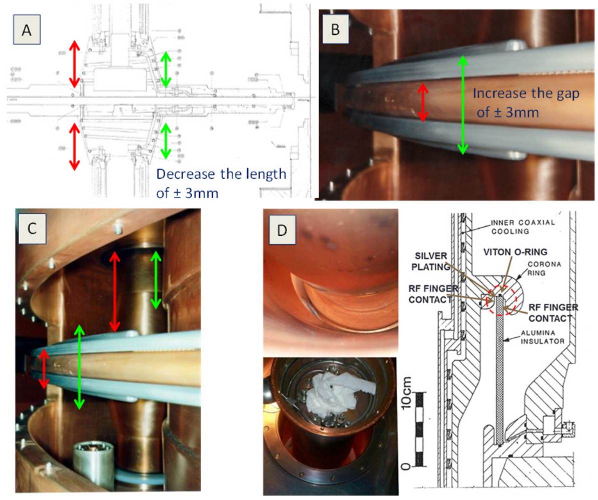

Figure 2: how to increase the gap between the dees.

At the maximum Dee voltage of 100 kV the insulator dissipation should not exceed 200 W [6]. All the geometry design around the insulator (pure alumina 99.7%) allows for safe mechanical and electrical working conditions. With these kind of constraints, even a modification of ±3mm can introduce limitations to the parameters of the cavity, such as bandwidth, power dissipation, voltage distributions, impedance matching, etc. For this reason, a detailed 3D numerical simulation of the modified RF cavity, using 3D commercial electromagnetic simulators, CST Microwave Studio [7] and COMSOL multiphysics [8] comparing them to significant experimental results, through network analyser measurements, has been done. The original frequency range of 15-48 MHz is achieved despite the reduction of ±3 mm. The voltage distribution, especially in the critical area, shown in Fig. 2D, around the main insulator, between the inner and the outer coaxial, near the antinode maximum dee voltage, is under the limit. The input impedance matching, through the coupling capacitor, is more or less within the present range of values [9]. The global RF cavity simulated model of the cyclotron is shown in Fig. 3.

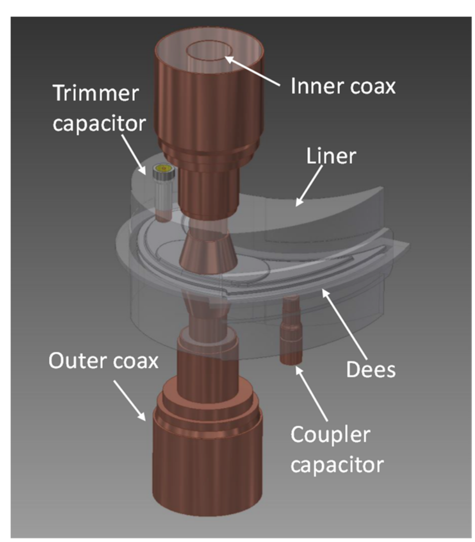

Figure 3: 3D model of RF cavity of the cyclotron.

ISBN: 978-3-95450-205-9 doi:10.18429/JACoW-Cyclotrons2019-WEA02

The dees, the inner/outer coaxial, the trimmer and the coupler capacitors have been included in the software simulations. Another important modification, to increase the vertical gap in the acceleration chamber, is related to the liner. The modification of the present one is not possible and a new liner has been redesigned. We are confident, using modern construction techniques, of reducing the present 14 mm thickness of 3 mm and of greatly minimizing the welding points too, in order to prevent leaks in the acceleration vacuum chamber. The current vacuum liner level of 1 mbar with a pumping system of 300 m^3/h is nowhere near the value of 10^{-1} mbar with a pumping system of 30 m^3/h, of only 4 - 5 years ago. This is another important reason to replace the upper and lower liner of the cyclotron in Fig. 4.

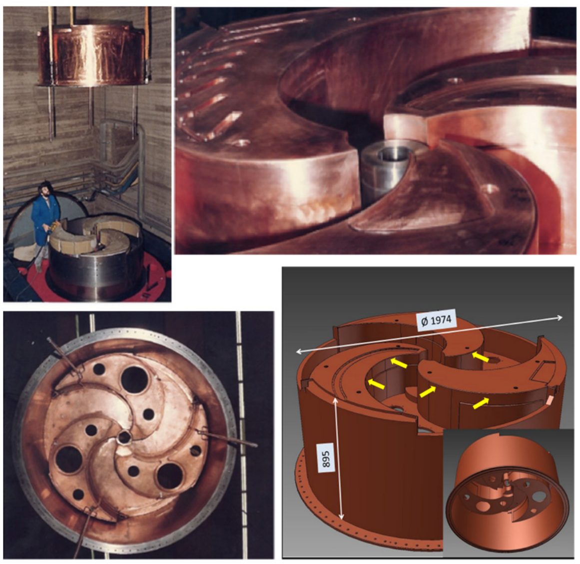

Figure 4: Liner assembling phases, about 30 years ago, the yellow arrows show the possible vacuum leakages in the welding points between vertical and horizontal wall.

Electronic modifications

An important refurbishment of the main power amplifiers has been completed recently. The insertion of a solid state amplifier (SSA) has substituted the obsolete first stage of the full tube RF power amplifier as shown in Fig. 5. All the 3 power amplifiers of the RF system are equipped with this solid state driver configuration plus a matching box to adapt the standard 50 Ω output of the 1st SSA stage with the final stage of the tube amplifier, as Fig. 6 shows. The main reason to transform the full tube amplifier to a hybrid tube-SSA configuration was the end of production of the first stage tube, a Thales RS1054. We were obliged in changing the 1st stage and we adopted a new technology according to the trend of the power telecommunication devices in the range of power and frequency of our interest: 15 - 50 MHz, 1 - 50 kW [10]. The beams produced by the present cyclotron need an RF power below 30 kW CW. To reduce the power consumption and to increase the life of the tetrodes, the original final power of 75 kW was adapted to the more relaxed output power of 20-30 kW. With the cyclotron upgrade, the final power of the extracted beam between 1 and10 kW needs about 30% more of the current RF Dee voltage.

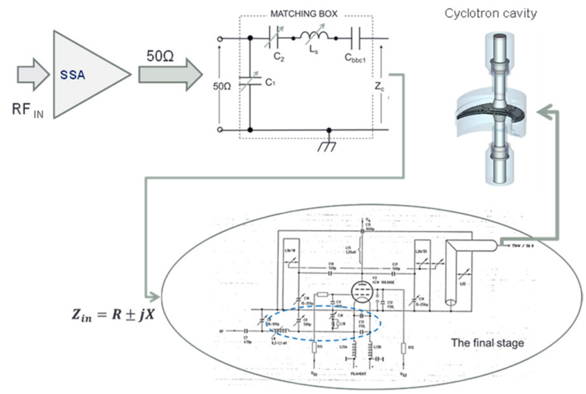

Figure 5: Block diagram of the refurbished amplifier.

It means a new optimization of the amplifier parameter to increase the power up to 40-50 kW. Some preliminary studies are in progress and we are confident to adopt soon the proper modifications to increase the final power.

The LLRF is following the same refurbishment and upgrade trend [11]. The migration from the platform Visual Basic to LabView is on the way, the complete substitution of old and obsolete part of the hardware is in progress, a new automatic tool of phase and amplitude adjustment in order to maximize the output beams is under developing. All the LLRF is made in house, mostly of the HLRF too. The LLRF working in progress between old analog equipment and new digital platforms are shown in Fig. 6.

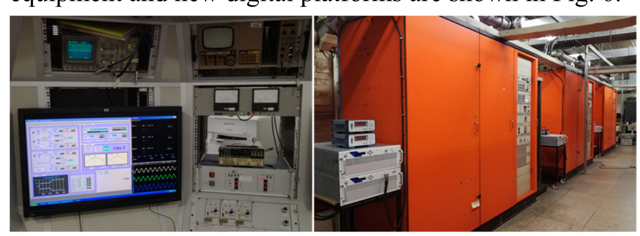

Figure 6: LLRF working in progress and HLRF.

CONCLUSION

The developing of the RF system related to the cyclotron upgrade is already planned and most of the points are on the way. Since the expected time to dismount and to assemble the cyclotron is about 18 months, we expect the restart the RF system and the cyclotron in two years.

REFERENCES

[1] L. Calabretta, A. Calanna, G. Cuttone, G. D'Agostino, D. Rifuggiato, and A. D. Russo, "Upgrade of the LNS superconducting cyclotron for beam power higher than 2-5 kW", in *Proc. 21th Int. Conf. on Cyclotrons and their Applications (Cyclotrons'16)*, Zurich, Switzerland, Sep. 2016, pp. 7-10. doi:10.18429/JACoW-Cyclotrons2016-MOA02

[2] F. Cappuzzello *et al.*, "The NUMEN project: Nuclear matrix elements for neutrinoless double beta decay", *Eur. Phys. J. A.*, vol. 54, no. 5, art. no. 72, May 2018. doi:10.1140/epja/i2018-12509-3

ISBN: 978-3-95450-205-9 doi:10.18429/JACoW-Cyclotrons2019-WEA02

[3] P. Russotto *et al.*, "Status and perspectives of the INFN-LNS in-flight fragment separator", *J. Phys. Conf. Ser.*, vol. 1014, p. 012016, 2018. doi:10.1088/1742-6596/1014/1/012016

[4] G. D'Agostino, L. Calabretta, A. Calanna, and D. Rifuggiato, "Extraction by Stripping in the IFNS-LNS superconducting cyclotron: Study of the extraction trajectories", in *Proc. 21th Int. Conf. on Cyclotrons and their Applications (Cyclotrons'16)*, Zurich, Switzerland, Sep. 2016, pp. 160-163. doi:10.18429/JACoW-Cyclotrons2016-TUC03

[5] G. Gallo *et al.*, "Mechanical modifications of the median plane for the superconducting cyclotron upgrade", in Proc. 22th Int. Conf. on Cyclotrons and their Applications (Cyclotrons'19), Cape Town, South Africa, Sep. 2019, MOP013, this conference.

[6] A. Caruso, "The RF system of the k-800 superconducting cyclotron at INFN-LNS", in *Proc. InPAC'13*, Calcutta, India, Nov. 2013, paper IT-15.

[7] CST microwave studio, www.cst.com

[8] *Comsol Multiphysics Reference Manual*, version 5.3, www.comsol.com

[9] G. Torrisi *et al.*, "3D Radio frequency simulation of the LNS superconducting cyclotron", in Proc. 22th Int. Conf. on Cyclotrons and their Applications (Cyclotrons'19), Cape Town, South Africa, Sep. 2019, FRB03, this conference.

[10] A. Caruso, F. Caruso, A. Longhitano, A. Spartà, G. Primadei, and J. Sura, "Hybrid configuration, solid state-tube, revamps an obsolete tube amplifier for the INFB K-800 superconducting cyclotron", in *Proc. 21th Int. Conf. on Cyclotrons and their Applications (Cyclotrons'16)*, Zurich, Switzerland, Sep. 2016, pp. 263-266. doi:10.18429/JACoW-Cyclotrons2016-WEB02

[11] A. Caruso, F. Consoli, A. Longhitano, A. Spartà, and L. Xia, "New PC-based control for the RF system at INFN/LNS", in *Proc. 12th Int. Conf. on Accelerator and Large Experimental Control Systems (ICALEPCS'09)*, Kobe, Japan, Oct. 2009, paper THP040, pp. 744-746.

ISBN: 978-3-95450-205-9 doi:10.18429/JACoW-Cyclotrons2019-WEB01

STATUS OF FFAS (MODELLING AND EXISTING/PLANNED MACHINES)

J.-B. Lagrange*, D. Kelliher, S. Machida, C. Prior, C. Rogers, ISIS/RAL/STFC, UK

Abstract

Since their rebirth two decades ago, great progress has been made in Fixed Field alternating gradient Accelerator (FFA) design, with different optical concepts and technological developments. Several machines have been built, and others are planned. The talk will review the recent progress around the world.

INTRODUCTION

A Fixed Field alternating gradient Accelerator (FFA) is defined as a circular particle accelerator, with a static guide field, like cyclotrons, and focusing and defocusing elements alternated to provide a strong focusing similar to modern synchrotrons. This principle is not new and came shortly after the discovery of the alternating gradient focusing [1] in the 1950s, in Japan [2], in USSR [3] and USA [4, 5], independently. Electron models were built shortly after its discovery by the Midwestern Universities Research Association (MURA) group [6–8] in the USA, but after it closed in 1967, FFA development was paused for about 40 years. If cyclotrons benefitted from the spiral geometry developed with FFAs [4,5], pulsed synchrotrons, more suitable to reach the energy frontier, were favoured over FFAs for high energy physics. However, the importance of the beam power over the final energy has been growing recently, since intense sources of secondary particles from high-power proton beams are now a priority in several fields. An FFA would be a good candidate for such proton drivers since it can indeed reach relativistic energies, contrary to cyclotrons, and fixed field gives the possibility for higher repetition rates and at a more energy efficient operation than in Rapid Cycling Synchrotrons (RCS).

Since the rebirth of the FFAs twenty years ago, several machines have been designed and built in Japan [9–13], and in the UK [14], with several of them still in activity, like the ADS complex [15] and the MERIT experiment [16] at Kyoto University and the 150-MeV ring at Kyushu University [17]. Several machines are planned for the near future or being commissioned at the moment. At CERN, the nuSTORM project aims to study neutrino interactions with a muon-decay racetrack ring composed of FFA magnets [18]. In the USA, to demonstrate the feasibility of the use of FFA arcs in the eRHIC project [19], the Cornell-BNL Energy recovery linac Test Accelerator (CBETA) is under commissioning [20, 21]. In the UK, a major upgrade of the ISIS synchrotron is currently under study [22] and the FFA option is under consideration. A test ring is planned at RAL to demonstrate the capability of the FFA to deliver a high-power and short pulse proton beam for spallation neutrons [23].

Several simulation codes are now available to model FFAs. Since the beam orbit in an FFA moves spatially with momentum, synchrotron simulation codes, which assume a central orbit independent of momentum, are unsuitable for studying FFAs. However, cyclotron codes and more generally static field codes including OPAL [24], Zgoubi [25], SCODE, MUON1 and FIXFIELD among others are now used to design FFAs. The first three integrate space charge to study high intensity effects.

FFAs are usually designed with an increasing radius, but excursion can be also done in the vertical direction. It has been first proposed in 1955 [27] as an "electron cyclotron". It has been rediscovered recently [28]. Vertical FFA (vFFA) could be an asset when it comes to accelerate ultra-relativistic particles, because of its quasi-isochronicity. This arrangement has several other advantages. First, it results in an orbit radius independent of momentum, like synchrotrons. Second, the horizontal dispersion function and the momentum compaction factor are zero, with infinite transition energy. Third, the scaling property is separated from the geometrical arrangement of the lattice footprint. In principle, the ring could have any shape and it would still be possible to maintain a scaling property as long as the vertical magnetic field satisfies the design shape of scaling magnets. Finally, a rectangular shape for the main magnets and the coil geometry is simpler compared to the spiral magnet of horizontal FFA.

This paper will present the new concepts in terms of lattice first for the horizontal excursion FFA, and then for the vertical excursion FFA.

HORIZONTAL EXCURSION FFA

DF Spiral

To keep the linearised transverse motion equations independent of momentum, the vertical component in the horizontal mid-plane of the magnetic field B_z varies with radius r according to the so-called scaling law, following

$$B_z = B_0 \left(\frac{r}{r_0}\right)^k \mathcal{F}\left(\theta - \ln\frac{r}{r_0}\tan\zeta\right), \tag{1}$$

with k the constant geometrical field index, r_0 the reference radius r_0, B_0 the field at that radius, ζ the constant logarithmic spiral angle and $\mathcal{F}$ an arbitrary fringe field fall-off function.

There are two types of zero-chromatic horizontal FFA, the radial type (case where $\zeta = 0$) and the spiral type. In the radial sector FFA, the alternating gradient is achieved with reverse bend magnets, while designing a lattice with logarithmic spiral FFA magnets gives a constant edge focussing independent of the beam momentum. Spiral FFAs thus have a smaller circumference than radial sector FFAs,

* jean-baptiste.lagrange@stfc.ac.uk

ISBN: 978-3-95450-205-9 doi:10.18429/JACoW-Cyclotrons2019-WEB01

but the possibility of adjusting focussing in the transverse plane is very limited. The field gradient of the main magnets could be changed if pole-face winding coils are used. However, this would only allow adjustment of the transverse tune in a very confined range, which could be a problem for the initial commissioning, especially for high current proton accelerators where the tune depends on the beam current.

A DF spiral lattice, which features normal and reverse bending magnets with a spiral edge angle, is a compromise between machine circumference size and tune flexibility [26]. In the same way, this method could be used in cyclotrons to offer better control over dynamics and would be useful in high-intensity machines. The number of cells is chosen as a multiple of 5 to give the largest resonance-free space between an integer and a quarter integer. A systematic 5th order resonance indeed coincides with an integer when the periodicity of the lattice is a multiple of 5, while space charge driven resonances at a quarter integer prohibit an operating tune just above a quarter integer. Almost equal horizontal and vertical tunes are chosen because it is the empirical best operating point of the most recently built high current accelerators, e.g. SNS and J-PARC. Parameters of an example of such a lattice is given Table 1, designed for ISIS-II.

Table 1: Parameters of DF Spiral 1.2 GeV FFA

Parameter	Value
Kinetic energy	0.4 - 1.2 GeV
Reference radius	24 m
Number of cells	25
Packing factor	0.35
Straight section	3.58 m
Spiral angle	62 deg
k-index	20.6
Ratio Bd/Bf strength	-0.443
Orbit excursion	0.8 m
Cell tune (H, V)	(0.2073, 0.2098)
Ring tune (H, V)	(5.18, 5.24)
Transition gamma	4.6

Figure 1 shows the top view of the DF spiral lattice. Figure 2 shows the vertical magnetic field strength along the closed orbit and the beta function at the extraction momentum.

Tilted Sector FFA

The main problem of the spiral geometry is the difficulty to manufacture the main magnets, especially for a superconducting design. It is also a challenge to incorporate square shape elements in drift sections, like cavities. A tilted sector type of magnet would be an advantage to solve these issues, while keeping edge focusing and thus vertical stability for high energy machines. A scheme of such a machine is presented in Fig. 3. However, a numerical solution of the field is necessary to control the tune with such a technique, since analytical solution is not available in this case.

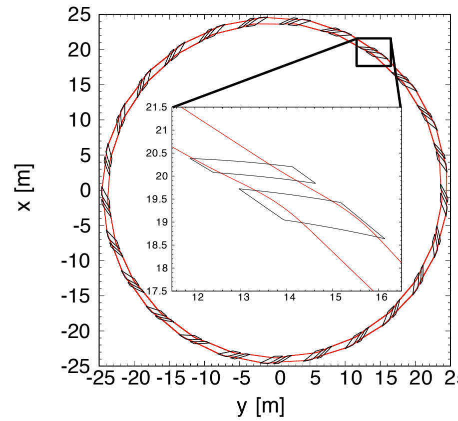

Figure 1: Spiral FFA ISIS upgrade lattice with 25 cells with closed orbits of injection and extraction momenta.

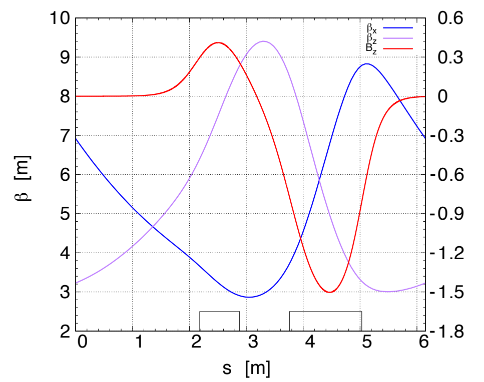

Figure 2: Vertical magnetic field on the median plane and beta functions of the DF spiral cell at extraction energy (1.2 GeV).

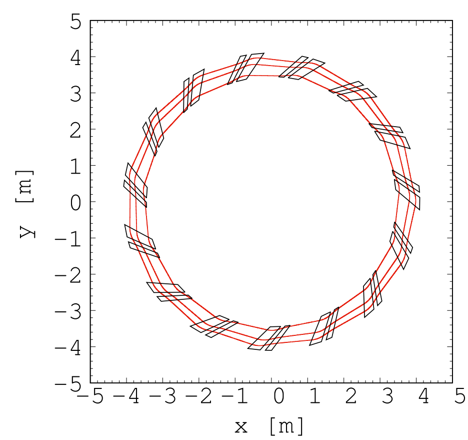

Figure 3: Scheme of a tilted sector FFA solution.

VERTICAL EXCURSION FFA

Simulation

In a vFFA, the particle motions in horizontal and vertical planes are no longer independent, making numerical simulation necessary to study beam dynamics in such machines. There is no established code designed to model vFFA, so extensive effort is under way to develop such codes. The

ISBN: 978-3-95450-205-9 doi:10.18429/JACoW-Cyclotrons2019-WEB01

field used in the simulation code is expanded in Cartesian coordinates (h, v, l) in terms of polynomial in the horizontal direction h from the ideal mid-plane field (the mid-plane for a vFFA is a zero-displaced plane in the horizontal direction) so that the fields satisfy Maxwell's equations. In this case, the zero-chromaticity condition can be obtained with an exponential increase of the magnetic field in the vertical direction v. In the mid-plane $h = h_0$, the field is then defined as

$$\begin{cases} B_{h0}(h_0, v, l) = 0 \\ B_{v0}(h_0, v, l) = B_0 e^{m(v-v_0)} \mathscr{F}(l) \\ B_{l0}(h_0, v, l) = \dfrac{B_0}{m} e^{m(v-v_0)} \mathscr{F}'(l) \end{cases}, \tag{2}$$

with m the constant normalised field gradient, $\mathscr{F}$ an arbitrary fringe field fall-off function. It is worth noticing that the parameters of the magnet for its design include both vertical and longitudinal components in the mid-plane.

Parameters of the test ring lattice planned to study the feasibility for ISIS-II presented above are presented in Table 2. Figure 4 shows the top and side view of the vFFA test ring cell. Figure 5 shows the magnetic field components along the orbit at the extraction momentum.

Table 2: Parameters of Test Ring vFFA

Parameter	**Value**
Kinetic energy	3 - 12 MeV
Reference radius	3.9789 m
Number of cells	10
Packing factor	0.32
Straight section	1.0 m (long), 0.5 m (short)
m-index	1.6 m^{-1}
Ratio Bd/Bf strength	-0.47
Orbit excursion	0.4 m
Cell tune (H, V)	(0.19, 0.16)
Transition gamma	infinite

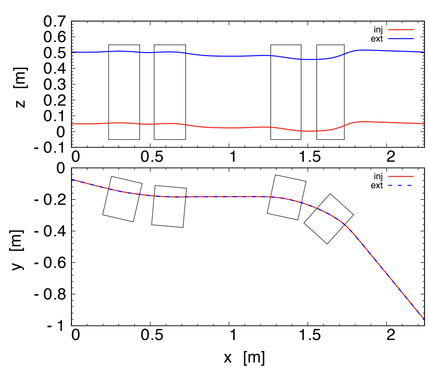

Figure 4: vFFA test ring cell from the side (top part) and from the top (bottom part).

SUMMARY

The contribution of FFAs to cyclotrons has been tremendous over the years, with the spiral geometry to increase

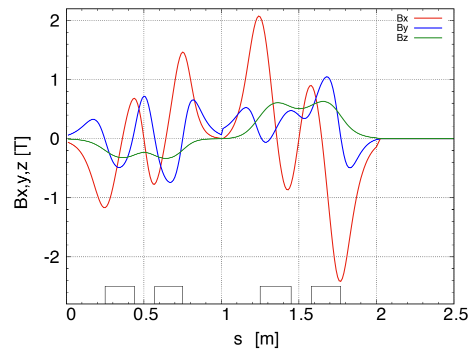

Figure 5: Magnetic field components on the closed orbit in the vFFA test ring cell at extraction momentum.

vertical stability, the addition of negative bend to increase control over dynamics, and the vertical excursion to have an isochronous machine for relativistic particles.

REFERENCES

[1] E. D. Courant, M. S. Livingston, and H. S. Snyder, "The strong-focusing synchroton: a new high energy accelerator", *Phys. Rev.*, vol. 88, no. 5, pp. 1190–1196, 1952. doi:10.1103/PhysRev.88.1190

[2] T. Ohkawa, in: Symposium on Nuclear Physics of the Physics Society of Japan, 1953.

[3] A.A. Kolomensky, V.A. Petukhov, and M.S. Rabinovich, "Some problems in the theory of cyclic accelerators", Academy of Sciences of the USSR, Moscow, 1955, p. 7.

[4] K. R. Symon, D. W. Kerst, L. W. Jones, L. J. Laslett, K. M. Terwilliger, "Fixed-field alternating-gradient particle accelerators", *Phys. Rev.*, vol. 103, no. 6, pp. 1837–1859, 1956. doi:10.1103/PhysRev.103.1837

[5] F. T. Cole, "O CAMELOT! A memoir of the MURA years", (section 6.1), 1 April 1994, reproduced in *Proc. 16th Int. Conf. on Cyclotrons and their Applications (Cyclotrons'01)*, East Lansing, MI, USA, May 2001, http://jacow.org/c01/cyc2001/extra/Cole.pdf

[6] F. T. Cole, R. O. Haxby, L. W. Jones, C. H. Pruett, and K. M. Terwilliger, "Electron model fixed field alternating gradient accelerator", *Rev. Sci. Instrum.*, vol. 28, no. 6, pp. 403–420, 1957. doi:10.1063/1.1715895

[7] D. W. Kerst *et al.*, "Fixed field alternating gradient accelerators with spirally ridged poles", *Phys. Rev.*, vol. 98, no. 4, p. 1153, May 1955, in: Minutes of the Meeting of the Division of Fluid Dynamics, Virginia, USA, Nov., 1954, p. 1153. doi:10.1103/PhysRev.98.1139

[8] D. W. Kerst *et al.*, "Electron model of a spiral sector accelerator", *Rev. Sci. Instrum.*, vol. 31, no. 10, 1076–1106, 1960. doi:10.1063/1.1716818

[9] M. Aiba *et al.*, "Development of a FFAG Proton Synchrotron", in *Proc. 7th European Particle Accelerator Conf. (EPAC'00)*, Vienna, Austria, Jun. 2000, paper MOP1B21, pp. 581–583.

[10] S, Machida *et al.*, "Commissioning of 150 MeV FFAG synchrotron", in *Proc. 9th European Particle Accelerator Conf. (EPAC'04)*, May 2004, paper THPLT066, pp. 2643–2645.

ISBN: 978-3-95450-205-9 doi:10.18429/JACoW-Cyclotrons2019-WEB01

[11] C. H. Pyeon *et al.*, "First injection of spallation neutrons generated by high-energy protons into the Kyoto University Critical Assembly", *J. Nucl. Sci. Tech.*, vol. 46, no. 12, pp. 1091–1093, 2009. doi:10.3327/jnst.46.1091

[12] Y. Mori, "Development of FFAG accelerators and their applications for intense secondary particle production", *Nucl. Instrum. Methods, Sect. A*, vol. 562, no. 2, pp. 591–595, 2006. doi:10.1016/j.nima.2006.02.044

[13] K. Yoshimura, "Prism overview", *Nucl. Instrum. Methods, Sect. A*, vol. 503, nos. 1–2, pp. 254–257, 2003. doi:10.1016/S0168-9002(03)00688-0

[14] S. Machida *et al.*, "Acceleration in the linear non-scaling fixed-field alternating-gradient accelerator EMMA", *Nature Phys.*, vol. 8, pp. 243–247, 2012. doi=10.1038/nphys2179

[15] Y. Ishi *et al.*, "Recent experimental results of the accelerator drive System with a sub-critical nuclear reactor (ADS) programme", in *Proc. 22nd Int. Conf. on Cyclotrons and their Applications (Cyclotrons'19)*, Cape Town, South Africa, Sep. 2019, paper MOA01, this conference.

[16] H. Okita *et al.*, "Beam optics study on FFA-MERIT Ring", in *Proc. 10th Int. Particle Accelerator Conf. (IPAC'19)*, Melbourne, Australia, May 2019, pp. 613–615. doi:10.18429/JACoW-IPAC2019-MOPRB019

[17] T. Fujinaka *et al.*, "Commissioning of FFAG accelerator at Kyushu University", in *Proc. 1st Int. Particle Accelerator Conf. (IPAC'10)*, Kyoto, Japan, May 2010, paper MOPEC038, pp. 543–545.

[18] J.-B. Lagrange *et al.*, "Racetrack FFAG muon decay ring for nuSTORM with triplet focusing", *J. Instrumentation*, vol. 13, no. 9, p. P09013, Sep. 2018. 10.1088/1748-0221/13/09/P09013

[19] C. Montag, "eRHIC - an electron-ion collider at BNL", in *Proc. 23rd Int. Spin Symposium (SPIN'18)*, Ferrara, Italy, Sep. 2018, *Proc. of Science*, vol. 346, p. 158, 2019. doi:10.22323/1.346.0158

[20] D. Trbojevic *et al.*, "CBETA - Cornell University Brookhaven National Laboratory Electron Energy Recovery Test Accelerator", in *Proc. 8th Int. Particle Accelerator Conf. (IPAC'17)*, Copenhagen, Denmark, May 2017, pp. 1285-1289. doi:10.18429/JACoW-IPAC2017-TUOCB3

[21] C. M. Gulliford *et al.*, "CBETA beam commissioning Results", in *Proc. 10th Int. Particle Accelerator Conf. (IPAC'19)*, Melbourne, Australia, May 2019, pp. 748–750. doi:10.18429/JACoW-IPAC2019-MOPRB076

[22] J. Thomason, www.isis.stfc.ac.uk/Pages/ISIS-II\%20Roadmap.pdf

[23] J.-B. Lagrange *et al.*, "Progress on design studies for the ISIS II Upgrade", in *Proc. 10th Int. Particle Accelerator Conf. (IPAC'19)*, Melbourne, Australia, May 2019, pp. 2075–2078. doi:10.18429/JACoW-IPAC2019-TUPTS068

[24] www.gitlab.psi.ch/OPAL/src/wikis/home

[25] F. Meot, "The ray-tracing code zgoubi", *Nucl. Instrum Methods, Sect. A*, vol. 427, pp. 353–356, 1999. doi:10.1016/S0168-9002(98)01508-3

[26] S. Machida, "Scaling fixed-field alternating-gradient accelerators with reverse bend and spiral edge angle", *Phys. Rev. Lett.*, vol. 119, p. 064802, 2017. doi:10.1103/PhysRevLett.119.064802

[27] T. Ohkawa, JPS meeting, 1955.

[28] S. Brooks, "Vertical orbit excursion fixed field alternating gradient accelerators", *Phys. Rev. Spec. Top. Accel. Beams*, vol. 16, p. 8, 2013. doi=10.1103/PhysRevSTAB.16.084001

22nd Int. Conf. on Cyclotrons and their Applications Cyclotrons2019, Cape Town, South Africa JACoW Publishing
ISBN: 978-3-95450-205-9 doi:10.18429/JACoW-Cyclotrons2019-WEB03

FACTORS INFLUENCING THE VORTEX EFFECT IN HIGH-INTENSITY CYCLOTRONS

C. Baumgarten*, Paul Scherrer Institut, 5232 Villigen PSI, Switzerland

Abstract

We discuss factors that have potential influence on the space charge induced vortex motion of particles within high intensity bunches (curling of bunches, Gordon 1969) in isochronous cyclotrons. The influence of the phase slip due to deviations from strict isochronism determines if the bunches of a specific turn are above, below or at "transition", and hence whether stable vortex motion of the bunches is possible at all. Secondly there are possible longitudinal and transverse effects of rf acceleration, the former depending on the bunch phase ("bunching" or "debunching"), the latter depending on the gradient of the accelerating voltage. High accelerating voltages in the first turns call the applicability of adiabatic approximations and analytic methods into question. The influence of the rf acceleration is expected to be significant only at low beam energy, i.e. should have small or even negligible effect beyond the central region of compact machines.

INTRODUCTION

Due to their operation principle, isochronous cyclotrons provide no longitudinal focusing of particles within a bunch. In case of high beam intensity, the natural expectation would be that the presence of the space charge force has a defocusing effect in all directions. However, as explained by Gordon and others [1–8], the space charge force combines with the cyclotron specific coupling between longitudinal and transverse motion thus leading to a parasitic effective longitudinal focusing. This effective focusing was confirmed by bunch shape measurements in the PSI Injector II cyclotron [6,9,10] and allows to operate this machine at high intensities without flattop resonators. The phase of the former flattop resonators has been reversed in order to increase the energy gain per turn.

Because of the inherent nonlinearity and complexity of the problem, a full analytical treatment has not been found to date. Here we refer to a linear approximation that has been suggested [7, 8] and used to understand the phenomenon in general. In Ref. [8] the linear model is used to develop a numerical code that allows to determine conditions for beam matching. This simple linear model effectively approximates the cyclotron by a constant focusing channel (CFC), and allows to derive some conclusions concerning the stability of the vortex effect. These conclusions have been compared with numerical studies using the particle-in-cell (PIC) code OPAL [11, 12]. The numerical simulations revealed that Gaussian beams which fulfill the linear matching conditions, are indeed (meta-) stable, but only under appropriate boundary conditions [8, 13]. Significant deviations from isochronism (strong phase excursions), for instance, are able to drive the beam out of the region of stability and may cause strong halo formation [13]. Here we present some results concerning effects of the acceleration voltage. These effects are expected to be important at low beam energy, i.e. during beam formation in the central region of the cyclotron.

CENTRAL REGION

A typical simplifying assumption used in previous studies is that of adiabatic acceleration, i.e. that the energy gain per turn (or per Dee gap) is small compared to the considered beam energy. This assumption is known to be questionable

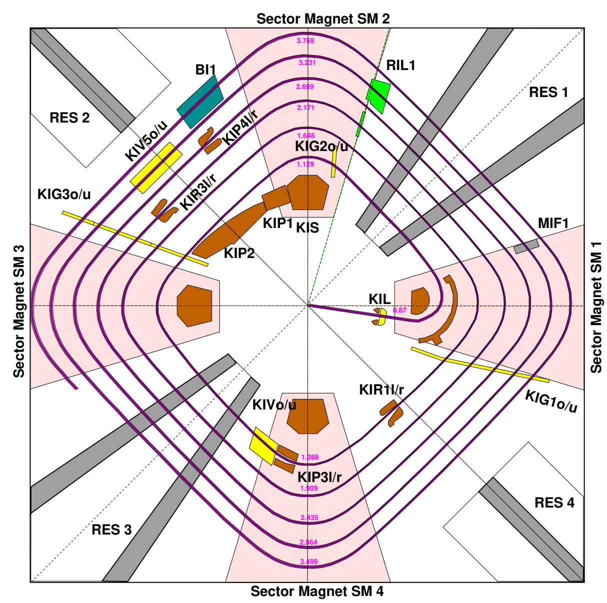

Figure 1: Layout of the central region of Injector 2.

in the first turns of Injector 2 (see Fig. 1): the DC beam of a Cockcroft-Walton preaccelerator passes a buncher before it is guided by an axial injection line towards the median plane. The injected beam energy is 870 keV, but the energy gain in the first resonator is of order ≈ 350 keV, and hence too large to safely presume adiabaticity.

We performed OPAL simulations of the acceleration of 2 mA beam for 3 different acceleration voltages with an initial distribution matched to a closed 1 MeV orbit in Injector 2. A too high accelerating voltage severely disturbs the vortex effect and leads to deformed bunches with increased halo formation as shown in Fig. 2. Figure 3 shows the number or particles versus distance from the bunch center and the corresponding integral. These results provide evidence that even in the case of well-matched beam injection, non-adiabatic acceleration causes halo formation and thus requires appro-

* christian.baumgarten@psi.ch

ISBN: 978-3-95450-205-9 doi:10.18429/JACoW-Cyclotrons2019-WEB03

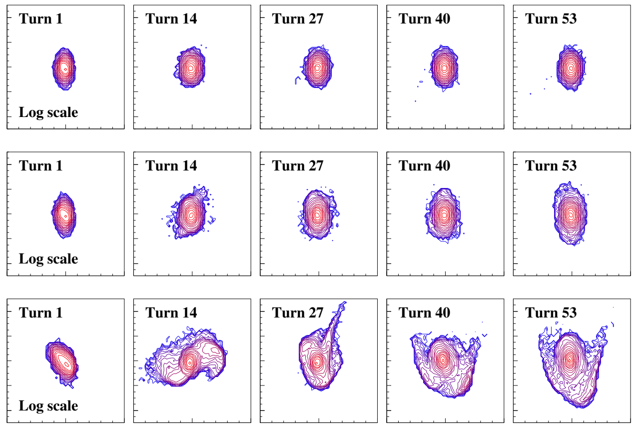

Figure 2: Top view contour lines (with logarithmic scale) of bunches with increasing turn number from left to right and (top to bottom) 25 %, 50 % and 100 % of nominal accelerating voltage, computed with OPAL.

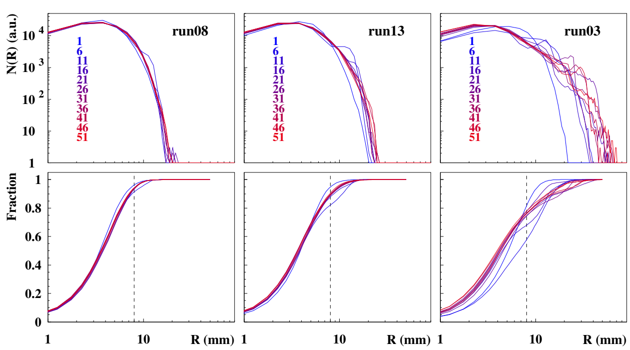

Figure 3: Radial distribution (top) and integral (bottom) for bunches with increasing turn number (blue to red). From left to right 25 %, 50 % and 100 % of nominal accelerating voltage, computed with OPAL. The dashed line is a guide to the eye.

priate beam collimation in order to achieve well separated turns and minimal extraction losses.

LINEAR MODEL

In order to discuss further disturbances due to acceleration and rf parameters, it is of advantage to review and extend the linear model developed in Ref. [8]. The effect of deviations from isochronism have been discussed in some detail in Ref. [8, 13] and are not considered here.

Since there are no linear terms that couple the longitudinal or transverse-horizontal motion to axial motion, the 6D problem can be split into a 2D treatment of axial and a 4D treatment of median plane motion. Let $\psi = (x, x', z, \delta)^T$ be the local median plane coordinates of a test particle relative to the reference orbit, then the linear terms of the CFC approximation $\psi' = \mathbf{F}\,\psi$ are given by the Hamiltonian matrix $\mathbf{F}$:

$$\mathbf{F} = \begin{pmatrix} \cdot & 1 & \cdot & \cdot \\ -k_x + K_x & \cdot & K_{grad} & h \\ -h & \cdot & \cdot & \frac{1}{\gamma^2} \\ K_{grad} & \cdot & K_z\,\gamma^2 + K_{rf} & \cdot \end{pmatrix} \tag{1}$$

where $h = 1/r$ is the inverse radius, $k_x \approx h^2\,\gamma^2$ is the horizontal focusing term and $\gamma = (1 - v^2/c^2)^{-1/2}$ is the relativistic factor. K_x and K_z are the transverse horizontal and longitudinal space charge terms, respectively, K_{rf} represents linear (de-) bunching and K_{grad} represents the linear terms of the radial rf voltage gradient [14]. The space charge terms are, assuming optimal isochronism [8, 13, 15]:

$$\begin{aligned} K_x &= \frac{K_3\,(1-f)}{(\sigma_x+\sigma_y)\,\sigma_x\,\sigma_z} \\ K_z &= \frac{K_3\,f}{\sigma_x\,\sigma_y\,\sigma_z} \\ K_3 &= \frac{3\,q\,I\,\lambda}{20\,\sqrt{5}\,\pi\,\varepsilon_0\,c\,E\,\gamma\,(\gamma+1)} \end{aligned} \tag{2}$$

where I is the beam current, $\lambda = c/\omega_{rf}$, E is the kinetic energy and f is the “ellipsoidal form factor” which we assume to be $f \approx 1/3$. The eigenvalues $\pm\,i\,\Omega$ and $\pm\,i\,\omega$ of $\mathbf{F}$ are (see Fig. 4) [16]:

$$\begin{aligned} \Omega &= \sqrt{a/2}\,\sqrt{1+\sqrt{1-\chi^2}} \\ \omega &= \sqrt{a/2}\,\sqrt{1-\sqrt{1-\chi^2}} \end{aligned} \tag{3}$$

where $\chi^2 = 4\,b/a^2$ with

$$\begin{aligned} a &\equiv -\mathrm{Tr}(\mathbf{F}^2)/2 = \Omega^2 + \omega^2 \\ b &\equiv \mathrm{Tr}(\mathbf{F}^2)^2/8 - \mathrm{Tr}(\mathbf{F}^4)/4 = \Omega^2\,\omega^2 \end{aligned} \tag{4}$$

In order to have stable motion, the eigenfrequencies must be real which yields the condition $\chi^2 > 0$, hence $b > 0$, and finally (assuming $\gamma \approx 1$ in the central region)

$$b\,\gamma^2 = K_x\,(K_{rf} + K_z) - K_{grad}^2 > 0 \tag{5}$$

For the terms K_{rf} and K_{grad} we obtain:

$$\begin{aligned} K_{rf} &= h^2\,\frac{\gamma\,N_h\,q\,V\,\sin\phi}{2\,\pi\,(\gamma+1)\,E} \\ K_{grad} &= h\,\frac{\gamma\,q\,V'(r)\,\cos\phi}{2\,\pi\,(\gamma+1)\,E} \end{aligned} \tag{6}$$

where N_h is the harmonic number of the rf voltage, $q\,V(r)$ the maximal energy gain and ϕ the phase between bunch and rf. $V'(r) = \frac{dV}{dr}$ is the radial voltage gradient.

OPERATION WITH (DE-) BUNCHING PHASE

The K_{rf} term represents possible (de-) bunching effects, if the machine is not operated at zero phase. If the bunch lags behind $\phi > 0$, then particles ahead of the bunch center have a higher energy gain than particles in the bunch tail. Therefore tracking at starting phases of $\phi = 90°$ ($\phi = -90°$) can be used to analyze the debunching (bunching) phase without actual acceleration.

ISBN: 978-3-95450-205-9 doi:10.18429/JACoW-Cyclotrons2019-WEB03

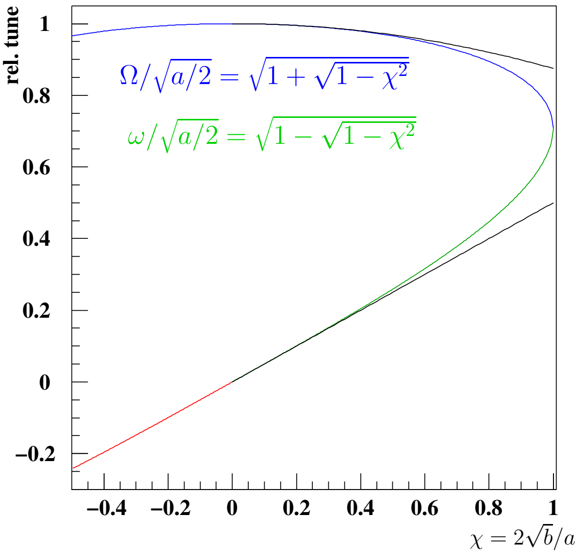

Figure 4: Horizontal and longitudinal tune in case of strong space charge.

For these cases, the linear model allows to compute the matching conditions for operation with a (de-) bunching phase. The results as shown in Fig. 5 indicate an increased (reduced) matched beam size for the debunching (bunching) phase. However, according to Eq. (5), the debunching phase

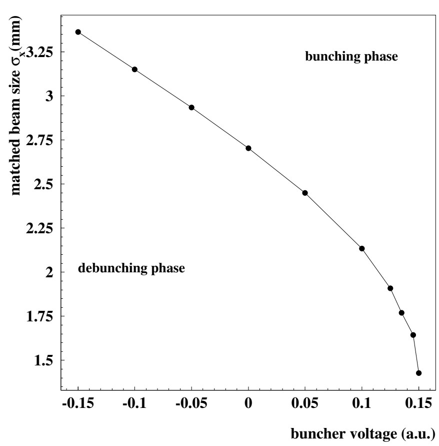

Figure 5: Matched horizontal bunch size σ_x versus buncher voltage for a 1 MeV beam coasting in Injector 2.

corresponds to $K_{rf} > 0$ and should theoretically provide a higher effective longitudinal tune and hence a better bunch stability. In order to test the expected effects with OPAL, we injected bunches at phases where no acceleration takes place, but (de-) bunching, that is, at $\phi = \pm 90°$. The model is confirmed by the plots in Figs. 6 and 7, which show that the bunching phase produces more halo, while the core stays more compact than in case of the debunching phase. Apparently the best compromize is to operate at $\phi \approx 0$ in order to avoid both, bunching and debunching effects.

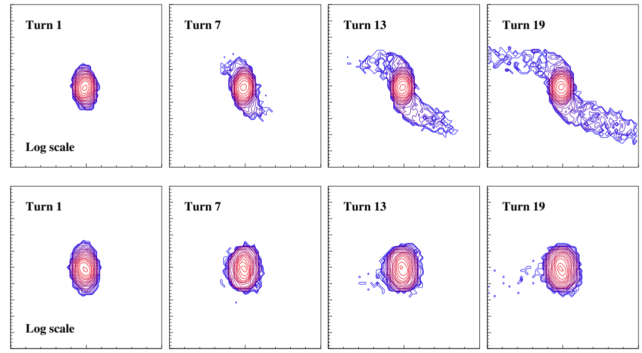

Figure 6: Top view contour lines (with logarithmic scale) of bunches with increasing turn number from left to right. Top: Bunching rf phase. Bottom: Debunching rf phase.

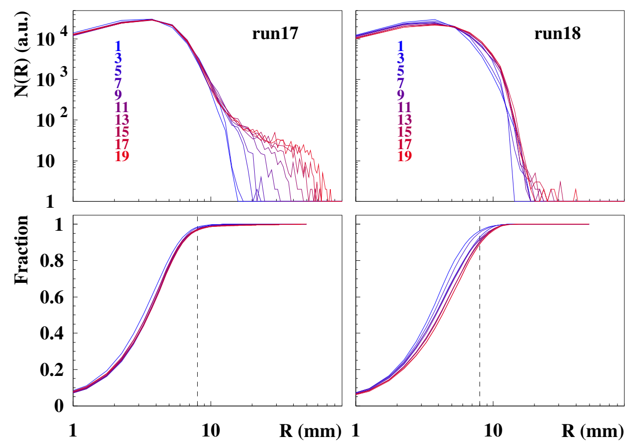

Figure 7: Radial distributions for bunching phase (left) and debunching phase (right).

STRONG VOLTAGE GRADIENTS

In order to investigate the influence of strong radial voltage gradients on the bunch, we generated a voltage profile with zero net voltage but significant voltage gradient at the bunch position. We then injected a matched bunch with (de-) accelerating phase $\phi = 0°$ ($\phi = 180°$), so that the bunch center "sees" no net voltage, but a positive (negative) voltage gradient. Figure 8 shows the resulting bunch form after some turns and Fig. 9 the corresponding radial distributions. The plots confirm that the presence of a voltage gradient reduces the bunch stability, especially in case of positive gradient. These results show that an attempt to circumvent the problem of adiabadicity by an rf design with a low starting voltage and high positive voltage gradient might result in new problems.

SUMMARY

We analyzed the possible effects of rf-acceleration on the vortex effect at low energy corresponding to the central region of a cyclotron with low injection energy as in case of the PSI Injector 2. OPAL simulations confirmed firstly that the matching condition sensitively depends on the assump-

ISBN: 978-3-95450-205-9 doi:10.18429/JACoW-Cyclotrons2019-WEB03

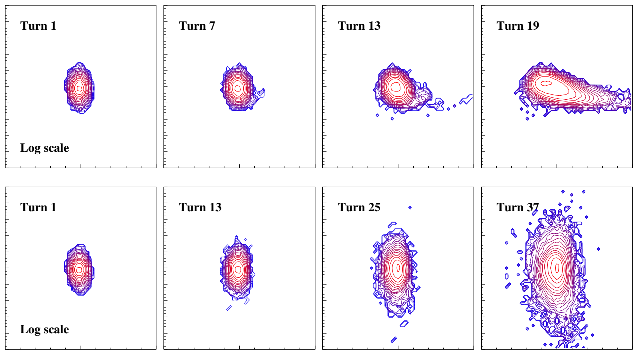

Figure 8: Radial distributions for positive (left) and negative (right) voltage gradient.

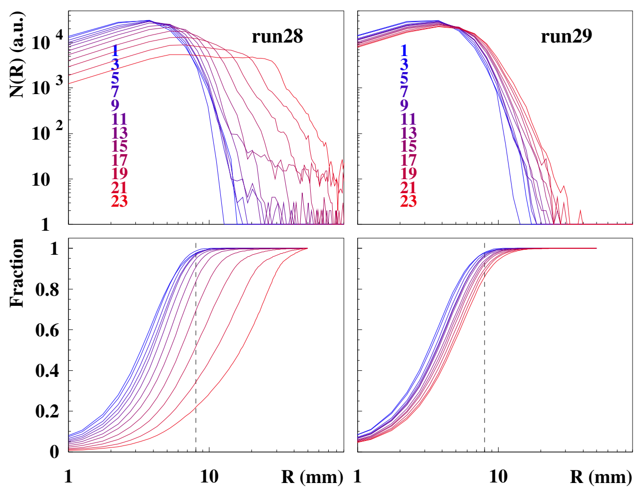

Figure 9: Radial distributions for positive (left) and negative (right) voltage gradient.

tion of adiabaticity. Secondly we found that (de-) bunching effects do not support the use of the vortex effect, i.e., do not significantly improve bunch stability. Finally we found that also strong voltage gradients have a potentially destructive effect on the vortex effect.

The latter effects can be avoided by an appropriate design of the rf system and/or by operation at the optimal phase $\phi = 0°$. The destructive effects of weak (de-) bunching or weak voltage gradients, respectively, become effective only after several turns. If the accelerating voltage is large, the beam will quickly achieve enough energy for these effects to be negligible.

To provide adiabaticity however, requires slow acceleration, i.e., a *small* accelerating voltage and is therefore in direct contradiction to the requirement of a low turn number and high turn separation. We conclude that – in case of electrostatic extraction – it is unavoidable to use an appropriate beam collimation system in the central region in support of proper beam formation and for the removal of beam halo. This of course requires sufficient energy gain and turn distance in order to place the collimators within the central region.

We believe that our results confirm the need for comprehensive numerical studies with suitable codes like OPAL in all cases where the use of the vortex effect is essential in order to achieve the design specifications of a high intensity cyclotron.

REFERENCES

[1] M. M. Gordon, "The longitudinal space charge effect and energy resolution", in *Proc. 5th Int. Cyclotron Conf. (Cyclotrons'69)*, Oxford, UK, Sep. 1969, pp. 305–317.

[2] A. Chabert, T. T. Luong, and M. Promé, "Separate sector cyclotrons beam dynamics", in *Proc. 7th Int. Conf. on Cyclotrons and their Applications (Cyclotrons'75)*, Zurich, Switzerland, Aug. 1975, *IEEE Trans. Nucl. Sci.*, vol. 22, no. 3, p. 1930, 1975.

[3] C. Chasman and A. J. Baltz, "Space charge effects in a heavy ion cyclotron", *Nucl. Instrum. Methods Phys. Res.*, vol. 219, pp. 279–283, Jan. 1984. doi:10.1016/0167-5087(84)90333-8

[4] S. Adam, "Calculation of space charge effects in isochronous cyclotrons", in *Proc. 1985 Particle Accelerator Conf. (PAC'85)*, Vancouver, BC, Canada, May 1995, *IEEE Trans. Nucl. Sci.*, vol. 32, no. 5, pp. 2507–2509, Oct. 1985. doi:10.1109/TNS.1985.4333962

[5] S. R. Koscielniak and S. Adam, "Simulation of space-charge dominated beam dynamics in an isochronous AVF cyclotron", in *Proc. 1993 Particle Accelerator Conf. (PAC'93)*, Washington, D. C., USA, May 1994, pp. 3639–3641.

[6] S. Adam, "Space charge effect in cyclotrons - from simulations to insights", in *Proc. 14th Int. Conf. on Cyclotrons and their Applications (Cyclotrons'95)*, Cape Town, South Africa, Oct. 1995, pp. 446–449.

[7] P. Bertrand and Ch. Ricaud, "Specific cyclotron correlations under space charge effects in the case of a spherical beam", in *Proc. 16th Int. Conf. on Cyclotrons and their Applications (Cyclotrons'01)*, East Lansing, MI, USA, May 2001, pp. 379–382.

[8] C. Baumgarten, "Transverse-longitudinal coupling by space charge in cyclotrons", *Phys. Rev. Spec. Top. Accel. Beams*, vol. 14, no. 11, p. 114201, 2011. doi:10.1103/PhysRevSTAB.14.114201

[9] R. Dölling, "Measurement of the time-structure of the 72 MeV proton beam in the PSI Injector-2 cyclotron", in *Proc. 5th European Workshop on Diagnostics and Beam Instrumentation (DIPAC'01)*, ESRF, Grenoble, France, paper PS05, pp. 111–113.

[10] R. Dölling, "Bunch-shape measurements at PSI's high-power cyclotrons and proton beam lines", in *Proc. 20th Int. Conf. on Cyclotrons and their Applications (Cyclotrons'13)*, Vancouver, BC, Canada, Sep. 2013, paper TU3PB01, pp. 257–261.

[11] J. J. Yang, A. Adelmann, M. Humbel, M. Seidel, and T. J. Zhang, "Beam dynamics in high intensity cyclotrons including neighboring bunch effects: Model, implementation, and application", *Phys. Rev. Spec. Top. Accel. Beams*, vol. 13, no. 6, p. 064201, 2010. doi:10.1103/PhysRevSTAB.13.064201

[12] Y. J. Bi, A. Adelmann, R. Dölling, M. Humbel, W. Joho, M. Seidel, and T. J. Zhang, "Towards quantitative simulations of high power proton cyclotrons", *Phys. Rev. Spec. Top. Accel.*

ISBN: 978-3-95450-205-9 doi:10.18429/JACoW-Cyclotrons2019-WEB03

Beams, vol. 14, no. 5, p. 054402, 2011. doi:10.1103/PhysRevSTAB.14.054402

[13] C. Baumgarten, "Transverse-longitudinal coupling by space charge in cyclotrons", in *Proc. 20th Int. Conf. on Cyclotrons and their Applications (Cyclotrons'13)*, Vancouver, BC, Canada, 2013, paper WE2PB03, pp. 315–319.

[14] R. W. Muller and R. Mahrt, "Phase compression and phase dialatation in the isochronous cyclotron", *Nucl. Instrum. Methods*, vol. 86, pp. 241-244, Sep. 1970.

[15] Frank Hinterberger, "Physik der Teilchenbeschleuniger" (in German), 2nd Ed., Springer, Heidelberg 2008.

[16] C. Baumgarten, "Analytic expressions for exponentials of specific Hamiltonian matrices", Feb. 2018 (version 3). arXiv:1703.02893

ISBN: 978-3-95450-205-9 doi:10.18429/JACoW-Cyclotrons2019-WEB04

BDSIM SIMULATION OF THE COMPLETE RADIONUCLIDE PRODUCTION BEAM LINE FROM BEAM SPLITTER TO TARGET STATION AT THE PSI CYCLOTRON FACILITY

H. Zhang†, R. Eichler, J. Grillenberger, W. Hirzel, S. Joray, D. C. Kiselev, N. P. van der Meulen, J. M. Schippers, J. Snuverink, R. Sobbia, A. Sommerhalder, Z. Talip
Paul Scherrer Institut, 5232 Villigen PSI, Switzerland
L. J. Nevay, John Adams Institute at Royal Holloway, University of London, Egham, UK

Abstract

The beam line for radionuclide production at the PSI Cyclotron Facility starts with an electrostatic beam splitter, which peels protons of a few tens of microamperes from the main beam around two milliamperes. The peeled beam is guided to a target station for the production of a variety of radionuclides. Beam Delivery Simulation (BDSIM), a Geant4 based simulation tool, enables the simulation of not only beam transportation through optics elements like dipoles and quadrupoles, but also particle passage through components like collimators and degraders. Furthermore, BDSIM facilitates user-built element with its accompanying electromagnetic field, which is essential for the modelling of the first element of the beam line, the beam splitter. With a model, including all elements from the beam splitter to the target, BDSIM simulation delivers a better description of the beam along the complete line, for example, beam profile, beam transmission, energy spectrum, as well as power deposit, which is of importance not only for present operation, but also for further development.

INTRODUCTION

The beam line for radionuclide production at the PSI Cyclotron Facility starts with an electrostatic beam splitter [1]. The splitter peels a beam of a few tens of microamperes from the main 72 MeV beam up to 2.4 mA intensity. The peeled beam gets a horizontal kick from the electrostatic field of the beam splitter, which creates a clearance more than 40 mm at the entrance of a septum magnet 3.395 m downstream. The peeled beam is then bent 17.5° away from the main beam, after passing the septum magnet, and is thereafter guided by the beam line to a target station for the production of a variety of radionuclides. The splitter is essential for the beam transportation. However, the splitter has so far been excluded from beam optics calculations, for example the envelope fit applying the program TRANSPORT [2]. The beam splitter is not a conventional beam transportation element. It is made of special materials, has a peculiar geometric form, and is accompanied with a 3D electrostatic field, while the beam transportation is correlated with all of these factors. It is therefore difficult to be defined by a conventional beam optics program, such as TRANSPORT or MADX.

Beam Delivery Simulation (BDSIM), a Geant4 based simulation tool, enables the simulation of not only beam transportation through optics elements like dipoles and quadrupoles, but also particle passage through components like collimators and degraders. Furthermore, BDSIM facilitates user-built elements in a wide range of geometrical forms and of practically any material. Importantly, an electromagnetic field can be attached to such a user-built element [3-5]. With a model, including all elements from the splitter to the target, BDSIM simulation delivers a better description of the beam along the complete line, for example, beam profiles at certain places, beam transmission through a degrader, power deposit on a component, as well as energy spectrum upon reaching the target. This is of importance not only for present operation, but also for further development.

SIMULATION

Electrostatic Field Analysis

The electrostatic field of the beam splitter is simulated with the program ANSYS. Figure 1 shows a quarter of the geometrical model of the splitter, as it is symmetrical about both horizontal and vertical middle planes. The septum consists of 117 tungsten strips 0.05 mm thick and 2 mm wide. The strips are tensioned onto a C-shaped structure with a 4-mm distance between the neighbouring strips, which gives a total length of 698 mm along the beam direction.

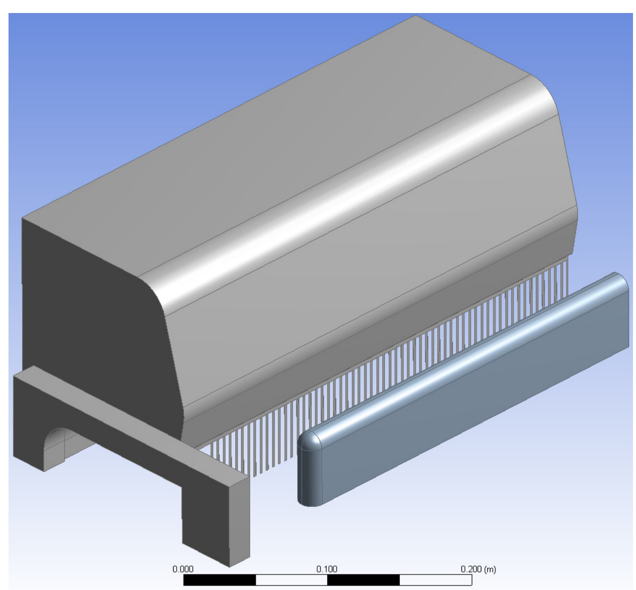

Figure 1: Geometrical model of beam splitter.

†hui.zhang@psi.ch

ISBN: 978-3-95450-205-9 doi:10.18429/JACoW-Cyclotrons2019-WEB04

The septum and the C-structure are grounded. The main beam passes through the field-free region inside the C-structure, a channel approximately 110 mm wide, 750 mm long, and 90 mm high. The cathode, 20 mm thick, 110 mm high, and 620 mm long, is placed 40 mm from the septum. A negative voltage of -105 kV is applied to the cathode. The peeled beam passes through the channel between the septum and the cathode and gets a kick towards the cathode. The cathode and the C-structure are protected by copper collimators. The electrostatic field analysis produces a 3D field map for BDSIM simulation. Figure 2 shows the electrostatic field on the horizontal middle plane. The field map is characterized with an approximately uniform field between the tungsten strips and the cathode, a fringe field at the entrance, and field fluctuation near the strips.

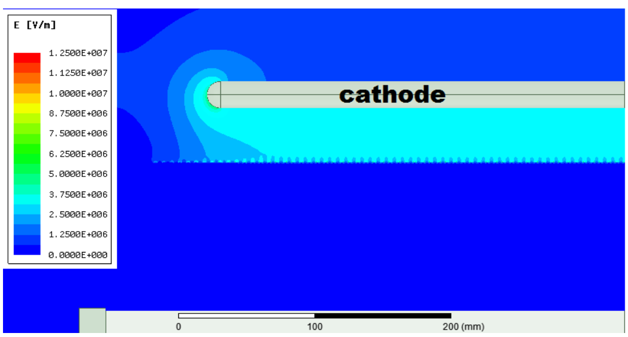

Figure 2: Electrostatic field on the horizontal middle plane.

Beam Line

Figure 3 shows the complete beam line from the beam splitter (left side) to the target (right side) for the BDSIM simulation. The specification for a dipole (in blue) or a quadrupole (in red) is similar to that of the program MADX. If necessary, yoke and coil may also be added. The collimator (in green) or the beam pipe is described by its aperture, length, and material.

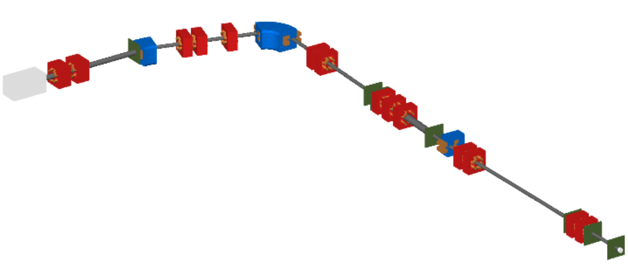
Figure 3: Complete beam line for BDSIM simulation.

For a special element like the beam splitter or the target assembly, the geometrical form and the material composition are specified with the Geometry Description Markup Language (GDML) [6]. For the target assembly, the shape and the material for each layer, e.g., Nb degrader or cooling water, are specified by a GDML file. The beam splitter is defined by the GDML file and the corresponding electrostatic field map. The beam line is then built up with each element lined in sequence.

BDSIM Simulation

The protons extracted from the Injector II cyclotron have energies around 72 MeV with a momentum spread of 0.1%. The beam is made wide and divergent in both directions when hitting the septum. The multiple Coulomb scattering inside the tungsten strips is the most interesting process. Nevertheless, a wide range of physics processes, including electromagnetic, hadronic and radioactive decay, are activated for the BDSIM simulation.

The septum is set to x=0, while the beam direction is parallel to the z-direction. The simulation starts at the entrance of the beam splitter. In consequence, the beam centroid has to be shifted to a negative position, x_0. The beam from the Injector II cyclotron is typically 1.8 mA in recent years, while the peeled beam is normally set to 50 µA. If the standard deviation of proton distribution along the x-axis is σ_x, x_0 is approximately $-1.9\sigma_x$.

BDSIM can generate a specified number of protons with (x, p_x, y, p_y, t, E) from a 6D sigma matrix with additional shifts for any components. The sigma matrix can be defined in the form of sigma*11*=64·mm·mm, sigma*12*=6·mm·mrad, and sigma*22*=0.64·mrad·mrad. Here sigm*ii* is the square of the standard deviation of the i^{th} component, whereas sigma*ij* represents the correlation between i^{th} and j^{th} components. The elements of the sigma matrix may be manually optimized so that the simulated beam size fits better with the measured one.

Protons can also be provided by an input file which specifies (x, p_x, y, p_y, t, E) for each proton. In this way, protons passing through the field-free region may be excluded from the simulation to save CPU time. Only protons hitting the septum and/or passing through the channel between the septum and the cathode will be tracked. As the peeled beam is typically 50 µA, while the main beam is typically around 1.8 mA, the simulation is, thus, more efficient.

RESULTS

Initially, two million protons are generated at the entrance of the vacuum chamber of the beam splitter, and then tracked along the beam line. Figure 4 (top, bottom) shows an x-p_x plot and a y-p_y plot, respectively, for all protons at the exit of the vacuum chamber, which is 0.206 m downstream from the last tungsten strip. The peeled beam gets a horizontal kick around 13.9 mrad. The peeled beam is no longer in an elliptical shape on the x-p_x plot. Most protons in the peeled beam are from the tip of the original x-p_x ellipse. In contrast, the elliptical shape on y-p_y phase space is almost undistorted.

Figure 5 (top) shows an x-y plot in front of the collimator of the septum magnet, which is 3.395 m downstream from the last tungsten strip. The beam is focused in the x-direction. A clearance around 45 mm is created, which is enough for the coil of the septum magnet. There are approximately 56000 protons in the peeled beam and 1.927 million protons in the main beam, respectively. In comparison, Fig. 5 (bottom) also shows an x-y plot, but only by tracking protons hitting the tungsten strips and/or passing through the channel between the septum and the cathode. Here, only

ISBN: 978-3-95450-205-9 doi:10.18429/JACoW-Cyclotrons2019-WEB04

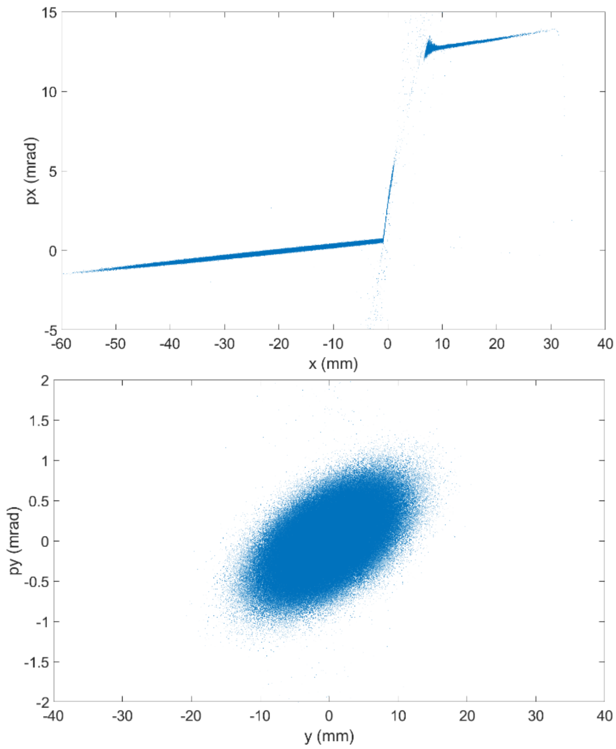

Figure 4 top: x-p_x plot, bottom: y-p_y plot at the exit of the vacuum chamber for the beam splitter.

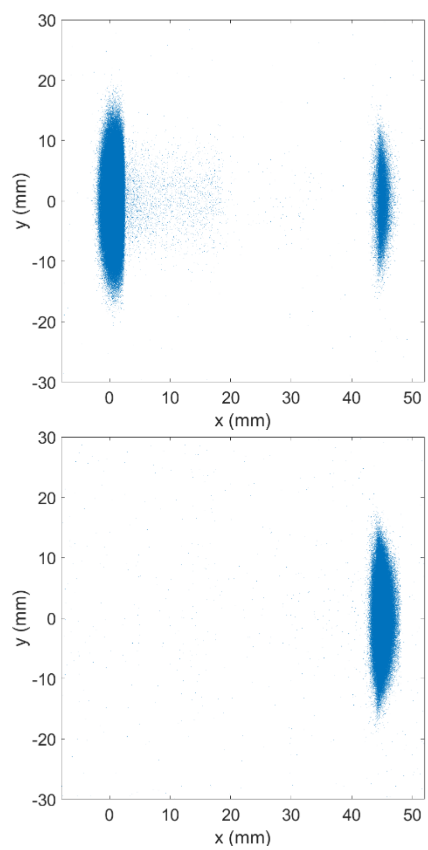

Figure 5: x-y plot for protons at the entrance collimator of the septum magnet. Top: all protons sampled from a 6D sigma matrix. Bottom: only protons hitting the tungsten strips and/or passing the channel between the strips and the cathode are tracked.

1.227 million protons are started. However, 1.113 million protons will pass through the collimator of the septum magnet. The simulation is, thus, far more efficient.

Figure 6 (top, bottom) shows the simulated horizontal and vertical beam profiles along with the measured ones at the location of the first and the last pairs of beam profile monitors, which is 6.771 m and 23.785 m downstream from the last tungsten strip, respectively. The horizontal profile is no longer symmetrical about its peak position and shows a longer tail on the left side.

Figure 7 shows a contour plot of the power deposited on-the vacuum window shortly before the target. The colour-bar indicates the power deposited in a 0.5×0.5 mm^2 area. The total power deposited in the 0.6 mm thick aluminium layer is around 63.28 W, while the beam power of 50 μA beam is 3.6 kW. Figure 8 shows the energy spectrum for the protons upon reaching the target after passing through cooling water and Nb degraders. The mean energy and the standard deviation are 16.35 MeV and 2.00 MeV, respectively, which is in agreement with an SRIM-2013 calculation [7].

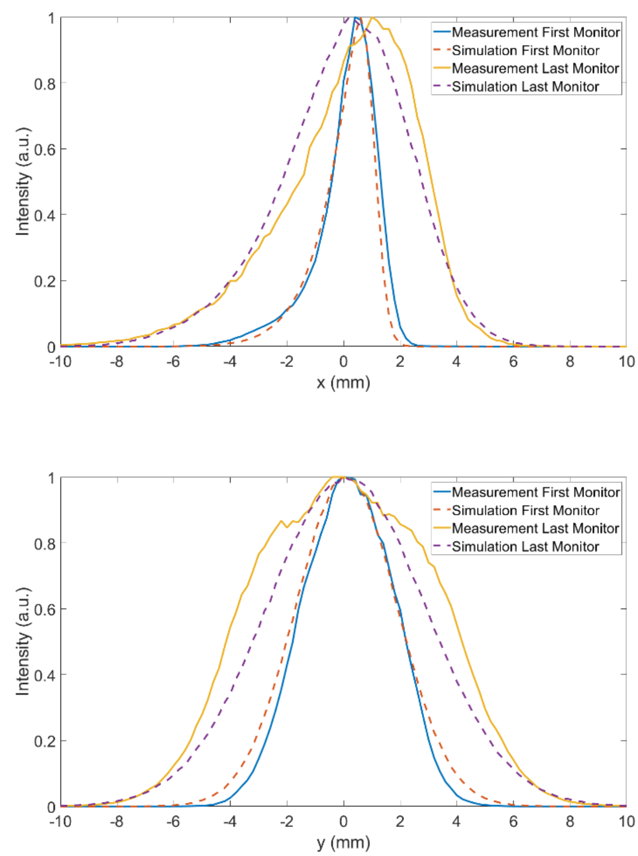

Figure 6: Measured and simulated beam profiles at the positions of the first and last pairs of beam profile monitors. Top: horizontal. Bottom: vertical.

ISBN: 978-3-95450-205-9 doi:10.18429/JACoW-Cyclotrons2019-WEB04

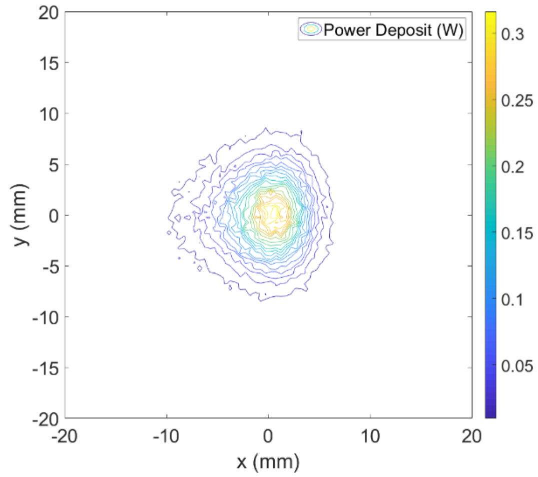

Figure 7: Power deposited on 0.6 mm thick aluminium vacuum window.

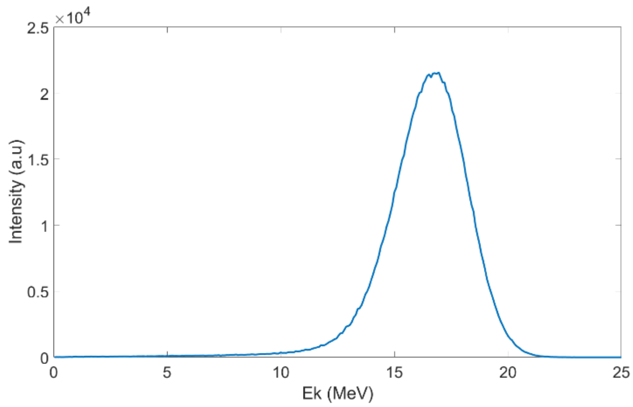

Figure 8: Energy spectrum upon reaching the target.

DISCUSSION

BDSIM simulation covers the complete beam line from the splitter to the target. The simulation predicts beam profiles at positions where beam profiles may also be measured. The beam size fits well with each other, especially in the vertical direction. The simulation also correctly predicts one-sided tails for horizontal profiles. Nevertheless, the simulated profiles deviate somewhat from the measured ones. The deviation arises from the following factors.

Firstly, it is a simplification to generate protons from a 6D sigma matrix. Although the beam profiles measured along the main beam line could be approximated with Gaussian peaks, many profiles differ significantly from Gaussian distribution. This indicates that it is rather an approximation to generate protons from a 6D sigma matrix for BDSIM simulation.

Secondly, for the simulation in horizontal direction the protons are not only scattered upon hitting the tungsten strips, but also kicked by the electrostatic field. The field is not uniform, but fluctuated, especially in the region near the strips. The strip has a special shape with extensions of 0.05 mm, 2 mm, and 90 mm in horizontal, longitudinal and vertical direction, respectively. However, the electrostatic analysis has to cover a volume with extensions of 566 mm, 1110 mm, and 360 mm in horizontal, longitudinal and vertical direction, respectively. The extremely thin strips make meshing difficult. The total number of elements reaches the computational limit, while the meshing around the thin edge is still not sufficiently refined. In consequence, the field near the thin edges is likely not as accurate as for other regions. Even if the field analysis could be significantly improved, it would still be difficult to create a field map to keep all details near the strips, especially near the thin edges. The field map created for present BDSIM simulation has steps of 0.05 mm, 2 mm and 5mm in horizontal, longitudinal, and vertical direction, respectively. The map is already large in size, but the field is still not accurate enough, for the region near the strips, in particular. Therefore, the proton passing nearby the strips is likely getting a different kick to an actual one.

Thirdly, several quadrupoles are specially constructed. For example, two quadrupoles directly after the beam splitter have a relatively larger aperture, specifically, an aperture 150 mm in diameter and 423 mm long. The fringe field effect can, thus, be no longer ignored, but has not yet been included in BDSIM simulation.

In summary, the improvement may come from all these three fronts, a better specification of the initial beam, an improved electrostatic field analysis and an optimized field map, and a better description of the quadrupoles with large apertures.

CONCLUSION

A model of the complete radionuclide production beam line is established for BDSIM simulation. The simulated beam profiles are comparable with the measured ones. The simulation also delivers power deposit on components of interest such as vacuum window and degrader. Energy spectrum of protons upon reaching the target may also be derived from the simulation. BDSIM simulation is, therefore, of importance not only for present operation but also for further development.

REFERENCES

[1] M. Olivo and H. W. Reist, “A beam splitter for the parasitic use of the 72 MeV proton beam line to produce isotopes”, in *Proc. EPAC’88*, Rome, Italy, Jun. 1988, pp. 1300-1302.

[2] J. Grillenberger, M. Seidel, and H. Zhang, “Beam optics considerations for isotope production on PSI cyclotron facility”, in *Proc. Cyclotrons’16*, Zurich, Switzerland, Sep. 2016, pp. 95-97. doi:10.18429/JACoW-Cyclotrons2016-MOP16

[3] BDSIM, http://www.pp.rhul.uk/bdsim/

[4] N. J. Nevay *et al.*, “BDSIM: An accelerator tracking code with particle-matter interactions”, Aug. 2018. arXiv:1808.10745

[5] S. Agostinelli *et al.*, “GEANT4—a simulation toolkit”, *Nucl. Instrum. Methods Phys. Res., Sect. A,* vol. 506, no. 3, pp. 250–303. doi:10.1016/S0168-9002(03)01368-8

[6] GDML, http://gdml.web.cern.ch/GDML/

[7] N. P. van der Meulen *et al.*, “The use of PSI’s IP2 beam line towards exotic radionuclide development and its application towards proof-of-principle preclinical and clinical studies”, presented at Cyclotrons’19, Sep. 2019, Cape Town, South Africa, paper TUA03, this conference.

ISBN: 978-3-95450-205-9 doi:10.18429/JACoW-Cyclotrons2019-WEC01

CONCEPTUAL DESIGN OF CENTRAL REGION FOR HIGH-TEMPERATURE SUPERCONDUCTING SKELETON CYCLOTRON (HTS-SC)

H. W. Koay†, M. Fukuda, H. Kanda, M. Nakao, T. Yorita
Research Centre for Nuclear Physics (RCNP), Osaka University, Japan

Abstract

A compact high-current accelerator is highly desirable for short and effective Boron Neutron Capture Therapy (BNCT) as well as radioisotopes production in a hospital environment. In accordance with this, a compact high-temperature superconducting skeleton cyclotron (HTS-SC) was proposed. HTS-SC is an air-core K-80 cyclotron with a relatively small extraction radius of 40 cm for a 50 MeV H^+ and 40 MeV D^+ beam. Owing to its compactness, a relatively high central magnetic field (>2.4 T) remains as a significant challenge for high current injection. This work describes a preliminary study of the injection using a spiral inflector and the central region design of the HTS-SC. Besides, the transverse beam dynamics are also discussed in order to investigate the upper limit of injection current.

INTRODUCTION

Since the first cyclotron developed by E.O. Lawrence and M. S. Livingston [1], it has been widely applied in various scientific researches and applications. In accordance with the advancement of high-temperature superconducting (HTS) tapes since these decades, the performance of a HTS cyclotron had also improved greatly to be more compact and efficient in producing high-energy or high-intensity beam with a lower power consumption. Following this trend, many works around the world have adopted HTS cyclotrons in various medical applications. However, most of them are relatively bulkier and of low-intensity (<100 μA), as they are mostly used to produce radioisotopes [2, 3]. In order to improve the versatility of HTS cyclotrons for direct therapeutic applications such as particle therapy or BNCT, beams of higher intensity are necessary. Therefore, this work wishes to propose a HTS skeleton cyclotron (HTS-SC) to produce a high-intensity beam for the previously proposed accelerator-based multi-port BNCT (AB-mBNCT) system, which can deliver multiple treatments at the same time [4], as well as the production of medical radioisotopes. Figure 1 shows the schematic of the applications of HTS-SC.

The proposed HTS-SC is an air-core (i.e. meaning of "skeleton") K-80 cyclotron with a small extraction radius of 40 cm for multiple-ion beams. It consists of 3 sector coils (SC) with a maximum spiral angle of 40°, 1 circular main coil (MC) of 60 cm radius and 7 small trim coils (TC) of radius varying from 5 cm to 45 cm. Owing to its compactness, a relatively high central magnetic field of about 2.4 T is required for a 50 MeV H+ beam. The radio frequency system consists of two 90° Dee locating directly opposite to each other, presently operating at a frequency from 34.5 MHz to 75 MHz with a maximum voltage of about 80 kV. Besides, an external injection system is required for the proposed HTS-SC in order to produce a high-intensity beam. As a part of the study of HTS-SC, this work will discuss about the conceptual design of its central region and its corresponding injection using a spiral inflector. As the space-charge effect is very important for a high-intensity beam at low energy, the transverse beam dynamics from the entrance of the inflector until several tenths of turns in the cyclotron are also discussed in order to investigate the upper limit of the injection current.

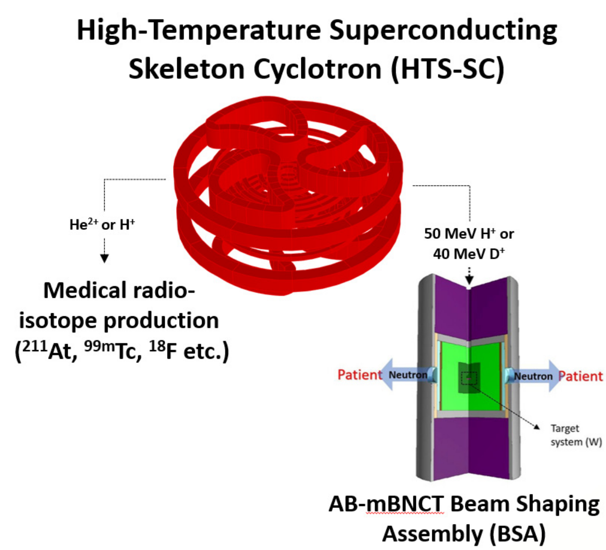

Figure 1: Schematic of the proposed HTS-SC and its application for AB-mBNCT as well as radioisotope production.

MATERIAL AND METHOD

Magnetic Field Distribution

The magnetic field distribution was calculated using the finite element magnetostatic (FEM) code TOSCA. The isochronous field is first estimated using Eq. (1).

$$< B(\overline{r}) > = \frac{B_O}{\sqrt{1-\beta(\overline{r})^2}} \quad (1)$$

After that, a better isochronous field was optimized by utilizing the orbital frequency obtained from OPAL (Object Oriented Parallel Accelerator Library) code developed by PSI [5]. The radial dependence of average magnetic field after optimization of isochronism is shown in Fig. 2.

ISBN: 978-3-95450-205-9 doi:10.18429/JACoW-Cyclotrons2019-WEC01

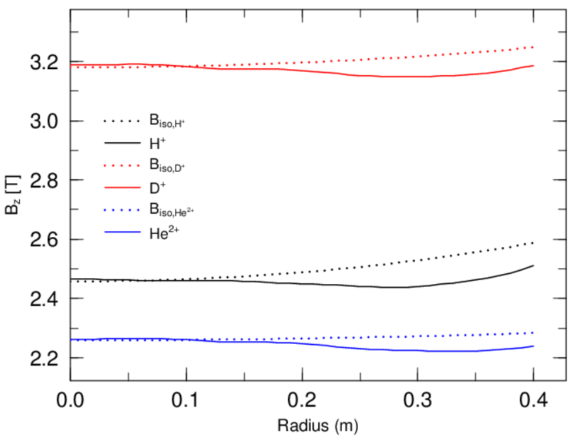

Figure 2: Average magnetic distribution for H^+ (black), D^+ (red) and He^{2+} (blue) ions up to 40 cm. Dotted lines show the analytical estimation of isochronous field using Eq. 1.

Central Region and Spiral Inflector

In order to inject the particles into median plane of HTS-SC, an inflector is needed. This work adopted a spiral inflector due to it is small-size and a relatively lower electric potential than other of the same kind. After considering the offset of beam at the inflector exit and the mechanical limitation of the bending structure, 40 keV was finally chosen as the injection energy. Table 1 shows the optimized parameters of the spiral inflector proposed in this study. Figure 3 shows the 3D CAD drawing of the spiral inflector and the central region of the HTS-SC. The average electric field distribution along the beam trajectory simulated by TOSCA is shown in Fig. 4.

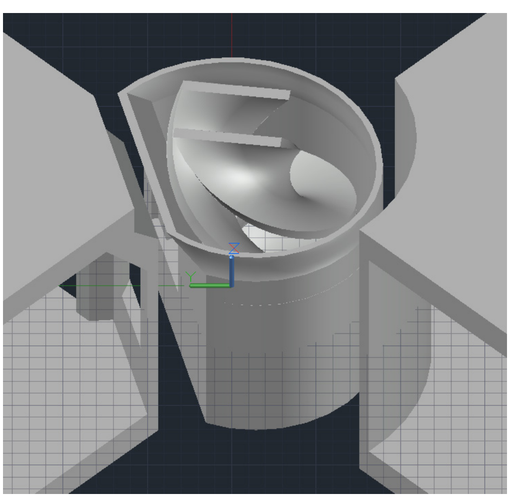

Figure 3: The 3D CAD drawing of the spiral inflector with the RF shield in the central region of HTS-SC.

RESULTS AND DISCUSSIONS

All the single-particle analysis and beam dynamics discussed in this work were performed by using SNOP developed by Victor Smirnov et al. [6]. Only single H^+ particle is involved in the following analysis, as this is the most important primary beam for AB-mBNCT neutron source.

The injection was assumed to be at 40 mm above the median plane, which is 4 mm above the entrance plane of the inflector.

Table 1: Optimised Parameters of the Spiral Inflector

Parameter	Value
Beam Energy	40 keV
Tilt (k')	0.17
Inflector Height (A)	3.6 cm
Electric Field (E_u)	20.93 kV/cm
Electrode gap (entrance)	8 mm
Aspect ratio (ξ)	2

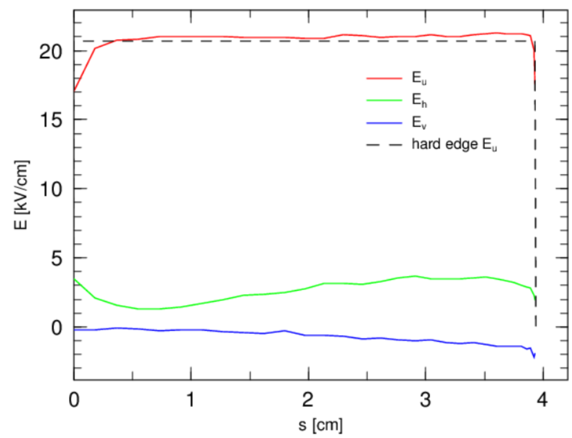

Figure 4: The electric field $\vec{E}$ directed in $\hat{u}$ (red), $\hat{h}$ (green), $\hat{v}$ (blue) along the beam trajectory simulated by TOSCA. The black dashed line represents the analytical hard edge E_u.

Single Particle Tracking

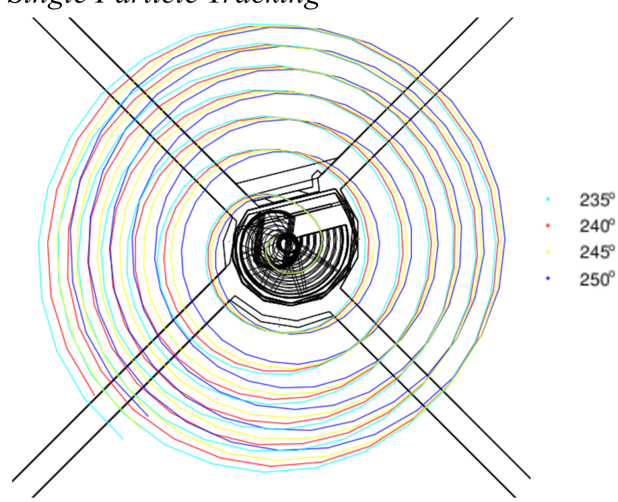

Figure 5: The accelerated orbits of H^+ ions from 40 keV to about 1.4 MeV with starting phases at 235° (cyan), 240° (red), 245° (yellow) and 250° (blue) respectively.

Beam Trajectory Simulations of the single particle tracking from injection above the inflector until the 6th turn were performed to show the feasibility of the design. The trajectory of the H^+ ion from 40 keV to 1.4 MeV with different starting phases from 235° to 250° at the median plane

ISBN: 978-3-95450-205-9 doi:10.18429/JACoW-Cyclotrons2019-WEC01

of the central region and the accelerating gaps are shown in Fig. 5.

Energy Gain Figure 6 shows the energy of the H^+ particle with an initial phase of 245°. Although the energy gain during the first 3 turns is just ~80% of the maximum energy gain due to the central bump of the magnetic field, this phase lag is reduced and almost fully recovered at the 6th turn. Also, the particle is crossing the gap when the electric potential is reducing. This enhances the axial focusing due to the Einzel focusing of the electric field.

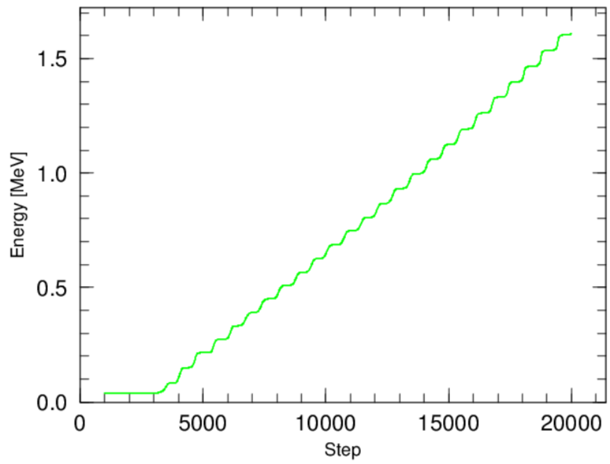

Figure 6: The energy gain of the H+ particle from 40 keV to about 1.6 MeV (up to the 6th turn).

Motion of Orbit Center Figure 7 shows the motion of the orbit centre to the 36th turn for particles of injection phases of 240˚, 245˚ and 250˚, respectively. The results show that the offset of the orbit centre is well confined within ±10 mm. This can easily be corrected by introducing first harmonic component into the acceleration.

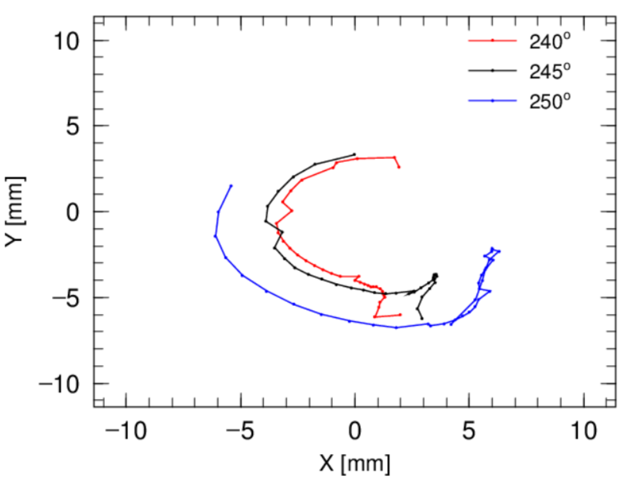

Figure 7: The motion of orbit centre (up to the 36th turn) in the central region for the particle with an injection phase of 240° (red), 245° (black) and 250° (blue) respectively.

Beam Dynamics

Beam Acceptance In order to determine the 6D phase acceptance of the central region (up to the 6th turn), an initial beam with (σ_x, σ_y) of (1.5 mm, 3 mm) and ($\sigma_{x'}$, $\sigma_{y'}$) of (30 mrad, 70 mrad) in trace spaces is generated at z = 40 mm. After passing through the spiral inflector, the particles which can survive up to the 6th turn gives the 6D beam acceptance of the injection system. However, as a spiral inflector couples the x-y motion of a particle, the acceptance contains x-y coupled component. This means that in order to perfectly match with the acceptance, an external beam skewer such as a quadrupole magnet is needed before injection into the spiral inflector. As far as this study is concerned, we are assuming a general injected beam without any coupling. Thus, only the projected beam acceptance is considered. The projected beam acceptance is about 29.8 π and 72 π mm·mrad in x and y direction respectively. The beam centre at the initial position in x-y real-space and x'-y' trace-space are shifted to (0.43 mm, 0.93 mm) and (2.9 mrad, -30.7 mrad) respectively due to the existence of fringing fields of the spiral inflector. Figure 8 shows the projected beam acceptance and the calculated rms emittance envelope.

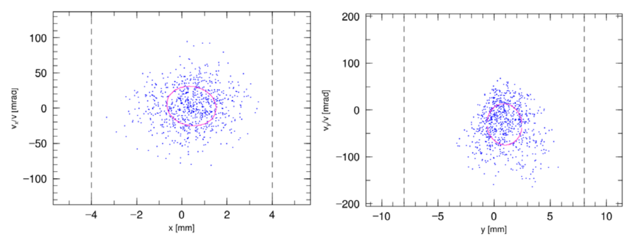

Figure 8: Projected beam acceptance of the central region of HTS-SC up to the 6th turn. The rms emittance bounded by the acceptance (pink line) is 29.8 π and 72 π mm·mrad in x and y respectively.

Current Dependence As the space charge effect is significant at low energy, the current dependence of the survival rate was also investigated. 3000 particles were injected (bounded by the projected acceptance shown in Fig. 8) from z = 40 mm. The surviving rate was then determined every 2000 step until the 36th turn in the cyclotron. The survival rate at different radii for different beam currents from 1 μA to 10 mA is shown in Fig. 9.

Generally, most of the particles are lost during the first turn (radius of < 30 mm) as they tend to hit the wall or ceiling of the Dee cavity. This kind of loss is magnified at high current owing to the existence of repulsive space-charge effect. This can be seen from the severe beam loss for the beam current of 5 mA (42%) and 10 mA (60%) during the first turn (r<30 mm). However, as particles accelerate, space charge effect is relieved and the beam loss is confined to be less than 10% until the 36th turn. This means that these particles are very likely to survive until extraction at the final turn. On the other hand, the beam loss of 1 μA, 0.1 mA and 1 mA are about 12%, 13% and 20% respectively up to 36th turn. This satisfactory result confirms the feasibility of the central region design for multi-particle motion.

ISBN: 978-3-95450-205-9 doi:10.18429/JACoW-Cyclotrons2019-WEC01

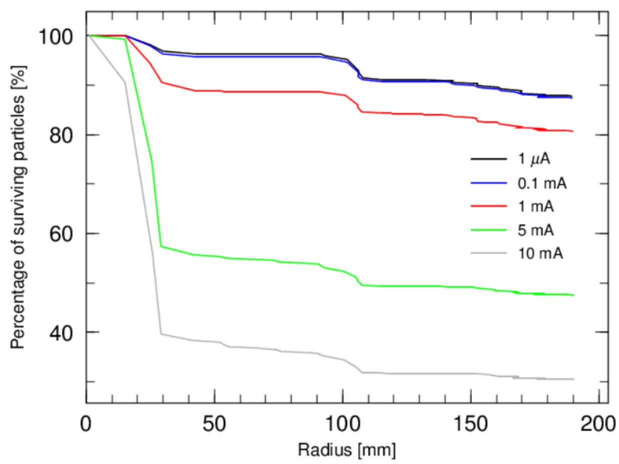

Figure 9: Percentage of surviving particles up to the 36th turn for beam current of 1 μA (black); 0.1 mA (blue), 1 mA (red), 5 mA (green) and 10 mA (grey) respectively.

Longitudinal Spread Besides the survival rate, the dependence of the longitudinal spread on to the space charge effect is also very important as the longitudinal spread of beam affects the beam resolution directly. Fig. 10 shows the longitudinal RMS spread for a 1 μA (Fig. 10(a)) and a 10 mA beam (Fig. 10(b)) up to the 36th turn for different initial rf phase width. As for the case of 1 μA beams, the longitudinal spread for a $\sigma_{rf} = 10^o$ is much wider than that of smaller width of 2.5^o or 5^o. However, this difference in rms is less significant for a 10 mA beam. This could be due to the enormous repulsive space charge effect that it overwhelmed any other causes, which could possibly increase the longitudinal spread of the beam. Besides, as the general trend, the rms difference in longitudinal direction due to different initial rf widths is becoming less significant as particles accelerate. This could be due to longitudinal bunching which might have taken place where particles that are lagged in phase are killed in the first few turns. This again proves our hypothesis that if particles can survive the first few turns, it is very likely for them to stay in the beam until the final turn, even for a high current beam.

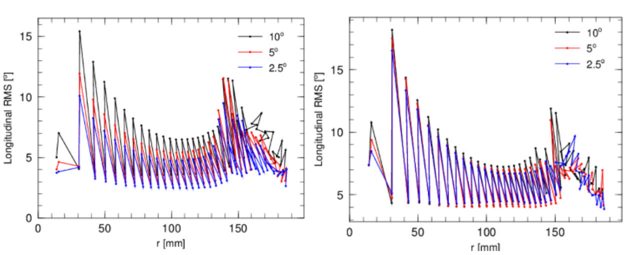

Figure 10: Longitudinal RMS spread for *left:* (a) 1μA, *right:* (b) 10 mA beam up to the 36th turn for initial rf phase width of σ_{rf}=2.5^o (blue), 5^o (red), and 10^o (black) respectively at azimuthal position of 90^o and 270^o.

Transverse Beam Size As beam growth at the central region is significant, the radial and axial rms were also studied using different injection current from 1 μA up to 10mA. Figure 11 shows the average motion in z direction, while Fig. 12 shows the RMS beam size in radial and axial direction respectively.

From Fig. 11, the mean axial motion of the beam, including the particles within 1 σ in z direction, are well confined within the axial aperture of ±20 mm for beams of 1 μA to 10 mA. In fact, the average motion as well as the beam rms are similar for these three different beam currents. This again shows that space charge effect is the most significant only at the first two turns. If the particles managed to survive, they are very likely to be able to stay in the coasting beam until the final turn. Figure 12, which shows the beam rms in r and z direction, also confirms this statement due to the similar rms growth for different beam currents.

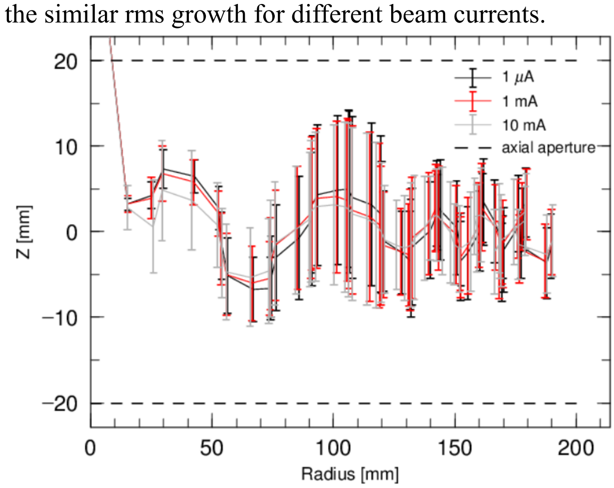

Figure 11: Average axial motion of the particles of beam current of 1 μA (black), 1 mA (red) and 10 mA (grey). Error bars represents 1 σ from the average trajectory.

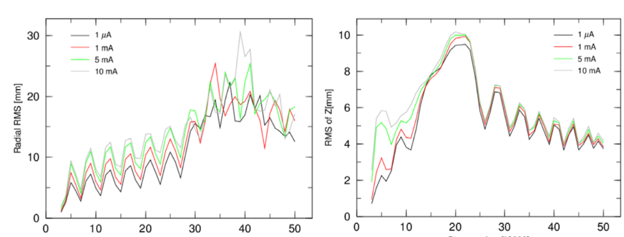

Figure 12: RMS (standard deviation) of the beam in radial (left) and axial (right) direction up to 36th turn. The beam current is 1 μA (black); 1 mA (red), 5 mA (green) and 10 mA (grey) respectively.

CONCLUSION

In conclusion, despite of the high central magnetic field of more than 2.4 T for H^+ beam, more than 80% of survival rate for a 1 mA beam is achieved by using the proposed spiral inflector of a high K value of >1.6. This satisfactory performance confirms the feasibility of the central region design in this work. Besides, this study also shows that most particles are killed during the first few turns. If we managed to increase the survival rate of the first few turns by introducing suitable coupling in x-y direction before injecting it into the inflector to improve the matching of the 6D acceptance, higher beam current is. Thus, additional elements such as a quadrupole magnet and an external buncher along the injection line shall remain as part of the next study. Furthermore, in order to confirm the survival

ISBN: 978-3-95450-205-9 doi:10.18429/JACoW-Cyclotrons2019-WEC01

rate of beams until extraction, the study of multi-bunch beam dynamics, coupled with the use of harmonic coils should also be performed in the coming future in order to check the neighbouring space-charge effect.

REFERENCES

[1] E. O. Lawrence and M. S. Livingston, "The Production of high speed light ions without the use of high voltages," *Physical Review,* vol. 40, no. 1, pp. 19-35, 1932. doi:10.1103/PhysRev.40.19

[2] A. E. Geisler *et al.*, "Commissioning of the Accel 250 MeV proton cyclotron", in *Proc. 18th Int. Conf. on Cyclotrons and Their Applications (Cyclotrons'07)*, Giardini-Naxos, Italy, Oct. 2007, pp. 9-14.

[3] V. Smirnov, S. Vorozhtsov, and J. Vincent, "Design study of an ultra-compact superconducting cyclotron for isotope production", *Nucl. Instrum. Methods Phys. Res., Sect. A*, vol. 763, no. 0168-9002, pp. 6-12, 2014. doi:10.1016/j.nima.2014.06.013

[4] H. W. Koay, M. Fukuda, H. Toki, R. Seki, H. Kanda, and T. Yorita, "Feasibility study of compact accelerator-based neutron generator for multi-port BNCT system," *Nucl. Instrum. Methods Phys. Res., Sect. A,* vol. 899, no. 0168-9002, pp. 65-72, 2018. doi:10.1016/j.nima.2018.05.025

[5] A. Adelmann, P. Calvo, M. Frey, A. Gsell, U. Locans, C. Metzger-Kraus, N. Neveu, C. Rogers, S. Russell, S. Sheehy, J. Snuverink, and D. Winklehner, "OPAL a versatile tool for charged particle accelerator simulations," *J. Comput. Phys.,* vol. arXiv preprint arXiv:1905.06654, 2019.

[6] V. L. Smirnov and S. B. Vorozhtsov, "SNOP – Beam dynamics analysis code for compact cyclotrons", in *Proc. 23rd Russian Particle Accelerator Conf. (RuPAC'12)*, Saint Petersburg, Russia, Sep. 2012, paper TUPPB008, pp. 325-327.

22nd Int. Conf. on Cyclotrons and their Applications Cyclotrons2019, Cape Town, South Africa JACoW Publishing
ISBN: 978-3-95450-205-9 doi:10.18429/JACoW-Cyclotrons2019-THA01

PRECISE MODELLING AND LARGE SCALE MULTIOBJECTIVE OPTIMIZATION OF CYCLOTRONS

J. Snuverink*, M. Frey, C. Baumgarten, A. Adelmann
Paul Scherrer Institut, 5232 Villigen PSI, Switzerland

SYNOPSIS

This contribution gives a summary of an invited presentation delivered at this conference.

The usage of numerical models to study the evolution of particle beams is an essential step in the design process of particle accelerators. However, uncertainties of input quantities such as beam energy and magnetic field lead to simulation results that do not fully agree with measurements. Hence the machine will behave differently compared to the simulations. In case of cyclotrons such discrepancies affect the overall turn pattern or alter the number of turns. Inaccuracies at the PSI Ring cyclotron that may harm the isochronicity are compensated by 18 trim coils. Trim coils are often absent in simulations or their implementation is simplistic. A realistic trim coil model within the simulation framework OPAL has been investigated. It was used to match the turn pattern of the PSI Ring (see Fig. 1). Due to the high-dimensional search space consisting of 48 simulation input parameters and 182 objectives (i.e. turns) simulation and measurement cannot be matched in a straightforward manner. Instead, an evolutionary multi-objective optimisation with more than 8000 simulations per iteration together with a local search approach was applied that reduced the maximum error to 4.5 mm over all 182 turns (see Table 1 and Figs. 2 and 3).

The results of this study have recently been published in their entirety in [1], to which the reader is further referred.

Table 1: Maximum absolute error (l_∞-norm), mean absolute error (MAE) and the mean squared error (MSE) of the best individual of the optimizer and local search compared to the measurement. In both cases the maximum error is at turn 2.

Method	**l_∞-norm** (mm)	**MAE** (mm)	**MSE** (mm^2)
optimizer	6.4	2.0	6.3
local search	4.5	1.4	3.4

REFERENCES

[1] M. Frey, J. Snuverink, C. Baumgarten, and A. Adelmann, “Matching of turn pattern measurements for cyclotrons using multiobjective optimization”, *Phys. Rev. Accel. Beams*, vol. 22, no. 6, p. 064602, 2019. doi:10.1103/PhysRevAccelBeams.22.064602

* jochem.snuverink@psi.ch

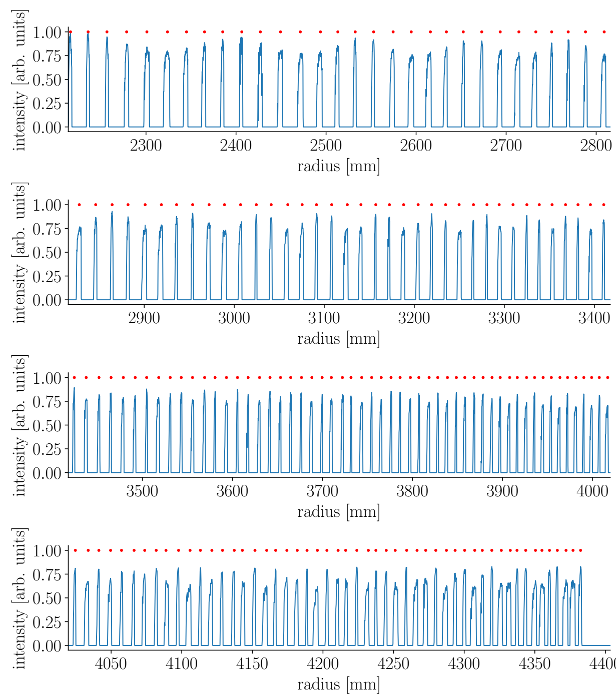

Figure 1: Histogram of the probe RRL measurement. The intensity is normalized. The red dots mark detected peaks.

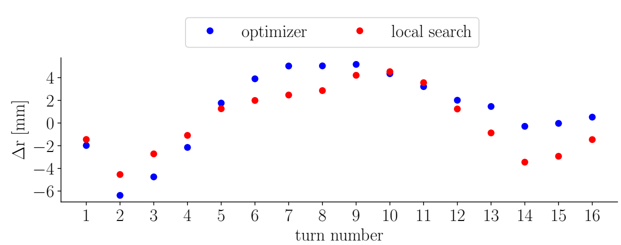

Figure 2: Error of the turn radius at RRI2 between measurement and simulation of the best individual obtained by multi-objective optimization and local search.

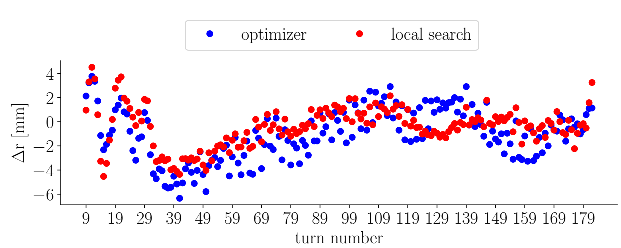

Figure 3: Error of the turn radius at RRL between measurement and simulation of the best individual obtained by multi-objective optimization and local search.

ISBN: 978-3-95450-205-9 doi:10.18429/JACoW-Cyclotrons2019-THA03

REACT AUTOMATION STUDIO: A NEW FACE TO CONTROL LARGE SCIENTIFIC EQUIPMENT

W. D. Duckitt, J. K. Abraham, iThemba LABS, Somerset West, South Africa

Abstract

A new software platform to enable the control of large scientific equipment through EPICS has been designed. The system implements a modern tool chain with a React front-end and a PyEpics back-end as a progressive web application. This enables efficient and responsive cross platform and cross device operation. A general overview of React Automation Studio as well as the system architecture, implementation at iThemba LABS, community involvement and future plans for the system is presented.

INTRODUCTION

Mobile phone and tablet technology have driven the need for cross platform and cross device applications that deliver an instantaneous user experience.

We were eager to be a part of this technical revolution, yet the tools available to us in the EPICS [1] open source community could not enable us to develop mobile based user interfaces (UI) for EPICS.

Having upgraded many of our systems to EPICS [1–4, 6] control and having developed several state-of-the-art EPICS-EtherCAT [1–3, 6, 7] control systems with Control Systems Studio (CS-Studio) [2, 3, 5, 6] operator UIs, we were poised with the problem of converting the remaining software systems for the rest of the facility to a similar standard.

We chose however to first investigate an alternative that involved creating a progressive web application (PWA) [8] framework for EPICS. The fruits of this investigation have led to the first release of a software framework to allow real-time, cross platform and cross device responsive UI creation for EPICS. This framework has been called React Automation Studio.

A general overview of React Automation Studio as well as the system architecture, implementation at iThemba LABS, community involvement and future plans for the system is presented in the sections below.

SYSTEM REQUIREMENTS

The goal of this first release was to a develop a containerised system consisting of a back-end to serve EPICS variables to a PWA front-end that could run cross platform and cross device.

For the back-end it was critical to incorporate user authentication and authorisation, whilst ensuring that it would not be necessary to manually declare process variables that needed to be served to the client. In other words the client must request the variables needed, and the back-end server should dynamically connect and relay the process variable meta and live data to the client.

For the client, the goal was to place a data connection wrapper on freely available React components and to build in the features for macro replacement of variable and system names. This was to allow for the creation of reusable operator interfaces to implement alarm handling and to add in diagnostic ability such as a probe interface where further information about the process variable is displayed.

Finally, the system should be sufficiently documented with use cases, examples and a front-end implementation guide.

Each of the goals have been achieved and the system overview is given below.

SYSTEM OVERVIEW

React Automation Studio has been containerised with Docker [9] and version controlled as a mono-repository using Git [10].

Each of the Docker containers are deployed as micro services and environment variables can be configured to deploy the system on different ports, to enable user authentication and authorisation or to serve the application on a unique URL or on the localhost. Separate Docker commands exist to load the development and production versions. These containerised environments allow for the precise versioning of packages used and prevents deployment dependency issues.

The software stack for React Automation Studio is shown in Fig. 1 and an overview of the system components are outlined below:

pvServer

We needed to develop a back-end server to relay the process variable (PV) data to the client. We initially evaluated a JavaScript back-end using a JavaScript EPICS channel access (CA) module, but we found the support and development to be limited and it also faced stability issues.

The chosen alternative is a Python [11] back-end which uses the well supported and well maintained PyEpics [12] CA module.

The resulting micro-service is the Python process variable server (pvServer). It is layered on the Flask [13] and Flask-Socket-IO [14] web application frameworks to serve the EPICS process variables to clients.

Communication between clients and the pvServer occurs between the data connection wrapper in the client components and the pvServer as follows:

The client initially makes a Socket-IO [15] connection to the pvServer. Depending on whether or not authentication is enabled the client will first be authenticated, and then the data connection wrapper will emit Socket-IO events to the pvServer requesting access to the EPICS variable.

Depending on the clients access rights, access is either denied or the socket connection is placed in a Socket-IO room

ISBN: 978-3-95450-205-9 doi:10.18429/JACoW-Cyclotrons2019-THA03

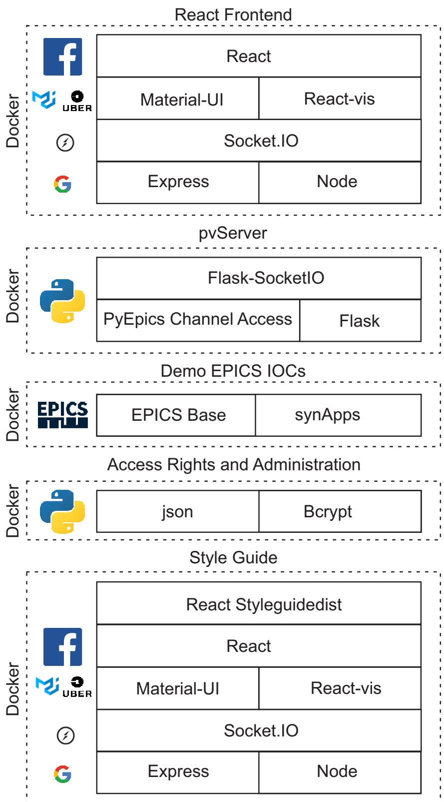

Figure 1: The React Automation Studio software stack.

with read-only or read-write privileges but with the same name as the PV. EPICS CA to the required process variables are established and the PyEpics PV is stored in a list, the connection and value change callbacks of the PyEpics CA are used to emit meta-data, connection status and value changes to the read-only and read-write rooms. The PV name is used as the event name.

In the data connection layer of the clients components, an event listener that is tied to the PV name is registered on the Socket-IO connection for each instantiation of the component. This allows efficient asynchronous updates of each listening component when the pvServer emits the PV's event update.

The only difference between the read-only and read-write rooms is that the write-access field of the meta-data has been changed to read-only based on the access rights and that for a read-write room the write access field is inherited from security rights defined by the EPICS IOC or gateway.

Similarly when writing to an EPICS variable, then depending on the access rights, the client is either granted or denied permission to write to the variable.

React Front-end

React [16] was chosen to develop the front-end for the PWA as it enabled the development of the front-end in a single language, i.e., JavaScript [17], as opposed to conventional web development in HTML, JavaScript and CSS. The UI interfaces that we have created are highly responsive and offer a real-time experience as is shown in the example of a mobile view in Fig. 2 and a desktop beam line control system in Fig. 3.

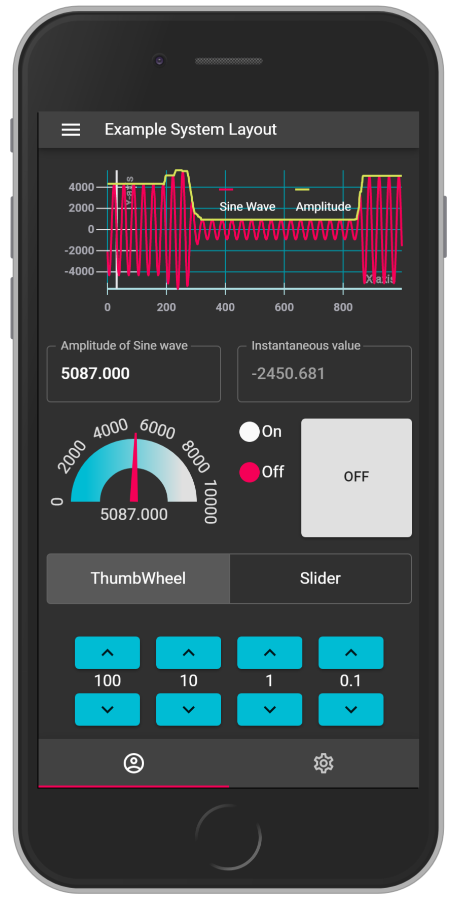

Figure 2: An example of a React Automation Studio mobile layout.

We have integrated selected components from the Material-UI [18] React component framework and the React-vis [19] graphing framework with our system to create user interfaces with the same features that we use in our current CS-Studio operator interfaces. These components have been integrated with a data connection layer which handles input and output, meta-data for labels, limits, precision, alarm sensitivity and initialisation from the pvServer.

Some components can handle multiple PVs such as graphs or single PVs i.e. text inputs. For each of the components, the PV's name can be declared using macros. The macros are replaced at component instantiation. This allows the design of complex user interfaces that can be reused by simply grouping the components and changing the global macro to point to another system.

The data connection layer can currently support EPICS process variables by adding "pva://" and local variables by adding "loc://" as prefixes to the component pv names. In the future, data connections to process variables of various protocols will be added, as well as new prefixes to indicate connection to these protocols.

ISBN: 978-3-95450-205-9 doi:10.18429/JACoW-Cyclotrons2019-THA03

Figure 3: An example of a wide screen operator display for the control of a beam line.

Demo EPICS IOC

The framework comes with a containerised demonstration IOC that enables the front-end demos to connect in real-time to a live system. The default EPICS port has been changed for the demo IOC to prevent multiple instances on different machines from influencing one another.

Access Rights and Administration

The URL, protocol selection for HTTPS or HTTP , authentication and server ports are controlled through the environment variables.

If React Automation Studio is installed on the localhost then there is no need to enable authentication as the host authentication system will protect access.

In this release, and with authentication enabled, the user name and password are managed through an administrator Docker environment through the command line. Passwords are stored on the server in encrypted format using Bcrypt [20]. In future releases this may be replaced by a web based administration page. The default authentication procedure can easily be modified to suit a different environment and point to an authentication server. The client is kept authenticated using an encrypted Jason Web Token (JWT) [21]. This JWT is used to check authorisation and access rights for every PV request and write. If the JWT is invalidated by the server then the user will be required to login.

Access rights can be controlled though a JSON file which contains user access groups and rules for defining PV access using regular expressions in the same way that the EPICS Gateway [22] access is defined. All of the components in React Automation studio currently indicate access rights to the PV.

Style Guide

A lot of effort was put into the documentation and a style guide based on React Styleguidedist [23] is used as the help function and to document the use of all the components from the source files. The current style guide is also interactive with a demo IOC. The properties of each of the components are documented and examples of their usage are shown.

IMPLEMENTATION AT iThemba LABS

React Automation Studio is currently being used as the control system front-end and overview screens for the Low Energy Radioactive Ion Beam (LERIB) [24] demonstrator which is part of the new South African Isotope Facility (SAIF) project. For LERIB it is used to control the motion control, vacuum systems, actuator systems and to display the status of the machine safety interlocking system. In total the various UIs currently connect up to 648 unique PVs from the same pvServer from multiple IOCs.

At the main separated sector cyclotron (SSC) complex, we have upgraded the harp beam diagnostics and Faraday cup front-end with a React Automation Studio front-end that controls all the harps and Faraday cups. For this system a total of 1683 unique process variables are connected to the UI from the same pvServer to multiple IOCs located on site.

We have also developed various engineering and mobile displays for other projects on site.

ISBN: 978-3-95450-205-9 doi:10.18429/JACoW-Cyclotrons2019-THA03

FUTURE PLANS AND COMMUNITY INVOLVEMENT

We are in the process of open-sourcing React Automation Studio and we encourage the community to get involved and collaborate with us on this project. The main release of React Automation Studio will contain all examples, source code and a style guide for implementation. We will also release boiler-plate example repositories that will contain simplified examples and staging areas that can be used by other laboratories to develop their own front-ends. We encourage interested persons to contact us via rasadmin@tlabs.ac.za.

In future releases we also hope to add in an interface to archived data, a dedicated alarm handler and a database abstraction layer to access saved settings.

CONCLUSION

iThemba LABS has successfully designed a new software platform to enable the control of large scientific equipment through EPICS via PWAs. The system is cross device and cross platform compatible. The operational readiness and stability of this software has been demonstrated and we encourage the EPICS community to test, evaluate and contribute to React Automation Studio.

REFERENCES

[1] EPICS, https://epics.anl.gov/

[2] W. D. Duckitt, J. K. Abraham, J. L. Conradie, M. J. Van Niekerk, and T. R. Niesler, "A new digital low-level RF control system for cyclotrons", in *Proc. 21th Int. Conf. on Cyclotrons and their Applications (Cyclotrons'16)*, Zurich, Switzerland, Sep. 2016, pp. 258–262. doi:10.18429/JACoW-Cyclotrons2016-WEB01

[3] W. D. Duckitt, J. L. Conradie, M. J. van Niekerk, J. K. Abraham, and T. R. Niesler, "The design and implementation of a broadband digital low-level RF control system for the cyclotron accelerators at iThemba LABS", *Nucl. Instrum. Methods Phys. Res., Sect. A*, vol. 895, Jul. 2018, pp. 1-9, ISSN 0168-9002. doi.org/10.1016/j.nima.2018.03.064

[4] I. H. Kohler *et al.*, "Progress in the conversion of the in-house developed control system to EPICS and related technologies at iThemba LABS", in *Proc. 13th Int. Conf. on Accelerator and Large Experimental Control Systems (ICALEPCS'11)*, Grenoble, France, Oct. 2011, paper MOPMS013, pp. 347–350.

[5] Control System Studio, http://controlsystemstudio.org/

[6] J. K. Abraham and W. D. Duckitt, "Integration of EtherCAT hardware into the EPICS based distributed control system at iThemba LABS", presented at the 22nd Int. Conf. on Cyclotrons and their Applications (Cyclotrons'19), Cape Town, South Africa, Sep. 2019, paper MOP015, this conference.

[7] R. Mercado, I. J. Gillingham, J. Rowland, and K. G. Wilkinson, "Integrating EtherCAT based IO into EPICS at Diamond", in *Proc. 13th Int. Conf. on Accelerator and Large Experimental Control Systems (ICALEPCS'11)*, Grenoble, France, Oct. 2011, paper WEMAU004, pp. 662–665.

[8] Progressive Web App https://developers.google.com/web/progressive-web-apps/

[9] Docker, https://www.docker.com/

[10] Git, https://git-scm.com/

[11] Python, https://www.python.org/

[12] PyEpics, https://cars9.uchicago.edu/software/python/pyepics3/

[13] Flask, https://palletsprojects.com/p/flask/

[14] Flask-SocketIO, https://flask-socketio.readthedocs.io/en/latest/

[15] Socket.Io, https://socket.io/

[16] React, https://reactjs.org/

[17] JavaScript, https://developer.mozilla.org/en-US/docs/Web/JavaScript

[18] Material-UI, https://material-ui.com/

[19] React-Vis, https://uber.github.io/react-vis/

[20] Bcrypt, https://pypi.org/project/bcrypt/

[21] Jason Web Token, https://tools.ietf.org/html/rfc7519

[22] EPICS Gateway, https://epics.anl.gov/extensions/gateway/index.php

[23] React Styleguidedist, https://github.com/styleguidist/react-styleguidist

[24] J. L. Conradie *et al.*, "The South African Isotope Facility", in *Proc. 9th Int. Particle Accelerator Conf. (IPAC'18)*, Vancouver, Canada, Apr.-May 2018, pp. 1240–1243. doi:10.18429/JACoW-IPAC2018-TUZGBF4

ISBN: 978-3-95450-205-9 doi:10.18429/JACoW-Cyclotrons2019-THB01

REVIEW OF HIGH POWER CYCLOTRONS AND THEIR APPLICATIONS

L. Calabretta, D. Rifuggiato, Istituto Nazionale di Fisica Nucleare- LNS, Catania, Italy
M. Maggiore, Istituto Nazionale di Fisica Nucleare- LNL, Legnaro, Italy

Abstract

An incomplete review of existing machines and of present new projects of high power cyclotrons is here presented. Both high energy and low/medium energy cyclotrons will be described. Specific requests for different fields of applications are also discussed.

INTRODUCTION

It is from the early years of the Eighties that the cyclotron community has proposed challenging cyclotrons to produce intense beams of kaons, antiprotons, neutrinos and other particles [1, 2] or to be used to drive subcritical reactors [3]. Unfortunately, up to now the cyclotron community was not able to get funds for none of these projects intended to surpass the performances of the TRIUMF and PSI cyclotrons. The main technical problems related to the construction of these projects are here discussed. Fortunately, the creativity of our community is again alive and new projects and ideas flourished.

HIGH INTENSITY LOW-MEDIUM ENERGY CYCLOTRONS

Low energy cyclotrons (15-30 MeV) are mainly used to produce radioisotopes, producing beams with intensity in the range 0.1-1 mA. But in the latest years the 30 MeV cyclotrons have also been used to drive BNCT facilities [4], and the perspective is towards increasing of this application, whose request is a beam current increase up to 2 mA or more.

The 70 MeV cyclotrons, supplied by IBA and BEST companies, are mainly used for the production of medical radioisotopes and their declared maximum intensity is about 1 mA. The wide range of energy of extracted beams varying from 35-70 MeV with the possibility to deliver two beams simultaneously make this kind of accelerator very flexible in use and particularly suitable to be employed as driver for multipurpose facilities. The SPES facility at LNL (Italy) [5] has already carried out the commissioning of the C70 cyclotron which will provide high power beams for nuclear research and radioisotopes R&D and in next future both RISP (Daejeon, Korea) [6] and iThemba (Cape Town, South Africa) laboratories will be equipped with cyclotrons with such performances.

The above energy range and current are appropriate to produce radioisotopes but an increase in the beam current would allow to increase the production rate for the present medical isotopes and also could open the opportunity to produce radioisotopes with small production cross sections or long half-lives.

The perspective to produce the ^{68}Ge/^{68}Ga generator for imaging diagnostic, through the reactions ^{71}Ga(p,4n)^{68}Ge and ^{69}Ga(p,2n)^{68}Ge, is very appealing to replace the usual ^{99}Mo/^{99m}Tc generator. Indeed, the half-life of the ^{68}Ge parent is of about 270 days while the lifetime of ^{99}Mo is only of 66 hours. Moreover, the half-life of the ^{68}Ga is just 68 minutes versus the 6 hours of the ^{99m}Tc.

Another interesting new radioisotope is ^{225}Ac, produced through the reaction ^{226}Ra(p,2n)^{225}Ac. This is a four alpha particles emitter and it is a wonderful tool for targeted radiotherapy. To produce efficiently this radioisotope it is convenient to use a proton beam with energy higher than 50 MeV and current in excess of 3-5 mA. This trend is confirmed by the new project TR100 [7] and by the interest of PSI to develop a dedicated beam line to the radionuclide production [8].

Another viable way to produce ^{225}Ac is bombarding Thorium target with a proton beam of about 450 MeV, as recently tested at TRIUMF [9].

Bombarding ^{232}Th by a proton beam with energy higher than 50 MeV is also a way to produce ^{213}Bi, another radioisotope that decays producing four alpha, also this is very appealing for radiotherapy.

An alternative production method to produce ^{213}Bi is through the reaction α+^{232}Th as presently investigated at GANIL [10]. Bombarding ^{232}Th with alpha particles allows to produce many different alpha emitters like ^{212}Pb, ^{213}Bi, ^{225}Ra, ^{225}Ac. The energy of the alpha beam must be higher than 50 MeV. These energies and the high current for α beam are not achievable with the present commercial cyclotrons but are in the energy range of the proposed IsoDAR cyclotron [11].

THE ISODAR CYCLOTRON

The IsoDAR compact cyclotron will be able to deliver up to 5 mA of H_2^+ beam with a maximum energy of 60 MeV/amu [11]. This cyclotron was designed to drive the experiment for sterile neutrino research [12] and as first stage of the cascade cyclotrons to perform the DAEδALUS experiment [13]. This cyclotron could also be used to accelerate He beam up to 240 MeV with intensity of about 1 mA (120 kW of beam power). The possible use of the IsoDAR cyclotron to produce huge amounts of medical radioisotopes for diagnostic and therapy, using both the high intensity proton beam and the He beam, are well described in a recent paper [14].

The large pole diameter of IsoDAR and the use of 4 RF cavities allow to extract the beam with high efficiency using the electrostatic deflector. For the extraction of protons also the stripping of H_2^+ molecule can be used. The feasibility to use a stripper foil with an intensity of 1.7 mA was tested with the 72 MeV proton beam at PSI [15].

The most serious problem to accelerate the high current beam is related to injection. The relatively low velocity and

ISBN: 978-3-95450-205-9 doi:10.18429/JACoW-Cyclotrons2019-THB01

the high intensity of the injected charged particles associated to the suppression of the effect of charge compensation makes much more effective the coulomb repulsion. As discussed in [16], the choice to accelerate H_2^+ mitigates this effect, nevertheless both the increase of particles energy and the bunching action may be suitable to get a high injection efficiency.

To achieve this goal, the design and construction of a RFQ to perform a Direct Injection Project [17] is in progress.

An alternative way to increase the injection efficiency is the use of a magnetic spiral inflector instead of the electrostatic device. This study was accomplished at LNS-INFN and it led to the optimization of a magnetic configuration based on a series of dipole Halbach rings [18] allowing to fit the ideal trajectory of the injected particles into the central region of a cyclotron, see Fig. 1. The Spiral Inflector Halbach Ring has been optimized to inject a 60 keV H_2^+ ion beam into the Isodar cyclotron [19].

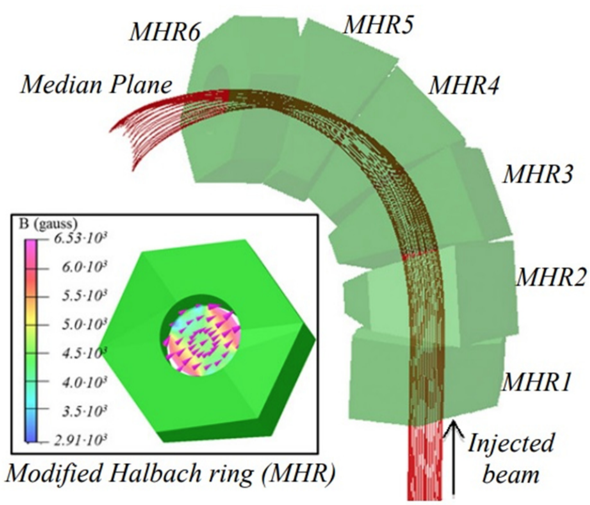

Figure 1: Layout of the six permanent magnets (MHR#) configuration to inflect the beam on the median plane of a cyclotron; into the box, magnetic field direction inside the inner region of the magic ring.

Compared to the usual electrostatic spiral inflector, the strength of the magnetic field is not adjustable during the injection operation, but the azimuth and vertical position of the magnetic inflector respect the cyclotron axis and median plane are tuneable. These two free parameters are very useful to match properly the median plane of the cyclotron and the right direction of the entering beam.

HIGH INTENSITY HIGH ENERGY CYCLOTRONS

Accelerators able to deliver proton beams with energy around 1 GeV and beam power in the range 2-10 MW are requested for experiments to investigate fundamental physics, to drive subcritical reactors for energy production, to drive new meson factories [20] and new neutron spallation sources in subcritical reactors [21]. Different approaches have been proposed and new projects are also presented at this conference [22].

The common feature of the three projects here discussed is the use of superconducting technology. The first project, studied by the INFN-LNS group [23, 24], is the two-stage cyclotron complex proposed to drive the DAEδALUS experiment to measure the CP-violation parameter δ_{CP} in the neutrino sector. The second is the single-stage superconducting cyclotron for H_2^+ proposed by P. Mandrillon [25] and the third is the stacked-cyclotron layout developed by P. McIntyre [26] at TAMU.

Superconducting Ring Cyclotron: DAEδALUS

The accelerator to drive the DAEδALUS experiment consists of two coupled cyclotrons. The first is the IsoDAR cyclotron, described in the previous section, able to accelerate H_2^+ up to 60 MeV/amu. The beam is extracted from this cyclotron by an electrostatic deflector. The second stage is a six sector Superconducting Ring Cyclotron (SRC) able to accelerate H_2^+ up to 800 MeV/amu, to be extracted by stripping [23]. Figure 2 shows the layout of this cyclotron complex. The stripper foil is placed in a region where the magnetic field stays around 0.1-0.15 T.

This low field allows to collect the removed electrons on a catcher. In Fig. 2, the trajectory of the extracted beam, crossing the central area of the cyclotron and exiting after half a turn, is shown. A small steering magnet placed in the central region is useful to drive the extracted trajectory, and to control the vertical beam envelope.

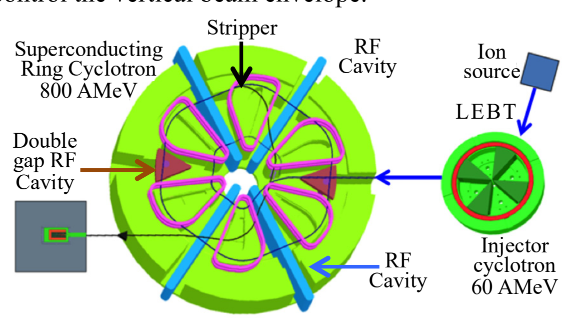

Figure 2: Layout of the two stage cyclotron complex. The SRC is equipped with four single gap RF cavities and two double gap cavities (brown). The stripper position and the extraction trajectories are also shown.

The choice to have just six sectors allows to have enough room to install RF cavities similar to those used in the PSI ring cyclotron. The use of only 4 cavities in an SRC with 6 sectors poses a problem of uncontrolled radial and vertical beam growth when the resonance $\nu_r = 2$ is crossed [27]. This problem has been solved by adding two additional double-gap RF cavities at the outer radii.

The use of a reduced number of cavities, the absence of flattop cavities, and the use of superconducting sector magnets allow to increase the conversion efficiency, from electric power grid to the 10 MW beam, up to about 60%.

The design of the superconducting sector magnet (see Fig. 3) is quite similar to the RIKEN Superconducting Ring Cyclotron. It was performed in collaboration with the Plasma Science and Fusion Center of MIT [28].

ISBN: 978-3-95450-205-9 doi:10.18429/JACoW-Cyclotrons2019-THB01

The Beam dynamics studies along the acceleration were simulated using the OPAL code [29].

The most serious problem posed by the acceleration of H_2^+ is the dissociation of many long-lived vibrational states. The electron binding energies of these vibrational states are very low, therefore they can be dissociated by electromagnetic stripping in the high magnetic fields. These high vibrational states could be removed at the source level.

Alternatively, it is also possible to remove the most dangerous of the less-bound vibrational states introducing dangerous of the less-bound vibrational states introducing a magnetic field bump with amplitude of 0.3 T and azimuthal extension of 1°-2° on each sector of the SRC. The field bump can be produced by small permanent magnets installed at the proper azimuth on the hills. Choosing properly the azimuth of the magnetic bumps for each energy, the trajectories of the protons dissociated by electromagnetic Lorentz go to inner radii and arrive outside of the vacuum chamber where can be collected [27].

Single Stage Superconducting Cyclotron

AIMA company has proposed a single stage cyclotron able to accelerate H_2^+ [25] up to 800 MeV. Although the iron pole consists of six separated sector and the field has a symmetry six, the magnetic field is powered by one pair of superconducting coils, with very complex shape. The coil is wrapped around the outer part of the six sectors but in the inner region it is bent in the opposite direction through the valley. The two coils are symmetric vs. the median plane, but they are not parallel to the median plane.

The beam acceleration is performed by six $\lambda/2$ double-gap RF cavities. To leave room for installation of the six RF cavities, the upper and lower coils increase their distance from the median plane in the inner regions.

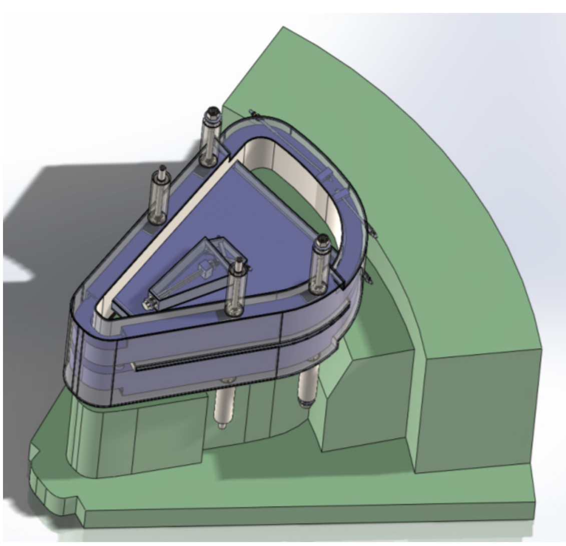

Figure 3: A sector of the SRC. The half lower part of iron, the cryostat and the tie rods, to maintain the superconducting coils in the proper position are shown.

The layout of the cyclotron is shown in Fig. 4. Beam extraction is performed by the stripper placed at the exit of the main sector, and beam trajectory is bent toward the outer radii, see Fig. 5. A key innovation of this project is the insertion in each valley of two wedges of iron , where direction of the magnetic field is reversed.

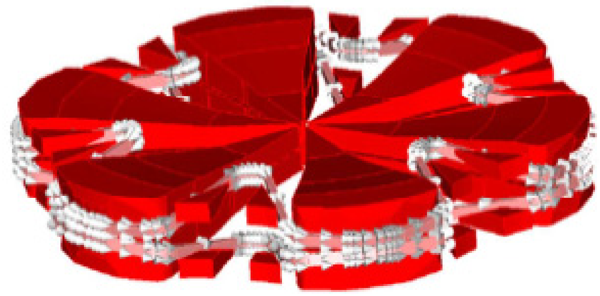

Figure 4: the magnetic circuit of the H_2^+ 800 MeV/amu single stage cyclotron.

This solution increases greatly the vertical focusing, avoids spiralling the sector edges, and allows to bend towards the outer radii the trajectory of protons extracted by stripper. This elegant extraction method could probably also be implemented in the DAEδALUS ring cyclotron.

Another innovative solution, to mitigate the space charge effects, is the use of three independent ion sources. This solution mitigates both the beam ripple and the risk of beam trips, a serious issue for the Accelerator-Driven Reactors System.

The 6 RF resonators have a special shape to fit the valley space with the coil cryostat. The RF cavities are designed to work at 36.3 MHz in harmonic 6, and the simulated quality factor Q of the cavities is 6200. The accelerating voltage rises from 150 kV to 450 kV from the inner to the outer radii. The maximum energy gains per turn at the extraction radius should be higher than 5 MeV/turn.

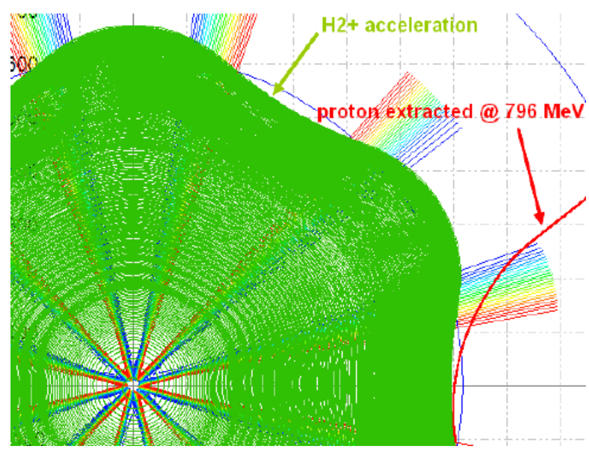

Figure 5: The trajectory of a H_2^+ reference particle along the acceleration path (green lines) and of the extracted proton (red line). The radial lines shown the electrical gradient produced by the RF cavities.

Critical issues of this project are the complexity of the superconducting coil shape and its dimensions, about 50 m long. The coil does not stay in a plane and the bending curvature of the coil is reversed at the inner radius.

ISBN: 978-3-95450-205-9 doi:10.18429/JACoW-Cyclotrons2019-THB01

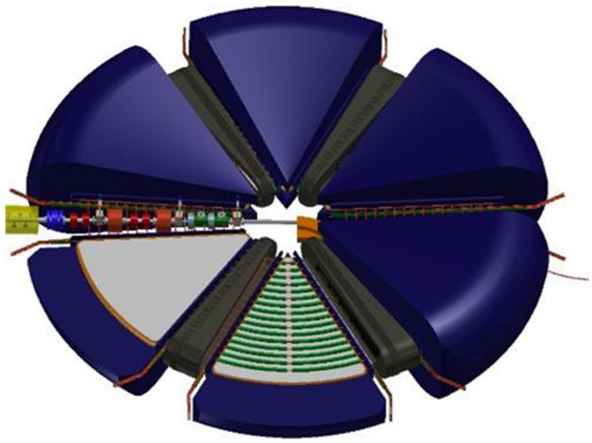

Figure 6: View of the 100 MeV SFC, showing the 16-turn spiral trajectory, the superconducting slot cavities (dark grey), and the beam transport channels (green).

A further issue is the amount of beam losses due to the interaction of the beam with residual gas: the vacuum has to be better than 8×10^{-7} Pa in order to maintain the beam losses below 150 W. The issue of the dissociation of the vibrational states contained in the H_2^+ beam has to be evaluated too. Probably, this problem could be solved inducing the electromagnetic dissociation by permanent magnets placed at proper azimuth, similar solution proposed for the DAEδALUS ring cyclotron [27].

Strong Focusing Superconducting Cyclotron

An alternative approach to achieve a 1 GeV 10 mA proton beam to drive ADS, was proposed by P. McIntyre [26] of TAMU. The proposal consists to use a two stage of acceleration performed by cyclotrons, but each stage consists of 6 stacked flux coupled isochronous cyclotron, to mitigate both the problems of space charge and cost. The TAMU group has developed new ideas both about new superconducting RF cavities and Strong Focusing Cyclotron (SFC).

In particular, the group is focused on the design of the first stage of SFC to accelerate a 100 MeV proton beam [30]. This is a separated orbit cyclotron similar to the TRITRON project [31], where the beam is forced to circulate through the transporting channel placed in the hills, see Fig. 6. According to their latest simulations this solution allows to accelerate beams with intensity up to 10-20 mA.

The SFC concept is based on the use of a local magnetic channel to focus the beam both radially and vertically. This is achieved using single layer Panofsky quadrupole with superconducting coils (MgB_2). A cable layer windings, wound as window frame, produce a dipole field used to tune the magnetic fields of each channel to match the isochronism.

An additional advantage of the SFC is the straight shape of the sectors edges. This feature simplifies greatly the insertion of the RF cavities. Since the huge turn separation implies a very high energy gain per turn, a further important contribution of the group is the design of new superconducting RF cavities [32].

Unfortunately, the acceleration of high proton beam current in the range 10-20 mA means a huge beam loading effect especially for superconducting cavities and consequently the beam instability or eventual ion source trips could produce serious problems at the RF cavities. Moreover, the tuning of the machine could be not very easy according to the previous experience of the TRITRON project.

CONCLUSION

The two frontiers of cyclotron accelerators are the beam current intensity and the high energy. According to the contribution at the present conference the goal to overcome the beam current limit of 2 mA seems to be feasible in the next years especially for the low/medium energy cyclotrons. Vice-versa, to achieve the 800 MeV needs important investments and depends also upon factors external to our community. Although the cyclotron is one of the oldest particle accelerator, it is impressive how the cyclotron community is able to propose interesting new tools [33], projects, innovations, and applications.

REFERENCES

[1] W. Joho, "ASTOR, Concept of a combined acceleration and storage ring for the production of intense pulsed or continuous beams of neutrinos, pions, muons, kaons and neutrons", in *Proc. 10th Particle Accelerator Conf. (PAC'83)*, Santa Fe, NM, USA, Mar. 1983, pp. 2083-2086.

[2] R. Laxdal, M. K. Craddock, W. Joho, G. H. Mackenzie, J. R. Richardson, and L. C. Teng, "Matching an isochronous cyclotron to a synchrotron to provide a high intensity injector", in *Proc. 10th Particle Accelerator Conf. (PAC'83)*, Santa Fe, NM, USA, Mar. 1983, pp. 2013-2016.

[3] N. Fiétier, P. Mandrillon, and C. Rubbia, "A cyclotron-based accelerator for driving the energy amplifier", in *Proc. 14th Int. Cyclotron Conf. and their Applications (Cyclotrons'95)*, Cape Town, South Africa, Oct. 1995, paper L-02, pp. 598-605.

[4] T. Mitsumoto *et al.*, "BNCT system using 30 MeV H- cyclotron", in *Proc. 19th Int. Conf. on Cyclotrons and their Applications (Cyclotrons'10)*, Lanzhou, China, Sep. 2010, paper FRM2CCO04, pp. 430-432.

[5] Selective Production of Exotic Species (SPES), Laboratori Nazionali di Legnaro, Italy. `http://www.lnl.infn.it/_spes/`

[6] `https://www.risp.re.kr/eng/orginfo/intro_project.do`

[7] Y.-N. Rao, R. A. Baartman, Y. Bylinskii, T. Planche, and L. G. Zhang, "Conceptual design of TR100+: An innovative superconducting cyclotron for commercial isotopes production", presented at the 22nd Int. Conf. on Cyclotrons and their Applications (Cyclotrons'19), Cape Town, South Africa, Sep. 2019, paper THB03.

[8] N. P. van der Meulen *et al.*, "The use of PSI's IP2 beam line towards exotic radionuclide development and its application towards proof-of-principle preclinical and clinical studies",

ISBN: 978-3-95450-205-9 doi:10.18429/JACoW-Cyclotrons2019-THB01

presented at the 22nd Int. Conf. on Cyclotrons and their Applications (Cyclotrons'19), Cape Town, South Africa, Sep. 2019, paper TUA03.

[9] A. K. H. Robertson *et al.*, "Design of a Thorium metal target for 225Ac production at TRIUMF", *Instruments*, vol. 3, no. 1, Feb. 2019. doi:10.3390/instruments3010018

[10] A. M. Frelin-labame *et al.*, "R&D activities for the production of radioisotopes at GANIL", presented at the SPES workshop, Legnaro, Italy, Jan. 2019, unpublished.

[11] A. Adelmann *et al.*, "Cost-effective design options for IsoDAR" Oct. 2012. arXiv:1210.4454

[12] A. Bungau *et al.*, "Proposal for an electron antineutrino disappearance search using high-rate ^{8}Li production and decay", *Phys. Rev. Lett.*, vol. 109, p. 141802, Oct. 2012. doi:10.1103/PhysRevLett.109.141802

[13] L. Calabretta, M. M. Maggiore, L. A. C. Piazza, and D. Rifuggiato, "A multi MegaWatt cyclotron complex to search for CP violation in the Neutrino sector", in *Proc. 19th Int. Conf. on Cyclotrons and their Applications (Cyclotrons'10)*, Lanzhou, China, Sep. 2010, paper TUA1CIO01, pp. 298-303.

[14] J. R. Alonso, R. Barlow, J. M. Conrad, and L. H. Waites, "Medical isotope production with the IsoDAR cyclotron", *Nat. Rev. Phys.*, vol. 1, Aug. 2019. doi:10.1038/s42254-019-0095-6

[15] R. Dölling, R. Dressler, and L. Calabretta, "A test of stripper foil lifetime in PSI's 72 MeV proton beam", in *Proc. 61st ICFA Advanced Beam Dynamics Workshop on High-Intensity and High-Brightness Hadron Beams (HB'18)*, Daejeon, Korea, Jun. 2018, pp. 338-341. doi:10.18429/JACoW-HB2018-WEP2PO033

[16] L. Calabretta and D. Rifuggiato, "Superconducting cyclotrons for acceleration of H_2^+", in *Proc. 15th Int. Cyclotron Conf. and Their Applications (Cyclotrons'98)*, Caen, France, Jun. 1998, paper J-02, pp. 665-668.

[17] D. Winklehner, "Beam dynamics and preliminary design of the RFQ direct injection project", presented at the 22nd Int. Conf. on Cyclotrons and their Applications (Cyclotrons'19), Cape Town, South Africa, Sep. 2019, paper WEB05.

[18] D. Campo and L. Calabretta, private communication.

[19] K. Halbach, "Design of permanent multipole magnets with oriented rare earth cobalt materials", *Nucl. Instrum. Methods*, vol. 169, no. 1, pp. 1–10, Feb. 1980. doi:/10.1016/0029-554X(80)90094-4

[20] R. Cywinski *et al.*, "Towards a dedicated high-intensity muon facility", *Physica B*, vol. 404, pp. 1024-1027, Apr. 2009. doi:10.1016/j.physb.2008.11.203

[21] V. L. Aksenov, "DNS-IV project: Present status and trends", presented at advanced ideas and experiments for DNS-IV workshop, Dubna, Russia, Dec. 2018.

[22] T. J. Zhang, "A new solution for cost effective, high average power (2 GeV, 6 MW) proton accelerator and its R&D activities", presented at the 22nd Int. Conf. on Cyclotrons and their Applications (Cyclotrons'19), Cape Town, South Africa, Sep. 2019, paper FRA01.

[23] D. Campo *et al.*, "High intensity compact cyclotron for ISODAR experiment", in *Proc. 20th Int. Conf. on Cyclotrons and their Applications (Cyclotrons'13)*, Vancouver, Canada, Sep. 2013, paper WEPPT030, pp. 384-386.

[24] D. Winklehner *et al.*, "High power cyclotrons for neutrino experiments", in *Proc. 5th Int. Particle Accelerator Conf. (IPAC'14)*, Dresden, Germany, Jun. 2014, pp. 788-790. doi:10.18429/JACoW-IPAC2014-MOPRI078

[25] M. Conjat, J. Mandrillon, and P. Mandrillon, "Cyclotron drivers for accelerator driven systems", in *Proc. ThEC13 Conf.*, Geneva, Switzerland, Oct 2013. doi:10.1007/978-3-319-26542-1_37

[26] P. McIntyre, G. Kim, D. May, and A. Sattarov, "A superconducting isochronous cyclotron stack as a driver for a Thorium-cycle power reactor", in *Proc. 19th Particle Accelerator Conf. (PAC'01)*, Chicago, IL, USA, Jun. 2001, paper WPPH062, pp. 2593-2595

[27] L. Calabretta and F. Meòt, "Cyclotrons and FFAG accelerators as drivers for ADS", *Rev. Accel. Sci. Technol.*, vol. 8, pp. 77-97, Jan 2015. doi:10.1142/S1793626815300054

[28] A. Radovinsky *et al.*, "Engineering study of sector magnet for the DAEδALUS experiment", *IEEE Trans. Appl. Supercond.*, vol. 24, p. 4500204, June 2014. doi:10.1109/TASC.2013.2281855

[29] J. J. Yang *et al.*, "High-power cyclotron beam dynamics-Space charge effects beam loss", *Nucl. Instrum. Methods Res., Sect. A*, vol. 704; pp. 84-91, 2013. doi:10.1016/j.nima.2012.12.050

[30] S. Assadi, P. M. McIntyre, A. Sattarov, and N. Pogue, "Nonlinear beam dynamics studies of the next generation strong focusing cyclotrons as compact high brightness, low emittance drivers", in *Proc. 6th Int. Particle Accelerator Conf. (IPAC'15)*, Richmond, VA, USA, May 2015, pp. 656-658. doi:10.18429/JACoW-IPAC2015-MOPMA047

[31] A. Cazan, P. Schutz, and U. Trinks, "Commissioning of the first separated orbit cyclotron triton", in *Proc. 15th Int. Cyclotron Conf. and Their Applications (Cyclotrons'98)*, Caen, France, Jun. 1998, paper C-04, pp. 323-326.

[32] J. Gerity, S. Assadi, P. M. McIntyre, and A. Sattarov, "Beam dynamics studies for a strong-focusing cyclotron", in *Proc. 9th Int. Particle Accelerator Conf. (IPAC'18)*, Vancouver, Canada, Apr.-May 2018, pp. 3522-3525. doi:10.18429/JACoW-IPAC2018-THPAK118

[33] T. Planche, "Designing cyclotrons and FFAs from their orbits", presented at the 22nd Int. Conf. on Cyclotrons and their Applications (Cyclotrons'19), Cape Town, South Africa, Sep. 2019, paper FRB01.

ISBN: 978-3-95450-205-9 doi:10.18429/JACoW-Cyclotrons2019-THB02

PRODUCTION OF 70 MeV PROTON BEAM IN A SUPERCONDUCTING CYCLOTRON

V. Smirnov† and S. Vorozhtsov, Joint Institute for Nuclear Research, Dubna, Russia

Abstract

Production of 70 MeV proton beams with help of a cyclotron-type facility is one of highly requested tasks presently. Such beams are used for medical applications including direct tumor irradiation and also for production of medical isotopes. The applications mentioned above dictate corresponding requirements imposed on the beam quality and intensity. For proton therapy treatment it is sufficient to have 300 to 600 nA output beam current with rather strict tolerance on the transverse beam quality. On the other hand, for the isotope production the major requirement is high enough beam intensity (hundreds μA) with less demanding beam quality. Nowadays, for production of the proton beams in the energy range considered cyclotrons with resistive coil weighting ~140 to 200 t are mostly used. In these cyclotrons two extraction methods – with electrostatic deflector and with stripping foils – can provide somewhat different quality of the output beam. In given report a possibility of using a superconducting cyclotron instead of room-temperature one is considered. To this end, acceleration of various ions was investigated with analysis of the main facility parameters and resulting output beams.

INTRODUCTION

Nowadays, the majority of cyclotrons intended for production of proton beams with energy about 70 MeV have rather low magnetic field in range of 1 to1.4 T [1-2]. As a result, the facility has footprint of 4 to 6 m and weight above 140 t. Application of higher level of magnetic field for such machines based on superconductive technology permits designing of accelerator with substantially lower size and weight. But application of high magnetic fields introduces some limitations in the cyclotron design. For example, acceleration of H^- ions in the selected energy range becomes practically impossible in high magnetic field due to massive particle losses by Lorentz stripping. On contrary, in room-temperature machines acceleration of H^- ions are widely used that provides a highly effective particle extraction near 100% by stripping foils with a possibility of some energy variation of the output beam. So, in the superconducting cyclotrons either protons or H_2^+ ions can be used for acceleration. The latter has a strong enough coupling of outside electron with the nucleon to stay stable even in considered high magnetic field of the facility. In case of protons an application of an electrostatic deflector for particles extraction leads to somewhat lower extraction efficiency and fixed energy of the output beam. On the other hand, for extraction of accelerated H_2^+ ions a stripping foil can be used. This will increase the output proton beam intensity twice compared to the internal H_2^+ beam current: each H_2^+ ion generates 2 protons downstream the stripping foil. The price in this case would be essentially bigger size of the facility compared to the cyclotron for proton acceleration with the same central magnetic field.

The goal of present work is investigation of various variants of superconducting cyclotrons for production of proton with output energy about 70 MeV in terms of their main technical parameters and extracted beam characteristics. Comparison of obtained parameters with that for existing commercial cyclotrons is also included. The highly realistic computer modelling of the proposed accelerators was performed with usage of spatial distributions of the facility electromagnetic fields and careful beam dynamics analysis.

PROTON CYCLOTRON

The 70 MeV cyclotron for acceleration of ions with charge to mass ratio 1 has K-value 70 MeV. So, in the paper we adopt K70 as a name for the machine. For protons the main limitation for the magnetic field level relates to the possibility of the practical realization of the machine central region. Calculations show that for magnetic field above 2.9 T it will be highly problematic to design the required center structure since it is almost impossible to install the spiral inflector infrastructure in the region: there is no room for potential connections to the inflector electrodes. The inflector diameter together with its RF shield is less than 25 mm for 2.9 T central magnetic field. The cyclotron magnetic system has 4-fold structure based on spiral sectors (Fig. 1). The valley axial gap 450 mm permits placement of 2 spiral RF cavities operating on the 2nd harmonic with frequency 88 MHz. The peak dee voltage of 30 kV is limited by consumption power in the system. The axial gap between the sectors reduces from 30 mm in the central region to 22 mm at the final radius. Parameters of the superconducting coil and required space around it for placement of the cryostat were selected looking at similar configurations of the successfully operating cyclotrons. The engineering current density in the coil is 75 A/mm^2 as result of this approach. The obtained eventually magnetic field distribution provides a sufficient axial focusing of the beam with axial betatron frequency being above 0.2 in the whole radial range (but the very center). The resulting diameter of the cyclotron is less than 2 m and its weight ~18 t.

† vsmirnov@jinr.ru.

ISBN: 978-3-95450-205-9 doi:10.18429/JACoW-Cyclotrons2019-THB02

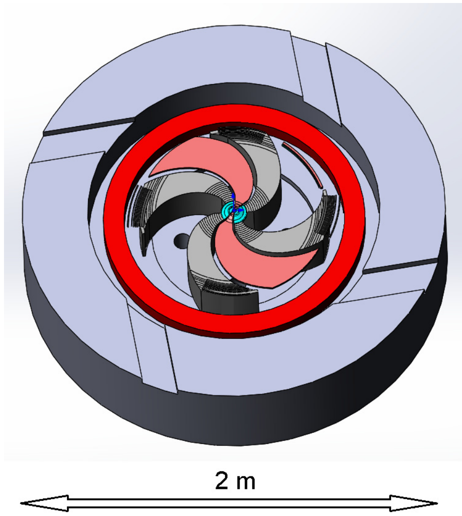

Figure 1: Cyclotron magnetic system.

The central region design permits both external and internal ion source applications. To change the mode of the operation the only dee tips should be replaced. The spiral inflector and internal PIG ion source are inserted axially to the working positions. The corresponding opening in the magnet return yoke and the pole are foreseen for both regimes. More detailed investigation of the beam dynamics was performed for operation with the internal ion source.

The central region design provides high efficiency of the beam transmission about 30% and good centering of the accelerated particle orbits with the amplitudes of the radial betatron oscillation being on average less than 1 mm in the whole working radial range. The cyclotron extraction system consists of electrostatic deflector with 110 kV/cm field strength and two passive magnetic channels. The first magnetic harmonic introduced by the channels will be compensated by corresponding magnetic elements installed just opposite the channels azimuthally. Besides the septum and anti-septum, the magnetic channels have also a set of the shimming plates to minimize the field perturbation in the region of the final internal orbits of the accelerated particles.

The beam extraction efficiency about 60% was obtained by the simulations. In compliance with the purpose of the study the only main characteristics of the cyclotron were defined for comparison to other designs without detailed optimization of the extraction system. The beam quality of 14 π·mm·mrad (horizontal emittance) and 1 π·mm·mrad (axial emittance) were obtained for the extracted beam. Despite of very small size of the spiral inflector (Fig. 2), the preliminary analysis shows that it is possible to converge to the technically realized construction of the unit. Installing a buncher to the axial injection line it is possible to reach about 30% beam transmission efficiency through the central region after carefully matching of the beam emittance to the acceptance of the cyclotron. Given adopted limitation on the beam loss power to be below 1 kW [3] and optimistic extraction efficiency of ~87%, the internal beam intensity should be below 120 μA, i.e., extracted beam current will be 100 μA. The extraction efficiency about 90% could be obtained using a set of phase slits in the central region. In the internal ion source regime, the beam intensity at injection can exceed 60 μA. Extracted beam current in this case can reach ~14 μA.

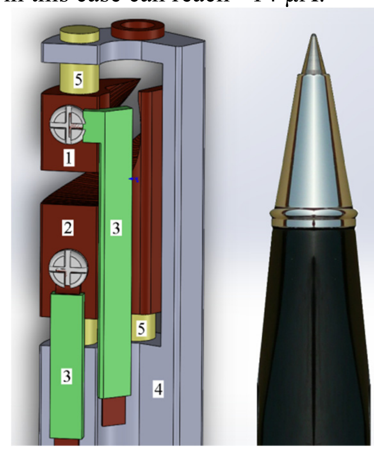

Figure 2: Structure of spiral inflector: 1 – upper electrode, 2 – lower electrode, 3 – potential connections, 4 – electrode fixation, 5 – ceramic isolators.

H_2^+ CYCLOTRON

As an example of H_2^+ accelerator for obtaining 70 MeV proton beam the superconducting cyclotron K280 [4] can be considered. The facility is planned as an injector of carbon beam to hadron therapy complex [5]. The cyclotron has 3-fold magnetic structure with the central magnetic field of 2.64 T (Fig. 3). All valleys are occupied by the spiral cavities operating on 3rd RF harmonics with frequency 60.8 MHz and peak voltage 90 kV. The cyclotron has uniform 52 mm gap between the sectors, which is sufficient for placement all elements of the extraction system. The engineering current density in the coil is selected to be 70 A/mm^2. Diameter of the cyclotron is 3m and its magnet weight is ~70 t.

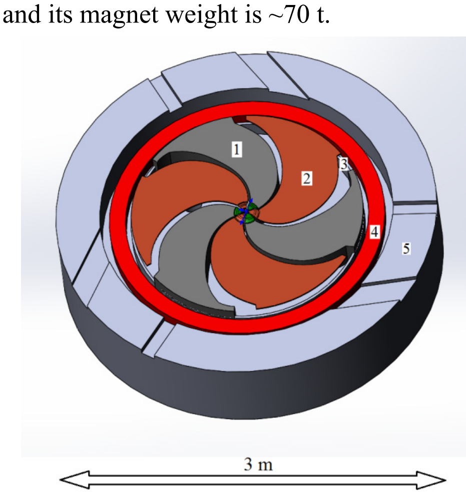

Figure 3: Cyclotron K280: 1 – sector, 2 – dee, 3 – valley shim, 4 – coil, 5 – yoke.

As an external ion source, ECRIS SUPERNANOGAN [6] can be used for production H_2^+ ions with intensity above 1 emA at maximal extraction voltage of 30 kV. The ion source is placed 3 m above the cyclotron median plane.

ISBN: 978-3-95450-205-9 doi:10.18429/JACoW-Cyclotrons2019-THB02

The main magnet fringe field is sufficiently small at the position of the source. The designed low energy beam transport line (LEBT) connects the source with the cyclotron. After passing through the horizontal section of the LEBT, where the analyzing magnet focuses ions in both transverse directions, the beam enters the axial injection line. The beam intensity in the LEBT can be measured by a Faraday cup, and the beam adjustment can be performed by the electrostatic steerer. There are also three room-temperature 200-mm solenoids for transverse focusing of the beam. The axial magnetic field produced by the cyclotron magnet in the injection line is rather high, leading to strong over-focusing of the particles. This induces large angular spread in the beam. The effect can be mitigated with the help of the solenoid closest to the main magnet. The solenoid field direction is opposite to that of the cyclotron. In the line the sine-wave buncher ensures longitudinal focusing of the injected beam.

The tune diagram shows that there is no crossing of dangerous resonances in the acceleration range except the very last turns, where the following resonances occur: parametric resonance ($2Qz=1$) and coupling resonances of the third and fourth order ($Qr-2Qz=0$, $2Qr+2Qz=3$, $2Qr-2Qz=1$).

The central region structure was carefully optimized to provide the best axial focusing and centering of the initial turns in the cyclotron. The spiral inflector design with its RF shielding allows sufficient space for the inflector potential leads. In compliance with the transverse size of the beam the inflector aperture was chosen to be 4 mm. The electrical radius of the inflector is 20 mm for potential at the electrodes of ±6 kV. The magnetic radius of the inflector is 13.4 mm. The inflector itself moves into the cyclotron axially to its working position inside the RF shielding attached to the dummy dees. There is a possibility of rotating the inflector inside the RF shield by several degrees for better matching of the injected beam to the central region acceptance. In the central region there are several posts attached to the dees and dummy-dees to provide sufficient scraping of the so-called “tails” from the injected beam distribution over its cross section and, simultaneously, to increase the rigidity of the unit structure (Fig. 4). The axial aperture available for the beam passage is 6 mm on initial turns.

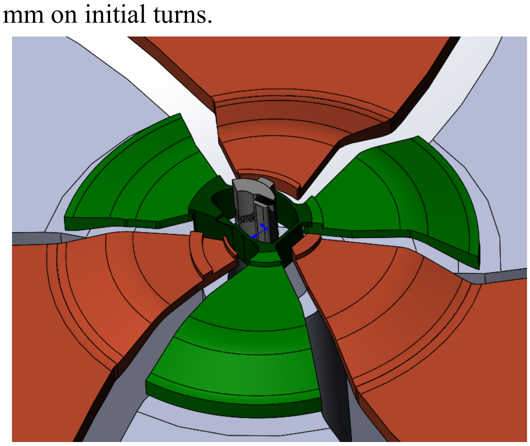

Figure 4: Central region structure of the K280 cyclotron.

The high-efficiency extraction of the proton beam can be obtained by stripping the H_2^+ ions on the foil placed inside the vacuum chamber of the accelerator. The method permits varying the output beam energy in a limited range. Calculation the energy variation by changing the stripping foil position shows a drastic difference in the trajectories corresponding to various energies with no point in the cyclotron magnet yoke where these tracks belonging to different energies converge. For example, protons of relatively low energy of 35-40 MeV make two turns in the vacuum chamber, and their trajectories in the magnet yoke are fairly separated from the corresponding paths of protons with higher energy, namely, 60-70 MeV (Fig. 5). Also, strong dependence of the beam axial envelope on the stripping foil position takes place. This effect limits the permissible energy variation of extracted protons by above mentioned 60-70 MeV range.

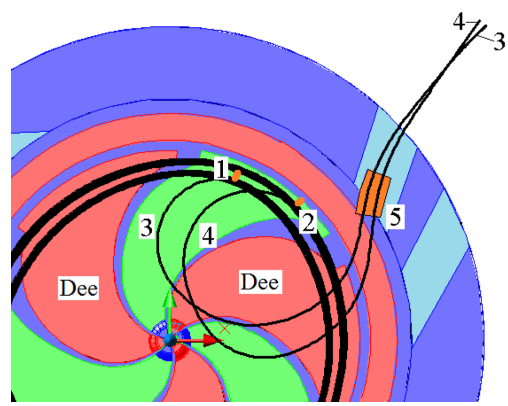

Figure 5: Extraction protons from K280 by stripping foil: 1 – the foil location for extraction of 60 MeV protons, 2 – the foil location for extraction of 70 MeV protons, 3 – trajectory of 60 MeV protons, 4 – trajectory of 70 MeV protons, 5 – bending magnet for steering proton beams with output energy in the range 60-70 MeV.

3D simulation of the proton extraction by stripping H_2^+ ions shows that the axial size of the H_2^+ beam on the stripping foil reaches ~6 mm. The axial focusing of the proton beam downstream the stripping foil is not sufficient. As a result, the axial envelope of the proton beam increases drastically to 30-50 mm at the exit of the magnet yoke (Fig. 6), the main reason for that being the axial over-focusing near the main coil. The improvement can come from installation of a combined-function-dipole in the yoke outlet window. In addition to the increased axial focusing, the dipole can provide also converging of 60 to 70 MeV proton paths to a common switching magnet for their transport downstream a single versatile set of the beam lines. Calculations show that the extraction efficiency by the stripping reaches ~95% in this case. Given the ion source H_2^+ ions intensity of 1 mA and accelerated particle current of 440 μA upstream the stripping foil, the output proton beam current can reach ~800 μA. Calculated horizontal and axial emittances of the output beam are 30 and 20 π·mm·mrad correspondingly with energy spread of ±0.67%.

ISBN: 978-3-95450-205-9 doi:10.18429/JACoW-Cyclotrons2019-THB02

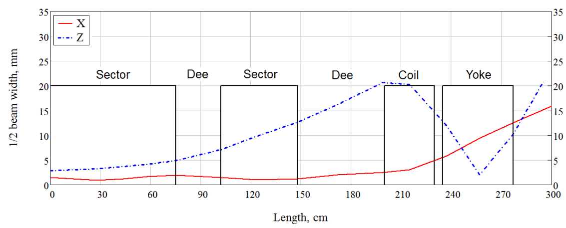

a)

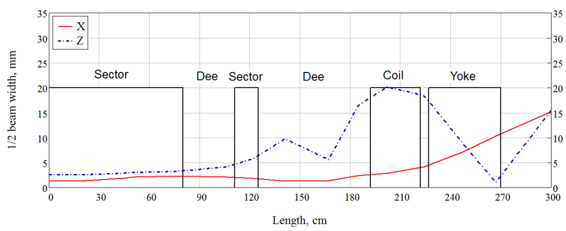

b)

Figure 6: Extracted beam envelopes with energy of 70-MeV (a) and 60-MeV protons (b).

CONCLUSIONS

Application of high magnetic fields in a superconducting cyclotron for final energy of 70 MeV does not permit acceleration of H^- ions. So, protons or H_2^+ ions can be used instead. Selection the proton as an accelerated particle has some disadvantages (no possibility of the output energy variation, lower extraction efficiency) compared to H^- acceleration variant. But the size and weight of the proton superconducting cyclotron are smaller by 2-3 times and by 7-10 times correspondingly (Table 1). Also, the proton cyclotron can provide a good quality of the output beam, which is in compliance with its possible medical application. A superconducting cyclotron for H_2^+ ions acceleration with K-value of 280 MeV is 4 times heavier compared to corresponding superconducting proton cyclotron at the same energy of the output beam. But even in this case the cyclotron is by several times lighter than a room-temperature machine for the same application. Also, usage of the stripping foil for beam extraction will ensure a number of positive features mentioned in the text of the paper. Besides, the K280-variant of the cyclotron can be designed with 4-sectors magnetic structure with even higher magnetic field. This will reduce the size of the machine even more. Another optimization would be a decreasing the acceleration voltage leading to lower RF consumption power. Application of 2 instead of 3 dees also can be considered to make the design simpler and more reliable. All calculations conducted for the design of the cyclotrons were performed for realistic configurations that were as much as possible close to the existing and successfully operational facilities. In this context it is worthwhile to mention selection of moderate engineering current density in the main coil of the cyclotron magnet, assignment of sufficient space for cryostat and extraction system elements et al.

REFERENCES

[1] IBA, https://www.iba-radiopharmasolutions.com/products/cyclotrons#cyclone-70

[2] V. Sabaiduc *et al.*, "BEST 70P cyclotron factory test", in *Proc. IPAC'15*, Richmond, VA, USA, 2015. doi.org/10.18429/JACoW-IPAC2015-THPF003

[3] H. Blosser, D. Johnson, D. Lawton, F. Marti, R. Ronningen, and J. Vincent, "A compact superconducting cyclotron for the production of high intensity protons", in *Proc. PAC'97* Vancouver, BC, Canada, Canada, May 1997, pp. 1054-1056.

[4] V. Smirnov, S. Vorozhtsov, F. Taft, and T. Matlocha, "Superconducting 70 AMeV cyclotron-injector for a hadron therapy complex", *Nucl. Instr. and Meth., Sect. A*, vol. 934, Apr. 2019. doi:10.1016/j.nima.2019.03.099

[5] V. L. Smirnov and S. B. Vorozhtsov, "Feasibility study of a cyclotron complex for hadron therapy", *Nucl. Instr. and Meth., Sect. A*, vol. 887, pp. 114–121, Apr. 2018. https://doi.org/10.1016/j.nima.2018.01.046

[6] Supernanogan, http://www.pantechnik.com

Table 1: Summary Table of Parameters

Description	K70	K280	IBA Cyclone 70	BEST 70	NIIEFA C80
Ion	p	H_2^+	H^-	H^-	H^-
Energy, MeV	70	60-70	30-70	35-70	40-80
Beam intensity, µA	100	800	750	700	200
Injection type	Cusp/PIG	ECR	Cusp	Cusp	Cusp
Dimensions: D×H, m	2.0/1.0	3.0/1.4	4.0/3.8	4.5/1.7	5.7/2.6/3.4
Weight, t	18	70	140	195	250
Central magnetic field, T	2.89	2.64	1.0	0.95	1.35
Extraction type	ESD	Stripping	Stripping	Stripping	Stripping
RF voltage	30	90	50	70	60
Country	Russia	Russia	Belgium	Canada	Russia

ISBN: 978-3-95450-205-9 doi:10.18429/JACoW-Cyclotrons2019-THB03

CONCEPTUAL DESIGN OF TR100+: AN INNOVATIVE SUPERCONDUCTING CYCLOTRON FOR COMMERCIAL ISOTOPES PRODUCTION*

Y.-N. Rao†, R. Baartman, I. Bylinskii, T. Planche, L. G. Zhang[1], TRIUMF, Vancouver, Canada
[1]also at Huazhong University of Science and Technology, Wuhan, China

Abstract

Utilizing dedicated cyclotrons to produce medical isotopes is an arising technology in hospitals across Canada. An excellent example is that in Jan. 2015, the CycloMed99 team, led by TRIUMF, demonstrated a breakthrough in producing the world's most highly used medical isotope, Tc-99 m, on existing medical cyclotrons. Now we propose to design an innovative H_2^+ superconducting cyclotron TR100+ for the production of commercially valuable radioisotopes. This project will be aiming at proton energy of 70 – 150 MeV and proton current of ~800 µA, since (i) cyclotron in this energy range is not developed world-wide; (ii) in this energy range numerous highly interested and increasingly demanded radionuclides can be produced, e.g. Sr-82 and Ac-225. Our machine shall be designed to accelerate H_2^+, by injection from external ion source and extraction by stripping. This shall allow to extract proton beam of variable energies with very high extraction efficiency, thus allow to reduce activation caused by beam losses. The basic parameters of our machine and simulations of stripping extraction will be presented in this paper.

OVERVIEW

There are two main types of commercial medical cyclotrons [1]: (i) those for medical isotope production, and (ii) those for proton therapy. The former are typically high-current low-energy (1 mA, 7 – 30 MeV) H^- machines, while the latter are low-current high-energy (1 µA, 200 – 400 MeV) proton machines. There are several well-established vendors [1] in each of these markets: ACSI, GE, Varian, IBA, Siemens, Sumitomo and Still River; and emerging players such as BEST and CIAE (China). From this overview it becomes apparent that 7 – 30 MeV and 200 – 250 MeV medical cyclotrons are well covered in the market by multiple strong players.

However, contrastingly, the 70 – 150 MeV range is not well represented; there being only few outliers at 70 and 100 MeV: the Best Cyclotrons 70P (in Legnaro, Italy) [2], the IBA C70 (in Nantes, France) [3], and CYCIAE-100 in Beijing [4]. All these are accelerating H^- to extract protons by stripping, in which a dominant factor limiting the beam intensity is the beam losses due to the electromagnetic stripping of the second electron during acceleration. To reduce activation of the accelerator system, caused by the resulting beam spills, the losses have to be kept low. This requires the magnetic field to be lower, the higher the machine energy, which in turn leads to the larger magnet size. Since the cost of the cyclotron rises with magnet size, the commercial H^- cyclotron balances acceptable losses versus size, ending up at a compromised energy of ~70 MeV [5].

Another option is to use protons directly, without stripping. But this extraction method requires well separated turns, which is achieved with a large radius of the machine and a high accelerating voltage, making the cyclotron very expensive. Proton machines for the therapy (up to ~1 µA extraction) can hardly reach an extraction efficiency above 80% [6, 7]. If they were for high current, they would not be able to run, because too much beam would get lost at extraction, exacerbating the neutron production and machine activation problem.

To overcome these limitations and reliably deliver high current (≥500 µA) proton beam on target, we intend to accelerate H_2^+, two protons bound by a single electron, with a binding energy much larger than the H^- case. This implies that a much higher magnetic field can be used in a compact cyclotron with significantly reduced magnet size and consequently lower costs.

In this energy range up to 150 MeV, numerous highly interested and increasingly demanded radio-nuclides can be produced, either as parent nuclei for generator use, or directly as an active pharmaceutical ingredient. For example, the two isotopes Actinium-225 and Bismuth-213 are anticipated to drive radiopharmaceutical developments for the researches of cancers (Melanoma, Prostate and Pancreatic) conducted at BCCA in Canada, and to expand in the world leading radionuclide imaging program. Another example, the isotope Strontium-82 (Sr-82) is used exclusively to manufacture the generators of Rubidium-82, which is the most convenient Position Emission Tomography (PET) agent in myocardial perfusion imaging. Over the last years, the demand for the Sr-82 from pharmaceutical industry has been growing, and such a demand is anticipated to continue to grow for the next 20 years. Other commercially relevant medical isotopes that can be produced from proton beams in the energy range 70 – 150 MeV include At-211, Ti-45 and Ra-223. With additional development, access to isotopes such as Ra-224, Pb-212 and Bi-212 will be possible. To date, virtually all Sr-82 is produced at large research facilities which are primarily used for scientific researches, and in most cases is partially subsidized. Using dedicated cyclotrons to produce medical isotopes is an arising technology in hospitals across the world.

Commercial superconducting (SC) cyclotrons are becoming ever more compact due to the introduction of successive

* TRIUMF receives funding via a contribution agreement through the National Research Council of Canada.
† raoyn@triumf.ca

ISBN: 978-3-95450-205-9 doi:10.18429/JACoW-Cyclotrons2019-THB03

generations of conductor technology for the magnet windings. The application of superconducting design has two evident advantages [6]. Firstly, the superconducting coils allow the machine to have extremely good reproducibility and linearity in the magnetic field with respect to the changes in the coil current, because the field-shaping iron and yoke get completely saturated in a strong field (> 2 T) of the coils; there is barely hysteresis effect. The magnetic field is dominated by the coil current. Secondly, the power consumption is at least 10 times less, and the machine's total weight is 2 times lighter than any normal-conducting cyclotron [7, 8] of identical energy. However, compactness is not necessarily a virtue. There should be a cost optimum in a design for a medical isotope production machine that adopts more mature and (comparatively) lower field conductor technology.

Since 20 years ago the idea of H_2^+ cyclotron was initially proposed [9, 10], there were not many studies devoted on this until the SCENT project [11], the IsoDAR and DAEδALUS Projects [12, 13] were brought up. The former is for an extraction energy of 260 MeV for proton therapy, while the latter is for energy up to 800 MeV/n for neutrino physics research. Although none of these machines has been built yet, it's conceived that the H_2^+ cyclotron will come into the market within the next few years because of its advantages.

BASIC DESIGN CONCEPT

The scale of our machine is set by the proton energy (up to 150 MeV), the superconducting magnet technology, the high-current (up to 2 mA) H_2^+ external ion source, the stripping of H_2^+ to extract protons (up to 800 µA), and the multiple external production targets, etc. A conceptual design was carried out for the superconducting cyclotron. It's a 4 sector compact machine of 3.8 m diameter, 2.0 m height, and 4 deep-valleys. The two opposite valleys accommodate rf cavities and the other two house diagnostic elements. Two RF cavities operating in 4th harmonic at a fixed frequency of ~97 MHz, accelerate the H_2^+ with a maximum dee voltage of 120 kV. Table 1 summarizes the main parameters of the cyclotron.

MAGNETIC FIELD DESIGN

The magnet was modelled with OPERA-3D (see Fig. 1). Using the deep-valley concept, the poles are shaped to achieve an adequate axial focusing and good isochronism, by azimuthal profiling of the sectors as well as by grooving and shimming of the sectors. The sector's azimuthal width varies from ~ 40° in the center to ~ 46° at outmost edge, while the spiral angle changes from ~ 20° to ~ 70° at maximum. The pole gap maintains at ~4.5 cm. The magnet is energized by a pair of superconducting coils, symmetrically placed above and below the median plane. These coils operate at current density of 46 Amp/mm^2, creating an average magnetic field of 3.1 T in the centre, up to 3.7 T at radius of ~1.0 m.

Figure 2 shows the contour of the magnetic flux density in the median plane. The field isochronism is better than $\pm 5 \times 10^{-4}$ over the acceleration region (see Fig. 3). The phase excursion is less than ±30° throughout, assuming a peak energy gain of 0.4 MeV per turn (see Fig. 4).

Table 1: TR100+ Main Parameters

Parameters	**Values**
Particle accelerated	H_2^+
Injection energy (keV/n)	25
Extraction energy (MeV/n)	100−150
Number of sector	4
Pole radius (cm)	106.5
Hill gap (cm)	4.5
Mean magnetic field (T)	3.1−3.7
Max. magnetic field (T)	4.5
Injection scheme	Axial + external ion source
Extraction	*p* by stripping extraction
Coils	2 superconductors
Max. current density (A/mm^2)	46
Number of cavities	2
RF harmonic number	4
RF frequency (MHz)	~97

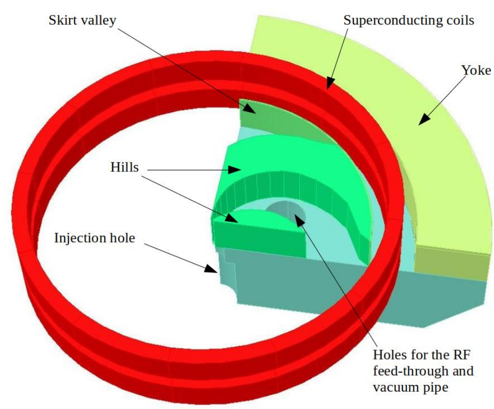

Figure 1: 1/8 OPERA model of the main magnet, mainly composed of the pole with spiral sector, skirt valley, yoke and superconducting coil (illustrated in various colors). The skirt valley serves to compensate for the isochronous field in the extraction region as well as to create a positive field gradient in the valley for the beam extraction.

The optimized magnetic field provides a vertical tune rapidly reaching above 0.2 and not crossing the coupling resonance $\nu_r - \nu_z = 1$. See Fig. 5.

EXTRACTION STUDIES

We extract protons by stripping of H_2^+. Placing the stripper properly (on the hill) can't only pull the protons to the outside of cyclotron in a decent path, but also deliver different energy protons to the same cross-over point in one turn. As an example, Fig. 2 shows the extraction trajectories of 140 and 150 MeV/n protons, where the radial distance is greater than 5.5 cm from the machine centre. Further studies (involving the centre region modelling) are needed to find out whether or not this is sufficient for the proton beam to get around

ISBN: 978-3-95450-205-9 doi:10.18429/JACoW-Cyclotrons2019-THB03

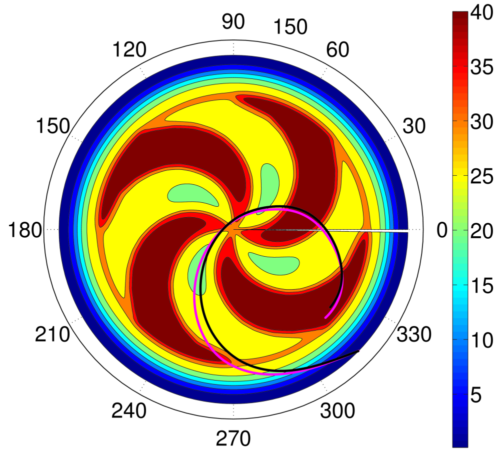

Figure 2: The contour of $B_z(r,\theta)$ in the median plane, and the extraction trajectories of 150 MeV (magenta) and 140 MeV (black) protons after being stripped. Both trajectories arrive at the same location where the field falls off to zero. The maximum field strength is ~45 kG on the hill.

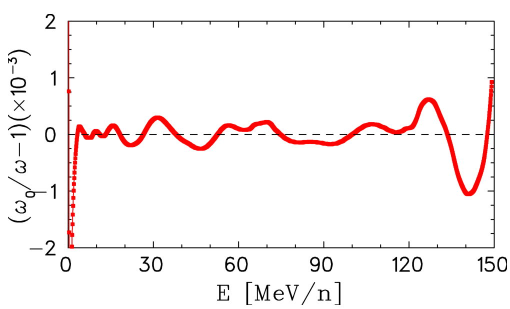

Figure 3: The isochronism parameter $(\omega_0/\omega-1)$ vs. energy, where ω_0 and ω are resp. the nominal rf angular frequency and the revolution angular frequency of particle along the SEO in the modeled magnetic field map.

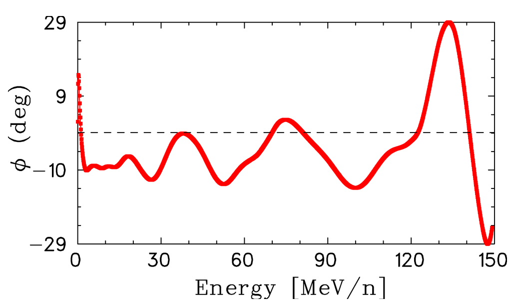

Figure 4: The rf phase vs. energy, showing that the excursion stays within ±30° over the entire energy range, assuming a peak energy gain of 0.4 MeV per turn.

the centre posts. Other lower extraction energies could be delivered from the other extraction ports.

Multi-particle simulation was done to calculate the extraction envelope, assuming a circulating emittance of 0.54 π.mm.mrad (4rms, normalized). Before entering the fringe field, the beam radial size is smaller than 0.25 cm while the axial size is smaller than 1.25 cm (2rms), well within the pole gap. However, after entering the fringe field,

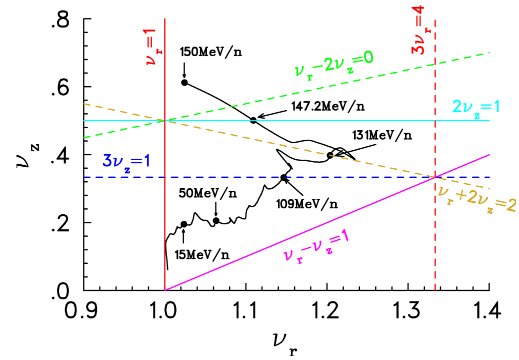

Figure 5: The tune diagram. Note that the coupling resonance $\nu_r - \nu_z = 1$ is preferably avoided; however the half-integer resonance $2\nu_z = 1$ occurs at ~147.2 MeV/n.

the radial size gets defocused continuously while the axial size gets over-focused (see Fig. 6). This suggests that magnetic channels need to be configured to compensate for these.

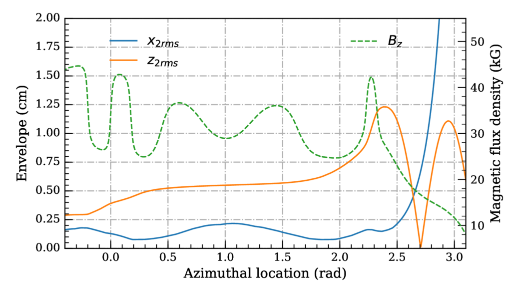

Figure 6: The axial (orange, solid) and radial (blue, solid) beam sizes (2rms) of 150 MeV protons. Also shown is the magnetic field strength along the extraction trajectory (green, dash).

INTENSITY LIMITATION

The acceleration process of H_2^+ in a compact cyclotron is similar to that of H^-: in both cases the space charge effects are strongest on the first turns. The intensity limit is due both to the vertical space charge tune shift and to the longitudinal space charge effect. Both effects give similar upper limits in the TR30 case [14]. The measurements for the TR30 demonatrated 1.0 mA beam current accepted under 5 mA injected dc beam. For the TR100+, we simply scale the expected current limit of H_2^+ using the formula (7) given in [14]:

$$\hat{I}_{max(vert)} = \beta \left(\frac{\nu_{z0} b_{max}}{R_\infty} \right)^2 \frac{I_0}{4}\,. \tag{1}$$

For the TR100+, we have $R_\infty \simeq 2.0$ m and I_0 twice as large as for the TR30. We assume $\nu_{z0} \sim 0.1$ and the same values of β as well as of the vertical aperture. These give ~ 40% of the space charge limit of TR30, that is, 400 μA H_2^+ expected from the cyclotron. This means 800 μA protons after stripping. However, this requires twice higher injection energy of H_2^+, that is, 50 keV. Also, to gain enough radius on the first 2 turns, it requires to maintain the energy twice as large on these turns because $\beta = \sqrt{2E/mc^2}$. So the rf voltage has to be twice as high.

ISBN: 978-3-95450-205-9 doi:10.18429/JACoW-Cyclotrons2019-THB03

BEAM LOSSES

We concentrate on two types of H_2^+ beam loss: electromagnetic dissociation (Lorentz stripping) and interactions with residual gas. The binding energy of the last electron is 2.75 eV, ~ 3.6 times larger than the binding energy in the H^- case. This bind can be dissociated by the electric field, generated from the motion of the ion in the magnetic field. The equivalent electric field in the rest frame of the ion is represented as

$$E = 3\beta\gamma B\,, \tag{2}$$

where B is the static magnetic field in Tesla, β and γ are relativistic factors of ion motion, and the electric field is given in MV/cm. At 150 MeV/n in a magnetic field of 3.5 Tesla, the electric field is 2.1 MeV/cm. The H_2^+ survival issue is complicated by the large number of stable vibrational states [15]. In terms of the calculations performed by Hiskes [16], ions in a vibrational state $\nu > 16$ will dissociate during acceleration; roughly 2% of the beam would be lost into the vacuum chamber.

The circulating ions can lose their orbital electron as they travel along the acceleration path due to interactions with the residual gas. The fractional beam particles which survive is given by [17]

$$\frac{N}{N_0} = \exp\left(-3.35\times 10^{16}\int \sigma_L(E)\,P\,dL\right)\,, \tag{3}$$

where P is the vacuum pressure in torr (3.35×10^{16} is the number of molecules/cm^3/torr), and L is the path length in cm. The cross section of electron loss is

$$\sigma_L(E) = 4\pi a_0^2\left(\frac{V_0}{V}\right)^2\frac{Z_t^2+Z_t}{Z_i}\,, \tag{4}$$

where V is the ion velocity, while V_0 and a_0 are the characteristic Bohr velocity and radius. Z_t and Z_i are the atomic number of the residual gas and of the incident ion respectively. We estimated the beam losses along the acceleration path. To achieve an amount of loss below 1.0% during the acceleraion, the vacuum has to be better than 1.0×10^{-7} torr.

CONCLUSION

An initial design was carried out to evaluate the feasibility of building a superconduting cyclotron to accelerate H_2^+ beam up to 150 MeV/n, by stripping extraction to deliver protons of 800 µA. The design goal seems to be feasible with the present technology. Next, the centre region and injection line will be studied. Further optimizations of the spiral shape of the sector and of the coils are needed to provide a better vertical focusing and to lower magnetic forces, taking into account the design of rf cavities to be operated at high voltage and high power. Moreover, some physics questions need to be answered about the vibrational state population of the beam coming from ion source.

REFERENCES

[1] P. Schmor, "Review of cyclotrons used in the production of radio-isotopes for biomedical applications", in *Proc. Cyclotrons'10*, Lanzhou, China, Sep. 2010, paper FRM2CIO01, pp. 419–424.

[2] V. Sabaiduc *et al.*, "New high intensity compact negative hydrogen ion cyclotrons", in *Proc. Cyclotrons'10*, Lanzhou, China, Sep. 2010, paper MOPCP017, pp. 81–83.

[3] J. Martino, "Arronax, a high intensity cyclotron in Nantes", in *Proc. Cyclotrons'07*, Giardini-Naxos, Italy, Oct. 2007, pp. 215–218.

[4] T. J. Zhang *et al.*, "Design & construction status of CYCIAE-100, a 100 MeV H^- cyclotron for RIB production", *Nucl. Instrum. Methods Phys. Res., Sect. B*, vol. 266, pp. 4117–4122, 2008. doi:10.1016/j.nimb.2008.05.021

[5] B. F. Milton, "Commercial compact cyclotrons in the '90s", in *Proc. Cyclotrons'95*, Cape Town, South Africa, Oct. 1995, paper C–01, pp. 99–106.

[6] H.-U. Klein *et al.*, "Design, manufacturing and commissioning of compact superconducting 250 MeV cyclotrons for proton therapy: A short report from the field", IEEE/CSC & ESAS European Superconductivity News Forum, Oct. 2007.

[7] Y. Jongen, "Review on cyclotrons for cancer therapy", in *Proc. Cyclotrons'10*, Lanzhou, China, Sep. 2010, paper FRM1CIO01, pp. 398–403.

[8] W. Beeckman *et al.*, "Preliminary design of a reduced cost proton therapy facility using a compact, high field isochronous cyclotron", *Nucl. Instrum. Methods Phys. Res., Sect. B*, vols. 56-57, pp. 1201-1204, May 1991. doi:10.1016/0168-583X(91)95131-V

[9] L. Calabretta and D. Rifuggiato, "Superconducting cyclotrons for acceleration of H_2^+", in *Proc. Cyclotrons'98*, Caen, France, Jun. 1998, paper J–02, pp. 665–668.

[10] L. Calabretta *et al.*, "High intensity proton beams from cyclotrons for H_2^+", in *Proc. PAC'99*, pp. 3288-3290, 1999.

[11] L. Calabretta *et al.*, "A novel superconducting cyclotron for therapy and radioisotope production", *Nucl. Instrum. Methods Phys. Res., Sect. A*, vol. 562, pp. 1009–1012, Jun. 2006. doi:10.1016/j.nima.2006.02.083

[12] M. Abs *et al.*, "Multi-megawatt DAEδALUS cyclotrons for neutrino physics", 2012. arXiv:1207.4895

[13] D. Winklehner, "Updated physics design of the DAEδALUS and IsoDAR coupled cyclotrons for high intensity H_2^+ beam production", 2017. arXiv:1708.06412

[14] R. Baartman, "Intensity limitations in compact H^- cyclotrons", in *Proc. Cyclotrons'95*, Cape Town, South Africa, Oct. 1995, paper H–02, pp. 440–445.

[15] H. Hus *et al.*, "Dissociative recombination of electrons with H_2^+ in low vibrational states", *Phys Rev Lett.*, vol. 60, pp. 1006-1009, Mar. 1988. doi:10.1103/PhysRevLett.60.1006

[16] J. R. Hiskes, "Dissociation of molecular ions by electric and magnetic fields", *Phys. Rev.*, vol. 122, pp. 1207-1217, May 1961. doi:10.1103/PhysRev.122.1207

[17] H.-D. Betz, "Charge states and charge-changing cross sections of fast heavy ions penetrating through gaseous and solid media", *Rev. Mod. Phys.*, vol. 44, pp. 465-539, Sep. 1972. doi:10.1103/RevModPhys.44.465

ISBN: 978-3-95450-205-9 doi:10.18429/JACoW-Cyclotrons2019-THB04

DEVELOPMENT OF A TRANSPARENT PROFILER BASED ON SECONDARY ELECTRONS EMISSION FOR CHARGED PARTICLE BEAMS

C. Thiebaux†, Y. Geerebaert, F. Magniette, P. Manigot, M. Verderi
LLR CNRS-Ecole polytechnique, Palaiseau, France
F. Haddad[1], C. Koumeir, F. Poirier, Cyclotron ARRONAX, Saint-Herblain, France
B. Boyer, E. Delagnes, F.T. Gebreyohannes, O. Gevin
IRFU-CEA, Université Paris-Saclay, Gif-sur-Yvette, France
G. Blain, N. Michel, N. Servagent, T. Sounalet
Laboratoire SUBATECH IMT Atlantique, Nantes, France
[1]also at SUBATECH, Nantes, France

Abstract

The PEPITES[1] project aims at realizing an operational prototype of an ultra-thin, radiation-resistant profiler able to permanently operate on mid-energy (O (100 MeV)) charged particle accelerators. Initially motivated by the needs of protontherapy, the proposed development may have a range of applications that is well beyond the foreseen framework.

INTRODUCTION

Beam profiling during patient treatment in hadrontherapy requires ultra-thin monitors to preserve the high beam quality. For detectors upstream in the line, a material budget as low as ~15 µm water-equivalent is needed. Besides, the current trend of dose escalation to treat highly resistant tumors implies challenging requirements to the monitor in terms of radiation hardness and dynamic range.

To fulfil these requirements, PEPITES, a new type of transparent beam profiler (< 10 µm water-equivalent thickness (WET)) is under development. It will equip the beam line of the ARRONAX cyclotron [1] and will be used daily to monitor the beam during radiobiological and preclinical experiments [2]. The profiler will measure the lateral beam shape in a broad range of energy (15-70 MeV) and a wide range of intensity (100 fA-10 nA), for alpha, proton and deuteron particles.

PRINCIPLES

PEPITES uses secondary electron emission (SEE) for the signal as it requires only a minimal thickness of material (~10 nm); very linear, it also offers a great dynamic. The SEE yield is proportional to the dE/dx of the beam particles [3, 4] and is independent of the beam intensity up to current far beyond expected needs both for medical use and radiobiology needs. The lateral beam profile is sampled using segmented electrodes, constructed by thin film methods. Gold strips, as thin as the electrical conductivity allows (50 nm), are deposited on an as thin as possible insulating substrate which, in contrast with conventional systems like ionization chambers, are free from mechanical constraints and can be as thin as achievable. Aromatic polyimides (PI), such as Kapton® or CP1™, are chosen as polymer substrate due to their insulating properties and resistance to radiation [5]. When crossing the gold, the beam ejects the electrons by SEE, the current thus formed in each strip allows the sampling.

The thinness of the monitor disturbs very little the incident beam, which can then be delivered to the patient while keeping the profiler in the line, ensuring continuous monitoring. Also, it makes the energy deposit very small allowing the monitor to tolerate higher currents than existing systems without suffering from overheating problems. Besides, the absence of mechanical efforts on the membranes makes radiation damages of less consequence than with classical systems like ionization chambers allowing to extend the operation duration of the system.

Prototype Layout

The layout of the prototype is shown in Fig. 1. It will consist of four electrodes: two segmented cathodes each facing an anode (with a 15 mm gap) biased at 100V to ensure the collection of secondary electrons emitted by the strips. The four electrodes are made of 50 nm thick gold deposited by chemical vapor phase on polymer membranes: 32 strips for cathodes and fully metallized anodes. The membranes are made of 1.5 µm thick CP1™, a colorless polyimide developed by the NeXolve company [6]. Initially developed for solar sails, its availability in very small thickness and the presence of aromatic cycles in its structure, thus making it extremely resistant to radiation, make it an element of choice for the construction of the detector.

The profiler is divided into two mechanically independent blocks for the measurements of the beam position and lateral shape in the two directions (X and Y). The signals from the strips can be rather low as resulting from SEE (about 10% yield) and spreading of the beam over the strips. A dedicated low-noise Application Specific Integrated Circuit (ASIC) chip being developed at CEA

† thiebaux@llr.in2p3.fr
[1]Profileur à Electrons secondaires Pour Ions ThérapeutiquES

ISBN: 978-3-95450-205-9 doi:10.18429/JACoW-Cyclotrons2019-THB04

will read independently each strip present on each of the two blocks. The whole system will operate in the vacuum of the beam line and will be put online and offline by a translation movement device.

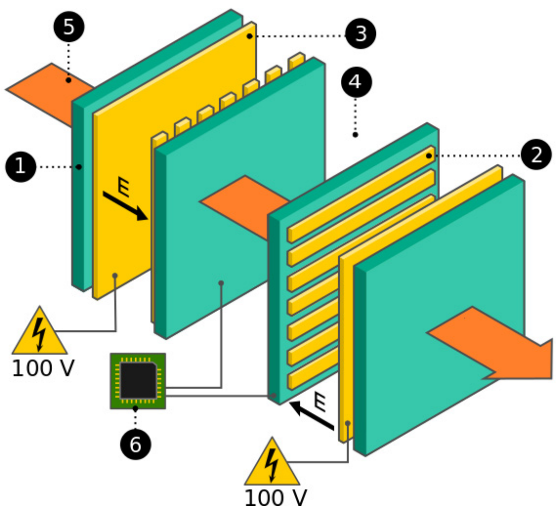

Figure 1: Schematic layout of PEPITES prototype. CP1™ membranes (1) sustain 50 nm thick gold strips (2) or are fully metallized (3). They stand in vacuum (4) where the beam (5) crosses the strips and produce secondary electrons. The signals coming from each strip are read by a dedicated readout chip (6). The final prototype will be made of 32 strips cathodes (2).

BEAM TESTS AND RESULTS

The technique was validated at ARRONAX with 68 MeV proton beams for intensities from 100 fA to 10 nA [7]. SEE is being characterized up to 100 nA at ARRONAX and medical energies (70-230 MeV) at Orsay Protontherapy Center (CPO – Institut Curie).

Several irradiation campaigns were conducted to assess the radiation resistance of the various materials and components of the detector. We undertook to irradiate several samples with gold strips on CP1™. The irradiations were done with the samples in vacuum, to mimic the real conditions of the final monitor.

Doses of 10^8 Gy and 10^9 Gy were delivered at LSI ("Laboratoire des Solides Irradiés", Ecole polytechnique) with 2 MeV electrons beams with current up to 25 µA, irradiating a surface of 1 cm of diameter on the sample. For the highest dose, the irradiation duration was 25 hours. Only the sample receiving the highest dose showed a light brown coloration of the CP1™ side without geometrical distortion of the sample. That observed effect is far to impact the integrity of the system, meaning that even higher doses could be tolerated.

We irradiated two samples at the CSNSM ("Centre de Sciences Nucléaires et de Sciences de la Matière", Orsay, France): one received a 10^8 Gy dose with 2 MeV protons, with a beam current of 100 nA during 90 minutes on a surface of about 1 cm^2, and a second was irradiated with 200 keV protons entering from the CP1™ side, so that protons stopped at the CP1™-gold interface in order to stress this interface to eventually favor gold delamination. In this context, where protons can stop into the material, nuclear recoil effects become important. Such effect should be rather aggressive on the material structure, displacing atoms, and would then mimic nuclear interaction effects that would also break the structure by destroying atoms. As a result, no significant effect was seen on the two irradiated samples.

Potential radiation induced permanent damages on polymeric substrates were specifically studied at ARRONAX [8]. Kapton® was considered on a first step and irradiated with 68 MeV proton beams. Both dynamics and permanent damages were observed and characterized using UV-Vis spectroscopy and scanning electron microscope. The permanent damages have occurred due to the irradiation with a high level of fluency (~7×10^{15} H^+/cm^2). Nevertheless, it should be noted that this high fluency level corresponds to several years of detector radiations exposure in a proton therapy center and opens the possibility to operate the PEPITES detector on a long-term basis. The next step is to characterize the damage of an irradiated CP1™ membrane with and without a deposited nanometric gold layer. The conductivity measurements will also be performed during and after irradiation. It will provide crucial information concerning the impact of the electrical properties evolution of CP1™ on the PEPITES detector performance.

FUTURE AND PLANS

Additional studies will be conducted on potential radiation induced damages on CP1™ at very high doses.

A demonstrator with dedicated electronics will be installed at ARRONAX and used routinely. It will be placed at the end of the beam line and will require an adaptation of this line in order to accommodate the detector. The performances of the system and its behavior over time will thus be characterized.

CONCLUSIONS

We propose a new type of beam profiler, PEPITES, using secondary electron emission. Build with thin film techniques and using very thin materials, the detector has WET of less than 10 µm. Studies of radiation induced damages have shown than the detector integrity will remain up to dose far beyond the medical yearly needs.

ACKNOWLEGMENTS

This project is funded, in part, by the French National Agency for Research (ANR), France (ANR-17-CE31-0015) and the labex P2IO. It has been also, in part, supported by an ANR grant called "Investissements d'Avenir", Equipex Arronax-Plus (ANR-11-EQPX-0004), Labex IRON (ANR-11-LABX-18-01) and ISITE NExT (ANR-16-IDEX-0007).

ISBN: 978-3-95450-205-9 doi:10.18429/JACoW-Cyclotrons2019-THB04

REFERENCES

[1] F. Poirier *et al.*, “Studies and upgrades on the C70 Cyclotron Arronax”, in *Proc. 21th Int. Conf. on Cyclotrons and their Applications (Cyclotrons'16)*, Zurich, Switzerland, Sep. 2016, pp. 235-237. doi:10.18429/JACoW-Cyclotrons2016-TUD02

[2] C. Koumeir *et al.*, “The radiobiological platform at Arronax”, *Radiat. Prot. Dosim.*, vol. 183, no, 1-2, pp. 270-273, 2019. doi:10.1093/rpd/ncy301

[3] E. J. Sternglass, “Theory of secondary electron emission by high-speed ions”, *Phys. Rev.*, vol. 108, no. 1, pp. 1-12, Oct. 1957. doi:10.1103/PhysRev.108.1

[4] J. Chou, “Transport theory for kinetic emission of secondary electrons from solids by electron and ion bombardment”, *Nucl. Instrum. Methods*, vol. 170, no. 1, pp. 317-320, 1980. doi:10.1016/0029-554X(80)91032-0

[5] E. A. Plis *et al.*, “Review of radiation-induced effects in Polyimide”, *Appl. Sci.*, vol. 9, no. 10, May 2019. doi.org/10.3390/app9101999

[6] https://www.nexolvematerials.com

[7] B. Boyer et al., “Development of an ultra-thin beam profiler for charged particle beams”, Nucl. Instrum. Methods Phys. Res., Sect. A, vol. 936, pp. 29-30, 2018. doi:10.1016/j.nima.2018.09.134

[8] S. Elidrissi-Moubtassim et al., “Exploring radiation hardness of PEPITES, a new transparent charged particle beam profiler”, presented at the 13th European Conference on Accelerators in Applied Research and Technology (ECAART13), Split, Croatia, May 2019, unpublished.

ISBN: 978-3-95450-205-9 doi:10.18429/JACoW-Cyclotrons2019-THC01

SHE FACTORY: CYCLOTRON FACILITY FOR SUPER HEAVY ELEMENTS RESEARCH

S. N. Dmitriev, Yu. Ts. Oganessian, G. G. Gulbekyan, I. V. Kalagin†, B. N. Gikal, S. L. Bogomolov, I. A. Ivanenko, N. Yu. Kazarinov, G. N. Ivanov, N. F. Osipov, S. V. Pashchenko, M. V. Khabarov, V. A. Semin, A. V. Yeremin, V. K. Utyonkov
Joint Institute for Nuclear Research, Flerov Laboratory of Nuclear Reactions, Dubna, Russia

Abstract

The synthesis of heavy and the heaviest elements and the study of their nuclear and chemical properties are of highest priority in the basic research programme of the Flerov Laboratory of Nuclear Reactions of the Joint Institute for Nuclear Research in Dubna (FLNR JINR). The synthesis of super heavy elements (SHE) with atomic numbers 113-118 has been achieved in the ^{48}Ca-induced reactions. The seventh period of the Periodic Table has been completed. In accordance with the development program, the first in the world SHE Factory was built at the Laboratory on the basis of the new DC280 cyclotron which was commissioned in 2019. DC280 has to provide intensities up to 10 pμA for ions with atomic masses over 50. The main task of the Factory is the synthesis of new chemical elements with atomic numbers 119 and higher, as well as a detailed study of the nuclear and chemical properties of previously discovered super heavy elements. The Factory are being equipped with target materials, new separators and detectors for the study of the nuclear, atomic and chemical properties of the new elements.

INTRODUCTION

Since 1998 priority experiments on synthesis of new superheavy elements (SHE) with atomic numbers of 114-118 in reactions of ^{48}Ca ions with actinide targets (^{242,244}Pu, ^{243}Am, ^{245,248}Cm, ^{249}Bk, ^{249}Cf) have been carried out at the FLNR JINR on the U400 accelerating complex. Over 50 new isotopes of elements 104 to 118 with maximum neutron excess were for the first time produced and their decay properties were determined in these investigations. The International Unions of pure and applied physics (IUPAP) and chemistry (IUPAC) recognized the priority of Dubna in the discovery of elements 114-118. The seventh period of the Periodic Table has been completed. The discovery of the new domain (island) of stability and the very fact of existence of SHE have posed a number of new questions associated with fundamental properties of nuclear matter. Can even heavier nuclei exist? Is the "Island of Stability" of SHE the last one on the Chart of the Nuclides? Can the superheavy nuclei be formed in the process of nucleosynthesis like those stable and long-lived nuclei in the groups of Pt, Pb, and U-Th found in Nature? What is the limit of Mendeleev's Table? How much are the chemical properties of SHE similar to those of their lighter homologues? Direct synthesis of elements with Z > 118 in fusion reactions means using projectiles heavier than Ca, since the capability of high-flux reactors to produce target material is limited to Cf isotopes. It is expected that production cross sections of nuclei with Z = 120 in the reaction ^{54}Cr+^{248}Cm and nuclei with Z = 119 via ^{50}Ti+^{249}Bk will be about ten times lower than those of production of ^{294}Og in experiments with ^{48}Ca. For more detailed studying nuclear - physical and chemical properties of SHE it is necessary significantly increasing efficiency of experiments [1]. For the solution of this task the first in the world Factory of superheavy elements (SHE Factory) was created at the FLNR JINR in 2019.

Figure 1: Building of SHE Factory.

SHE FACTORY

Creation of the SHE Factory was associated with developing the FLNR experimental basis in several directions. These directions are:

- creation of the new powerful accelerator of stable and long-living isotopes with mass range A = 4-238 with intensity up to 10 pμA for A ≤ 50 and energy up to 8 MeV/nucleon;
- construction of a new experimental building and infrastructure for placing the accelerator with five channels for transportation of beams to 3 experimental halls (total area up to 1000 m^2), equipped with systems of shielding and control matching the class two of operations with radioactive materials;
- development of new separating channels, development of new detection modules for the study of nuclear, atomic, and chemical properties of new elements;
- production of new target materials and development of techniques of making targets with high thermal and radiation stability;
- development of a base for research with intense ion beam in related fields of science and technology.

ISBN: 978-3-95450-205-9 doi:10.18429/JACoW-Cyclotrons2019-THC01

The SHE Factory situated in the stand-alone new building of the FLNR (Fig. 1). The building comprises a hall for accelerator, rooms for auxiliary equipment, offices for service staff and the experimental area which divided into three separated halls. Each experimental hall is radiation shielded. The total experimental area is about 1000 m^2.

Figure 2: DC280 cyclotron, where: 1- main magnet, 2-HV injection system, 3-RF resonator, 4- beam lines.

DC280 Cyclotron

As an accelerator for the SHE Factory the new DC280 cyclotron was created (Fig. 2). The DC280 was designed at the FLNR, the cyclotron intended for carrying out fundamental and applied investigations with ions from He to U, with the range of atomic mass to charge ratio of A/Z = 4 - 7.5, produced by an ECR ion source. Energies of accelerated ions may vary from 4 up to 8 MeV/nucleon. The DC280 has to produce ion beams with intensity up to 10 pμA for ions with A ≤ 50.

Table 1: DC280 Cyclotron - Basic Technical Solutions

Parameter	Goals
High injecting beam energy (up to 80 kV/Z)	Decreasing space charge factor. Decreasing beam emittance. Effective transportation of ions through injection and capture into acceleration.
High gap in the center	Space for a long spiral inflector.
Low magnetic field (up to 1.3 T)	Large starting radius. Good orbit separation. Low deflector voltage.
High accelerating voltage (up to 130 kV)	Higher turns separation. Lower losses of ions on the rest gas in the vacuum chamber.
Beam extraction by the electrostatic deflector with using a flat-top system	Effective ion extraction. Better beam quality.

The DC280 cyclotron was developed as the accelerator with high transmission of ion beams from the ion source to experimental setups (up to 50%) that allows us to carry out experiments with expensive rare isotopes such as ^{48}Ca at low material consumption. Also, maximal ion current from the ion source is limited from above, especially for metallic ions, therefore high transmission efficiency is necessary. The basic technical solutions which have formed the base of the DC280 cyclotron project are shown in the Table 1.

The main design parameters of the cyclotron specified in Table 2. Configuration of the DC280 cyclotron is shown in Fig. 3.

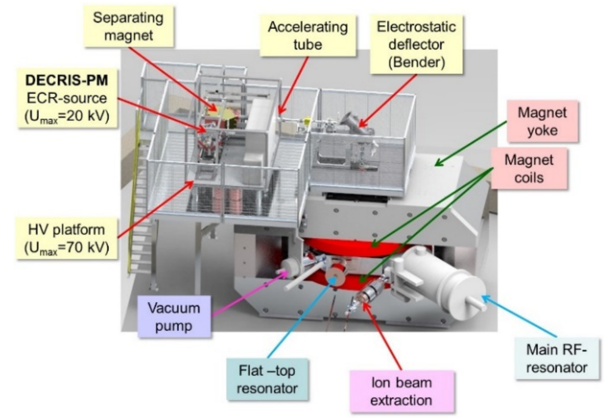

Figure 3: DC280 configuration.

Figure 4: DECRIS-PM source at HV platform, where 1- the source body, 2 – focusing solenoid.

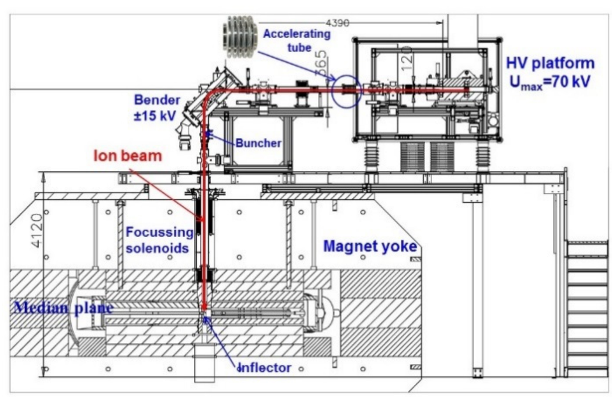

Figure 5: Scheme of the DC280 axial injection.

The DC280 equipped with the high voltage injection system which arranged above the main magnet [2]. The system consists of the high voltage (HV) platform with the DECRIS-PM ECR ion source, the maximal voltage at the platform is 70 kV. The DECRIS-PM is the source with permanent magnet structure created at the FLNR (Fig. 4) [3]. The source extraction voltage is up to 20 kV.

ISBN: 978-3-95450-205-9 doi:10.18429/JACoW-Cyclotrons2019-THC01

The first focusing solenoid, the 90° analysing magnet, the diagnostic box, the vacuum system and power supplies also installed on the HV platform. After the HV platform, ion beam with energy up to 80 keV/Z is focused by the second solenoid and turned to the DC280 center by spherical electrostatic deflector (bender) (Fig. 5).

The polyharmonic buncher (3 harmonics) [4] and 2 focusing solenoids situated in the vertical part of the injection line. The spiral inflector with quadrupole electrostatic lens at the exit (Fig. 6) is in the cyclotron center to bend the ion beam into the DC280 median plane [5].

For further development of the DC280 creation of a superconducting ECR ion source and the second HV platform which is planned for production of intensive ion beams of elements up to ^{238}U.

Table 2: Main Design Parameters of DC280

Parameter	Value
Injecting beam potential	Up to 80 kV
Pole diameter	4 m
A/Z range of ions	4-7,5
Magnetic field	0,6-1,3 T
K factor	280
Gap between plugs	400 mm
Valley/hill gap	500/208 mm/mm
Magnet weight	1100 t
Magnet power	300 kW max
Dee voltage	2x130 kV
RF power consumption	2x30 kW
Flat-top dee voltage	2x13 kV
Flat-top power consumption	2x2 kW
Beam orbit separation	10-16 mm
Deflector length	1,3 m
Deflector strength	90 kV/cm max
Magnetic channel length	0,9 m
Magnetic channel gradient	4,6-8,4 T/m
Efficiency of beam transfer	>50%

The DC280 is the isochronous cyclotron with four pairs of focusing sectors. The cyclotron has a compact type magnet. The aperture between the sectors is 208 mm that is enough to place Flat-Top dees and 4 pairs of harmonic correcting coils.

Table 3: Designed Beam Parameters of DC280

Ion	Ion energy [MeV/nucleon]	Intensity [pps]
^{7}Li	4	1×10^{14}
^{18}O	8	1×10^{14}
^{40}Ar	5	6×10^{13}
^{48}Ca	5	6×10^{13}
^{54}Cr	5	2×10^{13}
^{58}Fe	5	1×10^{13}
^{84,86}Kr	5	2×10^{12}
^{136}Xe	5	1×10^{14}
^{238}U	7	5×10^{10}

The wide range of the magnetic field levels 0.64-1.32 T allows to make smooth variation of the beam energy in a range 4-8 MeV/nucleon/nucleon. For operative optimization of the magnetic field the 11 radial correcting coils are utilized. The designed beam phase deviation at acceleration is not more than ±2° for ^{48}Ca, and about ±15° for edge operation modes.

Accelerating system of the DC280 consists of two main 45° dees and two flat-top 20° dees combined with RF- resonators (Fig. 7) [6].

The ion beam extraction system of the DC280 equipped with the electrostatic deflector (Fig. 8) and the passive focusing magnetic channel.

The deflector gap is 1 cm and voltage on the potential electrode is up to 90 kV. Designed parameters of extracted ion beams specified in Table 3.

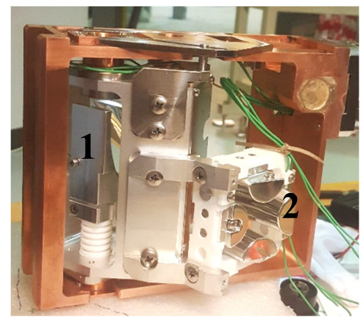

Figure 6: The spiral inflector with quadrupole electrostatic lens, where 1- inflector electrodes, 2 - electrostatic lens electrodes.

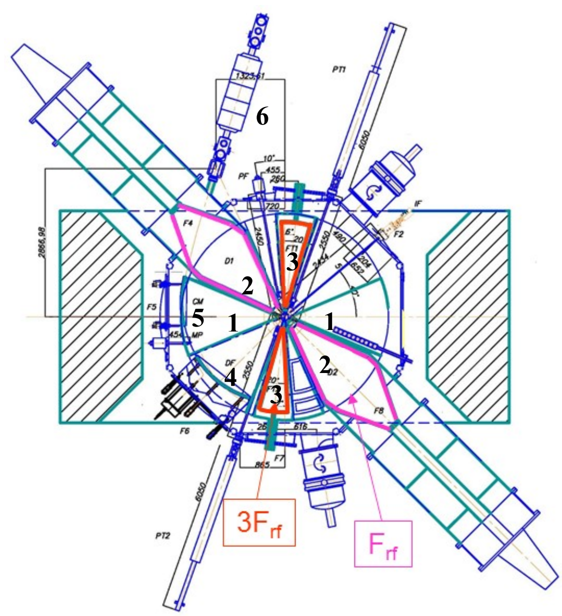

Figure 7: Scheme of the DC280, where: 1-sectors, 2- main dees with resonators, 3- flat- top dees, 4- deflector, 5- passive magnetic channel, 6- beam extraction line, F_{rf} - frequency of RF generators.

After extraction from the cyclotron ion beams are transported inside the extraction beam line to the TM switching magnet. After the TM there are five beam transport lines. Beam lines N3 and N4 are utilized to transport accelerated ion beams to GFS-II and GFS-III gas-filled separators (Fig. 9).

ISBN: 978-3-95450-205-9 doi:10.18429/JACoW-Cyclotrons2019-THC01

The beam focusing in beam lines is provided by set of quadrupole lenses having magnetic field gradients up to 7.7 T/m.

GFS-II and GFS-III gas-filled separators operate with internal vacuum is about 1 Torr (H_2). Vacuum in beam lines is about $5 \cdot 10^{-7}$ Torr. The differential pumping (DP) system situated between the last beam line quadrupole and the target will be utilized to separate vacuum in separators and beam lines. The ion beam has to be transported through a system of collimators of the DP with minimal losses [7].

The beam diagnostics consists of Faraday caps, slit collimators, sector aperture diaphragms, ionization beam profile monitors and pickups for TOF energy measurement.

The maximal ion beam power in the beam lines can be up to 2.5 kW. Special water cooled aperture diaphragms installed along the beam lines to protect them against damaging by ion beams. Also we can use formation of pulsed beam with 150 Hz repetition rate by using an electrostatic beam chopper in injection line. The chopper control can be operated with adjustable beam duty cycle.

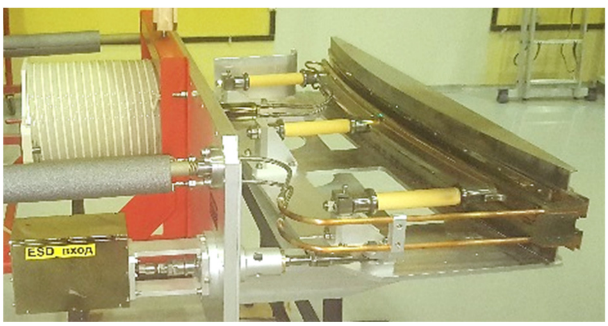

Figure 8: Electrostatic deflector.

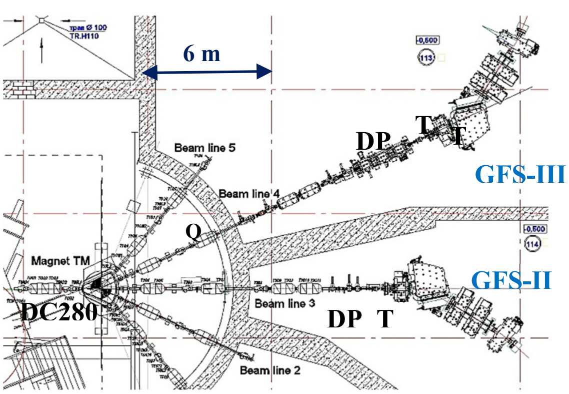

Figure 9: Scheme of beam lines in the SHE Factory building, where Q; quadrupole lens (triplet and doublets), DP; differential vacuum pumping, GFS-II and GFS-III: gas-filled separators at N3 and N4 beam lines, T- targets.

Experimental Results

The DECRIS-PM ECR ion source was tested at the FLNR testing bench. The maximal ion intensities of the source shown in Table 4.

The first beam of $^{84}Kr^{+14}$ ions was accelerated in the DC280 cyclotron on 26.12.2018. The first beam of $^{84}Kr^{+14}$ ions was extracted from the DC280 cyclotron on 17.01.2019. At the DC280 commissioning stage ion beam intensity was not more than 0.2 pμA.

Then, we carried work on test acceleration of $^{84}Kr^{+14}$, $^{12}C^{+2}$ and $^{40}Ar^{+7}$ ions together with improvement of operation of all the cyclotron systems. The DC280 was in testing operation about 3 months. Acceleration time for $^{12}C^{+2}$ ions was only few hours and ion currents were restricted to avoid excess equipment activation by neutrons at tests. Reached currents of accelerated and extracted ions with energy of 5.9 MeV/nucleon are shown in Table 5. Coefficients of ion capture into acceleration with and without the buncher shown in Table 6.

For today, the maximal extracted intensities in CW mode of operation are: 10 pμA for $^{12}C^{+2}$ (beam power is P_{beam}=0,71 kW), 6 pμA for $^{40}Ar^{+7}$ (P_{beam}=1,4 kW) and 1.32 pμA for $^{84}Kr^{+14}$ (P_{beam}=0,67 kW).

Table 4: Ion Intensities From DECRIS-PM

Ion	A/Z	Intensity [pμA]
$^{24}Mg^{+5}$	4,8	90
$^{40}Ar^{+8}$	5	115,8
$^{48}Ca^{+9}$	5,3	24,4
$^{50}Ti^{+9}$	5,6	10
$^{58}Fe^{+9}$	6,2	9,4
$^{84}Kr^{+15}$	5,6	12
$^{136}Xe^{+20}$	6,8	3,9

Table 5: Ion Beam Parameters of DC280 at 5.9 MeV/n

Ion	I_{HVP} [eμA]	I_{INJ} [eμA]	I_{in} [eμA]	I_{out} [eμA]	I_{EXTR} [eμA]
$^{12}C^{+2}$	69,7	59,5	37,8	31,3	20
$^{40}Ar^{+7}$	100,3	91	63	53	42
$^{84}Kr^{+14}$	45,6	40,5	25	21,3	19

I_{HVP}: ion current from ECR after HV platform; I_{INJ} ion current after bender and buncher, R_{in} = 40 cm; I_{in} ion current in the DC280 center, R_{in} = 40 cm; I_{out}: ion current near the DC280 extraction radius, R_{out} = 175 cm; I_{EXTR}: ion current in the extraction beam line.

Table 6: Coefficients of Ion Capture Into Acceleration

Ion	I_{INJ} [eμA]	Without buncher	With buncher
$^{12}C^{+2}$	59,5	11,5%	63,5 %
$^{40}Ar^{+7}$	91	12,2%	69,2 %
$^{84}Kr^{+14}$	40,5	14,1%	61,7 %

Unfortunately, we could not use flat-top resonators at test acceleration due some technical problems, therefore further increasing of ion currents was possible only with using the electrostatic beam chopper to avoid possible damaging of the deflector. When the chopper was operated with beam duty cycle of 25% we observed extracted current of $^{40}Ar^{+7}$ ions which was equivalent to I_{EXTR} = 63 eμA (9 pμA, P_{beam} = 2,1 kW) at I_{INJ} = 150 eμA (21,4 pμA).

The HV platform voltage was U_{HVP} = 47.2 kV for $^{12}C^{+2}$ and $^{84}Kr^{+14}$ ions, for $^{40}Ar^{+7}$ ions it was U_{HVP} = 44.2 kV. The extraction voltage of DECRIS-PM was 15 kV for all the

ISBN: 978-3-95450-205-9 doi:10.18429/JACoW-Cyclotrons2019-THC01

ions. The acceleration frequency was 9 MHz, the optimal RF voltage on the main dees was 115 - 120 kV. The deflector voltage was about -75 kV. Vacuum was: 5-7·10^{-8} Torr in injection, about 8·10^{-8} Torr in the cyclotron vacuum chamber and 2-3·10^{-7} Torr in the beam line N3.

Besides that, we carried out brief acceleration of $^{40}Ar^{+6,+7,+8}$ ions at acceleration frequencies of 8.3 MHz and 9.8 MHz, with the aim to check DC280 operation at lower (5 MeV/nucleon) and higher (7 MeV/nucleon) ion energies. Reached intensities of ion beams extracted with the energies were from 3 to 6 pμA depending on cyclotron tuning.

Experimental Setups

As the first experimental set-up for experiments on the synthesis and study of SHE, the GFS-II gas-filled separator has been chosen. The separator comprises the Q1-D1-Q2-Q3-D2 ion optical scheme (Fig. 10). The main magnet D30° with a deflection angle of 30°, rotated rear pole face and a gap of 120 mm separates synthesized heavy nuclei from background particles. The dipole D10° with a deflection angle of 10° reduces the background from light high-energy particles, e.g. protons, alpha-particles.

The separator (Fig. 11) had been manufactured by the SigmaPhi firm (Vannes, France) and installed at the beam line N3 (Fig. 9) of the SHE factory experimental hall designed in compliance with class II radiation safety requirements for work with high radioactive targets made of transuranium isotopes. The GFS-II was commissioned and ready for operation. The first beam of $^{40}Ar^{+6}$ ions was transported to the GFS-II beam stopper on 09.09.2019.

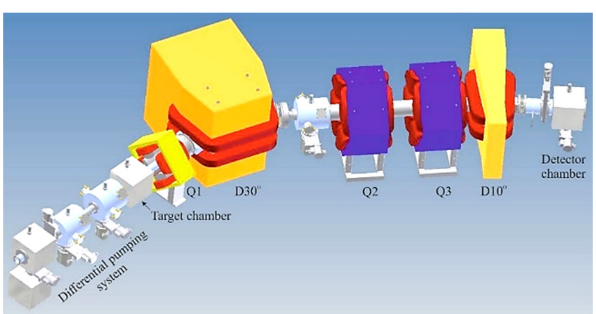

Figure 10: Configuration of GFS-II gas-filled separator, where Q- quadrupole lenses, D- dipole magnets.

Figure 11: GFS-II gas-filled separator.

During the first stage of testing the properties of the separator, the detection and data acquisition systems will be studied using ^{40}Ar+natYb, ^{48}Ca+natYb, $^{48}Ca+^{206}Pb$ reactions. Tests will be continued using $^{48}Ca+^{242,244}Pu$ and the $^{48}Ca+^{243}Am$ reactions. Several hundred decay events of Fl and Mc isotopes are expected to be recorded. After completion of these tests, it is planned to start the synthesis of new superheavy elements in reactions of ^{50}Ti and ^{54}Cr ions with ^{248}Cm, ^{249}Bk and $^{249\text{-}251}$Cf isotopes. The experiments will be conducted in a broad international cooperation.

The second experimental set-up is the GFS-III separator which also was made by the SigmaPhi. The GFS-III has the same ion optical scheme except D2 magnet which has the deflection angle of ±15°. The experimental setup will be installed on the beam line N4. The GFS-III will be utilized for nuclear spectroscopy. The first stage of testing the detection and data acquisition systems will be studying of Mc isotopes- products of the $^{48}Ca+^{243}Am$ reactions. Also, GFS-III will be used as a pre-separator for chemical experiments with SHE.

CONCLUSION

The SHE Factory was commissioned in 2019. The beam parameters of the DC280 cyclotron are close to required ones for testing of the first experimental setup - GFS-II separator in 2019. The GFS-II is ready for the first experiments on the synthesis and study of SHE.

REFERENCES

[1] S. Dmitriev, M. Itkis, and Y. Oganessian, "Status and perspectives of the Dubna superheavy element factory", in *Proc. Nobel Symposium NS160 - EPJ Web of Conferences*, vol. 131, 2016, pp. 1-6. doi:10.1051/epjconf/201613108001

[2] G. G. Gulbekyan *et al.*, "The project of beam transportation lines for the DC-280 cyclotron at the FLNR JINR", in *Proc. 24th Russian Particle Accelerator Conf. (RuPAC'14)*, Obninsk, Russia, Oct. 2014, paper THPSC09, pp. 336-338.

[3] S. L. Bogomolov *et al.*, "Production of high-intensity ion beams from the DECRIS-PM-14 ECR ion source", *Phys. Part. Nuclei Lett.*, vol. 15, no. 7, pp. 878–881, 2018. doi:10.1134/S1547477118070191

[4] I. V. Kalagin *et al.*, "Multigap and polyharmonic bunching systems at FLNR cyclotrons", in *Proc. 25th Russian Particle Accelerator Conf. (RuPAC'16)*, Saint Petersburg, Russia, Nov. 2016, pp. 447-449. doi:10.18429/JACoW-RUPAC2016-WEPSB038

[5] G. Gulbekian *et al.*, "Injection and acceleration of intense heavy ion beams in JINR new cyclotron DC280", in *Proc. 13th Int. Conf. on Heavy Ion Accelerator Technology (HIAT'15)*, Yokohama, Japan, Sep. 2015, paper MOA2C02, pp. 30-32.

[6] G. G. Gulbekyan *et al.*, "High-frequency acceleration system of the DC280 cyclotron", *Phys. Part. Nuclei Lett.*, vol. 9, no. 8, pp. 637-642, 2012. doi:10.1134/S1547477112080067

[7] N. Yu. Kazarinov *et al.*, "Beam lines for gas filled separator experiments at DC280 cyclotron", in *Proc. 26th Russian Particle Accelerator Conf. (RuPAC'18)*, Protvino, Russia, Oct. 2018, pp. 272-275. doi:10.18429/JACoW-RUPAC2018-TUPSA60.

ISBN: 978-3-95450-205-9 doi:10.18429/JACoW-Cyclotrons2019-THC02

FIRST BEAMS PRODUCED BY THE TEXAS A&M UNIVERSITY RADIOACTIVE-BEAM UPGRADE*

D. P. May, F. P. Abegglen, J. Ärje, H. Clark, G. J. Kim, B. T. Roeder, A. Saastamoinen, G. Tabacaru, Texas A&M University, Cyclotron Institute, Texas A&M University, College Station, TX 77845, USA

Abstract

The first test beams of radioactive ions produced by the ion-guide-on-line (IGOL) system coupled to an electron-cyclotron-resonance ion source for charge-breeding (CB-ECRIS) have been accelerated to high energy by the Texas A&M K500 cyclotron. The radioactive ions were produced by energetic protons, provided by the K150 cyclotron, impinging on foil targets. Low charge-state ions were then swept by a flow of helium gas into an rf-only sextupole ion-guide (SPIG) which transported them into the plasma of the CB-ECRIS. The K500 cyclotron and beam-line transport were tuned with analog beam before tuning the radioactive beam.

INTRODUCTION

Reference [1] gives a complete description of the Texas A&M upgrade. As part of the upgrade the K150 cyclotron has been re-commissioned to use as a driver for the production of radioactive ions. The method is to first stop radioactive products from beam-target collisions and transport them as low-charge-state ions using the IGOL technique. This technique was pioneered and continues to be developed at the University of Jyväskylä Cyclotron Laboratory [2]. Using this technique, a light-ion guide (LIG) is being developed where reaction products result from energetic, light-ion beams (p, d, ^{3}He, or α) impinging on a foil target. These products remain as 1+ ions and can be injected into CB-ECRIS for charge-breeding to higher charge states. A low-energy beam of ions of one selected high charge-state is then transported to the K500 superconducting cyclotron for acceleration to high energy. Figure 1 illustrates the scheme where protons and deuterons result from stripped accelerated negative ions. The high-energy radioactive beam is transported from the K500 to a detector station for analysis. Eventually the radioactive beams will be used for experiments.

LIGHT ION GUIDE AND SPIG

For LIG an energetic beam of light ions impinges on a thin foil target to produce radioactive products (via (p, n) for example) that then exit the target to encounter a rapid flow of helium gas. The products are mainly in the ionized state, and in the helium this ionization is reduced to the 1+ charge-state, taking advantage of the unfavorable energetics of neutralization of 1+ heavy ions colliding with neutral helium. The flow of helium through the target cell ushers the 1+ ions through an orifice into a highly pumped region where a large fraction of the helium is pumped away. Originally the ions were guided by a small electric field through an aperture in a skimmer electrode after which they could be accelerated to form a low energy (~10 kV) beam.

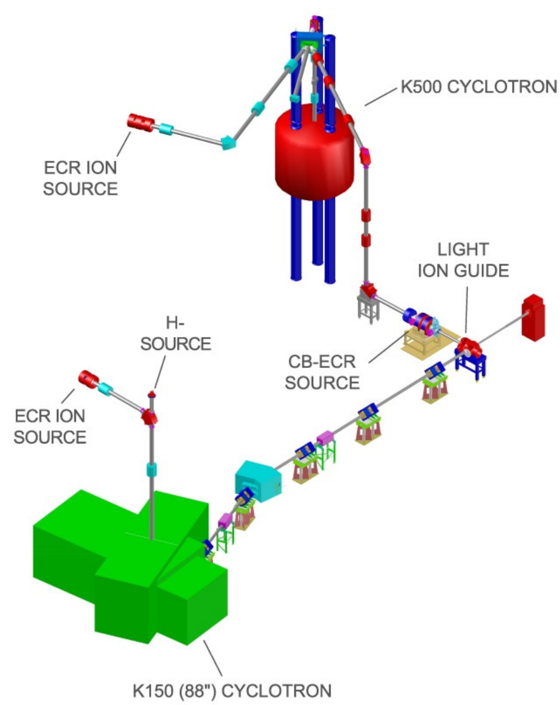

Figure 1: Simplified layout of the Texas A&M light-ion-guide scheme.

One disadvantage of the skimmer is that the ions can encounter a significant pressure of helium in the acceleration region which introduces an energy spread in the beam. In order to counter this, a system was introduced where before acceleration the thermalized ions travel along a SPIG through a sequence of pumping baffles before being accelerated [3]. References [4, 5] detail the development of the SPIG which consists of a parallel array, usually sextupolar, of conducting rods or vanes with low-power, high-frequency rf impressed. The rods are alternately phased by 180° so that rf fields of parabolically increasing intensity are set up in the interior of the sextupole. Ions travel through the channel between the rods contained by the rf fields while a larger fraction of the helium is pumped away. In reference 3 it is shown that ions accelerated by some initial voltage of several

*Work supported by U. S. Dept. of Energy Grant DE-FG02-93ER40773

ISBN: 978-3-95450-205-9 doi:10.18429/JACoW-Cyclotrons2019-THC02

hundred volts are thermalized by collisions with the high pressure of helium before the first pumping baffle and even cooled. As a consequence, the ions exit the SPIG into the low pressure region with only a thermal energy spread.

INITIAL SET-UP

Figures 2 and 3 illustrate the LIG-to-CB-ECRIS geometry and the target-cell. Three large Roots blowers are used to handle the large flow of helium gas exiting the target-cell. At first the SPIG was modelled after reference [3] and consisted of two sections with two pumping baffles, the first and second sections approximately 8 cm and 40 cm long, respectively, and used 4 mm diameter stainless steel rods arrayed around a 10 mm inner diameter. The exciting frequency was approximately 2 MHz and tuned to minimize reflected power. The target-cell and SPIG were held near the extraction voltage of the CB-ECRIS, and the 1+ beam subsequently accelerated to ground immediately after the SPIG. Table 1 lists four reactions that were focused on.

Table1: Reactions

Reaction	Cross-section [mb] @ E_p[MeV]	Half life
^{64}Zn(p,n)^{64}Ga	161 @ 14.3	2.6 m
^{58}Ni(p,n) ^{58}Cu	40 @ 14.3	3.2 s
^{46}Ti(p,n) ^{46}V	124 @ 14.3	422 ms
^{114}Cd(p,n) ^{114}In	510 @ 10.3	71.9 s

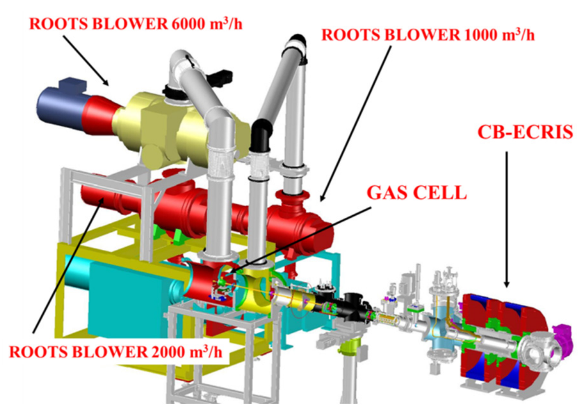

Figure 2: LIG and CB-ECRIS.

The 14 GHZ CB-ECRIS [6] is located 2.5 meters from the target-cell. Since it is constructed with a totally surrounding hexapole, it is difficult to achieve a symmetric geometry on the injection end due to microwave and gas injection. This symmetry is important in the volume where injected beams are encountering the electric field that decelerates the beam into the plasma chamber [7]. Various injection geometries have been tried, including one where the plasma chamber was opened up and extended on the injection end and the microwaves injected into the extension. Charge-breeding was observed for ^{64}Ga, ^{58}Cu, and ^{114}In with 1% being the highest efficiency obtained for one charge-state.

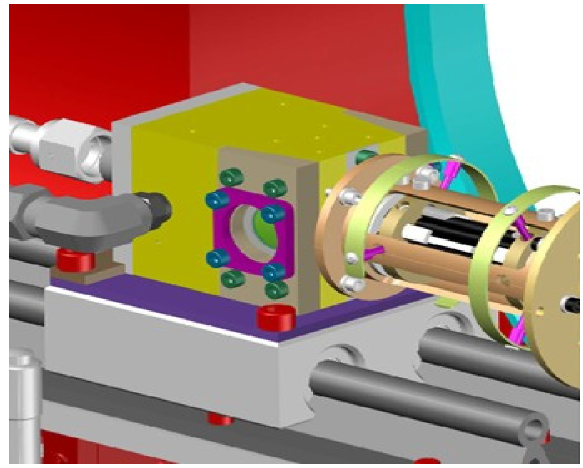

Figure 3: The target-cell and first SPIG section.

DIRECT SPIG INJECTION

The short distance between the target-cell and the CB-ECRIS made alignment and proper focus of the 1+ beam difficult. Also larger target-cell apertures and higher target-cell pressures caused higher concentrations of helium to migrate into the acceleration region and even into the CB-ECRIS. Finally, there was the possibility that a portion of the plasma was back-extracted by the presence of grounded elements in the injection region. With these considerations in mind, in the next phase a method of direct injection of the radioactive ions produced by the IGOL system was investigated. With this method the ions travel from the target cell along an extended SPIG directly into the CB-ECRIS plasma chamber, and these problems can be more easily avoided.

As a first test a 1 meter-long SPIG was positioned through of a Glaser lens that was similar to the coil on the injection end of the CB-ECRIS and capable of producing a comparable magnetic field. Transport of ions along the SPIG was little affected by the full field of the Glaser as its coil current was increased to its maximum.

Next an aluminosilicate ion gun fabricated by HeatWave Labs, Inc. for the production of singly-charged alkali ions was placed at the entrance of 40 cm long SPIG, and the exit end of the SPIG placed on axis near the maximum axial magnetic field at the injection end of the CB-ECRIS (Fig. 4). This arrangement resulted in a good charge-breeding efficiency (Fig. 5), although this was difficult to precisely quantify due to the difficulty of measuring the output from the SPIG directly. An estimate of the output was made using a measurement of the current hitting the plasma chamber added to the current measured hitting a faraday cup down-stream of the CB-ECRIS with no high voltage applied to the plasma chamber or SPIG. This measurement indicated an efficiency as high as 10% into one charge-state (8.4 pnA of $^{133}Cs^{24+}$ out of 70 pnA of $^{133}Cs^{1+}$ measured hitting the plasma chamber and 15 pnA hitting the down-stream faraday cup). The efficiency peaked at a difference between the source voltage and the CB-ECRIS voltage of

ISBN: 978-3-95450-205-9 doi:10.18429/JACoW-Cyclotrons2019-THC02

8.5 V with 5.8 V FWHM. Charge-breeding of potassium demonstrated similar results.

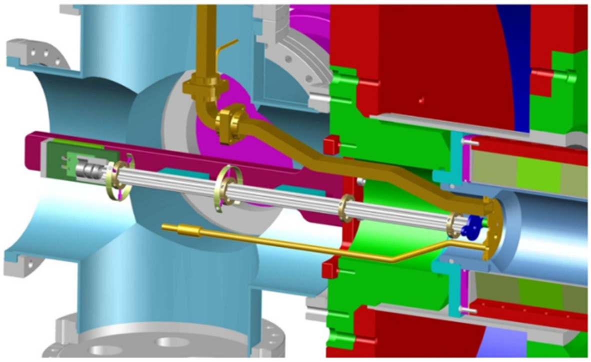

Figure 4: 40 cm SPIG injecting directly into the plasma chamber of the CB-ECRIS.

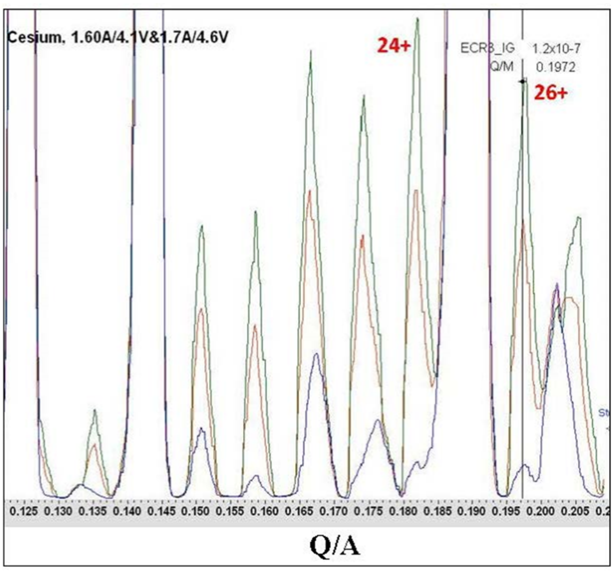

Figure 5: Spectrum of charge-bred ^{133}Cs for two ion-source outputs. The largest peaks are charge-states of oxygen and nitrogen, the underlying peaks are background.

One observation is that the efficiency of charge-breeding continued to improve as the vacuum improved, although as shown by Fig. 5 there was still the presence of oxygen (from water vapour) and nitrogen (from small leaks). The vacuum never improved at the injection end of CB-ECRIS to below 1×10^{-7} Torr, and the introduction of support gas only served to depress the charge-breeding efficiency. The charge-state distribution was quite high even though the microwave power was low (88 watts as measured at the transmitter above the cave shielding). The total extracted current was less than 80 µA.

Figure 6 illustrates the direct injection scheme and Fig. 7 shows the installed SPIG positioned in the injection end of CB-ECRIS (opposite extraction). The SPIG is made up of vanes instead of rods for more structural stability. In addition to the two pumping baffles from the former scheme, there are two additional baffles with pumping by turbo-molecular pumps in between. The entire LIG to CB-ECRIS system was tested first using a $^{133}Cs^{1+}$ source at the position of the target cell and then using a radioactive thorium source placed in the target cell. Both tests yielded about 50% global efficiency.

Finally, a proton beam was used to create products for acceleration by the K500 cyclotron. The charge-breeding efficiency was much improved. Intensities of $^{64}Ga^{14+}$, $^{63}Zn^{14+}$, $^{114}In^{20+}$ and $^{112}In^{21+}$ were 680, 897, 610 and 974 ions/µC, with production per unit cross-section of 4.2, 1.7, 1.1, and 1.2 ions/µC-mbarn, respectively.

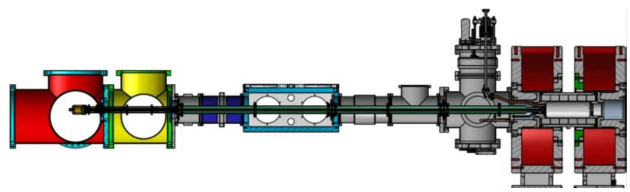

Figure 6: 2.5 meter SPIG joining LIG to CB-ECRIS.

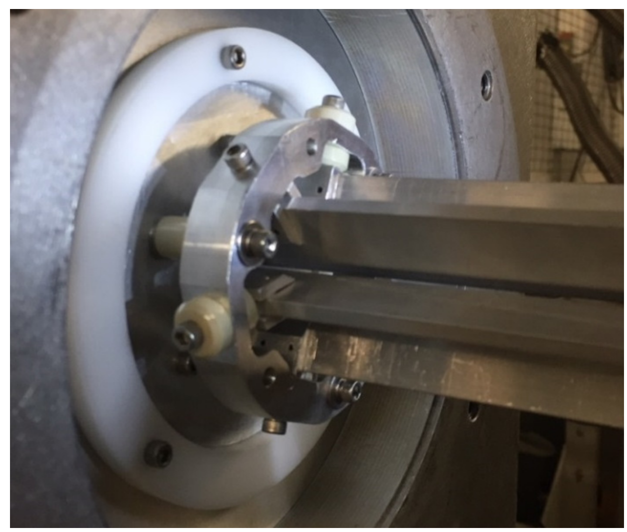

Figure 7: Vaned SPIG and pumping baffle.

CYCLOTRON ACCELERATION OF RIBS

The next step was the attempt to accelerate charge-bred radioactive ions and then detect them along with contaminating ions in order to determine the purity of the accelerated beams. Close analogs were used as described in [8], so it is certain that the radioactive ions were accelerated, but because of recently low proton-beam intensity most beams were totally obscured by contaminants. Contaminants included elastics from the target cell as well as close heavier analogs arising from the CB-ECRIS. Oxygen and nitrogen both were always present in CB-ECRIS and were thus convenient to use as analogs.

To address these issues it was decided to produce ^{112}In ($\tau_{1/2}$=15 m) by the (p, 3n) reaction on a ^{114}Cd target,

ISBN: 978-3-95450-205-9 doi:10.18429/JACoW-Cyclotrons2019-THC02

charge-breed to 21+, accelerate to 14.0 AMeV and detect using the Momentum Achromat Recoil Spectrometer (MARS) [9]. As detailed in [10] a beam of ^{109}Ag at 14.0 AMeV from the K500 was used to calibrate the ΔE/E silicon detector at the focus of MARS. The beam impinged on a thin carbon foil at the entrance of MARS in order to strip to the higher charge-states that the MARS magnetic dipoles could handle. Q/M ratios of ^{112}In^{21+} and ^{16}O^{3+} are 0.18768 and 0.18758, respectively, so the frequency shift from ^{16}O to ^{112}In was calculated to be +6.5 kHz. After tuning the ^{16}O^{3+} to MARS and then making the frequency shift, the rigidity of MARS was set to observe the 34+ through 41+ charge-states of ^{112}In. Particles with mass 112 dominate the spectra along with a few other ions with Q/M ≈ 3/16.

Measurements were taken with the proton beam "on" and "off" the LIG target for 3 minutes each. A sample of these is shown in Fig. 8 for the ^{112}In^{39+} setting. The ^{112}In disappears when the proton beam "off" (Fig. 8). A maximum rate of 100 counts/sec for ^{112}In^{39+} was observed with 2 μA of proton beam. With the other charge-states considered, 330 pps of ^{112}In^{21+} were delivered to target, and assuming 10% acceleration efficiency 3.3×10^3 pps. of ^{112}In^{21+} were produced for a 2 μA proton beam.

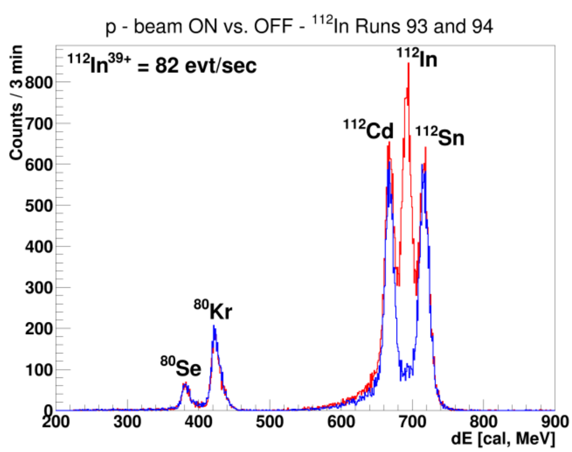

Figure 8: ΔE spectra showing the ^{112}In^{39+} measured in the MARS focal plane. Blue corresponds to proton beam "off" and red to proton beam 'on".

FUTURE PROGRESS

^{112}In^{21+} is the first re-accelerated radioactive ion beam at the Texas A&M Cyclotron Institute. Since this experiment the intensity of the K500 H-minus-to-proton beam has been increased by more than a factor of ten by fixing leaks in the K150 in addition to adding more cryopumps at the cyclotron periphery. Scaling of the LIG production with light-ion intensity needs to be tested, and higher production will make tuning easier and beam purity higher.

Direct injection by a SPIG proved an efficient and easily tuned alternative to the accel-decel scheme. However, fitting the SPIG into the existing transfer line has resulted in making alignment and servicing difficult and time consuming. In an effort to solve this problem, a new chamber is now being designed specifically for the SPIG. It will incorporate a single, long port through which the SPIG can easily be removed, or inserted and aligned. Also, room for diagnostics with a possible moveable section of the SPIG is being considered. Finally, strategies for increasing efficiencies for all species and decreasing breeding times and contamination will be explored.

Finally, the performance of the CB-ECRIS can be improved with the repair of small air leaks and the substitution of a low-power, variable frequency travelling-wave-tube microwave (TWTA) amplifier for the high-power klystron, 14.5 GHz transmitter [7].

REFERENCES

[1] D. P. May *et al.*, "Progress toward the facility upgrade for accelerated radioactive beams at Texas A&M", in *Proc. 20th Int. Conf. on Cyclotrons and their Applications (Cyclotrons'13)*, Vancouver, Canada, Sep. 2013, paper MO2PB03, pp. 22-24.

[2] J. Ärje *et al.*, "The ion guide isotope separator on-line, IGISOL", *Nucl. Instrum. Methods Phys. Res., Sect. A*, vol. 247, no. 3, Jul. 1986, pp. 431-437. doi:10.1016/0168-9002(86)90404-3

[3] P. Karvonen *et al.*, "A sextupole ion beam guide to improve the efficiency and beam quality at IGISOL", *Nucl. Instrum. Methods Phys. Res., Sect. B*, vol. 266, no. 21, Nov. 2008, pp. 4794-4808. doi:10.1016/j.nimb.2008.07.022

[4] H. J. Xu, M. Wada, J. Tanaka, H. Kawakami, I. Katayama, and S. Ohtani, "A new cooling and focusing device for ion guide", *Nucl. Instrum. Methods Phys. Res., Sect.* A, vol. 333, no. 2-3, Sept. 1993, pp. 274-281. doi:10.1016/0168-9002(93)91166-K

[5] M. Wada, "Genealogy of gas cells for low-energy RI-beam production", *Nucl. Instrum. Methods Phys. Res., Sect. B*, vol. 317, Dec. 2013, pp. 450-456. doi:10.1016/j.nimb.2013.08.062

[6] W. D. Cornelius, "Design of a charge-breeder ion source for Texas A&M University", in *Proc. 18th Int. Workshop on ECR Ion Sources (ECRIS'08)*, Chicago, IL, USA, Sep. 2008, paper WECO-B01, pp. 185-193.

[7] R. Vondrasek *et al.*, "Charge breeding results and future prospects with electron cyclotron resonance ion source and electron beam ion source", *Rev. Sci. Instrum.*, vol. 83, no. 02, 2012. doi:10.1063/1.3673629

[8] D. P. May *et al.*, "Status of the Texas A&M University Cyclotron Institute", in *Proc. 21th Int. Conf. on Cyclotrons and their Applications (Cyclotrons'16)*, Zurich, Switzerland, Sep. 2016, pp. 281-284. doi:10.18429/JACoW-Cyclotrons2016-THA04

[9] R. E. Tribble *et al.*, "MARS: A momentum achromat recoil spectrometer", *Nucl. Instrum. Methods Phys. Res., Sect.* A, vol. 285, no. 3, 1989, pp. 441-446.

[10] B. T. Roeder, F. P. Abegglen, J. Ärje, G. J. Kim, A. Saastamoinen, and G. Tabacaru, "Identification of ^{112}In: first re-accelerated radioactive light-ion-guide beam", Cyclotron Institute Progress in Research Texas A&M Univ. 2018-2019, p. IV-17.

ISBN: 978-3-95450-205-9 doi:10.18429/JACoW-Cyclotrons2019-THC03

DESIGN OF ACCELERATOR MASS SPECTROMETER BASED ON CYCLOTRON

H. Namgoong[1], H. S. Kim[2], J. C. Lee[2], D. H. Ha[1], M. Ghergherehchi[1] J. S. Chai[1,†]
[1]Department of Electrical and Computer Engineering, Sungkyunkwan University, 2066 Seobu-ro, Jangan-gu, Suwon, Gyeonggi-do, Korea
[2]College of Information & Communication Engineering, Sungkyunkwan University, 2066 Seobu-ro, Jangan-gu, Suwon, Gyeonggi-do, Korea

Abstract

In this paper, we present a cyclotron accelerator mass spectrometry system based on artificial intelligence. Cyclotron based AMS system are consist of cyclotron, ion source, RF buncher, dipole magnet and triplet quadrupole, detector. This Cyclotron based AMS system optimized the detection efficiency of $14C^-$ particles through artificial intelligence algorithms. Cyclotron was designed with a mass resolution of 5000, AVF electromagnet with 4 sectors. RF system was designed as RLC circuit consisting of Dee of which angle is 20 degrees. The stripping method was used of extraction. The ion source of AMS uses Cs sputtering source with Einzel lens and RF buncher. In this system, AI algorithm is applied to the detection and analysis algorithm through artificial neural network development to overcome the mass resolution time and precision by $14C^-$ sample number. The AMS has been designed and detailed hardware production is underway, and the system will be integrated in 2020 to carry out the mass decomposition experiment.

INTRODUCTION

In accelerator mass spectrometry, tandem accelerator is mainly used. Sungkyunkwan University developed cyclotron-based AMS cyclotron see Fig. 1. The advantage of the cyclotron-based AMS system is reducing the size and cost of the entire system. because cyclotron itself acts to separate the particles [1].

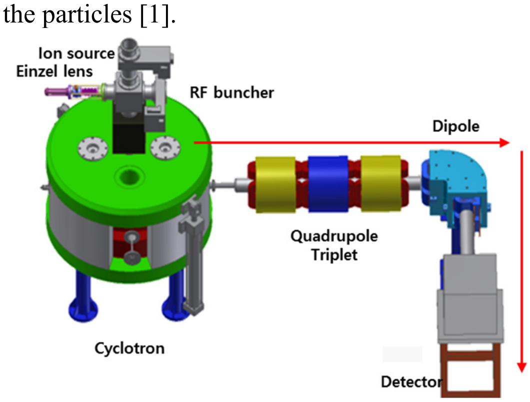

Figure 1: 3D drawings of Accelerator Mass Spectrometry based on cyclotron.

The tandem type accelerator is an electrostatic type, and the finally discharged particles are DC type. In the case of cyclotron, the electric field of RF emits the emissive particles in AC form. So Relatively fewer samples than static AMS. To solve this problem, we add artificial intelligence to increase the accuracy of the analysis.

The 3D drawing of cyclotron for AMS is shown in Fig. 2 and specification table of AMS cyclotron is shown as Table 1. This cyclotron is for accelerating carbon-14 beam.

DESIGN AND SYSTEM DESCRIPTION

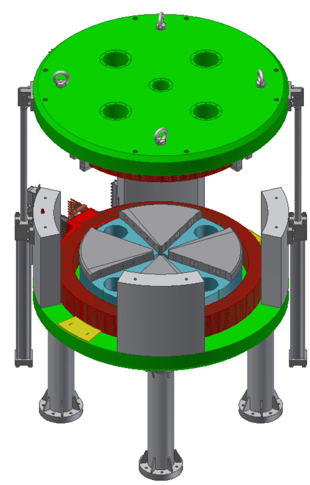

Figure 2: 3D drawings of cyclotron for AMS.

Table 1: AMS Cyclotron Magnet Specification

Parameter	Value
Maximum energy	200 keV
Beam species	Carbon-14 negative
Ion source	Cs sputtering
Number of sectors	4
Hill angle	60°
Valley angle	40°
Pole radius	0.510 m
Extraction radius	0.453 m
Hill / Valley gap	0.25
Harmonic number	10
Radio frequency	5.8 MHz
Radial tune	~ 1.01
Vertical tune	0.4
B-field (min., max.)	0.137, 0.687 T

† jschai@skku.edu

ISBN: 978-3-95450-205-9 doi:10.18429/JACoW-Cyclotrons2019-THC03

Maximum energy of carbon-14 beam is 200 keV. We select the harmonic number of 10, turn number is 159 turns. Because of this value is relate with mass resolution. Mass resolution is very important value at the AMS system. The mass resolution of AMS cyclotron is about 5000 [2]. The cyclotron has been manufactured and is currently undergoing magnetic field measurement and shimming.

The 3D model of magnet 3D model of magnetic field measurement instrumentation for AMS cyclotron is shown in Fig. 3. The hall sensor probe was on the bracket (1). It will rotate mid-plane of magnet. The step motor (2) was installed at the center of magnet, which is connected with rotation jig directly. The Rotation plate (3) prevent the rotation jig form tilting when magnetic field measurement instrumentation operates. The hall probe sensor had been moved by spur gear (4) and ratchet gear (5) along the radial direction. The Linear guide (6) supports hall probe sensor.

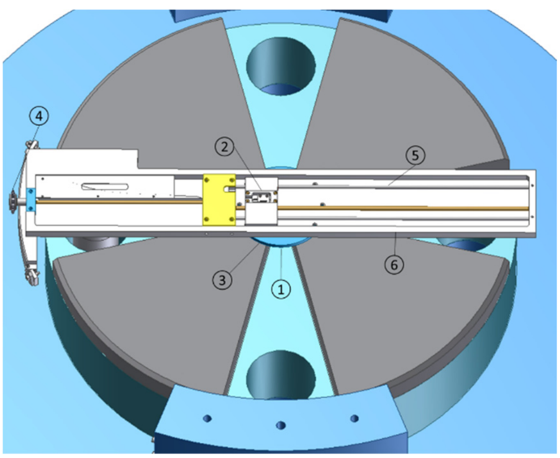

Figure 3: 3D drawing of magnetic field measurement system for AMS cyclotron.

The 3D drawings of Dee electrode are shown in Fig. 4 and specification table of Dee electrode is shown as Table 2.

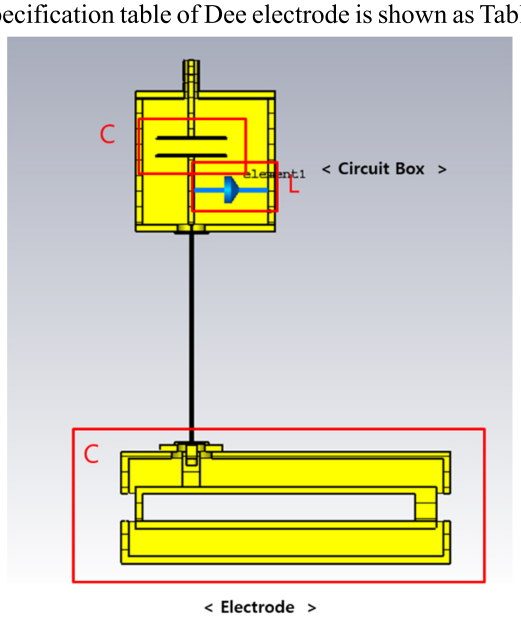

Figure 4: 3D drawing of Dee electrode for AMS cyclotron.

We designed a circuit box to match impedance and frequency. The circuit box is composed of capacitance and inductance. Approximate frequencies are set through inductance, impedance and detail frequency is set through capacitance [3].

We designed each components of the accelerator mass spectrometry beam line. Each component has been manufactured and is currently being tested for each part. Each component. Each component is shown in Figs. 5-7.

Table 2: Dee Electrode Specification

Parameter	Value
Vacc	300 V
Frequency	5.8 MHz
Accelerating distance	138 - 453 mm
Dee angle	20°
Number of Dee	2

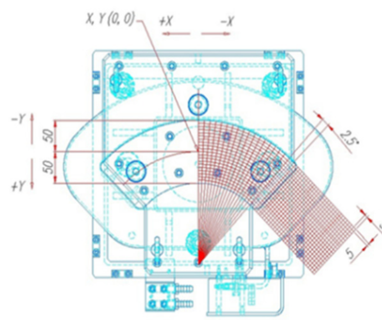

Figure: 5 Dipole magnet for AMS beamline.

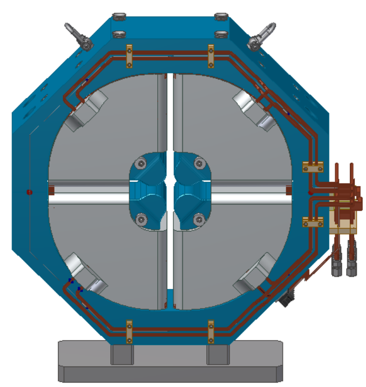

Figure 6: Quadrupole magnet for AMS beamline.

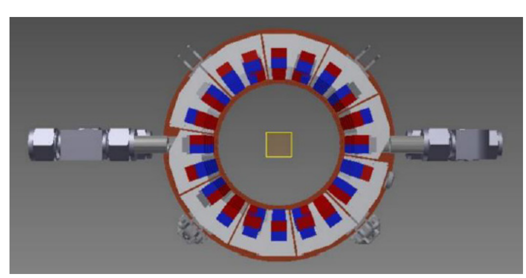

Figure 7: Ion source for AMS cyclotron.

ISBN: 978-3-95450-205-9 doi:10.18429/JACoW-Cyclotrons2019-THC03

Compared to tandem accelerators, acceleration particles are relatively small. Figure 8 is a block diagram of the accelerator control system based on neural network. The cyclotron control system for AMS uses data acquisition and logging of the accelerator drive parameters and combines this data with machine learning technology for cyclotron tuning and detector particle sorting. In order to implement the machine learning-based cyclotron control algorithm, the resonance point variation is simulated by the RLC model and the acceleration cavity output voltage is constructed in the form of time domain simulation. In addition, Normal distribution is analyzed by reflecting random noise components such as thermal noise amplifier noise [4].

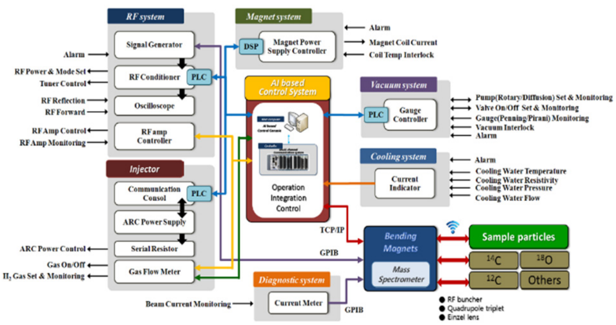

Figure 8: AI-based accelerator control system configuration diagram.

RESULTS AND DISCUSSIONS

A magnetic field measuring device for cyclotron for AMS was developed. The magnetic field 3D mapping was performed using the developed measurement instrument and the result is shown in Fig. 9.

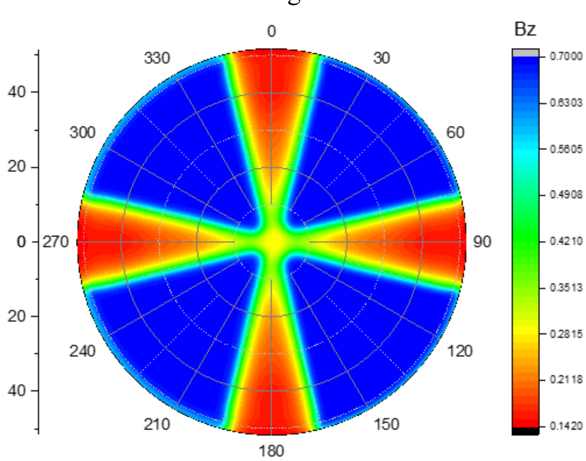

Figure 9: Magnetic field mapping data of AMS cyclotron.

The control system was constructed using the Adventure Actor Cricket method, which is a kind of reinforcement learning, and the learning was conducted by finding a policy that maximizes the reward.

The neural network was implemented inside the NI CRIO controller and we could see it converge around the resonance point, as shown in Fig. 10.

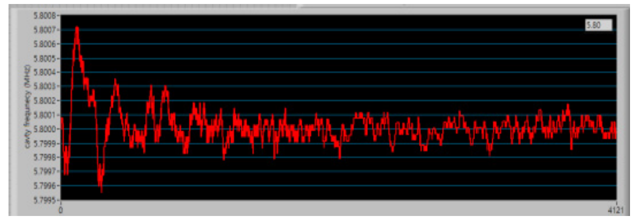

Figure 10: A2C resonance control learning process at 5.8 MHz constant resonance point.

CONCLUSION

We have developed a cyclotron based AMS system. Each component has been developed and tested Cyclotron-based AMS systems are currently under test. It also aims to operate in 2020. Based on machine learning, we develop an AI system that improves particle extraction accuracy and controls optimal isochronous magnetic field and RF frequency according to particle type.

ACKNOWLEDGMENT

This work was supported by Radiation Technology R&D program through the National Research Foundation of Korea funded by the Ministry of Science, ICT & Future Planning. [2017M2A2A4A02020347, Development of an Accelerator Mass Spectrometer based on Artificial Intelligence].

REFERENCE

[1] Jong-Won Kim *et al.*, "Design study of a compact cyclotron for accelerator mass spectrometry", *J. Korean Phys. Soc.*, vol. 54, pp. 580-585, Feb. 2009. doi:10.3938/jkps.54.580

[2] D. J. Clark, "Invited Paper: Cyclotrons as Mass Spectrometers", in *Proc. 10th Int. Cyclotron Conf. and Their Applications (Cyclotrons'84)*, East Lansing, MI, USA, Apr.-May 1984, paper L03, pp. 534-539.

[3] P. K. Sigg, "RF for cyclotrons", CERN, Geneva, Switzerland, Jun. 2005, pp. 231-252. doi:10.5170/CERN-2006-012.231

[4] I. Grondman *et al.*, "A survey of actor-critic reinforcement learning: Standard and natural policy gradients", *IEEE Trans. Syst. Man Cybern. Part C Appl. Rev.*, vol. 42, no. 6, pp. 1291-1307, 2012. doi:10.1109/TSMCC.2012.2218595

ISBN: 978-3-95450-205-9 doi:10.18429/JACoW-Cyclotrons2019-THC04

3D PRINTING FOR HIGH VACUUM APPLICATIONS

C. R. Wolf, F. B. Beck, L. Franz, V. M. Neumaier
Hochschule für Angewandte Wissenschaften, 96450 Coburg, Germany

Abstract

The 3D printing technology has made the leap from a home-based private practice to industrial manufacturing. Due to the increasing reliability of printers and increasing material diversity, especially in the metal sector, double-digit percentage growth rates are possible in the future.

This thesis deals with the manufacturing of parts made by 3D printing for high vacuum application. Different components are printed and examined for their vacuum compatibility.

As shown furthermore, conventionally made standard components can be vacuum tight welded to printed parts. This enables a cost-effective production with more complex components, such as a vacuum chamber. In addition, functional components can already be realized in the manufacturing process. The integration of a system of flow channels directly into the wall of a chamber is just one example. Thus, such a chamber can be heated during evacuation and effectively cooled in later operation.

INTRODUCTION

There is almost nothing left today that cannot be created by 3D printers. This doesn't only apply to the private sector, but increasingly also to the industrial environment.

The reason for this is the growing reliability of the process. Industrial 3D printers are fully automated machines that today can produce more cheaply, more reliably, and faster. Table 1 shows growth rates of 13 - 23% per year, with a market volume of 22.5 billion euros in 2030 [1].

Table 1: Compound Annual Growth Rate

Business	CAGR until 2030	Market Vol. 2015 in Billion €	Market Vol. 2030 in Billion €
Aerospace	23%	0.43	9.59
Medicine	23%	0.26	5.59
Automotive	15%	0.34	2.61
Industry	14%	0.44	2.98
Retail Trade	13%	0.30	1.89

Advantages of 3D printing

The 3D printing technology allows a lot of freedom in the design. In addition, the geometry of the component can be optimized so that a significant weight saving is possible and the part still meets the requirements of the strength. This topology optimization leads to a lightweight design of the parts, which is particularly important in the aerospace industry. In addition, compared to the milling out of the solid, a significant material savings is achieved here because no superfluous material (with the exception of any support structures) must be removed and and nearly no waste material is produced during production.

Since no moldings and other tools are necessary for the production of 3D printed components, there are no further costs. Another advantage results from the possibility of adding hollow and lattice structures, which can be used for the integration of a cooling system.

The fact that, apart from plastic, more and more materials are available, especially metals such as stainless steel, aluminum, titanium or similar and open new areas of application for 3D printing. Thus, in the present thesis, the application of this method in vacuum technology is examined.

Vacuums

When talking about vacuum technology, one has to specify the term vacuum more precisely (e.g., Fig. 1) because the different pressure ranges [2] place different demands on equipment and materials.

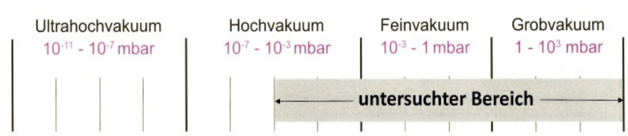

Figure 1: Pressure ranges.

This work is limited to the area of high vacuum. The limitation is due to the simple handling of the components and the existing pumping station, with which a minimum of 10^{-5} mbar is not undercut.

PRINTING OF THE COMPONENTS

LaserCUSING

The components investigated in this thesis were made of stainless steel 1.4404 using the process named LaserCUSING® patented by Concept Laser.

LaserCUSING® is an additive process in which components based on CAD data are produced layer by layer from the finest metal powder. The powdered metal is directly melted by a laser, which moves off the component cross-section. As a result of the subsequent cooling, the material solidifies. After a layer has been produced in this way, the building platform is lowered, a new layer of powder is applied and generated analogously to the next component cross-section. The structure of the part thus takes place layer by layer with a layer thickness of 15-500 microns.

ISBN: 978-3-95450-205-9 doi:10.18429/JACoW-Cyclotrons2019-THC04

The Printed Connector

The first 3D-printed component was a simple connector with two flanges DN40 on each side - here called the "3D-printed KF-SC DN-40".

Due to the use of powder in the production, 3D-printed parts have a certain surface roughness, which must be smoothed by reworking.

Another consequence of the layered structure is the fact that in overhangs with an angle smaller than 45° support structures - as shown in Fig. 2 - are necessary. They must be removed in the aftermath.

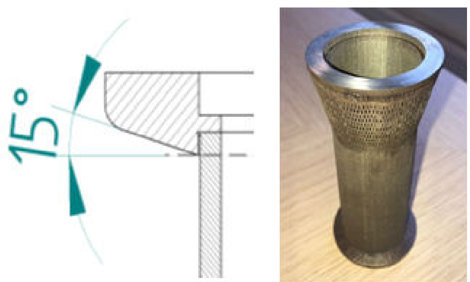

Figure 2: Support structures.

The Welded Connector

Due to an elaborate post-processing, it is clear that the 3D printing of standard components will hardly be worthwhile. Consequently, in order to achieve an economic use of this technology, it is necessary to retrofit the printed components with standard parts from conventional manufacturing.

For this purpose, a simple tube with an outside diameter of 41 mm and an inside diameter of 38 mm was printed and completed on one end by a welding flange and on the other side by a flange with a tube (e.g., Fig. 3).

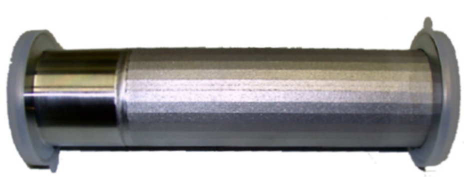

Figure 3: 3D-welded KF-SC DN-40.

The two different welds could be attached without problems. This meant that no further reworking was required. The present pipe - hereinafter referred to as "3D-welded KF-SC DN-40" - has the dimensions: r_i = 19 mm (inner radius) and h = 160 mm (length). This results in a volume V of 0.18 liters and an (inner) surface of 0.019 m^2.

With both parts a high vacuum of $1.5 \cdot 10^{-5}$ mbar was reached without problems.

LEAKAGE RATE MEASUREMENT

Experimental Setup and Implementation

To test the vacuum capability of the 3D-printed components by measuring the leak rate, the company VACOM offers the necessary equipment. The experimental set-up is shown in Figs. 4 a) and b).

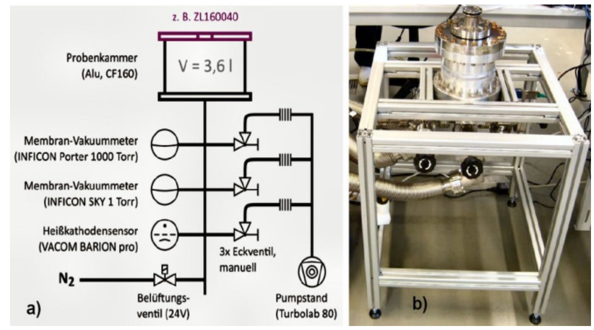

Figure 4: Experimental setup.

Before the actual examination a background measurement of the chamber without specimen was performed. Here, as with the test objects, the pressure increase Δp was recorded over a period of Δt = 24 h (e.g., Fig. 5). With the pressure increase rate Δp / Δt, taken from the corresponding diagram, the leak rate Q for the test component is calculated according to the equation:

$$Q = \frac{\Delta p}{\Delta t} \cdot V - Q_{background}$$

As a comparison to the printed component, a straight connector KF-SC DN-40 (V = 0.145 l) made of stainless steel is used. Furthermore, the influence of a pre-treatment can be checked by cleaning the 3D-welded KF-SC DN-40 with isopropanol in an ultrasonic bath and rerun the pressure increase measurement.

Evaluation

The measurement results are shown in Fig. 5.

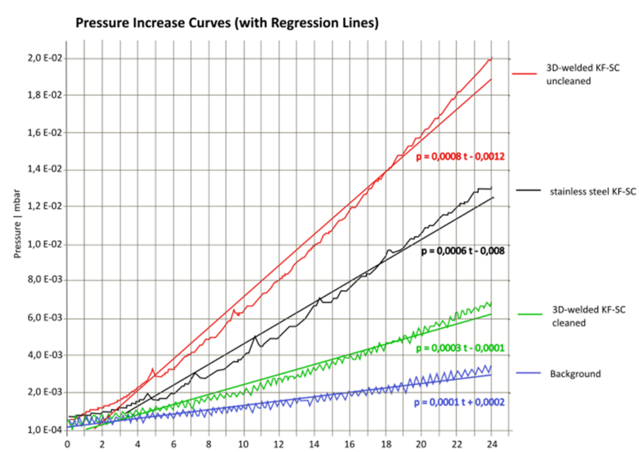

Figure 5: Leak rates.

As can be seen from Table 2, the 3D-welded KF-SC DN-40 in the uncleaned state behaves slightly worse than a conventionally manufactured component KF-SC DN-40 made of stainless steel.

When cleaned, the 3D printed part is even better than the conventional one.

ISBN: 978-3-95450-205-9 doi:10.18429/JACoW-Cyclotrons2019-THC04

Table 2: Leakage Rates

Component	Pressure Increase mbar/s	Leakage Rate mbar·l/s
Background	$2.78 \cdot 10^{-8}$	$1.00 \cdot 10^{-7}$
3D Welded KF-SC DN40 uncleaned	$2.22 \cdot 10^{-7}$	$7.39 \cdot 10^{-7}$
Edelstahl KF-SC DN40	$1.67 \cdot 10^{-7}$	$5.25 \cdot 10^{-7}$
3D Welded KF-SC DN40 cleaned	$8.33 \cdot 10^{-8}$	$2.15 \cdot 10^{-7}$

THE VACUUM CHAMBER

Following the successful test of the 3D-welded KF-SC DN-40, the 3D-printing of a complete vacuum chamber took place using the main advantages of 3D-printing, i.e. form independence and integration of functionality. The basic body of the vacuum chamber was supplemented with a complex geometry and integrated flow channels and completed by welding standard components. In addition to a cost-effective production by avoiding unnecessary rework, this method also has the advantage of a flexible adaptation to different customer requirements.

Figure 6 a) and b) show different CAD models of the vacuum chamber and Fig. 7 gives an insight into the manufacturing process of the base body of the recipient from the powder bed.

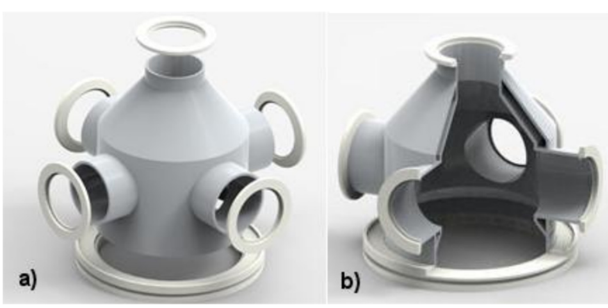

Figure 6: CAD-models of the chamber.

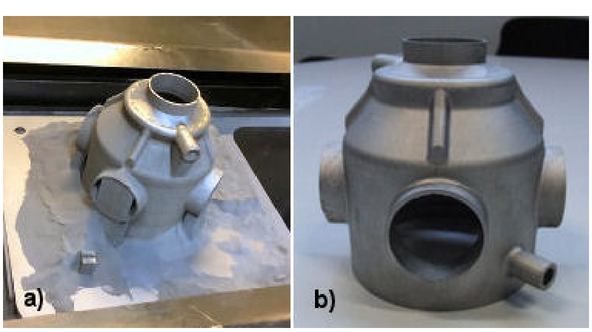

Figure 7: Production of the chamber.

Figure 8 shows the system of flow channels as an example of possible functional integration. Through the flow channels, the recipient can be heated during evacuation and alternatively cooled when needed in operation.

The exact shape of the channels was determined by a CFD-program to ensure optimal flow conditions.

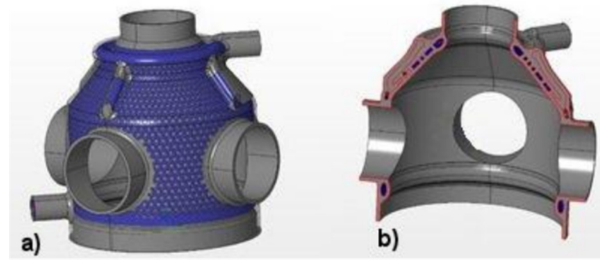

Figure 8: Flow channels.

Figure 9 shows the 3D-printed vacuum chamber ready for practical laboratory use.

Figure 9: 3D-printed vacuum chamber.

CONCLUSION

The present work shows that metal-based 3D printing can meet the requirements of vacuum technology in the area of high vacuum. Now the step is in the ultrahigh vacuum, i.e., in pressure ranges smaller than 10^{-7} mbar. While in high vacuum the leakage rate is essentially attributable to the Viton flange gaskets and the material properties, for example the roughness of the surface, are not yet effective, they will have a decisive influence when the pressure falls below 10^{-7} mbar. How big this influence ultimately is, must result in appropriate tests, which require a much greater effort.

The use of the described production technology will actually depend on how the advantages can be used properly. Especially for single production and prototypes, 3D printing technology can be of considerable benefit. This is particularly due to the freedom in geometry and the possibility of function integration, such as the realization of a surface heating system.

The interest of the cooperation companies is expressed in Mr. Dinkel's (company Robert Hofmann GmbH) quote: “For us the field of vacuum technology is a highly attractive market because often individually complex components with materials available in 3D printing are needed”.

ISBN: 978-3-95450-205-9 doi:10.18429/JACoW-Cyclotrons2019-THC04

ACKNOWLEDGEMENTS

The authors thank Prof. Dr. Prechtl for his professional help on every question and providing the laboratory and the necessary equipment.

We thank Mr. Jürgen Dorn for his support in carrying out the experiments.

Furthermore, we thank the company Robert Hoffmann GmbH in Schney for the generous support of our project. Our special thanks go to Mr. Michael Dinkel, who printed out the parts described in the thesis, reworked them and also helped us with technical questions at any time.

A big thank also goes to the company VACOM Vacuum Components & Measuring Technology GmbH in Jena and here to Mr. René Bauer for the excellent advice, the welding of the components and the performed tests, the results of which gave us new courage.

REFERENCES

[1] Strategy&-Analyse, https://www.strategyand.pwc.com/

[2] VACOM, Die kleine Fibel der Vakuum-Druckmessung. Jena, Germany, VACOM Vakuum Komponenten & Messtechnik GmbH, 2011, pp. 2-3.

ISBN: 978-3-95450-205-9 doi:10.18429/JACoW-Cyclotrons2019-THD01

PHYSICS AND TECHNOLOGY OF COMPACT PLASMA TRAPS*

D. Mascali†, G. Castro, L. Celona, S. Gammino, O. Leonardi, M. Mazzaglia, E. Naselli[1], G. Torrisi
Istituto Nazionale di Fisica Nucleare, Laboratori Nazionali del Sud, Catania, Italy
[1]also at Name of Università degli Studi di Catania, Dip.to di Fisica e Astronomia, Catania, Italy

Abstract

ECR Ion Sources are deemed to be among the most performing ion sources feeding particle accelerators, cyclotrons in particular. Improvements of their performances strictly depend on the knowledge of plasma physics in compact magnetic traps. The paper will comment on the results obtained by the INFN-LNS team and international collaborators by means of a multi-diagnostics setup able to monitor the evolution in space and time of several plasma parameters, simultaneously with beam extraction and analysis in the LEBT, in single vs. double frequency operations, including the RF power and magnetic field scalings, and exploring regimes dominated by plasma turbulence. The results are relevant for the operations of existing ion sources and for the design of new ones. Compact magnetic traps fashioned in a similar way of ECRISs can be considered as an experimental environment by itself: we are exploring this opportunity relying to the in-plasma measurements of radionuclides lifetimes (in particular, beta-decaying elements): CosmoChronometers or nuclei involved in the s-process nucleosynthesis are among the case studies, opening new perspectives in the nuclear astrophysics field.

INTRODUCTION

This paper describes the complex setup of diagnostics tools supported and developed in the frame of INFN-LNS activities on ion sources along the years. Efforts about diagnostics for ECR Ion Sources by other groups in the world are also mentioned. Plasma diagnostics have been developed in the ECRIS community for measuring plasma density and temperatures in a space and time resolved way, thus investigating the spatial structure of the plasma and its temporal behaviour, in stable and turbulent regimes. Precise measurements of parameters are crucial to correlate plasma vs. beam properties. Also in the perspective to use ECR ion traps for studying nuclear β-decays, thus correlating eventual variation of the lifetime to the plasma properties, plasma diagnostics play a fundamental role. The relevance on R&D for new diagnostics tools in ECR ion sources is witnessed by a plenty of publications [1-11].

DIAGNOSTICS TOOLBOX AT INFN-LNS

INFN has supported along the years the efforts of LNS R&D group on plasma based ion sources in the design and implementation of advanced diagnostics techniques, under the experiments HELIOS, RDH and VESPRI and, last, in the frame of PANDORA Feasibility Study. Of the list below, it is worth mentioning the A3 technique (the X-ray pin-hole camera) that has allowed to characterize the plasma morphology and to perform space resolved spectroscopy (thus evidencing the local displacement of electrons at different energies, as well as of plasma ions highlighted by fluorescence lines emission) versus the main tuning parameters such as the pumping wave frequency and the strength of the confining magnetic field. A summary of the diagnostics tools now composing the “arsenal” (described in details in [10, 11]) available or under design/installation at INFN-LNS is here presented, grouping them in four cathegories according to ther property of the plasma that we want to measure:

A. Warm & Hot electrons Temperature
 • A1 – Continuous and characteristic X radiation E<30 keV measured by SDD detectors;
 • A2 – Hard X-rays (E>50 keV, up to hundreds keV) by large volume HpGe detectors;
 • A3 –X-rays (1<E<20 keV) pin-hole camera with high energy resolution (around 150 eV) for space resolved X-ray spectroscopy;
B. Cold Electron Temp. & Density
 • B1 – Space Resolved Optical Emission Spectroscopy (space resolution less than 100 μm and spectral resolution of about 10^{-2} nm in the range 200-900 nm;)
 • B2 – Line integrated density measurement through microwave interferometry;
 • B3 – Faraday-rotation diagnostics (horn antennas coupled to Orthomode Transducer for polarimetry);
C. Ion Temperature
 • C1 – Measurement of X-ray fluorescence lines broadening through high resolution) X-ray spectroscopy, by using doubly curved crystals coupled to polycapillars;
 • C2 – Space resolved measurements are possibile with a Polycapillar+doubly-curved-crystal+CCD (X-ray sensitive) camera in a “pin-hole method” scenario;
D. On-line Charge State Distribution (CSD)
 • D1 – Space Resolved Optical Emission Spectroscopy:
 • D2 – X-ray fluorescence lines shift through high resolution); X-ray spectroscopy (curved crystals + polycapillar);
 • D3 – Space resolved measurements: Polycapillar+doubly-curved-crystal+CCD (X-ray sensitive) camera in a “pin-hole method” scenario;

A rendered view of the several diagnostics is illustrated in Fig. 1.

* Work supported by 5th Nat. Comm. of INFN under the project PANDORA.
† e-mail: davidmascali@lns.infn.it

ISBN: 978-3-95450-205-9 doi:10.18429/JACoW-Cyclotrons2019-THD01

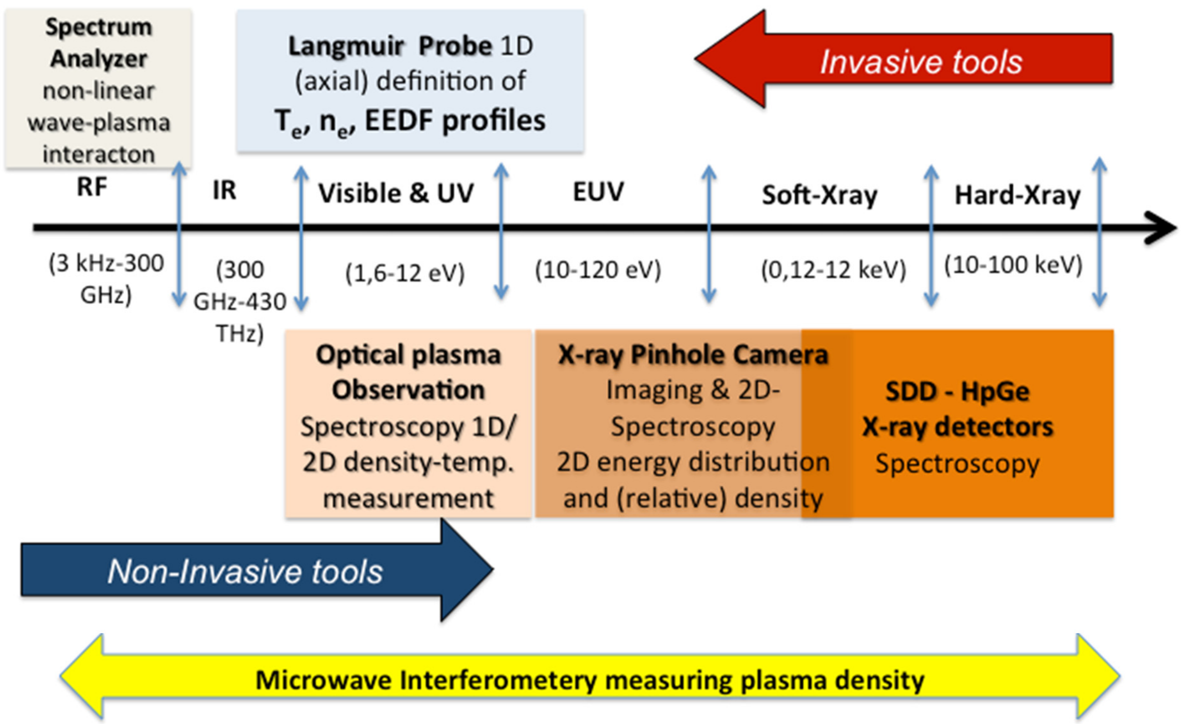

Figure 1: Render view of the several diagnostics tools needed (and already partially available at LNS) for characterizing microwave generated plasmas.

Other groups worldwide have used multi-diagnostics systems to provide a complete picture of how the plasma behaves under different sources parameters, in quiescent and/or turbulent regimes, exploring the role played by the RF field and by the magnetic confinement in simple-mirror and/or B-min configurations [1-6].

DIAGNOSTICS OUTCOMES

The outcomes of diagnostics measurements are of paramount importance in a number of applications. The operations of existing devices can be improved in a relevant way. The design of the new ones, can benefit hugely from a better understanding of ECRIS underlying physics.

The work done by Finnish and Russian groups [8, 11] about study of turbulence in ECRIS and ECRIS-based charge breeders, for instance, allows to find the so-called "stability islands". They are regions in the parameters space (operational power, magnetic field, frequency, etc.) where their combinations allow stable operations (low beam ripple, low plasma pollution by contaminants from the chamber walls, etc.) and high performances.

At INFN-LNS, the special magnetic field of the AISHa source (see Figs. 2 and 3: AISHa is an advanced ECRIS formerly designed for hadrontherapy purposes, but suitable for production of intense beams of any element) has been addressed to minimize the production of suprathermal electrons which are produced under certain profiles of the axial magnetic field [13].

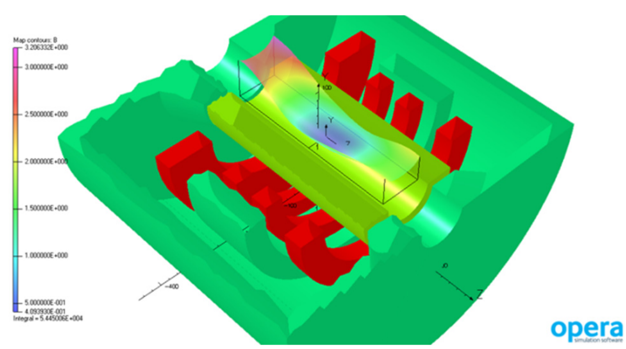

Figure 2: Magnetic system of the AISHa source with the trend of the axial field.

In particular, the field was studied to minimize the hot electron component and to optimize the ECR heating process by controlling the field gradient at injection and extraction and the resonance length. For the AISHa source it has been decided to adopt a solution employing four coils which permits to have a good control on the above cited parameters.

The microwave injection system has been designed for maximizing the beam brilliance and minimizing the beam emittance through a fine frequency tuning within the 17.3-18.4 GHz band.

Both the role of the magnetic field and frequency tuning were for a long time investigated in terms of plasma relative parameters, measured by X-ray spectroscopy especially [13-16].

ISBN: 978-3-95450-205-9 doi:10.18429/JACoW-Cyclotrons2019-THD01

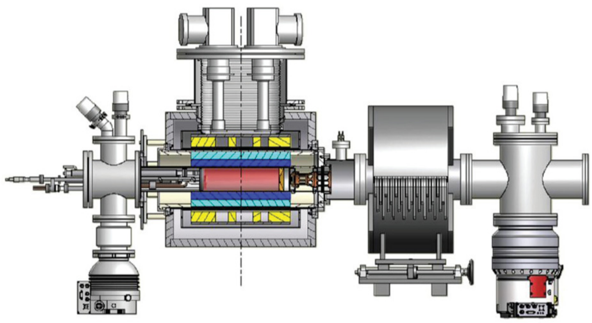

Figure 3: AISHa The layout of the source.

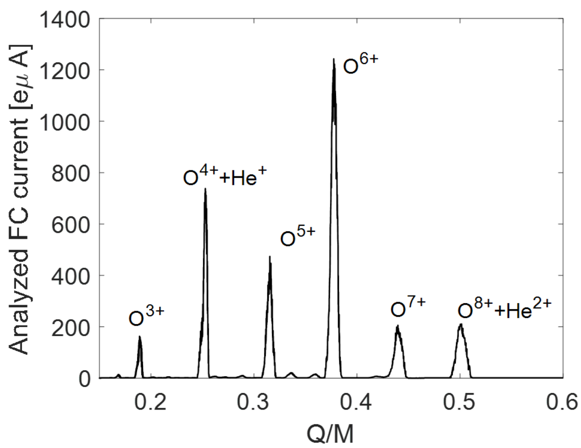

Figure 4: AISHa produced Oxygen charge state distribution for the ion source tune optimized on O6+ charge state.

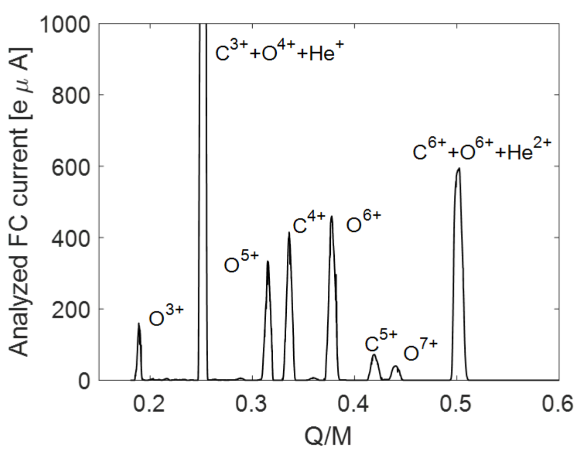

Figure 5: AISHa produced Carbon charge state distribution for the ion source tune optimized on C4+ charge state.

AISHa is now under the commissioning phase, which has been addressed especially to the production of light elements for hadron therapy and fundamental physics.

Table 1: AISHa First Performances

Charge State	Beam current [μA]	Requirement [μA]
$^{16}O^{6+}$	1200	400
$^{16}O^{7+}$	200	200
$^{12}C^{4+}$	420	400
$^{12}C^{5+}$	75	200
$^{40}Ar^{11+}$	155	//
$^{40}Ar^{12+}$	140	//

The ion beam currents produced by AISHa are reported in Figs. 4 and 5, for oxygen and carbon [17]. Table 1 summarizes beam currents for several ions, comparing them with the design requirements and goals. It is remarkable that more than 1 mA of O^{6+} has been produced. In particular, the requirements about the performances of AISHa for these beams were determined, other than from expectations of future hadrontherapy facilities, especially from the requirements of the INFN Superconducting Cyclotron upgrade project. AISHa, in fact, it is expected to become the main ion injector for the upgraded accelerator, that should be able to produce intense ion beams for fundamental research in the 2-10 kW range of output beam power [18].

From Table 1 it can be seen that most of the requirements have been already fulfilled, whilst for some others further commissioning and upgrades are needed. In particular, it is expected to achieve higher performances by an upgrade of the RF heating system through the installation of a 21+18 GHz Klystron Amplifier, in order to operate in Two Frequency Heating mode up to 21 GHz, that should be still feasible according to the maximal B-field in the trap.

BEYOND ECRIS: ECR ION TRAPS FOR NUCLEAR DECAY STUDIES

This section presents the underlying idea of the PANDORA project [19]: it is a new plasma trap designed to perform interdisciplinary research. The main goal is specially to make for the first-time nuclear β-decays measurements of astrophysical interest in magnetized plasmas as a function of ionisation state [20, 21]. The basic idea is that inside a compact plasma trap (sketched in Fig. 6, including the diagnostics surrounding the setup) the radionuclides can be trapped in a dynamical equilibrium for several hours or even days, with a locally stable density, temperature and charge state distribution (CSD). The latter can be modulated according to the RF power level sustaining the plasma, the magnetic field strength, the background pressure, etc. This will allow to characterize decay rates with respect to the CSD variation, and versus the plasma density and temperature, in a stellar-like condition at least as concerns the CSD conditions (e.g., like in the stellar cores or resembling primordial nucleosynthesis conditions).

ISBN: 978-3-95450-205-9 doi:10.18429/JACoW-Cyclotrons2019-THD01

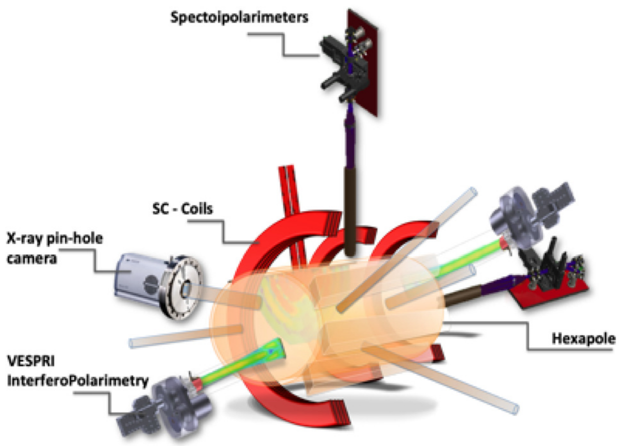

Figure 6: Sketch of the ECR ion trap surrounded by several diagnostics tools for investigating β-dacays in plasmas.

The densities of the multiply-charged ions to be confined for providing meaningful information concerning decay rates in plasmas will require a MHD - MagnetoHydroDynamically stable regime of trapping. MHD stability will be an important condition to investigate nuclear decays, since a stationary plasma state is needed in order to correlate nuclear phenomena with plasma observables, especially average charge state, temperature and density.

In summary, the experimental procedure includes:

- A "buffer plasma" is created by He, O or Ar up to densities of 10^{13} cm^{-3};
- The isotope is then directly fluxed (if gaseuous) or vaporized by appropriate ovens and then fluxed inside the chamber to be turned into plasma-state;
- Relative abundances of buffer vs. isotope densities range from 100:1 (if the isotope is in metal state) to 3:1 (in case of gaseous elements);
- The plasma is maintained in dynamical equilibrium by equalizing input fluxes of particles to losses from the magnetic confinement.

The in-plasma activity can be determined by measuring the number of decays vs. time, and this can be done by tagging them from products-emitted γ-rays, and as a function of the average ionisation state (predictions and extrapolations to astrophysical plasmas are also here included). Calculations say that under dynamical equilibrium the number of decays scales linearly with the radio-isotope activity λ.

Figure 7 illustrates a render view of the whole setup, including the magnetic trap and the array of HpGe detectors needed for tagging the decays via γ-rays detection (14 detectors are needed to achieve 1% approximately of overall efficiency).

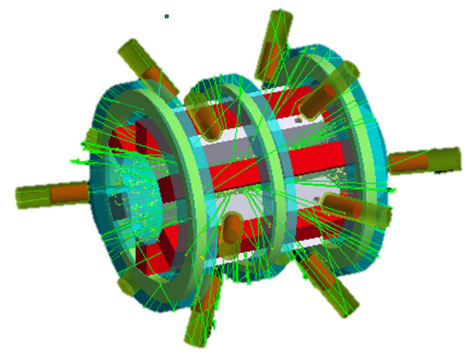

Figure 7: Geant-4 simulation of the overall PANDORA setup, including the trap and the array of 14 HpGe γ-rays detectors.

In this perspective, the simultaneous use of different diagnostics is crucial, since if and how the decay times would be affected by the plasma environment critically depend on local values of plasma density and temperature.

PANDORA has been funded as a feasibility study during 2017-2019, and for the full realization in the period 2020-2024. First results, after completing the construction of both the trap and the detector array, are expected by 2023.

CONCLUSION

The paper has reported about role played by the plasma diagnostics in research and development in ECR ion source field. Some recent results about the AISHa source, whose magnetic system as well as RF injection have been designed according to previous experiment on plasma properties measurements by X-ray diagnostics, have been reported, in view of the major upgrading of the INFN-LNS superconducting cyclotron. The efforts paid in diagnostics and design of advanced sources has produced a relevant outcome for application of ECR Ion Trap in the field of Nuclear Astrophysics. The PANDORA project has been presented, discussing about the future measurement of β-dacaying isotopes lifetimes in magnetized plasmas.

In perspective, the diagnostics could allow to tune the ECR Ion Source in a better way, also finding precursor of instabilities and/or allowing to implement new techniques for suppressing plasma turbulences, thus getting more stable and more intense beams [22, 23].

ACKNOWLEDGEMENTS

The authors gratefully acknowledge the contribution of Alessio Galatà, Paolo Romano, Gianluigi Cosentino, Claudia Caliri, Domenico Santonocito, Maurizio Busso, Alberto Mengoni, Cristian Massimi, Franco Chines, Gianni Manno, Salvo Marletta, Salvo Vinciguerra, Giuseppe Pastore, Maurizio Castro.

ISBN: 978-3-95450-205-9 doi:10.18429/JACoW-Cyclotrons2019-THD01

REFERENCES

[1] O. Tarvainen *et al.*, "Injected 1+ ion beam as a diagnostics tool of charge breeder ECR ion source plasmas", *Plasma Sources Sci. Technol.,* vol. 24, p. 035014, 2015. doi:10.1088/0963-0252/24/3/035014

[2] O. Tarvainen *et al*., "Diagnostics of a charge breeder electron cyclotron resonance ion source helium plasma with the injection of 23Na1+ ions", *Phys. Rev. Accel. Beams*, vol. 19, p. 053402, 2016. doi:10.1103/PhysRevAccelBeams.19.053402

[3] C. Mallick, M. Bandyopadhyay, and R. Kumar, "Plasma characterization of a microwave discharge ion source with mirror magnetic field configuration", *Rev. Sci. Instrum.,* vol. 89, p. 125112, 2018. doi:10.1063/1.5048292

[4] R. Racz, S. Biri, Z. Perduk, and J. Pálinkás, "First results on radial and azimuthal dependence of plasma parameters in a hexapole-trapped ECR discharge", in *Proc. 17th Int. Conf. on Ion Sources*, Geneva, Switzerland, Sep. 2017, *AIP Conf. Proc.,* vol. 2011, no. 1, p. 020010, 2018. doi:10.1063/1.5053252

[5] R. Rácz, "Effect of the two-close-frequency heating to the extracted ion beam and to the X-ray flux emitted by the ECR plasma", *J. Instrum.,* vol. 13, no.12, p. C12012, 2018. doi:10.1088/1748-0221/13/12/c12012

[6] R. Kronholm *et al.*, "Spectroscopic study of ion temperature in minimum-B ECRIS plasma", *Plasma Sources Sci. Technol., vol.* 28, no. 7, p. 075006, 2019. doi:10.1088/1361-6595/ab27a1

[7] M. Giarrusso *et al.*, "High resolution spectropolarimetry: from Astrophysics to ECR plasmas", *J. Instrum.,* vol. 13, no. 11, p. C11020, 2018: doi:10.1088/1748-0221/13/11/C11020

[8] I. Izotov *et al.*, "Measurement of the energy distribution of electrons escaping minimum-B ECR plasmas", *Plasma Sources Sci. Technol.,* vol. 27, p. 025012, 2018. doi:10.1088/1361-6595/aaac14

[9] O. Tarvainen et al., in *Proc. 17th Int. Conf. on Ion Sources: AIP Conference publications*, 2011, (2018), p. 070006.

[10] S. Biri *et al.*, "Multi-diagnostic setup to investigate the two-close-frequency phenomena", *J. Instrum.,* vol. 13, no. 11, p. C11016, 2018. doi:10.1088/1748-0221/13/11/C11016

[11] D. Mascali *et al.,* "Electromagnetic diagnostics of ECR-Ion Sources plasmas: optical/X-ray imaging and spectroscopy", *J. Instrum.* vol. 12, p. C12047, 2017. doi:10.1088/1748-0221/12/12/C12047

[12] A. G. Shalashov, M. E. Viktorov, D. A. Mansfeld, and S. V. Golubev, "Kinetic instabilities in a mirror-confined plasma sustained by high-power microwave radiation", *Phys. Plasmas,* vol. 24, p. 032111, 2017. doi:10.1063/1.4978565

[13] S. Gammino, D. Mascali, L Celona, F. Maimone, and G. Ciavola, "Considerations on the role of the magnetic field gradient in {ECR} ion sources and build-up of hot electron component", *Plasma Sources Sci. Technol.,* vol. 18, no. 4, p. 045016, 2009. doi:10.1088/0963-0252/18/4/045016

[14] D. Mascali *et al.*, "X-ray spectroscopy of warm and hot electron components in the CAPRICE source plasma at EIS testbench at GSI", *Rev. Sci. Instrum.*, vol. 85, p. 02A956, 2014. doi:10.1063/1.4858115

[15] D. Mascali *et al.,* "Electron cyclotron resonance ion source plasma characterization by X-ray spectroscopy and X-ray imaging", *Rev. Sci. Instrum.*, vol. 87, no. 2, p. 02A510, 2016. doi:10.1063/1.4939201

[16] R. Racz *et al.*, "Electron cyclotron resonance ion source plasma characterization by energy dispersive x-ray imaging", *Plasma Sources Sci. Technol.,* vol. 27, no. 7, p. 075011, 2017. doi:10.1088/1361-6595/aa758f

[17] L. Celona *et al.*, "Experimental characterization of the AISHA ion source", *submitted to Rev. of Sci. Instrum.*

[18] L. Calabretta, A. Calanna, G. Cuttone, G. D'Agostino, D. Rifuggiato, and A. D. Russo, "Upgrade of the LNS superconducting cyclotron for beam power higher than 2-5 kW", in *Proc. 21th Int. Conf. on Cyclotrons and their Applications (Cyclotrons'16)*, Zurich, Switzerland, Sep. 2016, pp. 7-10. doi:10.18429/JACoW-Cyclotrons2016-MOA02

[19] D. Mascali *et al.*, "PANDORA, a new facility for interdisciplinary in-plasma physics", *Eur. Phys. J. A.,* vol. 53. No. 7, p. 145, 2017. doi:10.1140/epja/i2017-12335-1

[20] Y. A. Litvinov and F. Bosch, "Beta decay of highly charged ions", *Rep. Prog. Phys.,* vol. 74, no. 1, p. 016301, 2011. doi:10.1088/0034-4885/74/1/016301

[21] K. Takahashi, R. N. Boyd, G. J. Mathews, and K. Yokoi, "Bound-state beta decay of highly ionized atoms", *Phys. Rev. C.* vol. 36, p. 1522, 1987. doi:10.1103/PhysRevC.36.1522

[22] E. Naselli *et al.*, "Impact of two-close-frequency heating on ECR ion source plasma radio emission and stability", *Plasma Sources Sci. Technol.,* vol. 28, no. 8, p. 085021, 2019. doi:10.1088/1361-6595/ab32f9

[23] R. Rácz *et al.*, "Effect of the two-close-frequency heating to the extracted ion beam and to the X-ray flux emitted by the ECR plasma", *J. Instrum.,* vol. 13, no. 12, p. C12012, 2018. doi:10.1088/1748-0221/13/12/C1

ISBN: 978-3-95450-205-9 doi:10.18429/JACoW-Cyclotrons2019-THD02

CENTRAL REGION UPGRADE FOR THE JYVÄSKYLÄ K130 CYCLOTRON

T. Kalvas*, P. Heikkinen, H. Koivisto
University of Jyväskylä, Department of Physics, Jyväskylä, Finland
E. Forton, W. Kleeven, J. Mandrillon, V. Nuttens
Ion Beam Applications (IBA), Louvain-la-Neuve, Belgium

Abstract

The Jyväskylä K130 cyclotron has been in operation for more than 25 years providing beams from H to Au with energies ranging from 1 to 80 MeV/u for nuclear physics research and applications. At the typical energies around 5 MeV/u used for the nuclear physics program the injection voltage used is about 10 kV. The low voltage limits the beam intensity especially from the 18 GHz ECRIS HIISI. To increase the beam intensities the central region of the K130 cyclotron is being upgraded by increasing the injection voltage by a factor of 2. The new central region with spiral inflectors for harmonics 1–3 has been designed. The new central region shows better transmission in simulations than the original one for all harmonics and especially for h=2 typically used for nuclear physics. The engineering design for the new central region is being done.

INTRODUCTION

The Jyväskylä K130 cyclotron [1] is a normal conducting multi-particle multi-energy accelerator that has been in operation since 1992. The cyclotron has been used for more than 160 000 hours providing beams from H to Au with energies ranging from 1 to 80 MeV/u. Currently about 3/4 of the running time is used for nuclear physics research and 1/4 for industrial applications. The main application is space electronics irradiation testing, which is done by accelerating ion beam cocktails at 9.3 Mev/u and 16.2 MeV/u [2], while the majority of the heavy ion beams for the nuclear physics program are run at energies close to 5 MeV/u.

The typical injection voltage used for nuclear physics beams is around 10 kV. Such a low voltage limits the available accelerated beam intensity due to several effects. The beams produced by electron cyclotron resonance ion sources (ECRIS) have a strong divergence due to the magnetic field of the ion source and especially when tuned for medium charge states and high intensities, also the space charge effects will limit the beam intensity available for acceleration. Also, typical normalized rms-emittance of a beam produced by modern ECRIS is about 0.1 mm mrad [3], which equates to about a geometric envelope emittance of 200 π.mm.mrad for Ar^{8+} accelerated with 10 kV injection voltage, assuming a KV-distribution. As the K130 cyclotron has an acceptance of 100 π mm mrad part of the beam is obviously lost. All of these effects can be mitigated by increasing the injection voltage. Using the recently commissioned 18 GHz ECRIS HIISI [4–6] at Jyväskylä it has been observed that produced beam intensities of medium charge states such as Ar^{8+} double as source voltage increases from 10 kV to 20 kV. Therefore, a project has been initiated to redesign and upgrade the central region of the K130 by increasing the injection voltage by a factor 2.

PLAN FOR REDESIGN

The K130 has a broad operation range by being able to accelerate particles with two 78° dees with 10–21 MHz RF at a maximum of 50 kV using harmonic modes h =1–3. Injection of beams is done axially using separate spiral inflectors for each of the three harmonic modes. The inflectors can be switched through the axial bore using an automatic changer. The inflector housing is fixed and common to all harmonic modes. Each of the harmonic modes has a fixed design orbit leading to a well-centered acceleration. The injection voltage therefore scales as

$$U_{\mathrm{inj}} = \frac{q}{2m} B_0^2 r_{\mathrm{inj}}^2, \tag{1}$$

where q and m are the particle charge and mass, B_0 is the cyclotron magnetic flux density on axis and r_{inj} is the injection radius. The dee voltage V_{dee} scales linearly with U_{inj} for a fixed design orbit. Only slight centering errors of < 5 mm can be corrected using harmonic coils.

For the upgrade of the central region the fixed design orbits and injection radii are redefined. The original injection radii 13.1, 18.8 and 18.8 mm for harmonic modes 1, 2 and 3 respectively [7] are replaced by 18.5, 26.6 and 26.6 mm – i.e. the radii are multiplied by $\sqrt{2}$. The proportionality constant between V_{dee} and U_{inj} was halved to keep the number of turns in the accelerator almost constant. The magnetic design of the machine was left as originally designed with a 20° integrated phase slip at the central field bump and isochronous field elsewhere until the extraction.

DESIGN PROCESS

The new central region was designed using IBA tracking code AOC [8], which numerically integrates the equations of motion in static magnetic fields and RF electric fields. The 3D magnetic fields were produced using first order expansion of 2D maps measured in the end of 1980s when the cyclotron was built. The electric fields were constructed assuming that $\vec{E}(\vec{r},t) = \vec{E}'(\vec{r})\cos(t)$, where $\vec{E}'(\vec{r})$ is a static electric field computed by Vector Fields Opera [9] and imported to AOC on a set of regular grids in cylindrical coordinates.

* taneli.kalvas@jyu.fi

ISBN: 978-3-95450-205-9 doi:10.18429/JACoW-Cyclotrons2019-THD02

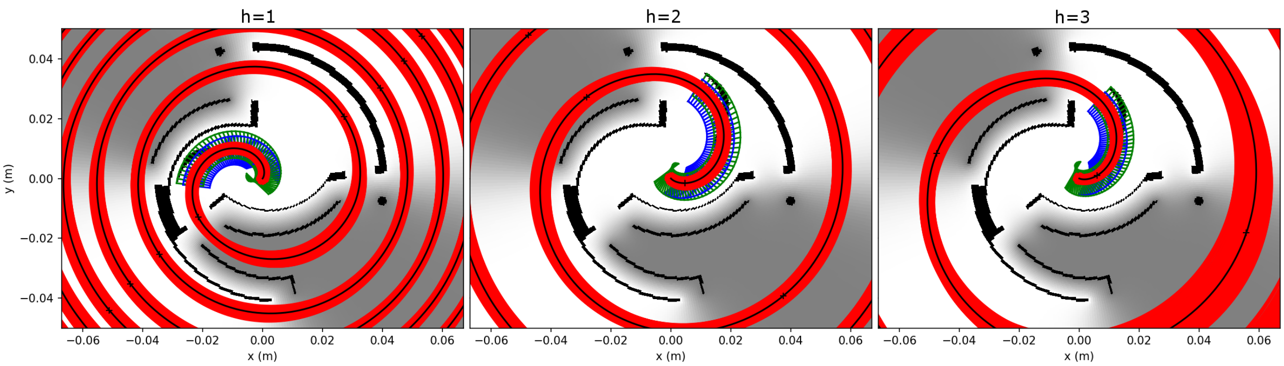

Figure 1: The new central region of the K130 with all three harmonics. The beam depicted in red has a geometrical envelope emittance of 100 π mm mrad at the inflector entrance and all particles are injected at phase 0°. The black line is the reference orbit with particle location at the time of dee voltage maxima marked with a cross.

The new central region design was made using three beams: (1) 30 MeV H^- beam accelerated with the first harmonic mode with V_{inj} = 11.5 kV and V_{dee} = 18.1 kV, (2) 200 MeV $^{40}Ar^{8+}$ accelerated with h = 2 using V_{inj} = 20.6 kV and V_{dee} = 24.5 kV, and (3) 200 MeV $^{40}Ar^{8+}$ accelerated with h = 3 using V_{inj} = 20.6 kV and V_{dee} = 36.0 kV. These beams are representative of typical medium energy, high intensity beams accelerated at Jyväskylä.

The new central region was designed with an iterative process, which started with the original central region geometry. First, on the cyclotron midplane, the injection location and angle leading to a minimum centering error of the accelerated orbit was searched for at the injection phase which leads to the maximum energy gain per turn at high energies. This was done for each of the harmonics, after which the geometry was modified to give space for the beams or to intentionally change the orbits by changing the acceleration gap angles and thus avoiding collimation. This process was repeated until a satisfactory solution was acquired.

After finding the well-centered reference orbits the spiral inflectors were designed to deflect a particle propagating along the axis of the accelerator to the desired orbit. The original inflectors of the K130 were made according to the analytic Belmont-Pabot formula [10]. This time the inflectors were designed in AOC using a numerical model producing the deflecting electric field in the particle tracking routine. The difference of the inflectors produced by this method when compared to Belmont-Pabot solution is that the gap between the inflector electrodes can remain constant even with a nonzero tilt parameter k. The tradeoff is that with a constant gap the inflector will be longer in length as a fraction of the electric field is used to adjust the horizontal turning radius. In this case the constant gap solution was found to have a higher transmission. For each of the inflectors there is an infinite number of solutions that deliver the beam to the desired orbit. For the K130 the largest bending radius A was chosen, which produces an inflector that both fits within the central region case and avoids affecting the accelerating field distribution. The tilt parameter k and the rotation θ were found to deliver the reference particle to

Table 1: The New Spiral Inflector Parameters

Harmonic mode:	**1**	**2**	**3**
Spiral height A (mm)	36	45	34
Tilt parameter k	0.497	0.560	0.604
Injection radius (mm)	18.5	26.6	26.6
Gap height (mm)	5	5	5
Gap width	10	10	10
Maximum V_{inj} (kV)	31.8	42.0	28.6
Maximum V_{sprl} (kV)	±4.41	±4.67	±4.21

the centered orbit. The inflector gap height and width were chosen to have the same values as in the original inflectors, 5 and 10 mm respectively. The inflector parameters selected for the new central region are shown in Table 1. The physical models of the inflector geometries built from the solved central trajectories were trimmed in length to take in account the effects of the fringe field. At the start of the inflector the length was trimmed to achieve centering of the reference particle inside the inflector and at the end trimming was done to minimize the vertical oscillation of injected particle around the midplane. For example, for the second harmonic inflector the calculated centering error within the inflector is less than 0.15 mm and the vertical oscillation in the acceleration region is less than 0.2 mm. The engineering models for the inflectors were produced using a custom computer program defining the geometry in the openly documented IGES file format [11].

The central region geometry with the inflectors and the beams for all three harmonics are presented in Figure 1. The transmission of a KV-distributed beam with a geometrical envelope emittance of 100 π mm mrad injected at the inflector entrance at phase 0° is 99 %, 93 % and 98 % through the inflectors and central region for harmonics 1–3 respectively. For a beam with 125 π mm mrad emittance the corresponding transmissions are 87 %, 82 % and 88 %. For a 100 π mm mrad emittance beam with a phase distribution of 0–360° (DC beam) the transmission is 10 %, 14 % and 12 % for the different harmonics. The transmission is mainly limited

ISBN: 978-3-95450-205-9 doi:10.18429/JACoW-Cyclotrons2019-THD02

by the loss of vertical focusing outside the 56° acceptance of h =2–3 modes and 46° acceptance of h =1 mode as presented in Figure 2. The transmission of the DC beam is therefore somewhat better than of the original central region (9 %) for the same geometrical emittance beam [7].

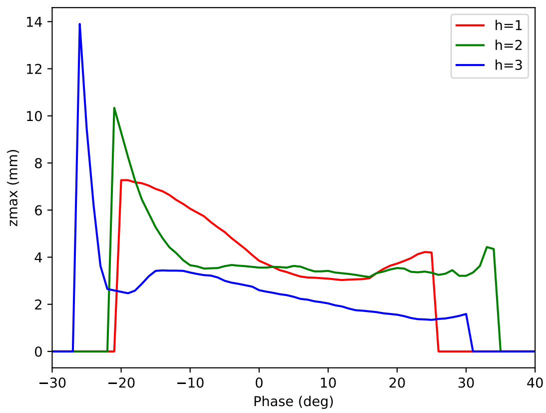

Figure 2: The maximum vertical position of a particle launched at the end of the inflector off the midplane, at z = 1 mm as a function of the starting phase. A non-zero value is shown only for particles reaching the extraction. Zero phase refers to the phase producing the highest energy gain per turn for a particle launched on the midplane.

Some studies were performed with bunched beams. With h = 2, for example, a transmission of 46 % was achieved (a gain factor of 3.5 compared to a DC beam) without considering the space charge effects. With the space charge model of AOC turned on one could evaluate the throughput of the bunched beam taking in account the repulsive space charge forces. Unfortunately to evaluate the maximum transmission with space charge a global optimization should be done to the injection line by adjusting the initial phase space distribution, bunching parameters and focusing between the buncher and the inflector. Due to the computation time of such a calculation it has not yet been done.

The centering of the injected beam with h = 2 and h = 3 is presented in Figure 3. The central region has been designed to minimize the centering error of the reference orbit, the orbit injected at the center of the inflector. The reference orbit is drawn in black. It can be seen that the centering error is of the order of 1 mm. The rest of the 100 π mm mrad beam is drawn in red. For the h = 2 the maximum centering error within the beam is < 5 mm, which enables an efficient extraction of the accelerated beam from the cyclotron. The h = 1 case is simiar. On the other hand, for the h = 3 case the beam contains particles with centering errors of up to 25 mm. This is not due to the new central region design as the same is also observed for the original central region, but it is an effect that takes place because in the case of h = 3 the phase advance within a single dee is 3 × 78° = 234°. Once the phase advance is larger than 180° small errors in particle phase become amplified causing the centering error to grow. The large centering error spread causes losses in the extraction, which is a known problem on the K130 with h = 3. The effect could be corrected by decreasing the dee angle in the central region, but this would decrease the energy gain per turn of the already critical h = 1 case. Therefore, for now the dee angle originally selected for the K130 is accepted as a compromise.

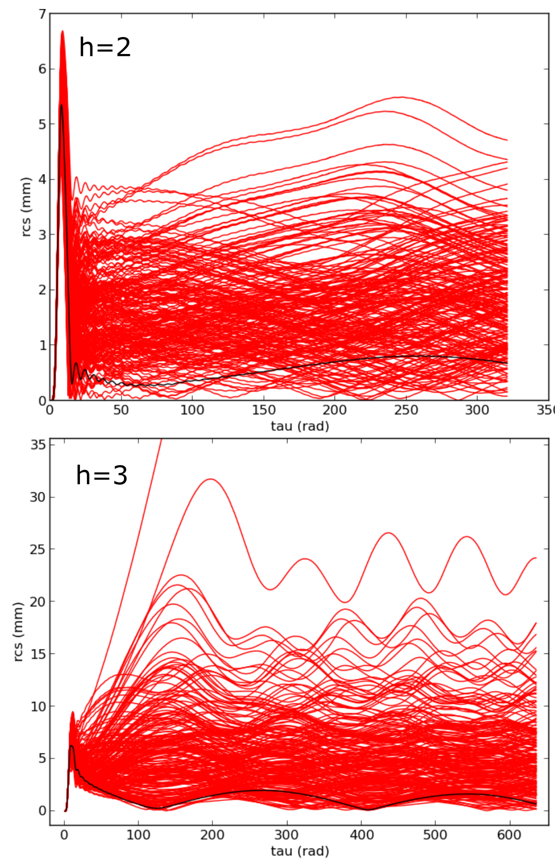

Figure 3: Centering of the full injected beam for h = 2 and h = 3. The reference orbit is drawn in black.

OUTLOOK

The physics design of the new central region is mostly done. Some simulation studies with space charge and bunching are still being made, but it is expected that no changes will be made to the design presented in this paper. Therefore, the engineering design for the project is already being made. The number of modified parts due to the redesign is rather small. The inflectors and their supporting structures, the central region case, the dee and the dummy-dee tips and the upper magnetic steel plug need to be remade. The magnetic upper magnetic steel plug is made of two parts with the outer one being fixed and acting as a part of the vacuum chamber. The inner part of the plug is removed together with the inflector by the inflector changer. Currently the aperture in the outer part is ⌀70 mm, but the h = 2, largest of the new inflectors will require a free space of at least ⌀75 mm to fit through. The engineering and machining of the new parts

ISBN: 978-3-95450-205-9 doi:10.18429/JACoW-Cyclotrons2019-THD02

should be done during the first months of 2020 allowing the experimental characterization and commissioning of the new central region during 2020.

REFERENCES

[1] E. Liukkonen, "New K130 cyclotron at Jyväskylä (Invited Paper)", in *Proc. Cyclotrons'92*, Vancouver, Canada, Jul. 1992, paper I–03, pp. 22–27.

[2] T. Kalvas *et al.*, "Application and development of ion-source technology for radiation-effects testing of electronics", *Nucl. Instrum. Methods Phys. Res., Sect. B*, vol. 406, pp. 205-209, 2017. doi:10.1016/j.nimb.2017.02.051

[3] D. Leitner *et al.*, "Ion beam properties for ECR ion source injector systems", *J. Instrum.*, vol. 6, p. P07010, 2011. doi:10.1088/1748-0221/6/07/P07010

[4] H. A. Koivisto *et al.*, "HIISI, new 18 GHz ECRIS for the JYFL accelerator laboratory", in *Proc. ECRIS'14*, Nizhny Novgorod, Russia, Aug 2014, paper TUOMMH05, pp. 99–103.

[5] T. Kalvas, H. A. Koivisto, K. Ranttila, and O. A. Tarvainen, "Thermal design of refridgerated hexapole 18 GHz ECRIS HIISI", in *Proc. ECRIS'14*, Nizhny Novgorod, Russia, Aug. 2014, paper WEOMMH04, pp. 114–119.

[6] T. Kalvas *et al.*, "Status of new 18 GHz ECRIS HIISI", *AIP Conf. Proc.*, vol. 2011, p. 040006, 2018. doi:10.1063/1.5053280

[7] P. Heikkinen and M. Rinta-Nikkola, "Ion optics in the Jyväskylä K130 cyclotron", in *Proc. Cyclotrons'92*, Vancouver, Canada, Jul. 1992, paper IXA–05, pp. 392–395.

[8] J. G. M. Kleeven *et al.*, "AOC, a beam dynamics design code for medical and industrial accelerators at IBA", in *Proc. IPAC'16*, Busan, Korea, May 2016, pp. 1902–1904. doi:10.18429/JACoW-IPAC2016-TUPOY002

[9] Opera simulation software, version 19, Dassault Systémes. https://operafea.com/

[10] J. L. Belmont *et al.*, "Study of axial injection for the Grenoble cyclotron", *IEEE Trans. Nucl. Sci.*, vol. 13, pp. 191-193, 1966. doi:10.1109/TNS.1966.4324204

[11] Initial graphics exchange specification IGES 5.3, U.S. Product Data Association, 1996.

ISBN: 978-3-95450-205-9 doi:10.18429/JACoW-Cyclotrons2019-THD03

AN IMPROVED CONCEPT FOR SELF-EXTRACTION CYCLOTRONS

W. Kleeven*, E. Forton
Ion Beam Applications (IBA), Louvain-la-Neuve, Belgium

Abstract

A study is made for an improved concept of self-extraction in low and medium energy cyclotrons to be used for production of medical isotopes. The prototype of the self-extracting cyclotron was realized around the year 2001. From this machine, currents higher than 1 mA were extracted and transported to a Pd-103 production target. However, at the higher intensities, the extraction efficiency was dropping to about 70-75%, and the extracted emittance was rather poor, leading to additional losses in the beamline. Several improvements of the original concept are proposed: i) the beam coherent oscillation (as needed for good extraction) is no longer generated with harmonic coils, but is obtained from a significant off-centring of the ion source, ii) the cyclotron magnet has perfect 2-fold symmetry, allowing the placement of two internal sources and dual extraction on two opposite hill sectors, iii) a substantial improvement of the magnetic profile of the hill sectors. Simulations show an extraction efficiency up to almost 93% and emittances at least a factor 3 lower as compared to the original design. The new magnetic design is shown, and results of beam simulation are discussed.

THE PROTOTYPE

The principle of self-extraction is known already for almost 20 years [1]. During extraction, the beam crosses the region of decreasing magnetic field near the pole edge. In existing isochronous cyclotrons, the pole gap usually is large, leading to a gradual radial field fall-off and resulting in a loss of isochronism and ultimate deceleration of the beam. An extraction system is needed to transfer the beam from the limit of isochronous acceleration to the limit of radial focusing. Self-extraction is based on creating a sharp transition from the isochronous to the instable region such that the latter can be reached before falling out of RF accelerating resonance and such that the beam can escape spontaneously from the cyclotron. The prototype (Figure 1) was realized by IBA in the beginning of this century [2].

The cyclotron has unconventional features with respect to typical commercial machines. The pole gap decreases quasi-elliptically towards larger radii. The pole on which the beam is extracted, is radially longer than the others and in it, a groove is machined. This creates a field shape with a sharp dip that acts like a septum and at the same time provides optics for the extracted beam. In order to maximize the extraction, harmonic coils are used to enhance the turn separation at the entrance of the extraction path. A permanent magnet gradient corrector, is placed immediately at the exit of the pole to provide radial focusing to the diverging beam. The small part of the beam, which is not properly

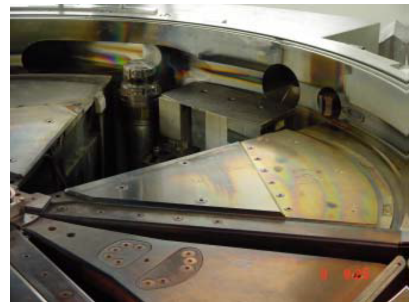

Figure 1: The extraction path in the prototype, showing the groove in the long pole, the gradient corrector and the beam separator. The harmonic coils are placed underneath aluminium pole covers.

extracted, is intercepted on a beam stop (the beam separator) that is placed immediately at the pole exit, in between the circulating and the extracted beam. This beam separator (BS) is designed for low activation and high thermal load. The prototype successfull extracted beams almost up to 2 mA. However, rather poor beam quality was observed and also the extraction efficiency was limited to about 80% at low intensities and about 70% to 75% at higher intensities. This drop (partly) relates to an increase of the dee-voltage ripple resulting from the noisy PIG-source and beam-loading. Although encouraging, the prototype was not yet good enough for industrial applications. The measured beam-quality and extraction efficiency at low intensities agreed quite well with simulations.

Table 1: Cyclotron Main Design Parameters

Cyclotron Type	**Compact Isochronous**
particle	proton
injection	dual internal PIG-source
extraction radius/energy	52 cm; 14 MeV
rotational symmetry	2-fold (quasi 4)
B_{ave} and B_{max}	1.15 T; 1.9 T
quasi-elliptical gap	16 mm < g < 40 mm
minumum gap at extraction	18 mm
pole radius short/long	54 cm/57 cm
number of dees/angle	2; 36°
RF frequency/mode	69.1 MHz; h = 4
dee-voltage	55 kV
available RF power	200 kW

IMPROVEMENTS OF THE DESIGN

Table 1 shows the main design parameters of the cyclotron. Several improvements of the prototype are proposed [3]: i) The groove is replaced by a plateau. This lowers the strong magnetic sextupole component in the extraction path and

* willem.kleeven@iba-group.com

ISBN: 978-3-95450-205-9 doi:10.18429/JACoW-Cyclotrons2019-THD03

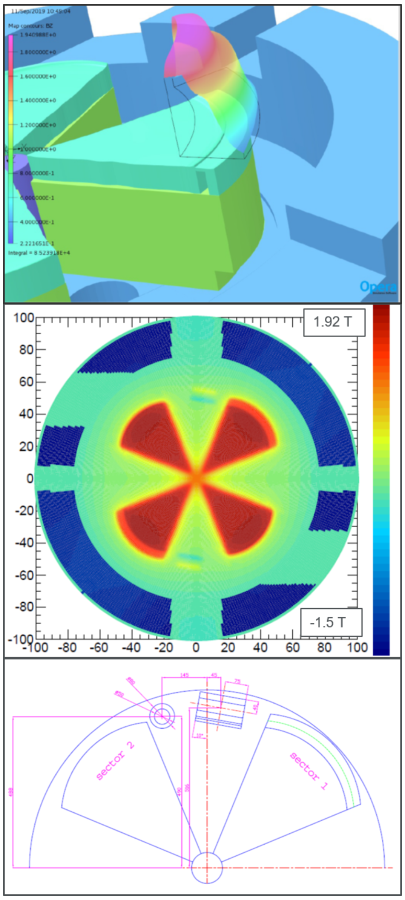

Figure 2: Lower: principal design features of the magnetic structure with the long pole and its plateau, the short pole, the permanent magnet gradient corrector and the beam separator. Middle: a zone plot of the median plane magnetic field. Upper: Finite element model of the cyclotron, showing design features of the extraction pole and the magnetic field histogram in the plateau region. At the plateau radius, the vertical gap changes from 18 mm to 28 mm.

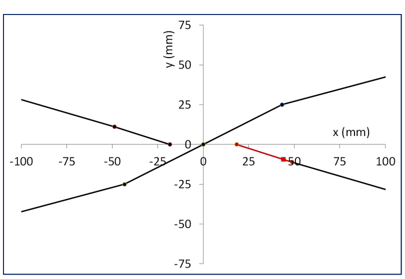

Figure 3: For the beam-simulation, the accelerating gaps were represented as a series of connected straight lines.

thereby strongly enhances the quality of the extracted beam. ii) The varying quasi-elliptical pole gap is no longer constant along circles but is constant along the equilibrium orbits of the particles. Such, the transition from the internal stable towards the non-stable extracted orbit becomes steeper, enhancing extraction efficiency. iii) The enhanced turn separation at extraction is no longer created with harmonic coils, but by an off-centring of the ion source. This substantially increases the extraction efficiency. iv) Strategic collimators are placed immediately on the first turn. This lowers the undesired beam losses at extraction. v) The cyclotron is designed with 2-fold rotational symmetry (with two long poles and two shorter poles). At the same time, two identical internal PIG ion sources are placed at opposite angles in the cyclotron centre. This allows to (simultaneously) accelerate two beams and to extract those on the two opposite longer poles. Beam produced at the first (second) ion source extracts only towards the first (second) exit port. In this way it can be chosen to irradiate only one of the production targets or both simultaneously. We note that in the prototype, currents up to 13 mA could be extracted from the ion source [1]. Figure 2 illustrates the main design features.

DESIGN OPTIMIZATION

For a given magnetic design, many beam simulations were carried out in order to find an optimum central region, resulting in highest extraction efficiency and beam quality. For this purpose the accelerating gaps were represented by a series of connected straight lines (see Figure 3) and the electric fields perpendicular to these lines by Gaussian distributions. The most important optimization parameters in this layout are the position of the ion source (r, θ) and the angle of the first gap with respect to the x-axis.

About 600 different central region geometries were evaluated. For each case a beam of 3000 particles was injected from the PIG-source in the first gap, accelerated up to full energy and then extracted. The injected phase space (see Table 2) was very large such that it filled the full central region acceptance. Figure 4 shows a typical central region beam pattern. The ion source is off-centered so much that the

Table 2: Initial beam properties used in the simulations

number of particles	3000
energy	100 eV
RF-phase	$0° < \Phi_{RF} < 110°$
half-beam width/height	1 mm; 2 mm
normalized/emittance (100%)	0.23/500 π mm-mrad

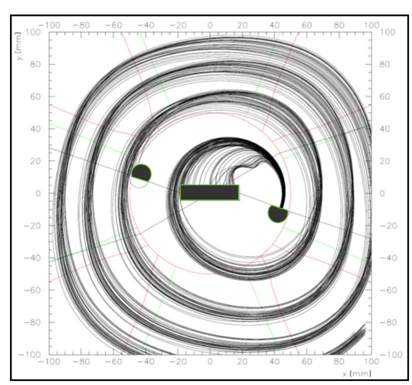

Figure 4: A typical injection simulation, showing the two ion sources, the beam passing in between them, the accelerating gaps and the beam stop removing unwanted orbits.

ISBN: 978-3-95450-205-9 doi:10.18429/JACoW-Cyclotrons2019-THD03

first turn passes in between the two (symmetrically placed) ion sources. A beam stop is placed at this position, that removes the part of the beam that is not properly accelerated or extracted. In the simulations, the second ion source also serves as an additional collimater that further cleans the beam. In a practical design, this collimator may be placed elsewhere and further optimized in order to futher improve the extraction. Figure 5 shows a 3D simulated extracted beam super-imposed on the FEM-model of the magnet.

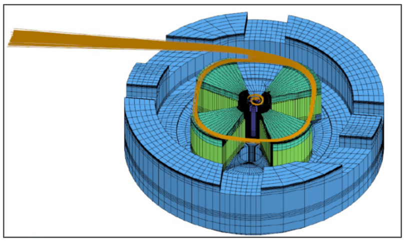

Figure 5: A simulated extracted beam also showing the part that is intercepted on the beam separator.

RESULTS

The best ion source position found in the optimization process is at the radius of 45 mm with the first accelerating gap angle at -20 degrees. This position results in a beam coherent oscillation of about 20 mm. Figure 6 shows a simulation of a differential probe track taken at an azimuth of 120° (just beyond the beam separator BS1). The beating

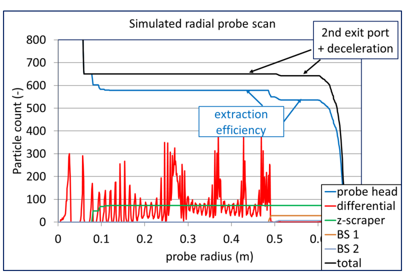

Figure 6: Simulation of a differential probe track showing turn-pattern, accumulated beam losses and beam transmission as function of radius.

Table 3: Simulated Extraction Efficiency and Beam Losses

number of injected particles = 3000 CENTRAL REGION LOSSES		
2nd ion source (18 mm)	398	
dee-connection block	1462	
vertical on dees	497	
vertical beam scraper	73	
number of particles accelerated	578	
EXTRACTION LOSSES		
beam separator 1	28	4.8%
beam separator 2	6	1.0%
second exit port	4	0.7%
back-accelerated	4	0.7%
EXTRACTION EFFICIENCY = 92.7%		

behavior seen in the turn pattern (red curve) is due to the beam off-centering. The blue curve represents the particle count on the integral part of the probe. Also shown are the losses on a vertical beam scraper (gap=12 mm) in the center, and the losses on the beam separators BS1 and BS2 (4.8% and 1.0% respectively). The black curve shows the sum of all signals. The slight dip in this curve at 50 cm is due to i) loss of isochronism and deceleration of a small fraction of the particles (0.7%) and ii) extraction towards the opposite exit port (0.7%). Table 3 shows an account on all losses. The considerable loss in the central region is due partly to the oversized injected phase space and partly to beam cleaning by collimation.The second ion source diameter is used for fine-tuning this collimation. Figure 7 shows that

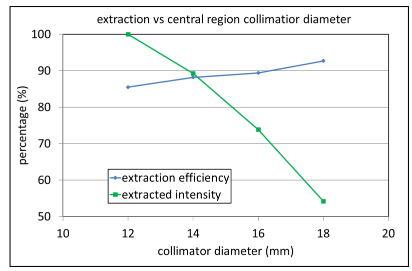

Figure 7: Dependence of extraction efficiency and intensity on the central region collimator size.

the extraction efficiency improves from about 87% to 93% by increasing this diameter from 12 mm to 18 mm. Figure 8

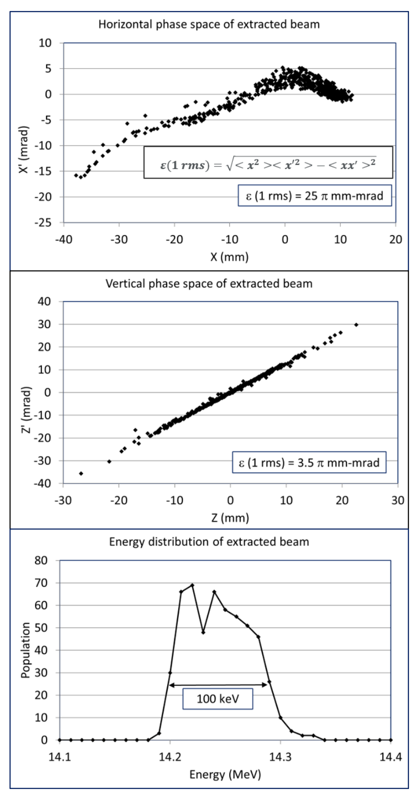

Figure 8: Horizontal phase space (upper), vertical phase space (middle) and energy spectrum (lower) of the simulated extracted beam.

ISBN: 978-3-95450-205-9 doi:10.18429/JACoW-Cyclotrons2019-THD03

shows the phase space properties and the energy spread of the extracted beam. The emmitances are at about a factor 3 better as compared to the prototype [2]. Such a beam can easily be transported to an isotope production target within a beamline with quadrupole apertures of 100 mm.

CONCLUSION

The improved design looks promissing: compared to the prototype it shows a substantial increase of extraction efficiency and also a much better beam quality. It is foreseen to continue this study. The following routes may lead to further improvements: i) increase of the extraction radius, ii) reduction of the elliptical gap in the long poles, iii) an improved positioning of collimators in the central region and iv) improvement of the dee-voltage regulation loop.

REFERENCES

[1] W. Kleeven *et al.*, "The self-extracting cyclotron", in *Proc. Cyclotrons'01*, East Lansing, MI, USA, May 2001, paper L–1, pp. 69-73.

[2] W. Kleeven, S. Lucas, J.-L. Delvaux *et al.*, "The IBA self-extracting cyclotron project", *Nukleonika*, vol. 48, pp. S59–S67, 2003.

[3] E. Forton and W. Kleeven, "High current cyclotron", European Patent Office, patent EP3024306B1.

ISBN: 978-3-95450-205-9 doi:10.18429/JACoW-Cyclotrons2019-FRA01

A NEW SOLUTION FOR COST EFFECTIVE, HIGH AVERAGE POWER (2 GeV, 6 MW) PROTON ACCELERATOR AND ITS R&D ACTIVITIES*

Tianjue Zhang†, Ming Li, Tianjian Bian, Chuan Wang, Zhiguo Yin, Shilun Pei, Shizhong An, Fei Wang, Fengping Guan and the Cyclotron Team at CIAE
China Institute of Atomic Energy, Beijing 102413, P. R. China

Abstract

Due to the successful construction of a 435-ton magnet for CYCIAE-100, it has been proved that the gradient adjustment of magnetic field along radius can effectively enhance the vertical focusing during the isochronous acceleration. This key technology was applied to the general design of a 2 GeV CW proton accelerator, the energy limitation of the isochronous machine is increased from ~1 GeV to 2 GeV, by our contribution of the beam dynamics study for high energy isochronous FFAG.

This paper will introduce CIAE's engineering experience of precision magnet, beam dynamics by single particle tracking and the advantages of beam dynamics simulation based on large-scale parallel computing. The cost-effective solution for such a 2 GeV high power circular accelerator complex will be presented in detail after the brief introduction about the high power proton beam production by the CYCIAE-100.

INTRODUCTION

The 100 MeV compact cyclotron, CYCIAE-100 was approved formally to start the construction in 2011[1], and the first proton beam was extracted on July 4, 2014. In 2017, the 200 μA proton beam development was conducted, and in 2018, the production of high power beam from 20 kW to 52 kW had been delivered successfully to the beam dump, which was quantitatively predicted ten years ago [2]. After about 8 years of construction, installation, beam commissioning and operation, various proton beam intensities from 2 pA to 520 μA can be provided for users for different applications. The Fig. 1 shows the 520 μA beam with the bunching effect of about 1.6 at the high current operation. The beam was measured by the beam dump at the end of the beam line for isotope production.

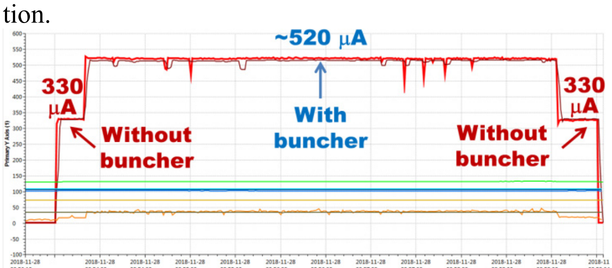

Figure 1: The 52 kW CW Proton Beam Production.

* Work supported by the basic research fund from the Ministry of Finance of China and Yong Elite Scientists Sponsorship Program by CAST under Grant of BRF201901 & 2018QNRC001.
† email address: 13641305756@139.com

During the construction of the 435-ton large-scale precision magnet for CYCIAE-100, we noticed that the 2nd order pole profile adjustment of magnetic field gradient along radius can effectively enhance the vertical focusing from the energy of 70 MeV to 100 MeV for such a AVF cyclotron [3]. This technology is also applied to pole profiles of the F & D magnets by two 3rd order functions respectively for the general design of a 2 GeV CW proton accelerator, which is using the 800 MeV cyclotron as an injector [4].

GENERAL CONSIDERATIONS IN OVERALL DESIGN OF 2 GEV CW FFAG

There are three different types of constructed accelerators for high power proton beam production: the cyclotron, LINAC and RC synchrotron. The average power of the accelerators currently is from 0.2 MW to 1.4 MW. The proton accelerator with highest beam power under construction is the ESS's SC LINAC, with a beam power of 5 MW [5]. The FermiLab researcher reported the energy efficiency of the three operational accelerators with the highest beam power in the world [6]. The energy efficiency of the PSI cyclotron is about 3 times of the other types. In order to develop high average beam power, high power efficiency and high cost effective proton machine, the isochronous accelerator is a good technical route, if it can break through the energy limitation of 1 GeV, which is presented by Dr. Y. Ishi [7]. Based on the basic FFAG idea, the research for a new solution for cost effective, high average power, 2 GeV proton accelerator was first proposed at CIAE in 2013. Combining the engineering experiences on large radial range varying gradient magnet in CYCIAE-100 and the strong focusing in FFAG, we achieve isochronous acceleration up to 2 GeV. The overall design has been basically completed after several years of research, simulation and optimization. It is a fix frequency, CW FFAG accelerator. Its layout with 100 MeV pre-injector, 800 MeV injector and 10 FDF cell CW FFAG is shown in Fig. 2, and the main parameters in Table 1.

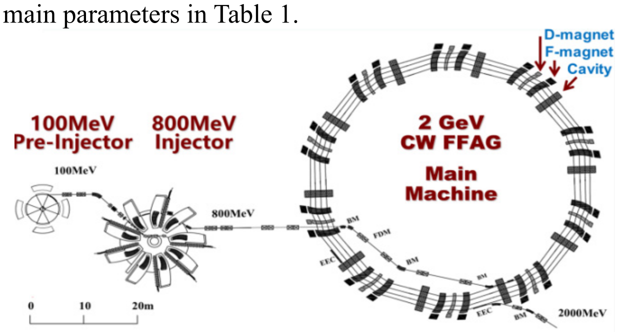

Figure 2: The layout of the circular accelerator complex.

ISBN: 978-3-95450-205-9 doi:10.18429/JACoW-Cyclotrons2019-FRA01

Table 1: The Main Parameters of 2 GeV Circular Accelerator Complex

Accelerator	**100 MeV Injector**	**800 MeV Booster**	**2 GeV FFAG**
Type	Separated-sector cyclotron	Spiral-sector cyclotron	CW FFAG
Overall diameter（m）	6.1	16	54
Lattice structure	FO	FO	OFoDoFO
Magnet Type	Warm	Warm	HTS
Average field(T)	0.36~0.41	0.54~0.90	F:1.5~2.7 / D:1.0~2.4
Sector number	4	9	10
Main cavity number	2	5	10
Cavity type	Double gap	Single gap	Single gap
RF Frequency(MHz)	44.4	44.4	44.4
Harmonic number	4	6	26
RF peak voltage(kV)	500	800~1000	~1200

Its basic characteristics are as follows:

- Comparing with an isochronous cyclotron, the 3rd order varying radial gradient of the magnetic field and FFAG's FDF Lattice are introduced to obtain isochronism at higher energy and bigger transverse acceptance. The two 3rd order field distributions, combining with the traditional spiral angles, angular widths and the fringe field shimming of the F & D magnets, bring more degrees of freedom to realize the isochronism and optimize the tune in the diagram.
- More than 9 m straight drift for the installation of up to 10 RF cavities to increase the energy gain per turn to 10 MeV, and for the beam injection /extraction.
- The 10 cell magnets and 10 RF cavities are arranged strictly in 10-fold symmetry to avoid driving low-order resonance.
- From the PSI's experience, the beam intensity, dominated by the space charge, is proportional to the third power of the energy gain per turn [8]. Based on that, the beam intensity is ~ 6 mA for 10 MeV energy gain per turn & big transverse acceptance of FFAG. It is conservatively estimated to be 3mA for this design.

BASIC BEAM DYNAMICS

As a nonlinear non-scaling FFAG [9], the challenge of isochronous FFAG lattice design is to maintain the isochronism up to 2 GeV and optimize the tune for resonance crossing. More challenges to design the basic beam dynamics, are from the large orbit oscillation of the FFAG machine and a large numbers of freedoms, which including the F & D magnet field and their gradient, the distance between the F and D, the straight drift section, the angular width and spiral angle of F or D magnet, etc.

A genetic-based multi-objective optimization algorithm is developed and applied to the CW FFAG optimization. The isochronous orbit and betatron tune of selected multi-energies are the goal of optimization. In order to obtain sensitive freedom variables for optimization, several methods are adopted:

- The magnetic field fitted by high-order polynomial (third order polynomial is used in this design);
- Spiral angle of F and D magnet change with radius;
- Angular width of F and D magnet increase monotonically with radius.

At the beginning of the acceleration, the isochronous condition is relaxed a little to avoid the resonance $\nu_r = 2$ crossing, just as shown in Fig. 3 and Fig. 4. In order to obtain the isochronism, the radial tune naturally grows with energy, so the tune optimization is a big challenge, as illustrated in Fig 3. The 10 MeV energy gain per turn with this 10-fold symmetry structure are helpful to cross the resonance quickly. The integrated phase shift is well controlled within $\pm 15°$, as shown in Fig 4.

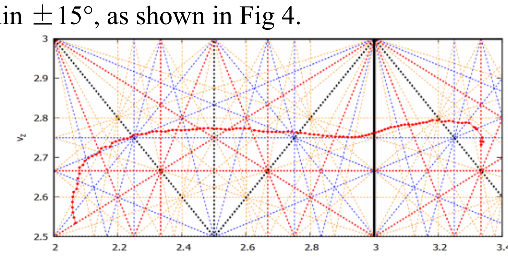

Figure 3: Tune diagram.

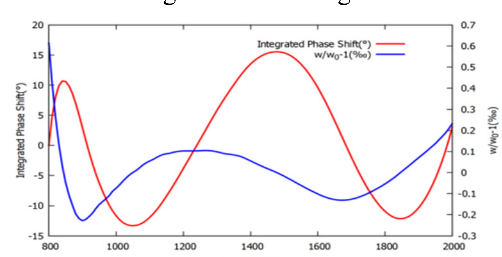

Figure 4: The isochronous behavior.

At the injection of 800 MeV proton beam into the FFAG machine, the radial acceptance is as big as 20 cm, and the vertical acceptance is also big enough, as shown in Fig 5. Although the basic beam dynamics is calculated based on the single particle, we can use:

$$i_{limit} = \Delta z \nu_Z^2 \omega_0 \varepsilon_0 \frac{\Delta\Phi}{2\pi} \frac{\Delta V}{Q_e}$$

to estimated how much ν_z shift can be caused by accelerated beams of 3 mA and 6 mA, respectively, where ε_0 is the dielectric constant, ω_0 is orbital angular frequency, Δz is

ISBN: 978-3-95450-205-9 doi:10.18429/JACoW-Cyclotrons2019-FRA01

the height of beam, ΔV is the energy gain per turn, ΔΦ is the phase width. Qe is the charge. The decrement of ν_z at 6 mA is only at 10^{-3} level. It demonstrates again that the 3 mA/6 MW is a conservative design.

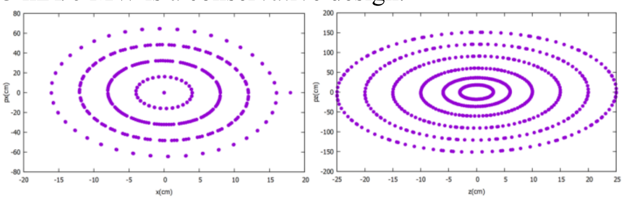

Figure 5: The radial (left) and vertical (right) phase space at 800 MeV.

RESONANCE STUDY & FUNDAMENTAL DESIGN FOR EXTRACTION

For the high power accelerator, resonance crossing is a key factor to impact the beam quality and hence increase the possibility of beam loss. The main resonances are shown in Fig. 6. These resonances are divided into two categories. One is driven by the external imperfection field, which is generally small, so only the low-order resonances need to be taken care of. The others are driven by the main field, such the average field gradient, the 10th harmonic field, etc., thus even a high order term may influence the beam quality. Among these resonances, the first order resonance $\nu_r = 3$, driven by third harmonic field B_3, is the most sensitive. Fig 7 gives the radial beam profile with and without third harmonic field near the resonance. Even a 3rd harmonic of 1 Gs leads to the beam envelop growth, which imposes strict requirements on the control of 3rd harmonic. Therefore, method to compensate the B_3 should be further investigated in this design. Also, the vertical beam profile study shows the radial and vertical coupled resonances driven by the main field have little effect on the vertical beam envelop.

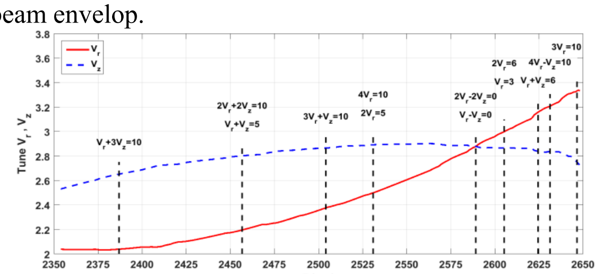

Figure 6: The tune values varying with radius and the main resonances crossed in the machine.

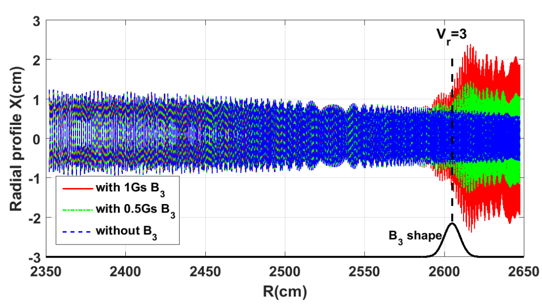

Figure 7: The radial beam profile during acceleration with and without third harmonic field near the ν_r=3 resonance.

Further, the fundamental design for the extraction is considered, mainly emphasizing on the turn separation at extraction. For a single particle, the turn separation for a cyclotron can be expressed as [10]

$$\triangle r = \triangle r_0 + \triangle x \sin(2\pi n \nu_r \theta) + x \triangle \sin(2\pi n \nu_r \theta)$$

Where $\triangle r_0$ is the separation from the energy gain, $\triangle x$ is the radial oscillation amplitude growth driven by resonance, and the third term is from the precessional motion. In the 2 GeV machine, the turn separation from 10 MeV energy gain is about 10 mm. Five more cavities are considered to be added and hence increase the turn separation to 15 mm. The radial beam profile illustrated in Fig.8 indicates the $2\nu_r=5$ resonance driven by the 5-fold symmetry of the electric field has little impact on the beam quality. In the physic design, the beam keeps stay near the $3\nu_r=10$ resonance for a long time, expecting to get larger turn separation. From Fig. 7 we know, this resonance brings little oscillation growth to the radial beam maybe due to the high order, may not helpful to increase the turn separation. The precession method is adopted for that as well. As the radial tune value is near 3.33 at extraction, with beam off centered at injection, beam can be separated significantly under the effects of precessional motion as illustrated in Fig. 9. In this simulation, 15 π.mm.mrad phase ellipse is used, corresponding to 1 cm radial oscillation amplitude at 800 MeV. 1 cm off-centered and 2 cm off-centered injection could increase the turn separation to 2 cm and 3 cm respectively, which seems to be enough for high power beam extraction. However, the beam quality with larger off-centered during acceleration should be studied further.

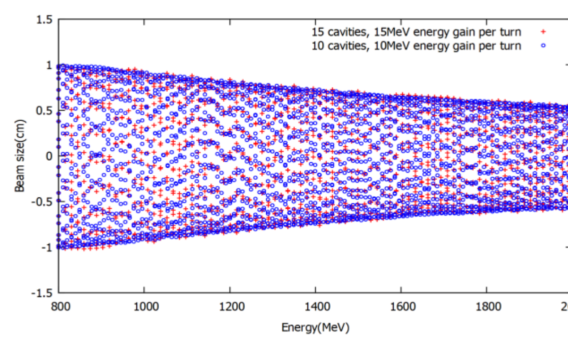

Figure 8: The radial beam profile with 10 and 15 cavities for acceleration.

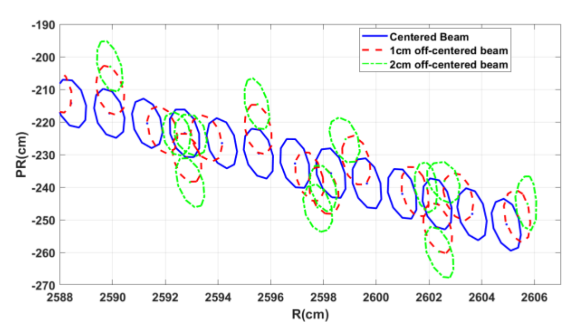

Figure 9: The radial phase space during accelerator with centered, 1 cm off-centered and 2 cm off-centered beam.

ISBN: 978-3-95450-205-9 doi:10.18429/JACoW-Cyclotrons2019-FRA01

R&D ACTIVITIES OF KEY COMPONENTS

Magnet System

Ten FDF periodic cells, each contains two bending (focusing) magnets and one reverse bending (de-focusing) magnet, form the whole 2 GeV FFAG lattice ring. Unlike the scaling FFAG scheme, where the required magnetic field is proportional to the k-th power of the orbit radius where k is the field index of the accelerator [11], the required magnetic field for the proposed 2GeV FFAG is non-parametric. The magnetic field is calculated by particle tracking during the lattice design. The variable spiral angle scheme is adopted to optimize ν_z, and the spiral angle grows from 5◦ to 30◦ with the orbit radial growth. The 3D FEM model and the magnetic field of the D-magnet and the two focusing magnets are shown in Fig10 and in Fig 11.

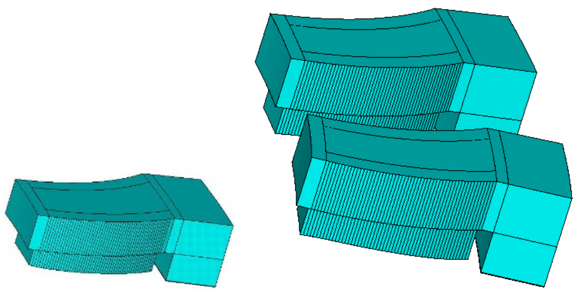

Figure 10: The 3D model of the defocusing magnet and the two focusing magnets.

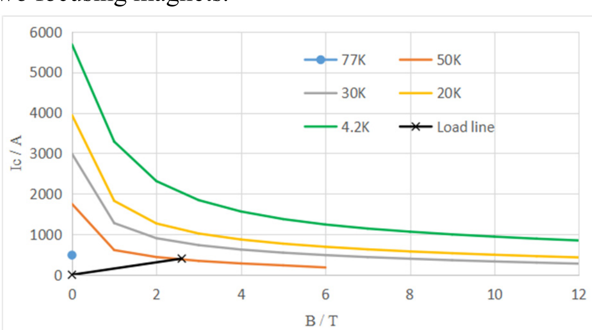

Figure 11: The load line of the HTS superconducting coil for the defocusing magnet.

Considering we have successful experiences in designing and machining of pole gap fitted with 2nd order polynomials for CYCIAE-100, and also considering the required 3rd order polynomial of magnetic field, n=3 will be used in the further magnet pole gap design.

$$g_{k(k=d,f)} = a_{k,0} + \sum_{i=1}^{n} a_{k,i}\, r^i$$

The magnetic field in the extraction radius of 2 GeV in defocusing magnet and the focusing magnet are ~-.4 T and ~2.7 T respectively. As the 2 GeV FFAG is designed to operate at high power, the 2nd generation REBCO superconducting magnet solution with both radiation resistant and thermal stable properties is preferred. The operating current of the D-magnet is 400 A @ 2.6 T, 30 K, about 50% of the Ic, as is shown in the load line drawing in Fig 11. The basic design parameters of the HTS defocusing magnet are shown in Table 2. As the SC magnet technology using 2nd generation HTS for accelerator is still under development world-wide [12, 13], an R&D project for 1/4 scale HTS D-magnet has been initiated recently to develop HTS coil winding, fixing, quench detection and protection technologies, especially for HTS coil with concave shape.

Table 2: The Parameters of the HTS D-Magnet

Item	**D-magnet**
Radial length of pole	3.78 m
Average azimuthal length of pole	~1.44 m
Total weight	~316 t
1/2 Pole gap distance	14~167 mm
Total Ampere turns	264000 AT
Total length of HTS wires	~14 km

RF System

The RF system includes all the hardware through which energy flows from the AC line to the RF cavities, and it is comprised of ten modules evenly spaced on the circumference of the accelerator. Fig. 12 shows one typical module of the high-power RF system schematically. The RF system will start up from the self-excitation mode and then change to the drive mode for the beam acceleration under the precise control of a fully digital Low-level RF controller.

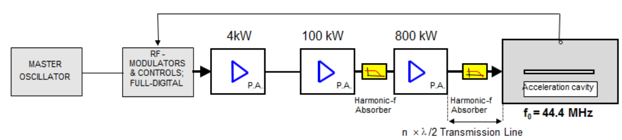

Figure 12: One typical module of the high-power RF system for the 2GeV FFAG.

Figure 13 shows the four geometries of the 44.4 MHz waveguide-type cavities for this machine, they are the: rectangular (1), omega (2), racetrack (3) and boat (4) shapes. The rectangular cavity is often used due to its simplicity for fabrication. But the research of PSI ring cyclotron indicated that the Omega cavity has a higher Q-factor [14], successfully for the ring cyclotron for 3 mA upgrade. For the 2 GeV FFAG, the peak cavity voltage averaged radially in the beam aperture is demanded to be 1.3 MV, in corresponding to a maximum value of ~1.4 MV due to the non-uniform radial distribution. By keeping some safety margin, max. 2 MV cavity voltage is determined in the design. In this situation, it is found that there are new designs so called as the racetrack and the boat cavities with even higher Q-factors.

The beam aperture of 2.8 m x 0.15 m required from beam dynamics, the RF performance of the four geometries of the 44.4 MHz waveguide-type cavity were evaluated and listed in Table 3. To keep the beam transit time factor higher than 0.95 with energy range from 800 MeV to 2 GeV, the acceleration gap is set to be 0.8 m.

ISBN: 978-3-95450-205-9 doi:10.18429/JACoW-Cyclotrons2019-FRA01

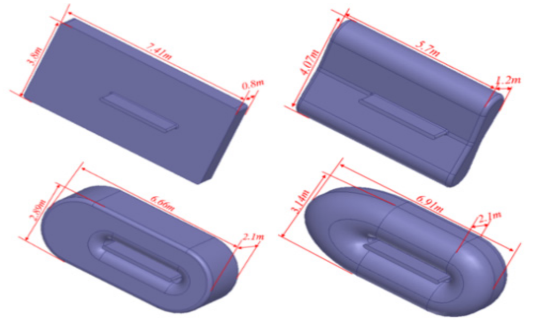

Figure 13: Four geometries of the waveguide-type cavity.

Table 3: Simulated RF Performance for the Four Geometries of the Cavity

Item	1	2	3	4
Frequency (MHz)	44.42	44.41	44.38	44.40
Operating mode	TM 110	TM 110	TM 110	TM 110
Quality factor	58497	74673	85832	92100
Shunt impedance (Max, MΩ)	5.38	10.08	19.29	20.14
Shunt impedance (Min, MΩ)	2.43	2.15	10.41	10.95
Power dissipation (kW@2MV)	743	397	207	199

Figure 14 shows the shunt impedance vs radial position relative to the beam aperture centre, the square root of the impedance is proportional to the cavity voltage amplitude in the acceleration gap. Though the boat one is the best from the simulation, the manufacture might be a little bit harder than the others, but from the on-line tuning point of view by deforming the cavity curved parts, the boat cavity is still a better choice.

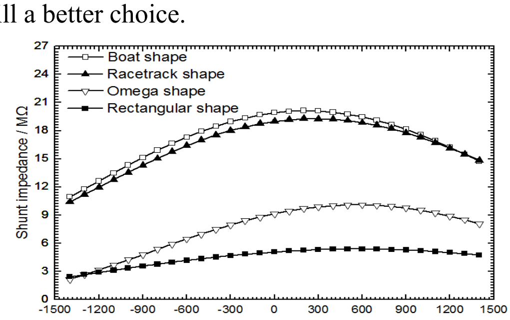

Figure 14: Relationship between the shunt impedance and the radial position relative to the aperture centre.

In order to obtain the fabrication technology of the boat cavity, and conduct the high-power RF conditioning study with the simulated beam-on scenario in the future by using the existing power source for the 230 MeV superconducting cyclotron, a 71.26 MHz scaled-down cavity prototype has been designed. Supported by the domestic industry, the discussion on the manufacture is ongoing with the potential providers.

CONCLUSION

The high power accelerator plays an important role in the internal accelerator field due to its diverse application. Based on the extensive experience of successful construction commissioning and operation of the CYCIAE-100 machine, a CW FFAG is proposed by CIAE to produce 2 GeV/6 MW beam. Beam dynamics results show a good isochronism towards 2 GeV and have a very large acceptance of the beam phase space. Resonance analysis shows the beam quality should be guaranteed when the 3rd harmonic imperfection field is compensated. The turn separation can be increased to 2~3 cm with 5 additional cavities and off-centered injection, which seems to be enough for 6 MW beam extraction. R&D Activities for key components, such as the HTS magnet and the RF system, are conducted for the 2 GeV high power circular accelerator complex.

ACKNOWLEDGEMENTS

We would like to extend our cordial gratitude to experts from TRIUMF, PSI, INFN-LNS and the international cyclotron community for their long-term support, and the recent email discussion with Dr Calabretta and Dr Rao about the beam physics for the 2 GeV machine.

REFERENCES

[1] T. J. Zhang *et al.*, "Progress on construction of CYCIAE-100", in *Proc. Cyclotrons'10*, Lanzhou, China, paper TUA2CIO01, pp. 308-313.

[2] J. J. Yang, H. J. Yao, and T. J. Zhang, "Physics problem study for a 100 MeV, 500 microamp H- beam compact cyclotron", in *Proc. ICAP'09*, San Francisco, CA, USA, Aug.-Sep. 2009, paper TH2IODN04, pp. 224-228.

[3] T. J. Zhang *et al.*, "Design, construction, installation, mapping and shimming for a 416-ton compact cyclotron magnet" *IEEE Trans. Appl. Supercond.*, vol. 26, no. 4, pp. 1-5. Jun. 2016, doi:10.1109/TASC.2016.2524535

[4] T. J. Zhang *et al.*, "Conceptual design of an 800 MeV high power proton driver", *Nucl. Instr. Methods Phys. Res. B*, vol. 269, no. 24, Dec. 2011 pp. 2964–2967. doi.org/10.1016/j.nimb.2011.04.053

[5] M. Eshraqi *et al.*, "The ESS LINAC", in *Proc. IPAC'14*, Dresden, Germany, Jun. 2014, pp. 3320-3322. doi:10.18429/JACoW-IPAC2014-THPME043

[6] V. P. Yakovlev, J. Grillenberger, M. Seidel, S.-H. Kim, and M. Yoshii, "The energy efficiency of high intensity proton driver concepts", in *Proc. IPAC'17*, Copenhagen, Denmark, May 2017, pp. 4842-4847. doi:10.18429/JACoW-IPAC2017-FRXCB1

[7] Y. Ishi, "Overview of FFAG", presented at FFAG School, Kumatori, Japan, Sep. 2018. http://www.rri.kyoto-u.ac.jp/beam_physics_lab/ffag18/documents/FFA18school_Ishi.pdf

[8] M. Seidel *et al.*, "Production of a 1.3 megawatt proton beam at PSI", in *Proc. IPAC'10*, Kyoto, Japan, paper TUYRA03, pp. 1309-1313.

ISBN: 978-3-95450-205-9 doi:10.18429/JACoW-Cyclotrons2019-FRA01

[9] C. Johnstone *et al.*, “1 GeV CW nonscaling FFAG for ADS, and magnet parameters”, in *Proc. IPAC’12*, New Orleans, LA, USA, paper THPPRO63, pp. 4118-4120.

[10] W. M Schulte *et al.*, “A method to obtain single turn extraction for a large phase width in cyclotrons”, *IEEE Trans. Nucl. Sci.*, vol. 26, no. 2, pp. 2392-2395, 1979. doi:10.1109/TNS.1979.4329884

[11] M. Yoshimoto *et al.*, “The magnet design study for the FFAG accelerator”, *IEEE Trans. Appl. Supercond.*, vol. 14, no. 2, pp. 397-401, Aug. 2004. doi:10.1109/TASC.2004.829680

[12] H. Song *et al.*, “2G HTS coil technology development at SuperPower”, *IEEE Trans. Appl. Supercond.*, vol. 25, no. 3, pp. 1-6, Jun. 2013. doi:10.1109/TASC.2012.2233837

[13] G. A. Kirby *et al.*, “Accelerator-quality HTS dipole magnet demonstrator designs for the EuCARD-2 5-T 40-mm clear aperture magnet”, *IEEE Trans. Appl. Supercond.*, vol. 25, no. 3, pp. 1-5, Oct. 2014. doi:10.1109/TASC.2014.2361933

[14] H. Fitze *et al.*, “Development of a new high power cavity for the 590 MeV ring cyclotron at PSI”, in *Proc. PAC’99,* New York, USA, 1999, paper MOP58, pp. 418-422.

ISBN: 978-3-95450-205-9 doi:10.18429/JACoW-Cyclotrons2019-FRA02

CURRENT STATUS OF SUMITOMO'S SUPERCONDUCTING CYCLOTRON DEVELOPMENT FOR PROTON THERAPY

H. Tsutsui†, Y. Arakawa, Y. Ebara, A. Hashimoto, M. Hirabayashi, T. Hirayama, N. Kamiguchi, J. Kanakura, Y. Kumata, Y. Mikami, H. Mitsubori, T. Miyashita, T. Morie, H. Murata,H. Oda, H. Ookubo, T. Sakemi, M. Sano, T. Tachikawa, N. Takahashi, K. Taki, T. Tsurudome,T. Watanabe, J. Yoshida
Sumitomo Heavy Industries, Ltd., Tokyo, Japan

Abstract

Sumitomo Heavy Industries, Ltd. is developing a compact superconducting isochronous 230 MeV cyclotron for proton therapy. It is designed to produce 1000 nA proton beams for high dose rate cancer treatment.

The cyclotron magnet, which includes a liquid-helium-free cryostat, has been fabricated and the magnetic field has been measured. Magnetic field distribution and parameters such as horizontal and vertical tunes agreed well with the original design. A 120 kW solid-state RF system is being tested. Other components such as the ion source and electrostatic deflector are being fabricated. After the testing of individual components, they will be assembled and beam testing will be scheduled at a new test site.

INTRODUCTION

Sumitomo Heavy Industries, Ltd. developed a normal conducting AVF proton cyclotron P235 in the 1990s [1]. Today, several P235 cyclotrons are in operation for cancer treatment.

In 2012, the basic design of a superconducting (SC) cyclotron [2] was established to reduce the size and cost of the system. The narrow pole-gap design makes the size smaller than existing isochronous cyclotrons for this purpose. Two h = 2 cavities and one supplementary h = 4 cavity are used to obtain large turn separation at the electrostatic deflector (ESD).

SC cyclotron components have been fabricated and tested since 2017. Figure 1 shows the magnet assembled in 2018. In the following sections, the current status of cyclotron component development and beam dynamics are discussed.

Figure 1: Superconducting cyclotron magnet. Diameter of the yoke is 2.8 m.

† hiroshi.tsutsui@shi-g.com

The detailed design started in 2015 [3]. The updated design parameters are listed in Table 1. Some parameters such as beam current have been changed to meet high dose rate therapy requirements. The supplementary h = 4 cavity has been removed to further reduce costs. To achieve turn separation with low acceleration voltage, a precessional extraction scheme was adopted.

Table 1: Main Design Parameters of the SC Cyclotron

Description	**Parameter**	**Unit**
Particle species	Proton	
Energy	>230	MeV
Beam current (max.)	1000	nA
RMS emittance	~ 1	π mm.mrad
RMS momentum spread	<0.1%	
Extraction efficiency	>70%	
Extraction radius	0.6	m
Average magnetic field	3.1–3.9	T
Yoke size	ϕ2.8 m × 1.7	m
Yoke weight	65 t	t
Coil material	NbTi/Cu	
Stored energy	5.1	MJ
Magnetic induction	9.7×10^5	AT/coil
Main coil current	442	A
Coil cooling time	14	days
Field ramp up time	<1.5	h
Quench recovery time	<24	h
RF frequency	95.2	MHz
Harmonic number	2	
Dee voltage	50–75	kV
RF wall loss	<120	kW

CYCLOTRON COMPONENTS

Cryogenic System

The cryostat [4], as shown in Fig. 2, was fabricated in 2018. Two NbTi coils are supported by four horizontal and four vertical structures. The coils are conduction cooled by four 4 K Gifford–McMahon cryocoolers (RDE-412). After the cryostat was assembled in the yoke, its performance was tested. The cooling time of the coils from room temperature to 4.2 K was 14 days, as shown in Fig. 3. Ramp-up time from 0 A to 488 A was 1.5 h. Quench protection of SC coils was done by a 1.1 Ω dump resistor. To date, we

ISBN: 978-3-95450-205-9 doi:10.18429/JACoW-Cyclotrons2019-FRA02

have not experienced a quench except during scheduled quench tests. The recovery time from a quench is 17 h.

Figure 2: Cryostat of the cyclotron.

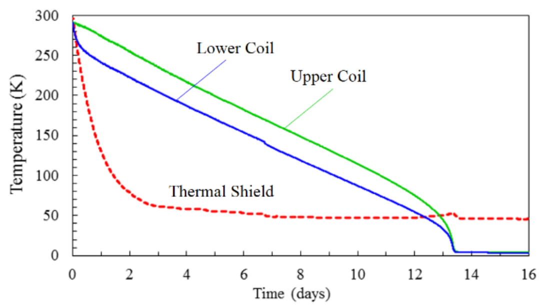

Figure 3: An example of SC coil cooling test.

Magnet

The pole and yoke were assembled in 2018. Figure 4 shows the inside of the magnet. The span angles of four sectors were designed to be as small as possible to achieve large acceleration voltage by h = 2 cavities. The average magnetic field was 3.1 T in the center region, and 3.9 T at the extraction radius. Magnetic field maps were measured by a newly developed mapping system [5]. It took approximately 2.5 h to complete one full map without magnetic channels (MC) with six Hall probes.

Figure 4: Cyclotron pole and extraction harmonic coils.

After adding the calculated magnetic field perturbation induced by MCs, the field map shown in Fig. 5 was used to calculate the field error from the isochronism. The error was adjusted three times by pole machining. The machining dimensions were determined using "saturated iron" approximation. The discrepancy between the measured and calculated values was approximately 10%. After machining, the isochronism was obtained as shown in Fig. 6.

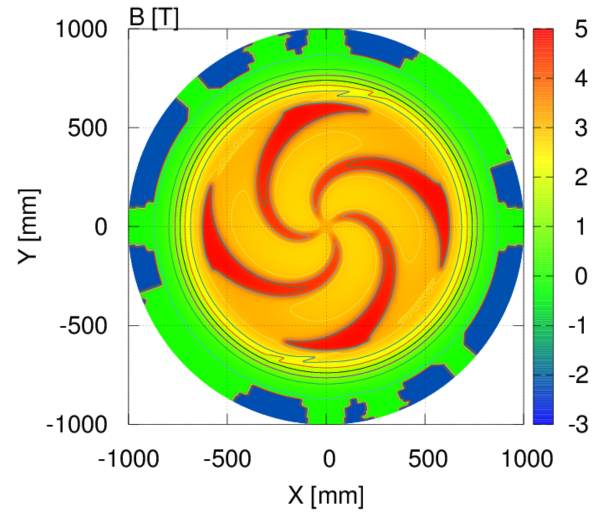

Figure 5: Magnetic field map. R < 630 mm region was measured by Hall probes [5]. The outside region was obtained by 3D calculation [6].

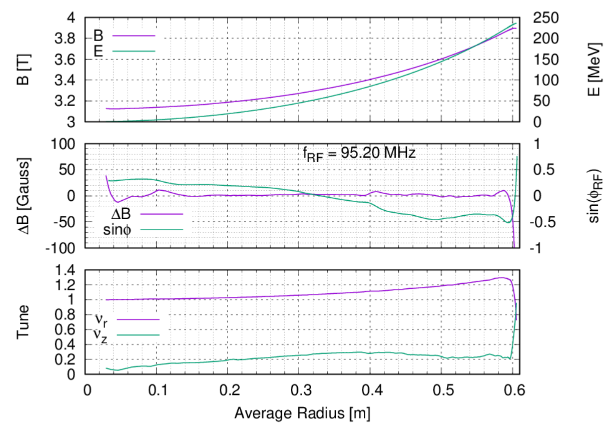

Figure 6: Parameters during acceleration.

RF System

Two opposite valleys will be occupied by RF cavities. The average Dee voltage is 50 kV in the center region, and greater than 75 kV in the outer region. The estimated total wall loss was below 100 kW by 3D calculation. Mock-up cavity low-level testing was completed in 2018. Now, the outer walls of actual cavities are being built. Simultaneously, a 120 kW, 95.2 MHz solid-state amplifier is being tested. After the cavities are installed in valleys, low-power testing will begin in early 2020.

Ion Source and Center Region

Hot-cathode-type Penning ionization gauge (PIG) ion source will be used. The ion source was tested in a 3 T magnetic field, and sufficient beam current was extracted. A vertical chopper will be equipped to perform fast beam on/off. Two sets of center harmonic coils (C-HC) are used to perform beam centering [7]. Modifiable phase slit and vertical slit are positioned to obtain high extraction efficiency.

ISBN: 978-3-95450-205-9 doi:10.18429/JACoW-Cyclotrons2019-FRA02

Extraction

Beam extraction will be performed by one ESD and two MCs (MC1, MC2). In order to remove the B_{z1} component produced by MCs, dummy MCs (C-MC1, C-MC2) are placed in the counter positions. Harmonic coils (E-HC), as shown in Fig. 4, were placed in the valleys to create adequate B_{z1} components for precessional extraction. The structure of MC1 is shown in Fig. 7. MC2 consists of three iron bars. The average field gradients of MC1 and MC2 are 21.8 T/m and 26.1 T/m, respectively. MC1 and MC2 were fabricated before magnetic field measurements. Magnetic field distributions induced by MCs were measured at several points near the MCs, which is consistent with the calculations by Opera-3D [7].

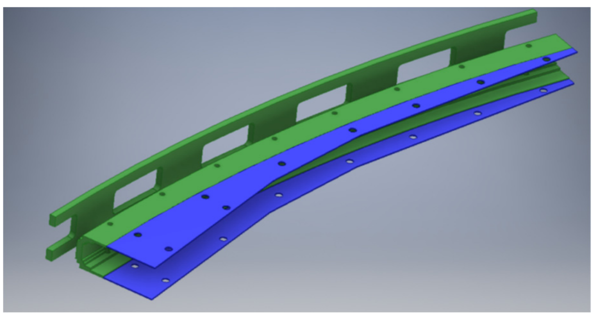

Figure 7: Magnetic channel 1.

Diagnostics

Since the sector spiral angle is large, it is difficult to insert one straight radial probe into the cyclotron center. Instead, several vertically movable probes will be set in a valley for measuring beam current and checking isochronism. A radial probe will be placed between MC1 and MC2 to optimize the beam extraction efficiency. Horizontal and vertical collimators will be set downstream of MC2. Beam loss current will be monitored on each side of the collimator.

Vacuum

The vacuum chamber consists of upper and lower poles, and the inner wall of the cryostat. Two 10-in aperture cryopumps (Canon-Anelva P-101C) will be installed to achieve better than 0.7 mPa within 2 h. The system will be tested in 2020.

BEAM DYNAMICS

In order to gain enough turn separation and reduce RF phase slippage during the precessional extraction process, the structures of sectors and MC1 were optimized. Figure 8 shows the tune diagram. The horizontal tune at extraction was determined to be $\nu_r = 0.9$. The turn separation was in the mm order R = 602 mm, as shown in Fig. 9. In this simulation, B_{z1}= 0.4 mT was applied by E-HCs. The RF phase excursion during $\nu_r = 1.3$ to 0.9 was $\delta\sin(\phi) = 0.5$, which might be allowable. The vertical tune near the extraction region is always larger than 0.2, which may be preferable for reducing beam loss. The best simulated extraction efficiency was approximately 80% by careful tuning of C-HC and E-HC parameters.

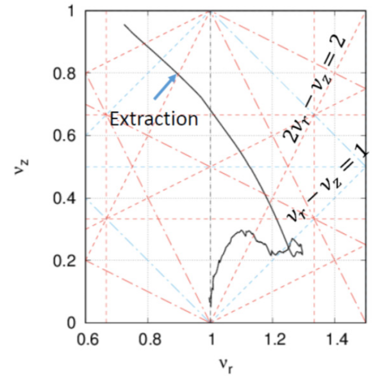

Figure 8: Tune diagram.

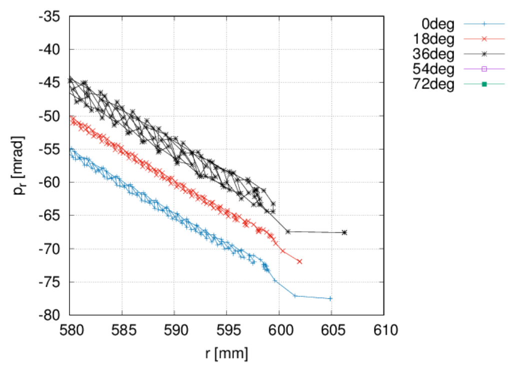

Figure 9: (r, r') phase plot around the extraction radius. ESD is placed at R = 602 mm. An offset of 5 mrad is artificially added to avoid overlapping.

CONCLUSION

Most SC cyclotron components have already been designed and are currently being built. The SC magnet was built and the specified magnetic field was successfully excited. Isochronous field was obtained by pole machining.

At Ehime Works' Saijo plant, a new building for cyclotron beam testing is under construction. Whole components of the SC cyclotron will be assembled at the new site and beam testing will start in 2020.

REFERENCES

[1] A. Goto, T. Tachikawa, Y. Jongen, and M. Schillo, “Cyclotrons”, in *Compr. Biomed. Phys.*, A. Brahme, Ed., Elsevier, 2014, pp. 179-195. doi:10.1016/B978-0-444-53632-7.00612-2

[2] H. Tsutsui *et al.*, “Design Study of a Superconducting AVF Cyclotron for Proton Therapy”, in *Proc. Cyclotrons’13*, Sep. 2013, paper MO3PB02, pp. 102-104.

[3] H. Tsutsui *et al.*, “Status of Sumitomo’s Superconducting Isochronous Cyclotron Development for Proton Therapy”, in *Proc. AccApp’17*, Quebec, Canada, Aug. 2017, pp. 412-419.

[4] J. Yoshida *et al.*, “Excitation Test of Superconducting Magnet for 230 MeV Isochronous Cyclotron for Proton Therapy”, in *Proc. 26th Int. Conf. on Magn. Tech.*, Triumf, Vancouver, Canada, Sep. 2019, *IEEE Trans. Appl. Supercond.*, to be published.

[5] Y. Ebara *et al.*, “Field mapping of Sumitomo superconducting cyclotron”, presented at Cyclotrons’19, Sep. 2019, paper MOP026, this conference.

ISBN: 978-3-95450-205-9 doi:10.18429/JACoW-Cyclotrons2019-FRA02

[6] *Opera-3d Reference Manual*, ver. 14.0, https://operafea.com/opera-3d-dynamic-electromagnetics-module

[7] N. Kamiguchi *et al.*, "Development of a Center Region for New Sumitomo Cyclotron", presented at Cyclotrons'19, Sep. 2019, paper TOP035, this conference.

ISBN: 978-3-95450-205-9 doi:10.18429/JACoW-Cyclotrons2019-FRA03

ENERGY REDUCTION OF VARIAN'S ProBeam 250 MeV CYCLOTRON TO 226 MeV

A. Roth, E. Akcöltekin, O. Boldt, F. Klarner, H. Röcken, T. Stephani, J. C. Wittschen
VARIAN Medical Systems Particle Therapy GmbH, Troisdorf, Germany

Abstract

With its superconducting 250 MeV isochronous proton cyclotron AC250, Varian uses a powerful accelerator for the ProBeam particle therapy systems. However, data from clinical operation has shown that the vast majority of treatments is only making use of proton ranges of less than 30 cm WET (water equivalent thickness), i.e. beam energy of 218 MeV at the patient. This led to a decision at Varian in Dec 2018 to conduct a redesign program with the goal to reduce extraction energy of the ProBeam cyclotron to 226 MeV. We present beam dynamics simulations for the AC226 beam acceleration and extraction. They actually show that only a reduced main coil current and adapted magnetic shimming process, as well as a slightly lower RF frequency is needed for re-tune. Furthermore, results indicate that a similar performance as compared to the AC250 can be expected. A first of its kind (FOIK) AC226 cyclotron is built by seamless integration into Varian's production process. The magnetic field measurement and shimming is completed, in-house RF and beam commissioning is planned for autumn 2019. We report on the status of the FOIK machine.

ProBeam CYCLOTRON

Varian's Proton Solutions (VPS) business unit provides with its superconducting isochronous proton cyclotron AC250 a powerful accelerator for the ProBeam proton therapy platform. With a fixed extraction energy of 250 MeV and extracted beam currents of up to 800 nA, this cyclotron drives proton therapy centers worldwide, many of them already in clinical operation, others currently in an installation and commissioning phase.

Design details of this cyclotron and factory testing including RF and beam commissioning were already reported in [1, 2]. The current status of VPS cyclotron series production is presented in [3].

ENERGY REDUCTION TO 226 MeV

Motivation

During the last decade, analysis of clinical cases has shown that the vast majority of treatments is only making use of proton ranges of less than 30 cm WET (water equivalent thickness), which corresponds to a beam energy of 218 MeV at the patient. Taking into account energy losses and necessary energy degradation of a few MeV from cyclotron exit to gantry isocenter, the corresponding beam extraction energy is 226 MeV. Consequently, the current 250 MeV ProBeam cyclotron is somewhat overdesigned in terms of beam energy, leading to potentially higher building cost for the customer, esp. due to more stringent shielding requirements.

Furthermore, in either case an energy degrader installed behind the cyclotron extraction must be used which lowers the beam energy by moving graphite wedges into the beam path. The energy degradation also leads to significant, needless reduction of beam intensity. This effect can be minimized when the cyclotron generates a lower energy beam already by design, which then results in a lower requirement for the extracted beam current to be provided by the cyclotron.

Therefore, VPS decided in December 2018 to redesign the ProBeam AC250 cyclotron for 226 MeV extraction.

Basic Concept

To achieve a fast integration of the new AC226 machine in VPS's ongoing production, the changes must be as limited as possible. VPS therefore decided not to change the extraction radius of the cyclotron of 816 mm (radius of the septum of the first extraction deflector ED1). Then the extraction of 226 MeV protons requires a lower magnetic field[1] B_{extr} of 2.82 T at 816 mm. Accordingly, the magnetic field[2] B_0 at the cyclotron center needs to be reduced and determines a slightly lower revolution frequency which finally results in change of the 2nd harmonic RF frequency f_{RF} from 72.8 MHz to 70.3 MHz. Since the RF acceleration voltage (roughly 80 kV in the center) is not changed, the mean number of turns until the protons reach extraction radius is decreased to about 580. A comparison of relevant cyclotron parameters for 226 MeV and 250 MeV machines is summarized in Table 1.

Table 1: ProBeam Cyclotron Key Parameters 226 MeV vs. 250 MeV

Parameter	226 MeV	250 MeV
R_{extr}	816 mm	816 mm
B_{extr}	2.82 T	2.98 T
$^2B_0$	2.27 T	2.35 T
I_{coil}	~148 A	~162 A
f_{RF}	70.3 MHz	72.8 MHz
# turns	~580	~650

In practice, adaption and isochronism of the shape of the averaged magnetic field from cyclotron center to extraction can be achieved by reducing the excitation current I_{coil} of the superconducting main coil and by a proper modification of the magnetic shimming of the iron poles.

[1] Azimuthally averaged magnetic field.
[2] $B_0 = B_{\mathrm{extr}} / \gamma$.

ISBN: 978-3-95450-205-9 doi:10.18429/JACoW-Cyclotrons2019-FRA03

In order to operate the AC226 cyclotron at the lower RF frequency, an adaption of the high-power RF amplifier is needed which is designed according to VPS's specifications by the Cryoelectra GmbH, Germany. The bandwidths of the digital LLRF and the cavity system (four spiral-shaped dees) are large enough so that both systems did not require a design change. The eight stems with movable shorting plates of the cavity system provide sufficient tuning range to shift the resonance frequency of the accelerating mode to 70.3 MHz.

Implementation into Series Production

End of 2018, VPS decided to transfer the S23 cyclotron (23rd cyclotron of VPS's production series) – which at that time was ready for magnetic field mapping in the factory – into the first AC226 machine. In the first quarter of 2019, the field mapping and shimming for 226 MeV were conducted. This first of its kind (FOIK) AC226 machine marked the starting point for a seamless adaption of VPS's cyclotron manufacturing. Simultaneously, a comprehensive beam dynamics simulation program was conducted and showed that smooth integration in the series production without major design changes is possible.

MAGNETIC SHIMMING PROCESS

The field of the FOIK has been measured with VPS's standard magnetic field mapping machine using a search coil, voltage integration, and absolute calibration by NRM measurements. Based on these field data, the phase advance per turn as well as the radial (ν_r) and vertical (ν_z) betatron frequencies were determined by equilibrium orbit computations up to 226 MeV. Required changes of the magnetic field shape to ensure isochronism as well as radial and vertical beam focusing were determined and transferred to precision machining of the shim plates[3]. The complete process for the FOIK consisted of one pre-machining step and two iterative steps of field mapping, computation, machining, and verification measurements. The final verification is presented in Figure 1 and Figure 2 and shows similar or even better results for isochronism and focusing properties as compared to the AC250 cyclotrons.

BEAM DYNAMICS SIMULATIONS

The shimming and equilibrium orbits computations presented above, and following beam dynamics simulations were conducted with the particle tracking software CYCTRACK, an in-house developed code of ACCEL[4], derived in parts from the NSCL tracking codes Z3CYCLONE and SPRGAP [4]. Based on electrical field maps existing for the 250 MeV cyclotrons and measured magnetic field maps from FOIK field mapping, tracking computations were performed starting from the chimney opening of the internal ion source (IS) up to the target energy of 226 MeV and through the extraction channel. Starting conditions of the protons at the chimney were varied over a complete set of horizontal and vertical positions and angles as well as starting phases[5], representing a realistic beam of a few thousand particles.

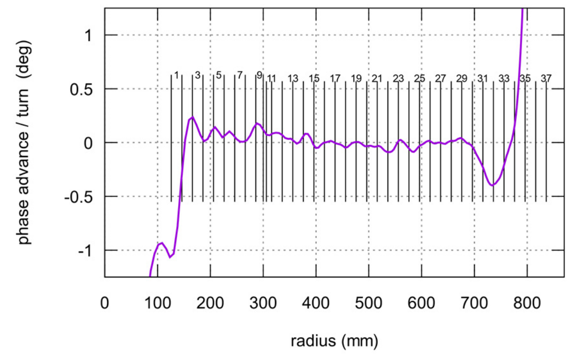

Figure 1: Phase advance per turn vs. cyclotron radius after completion of AC226 shimming. #1 - #37 indicate radial positions of the milling stripes on the shim plates.

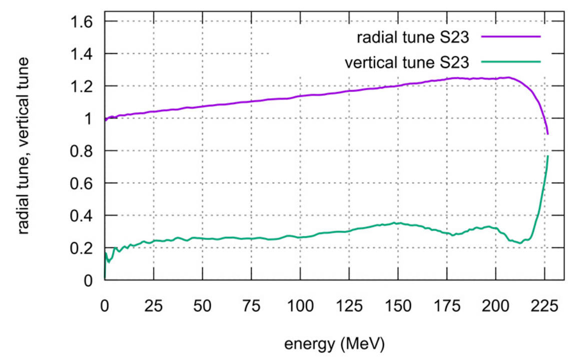

Figure 2: Tunes (ν_r and ν_z in units of revolution frequency) vs. beam energy for AC226. The vertical focusing for energies larger than 10 MeV exceeds 0.2 (for AC250 it was only 0.15).

Central Region Simulations

Figure 3 shows a tracking simulation in the horizontal plane of the central region (CR) with 6125 particles started at the IS. After transit through the puller nose of dee 1, the beam has to pass the first fixed (phase) slit (FS) in dee 2 nose. Starting phases at the IS were varied from 226° to 231° in one-degree steps which ensured that the beam was radially covering the complete FS. Radial position and width of the FS were optimized for a central passage through the subsequent dee noses and for a good compromise between beam intensity output from the FS and clear turn separation at higher radii[6]. Compared to the FS usually used for the AC250 beam commissioning, its radial position was shifted by about 1 mm outside for these tracking computations to take the slightly larger radius of the beam into account.

Based on the presented results which are supported by further simulations also for the vertical phase space and

[3]Iron plates mounted on top of each magnet hill allowing to remove material for magnetic shimming along 37 dedicated stripes at the hill edges.
[4]ACCEL Instruments GmbH, acquired by Varian in 2007.

[5]Starting phase is defined as phase in degrees with respect to the phase of the RF field.
[6]Turn separation at higher radii is essential to achieve a sufficient dynamic range for setting the cyclotron beam current for clinical applications via adjustable slits positioned at 20 cm radius.

ISBN: 978-3-95450-205-9 doi:10.18429/JACoW-Cyclotrons2019-FRA03

compared to similar simulations for the AC250 machine, e.g. [5], it was concluded that no hardware changes in the CR for AC226 are needed.

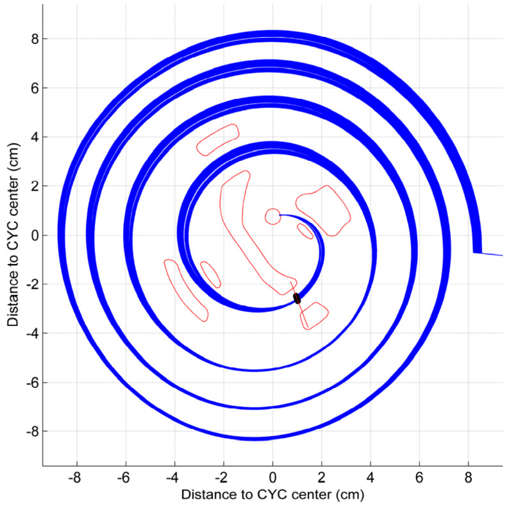

Figure 3: Tracking simulations in horizontal midplane of the CR with RF dee noses (red contours): 60% of the protons started at IS are stopped at FS edges (black dots) within dee 2 nose, protons passing the FS are accelerated further without any beam loss.

Beam Extraction Studies

The extraction path of the ProBeam cyclotron comprises two electrostatic deflectors (ED1, ED2) and six passive magnetic elements (combined dipoles/quadrupoles, M1 – M6) guiding the beam into the exit tube. Using eight adjustable trim rods (TR) positioned close to the $\nu_r = 1$ resonance, a 1st harmonic magnetic field bump is created for separation of the accelerated beam into ED1.

To extend the available magnetic field data from FOIK field mapping also along the extraction path, magnetic field maps computed for a complete cyclotron model with the TOSCA software package were patched to the measured data. On that base, detailed studies of the beam extraction have been conducted. As an example, in Figure 4 the continuation of the CR tracking simulation presented in Figure 3 is shown along the extraction path and in vertical phase space. The extracted beam is characterized by no particle losses in M1 to M6 and only minor losses at or within the EDs, by a mean energy of (226.2 ± 0.1) MeV, and by a vertical beam width (1σ) of ±2 mm.

By optimization of hardware settings and operational parameters in the simulation like main coil current, TR settings, ED field strengths, positions of EDs and magnetic elements, overall extraction efficiencies[7] (EE) in the range of 70% to 85% could be finally calculated.

During these studies, it turned out that to obtain such high EEs it was required to increase the electrical fields of the EDs by up to 20% as compared to the AC250 settings, resulting in absolute values of up to 110 kV/cm for AC226. The higher deflection field is required to compensate the stronger radial beam focusing of $\nu_r = 0.95$ at extraction energy, whereas ν_r is 0.74 in case of AC250.

[7]The overall extraction efficiency is calculated by #protons extracted out of the CYC (CYC exit), divided by #protons passed the FS.

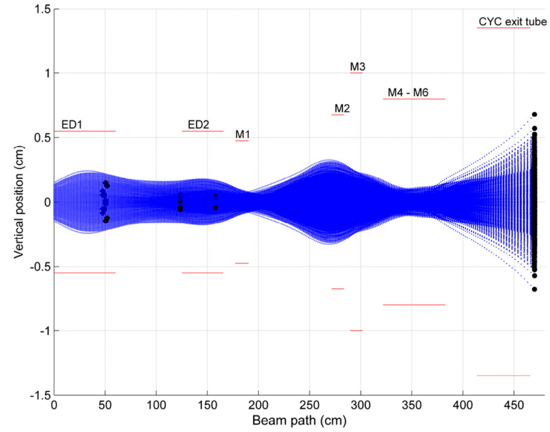

Figure 4: AC226 extraction: vertical proton position vs. beam path in the extraction channel. Aperture of EDs and M1-M6 are shown by red lines. Black dots indicate protons extracted or stopped at ED1 or ED2 (protons stopped by the septum edge of ED1 at position 0 cm are not marked).

Extraction Energy

During beam commissioning, measurement of overall EE in dependence of main coil current is a standard method to determine the working point and stability of the cyclotron which is especially important for clinical operation. Consequently, several sets of extraction tracking computations for different coil currents were performed. In addition to EE calculations, the mean energy of the extracted beam was determined with the goal to tune the cyclotron by optimization of the RF frequency to the target extraction energy of (226.0 ± 0.5) MeV.

In Figure 5, the overall EEs (FS to CYC exit, green curve) obtained from tracking computations for main coil currents between 147.77 A and 147.85 A and for an optimized RF frequency of 70.2803 MHz are shown. Within a coil current range of 25 mA an overall EE larger than 70% could be achieved while the mean number of turns reached a minimum value of around 580. Based on the number of protons reaching the exit of ED1, a second EE value (FS to ED1 exit) was calculated (purple curve in Figure 5). This EE is higher than the overall EE, showing that further optimization of settings and element positions, e.g. of ED2 and M1 - M6, could result in even higher overall EEs. For the highest overall EE of 83% at a coil current of 147.82 A, the extraction energy averaged over all extracted protons (#2131) is (226.3 ± 0.1) MeV.

STATUS FOIK AC226

The beam dynamics simulations for the AC226 cyclotron show a similar or even better performance as compared to simulation results obtained for AC250. No design changes in addition to the modified magnetic shimming for 226 MeV had to be implemented into the FOIK, and the regular manufacturing process (installation of RF structure and further subcomponents, transport and installation into factory test-cell) was completed in August 2019.

ISBN: 978-3-95450-205-9 doi:10.18429/JACoW-Cyclotrons2019-FRA03

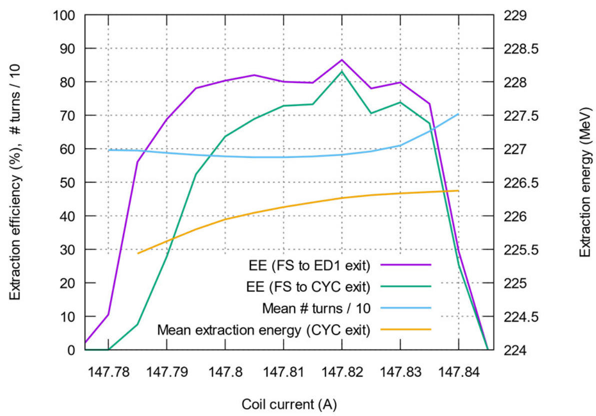

Figure 5: EE simulations for different main coil currents and optimized RF frequency of 70.2803 MHz to tune AC226 close to an extraction energy of 226 MeV. Optimum working point is around 147.82 A.

Adaption of RF Amplifier

In July 2019, Cryoelectra GmbH finalized the adaption of their existing high power, solid-state 72.8 MHz RF amplifier (model 312C) using newly designed splitter and combiner units for 70.3 MHz. This new RF amplifier (313A) is operating with the same RF power amplification modules than used for 312C amplifier. The 313A was successfully tested up to an RF output power of more than 130 kW on a water load in VPS's factory.

RF and Beam Commissioning

In September 2019, the RF commissioning process of the FOIK AC226 was started. Figure 6 shows a low power mode measurement via the coaxial RF line and dee pick-ups using a network analyzer. Positions of the eight shorting plates in the stems were adjusted to achieve a uniform balance of the electric fields and to tune the resonance frequency of the desired push-pull mode (1st mode) close to the RF frequency of 70.28 MHz.

With the 313A amplifier in operation, the cavity system of the FOIK is currently conditioned. After reaching stable RF operation at the nominal power of 115 kW, the AC226 beam commissioning will start. An integral part of the beam commissioning will be the verification of key specifications, e.g. overall EE and final beam energy. To determine the beam energy, a water phantom is currently installed in the test cell allowing Bragg peak range measurements.

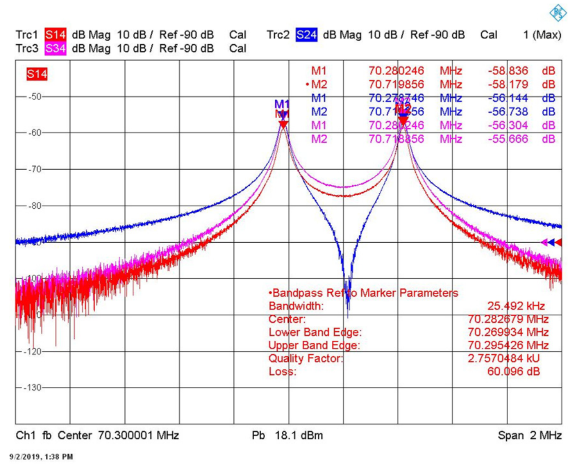

Figure 6: Mode measurement of FOIK AC226 cyclotron under vacuum using pick-up signals from dee 1 (red curve), dee 2 (blue curve) and dee 3 (magenta curve): 1st mode (push-pull mode) tuned to 70.28 MHz and same level as 3rd mode (pull-pull mode), while 2nd mode is suppressed.

CONCLUSION

On a short timeline, VPS realized a re-design program to reduce the energy of the ProBeam cyclotron to 226 MeV. Detailed tracking simulations for AC226 indicate that a similar performance as for the AC250 machine can be expected. Only ten months after the project kick-off RF commissioning of the FOIK started and the first extraction of 226 MeV beam is planned for October 2019.

ACKNOWLEDGEMENT

We thank Christian Baumgarten (PSI, Switzerland) for fruitful discussions and remarks.

REFERENCES

[1] A. E. Geisler *et al.*, "Commissioning of the accel 250 MeV proton cyclotron", in *Proc. 18th Int. Conf. on Cyclotrons and their Applications (Cyclotrons'07)*, Italy, Oct. 2007, pp. 9-14.

[2] H. Röcken *et al.*, "Progress at Varian's superconducting cyclotrons: A base for the ProBeam platform", in *Proc. 20th Int. Conf. on Cyclotrons and their Applications (Cyclotrons'13)*, Vancouver, Canada, Sep. 2013, pp. 55-57.

[3] O. Boldt *et al.*, "Manufacturing and commissioning of cyclotrons in a series production at Varian", presented at the 22nd Int. Conf. on Cyclotrons and their Applications (Cyclotrons'19), Cape Town, South Africa, Sep. 2019, paper TUP017, this conference.

[4] MSU NSCL Accelerator Group: Z3CYCLONE Instruction Manual, Version 4.0, Michigan State University, East Lansing, 2 March 1993.

[5] C. Baumgarten *et al.*, "A beam profile measurement in the ACCEL 250 MeV medical proton cyclotron", *Nucl. Instrum. Methods Phys. Res., Sect. A,* vol. 569, pp. 706-712, Dec. 2006. doi:10.1016/j.nima.2006.09.077

ISBN: 978-3-95450-205-9 doi:10.18429/JACoW-Cyclotrons2019-FRA04

CYCLOTRONS BASED FACILITIES FOR SINGLE EVENT EFFECTS TESTING OF SPACECRAFT ELECTRONICS

V. S. Anashin†, P. A. Chubunov, A. S. Bychkov, A. E. Koziukov, ISDE, Moscow, Russia
I. V. Kalagin, S. V. Mitrofanov, JINR, Dubna, Russia

Abstract

Space radiation is the main factor limiting the operation time of the onboard equipment of the spacecraft due to the radiation effects occurring in the electronic components. With a decrease in the size of semiconductor structures, the sensitivity to the effects of individual nuclear particles increases and hitting one such particle can cause an upset or even failure of a component or system as a whole. Since the phenomenon occurs due to the impact of a separate particle, these radiation effects are called Single Event Effects (SEE). To be sure that the electronic component is operational in space, ground tests are necessary. SEE tests are carried out on test facilities that allow accelerating heavy ions from C to Bi to energies from 3 to a few dozen MeV/A. Cyclotrons are best suited for this purpose. In this paper, the installations created by request of ISDE based on the cyclotrons of FLNR JINR are described.

INTRODUCTION TO THE SEE TESTING

Space ionizing radiation consists of Earth's radiation belts, galactic cosmic rays and solar energetic particles. Their effect results in different effects in semiconductor microelectronic components. Figure 1 shows the variety of cosmic radiation, its composition and the types of radiation effects it induce.

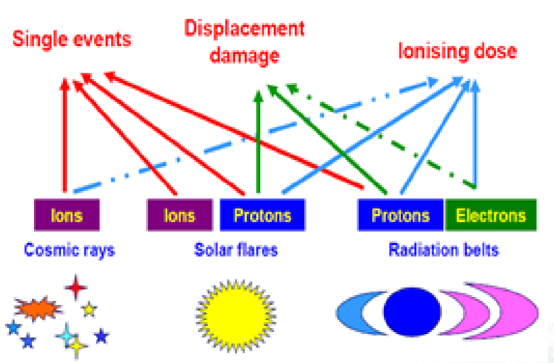

Figure 1: Types of space radiation.

The physical mechanism of interaction between a semiconductor structure and a heavy ion and a proton is illustrated in Fig. 2. The ion induces direct ionization while the proton induces secondary ionization due to knocking out atoms of the semiconductor material.

In the figures below you can see examples of the electronic components failure as a result of heavy ions exposure.

† npk1@orkkniikp.org

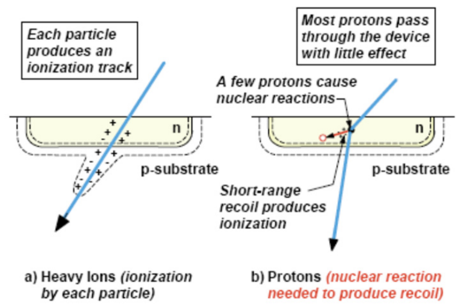

Figure 2: Mechanism for heavy ion and proton SEU effect.

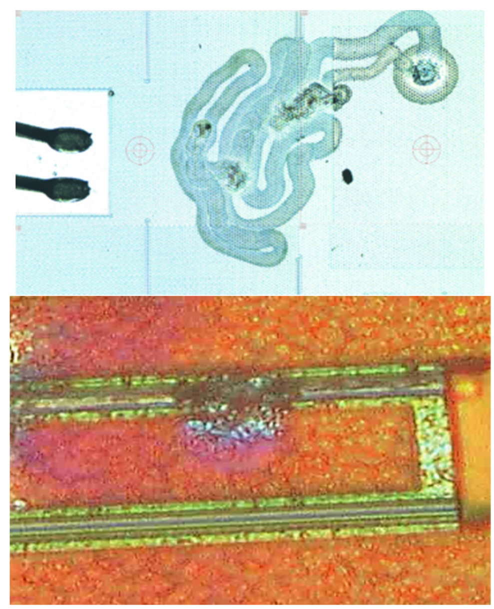

Figure 3: Examples of electronic components failure.

Table 1 represents a classification of heavy ion induced single event effects.

SEE testing is carried out with: Ion accelerator (dominating), Proton accelerator, Laser simulator (result calibration on the ion or proton accelerators is necessary!).

Guidelines using for SEE testing: "Methods of high energetic protons and heavy ions radiation testing of digital VLSI ICs performed on charged particles accelerators", "Methods of high energetic protons and heavy ions radiation testing of analog and mixed ICs performed on charged particles accelerators", "Methods of high energetic protons and heavy ions radiation testing of power MOSFETs performed on charged particles accelerators", "Methods of ICs radiation hardness characteristics calculation in the results of heavy ion facility direct experiments".

ISBN: 978-3-95450-205-9 doi:10.18429/JACoW-Cyclotrons2019-FRA04

Table 1: SEE Classification

Type / Subtype	Description	Impact	Susceptible Electronics
SEU (Single Event Upset) / MBU (multiple-bit upset), MCU (multiple-cell upset), SMU (single-word multiple-bit upsets)	Upset in a regular logic as a bi-stable structure information loss, including multiple	Recoverable failure	Storage and Logical Devices
SEDU (Single Event Destructive Upset)	Single bit corruption	Destructive Failure	Storage and Logical Devices
SEL (Single Event Latch-up)	Radiation latching induced by turning on a parasitic thyristor-like structure	Recoverable effect with possible destructive failure	CMOS, BiCMOS
SEHE (Single Event Hard Error)	Microdose effect (local energy deposition in a sensitive volume with following dose failure)	Recoverable or destructive failure	Storage elements and Logical Devices
SEFI (Single Event Functional Interrupt)	Function Interrupt Effect	Operation failure	Complex Devices
SEB (Single Event Burnout)	Burnout effect in power MISFETs, caused by opening of parasitic bipolar transistor	Destructive failure	High-voltage transistors
SEDR (Single Event Dielectric Rupture) / SEGR (Single Event Gate Rapture)	Dielectric rupture effect/ Gate dielectric rupture effect in MISFETs	Destructive failure	High-voltage devices with MOS-structures
SET (Single Event Transient)	Ionizing reaction (current or voltage pulses in output circuit)	Short-time failure	Analog Devices prevalent
SESB (Single Event Snapback)	Parasitic n-p-n transistor occurrence in n-channel (Secondary breakdown effect)	Destructive failure	N-channel MOS and SOI transistors

Typical Test Procedure for corresponding type of facility: "SEE test procedure for Roscosmos Test Facilities with the use of U-400 and U-400M accelerators" (All documents are based on MIL-STD-833, ASTM F1892, ESCC 25100 and detail them).

Typical SEE Test Procedure included: Studying the features of the test object, possible effects, Selection of the electrical parameters for monitoring and irradiation modes, the choice of test and measuring equipment; Test Plan Development and Agreement with Customer; lot Identification (incl. electrical measurements); Samples Preparation (De-capsulation); Test Setup Design (PCB); Test Software Development; Test Setup Adjustment and Trial Run; Test Setup Assembling in Irradiation Chamber; Irradiation Process; Test Results Calculation and Interpretation; Test Report Development.

TEST FACILITY

SEE facilities based on the FNRL JINR accelerators are used for electronic components testing. The layout is shown in Fig. 4. Specifications of the test facilities are listed in Table 2.

The scanning system provides an increase of irradiation area from 4-10 cm to 11.5-20 cm with minimum non-uniformity (Figs. 5 and 6).

Figure 7 shows the typical configuration of the test chamber.

ISBN: 978-3-95450-205-9 doi:10.18429/JACoW-Cyclotrons2019-FRA04

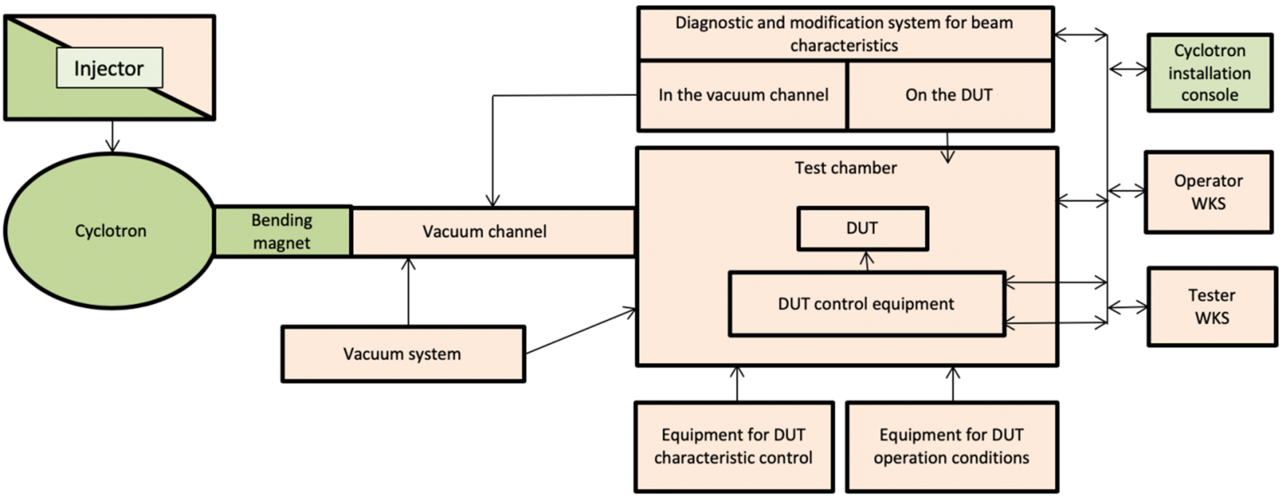

Figure 4: General structure of the SEE test facilities based on ion sources. Green for JINR; Beige for ISDE.

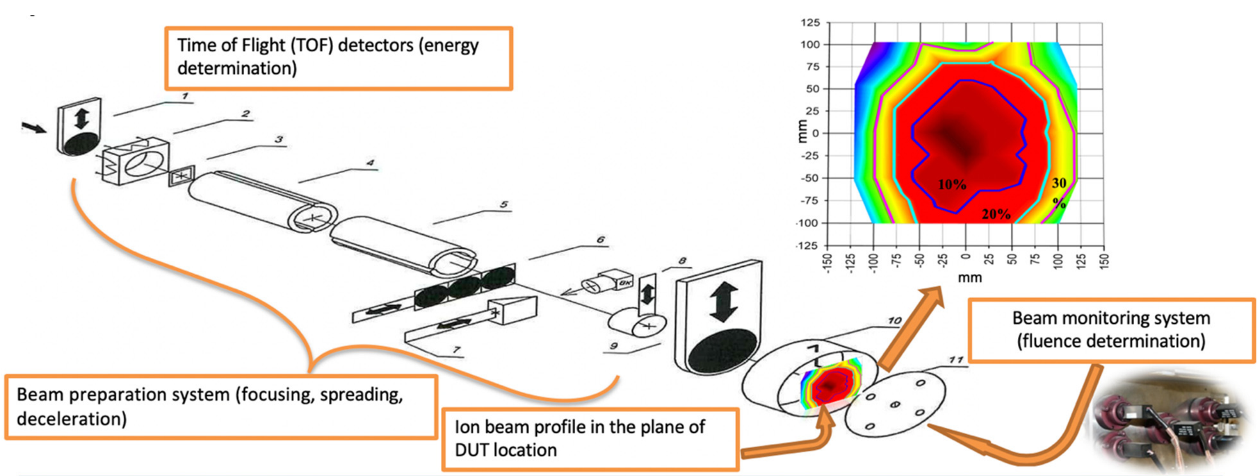

Figure 5: Beam transfer channel layout. 1- slide gate; 2- bending magnet; 3- diaphragm; 4- X-axis magnetic scanner; 5- Y-axis magnetic scanner; 6- degraders; 7- luminophore; 8- Faraday cup; 9- slide gate; 10- target node;11- beam monitoring system.

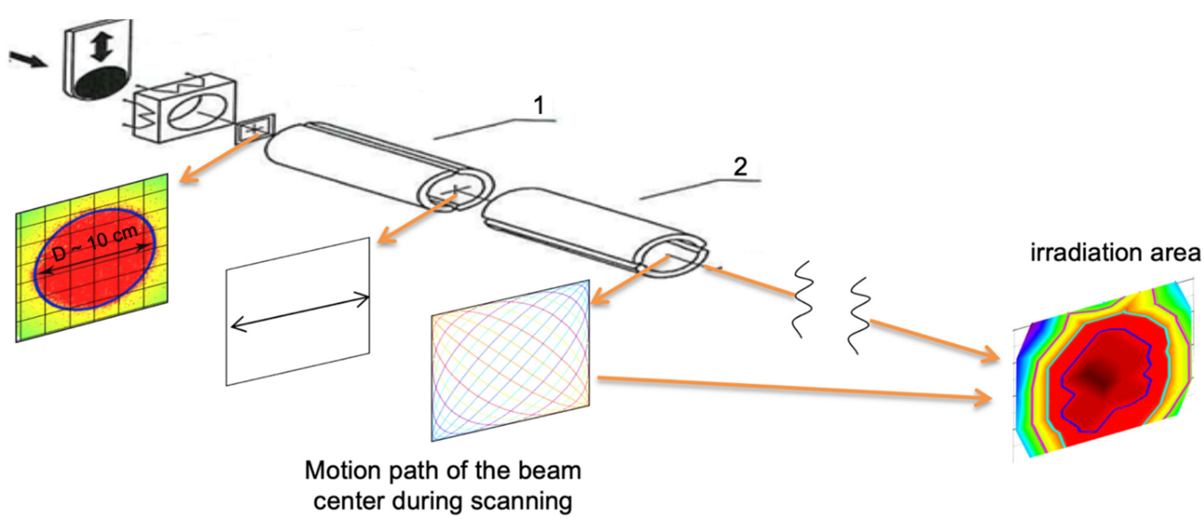

Figure 6: Beam modification system. 1- X-axis magnetic scanner; 2- Y-axis magnetic scanner.

ISBN: 978-3-95450-205-9 doi:10.18429/JACoW-Cyclotrons2019-FRA04

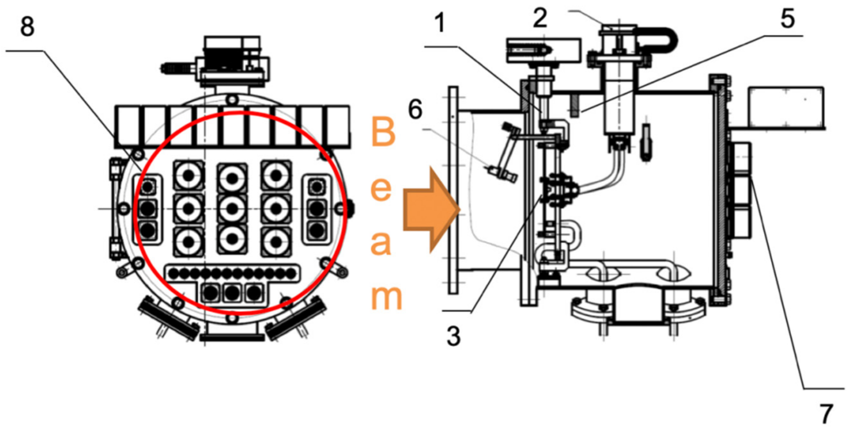

Figure 7: Vacuum test chamber. 1- rotary support frame; 2- conductive heating and cooling device; 3- PCB with a DUT; 4- flexible online detectors; 5- webcam; 6- non-contact heater; 7- beam monitoring system; 8- DUT/measuring instrumentation interfaces.

Table 2: Basic Technical Features of the SEE Test Facilities Based on Ion Sources

Technical features	IS OE PP (LE)	IS OE VE-M (HE)	IS OI 400-N (LE)
Ion source	Cyclotron U-400M FLNR	Cyclotron U-400M FLNR JINR	Cyclotron U-400 FLNR
E [MeV/u]	3 - 6	15 - 40 (60 for light ions)	3 - 9
Flux [part./(cm^{2}s)]	10x10^5	10 * 10^5 (10^4 for Bi)	10 *10^5
Non-uniformity, %	± 15	± 10	± 10
Ions	C, O, Ne, Ar, Fe, Kr, Xe, Bi	Ne, Ar, Kr, Xe (C, O, Fe, Bi)	C, O, Ne, Ar, Fe, Kr, Xe, Bi
LET (Si), [MeV• cm^2/mg]	1 - 100	1 - 98(with degraders)	1 - 100
Range in Si [μm]	> 30	130 - 2000	> 30
Irradiation area, mm	200 x 200	Ø 60 (Ø 40 for Bi)	150x200
Operational pressure	2.2x10^{-3} Pa	Forevacuum/atmosphere	2.2x10^{-3} Pa
Pumping time [min]	6	5/0	8
Temp. [˚C]	-40 to 125	-40 to 125	-40 to 125

IC tests are performed in at a temperature from -40 to 125 °C with the help of special equipment. Heating and cooling is carried out through thermal contact between a DUT and several thermoelectric coolers (TEC) on Peltier elements (Fig. 8).

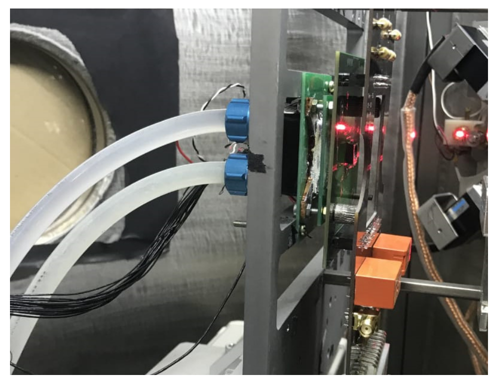

Figure 8: Heating and cooling facility.

HEAVY-ION FLUENCE DETERMINATION PROCEDURES

The fluence evaluation method is quasi-on-line (on-line - scintillators, off-line – track detectors) and yet it shows excellent accuracy.

On-line detectors are used to determine the moment for 10^5 for Power MOSFETs).

To obtain a precise value, the track detectors placed close to the DUT are used.

For operational evaluation of ion fluence in the DUT location the K coefficient is determined. K interrelates fluence according to track detectors ($\Phi_{track\ detectors}$) and dimensionless quantity characterizing ion fluence according to data from online monitoring counters (Φ_{count}).

$$\Phi_{track\ detectors} = K^* \ \Phi_{coun}. \quad (1)$$

The methodology of fluence determination consists in a TD positioning close to the DUT (Fig. 9), irradiation, chemical etching of the TD after irradiation, holes calculation and determination of the true fluence value in the TD location or all over the beam profile, and non-uniformity determination.

ISBN: 978-3-95450-205-9 doi:10.18429/JACoW-Cyclotrons2019-FRA04

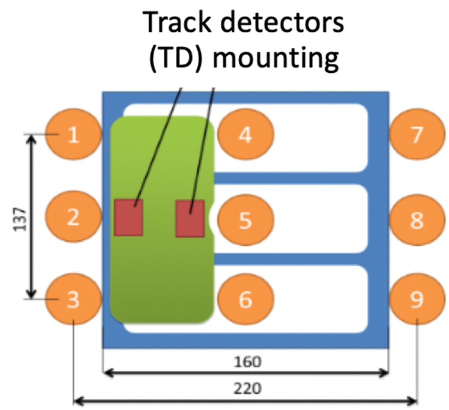

Figure 9: DUT Position.

Based on the data obtained, a map of non-uniformity was plotted (Fig. 10). The typical shape of the ion beam is in the form of a “Gaussian” curve with a “plateau” that is clearly distinguished in the central region of irradiation.

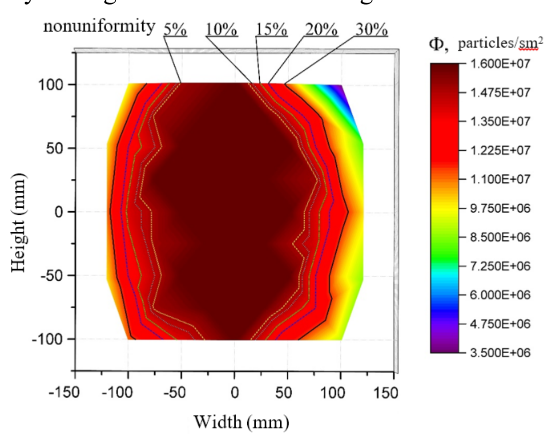

Figure 10: Beam profile with designated zones of non-uniformity.

Based on the map of non-uniformity, it can be concluded that in almost the entire irradiation area (150 x 200 mm^2) a non-uniformity of no more than 30% is provided. However, regardless of the entire irradiation field non-uniformity in the standard zone (100 x 150 mm^2) of the samples location (Fig. 11), the non-uniformity does not exceed 10%.

ION BEAM CHARACTERISTICS DETERMINATION

For determination of the ion energy, the Time of Flight technique is used (Fig. 12).

The energy measurement method based on one-to-one correspondence between the kinetic energy E_k and the particle velocity *v.*

Energy measurements are performed once after ion ejection (may be repeated if required).

This method provides energy determination with up to 2% accuracy.

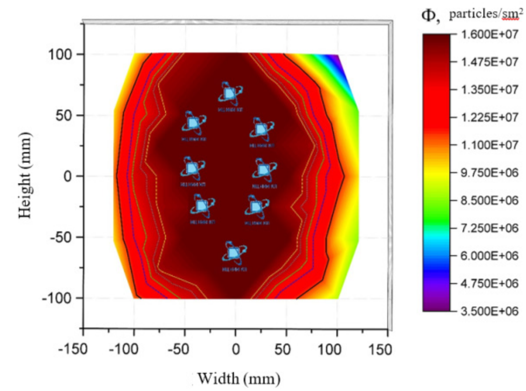

Figure 11: Beam profile with recommended sample area.

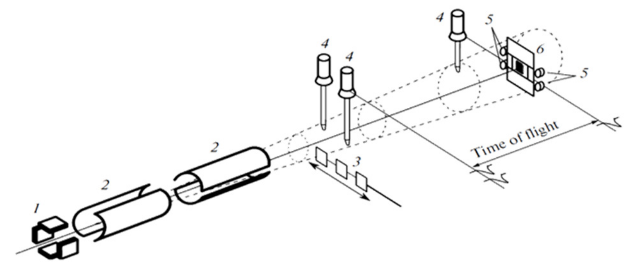

Figure 12: Beam profile with designated zones of nonuniformity. 1- bending magnet; 2- X-Y magnet modification system; 3- degrader foils set; 4- Scintillation detectors TOF; 5- Scintillation detectors; 6- DUT.

DIRECTIONS FOR THE DEVELOPMENT OF TEST FACILITIES

Improvement the accuracy of technical characteristics. Creation of on-line beam monitoring system (energy, non-uniformity, flux, fluence, etc.).

Creation of test facilities with milli- and micro- beams for fundamental investigations.

Creation of technological bench for ensuring decapsulation of electronic components.

Creation of new test facilities based on accelerators that exist or under development in JINR.

CONCLUSION

ISDE in collaboration with JINR operates the modern high-quality SEE Test Facilities, which allow to make the best use of up to 4000 hours of the test time per year and provide tests of electronic components of all functional classes to all types of radiation effects, taking into account the specific technical features.

ISBN: 978-3-95450-205-9 doi:10.18429/JACoW-Cyclotrons2019-FRB01

DESIGNING CYCLOTRONS AND FIXED FIELD ACCELERATORS FROM THEIR ORBITS*

T. Planche†, TRIUMF, Vancouver, Canada

Abstract

The transverse motion of particles in fixed field accelerators with mid-plane symmetry is entirely determined by the properties of the closed orbits. In this study I exploit this property to produce a variety of isochronous magnetic distributions. All the results presented in this paper are verified using CYCLOPS simulations.

INTRODUCTION

The transverse tunes of separated sector cyclotrons, and other fixed-field accelerators, can be estimated "on the back of an envelope" using the hard-edge approximation and the concatenation of drift-edge-bend-edge-drift transfer matrices, see for instance Refs. [1–4]. In this paper, I try to go a little further by presenting a way to calculate exactly the transverse tune from the non-hard-edge shape of the closed orbits. The only approximation is that the magnetic field presents a mid-plane symmetry.

The first section is a review of the derivation of the Hamiltonian for linear motion in a magnet with median plane symmetry [5]. The second section is dedicated to derive the relations between the parameters of this Hamiltonian and the geometry of the closed orbit. In the third section, I present examples of isochronous field distributions, and verify my calculations using CYCLOPS. My intention is to show that it is possible to design a cyclotron starting from its orbits, rather than from its field.

In the last section I present an example of application of this method to a non-isochronous fixed field accelerator.

LINEAR MOTION HAMILTONIAN

Let's consider a charged particle with mass m and charge q travelling in empty space on a closed orbit, under the sole influence of a static magnetic field. Let's also assume that the closed orbit is contained in a plane. Let $\rho(s)$ be the curvature of the closed orbit, and (x, y, s) be the Frenet-Serret coordinates around it. Let the plane of the orbit be the $y = 0$ plane, and let the magnetic field be everywhere normal to this plane:

$$(\nabla \times \mathbf{A})(0,0,s) = \begin{pmatrix} 0 \\ B_0(s) \\ 0 \end{pmatrix}, \tag{1}$$

where $B_0(s) = B(0,0,s)$. The vector potential should also satisfy the absence of source along the orbit, which is:

$$(\nabla \times \nabla \times \mathbf{A})(0,0,s) = \mathbf{0}\,. \tag{2}$$

Using the definition of the curl operator in the planar Frenet-Serret system:

$$\nabla \times \mathbf{A} = \left(\frac{1}{h}\frac{\partial A_s}{\partial y} - \frac{\partial A_y}{\partial s}, \frac{\partial A_x}{\partial s} - \frac{1}{h}\frac{\partial A_s}{\partial x}, \frac{\partial A_y}{\partial x} - \frac{\partial A_x}{\partial y} \right),$$
$$h = 1 + x/\rho, \tag{3}$$

and considering a vector potential in the form of a truncated power series about the equilibrium orbit [6], we find by inspection that the following vector potential

$$\begin{aligned} A_x &= 0\,, \\ A_y &= \frac{\partial B}{\partial s} x y\,, \\ A_s &= -\frac{B}{2\rho}\left(x^2(1+n) + y^2 n\right) - xB\,, \end{aligned} \tag{4}$$

satisfies Eq. (1). It also satisfies Eq. (2) provided that:

$$n = -\frac{\rho}{B_0}\left.\frac{\partial B}{\partial x}\right|_{x=y=0}, \tag{5}$$

which is the standard definition of the magnetic field index.

Let's now consider the Courant-Snyder Hamiltonian [6]

$$H(x, P_x, y, P_y, t, -E; s) = qA_s - \left(1 + \frac{x}{\rho}\right)\sqrt{\frac{E^2}{c^2} - m^2c^2 - (P_x - qA_x)^2 - (P_y - qA_y)^2}\,, \tag{6}$$

where E, P_x, P_y and t are, respectively, the particle's total energy, transverse canonical momenta, and time of flight. For the longitudinal coordinates to be, like the transverse ones, deviations for the reference particle's coordinates, we proceed to the canonical transformation $(t, -E) \longrightarrow (z = s - \beta ct,\ \Delta P = \frac{\Delta E}{\beta c})$ using a generating function of the second kind:

$$F_2(t, \Delta P) = \left(\frac{s}{\beta c} - t\right)(E_0 + \beta c \Delta P)\,. \tag{7}$$

where the constants βc and E_0 are, respectively, the reference particle velocity and total energy. The new Hamiltonian is obtained by adding $\frac{\partial F_2}{\partial s} = \frac{E_0}{\beta c} + \Delta P$ to the old one.[1]

Without changing the dynamics, we scale all the momenta by the constant reference particle's momentum $P = \frac{1}{c}\sqrt{E_0^2 - m^2c^4}$. The scaled momenta become:

$$\begin{aligned} p_x &= P_x/P\,, \\ p_y &= P_y/P\,, \\ p_z &= \Delta P/P\,, \\ h &= H/P\,. \end{aligned} \tag{8}$$

Expanding the resulting Hamiltonian to second order in x, y, z, p_x, p_y, and p_z, we find that all first order terms vanish

* TRIUMF receives funding via a contribution agreement with the National Research Council of Canada.
† tplanche@triumf.ca

[1] One can verify that the partial derivative of F_2 w.r.t. the old position t gives the old momentum $-E$. The new position z is obtained from the partial derivative of F_2 w.r.t. the new momentum ΔP.

ISBN: 978-3-95450-205-9 doi:10.18429/JACoW-Cyclotrons2019-FRB01

provided that:

$$\rho = \frac{P}{qB_0}\,, \tag{9}$$

and

$$\beta = Pc/E_0\,. \tag{10}$$

In other words, under these two conditions, a particle placed right on the reference orbit will remain on it. Removing the constant terms, which do not contribute to the dynamics, the Hamiltonian becomes:

$$h = \frac{x^2}{2}\frac{1-n}{\rho^2} + \frac{y^2}{2}\frac{n}{\rho^2} + \frac{p_x^2}{2} + \frac{p_y^2}{2} - \frac{p_z x}{\rho} + \frac{p_z^2}{2\gamma^2}\,, \tag{11}$$

where $\gamma = \frac{1}{\sqrt{1-\beta^2}}$.

The equations of motion that derive from this quadratic Hamiltonian can be written in matrix form as:

$$\mathbf{X}' = \mathbf{F}\mathbf{X}\,, \tag{12}$$

where a prime $'$ denotes a total derivative w.r.t. the independent variable s. The matrix $\mathbf{F}$:

$$\mathbf{F} = \begin{pmatrix} 0 & 1 & 0 & 0 & 0 & 0 \\ \frac{n(s)-1}{\rho(s)^2} & 0 & 0 & 0 & 0 & \frac{1}{\rho(s)} \\ 0 & 0 & 0 & 1 & 0 & 0 \\ 0 & 0 & -\frac{n(s)}{\rho(s)^2} & 0 & 0 & 0 \\ -\frac{1}{\rho(s)} & 0 & 0 & 0 & 0 & \frac{1}{\gamma^2} \\ 0 & 0 & 0 & 0 & 0 & 0 \end{pmatrix} \tag{13}$$

is the infinitesimal transfer matrix, and

$$\mathbf{X} = \begin{pmatrix} x \\ p_x \\ y \\ p_y \\ z \\ p_z \end{pmatrix} = \begin{pmatrix} x \\ x' \\ y \\ y' \\ z \\ \gamma^2 z' \end{pmatrix} \tag{14}$$

is the particle state vector.

LINEAR OPTICS FROM GEOMETRY

The objective of this section is to derive the relation between the geometry of the closed orbits and the coefficients that appear in the Hamiltonian of Eq. (11).

Let's consider an ensemble of closed orbits given by:

$$r(a,\theta)\colon \mathbb{R}^+ \times \mathbb{R} \to \mathbb{R}^+\,, \tag{15}$$

where θ is the azimuth and a is an orbit scale factor. For the orbits to be closed, r must be periodic:

$$r(a,\theta + 2\pi/N) = r(a,\theta + 2\pi/N) \text{ with } N \in \mathbb{N}^*\,. \tag{16}$$

Let's also assume that for all a and θ:

$$\frac{\partial r}{\partial a} > 0\,; \tag{17}$$

this will ensure that the closed orbits with different scale factor (i.e. corresponding to different energies) do not cross over. The infinitesimal length increment of the orbit is given by (see Fig. 1):

$$\frac{\mathrm{d}s}{\mathrm{d}\theta} = \sqrt{r^2 + \left(\frac{\partial r}{\partial \theta}\right)^2}\,, \tag{18}$$

which leads to the orbit circumference:

$$\mathcal{L}(a) = \int_0^{2\pi} \sqrt{r^2 + \left(\frac{\partial r}{\partial \theta}\right)^2}\,\mathrm{d}\theta\,. \tag{19}$$

The isochronous condition sets the relation between the circumference of the orbit and the particle energy through:

$$\beta = \frac{\mathcal{L}(a)}{r_\infty} \tag{20}$$

where $2\pi r_\infty$ is the circumference of the orbit of a particle travelling at the speed of light. The curvature of the orbit is given by:

$$\rho(a,\theta) = \frac{\left(r^2 + \left(\frac{\partial r}{\partial \theta}\right)^2\right)^{3/2}}{r^2 + 2\left(\frac{\partial r}{\partial \theta}\right)^2 - r\frac{\partial^2 r}{\partial \theta^2}}\,. \tag{21}$$

The field index writes, using Eqs. (5) and (9):

$$n = -\frac{q\rho^2}{P}\frac{\partial B}{\partial x} = \frac{\partial \rho}{\partial x} - \frac{\rho}{P}\frac{\partial P}{\partial x}\,. \tag{22}$$

Using the chain rule, and the relations between infinitesimal

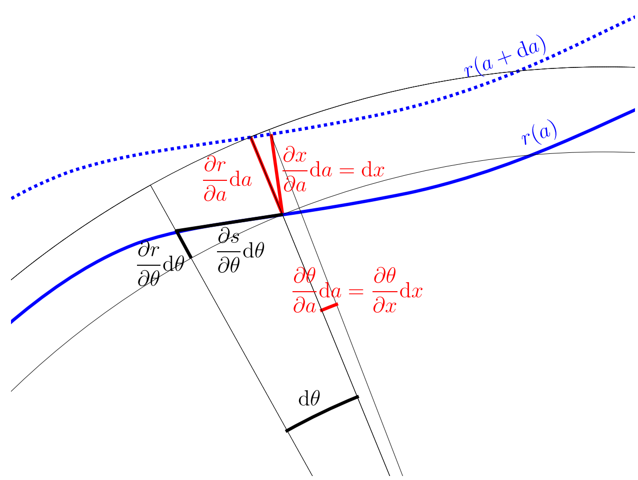

Figure 1: Relations between infinitesimal quantities around the closed orbit (the thick blue line); $\mathrm{d}\theta$ and $\mathrm{d}a$ represent infinitesimal variations in θ and a respectively.

quantities (see Fig. 1):

$$\frac{\partial \rho}{\partial x} = \frac{\partial \rho}{\partial a}\frac{\partial a}{\partial x} + \frac{\partial \rho}{\partial \theta}\frac{\partial \theta}{\partial x} = \frac{1}{r}\left(\frac{\partial \rho}{\partial a}\frac{\frac{\mathrm{d}s}{\mathrm{d}\theta}}{\frac{\partial r}{\partial a}} - \frac{\partial \rho}{\partial \theta}\frac{\frac{\partial r}{\partial \theta}}{\frac{\mathrm{d}s}{\mathrm{d}\theta}}\right)\,, \tag{23}$$

where $\frac{\mathrm{d}s}{\mathrm{d}\theta}$ is given by Eq. (18). Finally:

$$\frac{\partial P}{\partial x} = \frac{\mathrm{d}\beta}{\mathrm{d}a}\frac{mc}{r\left(1-\beta^2\right)^{3/2}}\frac{\frac{\mathrm{d}s}{\mathrm{d}\theta}}{\frac{\partial r}{\partial a}}\,, \tag{24}$$

where β is given by Eq. (20). All the coefficients that appear in Eq. (11) are given by r and its partial derivatives: ρ from Eq. (21), γ from Eq. (20), and n from Eqs. (20) and (22) to (24).

Now that we know how to write linear-motion Hamiltonian explicitly, we can calculate the transverse tunes. This is done by numerically integrating a θ-based version of Eq. (12):

$$\frac{\mathrm{d}\mathbf{X}}{\mathrm{d}\theta} = \mathbf{X}'\frac{\mathrm{d}s}{\mathrm{d}\theta} = \mathbf{F}\mathbf{X}\frac{\mathrm{d}s}{\mathrm{d}\theta} \tag{25}$$

ISBN: 978-3-95450-205-9 doi:10.18429/JACoW-Cyclotrons2019-FRB01

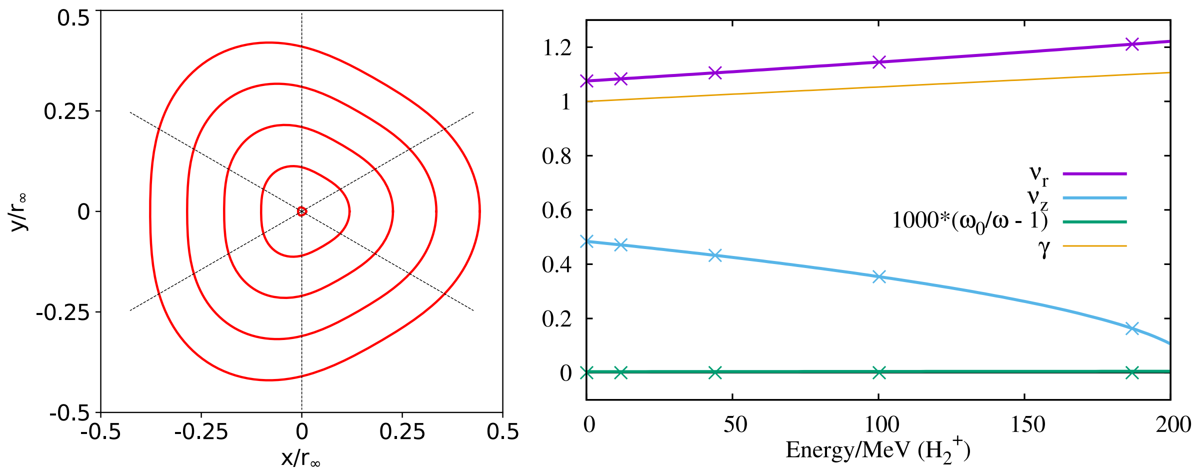

Figure 2: **Left**: the red lines represent 5 closed orbits with scale value a ranging between $0.01 \times r_\infty$ and $0.41 \times r_\infty$; the black dotted lines are lines of constant ϕ value. **Right**: corresponding horizontal (purple) and vertical (blue) tune variation with energy; the green curve represents the relative variation of the revolution frequency; the orange line represents the Lorentz factor γ.

over one period for two different sets of initial transverse state vectors: $\mathbf{X} = (1,0,1,0,0,0)^\mathsf{T}$ and $\mathbf{X} = (0,1,0,1,0,0)^\mathsf{T}$, see for instance Ref. [7].

To verify the tune calculated from numerical integration of Eq. (25), I also run CYCLOPS using 2-dimension field maps constructed by evaluating on a polar grid:

$$B(r,\theta) = \frac{\beta(a(r,\theta))}{\sqrt{1-\beta^2(a(r,\theta))}} \frac{m}{q\rho(a(r,\theta),\theta)}, \qquad (26)$$

where $\rho(a,\theta)$ is given by Eq. (21), $\beta(a)$ is given by Eq. (20). $a(r,\theta)$ is calculated from $r(a,\theta)$ using numerical root finding.

The source code used to calculate tunes and generate fields maps for all the examples presented below is available on: `https://gitlab.triumf.ca/tplanche/from-orbit`

EXAMPLES

Let's now consider an ensemble of closed orbits written in the form of a truncated Fourier series:

$$r(a,\theta) = a\left[1 + C(a)\cos\left(N(\theta - \phi(a))\right)\right], \qquad (27)$$

where N is the number of sectors.

Table 1: Examples of Orbit Shape Parameters. The names in the first row refer to the titles of the corresponding subsections.

	Gordon		spiral		N = 3 flat tunes		N = 5 flat tunes	
a/r_∞	C	ϕ	C	ϕ	C	ϕ	C	ϕ
0.01	0.08	0	0	0	0	0	0	0
0.11	0.08	0	0.04	0.319	0.0885	0.531	0.0614	0.827
0.21	0.08	0	0.04	0.719	0.0980	0.513	0.0748	0.94
0.31	0.08	0	0.04	1.082	0.0882	0.362	0.0712	0.992
0.41	0.08	0	0.04	1.427	0.0632	0.147	0.0591	1.103

3-sector Soft-edge Gordon Cyclotron

The first example I propose to study is a soft-edge version of Gordon's radial-sector cyclotron [1]. I choose the number of sectors $N = 3$, and $C(a) = 0.08$ for all a. In other words, all closed orbits are photographic enlargements with no rotation, see Fig. 2.

H_2^+ is chosen as the injection particle to run the CYCLOPS. Results are presented in Fig. 2. Agreement between the calculation from geometry (crosses) and using a field map with CYCLOPS (solid lines) is perfect. As expected, the field is isochronous: the maximum relative deviation from isochronism calculated by CYCLOPS is of the order of 10^{-5}. Note that the results presented in Fig. 2 are independent of the value chosen for r_∞.

3-sector Spiral Cyclotron

In all the following examples I define $C(a)$ and $\phi(a)$ as cubic splines constrained at 5 knots ranging from $a = 0.01 \times r_\infty$ to $a = 0.41 \times r_\infty$, see Table 1. I also impose the most central orbit to be circular, i.e. $C(0.01 \times r_\infty) = 0$. The intention is to account for the fact that closed orbits with a radius comparable with the magnetic gap are, in practice, very close to perfect circles.

For the second 3-sector example, I choose $C = 0.04$ for the outer orbits. I use the 'minimize' function form SCIPY.OPTIMIZE to minimize the variation of the vertical tune by adjusting the value of ϕ of the 4 outer orbits. The result is presented in Table 1 and Fig. 3. The agreement between the calculation from geometry and using a field map with CYCLOPS is again perfect, and the result is independent of the choice r_∞.

3-sector Cyclotron with Flat Transverse Tunes

For the third 3-sector example, I let both C and ϕ vary for the 4 outer orbits, with the objective to minimize the variation of both transverse tunes. The result is presented in Table 1 and Fig. 5. This example is not dissimilar to the one presented in Ref. [8], except that the relative variation of the revolution frequency is here of the order of 10^{-5}.

ISBN: 978-3-95450-205-9 doi:10.18429/JACoW-Cyclotrons2019-FRB01

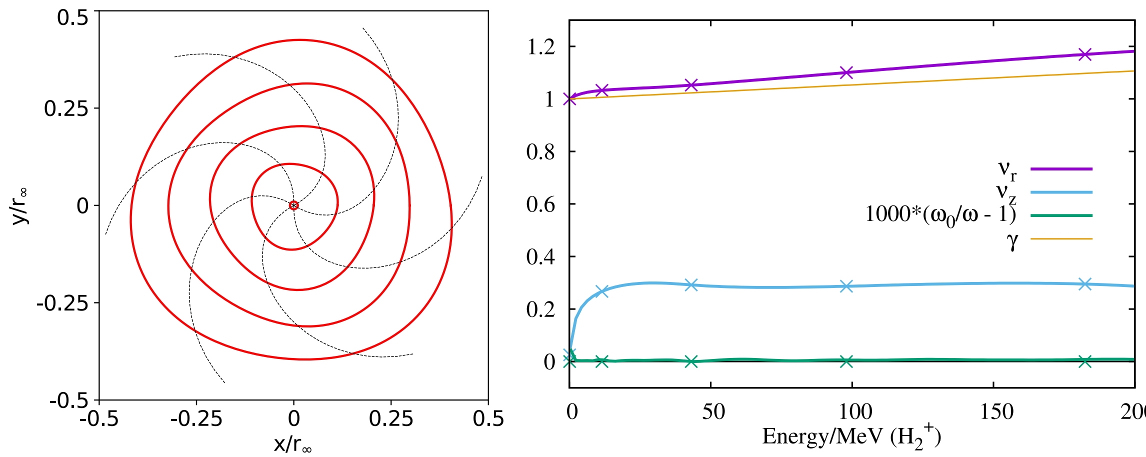

Figure 3: 3-sector spiral sector cyclotron example. Crosses show results calculated from the geometry of the orbits. The solid lines show results obtained using a field map and the computer code CYCLOPS. For a detailed plot description, please refer to the caption of Fig. 2.

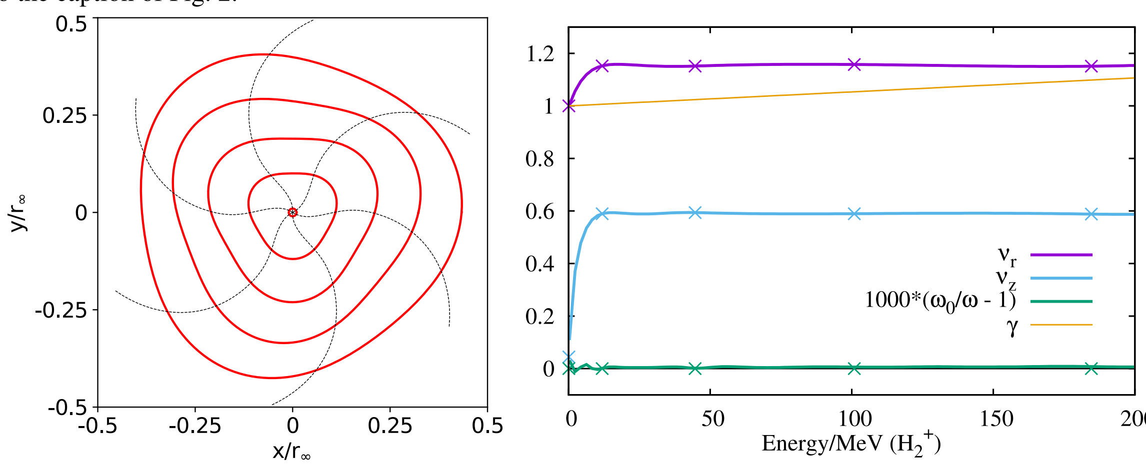

Figure 4: 3-sector spiral sector cyclotron example with stabilized radial tune. Crosses show results calculated from the geometry of the orbits. The solid lines show results obtained using a field map and the computer code CYCLOPS. For a detailed plot description, please refer to the caption of Fig. 2.

5-sector Cyclotron With Flat Transverse Tunes

The fourth example is a 5-sector version of the previous example. The result is presented in Table 1 and Fig. 5.

SCALING FFA

One may, for instance, substitute the isochronous condition, that is Eq. (20), by the following scaling law [9]:

$$P(a) = P_0 \left(\frac{a}{a_0}\right)^{k+1} \tag{28}$$

where P is the momentum associated with the closed orbit; k, P_0, and a_0 are constants. If $C(a)$ is kept constant, and $\phi(a)$ is chosen to follow a logarithmic spiral [9]:

$$\phi(a) = \tan(\zeta) \ln\left(\frac{a}{a_0}\right), \tag{29}$$

the resulting machine is scaling fixed field accelerator (FFA). It is not isochronous[2] and may be called a synchro-cyclotron. In the particular case $\zeta = 0$, the machine has radial sectors.

[2] except immediately around the transition energy given by $\gamma = \sqrt{k+1}$

As a scaling FFA example I choose $N = 4$, $C = 0.02$, $k = 0.2$ and $\zeta = 60$ degree. As expected the transverse tunes calculated using the geometrical parameters of the orbits are constant, see Fig. 6. Agreement with CYCLOPS is again perfect. These results have also been crosschecked using the analytic field model of the code FIXFIELD [10].

CONCLUSION

I have described a method to generate fixed field distributions starting from the geometry of the closed orbits. This method is useful to rapidly produce isochronous field maps without the need for finite element calculations. Among the few isochronous examples presented in this paper, two have stabilized vertical and radial tunes. These two examples have in common their non-monotonic radial variation of the magnetic flutter and spiral angle.

REFERENCES

[1] M. Gordon, "Orbit properties of the isochronous cyclotron ring with radial sectors," *Annals of Physics*, vol. 50, no. 3, pp.

ISBN: 978-3-95450-205-9 doi:10.18429/JACoW-Cyclotrons2019-FRB01

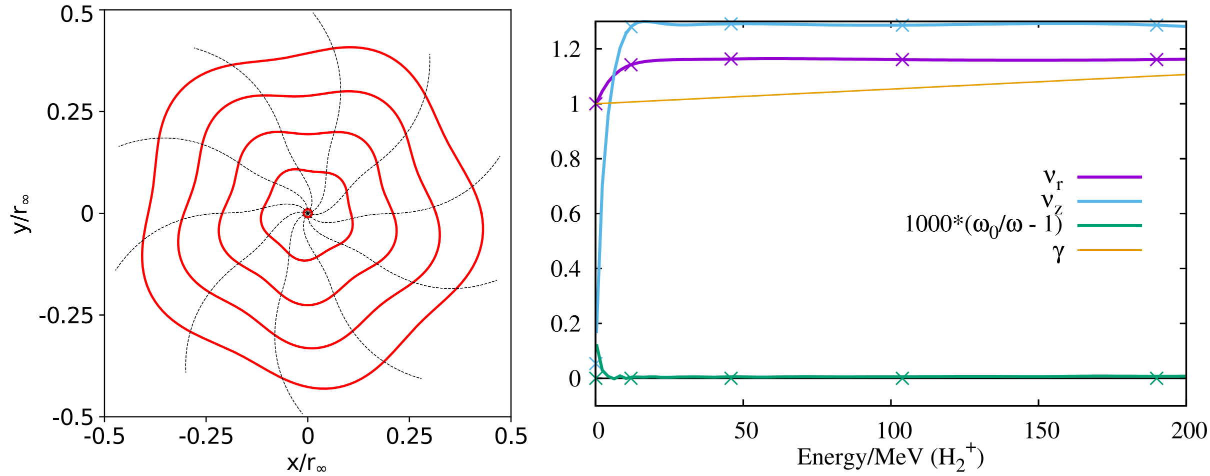

Figure 5: 5-sector cyclotron example. Crosses show results calculated from the geometry of the orbits. The solid lines show results obtained using a field map and the computer code CYCLOPS. For a detailed plot description, please refer to the caption of Fig. 2. Note the negative bends.

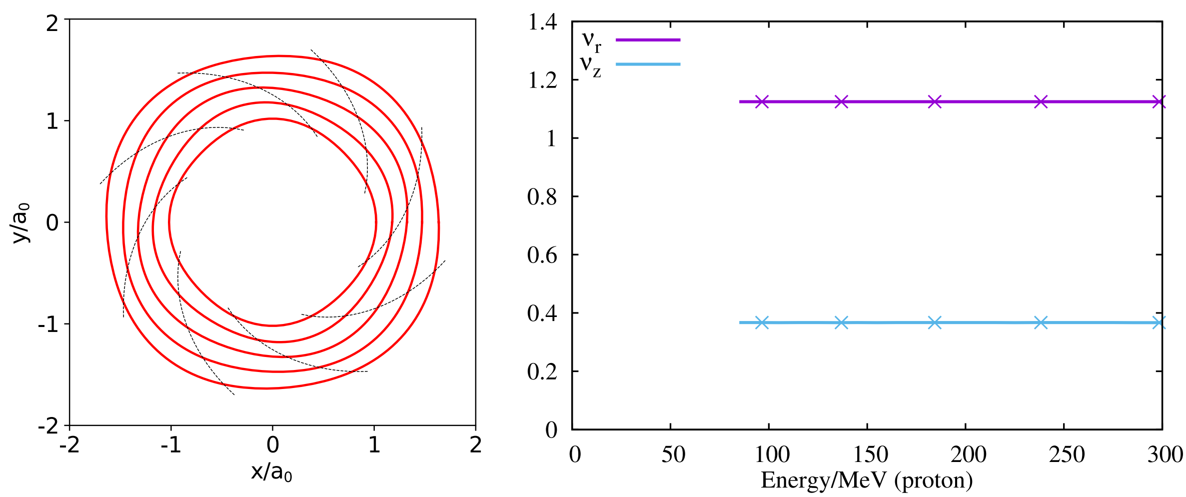

Figure 6: 4-sector spiral scaling FFA example. Crosses show results calculated from the geometry of the orbits. The solid lines show results obtained using a field map and the computer code CYCLOPS.

571–597, 1968. doi:10.1016/0003-4916(68)90132-2

[2] W. Joho, "Simulating cyclotron sector magnets with the computer program TRANSPORT," TRIUMF, Tech. Rep. TRI-BN-82-12, 1982. http://lin12.triumf.ca/text/2002FFAG/TRI-DN-82-12.PDF

[3] J. Botman, "Ring cyclotrons with return field gullies," TRIUMF, Tech. Rep. TRI-BN-82-20, 1982. http://lin12.triumf.ca/text/2002FFAG/TRI-DN-82-20.PDF

[4] M. Craddock and K. Symon, "Cyclotrons and fixed-field alternating-gradient accelerators," *Rev. Accel Sci. Technol.*, vol. 1, no. 01, pp. 65–97, 2008. doi:10.1142/9789812835215_0004

[5] R. Baartman, "Linearized Equations of Motion in Magnet with Median Plane Symmetry," TRIUMF, Tech. Rep. TRI-DN-05-06, 2005.

[6] E. Courant and H. Snyder, "Theory of the alternating-gradient synchrotron," *Annals Phys.*, vol. 3, no. 1, pp. 1 – 48, 1958. doi::10.1016/0003-4916(58)90012-5

[7] C. Meade, "Changes to the main magnet code," TRIUMF, Tech. Rep. TRI-DN-70-54-Addendum4, 1971. http://lin12.triumf.ca/design-notes/1970/TRI-DN-70-54.Addendum4.PDF

[8] D. Bruton *et al.*, "A compact and high current FFAG for the production of radioisotopes for medical application", in *Proc. IPAC'16*, Busan, Korea, 2016. doi:10.18429/JACoW-IPAC2016-TUPOY023

[9] K. R. Symon, D. W. Kerst, L. W. Jones, L. J. Laslett, and K. M. Terwilliger, "Fixed-field alternating-gradient particle accelerators," *Phys. Rev.*, vol. 103, pp. 1837–1859, Sep 1956. doi:10.1103/PhysRev.103.1837

[10] J.-B. Lagrange, D. J. Kelliher, S. Machida, C. R. Prior, and C. T. Rogers, "Status of FFAs (Modelling and Existing/planned Machines)", presented at the Cyclotrons'19, Cape Town, South Africa, Sep. 2019, paper WEB01.

ISBN: 978-3-95450-205-9 doi:10.18429/JACoW-Cyclotrons2019-FRB02

FLNR JINR ACCELERATOR COMPLEX FOR APPLIED PHYSICS RESEARCHES: STATE-OF-THE-ART AND FUTURE

S. Mitrofanov†, P. Apel, V. Bashevoy, V. Bekhterev, S. Bogomolov, O. Borisov, J. Franko, B. Gikal, G. Gulbekyan, I. Ivanenko, I. Kalagin, N. Kazarinov, V. Mironov, V. Semin, V. Skuratov, A. Tikhomirov, Joint Institute for Nuclear Research, 141980 Dubna, Russia

Abstract

The main activities of FLNR, following its name -- are related to fundamental science, but, in parallel, plenty of efforts are paid for practical applications. Certain amount of beam time every year is spent for applied science experiments on FLNR accelerator complex. The main directions are: the production of the heterogeneous micro - and nano-structured materials; testing of electronic components (avionics and space electronics) for radiation hardness; ion-implantation nanotechnology and radiation materials science. Status of all these activities, its modern trends and needs will be reported. Basing on FLNR long term experience in these fields and aiming to improve the instrumentation for users, FLNR accelerator department announce the design study for a new cyclotron, DC140, which will be dedicated machine for applied researches in FLNR. Following the user's requirements, DC140 should accelerate the heavy ions with mass-to-charge ratio A/Z of the range from 5 to 8 up to fixed energies 2 and 4.8 MeV per unit mass. The first outlook of DC140 parameters, its features, layout of its casemate and general overview of the new FLNR facility for applied science is presented.

INTRODUCTION

The main point is that for applied science people use powerful machines which were created and developed to solve the wide range of fundamental research. The usage of 'science' accelerators for such activities is connected which high cost of beam time and difficulty to meet quick changes of user's requirements. Also, there is a "time lack" problem when application begins to demand the beam time more than accelerator centre could provide to it in parallel with its scientific plan's realization. Usually, it means that all technical "bugs" and methodological questions were successfully fixed and answered, and users requesting the time as much as they could. That's why Flerov Laboratory of Nuclear Reaction of Joint Institute for Nuclear Research starts the Design Study of the dedicated applied science facility based on the new DC130 cyclotron. The irradiation facility will be used mainly for the following applications: creation and development of track membranes (nuclear filters) and the heavy ion induced modification of materials; activation analysis, applied radiochemistry and production of high purity isotopes; ion-implantation nanotechnology and radiation materials science; testing of electronic components (avionics and space electronics) for radiation hardness.

† mitrofanov@jinr.ru

RADIATION MATERIAL SCIENCE

Characterization and monitoring of structural defects enhanced by ~100 MeV heavy ions in nuclear ceramics represents an important issue. Besides many intriguing fundamental science questions, these experiments may be of considerable practical value in view of such pressing problems such as radiation stability of inert matrix fuel hosts and coated fuel particles. Materials to be employed as inert matrices for transmuting of minor actinides by means of nuclear reactions should obviously present suitable characteristics as hosts for the actinides and as targets for the irradiation in a reactor. A key parameter to be considered is the resistance to radiation damage due to neutron exposure, gamma and beta radiation, self-irradiation from alpha decay, and fission fragments. Structural modifications induced by fission products, i.e. atoms with a mass ranging from 80 to 155 and an energy of about 100 MeV, still remain uncertain because the effects cannot be investigated using classical low-energy ion implanters. To date, only limited data concerning the microstructural response of non-fertile ceramics to ion irradiation of fission energy are available and external bombardment with energetic ions offers a unique opportunity to simulate fission fragment-induced damage.

The main objective of ongoing projects in radiation material science in FLNR is to determine the radiation tolerance of several oxides, carbide and nitride based ceramics (MgO, Al_2O_3, ZrN, SiC, Si_3N_4, A_lN), considered as candidates for inert matrix fuel hosts, irradiated with high-energy heavy ions, simulating fission fragments impact. Our central objectives are:

a) To study the structural changes and mechanical stresses induced by swift heavy ions as function of ion fluence, irradiation temperature and ionizing energy loss;
b) To elucidate the dense ionization effect on pre-existing defect structures in irradiated materials;
c) To compare the radiation stability of nanocrystalline and bulk ceramics.

TRACK – ETCHING MEMBRANE

In the 1970s, advances in heavy-ion accelerator technology resulted in the idea to replace the fission fragment irradiation with bombardment by high energy, multiply charged ions. The advantages of the accelerator irradiation method are the following: (i) there is no radioactive contamination of the irradiated material because the ion energy is normally below the Coulomb barrier; (ii) all of the bombarding particles are identical; (iii) the ions have a

ISBN: 978-3-95450-205-9 doi:10.18429/JACoW-Cyclotrons2019-FRB02

larger penetration depth in the polymers; (iv) it is easier to produce high density track arrays; (v) particles heavier than fission fragments can be used for highly radiation-resistant materials; and (vi) it is easier to control the impact angle to produce either arrays of parallel tracks or those with special angle distributions. The only disadvantages of ion beams are that they are less stable over time because of transient fluctuations in intensity, and they have a higher cost. Firstly, the U-300 cyclotron at the Flerov Laboratory of Nuclear Reactions (JINR, Dubna) was employed to produce a track membrane from a polyester film. Accelerated xenon ions, with energy of 1 MeV/u and intensity of 10^{12} s^{-1}, were found to be a good substitute for fission fragments. High intensity, heavy-ion beams provided new advantages, such as higher pore densities, larger membrane thickness, and control over the angle of incidence. The use of heavy-ion accelerators equipped with specialized beam channels, sophisticated irradiation chambers, and beam diagnostics made it possible to fabricate micro- and nanoporous materials with unique structural parameters that could not be obtained using fission fragments. Since then, following the advances was achieved using FLNR accelerating complex the applications of track membranes can be categorized into three groups: process filtration, analytical filtration, and permeable supports. Within each group, there are a number of particular uses. Typical areas where the use of track membranes are especially beneficial, are air monitoring; water analysis; blood filtration; cell culture; analytical methods (gravimetry, microscopy, emission spectroscopy, X-ray fluorescence, and others); bacteria removal and analysis; HPLC (high performance liquid chromatography) sample preparation; nucleic acid studies; oceanographic studies; healthcare; biosensors. With the capability to create either a single track or regular pattern with a preset number of tracks, the track etching technique allows the fabrication of nano and microengineered membranes, with finely tuned geometrical parameters.

SEE TESTING

On-board equipment of spacecraft is exposed to ionizing radiation from the Earth's natural radiation field, as well as galactic and solar cosmic rays during its operation. There are two types of effects in microelectronic circuits caused by radiation: 1 - those related to accumulated dose; and 2 - those caused by a singular hit of a swift heavy ion (single event effect, SEE). Despite its relatively minor contribution (~1%) of the total amount of charged particles, it is heavy ions that cause the most damage to microelectronics hard ware components due to the high level of specific ionization loss. Hence, to reproduce the effects of the heavy ion component of cosmic radiation for the prediction of electronic device radiation hardness usage of low intensity (up 10^6 ions cm^{-2} s^{-1}) heavy ion beams with linear energy transfer (LET - the measure of energy losses per path length in the material) levels in silicon, specific for the ion energy range of 50 - 200 MeV/u, is supposed. Taking into account that actual integrated circuits in metal and plastic packages, as well as ready to use electronic boards need to be tested, ion beams with energies in the range of 3-50 MeV/u are used in model experiments.

The SEE testing facility was established at the U400M cyclotron at the accelerator complex of the Flerov Laboratory of Nuclear Reactions (FLNR) of the Joint Institute for Nuclear Research (JINR) in 2012. The U400M cyclotron is designed to accelerate ion beams in two modes: in the energy ranges of 19-52 and of 6-9 MeV/u. Using this feature, two dedicated beam lines with low and high energy modes were created and successfully lunched.

Testing was carried out according to the procedure based on international standards, such as EIA/JESD57 and ESCC25100. The standards apply to ions with energies <10 MeV/u. These standards have the following requirements to the ion beam: set of ions with different LET values in the material of tested devices should be used in the tests. There should be no impurities of other atoms in the irradiating ion beams. In this case it is impossible to clean out the ion beam of impurities, a minor presence of impurities is allowed, and their content must be known. It is required by the standards that the LET be known with an accuracy no worse than ±10%. Based on this, the energy of the ions must be measured with the same accuracy. The accepted method of SEE testing requires measurements of ion flux in the range from 1 to 10^5 ions (cm^{-2} s^{-1}), ion fluence up to 10^7 ions/cm^2, beam uniformity at the DUT, and energy of ions.

DC 140 PROJECT

From the common user's requirements, operation simplicity and cost reasons the main parameters of future machine were chosen. The facility will be based on new DC140 isochronous cyclotron: multiparticle, double - energy machine, capable with light and heavy ions up to bismuth (2 and 4.8 MeV/u).

The research works on radiation physics, radiation resistance of materials and the production of track membranes will be carrying out by using the ion beams with energy of about 2 MeV per unit mass and A/Z ratio in the range from 7.58 to 8.0. Besides these, testing of avionics and space electronics by using of ion beams (^{20}Ne, ^{40}Ar, ^{84,86}Kr, ^{132}Xe, ^{197}Au or ^{209}Bi) with energy of 4.8 MeV/u and with mass-to-charge ratio A/Z in the range from 5.0 to 5.5, will be proceeded. One of the significant requirements for this application is the "ion cocktail" means mixed of highly charged heavy ions with the same or very close mass/charge ratios produced and injected in the same time. Once the ions will be accelerated, the different species will be separated by the fine tuning of the cyclotron magnetic field. This issue allows switching the type of ions quick and will reduce the time which user should spend for full scale testing of its samples.

The idea is to effectively use existing stuff to modernize and totally upgrade the old U200 machine which was decommissioned in 2013, because of being outdated

ISBN: 978-3-95450-205-9 doi:10.18429/JACoW-Cyclotrons2019-FRB02

physically and technologically. The design will be based on existing systems of IC100 and U200 cyclotrons.

The working diagram of DC140 cyclotron is shown in Fig. 1. The acceleration of ion beam in the cyclotron will be performed at constant frequency f = 8.632 MHz of the RF-accelerating system for two different harmonic numbers h. The harmonic number h = 2 corresponds to the ion beam energy W = 4.8 MeV/u and value h = 3 corresponds to W = 2.877 MeV/u. The intensity of the accelerated ions will be about 1 pμA for lighter ions (A < 86) and about 0.1 pμA for heavier ions (A < 132).

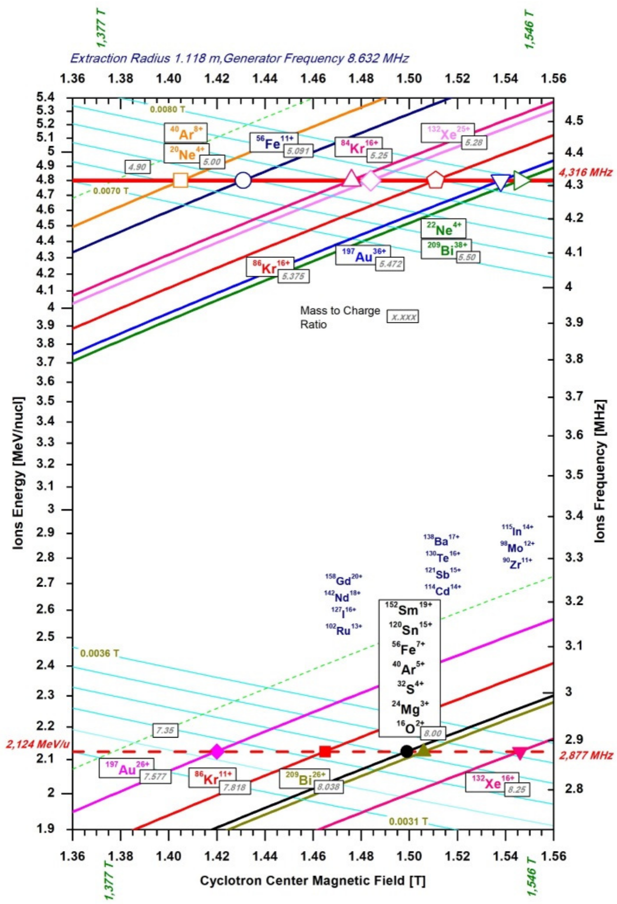

Figure 1: Working diagram of DC140 cyclotron with ^{209}Bi.

The axial injection system and its beam line for new accelerator will be adapted from the existing IC100 cyclotron systems.

In the frame of reconstruction of U200 to DC140 it is planned to upgrade the cyclotron magnetic structure, replace the magnet main coil and renovate RF system. Other systems: beam extraction, vacuum, cooling, control electronics and radiation safety will be new.

EXPERIMENTAL BEAM LINES

The set of the experimental beam lines will include track membrane line; SEE testing line and radiation physics line. The scheme of the experimental beam lines is shown in Fig. 2. The common part of the channel consists of extraction bending magnet, the quadrupole lens triplet and commutating magnet. The centre of the extraction bending magnet is an object point for all beam line. These beam lines will consist of standard subsystems: ion beam transportation system, beam scanning system, beam monitoring system, energy measurement system and user's vacuum test chamber with a mounting, positioning and moving assembly to hold or move the sample in the irradiation field. The experience of working at U400, U400M cyclotrons and existing FLNR apply science facilities will be used during developing the experimental channels for these applications.

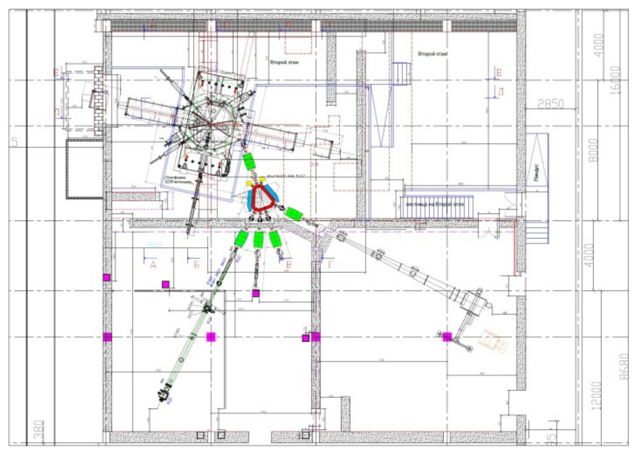

Figure 2: DC140 cyclotron – layout of its casemate and general beam lines overview.

CONCLUSIONS

At present time, Flerov Laboratory of Nuclear Reaction begins the works under the conceptual design of the dedicated applied science facility based on the new DC140 cyclotron. The main characteristics of the new DC140 cyclotron are defined and fit main user requirements well. This dedicated facility is intended for track pore membranes production; SEE testing and radiation materials science. The detailed technical project and the costs estimation will be ready in December 2019. The project is planned to be realised in 2020 - 2022 and will provide the first beam for users before 2023.

ISBN: 978-3-95450-205-9 doi:10.18429/JACoW-Cyclotrons2019-FRB03

3D RADIO FREQUENCY SIMULATION OF THE INFN-LNS SUPERCONDUCTING CYCLOTRON

G. Torrisi*, L. Neri, L. Allegra, L. Calabretta, A. Caruso, G. Costa,
G. Gallo, A. Longhitano, D. Rifuggiato
INFN-LNS, Catania, Italy

Abstract

An upgrade plan of the Superconducting Cyclotron operating at INFN-LNS is ongoing. In this paper, a 3D numerical model of the Cyclotron radio frequency cavity is presented. Simulations include the coaxial sliding shorts, liner vacuum chamber, coupler, trimming capacitor and the Dees structures. CST microwave studio software has been used for numerical computation. RF simulations are mandatory also in order to analyze the field in the beam region and evaluate the impact of different Dees geometry and eventual field asymmetries. Moreover, 3D COMSOL Multiphysics simulations have been carried out in order to couple the electromagnetic field solution to a custom beam-dynamics code developed in Matlab as a future plan. Time evolution of accelerated beam and electromagnetic field make also possible to verify the magnetic field synchronization. Experimental validation of the developed model will be also presented.

INTRODUCTION

The INFN-LNS Superconducting Cyclotron (SC) is a three sector compact machine with a wide operating range, able to accelerate heavy ions with values of q/A from 0.1 to 0.5 to energy from 2 to 100 AMeV [1]. The SC has been in operation for more than 20 years for nuclear physics experiments, which require low intensity beams. Up to now the maximum beam power has been limited to 100 W due to the beam dissipation on the electrostatic deflectors. To fulfill the request of users aiming to study rare processes in Nuclear Physics [2, 3], the beam power has to be increased up to 2-10 kW for ions with mass lower than 40 a.m.u., and extracted by stripping [4–6]. The feasibility of extraction by stripping through an optimized extraction channel with an increased transverse section has been studied in [7–9]. In the meantime, the RF system has gone through many improvements for more reliable operation of the cyclotron [10, 11]. Moreover, the vertical gap between the dees of the acceleration chamber is planned to be increased from the present 24 mm up to 30 mm by renewing the existing liners and trim coils [12]. This paper describes a numerical study of the RF cavity of the INFN-LNS SC, especially focused on the eventual vertical asymmetry at the dee gap. RF driven-field simulations allow to investigate the fundamental accelerating mode and eventual RF leakages and asymmetries [13–16].

* giuseppe.torrisi@lns.infn.it

RF NUMERICAL MODEL VS EXPERIMENTAL RESULTS

The 3D model was created by using Autodesk Inventor [17] to provide a proper geometry with the actual dimensions to the 3D commercial electromagnetic simulators, CST Microwave Studio [18] and COMSOL multiphysics [19]. In particular, COMSOL could be used connected to a MATLAB-developed beam dynamics code [8]. In Fig. 1 the overall geometry of the simulated model of RF cavity of the LNS SC it is shown: the dee stems, the trimmer, the coupler and the dees have been included into the simulation. Figure 2 shows the CST MWS simulated 3D Electric field distribution vector (left) and intensity (right). The RF Cavity has a

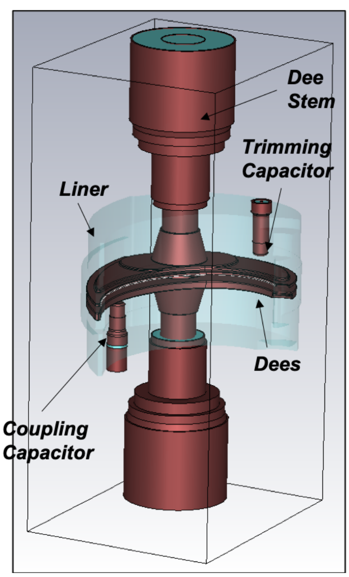

Figure 1: Overall geometry of the simulated model of RF cavity of the LNS Superconducting Cyclotron (SC).

capacitive coupled power input, while, on the other side of cyclotron, cavity has a tuner. Both the components are controlled by external motor for tuning of the cavity matching and frequency. For COMSOL simulations (see Fig. 3), we added an external lateral volume in correspondence of the dee plane to the previous geometry, in order to simulate the "accelerating" electric field for the beam-dynamics code.

As experimental validation of the developed model we performed driven RF simulation by varying the coupler and trimmer position. Figure 4 shows that a good impedance matching (in terms of $|S_{11}|$) can be obtained by moving the coupler towards the dee-plane. The comparison between the numerical results of Fig. 4 and the experimental results

ISBN: 978-3-95450-205-9 doi:10.18429/JACoW-Cyclotrons2019-FRB03

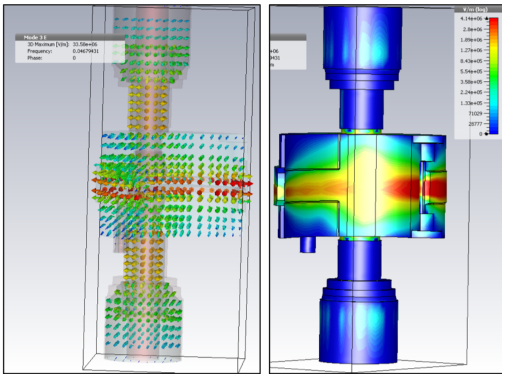

Figure 2: CST MWS simulated 3D Electric field distribution vector (left) and intensity (right).

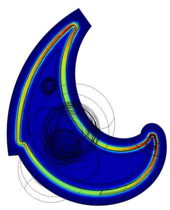

Figure 3: COMSOL Numerical simulation result: Electric field norm on the median dee-plane.

of Fig. 5 confirms also that the tuner positioning allow a fine-tuning of the resonant frequency. The RF scattering parameters have been computed and are in agreement with the parameters measured on the cyclotron: both in simulation (Fig. 4) and measurement (Fig. 5), we can observe a frequency downshift of the resonant frequency by moving the coupler from the initial position (“c=start”) towards the median plane (“c=+30 mm” in simulation, “c=+25 mm and c=+50 mm” in measurements).

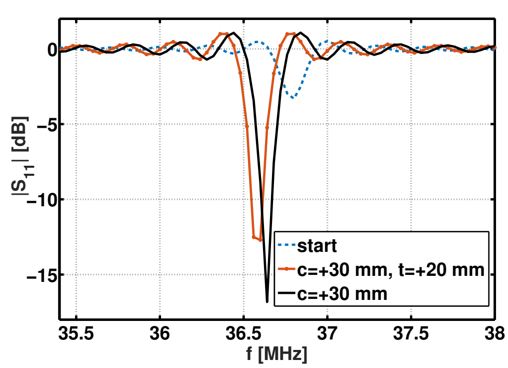

Figure 4: CST MWS Numerical simulation results: Comparison of the reflection coefficient $|S_{11}|$ for three different configurations obtained by varying the coupler and the trimmer vertical positions (“c” and “t” in the legend). In the legend, “start” indicates that coupler and trimmer have a distance from the dee-plane of 146 mm. The sign “+” means to get closer to the dee-plane with respect to the “start” position.

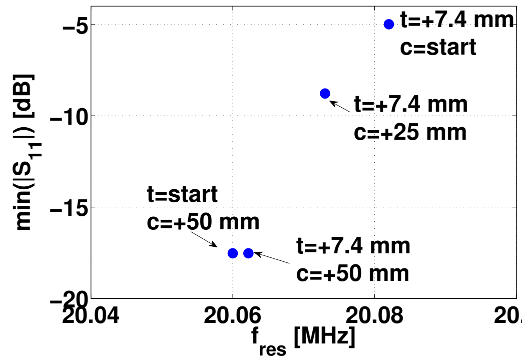

Figure 5: Measured results with Network analyzer: Comparison of the minimum reflection coefficient (min($|S_{11}|$)) for different configurations obtained by varying the coupler and the trimmer vertical positions (“c” and “t” in the legend).

ELECTROMAGNETIC STUDY OF DEES ASYMMETRY

Due to the different size of the beam for the SC upgrade plan [5], the vertical gap between the dees has to be increased from 25 to 31 mm, 6 mm of difference, 3 mm up and 3 mm down. This modification results in the length reduction of the conical connection between the stem (inner coaxial) and the dee (see the comparison of the “old” and “new” geometry in Fig 6).

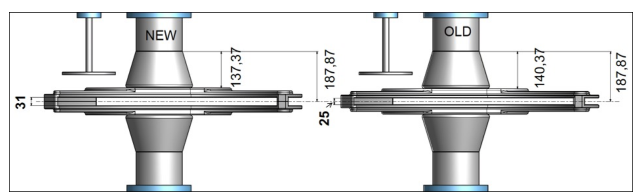

Figure 6: Comparison of the “old” and “new” geometry (sizes in mm-unit): the reduction of the length of the conical connection between the stem (inner coaxial) and the dee from 140.37 mm (on the right) to 137.37 mm (on the left) increases the dee vertical gap size Δg from 24 to 30 mm in the “new geometry”.

Using the CST Microwave Studio, we checked the proposed length reduction, of ± 3 mm (up and down), of the conical connection (dee-inner coax), can be accepted, in terms of maximum electric field distribution, around the critical zone of the nose, electric field along the vertical axis (see Fig. 7) and no parasitic modes appear. In order to host the new stripping extraction system, a new dee geometry has been proposed. In this Section, we evaluate the impact of the different dee geometry on the electric field distribution on the medium plane using the CST Microwave Studio. For the simulations, three models were created: the actual geometry (Fig. 8 (a)) used as a reference for RF simulations preserving the actual cavity structure; a second asymmetric model (Fig. 8 (b)) with the top actual dee and the new bottom; a third model where both the dees have the new geometry (Fig. 8 (c)). In order to explore the eventual presence of parasitic

ISBN: 978-3-95450-205-9 doi:10.18429/JACoW-Cyclotrons2019-FRB03

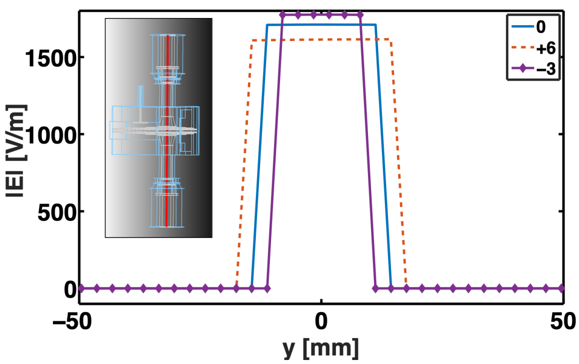

Figure 7: Norm of electric field along the vertical axis (red line in the inset) crossing the dee of the RF cavity for different values Δg of the vertical gap between the dees.

electric field components, the resulting electric field orthogonal to the medium (accelerating) plane is shown in Fig. 9 (plotted on the same plane). As we would expect, Fig. 9 (a) shows the unwanted electric field component is near zero in the first symmetric case (actual geometry, Fig. 8 (a)). On the other hand, the geometrical asymmetry of the second case (asymmetric model Fig. 8 (b)) gives rise to undesired electric field intensity (Fig. 9 (b)) in the central part of the dee medium plane. This undesired effect can be only partially avoided by using the third case geometry (Fig. 8 (c)): anyway, in this latter case, Fig. 9 (c) shows fringing field due to the “edge” effect ot the “new” dees.

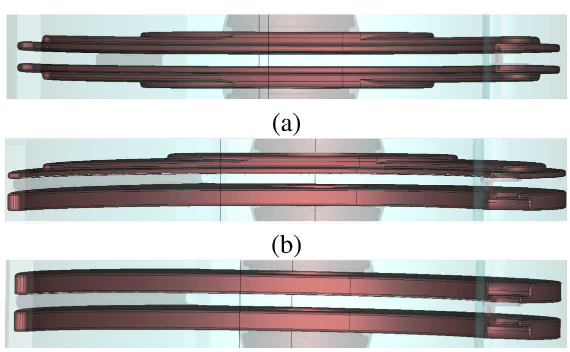

(a)

(b)

(c)

Figure 8: 3D view of the Dees geometry: a) current configuration. b) asymmetric configuration with the new dee; c) symmetric configuration with the new dees.

CONCLUSION

A better understanding of RF behavior in the SC was possible by using Electromagnetic 3D simulation. Close agreement between measured and computed S-parameters demonstrates the usefulness of the simulation. The full structure model of the cyclotron was used to study eventual asymmetry. This model simulation can be further used to study the center region of the accelerator, RF leakages, parasitic modes. 3D COMSOL Multiphysics simulations could be carried out in order to couple the electromagnetic field solution to a custom beam-dynamics code developed in Matlab as scope of future work.

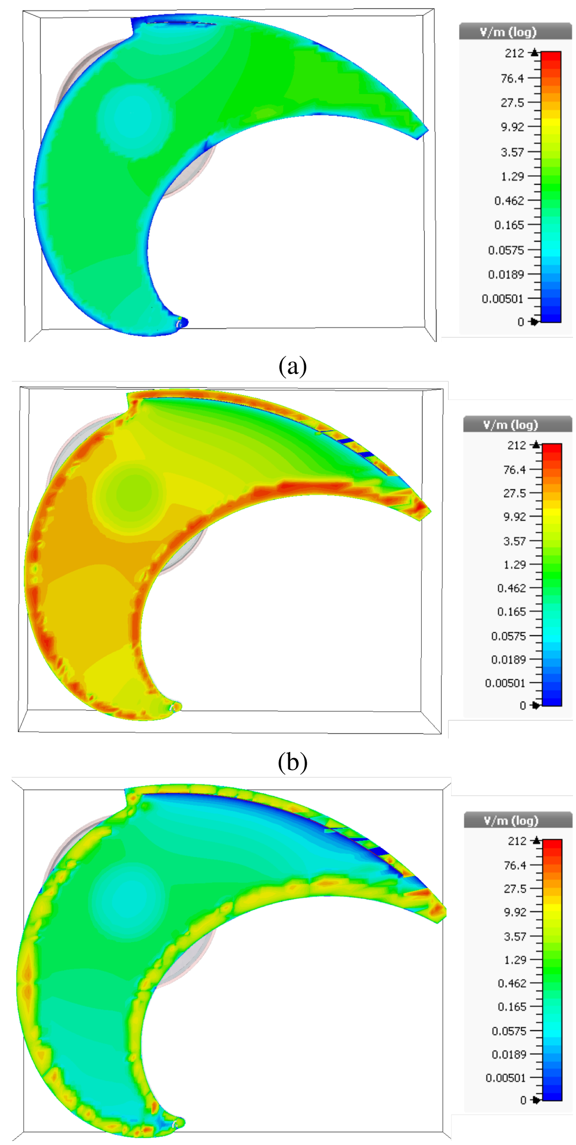

(a)

(b)

(c)

Figure 9: Cross Section view of the Electric field (same scale) for the three geometry: a) current configuration. b) asymmetric configuration with the new dee; c) symmetric configuration with the new dees

REFERENCES

[1] L. Calabretta *et al.*, “Commissioning of the K800 INFN Cyclotron,” in *Proc. Cyclotrons’95*, Faure, Cape Town, South Africa, 8-13 Oct 1995, p. A02, 1996.

[2] F. Cappuzzello, F, M. Cavallaro, C. Agodi, M. Bondì, D. Carbone, A. Cunsolo, and A. Foti, “Heavy-ion double charge exchange reactions: A tool toward $0\nu\beta\beta$ nuclear matrix elements,” *Eur. Phys. J. A*, vol. 51, no. 11, p. 145, 2015. doi:10.1140/epja/i2015-15145-5

[3] F. Cappuzzello *et al.*, “The NUMEN project: NUclear Matrix Elements for Neutrinoless double beta decay,” *Eur. Phys. J. A*, vol. 54, no. 5, p. 72, 2018. doi:10.1140/epja/i2018-12509-3

[4] A. Calanna *et al.*, “Proposal to increase the extracted beam power from the LNS-INFN Superconducting Cyclotron,” in

ISBN: 978-3-95450-205-9 doi:10.18429/JACoW-Cyclotrons2019-FRB03

Proc. HIAT2015, Yokohama, Japan, Sep. 2015, pp. 23–26. doi:10.18429/JACoW-HIAT2015-MOA1C03

[5] L. Calabretta, A. Calanna, G. Cuttone, G. D'Agostino, D. Rifuggiato, and A. D. Russo, "Upgrade of the LNS superconducting cyclotron for beam power higher than 2-5 kW," in *Proc. Cyclotrons'16*, Zurich, Switzerland, Sep. 2016, pp. 7–10. doi:10.18429/JACoW-Cyclotrons2016-MOA02

[6] A. Calanna, "High-intensity extraction from the Superconducting Cyclotron at LNS-INFN," *Nuovo Cimento C Geophysics Space Physics C*, vol. 40, p. 101, Mar. 2017. doi:10.1393/ncc/i2017-17101-y

[7] G. D'Agostino, L. Calabretta, W. J. G. M. Kleeven, and D. Rifuggiato, "A central region upgrade of the K800 Superconducting Cyclotron at INFN-LNS," in *Proc. IPAC'19*, Melbourne, Australia, May 2019, pp. 1975–1978. doi:10.18429/JACoW-IPAC2019-TUPTS023

[8] L. Neri, G. D'Agostino, L. Calabretta, D. Rifuggiato, A. Russo, and G. Torrisi, "3D Magnetic optimization of the new extraction channel for the LNS Superconducting Cyclotron," presented at the Cyclotrons'19, Cape Town, South Africa, Sep. 2019. doi:10.18429/JACoW-Cyclotrons2019-MOP014, to be published

[9] G. Gallo, G. Costa, L. Allegra, L. Calabretta, G. Messina, M. Musumeci, D. Rifuggiato, and E. Zappalà, "Mechanical modifications of the median plane for the Superconducting Cyclotron upgrade," presented at the Cyclotrons'19, Cape Town, South Africa, Sep. 2019. doi:10.18429/JACoW-Cyclotrons2019-MOP013, to be published

[10] A. Caruso, "The RF System of the K-800 Superconducting Cyclotron at INFN-LNS," in *Proc. InPAC'13*, Nov 2013, Kolkata, India, paper InPAC2013IT15.

[11] A. C. Caruso, F. Caruso, A. Longhitano, A. Spartà, G. Primadei, and J. Sura, "Hybrid configuration, solid state-tube, revamps an obsolete tube amplifier for the INFB K-800 Superconducting Cyclotron," in *Proc. Cyclotrons'16*, Zurich, Switzerland, Sep. 2016, pp. 263–266. doi:10.18429/JACoW-Cyclotrons2016-WEB02

[12] G. Gallo, L. Allegra, G. Costa, E. Messina, and E. Zappalà, "Mechanical aspects of the LNS Superconducting Cyclotron upgrade," in *Proc. Cyclotrons'16*, Zurich, Switzerland, Sep. 2016, paper THP09, pp. 322–324. doi:10.18429/JACoW-Cyclotrons2016-THP09

[13] J. J. Livingood, *Principles of Cyclic Particle Accelerators*, London: D. van Nostrand Co, 1961.

[14] V. Afzalan, H. Afarideh, R. Azizi, M. Ghergherehchi, and J. S. Chai, "Design and simulation of cavity for 10 MeV compact cyclotron," in *Proc. Cyclotrons'13*, Vancouver, Canada, Sep. 2013, paper TUPPT023, pp. 200–202.

[15] A. K. Mitra, Y. Bylinski, N. Mehboob, R. L. Poirier, and V. Zvyagintsev, "Simulation of RF structure of TRIUMF cyclotron with HFSS," in *Proc. Cyclotrons'04*, Tokyo, Japan, Oct. 2004, paper 20P29, pp. 365-367.

[16] M. Mohamadian, H. Afarideh, M. Ghergherehchi, S. Sabounchi, and M. Salehi, "Equivalent circuit model of cyclotron rf system," in *Proc. Cyclotrons'16*, Zurich, Switzerland, Sep. 2016, pp. 39–41. doi:10.18429/JACoW-Cyclotrons2016-MODM03

[17] Autodesk, "Autodesk Inventor."

[18] CST, "CST Microwave Studio," 2017.

[19] "Comsol Multiphysics reference manual, version 5.3.

List of Authors

Bold papercodes indicate primary authors; ~~crossed out~~ papercodes indicate 'no submission'

— A —

Abegglen, F.P.	THC02
Abraham, J.K.	MOB02, **TUP004**, TUP007, THA03
Adachi, T.	TUP024
Adam, T.	MOP021
Adant, B.	TUP009
Adelmann, A.	MOP034, ~~**WEB02**~~, THA01, ~~**THA02**~~
Afarideh, H.	MOP032, ~~TUA05~~
Agustsson, R.B.	TUP029
Ahn, J.-K.	TUP028
Akcöltekin, E.M.	FRA03
Akhdar, H.F.	TUP025
Allegra, L.	MOP013, MOP014, FRB03
Alrumayan, F.M.	TUP025, TUP026
An, S.	**MOP006**, MOP007, MOP008, MOP010, MOP011, TUP031, FRA01
Anashin, V.S.	FRA04
Anderson, H.	MOB02
Anthony, L.S.	MOB02
Antoine, S.	~~MOB03~~
Antonini, P.	**TUP010**, TUC01
Antos, M.	TUA04
Aoki, T.	TUP036, TUP037
Apel, P.Yu.	FRB02
Arakawa, Y.	FRA02
Ärje, J.E.	THC02
Azaiez, F.	MOB02

— B —

Baard, S.	MOB02
Baartman, R.A.	THB03
Babaee, S.	MOP032
Bark, R.A.	MOB02
Barnard, A.H.	MOB02, **MOP016**
Bashevoy, V.	FRB02
Baumann, P.	TUP016
Baumgarten, C.	**WEB03**, THA01
Beck, F.B.	THC04
Beeckman, W.	~~**MOB03**~~
Běhal, R.	MOP022
Bekhterev, V.	FRB02
Belver-Aguilar, C.	TUA02
Bertora, L.	TUB03
Beukes, P.	MOB02
Bian, T.J.	FRA01
Blain, G.	TUP006, THB04
Bogomolov, S.L.	**MOP017**, THC01, FRB02
Boldt, O.	**TUP017**, FRA03
Boso, A.	TUP012
Boucher, S.	TUP029
Boyer, B.	THB04
Braccini, S.	TUA03, **TUA02**
Brandenburg, S.	TUC03
Brijar, F.	TUA04
Bromberg, L.	~~TUB01~~
Broodryk, J.I.	MOB02, MOP016
Brutscher, J.	MOP025
Buffler, A.	TUP012
Bulteau-harel, F.	TUP006
Bundesmann, J.	TUP007, **TUP020**, TUP021, TUC02
Bunyatov, K.	TUB02
Buriola, L.	TUP010
Bychkov, A.S.	FRA04
Bylinskii, Y.	THB03

— C —

Cailliau, P.	TUP009
Calabretta, L.	MOP001, MOP002, MOP013, MOP014, TUP011, WEA02, **THB01**, FRB03
Calvo, P.	**MOP034**
Cao, L.C.	TUP005
Carrozzi, A.	TUB03
Caruso, A.C.	MOP001, MOP013, **WEA02**, FRB03
Carzaniga, T.S.	TUA02
Castro, G.	THD01
Celona, L.	THD01
Cervenka, V.	MOP023
Chai, J.-S.	MOP028, MOP029, MOP030, MOP031, ~~TUA05~~, TUP030, THC03
Chao, C.	MOP001
Chen, G.	**MOP001**, MOP002
Chen, Y.	MOP001, MOP003
Chiavassa, S.	TUP006
Chubunov, P.A.	**FRA04**
Čihák, M.	**MOP022**
Clark, H.L.	THC02
Conradie, J.L.	**MOB02**, MOP016, MOP017, TUP007
Cordini, D.	TUC02
Cornelius, B.	MOB02
Cornell, J.C.	MOB02
Costa, G.	MOP013, MOP014, WEA02, FRB03
Cuhra, M.	TUA04
Cui, T.	MOP011, TUP031
Cvachovec, F.	TUA04
Czakoj, T.	TUA04

ISBN: 978-3-95450-205-9

ISBN: 978-3-95450-205-9

ISBN: 978-3-95450-205-9

ISBN: 978-3-95450-205-9

ISBN: 978-3-95450-205-9

ISBN: 978-3-95450-205-9

Institutes List

AEC
Bern, Switzerland
- Belver-Aguilar, C.
- Braccini, S.
- Carzaniga, T.S.
- Dellepiane, G.
- Haeffner, P.
- Scampoli, P.

Al-Imam Mohammad Ibn Saud University
Riyadh, Kingdom of Saudi Arabia
- Akhdar, H.F.

ASG
Genova, Italy
- Bertora, L.
- Carrozzi, A.
- Serra, A.

ASIPP
Hefei, People's Republic of China
- Chao, C.
- Chen, G.
- Chen, Y.
- Ding, K.Z.
- Huang, X.Y.
- Li, J.
- Liu, G.
- Long, X.Y.
- Pei, K.
- Peng, Z.
- Song, Y.
- Wu, Z.
- Xu, Y.
- Yu, C.
- Zhang, X.
- Zhao, Y.

AUT
Tehran, Iran
- Afarideh, H.
- Babaee, S.
- Mohamadian, M.
- Pashaei, H.
- Salmani, N.

Catania University
Catania, Italy
- Naselli, E.

CEA-IRFU
Gif-sur-Yvette, France
- Boyer, B.
- Delagnes, É.
- Gebreyohannes, F.T.
- Gevin, O.

Charite
Berlin, Germany
- Cordini, D.
- Ehrhardt, V.H.
- Gollrad, J.
- Heufelder, J.
- Stark, R.
- Weber, A.

CIAE
Beijing, People's Republic of China
- An, S.
- Bian, T.J.
- Cao, L.C.
- Cui, T.
- Fu, Z.H.
- Ge, T.
- Guan, F.P.
- Guan, L.L.
- Hou, S.G.
- Huang, P.
- Ji, B.
- Ji, L.Y.
- Jia, X.L.
- Jiang, H.
- Li, M.
- Li, S.Q.
- Li, Y.Q.
- Liu, Z.W.
- Lv, Y.L.
- Pan, G.F.
- Pei, S.
- Wang, C.
- Wang, F.
- Wang, L.
- Wang, S.L.
- Wei, S.M.
- Wen, L.P.
- Xie, H.D.
- Xing, J.S.
- Yin, M.
- Yin, Z.G.
- Zhang, T.J.
- Zheng, X.
- Zhu, F.Zhu.

CIEMAT
Madrid, Spain
- Calvo, P.
- Oliver, C.

CMRP
Wollongong, Australia
- Oborn, B.

CNRS - DR17
RENNES, France
- Poirier, F.

ISBN: 978-3-95450-205-9

Cyclotron ARRONAX
Saint-Herblain, France
- Bulteau-harel, F.
- Durand, T.
- Goiziou, X.
- Haddad, F.
- Koumeir, C.
- Poirier, F.
- Sengar, A.
- Trichet, H.

Ernes
Coburg, Germany
- Beck, F.B.
- Franz, L.
- Neumaier, V.M.

FZJ
Jülich, Germany
- Demary, N.
- Felden, O.
- Fröhlich, N.-O.
- Gebel, R.
- Valdau, Y.

GANIL
Caen, France
- Delahaye, P.
- Dubois, M.
- Kamalou, O.
- Savalle, A.

Helmholtz-Zentrum Dresden-Rossendorf
Dresden, Germany
- Preusche, S.

HFCIM
HeFei, People's Republic of China
- Gu, K.
- Wang, Z.

HiLASE Centre, Institute of Physics ASCR, v.v.i.
Dolní Břežany, Czech Republic
- Cervenka, V.

Hitachi Ltd.
Ibaraki-ken, Japan
- Aoki, T.
- Hori, C.
- Nakashima, Y.
- Noda, F.
- Seki, T.

Hitachi Ltd., Hitachi Research Laboratory
Ibaraki-ken, Japan
- Hae, T.
- Hiramoto, H.

HS Coburg
Coburg, Germany
- Wolf, C.R.

Huazhong University of Science and Technology, State Key Laboratory of Advanced Electromagnetic Engineering and Technology,
Hubei, People's Republic of China
- Fan, K.
- Yan, Y.
- Zhang, H.J.

HUST
Wuhan, People's Republic of China
- Zhang, L.G.

HZB
Berlin, Germany
- Bundesmann, J.
- Damerow, T.
- Denker, A.
- Fanselow, T.
- Hildebrand, D.
- Hiller, U.
- Holz auf der Heide, J.
- Kailouh, I.
- Kourkafas, G.
- Ozierenski, S.
- Rethfeldt, C.
- Röhrich, J.
- Seidel, S.
- Zimmer, C.

HZDR
Dresden, Germany
- Knieß, T.
- Kreller, M.

IBA
Louvain-la-Neuve, Belgium
- Adant, B.
- Cailliau, P.
- Dabin, J.
- Ellis, K.
- Forton, E.
- Geets, J.-M.
- Kleeven, W.J.G.M.
- Mandrillon, J.
- Nuttens, V.
- Ponter, T.S.
- Smeets, J.
- van der Kraaij, E.
- Verbruggen, P.

IBS
Daejeon, Republic of Korea
- Kang, J.
- Kim, J.-W.
- Kim, J.H.
- Shin, T.S.

ICO
Saint - Herblain, France
- Chiavassa, S.
- Delpon, G.

ISBN: 978-3-95450-205-9

IMP/CAS
Lanzhou, People's Republic of China
- Mao, L.J.
- Sun, L.T.
- Wang, B.
- Wu, B.M.
- Wu, W.
- Xia, J.W.
- Yang, J.C.
- Yang, L.
- Yang, W.Q.
- Yao, Q.G.

INFN/LNL
Legnaro (PD), Italy
- Antonini, P.
- Lombardi, A.
- Maggiore, M.
- Pranovi, L.

INFN/LNS
Catania, Italy
- Allegra, L.
- Calabretta, L.
- Caruso, A.C.
- Castro, G.
- Celona, L.
- Costa, G.
- D'Agostino, G.
- Gallo, G.
- Gammino, S.
- Leonardi, O.
- Longhitano, A.
- Mascali, D.
- Mazzaglia, M.
- Messina, E.
- Musumeci, M.S.
- Naselli, E.
- Neri, L.
- Rifuggiato, D.
- Russo, A.D.
- Spartà, A.
- Torrisi, G.
- Zappalà, E.

IPHC
Strasbourg Cedex 2, France
- Adam, T.
- Osswald, F.R.
- Traykov, E.K.

IRSN
Saint-Paul-Lez-Durance, France
- Lacoste, V.

ISDE
Moscow, Russia
- Bychkov, A.S.
- Chubunov, P.A.

iThemba LABS
Somerset West, South Africa
- Abraham, J.K.
- Anderson, H.
- Anthony, L.S.
- Azaiez, F.
- Baard, S.
- Bark, R.A.
- Barnard, A.H.
- Beukes, P.
- Broodryk, J.I.
- Conradie, J.L.
- Cornelius, B.
- Cornell, J.C.
- De Villiers, J.G.
- Du Plessis, H.
- Duckitt, W.
- Fourie, D.T.
- Hogan, M.E.
- Kheswa, N.Y.
- Kohler, I.H.
- Lussi, C.
- Maleka, P.P.
- Mira, J.
- Mostert, H.W.
- Naidoo, C.
- Ndlovu, N.B.
- Nemulodi, F.
- Sakieldien, M.
- Smit, F.D.
- Spannenberg, V.F.
- Steyn, G.F.
- Stodart, N.
- Strydom, I.L.
- Thomae, R.W.
- Van Niekerk, M.J.
- van Schalkwyk, P.A.

JAEA/J-PARC
Tokai-mura, Japan
- Fuwa, Y.

JAI
Egham, Surrey, United Kingdom
- Nevay, L.J.

JCNS
Jülich, Germany
- Rimmler, M.

JINR
Dubna, Moscow Region, Russia
- Apel, P.Yu.
- Bashevoy, V.
- Bekhterev, V.
- Bogomolov, S.L.
- Bunyatov, K.
- Dmitriev, S.N.
- Efremov, A.A.
- Franko, J.

ISBN: 978-3-95450-205-9

- Gikal, B.
- Gulbekyan, G.G.
- Gurskiy, S.
- Ivanenko, I.A.
- Ivanov, G.N.
- Kalagin, I.V.
- Karamyshev, O.
- Karamysheva, G.A.
- Kazarinov, N.Yu.
- Khabarov, M.V.
- Kuzmenkov, K.I.
- Mironov, V.
- Mitrofanov, S.V.
- Oganessian, Y.T.
- Osipov, N.F.
- Pashchenko, S.V.
- Popov, D.P.
- Pugachev, D.K.
- Semin, V.A.
- Shirkov, G.
- Shirkov, S.G.
- Skuratov, V.A.
- Smirnov, V.L.
- Tikhomirov, A.
- Vorozhtsov, S.B.
- Yazvitsky, Yu.

JINR/DLNP
Dubna, Moscow region, Russia
- Karamyshev, O.
- Malinin, V.

JINR/FLNR
Moscow region, Russia
- Popeko, A.G.
- Utyonkov, V.K.
- Yeremin, A.V.

JYFL
Jyväskylä, Finland
- Heikkinen, P.M.T.
- Kalvas, T.
- Koivisto, H.A.

KEK
Ibaraki, Japan
- Adachi, T.
- Miyake, Y.

KEK, Tokai Branch
Tokai, Naka, Ibaraki, Japan
- Nagatani, Y.
- Yamazaki, T.

King Faisal Specialist Hospital and Research Centre
Riyadh 11211, Kingdom of Saudi Arabia
- Alrumayan, F.M.
- Hendy, A.M.

Korea Basic Science Institute
Busan, Republic of Korea
- Kim, S.J.
- Park, J.Y.
- Won, M.

Korea University
Seoul, Republic of Korea
- Kumwenda, M.J.
- Lugendo, I.J.

KRO
Bern, Switzerland
- Weber, D.C.

KSU
Riyadh, Kingdom of Saudi Arabia
- Kassim, H.A.

KVI-CART
Groningen, The Netherlands
- Brandenburg, S.
- Jones, B.N.
- van Goethem, M.-J.

Kyoto University, Research Reactor Institute
Osaka, Japan
- Fuwa, Y.
- Ishi, Y.
- Kuriyama, Y.
- Mori, Y.
- Okita, H.
- Suga, K.
- Uesugi, T.

LBNL
Berkeley, California, USA
- Phair, L.
- Sabbi, G.L.
- Todd, D.S.
- Xie, D.Z.

LHEP
Bern, Switzerland
- Braccini, S.

LLR
Palaiseau, France
- Geerebaert, Y.
- Magniette, F.
- Manigot, P.
- Thiebaux, C.
- Verderi, M.

ISBN: 978-3-95450-205-9

Masaryk University
Brno, Czech Republic
- Matej, Z.
- Mravec, F.

MIT
Cambridge, Massachusetts, USA
- Lanza, R.C.
- Winklehner, D.

MIT/PSFC
Cambridge, Massachusetts, USA
- Bromberg, L.
- Minervini, J.V.
- Radovinsky, A.

Naples University Federico II
Napoli, Italy
- Scampoli, P.

NPI
Řež near Prague, Czech Republic
- Běhal, R.
- Čihák, M.
- Krist, P.
- Matlocha, T.
- Poklop, D.
- Stursa, J.
- Zach, V.

NPL
Middlesex, United Kingdom
- Boso, A.

Nuclear Research Institute Řež plc
Řež, Czech Republic
- Antos, M.
- Brijar, F.
- Cuhra, M.
- Czakoj, T.
- Košťál, M.
- Losa, E.
- Rypar, V.
- Schulc, M.
- Simon, J.
- Vadjak, S.

OncoRay
Dresden, Germany
- Gantz, S.
- Hoffmann, A.
- Karsch, L.
- Lühr, A.
- Pawelke, J.
- Schellhammer, S.

PAC
Batavia, Illinois, USA
- Johnstone, C.

Private Address
Dresden, Germany
- Brutscher, J.

PSI
Villigen PSI, Switzerland
- Adelmann, A.
- Baumann, P.
- Baumgarten, C.
- Duperrex, P.-A.
- Dölling, R.
- Eichler, R.
- Fernandez Carmona, P.
- Frey, M.
- Gamma, G.G.
- Grillenberger, J.
- Grundler, P.V.
- Gsell, A.
- Hasler, R.
- Hirzel, W.
- Joray, S.
- Kiselev, D.C.
- Laube, D.
- Meer, D.
- Ovinnikov, V.
- Psoroulas, S.
- Reggiani, D.
- Rohrer, M.
- Rüttimann, P.
- Schippers, J.M.
- Schneider, M.
- Senn, R.
- Snuverink, J.
- Sobbia, R.
- Sommerhalder, A.
- Talip, Z.
- van der Meulen, N.P.
- Weber, D.C.
- Zhang, H.

Pusan National University
Pusan, Republic of Korea
- Ahn, J.-K.
- Lee, J.W.

Radan s.r.o.
Barchov, Czech Republic
- Vozáb, J.

RadiaBeam
Marina del Rey, California, USA
- Agustsson, R.B.
- Boucher, S.
- Kutsaev, S.V.
- Smirnov, A.Yu.

RCNP
Osaka, Japan
- Fukuda, M.
- Hara, S.
- Hara, T.
- Hatanaka, K.
- Kamakura, K.
- Kanda, H.
- Koay, H.W.
- Morinobu, S.
- Morita, Y.
- Nagayama, K.

ISBN: 978-3-95450-205-9

- Nakao, M.
- Omoto, K.
- Saito, T.
- Takeda, K.
- Tamura, H.
- Tomono, D.
- Yasuda, Y.
- Yorita, T.

RIKEN
Saitama, Japan
- Miyake, Y.M.

RIKEN Nishina Center
Wako, Japan
- Dantsuka, T.
- Fujimaki, M.
- Fukunishi, N.
- Goto, A.
- Hasebe, H.
- Higurashi, Y.
- Ikezawa, E.
- Imao, H.
- Kamigaito, O.
- Kidera, M.
- Komiyama, M.
- Kumagai, K.
- Maie, T.
- Nagatomo, T.
- Nakagawa, T.
- Nakamura, M.
- Nishi, T.
- Ohnishi, J.
- Okuno, H.
- Ozeki, K.
- Sakamoto, N.
- Suda, K.
- Uchiyama, A.
- Watanabe, T.
- Watanabe, Y.
- Yamada, K.

Royal Holloway, University of London
Surrey, United Kingdom
- Nevay, L.J.

SHI
Kanagawa, Japan
- Arakawa, Y.
- Ebara, Y.
- Hashimoto, A.
- Hirabayashi, M.
- Hirayama, T.
- Kamiguchi, N.
- Kanakura, J.
- Kumata, Y.
- Kusuoka, S.
- Mikami, Y.
- Mitsubori, H.
- Miyashita, T.
- Morie, T.
- Murata, H.
- Oda, H.
- Onda, T.
- Ookubo, H.
- Sakemi, T.
- Sano, M.
- Tachikawa, T.
- Takahashi, T.
- Taki, K.
- Tsurudome, T.
- Tsutsui, H.
- Watanabe, T.
- Yoshida, J.Y.

SIGMAPHI S.A.
Vannes, France
- Antoine, S.
- Beeckman, W.
- Forest, F.
- Jehanno, P.J.
- Jivkov, P.
- Leray, M.J.
- Milpied, X.
- Nignol, C.
- Tasset-Maye, O.

SKKU
Suwon, Republic of Korea
- Chai, J.-S.
- Gad, Kh.M.
- Ghergherehchi, M.
- Ha, D.H.
- Kim, H.S.
- Lee, J.C.
- Namgoong, H.

STFC/RAL/ISIS
Chilton, Didcot, Oxon, United Kingdom
- Kelliher, D.J.
- Lagrange, J.-B.
- Machida, S.
- Prior, C.R.
- Rogers, C.T.

SUBATECH
Nantes, France
- Blain, G.
- Fattahi, M.
- Haddad, F.
- Michel, N.
- Servagent, N.
- Sounalet, T.
- Vandenborre, J.

Texas A&M University Cyclotron Institute
College Station, Texas, USA
- Ärje, J.E.
- Abegglen, F.P.
- Clark, H.L.
- Kim, G.J.
- May, D.P.
- Roeder, B.T.
- Saastamoinen, A.
- Tabacaru, G.

ISBN: 978-3-95450-205-9

TRIUMF
Vancouver, Canada
- Baartman, R.A.
- Bylinskii, Y.
- Planche, T.
- Rao, Y.-N.
- Zhang, L.G.

UCT Physics
Cape Town, South Africa
- Buffler, A.
- Geduld, D.
- Hutton, T.
- Leadbeater, T.

UI PET
Skopje, Republic of North Macedonia
- Filipovski, Z.

United Rocket and Space Corporation, Institute of Space Device Engineering
Moscow, Russia
- Anashin, V.S.
- Koziukov, A.E.

Univ. degli Studi di Padova
Padova, Italy
- Buriola, L.

University of Defence
Brno, Czech Republic
- Cvachovec, F.

University of Zurich, University Hospital
Zurich, Switzerland
- Weber, D.C.

USTC
Hefei, Anhui, People's Republic of China
- Xu, S.W.

VMS-PT
Troisdorf, Germany
- Akcöltekin, E.M.
- Boldt, O.
- Eichel, M.
- Klarner, F.
- Lucht, S.
- Netterdon, L.
- Roth, A.
- Röcken, H.
- Seher, M.
- Stephani, T.
- Wiesner, M.
- Wittschen, J.C.